The *Telstar* Experiment

By A. C. DICKIESON

(Manuscript received February 6, 1963)

The papers that follow describe in depth the satellite and ground systems designed for the Telstar experiment and give the results to date. The purpose of this introduction is to set the scene in which the project was undertaken and to state some general conclusions.

Bell System interest in satellite communication had been aroused when in 1955, Dr. John R. Pierce published calculations showing the possible usefulness of satellites to communication. Dr. Pierce discussed the relations among power, bandwidth, antenna gain, and orbit parameters. Sputnik in 1957 started the procession of man-made satellites.

In 1960, with the launching of a large aluminum-coated balloon by the National Aeronautics and Space Administration, the famous Echo experiments[1] were conducted between a transmitting and receiving station set up by Bell Telephone Laboratories at Holmdel, New Jersey, and a companion station at Goldstone, California, designed and operated by Jet Propulsion Laboratory.

The Echo experiments produced the first two-way telephone conversations via satellite. They also confirmed predictions of the radio path loss to be encountered, the stability of the radio medium, and the low noise picked up by a well designed antenna pointing at the sky.

These results were studied at Bell Laboratories in the context of the Bell System's long-term interest in overseas communication. The first New York-London commercial voice circuit was established by long-wave radio in 1927 and was followed by short-wave (HF) circuits in 1929. Over the years, a network of some 240 radio circuits has been constructed, connecting the United States to 140 countries.

By the end of the late 1940's it had become evident that the frequency space available in the HF range was not sufficient to support the volume

of worldwide communication that was developing. It was clear also that because of physical limitations inherent in the very nature of the radio transmission medium, the reliability and quality of the resultant telephone circuits would leave something to be desired.

At this time the development of repeatered, multi-channel submarine cable was pressed forward. The first transatlantic cable of this type was placed in service in 1956,[2] followed in rapid succession by many others. The submarine cable network is expanding rapidly, providing high quality and reliable communication service.

The Echo experiments opened the possibility of applying microwave radio relay technology to transoceanic links. The line-of-sight transmission characteristic of microwaves had prevented their use over the oceans until the possibility of a "microwave repeater in the sky" appeared.

As we studied the problem of satellite communication, it became apparent that we had most of the tools to do the job in the fruits of previous research and development in widely scattered fields. Transistors and diodes, solar cells, low-noise maser amplifiers, long-lived traveling-wave tubes, horn-reflector antennas, FM-feedback receivers — these and other essential tools were available.

It was recognized that there was a long step in development needed to fit these essential but separate elements into a coordinated working system. Also, numerical knowledge of the characteristics and magnitude of radiation in the Van Allen belt was not adequate as a basis for design of a long-lived satellite.

It was decided, therefore, to design and build an experimental satellite communication system. To this end, the A.T.&T. Co. entered into a cooperative agreement with NASA; A.T.&T. to design and construct a satellite and NASA to launch it into space, with A.T.&T. paying its own costs plus reimbursing NASA for the cost of launching and for certain tracking and telemetry services.

In setting the objectives for the experiment, the desideratum was the simplest experiment that would answer the really critical questions, leaving until a later round of design the optimization of trade-offs and the development and construction of a commercial operating system. Thus, the objectives were:

1. To look for the unexpected.
2. To demonstrate the transmission of multichannel two-way telephony, television, data and facsimile via satellite.
3. To build a very large ground station antenna and find out how to point its extremely sharp beam very accurately at the satellite.

4. To gain a firm understanding of the problems of measuring orbital parameters and predicting satellite positions.

5. To gain a better numerical knowledge of the character and intensity of radiation in the Van Allen belt.

6. To face the problems of designing for long life and reliability of electronic equipment for operation in the space environment.

It was decided to install a microwave repeater in the satellite. While the passive reflector of the Echo type has advantages, calculations indicated that the transmitter power required for television bandwidths would be excessive unless balloons of a size well beyond the present state of the art were used.

Study of available boosters led to the Delta configuration of the Thor as the simplest and most reliable rocket for these purposes. Its relatively limited lifting capacity set a bound of about 180 pounds for a useful orbit. This was established as: apogee 3450 miles, perigee 575 miles, inclination to equator 45°. The apogee is high enough to give good mutual visibility between northeastern United States and western Europe. Calculations for a working worldwide system indicate the desirability of circular orbits at 6000–8000 mile elevations; however, these were not achievable with the Delta vehicle.

The weight restriction now forced the decision to install only a single, one-way amplifier in the satellite, rather than two. This permits one full-band signal to be sent one way, or two (or more) narrow-band signals to be sent two ways. Also, the solar cell power supply capacity was limited to less than that required to operate all of the electronic circuits continuously. It was necessary, therefore, to use a nickel-cadmium storage battery to handle the peak loads, with means to turn the amplifier on and off by command from the ground.

If the satellite presented one face to the earth at all times, it would be possible to use directional antennas, with consequent gain in signal strength. While such arrangements exist as concepts, it was not practicable to apply them in this experiment. It was decided to stabilize the position of the satellite by spinning it around one axis, like a child's top. This fitted well into the Delta vehicle; the third stage of the Delta is a solid-fuel rocket which is spun during firing for reasons of stability and equalization of thrust. The payload is thus spinning at the time of ejection.

It was decided that the satellite antennas should receive and transmit circularly polarized waves, so as not to require polarization tracking by the ground system. Consideration of the geometrical relations between the earth and the spinning satellite in an inclined, elliptical orbit indi-

cated the desirability of omnidirectional antennas if communication is to be maintained unhampered at all times and places. Such a design is not possible; thus the design objective was to achieve the broadest coverage obtainable. Calculations indicated that with the antenna pattern attainable and with the satellite launched with its spin axis perpendicular to the sun line, its aspect with respect to locations in the northern hemisphere would be satisfactory for long periods.

To gain more numerical understanding of the distribution of radiation in the Van Allen belt, it was decided to include a rather complicated array of sensors and measuring devices in the satellite. Clearly, to return this information to earth required radio telemetry. Parts of some and all of other orbits are not visible from the BTL stations. Thus it was made part of the cooperative agreement with the National Aeronautics and Space Administration that their Minitrack stations around the world would collect telemetry from the satellite. For this reason, the telemetry frequency was chosen in the band around 136 mc for which the Minitrack stations were already equipped.

The necessity to turn the communication repeater on and off (because of power capacity limitations) established a need for a radio command channel. Further consideration of the over-all problem indicated the desirability of additional command capability. Since it seemed likely that it might be desirable for some Minitrack stations to issue commands, it was decided to use a frequency near 120 mc for this purpose, and to use a command format for which the Minitrack stations were equipped.

The choice of frequencies for the communications repeater was more complicated. Previous research had indicated that the preferred frequencies lie between 1000 and 10,000 mc. In the United States, and generally in the rest of the world, these frequencies have all been allocated for various terrestrial uses. The newcomer, satellite communication, has to work its way into this established pattern. This presents a complex international question which is not yet resolved.

In the meanwhile, though, it seemed most practical to assume that at least initially satellite communication of the Telstar type would have to share frequencies with terrestrial systems; hence it became important to examine the conditions of compatibility. After considerable study,[3] and consultation with various foreign communication agencies, it was concluded that for a start it was most practical to share frequencies with the point-to-point, common carrier microwave relay systems. These are the frequency bands 3700–4200 mc and 5925–6425 mc.

It was decided to use the 4000-mc band for the down direction, from satellite to ground, so as to minimize the deleterious effects of rain on the

received signal and noise. The 6000-mc band is used for the up direction. The wide frequency separation between the two directions simplifies sharing of the ground antenna and minimizes interference effects in the satellite. The A.T.&T.Co. applied for and received from the Federal Communications Commission research-experimental licenses for satellite and ground stations.

Sharing of frequencies with terrestrial systems had an effect on the choice of the site for the ground station. A location in the northeast part of the United States was wanted, so as to minimize the great circle distance to western Europe. Separation from large cities and from existing or probable microwave radio relay stations operating in the 4000- or 6000-mc bands was desirable.

Fairly flat ground was desired for the installation of initially one, and later several, large antennas. For best protection against interference, the site should be ringed by hills. Finally, the site should have road access, power, water, and living facilities nearby. All of these were found at a location near Andover, Maine.

Study of the over-all system parameters lead to the conclusion that a large ground antenna with minimum power in the satellite was the economical choice. Research work at the Bell Laboratories Holmdel Radio Research Laboratory had culminated in the construction of a horn-reflector antenna with 400 square feet of aperture. This was used very successfully in the Echo experiments. The particular virtue of the horn-reflector type is that it has very low side lobes; hence it does not pick up extraneous noise from the ground when it is pointed even a few degrees above the horizon. Besides being very broad-band, it can be designed so that the receiving equipment does not move with elevation motions of the horn.

It was decided to design and build a horn-reflector antenna with 3600 square feet of aperture. The very sharp beam of such an antenna would stretch our ability to point it accurately at the satellite. To preserve the accuracy of the antenna, and to permit it to operate in all kinds of weather (including the 90 inches of snow to be expected in Maine), an air-inflated covering or radome was added.

Study of the antenna-pointing problem led to the conclusion that the satellite should radiate a low-level microwave signal whenever the communications transmitter is turned on. This has two uses. It permits very precise tracking of the satellite, and hence accurate determination of its orbit. Also, it facilitates the design of an autotrack system that automatically optimizes the pointing of the ground antenna once its beam is placed on the satellite.

It was decided to design for tape-controlled pointing of the antenna, as well as for slaving to a small, precise autotracking dish. The objective was to acquire knowledge of the advantages and limitations of several methods of antenna pointing.

To receive telemetry at 136 mc, and to transmit commands at 120 mc, it was decided to construct a directional antenna with autotrack capability. This would lock on to the 136-mc telemetry carrier normally radiated from the satellite. The relatively broad beam (about 20°) of this antenna facilitates finding the satellite in space, even with quite crude orbit prediction. It was decided to arrange for slaving of the precision tracker to the command antenna, so that we could go through the sequence of acquiring the satellite with the 20° command antenna, having it direct the 2° beam of the precision tracker to the right position, and then have the precision tracker give instructions to the horn-reflector antenna.

To make the most of the very good noise performance of the horn-reflector antenna, the communications receiver was designed to use a traveling-wave maser operating in liquid helium. Also, to improve the breaking point of the receiver, (i.e., to permit the receiver to reach deeper into noise for very weak signals) the technique of FM-feedback is used. This method was invented at Bell Telephone Laboratories some years ago, and was applied very successfully in the Echo experiment.

Thus the main outlines of the Telstar experiment were established. The plans were discussed in considerable detail with the communication agencies in England, France and Germany. All three decided to build ground stations to work with Telstar; the German station was planned for operation in 1963 or 1964, while the British and French set it as an objective to be ready on or near the time of the first Telstar satellite launching. In the meanwhile, NASA discussions led to the agreement that the Bell System, British and French stations would be equipped to operate with Project Relay, along with other stations such as those planned in Italy, Brazil, and elsewhere. To simplify the hardware situation at the ground stations, it was agreed to have Project Relay use the same frequency plan as Telstar for the downward direction.

GENERAL CONCLUSIONS

The Telstar satellite was launched in the early morning of July 10, 1962. On the first pass usable from Andover, demonstrations were made of speech and television transmission. These transmissions were carried on between distinguished audiences in Washington, D.C., and

Andover, Maine. Also the first transmission of a telephoto picture was achieved. The procedure was also televised for the national networks. In the midst of this program, word was received that the French station at Pleumeur-Bodou was receiving picture and sound perfectly. The British station at Goonhilly was receiving the signal, but was not able to utilize it because of a turnover in polarization at the antenna.

On the next pass, six two-way telephone circuits were set up through the Telstar system, and various people in Washington and Andover talked to people around the United States. Also, high-speed data messages were sent successfully. On the next day, television signals were received from Pleumeur-Bodou and Goonhilly.

In the next several months, in addition to more than 250 technical tests covering every aspect of transmission, there were some 400 demonstrations. These included multi-channel telephony, telegraphy, data, telephoto and other facsimile transmissions. Transatlantic television was demonstrated 47 times, and on 5 of these occasions the transmission was in color. At the same time, a great deal of telemetry data were received, covering conditions in the Van Allen belt, temperatures, degradation of the solar cell plant, spin rate, voltages, etc.

During the fourth week of November, 1962, the command channel began to act erratically. Increasing difficulty was encountered in having it accept commands. Since it seemed possible that control might be lost, arrangements were made to leave the telemetry on continuously rather than switching it on and off. Also, the traveling-wave tube was not energized at all, lest loss of control should leave this heavy drain on continuously and thereby ruin the batteries. After the 1242nd orbit on November 23, 1962, the command channel ceased responding.

It was known from previous studies[4] that radiation may produce important effects on transistors. Telstar telemetry data indicated that the density of electrons of high energy was much higher than had been anticipated. The working hypothesis was formed that the command circuit failure was caused by radiation damage to certain of the transistors in the command decoder. Careful study of previous data indicated that one of the two command decoders had failed in August of 1962.

During November, our command stations in the northern hemisphere were addressing the Telstar satellite near the perigee of its orbit, while it was traversing the worst part of the Van Allen belt. The possibility existed that the radiation damage effects would be less serious while the satellite was nearer apogee. Thus attempts were made to command the satellite from the Minitrack station at Johannesburg, South Africa, but without success.

In the meanwhile, laboratory tests had pointed to certain transistors as being the most likely sources of trouble. Special codes were devised to take advantage of certain circuit features that would permit by-passing these particular transistors. On December 20, 1962, one of these modified codes was successfully transmitted to the satellite. In subsequent operations, all voltages were removed from the command decoders. As had been predicted, this action allowed recovery of the transistors. On January 4, 1963, during orbit 1628, public demonstrations of live television to and from Europe were concluded. Telstar by then was responding properly to all normal commands.

On February 14, 1963, there began to be indications that the operation of the command system was beginning to degrade again. The satellite began to take longer and longer to respond to the normal command codes. By February 20, it did not respond to the normal codes. During this period, the response to the modified codes was solid.

On February 21, the satellite misinterpreted a command and operated the relay that disconnects most of the electronic system from the power plant. Since then to the present writing (March 18), the Telstar satellite has not responded to even the modified commands.

The results of the Telstar experiments are given in detail in the following papers. Two general conclusions can be drawn:

1. Design of a second-generation Telstar satellite could be approached by Bell Telephone Laboratories with confidence as an engineering project. Where uncertainties exist, they have to do with the conditions existing in space.

2. Problems of the ground station are clearly understood. The usual design trade-offs and optimizations can be made with real understanding. The second-generation ground station will be considerably simpler than the first experimental station at Andover.

REFERENCES

1. B.S.T.J., Project Echo issue, **40**, July, 1961.
2. B.S.T.J., Transatlantic Cable issue, **36**, January, 1957.
3. Curtis, H. E., Interference between Satellite Communication Systems and Common Carrier Surface Systems, B.S.T.J., **41**, May, 1962, p. 921.
4. Peck, D. S., Blair, R. R., Brown, W. L., and Smits, F. M., Surface Effects of Radiation on Transistors, B.S.T.J., **42**, January, 1963, p. 95.

The Research Background of the *Telstar* Experiment

By A. B. CRAWFORD, C. C. CUTLER, R. KOMPFNER and L. C. TILLOTSON

(Manuscript received March 5, 1963)

For several years before the launch of the Telstar satellite, research effort was directed toward an experiment with an active satellite capable of relaying a broadband communication channel. The intention was to utilize and test a number of novel techniques which had become available, to explore those areas in which the current technology was lacking, and to demonstrate the feasibility of this means of communication. This paper describes some of this work, the background of facts and beliefs on the basis of which a number of important choices were made, and the general state of the radio art upon which the Telstar program was built.

I. INTRODUCTION

The Telstar satellite communications experiment, like all achievements in technology and engineering, has many roots. Some of these roots are as broad and old as science itself; others are rather recent and include modern rockets, missile guidance, and general space technology. Other more modest but essential roots grew from an early appreciation of the potential of satellite communication and the steps taken in the area of communication technology to foster its growth.

Bell Telephone Laboratories interest in the possibility of using artificial earth satellites for communication purposes began in 1955 with the publishing of the article on "Orbital Radio Relays"[1] by J. R. Pierce. It is significant, however, that some of the research which was relevant to the success of the satellite predated this publication by a decade or more.

The material presented here consists of a summary of scientific and technological knowledge and advances which were important to the satellite program. It also contains the pertinent parts of a memorandum dated August 24, 1959, which summarizes the background and views

that led to work toward a particular sort of experimental communication satellite. This memorandum expresses better than could be done retrospectively the thinking that led to the course of research activity which followed.

Bell Laboratories activities which followed the publication of Pierce's article and which culminated in the Telstar satellite experiment can be divided into five rather distinct periods of approximately one year each:

(*i*) 1958 Preliminary studies
(*ii*) 1959 Initiation of research and development programs
(*iii*) 1960 Experimentation and verification
(*iv*) 1961 Intensive development
(*v*) 1962 System construction and test.

The year 1958 was one for imagination and invention. The activities consisted principally of paper studies of the many system possibilities which were made possible by satellites, and resulted in a number of memoranda and published papers[2,3,4,5] which provided guide-lines for subsequent activities. Systems proposed in Bell Telephone Laboratories were conservative by many standards but relatively realistic if we judge by the fact that most of the factors which have so far proven to be important to the problem were well evaluated at that time. The most notable exceptions have been the unforeseen radiation hazard and the degradation of two-wire circuits with echo suppression by delay, which has dampened an early enthusiasm for 24-hour "stationary" satellites.

During 1959 several research and development programs were initiated which led directly to the Telstar experiment. An ad-hoc group containing people from many disciplines throughout the organization was formed to initiate activities in the areas which needed attention. It is principally the early work of this group which is described in this paper.

By 1960 laboratory work was well under way on several of the problems. During the year, the Project Echo experiment[6] was carried out and provided valuable experience with many of the elements inherent in a satellite communication system. Prototype models of the traveling-wave tube used in the Telstar satellite were built and put on life test, and life tests on batteries and other components were also started. Discussions with others working in the field led to an appreciation of the environmental problems and the necessity of radiation shielding. During this time, studies of radiation damage to solid-state devices were undertaken in cooperation with Brookhaven Atomic Energy Laboratories, which led to the design of the radiation-sensing package

and the radiation protection used on the satellite. A general electrical-mechanical configuration of the satellite was also proposed, although many important problems remained to be worked out.

Early in 1961 intensive development of the satellite began and is described elsewhere in this issue. The present paper discusses the more important parts of the research program which preceded the development project.

II. RESEARCH LEADING TO THE STATE-OF-THE-ART

If the Telstar satellite had been built using the state-of-the-art of a decade ago, it would have been a very different satellite. The evaluation of the sky noise temperature, the development of the low-noise maser amplifier, the appreciation of the low-noise properties of the horn-reflector antenna, and the solving of the problem of demodulation of large-index frequency modulation using feedback combined to reduce the power requirement on the satellite by two or three orders of magnitude (about 20 db in effective noise temperature and 5 db in FM threshold improvement). Similarly, advances in solid-state electronics reduced power requirements, size and weight enormously. In the following pages, we will outline some of the more significant parts of the general research activities which produced the state-of-the-art upon which the Telstar satellite was built, and we then will describe work done more recently, specifically to implement satellite communication. Less attention will be given to a number of areas which were of vital importance to the success of the experiment, such as the development of solid-state electronics, microwave electronics and large computers, since these are covered in other papers.

2.1 *Low-Noise Receivers*

Research leading to the understanding of the effective temperature of the sky has gone on intermittently for several decades and has yielded important results, culminating in the determination of the now well known relationships[7] of sky noise temperature vs frequency and elevation angle. These relationships were vital to the choice of frequencies for space communication, and the realization that these very low effective sky noise temperatures existed revealed the possibility of utilizing the properties of masers and low-noise antennas.

Most work on antennas in the past has been directed toward producing high area efficiency in terms of the gain or directivity of the antenna, properties which are not uniquely related to the noise properties. How-

ever, the horn-reflector antenna,[8,9] developed for terrestrial microwave relay systems, was found to have an effective noise temperature of only one to two degrees Kelvin.[10]

The low-noise character of sky-directed antennas would be of little use were it not for the extremely low-noise microwave amplifiers which came into being just as satellite communications became a possibility. The microwave maser amplifier,[11] having a noise temperature of two or three orders of magnitude lower than the best previously existing amplifiers, grew out of a decade or more of physical research in microwave molecular spectroscopy and paramagnetic resonance in solids. The parametric amplifier, similarly, was the product of years of work in solid-state physics and nonlinear circuit theory.[12,13]

Research and development in these three low-noise areas were greatly stimulated by the prospect of satellite relays. Research on atmospheric absorption and radiation, particularly in the presence of high humidity and rainfall, was intensified because of this prospect.[14] Traveling-wave masers played key roles in both the Echo[15] and Telstar experiments; those used in the Telstar Project were among the first masers with truly broadband capability. Antenna development (larger horns and Cassegrainian antennas) was likewise spurred by the fact that new low-noise and large-size requirements had to be met.

2.2 *Electron Devices*

Perhaps the most remarkable contribution to the state-of-the-art came from solid-state physics. Few components used in the satellite or on the ground are not at least in part the product of research in this area of physics. The maser and parametric amplifier have already been mentioned. All of the active elements in the satellite, except the traveling-wave tube, are solid-state devices, none of which was beyond an early state of development a decade ago. The availability of the reactance diode used in the frequency multipliers and the high-frequency transistor could scarcely have been more timely.[13]

Microwave tube development was likewise timely. Five years before the Telstar experiment there were no CW microwave tubes of adequate power for ground station operation, and the long life and reliability required in space were just beginning to be obtained. These efforts, directed toward more conventional applications, were almost directly applicable to the space problem.

Development in other areas, such as missile tracking and computers, as well as the chemistry of plastics and adhesives, also helped to provide

a state-of-the-art conducive to the development of satellite communications; but it is perhaps more appropriate to consider those problems which were newly posed by the new prospect. These problems ranged from satellite components and construction to considerations of celestial mechanics and geography necessary to establish probability statistics of mutual visibility between stations.

III. THE SATELLITE RESEARCH PROGRAM

In the face of a bewildering variety of options, it was necessary in 1959 to settle on a particular plan of action which would define the next nearest goal and the steps needed to attain it. This plan had to be sufficiently concrete to make it possible to identify the various problems and to help in getting people interested in solving them; at the same time it had to be flexible to allow for unexpected discoveries and developments.

Such a plan, embodying much of the thinking of Bell Laboratories at that time, was presented in an unpublished company memorandum dated August 24, 1959. In view of the influence of this memorandum on the subsequent course of events, we feel that the readers' interests are best served by reproducing below the relevant parts of this memorandum,* including even those parts about which we might feel differently now. It will be seen that while a number of important choices and decisions were made at a relatively early date and were adhered to subsequently, there were other choices, such as the traveling-wave tube power level, the modulation bandwidth and the choice of frequencies, which had to be changed to meet new requirements.

An important change in outlook has resulted from tests of the effect of long delays and echo suppressors on telephone users. The degradation due to delay has not been precisely defined over the total range of interest in satellite communications, but present evidence strongly favors an approach which minimizes the delay. Thus our initial enthusiasm for a 24-hour system as an ultimate goal has been considerably dampened, and the low-altitude system, proposed in the memorandum as the first experiment, has become more attractive.

The fact that the document reproduced here was a plan, a program of action only and conditioned by the time it was written, should be kept clearly in mind by the reader.

---

* Only sections which are pertinent to the subsequent activities and which led to the Telstar experiment are included here.

Active Satellite Repeaters: Interim Report I

By L. C. TILLOTSON

ABSTRACT

An experiment employing an active repeater in orbit at an altitude of about 2500 miles is discussed. The system would provide an experimental circuit having a bandwidth of 5 mc and suitable for TV or multiplex telephony between the U.S.A. and Europe for periods of up to 30 minutes. Broadband frequency modulation would be used to ease power requirements on board the satellite. Possible interference between the space system and existing services is discussed briefly. Some of the problems which must be solved before such a system can be considered feasible are outlined.

Active versus Passive Repeaters

As the title indicates, we are here concerned primarily with active repeaters. This comes about in part because passive repeaters are already receiving considerable attention at Bell Telephone Laboratories* and in part by the writer's conviction that passive satellites are best for military systems, particularly if the orbiting body is chosen for its immunity to enemy action, and that active satellite repeaters will be more useful in civilian activities.

For long-haul point-to-point service, a repeater in a synchronous (24-hour) equatorial orbit is very attractive. The main disadvantages, in addition to the large distances involved, are the $\frac{1}{4}$-second round trip delay and the fact that the satellite is not visible near the north and south poles. The latter is more important to military than to civilian communications. An unoriented passive reflector at this altitude is prohibitively large. On the other hand, if it is to be successful, an active repeater must be built from *reliable* components. Herein lies the challenge....

Frequency Allocations

Space-borne repeaters will obviously have to compete with other types for frequency allocations. This problem could be considerably reduced if bands presently assigned to the common carriers are also used for common carrier activities in space, the only real difference being that the satellite radio repeaters would be located on very high altitude platforms. If a given frequency band is to be used for space and earth-based repeaters simultaneously, several possible interference paths must be studied and controlled.† These are:

* Both passive and active satellite repeaters are considered at some length a memorandum by C. C. Cutler dated 1/12/59. Many of the proposals in this memorandum are based in part on this work. [Later published, Ref. 5.]

† Since we also propose to use the same frequency for several satellite repeaters, relying upon spatial separation and antenna discrimination for protection, this subject must also be investigated but it is not part of the present consideration.

1. Interference to earth-based receivers caused by satellite-borne transmitters.
2. Interference to earth-based receivers caused by space system ground-terminal transmitters.
3. Interference to space system ground-terminal receivers by earth-based transmitters....

Proposed Experiment

A system with a 5-mc baseband and a snr of 40 db which uses a repeater circulating in a 2500-mile polar orbit could provide a TV circuit to Europe with a common visibility time from Holmdel and Paris of up to 30 minutes. The communication system parameters are listed in Fig. 2 [Table I in this

TABLE I—ACTIVE SATELLITE REPEATER SYSTEM PARAMETERS
(Fig. 2 of 8/24/59 memorandum)

Experimental path	USA (Holmdel)—Europe (Paris)
Satellite, altitude	2500 miles
orbit	circular polar
period	2 hours 55 minutes
velocity	14,450 mph (4 mps)
Mutual visibility time, best pass	approx. 30 minutes $7\frac{1}{2}°$ above horizon
Maximum range to satellite	4600 miles
Maximum path loss	130 db
Minimum range to satellite	2500 miles
Minimum path loss (reference value)	125 db
Ground antenna effective area	1700 ft² (60-foot dish)
Temperature of ground receiver	30° Kelvin
Noise in 10-mc band	−144 dbw
Power of ground transmitter	1 kw
Satellite antenna	isotropic −3 db
Temperature of satellite receiver	3000° Kelvin
Noise in 100-mc band	−114 dbw
Power of satellite transmitter	1 watt
With satellite at *maximum* range:	
Margin relative to system objective	−1 db
Margin about FMFB threshold (C/N = 12 db)	2 db
Modulation	Large-index FM
Improvement factor	21 db
Baseband	5 mc
RF band (30 db down)	104 mc
Radio frequency	6 kmc
S/N for TV, p.t.p. signal to rms noise	48 db
Noise in message channel	38 dba at zero level
Number of message channels	500 to 1000

paper]; possible repeater arrangements are described in a later section entitled "Satellite Microwave Repeaters".

The philosophy used in the design of the experiment is as follows:

(*i*) *Minimum requirements on the propulsion and guidance equipment used to inject the payload into orbit.* Thus the satellite is assumed to be either completely unoriented and hence tumbling through space or, at most, spin-stabilized, and hence precessing only very slowly. This choice must be determined by further study of the satellite antenna and orbit injection problems.

(*ii*) *Minimum possible payload size and weight.* This is achieved mostly by limiting the experiment to a single one- or two-way channel and by using a receiver which trades bandwidth for snr in an advantageous manner. This makes it possible to keep the satellite transmitter power down to one watt. Special care will also need to be taken in the design of the microwave tube to achieve maximum efficiency. Since one of the larger components of the payload weight will be solar cells and storage batteries, this will be reflected directly in the total weight of the package.

(*iii*) *The space-borne apparatus must be compatible with our long-range objectives.** Since the path loss to an unoriented satellite at 2500 miles altitude is nearly equal to that for a 22,300-mile attitude-stabilized repeater with a 19-db antenna, the satellite electronics can be essentially the same at both altitudes. This is very desirable since even a "minor" change in the design of long-life apparatus may mean starting over.

(*iv*) *The space-borne apparatus must have maximum possible life.* Almost every design parameter must be considered here. Some of the most important are:

(a) *Low transmitter power.* Tubes in the one- to ten-watt power range have a longer operational life than those in the 100- to 1,000-watt range. As shown in a memorandum† by D. A. Chisholm et al, tube life decreases rapidly as cathode current density is raised. High-power tubes call for high cathode current densities. It is expected that a one-watt TWT can be built with a cathode current density not to exceed 50 ma/cm^2. Such a tube would have an "expected" life of 10 to 20 years. Low power is also important in the satellite because waste heat dissipation is a problem at best.

(b) *Only one microwave tube per repeater channel and maximum use of solid-state devices operated in a conservative manner.*

(c) *Simplest possible repeater circuit arrangements consistent with a useful communication capability.* It seems clear that components left out will never cause trouble. However, this must be achieved by straightforward design rather than by resorting to "trick" circuits which make repeater performance unduly sensitive to component characteristics.

(d) *The space electronics must not quickly become obsolete because of advances in the art.* We propose a "straight-through" repeater having a

* Soon after this memorandum was issued, experiments with delay on a two-wire telephone circuit indicated that there is a very serious problem in the use of a synchronous satellite in two-way telephony.

† Contents of this memorandum are presented in Ref. 16.

bandwidth of 100 mc and providing a minimum cnr of 15 db at the earth-based receiver....

Satellite Microwave Repeaters

Although there are many possible apparatus arrangements which could be used for satellite repeaters, there are only two broad categories. The first type puts out what it receives, but at higher level and perhaps shifted in frequency. This is essentially a broadband straight-through amplifier which will handle any signal within the range of its performance characteristics. Such an arrangement has two outstanding advantages.

(*i*) Great changes in ground-based apparatus, modulation techniques, etc., can be made with no reaction on the satellite repeater. This will help to avoid obsolescence caused by advances in the state of the art, which is an important consideration when development of very reliable apparatus which takes years to complete is being started.

(*ii*) Since the signal handling at the satellite is simple, i.e., just amplification, simple circuit arrangements and relatively few components can be used. In spaceborne apparatus this is a vital consideration, at least for the present.

The second type processes the signal during its passage through the repeater. Examples are: demodulating-remodulating repeaters, or receivers and transmitters connected back to back; pulse-regenerating repeaters, receivers which employ a correlation detector feeding a local transmitter; and very advanced types which include on-board computers for error correction, key stream generation, path selection (antenna pointing), orbit parameter control, etc. The disadvantages of this type are rather obvious:

(*i*) We must decide the system mode of operation in considerable detail before launching. Any important change will require a new satellite.

(*ii*) Most of these schemes require an untenable amount of complication in on-board apparatus.

Since even the simplest schemes will require a major effort to achieve adequate reliability in the space environment, we shall consider only the simplest possible versions of each of the two basic repeater types.

Straight-Through IF Repeater

Two variations of a possible IF type repeater are shown in Figs. 8 and 9 [Figs. 1 and 2 in this paper]. In type I the IF amplifier, up and down converter, frequency shift oscillator and local (microwave) oscillator, would all be realized by using solid-state devices. Since a real microwave transistor is doubtful, especially on the required time scale, local oscillator power would need to be obtained by harmonic generation from a transistor oscillator operating at several hundred megacycles. Of course, if all this can be achieved, the repeater will require only one microwave tube. If not, then repeater type II, shown on Fig. 9 [Fig. 2], is a possibility. This arrangement exploits the bandwidth of the TWT to provide a microwave oscillator at a different frequency, but at the same time it is being used as a

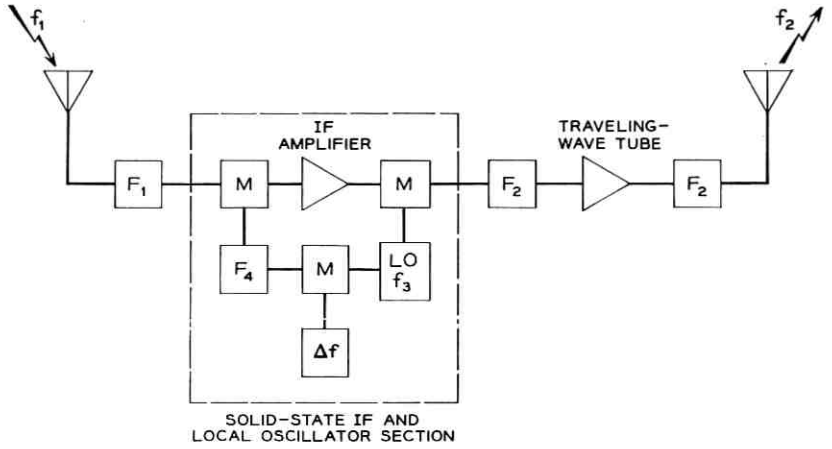

Fig. 1 — IF repeater type I (Fig. 8 of 8/24/59 memorandum).

signal amplifier. There are intermodulation troubles here, too, but the local oscillator power can be kept 20 db or more below the signal power, which should be very helpful in solving this problem.

At present, the most likely choice appears to be an IF repeater of type I or II, as shown in Figs. 8 and 9 [Figs. 1 and 2]....

Satellite Repeater Design

(*i*) *Life.* While launching costs are expected to decrease markedly as the operation moves from R and D into an operational phase and as more effi-

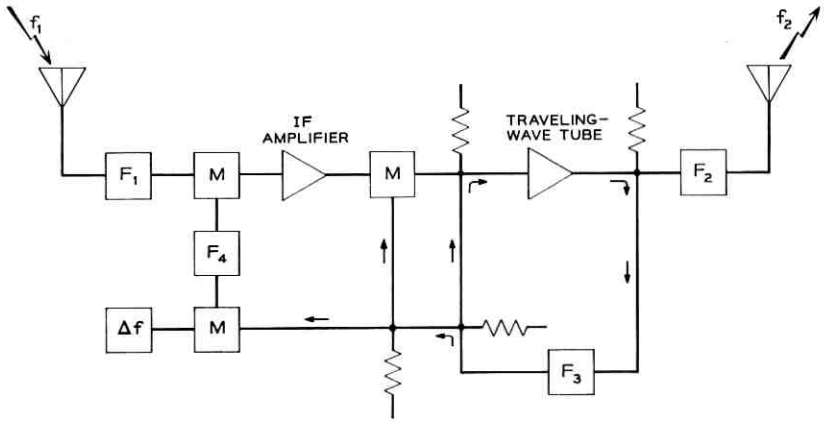

Fig. 2 — IF repeater type II (Fig. 9 of 8/24/59 memorandum).

cient propulsion systems become available, the cost of placing a repeater in orbit seems likely to remain as a major item of expense. Even if this were not so, it would still be important that the repeater last as long as possible in order to avoid cluttering up space with unusable derelicts. Hence, both for economic and political reasons, a long-life repeater appears essential. It is suggested that our goal be the same as for undersea cables — 20 years. More knowledge of the space environment than we now possess is likely to be required before such an ambitious goal can be achieved, but it is not too early to define our objective. Also, in order to make the first experiment appear successful, from both economic and psychological points of view, the first satellite should not be launched until it has a high expectancy of living at least one year.

(*ii*) *Size and Weight.* Clearly, both size and weight should be held down, but not at the price of compromising on performance. The successful launching of a device which then fails to operate will avail us less than nothing. An over-all weight in the vicinity of 100 pounds and a surface area of 20 square feet for solar cells appears reasonable from both the propulsion and electronic subsystem viewpoints. As propulsion systems with greater capabilities become available, they can be used to launch a multichannel repeater or several satellites at one time, or both. The basic repeater design can remain unchanged, if it is right in the first place. For example, the experimental single-channel one-way repeater discussed above could be used to build up a multichannel two-way repeater....

* * *

About the time the memorandum reproduced above was written, work was started on a number of problems defined therein in several places, both within the Research Division and in other Divisions of Bell Telephone Laboratories. Since much of this work is treated in considerable detail in this issue and elsewhere, we shall treat each topic with only the amount of detail appropriate to this historical introduction.

3.1 *Project Echo*

Early in 1959 preparation was begun for the Project Echo experiment,[6] and this work dominated our satellite communication activity for a time. Interest in the passive satellite was spurred by realization of the magnitude of the job of building an adequate active satellite, and the desire to gain early experience with systems. It was also believed that a system based on passive satellites might be created before the reliability of active satellites could be proven.

Bell Laboratories cooperated with the National Aeronautics and Space Administration, Jet Propulsion Laboratories, Naval Research Laboratories and others in formulating and carrying out the communication part of the Echo experiment. For this purpose a ground station with transmitter, receiver and satellite-tracking facility was established at

Holmdel, New Jersey. As is now well known, single-channel two-way voice communication, facsimile transmission, etc., were demonstrated over transcontinental paths; transmission characteristics were measured; and valuable operational experience was obtained using the 100-foot aluminized balloon reflector. This work spurred large ground station tracking and control and receiver development, and contributed valuable assurance that there were no propagation anomalies except for atmospheric refractive effects at low elevation angles. Experience with the large horn-reflector antenna with its complement of low-noise components, experience with orbit prediction and tracking, and experience with wide-index feedback FM demodulators were of considerable value in subsequent design of the much larger ground station used for the Telstar experiment. Portions of the ground station constructed for Echo were also eventually used in connection with the Telstar experiment.[17]

3.2 *Satellite Electronics*

The most critical component of the spacecraft itself was considered to be the traveling-wave tube. Fortunately, the development of tubes for terrestrial microwave relay systems had recently demonstrated as much as a five-year life span for such tubes, and their use in missile systems had shown that they could be made light and rugged enough. To design and build a tube for particular performance objectives — frequency, gain and power level — and with an aim toward even longer life, was no trivial task, and it was felt that at least a two-year lead time would be needed. To complicate the matter, the assignment of frequencies for an experiment with communication satellites could not be rushed. Consequently, some long guesses had to be made, and work on a one-watt tube at 6000 megacycles was started because this seemed a most likely possibility. The eventual change to two watts at 4000 megacycles was not so great as to void much of the work that was done. A full account of this work is presented elsewhere in this issue.[16]

Experience with an experimental light-route radio relay gave confidence that the solid-state devices and microwave circuitry used therein could be adapted to the design of a broadband repeater in space, and there was considerable experience upon which to draw. Several repeater circuit configurations were considered, and the straight-through IF configuration was favored because it made more straightforward use of existing circuitry.

3.3 *Satellite Power Supply*

Since the satellite power supply accounts for an appreciable part of the total satellite weight, it was essential that the most efficient design be used. While several schemes, including nuclear reactors and isotope power supplies, had been proposed, the only feasible means (1959–1960) was to use solar cells and a storage battery, together with a solid-state converter to change the low battery voltage to the various potentials required by the electronic circuitry. Study of the solid-state power converter, which was started at this time, benefited from considerable related experience with dc-to-dc converters for terrestrial microwave systems and for various military applications. The main problem was one of reliability. How this was obtained is described elsewhere in this issue.[18]

A storage battery of suitable design was not available; existing cells suffered from a lack of control during the manufacturing process and from a tendency to leak. There was also considerable question about cell life under continuous deep cycling and the effects of a long continued overcharge. Some of the early results obtained from a fundamental investigation started at this time have been published.[19,20,21] Early work on solar cells consisted mostly of radiation damage studies, since this was expected to be the most crucial problem; considerations were also given to temperature control and mounting arrangements.

3.4 *The Satellite Antenna*

The satellite antenna posed a difficult problem because of the conflicting mechanical and electrical requirements. Since the satellite diameter would inevitably be many wavelengths at the operating frequency, severe shadowing would occur if a nondirectional antenna was mounted near the surface. Erection of extensible arms in space had proven risky at best; and even if this were achieved, a sufficiently flexible low-loss microwave transmission line was not available.

A solution to the electrical problem was to divide the spherical satellite into two parts, separated by a radial transmission line which fed a circumferential slot radiatior. This antenna configuration was studied analytically and checked experimentally and found to produce a pattern acceptable for a spin-stabilized satellite.[22] However, this basic structure, consisting of two hemispheres insulated from each other by a small slot, posed severe mechanical and thermal problems in the satellite design. A multiplicity of closely spaced "boxes" fed in-phase by an array of

coaxial cables and arranged to radiate circular polarization[23] provided an acceptable solution which was adopted in the development models of the Telstar satellite.

3.5 *The Satellite Structure*

Since it was desired to build a satellite which would have a long useful life, and there was no assurance of being able to provide attitude control, it was important that the satellite not be dependent upon orientation relative to the sun or the earth. For this reason an approximately spherical shape was chosen, and solar cells were distributed more or less uniformly so that the power generated would not depend upon solar aspect.

The early work was on a larger framework than used on the Telstar satellite, because continuous operation was envisaged, but work on the structure, heat flow and vibration damping paved the way for the later design.[24]

3.6 *Mutual Visibility Problems*

A crucial factor in the design of satellite communication systems is the problem of mutual visibility statistics. It was easy to derive a first-order approximation to the operational statistics for particular ground terminals and satellite orbit. To get a more general solution was a good mathematical problem which was solved in an interesting fashion.[25] It is clear from this work that a practical real-time, low-altitude satellite system for use between the United States and Europe should use polar, or at least steeply inclined, orbits at an altitude of several thousand miles. Other orbits are more suitable for other paths, and it appears that a global system would make good use of both polar and equatorial orbits. Before the radiation hazard was appreciated, it was thought that a 2,500-mile orbital altitude represented a logical compromise between the many factors involved, but to ease the radiation problem, and for other reasons, higher altitudes are now favored. The 24-hour synchronous satellite was, of course, expected to be much better from this point of view, but was ruled out of early consideration because of the more severe technical problems.

3.7 *The Delay and Echo Problem*

A most interesting research problem has been that of the delay and echoes inherent in long two-wire telephone circuits. The literature of a generation ago has a lot to say on this subject, and set a limit on the largest acceptable delay in a two-way, two-wire telephone circuit.

Heretofore, it has not been too difficult to stay within such a limitation, but it was soon clear that any double-hop, low-altitude system or single-hop synchronous satellite system would exceed this standard by a considerable amount. Early (1959) and simple experiments indicated that delay alone (in four-wire circuits) was not a problem, but that eliminating the echo in the presence of a delay up to 0.6 second was not a trivial problem.

It was soon apparent that this problem strongly involved user psychology as well as some severe technological problems. Circuits were devised which worked very well with some individuals and very poorly with others. Accordingly, in addition to work on specific apparatus for echo suppression, a user preference testing program was inaugurated. Tests were conducted over several years using a number of echo suppression techniques, including those of competitive companies. The user reaction to circuits with the best available echo suppressors and delays corresponding to only a single 24-hour satellite link is of serious concern in commercial telephony. This question still remains a fruitful area of research.[26]

3.8 *The Ground Station Antenna*

During the early planning for an active satellite experiment, it became evident that a low-noise antenna larger than any then in existence would be required. Design, construction, and test of the 20 × 20-ft horn reflector for Project Echo were sufficiently advanced to make clear that such an antenna would also be acceptable for use with an active satellite. Hence, plans were initiated for a 60 × 60-ft horn-reflector antenna of similar design. It was suggested by the mechanical designers that a conical horn might ease some of the structural problems. As a result of this suggestion, an analysis and an experimental check were made of the gain and pattern of such an antenna[27] which showed that performance equal to that of the older rectangular horn-reflector antenna could be obtained.

With antennas of the size contemplated, it is desirable that steering (autotrack) information be derived from the antenna itself. Prior research on waveguide modes provided a solution to this problem[28] and a multimode autotrack system was developed which contributed greatly to the Telstar operation.[29]

3.9 *Modulation*

A large number of possible modulation methods were considered for both passive and active satellites. During the Project Echo experiment

amplitude modulation, phase modulation, single-sideband and frequency modulation (FM) were used. When complexity, power requirements on the satellite, and frequency spectrum limitations were all considered, it was not difficult to settle on wide-index FM as the most desirable. FM seemed desirable even for spectrum conservation because the relative freedom from interference greatly reduces the required geographical separation of stations sharing the same band.

The desirability of FM was greatly enhanced by the promised advantage of feedback in reducing the receiver threshold power.[30] Early attempts to use feedback demodulation failed to demonstrate the expected advantage, because of the seeming conflict between the IF band-shape requirements of the noise elimination and feedback stability criteria. A considerable amount of rather difficult theoretical and experimental work was necessary to resolve this difficulty, and the improvement obtained,[31,32,33] first for Project Echo and later in the broadband Telstar receiver, was very near the amount expected on more intuitive grounds.

IV. TRANSITION FROM THE RESEARCH TO THE DEVELOPMENT PHASE

Up to 1960, Bell Laboratories activity in satellite communication centered in an ad hoc group representing many parts of the organization. No large expenditure had been committed, and in fact it was not known at this date when, if ever, a satellite for other than government purposes would be launched. The work was undertaken because of a firm conviction of its eventual importance to the Bell System and because it posed problems which the technical staff found interesting and challenging. It was made possible by the freedom granted to the research groups to enter new areas which they found promising, long before it was possible to evaluate the commercial importance of the new field of activity.

Where does research end and development begin? It must be clear to the reader that there is as much "development" described in the foregoing paragraphs as there is research. However, there came a time in the course of events when a clear-cut change in the nature of the effort took place. Prior to the fall of 1960, "research," motivated primarily by the desire to solve crucial and interesting problems, dominated the Bell System activities in this field. After the fall of 1960, the activities were dominated by the dedication and commitment to produce a working experimental system in the shortest possible time. This paper covers only the earlier effort when activities were based on a hope rather than

a commitment, were directed toward components more than toward a system, and before most of the people who made the Telstar experiment work had become involved. In the two years that followed, a number of important changes in the plan took place, and the pace accelerated many fold. The earlier contributions seem pale beside the later achievement, but small as the beginnings were, they played an important part in getting the Telstar satellite program under way.

REFERENCES

1. Pierce, J. R., Orbital Radio Relays, Jet Propulsion, **25,** April, 1955, pp. 153–157.
2. Pierce, J. R., and Kompfner, R., Transoceanic Communication by Means of Satellites, Proc. I.R.E., **47,** March, 1959, pp. 372–380.
3. Pierce, J. R., and Cutler, C. C., Interplanetary Communication, Advances in Space Science, **1,** Academic Press, Editor Fredrich I, Ordway III, New York, 1959, pp. 55–109.
4. Tillotson, L. C., Active Satellite Repeaters, Signal, **14,** No. 11, July, 1960, pp. 48–50.
5. Cutler, C. C., Radio Communication by Means of Satellites, Advances in Ballistic Missile and Space Technology, Proc. Fourth AFBMD/STL Symposium, **3,** Pergamon Press, 1961, pp. 254–271.
6. B.S.T.J., **40,** July, 1961, entire issue.
7. Hogg, D. C., Effective Antenna Temperature Due to Oxygen and Water Vapor in the Atmosphere, J. Appl. Phys., **30,** September, 1959, pp. 1417–1419.
8. Friis, H. T., and Beck, A. C., U. S. Patent 2,236,393, filed 3/1/39, issued 3/25/41.
9. Crawford, A. B., Hogg, D. C., and Hunt, L. E., A Horn-Reflector Antenna for Space Communication, B.S.T.J., **40,** July, 1961, p. 1095.
10. DeGrasse, R. W., Hogg, D. C., Ohm, E. A., and Scovil, H. E. D., Ultra-Low Noise Antenna and Receiver Combination for Satellite and Space Communication, Proc. Nat. Elect. Conf., **15,** 1959, p. 370.
11. DeGrasse, R. W., Schulz-DuBois, E. O., and Scovil, H. E. D., The Three-Level Solid-State Traveling-Wave Maser, B.S.T.J., **38,** March, 1959, p. 305.
12. Manley, J. M., and Rowe, H. E., Some General Properties of Nonlinear Elements — Part I, General Energy Relations, Proc. I.R.E., **44,** July, 1956, pp. 904–913.
13. Uhlir, A., Jr., The Potential of Semiconductor Diodes in High-Frequency Communications, Proc. I.R.E., **46,** June, 1958, p. 1099.
14. Hogg, D. C., and Semplak, R. A., The Effect of Rain on the Noise Level of a Microwave Receiving System, Proc. I.R.E., **48,** December, 1960, p. 2024.
15. DeGrasse, R. W., Kostelnick, J. J., and Scovil, H. E. D., The Dual Channel 2390 mc Traveling-Wave Maser, B.S.T.J., **40,** July, 1961, p. 1117.
16. Bodmer, M. G., Laico, J. P., Olsen, E. G., and Ross, A. T., Satellite Traveling-Wave Tube, B.S.T.J., this issue, Part 3.
17. Jakes, W. C., Jr., Participation of the Holmdel Station in the *Telstar* Project, B.S.T.J., this issue, Part 2.
18. Bomberger, D. C., Feldman, D., Trucksess, D. E., Brolin, S. J., and Ussery, P. W., The Spacecraft Power Supply System, B.S.T.J., this issue, p. 943.
19. Thomas, U. B., The Oxides and Hydroxides of Nickel, Their Composition, Structure, and Electrical Properties, presented to the Electro-Chemical Society, Ottawa, Canada, October, 1958.
20. Thomas, U. B., Battery Considerations for a Communication Satellite, presented at the American Rocket Society Energy Conversion for Space Power Conference, Santa Monica, California, September, 1960, published in Progress in Astronautics and Rocketry, **3,** ARS series, Chapter 34, 1961, pp. 497–514.

21. Thomas, U. B., Kinetic Basis for the Operating Characteristics of Sealed Nickel-Cadmium Batteries, presented at the Third International Symposium on Batteries, Bournemouth, England, October, 1962, published in the Proceedings.
22. Bugnolo, D. S., A Quasi-Isotropic Antenna in the Microwave Spectrum, I.R.E. Trans. on Antennas and Propagation, AP-10, No. 4, July, 1962, p. 377.
23. Bangert, J. T., Engelbrecht, R. S., Harkless, E. T., Sperry, R. V., and Walsh, E. J., The Spacecraft Antennas, B.S.T.J., this issue, p. 869.
24. Hryeak, P., Koontz, D. E., Maggs, C., Stafford, J. W., Unger, B. A., and Wittenberg, A. M., The Spacecraft Structure and Thermal Design Considerations, B.S.T.J., this issue, p. 973.
25. Sinden, F. W., Geometric Aspects of Satellite Communication, I.R.E. Trans. on Space Electronics and Telemetry, **6,** September–December, 1960, p. 146.
26. News Feature in the Bell Laboratories Record, Simulating Speech through Space, **38,** August, 1960, pp. 296–298.
27. Li, Tingye, and Turrin, R. H., Performance Characteristics of a Conical Horn-Reflector Antenna, presented at URSI Spring Meeting, Washington, D.C., April 30 to May 3, 1962.
28. Miller, S. E., Multimode Automatic Tracking Antenna System, Patent No. 2,931,033, filed 7/19/55, issued 3/29/60.
29. Cook, J. S., and Lowell, R., The Autotrack System, B.S.T.J., this issue, Part 2.
30. Chaffee, J. G., The Application of Negative Feedback in Frequency-Modulation Systems, B.S.T.J., **18,** July, 1939, pp. 385–403.
31. Ruthroff, C. L., FM Demodulators with Negative Feedback, B.S.T.J., **40,** July, 1961, p. 1149.
32. Enloe, L. H., Decreasing the Threshold in FM by Frequency Feedback, Proc. I.R.E., **50,** January, 1962, pp. 18–30.
33. Ruthroff, C. L., and Bodtmann, W. F., Design and Performance of a Broadband FM Demodulator with Frequency Compression, Proc. I.R.E., **50,** No. 12, December, 1962, pp. 2436–2445.

The *Telstar* Satellite System

By D. F. HOTH, E. F. O'NEILL and I. WELBER

(Manuscript received March 15, 1963)

This paper describes the Telstar system and discusses the over-all system design. System considerations, the orbit selection and frequency allocation considerations are covered. A general description of the Telstar satellite and Andover, Maine, ground station provides background for companion articles in this series. Finally, the transmission performance is given with some discussion of system parameters.

I. INTRODUCTION

The Telstar system consists of the active communication satellite repeater in orbit and ground facilities to work with it. The satellite was designed and built by Bell Telephone Laboratories and launched by the National Aeronautics and Space Administration (NASA) under the terms of a cooperative agreement. Bell Laboratories built the ground station at Andover, Maine, and furnished launch support equipment at Cape Canaveral. The station at Holmdel, New Jersey,[1] originally built for the Echo project, was modified to work with the Telstar system. Participating European stations were constructed at Goonhilly Downs in England, Pleumeur-Bodou in France, and Fucino in Italy by telecommunications agencies in the respective countries.

This paper gives a general description of the Telstar satellite system. It starts with a discussion of the over-all system design. This is followed by a more detailed discussion of the factors affecting the choice of the orbit and of the operating frequencies. The satellite, the Andover ground station, and the equipment at Cape Canaveral are next described and, finally, certain important transmission parameters are presented.

II. SYSTEM OBJECTIVES

The system was designed to meet the following objectives:

(1) To demonstrate broadband microwave transmission through an active satellite.

Specifically, this included the transatlantic transmission of high-quality television with sound, or the equivalent of 600 one-way telephone channels. It was also desired to test the transmission of a limited number of two-way telephone channels using a common amplifier in the satellite. A further transmission objective was to demonstrate that other services, such as data, telegraphy and telephoto, could be sent through the satellite.

(2) To test the operation of a ground station capable of transmitting to, and receiving from, the satellite while tracking it.

This involved the simultaneous operation of a high-power broadband transmitter and an ultra-low-noise receiver through a common horn-reflector antenna. An important aspect of the ground station tests was the trial of several means of acquisition and tracking of the satellite, and the steering of the antenna by both programmed and autotrack methods.

(3) To obtain data on the space environment and its effect on the satellite.

For this purpose, equipment is carried to measure particle radiation in space, as well as temperatures, voltages and other conditions in the satellite. Telemetry is provided to relay this information to the earth.

III. GENERAL SYSTEM CONSIDERATIONS AND FEATURES

A satellite communications system differs in major respects from other kinds of radio communications systems, and hence the various constraints faced by the designer differ in nature or emphasis. In this section, the major constraints which influenced the design of the Telstar system and the way in which they affected the system parameters are discussed in a general way. Major system features are given. Subsequent sections will discuss these matters in more detail.

The principal factors affecting the choice of the parameters of the Telstar system were the following:

(1) In order to provide mutual visibility across the Atlantic for periods of useful length, it was necessary to place the satellite in an orbit above 2000 miles. On the other hand, the weight which could be launched into a satisfactory orbit with available launch vehicles was limited.

(2) It was necessary to choose operating frequencies at which the sky noise and atmospheric absorption would be low and where sufficient bandwidth for television and other broadband services could be obtained. It was also necessary to consider interference between the satellite system and other radio services.

(3) Because of the long distances involved, radio path losses are very great. In addition, the effective radiated power of the satellite was limited by the primary power obtainable within the weight restrictions and because of the impracticality of using directive antennas in the satellite. The signal power received at the ground antenna, therefore, is very weak compared with levels normally received in overland radio relay systems.

(4) It was desired to design a satellite with a high probability of surviving the launch and which would last as long as possible in the space environment. This consideration affected the design and weight of the satellite in many ways, including selection of reliable components, rugged construction and protection against particle radiation.

All of these factors interact with each other and, as a result, there is no uniquely logical order in which the design choices can be developed in a step-by-step manner. Probably the choice of operating frequencies is the best starting point.

Considerations of bandwidth, propagation and radio noise narrow the choice of operating frequencies to the region between one and ten gigacycles, as will be discussed in more detail in a later section. These factors, together with hardware considerations and problems of coordination with other radio services, led to operation in the 3700–4200-mc and 5925–6425-mc common-carrier bands. The low power received at the ground led to the choice of the lower frequency band for the down path because these frequencies are better from the standpoints of radio propagation and noise.

At the operating frequencies chosen, noise from the sky is very low (as much as 20 db lower than that radiated by the earth into terrestrial microwave antennas) and thus very weak signals can be used. Advantage could be taken of this by using a low-noise ground antenna and a helium-cooled maser amplifier at the input to the ground receiver. A horn reflector was chosen because it has very low gain a few degrees off the main beam and thus would pick up very little noise from terrestrial sources. To further improve reception, it was decided to build at Andover the largest, and thus highest-gain, horn-reflector antenna that could be designed with confidence that it could be steered accurately enough to track the satellite. This antenna has a 3600-square-foot aperture.

Even with the low-noise antenna and maser, it was necessary to employ every possible technique for achieving high quality transmission with weak signals. This led to the choice of wide-swing frequency modulation for the down path, since it permits good baseband signal-to-noise ratios with poor radio-frequency carrier-to-noise ratios. The use of a frequency compression demodulator (also referred to as an FM feedback

receiver) permits operation with lower carrier-to-noise ratios than is possible with a conventional FM detector. For satellite simplicity and other reasons, FM was also chosen for the up path. The satellite amplifies the signal but does not alter the modulation.

The Andover ground station provides adequate transmission performance for the down link out to a range of more than 8000 nautical miles with a satellite effective radiated power of 2 watts. A 2-kw transmitter on the same antenna provides similar performance for the up link.

If antenna gain could be used in the satellite, the actual RF power could be less than 2 watts and this could be traded for other simplifications in the satellite or ground station, or for improved transmission performance. There are a number of possible techniques for achieving this, including the use in the satellite of earth pointing attitude stabilization along with a directive antenna, steerable phased arrays or provision for switching several directive antennas. These possibilities were discarded for various reasons, including the state of the art, the time it would have taken to develop them, and the desire for a simple satellite. Instead, an antenna system which is nearly isotropic is employed. To minimize the effects of nulls on communication, the satellite is spin stabilized around the axis of symmetry of the antenna system.

A traveling-wave tube was chosen for the satellite output amplifier, since it could provide sufficient power with good efficiency and because it would provide a wide bandwidth. Prior experience with missile-borne traveling-wave tubes had demonstrated that they could be made rugged enough to withstand a rocket launch. All other circuits employ solid-state devices.

Solar cells were chosen as the only practical source of primary power for the satellite. To supply the power required for the communication equipment directly from the solar cells would mean more cells and thus more weight than was possible within the weight and size limitations on the satellite. Therefore, a nickel-cadmium storage battery charged by the solar cells supplies the communications equipment during operation. Command circuits are provided to turn off the communications equipment so the batteries can be charged and to perform a number of other functions.

Facilities for measuring trapped particle radiation and its effect on solid-state devices are provided. Telemetry provides information on the condition of the satellite and on the results of the radiation experiment. The satellite is approximately spherical, with a diameter of 34 inches, and weighs approximately 170 pounds.

The launch vehicle was a major factor in the Telstar experiment.

Very early in the planning of the project, consideration was given to possible vehicles which might be capable of putting a sufficient payload into a satisfactory orbit. For reasons of availability and reliability, the NASA Delta vehicle was chosen. Since it could not launch the payload into a high enough circular orbit, an elliptical orbit with an apogee of about 3000 nautical miles and a perigee of about 500 nautical miles was chosen. The orbit is inclined 45° to the equator. When apogee is over the North Atlantic, there are several good periods of mutual visibility between Europe and Andover daily.

Table I lists the major parameters of the Telstar system.

IV. ORBIT SELECTION

As indicated in the preceding section, it was necessary to place the satellite in a high enough orbit to give satisfactory periods of mutual visibility across the Atlantic. The problem is illustrated by Fig. 1.* It shows lunes of mutual visibility for communication between Andover, Maine, and either Goonhilly Downs in England or Pleumeur-Bodou in France, assuming minimum antenna elevation of 7.5°. For a particular height, the subsatellite point on the earth's surface must be within the corresponding lune if the satellite is to be mutually visible. As the height gets lower, the lune becomes smaller. At the same time, the orbit period becomes shorter so that the subsatellite point moves more rapidly over the earth. The net result is fewer and shorter useful passes. The lune would vanish at 475 nm height.

The inclination of the orbit also affects visibility, since the satellite never passes over regions whose latitudes are higher than the inclination. Thus, only part of the visibility lune may actually be useful for communication. The best choice of orbit inclination depends on the particular points on the earth between which communication is desired; for the points of principal interest here a high inclination is best. Thus, for the Telstar satellite, an orbit was desired with the highest altitude and inclination possible with the available launch vehicle and launch location.

The launch vehicle used is a major factor in any satellite experiment. Rockets capable of orbiting significant payloads do not exist in such variety that the problem can be approached with a set of requirements on *them* as an end result. On the contrary, it is almost inevitable that an available vehicle must be found and the experiment framed within its capability. This, in effect, limits the achievable orbits and sets weight and size limits on the satellite.

---

* For a more complete discussion of satellite visibility, see Ref. 2.

TABLE I — PRINCIPAL FEATURES OF THE *Telstar* SYSTEM

TRANSMISSION

- Signals handled
  - Television
  - 600 one-way telephone channels (simulated by noise)
  - 12 two-way telephone channels
- Modulation — FM
- RF bandwidth
  - Ground station — 25 mc
  - Satellite — 50 mc
- Frequencies
  - Communication up — 6389.58 mc
  - Communication down — 4169.72 mc
  - Beacon — 4079.73 mc
  - Telemetry and beacon — 136.05 mc
  - Command — about 123 mc
- Polarization
  - Microwave channels — circular
  - VHF beacon — linear
  - Command — circular

SATELLITE

- Size, shape, and weight — 34-inch sphere, 170 pounds
- Orbit
  - Perigee 514.21 nm
  - Apogee 3051.37 nm
  - Inclination 44.8°
- Launch — Delta vehicle from Cape Canaveral
- Repeater configuration — IF type: amplifies, shifts frequency, does not alter modulation
- Communications antennas — approximately isotropic, circularly polarized
- RF power output — 2 watts
- Power plant
  - Silicon n-on-p solar cells — shielded
  - Ni-Cd storage battery
- Stabilization
  - Spin with axis normal to plane of ecliptic
  - Magnetic torquing coil control
- Radiation experiments — proton and electron
  - Flux in several energy ranges
  - Radiation damage to special solid-state devices

ANDOVER GROUND STATION

- Communications antenna
  - 3600 square foot horn reflector
  - Inflated radome
  - Pointing by tape drive, autotrack, slave to precision tracker
- Communications transmitter — 2 kw
- Communications receiver — maser input, frequency compression demodulator
- Noise temperature — 32° K at zenith

The capabilities of the possible launch vehicles were analyzed. The most readily available was the Delta vehicle used by NASA for the Echo launch and planned to be the vehicle for many other space experiments. It was also believed to be reliable, as has since been borne out by a long succession of successful launches. The initial weight objective

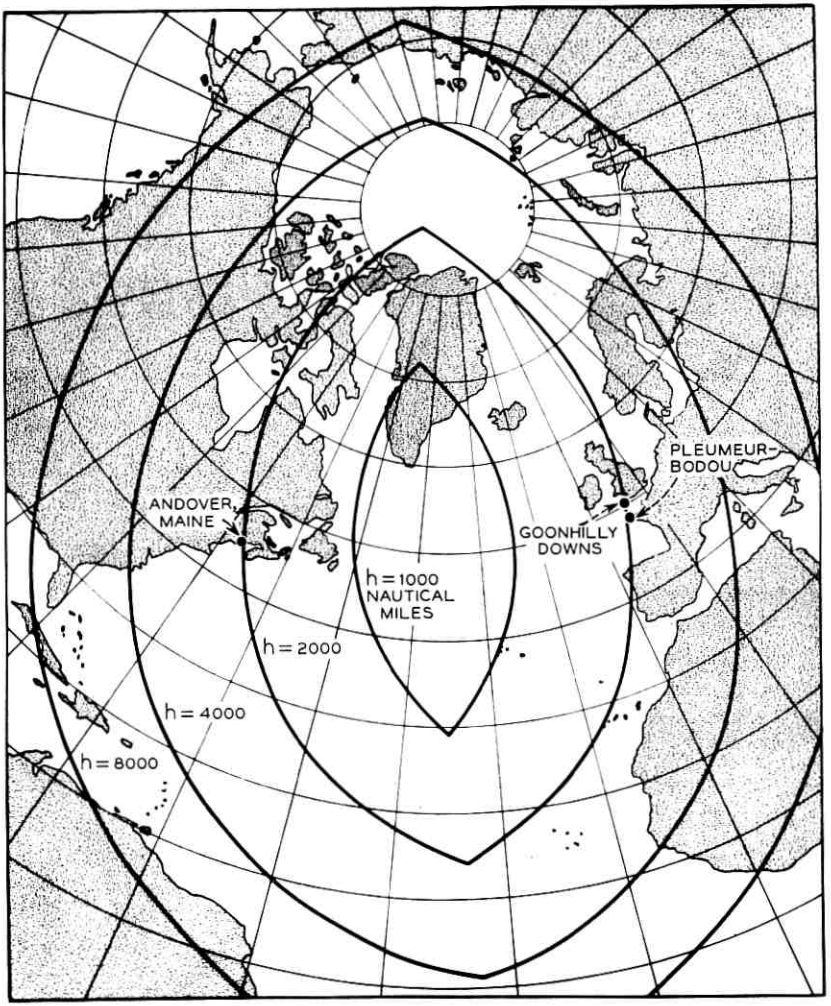

Fig. 1 — Useful regions for various heights above surface of earth.

for the Telstar spacecraft was 125 pounds, but as the real problems of design were met and solved, it became apparent that the satellite would weigh about 170 pounds. With this weight, analysis indicated that the Delta vehicle, launched from Cape Canaveral, would achieve a circular orbit only about 1000 nautical miles high with 42° inclination. This would result in only about three passes per day, typically only five minutes long, with mutual visibility across the Atlantic.

In spite of this disadvantage, the availability and reliability of the

Delta made it an attractive vehicle. Therefore, attention was turned to the possibilities of an elliptical orbit. By accepting a low perigee, an apogee much higher than 1000 miles could be achieved. If the apogee were located well north of the equator, satisfactory periods of mutual visibility could be achieved across the North Atlantic. Table II shows the orbit parameters chosen, together with those actually achieved.

Fig. 2 shows the suborbital track of the Telstar satellite for the first 24 hours after launch. With a period of 158 minutes, the satellite completes nine orbits in 23 hours, 42 minutes, accounting for the near retracing of the first track on the tenth orbit. Those periods when the satellite was mutually visible across the Atlantic are shown by heavy solid lines. Additional time when it was visible from Andover only are shown by light solid lines. Other periods are shown dashed.

It will be noted from the table that the initial apogee was south of the equator — not the best position from the standpoint of visibility. However, the line of apsides advances about 2° per day, and after launch the apogee moved in a northerly direction. It reached its northernmost point in about 50 days and then started to move southward. This gave a period of about three months during which visibility was good, followed by a period of poor visibility. Fig. 3 shows visible time per day when the satellite is at least 7.5° above the horizon. Initially, there were three or four passes per day, each lasting 10–20 minutes, during which the satellite could be used for transatlantic communication. Seven weeks later, with the apogee in its best position, there were four or five passes daily, each lasting 20–40 minutes.

Another orbit parameter is spin-axis orientation. For optimum output from the solar power plant and favorable heat balance, it was desired to have the spin axis perpendicular to the sun line. If this attitude is to be maintained as the earth carries the satellite with it around the sun, the axis must also be normal to the ecliptic plane. The desired inclination of the orbit was achieved by dog-leg maneuvers during the launch. Thus, while the orbit plane is inclined 45° to the equator, the direction

TABLE II — ORBIT OF THE *Telstar* SATELLITE

	Proposed	Actual Orbit (NASA Minitrack)
Perigee	500 nm	511.9 nm
Apogee	3000 nm	3043.2 nm
Inclination	45.43°	44.8°
Period	156.47 min.	157.6 min.
Initial apogee latitude	8.59°S	11.92°S
Apsidal advance	2.02°/day	1.98°/day

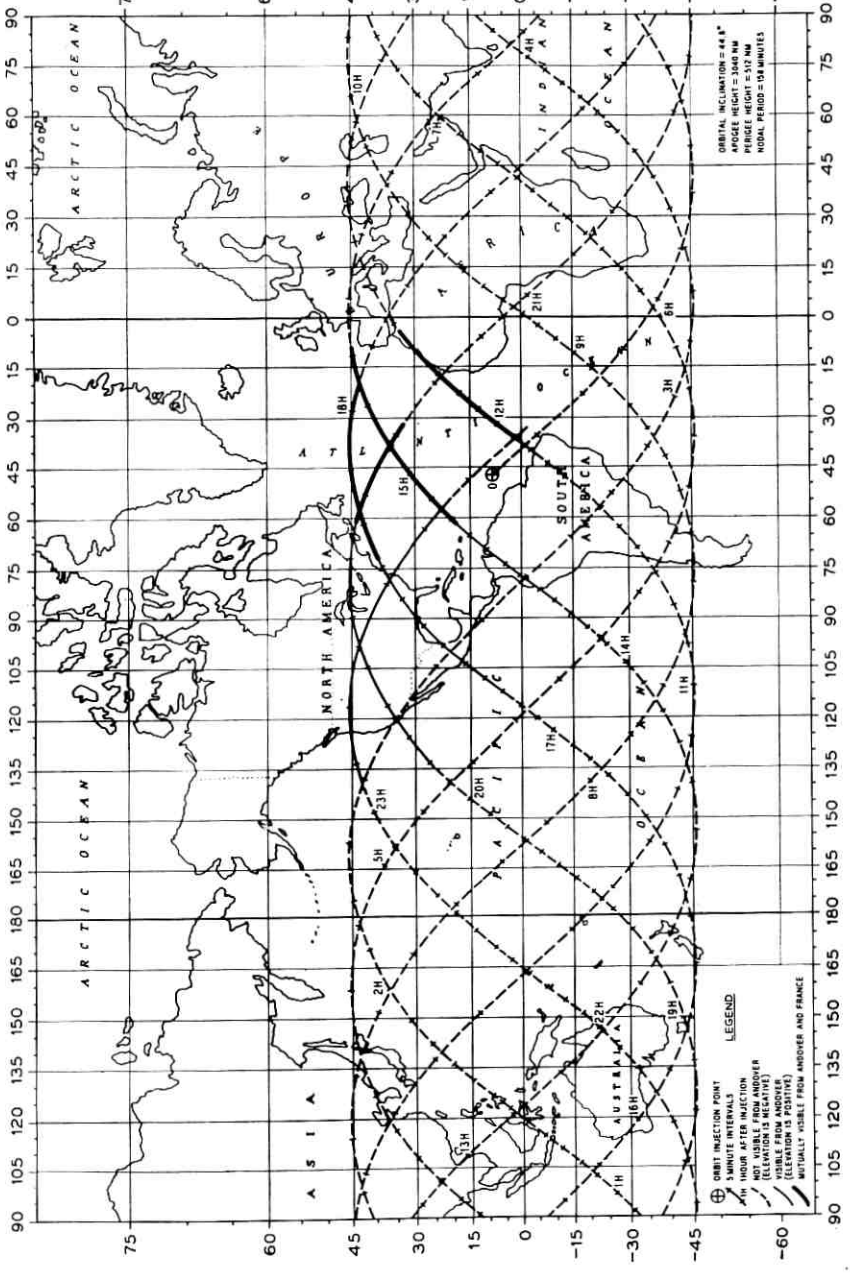

Fig. 2 — Suborbital tracks and mutual visibility for first 24 hours.

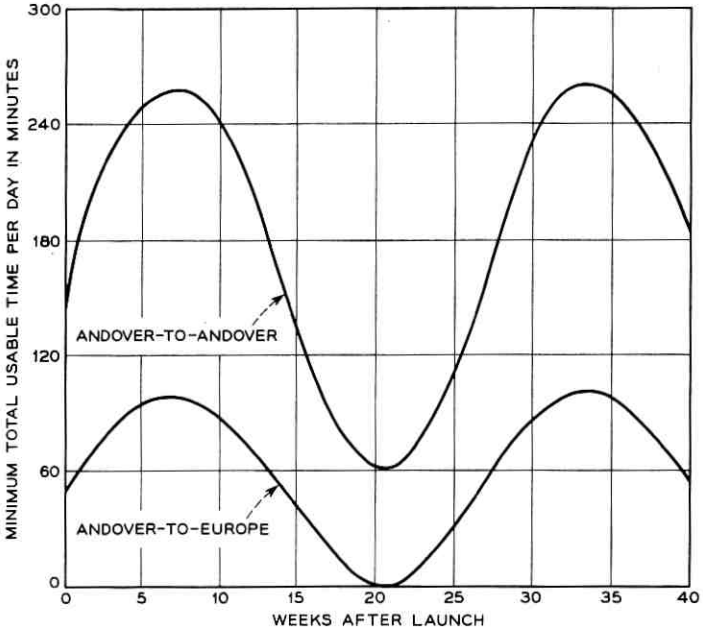

Fig. 3 — Minimum usable time per day.

of the final thrust of the third-stage rocket, and hence the orientation of the spin axis, was at a higher inclination to the equator — actually 67°. By choosing the time of launch, the 23° inclination of the earth's axis with respect to the ecliptic plane was added to this, resulting in a spin-axis attitude almost perpendicular to the ecliptic plane. The axis precesses with time because of the torque created by the residual magnetic moment of the satellite in the earth's field. To correct this precession, a magnetic torquing coil is provided in the satellite which can be turned on from time to time to control the position of the spin axis.

The elliptical orbit of the Telstar satellite is also desirable for the radiation experiment, since it covers a large part of the inner Van Allen belt and, with its apogee in northerly or southerly positions, it passes through a portion of the outer Van Allen belt.

V. CHOICE OF OPERATING FREQUENCIES

The frequencies used by the Telstar system include those required for the communications channel and for a microwave beacon used in tracking. They also include VHF channels for transmitting commands

to the satellite and for the VHF beacon and telemetry. The VHF channels were chosen to fit in with the facilities of NASA Minitrack stations.

Factors in the choice of the communications frequencies included propagation, noise, and interference within the satellite system and with other services. These were considered not only with respect to the experiment, but also from the point of view of later commercial systems. These factors lead to the choice of frequencies in the region between one and ten gigacycles.

5.1 *Propagation and Noise*

The 1- to 10-gc region is the same part of the spectrum commonly used for terrestrial radio relay systems, but the critical transmission factors are different. Radio relay systems are subject to severe selective fading due to multipath effects. When enough margin is provided for fading, atmospheric absorption is unimportant except at the upper edge of the band. Radio relay antennas, since they are pointed horizontally, receive thermal noise from the earth, and this puts a floor on the effective noise temperature of the system. On the other hand, in satellite systems, selective fading is nonexistent, except at very low elevation angles of the ground antennas. Noise received from the sky in favorable parts of the spectrum is much lower than thermal noise from the earth, so that low-noise amplifiers such as the solid-state maser can be used effectively.

Receiving system noise temperatures of satellite ground stations can be made very low compared with the approximately 300°K temperature of the earth. For example, the Andover station has an effective temperature, excluding sky noise, of about 30°K. Thus, sky noise temperatures in the tens of degrees are significant.

At one gigacycle, cosmic noise can be as high as 30°K and becomes greater at lower frequencies.[3] Above one gigacycle, sky noise due to air, water vapor and rain increases as frequency increases. Noise due to air and water vapor alone is worst at low antenna elevation angles. For an elevation of 7.5°, it is about 15°K at 1 gc and 30–60°K at 10 gc. More serious is the effect of rain. Zenith measurements at 6 gc have produced values in excess of 100°K during very heavy rainfall.[4] Unpublished data indicate that, for the same rain conditions, noise will generally be higher for low antenna elevation angles. The effect is highly dependent on frequency with the lower frequencies showing less noise.

When a radome is used, as at the Andover station, there is an additional source of noise during rain due to reflection and absorption from the wet radome. Particularly with high antenna elevation angles,

this may be the most important source of added noise. More data on this effect are needed, but they are not expected to alter conclusions regarding the choice of frequencies.

Not only is the noise temperature of the sky increased by rain, but the signal is attenuated because the raindrops scatter and absorb it. This effect is also strongly dependent on frequency, since it depends on the size of the raindrops measured in wavelengths. At 4 gc, a rainfall of five inches per hour causes about 0.2 db excess attenuation per mile of rainstorm traversed.[5] At 6 gc, the increase is about 1.5 db per mile of rainstorm. Although this rate of fall is very high, it does occur quite often for short periods during thunderstorms. The core of a thunderstorm may be some five miles in diameter. Thus it can be seen that excess attenuations of some 1 db at 4 gc and 7 db at 6 gc are indeed likely to occur a small fraction of the time, and lesser increases will occur more often. At frequencies higher than 6 gc, the excess attenuation will be higher — for instance, as much as 50 db at 11 gc.

5.2 *Frequency Allocation Considerations*

Frequencies in the 1- to 10-gc range are allocated internationally by the Radio Regulations resulting from the Administrative Radio Conference (Geneva, 1959) to a variety of services. Allocations differ in the three regions of the world recognized in the Geneva frequency tables, and there are numerous footnotes to the tables and reservations to the convention calling attention to national deviations from the tables. Furthermore, in the United States, there are further distinctions, particularly between government and nongovernment allocations.

It may be difficult for satellite communications systems to share frequencies with some of these services. For example, radio location and navigation services generally use very high power transmitters and very sensitive receivers, and hence may both cause interference to, and receive interference from, sharing services. Radio astronomy by its very nature uses very sensitive receivers, and would be vulnerable to interference from sharing services. The frequencies allocated to space research are scarcely wide enough to support a commercial satellite system on a world-wide basis.

Consideration of the variety of services in the 1- to 10-gc region led to the conclusion that the frequency space necessary for the Telstar satellite communications system could best be found by sharing with common-carrier radio relay systems. Specifically, these bands are 3700–4200 mc* and 5925–6425 mc. These bands are included in the October 22,

* In Europe, the band 3700–3800 mc is presently used for other services.

1962 "Draft Proposals of the United States of America for the Extraordinary Administrative Radio Conference for Space Radio Communication," to be presented at the conference scheduled by the International Telecommunications Union to be held at Geneva, Switzerland starting October 7, 1963.

5.3 *Coordination with Existing Terrestrial Systems*

When satellite systems share the same frequency bands with radio relay systems, it is necessary to consider four separate interference paths:

(1) satellite system ground transmitter to radio relay receivers,
(2) radio relay transmitters to satellite system ground receivers,
(3) radio relay transmitters to satellite receivers, and
(4) satellite transmitters to radio relay receivers.

The first two interferences are peculiar to the ground station sites and can be controlled by properly engineering the exposures between the satellite ground stations and radio relay routes.[6] The last two interferences must be considered on a world-wide basis, since they involve radio relay stations anywhere within view of the satellites with which frequencies are shared. These interferences must be kept acceptably small by agreement as to permissible parameters for both satellite and radio relay systems. Studies show that such coordination is possible with reasonable parameters of the terrestrial and satellite communications systems.[7]

Radio-frequency channel arrangements for the 4-gc and 6-gc common-carrier bands are given by C.C.I.R. Recommendations No. 278 and 280 (Los Angeles, 1959)* and are shown in Fig. 4. The microwave frequencies finally chosen for the Telstar system are indicated, with ground-to-satellite transmission at 6-gc and satellite-to-ground transmission at 4-gc. The high end of each band was chosen because, at least in the United States, it has been the custom to build up radio relay routes from the low-frequency end of the band and because, as previously mentioned, other services use the 3700–3800-mc band in Europe. While the frequency-sensitive factors favor 6-gc for the up direction and 4-gc for the down direction, the balance is not so overwhelming that the opposite choice is impractical. In the future it may be desirable to double satellite frequency usage by operating both ways simultaneously.

VI. THE *Telstar* SATELLITE

The Telstar satellite is a microwave repeater that receives signals from the earth, amplifies them and retransmits to the earth. The trans-

* These two recommendations were modified at the Plenary Meeting of the C.C.I.R. at Geneva, 1963, but the frequency arrangements are unchanged.

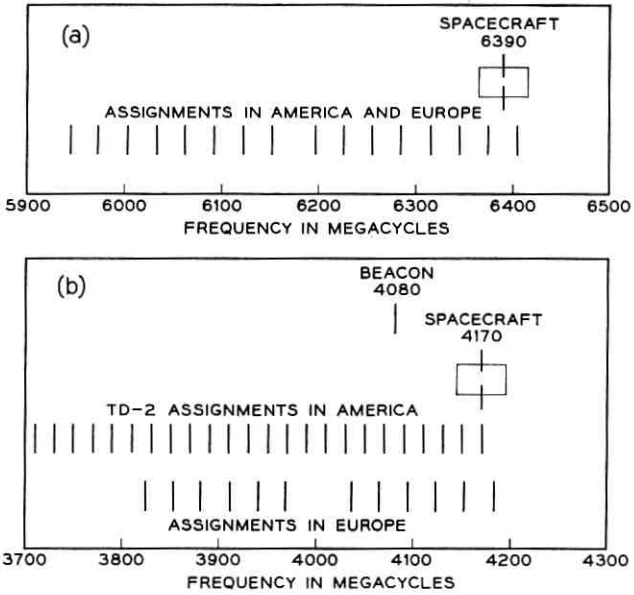

Fig. 4 — Frequency plan: (a) 6-gc common-carrier assignments, (b) 4-gc common-carrier assignments.

mission through the satellite is shown in Fig. 5. FM radio signals with a carrier at 6390 mc are received in an antenna, converted to 90 mc and amplified in an IF amplifier which supplies most of the repeater gain. The signals are then converted up to 4170 mc, amplified in a traveling-wave tube (TWT) and radiated from a separate antenna at a level of 2 watts. The beat frequency tones for the converters originate in crystal oscillators operating at about 16 mc. These frequencies are multiplied in a series of transistor and varactor doublers to the required microwave frequencies.

An interesting feature is the use of the TWT to amplify the up-converter local oscillator tone as well as the signal. This is done by combining the tone with the signal in a filter before the TWT, amplifying them together and then separating the tone from the signal in a separation filter at the TWT output. The separation filter is deliberately made "leaky" to the 4080-mc tone so that part of it is radiated as the microwave beacon for precision tracking. The 6300-mc down-converter tone is obtained by combining the 4080-mc up-converter tone with 2220 mc obtained from a separate oscillator and multiplying chain.

The primary power for the satellite is obtained from solar cells.

Silicon n-on-p cells were chosen because of their greater resistance to radiation. Radiation effects were further reduced by shielding the cells with 30 mils of synthetic sapphire. Fifty groups of cells are connected in parallel, each group containing 72 cells in series for a total of 3600 cells. The power required to operate the communication circuits, especially the TWT, is greater than the average output of the cells. A nickel-cadmium storage battery is provided to carry the peak load and also to permit operation during eclipse. The output of this battery is normally in the range of 24–27 volts. This is regulated to 16 volts, which is used directly for most of the solid-state circuits, or converted in dc-to-dc converters to the higher voltages needed for the TWT.

Since the satellite cannot be operated continuously because of power limitations, it is turned on and off by radio commands from the earth. The commands are transmitted at about 123 mc, which is received through a VHF antenna on the satellite. The command signals are amplified in command receivers, decoded, and used to operate relays which turn the communications repeater on and off. Commands are also used to turn the radiation experiment off and on, to switch between two telemetry encoders, to actuate the magnetic torquing coil and to turn the main power off and on. Duplicate command receivers and decoders are included for reliability.

The satellite transmits a continuous beacon signal at 136 mc from

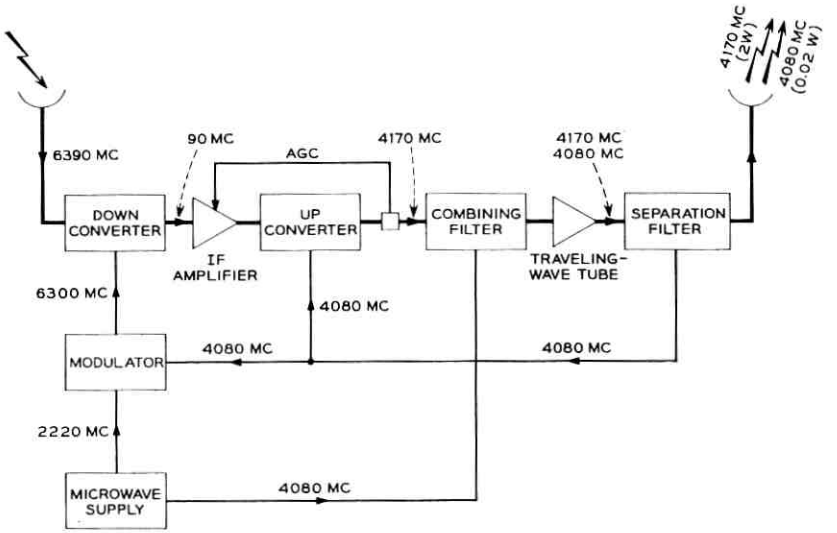

Fig. 5 — Telstar communications repeater

the same antenna used to receive commands. This is used for acquisition and coarse tracking. In addition to its use as a tracking beacon, the 136-mc signal is used as a carrier for telemetry to ground receivers. One hundred and twelve different items are measured each minute and the data transmitted to the ground by low-frequency modulations on this carrier. Measurements include information on temperatures, pressure, currents, and voltages, the state of several relays, RF power transmitted from the satellite and received signal strength at the satellite, as well as the results of the radiation experiment.

The radiation experiment is an important part of the Telstar spacecraft electronics. This experiment measures the flux of protons and electrons at several energy levels and the cumulative effect of the incident radiation on several specially designed semiconductor devices.

An external view of the satellite is shown in Fig. 6. It is a nearly spherical structure, $34\frac{1}{2}$ inches in diameter, weighing 170 pounds. It spins about an axis which is vertical in the picture. While the satellite was placed in orbit with the spin axis nearly perpendicular to the ecliptic plane, it is designed to operate, although on a reduced cycle, with the spin axis in any relation to the sun. For this reason, the solar cells are distributed approximately uniformly about the sphere.

Two equatorial bands of rectangular ports make up the microwave communications antennas. The smaller ports receive signals from the earth at 6390 mc and the larger ports transmit at 4170 mc. The design of the ports and the L-shaped diagonal probes is such that circularly polarized signals of opposite sense are received and transmitted in a nearly isotropic pattern. The pattern and circular polarization permit transmission through the satellite from all aspects without polarization tracking or loss due to cross polarization. Using opposite senses of circular polarization for the up and down paths helps to isolate the receiver from the transmitter both in the satellite and in the ground station.

The VHF command and telemetry antenna is a helical structure. It is also nearly isotropic, but is linearly polarized. Sensors for measuring solar aspect, radiation in the Van Allen belts, and the effects of this radiation, are located at several points on the outer surface. Three mirrors on the outer shell are used to reflect sunlight to the earth. Optical equipment at Holmdel, N. J., is used to observe these flashes and aid in the determination of the spin-axis orientation.

The outer structure consists of an aluminum skin on a magnesium frame. Within this outer shell and frame, a hermetically sealed cylindrical canister containing practically all the electronic circuits is suspended by nylon laces. This laced suspension provides thermal isolation from

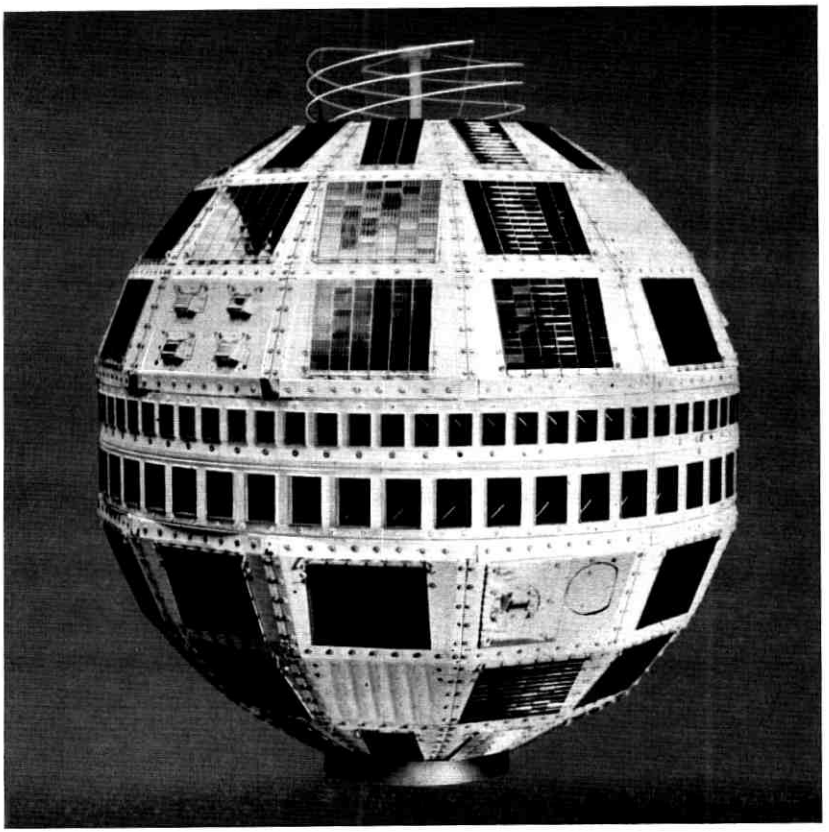

Fig. 6 — The Bell System's experimental communications satellite as it appeared before launch.

the outer shell and effectively attenuates the higher-frequency components of vibration experienced during the launch.

The circuits and subassemblies in the canister are individually encased in polyurethane foam, and the entire interior of the canister assembly is foamed as a unit and the covers welded on. The foam provides a lightweight support for the electronics and greatly reduces the effects of vibration on the subassemblies. It is extremely difficult, though not impossible, to make a repair if a failure should occur after the final foaming and welding operation. The principal reliance is on achieving a reliable unit before this step is taken.

Six complete flyable models were constructed in addition to a prototype and several special-purpose development models.

VII. THE ANDOVER GROUND STATION

The Andover ground station provides means for transmitting to and receiving from the Telstar satellite. The station includes the communications antenna, associated transmitting and receiving equipment, and means for steering the antenna to follow the satellite.

A separate microwave precision tracker is used for orbit determination. A VHF command tracker is used for acquisition and coarse tracking and for transmission of commands to and reception of telemetry from the satellite. The station has computers for the data processing involved in tracking and orbit determination and to reduce experimental data.

7.1 *The Andover Site*

In selecting the site for the Andover ground station, a location was picked which would be suitable for commercial operation as well as for the experiment. Several factors were taken into consideration,[8] principal among which were proximity to Europe and freedom from interference, existing or potential. Obviously, a site in the northeastern United States would best satisfy the first criterion.

Computations indicated that if interference was to be kept to tolerable levels, TD-2 and TH stations operating close to satellite frequencies should be at least 150 miles away if their antennas are aimed directly at the ground station. Average terrain was assumed. For other orientations of the radio relay antennas, a minimum of 40 miles was used. These values are believed to be quite conservative.[6]

Using these criteria, a number of areas in the northeastern states were selected as possibilities. Of these the one in western Maine was most promising. A siting team explored this area and selected the Andover site. Profile studies were made to existing and proposed radio relay stations and showed that interference at the Andover site would be negligible. Subsequent interference measurements confirmed this conclusion.

The location of the station is shown in Fig. 7. It is situated in western Maine close to the New Hampshire border. The site is nearly as close to Europe as is possible in the United States and is well removed from existing and potential radio relay routes. On the other hand, it is close enough to existing radio relay telephone and television routes for economical interconnection.

The connecting link consists of a four-hop system with two sections of TD-2 and two sections of TJ (11 gc) to enter the site. By using TJ for the sections closest to the site, and utilizing frequencies at the low

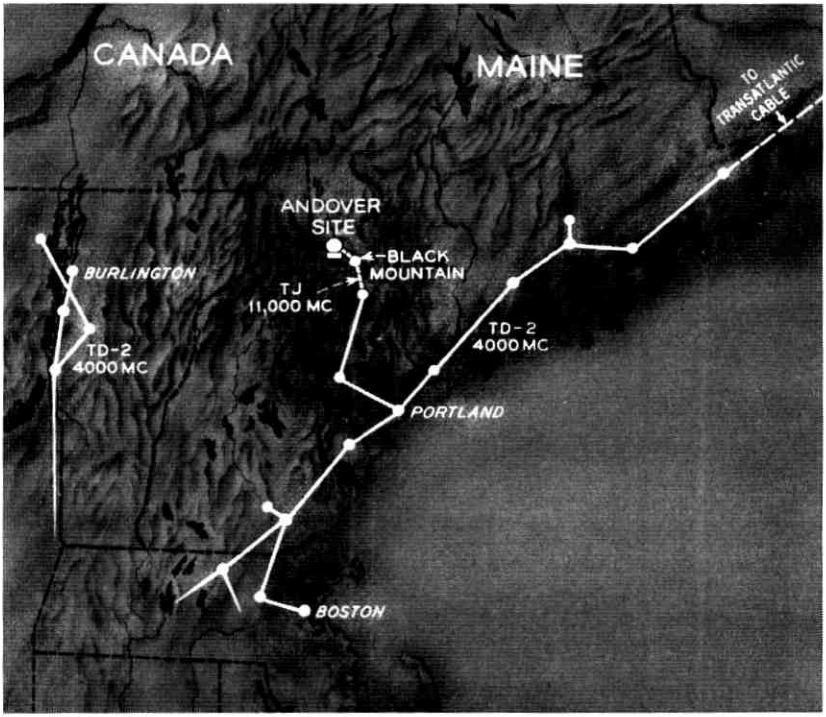

Fig. 7 — Map showing Andover site.

end of the TD-2 band, interference from the entrance link into the ground receiver has been completely avoided.

Fig. 8 is a general aerial view of the Andover site. The station is located in a wide shallow valley about 8 to 10 miles in diameter. The situation is such that additional shielding is obtained in almost all directions by surrounding hills. These are not high enough, however, to interfere significantly with the visibility of the satellite. The profile of the optical horizon from the site of the antenna is shown in Fig. 9. The tower in the foreground of Fig. 8 is for the last station of the radio entrance link. This tower houses, in addition to the TJ repeater, an electrical model of the satellite for calibrating the ground station.

A close-up aerial view of the station is shown in Fig. 10. The station is situated on a tract of about 1100 acres on top of a low rounded hill at an elevation of about 900 feet in the center of the valley. This area is large enough to permit future expansion for commercial operation. The most prominent feature of the station is the large inflated radome that

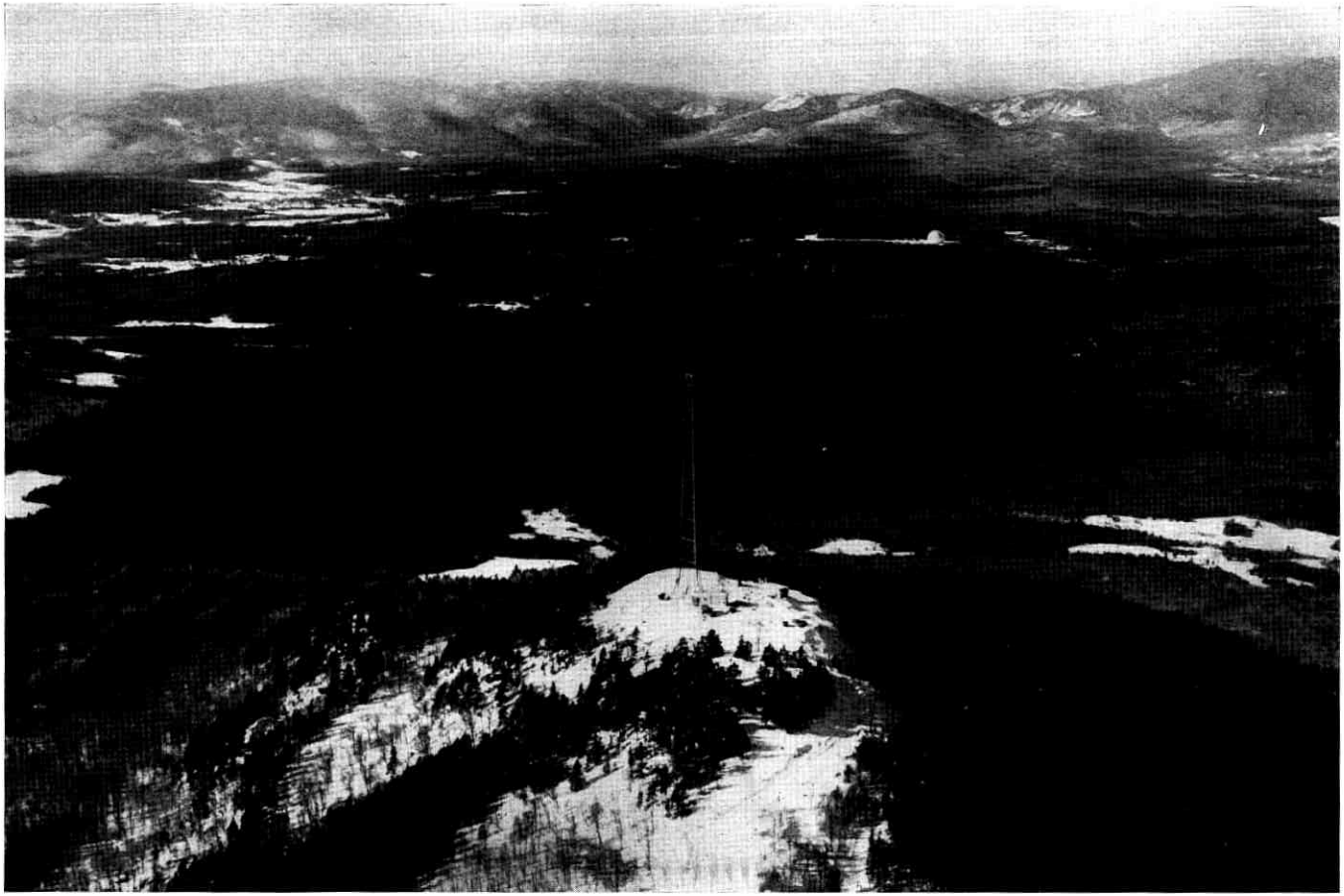

Fig. 8 — Aerial view of site

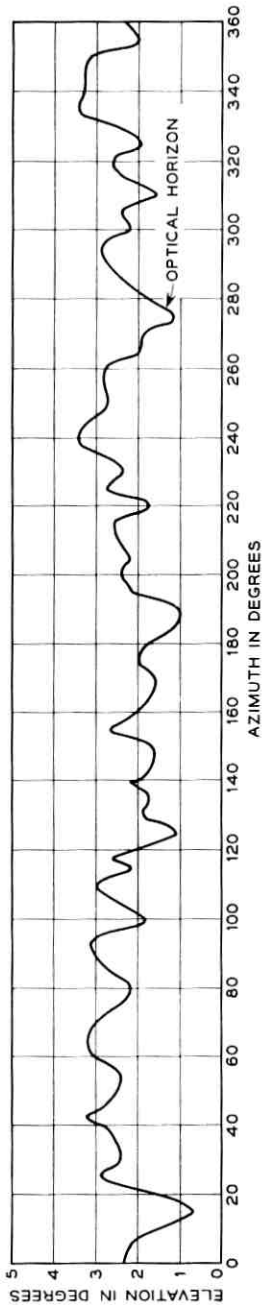

Fig. 9 — Optical horizon at Andover.

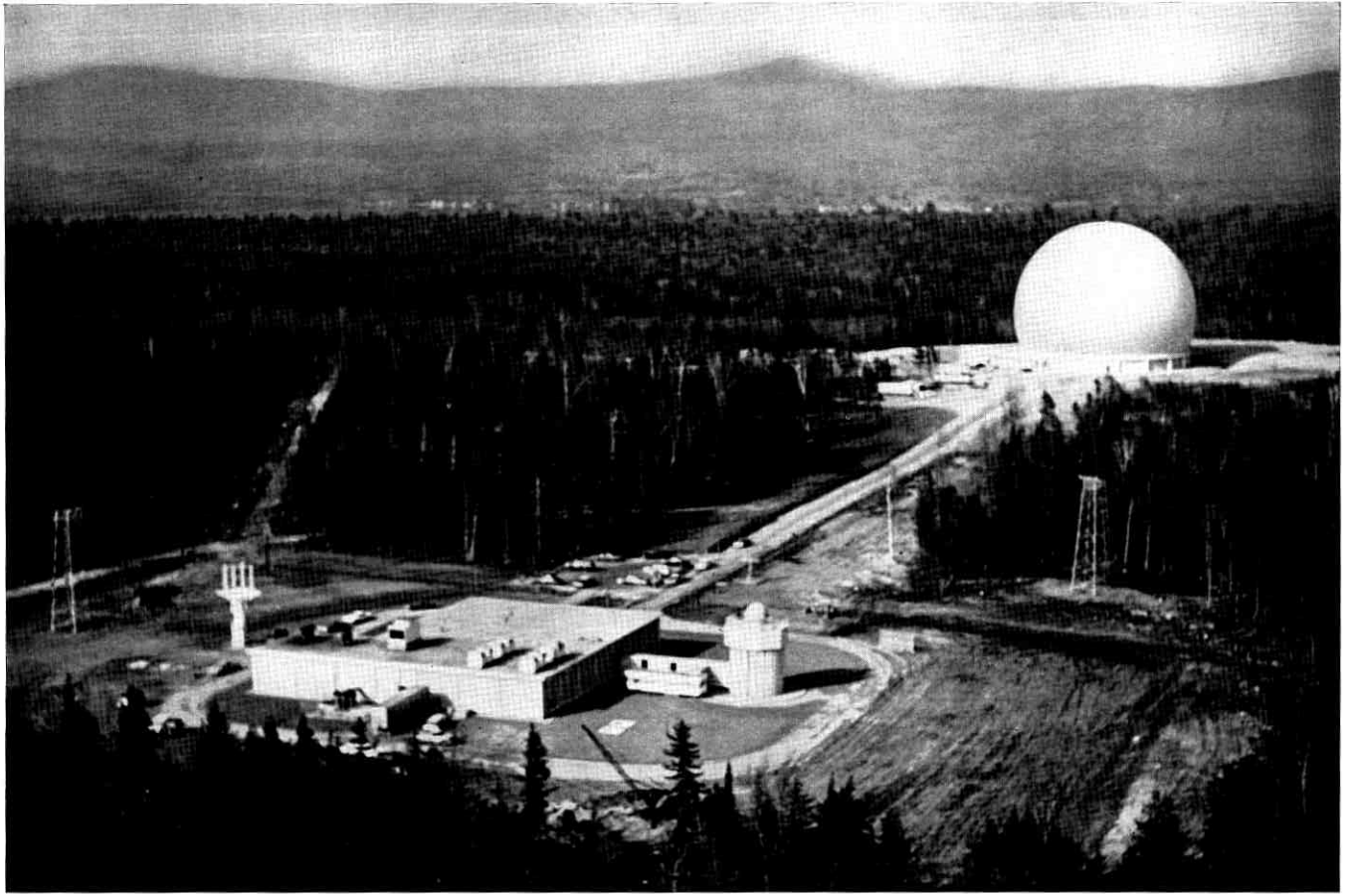

shelters the horn antenna. It is made of rubberized Dacron and is 210 feet in diameter and 165 feet high. The control building in the foreground houses the equipment for terminating the telephone and television circuits brought into the station by the entrance link. It contains the equipment for making transmission tests through the satellite, as well as the heating plant for the station and diesel generators for power. Flanking the control building on the right is the precision tracking antenna on a concrete pylon and, on the left, the quad-helix command tracker antenna.

7.2 *Ground Station Transmission Plan*

A general transmission plan of the station is shown in Fig. 11. Tests or demonstrations that originate at other locations are received at 11 gc and demodulated to baseband in the control building. The link from the control building to the large horn is by video pairs. This is carried to equipment rooms on the antenna structure through slip rings. The baseband signals are used to frequency modulate the 6390-mc ground transmitter, which is connected to the horn through diplexing equipment. Incoming signals from the satellite at 4170 mc are connected to the radio receiver through the diplexer and demodulated to baseband in the equipment room and then transmitted to the control building by video pairs.

7.3 *Horn-Reflector Antenna*

The communications antenna at Andover is a much enlarged version of similar antennas widely used on Bell System microwave relay routes. A horn reflector of this type with a 20 × 20 foot aperture was used at Holmdel in the Echo experiments. Fig. 12 shows a model of the Andover antenna.* For structural reasons, the horn at Andover is conical rather than pyramidal, as was the case in the smaller versions. The antenna rotates in azimuth on two concentric rails and in elevation about the axis of the conical feed horn on two large bearings. Two equipment rooms are carried on the structure. The maser is in the upper room near the apex of the horn.

This configuration has several advantages over other possible forms. It is very broadband, presents an excellent impedance to the transmitter, and the parabolic surface is efficiently illuminated. Most im-

* Since the antenna was built under the radome and has never been exposed, it has not been possible to obtain a really satisfactory picture of the actual hardware.

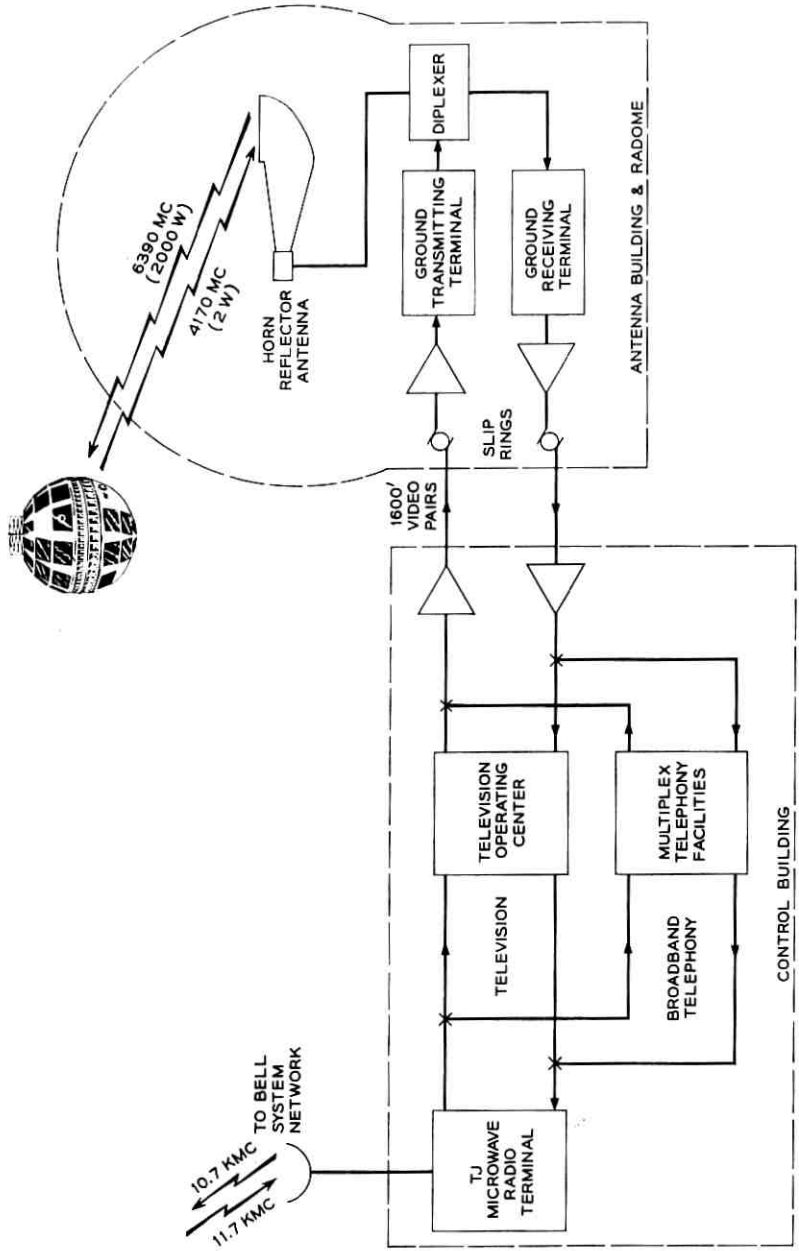

Fig. 11 — General transmission plan — Andover.

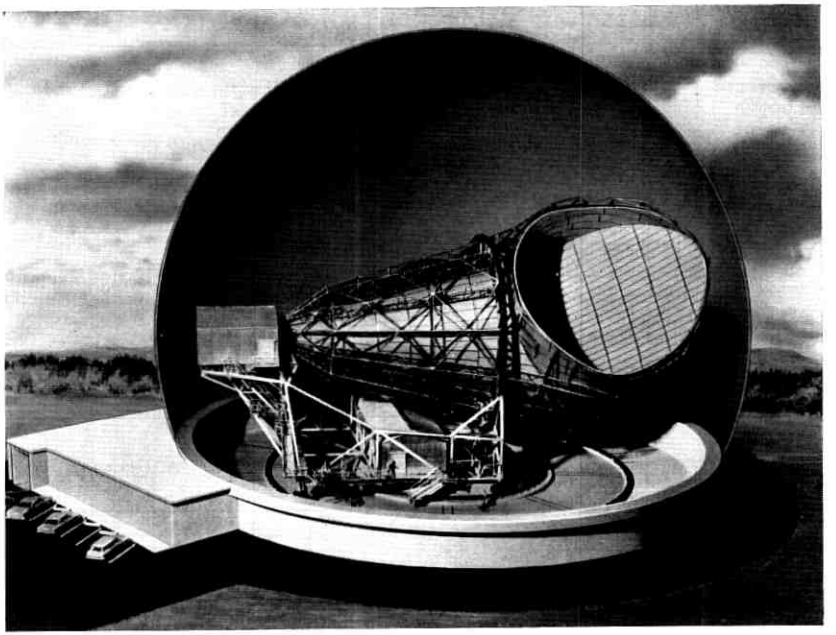

Fig. 12 — Model of Andover, Maine, antenna.

portant, however, for the present application, the antenna has very low side and back lobes and may be connected to the receiver with short, low-loss connections resulting in a low system noise temperature.

Table III gives the principal physical and performance characteristics of the Andover horn. The details of performance are covered in later papers in this series. The precision achieved on the critical parabolic surfaces is such that operation at frequencies considerably higher than 6000 mc is possible. Pointing calibration was made by tracking radio stars. The structural distortions indicated by these calibrations are corrected for in the electronic antenna direction system. The corrections are known with sufficient accuracy that, with good ephemeris data, the antenna beam may be pointed at the satellite within a small fraction of a beamwidth.

All connections to the antenna are made through slip rings located around a pintle bearing at the azimuth axis. This permits free rotation of the antenna. Cooling water, power and control leads are also carried through rotating joints and slip rings in the pintle bearing.

TABLE III — HORN-REFLECTOR ANTENNA

Structural Characteristics		
Aperture	3600 square feet	
Length	177 feet	
Weight	380 tons	
Reflector accuracy	0.060 inch (1 sigma)	
	Azimuth	Elevation
Tracking and Slewing		
Maximum tracking velocity	1.5 deg/sec	1.5 deg/sec
Maximum slewing velocity	1.5 deg/sec	1.5 deg/sec
Maximum acceleration	1.3 deg/sec^2	3.0 deg/sec^2
Error during acceleration	0.26° per deg per sec^2	
	4170 mc	6390 mc
Performance		
Gain	58 db	61 db
Beamwidth (3-db points)	0.23 degree	0.16 degree

7.4 *Transmitter and Receiver*

The ground transmitter, shown in Fig. 13, provides an FM signal of 2000 watts maximum with a peak deviation of ±10 mc. The FM deviator and modulator amplifier stages are modified versions of TH radio transmitting equipment. The output stage is a power amplifier using a high-power traveling-wave tube.

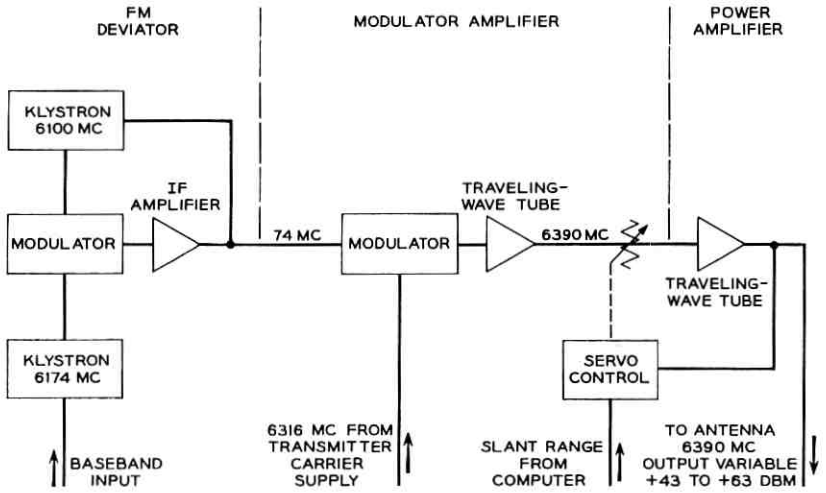

Fig. 13 — Block diagram — ground transmitter.

The center frequency is 6390 mc when the transmitter is used for television or other straight-away tests. It can be shifted ±5 mc for two-way message experiments. The servo control shown can be used to vary the output power to maintain a prescribed received power at the satellite. This is used in two-way telephone tests, where approximately equal carrier levels at the satellite are desired.

A block diagram of the receiver is shown in Fig. 14. Signals received through the antenna are first amplified 40 db by a traveling-wave ruby maser. They are then converted to a 74-mc IF frequency, where most of the receiver gain is obtained. The signals are then shifted back to the 6-gc band for demodulation in a frequency compression detector. This detector permits the baseband signal-to-noise advantage of wide-deviation FM to be realized without the loss in threshold level that would be suffered in a conventional detector of the same bandwidth. An effective compression of the noise band is achieved by feeding back part of the baseband output to a voltage-controlled local oscillator. The local oscillator follows the deviations of the incoming signal, and in this way the IF frequency deviations applied to the discriminator are reduced by the feedback factor. An improvement in threshold of 4–5 db is obtained by the feedback receiver. A standard FM detector operating at 74 mc may also be used.

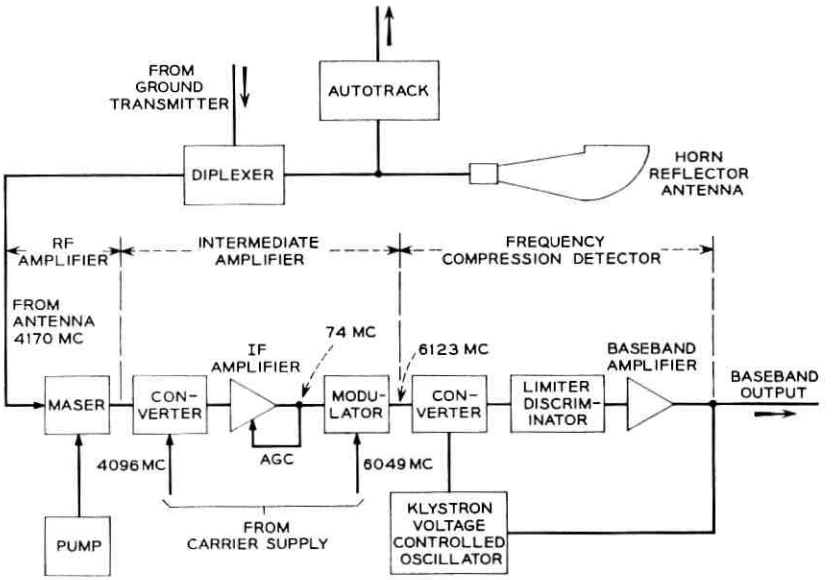

Fig. 14 — Block diagram — ground receiver.

The transmitter and receiver are located physically in the upper equipment room of the antenna structure. Unlike a conventional center-fed parabolic dish, the horn antenna allows for considerable equipment to be mounted at the feed. This has been used to good advantage at Andover, where feeder losses are kept to a minimum by locating the transmitter power stage and the maser close to the antenna feed.

7.5 *Tracking Equipment*

The tracking system at Andover consists of four parts. These are the: (1) command tracker and its control, (2) precision tracker and control, (3) horn-reflector antenna and control, and (4) computers. This is more elaborate than would be required for a commercial system. However, the flexibility that this arrangement provides is very useful in evaluating methods for future systems. Fig. 15 shows the four parts of the system and their interrelation.

The computer (IBM 1620) is programmed to derive drive tapes from any one of three different sources of information: (1) azimuth, elevation and time data from previous passes, (2) orbital elements, (3) X-Y-Z topocentric coordinates obtained from NASA. The drive tapes can be used to position all three antennas to the predicted position of the satellite. A different mode of operation which does not depend on accurate drive tapes is as follows.

The command tracker, with its wide beam of 20°, picks up the 136-mc beacon as the satellite rises above the horizon. When autotrack has been obtained with this antenna, the satellite is located to within 1°. If the telemetry indicates that the satellite is in satisfactory condition, the command sequence is started. By means of the three sequenced commands at 123 mc, the repeater in the satellite is turned on. At this time, the satellite transmits the 4080-mc beacon. With the precision tracker slaved to the command tracker, it can now acquire the microwave beacon with its 2° beam and autotrack. In this mode the precision tracker locates the satellite to within 0.02°. The horn antenna can then be slaved to the precision tracker and acquire the microwave beacon with its 0.2° beam and autotrack. Once this is accomplished, the horn can continue to autotrack without further aid.

The step-by-step procedure as outlined above is just one of many possible modes of operation. With good pointing information, the horn can be directed to acquire and then autotrack the satellite without going through the steps outlined above. This has been done on many occasions at Andover, and it is expected that a commercial system would be operated on this basis.

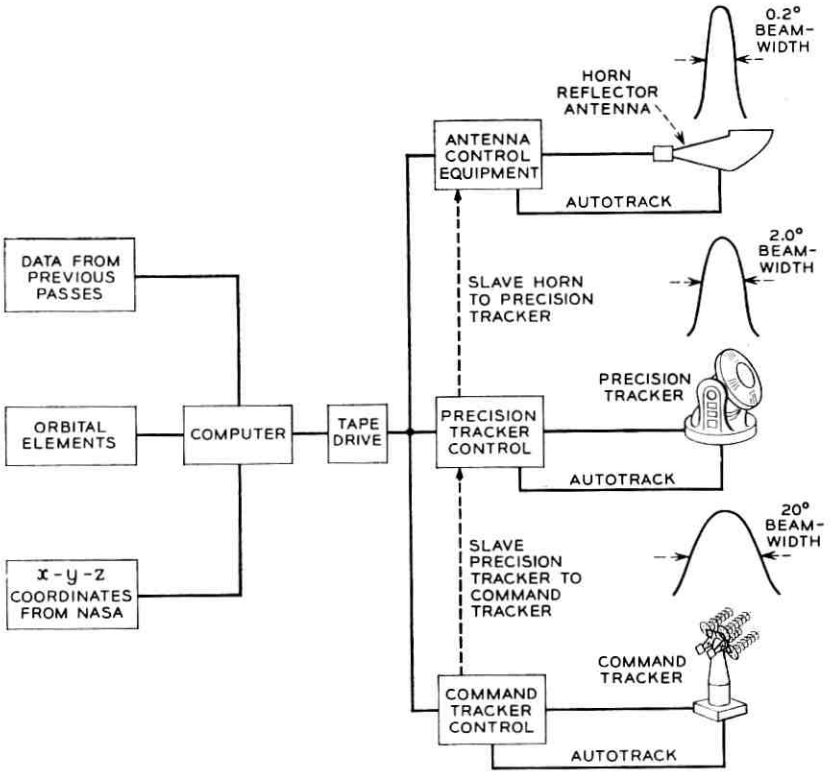

Fig. 15 — Block diagram of tracking system.

VIII. FACILITIES AT CAPE CANAVERAL

Special facilities were provided at Cape Canaveral for testing the satellite. Test equipment was located in three vans adjacent to Bell Laboratories' guidance facility and on the gantry. A command tracker like the one at Andover was provided. Compatibility of the radio frequency systems in a prototype model of the satellite with other systems involved in launching was verified about two weeks before launch. The flyable model was tested daily from the time of its arrival at the Cape and after mating with the third stage of the rocket, after spin balancing and on the gantry up to the time of launch. From lift-off, the satellite was tracked and telemetry monitored. During the following months, the facilities were used to augment Andover by receiving telemetry and, in some cases, by sending commands.

IX. TRANSMISSION PERFORMANCE

The broadband signals transmitted through the Telstar satellite were television and 600 telephone channels simulated by noise loading. In addition, the performance with 12 two-way voice channels was evaluated as well as performance with data and other special signals. Performance objectives for signals of these types have been established by the Bell System and the CCIR. Because of limitations imposed by the rocket on weight and, therefore, power, some compromise was necessary and the objectives were not met in all cases. However, the quality of these signals, when transmitted through the satellite link, is reasonably close to the objective for commercial service.

9.1 *Over-all Performance*

Table IV shows the performance with the satellite at a range of 5000 nm for the three main types of service considered: TV, 600-channel one-way telephony, and twelve-channel two-way telephony.

For TV transmission the audio signal is transmitted by frequency modulating a subcarrier located at 4.5 mc. This limits the bandwidth available for picture transmission to 3 mc. Other techniques for transmitting the sound would remove this limitation.

Two-way telephony is achieved by transmitting two carriers from two ground stations through the satellite simultaneously. These carriers are separated by ten megacycles with the carrier from Andover 5 mc above the normal center frequency and the carrier from Europe 5 mc below. Because of the lack of isotropy in the satellite antenna pattern, the two carriers may be received by the satellite with a 6-db level difference. Under this condition, compression in the TWT will cause the

TABLE IV — PERFORMANCE OF *Telstar* SYSTEM

Television	
Bandwidth	3 mc
Peak-to-peak signal to rms noise (unweighted)	41 db
Peak audio signal to rms noise	56 db
600-Channel One-Way Message	
Top telephone channel noise	49 dbrn 0*
Improvement with pre-emphasis	3 db
Noise in top telephone channel with pre-emphasis	46 dbrn 0
Twelve-Channel Two-Way Message	
Noise in top channel	45 dbrn 0

* Measured with 3A noise meter with C message weighting. 0 dbrn equals 1 picowatt at 1000 cycles.[9]

weaker carrier to be transmitted 10 db below maximum output power. The 45 dbrn 0 given in Table IV is based upon this weaker carrier power.

At 5000 nm, the quality achieved for TV transmission would be judged to be a slight picture impairment. Also under these conditions, the amount of noise in the poorest telephone channel would be 6 db more than the tentative CCIR objectives for a commercial grade circuit. For an experimental system, this performance is considered reasonable. The important consideration is that measured performance was consistent with actual parameters of the system, and that no unexplained degradations occurred.

9.2 *Fluctuation Noise*

The controlling parameter in a system such as this is noise. Table V shows the fluctuation noise performance for the ground-to-satellite and satellite-to-ground paths.

It will be noted from the Table V that the carrier-to-noise ratio in the down path is 15 db. Even with this low carrier-to-noise ratio, high quality performance is obtained by means of wide deviation FM. How-

TABLE V — FLUCTUATION NOISE

Up Path: Andover to satellite	
Maximum transmitted power (2 kw)	63 dbm
Ground waveguide losses	1 db
Ground antenna gain	61 db
Path loss (5000 nm)	187 db
Satellite antenna gain	0 db
Received carrier power	−64 dbm
Satellite antenna feed loss	2 db
Satellite receiver noise figure*	16.5 db
Noise power in 25-mc band	−83.5 dbm
Carrier-to-noise ratio in 25-mc band	17.5 db
Down Path: Satellite to Andover	
Satellite power (2 watts)	33 dbm
Path loss (5000 nm)	184 db
Satellite antenna gain	0 db
Ground antenna gain	58 db
Received carrier power	−93 dbm
System noise (50°K, 25-mc bandwidth)	−108 dbm
Carrier-to-noise ratio in 25-mc band	15 db

* The noise figure of the satellite as measured by a noise lamp is 13.5 db ±1 db. However, the noise does not have a flat spectrum over the band of interest and this number applies in the region where the noise is flat. Measurements made of the system noise spectrum using narrow-band analyzers indicate a satellite noise figure in the flat region of 15 db ±2 db. If the noise spectrum around the carrier is integrated over a 20-mc band, then an equivalent noise figure of 16.5 db ±2 db is obtained.

ever, at 10 db carrier-to-noise ratio a conventional FM receiver will start to rapidly degrade the demodulated signal. The carrier-to-noise ratio in the down path, being 15 db, is only 5 db above this threshold. Therefore, a frequency compression demodulator has been used in the Telstar system. This technique improves the threshold by about 5 db, allowing adequate margin against the onset of breaking. At 5000 nm range and with 50°K system noise temperature, the breaking margin due to the down link is 10 db. The ground to satellite path also contributes to the over-all system noise and reduces the breaking margin. With 2 kw radiated from the ground at 5000-nm range, the carrier to noise ratio at the satellite is 17.5 db. At this range for both the up and down path, the effect of the up path is to reduce the over-all carrier-to-noise ratio and the breaking margin by about 2 db. Most of the time the range is shorter and the performance is better.

A number of other factors may reduce the carrier-to-noise ratio and degrade the breaking margin. These are noncircular polarization, satellite antenna pattern, ground antenna mispointing and rain.

To the extent that the antennas at both ends of the link do not have circular polarization but are somewhat elliptic, i.e., have an axial ratio other than unity, there will be some loss of signal. The axial ratio of the Andover ground antenna system is in the order of 0.5 db and that of the satellite is 2 db in the equatorial plane. Maximum loss due to these axial ratios is about 0.1 db. When the satellite is viewed at angles 30° or more from the spin axis, the axial ratio may be as much as 4 db, but even under these conditions, the loss due to this effect is only 0.25 db.

The satellite antenna has essentially 0-db gain in the equatorial plane. It is down about 6 db at an angle $\pm 60°$ from the equator. The pattern is quite smooth around the spin axis with a ripple of about ± 1 db. This is adequate to maintain the signal above the FM threshold, especially since an unfavorable aspect and maximum range will rarely coincide.

The signal loss due to antenna mispointing is less than 0.1 db. This is due to the use of the vernier autotrack, which is capable of maintaining the antenna beam to within 0.005° of the satellite's position.

It has been observed that system noise temperature can increase to 130°K in the presence of heavy rain. This can be ascribed to the increase in sky noise and the effect of the wet radome. The degradation of carrier-to-noise ratio under these conditions is 4 db compared to conditions on a clear day with the antenna at zenith. With the system parameters described and the margin available, operation above threshold is still possible.

TABLE VI — FM DEVIATIONS

Video	
TV bandwidth	3 mc
Peak-to-peak frequency deviation (picture)	14 mc
Peak-to-peak frequency deviation (picture + aural subcarrier)	16.8 mc
Bandwidth of audio channel	8 kc
Peak-to-peak frequency deviation (audio on 4.5-mc aural subcarrier)	100 kc
600-Channel Noise Loading	
Peak frequency deviation due to noise loading signal	10 mc
RMS frequency deviation due to noise loading signal	1.77 mc
RMS frequency deviation per telephone channel	72 kc
Twelve-Channel Two-Way Message	
Baseband signal	60–108 kc
Peak frequency deviation for twelve channels	1 mc
RMS frequency deviation per channel	16 kc

9.3 *FM Deviations*

Based upon the fluctuation noise indicated in Table V, the required modulation indices were determined. These are given in Table VI.

9.4 *Amplitude and Phase Distortion*

The presence of amplitude and phase distortion causes transmission degradation which adds to that caused by thermal noise. This form of distortion does not affect the breaking margin, but adds to the noise at baseband. The most important forms of nonlinear distortions are envelope delay distortions[10] and differential gain. In a two-link radio relay system such as Telstar, this distortion can be made small compared to thermal noise. In the allocation of system impairments, the total for intermodulation noise is 36 dbrn at the 0-db transmission level. Fig. 16

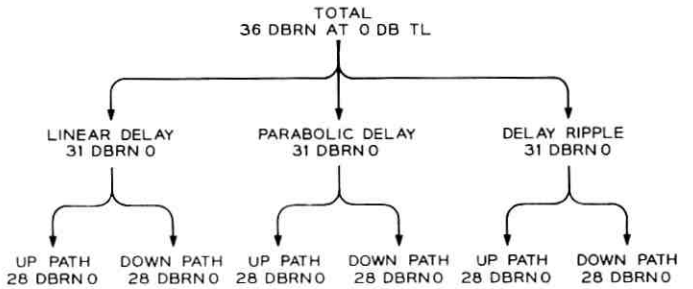

Fig. 16 — Allocation of intermodulation noise.

TABLE VII — DELAY DISTORTION OBJECTIVES

Frequency with respect to carrier — mc	±2	±4	±6	±8	±10
Linear delay distortion — nanoseconds	1.2	2.4	3.6	4.8	6
Parabolic delay distortion — nanoseconds	1.1	4.5	10	18	28
Delay Ripple					
Ripple periodicity — mc	0.3	0.6	1.5	3.0	6	15
Peak delay ripple — nanoseconds	30	15	6	3	1.5	1.5

indicates how this total is divided among the various sources. Assuming the parameters indicated previously for the 600-channel noise loading signal and the use of pre-emphasis,* Table VII indicates the delay distortion objectives. The figures indicated in Table VII apply to both the up-path and down-path equally.

The differential phase would be 4.2° if the objectives in Table VII are met. For N.T.S.C. color the requirement is 5°, so that this set of performance objectives is consistent. The performance measured for television and the 600 telephone channel simulated noise load indicates that these objectives have been met.

X. CONCLUSIONS

The Telstar system has demonstrated that wideband communications by means of an active satellite is feasible and that performance is predictable on the basis of system parameters. A ground station system has been tested and shown to be operable under a wide range of weather conditions and with a variety of tracking techniques. A large amount of data on the space environment has been gathered and analyzed and has added valuable information concerning the conditions which a satellite must withstand. The satellite, the Andover ground station, and the radiation experiment are discussed in more detail in companion papers.

REFERENCES

1. Jakes, W. C., Jr., Participation of Bell Telephone Laboratories in Project Echo and Experimental Results, B.S.T.J., **40**, July, 1961, pp. 975–1028; see also other papers in this Project Echo issue.
2. Rinehart, J. D., and Robbins, M. F., Characteristics of the Service Provided by Communications Satellites in Uncontrolled Orbits, B.S.T.J., **41**, September, 1962, pp. 1621–1670.
3. Pierce, J. R., and Kompfner, R., Transoceanic Communication by Means of Satellites, Proc. I.R.E., **47**, March, 1959, pp. 372–380.
4. Hogg, D. C., and Semplak, R. A., The Effect of Rain and Water Vapor on

* The pre-emphasis assumed starts at 3 mc with 6 db per octave slope and continues until a total of 10 db of pre-emphasis is reached.

Sky Noise at Centimeter Wavelengths, B.S.T.J., **40**, September, 1961, pp. 1331–1348.
5. Hathaway, S. C., and Evans, H. W., Radio Attenuation at 11 kmc and Some Implications Affecting Relay System Engineering, B.S.T.J., **38**, January, 1959, pp. 73–98.
6. Curtis, H. E., Interference between Satellite Communication Systems and Common Carrier Surface Systems, B.S.T.J., **41**, May, 1962, pp. 921–944.
7. Preparatory documents for Xth C.C.I.R. Plenary Assembly, particularly those submitted by the United States and the United Kingdom for Study Group IV.
8. Caserta, Nino, Engineering Considerations in the Selection of Andover, Maine, as the Location for the Bell System's Satellite Ground Station, A.I.E.E. Conference Paper, 62–328.
9. Cochran, W. T., and Lewinski, D. A., A New Measuring Set for Message Circuit Noise, B.S.T.J., **39**, July, 1960, pp. 911–932.
10. Bennett, W. R., Curtis, H. E., and Rice, S. O., Interchannel Interference in FM and PM Systems under Noise Loading Conditions, B.S.T.J., **34**, May, 1955, pp. 601–636.

A General Description of the *Telstar* Spacecraft

By R. H. SHENNUM and P. T. HAURY

(Manuscript received February 6, 1963)

The Telstar spacecraft design is discussed with emphasis on the electronics system. The description includes early planning, starting with frequency allocation considerations, and carries the program through electrical and mechanical design, construction and evaluation of the electronics system. The content is aimed at a broad introduction, depending on companion papers for many details of the spacecraft design.

I. INTRODUCTION

A description of the Telstar spacecraft presented in this paper is developed chronologically so that the reader may understand how each of the decisions influenced the design and construction which followed. Foremost in practical considerations affecting the satellite design was the selection of the Delta vehicle to launch the spacecraft.

II. BACKGROUND

Another paper of the series[1] outlines the needs for an orbit which would reach the vicinity of 3000 nautical miles apogee with a perigee of at least 500 nautical miles. The capability of the Delta vehicle to put a satellite into such an orbit, with the restriction of a launch from the Atlantic Missile Range and the desired inclination of the orbit plane to the equator of 45°, limited the permissible weight of the spacecraft to the order of 180 pounds. This weight limit was a severe restriction to incorporation of many ideas which were proposed early in the development. The second characteristic of the Delta which was influential in the Telstar spacecraft design was the existence of only two fairings and the decision not to undertake the development of a new one. The larger of the two, which had been tested repeatedly in satellite launchings and was large enough for our purposes, was selected as one which would be suitable for the spacecraft, as described in Section IX. The third aspect

of the Delta which was influential in planning the Telstar system was the need for spin stabilization of the third stage, which is a solid fuel motor without radio guidance. Typical spin rates of 200 revolutions per minute are used for this third stage and, while it would have been possible to despin the satellite after injection into orbit, it was judged desirable to utilize the spin for stabilization. In this way, the weight which would otherwise have been associated with a despin mechanism was saved. The detailed development of the structure of the frame, the shape of the spacecraft, and other mechanical aspects are treated in another paper in this issue.[2]

III. FREQUENCY ALLOCATION

Project Telstar was planned from the first as being primarily a communications experiment. However, other scientific experiments were also a very important part of the early planning. The selection of the frequency assignments used in Project Telstar is mentioned in Ref. 1. As discussed in that paper, some early thinking was based upon the assumption that new frequencies exclusively for the use of satellite communications could be assigned, and that interferences into and out of the ground receiver and transmitter, respectively, would be eliminated. It became apparent as the project developed, however, that such frequencies for exclusive use were not to be available for the Telstar experiment, so plans were developed for joint use of the 4-gc and 6-gc common-carrier bands with existing land-based microwave equipment. Both of these bands are in the broad spectral region where galactic noise is almost negligible compared to signals expected to be received at the ground station, and where atmospheric absorption is not a serious matter. The 4-gc band is, however, in the more favorable region and was chosen for the spacecraft microwave transmitter. The actual frequencies to be used were so chosen that they coordinated in the 4-gc region with existing TD-2 system assignments in this country and abroad, and in the 6-gc band with the TH system assignments, which are the same throughout the world. As seen in Fig. 1, the 16 satellite channels either coincide with existing common-carrier frequencies or fall approximately midway between bands. Concurrent work by H. E. Curtis was reported earlier.[3] His proposed frequency allocation plan, though very similar in most respects, resulted in frequencies slightly different from those actually used in the Telstar plan.

Although the Telstar repeater was conceived from the beginning as a single broadband amplifier, it was considered necessary that the frequencies used would be consistent with those which would later be

assigned to multichannel communications satellite systems. Allocations were studied and based on both six and eight channels allocated in each of the 500-mc* bands at 4 and 6 gc, respectively. The final choice of frequencies for the Telstar plan was based on an assignment which permits the eventual existence of eight broadband channels. In addition to the selection of frequencies for the broadband amplifier, a microwave beacon was an important part of the planning. Fig. 1 is a diagram giving the allocations both in the U. S. and in Europe in the 4- and 6-gc common-carrier bands and showing the location of the eight up and eight

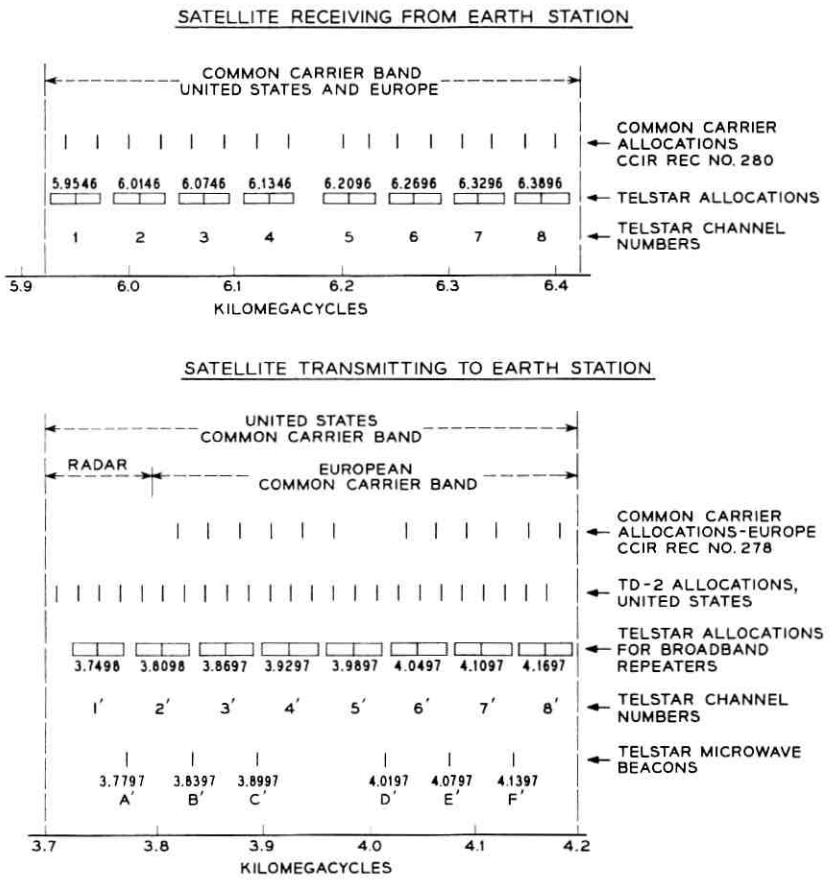

Fig. 1 — Frequency allocations

* Abroad, the 4-kmc band is narrower than the U. S. 500-mc assignment, as seen in Fig. 1.

down channels which are recommended for satellite use, as well as the frequencies for the associated microwave beacon tones. Channels 8 and 8′ with beacon E′ were used for Project Telstar.

To minimize the amount of electronic equipment in the spacecraft, the microwave beacon was obtained from the pump frequency of the up-conversion process. Consequently, the separation between the microwave beacon and the center of the broadband channel determined the midfrequency of the intermediate-frequency amplifier. The state of the art of transistor amplifiers for intermediate frequency use with proposed bandwidth of 50 mc dictated a center frequency above that which typically had been used for land-based microwave equipment. Preliminary designs of IF amplifiers which existed at the time of the beginning Telstar program made possible a center frequency of as high as 100 mc. The last constraint which was introduced into the calculations, and the one which in the final analysis proved to be the most limiting, was the requirement that the down conversion and the subsequent up conversion be accomplished by use of a pair of frequencies obtained from a coherent microwave carrier supply, with a single crystal-controlled oscillator producing both local oscillator signals. As will be noted in the discussion to follow, this last-stated objective was not to be attained, and an alternate method was adopted.

Fig. 2 shows a block diagram of the microwave carrier supply originally planned, with levels and frequencies sufficiently accurate for engineering purposes satisfying the previously stated requirements. This basic block diagram is readily expandable to obtain all necessary frequencies for an 8-channel system from a single crystal oscillator. Calculations by R. W. Hatch in unpublished work show that the noise associated with a non-

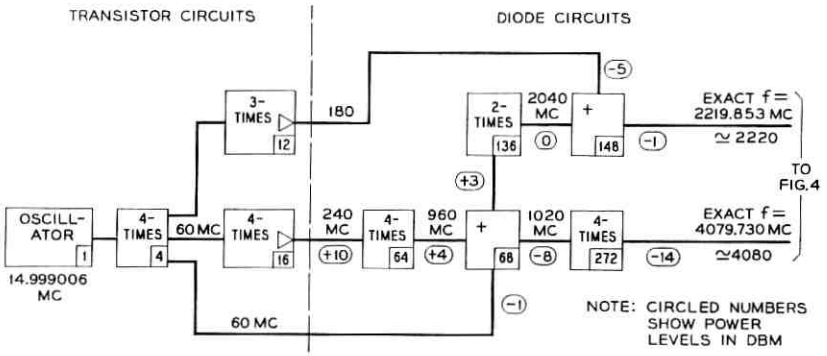

Fig. 2 — Single oscillator microwave carrier supply originally proposed.

coherent microwave carrier supply is not a major contributor to the over-all system noise. Despite the fact that it would have been desirable to eliminate this small noise contribution, the schedule of the Telstar program did not permit carrying to completion the circuitry indicated in Fig. 2. The decision was made about midway through the program (Aug., 1961) to implement the microwave carrier supply along the lines shown in Fig. 3, where two separate crystals are used. The resulting frequencies are the same as those in Fig. 2 to the first six significant figures. Better coordination with the existing land-based microwave systems could have been obtained by use of the two-oscillator approach. However, other parts of the program were so far advanced that a frequency change at that time was not possible.

IV. THE ELECTRICAL REQUIREMENTS OF THE MICROWAVE RECEIVER

The over-all signal-to-noise performance is summarized in a preceding paper.[1] Parts of this will be repeated and expanded in this discussion in order that an over-all description of the satellite proper may be contained within this paper. Data given here will supply the details necessary for the understanding of the block diagram of the communications repeater shown in Fig. 4. The nominal planned received signal for mid-range operation at the input to the converter is −60 dbm. There is an allocation of loss of 2 db between this point and the antenna, so that the nominal signal received into the antenna is −58 dbm. The IF amplifier operates with a midfrequency of approximately 90 mc and has a bandwidth requirement at the 1-db points of ±25 mc about this midfrequency. The automatic gain control was specified to operate over a signal range of approximately +5 to −12 db. The traveling-wave tube

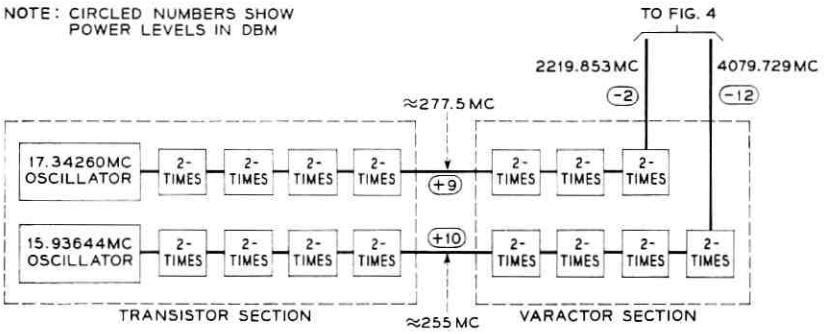

Fig. 3 — Final microwave carrier supply.

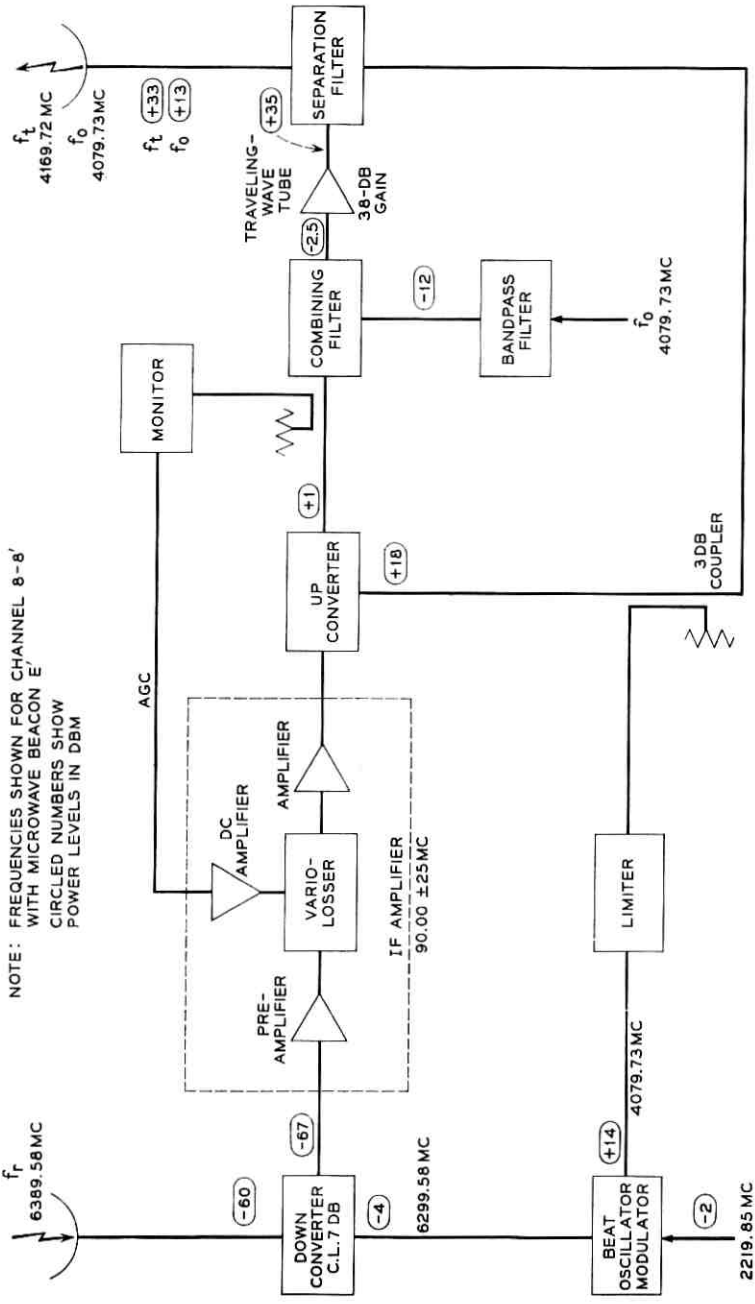

Fig. 4 — Telstar satellite amplifier simplified block diagram.

(TWT), the only electron tube in the Telstar satellite, amplifies two signals simultaneously. One, the main broadband signal with approximately 50 mc potential bandwidth, is required at an operating point in the tube at which the gain is 37.5 db and the power output is +35 dbm. The second signal at the output of the tube is 13 db lower than this main signal (i.e., +22 dbm), and under the condition of simultaneous existence of the two signals, separated in level by 13 db, the gain for the low-level signal is 35 db. The circuitry thus operates in a reflex mode such that the 4080-mc signal, which is one of the outputs of the microwave carrier supply, is combined with the main signal in the combining filter, amplified through the traveling-wave tube, and in the separation filter is largely transmitted back into the microwave repeater for use as the pump frequency in the up-conversion process. Part of the 4080-mc signal is also combined in the beat-oscillator modulator with a second output from the microwave carrier supply to produce the beat oscillator frequency for the down-conversion process. As will be discussed later, a small part of this 4080-mc signal at the output of the TWT is directed by the separation filter directly to the microwave transmitting antenna, where it is radiated to the earth station and used by the precision tracker and system autotrack for acquisition and tracking of the satellite. The radiated signal strength of the 4080-mc beacon at the output of transmitting antenna was required to be at a minimum power level of +13 dbm. The circuit design of the microwave repeater with its TWT in this dual-amplification mode with two signals widely separated in level was based on analytical predictions and early experimental work which was done by P. R. Wickliffe and reported in unpublished work. The experimental work was performed at 6 gc with traveling-wave tubes which were of sufficiently similar structure to the tube proposed for use in the Telstar repeater circuit that it was felt reasonable to extrapolate the results to the 4-gc operation.

V. THE ELECTRICAL DESIGN OF THE COMMUNICATIONS REPEATER

The operating levels of the communications repeater are given in the block diagram of Fig. 4. The design requirements have been discussed in the preceding section. This section describes briefly the realization of the system satisfying these requirements. The down-conversion system, consisting of down converter and its associated filters and beat oscillator signal from the microwave carrier supply, is in broad principle similar to those used in earlier land-based microwave systems.[4] The physical structure is, however, quite different and is based on operation of the

received signal and beat oscillator signal in orthogonal modes in a round waveguide. This is described in detail in another paper in this issue.[5] The noise figure and conversion loss, 12.5 db and 7 db respectively, resulting from this configuration, are both within the ranges which have been obtained at this frequency and bandwidth by earlier experimenters. However, the level of the beat oscillator signal (−4.0 dbm) to the down converter is substantially below that normally used. This low oscillator signal level was, of course, used because of the necessity to conserve power and to operate at the lowest practical level; however, small changes in power level are not troublesome with the regulation schemes provided. Similar statements concerning power levels can be made about almost every other block within the communications repeater.

The IF amplifier and associated automatic gain control will be described in considerable detail later in this issue.[5] The IF amplifier has a common-emitter doublet input stage working into a resistive load. The bandwidth of the IF amplifier is 50 mc, while the noise figure is 4.5 db. The 90-mc signal is amplified using broad-band common-emitter transistors with local shunt feedback. The amplifier is so designed that, should one of these transistors open circuit, the feedback network would operate to continue to provide a fairly flat transmission path without excessive loss.

The last two stages of the amplifier are common-base circuits. These circuits provide linear amplification at output power levels up to +6 dbm. A 20-db return loss is maintained at the output over the 50-mc frequency band. The maximum gain of the IF amplifier is 87 db. The gain of the amplifier is controlled using two similar resistive T-network diode variolossers. Each gives approximately 15 db of control range, more than satisfying the original requirement for a 17-db range.

The AGC variolossers are driven by a dc amplifier requiring four transistors. These are arranged in a differential input stage followed by two common-emitter stages. The sensing for the AGC is a measure of the signal output of the up converter, in contrast to the more usual method of monitoring the output of the IF amplifier. Since the up converter operates with relatively low pump power, its output is subject to some variations caused by temperature changes and aging. The action of the AGC compensates for these variations and ensures constant input to the TWT.

The up-converter is a balanced diode modulator in which the 90-mc signal is shifted to a frequency band centered at 4170 mc. It was designed for temperature stability and minimum susceptibility to fluctuations in

beat oscillator power. Consequently, the conversion gain of the device is low — only about 2 db.

The 4170-mc signal passes through a filter-monitor combination. The monitor is part of the AGC circuit, which ensures that the level of the signal fed to the TWT is constant. The monitor contains two separate diodes, mounted in the waveguide in a configuration designed to minimize directivity. The time and temperature stability of the monitor is better than ± 0.25 db.

The TWT amplifier is unusual for its high efficiency. A single-reversal permanent magnet is used for beam focusing in place of the customary straight field magnet such as that used in TH radio.[6] In addition to saving weight, this arrangement gives a substantial reduction in the associated magnetic dipole of the spacecraft, which must be neutralized by the addition of small magnets on the surface of the satellite to limit interaction with the earth's magnetic field. A net magnetic moment for the satellite of 1 ampere-turn meter squared was attained.

Some of the design parameters of the traveling-wave tube are given in Table I. It is of interest to note that the voltages and currents have been chosen to give maximum over-all efficiency, including the heater power, rather than maximum electronic efficiency. In the present design, lowering the collector voltage below the helix voltage increases the efficiency appreciably. The TWT is operated in the nearly linear region, where the output power is about 1.25 db below the saturation output power. This is done both to assure stability of the over-all circuit and to reduce intermodulation. The anode voltage is kept above the helix voltage to provide ion pumping. Further details describing the tube have been included in another article in this issue.[6]

The final microwave carrier supply provides local signals at approximately 4080 mc and 2220 mc. These frequencies are derived from crystal oscillators which drive transistors and varactor-multiplier chains as shown in Fig. 3. The two paths are similar except for the output stages, so only the one with the larger multiplication is discussed. The

TABLE I

Helix voltage	1500 volts
Anode voltage	1750 volts
Collector voltage	750 volts
Cathode current	17.5 milliamperes
Output power (saturated)	4.5 watts
Heater power	1.5 watts
Collector power	13 watts
Gain (saturated)	36.5 decibels

nominal 4080-mc (microwave-beacon frequency) path starts with a solid-state Pierce oscillator at about 15.9 megacycles. To ensure maximum short-term stability, the oscillator is operated at a high level. Since the crystal is driven hard, it is necessary to have crystals that are free from unwanted resonances at this operation level over the whole temperature range likely to be encountered. The long-term stability is determined mainly by the temperature characteristic of the crystals. All units manufactured met the specified limit of five parts per million, and in the Telstar satellite the microwave beacon has a stability of better than one part per million from 0 to 60°C. It is expected that the effect of aging will be of the order of one part per million per year.

The output of the oscillator is fed to a doubler stage and then the signal is alternately passed through transistor-doubler stages and amplifier stages until a frequency of 255 mc is reached. Temperature compensation is provided to the last four stages, keeping the output constant to 0.2 db over a range from $-10°$ to $+50°$C.

The 255-mc signal from the last transistor doubler is passed to a three-stage varactor multiplier using conventional lumped circuits. The output from these circuits is fed into a coaxial doubler, which connects the 4080-mc signal through a transducer into the combining network that feeds the traveling-wave tube. The units performed well and the entire harmonic-generator system showed less than 1.5 db variation in level over the temperature range 0 to 50°C.

VI. TELEMETRY AND COMMAND

The need for a telemetry system arises from three types of required measurements:

(a) communications experiment data such as transmitted and received signal strengths, and states of several relays;

(b) general "housekeeping" data such as temperatures, pressure in canister, currents and voltages of subsystems;

(c) radiation experiment measurements related both to integrated damage to solar cells and transistors and to counts of electrons and protons in several energy bands.

To simplify the telemetry in a way which is consistent with the design of the entire electronics system, it was decided to use a one-per-minute frame rate, which is very slow compared to normal industry standards. A tabulation of the necessary measurements in the three categories previously listed indicated that 118 channels would provide the required

data. The final channel assignment is described in some detail in another paper of this series.[7] The channels are approximately equally divided into the three categories which were listed earlier. Because of the needs of the radiation experiment for high accuracy, it was decided to use a PCM system with 7 bits, giving slightly better than 1 per cent basic coding accuracy and an over-all accuracy including the effect of gating of approximately 1 per cent. While most of the channels are sampled in analog fashion and converted to digital form, direct digital counts are used in much of the radiation particle counting, in order to increase the accuracy of the measurements. This is described in detail by Ref. 8 of this issue. The modulation scheme utilized to impress the telemetry information on the 136.05-mc VHF beacon (the power output of which is +23 dbm) involves two stages of modulation. The PCM signal is first changed to a frequency-shift form of modulation with frequencies of 3225 and 2775 cps representing the binary 1 and 0, respectively. This is then amplitude-modulated onto the 136.05-mc carrier. This form of modulation was utilized to keep the major sidebands far enough removed from the 136.05-mc carrier that it would be possible to utilize the carrier for tracking purposes in the presence of the telemetry signal. The percentage modulation was limited to 50 per cent to limit the sideband amplitudes and hence to ease tracking problems.

The need for a command system was established when the decision was made to operate the TWT only part time and to depend upon energy stored in a nickel-cadmium battery for the operation of the tube. The solar plant, when new, delivered slightly under 15 watts. This is expected to fall to two-thirds this value in a two-year period. With all the subsystems in the satellite operating simultaneously, the required power is more than twice that which is available from the new, undamaged solar plant. The command system provides sequential turn-on and turn-off of three voltages for the traveling-wave tube. The sequencing is controlled from the ground in order to permit the simplest possible satellite electronics system. In addition to the five commands which are utilized for TWT operation, commands are provided to turn the telemetry off and on and to switch or reverse the current in an orientation loop provided to correct spin-axis orientation, should this be required. Commands are also provided for test purposes to evaluate the operation of the two separate redundant command systems. Finally, it is possible to control a battery-cutoff relay which is provided to protect the nickel-cadmium cells from excessive discharge.

The command code structure was chosen to be consistent with that in use by the National Aeronautics and Space Administration Minitrack

network, (in order that the far-flung Minitrack stations would have command capability). The 15 command signals are at a frequency of approximately 123 mc and are modulated in a pulse-duration manner which is described in detail in Ref. 8. The block diagram, Fig. 5, shows the association of the command and telemetry and beacon systems, coupled through a diplexer to a common VHF antenna.

VII. ANTENNAS

Separate microwave antennas (pictured in Fig. 6) are used for the 6390-mc reception and the 4170-mc retransmission of the broadband microwave signal. The receiving antenna, the upper of the two equatorial units, consists of 72 boxes or ports which are coupled together with matched amplitude and phase so that the pattern of the antenna around the equatorial region of the satellite varies about 2 db peak-to-peak, as shown in Fig. 7(a). The antenna has reasonably uniform properties for an angle of $\pm 60°$ about the equator, leaving at either pole a cone with

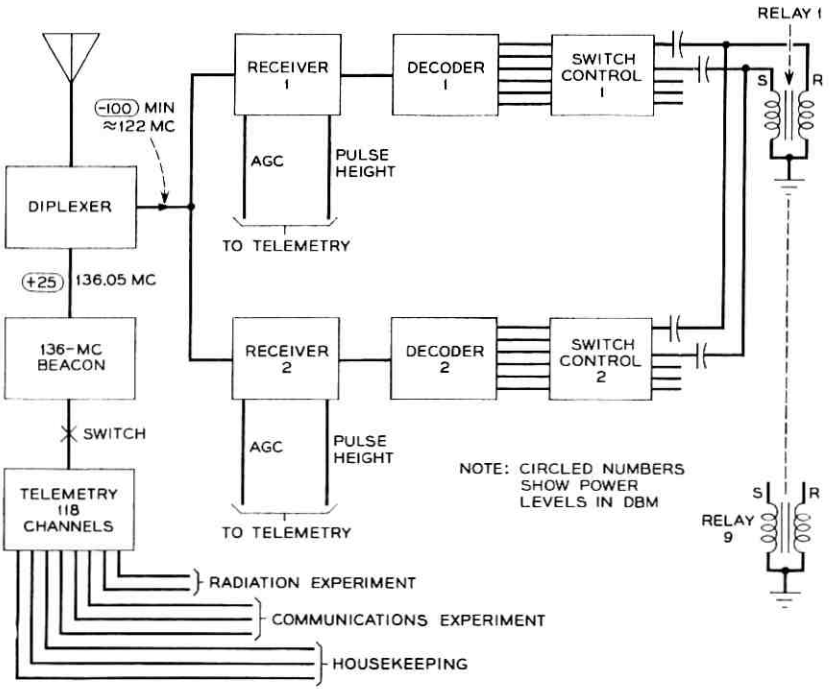

Fig. 5 — Telstar command and telemetry.

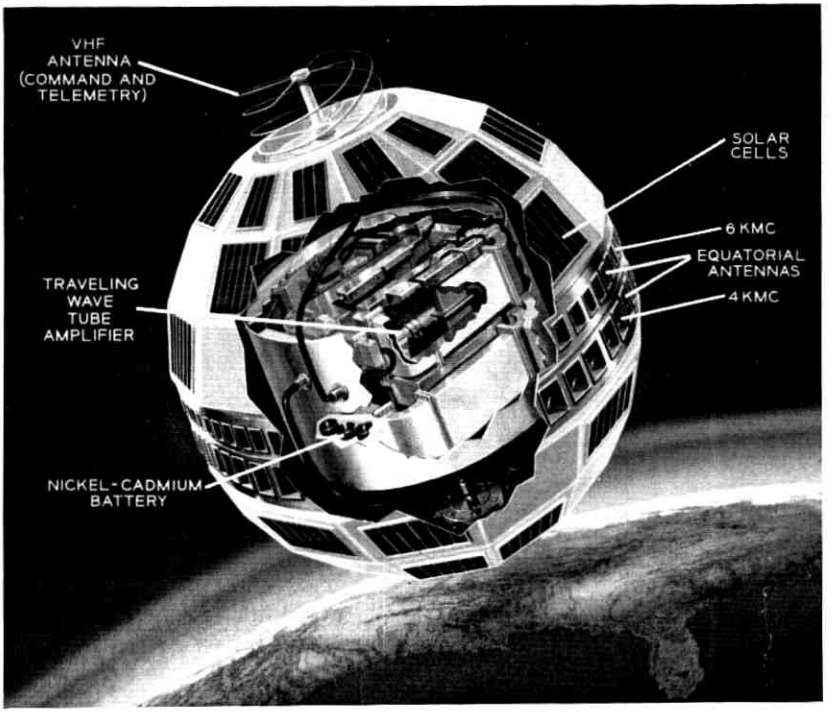

Fig. 6 — Spacecraft, showing antennas.

a half angle of 30° containing deep nulls. The details of the antenna are described by Ref. 9. The goal of the design was to produce a circularly polarizing antenna having a near isotropic pattern.

The microwave transmitting antenna is very similar to the one used for reception. It consists of 48 apertures, again equalized for amplitude and phase, and has radiation properties similar to those just described for the receiving antenna. The transmission loss between the receiving antenna and the down converter is approximately 2 db, while the loss between the output of the traveling-wave tube and the radiating apertures of the transmitting antenna is about 1.5 db. Contributing to these losses are the coaxial cables which couple the electronics canister to the radial power splitter and the cables which connect the outputs of the power splitters as antenna feeds to the hybrids. The transmitting and receiving power splitters are respectively 6-way and 9-way, which couple to as many hybrids. Each hybrid further subdivides by a factor of eight to couple to the individual ports of the respective antennas.

The VHF antenna is used both for transmission of the 136.05-mc

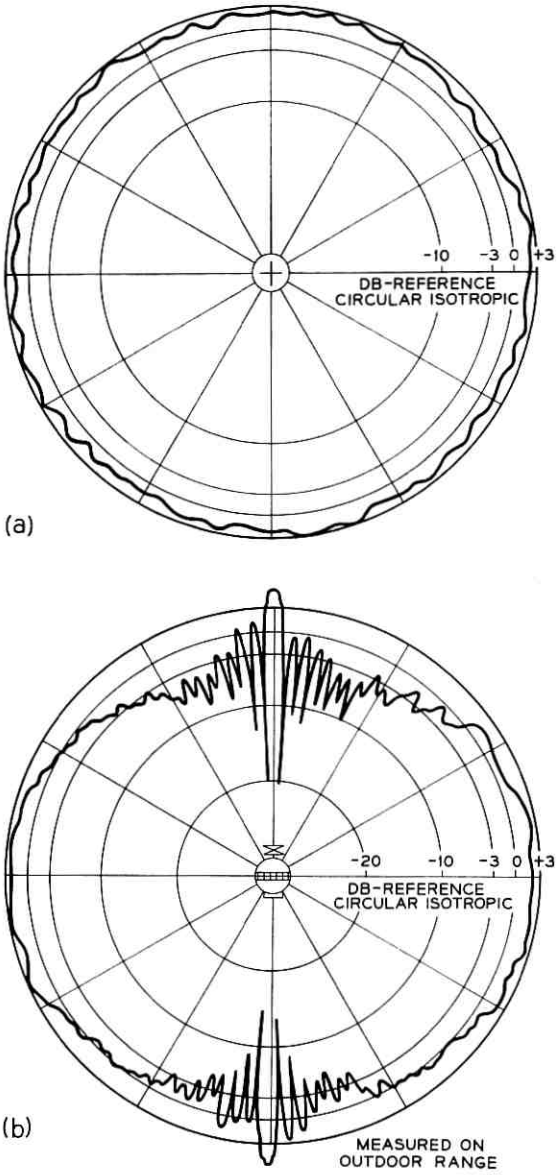

Fig. 7 — Antenna patterns at 6390 mc: (a) equatorial aspect; (b) polar aspect.

beacon signal, which is amplitude modulated with telemetry information upon command, and the reception of command signals at approximately 123 mc. The antenna is a quadrafilar helical unit which in free space produces a circular polarized signal over a wide angle. The half angle of the zone at each pole, where antenna gain is in excess of 6 db below the gain of an isotropic radiator, is approximately 20° (upper) or 10° (lower), as shown in Fig. 8(b).

The placement of this antenna close to the spacecraft as shown in Fig. 6 results in nearly linear polarization, since the proximity of the large metallic surface produces an image to cancel one component of the wave. The reasons for mounting this antenna close to the sphere are discussed in Section XI.

VIII. BATTERY AND POWER SUPPLY

The Telstar battery consists of 19 series-connected nickel-cadmium cells. Each cell has a nominal capacity of six ampere-hours and weighs eight ounces unmounted. The battery was made of 19 individual cells having essentially matched characteristics. The main voltage regulator is designed for satisfactory operation with maximum loads with an 18-cell battery, so there is series redundancy of one cell.

The main regulator provides -16 volts, regulated to ± 2 per cent. A minimum-loss design was of the greatest importance, and an efficiency of between 80 and 92 per cent is obtained as the output is varied from a light load to full load. There are two outputs from the regulator. The first output, feeding most of the solid-state circuits, has a ripple of less than 1 millivolt, rms. The other output is connected to the TWT supply.

The TWT supply is an unregulated dc-to-dc converter which provides heater, collector, helix and anode voltages for the tube. To conserve the life of the traveling-wave tube it is important that the voltages be applied and removed in a controlled time sequence. This is accomplished by commands from the ground which actuate magnetic latching relays within the satellite. Separate transformers for the high-voltage potentials are consequently required and are shown in Fig. 9. By use of new techniques in the oscillator portion of the converter it has been possible to achieve an efficiency as high as 70 per cent. The complete design of the regulator and converter is covered in another paper in this issue.[10]

IX. OVER-ALL STRUCTURE

As noted earlier, the structure of the Telstar satellite was determined largely by conditions inherent in the choice of the launch vehicle as

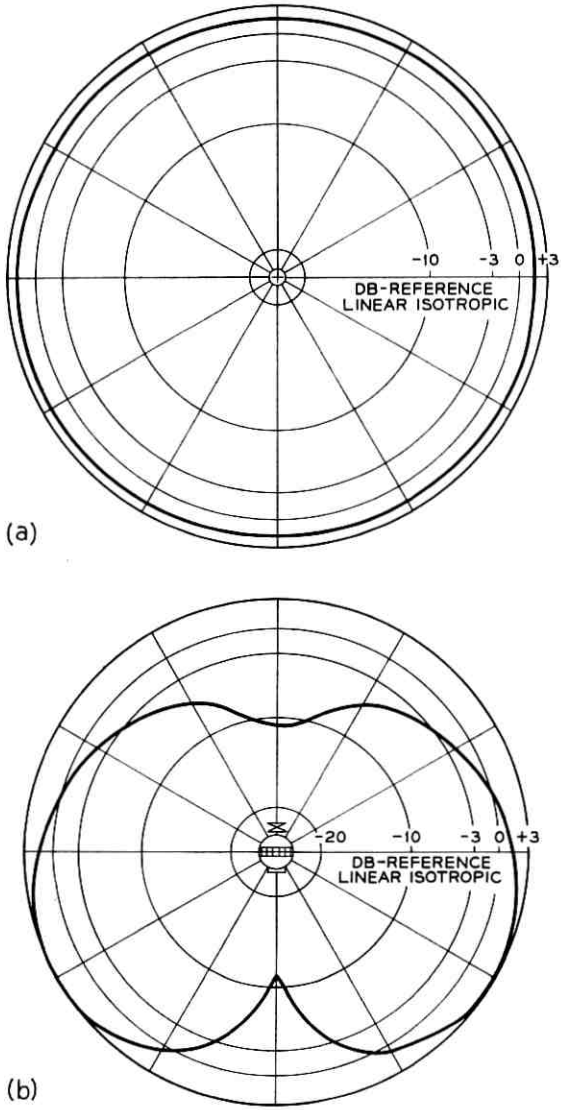

Fig. 8 — VHF antenna patterns: (a) equatorial aspect; (b) polar aspect.

well as fundamental decisions regarding the mission objectives. All studies and designs have been based on the use of the highly reliable Delta three-stage combination. Preliminary studies were directed toward an essentially spherical design with a diameter of about 27 inches and a weight of about 90 pounds. This early objective was a design that could

be accommodated in the low-drag fairing of the Delta vehicle. As more detailed examination of the electronics assembly progressed, it became apparent that the earlier proposals could not be attained within a reasonable schedule. It was then decided to examine the possibility of using a second nose fairing, originally developed for another program. This so-called "bulbous" fairing encloses more efficiently the volume needed for a spherical payload structure. With this alternative, a diameter of about 34 inches was made possible.

Concurrent with selection of the bulbous fairing, investigation was carried out on considerations of spacecraft weight versus orbital parameters. From this, it was established by engineers with NASA and

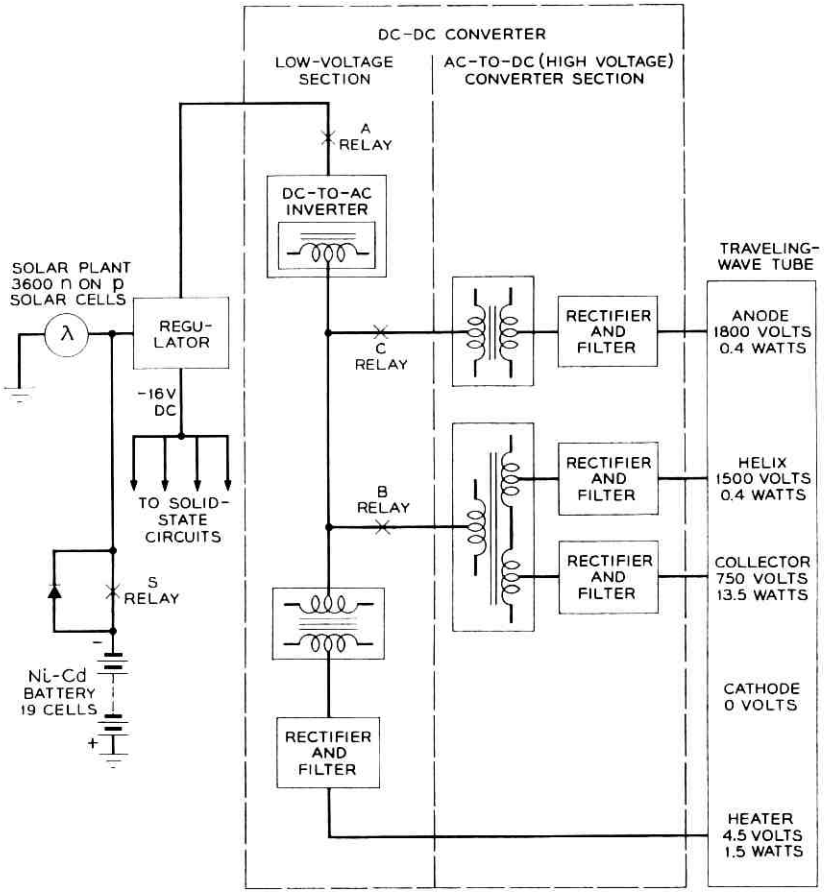

Fig. 9 — Power system.

Douglas Aircraft that a maximum payload of 180 pounds could be launched into an orbit consistent with the over-all objectives of the Telstar experiment. From design information available at that time, a maximum weight of 175 pounds was set as the limit for the Telstar spacecraft. Actual weights of six models completed for possible launch have ranged from 170.94 pounds for the model launched to 175.4 pounds.

The Telstar spacecraft structure was also influenced by the choice of spin stabilization, for which the reasons have already been discussed. The principal problems in this method are those related to dynamic and static balance of the payload about the spin axis and the requirement that the spin axis be that of major moment of inertia. As in most such designs, this is achieved by symmetry about the spin axis of the primary structure and judicious placement of masses not having natural balance by symmetry. Residual imbalance is, of course, removed by measurement and addition of trim weights as a final step in construction. In the satellite design, the major difficulty in optimizing the structure for spin stabilization was that of obtaining a low enough ratio of pitch to spin moments of inertia. A design requirement of 0.95 maximum was established and was attained with some compromise in performance of the VHF helical antenna. This antenna was to have been mounted on a telescoping mast and erected on firing a charge by closure of switches actuated by payload separation. Although the combined weight of mast and antenna was less than one pound, the effect on pitch moment was the deciding factor. The final mounting, although sacrificing 3 db in antenna performance, resulted in a more reliable design with an over-all saving in weight and an adequate ratio of pitch to spin moments. Mechanical and electrical testing were also simplified by this change.

In addition to spin-axis balance, the nearly spherical symmetry of Telstar is important in other respects. Foremost in these was the objective of near isotropy in the solar cell arrays.[2] The sphere-like outer shell permits placement of solar cell groups such that a reasonably uniform electrical output is obtained regardless of the relative orientation to the sun. The surfaces on which the solar cells are mounted are planar sections or facets rather than spherical sections. In this way all solar cells on a facet are illuminated to the same degree for maximum efficiency. The larger facets contain complete 72-cell groups (38 in number) while the 12 facets near each pole contain half-groups of 36 cells. The 24 half-groups combine in pairs to provide 12 complete groups, bringing the total to 50 groups providing 3600 cells. Facets not used for solar cell mounting and all other exposed outer surfaces are coated

with a plasma spray of aluminum oxide to effect the desired thermal balance.[2] Three facets carry optical mirrors for spin rate and orientation measurements by means of ground-based optical telescopes.[11]

The last factor to be discussed, wherein the choice of launch vehicle exerted particular influence, is related to the launch environment. Specifications covering shock and vibration tests had been effectively standardized for Delta missions and were invoked by NASA in the Telstar program. The severity of the tests for qualification of the prototype is 50 per cent greater than that for acceptance of models designated for launching. Included are random and sinusoidal vibration tests in three axes on all models. The prototype qualification tests also include constant acceleration and shock tests.[12] Levels of vibration input normal to the plane of the attachment fitting range from 2.3 g to 21 g between 5 and 2000 cps, with special requirements from 550–650 cps. In the latter range, a level of 40 g is used to simulate the resonant burning peculiar to the third-stage rocket. In order to isolate the sensitive electronics assemblies from the effects of shock and vibration, an isolation mounting comprising many strands of nylon cord was used. This support was designed to have a natural frequency of 40–45 cps, where the expected "g" input is of the order of 1.5 g along the spin axis. Maximum "g" levels experienced by the electronics assemblies due to qualification testing approach 20 g at resonance of the lacing support, while the higher-level inputs at frequencies above 50 cps are effectively damped, with occasional spikes of 5 to 10 g on the electronics section.

A simplified cross section showing relative positions of the major parts of the spacecraft is shown in Fig. 10. As shown, the electronics assembly occupies a large central volume of the structure. It is, in fact, a single assembly which is constructed and tested separately before insertion into the outer frame. All of the electronics subassemblies are contained in this "package" with the exception of portions of the radiation experiment, which had to be assembled close to detectors with which they were associated. The electronics package accounts for 85 pounds or essentially one-half the total spacecraft weight. Attached near the top and bottom of the cylindrical package are lacing rings through which the nylon lacing supports are stitched. The outer frame is a welded structure of magnesium tubing with an exterior skin of very thin aluminum panels. Whenever possible, these lightweight metals have been applied throughout for optimum utilization of their strength, weight, and heat conductivity, as applicable. Fabrication techniques and finishing problems were also of considerable importance.

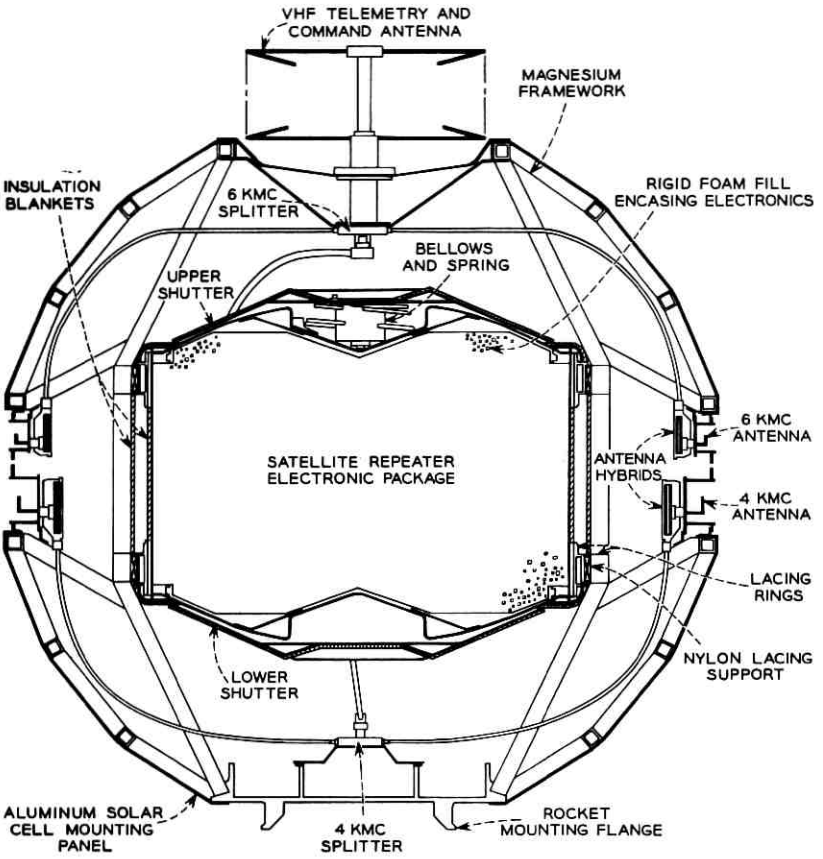

Fig. 10 — Cross section of spacecraft.

X. THE ELECTRONICS PACKAGE

The environment to be encountered during many months in orbit, as well as the conditions of launch, had strong influence on the design of the electronics package. The effects of high vacuum and Van Allen belt radiation on organic materials commonly used in electronic equipment were of particular concern. For this reason, many materials expected to be used in Telstar satellite designs were tested for the effects of radiation and vacuum. However, time did not permit adequate and conclusive tests on all such materials, especially since high-vacuum tests cannot be accelerated, but only extrapolated. This factor, coupled with the presence of high TWT voltages, led to the decision to enclose

the electronics in a hermetically sealed container which would carry an atmosphere into space. In this way, it could be assured that outgassing of organic materials would not contaminate finishes critical to thermal balance or solar cell operation. Also, any immediate hazard of high-voltage ionization and breakdown at low pressure was removed. While these were the primary objectives of the sealed container, fortuitous gains were improvement of shielding against electron radiation and completely valid tests of thermal characteristics on the laboratory bench.

Mention has been made of shock and vibration levels sustained by the electronics package during launch. In order that these inputs would not be further amplified by self-resonances within the electronics assembly, a somewhat radical approach was taken. In addition to the generally accepted procedure of encapsulating individual circuit packages, it was decided to fill the voids in the over-all assembly with polyurethane foam of the same type as that used for individual assemblies. This final encapsulation provided the major mechanical support for the TWT amplifier and waveguide components as well as for the transistorized units mounted with them. With the additional foam, the design of supporting brackets and testing for their adequacy could be minimized, if not ignored. Also, the retention of interconnecting wires prior to final encapsulation was essentially unnecessary. Consonant with this use of rigid foam is the avoidance of connectors except where essential to assembly and testing. All subassemblies are constructed with their wiring pigtailed from the units and color-coded. Interconnections are made with crimped sleeves covered over by heat-shrunk plastic tubing. The final assembly with foam fill in place might be equated to "launching" in the shop. However, repair, though difficult, is not impossible and the technique is believed to be consistent with the reliability objectives inherent in the program.

XI. THERMAL DESIGN WITHIN THE ELECTRONICS PACKAGE

Because of the almost complete filling of the electronics package with the rigid foam, appreciable heat transfer by gas convection cannot be expected. Hence, it was necessary to rely entirely on conductive heat transfer to remove power dissipated within the package to its outer walls, whence it could be radiated off. The comparatively massive waveguide structure (see Fig. 11), supplemented by heat conducting straps to attach it to the package cylinder wall, is the primary means of removing the heat. This was of particular significance at the TWT amplifier with a peak dissipation of 13 watts. Also, the chassis of a number of units, which accounted for the major part of the remaining dissipation,

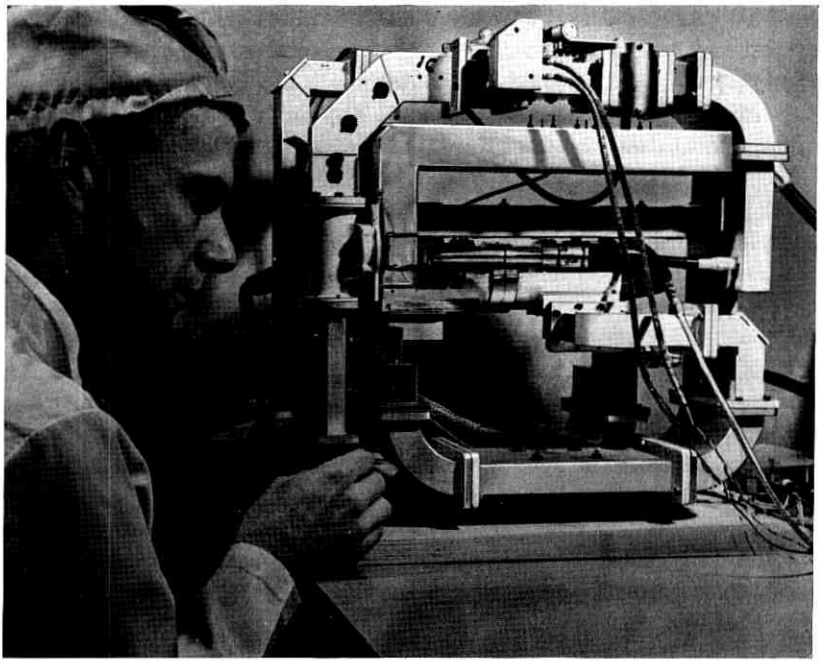

Fig. 11 — Waveguide structure.

were firmly attached to the waveguide structure. The power supply regulator was bonded directly to the cylinder wall, as were the cells of the nickel-cadmium battery. This treatment of the battery cells was most important, since during periods of overcharge almost all of the solar plant output may be dissipated in the battery as heat. Placing the cells in intimate contact with the cylinder wall avoided wide excursions in temperature at the cells. Similarly, the intimate bonding of all heat producing assemblies through the waveguide and package container avoided any significant localized heating, even with the peak dissipation associated with operation of the microwave repeater.

To verify the adequacy of the thermal design of the electronics package, an electrical analog was constructed of appropriate resistive and capacitive components and fed with currents corresponding to the various heat sources. The schematic of the analog circuit is shown in Fig. 12 with a table of current feed (temperature check) points. Continuously operating sources were separated from switched loads to permit precise simulation of operation in successive orbital passes. The electrical analog permitted evaluation in minutes of thermal charac-

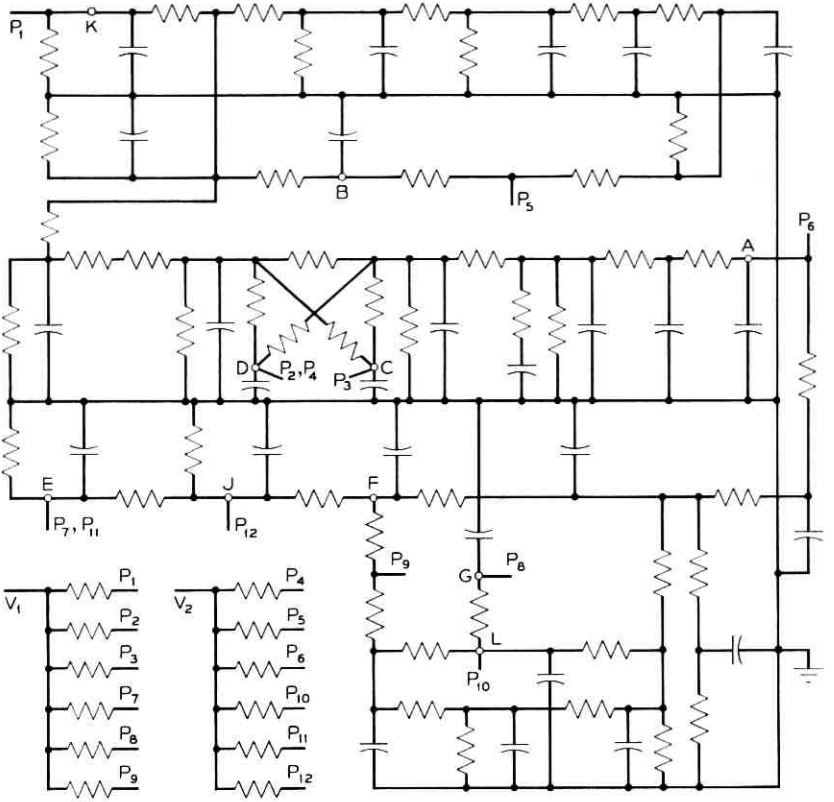

ANALOG POINT	TEMPERATURE MEASURED	ANALOG POINT	TEMPERATURE MEASURED
A	NEAR TWT COLLECTOR	F	COMMAND RECEIVER
B	IF AMPLIFIER	G	COMMAND SWITCH CONTROL
C	VHF BEACON TRANSMITTER	J	TELEMETRY
D	BEAT OSCILLATOR SUPPLY	K	COMMAND DECODER
E	POWER SUPPLY REGULATOR	L	DC–DC CONVERTER

NOTES

1. CIRCUIT GROUND CORRESPONDS TO CANISTER OF ELECTRONIC PACKAGE
2. V_1 FEEDS CONTINUOUS LOADS AND V_2 FEEDS LOADS SWITCHED BY COMMANDS

Fig. 12 — Electrical analog of thermal characteristics.

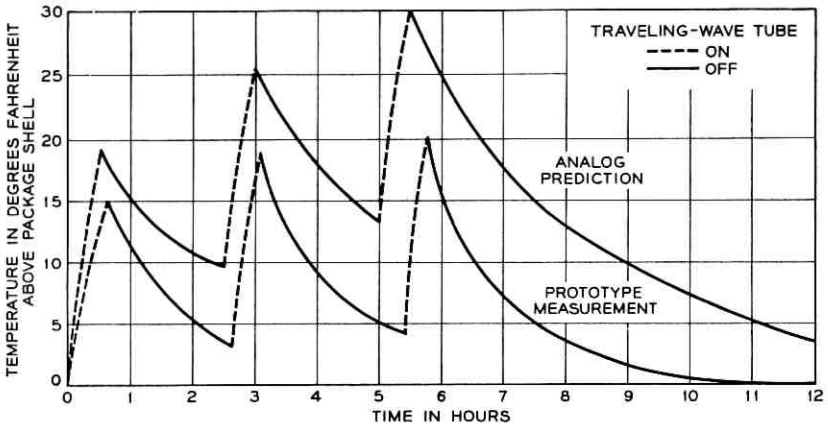

Fig. 13 — Predicted vs measured thermal performance of prototype spacecraft.

teristics actually realized in days (50 milliseconds = 1 hr.). Fig. 13 shows a comparison of results obtained at the TWT amplifier with the analog measurements to actual data obtained in thermal vacuum testing of the prototype model. The greater temperature rise shown by the analog data is indicative of the conservative approach taken in simplification of the analogous form. Temperature rises indicated by the analog, though consistently higher than actually realized, were within the objectives and confirmed the adequacy of the design.

XII. SUBASSEMBLIES FOR THE ELECTRONICS PACKAGE

Some further details of the design of the electronics package are of interest. The progress of the assembly before final encapsulation is shown at three stages in Fig. 14. Top and bottom views of the completely assembled unit are shown in Fig. 15. To reduce weight, the waveguide portions are constructed entirely of magnesium with silver plating to improve electrical performance. A layout was achieved which, if laid straight, would exceed 13 feet of $1'' \times 2''$ waveguide, but in which only 1 foot is simple waveguide and is not functional as a filter or other such component. In addition to the waveguide, 16 electronic units and 19 nickel-cadmium cells are assembled in the package. These are tabulated in Table II together with their approximate weights.

The total weight of waveguide components is 9.9 pounds while the TWT amplifier adds 7.1 pounds. The complete sealed container for the electronics weighs 13.9 pounds, and the foam for the final encapsulation varies in weight from 7 to 8 pounds.

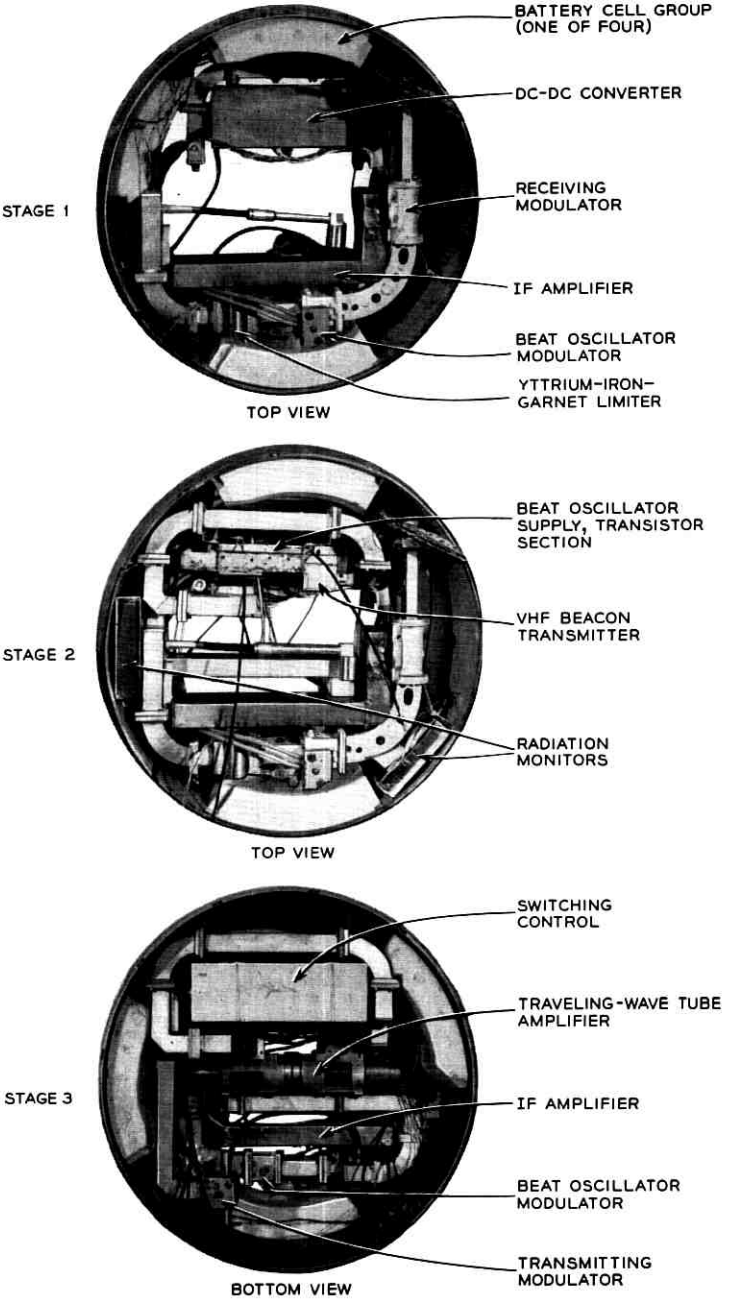

Fig. 14 — Assembly of electronics package.

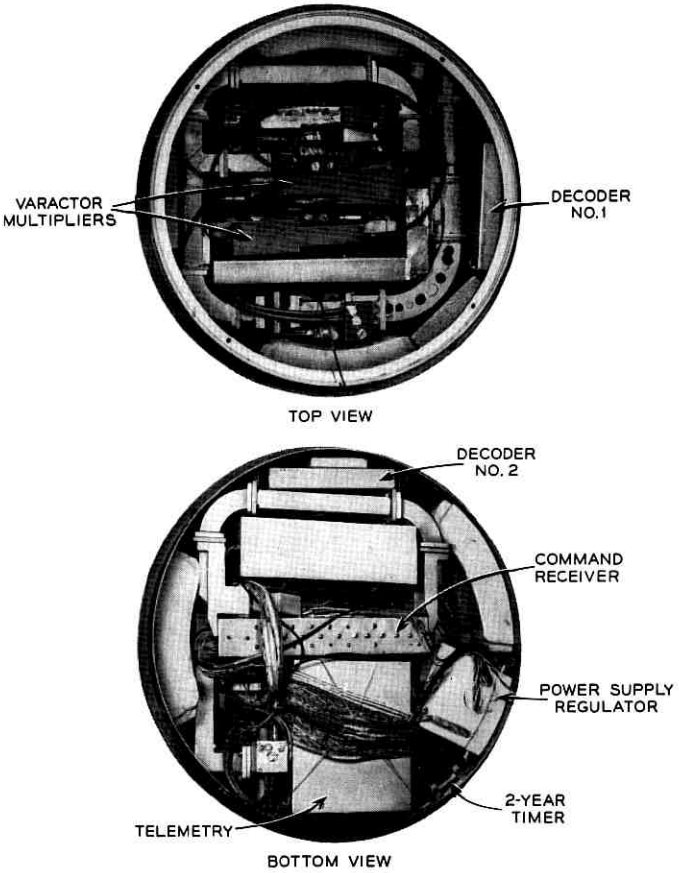

Fig. 15 — Completely assembled electronics package.

The designs of the individual units are quite varied in detail but fall nto three principal categories:

(a) For high-frequency circuits such as the IF amplifier and beat oscillator supply, a fabricated aluminum chassis is used in conjunction with epoxy-glass boards for mounting. After wiring and testing, the structure is encapsulated with certain areas of the chassis exposed. Electrical shielding is then completed by a 0.003-inch aluminum cover. Cover and chassis are gold-plated to facilitate soldering the shield to the exposed chassis. A view of the IF amplifier before encapsulation and shielding is shown in Fig. 16.

(b) The second type is devoted to circuits lending themselves to modular construction, such as the decoder in Fig. 17. Small modules

TABLE II

Unit	Approximate Weight (lbs)
1. IF amplifier and AGC	1.2
2. B.O. supply	0.9
3. Varactor multipliers (2)	0.63
4. Command receiver	1.32
5. Command decoders (2)	1.98
6. Command switch control (2)	2.26
7. VHF beacon transmitter	0.9
8. Telemetry	8.5
9. Power supply regulator	4.0
10. DC-to-DC converter	2.92
11. Ni-Cd battery (19 cells)	11.25
12. Radiation particle counters (2)	1.65
13. Two-year timer	0.57

are encapsulated separately and grouped on unit boards to perform the more complex functions. After interconnection, board and modules are again encapsulated.

(c) The last type is best described as a free-form construction to accommodate components too varied in size and shape for strict organization. One or more insulating mounting boards are used with a single step of encapsulation completing the unit. One of three boards from the power supply regulator pictured in Fig. 18 is typical of these.

XIII. CANISTER FOR THE ELECTRONICS PACKAGE

The container for the electronics package is made of $\frac{1}{16}$-inch 1100-type aluminum. The cylindrical section is fabricated of sheet with a seam

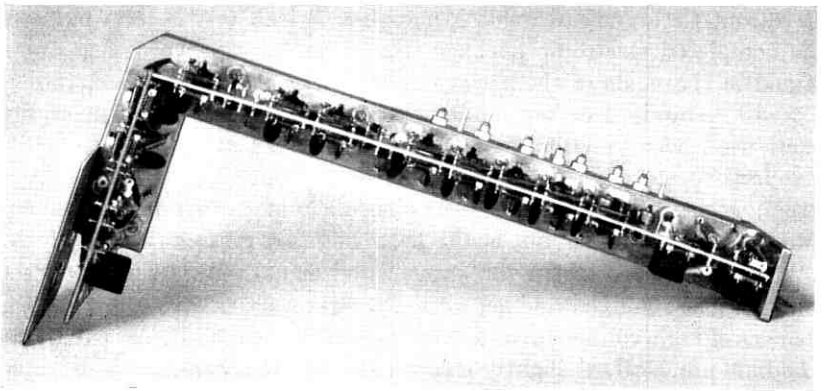

Fig. 16 — IF amplifier.

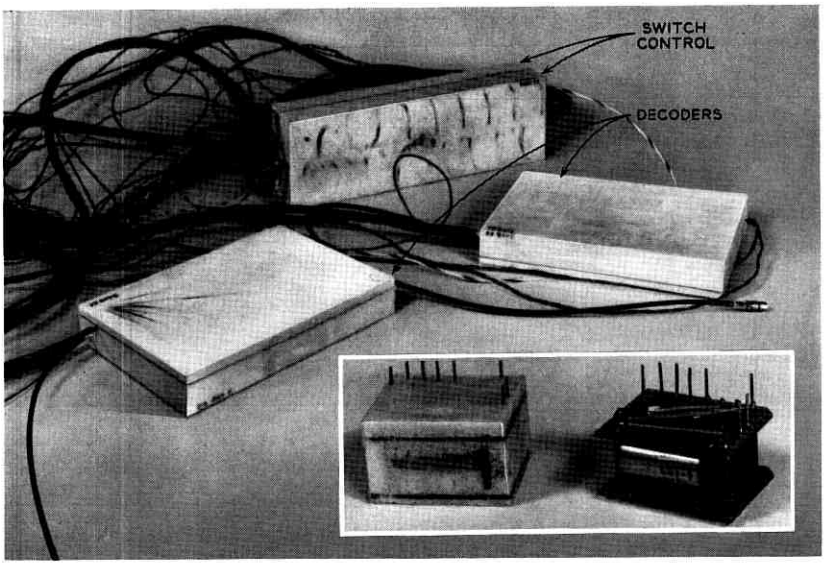

Fig. 17 — Modular construction — decoders and switch control.

weld, reinforced penetrations being provided at six locations for the electrical feed-throughs. The completed cylinder is gold-plated and polished on the exterior, after which glass-seal headers and coaxial feed-throughs are soldered into the penetrations. A helium leak check is made on each solder or glass seal before and after assembly and wiring. After foaming and temperature testing of the wired package, the top and bottom are closed by identical aluminum domes welded into place on an automatic argon-arc welding machine. A leak test is then made of the completed electronic package. Based on the reservoir of gas contained in the voids of the package assembly, a permissible leak rate of 8×10^{-5} standard cc/sec was computed for a 2-year life. The equipment used was sensitive enough to detect leaks in the order of 10^{-6} standard cc/sec or about two orders down from the permissible leak. Argon is used to make this test, since helium cannot be introduced into the package (helium would penetrate the glass envelope of the TWT and cause noise in the transmitted signal). As a final step the argon is also removed and replaced by carbon dioxide to minimize the chances of high-voltage breakdown inherent in the readily ionized argon. The final pinch-off, at slightly below atmospheric pressure, is also tested for leak by monitoring rise in pressure in a known evacuated volume.

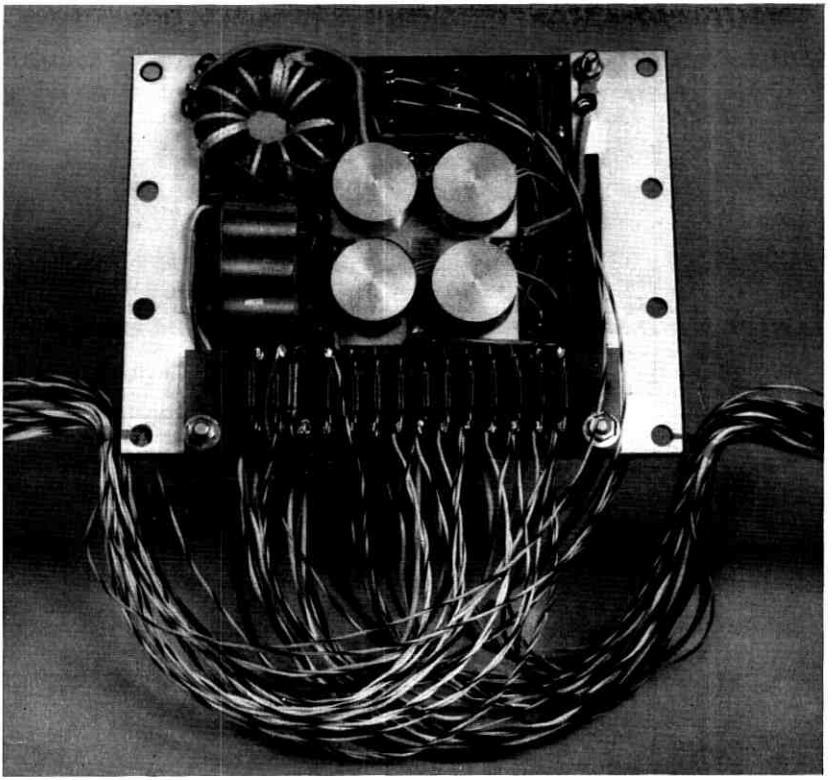

Fig. 18 — Free-form construction — portion of power supply regulator.

XIV. CONCLUSION

This paper has described the planning and general design of the Telstar satellite and attempts to give the reader an over-all picture of what the satellite contains. Several companion papers give very detailed descriptions of the various subassemblies and parts of the satellite. Another paper[13] discusses the importance of a reliable construction program. The relative simplicity and established performance of the circuit and equipment approaches described were basic to the development plan. Long life can best be attained, we believe, by a straightforward design based on a minimum of duplication and tried and proven design principles. The success of the Telstar program demonstrates the validity of this approach.

XV. ACKNOWLEDGMENTS

As in any corporate effort, many people made significant contributions to those phases of work described in this paper. The leadership and guidance of Messrs. A. C. Dickieson and E. F. O'Neill in the planning and early system layout are particularly worthy of mention.

REFERENCES

1. Hoth, D. F., O'Neill, E. F., and Welber, I., The *Telstar* Satellite System, B.S.T.J., this issue, p. 765.
2. Hrycak, P., Koontz, D. E., Maggs, C., Stafford, J. W., Unger, B. A., and Wittenberg, A. M., Spacecraft Structure and Thermal Design Considerations, B.S.T.J., this issue, p. 973.
3. Curtis, H. E., Interference between Satellite Communication Systems and Common Carrier Surface Systems, B.S.T.J., **41**, May, 1962, p. 921.
4. Sproul, P. T., and Griffiths, H. D., The TH Broadband Radio Transmitter and Receiver, B.S.T.J., **40**, November, 1961, p. 1521.
5. Davis, C. G., Hutchison, P. T., Witt, F. J., and Maunsell, H. I., The Spacecraft Communications Repeater, B.S.T.J., this issue, p. 831.
6. Bodmer, M. G., Laico, J. P., Olsen, E. G., and Ross, A. T., The Satellite Traveling-Wave Tube, B.S.T.J., this issue, Part 3.
7. Chapman, R. C. Jr., Critchlow, G. F., and Mann, H., Command and Telemetry Systems, B.S.T.J., this issue, p. 1027.
8. Brown, W. L., Buck, T. M., Medford, L., Thomas, E. W., Gummel, H. K., Miller, G. L., and Smits, F. M., The Spacecraft Radiation Experiments, B.S.T.J. this issue, p. 899.
9. Bangert, J. T., Engelbrecht, R. S., Harkless, E. T., Sperry, R. V., and Walsh, E. J., The Spacecraft Antennas, B.S.T.J., this issue, p. 869.
10. Bomberger, D. C., Brolin, S. J., Feldman, D., Trucksess, D. E., and Ussery, P. W., The Spacecraft Power Supply System, B.S.T.J., this issue, p. 943.
11. Courtney-Pratt, J. S., Hett, J. H., and McLaughlin, J. W., Optical Measurements on the *Telstar* satellite to Determine the Orientation of the Spin Axis and the Spin Rate, to be published.
12. Delchamps, T. B., Jonasson, G. C., and Swift, R. A., The Spacecraft Test and Evaluation Program, B.S.T.J., this issue, p. 1007.
13. Shennum, R. H., and Reid, E. J., The Design and Construction of the Electronics Package, B.S.T.J., this issue, Part 3.

The Spacecraft Communications Repeater

By C. G. DAVIS, P. T. HUTCHISON,
F. J. WITT and H. I. MAUNSELL

(Manuscript received January 28, 1963)

This paper describes the electrical characteristics of the waveguide components, the solid-state circuits and the traveling-wave tube used in the microwave communications repeater. The reflex-circuit method of obtaining local oscillator signals for the modulators and certain circuit stability problems are discussed.

I. INTRODUCTION

This paper describes the communications repeater portion of the Telstar satellite. This repeater receives the weak, −60 dbm nominal, FM signal from the earth at a center frequency of 6389.58 mc, shifts the frequency to 90 mc for amplification by transistors, shifts the frequency to 4169.72 mc for further amplification by the traveling-wave amplifier, and reradiates the signal at a minimum power of 33 dbm. The signals are received and transmitted through separate circularly polarized antennas which are nearly isotropic.[1] The satellite also radiates, for tracking purposes, a very stable microwave beacon signal at a frequency of 4079.73 mc and at a power of greater than 13 dbm. The bandwidth of the repeater is 50 mc, although to date only 25 mc has been used in the experiments because of bandwidth limitations of the maser in the ground receiver.

II. CIRCUIT OPERATION

The block diagram of the communications repeater, excluding power supply, is shown in Fig. 1; the numbers circled at various points in the circuit show the power levels in dbm. Fig. 1 shows exact frequencies, but for simplicity approximate frequencies will be used in the text. The signal path through the repeater is as follows.

The signal from the ground station is received by the nearly isotropic 6-gc antenna and is applied to the down converter at a nominal level of −60 dbm. A down converter shifts the center frequency to 90 mc where

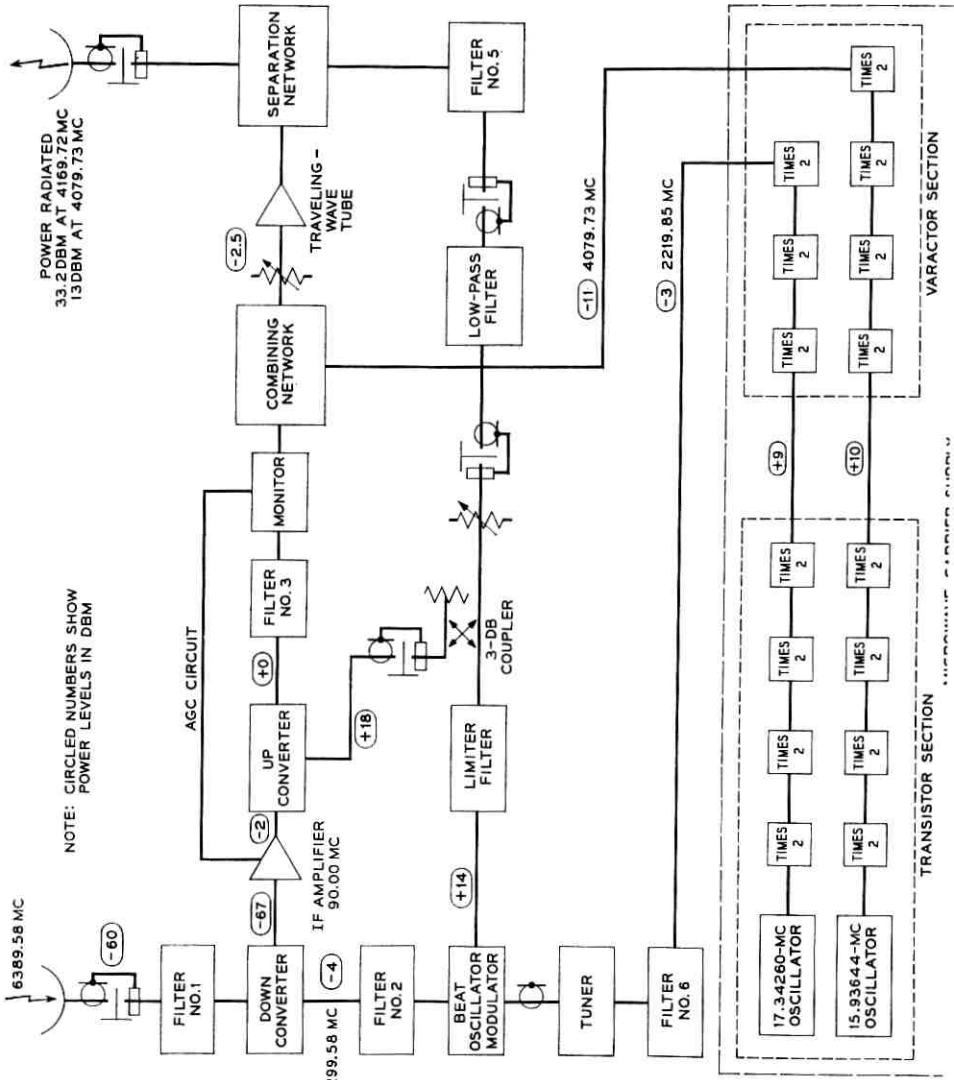

Fig. 1 — Communications repeater.

the signal undergoes gain of about 65 db in a 14-stage transistor amplifier. The signal is then applied to a balanced up converter which shifts the center frequency to 4170 mc. Varactor diodes are used in the up converter, so it provides some conversion gain. Filter 3 in the output of the up converter allows only the sum frequency (4080 + 90) mc from the up converter to pass into the monitor section. Silicon diodes in the monitor provide a dc output voltage which is a monotonic function of the power input to the monitor. This dc voltage, after amplification, controls the gain of the IF amplifier by changing the current through variolosser diodes in the IF amplifier. Because this automatic gain control (AGC) detector, the monitor, operates at 4 gc, the AGC loop includes the up converter and keeps the input power to the traveling-wave tube essentially constant as the input signal at 6390 mc varies from −55 to −72 dbm. Variations in the input signal are due to changes in satellite slant range and lack of isotropy in the receiving antenna. These variations are usually much less than 17 db when the transmitted power at 6390 mc is programmed. Ripple in the antenna pattern combined with spinning of the satellite causes the received signal to be amplitude modulated at frequencies of several hundred cycles per second. The frequency response of the AGC circuit is fast enough to smooth the amplitude modulation caused by the ripple in antenna gain.

After the signal passes through the monitor section, it is applied through a combining network to the traveling-wave tube (TWT). A card attenuator preceding the TWT is used so that small adjustments in tube drive can be made after the AGC adjustments have been completed. At the operating point selected for the tube, the gain for the 4170-mc signal is 37.5 db and the resulting power output is 35 dbm. The 4170-mc output of the TWT is applied to the transmitting antenna through a separation network which has an insertion loss of only 0.2 db at this frequency. However, the insertion loss of the transmitting antenna and connecting cables is 1.6 db, so the radiated power is 33.2 dbm.

The 4080-mc pump for the up converter is derived from a crystal oscillator at approximately 15.9 mc, followed by transistor and varactor frequency doublers. In order to obtain sufficient power for this up-converter pump, a special reflex circuit[2] using the TWT amplifier with a combining and a separation network is used, as shown in Fig. 1. In addition to furnishing the pump for the up converter, the 4080-mc amplified output of the TWT provides the microwave beacon needed for precision tracking and provides the pump for the beat oscillator (BO) modulator. The BO modulator furnishes the 6300-mc local oscillator for the down converter by combining the pump signal at 4080 mc with a signal at

2220 mc. The latter is also derived from a crystal oscillator and a series of frequency doublers. The yttrium-iron-garnet (YIG) limiter is used to ensure stability of the BO modulator under conditions of increased power at 4080 mc, conditions which exist when no 6-gc signal is transmitted to the satellite.

The gain of the TWT for the beacon signal is less than that for the communications signal, because the latter signal drives the tube into partial saturation: see Fig. 2. This graph shows the relationship of the power outputs at 4080 and 4170 mc when the 4080-mc input is constant and the 4170-mc input is varied. Three sets of curves also show the sensitivity of the tube to changes in the main regulator supply voltage; −16 volts is normal.* A circuit in the AGC amplifier changes the drive at 4170 mc to reduce the output variations if the supply voltage changes. Because two signals are amplified by the TWT, it is necessary to operate the tube about 1.5 db below saturation to reduce intermodulation to an acceptable level.

The reflex circuit is an electrically efficient way of obtaining sufficient power levels needed at 4080 and 6300 mc, but it introduces additional closed paths in the circuit, with the resulting possibility of instability. These closed paths are hereafter called feedback paths or loops, although the names are misleading because they are not used to improve circuit linearity or to realize the usual advantages of negative feedback. In this circuit, the feedback paths are undesirable by-products of the reflex method of obtaining the local oscillator signals for the converters.

The AGC circuit controls the gain of the IF amplifier so that the input signal power to the satellite is amplified by the proper amount to hold the power into the TWT constant. An increase in signal level of 3 db means a decrease in IF gain of 3 db with a corresponding 3-db decrease in noise drive to the TWT. The noise level to the TWT is low enough that noise amplification is linear, and that output noise increases almost linearly with a decrease in input signal so long as the signal falls within the AGC range.

When the input signal is removed, the gain of the IF amplifier is maximum and the noise drive to the TWT is enough to give a radiated noise power of 31 dbm in a 50-mc bandwidth. This noise will not cause trouble in any communications system unless the system uses the same frequency and has a very high-gain antenna pointed almost at the satellite. Sup-

* The variations in power output predicted from Fig. 2 are very pessimistic, because these data are shown for variations of ±3 per cent in supply voltage. The predicted variation at the end of 2 years is less than ±1 per cent, unless radiation damage is extensive.

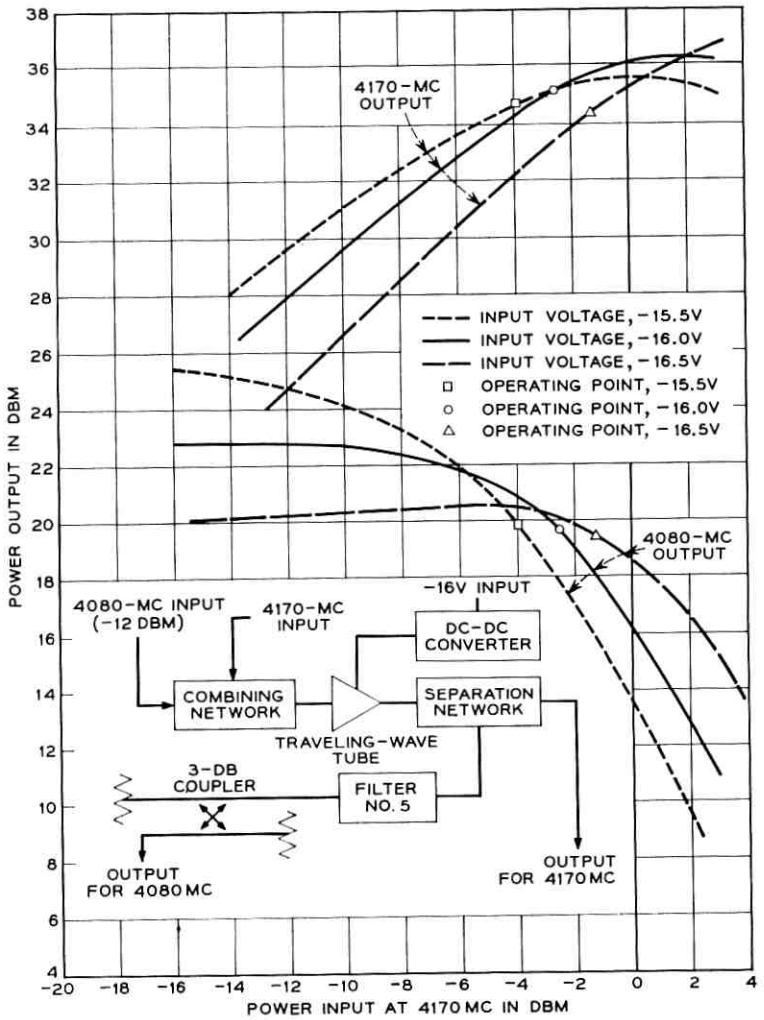

Fig. 2 — Operating characteristics for the traveling-wave amplifier.

pose, for example, there were two Telstar satellites in view, one turned on and in use, and the other turned on but having no input signal. The satellite not in use can increase the noise temperature of the Andover ground receiver by a maximum of only 2.2°K while the horn is pointing more than 3° away from the "noisy" satellite, and this would occur only when the slant range to the satellite is at its minimum possible distance of

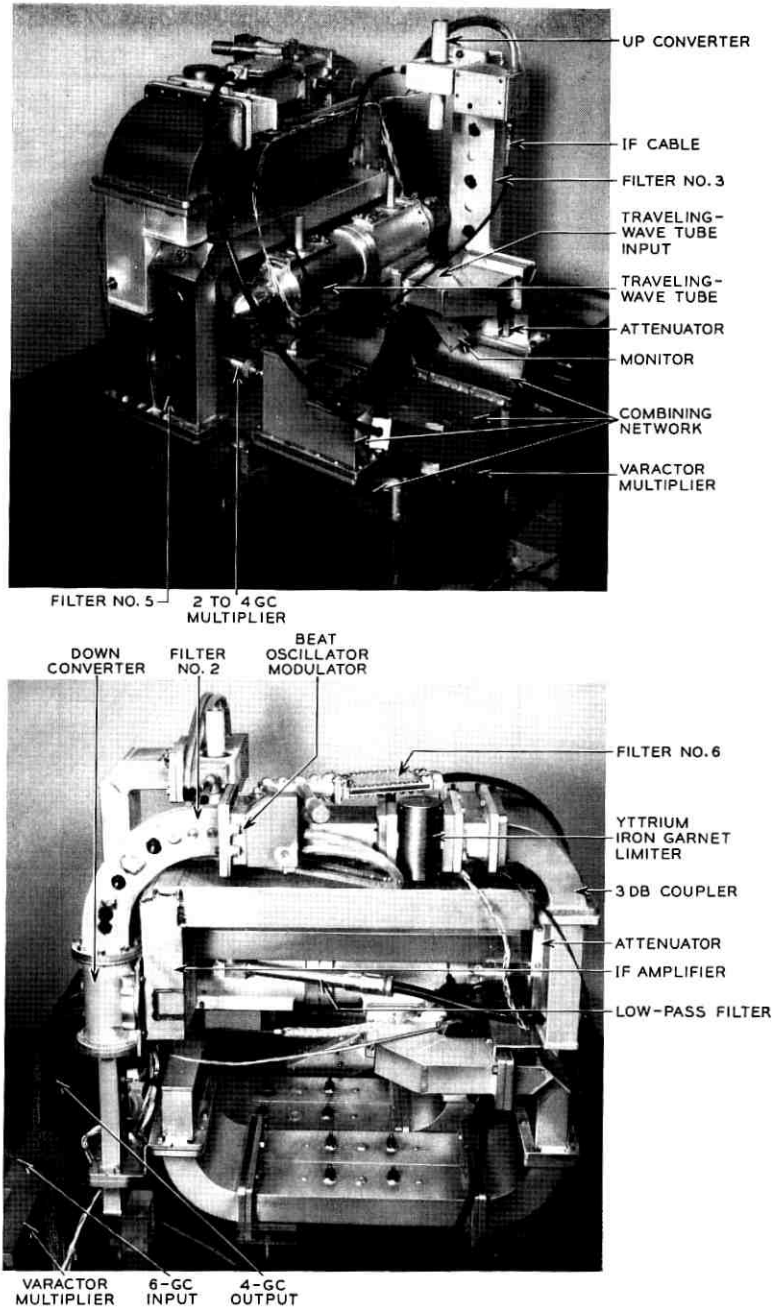

Fig. 3 — (a, b) Pictorial views of the repeater.

600 miles.[3] For a "normal" range of 2500 miles, the noise contribution from the "noisy" satellite when it is more than 3° from the beam of the ground antenna is less than 0.12°K.

When the spacecraft has no input signal, the TWT is not driven as hard as when a normal signal is used, so the microwave beacon power increases 2 db over its normal level. This extra power is advantageous, since the no-signal-input condition usually occurs when the ground tracking antennas are trying to acquire the satellite.

III. SUBASSEMBLY DESCRIPTIONS

In this section the various subassemblies of the repeater are described. The characteristics and unique features of the subassemblies are covered, but the descriptions are not intended to be design sections. Two views of the communications repeater, Figs. 3(a) and 3(b), show all the important subassemblies. All waveguide parts are made of magnesium; the 4-gc parts use WR187 guide, and the 6-gc parts use reduced-height WR137 guide. All subassemblies were tested before and after they were subjected to vibrational forces in excess of these expected in launch. The repeater must operate over a temperature range of 0° to 50°C, so all units were tested over at least this range.

3.1 *Down Converter*

The down converter shifts the 6390-mc broadband signal to an intermediate frequency centered at 90 mc. Fig. 4 shows the internal configuration of the down converter. The received signal passes through a waveguide filter into a circular cylindrical cavity in which two diodes are mounted. Inside the cavity, the signal power divides equally between the two diodes. The 6300-mc local oscillator signal is coupled into the opposite end of the cavity from a second waveguide filter; the principal axes of the two waveguides are at right angles to ensure isolation between the two frequencies present in the cavity. Input matching is provided at the signal input by the three screws which penetrate into the cavity as shown in the illustration. Two screws mounted in the waveguide close to the cavity are used to tune the local oscillator input.

The IF connection to each diode is decoupled to microwave signals by means of an RF choke which consists of two quarter-wavelength radial transmission lines. The resonant frequencies of the two lines are staggered to obtain high insertion loss over a wide bandwidth. The position of each choke along the IF output line is so chosen that an RF short circuit appears at the waveguide wall. The two IF output lines are parallel connected through coupling capacitors to the input of the IF ampli-

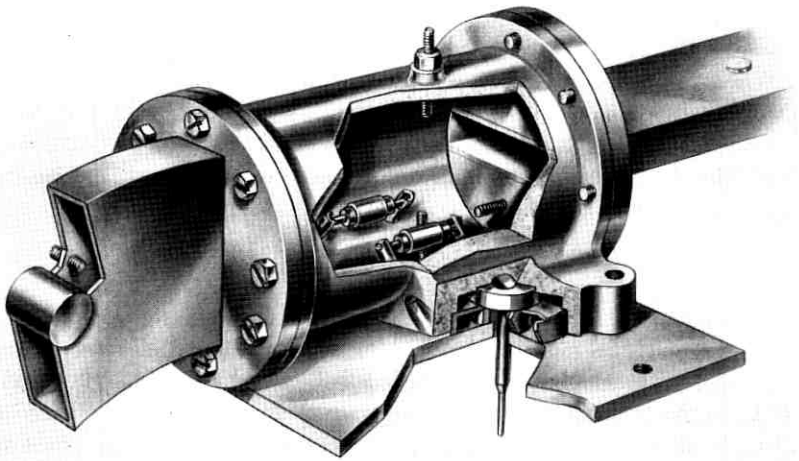

Fig. 4 — Internal structure of the down converter.

fier which is mounted directly onto the down converter. However, separate dc connections are made to the two IF output lines so that each diode may be forward biased for optimum performance.

It was experimentally determined that a good noise figure could be obtained most readily when the down converter was tuned to have a relatively narrow-band input match. The down converter is narrow banded by the presence of the resonant tuning screw placed between the two diodes, which reduces the bandwidth to about 120 mc. Narrow banding the down converter lessens the importance of the combination-frequency products generated by the modulator. With the down converter working into an IF amplifier with a noise figure of 4.5 db, the receiver noise figure is 12.5 db. Some improvement in noise figure would be obtained by increasing the level of the local oscillator signal; however, this would decrease the long-term stability and cause the properties of the down converter to be noticeably dependent on the exact level of the local oscillator signal. In the final design, the down-converter conversion loss is less than 7 db.

3.2 *IF Amplifier and AGC Circuit*

The IF amplifier provides the bulk of the amplification in the repeater, helps determine the repeater bandwidth,* and in conjunction with the

* One end of the receiver passband is determined by a high-pass filter at the input to the up converter.

microwave level monitor and the direct-coupled AGC amplifier provides automatic gain control.

Fig. 5 shows the levels encountered throughout the IF circuit. Note that the gain of the IF amplifier is adjusted by two variolossers whose losses are controlled by the output current of the AGC amplifier. The monitor for the AGC system is placed at the output of the up converter; thus the AGC system controls the input level to the traveling-wave tube.

3.2.1 *IF Amplifier*

Fig. 6 shows diagrammatically the basic design of the, IF amplifier, which uses diffused-base germanium pnp transistors throughout. Three different transistor IF amplifier configurations are employed.

The low-noise input stage consists of a common-emitter — common-emitter "doublet."[4] This configuration utilizes a large portion of the available power gain of the input transistor and thereby minimizes the effect on the over-all noise figure of the noise generated by the other transistors in the IF amplifier. A simple equalizer network is used at the output of the second transistor to compensate for the rolloff in gain of the doublet in the IF band. As one can see from Fig. 3(b), the input of the IF amplifier is physically located next to the down converter. A transformer with a 1:2 turns ratio is used between the down converter and the doublet to provide the proper mismatching for optimum noise figure. Averaged over the 65- to 115-mc band, the IF amplifier noise figure is 4.5 db, and the input impedance is about 30 ohms. The power gain of the doublet plus equalizer network is about 13 db.

To achieve the desired IF gain with a minimum number of stages while still realizing satisfactory aging and temperature performance characteristics, the common-emitter circuit with frequency-sensitive shunt feedback[4,5,6] is used for the large majority of IF amplifier stages. Frequency shaping is achieved by means of an RL network connected between base and collector. Consider the third transistor stage of Fig. 6. Resistor R_1 determines the low-frequency gain, and inductor L effectively removes the feedback at high frequencies and thereby plays the role of a broadbanding element. Resistor R_2 damps the resonance which occurs between the inductor L and the capacitive reactance presented by the transistor. Through adjustment of R_1, R_2 and L, gain and bandwidth can be exchanged; and the gain-bandwidth product is given approximately by f_T, the frequency at which the common-emitter short-circuit current gain is unity. The gain for each common-emitter shunt-feedback stage is approximately 8 db.

The principal requirement which dictates the selection of an IF out-

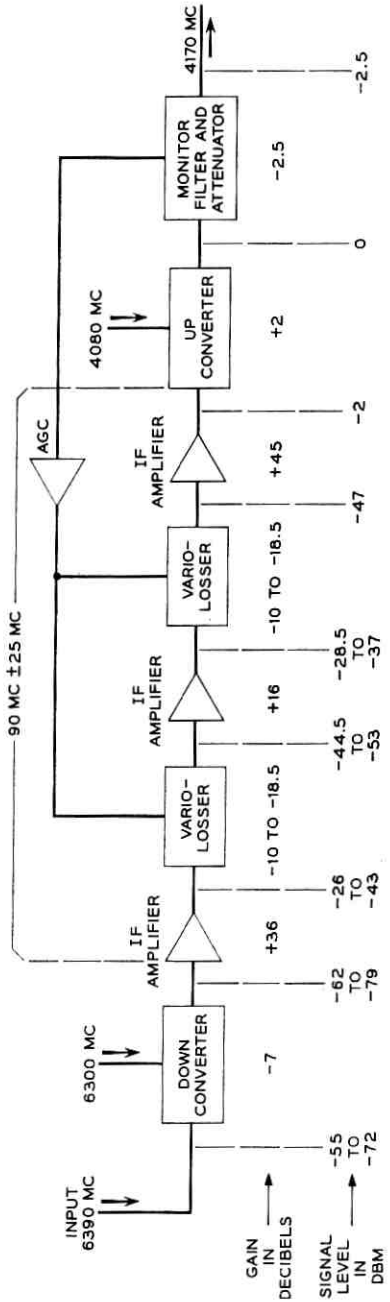

Fig. 5 — Level diagram of the IF amplifier.

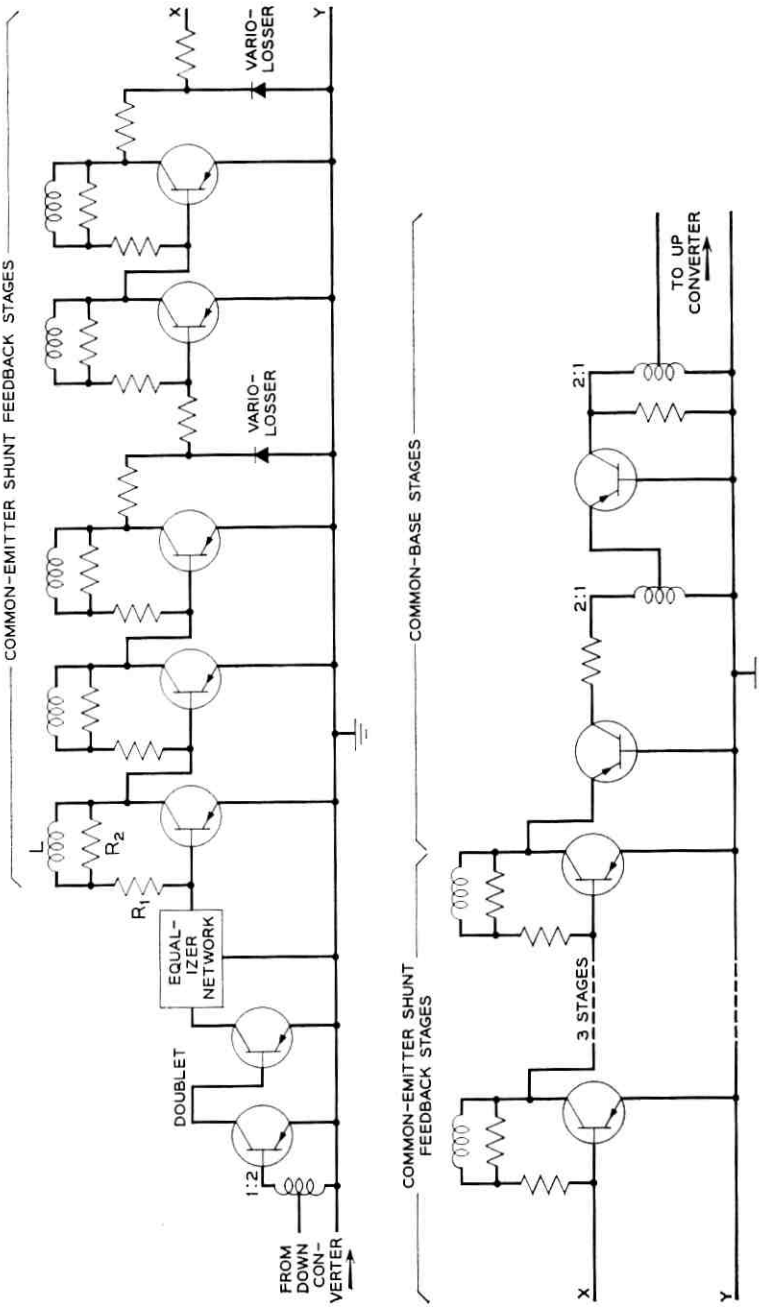

Fig. 6 — Basic circuits in the IF amplifier.

put stage configuration is that the desired undistorted output power should be achieved with minimum expenditure of dc power. For this reason the common-base configuration, with its inherently linear transfer characteristic, is used for the output stage and its driver. Two transformers, each with a 2:1 turns ratio, are used for current step-up between the common-base stages and at the output of the amplifier. Through the use of these transformers, each common-base stage provides about 5.5 db of power gain. The up converter, which is driven through a length of 75-ohm coaxial cable by the IF amplifier, must be driven by a generator with resistive impedance. An output return loss in excess of 20 db is achieved over the IF band. The output stage is capable of delivering up to +6 dbm into a 75-ohm resistive load.

The transmission characteristic of the complete IF amplifier with the variolossers set in the minimum loss condition is shown in Fig. 7. Note that over the 0° to 60°C temperature range the midband gain (nominally 87 db) changes 10 db and the tilt over the band varies from +1.5 db to −2.0 db. Delay slope over the band is less than 7 ns and AM-to-PM conversion is less than 0.4 degree per db. The circuit operates from a negative 16-volt supply and has a current drain of 90 milliamperes.

Conventional high-frequency wiring techniques are applied, and because of the inherent stability and low gain per stage of the configurations used, no interstage shielding is necessary.

3.2.2 *Variolossers*

The variolossers consist of a T-network containing two series resistors and a shunt low-capacitance germanium alloy diode used as a variable

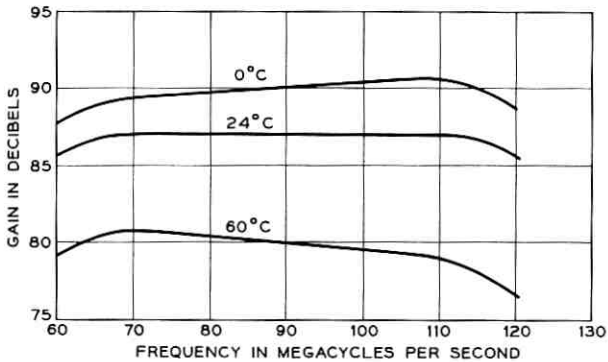

Fig. 7 — Transmission characteristics of the IF amplifier.

element. The resistors are large enough that they essentially mask out the reactive input and output impedances of the adjacent common-emitter shunt-feedback stages. They are small enough, however, to assure a low minimum loss for the variolossers. The loss of the variolossers is controlled by varying the direct current through the shunt diodes.

The placement of the variolossers in the IF amplifier is a compromise. If located too near the input, they cause too severe a degradation of noise figure during stronger input signal conditions. Placement too near the output of the amplifier will result in distortion due to rectification of the IF signal by the variolosser diodes.

The loss range of each variolosser is 15 db, and the minimum loss (relative to directly cascaded common-emitter shunt-feedback stages) is about 5 db. For the full 15-db loss variation at any temperature, the frequency distortion is less than 0.5 db; over the 0° to 60°C temperature range, the frequency distortion is negligible compared with that caused by other parts of the IF amplifier. The control current of 0 to 8 milliamperes flows through the two variolosser diodes. This current, which is a monotonic function of variolosser loss, is telemetered back to earth as an indication of the received signal strength at the satellite.

3.2.3 *AGC Amplifier and Loop Performance*

The AGC amplifier is a direct-coupled amplifier which provides control current for the variolosser diodes proportional to the difference between the dc output from the waveguide monitor and a dc reference voltage. The amplifier, which uses diffused-base silicon npn transistors, is shown diagrammatically in Fig. 8. In addition to providing high gain

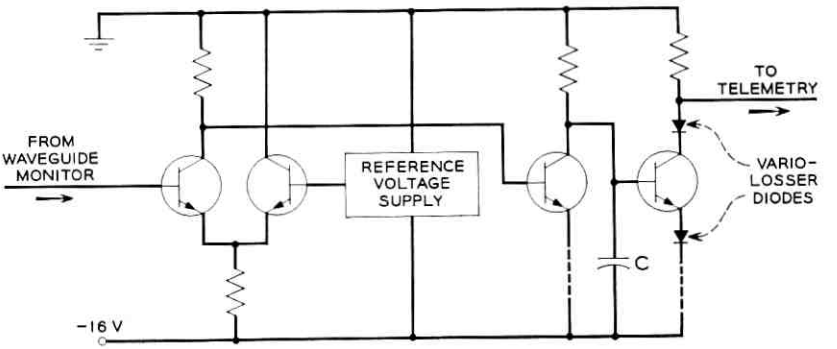

Fig. 8 — The AGC amplifier.

with low drift, the amplifier also has an adjustable feature which programs the reference voltage in accordance with variations in power supply voltage. Since the TWT uses the same power supply, the net effect of this feature is a compensation of the power supply dependence of the TWT overload characteristic through variation of TWT input level; see Fig. 2.

The differential input stage is followed by a common-emitter stage. One variolosser diode is driven from the emitter of the output stage and the other from the collector of that same stage; thus approximately equal currents flow through each variolosser diode. This diode-driving technique and the use of high-frequency transistors in the AGC amplifier (f_T = 250 mc) results in the frequency response of the AGC loop being controlled almost exclusively by capacitor C.

As has been mentioned previously, the AGC loop includes not only the IF amplifier, but also the up converter. Thus, the input level to the TWT is held relatively constant for variation in received signal strength, down converter loss, IF amplifier gain, and up converter gain. The dependence of TWT input level on received signal level is shown in Fig. 9. For received signal levels ranging between −55 and −72 dbm over a temperature range of 0 to 60°C, the input level to the TWT tube varies less than ±0.8 db.

Since the satellite is spinning and because the radiation pattern of the receiving antenna has ripples, the dynamic regulation of the AGC system must be effective for frequencies as high as 500 cps. The dynamic regulation of the AGC system is shown in Fig. 10 for several received signal levels.

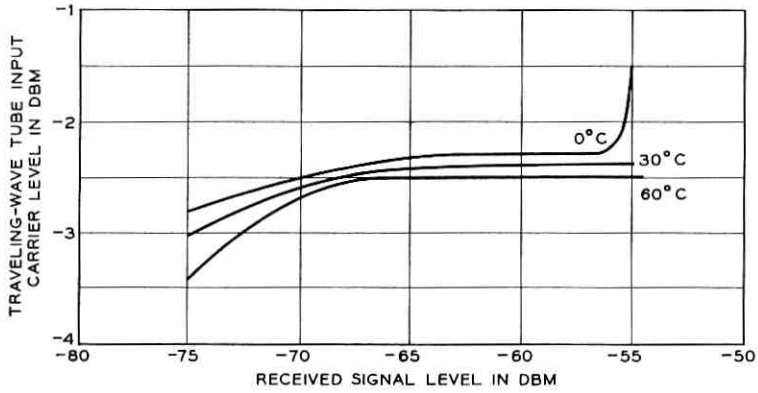

Fig. 9 — Tightness of the AGC system.

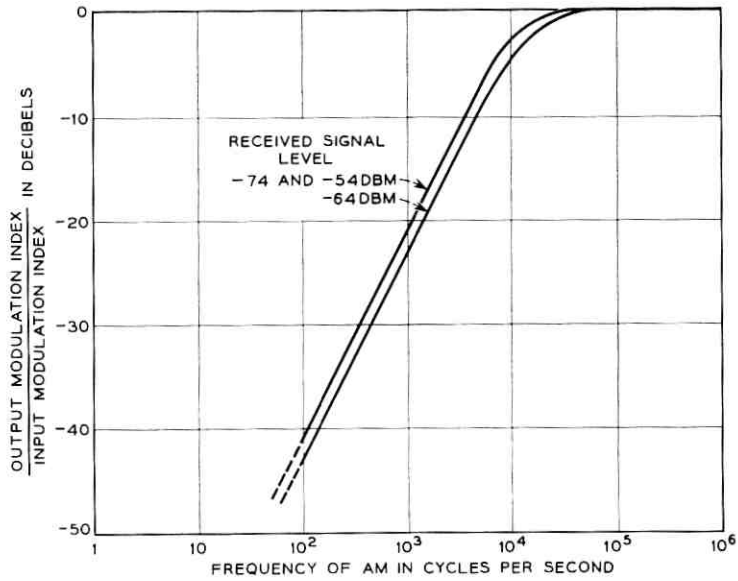

Fig. 10 — Dynamic regulation of the AGC system.

3.3 *Up Converter*

The output of the IF amplifier is connected through a short coaxial lead to the up-converter assembly, where the signal first passes through a high-pass filter. The over-all transmission characteristic of the filter is flat over the frequency band 65 mc to 115 mc, but has a minimum of 40-db rejection at frequencies below 50 mc. The up converter is a balanced diode modulator which was designed for good temperature stability and for low susceptibility to rapid fluctuations in the pump power level. To meet the special requirements imposed on the design of the converter, the diodes are operated in forward conduction and a conversion gain of about 2 db is obtained.

The up converter is designed around a hybrid junction; the output arm is waveguide, while the other three arms are coaxial, as shown in Fig. 11. Two of the arms containing the diodes also house matching transformers and second-harmonic rejection filters. The IF output leads are fed through hollow center conductors within the crystal arms and then through the center of a shorted coaxial stub. These leads are parallel coupled through capacitors to the input network and high-pass filter circuit mounted in the shielding can on the side of the up converter. DC bias voltages for the diodes are developed across self-bias resistors;

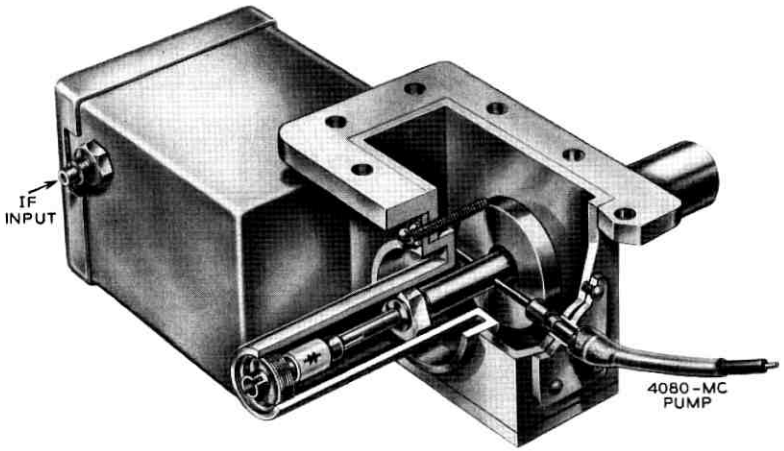

Fig. 11 — Internal structure of the up converter.

these voltages serve the secondary function of indicating the level of the pump signal for telemetry purposes. The waveguide filter on the output of the up converter is critically positioned to reflect the image frequency in correct phase to reinforce the modulator signal output power. Since the circuitry is adjusted to have a flat transmission characteristic, the return loss of the IF input to the up converter varies from 7 to 18 db over the 65- to 115-mc band.

The return loss at the microwave ports is in excess of 20 db. An important characteristic of the up converter is the relationship between the pump input level and the signal output level shown in Fig. 12. This relationship is vital to the AM stability of the circuit, a problem that will be discussed later in this article. Equally important is the absence of the pump signal at the output. Means are provided to adjust the balance of the converter to obtain a minimum loss of 30 db between the pump input and the signal output arm at normal operating levels.

3.4 *Waveguide Monitor*

The 4170-mc signal from the up converter passes through a filter and a monitor which consists of two similar diode mounts inserted one-quarter wavelength apart in a waveguide. Each diode, as shown in Fig. 13, is supported between two chucks, one on the end of the center conductor, the other in the center of a four-arm spider mounted in a die-

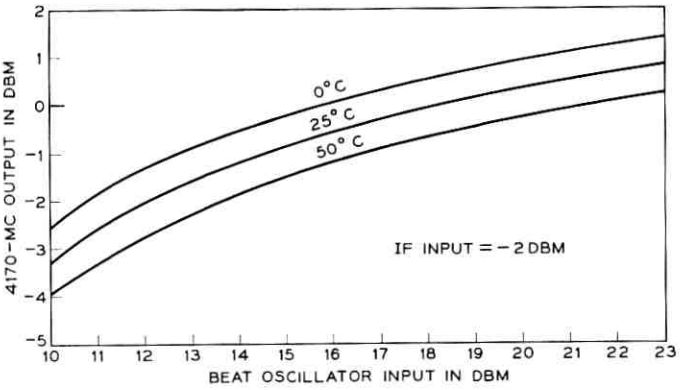

Fig. 12 — Operating characteristics of the up converter.

lectric support within the waveguide. The dc voltage developed across the diode appears between the center conductor and the outside conductor of the crystal mount, both parts being insulated from the waveguide itself. On the center conductor, a bucket-type choke determines the RF susceptance in series with the crystal.

The diode mounts are tested separately. To accommodate variations of the individual crystals, the position of the center conductor choke is varied until the impedance measured at the waveguide input and referred to the plane of the diode is found to be purely resistive. After the two diode mounts have been sealed and have passed their acceptance tests, they are mounted in the waveguide and load resistors and video-frequency decoupling components are added before foaming and final testing. No tuning or adjustment of the entire assembly is necessary.

The output voltage used for AGC purposes is derived by connecting the two diodes in series. Separation of the mounts by a quarter-wavelength along the waveguide ensures a design that is not too sensitive to the nature of the output termination. This eliminates the need for a directional coupler in this part of the circuit, thus simplifying the electronics package and reducing its size. The input-output characteristic of the monitor is shown in Fig. 14, where it will be seen that changes with temperature are relatively small. The monitor has a 20-db return loss into the waveguide input; its insertion loss is 1.5 db.

3.5 *Combining Network*

The function of the combining network is to provide a common connection to the TWT for both the communication and microwave beacon

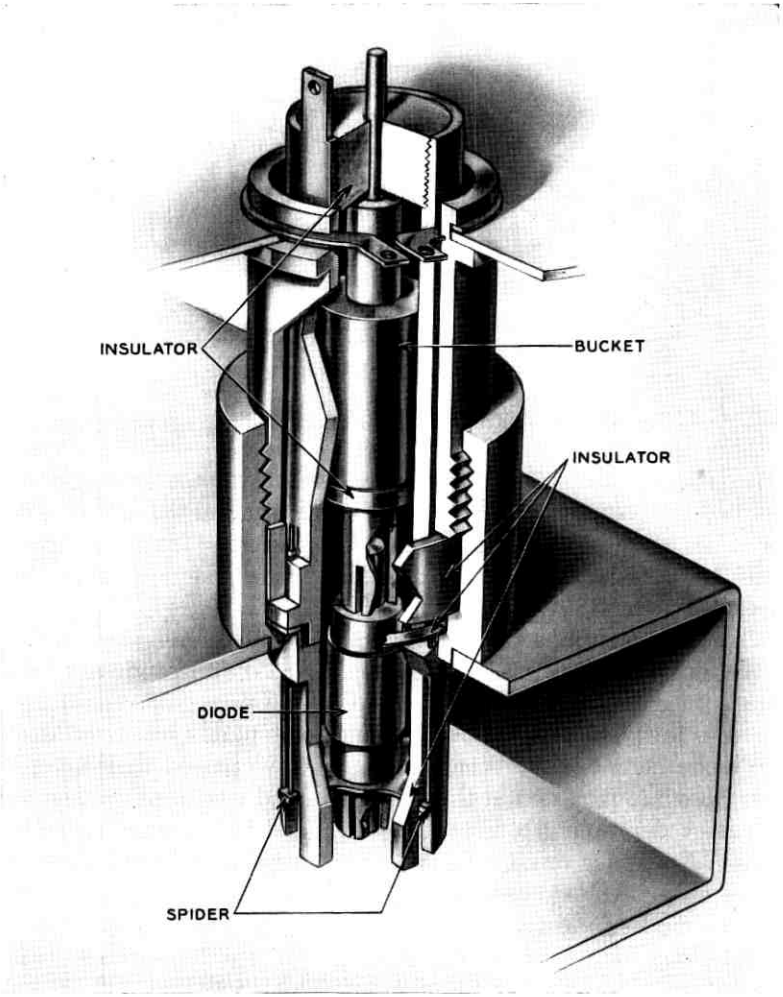

Fig. 13 — Internal structure of the monitor.

signals and at the same time provide isolation between these two inputs. This network consists of two 3-db couplers of the Riblet type,[7] two identical bandpass waveguide filters tuned to 4080 mc, and a matched termination; see Fig. 15.

The 4080-mc beacon signal input to filter B from coupler B lags the beacon signal input to filter A by 90° because of the nature of the coupler. The relative phase of the two signals is unaltered as the signals go

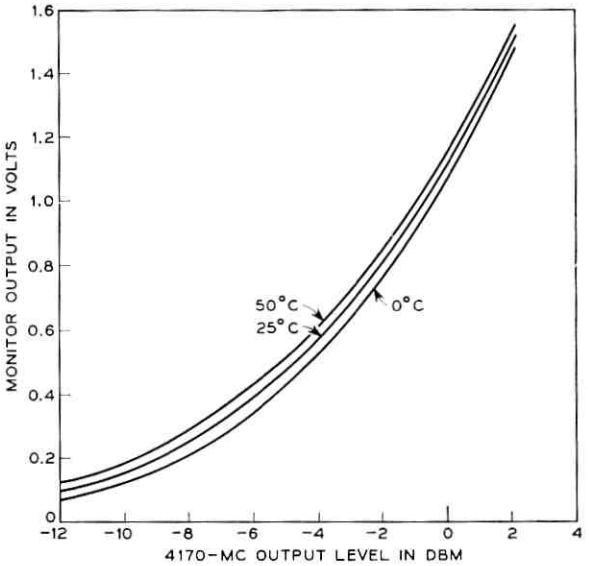

Fig. 14 — Voltage-power relations in the monitor.

through the identical two-section filters. At the output port, the signal from filter A is delayed 90° by coupler A, so at this point it is in phase with the signal from filter B. At the communications input port, the two equal-magnitude 4080-mc signals are 180° out-of-phase because the signal from filter B undergoes a 90° lag in going through coupler A, and it already lagged the output of filter A by 90°. Because of the cancellation of two 4080-mc signals at the 4170-mc input port, the only loss in the microwave beacon signal in this unit is due to the small ohmic losses.

The input signal at 4170 mc enters coupler A, and the nature of the coupler makes the input signal to filter B lag the input signal to filter

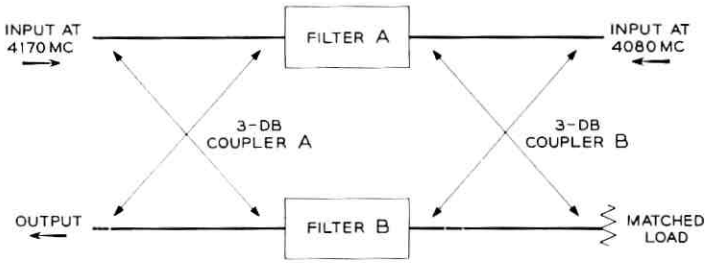

Fig. 15 — The combining network.

A by 90°. The relative phase of these signals is unchanged, as they are almost completely reflected from the filters which are tuned to 4080 mc. Thus, the phase relationship of the signals entering coupler A from the filter side is such that the two signals at the 4170-mc input port are 180° out of phase and the two signals at the output port are in phase. The isolation between the two input ports is greater than 30 db; the insertion loss at 4170 mc is 0.2 db; and the insertion loss at 4080 mc is 0.3 db.

3.6 *Separation Network*

The separation network, shown in Fig. 16, is similar to the combining network in that it comprises two 3-db couplers, two identical waveguide filters, and a matched termination. Because its filters are tuned to 4170 mc, signals near this frequency go through the separation network in the same manner that the signal at 4080 mc goes through the combining network. The filters are relatively broadband, so twenty per cent of the signal at 4080 mc leaks through the filters to the transmitting antenna, and eighty per cent is reflected from the filters. The behavior of the separation network to the reflected 4080-mc signal is similar to the behavior of the combining network to the 4170-mc signal. The 4080-mc signal level at the output port connected to the antenna is 7 db below the input signal. The insertion loss of the network in the band 4145 to 4195 mc is less than 0.2 db.

3.7 *Traveling-Wave Amplifier*

The type M4041 TWT is the only vacuum tube in the satellite. Since this tube is described in a separate paper,[8] only the circuit aspects are discussed here. The purpose of the tube is to provide power amplification for both the communications and microwave beacon signals. The operating characteristics of the tube, including the combining net-

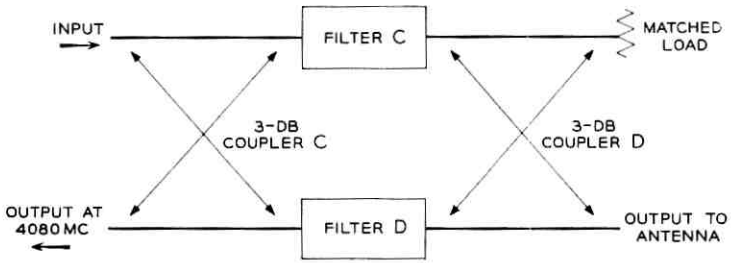

Fig. 16 — The separation network.

work, the separation network, and filter 5, are shown in Fig. 2. These filters are included in the circuit associated with Fig. 2 so the impedances seen by the tube will closely approximate those seen under actual operating conditions. The operating point was chosen well below the saturation power level of 36.5 dbm for four reasons.

First, operation in the near-linear region of the tube reduces the effect of amplitude changes in the communications signal causing amplitude changes in the microwave beacon signal. The circuit instability associated with this condition is discussed later in this paper.

Second, near-linear operation reduces the phase jitter of the microwave beacon signal. Stability of the beacon is important because both the precision tracker and the vernier autotrack systems phase lock on the signal. Even when the output load on the tube and the impedance of the source feeding the tube are perfectly matched, the power output is frequency sensitive. This means that when the communications signal is frequency modulated, the microwave beacon is amplitude and phase modulated. When the load impedance (the antenna) causes a reflection which is frequency sensitive, the above effect is made worse. Both types of modulation are decreased by operating below saturation. From the standpoint of the phase-locked tracking systems on the ground, the amplitude modulation is much less serious than the phase modulation.

The third reason for operating the TWT below saturation is the frequency characteristics of the up and down converters, the IF amplifier, and the monitor. None of these units has a perfectly flat frequency response, so an FM communications signal causes the instantaneous power drive to the tube to vary. This causes phase modulation (through AM to PM conversion) of the beacon and communications signals.

Finally, near-linear operation is desirable to reduce intermodulation of signals when the satellite is used for two-way communications experiments. This is true regardless of any effects on the microwave beacon.

The M4041 tube has very low AM-to-PM conversion when operated below saturation, so the first of the four reasons determines the operating point. With the operating point shown in Fig. 2, the net phase jitter or deviation of the microwave beacon as measured with the precision tracker[9] was less than the $\pm 5°$ "noise level" in the measuring equipment.

3.8 *Waveguide Limiter*

Because the level of the 4080-mc signal from the TWT varies with the level of 4170-mc signal, a waveguide limiter is used to stabilize the level of the 4080-mc signal at the input to the BO modulator. The lim-

iter comprises a half-height, half-wavelength waveguide cavity with a carefully oriented yttrium-iron-garnet (YIG)[10] single-crystal sphere supported in a dielectric material close to the side wall. The cavity is formed from two inductive irises; the reduced waveguide height improves the ratio of the volume of the YIG sphere to that of the cavity and appreciably reduces the size and weight of the permanent magnet required to bias the YIG sphere.

The sphere is highly polished to reduce the insertion loss to less than 0.75 db for operation below the limiting threshold. The power limiter is of the subsidiary resonance type. With the correct external magnetic field, above a critical power level a subsidiary resonance appears in the YIG crystal which is caused by the generation of spin waves at one-half the applied microwave frequency. With increasing power input, the power out of the device remains essentially constant because the excess RF energy goes into the generation of the spin waves or is reflected from the limiter.

The magnet is designed to produce a field of about 1200 gauss across a 0.4-inch gap. It consists of two truncated cones of magnetic material and two soft-iron pole pieces. The outer case, which is used as a magnetic return path, is designed to keep the external magnetic field to a minimum.

3.9 *BO Modulator*

The 6300-mc signal used as a receiver local oscillator is generated in the BO modulator shown in Fig. 17. It is a balanced upper-sideband up

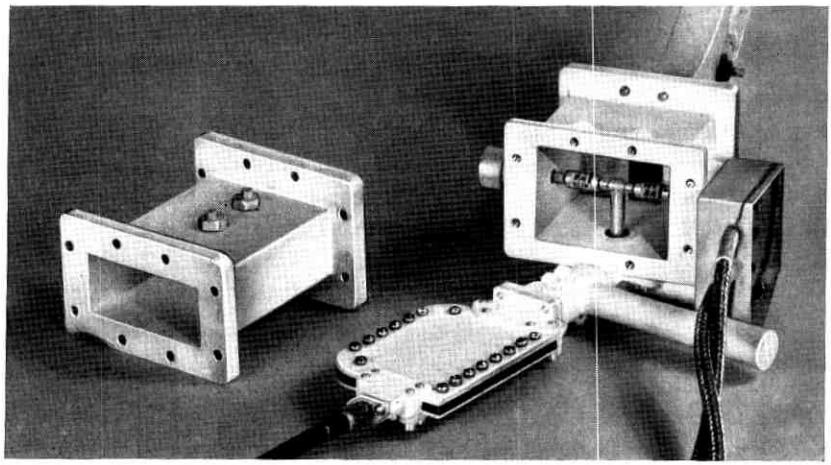

Fig. 17 — The BO modulator.

converter using gold-bonded varactor diodes which are mounted in line across a waveguide cavity. The 2220-mc input is connected to the center of the two diodes. Thus the diodes together with the center conductor of the 2220-mc coaxial input form a "T" inside and across the waveguide cavity. A two-section strip-line filter in the coaxial input provides decoupling to the higher frequencies present; the balanced structure is chosen to avoid generation of the 6300-mc signal across the 4080-mc input port, and all other necessary decoupling is provided by the natural cutoff frequencies of the waveguides used. No attempt was made to broadband the modulator since this was not necessary; the simplest possible matching device was provided in each transmission line external to the cavity. Adjustable tuning screws were used in the waveguide connections, while coaxial stub tuners were used at the 2220-mc input.

To ensure maximum stability, the modulator was operated somewhat conservatively, and the efficiency of the device was low. Due to filter losses there is a loss between the lower frequency input and the 6300-mc output of approximately 1.0 db.

3.10 *The Microwave Carrier Supply*

The local oscillator signals for the up and down converters are obtained by frequency multiplication following crystal-controlled oscillators, as shown in Fig. 18. These oscillators and the accompanying multipliers constitute the microwave carrier supply. The exact crystal frequencies are 17.342600 and 15.936440 mc. These frequencies are multiplied to provide nominal frequencies of 2220 and 4080 mc. As noted previously, the 4080-mc signal is further amplified by the TWT and used for the microwave beacon; it is also used as the pump for the up converter and mixed with the 2220-mc signal to provide the 6300-mc supply for the down converter.

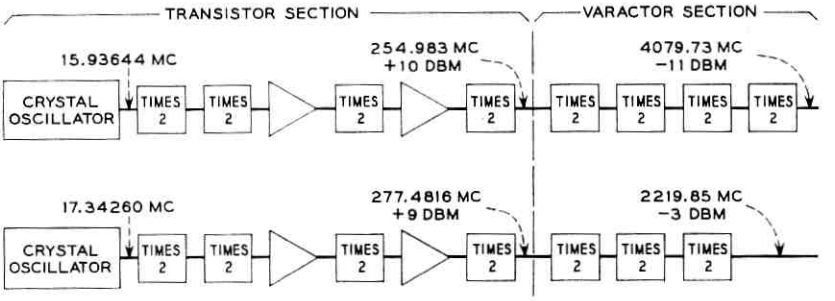

Fig. 18 — The microwave carrier supply.

A more detailed description of the components of the microwave carrier supply follows.

3.10.1 *Transistor Section*

The third overtone AT-cut crystals selected for use in the satellite had a frequency variation of only ±2 parts per million over a 0 to 50°C temperature range, so neither temperature stabilization nor temperature compensation was necessary. Good short-term stability was obtained by maintaining an RF crystal current of 6 milliamperes.

Since frequency multiplication decreases the ratio of signal power to noise power, it is necessary to start the multiplication process with an extremely pure signal. To obtain the spectral purity, extensive shielding, decoupling, and filtering were necessary to isolate the two transistor sections from each other, from the power supply, and from other oscillators in the satellite.

The transistor frequency doublers are class C amplifiers with a collector tank tuned to the second harmonic. The first and second multipliers are operated common-emitter, the third and fourth common-base. The efficiency of the third and fourth multipliers is improved by the inclusion of a full-wave rectifier in the input circuit.

3.10.2 *Varactor Octuplers*

Design of the varactor octuplers (250–2000 mc) is common for the two strings, only the tuning being different. The octupler consists of three doubler stages, each using lumped elements; early experimental work showed frequency doubling to be the most efficient means of multiplication.

The basic doubler circuit is shown in Fig. 19. The series resonant circuit in the output is resonant at frequency f, while the input trap is resonant at $2f$. The shunt input inductor is chosen to match the diode

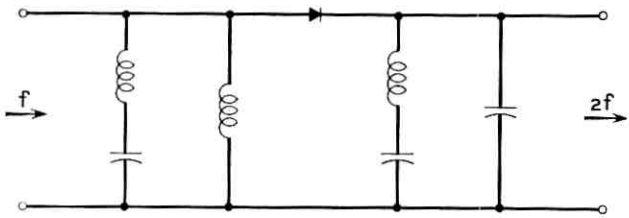

Fig. 19 — Basic varactor frequency doubler circuit.

impedance: the output capacitor is tuned for maximum output. Cascading of these stages requires additional tuning elements.

The first two stages are placed at zero bias by RF chokes connected to ground; the third stage is self-biased. Varactor diodes are Western Electric Co. units chosen for stability and high Q.

Shunt resistors were added around the diode in each stage to improve stability with changing input power level. The addition of these resistors also made tuning less critical and eliminated a problem of parametric oscillation. Critical cable lengths at both the input and output of each octupler were experimentally determined.

The octupler, before encapsulation, is shown in Fig. 20. Connections are made to the diodes through a cup welded to the small end of the diode and a shell screwed to the other. Tuning is accomplished with variable quartz capacitors and air inductors of 14-gauge tinned copper wire.

3.10.3 *The 2040- to 4080-mc Doubler*

This doubler, shown in exploded form in Fig. 21, uses the same principle as the varactor doubler described above. The diode is placed in a coaxial cable which terminates in a 4-gc waveguide. This waveguide effectively reflects the 2-gc energy. The input trap is provided by a quarter-wave sliding transformer.

A short length of rigid coaxial line matches the loop and waveguide to the diode. Output power at 4080 mc is set by rotating the output loop

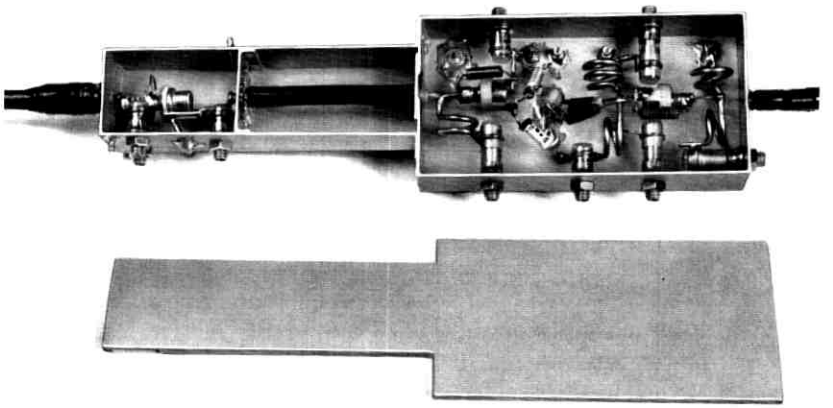

Fig. 20 — The varactor octupler.

Fig. 21 — The 2- to 4-gc doubler.

in the waveguide. The spring shown in the photograph presses the chuck and diodes against the center conductor of the rigid coaxial cable. The capacitor wire which slides inside the insulating sleeve is selected to tune the circuit. The decoupling afforded by this capacitor results in self-biasing of the diode.

3.10.4 *Over-All Design Considerations*

The microwave carrier supply must be self-starting, must be free of spurious oscillation and must maintain proper output level over the temperature range. The above conditions require special attention to tuning procedures, especially for the varactor multipliers.

As mentioned above, relative amplification of noise and spurious sidebands in each multiplier stage required close attention to suppression of these unwanted signals in the early transistor stages. All inherent noise sidebands at 2000 and 4000 mc are at least 40 db below the desired signal.

The crystal-oscillator frequency is initially adjusted to within ± 1 part per million of the desired frequency, and aging in two years is expected to be less than one part per million.

3.11 *Microwave Filters*

Because space in the electronics canister is so limited, all the waveguide filters utilize direct-coupled cavities. There are four single waveguide filters, two dual waveguide filters, one coaxial low-pass filter, one strip-line filter, and a YIG limiter which is also a filter. All data given in this section are for room temperature.

Filter 1 is a two-section filter which is designed to give a 20-db insertion loss at the image frequency, 6210 mc, of the receiver. This filter has a half-power bandwidth of 100 mc and an insertion loss of 0.2 db at the center frequency of 6390 mc.

Filter 2 is also a two-section filter. It is built in a gradual 90° H-plane bend. The insertion loss at the center frequency of 6300 mc is 1.2 db, and the half-power bandwidth is 16 mc. The filter was made narrow band

to give high insertion losses except at 6300 mc. The need for the high insertion losses is discussed in the stability section of this paper.

Filter 3 is a three-section filter connected between the up converter and the monitor; its purpose is to pass the signal at (4080 + 90) mc and reject the signal at (4080 − 90) mc. It also must provide about 20 db insertion loss at 4080 mc so leakage of the pump signal through the up converter will not contribute to the output of the microwave monitor. This filter has a 90-mc bandwidth and an insertion loss of 0.15 db at the 4170-mc center frequency.

Filter 4 is the YIG limiter. The YIG crystal is placed in a resonant cavity, which below the threshold has loaded Q of about 200.

Filter 5 is a five-section direct-coupled filter having a center frequency of 4080 mc and a half-power bandwidth of 20 mc; the insertion loss at 4080 mc is less than 1 db. This filter was made as narrow band as space allowed to give high insertion losses except at 4080 mc. The high insertion loss is needed to ensure stability in some of the closed circuits in Fig. 1, which are discussed in the stability section of this paper. In order to position the large filter (15-inch length) in a canister of reasonable size, it was necessary to build the filter with a 90° E-plane bend in one of the cavities. It was found that by measuring the electrical length of the well-matched 90° mitered bend, the distance between the inductive posts separated by the bend could be calculated, and the resulting filter had no measurable difference from the "same" filter made in straight waveguide. The 90° mitered bend was placed as near the center of one of the five cavities as possible.

Filter 6 is a two-section strip-line filter that has a half-power bandwidth of 100 mc centered at 2220 mc. The purpose of this filter is to prevent the pump signal and harmonics and beat frequencies of the two input signals to the BO modulator from going back into the microwave carrier supply. The filter has excellent temperature stability and has an insertion loss of 0.7 db at 2220 mc.

The dual filters used in the combining and separating networks are described in previous sections of this paper.

IV. CIRCUIT STABILITY

As stated previously, the circuit stability problem is complicated by the feedback paths which are inseparably connected with the reflex circuit of Fig. 1. Three feedback paths created by the reflex circuit, the coupling between the satellite output and input, and miscellaneous couplings are described in this section. The loops are shown in Fig. 22.

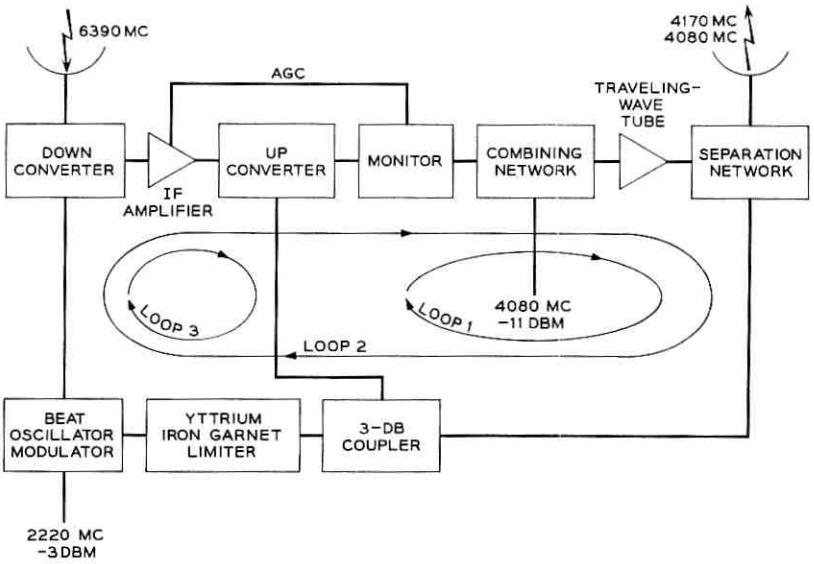

Fig. 22 — Simplified block diagram showing the feedback paths.

4.1 *Feedback Path One*

The circuit loop created by this feedback path from the separation network to the up converter includes the monitor, TWT and combining network. Two types of oscillation are possible in this loop.

The first is a straightforward RF oscillation. The TWT will act as an amplifier over a very wide frequency range; therefore the filters in this circuit were designed so at all frequencies there is margin against oscillation of at least 40 db at room temperature. This margin is made high because at least 30 db of this margin is due to the isolation between the pump input and signal output ports of the up converter, measured when it is new and the two diodes are balanced, and the isolation will be greatly reduced if one diode degrades. Also, the relatively narrow-band filters can change the margin by 5 db at the temperature extremes of 0 and 50°C. At frequencies high enough to allow higher-order modes to propagate in the waveguide, the waveguide filters give small insertion losses, so the low-pass coaxial filter was put in the circuit to provide the proper margin against oscillation at the higher frequencies. The coaxial filter has another use explained later in this article.

A second possible oscillation in this loop manifests itself in the form of amplitude modulation (AM) of existing signals. This is explained by showing that an AM signal applied to the input of the open loop causes

a similar AM signal at the output of the loop. If the amplitude and phase of the modulation envelope are proper, this circuit can oscillate in the AM mode; the phase of the carrier signal is not critical. Assume that the loop is opened at the input to the TWT and that an AM wave at 4170 mc is applied to the input. The data in Fig. 2 show that an increase in amplitude of the signal at 4170 mc results in a decrease in the output at 4080 mc. Thus, the envelope of the AM output at 4080 mc is 180° out-of-phase with the envelope of the input AM wave at 4170 mc. The amplitude-modulated wave from the output of the TWT goes through the separation network and filter 5 into the up converter. Unless the sidebands of the AM wave are attenuated more than the carrier, the output of the filter has the same general shape as the input to the filter. The curves in Fig. 12 show that if the pump signal to the up converter is amplitude modulated, the output signal at 4170 mc is also amplitude modulated, even though the modulation index of the output is much less than that of the input. If there is a phase delay in this loop corresponding to 180° at the modulation frequency, the AM feedback is positive; and if the modulation index of the signal at the output of the open loop is the same as or greater than the modulation index of the signal at the input to the loop, the circuit will oscillate in the AM mode when the loop is closed. It should be emphasized that the AM oscillation occurs only when there is a communications signal going through the TWT. The AM response of the various subassemblies in loop 1 are discussed in the next few paragraphs.

When the 4170-mc signal going into the TWT is amplitude modulated, both 4170- and 4080-mc signals from the tube are amplitude modulated. The degree of modulation of the beacon depends on the degree of modulation of the input signal and the operating point of the tube. The AM conversion gain (G_{cam}) of the TWT is defined at the ratio of the modulation index (m_{out}) of the beacon output to the modulation index (m_{in}) of of the input signal frequency. In decibels this is expressed as

$$G_{\text{cam}} = 20 \log_{10} \frac{m_{\text{out}}}{m_{\text{in}}}.$$

Since the ordinate and abscissa of Fig. 2 use the same scale, the TWT will have G_{cam} greater than 0 db when the magnitude of the slope of the beacon-output signal-input curve is greater than 45°. The operating point of the TWT is chosen so that the AM gain of the tube is less than 0 db and the power output at the signal frequency is near 35 dbm. Having the operating point below saturation is desirable, from the standpoints of AM gain and intermodulation of signals, but it is undesirable from a standpoint of obtaining maximum power output.

By selecting the proper biasing resistors for the diodes in the up converter, the output of the up converter can be made relatively independent of the 4080-mc pump signal (see Fig. 12), so this unit can be made to have very small (−18 db) AM conversion gain and thus provide good margin against AM instability for this loop.

At very low modulating frequencies, the feedback in this loop is negative because there is a 180° phase shift in the TWT and no phase shift in the up converter. However, at higher modulating frequencies, the phase delay in the various elements in this loop causes phase shifts of several hundred degrees, so the feedback at some frequencies is positive. The calculated delay for all the networks in the loop is approximately 75 ns; about 36 ns of this is due to the narrow-band filter 5.

If an AM signal with a modulating frequency f_b in loop 1 is delayed by T seconds, the envelope of the wave is shifted by

$$\varphi = 2\pi f_b T \text{ radians.}$$

When this phase angle φ is some odd multiple of 180°, the feedback will be positive because there is a constant 180° phase shift of the modulation envelope introduced in the TWT. Using these relationships and a 75-ns circuit delay, the lowest frequency f_b calculated to give positive feedback is 6.7 mc. When the circuit gain was adjusted to have more than 0 db (by changing the drive to the TWT), the output wave was amplitude modulated at 6.1 mc.

If the input wave to filter 5, which has a half-power bandwidth of 20 mc, is amplitude modulated at 6.1 mc, the sidebands and carrier all experience about the same insertion loss; so the AM gain of the filter is about 0 db. If, however, the modulating frequency is 20 mc, the next modulating frequency that gives positive feedback, the sidebands are attenuated 11 db more than the carrier; so the filter gives an AM gain of −11 db. Even if space were available to reduce the bandwidth of this filter, it would do no good because the filter delay, which contributes an appreciable part of the circuit delay, would increase and the frequency of oscillation would decrease, so the filter would have little effect on AM gain at the lower frequency. The remaining filters in this loop are quite broadband, so they have essentially 0-db AM gain.

The monitor circuit consists of two diodes inserted in the waveguide. The insertion loss caused by these diodes depends upon the resistors used in the self-biasing circuit; the smaller these biasing resistors, the higher the insertion loss. By putting selected capacitors across the biasing resistors, the monitor can be made to partially clip the peaks of the AM wave and have little effect on the troughs. By this means, the AM gain of the monitor is reduced to −3 db at f_b = 6 mc.

The final open-loop AM gain of the circuit was made as low as −18 db when the TWT voltages were normal. A decrease in tube supply voltages of 3 per cent causes the tube characteristics to change, and this can reduce this margin to −13 db.

If the 6390-mc received signal power is large enough to extend above the upper limit of the AGC circuit, the 4170-mc signal drive to the TWT is increased an amount depending on the input signal, and the AM conversion gain of the tube will be increased; see Fig. 2. This increase in signal drive to the TWT decreases the beacon output and the 4080-mc pump to the up converter and thus increases its AM conversion gain. An experiment on the ground has shown that if the 6390-mc input is increased to about −35 dbm, the AM oscillation will start, but does not damage the circuit. This high input level is not possible under normal orbital operating conditions.

4.2 *Feedback Path Two*

The local oscillator signal for the down converter is obtained by combining in the BO modulator the 4080-mc signal from the TWT with a 2220-mc signal from the microwave carrier supply. This method of obtaining the local oscillator signal creates feedback path two, which consists of the down converter, the IF amplifier, the up converter, the monitor, the TWT, the YIG limiter, the BO modulator, and several passive filters. Here, as in loop 1, two types of oscillation can exist, straight RF oscillation and AM oscillation.

In loop 2 a signal at frequency f, expressed in mc, in the IF amplifier will cause a frequency of $(4080 + f)$* mc in the output of the up converter. This signal is amplified by the TWT and is fed back through the separation network to the BO modulator through the YIG limiter. Even if the nonlinearities of the TWT and YIG limiter are neglected, this signal at $(4080 + f)$ mc plus the normal 4080-mc signal is combined in the BO modulator with the 2220-mc signal from the microwave carrier supply to give a frequency of $(6300 + f)$ mc. Going into the down converter is the "weak" signal at $(6300 + f)$ mc in addition to the strong local oscillator signal at 6300 mc. These signals are combined in the down converter to give an output frequency f. Since this frequency is the same as the assumed input frequency in the IF amplifier, this feedback loop can oscillate if the gain is large enough, even though the signal changes frequency three times in the loop. When no 6390-mc signal

* A frequency of $(4080 - f)$ mc is also present, but it is attenuated more than the higher frequency.

is applied to the down converter, the gain of the IF amplifier is about 87 db over a wide frequency range, and the gain of the TWT is greater than 42 db, so the total gain of the amplifiers in this loop is very high. As was the case in loop 1, the margin against oscillation was made 40 db or more because high insertion losses were obtained with two balanced modulators, the BO modulator and the down converter, and an unbalance in any one could change the insertion loss appreciably. In order to get the required margin for this loop, in which the combined gain of the amplifiers is at least 129 db, and still keep the microwave package small, two filters in this loop were built in waveguide bends: filter 5 has a 90° mitered E-plane bend, and filter 2 has a gradual 90° H-plane bend. Also to improve the margin, a high-pass filter was put at the input to the up converter.

The above discussion of loop 2 did not discuss the possibility of nonlinearity of the TWT. When the nonlinearity of the tube is considered and a frequency f occurs in the IF amplifier, there are output frequencies from the TWT of $m(4080 + f) \pm n(4080)$ mc, where m and n are integers. Many of these frequency components pass through the 4-gc filters because the frequencies are such that the waveguide can propagate higher-order modes. These frequencies can combine in the nonlinear limiter to produce frequencies of $4080 \pm f$, going into the BO modulator. For example, the 3×4080 component can combine in the limiter with the $4080 + (4080 + f)$ components to give a frequency of $(4080 - f)$ mc. This signal at $(4080 - f)$ mc combines with 2220-mc component to give a signal at $(6300 - f)$ mc which is fed into the down converter along with the normal 6300-mc signal. These two signals in the down converter give the original f frequency in the IF amplifier, so oscillation occurs if there is sufficient gain. There are many combinations of high frequencies which create this problem; only one example has been given. A three-section low-pass coaxial filter having an upper usable frequency of 4500 mc preceding the YIG limiter provides an insertion loss greater than 60 db above 6000 mc, and this is enough to eliminate oscillation of the type due to nonlinearities in the TWT and other elements.

The same AM problem exists in loop 2 as exists in loop 1, since the TWT is common to both loops. The YIG limiter does not eliminate the AM oscillation in either loop. Positive feedback occurs in loop 2 when the modulating frequency is about 2.5 mc, because the delay in this loop is approximately 200 ns. Four circuits are involved in loop 2 which were not in loop 1: (a) the BO modulator, (b) the YIG limiter, (c) the IF amplifier, and (d) the down converter.

The BO modulator was found to have an AM conversion gain of

approximately 0 db when the average pump input is +14 dbm (normal level) and the modulating frequency is below 2 mc. The AM gain decreases to about −3 db when the pump is increased to +16 dbm and increases to +2 db when the pump is decreased to +12 dbm. Decrease in AM gain with increase in modulating frequency is very small in the trouble region below 5 mc.

Characteristics of the YIG limiter show it has excellent limiting characteristics for slow variation in signal level; but unfortunately, when the envelope of the input is amplitude modulated at rates higher than 100 kc, the limiter has little effect on the peak-to-peak variations. Since the average value of the signal is limited, the limiter actually has AM gain. Under normal conditions the limiter has an AM gain of 3 db.

For purposes of AM analysis, the IF amplifier can be considered linear and thus has an AM gain of 0 db. At frequencies below a few thousand cycles, the AGC circuit reduces amplitude modulation, but at 20 kc and above it has virtually no effect; see Fig. 10.

The down converter alone has an AM conversion gain of about −15 db when the modulating frequency is less than 10 mc, and even less when the frequency is higher. However, in early tests on the down converter and IF amplifier together, the AM conversion gain was found to be greater than 0 db. The reason for the increase in gain is as follows. When an AM signal is used as the local oscillator for the down converter, the output will contain, among other signals, a signal at the modulation frequency. If the low-frequency circuitry preceding the first IF amplifier does not give sufficient attenuation to this modulating frequency, it can overload the first two stages and cause the output IF frequency to be amplitude modulated. When the front end of the IF amplifier was modified to properly attenuate the frequencies below 15 mc, the AM conversion gain of the down converter and IF amplifier was consistent with the value predicted from the gains of the units measured separately.

4.3 *Feedback Path Three*

As shown in Fig. 22, feedback path or loop 3 consists of the down converter, the IF amplifier, the up converter, the 3-db coupler and YIG limiter, and the BO modulator.

RF oscillation in this loop is very similar to the RF oscillation described in loop 2. Consider this loop opened at the IF amplifier, where an input signal at a frequency f in mc is applied. The sum and difference frequencies $(4080 + f)$ and $(4080 - f)$ mc, originating in the up converter, leak down the pump arm through the directional coupler and

into the BO modulator via the YIG limiter. In this modulator, the two frequencies combine with the 2220 mc to give $(6300 + f)$ and $(6300 - f)$ mc signals into the down converter. These signals combine with the normal 6300-mc signal in the down converter to give a signal f in the IF amplifier. Since this frequency is the same as the assumed input, the circuit can theoretically oscillate. Loop 3 has less gain than loop 2, and the conversion insertion loss from the IF arm to the pump input arm is very large (30 db). Conversion insertion loss is calculated using the ratio of the magnitude of the $(4080 \pm f)$ mc signal in the pump arm to the magnitude of the input signal at f mc. Loop 3 was analyzed after loop 2, and when the margin against RF oscillation in loop 2 was made 40 db, the resulting margin in loop 3 was greater than 50 db.

The AM problem of loops 1 and 2 is no problem in loop 3 because the AM conversion gain between the IF input and pump ports of the up converter is extremely low, and the YIG limiter and BO modulator give a combined AM gain of only a few db.

4.4 *Output-Input Coupling*

The TWT produces noise power over a wide range of frequencies including the satellite input and image frequency bands of 6390 and 6210 mc. Since the cutoff frequency for the TE_{20} mode in the waveguide used to make the filters in the separation network is 6300 mc, their insertion loss at 6390 mc is small. When the output of the repeater, less antennas, is connected to the input through an attenuator, the noise output from the repeater is 3 db higher when the attenuator setting is 27 db than when the attenuator is "infinite." The measured isolation between the transmitting and receiving antennas over the frequency range 6150 to 6450 mc is greater than 75 db in the temperature range -100 to $+100$°F, so the noise output of the TWT that is coupled into the down converter is negligible.

The coupling between the antennas at 4170 mc is not a problem because the input waveguide is below cutoff at this frequency and provides enough insertion loss to prevent the high power from the TWT from having any effect on the down-converter crystals.

4.5 *Miscellaneous Couplings*

Fig. 23 shows an end view of the cylindrical part of the electronics canister after all the electronics subassemblies have been mounted in the canister, but before it has been foamed and the metal domes have

been welded in place. After the domes are in place, the canister becomes a big echo box, and reducing the couplings between units to acceptable levels becomes very difficult. The power supply contains one flip-flop circuit operating at a fundamental frequency of 2.5 kc and another operating between 25 and 50 kc. Also, there are four crystal oscillators that are used to obtain the microwave carrier supply signals at 2220 and 4080 mc, the VHF beacon signal at 136 mc, and the local oscillator signal at 128 mc for the command receiver. The frequencies of the crystal oscillators (15.93644, 17.34260, 17.00625, and 31.9750 mc) and their harmonics, plus all harmonics from the flip-flop circuits, create a noise spectrum that can cause trouble in the IF amplifier and the converters. The problems associated with the myriad couplings in the canister were solved with extensive shielding, filtering, and patience.

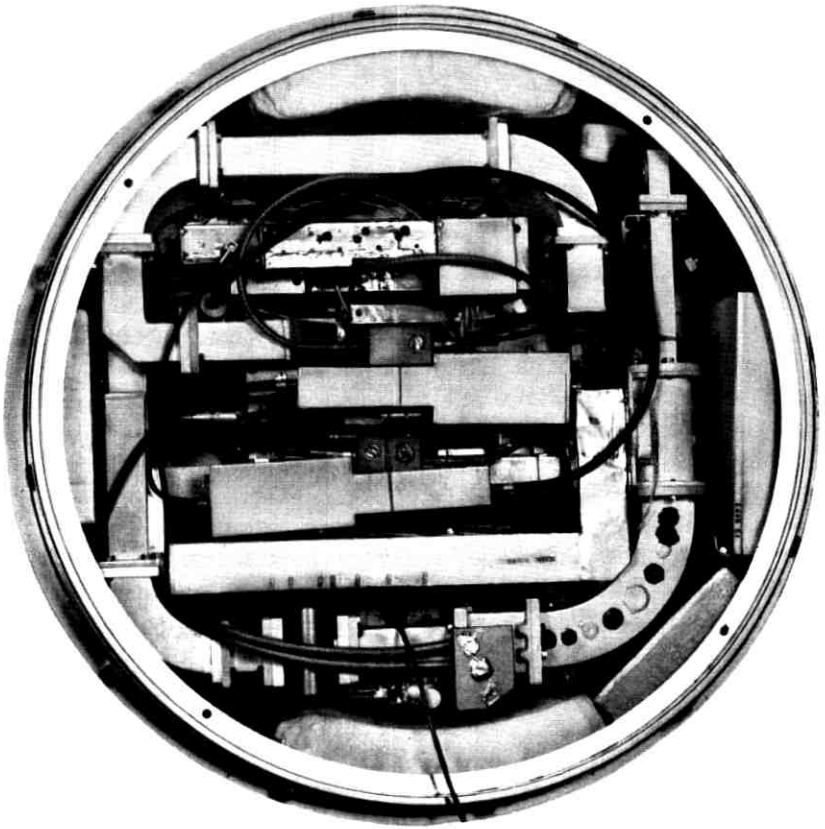

Fig. 23 — Electronic parts in the canister.

4.6 *Over-All Noise Performance*

The frequency modulation noise due to the satellite repeater is an important factor in the operation of the system as a whole. Consideration of this noise contribution is complicated by the complex nature of the repeater circuit because of the dual use of the traveling-wave tube. The predominant noise source is at the input to the IF amplifier. Operated as it is with a low level 6300-mc signal, the down converter does not add significantly to the noise, but there is considerable loss of signal power through the device, and the noise figure of the down converter and the IF amplifier together is as much as 12.5 db. Noise contributions due to other parts of the repeater, including the microwave carrier supply, increase this figure.

The noise figure of the satellite as measured before launch by a noise lamp is 13.5 db ±1 db.* However, the noise does not have a flat spectrum over the band of interest and this number applies in the region where the noise is flat.

V. CONCLUSIONS

The Telstar communications circuit is a broadband nondemodulating repeater. To obtain a high power efficiency the traveling-wave tube is caused to amplify two signals, a fact that somewhat complicates the circuit. Consequently, several stability problems exist which are overcome by the provision of frequency filters and by careful control of the nonlinearity of the circuits. Every portion of the circuit had to be specially designed for satellite use. Even where components were available with the required electrical performance, it proved necessary to seek reduced power consumption and to meet unusually stringent size and weight restrictions.

The circuit has given an exceptionally good performance. None of the complete assemblies that have been made have shown any significant variations of operating levels over the course of six months. Although no failure in this part of the satellite is expected, in many parts of the circuit sufficient margin has been built into the circuit that in the event of such a failure the circuit will continue to operate with reduced performance.

---

* Measurements made of the system noise spectrum using narrow-band analyzers indicate a satellite noise figure in the flat region of 15 db ±2 db. If the noise spectrum around the carrier is integrated over a 20-mc band, then an equivalent noise figure of 16.5 ±2 db is obtained.

VI. ACKNOWLEDGMENTS

The circuits described in this paper represents the combined efforts of so many key personnel that a complete listing is not practical. The work was done under the direction of R. H. Shennum, who suggested the use of the reflex circuit and most of the circuit arrangement.

REFERENCES

1. Bangert, J. T., Englebrecht, R. S., Harkless, E. T., and Sperry, R. V., The Spacecraft Antennas, B.S.T.J., this issue, p. 869.
2. Langford, F., Editor, *Radiotron Designer's Handbook*, Wireless Press, Sidney, Australia, pp. 1140–1146.
3. Hutchison, P. T., and Swift, R. A., Results of *Telstar* Satellite Space Experiments, B.S.T.J., this issue, Part 2.
4. Ballentine, W. E., Saari, V. R., and Witt, F. J., The Solid-State Receiver in the TL Radio System, B.S.T.J., **41**, November, 1962, pp. 1831–1863.
5. Ballentine, W. E., and Blecher, F. H., Broadband Transistor Video Amplifiers, Solid-State Circuits Conf., February, 1959, Digest, pp. 42–43.
6. Saari, W. R., Kirkpatrick, R. J., Bittmann, C. A., and Davis, R. E., Circuit Applications of a Coaxially Encapsulated Microwave Transistor, Solid-State Circuits Conf., February 1960, Digest, pp. 64–65.
7. Riblet, H., The Short-Slot Hybrid Junction, Proc. I.R.E., **40**, February, 1952, pp. 180–84.
8. Bodmer, M. G., Laico, J. P., Olsen, E. G., and Ross, A. T., The Spacecraft Traveling-Wave Tube, B.S.T.J., this issue, Part 3.
9. Anders, J. V., Higgins, E. F., Murray, J. L., and Schaefer, F. J., Jr., The Precision Tracker, B.S.T.J., this issue, Part 2.
10. Varnerin, L. J., Jr., Comstock, R. L., Dean, W. A., and Kordos, R. W., The Satellite Ferrimagnetic Power Limiter, B.S.T.J., this issue, Part 3.

The Spacecraft Antennas

By J. T. BANGERT, R. S. ENGELBRECHT, E. T. HARKLESS, R. V. SPERRY and E. J. WALSH

(Manuscript received February 13, 1963)

The spacecraft employs two microwave antennas for communications and a single VHF antenna for telemetry, beacon, and command functions. One microwave antenna centered at 6 gc is used to receive broadband signals from a ground transmitter while the other microwave antenna centered at 4 gc is used to transmit signals to a ground receiver. Each microwave antenna is composed of a large number of circularly polarized radiating elements equally spaced around the equator of the spacecraft and connected to the electronic receiver and transmitter by a complex precision feed system. The VHF antenna is a small multi-element helix mounted at the pole of the spacecraft and radiates a linearly polarized signal. All antennas provide nearly isotropic antenna patterns with the axis of symmetry corresponding to the spin axis of the spacecraft. The antenna systems were constructed of light, but rugged, materials and passed extensive electrical, mechanical, and thermal tests.

I. INTRODUCTION

The function of the spacecraft antennas is to receive and transmit two distinct classes of signals: broadband microwave frequencies for communication service, such as television; and narrow-band VHF for beacon, command, and telemetry.

The requirements on these antennas resulted from a thorough systems analysis which led to an intricate balance of many factors involving not only the spacecraft, but the ground station as well.

These factors include such vital questions as: the modulation method, the location of frequencies, the choice of polarizations, the degree of attitude stabilization, etc., and are discussed in companion papers.[1,2,3]

1.1 *Requirements*

One of the most important and difficult objectives was to make the patterns provided by both the microwave and VHF antennas as nearly

isotropic as possible. This is necessary because the spacecraft is spin stabilized; consequently the received and transmitted signal amplitudes will fluctuate by an amount depending on the anisotropy of the antenna pattern. In addition, the microwave antenna must receive right circularly polarized FM signals centered at 6390 mc and transmit left circularly polarized FM signals centered at 4170 plus a beacon signal at 4080 mc. The wide frequency separation and the opposite sense of circular polarization for the 4- and 6-gc signals suggests two microwave antennas. A single VHF antenna is used to receive command signals at 123 mc and to transmit a 136-mc beacon which can be amplitude modulated with telemetry information.

In a realistic allocation of the extremely valuable space in the spacecraft, the microwave antennas were assigned a band around the equator. This band had an outside diameter of 34.5 inches, a height of 6 inches, and a depth of 3 inches. In addition, a few extra cubic inches were available in the interior for the needed feed system. It was decided to mount the VHF antenna projecting outward from the top of the spin axis. All three antennas are shown in Fig. 1. The satellite maximum mass was

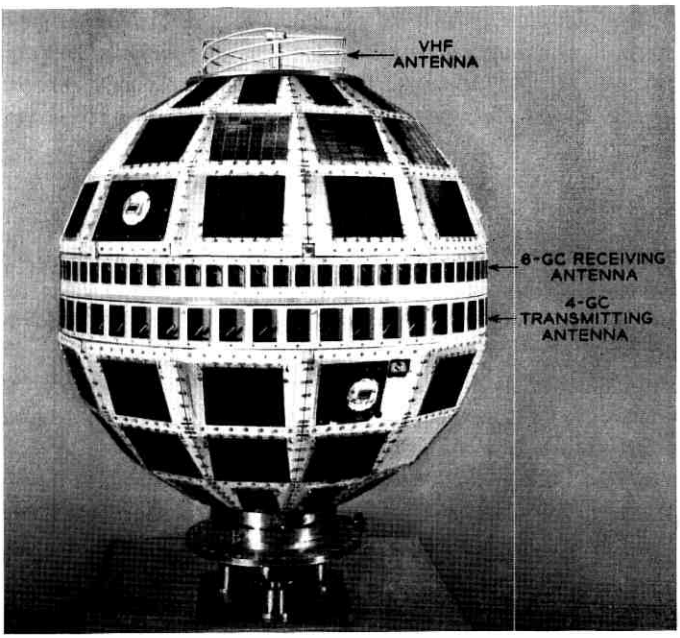

Fig. 1 — Spacecraft, showing microwave antennas and VHF antenna.

determined by the launch vehicle capabilities. The guiding design rule was that every item in the satellite was to be as light as possible. About 7 pounds was allotted to the complete antenna system. The completed satellite also had to be balanced and have a moment of inertia with respect to its spin axis such that there would be no tumbling effect while in orbit.

In addition to fulfilling the system's electrical performance requirements, the construction of the antennas had to be such that they would withstand the induced vibrational stresses of the launching and then continue at the desired level of performance in the high vacuum and extreme temperature variations of outer space. Furthermore, the antennas had to be able to withstand the high-energy nuclear particles as well as the low-energy microscopic particles found in space.

One of the most serious constraints affecting the antenna design was the necessity of building a full-scale electrical model in a total of twenty working days. It is clear that under such time pressure there was no opportunity to explore elegant proposals or to debate several alternatives. Only the most straightforward approach offering the highest probability of success could be pursued. An essential factor in the development was reliability. When reliability and urgency are both needed, new and unproven methods and materials are used only as a last resort. All materials and techniques, where possible, were proven ones. Those which were new were life tested within the limits allowed by the program's rapid pace.

A minor complication was the added requirement that the top and bottom hemispheres of Telstar be dc isolated from each other in order to reduce the eddy current damping of the spin energy. A continuous strip of insulated conductor was provided on the edge of the 4-gc radiator band to provide a bypass capacitor. Spring fingers on the 6-gc band provided continuous contact to one terminal of this RF bypass capacitor. A further complication was the need for the VHF antenna to operate during the launching operations.

Since the microwave antennas and the VHF antenna are distinct and independent systems, each will be described in separate sections of this paper.

II. MICROWAVE ANTENNA SYSTEM

The two microwave antenna systems shown schematically in Fig. 2 are each composed of an array of discrete radiating elements and a complex power distribution system to supply each element. The power distribution system consists of both resistive and reactive power dividers

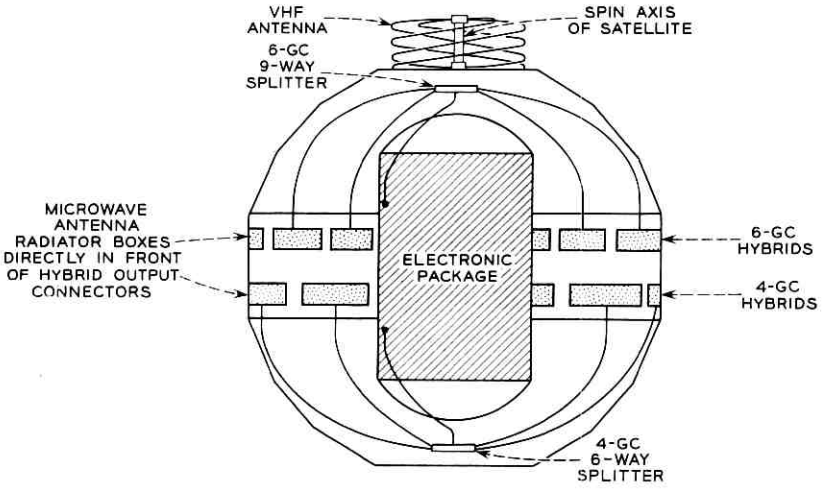

Fig. 2 — Schematic and physical arrangement of antennas in spacecraft.

and semiflexible coaxial cables. The various components of the microwave antenna systems will be described after a brief review of the basic theory underlying this approach.

2.1 *Basic Approach*

D. S. Bugnolo[4] has calculated the surface currents and radiation pattern for a large sphere excited by a great-circle slit. His analysis showed that good axial ratio and nearly isotropic radiation could be maintained to within about 20 degrees of the poles for both the 4-gc and 6-gc frequency bands on a 34.5-inch sphere. A straightforward method for exciting such a slit is by means of a radial disk line fed at the center of the sphere. Unfortunately this feed is impractical for a number of reasons. Bisecting the structures raises severe problems in maintaining structural rigidity between the two halves of the satellite and also impedes the heat flow necessary to minimize thermal gradients within the satellite. Furthermore, the electronic package occupies most of the volume at the center of the spacecraft. Elimination of the continuous radial disk line then suggests the use of some form of discrete approximation such as a belt of individually fed apertures to excite the two halves of the sphere. A further study of the problem revealed that less than one-half db of ripple would be produced in the far field pattern if discrete sources on the great circle were spaced closer than 0.8 wave-

length. For short intervals of time the path between satellite and ground station will intercept a constant latitude on the satellite. In order to avoid amplitude fluctuations of the received signal, the constant latitude of viewing should result in a constant amplitude signal, or the spin axis of the satellite must coincide with the symmetry axis of the radiation patterns. This coincidence can be provided by placing the radiating elements in two closely spaced bands near the equator of the spacecraft, one for the 4-gc transmitter and one for the 6-gc receiver. The use of two bands considerably reduces the individual bandwidth requirements for each set of radiating elements and the associated feed systems.

The variation in field pattern produced by discrete radiating elements near the equator of a sphere is a function of the sphere diameter and the number of elements. After calculating the minimum number of elements needed and allowing some margin, it was decided to employ 72 elements for the 6-gc antenna and 48 for the 4-gc antenna.

Several reservations about the performance of this system using the entire surface of the spacecraft as the radiator remained with the designers until near the end of the development. In particular, no theory was available to predict the interaction between the closely spaced sets of radiating elements at 4 gc and 6 gc and the modification of the radiation pattern by the facets and the solar cells which covered much of the surface area.

2.2 *Radiating Elements*

2.2.1 *Requirements*

Each radiating element must launch a circularly polarized wave over the frequency band of interest and at the same time provide a good impedance match for the feed system.

In view of the great importance of the individual radiating elements to the over-all performance, three alternate designs were considered before concentrating on the most promising one. Only a brief mention will be made of the first two as possibilities for future study.

2.2.2 *Two Early Realizations*

One early design of radiating element consisted of a circular opening on the satellite surface with a circular waveguide recessed into the satellite and fed by a probe from a coaxial line. Between the probe and aperture were two screws forming a quarter-wave plate. This structure worked very well over a wide band so long as sufficient space was pro-

vided between the coaxial probe and the screws forming the quarter-wave plate. Unfortunately, there was not sufficient room in the satellite to allow the circular waveguide to project into the satellite sphere as far as was necessary. When the structure was shortened, the coaxial probe and the quarter-wave plate coupled directly to each other's local fields and strongly interacted with each other. The network could still be tuned to produce circular polarization, but the bandwidth was very small (about 5 mc for a return loss exceeding 20 db).

Another early design proposed the use of a square aperture and waveguide which was excited by two probes, each fed by a coaxial line. By placing an extra 90° phase shift in one of the coaxial lines, circular polarization would be achieved. A serious disadvantage of this structure was the need for twice as many output ports on the power divider and twice as many coaxial connectors as well as provision for the additional 90° phase shift.

2.2.3 *Final Realization*

The final design shown in Fig. 3 employed a rectangular waveguide and aperture with dimensions large enough to propagate two cross-polarized modes (TE_{10} and TE_{01}). Since the two modes have different phase velocities, the length of rectangular waveguide could be adjusted to produce a 90° phase differential between the two polarizations, resulting in circularly polarized fields at the radiating aperture. A single probe was used to feed this structure, and because of space limitations it was decided to introduce the probe from the back wall of the radiating

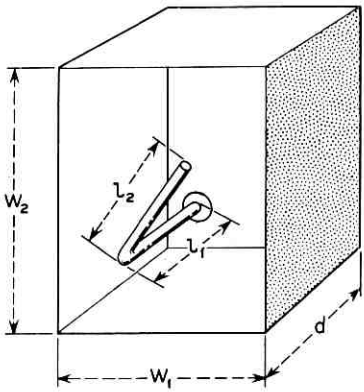

Fig. 3 — Radiating element for microwave antenna.

box. In order to obtain the 90° differential phase shift in as short a length as possible, one cross-sectional dimension of the box was chosen close to cutoff. The lowest frequency utilized in the 4-gc band is 4080 mc. The minimum dimension for propagation of this frequency in empty guide is 1.446 inches, so the narrow dimension was chosen to be 1.500 inches. The other cross-sectional dimension must be somewhat larger to provide a larger propagation constant, but not so large that the radiation patterns for the two polarizations are markedly different. A dimension of 2.100 inches was somewhat arbitrarily selected here. At band center of 4137 mc the two propagation constants are 0.658 radian per inch and 1.613 radians per inch. Therefore, in order to obtain a differential phase shift of $\pi/2$ radians, a path length of 1.65 inches is needed. Since the probe radiates in both directions in the box, some energy goes directly to the apertures and the rest is reflected from the back wall before reaching the aperture. Since there are also reflections from the radiating aperture, the effective path length is rather complex. The depth of the box was experimentally adjusted to 1.490 inches, which gave the best circular polarization for the radiated energy. The optimum axial ratio of the radiated energy is also dependent on the angle of the probe, which is close to 45 degrees.

After obtaining circularly polarized radiation, the remaining problem is to obtain a matched input impedance for the coaxial line. A 50-ohm dielectric bead support for the probe was designed and the two length dimensions of the probe, l_1 and l_2 in Fig. 3, were varied to obtain 50 ohms looking into the coaxial connector at the back of the box. The various adjustments for circularly polarized radiation and good impedance match interact with each other, so that considerable experimentation was found necessary to settle on dimensions which provided the necessary broadband performance. The 4-gc and 6-gc box dimensions are simply scaled in inverse frequency ratio.

Despite early recognition that the radiators would ultimately be magnesium extrusions for high strength-to-weight ratio and precision fabrication, the need for early demonstration of feasibility suggested the use of sheet metal techniques. The first radiating elements were made by cutting 15-mil brass sheet to the right size and shape and bending into the form of a rectangular box having four sides and a bottom, but no top. The adjoining edges were soldered to provide good electrical conductivity. The top edges were bent over at right angles to form lips which could be soldered to the cylindrical supporting midsection in which rectangular holes were punched. The first midsections were made in four parts to permit some tolerance in the associated

hemispheres. A hole was drilled in one corner of the bottom of the box to permit the insertion of a feed probe. The probe was supported by a coaxial connector soldered to the outside of the box bottom. The four quadrant radiator assemblies were fastened between a pair of smooth aluminum hemispheres to form a crude breadboard model. Although the tolerances which had been achieved in the dimensions of the radiators exceeded by several times the estimated allowable tolerances, the first radiation patterns were very encouraging in that they indicated the basic approach was sound, provided the physical structure could be fabricated to the necessary tolerances.

When final models were skillfully fabricated by Dow Metal Products of Bay City, Michigan, the radiating elements were formed as magnesium impact extrusions with a boss on the bottom which was drilled and threaded to serve as the shell of a coaxial connector. Despite the elaborate precautions taken during fabrication to hold the critical dimensions of the radiating elements, small departures from design center values combined in a complicated fashion to cause nonuniform electrical behavior. This problem was solved by shipping test equipment to the factory and selecting satisfactory boxes by measuring return loss over the frequency band of interest. The boxes were then magnesium welded into a wheel-like frame as shown in Fig. 4. During the welding process the frame and boxes were held rigidly in alignment by an elaborate

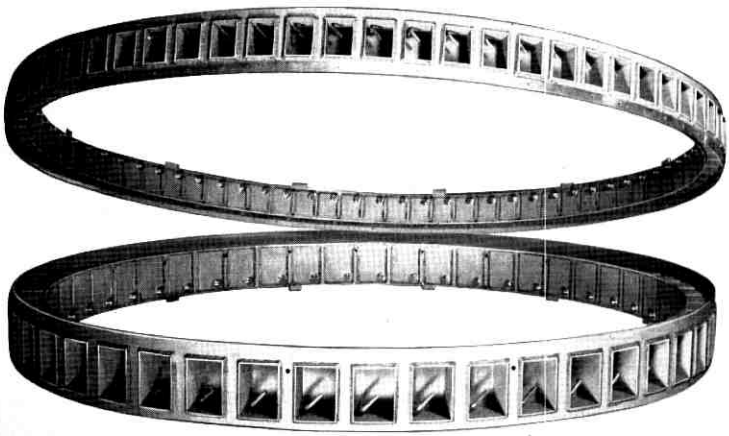

Fig. 4 — Microwave antenna radiating elements assembled into their frames before attachment to the spacecraft.

set of heavy steel jigs. The fixturing is such that when completed, the center of each connector lies within a few thousandths of an inch of a datum plane. The radiating probes were also accurately positioned by means of suitable fixtures before being clamped in place.

2.3 *Feed System of Microwave Antenna*

2.3.1 *Requirements*

Calculations showed that precise microwave distribution systems were required for funneling the 6-gc signals from the 72 receiving radiators to the single receiver within the satellite's electronics package, and similarly for fanning out the amplified 4-gc signals from the satellite's traveling-wave tube to the 48 transmitting apertures. The tolerable variations accumulated within the distributions systems must be restricted to about 15° peak-to-peak and 1 db peak-to-peak, of which no more than 5° and 0.5 db should be systematic.

2.3.2 *Single-Stage Reactive Distribution*

Initially, purely reactive single-stage distribution systems were investigated. These consisted simply of a 48-way power divider for the 4-gc band and a 72-way power divider for the 6-gc band. Each divider was arranged on a circular printed circuit board with a central input connector and the required number of output connectors around the periphery. Early measurements indicated that prohibitive manufacturing tolerances were required, not only for the power dividers themselves, but also for the connecting cables and radiators to keep the phase and amplitude variations within acceptable limits.

2.3.3 *Multistage Reactive and Resistive Distribution*

For the above reason, attention was directed toward multistage distribution systems using suitable resistive type power dividers which would provide isolation between output ports. The so-called resistive dividers are tree-like arrays of lossless hybrids, each with an internal terminating resistance. Furthermore, with this approach more flexibility was possible in the location and weight distribution of the various feed system components within the satellite.

Considering electrical performance alone, the arrangement chosen is one of many alternatives, some of which are undoubtedly better suited for precise microwave power distribution. The choice made resulted from consideration of available space between the radiating elements

and frame structure of the satellite, as well as from such constraints as minimum weight, minimum cross-section (to facilitate free internal heat exchange by radiation between the satellite hemispheres), maximum moment of inertia about the satellite's spin axis (in order to avoid tumbling), etc. The final 4-gc and 6-gc distribution systems chosen are illustrated schematically in Fig. 5. An assembled 72-way power divider for the 6-gc band is shown in Fig. 6. The reactive divider shown at the center is connected by coaxial cables to the nine resistive dividers mounted behind the radiating apertures.

2.3.4 *Reactive Power Dividers*

Centrally located in the 4-gc and 6-gc systems are a 6-way and 9-way reactive power splitter, respectively, connected to 50-ohm input and output cables. These dividers were produced on small circular printed circuit boards, with the input connector centrally located and the 6 or 9 outputs evenly spaced around the periphery as shown by Fig. 7. To maintain 50-ohm impedance levels on both the input and output cables, appropriate $\lambda/4$ transforming sections are incorporated in each of the 6 or 9 output lines near their common junction point. In addition, matching sections are built into the input connector of both the 4-gc

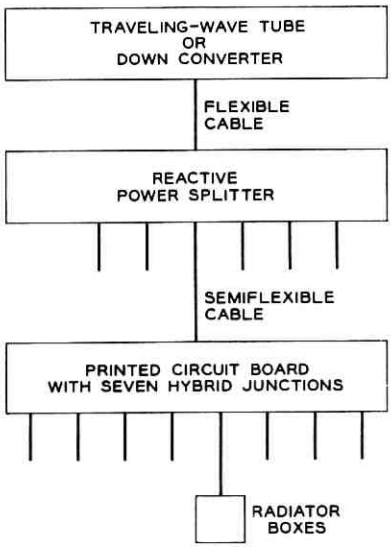

Fig. 5 — Block diagram of microwave antenna feed system.

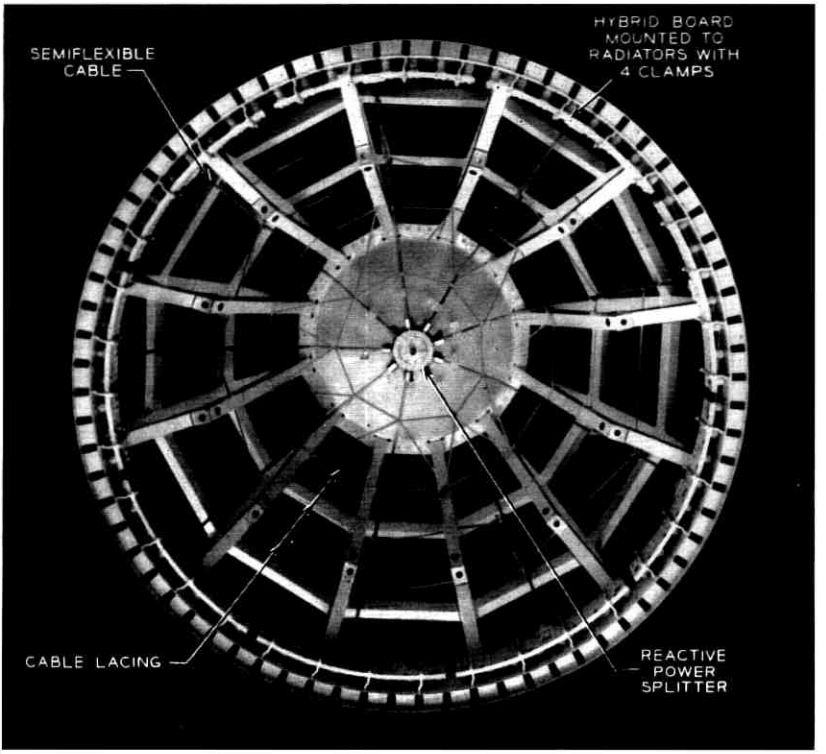

Fig. 6 — View of 6-gc antenna and feed system installed in spacecraft frame.

and 6-gc splitters to provide final over-all tuning of the complete antenna system.

2.3.5 *Resistive Power Dividers (Hybrids)*

Each hybrid board constitutes a resistive 8-way power divider. These hybrid boards are located around the satellite's equator and are curved so as to attach directly to the radiating apertures through special coaxial connectors. In this manner, each hybrid board is rigidly fastened to 8 transmitting or receiving apertures.

The configuration shown in Fig. 8 was chosen for the hybrids, which provides equal power split between ports 2 and 3 independent of frequency. Port 4 is terminated internally by a series resistance of $2Z_0$ (in this case 100 ohms) to maintain isolation between ports 2 and 3.

Fig. 9 shows the center conductor layout for the 4-gc hybrid board,

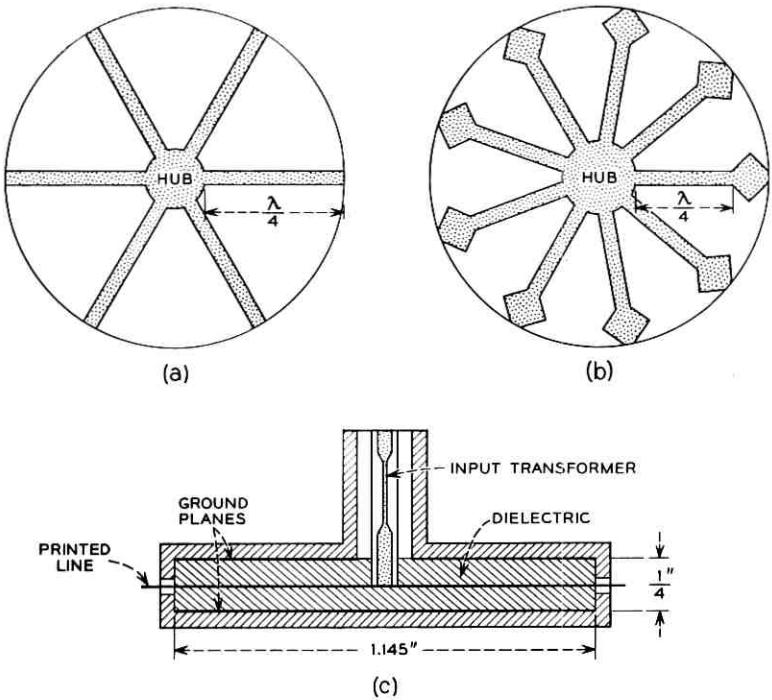

Fig. 7 — Reactive power splitter configuration: (a) 4-gc printed line; (b) 6-gc printed line; (c) cross-section showing input transformer.

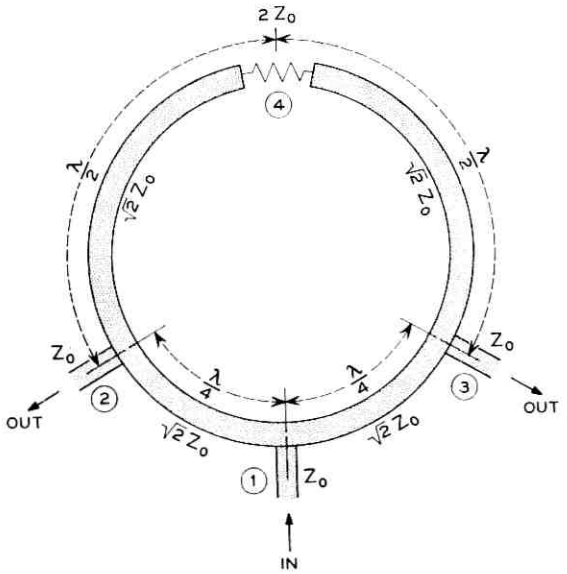

Fig. 8 — Transformed ring hybrid for frequency-independent symmetry.

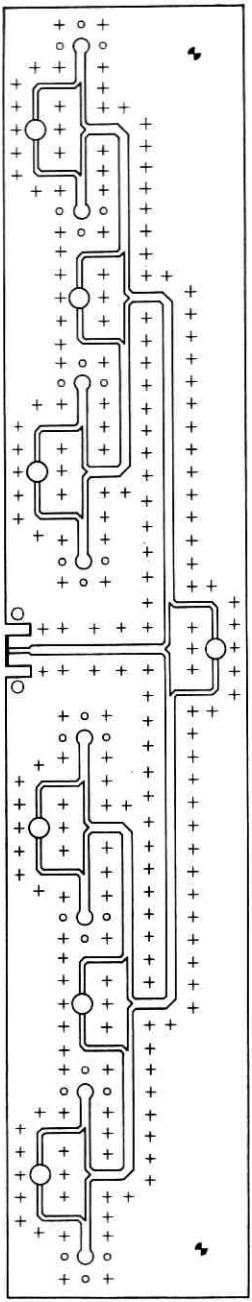

Fig. 9 — 4-ge hybrid printed circuit board.

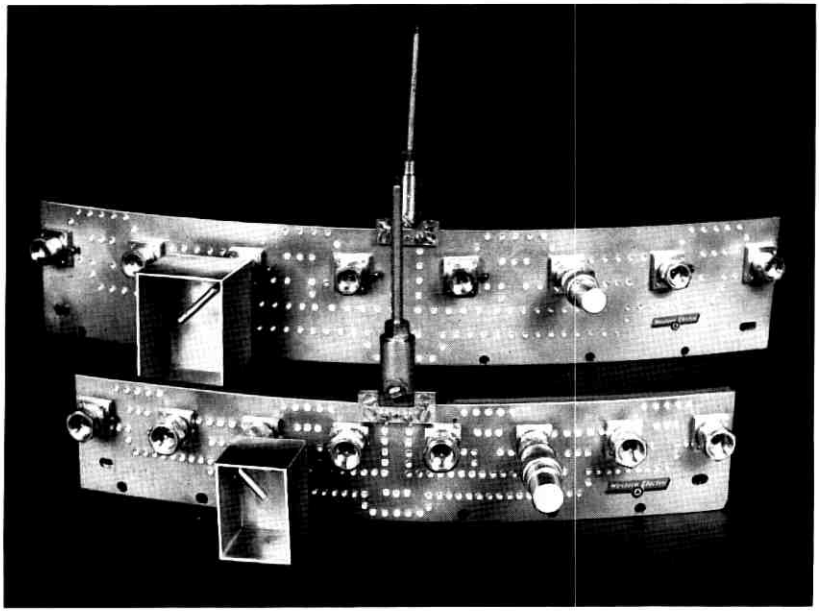

Fig. 10 — 4-gc and 6-gc resistive power dividers.

providing an 8-fold power division by cascading three hybrid stages from input to each output port. The dielectric material used is two sheets of 0.062-inch thick irradiated polyethylene ($\epsilon \approx 2.30$, $\tan \delta \approx 0.00005$). A 100-ohm miniature metal film resistor with flat ribbon leads fits into a circular recess in the dielectric boards and is soft-soldered to the adjoining center conductor to form port 4. Calculations show the absorption loss of the resistors to be $\approx$0.015 db per hybrid at 4 gc and $\approx$0.03 db at 6 gc. Thus, with the three cascaded hybrid stages in each board, the loss due to the 100-ohm resistors is approximately 0.05 db in the 4-gc boards and 0.1 db in the 6-gc boards.

Fig. 10 is a photograph of two assembled hybrid boards — one used at 4 gc and the other at 6 gc. A radiating box is attached to one output port of each hybrid and a short length of 0.160-inch coax is connected to the input ports.

Also noticeable on Fig. 10 are rows of rivets, each 0.090 inch in diameter, which serve both as mechanical fasteners and as electrical shorts around the center conductor, thus ensuring TEM wave propagation without measurable mode conversion. As a rule of thumb, these rivets must be spaced closer than $\lambda/4$ to provide effective shielding and must

be kept away from the center conductor edge by at least one dielectric thickness to prevent changes in characteristic impedance.

These hybrid distribution boards are an interesting use of extremely precise etched circuitry. Stability of performance and distribution of mass were two of the several factors that qualified them for use. The boards are curved riveted "sandwiches" consisting of four layers. The inner two are the dielectric with the etched circuit between them and with copper-clad surfaces adjacent to the outer two magnesium backing plates. All four are riveted together after the boards have been curved to approximately a 16-inch radius. Approximately 200 rivets are used in each board. The large number of rivets, dictated by electrical considerations, results in an extremely rugged and compact circuit board. The boards, 6 for the 4-gc and 9 for the 6-gc antennas, are immediately in back of, and are connected to, the radiating boxes by means of one coaxial connector per antenna box. Fig. 6 shows the hybrid boards as assembled behind the radiating elements. The control of both curvature and the position of the connectors was critical in order to insure proper mating with the radiator box stubs.

2.3.6 *Coaxial Cables*

A total of fifteen semiflexible 50-ohm coaxial cables connect the two central reactive power splitters located near the poles of the satellite to the associated resistive power splitters mounted behind the equatorial arrays of radiating elements. The coaxial is composed of a 43-mil copper wire encased in an irradiated polyethylene dielectric in the form of a helical winding with essentially zero space between turns. The sheath is a copper tube having a diameter of 160 mils and a wall thickness of 5 mils. These cables are sufficiently flexible to be bent so as to follow the contours of the satellite.

2.3.7 *Assembly of Radiating Elements and Feed*

The antenna bands and antenna feed were assembled to the satellite frame in such a manner as to prevent relative motion of the parts at their points of connection. The hybrid boards are rigidly clamped to the antenna bands through the use of four clamps per board, as shown in Fig. 6. The splitters are bolted directly to the frame at its poles and thus are rigidly held. Thus the relative motion that occurs between the hybrids and the splitters during the vibration of launch is accommodated by the bending of the semiflexible cables.

2.4 *Testing and Performance*

2.4.1 *Objectives*

In order to insure the best possible radiation pattern it was necessary to carry out an extensive program of electrical and mechanical tests on the individual components, various subassemblies, and the over-all system. The vital electrical objective is a good pattern, which is insured if microwave power generated or received in the electronics package is transmitted to or from each of the radiating elements with exactly the same phase and amplitude. These tests used a microwave bridge circuit incorporating a calibrated attenuator and phase shifter to measure the relative phase and amplitude between the output ports of the various components of the antennas as well as the over-all antenna assemblies. Phase and amplitude measurement accuracies of the bridge were approximately $\pm 2°$ and ± 0.1 db.

2.4.2 *Radiating Elements*

The radiating elements were checked for axial ratio and return loss over their operating bands. After brief experience with the fabrication of the radiating elements, it was apparent that realistic mechanical tolerances did not insure the necessary uniformity in electrical performance. A sensitive measure of the electrical performance of the individual boxes is the return loss. Return loss measuring equipment (a reflectometer setup) was moved to the fabrication plant, and the boxes were individually tested after they had been welded into the support bands. By electrical tests at the factory it was possible to use boxes in which the mechanical variations combined in a favorable manner and to replace subpar boxes before the whole assembly was removed from the welding fixtures. Although the factory tests indicated the acceptability of the radiators in a qualitative way, it was necessary to make more precise quantitative measurements in the laboratory. Uniformity of transmission through the boxes was checked by exciting them one at a time and terminating the open end of the radiator in a special test fixture. This fixture consisted of a short open-ended rectangular tube of lossy plastic with lips to fit into the mouth of the radiating box and a receiving box mounted on the other end of the tube. With this arrangement, the relative loss and phase of the individual radiators could be compared. These measurements showed a peak-to-peak loss variation of about 0.5 db and a peak-to-peak phase variation of about 8 degrees.

2.4.3 *Reactive Power Dividers*

All the printed circuit reactive power splitters were checked for equality of power division over their operating band. The matching section incorporated at the input to the power splitter was custom designed to allow for individual variations among the reactive and resistive dividers, cables, and radiating elements. The peak-to-peak variation of insertion loss and phase shift taken over the output ports of each splitter is given in Table I.

2.4.4 *Resistive Power Dividers (Hybrids)*

All hybrids boards were given complete electrical testing. Fig. 11 shows the phase and amplitude distribution of all the ports provided by the 4-gc boards; similar results were obtained for the 6-gc boards. Briefly, the peak-to-peak deviations on phase are approximately 8° at 4 gc and 10° at 6 gc, and on amplitude 0.3 db at 4 gc and 0.4 db at 6 gc. In addition, a variation from board to board existed in phase and to a smaller extent in amplitude, which is attributable to lack of precision in the attachment of the input connectors. This phase variation between boards amounted to 10° to 20° and was compensated by corresponding changes in length of the connecting coaxial cable. Input and output VSWR's were measured on all hybrid boards by means of microwave reflectometers and — for more accuracy — on a slotted line. Fig. 12 shows the input and output VSWR's on representative boards. The input match is shown for: (a) radiating elements attached to the output ports and (b) TNC terminations on the output ports. With the TNC terminations, the input VSWR is seen to be less than 1.4 to 1 for about 10 per cent bandwidth. Over the same bandwidths, the output VSWR's are under 1.4 to 1 for the 6-gc boards and under 1.1 to 1 for the 4-gc boards.

2.4.5 *Combined Radiating Elements and Feed*

After individual components, including connecting cables had been measured, the antennas were assembled on the spacecraft framework.

TABLE I—REACTIVE POWER DIVIDERS

Model	Peak-to-Peak Insertion Loss, db	Peak-to-Peak Phase Shift, degrees
Best 4-gc	0.2	1.4
Worst 4-gc	0.4	3.6
Best 6-gc	0.2	4.4
Worst 6-gc	0.55	5.3

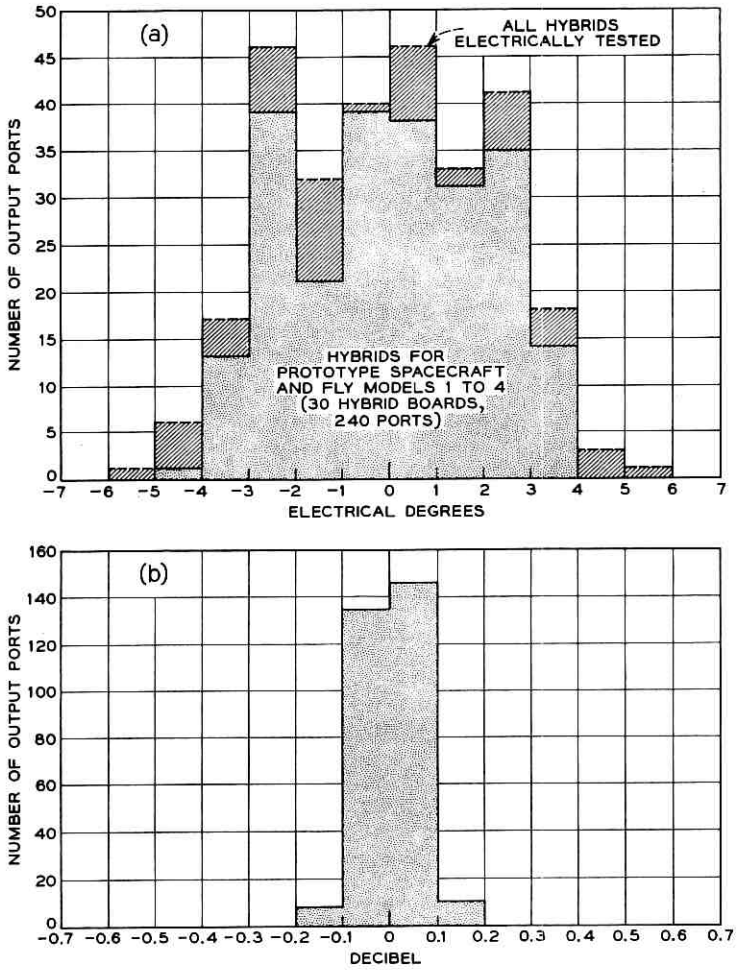

Fig. 11 — Distributions of measurements on the 4-gc hybrid boards: (a) phase distribution; (b) amplitude distribution.

A final check for uniformity of excitation was made of the complete assembly by comparing the phase and amplitude of the individual radiating elements. The test fixture for this purpose consisted of a band of absorbent material to fit around the satellite equator in which was embedded one of the previously described test fixtures for checking the individual radiators. By carefully selecting cable lengths, the average phase to each hybrid group could be accurately matched. This careful selection resulted in peak-to-peak variations as shown in Table II.

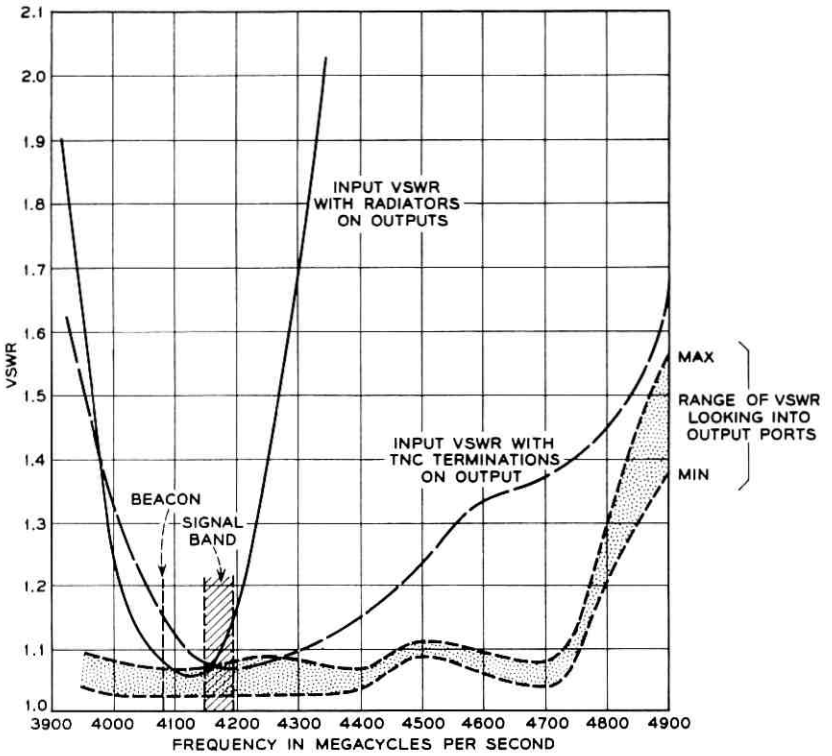

Fig. 12 — VSWR measurements on 4-gc hybrids.

2.4.6 *Over-all Patterns*

Most of the radiation patterns were obtained with an indoor anechoic chamber. These were checked later on an outdoor range with substantial agreement between results. Fig. 13 shows the results for the 6-gc receiving antenna system both for the equatorial and polar aspects. These patterns show the power relative to an isotropic circularly polarized antenna. The all-important equatorial pattern was especially gratifying, because it exhibited a peak-to-peak ripple of less than two db. The

TABLE II — RADIATING ELEMENTS AND FEED

Frequency, mc	Peak-to-Peak Insertion Loss, db	Peak-to-Peak Phase Shift, degrees
4170	1.1 db	10°
6390	1.4 db	14°

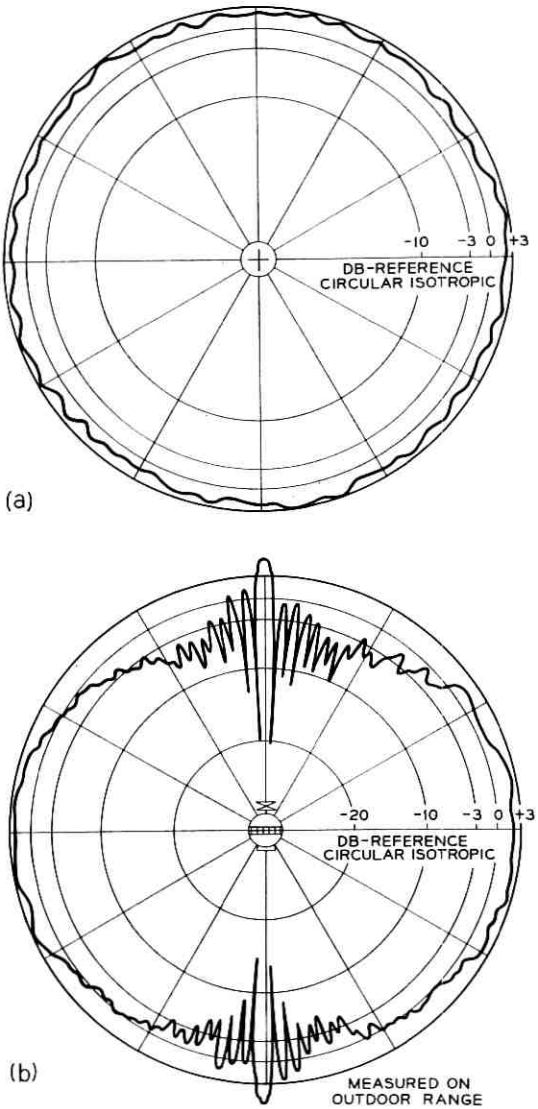

Fig. 13 — Antenna patterns at 6390 mc: (a) equatorial aspect; (b) polar aspect.

polar pattern is reasonably smooth except for the expected nulls near the poles. These patterns show the remarkably large solid angle of coverage provided by these antennas.

Fig. 14 presents the equatorial and polar aspects of the 4-gc transmitting antenna.

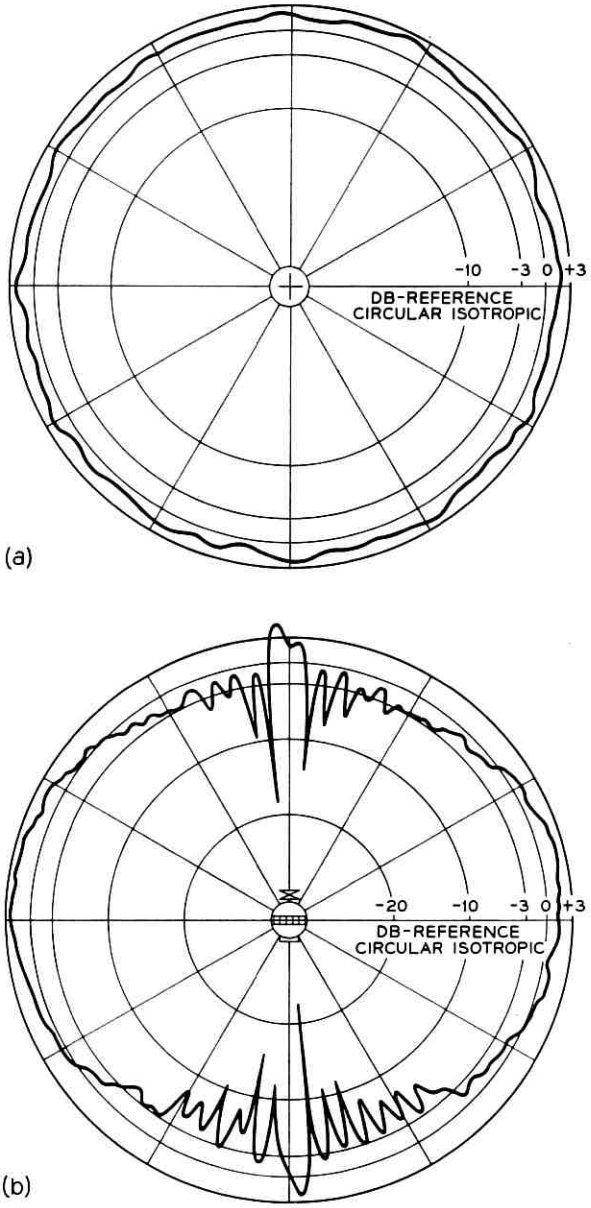

Fig. 14 — Antenna patterns at 4170 mc: (a) equatorial aspect; (b) polar aspect.

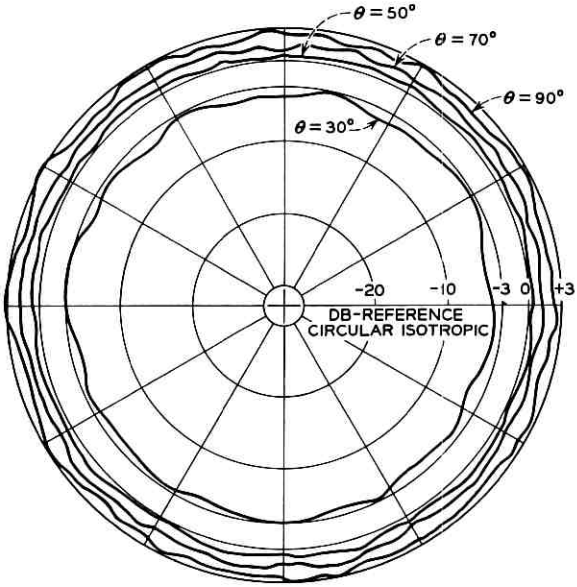

Fig. 15 — Constant-latitude antenna patterns at 4080 mc.

Fig. 15 shows measurements taken at different constant latitudes when measured in an indoor anechoic chamber. The satellite spin produces fluctuations in the received signal level corresponding to the ripples in these patterns. The curve marked $\theta = 90°$ corresponds to the equatorial aspect.

2.4.7 *Thermal and Vibration Considerations*

As pointed out in accompanying papers,[3,5] the spacecraft's spin-axis orientation should be perpendicular to the sun's rays for thermal reasons. The temperature of the antenna components is determined by the actual spin-axis orientation and the duration and frequency of eclipses of the satellite. Extrapolating the predicted skin temperature data in an accompanying article,[5] the temperatures noted in Table III are the ex-

TABLE III — PREDICTED TEMPERATURE EXTREMES

Component	Max. Possible Temp. Range (1 to 2 cycles)	Expected Temperature Range (2000 cycles)
Splitter	+34°C to −50°C	+20°C to −20°C
Hybrid	+10°C to −20°C	+10°C to −5°C
Cables	+40°C to −50°C	+20°C to −10°C

TABLE IV — TEMPERATURE CYCLING CAPABILITIES OF COMPONENTS

Splitter	+40°C to −100°C
Hybrid	+40°C to −100°C
Cables	+65°C to −100°C

tremes predicted, which could only occur once or twice during the satellite's two-year lifetime. In the same table, the temperature extremes are shown for the satellite when the spin axis is within ±30° of being normal to the sun. The range of temperature shown in both extremes includes the effects of full sunlit orbits and maximum eclipse conditions.

Extensive thermal tests were conducted on the hybrids, splitters and antenna cables to ensure that they were capable of withstanding the maximum possible temperature ranges listed above. Table IV is a summary of the temperature cycling capability of the components used in the spacecraft.

Because of the limited development time, extensive tests were not conducted at the more modest "expected temperature range." Based upon an analysis of the stresses which are built up under the extreme temperature cycling conditions and the number of cycles achieved in these tests, it can be confidently predicted that the antenna feed components are capable of withstanding the expected temperature limits for many thousands of cycles.

The thermal tests did disclose a number of weaknesses in the initial designs of the splitters and cables. Mechanical design changes based on these data eliminated the thermal cycling difficulties with the splitters. However, the cable difficulty was more fundamental. In the cable, relative motion occurred between the dielectric and both the inner and outer conductors as a result of temperature cycling. This resulted in a relative displacement of the three items after a few temperature cycles. Different materials and types of cables from a number of suppliers were tested, but all behaved in a similar manner. Through the cooperation of the Tellite Corporation of Orange, N. J., this serious problem was solved by incorporating a helical cut in the dielectric. The depth of the cut extended from the inner conductor to the outer conductor, so that the resulting configuration has a helical winding of dielectric with a small spacing between turns. This design accommodated the difference in expansion between the copper inner and outer conductors and dielectric material.

As a complete assembly the antenna structure was tested thermally in several ways. It was assembled into one of the thermal tester satellites and subjected to temperature cycling as encountered in the environ-

mental test chamber which included solar simulation. The temperature ranges under these conditions were equivalent to the expected temperature range for the high-temperature end, and equivalent to the extremes expected to be encountered for the low-temperature end. In addition, a laboratory test was conducted in which the antenna performance was checked while the poles of the satellite were being cooled down to the extreme low temperature with the antenna radiator section being kept at room temperature. This condition is more severe than that which could be encountered. The antenna satisfactorily passed all these tests.

Section 2.3.7 describes the attachment of the feed to the satellite. In view of the high acceleration levels to which the feed components are subjected and the complex nature of acceleration levels versus the frequency, the most realistic test for mechanical prove-in of the antenna feed structure is on an actual satellite. Hence, the antenna feed system as a whole was vibration tested only after it was assembled into a satellite frame. Accelerometers attached to various portions of the feed system showed a maximum reading at resonance of 260 g on one of the hybrids. Although subsequent electrical tests showed that the antenna systems were still usable, several mechanical weaknesses were uncovered. Further mechanical engineering changes in the mounting of the components eliminated the difficulties.

III. VHF ANTENNA SYSTEM

3.1 *Requirements*

The VHF antenna is used for beacon, telemetry, and command signals. This antenna should be nearly isotropic, have low dissipation loss and radiate circularly polarized waves. The size and position of the antenna is restricted in that it must not shade the solar cells. The VHF antenna is required to operate during the launching of the satellite as well as during orbit. This means that the antenna must radiate with substantially no change in pattern while the satellite is enclosed in the protective fairing and while mounted to the third stage of the rocket during the early phases of the launch. The dimensions of the fiber glass fairing placed upper limits on the height and diameter of the antenna in order to avoid interference during the severe vibration encountered during launch. The final dimensions of the antenna were chosen to make the antenna as large as possible within these restrictions.

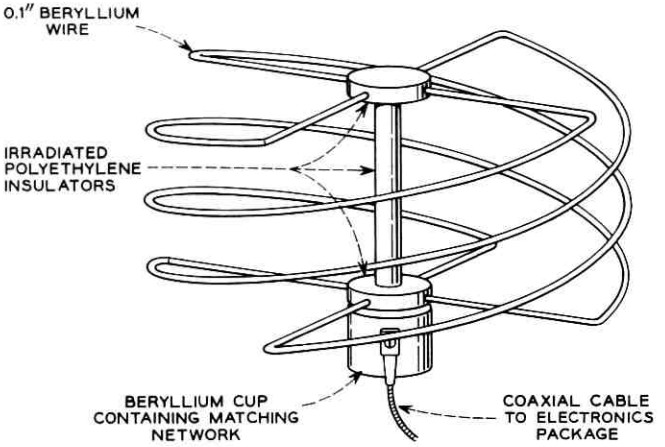

Fig. 16 — Sketch of VHF antenna.

3.2 *Initial Approach*

The decision to mount the communication antennas around the equator of the spacecraft eliminated that position for the VHF antenna. The requirement of nonshading of the solar cells eliminated the use of several sets of crossed dipoles located symmetrically about the satellite. It was therefore originally decided to use a small, multi-element, broadside helix mounted on an erectable mast. A sketch of this helix is given in Fig. 16. The antenna and mast would be collapsed during the launch, since the fairing dimensions would not allow the antenna to be extended, and upon injection into orbit an explosive charge would erect the mast and helix. During the launch a pair of auxiliary dipoles or whips mounted near the south pole of the satellite and fed by means of a directional coupler would maintain telemetry and command capability for the satellite. With this system, which was suggested by Wheeler Laboratories, Smithtown, N. Y., under Bell Laboratories contract, the helix radiated a circularly polarized wave with a pattern similar to that of a short dipole. This gives quite good coverage except near the poles of the satellite.

The helix may be thought of as an end-fed half-wave radiator coiled so as to look like a small loop antenna combined with a short dipole radiator. The loop field is in time quadrature and is at right angles to the dipole field. Circular polarization is obtained by adjusting the dimensions so that the magnitudes of the two field components are equal. The helix was designed by Wheeler Laboratories.[6] The antenna is a

small end-fed radiator with a high input impedance and its bandwidth is relatively small, in fact, considerably smaller than the 13-mc spread between the command and telemetry frequencies. Therefore, a matching network to avoid high standing wave loss was necessary. The dimensions were chosen such that the antenna was resonant at 129 mc, and the matching network provided a conjugate match as well as a transformation of impedance level at both frequencies. A circuit diagram of the matching network is given by Fig. 17.

Beryllium wire 0.1 inch in diameter was chosen to wind the helix because of its light weight and rigidity. A thin layer of gold was plated over the beryllium to reduce its dissipative loss. In order to provide the proper coefficient of emissivity to aid in the thermal balance of the spacecraft, the exterior portion of the antenna system was sprayed with an aluminum oxide coating by a plasma gun.

During the development a number of uncertainties arose to make an antenna on an erectable mast seem less and less desirable. The adverse effect on the moment of inertia was compounded, since the stringent requirements on the helix dimensions dictated elaborate jigs to insure these dimensions after the stress of launch and upon erection. The collapsed helix, while not a good radiator, did radiate enough to affect the patterns of the dipoles to an unpredictable extent if the vibration during launch caused the helix elements to intermittently touch one another. Also, the dipoles themselves affected the in-orbit pattern, not so much near the equator, but noticeably in the vicinity of both poles.

3.3 *Final Approach*

Because of these uncertainties it was decided to use the helix as a short vertically polarized dipole permanently mounted to the north pole of the satellite. Since the ground antenna used for the command and telemetry signals is circularly polarized, the problem of polarization

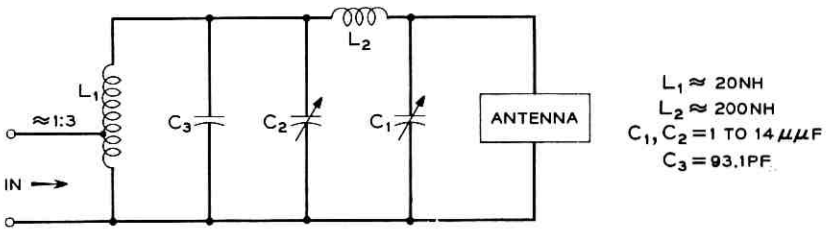

Fig. 17 — Schematic diagram of VHF antenna matching network.

tracking does not arise if the system can tolerate the additional 3-db loss. A careful study of the signal levels and path losses showed essentially no penalty for commandability and a small penalty for telemetry. Mounting the helix directly on top of the satellite resulted in the following advantages:

(a) Since the helix is not collapsed during launch, the whips and associated directional coupler can be eliminated.

(b) Since the helix is directly on the sphere, the additional cable length required for the erectable mast is eliminated. This results in a 0.5 db decrease in loss.

(c) The elimination of the mast erecting package results in an increase in reliability since the antenna would have been useless had the firing mechanism failed.

Since mounting the helix directly on top of the satellite destroys the balance between the loop and dipole radiation components, the dimensions were altered to insure that it would fit into the launch fairing, yet retain the same impedances. This alteration did not change the matching network and left the dipole component unaffected.

The matching network was adjusted while mounted on a model of the satellite. The model was mounted on the roof of the Hillside, N. J., laboratory, and final adjustments were made with the base of the helix and the network cup surrounded by dry ice; a thermocouple attached to the network cup indicated −75°C. Fig. 18 shows that the match at both frequencies is degraded as the temperature increases, but the

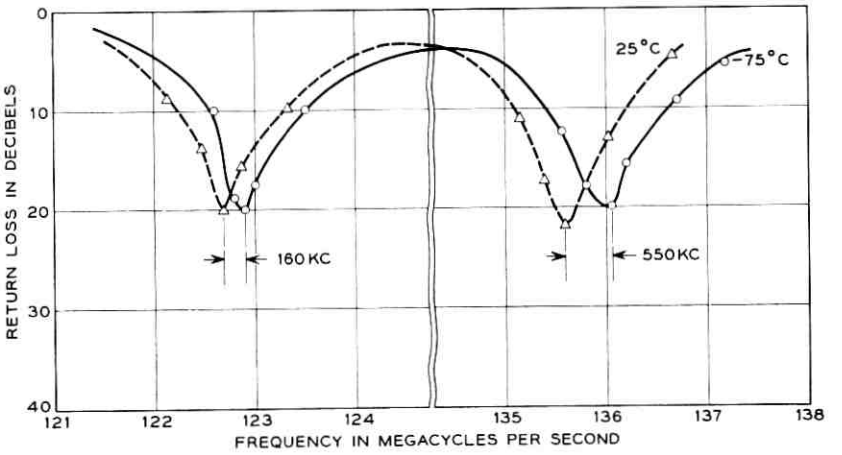

Fig. 18 — Return loss measurements of VHF antenna.

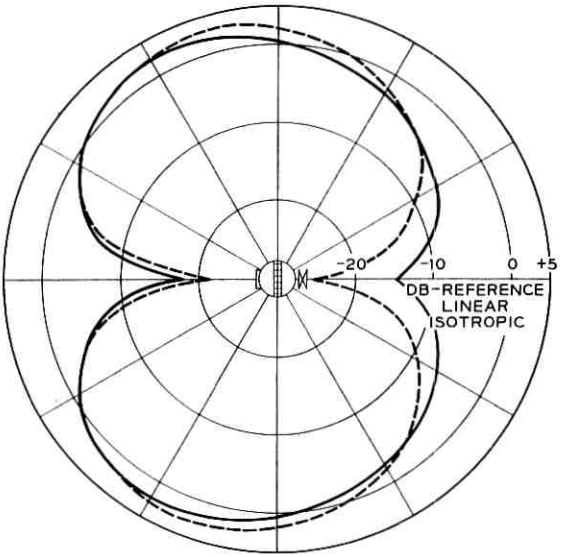

Fig. 19 — Polar aspect VHF antenna pattern at 123 mc: solid curve—measured pattern; dotted curve—calculated pattern.

antenna is still quite usable at +25°C, although, except at launch, it is never expected to be warmer than −50°C.

3.4 *Testing and Performance*

The radiation patterns of the antenna are perfectly uniform when viewed at a constant latitude and when the satellite is rotated about its spin axis. The pattern does vary as the satellite is rotated at right angles to the spin axis, as is shown by Fig. 19. This figure shows the radiation pattern at approximately 123 mc as well as a theoretical pattern assuming a lossless antenna. The differences in maximum gain points indicate a loss in the matching network and dissipation loss in the helix of 1.5 db at approximately 123 mc. The corresponding comparison at approximately 136 mc shows a loss of 2.5 db.

IV. CONCLUSION

Two high-performance, isotropic, circularly polarized, microwave antenna systems have been designed, constructed, and operated successfully in the environment of outer space. The radiation patterns demonstrate that by use of extremely precise techniques of magnesium

fabrication and printed wiring a spherical surface can be uniformly excited by as many as seventy-two discrete radiating elements.

In addition, reliable and efficient narrow-band radiation of VHF signals has been achieved by employing a multi-element helix with a matching network.

V. ACKNOWLEDGMENT

The authors wish to pay tribute to their many colleagues in Bell Telephone Laboratories and Western Electric who devoted their skill and energies far beyond the call of duty in making this development possible. Special mention should also be made of the wholehearted cooperation of many companies outside the Bell System.

REFERENCES

1. Dickieson, A. C., The *Telstar* Experiment, B.S.T.J., this issue, p. 739.
2. Hoth, D. F., O'Neill, E. F., and Welber, I., The *Telstar* Satellite System, B.S.T.J., this issue, p. 765.
3. Shennum, R. H., and Haury, P. T., A General Description of the *Telstar* Spacecraft, B.S.T.J., this issue, p. 801.
4. Bugnolo, D. S., A Quasi-Isotropic Antenna in the Microwave Spectrum, I.R.E. Trans. on Ant. and Prop., **AP-10,** No. 4, July, 1962.
5. Hrycak, P., Koontz, D. E., Maggs, C., Unger, B. A., Stafford, J. W., and Wittenberg, A. M., The Spacecraft Structure and Thermal Design Considerations, B.S.T.J., this issue, p. 973.
6. Wheeler, H. A., A Helical Antenna for Circular Polarization, Proc. I.R.E., **35,** December, 1947, p. 1484.

The Spacecraft Radiation Experiments

By W. L. BROWN, T. M. BUCK, L. V. MEDFORD, E. W. THOMAS, H. K. GUMMEL, G. L MILLER* and F. M. SMITS†

(Manuscript received March 22, 1963)

The radiation experiments on the Telstar spacecraft were designed to measure the electron and proton particle distributions in the region of space explored by the satellite orbit and to give information on the integral semiconductor radiation damage produced by these particles. A solar aspect experiment is included with the radiation experiments because of its direct importance to solar cell damage results. The design and the hardware for these experiments are described in the present paper. Results of the experiments are included in a companion paper in this issue.

I. INTRODUCTION

The radiation experiments on the Telstar spacecraft were designed to measure the distribution in energy, position, and time of electrons and protons trapped in the earth's magnetic field in the Van Allen belts. Such particle distributions characterize the radiation environment of the satellite, and in addition help provide an understanding of the mechanisms that are responsible for injection of particles into the Van Allen belts and for loss of particles from the belts. The radiation experiments also measure directly the integral radiation damage effects on semiconductors. Only magnetically trapped particles are important for damage considerations on the satellite, and only they are being examined in the particle experiments. The direct effects of primary cosmic rays are negligible, as are also the effects of solar protons which stream into the earth's polar regions but do not reach the Telstar satellite's extremes in latitude. However, these two classes of particles are important because of the secondary neutrons they produce in the earth's atmosphere, which subsequently decay in the trapped particle region and contribute both protons and electrons to the Van Allen belts.

Although the radiation belts have been examined in a large number of

* Brookhaven National Laboratory, Upton, Long Island, N.Y.
† Sandia Corporation, Sandia Base, Albuquerque, New Mexico.

experiments, the region of space traversed by the Telstar satellite has not previously been studied extensively. The satellite provides an unusually fine opportunity for quantitative observation of a large region that includes essentially the whole of the inner Van Allen belt as well as part of the high latitude "horns" of the outer belt. As it turned out, the satellite was to examine not only the natural particles in the radiation belts, as had been originally intended, but also particles artifically introduced into the belts by U. S. and Russian high-altitude nuclear explosions. These new particles were destined to play a major role in the radiation effects sustained by the satellite's electronic equipment.

The radiation experiments on the satellite are divided into those measuring radiation damage and those studying energetic particles. These will be discussed in detail in Sections III and IV, respectively. A solar aspect experiment which measures the orientation of the satellite with respect to the sun is also included as a part of the present paper, because it is essential to the radiation damage experiment on solar cells. It will be discussed in Section II.

II. SOLAR ASPECT

The attitude that the satellite presents to the sun is important for the performance of the solar cell power supply and for the temperature distribution of the satellite. The knowledge of this is also important for evaluation of the degradation of solar cells as a result of radiation damage, since changes in solar aspect affect the illumination of the cells whose output is being monitored. The satellite is spinning and, as a result, the satellite temperature and the average power from the solar power plant depend only on the angle α between the spin axis and the satellite-sun line, essentially the colatitude of the satellite-sun line with respect to the satellite. However, for a single solar cell or a group of cells which are parallel, the instantaneous output depends both on the colatitude of the satellite-sun line and its longitude φ with respect to the satellite. These two angles are determined in the solar aspect experiment.

The angles α and φ are determined by simultaneous measurement of the outputs of a group of six solar cells arranged as in Fig. 1. These cells have mutually perpendicular normals. In essence their directions are those of the faces of a cube. The three perpendicular axes defining the normals of the group could be located in any direction with respect to the spin axis of the satellite and still uniquely define the sun's position. For example, four cells could look out perpendicular to the spin axis and

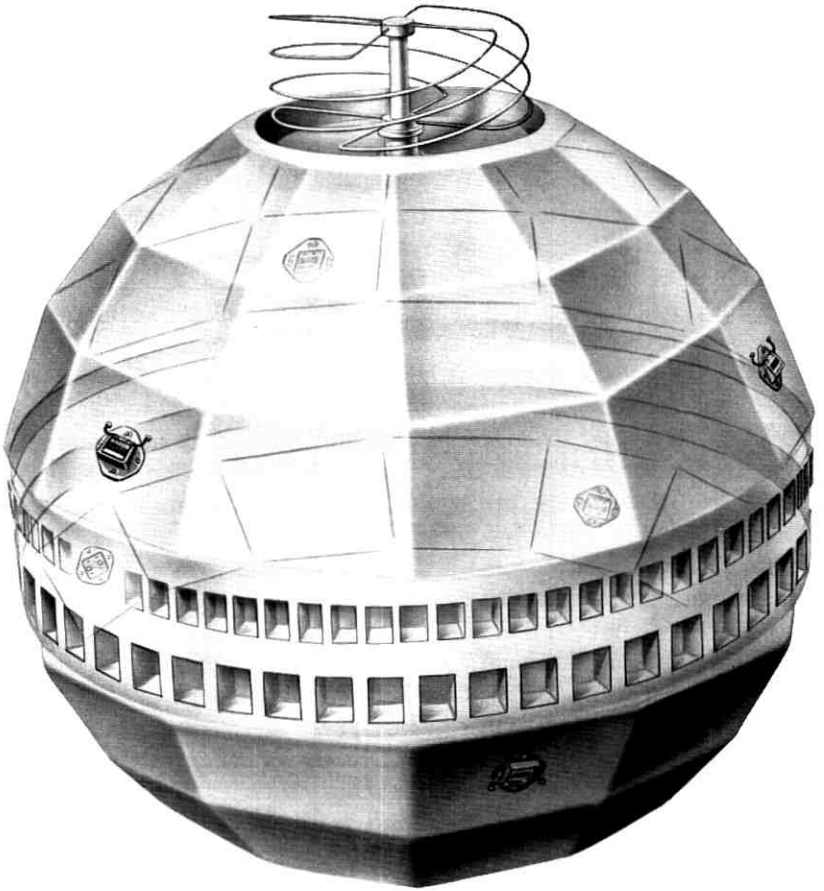

Fig. 1 — Placement of the solar aspect cells.

two in opposite directions along that axis. However, the arrangement of Fig. 1 has several advantages. The angle α is expected to be near 90 degrees, and reliable measurements near this angle are desired. With the cell positions of Fig. 1, one per cent measurements of the cell outputs define α and φ to one degree or better. Furthermore, as the instant of simultaneous measurement (determined by the telemetry frame rate) is not in general synchronous with the rotation rate of the satellite, the measurement of α depends in successive telemetry frames on different combinations of the six cells, so that failure or degradation of one is not disastrous.

The cells are mounted on the satellite facets nearest the antenna band to minimize the temperature extremes encountered as α departs from 90 degrees. The individual cells are of the same type (n-on-p) and are mounted with the same techniques used on the main solar power supply:[1] a ceramic base, platinum side strips and 30-mil sapphire covers. The cover width is much wider than a single cell, for uniformity in illumination and protection from radiation damage. Angle brackets orient the cell normals to 35 degrees above and below the satellite equator as required. With this mounting on the nearly spherical satellite surface, there are no shadowing and reflection problems of any consequence.

The six solar aspect cells were preirradiated with approximately 2×10^{16} 1-Mev electrons/cm^2 before mounting. This reduced their output under solar illumination by a factor of 2, but it reduced their sensitivity to further reduction in this number by radiation damage in space by a factor of at least 100.[1] The short-circuit current of each cell is measured as a voltage across a 2.75-ohm shunting resistor actually positioned in the telemetry interface circuitry inside the electronic canister. The currents for the six cells are sampled in a total of 600 microseconds, a time in which the satellite at its maximum rotation rate turns only by about one half of a degree. The timing is accurately known, so that an additional correction could be applied, but for this experiment the sampling is essentially instantaneous.

The telemetry examining the cell outputs has 100-millivolt full-scale sensitivity.[2] Changes in its gain are of relatively minor significance because the solar aspect angle really depends on ratios of the outputs of different cells. However, drifts in the amplifier zero would be quite serious. To provide a check on the zero, a seventh cell is placed inside the satellite skin and is covered with an opaque aluminum coating. To permit detection of zero drifts of either sign, a one-milliampere current is bled into the shunting resistor of this dark cell to offset its reading above zero by two telemetry bits.

The short-circuit current of an individual cell as a function of the angle of illumination with respect to its normal has been experimentally determined and is shown in Fig. 2. The shape does not depart substantially from a cosine law at small angles, but drops much more rapidly because of reflection losses toward grazing incidence. In addition to this calibration, interpretation of the telemetry readings to deduce the angle of illumination of a single cell involves temperature correction as illustrated by line A of Fig. 3. This is much larger than the temperature correction to the short-circuit current of nonirradiated cells, line B of the figure, because the recombination centers introduced by radia-

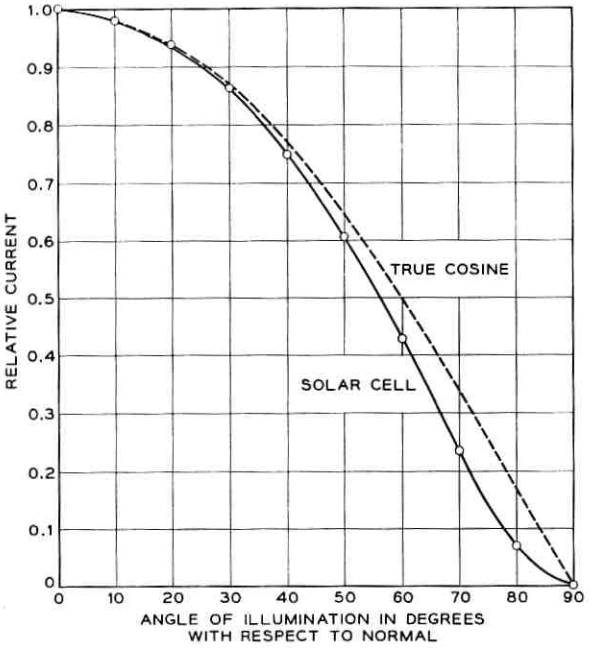

Fig. 2 — Solar cell short-circuit current vs angle of illumination.

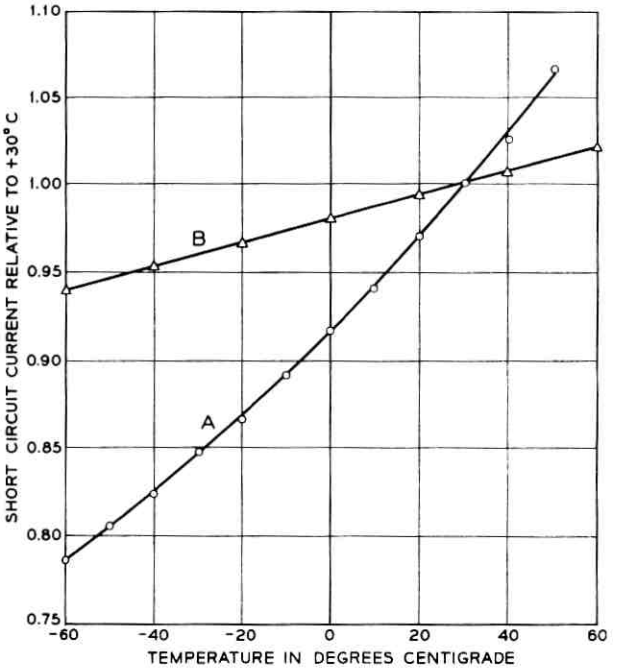

Fig. 3 — Temperature dependence of solar cell short-circuit current: (a) cell preirradiated with 2×10^{16} 1-Mev electrons/cm^2; (b) nonirradiated cell.

tion are quite different than those normally present. The operating temperatures in orbit range[3] from $-30°C$ to $+14°C$, but measurements have usually been made between $-10°C$ and $+5°C$.

Fig. 4 shows the anticipated output from the cells as a function of φ and for two values of α at 80 degrees and 90 degrees. In general, three cells are involved in the measurement, except at specific symmetry points where only two are illuminated, such as point A. The most critical measurement positions, those giving best definition to α and φ, are of type B, where three cells have substantial outputs and two are nearly alike. Such positions correspond to the sun being on the meridian of a cell in one hemisphere, and hence midway between the meridians of two cells on the other hemisphere. The ratio of the two nearly equal outputs to the one larger output is quite sensitive to α, and the ratio of the two nearly equal outputs to one another is very sensitive to φ. Because of the satellite rotation rate and its change with time, the sequence of one-minute measurements of the cell outputs will display a variety of patterns on different orbits of the satellite. Examples will be discussed

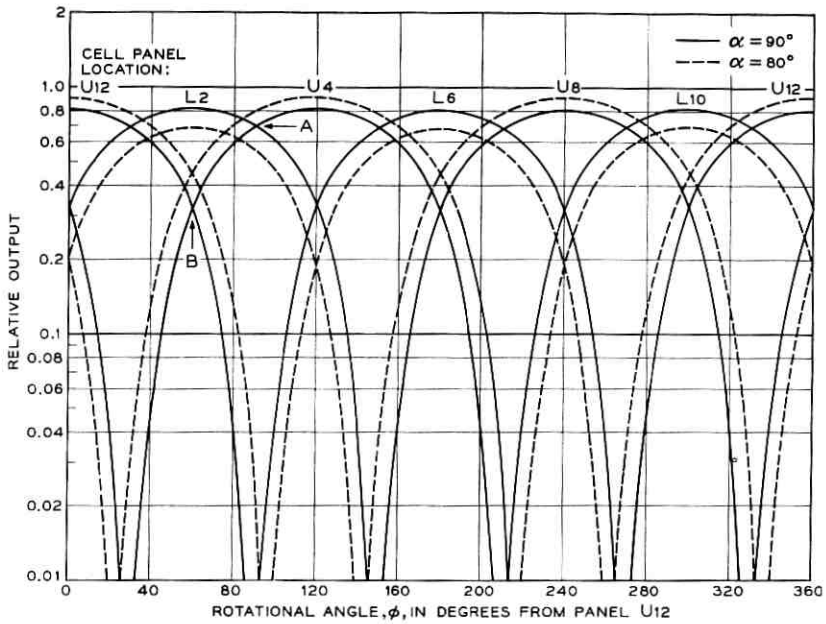

Fig. 4 — Anticipated dependence of the output of the solar aspect cells on the rotational angle of the sun with respect to the satellite for two different angles of the satellite spin axis with respect to the satellite-sun line.

in connection with the results of the radiation experiments in a separate paper.[4] The angle α can in general be determined from a single set of readings of the telemetry, but in practice many more points are used to avoid the possibility of error and to check on the reproducibility of the result obtained as different cells dominate in its determination.

III. RADIATION DAMAGE

3.1 *Solar Cells*

A solar cell damage experiment provides a direct measure of the degradation in short-circuit current due to radiation damage in three cells shielded by different thicknesses of sapphire. The cells are of the same type as the main solar power supply cells and the mounting is the same as for the solar aspect cells. It was not possible, using this mounting technique, to provide reliable attachment of thin covers, and hence the range in shielding thickness is narrower than would have been desirable. The cells are protected with 20, 25, and 30 mils of sapphire.

The group of three damage cells is mounted on the same facet of the satellite skin as one of the preirradiated solar aspect cells. This panel is shown in Fig. 5. The outputs of the damage cells are handled in the telemetry in the same way as those from the aspect cells, except that a 1.5-ohm resistor is used for a shunt because of the higher anticipated short-circuit current. The sampling time for the total of ten cells (six aspect, one zero-drift, three damage) is approximately 1100 microseconds.[2] The damage cells thus have the same illumination at the time of measurement as the solar aspect cell with the same orientation. With this arrangement, determination of changes in the unirradiated cells due to radiation damage can be made directly by comparison with that preirradiated aspect cell. The accuracy of the measurement depends markedly on the magnitude of all the outputs, but no correction for sun position is necessary in evaluating solar cell degradation. Furthermore, changes in illumination such as might arise from roughening of the sapphire surface by micrometeorites are not involved. Observation of the absolute current from the aspect cells measures this type of variation if it exists, although not distinct from changes in amplifier gain in the telemetry. Even if the aspect cell on the panel with the damage cell should fail, the redundancy of the determination of the solar aspect between remaining cells would make a continuing measure of damage possible without reliance on the absolute current. All of the cells in the aspect and damage parts of the experiment were measured with a spectral

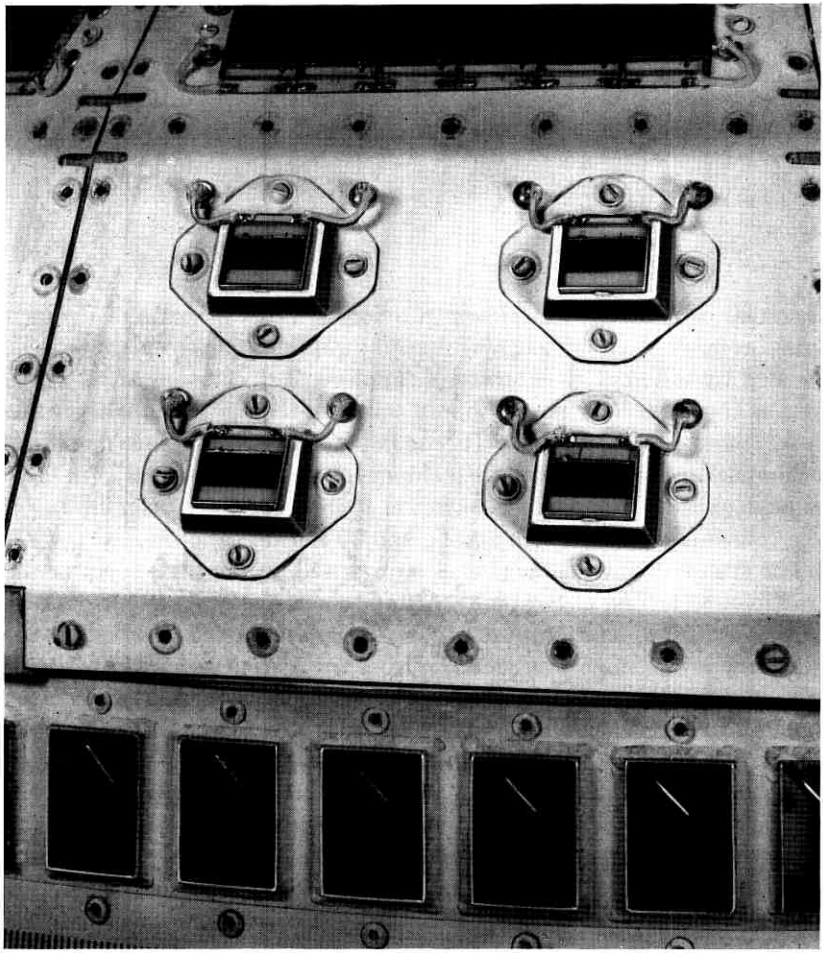

Fig. 5 — Radiation damage solar cell array. The lower right-hand cell is one of the six solar aspect cells.

analyzer developed by H. K. Gummel,[5] and predictions of their output under outer-space illumination were made. The shunt resistance choice was conservatively based on these measurements. For the damage cells the anticipated output was 52.5 milliamperes, the cells being similar within ±2 per cent. For the aspect cells, the predicted current was 23.5 milliamperes, with individual variations of less than ±3 per cent.

3.2 *Transistors*

To provide a direct measure of radiation damage in silicon independent of light, a group of npn diffused silicon transistors was specially fabricated. These devices provide a check on the solar cell results and permit extension of the study of shielding effectiveness to thinner shields. The degradation of solar cell performance under radiation results from a decrease in the lifetime of electrons (for n-on-p solar cells) in the p-type base material of the cell. This same property controls the α of transistors through the transport factor: the fraction of minority carriers introduced into the transistor base at the emitter which arrive at the collector junction. If lifetime is decreased by radiation damage, the light-created electrons (in the solar cell) and emitter-injected electrons (in the transistor) have increasing probability of recombination before they reach the solar cell junction or the transistor collector junction. Thus a direct comparison can be made between the results of one experiment and the other. As an experiment, the transistor has the advantage not only that the α measurement is independent of the sun, but also that the sensitivity to radiation damage can be made considerably greater by the use of a very wide base region.

The construction of the damage transistors is shown in Fig. 6. The device is made of the same kind of silicon used in solar cells (approximately one ohm-cm p-type) and the two junctions are made by solar cell junction diffusion techniques. These steps make a comparison of the results most direct. The transistor wafer is mounted on a pedestal close beneath the lid of the encapsulating Kovar can. For minimum shielding, the lid has been ground down to 3 mils from its normal 10-mil thickness. Through this thin lid the device sees particles over a 3.5-steradian solid angle.

The maximum sensitivity for damage measurement in transistors is limited by the maximum initial lifetime that can be maintained in the base region through device fabrication. The common-base current gain, α_{DC}, is related to the transport factor β across the base region as $\alpha_{DC} = \gamma\beta = I_c/I_e$, where γ is emitter efficiency, which we will assume to be independent of radiation damage. The lifetime τ of minority carriers in the base determines β in a device with base width W as

$$\beta = \operatorname{sech}\,(W/\sqrt{D\tau}) = \operatorname{sech}\,(W/L)$$

where D is a diffusion coefficient and L is the diffusion length for electrons in the p-type base. Radiation damage changes the lifetime[6] as

Fig. 6 — Construction of the radiation damage transistors.

$$1/\tau = 1/\tau_0 + K\Phi$$

where Φ is the integral flux of damaging particles and K depends on particle type and energy.

$$d\alpha/d\Phi = \gamma d\beta/d\Phi = -\frac{LK}{2D}\frac{W \sinh W/L}{\cosh^2 W/L}.$$

For small values of W/L, $d\alpha/d\Phi$ increases as W^2 for fixed L, the sensitivity to damage increasing with base width simply because the minority-carrier diffusion time increases and recombination processes become more evident. However, the expression has a maximum at $W \approx 1.5L$, corresponding to an α of about 0.43. Since τ_0 is limited by device processing, there is no advantage in increasing W beyond this point. In the damage transistors of the Telstar satellite, α is between 0.3 and 0.5 and the base width is on the order of 4 mils. As a result, the

devices have a low α cutoff frequency, about 100 kc. (Low-frequency cutoff and high damage sensitivity in transistors are almost invariably found together.[7] In examining components for potential susceptibility to damage, it is the low-frequency power devices that are of primary concern.)

The α_{DC} of the damage transistors is measured in the Telstar satellite in the circuit shown in Fig. 7. An approximately constant 0.5-milliampere dc emitter current is determined by the 8-volt zener diode and the 16.2-kilohm resistor in the emitter circuit. The extra diode in series with the zener partially compensates for change in the emitter current that would arise from the temperature dependence in the emitter junction. The collector current is read by the telemetry[2] as the voltage across the 16.2-kilohm collector resistor. With an α of 0.5, the output voltage has a maximum of approximately 4 volts. The output drops in proportion to α until it reaches the collector saturation current, specified in these devices to be less than 5 microamperes. This collector saturation current ultimately limits the minimum measurable α at two per cent of its initial value or less.

The relative change in α_{DC} in the transistors with radiation compared with the change in I_{SC} in solar cells is shown in Fig. 8. The initial rate of change of the transistor is somewhat greater, but even more striking is its continued high rate of change as the radiation proceeds. From the standpoint of a solar cell power supply, the decrease in the sensitivity to radiation with increasing damage is very helpful in providing extended life; but from an experimental standpoint, it makes evaluation of the damaging environment increasingly difficult.

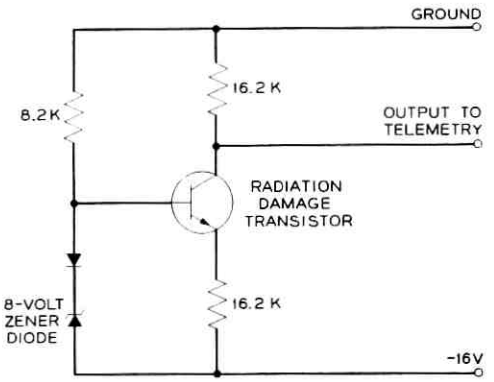

Fig. 7 — Radiation damage transistor circuit.

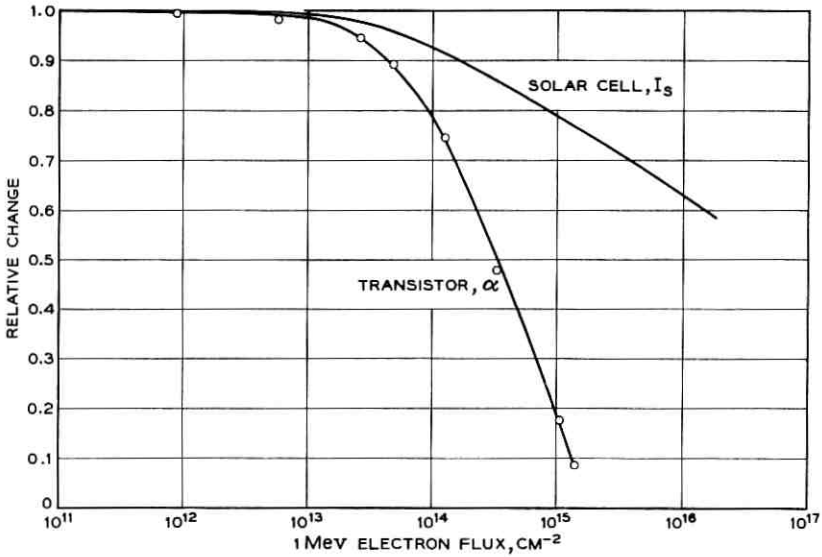

Fig. 8 — Comparison of radiation damage in solar cells and damage transistor.

Seven damage transistors are included in the transistor experiment, two each with three different shield thicknesses and a seventh which is heavily shielded and preirradiated to serve as a general check on the stability of the measurements. The devices and their associated circuits are assembled in a single package, shown in Fig. 9. This package (foamed and in a complete can) is mounted at a hole in the satellite skin, with its face almost flush with the surface of the satellite. The shield thickness of one of the pairs of devices, 35 mils of aluminum in addition to the 3-mil Kovar can, is comparable to the shielding of the main solar cell power supply, 30 mils of sapphire, and of one of the damage solar cells discussed in Section 3.1. The other two pairs have less shielding: 3-mil Kovar only and 3-mil Kovar plus 15 mils of aluminum.

IV. ENERGETIC PARTICLES

The Telstar satellite carries a group of four detectors designed to measure the spatial distribution and time variation of electrons and protons trapped in the earth's magnetic field and crude properties of their energy distribution. The satellite's orbit takes it through the most intense part of the inner Van Allen belt where protons of up to at least 500 Mev are known to exist[8] and where the proton flux increases with

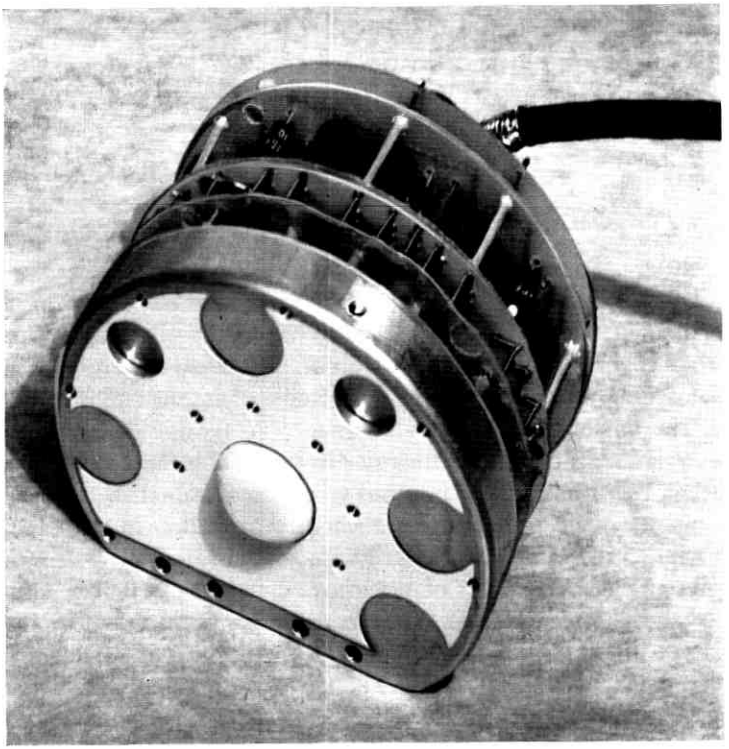

Fig. 9 — The radiation damage transistor assembly.

decreasing energy. The region also contains high fluxes of electrons whose intensity and energy distribution were poorly known. The orbit at high latitudes touches the horns of the outer Van Allen belt, which contains electrons and very low energy protons in concentrations that are highly variable as a result of solar activity.[9] One objective of the particle experiment is to establish a correspondence between the radiation damage in the solar cell power supply, the solar cells and transistors of the radiation experiment, and the distribution of particles responsible for the damage. Of even greater importance is the acquisition of data that will help provide a detailed understanding of the geophysical processes that produce and limit the radiation belts. Such an understanding is ultimately essential for assessing the radiation environment, not only in the Telstar satellite orbit but in other orbits of interest for communications satellite systems. In conceiving the experiments, no consideration was given to the possibility that effects of high-altitude

nuclear explosions might alter the belts in very significant ways,[10] although these artificial perturbations turned out to be of great importance. The next sections will describe the particle experiments, some details of the particle detectors, and some of the unique circuit features in the particle measuring experiments.

4.1 *The Particle Experiments*

The high particle intensity anticipated in the heart of the inner Van Allen belt requires the use of detectors which are fast and which have rather small geometrical factors (the product of the solid angle of particle acceptance and effective detector area). To avoid severe background problems that would arise if the solid angle of interest were made very small, the detector itself must be small. To permit discrimination of electrons from protons, some energy-proportional measurement is almost essential. To withstand the rigorous vibration of launch, a rugged device is required, and to provide for satisfactory operation in the vacuum of space, under the temperature variations of the satellite in orbit and in the presence of high levels of radiation, a device of great reliability is a necessity. Semiconductor particle detectors were selected as being nearly ideal. These are p-n junction devices which in effect are small solid-state ionization chambers.[11] They give output charge pulses proportional to the energy deposited by an incident charged particle in a disk-shaped active volume a few millimeters in diameter and a few tenths of a millimeter thick. They can be made with high reliability, as will be described in detail in Section 4.2. This kind of device has been extensively used in low-energy nuclear physics experiments in the last several years and provides high energy resolution[12] and relatively high speed.[13] In the Telstar experiment, the detectors are not being used as high-resolution devices or at their maximum capabilities of speed. Nevertheless, the nuclear physics experience with them has been invaluable in the satellite experiment design. Semiconductor detectors have been flown in the Injun and TRAAC satellites and in several Air Force satellites in the past two years, but very little of this information is yet available.

Three of the four detectors in the Telstar particle experiment measure protons, and the fourth measures electrons. Their energy ranges are:

low-energy protons	2.4–25 Mev
medium-energy protons	26–34 Mev
high-energy protons	>50 Mev
electrons	200 Kev–1 Mev (the detector response continuing to higher energies).

The outputs from the detectors time-share a single 14-bit register in the

telemetry, accumulating counts over periods between 3 and 15 seconds and reading out the register in all cases in two consecutive 7-bit telemetry words. The detectors are described individually in Sections 4.1.1 through 4.1.4.

4.1.1 *Low-Energy Protons (2.4 to 25 Mev)*

A cutaway view of the low-energy proton detector mount is shown in Fig. 10. The active p-n junction device is inside a transistor-like

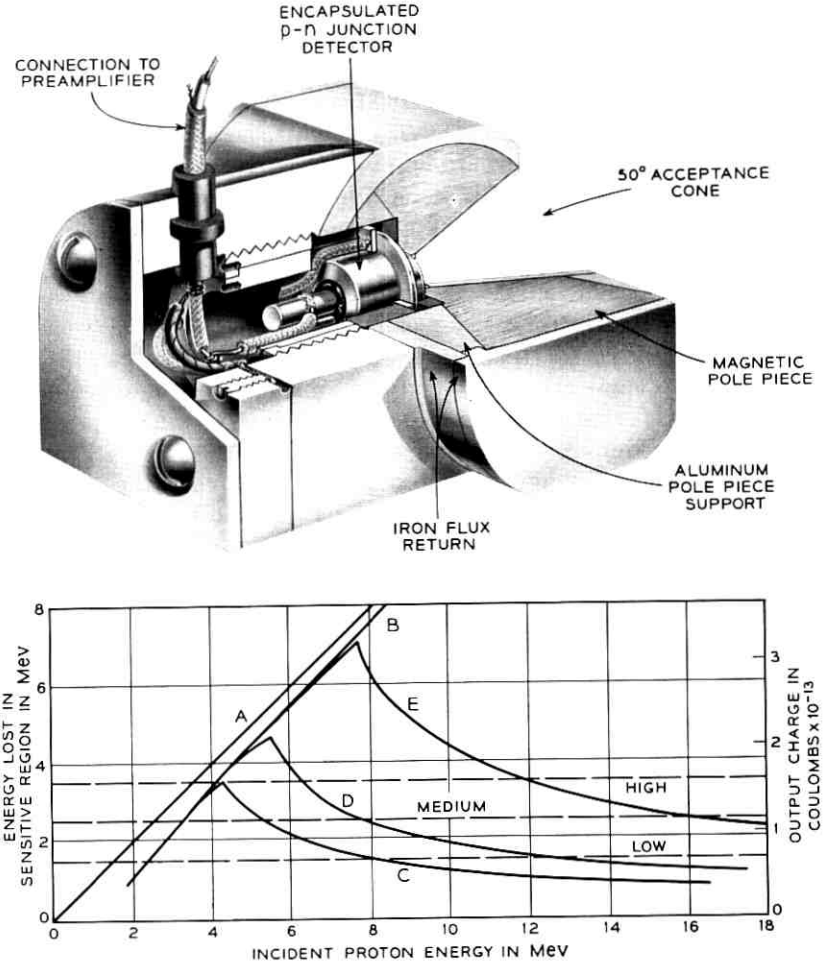

Fig. 10 — Cutaway view of the low-energy proton detector mount and the response of the detector to protons.

can (see Fig. 14, Section 4.2.1) surrounded by a relatively massive housing. The particles of interest enter through a cone with an acceptance angle of 50 degrees, truncated near its apex in an aperture 82 mils in diameter. Immediately behind this aperture is a Kovar window 80 mils in diameter and 0.3 mil thick which admits particles through the vacuum-tight enclosure of the detector encapsulation to the p-n junction device itself. Construction of this device is described in Section 4.2. The Kovar window excludes light, which would generate current in the device with high efficiency, and also removes protons with energies below 1.1 Mev and electrons below 15 Kev. A permanent magnet with tapered pole-pieces and a surrounding cylindrical soft steel magnetic flux return path provides a field in the acceptance cone that increases toward the apex and has a value of approximately 1500 gauss a quarter-inch from the detector. This magnet excludes electrons with energies below 300 Kev with increasing efficiency toward lower energies. It does so by deflecting them into the side walls of the cone, which is lined with aluminum to reduce electron back scattering. For electrons of 500 Kev or higher the magnetic exclusion efficiency becomes very low, and for all protons above a few Kev the magnetic field is insignificant in its effect. In directions outside the acceptance cone, the shielding of the detector is heavy enough to exclude protons of less than 80 Mev and electrons of less than 10 Mev. The detector mount extends behind the tubulation of the detector encapsulation to permit attachment of the detector to a coaxial preamplifier lead, still retaining the effective shielding.

The response of the detector to protons is illustrated in the lower half of Fig. 10. The electrical pulse developed by the detector is expressed in terms of the energy that an incident particle must leave in the detector to produce that pulse. One electron is available to the external detector circuit for each 3.5 ev of energy deposited by an energetic particle in the sensitive volume of the detector. This equivalence is independent of the particle type. The charge associated with an energy deposition is shown in the second vertical scale of the figure. The straight line A in the figure is a theoretical response just equal to the incident proton energy. The line B takes account of the effects of the 0.3-mil Kovar window and the diffused layer on the silicon detector, which together exclude protons of less than approximately 1.3 Mev and remove a smaller and smaller energy increment from protons of higher energy. The measured curves C, D and E correspond to three different effective detector thicknesses. This thickness is a little larger than the thickness of the p-n junction space-charge region — the region containing a high electric field. It is

variable with the bias on the detector. When the range of a proton just equals this thickness, the maximum energy loss and corresponding electrical pulse are obtained. For higher-energy protons less and less energy is left in the space-charge thickness. Curve C corresponds to a detector biased at 4.2 volts; D, 15 volts; E, 95 volts. The double-valued nature of each of these curves provides an energy band within which a pulse of a given size or larger can be observed. To change this band, either the sensitive thickness can be varied or the electrical pulse height discrimination level can be changed. In the low-energy proton detector, both of these variations are used. Nine distinct outputs can be obtained by measuring at each of three detector biases corresponding to curves C, D and E and by examining pulses within three different pulse height ranges marked by the horizontal lines on the figure: low, medium and high discrimination level.

The total span of energies covered by the detector is 2.4 to 25 Mev. However, it is not possible to measure a segment in energy close to the 25 Mev without including pulses from lower-energy particles as well. In a particle energy spectrum which falls rapidly with increasing energy, only an upper limit can be set on the number of the highest energy particles the detector is observing. The highest segment of energy which the present arrangement provides without a separate lower-energy component is that between 4.2 and 12 Mev, observed in the highest discrimination channel at the highest detector bias.

The probability that a single electron can produce a pulse as large as the 1.4 Mev of the lowest discrimination level is very small, less than one in 10^3. This is a result of the low rate of energy loss by electrons of this or higher energy. Pulse pile-up can occur from an anticipated high flux of low-energy electrons. The magnetic rejection reduces this problem for electrons of less than 300 Kev. Electrons of between 300 Kev and 600 Kev are of most serious concern. They are not well removed magnetically. They produce pulses comparable to their energy in many cases and pulse pile-up can reach the lowest discrimination level of the detector with only a three to fivefold multiplicity. A very high electron flux is needed to produce this pile-up, but a very high electron flux was measured in space during July, and the results of the low-energy proton detector consequently require careful examination.

The low-energy proton detector looks out perpendicular to the spin axis of the satellite through a hole in the satellite skin. It utilizes the single 14-bit register[2] in the telemetry for three seven-second periods during a one-minute telemetry frame, one period for the output of each

of the three discrimination levels. The detector bias is changed each frame, so that a complete sequence of nine readings requires three minutes.

4.1.2 *Medium-Energy Protons (26–34 Mev)*

The medium-energy proton detector mount is illustrated in Fig. 11. In this case the p-n junction detector is being used essentially on edge, particles of interest entering within a few degrees of perpendicular to the axis of the cylindrical detector disk and not nearly parallel to it as in the low-energy proton case. The acceptance aperture is a pair of 20-degree wedges like orange slices that have a common apex line through the junction device perpendicular to its cylindrical axis. This common apex line is parallel to the spin axis of the satellite. As the satellite makes half a rotation these wedges together sweep out a 4π solid angle. The detector is thus omnidirectional, sensing equally particles in all directions if its output is averaged over a time long compared to half a rotation of the satellite. As it is used, output pulses from the detector are summed for a 15-second period, corresponding to 45 complete rotations at the initial satellite spin rate. The detector protrudes through the skin of the satellite to permit essentially unobstructed access of particles to the wedges.

Protons penetrate this detector more or less along its diameter, and consequently can leave much larger amounts of energy in the space-charge region than was the case in the low-energy proton detector. The maximum path length is approximately 2.5 mm instead of about 0.4 mm as in the previous case. This makes it possible to set a high pulse height discrimination level, 11.4 Mev. No proton entering along the axis of the detector, or even at angles of up to 60° from the axis, can deposit enough energy to trigger this level. No electron is capable of triggering this level with any significant probability, no matter what its incident direction. Moderate shielding along the axis in the forward and back directions is used to remove problems of pulse pile-up, and very heavy shielding is used between 60° to the axis and the acceptance wedges to reject any protons of lower than 100 Mev. The detector should be extremely free from response to unwanted particles.

If the junction device were not surrounded by any material in the acceptance wedges, it would detect protons starting at an energy of 11.4 Mev. However, the thickness of the Kovar detector can wall (5 mils from the side) and an additional absorber placed within the acceptance wedges pushes this minimum energy up to approximately 26 Mev. The calculated detector response is shown in the lower part of Fig. 11. The curve represents the average response for protons incident over the ac-

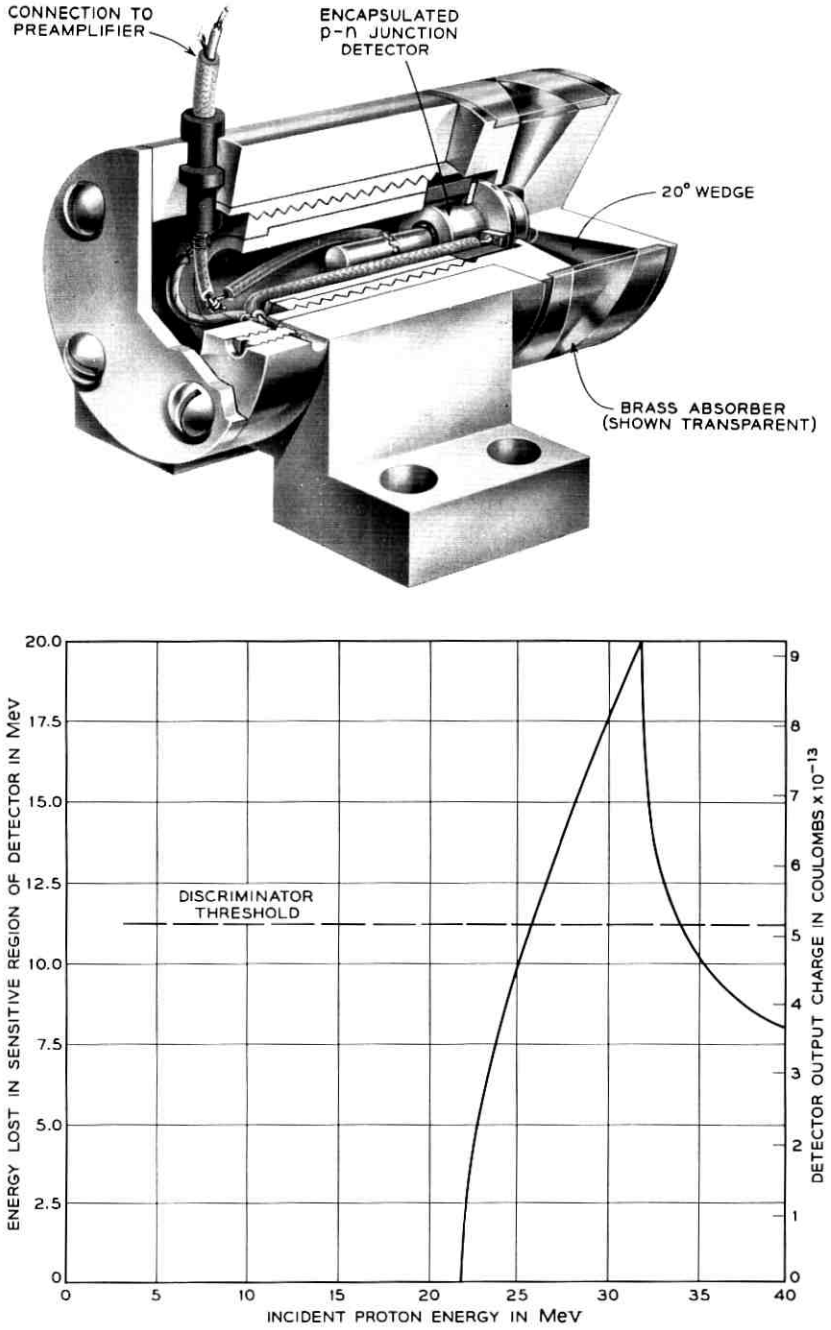

Fig. 11 — Cutaway view of the medium-energy proton detector mount and the calculated response of the detector to protons.

ceptance aperture. The shape for a particular angle of incidence and position of the particle path with respect to the disk diameter will vary because of the different path lengths the particles take. This detector supplies pulses from its single discrimination channel to the 14-bit register of the telemetry for a period of 15 seconds each telemetry frame.

4.1.3 *High-Energy Protons (>50 Mev)*

Energy discrimination in this detector is obtained by use of an absorber. The detector mount is shown in Fig. 12. The junction device is placed in the center of a hemispherical aluminum shell to provide an approximately uniform absorber over a 2π solid angle. The detector mount is inside the satellite skin, and taking into account the satellite structure near the detector, the effective threshold energy of the device is calculated to be approximately 50 Mev. The detector is not truly omnidirectional because of nonuniformity in the absorber thickness in different directions. However, because of the rotation of the satellite this lack of directional uniformity is largely averaged out. All pulses in the detector greater than 2.1 Mev are accepted. The calculated detector response for particles entering in a representative direction is shown in the lower part of Fig. 12.

The single discrimination channel of the high-energy detector makes use of the 14-bit telemetry register for 11 seconds of the one-minute telemetry frame.

4.1.4 *Electrons*

The electron detector mount is illustrated in Fig. 13. This mount protrudes through the satellite skin and looks out perpendicular to the spin axis. Particles are accepted in a cone having an angle of 20 degrees with an 82-mil diameter aperture immediately in front of the junction detector can. The deposition of energy by electrons in the sensitive volume of the detector is much less clearly related to the actual particle energy than is the case for protons. A 600-Kev electron may leave all its energy in a sensitive volume 0.43 mm thick (the thickness of the electron detector on the Telstar satellite); it may back scatter in the first fraction of this thickness and leave only a small part of its total energy; or it may penetrate entirely and leave less than all its energy to be detected. By examining the distribution of pulse heights produced in the detector, only a rough evaluation of the spectrum of incident electrons can be obtained, since the spectrum must be unfolded from the distribution of pulse heights produced by monoenergetic particle groups. (See Fig. 15, Section 4.2.3.1.) The probability that an electron of more

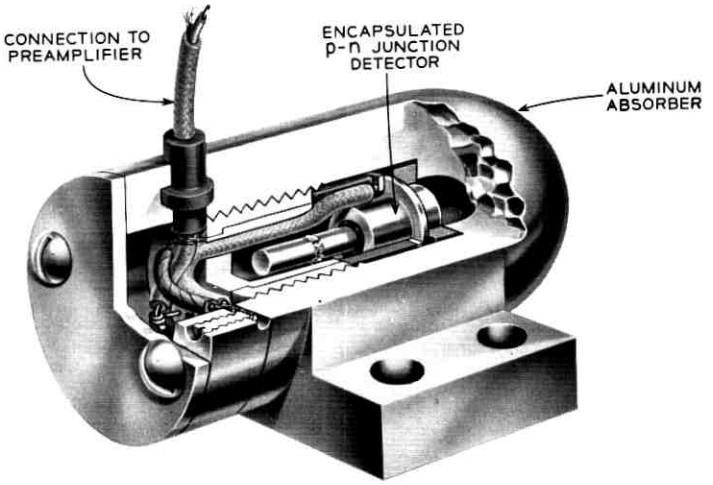

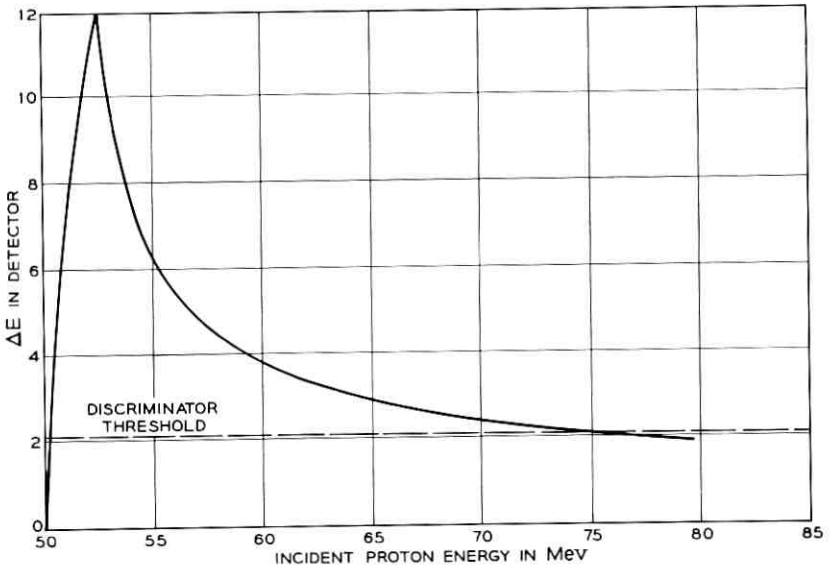

Fig. 12 — Cutaway view of the high-energy proton detector mount and the calculated response of the detector to protons.

than 1 Mev will leave all its energy in the sensitive detector thickness is very small. Such electrons can be detected by the lower energy pulses they produce, but their energy cannot be directly deduced.

In the Telstar electron detector, particle pulses are sorted into four pulse height channels: 180–280, 285–440, 390–615 and 635–990 Kev.

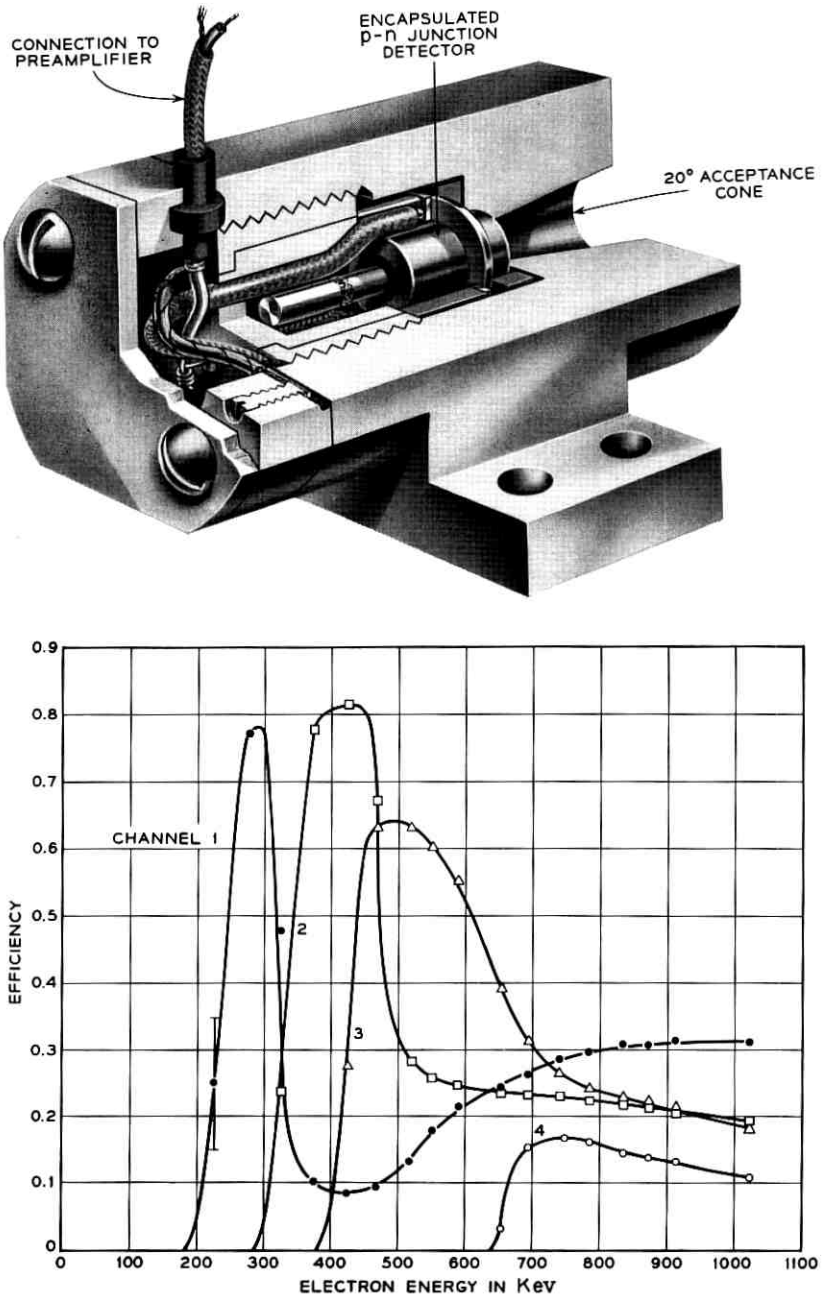

Fig. 13 — Cutaway view of the electron detector mount and the response of the detector to electrons.

The bottom edges of these channels correspond to 215, 315, 420 and 660 Kev, taking into account the energy lost by electrons in penetrating the 0.3-mil detector can window and an additional 1.6-mil aluminum absorber used to remove protons of less than 2.3 Mev. Pulses from two of the four channels are fed to the 14-bit telemetry register for three seconds each in every other telemetry frame. The second pair of channels, produced by a change in amplifier gain, is measured in the alternate frames.

The efficiency of each of the four channels for counting electrons up to approximately 1 Mev is illustrated in the lower part of Fig. 13. Each channel starts abruptly as the energy requirement of the channel is met, but retains a substantial efficiency at electron energies above the upper pulse height limit of the channel.

The electron detector is potentially susceptible to background problems from protons. The addition of the 1.6-mil aluminum absorber eliminates the problem for very low energy protons. In addition, the top pulse height channel is closed. Pulses in excess of 990 Kev will not be counted. To be recorded, protons must have energies greater than 2.4 Mev to penetrate the entrance window and leave at least 180 Kev in the detector, but energy less than 2.7 Mev, so they do not leave more than 990 Kev (a shield that just stops 2.3-Mev protons will extract less than 2.3 Mev from 2.7-Mev protons). This very narrow energy range for proton acceptance makes the proton contribution to the counting rate small except when the electron flux nears the minimum values that it has in the Telstar satellite's portion of space.

4.2 *Silicon p-n Junction Detectors*

Silicon p-n junction detectors were used in all the particle experiments, as described in Section 4.1. They satisfy the requirements of small size and rugged construction, high sensitivity, high speed, low noise, and in addition provide high reliability in the space environment where temperature and radiation intensity vary continuously. The construction and testing of these detectors will be discussed in the following sections.

4.2.1 *Mechanical Construction*

Surface reliability was recognized as a problem of major proportions in designing the Telstar satellite detectors. Surface control was achieved by adopting a hermetically sealed transistor-type encapsulation with a thin window. Such a window was permissible in this experiment, although it would not be for many nuclear physics experiments. The design which evolved is shown in a schematic cross-sectional view in Fig. 14. The

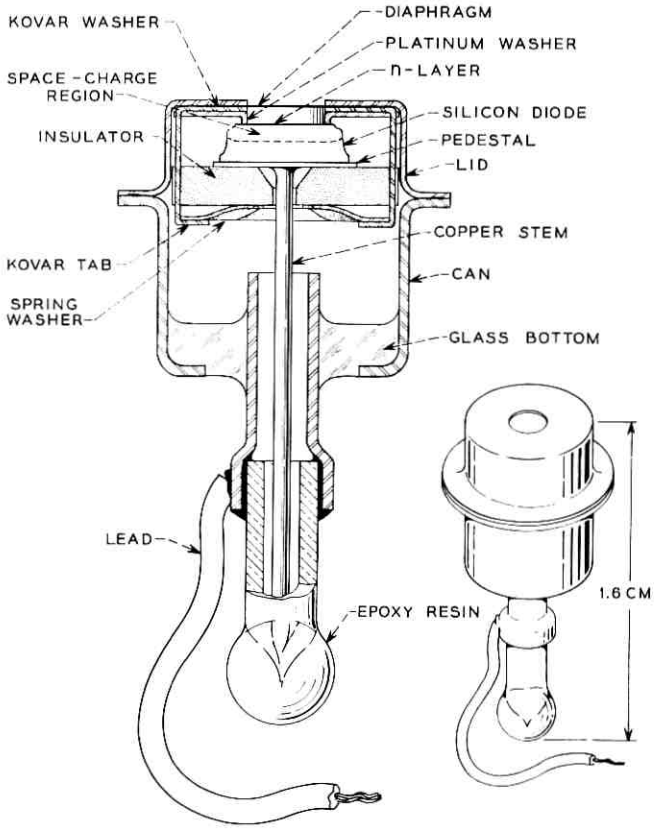

Fig. 14 — Cross-section view of encapsulated detector.

encapsulation consists of a Kovar can with a glass bottom and a metal tubulation, and a Kovar lid which is welded onto the can in final assembly. All Kovar parts are gold plated. The diode with the diffused n-layer looks out through the hole in the lid, which is covered by a Kovar diaphragm which may be as thin as 0.3 mil. The diaphragm is welded between the lid and a Kovar washer to make a good vacuum seal. The diode is pressed against a platinum washer which has a raised rim around the hole and thus provides contact to the n-layer. Contact to the back or p-region of the diode is made through the gold-plated Kovar pedestal alloyed to it. A good low-resistance contact is needed here to provide a pulse rise time of less than 0.2 μsec. A copper stem completes the connection to the tubulation and a stranded lead makes contact to it.

The p-region of the diode is insulated from the main body of the encapsulation by a ceramic insulator. A spring washer is compressed against the insulator by tabs which extend from the Kovar washer welded to the lid. After assembly the device is evacuated, baked at 200°C for an hour or more, cooled to room temperature, back filled with a suitable atmosphere and the tubulation pinched off. A drop of epoxy resin is used to protect the delicate feather edge of the pinch off.

4.2.2 *Materials and Processing*

The detector diodes are of the n-on-p type,[14] made by diffusing phosphorus into silicon of the highest available resistivity, i.e., about 10,000 ohm-cm to 20,000 ohm-cm. At 100 v the space-charge depth in this material is 0.30–0.45 mm. Deeper sensitive regions could have been obtained by using the lithium-drift technique[15] which produces a p-i-n structure with very close compensation in the middle, drifted region. However, preliminary tests showed that Li-drifted diodes are much more rapidly degraded by radiation damage than are the n-on-p diffused diodes and would have too short a life in the radiation environment the Telstar satellite was expected to encounter. They also exhibit a more complicated surface behavior.[16] The phosphorus diffusion is carried out at 1050°C, using P_2O_5 in an open tube system. A diffusion time of three hours gives a junction depth of about 4 microns. This "dead layer" or "window" is negligible compared to the thickness of the Kovar diaphragm. After diffusion, the slices are wafered and the small diodes then alloyed to pedestals, etched and encapsulated.

4.2.3 *Performance and Testing*

4.2.3.1 *Calibration and Counting Behavior.* Direct calibration of the particle detectors was carried out with electrons from a 1-Mev Van de Graaff generator and also with 17-Mev protons from the Princeton cyclotron.* Fig. 15 shows pulse height spectra for electrons of 5 different energies, taken on a detector with 100-v bias. These results differ only slightly from those corresponding to the 95-v detector bias in the satellite. It may be seen that the total absorption peak is quite high for 220 and 425-Kev electrons and then becomes progressively smaller until it has almost disappeared at 990 Kev. At the same time, a broader peak due to electrons which lose only part of their energy in the space-charge

* These calibrations were carried out with the kind cooperation of Professor R. Scheer of the Princeton University Physics Department.

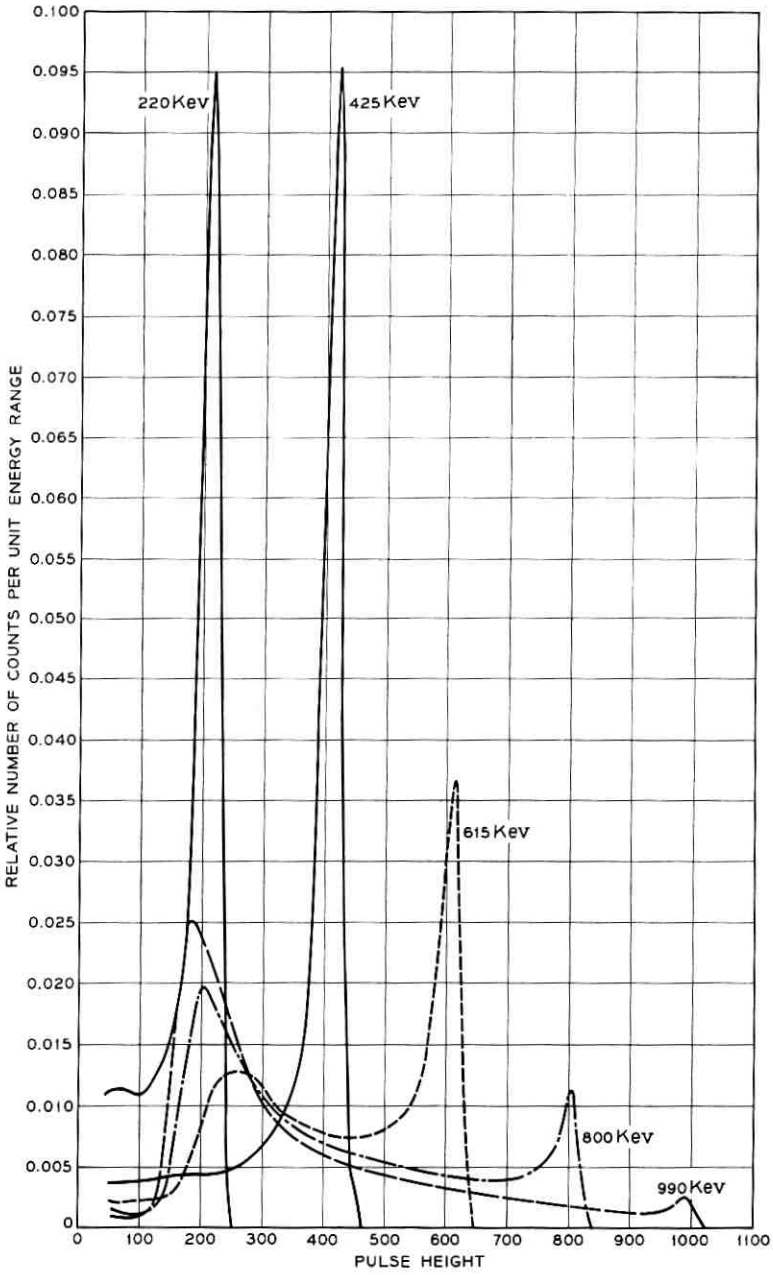

Fig. 15 — Pulse height spectra for electrons of five different incident energies. Pulse heights are indicated in terms of energy deposited by an electron in the sensitive region of the detector.

region is increasing in size.* By calibration with protons which, unlike electrons, have a precisely defined range at a given energy, the depth of this detector was found to be approximately 0.43 mm at 100 v.

Detector noise is an extremely important characteristic of the junction detector, particularly in the case of the electron detector, where pulses corresponding to particle energy losses in the detector of less than 200 Kev are to be measured. Spurious noise pulses which even approach this threshold level are serious because of the distortion they produce in the pulse height distribution. The noise in low-noise devices can be examined most easily, not in terms of the probability of finding a spurious pulse equivalent to 200 Kev, but as a broadening in the distribution of pulse heights produced in response to a series of uniform electrical pulses artificially introduced in the detector. The full width at half height of this pulse height distribution is measured and expressed in terms of an equivalent particle energy. Such noise linewidth measurements were obtained in all detectors under standard conditions, and in a number of cases whole sequences of noise measurements were made through a series of environmental tests.

4.2.3.2 *Reliability*

i. Surface Reliability. The essence of the surface reliability problem on the detectors is illustrated in Fig. 16, in which reverse current is plotted against bias for three representative cases. These curves were measured on different encapsulated units which were all good initially but which aged in different ways to arrive at the conditions shown. Curve A is a typical good, low-noise characteristic which is obtained with the surface (of the high resistivity p-side) nearly intrinsic or perhaps slightly n-type.[18] The current is 0.14 μa at 100 v and noise linewidth was 10 Kev. (Note that the current scale for A differs by a factor of 100 from that for B and C.) Curve B results from a strong n-type inversion layer over the p-region. The current is 48 μa at 100 v and the noise linewidth 85 Kev. The behavior depicted by curve C is due to an accumulation layer at the surface; i.e., the surface is more strongly p-type than the bulk. The charge in surface states is negative, and the resulting high field at the edge of the junction causes surface breakdown at many little spots around the junction. Even at 1 v, where the current is only 0.04 μa, the noise linewidth is 90 Kev, and at 5 v bias the noise is greater than 450 Kev. The diode represented by this type of characteristic is the noisiest of all for a given current. There is very good correlation between

* These results are similar to those of Ref. 17.

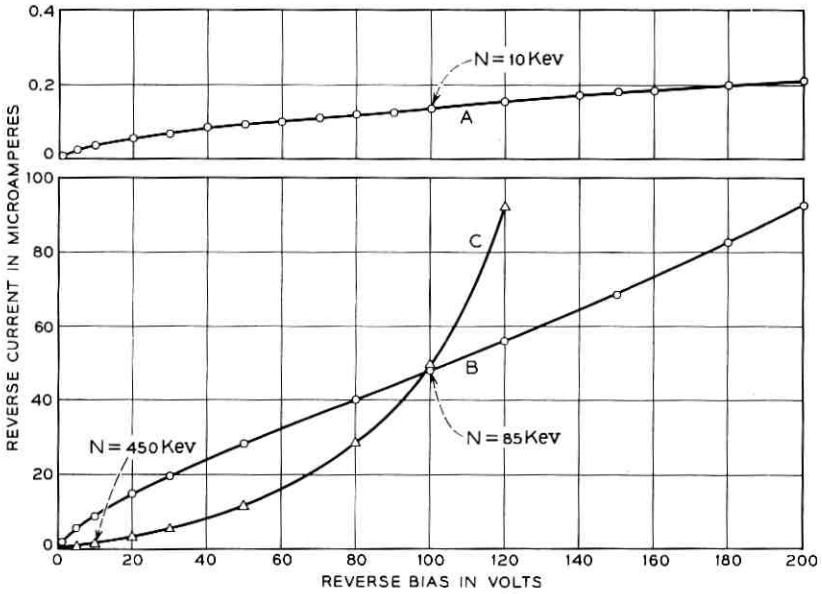

Fig. 16 — Typical reverse current-voltage characteristics for detector diodes with: (a) normal low-noise characteristic; (b) strong n-type inversion layer; (c) p-type surface accumulation layer. Note smaller scale for A. Noise linewidth values N are indicated at particular points on the curves.

noise and I–V characteristics* that has made it possible to predict noise by inspection of an I–V curve. Even a small departure from curve A toward the B or C conditions shows up as an increase in noise.

The maximum permissible noise linewidth was about 50 Kev for the electron detector, and several hundred Kev for the proton detectors. Newly fabricated detectors were all well below this, at about 10–15 Kev, but many of the early models developed poor I–V characteristics and high noise within a few weeks on shelf aging. Of the first 100 produced, only 44 survived after a few weeks. Transistions between characteristics of the type illustrated in Fig. 16 may be brought about very quickly by atmosphere changes or wet chemical treatments which shift the surface potential in known ways,[19] but the causes of long-term shifts on shelf aging, bias aging and temperature cycling are harder to detect and control. Nevertheless, by careful adjustment of surface potential by initial chemical treatments and by control of the ambient atmosphere

* Early studies of noise in the detectors were made in collaboration with H. C. Montgomery and L. K. Monteith. See also Ref. 16.

in the encapsulations it was possible to improve the yields to about 90–95 per cent by the end of the project. The processing will be described more fully in another paper.[20]

Indirect effects of radiation on the detector surfaces as a result of ionization of the ambient gas within the encapsulating can were considered, since such effects had recently been observed on transistors.[21] Selected groups of detectors were tested under intermittent bias and continuous bias in γ radiation of 50 rads/hr, approximately the average encountered in space. In general the effects have been rather small, although complicated. Changes do occur when the conditions are changed; as the bias or radiation is turned on or off the currents may increase or decrease, but after a few days in a new condition the current levels off at a new steady-state value. Detectors vary in their sensitivity to radiation for reasons not yet understood, but not many are severely affected by radiation at this dose rate level.

ii. Bulk Radiation Damage Effects. The effects of particle radiation on bulk properties of the detectors are not yet well understood, although it can be said that really serious effects are not expected in less than about a year. After a bombardment with about 10^{14} electrons/cm^2 of 1-Mev energy, a loss in pulse height begins to appear. The electron detector in the Telstar satellite has received damaging particles equivalent to about 5×10^{11} 1-Mev electrons/cm^2 day. On this basis one may expect that the electron data will begin to be affected by bulk damage after about six months in orbit, and that thereafter it may be necessary to estimate corrections by using damage measurements obtained on the ground. The low-energy proton detector, with the largest solid angle and the thinnest diaphragm, may be affected somewhat sooner. The medium and high-energy proton detectors with their thick shielding will not be affected until much later.

iii. Life Testing Program. Finished detectors were put through a life testing program which included:

(a) Vibration at frequencies from 50 to 2000 cycles/sec and accelerations of either 40 or 80 g's in both the longitudinal and transverse directions. Two typical detectors were subjected to 12 shock tests with successively higher accelerations, up to 1100 g, without any apparent damage.

(b) High humidity soaks at 95 per cent RH for 16 to 24 hrs, followed by vacuum pumping and exposure to oxygen. The surface sensitivity of the diodes is such that any leak would be easily detected by this test.

(c) Temperature and bias cycling in a vacuum chamber for at least one month. Temperature was cycled continuously from -50°C to

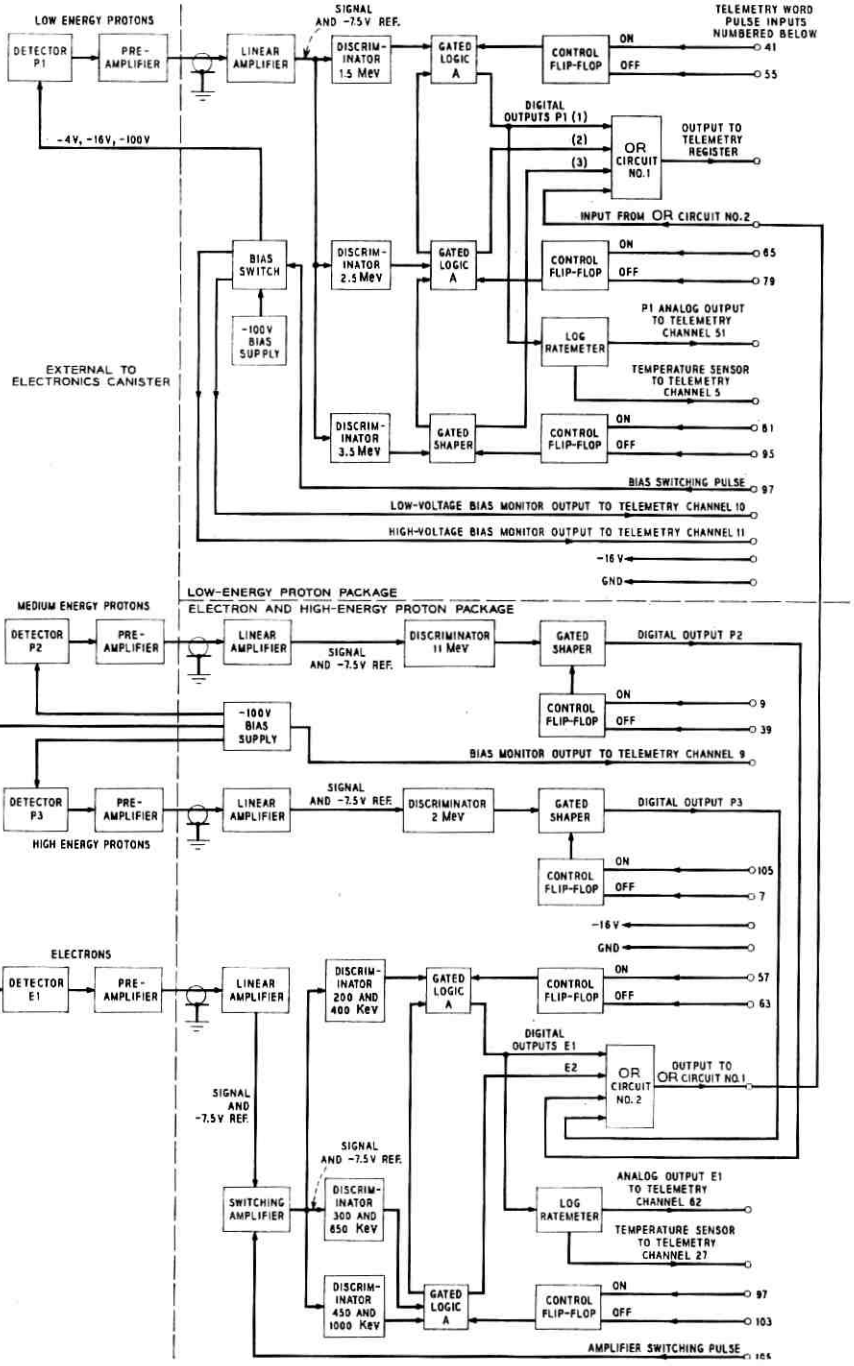

Fig. 17 — Radiation particle experiment block diagram.

+50°C with a period of 3 hours, while reverse bias of 120 v was cycling 20 minutes on and 1 hour off.

(d) Exposure to γ radiation at 50 rads/hr during bias cycling.

During all this testing and also during shelf-aging, accurate measurements of the reverse current-voltage characteristics were made frequently, as a very sensitive indication of surface stability. Only stable devices were selected for use.

4.3 *Electronic Circuits*

4.3.1 *Block Diagrams*

The electronic circuits of the radiation particle experiments are shown in block diagram form in Fig. 17. Each block represents the smallest part of a circuit that has an essentially independent function. The four detectors are at the left of the diagram. The function of the preamplifiers, which are to the right of the detectors, is to produce an output current pulse whose maximum is proportional to the charge produced in the detector by an incident particle. The linear amplifiers amplify this current pulse and present a proportionate output voltage pulse to one or more pulse amplitude discriminators. The discriminators produce an output current pulse of fixed shape for each input pulse above a threshold amplitude at the discriminator input. The gated logic and shaper circuits decide, for any input pulse, the highest discriminator threshold exceeded and produce an output pulse corresponding to that decision. The control flip-flops control the digital outputs and are turned "on" and "off" by signals from the telemetry timing circuits. Only one gated logic or shaper circuit is operative at any one time. All others are held off by their respective control flip-flop. The OR circuits combine all logic and shaper outputs on one output line to a register in the telemetry section. The log ratemeters take the average of the logarithm of the counting rate and present this average as a dc voltage to analog telemetry channels. A tristable multivibrator, bias switch and −100-volt bias supply provide three levels of bias to the low-energy proton detector.

Many of the problems encountered in the design of a satellite radiation measuring instrument are due to the random arrival of the particles and to their wide variation in energy. Problems of this nature are encountered in the analysis of the radiation from atomic nuclei and have been extensively treated in the literature.[22,23] In addition, electronic circuits for this application must be designed with adequate stability against changes in ambient temperature, supply voltage, and transistor parameters. Stability requirements are most severe in the linear amplify-

ing system and in the discriminators, where changes would shift the energy calibration of the experiment. In the amplifiers these requirements are met by the use of negative feedback through passive low-temperature coefficient elements in loops having large reserve gain.

Shifts in baseline with pulse rate are eliminated by using double RC differentiation to produce a bipolar pulse. The maximum counting rate of each experiment is limited to 100,000 pulses per second by the linear system shaping network and digital circuit recovery times.

Overload of the amplifying system by large input pulses is handled by arranging gains and bias so that overloads occur outside the feedback loops at the output of the preamplifier. The system quickly recovers from the overload with negligible baseline shift.

Electronic noise in the preamplifier is a limiting factor in the lowest energy of electrons that can be measured. A 25-Kev equivalent noise linewidth has been attained, a value well below the threshold of the lowest electron channel.

4.3.2 *Circuit Reliability*

With extended operation in space as a design goal, special attention was given to circuit reliability. Reliability has been enhanced through design simplicity, outstanding cases of which are the log ratemeters, bias supplies, and gated logic and shaper circuits which require only a single transistor to perform their function. Another method used to improve reliability was to design the system so that failure of a circuit would not terminate the entire experiment. The three proton experiments have been divided into independent parts so that the loss of one does not affect the operation of the others. In the low-energy proton and electron experiments, several independent discriminators enable collection of meaningful data even if a single discriminator fails. A -100-v bias supply common to three detectors is equipped with a diode OR circuit which, in the event of failure, would automatically switch in the -16-v satellite supply. Although performance would be limited at this reduced bias, useful data would still be received. Care was taken to avoid series failure mechanisms such as single power line filters and fuses. All circuits are separately decoupled and load limited.

4.3.3 *Linear System*

4.3.3.1 *Preamplifier.* The total detector output charge q_s produced by an incident particle is amplified in a linear system whose peak output voltage is proportional to q_s. A conventional method of doing this is

to amplify the voltage appearing across the total capacitance from input to ground. This voltage is

$$e_s = q_s/C_T$$

where e_s is the input signal voltage, and C_T is the total capacitance from the input to ground including the junction capacitance. In the solid-state detector, however, the junction capacitance changes with bias and ambient conditions, and consequently the voltage signal, e_s, would not always maintain the same relationship to the input charge.

An integrating preamplifier whose output is relatively unaffected by changes in detector capacitance is shown in Fig. 18.[24] The output voltage, e_o, is nearly equal to the input charge, q_s, divided by the feedback capacitance, C_F, if the open loop voltage gain is large. Thus the output signal is relatively insensitive to changes in detector capacitance. The preamplifiers in the Telstar satellite are of this type.

4.3.3.2 *Linear Amplifier.* After the preamplifier, the signal is amplified further in a linear current amplifier, which uses a two-transistor configuration described by Goulding.[25]

4.3.3.3 *Linear Signal Shaping.* The signal from the detectors is differentiated twice in the linear system with equal one-microsecond RC clipping networks, which are shown in Fig. 18. A resistor, R_C, of resistance such that R_CC_F equals one microsecond, is placed across the preamplifier feedback capacitor, C_F, to provide the first clip. A second clip is made by the combination of the output impedance of the preamplifier and a capacitor, C_C, between the preamplifier and the linear amplifier. The output resistance of the preamplifier is conveniently fixed

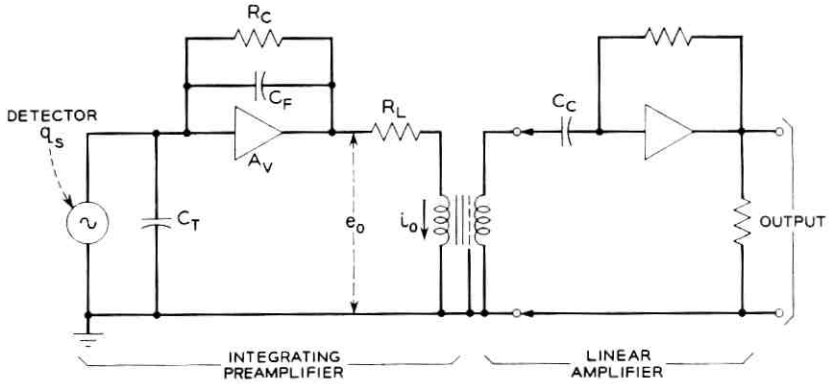

Fig. 18 — The linear system.

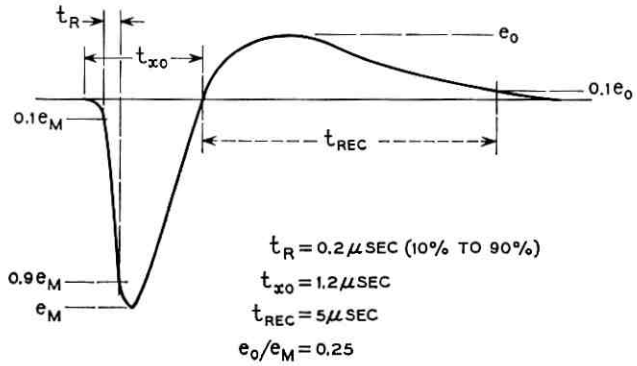

Fig. 19 — Linear amplifier output waveform.

by resistor R_L. The impedance looking into the input of the linear amplifier is very small (about 40 ohms), so it does not significantly affect the second clip time constant. The double-clipped signal as it appears at the linear amplifier output is shown in Fig. 19. The transformer at the output of the preamplifier contains an electrostatic shield to prevent coupling of common mode interference into the amplifier.

4.3.3.4 *Switching Amplifier.* The electron experiment, which is at the bottom of the block diagram, Fig. 17, has four levels of data but uses only two telemetry channels. This is accomplished by changing the gain of the linear amplifier system between successive telemetry frames. A plot of the electron channels for the electron analyzer is shown in Fig. 20. Three discriminators set the two channels shown by the solid lines.

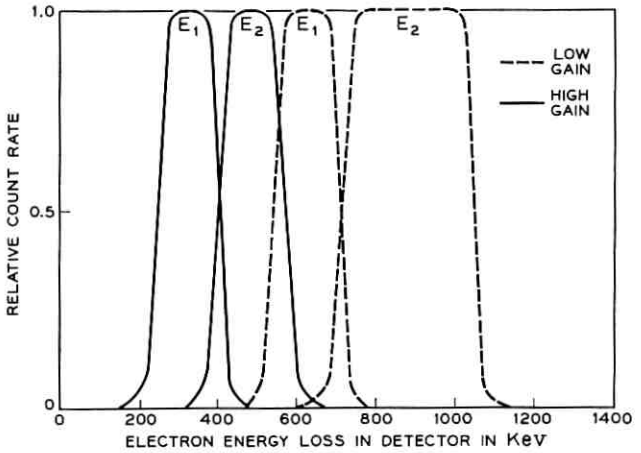

Fig. 20 — Response of electron channels as a function of input pulse height.

Decreasing the gain of the linear system shifts the energy thresholds up to those indicated by the dashed lines. In the satellite, the electron detectors count at one gain during a given telemetry frame and at another gain during the next frame.

The switching amplifier is shown in Fig. 21. The amplifier loop is similar to that of the ordinary linear amplifier. The gain of the amplifier is proportional to $1/R_4$ when transistor Q_3 is on, and $1/(R_4 + R_5)$ when Q_3 is off.

The switching transistor, Q_3, is driven by the bistable switch. The switching signal input is a timing signal from the telemetry package that occurs once each frame. An indication of the position of the bistable is telemetered.

4.3.4 *Digital System*

4.3.4.1 *Pulse Height Analyzers.* Two methods of pulse height analysis are conventionally used in random pulse height measurements: the stacked-discriminator method[22] and the pulse-height-to-time-converter method.[26] The relative simplicity of the stacked-discriminator analyzer was felt to be of commanding importance in this application.

In the stacked-discriminator analyzer each discriminator is biased at a different level or threshold. Any input pulse causes each discriminator whose threshold it exceeds to trigger and produce an output pulse. Since only the highest discriminator threshold exceeded is of interest,

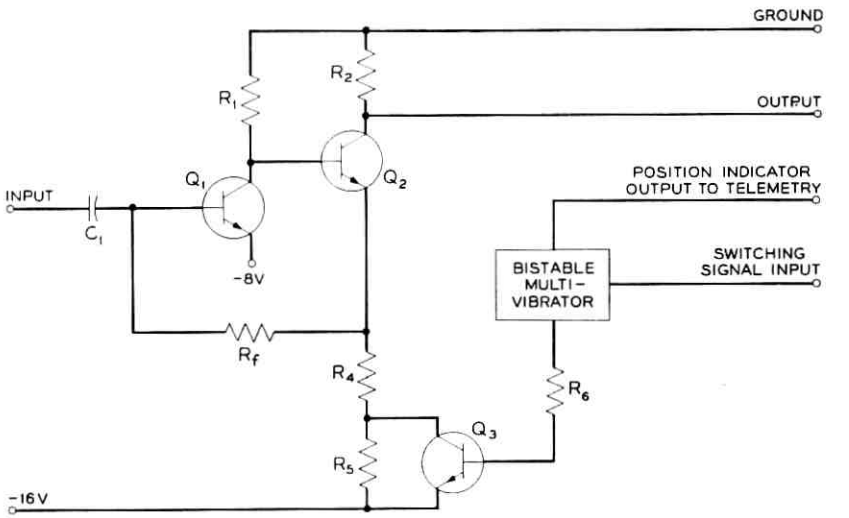

Fig. 21 — Switching amplifier (simplified).

logic circuits following the discriminators determine the one with the highest threshold that was triggered.

4.3.4.2 *Discriminator.* The characteristic most difficult to achieve in the design of a threshold discriminator for satellite use is thermal stability. The circuit used in the Telstar satellite (Fig. 22) is based on the emitter-coupled monostable multivibrator to take advantage of the inherent compensation of base-emitter voltage change with temperature. All other voltage drops that would affect threshold sensitivity are eliminated except an adjustable potential, V_t, that is derived from a zero temperature-coefficient reference element. An inductor, L_1, used instead of a base return resistor on the normally conducting transistor of the emitter-coupled pair, eliminates a temperature-sensitive voltage drop at that point.

A second-order effect on the threshold thermal stability is the variation of transistor beta with temperature. To trigger the multivibrator, the input signal must raise the base of Q_3, the normally "off" transistor, until its beta is large enough to produce a gain around the feedback loop of greater than one. At low temperatures the beta of Q_3 is reduced, so the input signal must be slightly larger than at higher temperatures. Nevertheless the discriminator threshold is quite stable. From $-50°C$ to $+50°C$ the threshold does not vary more than ± 1 per cent. The discriminator output, taken from the collector of Q_3, is a current pulse of about 600 μa, with a duration determined mainly by the shape of the input pulse.

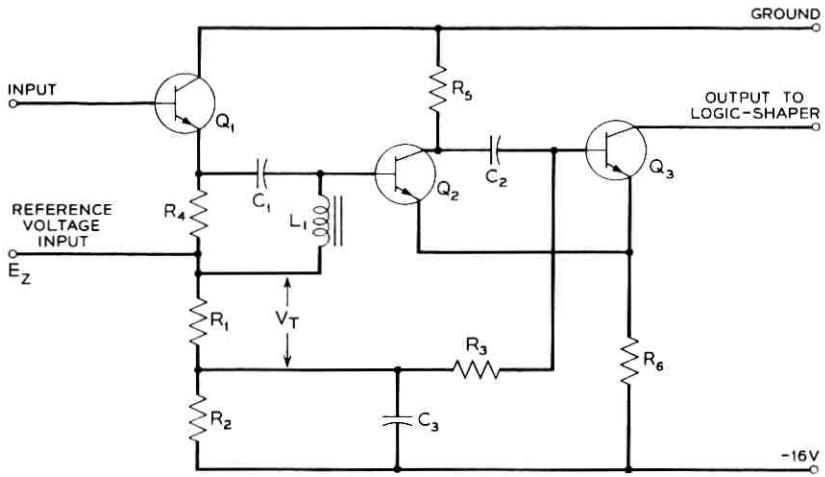

Fig. 22 — Discriminator circuit.

4.3.4.3 *Gated Logic Circuit.* The gated logic circuits have two functions: first, to determine the discriminator with the highest threshold that was triggered by a signal from the linear system; second, to produce an output pulse suitable for driving a coaxial cable and a register. Each discriminator's output is trying to turn a gated logic circuit on while at the same time keeping the one below it from turning on. A discriminator turns on a logic circuit only if the next higher discriminator does not produce an output during the rise of the pulse from the linear amplifier driving them. Since the input pulse has a finite rise time, a discriminator with a higher threshold will trigger later than one with a lower threshold. The logic circuit must delay its decision until the higher discriminators have had time to fire.

These operations are performed in an unusual manner in a modified blocking oscillator, shown in Fig. 23. Two input windings of a pulse transformer connect to the discriminator outputs, and a third winding that has the same number of turns as the input windings connects to the transistor base. The current in the base winding is the algebraic sum of the current in the input windings as long as the transistor is turned off. Winding 1 is connected to the upper discriminator in the direction that produces a base winding current that drives the base of Q_1 negative. Winding 2 is connected to the lower discriminator in the opposite phase; when this discriminator fires, the base of Q_1 goes positive.

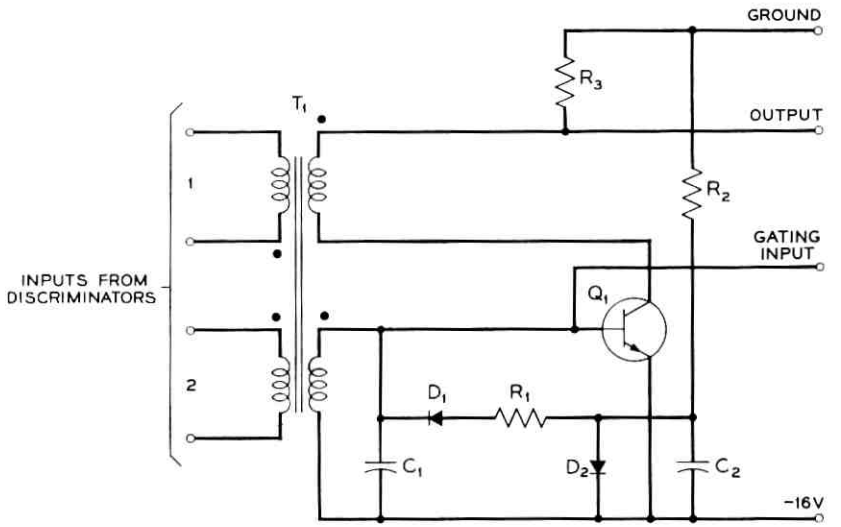

Fig. 23 — Logic-shaper circuit.

When the input pulse is large enough to trigger the lower but not the upper of two discriminators connected to a gated logic unit, the current pulse pours into C_1 and charges it linearly with time. Transistor Q_1 is normally biased off by holding the base at the emitter voltage. The capacitor C_1 must then charge to about 0.7 v before the transistor turns on. In the circuit shown, the input current from a discriminator is about 600 μa. The time required to charge the capacitor to 0.7 v is about 0.5 μsec, allowing the input pulse to rise to the next discriminator threshold if it will. If the next higher discriminator were to trigger during this 0.5-μsec period, its output current, pouring in the other input winding, would prevent the capacitor from charging enough to turn on Q_1.

When Q_1 does turn on, it operates as a blocking oscillator. Current in the collector circuit is fed back to the base and the transistor rapidly saturates. The saturation current is limited to about 2 ma by R_3. The inductance of the collector winding is such that the transistor is held on in saturation for about 4 μsec. Then Q_1 turns off and the energy stored in the transformer inductance is dissipated in resistor R_1, which is chosen to slightly underdamp the overshoot. With this damping the blocking oscillator is completely recovered in about 10 μsec. Diode D_1 prevents R_1 from taking any of the 600 μa charging current; diode D_2 biases diode D_1 so that R_1 is effective for the entire negative swing in the base circuit. Fig. 24(a) shows the base waveform for both conditions of operation: when just one discriminator fires (solid line), the capacitor charges linearly until the blocking oscillator fires; when both

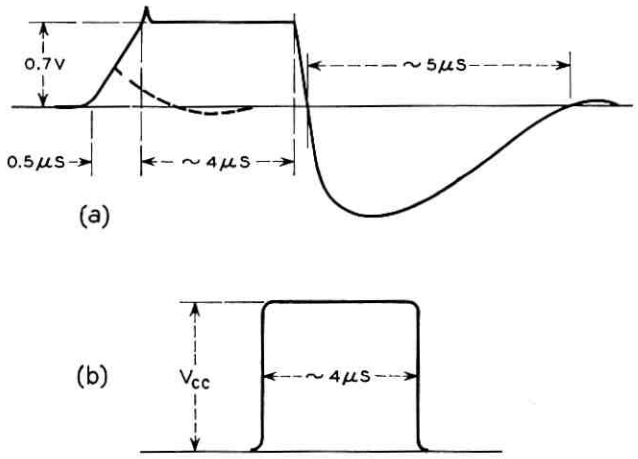

Fig. 24 — Logic shaper waveforms: (a) base waveform (b) output waveform.

discriminators fire (dashed line), the charge of the capacitor is stopped before the blocking oscillator fires. The shaper circuits are similar to the logic circuits, the chief difference being that only one input is provided. Fig. 24(b) shows the output waveform.

A 14-bit register[2] is provided in the telemetry package to accumulate the pulses from the radiation circuits. Time sharing of the outputs of the logic and shaper circuits into this register is accomplished by holding off all except one with saturating transistor gates connected between the gating inputs and −16 v. The gates are controlled by flip-flops shown in the block diagram. The flip-flops are switched by signals from the telemetry timing circuit. The timing is indicated by the telemetry word number given on the block diagram. Two word times are allowed between each counting period for read-out of the telemetry register. The OR circuits which combine all outputs onto one line are simply diode OR's and an emitter follower.

4.3.4.4 *System Response to Closely Spaced Pulses.* The handling of closely spaced pulses by the analyzer and linear system is somewhat complicated. Pulses further apart than about 7 μsec are essentially independent, since the system will have had time to recover sufficiently between them. (The 7 μsec limitation occurs in the logic circuit.) A pulse that occurs between 7 μsec and about 2 μsec after another is reduced in amplitude by the "undershoot" of the first pulse in the linear system as shown in Fig. 19. (The 2-μsec time is the recovery time of the discriminator.) If the reduced second pulse falls in a different channel than the first pulse it will be counted, but if it falls in the same channel as the first pulse it will not count, since the logic unit has not recovered from counting the first pulse. Signals that occur from 2 μsec to 0.6 μsec after a first pulse are distorted by the first pulse and are counted if their amplitude is sufficiently higher than the first pulse to trigger a discriminator that was not triggered by the first pulse. These signals (2.0 μsec to 0.6 μsec) cannot trigger discriminators that were triggered by the first pulse, since they have not sufficiently recovered. Signals occurring closer together than 0.6 μsec are indistinguishable and are counted as a single pulse that is larger than either of them. These effects are not considered as serious limitations on the system's performance in its intended application.

4.3.5 *Log Ratemeter*

The radiation experiment telemetry register has a capacity of 14 bits (16,383 counts). Whenever the register has filled and input pulses are still entering, it returns to zero and continues to count. In a region of

high activity the register may "overflow" several times, leaving an uncertainty in the total count. A log ratemeter[27] is used on the most sensitive levels to determine how many times the register has filled; during normal periods it provides redundancy. This circuit, which produces an output voltage that increases approximately as the log of the input pulse rate from 1 to 100,000 pps, contains a blocking oscillator which is triggered by the output of the logic circuit. The oscillator completely discharges a bank of five capacitors, differing by factors of 20, each time it fires. Isolating diodes enable the capacitors to discharge simultaneously but charge individually through large identical series resistors. Charging currents for the capacitors are added and integrated to produce an analog output voltage. This voltage is coupled to an analog telemetry channel, which is read out just before the digital information from the level to which the ratemeter is connected. The output is the average of the logarithm of the counting rate, an important consideration in the case of rapidly varying random pulse rates. A typical plot of output voltage vs input rate is shown in Fig. 25.

4.3.6 *Detector Bias*

4.3.6.1 *100-volt Bias Supply.* The −100-v bias supply is basically a free-running blocking oscillator driving a transformer with a 10:1 tertiary winding. The resulting high voltage is rectified and RC-filtered

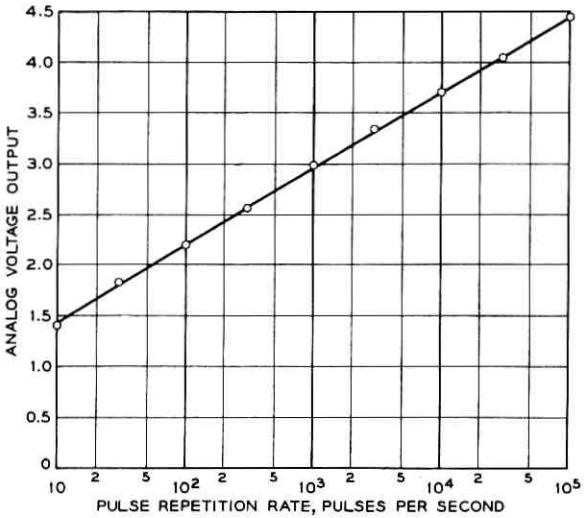

Fig. 25 — Ratemeter response.

in a conventional manner. However, the method by which load regulation is obtained is rather unique. DC feedback from a high-resistance divider on the output controls the oscillator repetition rate in proportion to the load by determining the charging time of a capacitor in the oscillator base circuit.

The detector load is nominally less than one microampere; load regulation is 0.1 per cent per microampere for loads up to 100 microamperes. Temperature stability is 0.05 per cent per degree centigrade.

4.3.6.2 *Tristable Multivibrator and Bias Switch.* The low-energy proton detector operates sequentially at three levels of bias. The tristable multivibrator circuit controls the position of the bias switch. A timing signal from the telemetry package switches the state of the tristable once each frame. The bias switch consists of transistor gates which turn off the −100-v bias supply and set the other levels of bias.

All three bias levels are monitored by an analog telemetry channel.

4.3.7 *Construction*

The detectors and their preamplifiers are mounted on the outer framework, with three of the four detectors protruding into space through holes in the satellite skin. The remainder of the radiation circuitry is located within the temperature-controlled electronics canister.

With the exception of the preamplifiers, the radiation electronics in the Telstar satellite are constructed in modules,[28] each represented by a square in the block diagram, Fig. 17. These modules consist of fiber glass epoxy circuit board wafers forming the top and bottom of a sandwich with components stacked like cordwood between them. Leads extend through a "mother board" on which all modules are mounted and interconnected. The entire subassembly is encapsulated in polyurethane foam, giving it good rigidity with little added weight. The radiation circuit is divided into two subassemblies to facilitate placement among the communications equipment complex within the canister.

V. PERFORMANCE IN SPACE

All parts of the radiation experiment have performed in space as expected and have provided a wealth of data, part of which will be described in a separate paper in this issue. The particle detectors, which are potentially susceptible to changes in their characteristics due to radiation surface effects,[21] have shown an internal consistency which indicates their continuing satisfactory operation after several months in space. This is true in spite of the higher radiation intensity encountered than

had been anticipated, and in spite of the often extensive periods of continuous bias under which the devices have been in operation, a condition which aggravates the radiation surface effects.

VI. ACKNOWLEDGMENTS

A large number of people have participated in an important way in this work. We wish in particular to acknowledge the contributions of: G. H. Wheatley, J. W. Rodgers, J. J. Darold and P. V. Chase in the development, production and testing of the particle detectors; W. M. Augustyniak in calibration of the detectors; B. H. McGahey in the development of the aspect and radiation damage solar cells; and D. J. D'Stefan, T. E. Davis, M. F. Slana, R. R. Blair and D. G. DeNure in the development and testing of the radiation damage transistors.

REFERENCES

1. Smith, K. D., Gummel, H. K., Bode, J. D., Cuttriss, D. B., Nielsen, R. J., and Rosenzweig, W., The Solar Cells and Their Mounting, B.S.T.J., this issue, Part 3.
2. Chapman, R. C., Jr., Critchlow, G. F., and Mann, H., The Telemetry and Command Systems, B.S.T.J., this issue, p. 1027.
3. Hutchison, P. T., and Swift, R. A., Results of *Telstar* Satellite Space Experiments, B.S.T.J., this issue, Part 2.
4. Brown, W. L., Gabbe, J. D., and Rosenzweig, W., Results of the *Telstar* Radiation Experiment, B.S.T.J., this issue, Part 2.
5. Gummel, H. K., and Smits, F. M., Testing of Solar Cells by Means of Spectral Analysis, Proc. of the Solar Working Group Conference, **2,** February 27, 28, 1962, pp. 3–17.
6. Loferski, J. J., and Rappaport, P., Radiation Damage in Ge and Si Detected by Carrier Lifetime Changes: Damage Thresholds, Phys. Rev., **111,** March, 1958, p. 432.
7. Easley, J. W., and Dooley, J. A., Fast Neutron Bombardment Reduction of Transistor Current Gain, J. Appl. Phys., **31,** June, 1960, p. 1024.
8. Freden, S. C., and White, R. S., Protons in the Earth's Magnetic Field, Phys. Rev. Letters, **3,** July 1, 1959, p. 9.
9. Van Allen, J. A., *Space Research,* Ed. H. K. Kallman Bijl, North Holland Publishing Co., Amsterdam, 1960, pp. 749–750.
10. Singer, S. F., Nuclear Explosions in Space, Nature, October 27, 1962, p. 301.
11. Brown, W. L., Introduction to Semiconductor Particle Detectors, I.R.E. Trans. Nuc. Sci., **NS-8,** 1961, pp. 2–10.
12. Blankenship, J. L., and Borkowski, C. J., Performance of Silicon Surface Barrier Detectors with Charge Sensitive Preamplifiers, I.R.E. Trans. Nuc. Sci., **NS-7,** 1960, p. 185.
13. Miller, G. L., Brown, W. L., Donovan, P. F., and MacIntosh, I. M., Silicon p-n Junction Particle Detectors, I.R.E. Trans. Nuc. Sci., **NS-7,** 1960, p. 185.
14. See I.R.E. Trans. Nuc. Sci., **NS-8,** January 1, 1961, and **NS-9,** June 1, 1962.
15. Pell, E. M., Ion Drift in an n-p Junction, J. Appl. Phys., **31,** February, 1960, pp. 291–302.
16. Monteith, L. K., M.S. thesis, Duke University, 1962.
17. McKenzie, J. M., and Ewan, G. T., Semiconductor Electron Detectors, I.R.E. Trans. Nuc. Sci. **NS-8,** 1961, pp. 50–53.
18. Buck, T. M., Proceedings of the Asheville Conference on Semiconductor Nuclear Particle Detectors, Dabbs, J. W. T., and Walter, F. J., Editors, NAS-NRC Pub. 871, 1961, p. 111.

19. Buck, T. M., and McKim, F. S., Effects of Certain Chemical Treatments and Ambient Atmospheres on Surface Properties of Silicon, J. Electrochem. Soc., **105,** December, 1958, pp. 709–714.
20. Buck, T. M., Wheatley, G. H., and Rodgers, J. W., to be published.
21. Peck, D. S., Blair, R. R., Brown, W. L., and Smits, F. M., Surface Effects of Radiation on Transistors, B.S.T.J., **42,** January, 1963, p. 95.
22. Elmore, W. C., and Sands, M., *Electronics*, McGraw-Hill, New York, 1949, pp. 241–249.
23. Chase, R. L., *Nuclear Pulse Spectrometry*, McGraw-Hill, New York, 1961, 22 pages.
24. Kelly, G. A., I.R.E. National Convention Record, Part 9, 1957, p. 63.
25. Goulding, F. S., Transistorized Radiation Monitors, I.R.E. Trans. Nuc. Sci., **NS-5,** 1958, pp. 38–43.
26. Wilkinson, D. H., Stable Ninety-Nine Channel Pulse Amplitude Analyzer for Slow Counting, Proc. Cambridge Phil. Soc., **46,** Part 3, 1950, p. 508.
27. Cooke-Yarborough, E. H., Counting-Rate Meter of High Accuracy, Proc. Inst. Elec. Engrs., London, 1951, p. 196.
28. Shennum, R. H., and Haury, P. T., A General Description of the *Telstar* Spacecraft, B.S.T.J., this issue, p. 801.

The Spacecraft Power Supply System

By D. C. BOMBERGER, D. FELDMAN, D. E. TRUCKSESS, S. J. BROLIN and P. W. USSERY

(Manuscript received February 11, 1963)

The power supply system in the Telstar spacecraft consists of a solar cell plant to convert solar radiation to electrical energy when the satellite is illuminated by the sun, a 19-cell nickel-cadmium battery to store energy, and a regulation circuit to supply constant output voltages over a wide variation in input voltages. Additionally, the power supply system provides switching to conserve power and allow battery recharging during periods between communications experiments.

I. INTRODUCTION

The power supply system used in the Telstar spacecraft employs a solar cell plant which converts solar radiation to electrical energy when the satellite is illuminated by the sun. During periods of eclipse and/or peak power drain of transmission, reserve power is provided by a 19-cell, nickel-cadmium battery. To conserve power and allow battery recharging, continuous power is supplied only to those circuits in the satellite necessary for ground tracking and command. All others are turned off when not required.

1.1 *Characterization of Loads*

The electrical systems in the spacecraft are divided into three major parts:

(a) the communications repeater, which contains the microwave transmitter, microwave receiver and microwave beacon;

(b) the radiation damage and particle distribution experiment;

(c) the command receivers, telemetry system, and VHF beacon transmitter.

The microwave transmitter contains a traveling-wave tube, the only electron tube in the satellite. The power requirements for the traveling-wave tube total 15.8 watts.

A transistorized dc-to-dc high-voltage converter was designed to achieve the desired voltages. The single converter provides all the required TWT power. All subsystems employ solid-state devices as active circuit elements and operate at 16 volts.

The power requirements for the microwave receiver and beacon total 3.2 watts. Together with the microwave transmitter, the power requirements for the communications experiment amount to 19.0 watts.

The instrumentation for the radiation damage and particle distribution experiment requires approximately 0.3 watt. For reliability, two command receivers are employed, each requiring 1.0 watt; the 136-mc VHF beacon transmitter requires 1.8 watts. The VHF beacon transmitter and the command receivers are continuously powered and require a total of 3.8 watts. The telemetry system requires approximately 0.9 watt.

The programming of the systems by ground command results in a power drain profile having three major levels. The first is the continuous drain of the VHF beacon transmitter and command system. This totals 3.8 watts. A second level adds the telemetry and radiation experiments which may be commanded "on"; the second level brings the total to 5.0 watts. The third level adds the power requirements of the communication repeater, resulting in a maximum power demand of 24 watts distributed among the several subsystems. An experiment considered typical for any 24-hour period is shown in the power profile of Fig. 1. The power level shown includes the losses of the high-voltage converter for the TWT and of the main 16-volt regulator. The details of these circuits are covered in later sections of this paper.

1.2 *Power System Design Considerations*

In addition to the specific power requirements of the electronic loads described in the preceding section, there are several general requirements which must be met by the power system.

(*i*) *Temperature Range* — An objective of the spacecraft thermal design was to attain an electronic canister temperature as close to 70°F as possible, regardless of the satellite spin-axis orientation with regard to the sun, during full sunlight, during maximum eclipse and with an estimated decrease in solar plant power from an initial 14 watts to 7 watts after a two-year life. Normal temperature range for these conditions over a two-year period was calculated to be 32°F to 70°F. Operational design limits of 15°F to 90°F were established for compo-

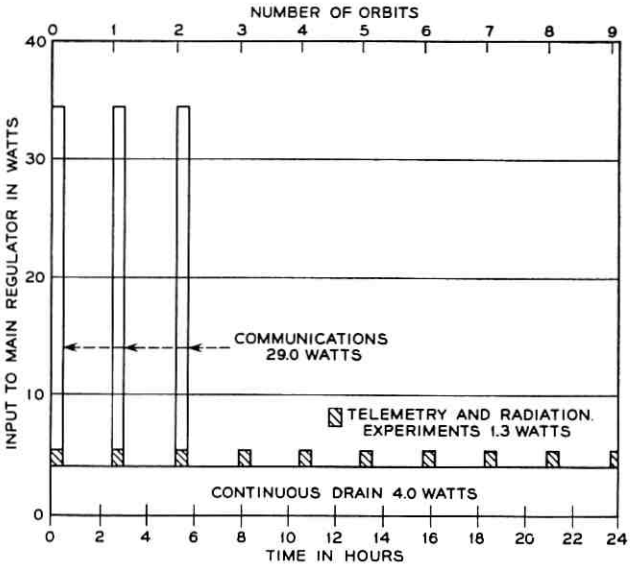

Fig. 1 — Power duty cycle referred to the input of the main regulator.

nents of the power system, and qualification tests include temperature checks at 0°F and 140°F.

(*ii*) *Efficiency and Weight* — Every effort was made to minimize the weight of the Telstar power system consistent with maintaining high power conversion efficiency, high reliability, and repeated operation in the radiation environment of the Van Allen belt. The battery and mounting weigh 11 pounds; the regulator and converter combined, including auxiliary control apparatus and wiring, weigh 7 pounds.

(*iii*) *Telemetry* — There are 30 channels of telemetry associated with the power system to provide information on its behavior. Battery voltage and temperature are monitored. The performance of the main regulator is assessed by monitoring various voltages and transistor case temperatures. The dc-to-dc converter is monitored by telemetering the heater voltage and collector current along with the helix and accelerator currents; in addition, the case temperature of switching transistors is monitored. Three channels are used to monitor the status of the relays associated with control sequence for commanding the TWT on. In addition, the current available from the solar cell plant is telemetered; this information, together with voltage measurements for the entire

nickel-cadmium storage battery, permits calculations of the available solar power to be readily made.

II. DESCRIPTION OF POWER SYSTEM

The Telstar power system employs silicon solar cells as the primary power source and a sealed nickel-cadmium storage battery which provides power for peak loads and for eclipse periods. An over-all block diagram is shown in Fig. 2. The number and arrangement of solar cells were designed to provide nearly constant power regardless of satellite attitude, at the value required to provide for the average power requirements of an orbit, including battery losses. The solar cell portion of the power system was designed to provide an initial power output of approximately 14 watts, which is sufficient to permit a flexible experimental program.

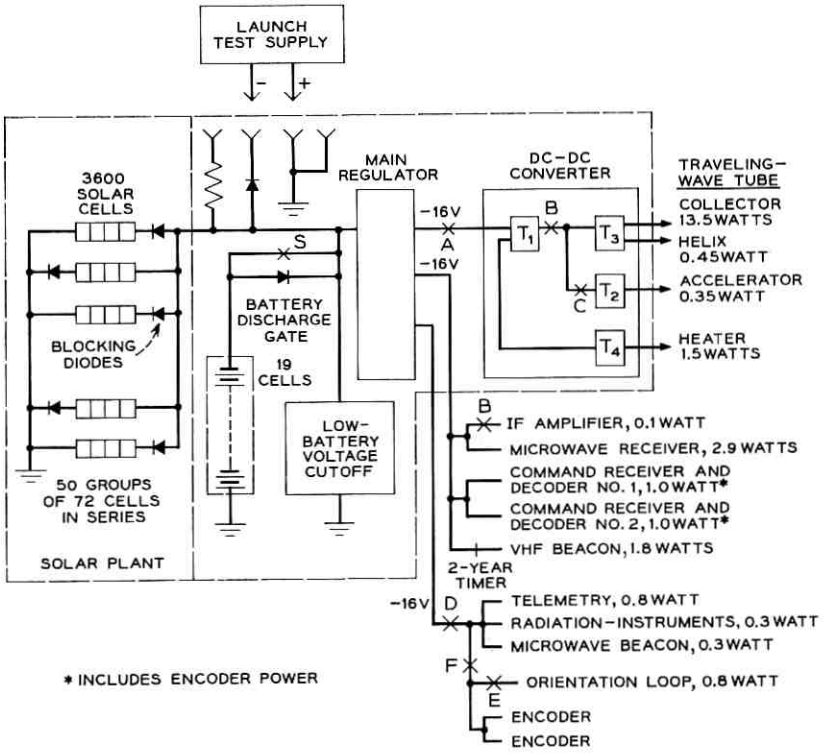

Fig. 2 — Block diagram of spacecraft power system.

The early objectives for the spacecraft included a minimum capability of 30 minutes per orbit for monitoring the telemetry and radiation experiments, with continuous use representing a desirable upper limit. An objective of at least 90 minutes per day was established for the communications experiments requiring operation of the TWT. The maximum duration of any single pass for which the spacecraft is usable to the Andover, Maine, station is approximately 60 minutes.

The objective of 90 minutes per day for communications experiments may be distributed among the visible orbits with the possibility of equal distribution in three consecutive orbits.

2.1 *Solar Power Requirements*

The solar power plant requirements were calculated by considering the continuous and peak power requirements of the electrical systems, the efficiency of the regulator and converter, the battery efficiency, the eclipse time per orbit, the duty cycle of the various intermittent loads, the orbital period, and total light time per day.

The following formula was developed to determine the required power from the solar cell plant:

$$P_S = (W_S/T_L) = [(W_L + kW_D)/T_L] \tag{1}$$

where W_S = energy supplied by the solar source in one periodic interval,
W_L = energy consumed in the load during the light periods,
W_D = energy consumed in the load during the eclipse periods,
k = ratio of the energy put into the battery during charging to the energy available from the charged battery, and
T_L = light period.

The energy efficiency factor, k, is a complicated function which depends on battery temperature, charge rate, depth of discharge, discharge rate, charge time, and cycle behavior. Laboratory data on commercial nickel-cadmium storage cells evaluated during the early stages of Telstar system development indicated that a typical charging efficiency for sealed nickel-cadmium cells, based on deep discharges and charge rates of $C/50$* to $C/20$ for complete recharge, was approximately 55 per cent. The value of k for a charging efficiency of 55 per cent was calculated to be 2.23. This value of k was employed in determining the required solar cell power output. During the short development period there

* C is the current which would flow out of the battery during discharge if the nominal capacity of the battery could be removed in one hour at constant current.

were a number of revisions in the power requirements of the several electrical systems, and a considerable amount of necessary interaction among the various development activities. The maximum required solar power was calculated to be 14 watts using (1) and maximum load and eclipse requirements. Current data on the specially developed nickel-cadmium cell indicate that an energy ratio factor k of approximately 1.5 can be achieved in the required temperature range, with charge rates of $C/40$ to $C/10$.

Telstar employs 3600 n-p silicon solar cells, made up into 50 groups of cells in parallel, each group containing 72 cells in series. A silicon diode is placed in series with each parallel string to prevent cells which are not illuminated by the sun from loading the illuminated cells and also to prevent the battery from discharging into the solar cell plant. The solar cell arrangement occupies approximately 35 per cent of the exterior surface of the spacecraft.

2.2 *The Storage Battery*

The storage battery contains 19 specially prepared sealed nickel-cadmium cells with a nominal capacity of 6 ampere-hours. Fig. 3 is a photograph of the cell, which is discussed in detail in a companion paper.[1] The 19-cell battery is mounted in the canister in 3 groups of 5 cells each and 1 group of 4 cells. Each cell is individually insulated from the canister with a thin polyethelene sleeve.

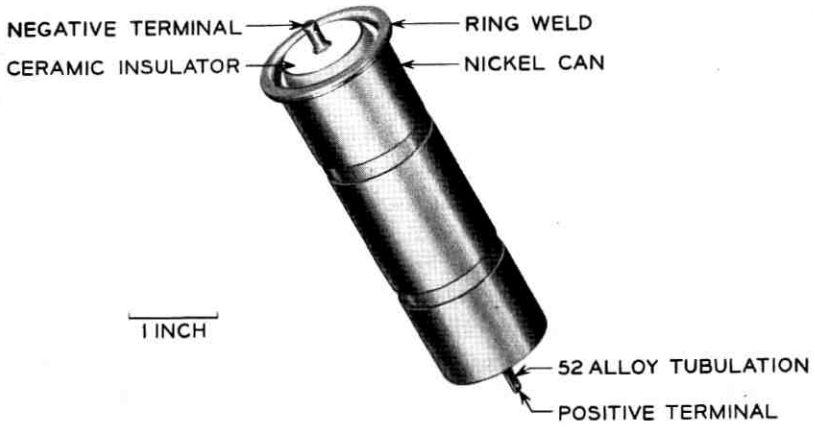

Fig. 3 — Nickel-cadmium cell for the spacecraft.

The battery is connected directly across the output of the solar cell plant through a diode normally bypassed by relay contacts. This diode circuit, called the "battery discharge gate," is described elsewhere in this paper. In this arrangement the maximum voltage of the solar power plant is 29.5 volts, which is the end-of-charge voltage of the 19-cell battery at the lowest expected temperature. The minimum voltage at the input to the main regulator is determined by the discharge voltage of the battery. The power system was designed to operate with a minimum voltage of 19.8 volts, based on 18 cells in the event of a short circuit of one cell.

2.3 *Main Regulator and dc-to-dc Converter*

The main regulator, shown in Fig. 2, provides a regulated voltage for the different loads from the varying battery voltage. A switching type series voltage regulator design was selected rather than quasi-linear series or shunt type regulators because of the higher efficiency that can be obtained with wide variations in battery voltage and load current. The main regulator provides three separate filtered outputs at nominally minus 16 volts. Separate filters are employed to reduce crosstalk between the command receivers, the radiation experiment and the switching transistor dc-to-dc converter. The efficiency of the regulator at maximum load is approximately 92 per cent.

The dc-to-dc high-voltage converter furnishes heater, anode, helix and collector voltages for the TWT, derived from the minus 16-volt supply. The converter is unregulated and its output regulation is governed by the changes in the minus 16-volt output of the main regulator and the load variations in the TWT. The over-all efficiency of the converter is approximately 70 per cent, including losses in the low-voltage command switching circuits. To conserve power, the converter is energized only during the communications experiment by sequential application of the TWT voltages by ground command.

The major items of the satellite power system are described in greater detail in the following sections, along with several auxiliary features.

III. NICKEL-CADMIUM STORAGE BATTERY

A sealed nickel-cadmium battery was selected for the spacecraft because this storage system is considered to be capable of

(a) accepting continuous overcharge during long periods of constant sunlight,

(b) displaying long cycle life under shallow depths of discharge and moderate life under deep discharges,

(c) being hermetically sealed, permitting long life in a space environment,

(d) operating in the temperature range of 15°F to 90°F, and

(e) providing nearly constant voltage during discharge.

3.1 *Battery Capacity*

Thermal calculations of the satellite chassis temperature indicated that the nominal battery temperature would be 70°F under conditions of initial available solar power of 14 watts and continuous sunlight. Data obtained with nickel-cadmium cells having a construction similar to those chosen for the power supply indicated that for a temperature of 70°F and a maximum cell voltage of 1.48 volts the overcharge current should not exceed $C/15$. Orbital predictions for the Telstar satellite indicated that early in life the satellite would be in continuous sunlight, under conditions of maximum available solar power, and would for long periods be operated with only the continuous power drain of the VHF beacon transmitter and command system. Under these conditions the charging power available to the battery would be approximately 10 watts, leading to a continuous charging current of approximately 0.36 ampere. To insure a safe continuous overcharge at this rate and a cell temperature of 70°F requires a cell having a nominal capacity of at least 5.4 ampere-hours. A smaller-capacity storage cell would require the addition of a battery charging current limiter.

In addition to the overcharge characteristics desired in the spacecraft battery because of long periods of continuous sunlight, consideration was necessarily given to the discharge capacity. Since the peak power required for a communications experiment exceeds the power available from the solar cells, the storage battery is subjected to many charge-discharge cycles during the satellite life. The battery is designed so that the peak load requirements can be met during at least three consecutive periods of longest eclipse. It is not feasible to completely recharge the battery during interim sunlight periods. Initially, 20 per cent was considered to be a safe maximum depth of discharge at the end of three peak eclipse time discharges. Each peak power drain represents a discharge of about 0.75 ampere-hour. Interim recharge is a function of the charge rate, cell temperature, and ampere-hour charge efficiency. For spacecraft nickel-cadmium cells the charge efficiency of partially discharged cells may range from 75 to 97 per cent. For the purpose of establishing a required cell capacity, the minimum recharge efficiency was used. Each charge interval between communications experiments returns approximately 0.5 ampere-hour; therefore at the end of the third consecu-

tive peak power drain, the capacity discharged from the battery is approximately 1.25 ampere-hours. Allowing this peak discharge to represent 20 per cent of the battery total capacity indicates that a 6.2-ampere-hour nominal capacity is required.

Consideration of the required continuous overcharge characteristics, along with the required discharge capacity, suggests that a battery having a nominal capacity of 6 ampere-hours is adequate for the spacecraft power system. Laboratory data on the power system performance obtained during the development program revealed satisfactory battery system behavior with maximum depths of discharge as high as 40 per cent when providing for frequent communication experiment usage during periods of greatest satellite visibility and maximum eclipse periods. Under these conditions, the battery may be discharged from a fully charged state during four consecutive orbits, with each discharge period equal to or greater than the maximum eclipse period. Fig. 4 illustrates the capacity removed from a fully charged storage battery as a result of the four consecutive peak power drains, three of which are

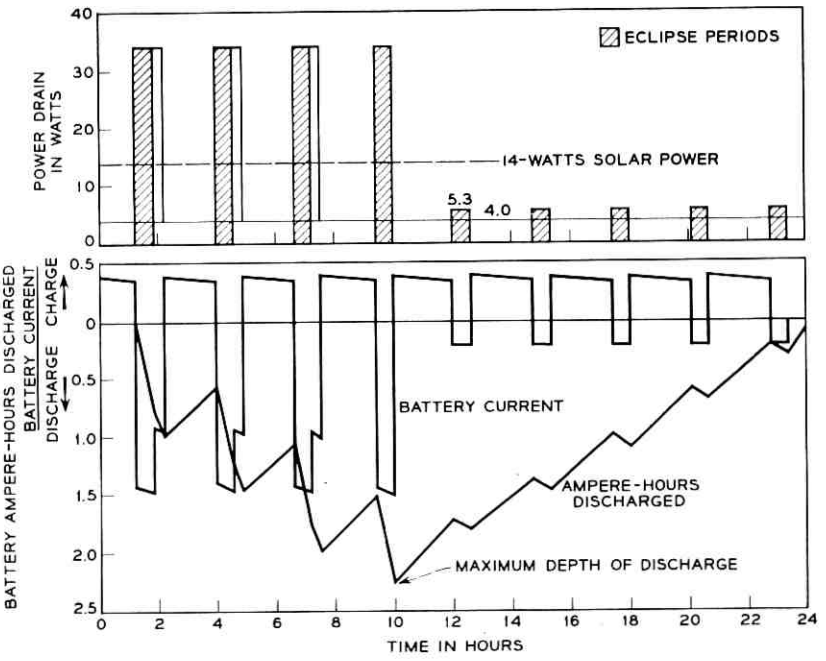

Fig. 4 — Battery charging and discharging, along with capacity removed from battery, during a typical 24-hour period.

for periods exceeding the maximum eclipse time. The maximum capacity removed is approximately 2.3 ampere-hours or 40 per cent of the available capacity of the battery, calculated on the basis of a charge efficiency of 75 per cent, a solar cell plant output of 14 watts, and illumination intervals and loads as shown in Fig. 4. This usage represents a large short-term discharge of the nickel-cadmium battery and requires that the sunlight periods during the balance of the day, approximately 11.5 hours in this illustration, be available for charging the battery to insure restoral of full battery capacity.

3.2 *Battery Energy Balance*

Analyzing the energy flow equations for the battery permits a flexible program involving communication experiments of varying duration. This analysis correlates the charging energy available from the solar cell plant, over any 24-hour period, with the energy requirements of the load. Thus, the power system designer can take into account different battery depths of discharge, reduced available solar cell power and different eclipse periods. Figs. 5 and 6 show the time allowable for com-

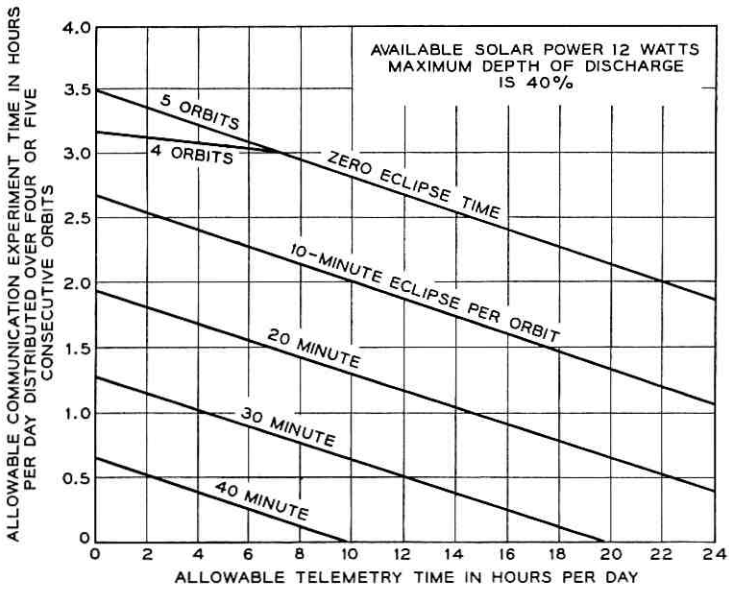

Fig. 5 — Allowable satellite utilization with communications experiments distributed over 4 or 5 consecutive orbits (solar power 12 watts).

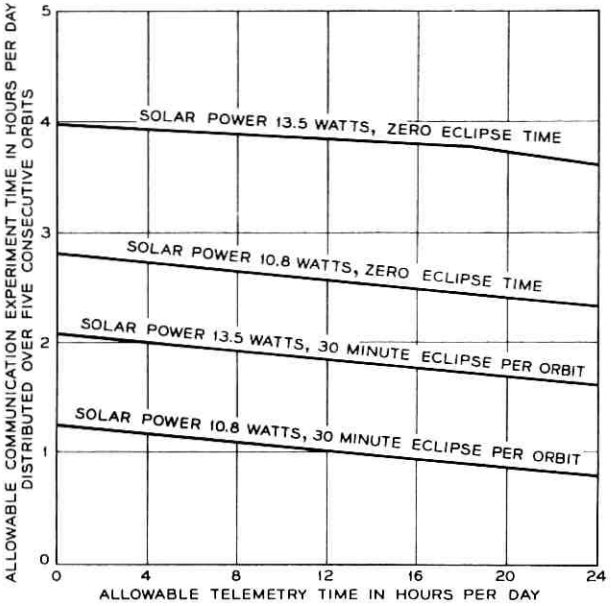

Fig. 6 — Allowable satellite utilization with communications experiments distributed over 5 consecutive orbits (variable solar power).

munication experiments as a function of the total time spent telemetering data to various ground stations. Families of such curves were developed for different values of available solar power, orbit eclipse time and battery depth of discharge, and for communication experiments distributed among 3, 4 and 5 consecutive orbits.

IV. MAIN REGULATOR

The principal function of the main regulator is to provide a regulated voltage with low ripple from the nickel-cadmium battery, whose voltage varies during the charge and discharge cycle. Fig. 7 is a photograph of the main regulator, packaged with a portion of the dc-to-dc converter. The main regulator is on the middle and bottom mounting boards of this package.

4.1 *Performance*

The main regulator supplies 16 volts ± 0.17 per cent output, for loads varying between 0.2 and 2.0 amperes and an input voltage between 19.8

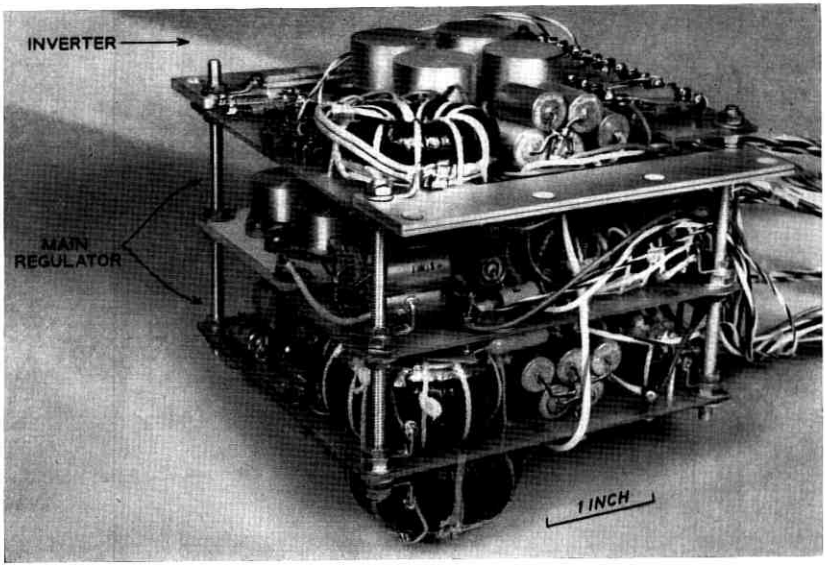

Fig. 7 — Main regulator assembly (unfoamed).

and 29.5 volts. The efficiency is approximately 92 per cent at maximum load and 85 per cent at minimum load.

Fig. 8 shows the basic performance characteristics of the regulator. Curves are drawn for conditions of minimum and maximum loading. The upper graph shows the output voltage vs input voltage; the flat portion is the region of regulation. The lower graph shows input current vs input voltage. The input current increases with input voltage until the minimum regulating voltage is reached. Then the input current falls off with increasing input voltage, since the regulator draws essentially constant power while regulating. Above the regulating range both the input current and output voltage increase with input voltage.

4.2 *Block Diagram of Main Regulator*

The block diagram of the main regulator is shown in Fig. 9. The dc input is "chopped" into a series of rectangular waves by means of a transistor switch. This switch is alternately a short circuit and an open circuit, dissipating relatively little power in either state.

The rectangular wave is imposed upon the main filter, a low-pass LC filter. The rectangular wave consists of alternate intervals of dc input voltage and ground; the main filter extracts the average of this

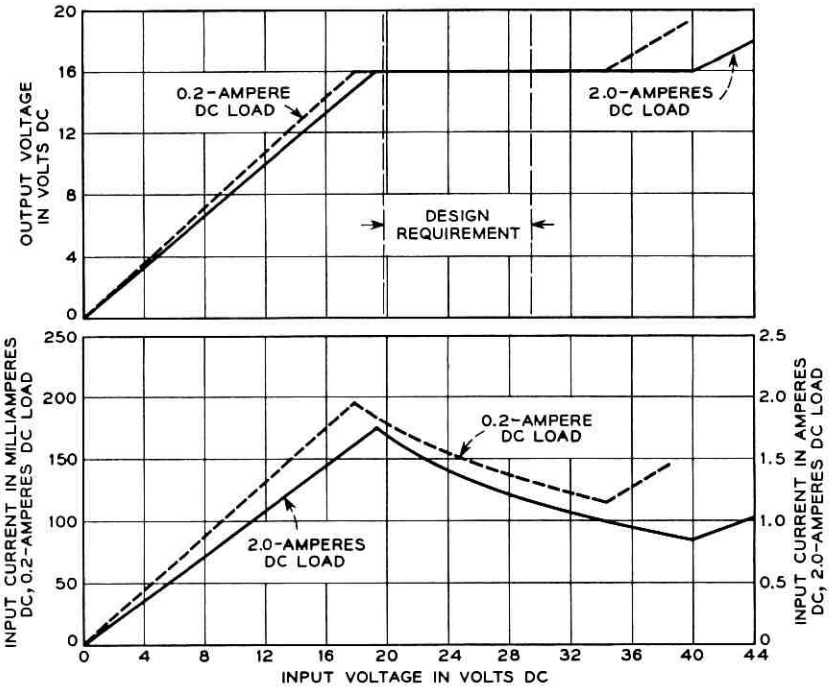

Fig. 8 — Main regulator nput-output characteristics.

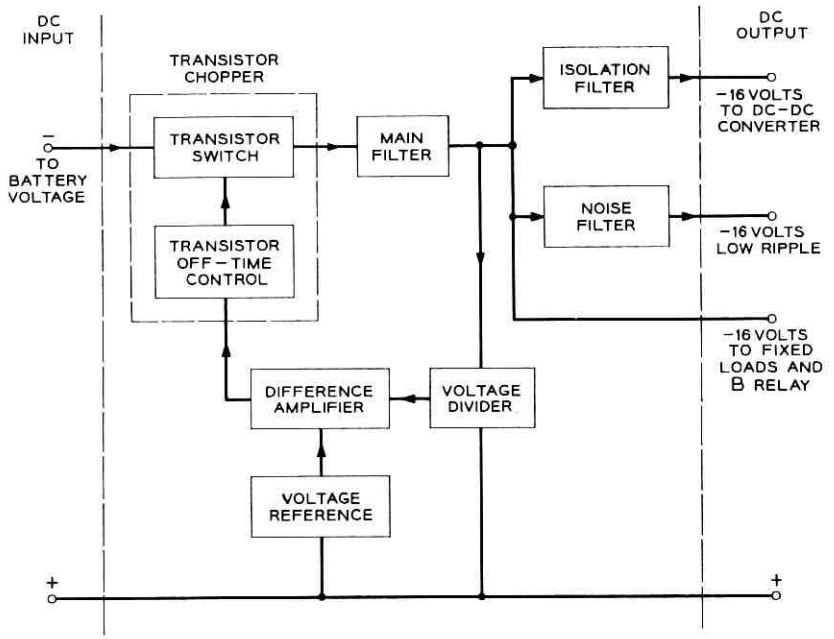

Fig. 9 — Block diagram of main regulator.

wave, which becomes the −16-volt output. Further filtering is provided by an isolation filter, which prevents interaction between the main regulator and the dc-to-dc converter. The noise filter provides an output whose fundamental component (at the main regulator frequency) is approximately 1 millivolt peak-to-peak.

The difference amplifier compares the output of the voltage divider, a fixed fraction of the output voltage (approximately 8.0 volts), with that of the voltage reference, a voltage regulator diode. If the output voltage goes above or below its correct value, an error signal is sent to transistor off-time control, which adjusts the off time, or time during which the transistor switch is an open circuit. This in turn controls the −16-volt dc output. The output voltage is thereby regulated by a closed feedback loop. The transistor switch and transistor off-time control can be considered as a single block, labeled "transistor chopper" in Fig. 9.

4.3 *Qualitative Discussion of Main Regulator*

4.3.1 *Design Approach*

Fig. 10 displays a simplified schematic of the transistor chopper. Transistor Q_1 is the switching power transistor, which alternates between cutoff and saturation to create rectangular waves. Since Q_1 regulates by

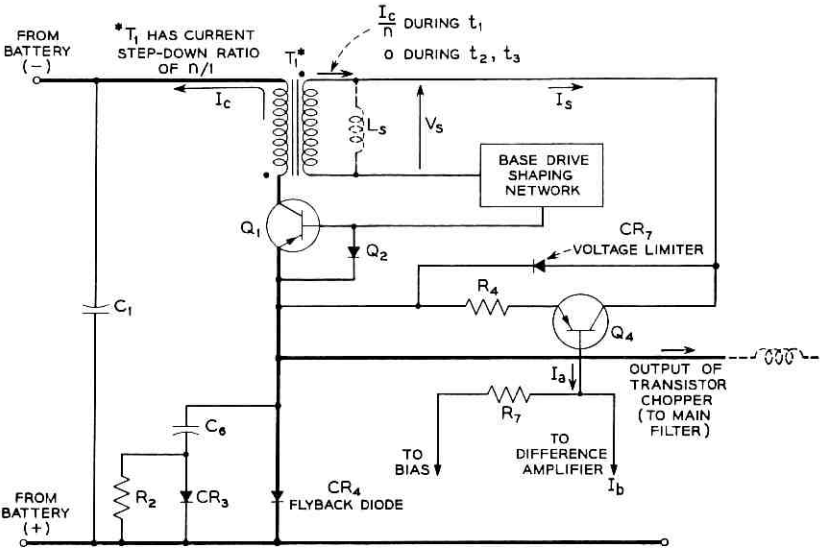

Fig. 10 — Simplified schematic main regulator of transistor chopper.

means of a switching mode, highly efficient regulation is possible. Given ideal components, a switching regulator can approach lossless regulation. This contrasts with the more familiar series or shunt type regulators where regulation is accomplished through a controlled dissipation of power.

While a switching regulator has the advantage of achieving high efficiency, it has the disadvantage of creating rectangular waves which must be filtered before application to the various loads. This filtering, to be efficient, is of the LC low-pass type and accounts for more than half the weight of the regulator. To minimize this weight it is desirable to switch at a relatively high frequency, where LC filtering is increasingly effective.

There are several practical limitations as to how high a frequency one can switch. First, there are the inevitable switching losses in transistor Q_1. While Q_1 dissipates little power in cutoff and saturation, the instantaneous power dissipated while switching from cutoff to saturation is high (roughly equal to one-half the input voltage multiplied by the load current, or 25 watts at 25 volts input and 2 amperes load), but the average loss is small because the switching times are very short compared to the over-all period. The power loss in Q_1 due to switching is approximately 0.5 watt. The switching frequency is approximately 20 kc at a 2-ampere load and 35 kc at a 0.2-ampere load.

The requirements for Q_1 were for a power transistor with fast rise and fall times and low saturation resistance (0.1 ohm). These requirements were met by an alloy-diffused germanium power transistor, a relatively recent semiconductor development. This type of transistor also proved to be less sensitive to proton bombardment than conventional germanium alloy power transistors.

The output of the transistor chopper feeds the inductor input filter (main filter). Diode CR_4, a flyback diode, maintains continuity of current in this inductor when Q_1 switches off. The network consisting of capacitor C_6, resistor R_2 and diode CR_3 improves the turn-off switching locus of transistor Q_1. Without this network, it would be necessary, on turn off, for Q_1 to block the entire input voltage, before CR_4 could start to conduct. However, with the network, C_6 charges up during the on time of Q_1 and can absorb current through C_6 and CR_3 as Q_1 starts to turn-off, without first requiring Q_1 to absorb the complete input voltage. Since C_6 charges and discharges every cycle, with power dissipated in R_2, it is obvious that losses in this network also increase with frequency.

Another source of frequency-dependent losses is the input inductor of the main filter. Here eddy current and hysteresis losses were minimized by the use of a powdered iron toroid.

Another frequency limitation besides losses is the storage time of transistor Q_1. While Q_1 has rise and fall times at least an order of magnitude shorter than those of a conventional germanium alloy transistor, its storage time is roughly equivalent (about 5 microseconds in a typical application). While the storage time does not appreciably affect efficiency, since Q_1 is saturated during this interval, it does affect frequency and the length of Q_1 on time, if it is allowed to become an appreciable percentage of the period. Since storage time is highly variable between transistors of the same code and also is reduced with time by proton radiation, it is desirable to have the circuit, rather than the storage time, predominate in controlling frequency.

Two other frequency limitations are the response times of transistor Q_4 and diode CR_4.

4.3.2 *Principle of Self-Excited Oscillations*

Transistor Q_1 in conjunction with current transformer T_1 forms a self-excited blocking oscillator. When Q_1 starts to turn on, the positive feedback polarity of T_1 causes current, I_s, to flow through CR_7 (forward biased), the emitter to base of Q_1 and the base drive shaping network, driving Q_1 further into saturation.

Inductor L_s represents the finite magnetizing inductance of the T_1 secondary. An ideal current transformer, of course, has infinite magnetizing inductance. The finite inductance of T_1 is deliberately controlled as a means of controlling the regulator switching frequency.

The waveforms of Fig. 11 relate the T_1 secondary voltage and current as a function of time and are idealized for simplicity. Assume Q_1 has just turned on. Then the current flowing out of the secondary of the "ideal" transformer is I_c/n, where I_c is the primary and transistor Q_1 collector current and n is the current stepdown turns ratio of T_1. Initially, L_s accepts no current and I_s, the "actual" transformer secondary current, is also I_c/n. This is displayed on the I_s waveform at $t = 0$. Since the idealized waveforms show a constant voltage, V_1, across T_1 secondary during the on time (t_1) of Q_1, then the current through L_s increases linearly with time, causing I_s to fall linearly with time. The total current out of the "ideal" secondary remains constant during t_1.

Since Q_1 has a large dc current gain (typically 150) over the load currents considered, it is reasonable to assume that I_s, which is also the base drive of Q_1, falls to zero before Q_1 switches off. At this time, the current through L_s is I_c/n, the entire "ideal" secondary current.

When Q_1 switches off, the "ideal" secondary current drops immediately from I_c/n to zero. At the same time, I_s reverses and initially becomes

$-I_c/n$ due to the demands of L_s. This current reverse biases Q_1 to maintain Q_1 in cutoff throughout the interval $t_2 + t_3$. Diode Q_2 bypasses the excess reverse current not needed to supply Q_1 reverse leakage currents.

Reverse current I_s passes through the parallel combination of CR_7 (reverse breakdown) direction and transistor Q_4. Resistor R_4 provides local negative feedback. At this point it is assumed that Q_4 acts as a current device, where collector current is independent of emitter-collector voltage. For a given value of I_s it is thus understood that either the base current to Q_4 is sufficient to saturate (zero voltage across Q_4) or the voltage across Q_4 is the breakdown voltage of limiter diode CR_7.

Referring once again to the waveforms of Fig. 11, t_2 is the interval during which limiter diode CR_7 conducts and t_3 is the interval during which Q_4 is saturated. The sum of t_2 and t_3 is the off time of Q_1. It will be noticed that T_1 secondary voltage, V_s, is much larger during t_2 (equal to $-V_2$) than during t_3 (equal to $-V_3$). As a consequence of this, I_s falls much more rapidly during t_2 than during t_3.

I_s is seen to fall rapidly till it reaches the value $-\beta I_a$, at which Q_4 saturates. β is the common-emitter current gain and I_a the base drive of transistor Q_4.

The off time of Q_1, and thus the dc output voltage, can be controlled

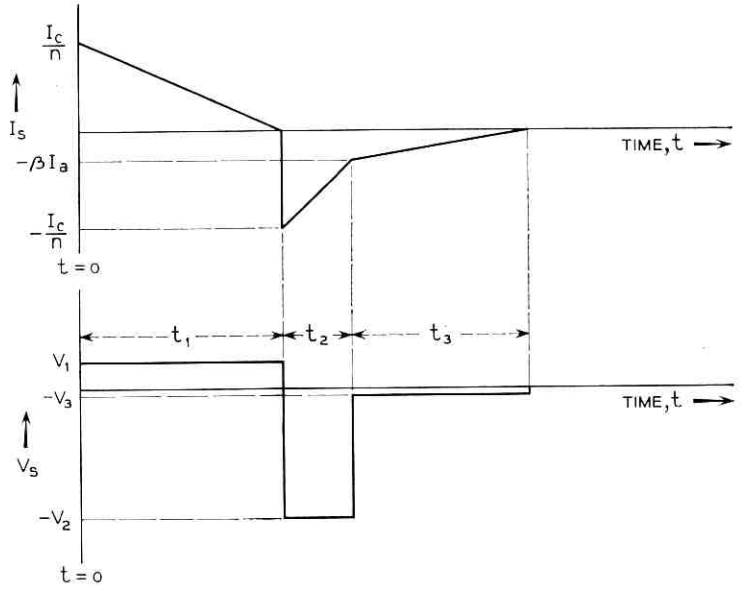

Fig. 11 — Waveforms of main regulator current transformer T_1.

by varying I_a . If I_a is zero, the reverse I_s will fall in the shortest possible time, minimizing the transistor Q_1 off time. If I_a equals $I_c/n\beta$, Q_4 will saturate as soon as Q_1 turns off, resulting in the longest possible off time. Regulation occurs only during the off time of Q_1 .

V. DC-TO-DC CONVERTER

The dc-to-dc converter furnishes high and low dc voltages for the TWT and a low dc voltage for the bias for the down converter. Important in the derivation of these voltages is the dc-to-ac inverter shown on Fig. 12; this inverter changes the −16-volt dc input voltage to an ac voltage which is applied to transformers. The secondaries of the transformers are applied to rectifiers and filters to obtain dc voltages. The converter is unregulated, and its output regulation is the sum of changes due to temperature and to load variations in the TWT. The over-all converter efficiency is approximately 71 per cent. A simplified diagram of the dc-to-dc converter is shown in Fig. 13.

To conserve power, the converter is energized only during the communications experiment. Command signals to the satellite to operate the traveling-wave tube and bias the down converter of the transmission equipment are accomplished by use of three magnetic-latching relays mounted in the power supply.[3] Relay A responds to the A command to the satellite, which causes the heater voltage to the TWT and the positive bias voltage for the down converter to be applied.[4] The B relay responds to the B command and causes the helix and collector voltages to be applied but no beam current to flow in the TWT when B relay is

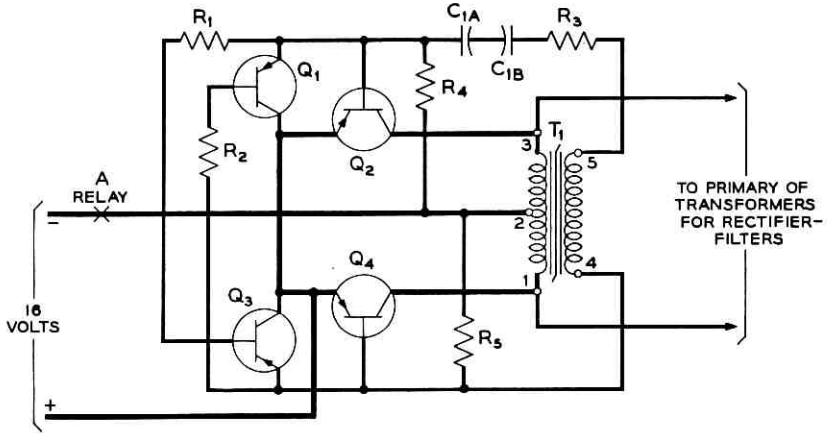

Fig. 12 — Schematic diagram of dc-to-ac inverter.

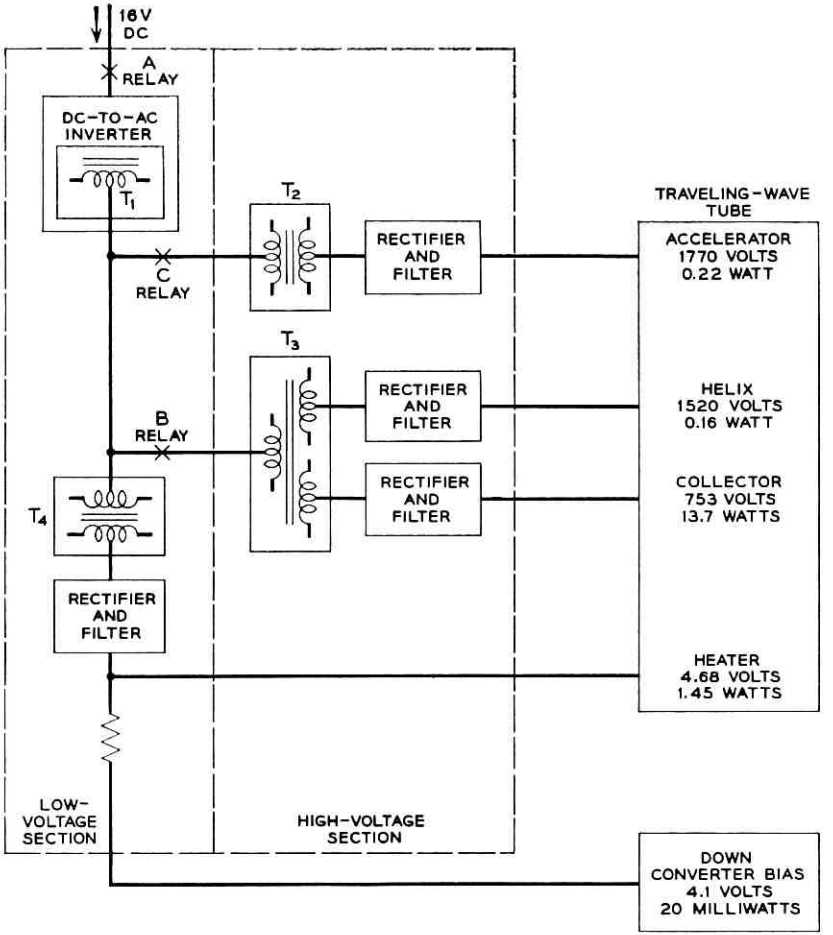

Fig. 13 — Block diagram of dc-to-dc converter.

closed. Beam current flows when the A, B and C relays are commanded on. This eliminates the possibility of other voltages being applied to the TWT prior to the heater voltage. After a minimum of three minutes warm-up time for the heater of the TWT, the C command to the satellite causes the accelerator voltage to be applied to the TWT. The CC command causes the accelerator voltage to be removed. The A and B relays respond to the AA command on turn-off. Switching in the low-voltage ac circuits provides a satisfactory means of effectively switching the high voltage to the TWT through the use of separate transformers for the helix-collector and accelerator rectifiers. The primaries of the transform-

ers are connected as required by the B and C relays to the dc-to-ac inverter. The inverter is operated from the −16-volt dc source by the A relay being commanded on.

5.1 *DC-to-AC Inverter*

A schematic diagram of the inverter is shown in Fig. 12. The inverter produces a square-wave ac voltage with a nominal frequency of 2.5 kc at full load. This frequency is selected to provide minimum transistor switching and transformer losses. Also, it is desirable that the switching frequency of the dc-to-ac inverter be separated from the switching frequency range of the −16-volt regulator. The dc-to-ac inverter, along with relays D, E and F, is mounted in the main regulator package. The D relay causes −16 volts to be applied to the converter for the TWT heater telemetry network in addition to applying −16 volts to other circuits in the satellite. Relay E is used to apply voltage to the orientation loop and relay F is used to switch operation of encoders 1 or 2.

A feedback winding on transformer T_1 (shown in Fig. 12) is provided to furnish the source voltage for the drive circuit of the "on" power transistor, Q_2 or Q_4. The simplified drive circuit shown in the schematic of Fig. 14 may be used to describe operation during the half-cycle that transistors Q_3 and Q_2 are conducting and transistors Q_1 and Q_4 are cut off.

The inverter-transformer saturates each half-cycle and transformer action ceases, so that the feedback voltage on the secondary winding collapses. This causes the "on" power transistor to fall out of saturation because of lack of base drive current necessary to maintain low emitter-to-collector voltage. Consequently, the voltage applied to the primary

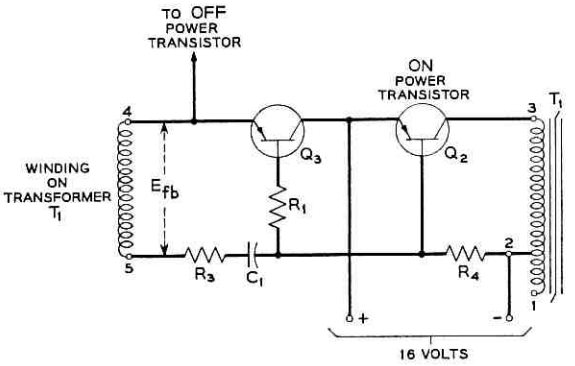

Fig. 14 — Simplified schematic of inverter drive circuit.

winding of transformer T_1 is reduced, causing a further reduction of feedback voltage. This action results in turning off the conducting transistor and turning on the transistor that has been cut off.

Since the power transistors require a finite time to turn off because of the storage time of the transistor, it is necessary to provide switching of the transistors so that at no time are transistors Q_2 or Q_4 conducting simultaneously. The collector current of the conducting transistor, Q_2 or Q_4, increases when transformer T_1 saturates because of the effective low impedance in the collector circuit. This increased current causes an increase of the power dissipation during switching of each half-cycle. To limit these losses and improve reliability, the base current of the power transistors is just sufficient to cause saturation at the time prior to turn-off but not large enough to cause excessive storage time. This is a value of base current determined for an expected degradation of gain due to aging and radiation damage. The base current is made large enough at the turn-on portion of the cycle to provide fast switching at each half-cycle, and the feedback is sufficient to initiate and maintain oscillation when the A, B, or C relays operate. The power transistor losses can be divided into three classifications: conduction, switching, and cutoff. The conduction losses are minimized by operating the power transistors in a saturated mode. The loss during switching is reduced by limiting the rise of collector current when the inverter-transformer saturates at the end of each conduction cycle. The drive circuit also provides negative base current to sweep out the minority carriers of the conducting transistor and reduce the transistor storage time. This helps prevent both power transistors from being on simultaneously, a condition which could result in catastrophic failure. Resistor R_4 provides initial base current to power transistor Q_2 when the A relay is commanded on. The magnitude of the base current is large enough to insure reliable starting of the inverter.

The base current for transister Q_2 (shown in Fig. 14) prior to switching is

$$i_{fb} = \frac{E_{fb} + (q_0/C_1)}{R_T} \exp - \frac{t_1}{R_T C_1}$$

where

E_{fb} = voltage of secondary winding on T_1

q_0 = charge on C_1 at time of switching

t_1 = $1/2f$, where f is the switching frequency, and

R_T = effective resistance of driver circuit for "on" transistor Q_2.

Also

$$R_T \approx R_3 + \frac{R_1}{h_{FE} \text{ of } Q_3}.$$

The waveform of the drive current is shown in Fig. 15.

When the A command is sent to the satellite, the −16 volts is applied to the inverter input. Oscillation is initiated and the output of the rectifier-filter provides power for the heater of the TWT. At the instant

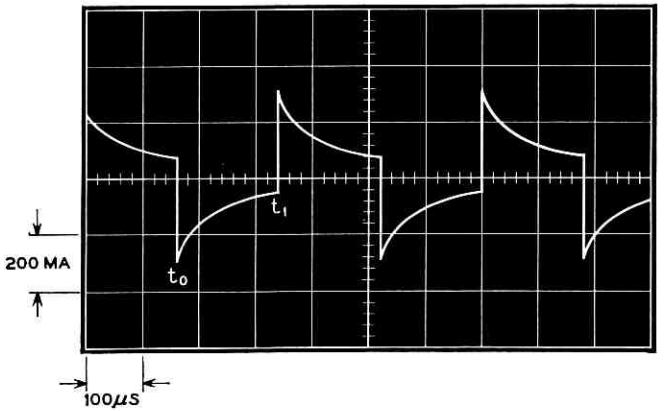

Fig. 15 — Waveform of inverter feedback current.

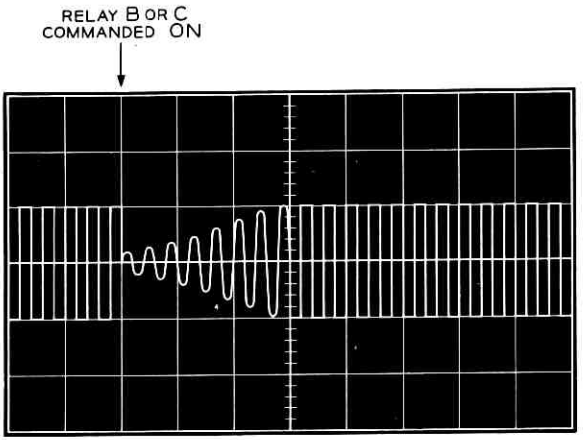

Fig. 16 — Inverter output voltage when relays B or C are commanded on.

the B and C relays operate, an effective short is placed on the output of the inverter due to the inrush current of the transformers connected when each relay operates. Also, the high-voltage capacitors in the rectifier-filter tend to draw large initial surge currents. To prevent excessive transistor collector power dissipation due to these transients, the drive circuit is designed to cause a gradual buildup to steady-state operation. Fig. 16 indicates the waveform produced on the output of the inverter when relay B or C is commanded on.

5.2 *Rectifier-Filter*

A photograph of the rectifier-filter section of the TWT power supply is shown in Fig. 17. Included in this unit are the telemetry networks for the heater voltage, collector, helix and accelerator currents.

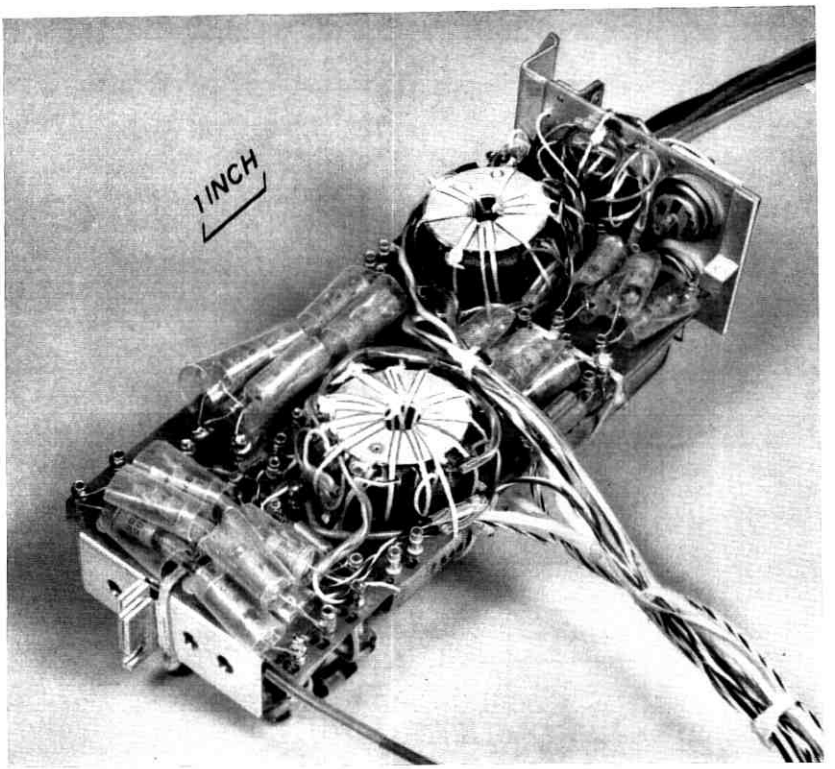

Fig. 17 — Traveling-wave tube power supply.

5.2.1 *Heater*

The square-wave ac voltage across the full primary of the inverter-transformer T_1 of Fig. 12 is applied to the primary of the heater-transformer, T_4, which provides bias and collector voltages for the transistorized synchronous rectifier Q_1 and Q_2 as shown in Fig. 18. The low voltage drop between the emitter and collector of the conducting transistor and

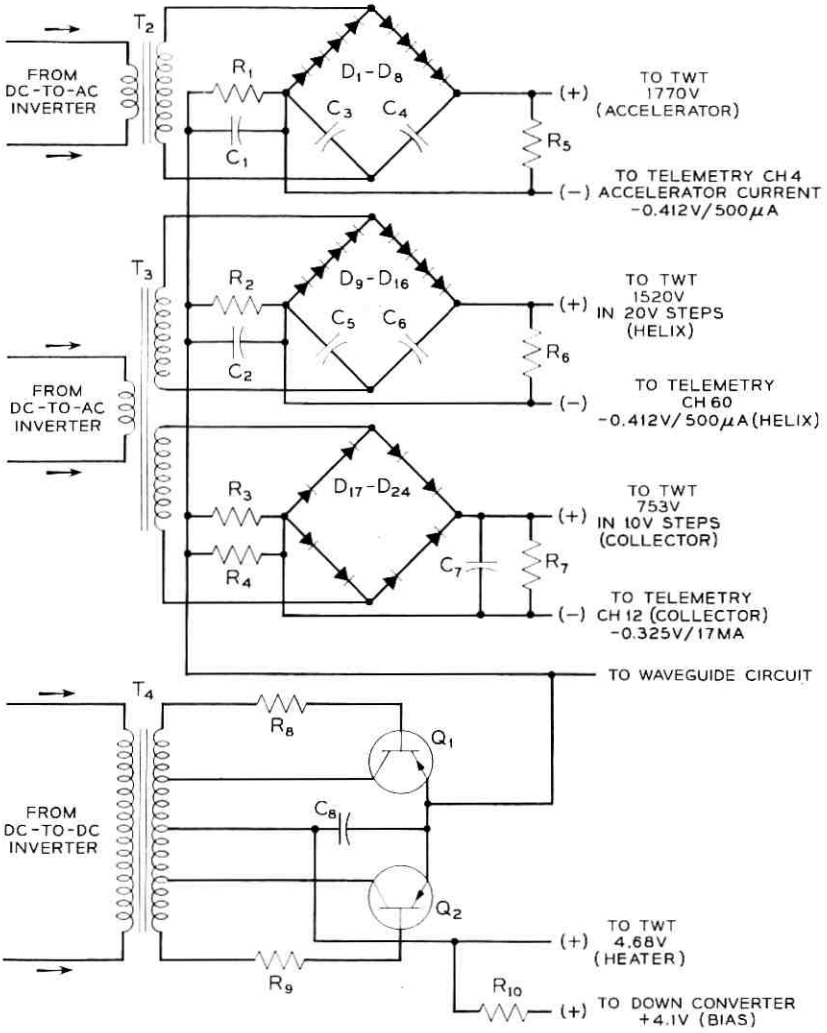

Fig. 18 — Schematic of traveling-wave tube power supply.

the small power necessary to maintain saturation affords an efficient means of obtaining dc for the heater of the TWT. Since the output is a rectified square-wave voltage, sufficient filtering is accomplished with only a capacitor filter.

5.2.2 *Helix-Collector*

Two separate secondary windings on transformer T_3 (shown in Fig. 18) provide helix and collector voltages for the TWT. One secondary winding is connected to a full-wave bridge rectifier and capacitor filter to obtain the dc voltage for the collector, and the other is connected to a voltage doubler rectifier-filter to obtain the dc voltage for the helix. A bleeder resistance across the collector output is provided to discharge the capacitor. Also, the bleeder in the helix rectifier prevents a rise of voltage at very low helix currents of 20 to 40 microamperes.

5.2.3 *Accelerator*

A separate transformer with one secondary is used to furnish high voltage for the voltage doubler rectifier-filter to obtain the dc voltage for the accelerator of the TWT. It is necessary to use a bleeder resistor to discharge the capacitors of the voltage doubler to prevent damage to the TWT.

5.3 *Performance*

5.3.1 *Heater* (A *Command On*)

Since the TWT heater resistance, when cold, is estimated to be approximately one-sixth the hot or steady-state resistance, there is a tendency for the heater to draw large initial current. Operational tests indicate that several cycles of the dc-to-ac inverter are required for the heater voltage to build up to full output. Steady-state operating temperature of the TWT heater is reached in approximately three minutes. The heater voltage is approximately 4.5 per cent higher with only the heater on than when the A, B, and C relays are on. This is due to the light load on the converter until there is TWT beam current. The slight over-voltage helps the TWT tube heater to stabilize in the three-minute warmup period.

5.3.2 *Heater, Collector and Helix* (A *and* B *Commands On*)

Since no beam current exists until the accelerator voltage is applied, there is a tendency for high voltage to be produced on the collector and

helix outputs during the time before the accelerator voltage is applied to the tube. A fixed minimum resistance load in the power supply reduces the rise of voltage on the collector of the TWT to less than 1150 volts, which is the maximum safe voltage for the filter-capacitor, transformer and TWT.

5.3.3 *Heater, Collector, Helix and Accelerator* (A, B, *and* C *Commands On*)

With the C relay on, there exists collector current of approximately 18 milliamperes, helix current between 20 and 50 microamperes with no RF drive to the TWT and 100 to 300 microamperes with RF drive, and an accelerator current between 100 and 150 microamperes. This current may build up to 500 microamperes after a year of operation in space. The most critical voltage on the TWT is the helix voltage. The regulation of this voltage is improved by designing the collector-helix transformer to have minimum leakage reactance on the helix winding of the transformer.

The power supply and TWT of each satellite are tested together prior to installation in the canister of the satellite. The final voltage and currents for optimum performance of the TWT are determined by observing the variation of RF output of the TWT when different voltage taps are selected on the transformers of the converter. The 16-volt dc input to the inverter is varied ±3 per cent, and taps are selected which give the smallest variation of RF output with the change of voltage to the TWT.

Measurements on the power supply and TWT of the spacecraft are given in Table I.

The total output power of the converter when the TWT is on is 15.48 watts. The input power is 21.8 watts. The efficiency is 71 per cent. The input current to the dc-to-ac inverter is 1.36 amperes. The bias voltage

TABLE I—MEASUREMENTS OF POWER SUPPLY AND TWT OF SPACECRAFT

Command	Item Measured	Volts	Current	Ripple
A only	heater	4.89	322 ma	
A + B	heater	4.850	320 ma	
	collector	1035	0	
	helix	1710	0	
A + B + C	heater	4.68	310 ma	135 mv
	collector	753	18.1 ma	310 mv
	helix	1520	110 μa	800 mv
	accelerator	1770	125 μa	600 mv
	down-converter bias	4.1	4.8 ma	

for the down converter is derived from the same rectifier-filter used to supply the heater voltage.

5.4 *Operational Tests*

The dc-to-ac inverter is combined with the −16-volt regulator to form a subassembly, and tests are made with the rectifier-filter section of the converter. The two units are foamed and then temperature cycled. The two subassemblies are soaked at −22°F and +140°F for six hours at each temperature. An operational temperature run is performed between +15°F and +105°F.

The −16 volts is operated continuously during the vibration test, and the states of relays A, B, C, and D are monitored. A change of state of the relays would have indicated that the TWT could have come on during launch.

Temperature cycling of the power supply in the canister includes soaking at 0°F and +125°F, and operation between +25°F and +90°F. During shake and environmental tests at Whippany[5] and extended transmission tests at the Murray Hill Laboratories, data from the power supply telemetry channels are evaluated to confirm that the power supply is performing satisfactorily.

VI. CONSTRUCTION FEATURES

Design and construction changes during the development period included the placement of aluminum caps on the transistors of the main regulator and inverter to reduce the effect of radiation damage. Separation of the high and low potential terminal posts gave greater assurance that corona would not occur.

VII. AUXILIARY FEATURES

7.1 *Two-Year Timer*

It was required that two years after spacecraft launching the VHF beacon of the satellite be irrevocably turned off to clear the radio channel; this is to be done by a timer which operates from an independent source of power. The timer consists of a tuning fork mechanically coupled to a gear train and switch to disconnect power to the VHF beacon transmitter. The oscillation of the tuning fork is maintained by means of a 360-cycle transistor oscillator driven by a battery. The power source is a single primary mercury cell with sufficient ampere-hour capacity to supply the current for 18,000 hours.

7.2 *Battery Discharge Gate*

There was need for a means to control remotely the discharge of the Ni-Cd battery by removing the loads after sealing the canister prior to launching. This switch must not prevent the charging of the battery by the solar cell plant. To perform this switching function a silicon diode, used as a gate, was connected in series with the battery. The diode was connected, as shown in Fig. 2, with its polarity in a direction to allow the solar cell plant to charge the battery, with the loss of its forward drop of approximately one volt. When load is to be supplied from the battery, the contacts of the S relay short out the diode. The S relay is operated under control of the command receiver in the satellite or by means of the low-voltage cutoff circuit.[3]

Before launching, the S relay is open and the diode gate prevents discharge of the battery between tests and during shipment. After launching, if it is determined from telemetered data that the battery is excessively discharged due to long periods of transmission, or due to low solar cell output voltage which could occur during extended periods of polar illumination of the satellite, the S relay can be opened to disconnect the load from the battery. The command receiver will operate with power from the solar cell plant, through the main regulator, making it possible to command the S relay to close, shorting the diode gate.

7.3 *Pre-Launch Test and Auxiliary Power Supply*

During the testing period of the satellite on the ground and during the launching period, the solar cells are not illuminated, so that an auxiliary source of power is required. A passive ferroresonant regulating circuit was used to eliminate the effects of input ac line voltage variations and limit the charging current to the maximum safe value for the nickel-cadmium battery.

VIII. PERFORMANCE

The performance of the Telstar power system has agreed very closely with the design objectives. Voltage requirements of all active elements of the satellite have been met, as evidenced both by the results of measurements before launch and by telemetry data after launch. The main regulator has successfully adjusted for a wide range of input voltage, as shown in Fig. 19. This figure presents the battery voltage time history for three different satellite passes within range of the Andover ground station.

The voltage behavior for orbit 414 is typical of an orbit in full sun-

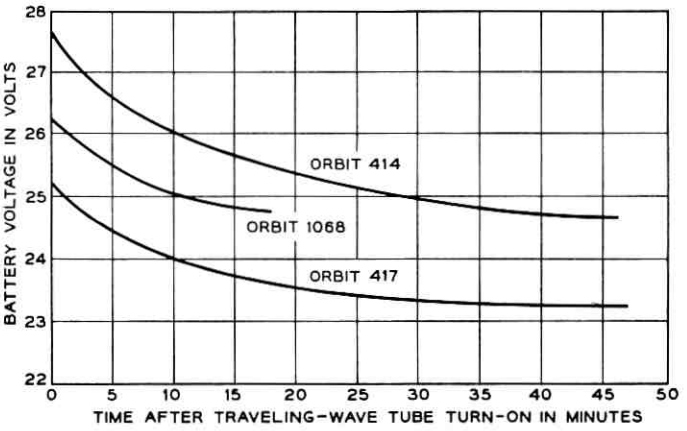

Fig. 19 — Input voltage to main regulator.

light with the battery fully charged at the beginning of the orbit; the communications experiment was in operation for nearly 50 minutes. A similar communications experiment was performed during orbits 415, 416 and 417. The voltage record for orbit 417, shown in Fig. 19, shows a substantially lower initial value as a result of battery discharge; at the end of orbit 417 the battery had been discharged to 60 per cent of its capacity.

The voltage data for orbit 1068 show a low initial voltage despite the fact that the battery was fully charged initially, for the reason that the satellite was in eclipse for the first 10 minutes of the orbit.

The state of charge of the battery has been monitored carefully through detailed histories of charge and discharge currents. These histories take into account actual solar plant current and actual load currents as reflected in telemetry data. Satellite use has been programmed so that at no time has the battery been discharged below 60 per cent of capacity.

IX. ACKNOWLEDGMENTS

Acknowledgment is hereby made of the contributions of many members of the Power Systems Laboratory, too numerous to mention by name.

REFERENCES

1. Bomberger, D. C., and Moose, L. F., Nickel-Cadmium Cells for the Spacecraft Battery, B.S.T.J., this issue, Part 3.

2. Feldman, D., and Thomas, U. B., Current Status of Sealed Nickel-Cadmium Storage Cells, Proc. of 1962 A.I.E.E. Pacific Energy Conversion Conference.
3. Chapman, R. C., Jr., Critchlow, G. F., and Mann, H., Command and Telemetry Systems, B.S.T.J., this issue, p. 1027.
4. Davis, C. G., Hutchison, P. T., Witt, F. J., and Maunsell, H. I., The Spacecraft Communications Repeater, B.S.T.J., this issue, p. 831.
5. Delchamps, T. B., Jonasson, G. C., and Swift, R. A., The Spacecraft Test and Evaluation Program, B.S.T.J., this issue, p. 1007.

The Spacecraft Structure and Thermal Design Considerations

By P. HRYCAK, D. E. KOONTZ, C. MAGGS, J. W. STAFFORD, B. A. UNGER and A. M. WITTENBERG

(Manuscript received March 22, 1963)

This paper covers the general structural and thermal design considerations of the Telstar satellite. The basic objectives were to maintain the electronic components in a near room temperature environment and to protect the electronics package from high-frequency vibration excitation. These objectives were realized by dividing the satellite into two lumped masses, the shell and the centrally located electronics package, and by utilizing nylon lacing for support of the electronics package. The package was provided with an active temperature control, regulating radiative heat flow between the skin and the package. Results of on-the-ground experimental evaluation and of telemetry data are given.

1. INTRODUCTION

The general size and shape constraints for the Telstar satellite have been reviewed in a previous paper.[1] The present paper discusses the important features of the spacecraft structural and thermal design.

The function of the spacecraft structure is to support and isolate the electronic components from the shock and vibration loads due to launch, and to provide a geometry compatible with an isotropic solar cell power plant.[2]

Since a majority of the critical components used in the electronics package were designed to operate in a room temperature environment, a major objective of the thermal design was to provide a package temperature as close to room temperature as possible. This objective was to be maintained during a two-year life in orbit. Therefore, all orbital effects on the satellite temperature had to be considered: full sunlight, maximum eclipse orbit, seasonal variation of the solar constant, satellite orientation, and long-term effects on surface coatings exposed to ultraviolet light and other radiation effects. Another thermal objective

was that the solar cell power plant operate at as low a temperature as practicable, for maximum efficiency in the conversion of solar energy to electrical power.

These apparently contradictory objectives — warm package and cold skin — were met by compacting the electronics components in a central container referred to as the "electronics package," isolating them from conductive heat transfer to the skin, and providing an active temperature control which regulates the radiant heat transfer from the electronics package to the colder skin. The power from the solar plant, which is dissipated in the electronics package, provides the heat to keep the electronics near room temperature.

The over-all design concept of the Telstar spacecraft structure is depicted in Fig. 1. A "ball-within-a-ball" configuration is employed. Those portions of the outer shell not used for supporting the solar cell power plant are coated with plasma-sprayed aluminum oxide, to keep the satellite skin temperature at about 30°F for best efficiency of the solar cell power plant. The inner "ball" contains the electronics circuitry, which is hermetically sealed from the high vacuum of space. The nylon lacing minimizes thermal conduction from the warm package to the colder skin. To minimize temperature effects on the chassis when

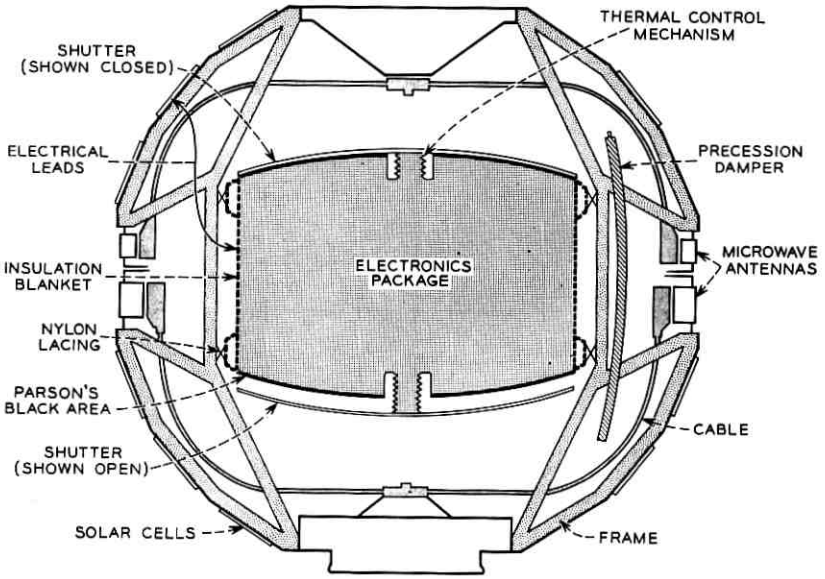

Fig. 1 — Sectional schematic of spacecraft.

the satellite is in either a fully sunlit orbital period or a maximum eclipse period, the radiative heat transfer between the insulated package and the satellite skin is varied by means of thermally actuated shutters. Fig. 2 shows the internal arrangement of the spacecraft parts.

The significant feature of the compact electronics package is that the critical components can be housed in a separate container and through suitable suspension be protected from the high-frequency vibration excitation due to launch. It seemed prudent to protect the electronics from high-frequency vibration excitation, since vibrational failure of electronic devices is most likely to occur in this frequency range. Nylon lacing which supports the electronics package provides both the high-frequency vibration and thermal conductive isolation. This arrangement required that the spacecraft structure support a lumped mass of about 85 pounds subjected to combined vibration and rocket thrust loading. During resonance of the electronics package in its nylon lacing support, the frame must support a combined loading of about 6000 pounds in the thrust direction.

The Telstar satellite is spin stabilized. In a geomagnetic field, its spin rate will be slowed down by induced eddy currents. For this reason, the

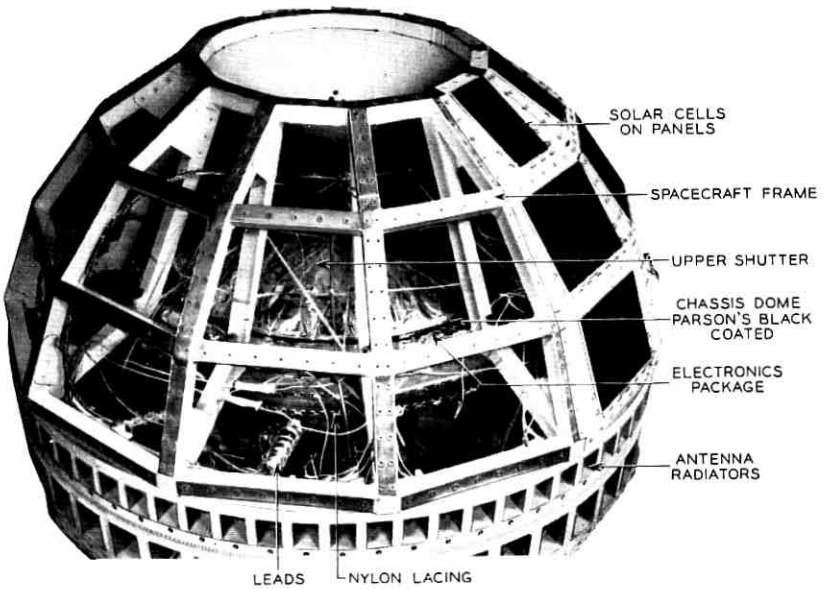

Fig. 2 — Side view of electronics package in spacecraft, showing upper shutter open.

shell is divided into two hemispheres, which are electrically insulated from each other.

Precession dampers are required to keep the satellite spinning about its principal axis of maximum moment of inertia, which is also the symmetry axis of the antenna. Disturbances which could cause a spinning satellite to have short-time precession (wobble) are electromagnetic torques, the uneven forces imparted by the spring during separation from the rocket, and collisions with meteoroids. Precession dampers quickly remove this wobble.[3]

II. SPACECRAFT CONSTRUCTION AND DESIGN

2.1 *Frame Construction and Design*

The frame of the Telstar satellite is the basic load carrying structure. It must support all other components, and it comprises 13 per cent of the total spacecraft weight of about 170 pounds. The frame provides support for the skin, which is roughly spherical in shape and has a nominal diameter of 34.5 inches. The frame is of an all-welded construction, fabricated from $\frac{3}{4}$-inch square ZK-21-A magnesium alloy tubing with a wall thickness of 0.025 inch. The frame is constructed in two parts, as shown in Fig. 3.

The sections of the frame are made of 12 truss assemblies, 30 degrees apart; the assemblies are joined by chordal members at their exterior

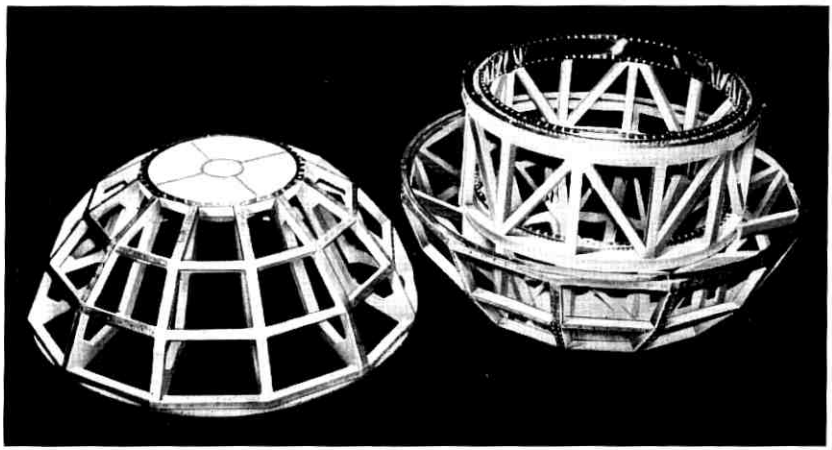

Fig. 3 — Spacecraft frame: upper half at left, lower half at right.

joints. The size of the facets, which is determined by the spacing of the truss assemblies, was selected to provide mounting surfaces of sufficient size for the solar cell modules.[2] One-half of the framework contains additional structural members, which form a cylindrical cage to support the 85-pound electronics package. The end rings of this cage are made from AZ-31-B-H24 magnesium alloy and contain radial holes with eyelet inserts for lacing the electronics package mounting rings to the frame. A machined AZ-31-B-H24 magnesium alloy plate, which is used to attach the spacecraft to the launch vehicle, is welded to this portion of the frame. In addition, several diagonal members are incorporated into this part of the framework to provide torsional and lateral rigidity.

Because of the mass of the electronics package, the combined sustained acceleration loading due to the thrust of the launch vehicle and the vibrational loading due to the first resonance of the electronics package had to be given special consideration in the frame design. The average (mean) stress in the frame members was limited to a value below the minimum guaranteed compressive yield stress of the ZK-21-A magnesium alloy tubing. The mean stress figure included an appropriate weld efficiency factor, which was determined experimentally. Sufficient rigidity was provided in the construction to minimize secondary bending stresses in the frame members. Limiting the average stresses in the frame members to values below the compressive yield stress of the ZK-21-A tubing and minimizing secondary bending stresses precluded any possibility of a frame collapse due to the combined loading. For the spacecraft, the allowable buckling stress for the frame members exceeded the compressive yield stress for the ZK-21-A tubing.

The hemispherical portions of the frame are electrically insulated from each other to limit the eddy current paths of the satellite. The frame halves are connected by insulated steel bolts, the only structural connection between the two portions of the frame. The 6-kilomegacycle antenna is supported by the upper half of the framework, and the 4-kilomegacycle antenna by the lower half of the framework. Except for internal wiring, these two antennas are dc-insulated from each other.[4]

The faceted surfaces formed by the truss and chordal members support the panels which form the skin on which the solar cell modules are mounted. The solar cell modules which compose the solar power plant are attached to these panels by beryllium copper tabs pulled through mounting slots in the panels and twisted to provide intimate contact of the modules to the panels.[2] The solar cell panels are attached to the frame by screws held in place by lockwashers.

2.2 *Solar Cell Panel Construction and Design*

Design objectives for the panels which support the solar cell modules were: (a) minimum weight consistent with structural rigidity requirements, (b) flat exterior panel surface to provide good contact with solar cell modules, and (c) thermal behavior of panels equivalent to that of thin, uniform sheets.

The panels, shown in Figs. 4 and 5, are of an integrally stiffened design. They are of brazed construction, fabricated from 6061-T6 aluminum alloy. Total weight of the panels, excluding modules, is 4 per cent of the satellite weight. The panels essentially consist of a cover sheet with so-called "hat" sections brazed on the inside face (i.e., face interior to the spacecraft) of the cover sheet. The hat sections have large holes which provide for radiant heat transfer by eliminating the effect of the additional reflective surface of the hat section. The brazed construction provides good thermal conduction throughout the panel.

The fundamental frequency of the solar cell panels with modules attached occurs at approximately 200 cps when the panels are screwed to the spacecraft frame. The panel design was a compromise between weight and fundamental frequency. From a structural standpoint, it would have been desirable to design for a resonant frequency above 2000 cps; however, the weight penalty would have been enormous even

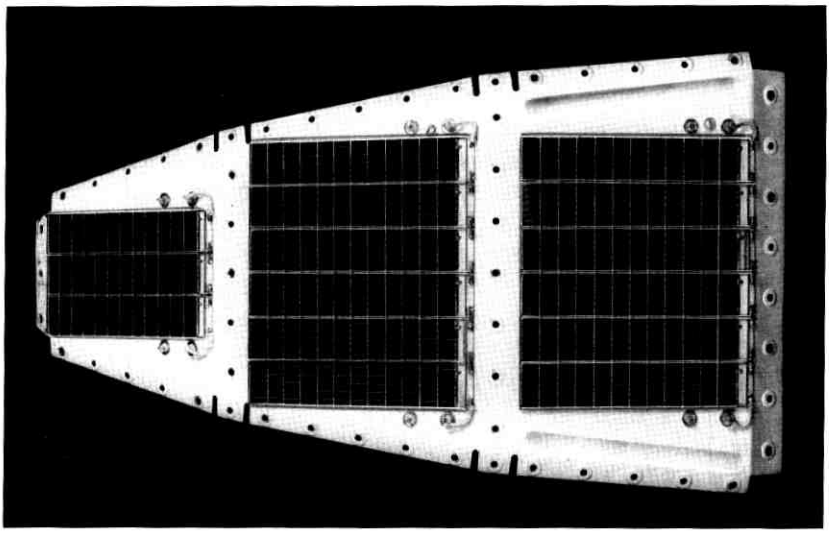

Fig. 4 — Front view of complete solar cell panel.

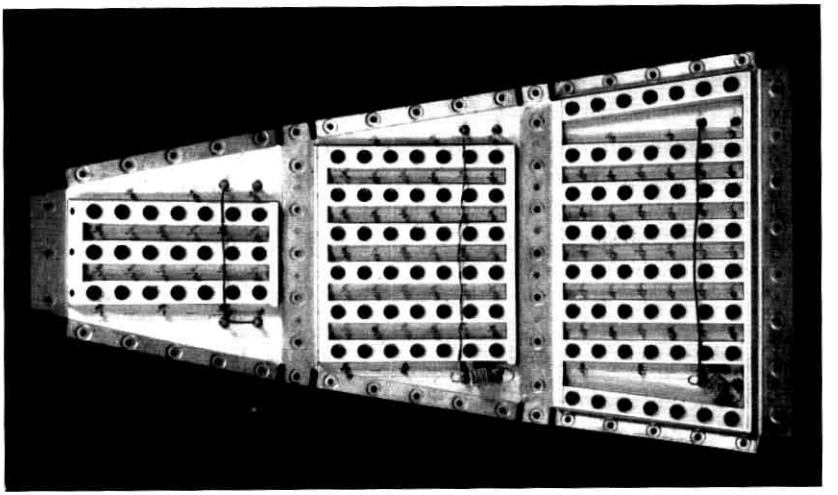

Fig. 5 — Rear view of solar cell panels, showing hat sections.

if such a design could have been achieved. The 200-cps resonance was selected to provide a minimum-weight design which also minimizes deflections of the panel during vibration to avoid damaging the solar cell modules.

Magnesium had been considered for the solar cell supporting panels, with the objective of achieving minimum weight. However, satisfactory brazing techniques were not available for magnesium, and welded construction would have been required. This in turn would have required thicker sections, and the magnesium panel would have weighed about 50 per cent more than the aluminum panel adopted.

2.3 *Insulation Support for the Electronics Package*

As mentioned previously, the electronics package is supported by nylon lacing to isolate the package from the high-frequency vibrations of launch and, for thermal reasons, to minimize conductive heat transfer to the skin. The spacecraft qualification test specification[5] suggests the desirability of placing the fundamental resonance of the electronics package below 50 cps; below this frequency, the g level applied to the base of the satellite is minimum (i.e., 0-to-2.3 g peak).

Braided nylon cord was selected for the electronics package lacing because its spring constant would place the fundamental frequency of the electronics package at approximately 42 cps, and yet would have

sufficient strength to support the package under combined loading due to sustained acceleration plus first resonance of the electronics package. Fig. 6 shows that the first resonance of the electronics package occurs at 40 cps; above 40 cps the package is essentially vibrationally isolated from the frame. A similar situation exists for the lateral direction, where the first resonance occurs at 15 cps. Techniques utilizing small spring balances were developed to control the pretensioning of the lacing; as a result, the fundamental frequency of the package was found to be reproducible within a few cps.

In addition to isolating the electronics package from high-frequency vibration, the lacing also supports the package under combined loading and behaves approximately as though it were a linear spring. In the direction of the thrust axis under combined loading, the nylon lacing must withstand a 4050-pound load. Individual braided nylon cord strands are subjected to a load of 32 pounds, which is well below the knot breaking strength of 60 pounds.

Extensive testing of nylon, Dacron, and fiber glass cords was performed to determine their structural characteristics in order to select the appropriate fiber cord with which to lace the electronics package. Load-deflection curves, ultimate strength (unknotted), knot breaking strength, and creep data were obtained for all fibers. The fiber glass cord was rejected for use because of its poor dynamic strength properties. In addition to other tests, the Dacron and nylon cords were subjected to temperature, humidity, high vacuum, and proton and electron radiation

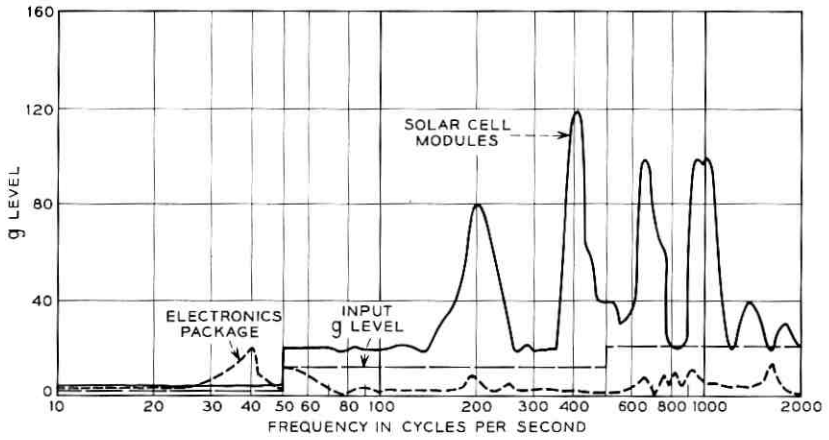

Fig. 6 — Response of electronics package and solar cell modules to sinusoidal vibration excitation in the thrust direction.

tests equivalent to two years in space. Although these tests indicated that there should be no problem with the nylon cord in high vacuum for the desired life of two years, reliability considerations dictated that several pieces of Dacron cord, which is a good deal more space stable than nylon, should also be used to completely insure support of the electronics package.

2.4 *Structural Design Testing*

The objective of the structural design testing program is to ensure that the complete spacecraft will meet the requirements of the qualification level tests.[5] It should be noted that the qualification level testing does not include the combined effects of sustained acceleration loading due to the thrust of the launch vehicle and vibrational loading due to the first resonance of the electronics package. Nevertheless, combined loading effects were simulated on an early test model. To meet these objectives, an extensive mechanical test program was instituted in August, 1961, to ensure that (a) the frame structure was capable of withstanding qualification level tests and combined loading, (b) the electronics package was protected from high level vibration excitation during launch, and (c) the spacecraft structure responses during vibration testing were known. The last item determines the appropriate testing levels which should be assigned to the parts connected directly to the satellite frame. Some of these parts are (a) solar cell modules, (b) precession dampers, (c) antenna feed structure, and (d) radiation experiments.

During this extensive structural evaluation program, two vibration test model spacecraft, a structural frame model and a mechanical development model, were used. In October, 1961, the first full-size test model was subjected to shock, centrifuge, and vibration qualification level tests. This model successfully passed the tests and provided the vibration spectrum that the spacecraft components associated with the shell would have to sustain. It also demonstrated that the nylon lacing performed its function of substantially isolating the electronics package from high-frequency vibration excitation. It should be observed that this frame withstood many hours of vibration testing at qualification level, in contrast to the few minutes encountered during launch.

Fig. 6 shows the vibration response of the electronics package and solar cell modules. The required input level to the spacecraft is shown by the heavy dashed line. The design objective of protecting the electronics components from high frequency levels has been substantially achieved. The 20-g level at one discrete frequency at approximately 40 cps is not

undesirable, because electronic components do not have resonances at such a low value. The solar cell modules are subjected to levels as high as 80 to 120 g at several narrow-frequency bands. Amplification factors of 5:1 to 10:1 result from frame resonances, and are to be expected in a structure which is as large as 3 feet in diameter. During resonance dwell tests, which are conducted at the third-stage rocket resonances of 550 to 650 cps, the solar cell modules reached levels as high as 200 g with a 42-g input to the base of the spacecraft.

Another series of vibration tests was performed, using a second vibration test model as a vehicle for the design testing of components which are attached to the frame. Many tests were conducted on the antenna feed structure and techniques were developed for securing their cables.[4] Tests were also performed to develop the best techniques for securing the many leads and cables connected between the electronics package and frame components. The leads are about 9 inches long, to minimize thermal conduction from the package to the skin.

As mentioned previously, qualification level tests in themselves do not supply absolute proof of the adequacy of the frame and lacing under possible combinations of sustained acceleration and vibration loading due to the first resonance of the electronics package. Static simulation of the possible modes of combined loading were performed on one of the first frames at Lehigh University, Bethlehem, Pennsylvania. The test setup is shown in Fig. 7. All loads were applied to a canister whose outline was similar to that of the electronics package. The canister was specially designed so that the vertical, lateral and torsional loads could be applied to the frame. The method of load application was a conservative approximation to the actual case. The three basic loading conditions, which were applied individually and in suitable combinations, are given in the Table I.

The deflection of the dummy electronics package was measured and strain gauge readings of the various frame members taken. The recorded strains and the stresses calculated therefrom show that the basic spacecraft frame has a margin of safety of 46 per cent for the static loads applied, where due consideration of weld efficiency has been taken into account. The actual margin of safety is somewhat less than 46 per cent, because the static test performed does not completely simulate the fatigue effects of combined vibration and thrust loading. With the present state of the art, this type of test is not possible. Nevertheless, the extensive vibration tests which were conducted on the other models, coupled with the static test, left little room for doubt that the frame is capable of withstanding the actual launch conditions.

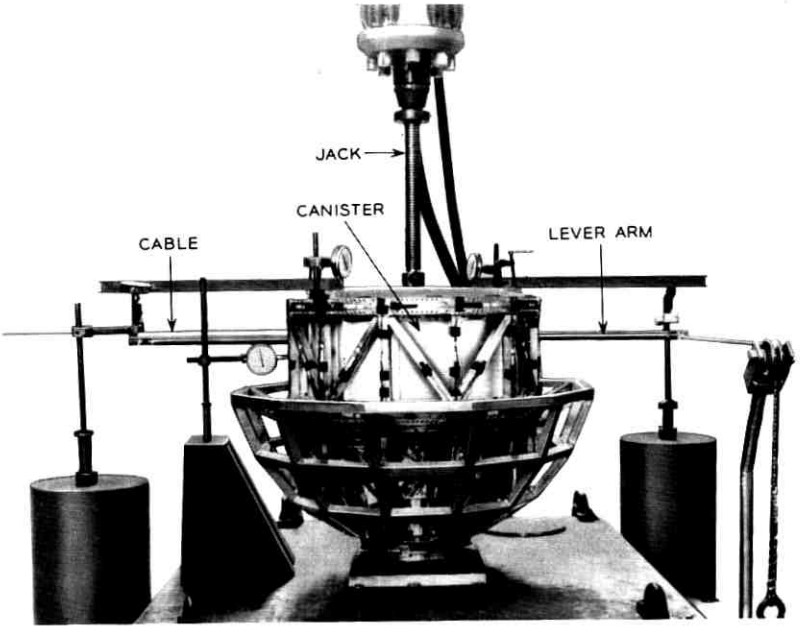

Fig. 7 — Spacecraft static test setup.

TABLE I

Direction of Loading	Due to Sustained Acceleration of 170-lb Satellite	Due to First Resonance of 90-lb Electronics Package	Total Maximum Load
Thrust axis	(25 g) (170 lb) = 4250 lb	(20 g) (90 lb) = 1800 lb	(4250 lb + 1800 lb) = 6050 lb
Transverse (lateral) axis	(2.25 g) (170 lb) = 382 lb	(6 g) (90 lb) = 540 lb	(382 lb + 540 lb) = 922 lb

Direction of Loading	Maximum Torque due to Spin-Up	Residual Torque at End of Spin-Up
Torsional moment about spin axis due to flexibility of electronics package mounting	3000 in-lbs	1500 in-lbs

Note: In the thrust direction, the 25-g sustained acceleration is from the rocket thrust and the 20-g vibration acceleration is the level imparted to the package during its resonance. In the transverse direction, the accelerations were determined on a similar basis.

The apparent weight of the satellite along the thrust axis in the 550 to 650-cps frequency range was determined so as to establish the necessary vibration level to be applied in the simulation of the combustion resonance dwell test.[5] Since the apparent spacecraft weight was of the order of 7 pounds, the combustion test should have been conducted at an 86-g input level over the 550- to 650-cps band. However, vibration equipment was not available to conduct the tests at this high level. Development model spacecraft were tested at a 75-g input level over the required frequency band. As a result of these high-level tests, minor modifications were made to the method of attaching the solar cell modules to the panels and to the interconnections between them. These tests also reconfirmed the adequacy of the spacecraft frame and were useful in proving in many of the components attached to the spacecraft shell structure. Details on qualification tests on the final model are given in Ref. 5.

In December, 1961, a mechanical development model spacecraft, complete except for the electronics package, was subjected to all mechanical tests at qualification level. A dummy weighted canister was used instead of the actual electronics package. This model successfully passed all development tests without failure. In subsequent testing, this model was subjected to the equivalent of four complete qualification-level vibration tests without any failure of any component part.

III. THERMAL DESIGN OF THE SPACECRAFT*

3.1 *Requirements and Design Approach*

The introductory section of this paper outlined the two major thermal design objectives for the Telstar satellite: to provide an environment for the electronics components as close to 70°F as possible, and to maintain the solar cell power plant at as low a temperature as practical. This section of the paper covers the spacecraft thermal design in greater detail.

The temperature of the electronics package shell is used as a reference point to describe the environment for the electronic components. This reference point, of course, is not at the actual temperature of the components themselves. In the design of the electronics package, high-conduction paths were provided to minimize temperature differentials between the components and the package wall. Detailed studies of operating tem-

* Two comprehensive reports on the Telstar satellite thermal design and analysis, including the results of space simulation tests, were submitted to NASA in March and May, 1962. Substantially all of the thermal information reported upon in this paper was included in the foregoing reports.

peratures of internal components provided temperature limits of 15°F to 90°F on the package wall to assure satisfactory operation of the electronics circuitry.[1] Nevertheless, a 70°F objective for the package wall temperature was established, since practically all component life test data were obtained at room temperature.

A knowledge of the temperature distribution over the surface of the satellite was required to determine the power available from the solar cell plant and to establish temperature extremes to which the components attached to the skin would be subjected. These temperature ranges had to be determined in relation to the extremes of the satellite thermal environment.

The thermal and long-life requirements made a good portion of the practical experience gained with other artificial satellites not directly applicable to the Telstar satellite,[6] and new concepts in the over-all thermal design had to be explored. In particular, thermal analysis disclosed that an active temperature control system was required to minimize temperature variations in the electronics package during a long lifetime in orbit. The control system chosen was unique in that it regulated only the radiative coupling between the package and the skin, while the temperature of the skin itself was to be controlled by passive means. In the early development stages, very little was known of this type of temperature control. Instead, detailed information on an active skin-temperature control, as originally proposed by Hanel[7] or by Acker,[8] was available.

3.2 *Thermal Radiation Environment of the Telstar Satellite*

There are two kinds of thermal radiation which affect Telstar's thermal design: the primary radiation coming directly from the sun and the secondary radiation. Secondary radiation intercepted by the satellite consists of albedo radiation and the earth's infrared radiation. Albedo is solar radiation reflected by the earth. Since energy can be gained or lost in the space environment only by radiation, the extremes of the total radiative heat input had to be determined as the starting point of the entire thermal design.

Direct solar radiation is the major contributor of incident energy, amounting to about 84 per cent of the energy received by the satellite when it is in a fully sunlit orbit. However, this energy may be reduced significantly when the satellite is in an eclipsed orbit. During a maximum 45-minute eclipse in the satellite orbit, the orbital average primary energy will be reduced to 70 per cent of its full sunlit value. In addition,

the direct solar radiation, which may be expressed in terms of the solar constant S, varies ± 3.3 per cent in the course of one year.

The significance of the reflected radiation would, in general, depend on the orientation of the satellite; only in the case of a spherical satellite with an isotropic surface are the effects of the orientation eliminated. Geometrically, the spacecraft was considered to be a sufficiently close approximation to a sphere with an isotropic surface. In addition, the reflected radiation would depend on the altitude of the satellite and its phase angle, defined as the angle between the line joining the sun and the center of the earth and that between the satellite and the earth's center. For a general elliptical orbit, both the altitude and the phase angle will vary with time. The situation is somewhat simpler with regard to the infrared radiation of the earth, which is to a first approximation dependent on the altitude only. The further details of the secondary radiation problem in its relation to spherical satellites have been outlined in a special study.[9]

3.3 *Thermal Model of Telstar Spacecraft and Its Environment*

In the following, as a thermal model, the satellite will be considered to consist of two lumped masses: M_S, with thermal capacitance C_S, corresponding to the skin; and M_P, with thermal capacitance C_P, corresponding to the electronics package of the satellite. Since the package is thermally insulated from the skin by means of a high conductive resistance, all heat transfer between M_S and M_P will have to take place by radiation. Then the package will be, in the steady state, essentially in radiative equilibrium with the skin. In particular, if the time constant of the package is long with respect to the orbital period, a sufficiently close approximation to the steady-state heat transfer will be realized at all times. In other words, the package will then be only very little thermally disturbed by short-term temperature fluctuations of the skin caused by an individual eclipse of the satellite, but will have to adapt itself to long-term orbital changes, i.e., drastic variations of the eclipse periods and seasonal variation in the solar constant.

The long time constant of the package is realized by its high heat capacity and by the application of a low-emissivity material over its surface. The use of the linear concept of a time constant with respect to the relations involving the fourth-power law of radiation is only a convenient approximation.

For a sufficiently uniform temperature prevailing within the package, the temperature extremes of the package will be based on the extremes of the heat radiation intercepted by the skin. This dependence may be

expressed in terms of a reference skin temperature, as discussed in Section 3.4. An expression for such a reference skin temperature, $\bar{T}_s$, is given by

$$\bar{T}_S = \left(\frac{S}{4\sigma}\right)^{\frac{1}{4}} \left[\frac{\bar{\alpha}}{\bar{\epsilon}} \left(1 - \frac{t_e}{t_o} + \bar{a}\bar{f}\right) + \tfrac{1}{4}\,(1 - \bar{a})\bar{g}\right]^{\frac{1}{4}} \tag{1}$$

where S is the solar constant, σ the Stefan-Boltzmann constant, $\bar{\alpha}$ the over-all value of solar absorptivity of the skin of the satellite, $\bar{\epsilon}$ the over-all value of the infrared emissivity of the satellite, t_e the eclipse time, t_o the orbital period, $\bar{a}$ the mean value of the earth's albedo, $\bar{f}$ the mean integral value of the albedo, and $\bar{g}$ the mean integral value of the earth's infrared radiation. Equation (1) is derived from the consideration that the orbital mean average temperature of the skin of the satellite, $\bar{T}_S$, can be determined from a balance between the total heat energy absorbed over one orbit and the energy emitted by the satellite during the same orbit, according to the Stefan-Boltzmann law. This equation applies for an isotropic sphere and represents the effective radiation temperature of the skin; for the important special case of two lumped masses, M_S and M_P, it may be used to obtain a convenient reference temperature for the instrument package, as will be shown below.

For an elliptical orbit, the speed of the satellite varies according to Kepler's law, which states that equal areas are swept out in equal times by the radius vector. Therefore, in getting the values of $\bar{f}$ and $\bar{g}$, time must be taken as the weighting factor. The integration itself is best carried out numerically.

To get the upper limit for $\bar{T}_S$, one has to consider that, in general, the contribution due to the eclipse time t_e is relatively more important than that due to $\bar{f}$ and $\bar{g}$. Therefore, it is sufficiently accurate to calculate $\bar{f}$ and $\bar{g}$ for the case where $t_e = 0$ is combined with the largest possible albedo effect. This is the case when the satellite just grazes the earth's shadow at apogee.

Similarly, one can set the lower limit on $\bar{T}_S$ by considering in (1) the longest eclipse time t_e compatible with the given orbital configuration. These two temperature extremes $\bar{T}_{\max,S}$ and $\bar{T}_{\min,S}$ can, for a given orbit and $\bar{\alpha}/\bar{\epsilon}$, be conveniently expressed in terms of an equivalent solar constant S_{eq}

$$\bar{T}_S = \left(\frac{S_{\text{eq}}}{4\sigma}\,\frac{\bar{\alpha}}{\bar{\epsilon}}\right)^{\frac{1}{4}}. \tag{2}$$

For an orbit of 500 nm perigee and 3000 nm apogee, $\bar{T}_{\max,S}$ corresponds to $S_{\text{eq}} = 1.19\ S$, and $\bar{T}_{\min,S}$ to $S_{\text{eq}} = 0.917\ S$. A value of $\bar{\alpha}/\bar{\epsilon}$ of 0.65

was obtained from calculations based upon the individual surface properties of the skin exterior and was subsequently confirmed by space chamber measurements on several spacecraft models, as will be described later.

For a given S_{eq} and $\bar{\alpha}/\bar{\epsilon}$, the temperature $\bar{T}_S$ can be easily calculated from (2). If this temperature is reached (for example, in the space chamber), it means that the satellite has been exposed to the equivalent "full sunlight" or "maximum eclipse" corresponding to the maximum and the minimum values of S_{eq}, respectively. Thus experimental determination of temperature extremes of all internal components becomes a possibility.

3.4 *Thermal Design Considerations for Electronics Package*

The information on S_{eq} and the extremes of $\bar{T}_S$ may be used in the design of the electronics package in the following way: in the steady state, and in the absence of heat conduction to the skin, the package will assume the temperature $\bar{T}_P$ defined by the equation

$$Q_P = A_p h\sigma[\bar{T}_P^4 - \bar{T}_S^4] \tag{3}$$

where Q_P is the heat power developed in the package due to the operation of its electronic components and battery charging and h is the overall effective emissivity of the package-skin system. A_p is the surface area of the package.

For a package with a high internal thermal conductivity as a feature of its design, $\bar{T}_P$ will not differ significantly from the operating temperatures of its internal components. The extremes on $\bar{T}_P$ will be obtained from (3). The extreme values of Q_P depend, for a given design of the solar-cell power plant, upon the orientation of the spin axis of the satellite with respect to the sun (a major factor in the output of the solar cells) and upon radiation damage to the solar power plant in space.

The solar plant output has been calculated to be $Q_{P,\min} = 7$ watts if the spin axis stays parallel to sun rays for an extended period of time, and $Q_{P,\max} = 14$ watts for the initial power with the spin axis perpendicular to the sun's rays.[2] The minimum power figure took into account a 30 per cent deterioration factor due to the space environment during a two-year period, and also included the effects of shading during the eclipse time. The minimum power figure also considered the elevated temperatures of the active areas of the solar cell plant that result from the parallel orientation of the spin axis with respect to the sun's rays. The higher power figure reflects the fact that, for a spin-stabilized

satellite with the proper orientation of the spin axis, spinning is effective in reducing the solar cell temperatures, with improved conversion efficiency. For thermal tests, a conservative value of 16 watts was used for the maximum power, a value based upon very early estimates of the maximum possible power from the plant.

For a given h, the extremes of the calculated values of Q_P and $\bar{T}_S$ will determine the extremes of $\bar{T}_P$ from (3). The calculated extremes of $\bar{T}_P$ must then fall into the range of temperatures compatible with efficient and reliable operation of all temperature-sensitive package components. The design objectives of maintaining a temperature range of 15°F–90°F on the periphery of the electronics package were the result of an assessment of the reasonable minimum and maximum operating temperatures of the vital components of the package.[1] Initial calculations indicated that these temperature requirements for $\bar{T}_P$ could not be maintained for a fixed h because of the rather drastic changes in S_{eq} and Q_P discussed above. In addition, with respect to $\bar{T}_P$ certain safety margins had to be taken into consideration to account for changes in surface properties of the skin due to the space environment, and to include unavoidable differences between individual satellite models due to processing and assembly. One way of doing this would have been to include the expected variation of $\bar{\alpha}/\bar{\epsilon}$ in the calculation of S_{eq}, with the alternative of simply adding reasonable safety margins to the skin temperature directly.

It was determined that $\bar{\alpha}/\bar{\epsilon} \pm \Delta(\bar{\alpha}/\bar{\epsilon}) = 0.65 \pm 0.1$ was a realistic figure, based on possible variation of the properties of the skin, both initially and after the satellite was subjected for a long time to the space environment. Using the figure of 0.65 for $\bar{\alpha}/\bar{\epsilon}$, $\bar{T}_S$ for a fully sunlit condition is 12°F, and for the maximum eclipse time of 45 minutes, $\bar{T}_S$ is −18°F. In practice, the effect of this variation in $\bar{\alpha}/\bar{\epsilon}$ could be reflected in its influence on package temperatures by applying a safety margin of ±18°F directly to the skin. The ±18°F safety margin is also the figure recommended by NASA from their experience. As will be pointed out later, the calculated values plus 18°F margins were used for space chamber simulation.

3.5 *Active Temperature Control System*

In the foregoing discussion it was pointed out that the effective emissivity parameter h in (2) would have to be made variable in a suitable way to maintain a range of 15°F–90°F for the electronics package shell. The variable emissivity would also assist in maintaining the shell close to the room temperature objective previously mentioned.

This was accomplished by providing thermostatically controlled "black areas" on surfaces that had to be otherwise insulated to keep the general temperature level of the package higher than the skin reference temperature. The black areas on the surface of the package were obtained by coating with Parson's black lacquer.* Because of the relatively large surface area of the package and the small amount of power available for heating it internally, the whole package exterior was insulated with up to 30 layers of aluminized Mylar, with fiber glass separators.

The amount of exposed black area was controlled by two independently operated, umbrella-type shutters (Fig. 1) that could close very tightly for situations where maximum eclipse and low power input would require a relatively low value of the effective emissivity h. The control element was a bellows filled with n-pentane, designed to be completely open at 75°F and fully closed at 55°F. Because the bellows had to operate in the vacuum environment, a spring arrangement was used to keep the operating fluid at nearly constant pressure. Experimentally, it was verified that the required h range of $0.05 \leqq h \leqq 0.1$ had been achieved. It must be stated here, however, that the active thermal system designed for the Telstar satellite had to respond primarily to the long-term changes in orbital parameters for purposes of temperature stabilization. For short-term temperature changes (such as those due to a single eclipse), the particular radiative coupling chosen, together with the long time constant of the package with the shutters nearly closed, provided for a temperature response of the package of less than 3°F, as telemetered from the satellite in orbit. It was found experimentally that, should one of the shutters fail, the temperature of the package wall would only slightly exceed the 15°F–90°F range.

3.6 *Thermal Design of Satellite Skin*

The energy conversion efficiency of solar cells is temperature dependent; the operating efficiency increases as the temperature is reduced. A design objective of approximately 30°F was determined to be a practical average temperature for solar cell operation. This value was based on a compromise between the power required from the solar cell plant, the area on the skin used as cooling areas, and the influence of shell temperature on the package temperature (3). Therefore, the overall temperature level of the skin has to be low. Since the $\bar{\alpha}/\bar{\epsilon}$ of the

* Parson's black lacquer, distributed by Eppley Laboratories, Newport, R. I.

sapphire-covered solar cell module was about 1.5, additional cooling areas of low absorptivity and high emissivity were dispersed between banks of solar cells.* For the cooling areas, surfaces covered with plasma-jet deposited aluminum oxide with $\alpha/\epsilon = 0.26$ were used. This arrangement resulted in the characteristic checkered appearance of the spacecraft shell, which has an over-all value of $\bar{\alpha}/\bar{\epsilon} = 0.65$ for the entire skin.

In addition to having low absorptivity, the external surface finish must be adherent and stable in space to assure that the cooling effect will be maintained. The surface properties of the 5-mil layer of rough aluminum oxide should be insensitive to change because of abrasion by micrometeoroids in space. The stability of plasma-sprayed aluminum oxide coatings was evaluated in the laboratory, prior to their final selection, by examining their absorptivity and emissivity and by measuring changes in these values with exposure to high vacuum, ultraviolet radiation and electron bombardment. Because the material is a fused inorganic compound, it exhibits high-vacuum stability. Also, its optical properties are more stable than the optical properties of other materials which might have been used for this purpose. The absorptivity of the aluminum oxide surface increased from 0.21 to 0.24 when exposed to ultraviolet radiation equivalent to 8 months in orbit. Thereafter, the absorptivity did not change with further irradiation equivalent to 18 months in orbit. Other tests showed that absorptivity increases from 0.21 to 0.25 after radiation with 100-Kev electrons equivalent to three months in orbit. Additional electron radiation did not cause further change in the absorptivity. The emissivity of the aluminum oxide coating does not change with any of the environmental stresses described above. Therefore, the skin temperature of the satellite should increase slowly with its time in orbit; this will be discussed later in more detail.

A separate investigation[10] was conducted to establish the minimum spin rates for which satellite surface temperatures are radially uniform, so that local surface temperatures are symmetrical with respect to the spin axis. This investigation showed that a spin rate of 3 to 4 rpm is adequate to achieve a radially symmetric temperature distribution. Spinning the satellite, with proper alignment of the spin axis with respect to the sun, reduces the temperatures of the areas in sunlight below those of comparable areas on a nonspinning satellite.

In the above temperature calculations, thin-shell techniques for temperature distribution in the skin have been used. This was again

* The solar cells were covered with sapphire windows to protect them against space hazards. The module was designed to minimize the greenhouse effect due to the presence of the sapphire windows, and to conduct heat efficiently to the skin structure of the satellite.

mainly possible because of the effective separation of the satellite into two lumped masses, that of the skin and that of the package, and through careful elimination of conduction between them. In order to reduce the temperature of areas directly exposed to the solar light, a provision was made for internal radiative heat exchange between hot and cold portions of the skin. Internal radiation has also been found to be very effective in reducing the undesirable temperature differences between the aluminum oxide covered areas of the skin and the areas occupied by the solar cell modules.

The internal surface of the satellite shell and the frame were coated with a white polyurethane paint. Since the finish for the inside of the satellite is not subject to ultraviolet radiation and is less susceptible to electron damage than the external finish, the principal factors to be considered in its selection are high emissivity, vacuum stability and ease of application. The organic finish was chosen in preference to aluminum oxide primarily because it could be applied without the danger of thermally stressing the panels and the satellite frame. The white polyurethane finish has an emissivity of 0.85 and does not change with exposure to vacuum at the temperatures of the satellite shell in orbit.

Methods for calculating local surface temperatures for several orientations of a spinning satellite have been derived.[11] In the design stage of the spacecraft, surface temperature distribution was calculated using the above techniques, which take into account the local variation of the $\bar{\alpha}/\bar{\epsilon}$ due to inhomogeneous composition of the individual satellite facet surfaces, internal radiation and orientation of the spin axis with respect to the sun rays.

If can be shown that the appropriate formulas are, for the jth facet, whose normal makes the angle θ_j with the sun rays

$$T_j = \bar{T}_j \frac{\sqrt{2}}{(1 + \beta_j')^{\frac{1}{4}}} (\cos \theta_j + \beta_j/4)^{\frac{1}{4}} \tag{4}$$

for the case of spin axis being parallel to sun rays, and

$$T_j = \bar{T}_j \frac{\sqrt{2}}{\pi^{\frac{1}{4}}(1 + \beta)^{\frac{1}{4}}} \left[\cos (90° - \theta_j) + \frac{\pi}{4} \beta_j\right]^{\frac{1}{4}} \tag{5}$$

for spin axis perpendicular to sun rays.

For the intermediate orientations, similar formulas have been developed. In (4) and (5), T_j refers to T as a function of the local values of α_j and ϵ_j. The term β stands for the contribution due to the internal radiation (which depends on the internal emissivity, ϵ_i) and is defined as $\beta_j = \epsilon_i/\bar{\epsilon}_j$. Since for the case of the spin axis being aligned with the

sun rays (4) the effect of the instrument package is to reduce the internal heat transfer the "effective value" of β, β', is used instead of the full value of β. As a first approximation, β' is proportional to the amount of free area at the equator of the satellite and to β. The results of temperature calculations using (4) and (5) are shown in Table II; the temperatures for 30° and 60° orientations calculated by other equations are also included. For comparison, some telemetered data from orbits 9 and 17 are shown.

The temperatures listed in Table II were intended to be limiting values, so that the power output calculated from the solar cell plant would not be over-optimistic. For the indicated temperatures, a safety margin of 18°F was included to take care of changes in coating characteristics in space, solar cell module thermal impedance and variations in the secondary radiation from the earth. The calculated temperature extremes for the solar cell modules when the satellite spin axis is parallel to the sun are 150°F for the pole nearest the sun and −150°F for the pole away from the sun after a 45-minute eclipse. These limits were used for the design of the solar cell modules and antenna feed components.[2,4]

In the temperature calculations, the secondary radiation effects were included as average values regardless of satellite altitude and spin axis orientation in relation to the earth, whereas telemetered temperatures include secondary radiation effects for the particular altitude and orien-

TABLE II—LOCAL TEMPERATURE DISTRIBUTION OF SOLAR CELL BANDS* (°F)

Band	Calculated				Telemetry Data from Space	
					Orbit 9	Orbit 17
	Angle Between Spin Axis and Sun Rays					
	0°	30°	60°	90°	90°	90°
1	156	120	59	27	26	19
2	145	111	77	46	38	32
3	55	46	46	34	36	35
4	†	−94	−29	34	43	45
5			−41	46	30	32
6			−92	27	26	29

* A band is a faceted zone of the skin contained between two planes which are perpendicular to the spin axis of the satellite. The bands are numbered in the table starting at one pole. Bands 1 and 6 are at the poles; bands 3 and 4 are adjacent to the communications antennas.

† Temperatures for bands that do not see the sun directly have not been included in the table.

tation of the satellite at the time the data were taken. In view of these factors, results compare very favorably with predictions.

IV. SATELLITE TESTS IN THE SPACE SIMULATOR

Experimental evaluation of the thermal design of the spacecraft was conducted in a space simulation chamber, with solar radiation provided by carbon arc lamps. The thermal test program had a twofold objective. The first objective was determination of the over-all ratio of solar absorptivity to infrared emissivity of the complete satellite, to verify calculations based upon individual measurements of the satelite's exterior surfaces. Such tests were performed on several satellites with various orientations of the spin axis to the light beam from the solar simulator. With the $\bar{\alpha}/\bar{\epsilon}$ ratio known, the thermal environment for the electronics package can be determined from (2) and (3). The other objective was to simulate extreme orbital conditions, such as full sunlight and maximum eclipse periods, so that the anticipated thermal performance in space could be verified by on-the-ground tests.

4.1 *Determination of $\bar{\alpha}/\bar{\epsilon}$ from Simulator Tests*

The appendix describes the space simulation facility and presents the method used to calibrate the chamber. The black- and Al_2O_3-coated satellite experiments determined the average values of solar flux and infrared flux for the case when a real spacecraft was tested in the chamber.

Using these values, four satellite shells were tested in the space chamber under various conditions of illumination to determine the average value of $\bar{\alpha}/\bar{\epsilon}$. These tests were conducted with illumination normal to the spin axis; see Table III. The average $\bar{\alpha}/\bar{\epsilon}$ of the four satellites for illumination normal to the spin axis is 0.702. An experiment was also conducted to determine the variation in $\bar{T}_s$ for spin-axis orientations to the arc lamps of 0°, 30°, 60° and 90°, and showed that $\bar{T}_s$ varied by less than 1.5 per cent for these four orientations.

TABLE III

Satellite Shell	Average $\bar{\alpha}/\bar{\epsilon}$
Mechanical model	0.700
Prototype	0.699
Flyable model no. 1	0.695
Flyable model no. 2	0.716

The $\bar{\alpha}/\bar{\epsilon}$ ratio determined in the space chamber experiments is well within the design tolerance for $\bar{\alpha}/\bar{\epsilon}$ of 0.65 $\pm$ 0.1. Using this median value for $\bar{\alpha}/\bar{\epsilon}$ of 0.65 with the S_{eq} from Section 3.3 ranging from 0.917 to 1.19, the temperature extremes that the satellite skin will experience in its intended orbit will be $\bar{T}_{s,\text{low}} = -18°\text{F}$ and $\bar{T}_{s,\text{high}} = 12°\text{F}$. With an 18°F safety margin, limiting mean skin temperatures are $\bar{T}_{s,\text{low}} = -36°\text{F}$ and $\bar{T}_{s,\text{high}} = 30°\text{F}$. These limiting temperatures were simulated in the chamber with an arc lamp schedule of 2.93 lamps and 1.57 lamps respectively. The lamp schedule refers to the average number of lamps in operation during a test, where a fractional lamp represents the ratio of its "on" time to total test time. Fig. 8 is a plot of mean spacecraft shell temperatures as a function of the arc lamp schedule for four shells tested in the space chamber.

4.2 *Space Simulation Tests*

During development, many thermal tests were performed on two thermal models and on the mechanical development model. These models were essentially complete, except that a dummy electronics package with heat dissipation means was used in lieu of actual components in the package. Except for thermal conductivity effects internal

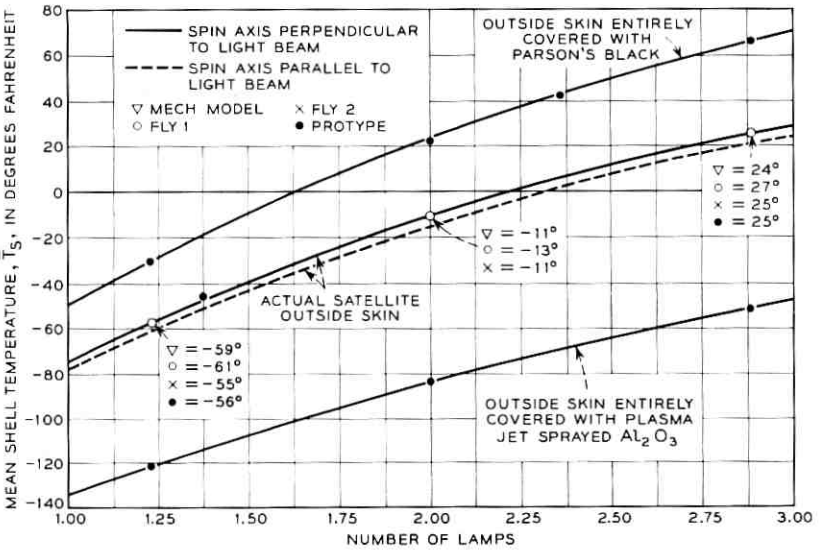

Fig. 8 — Mean shell temperature test results.

to the electronics package, these thermal models duplicated in every respect the thermal behavior of the complete spacecraft in the chamber. These tests were performed to determine the $\bar{T}_s$ of several spacecraft shells, to develop the required degree of emissivity control for the electronics package, to develop support techniques to minimize thermal conduction along the leads from the package to the skin, and to evaluate the operation of the thermal control mechanisms.

In addition, thermal tests were performed on the mechanical development model to evaluate the electronics package temperatures under extreme conditions. The tests listed below were of particular interest in comparing on-the-ground predictions with space performance. The test conditions were:

(a) initial conditions in orbit — maximum power in electronics package (16 watts), full sunlight, +18°F margin on satellite skin, spin axis perpendicular to solar simulator beam, and

(b) end-of-life conditions (two years) — minimum power in electronics package (7 watts), maximum eclipse, −18°F margin on satellite skin, spin axis perpendicular to solar simulator beam.

These test conditions were more stringent than those predicted for the spacecraft in orbit, for the following reasons:

(a) With the initial highest power from the solar plant dissipated in the electronics package, the satellite skin temperature included the +18°F safety margin for a full sunlit orbit. Part of this safety margin was for space deterioration effects on the surface coatings, which tend to warm the skin. Based upon measurements of the surface coating deterioration, this condition would not occur until after several months in orbit, at which time the power from the solar plant would be lower.

(b) With the minimum power at the end of two years in space dissipated in the electronics package, the satellite skin temperature was operated with a −18°F safety margin for a fully eclipsed orbit. After two years in orbit, the skin temperature would have been higher than its initial value because of deterioration of the surface coatings.

Nevertheless, these tests were conducted in this manner to be sure that the 15°F to 90°F limits could be met under extreme theoretical conditions. The results of these two extreme tests are given in Table IV along with the anticipated temperatures.

It is interesting to compare the actual package wall temperatures encountered in space with those predicted by the foregoing tests. Fig. 9 is a graph of the package wall temperatures versus time for the satellite's first seven months in orbit. Also included are the eclipse times, which significantly affect package temperatures as well as the power dissipated

TABLE IV

(a) Initial Conditions (Full Sunlight — 16 Watts Maximum Power)

Measured Package Wall Temperature with +18°F Margin on Skin	Anticipated Package Wall Temperature in Space
87°F	73°F*

(b) End of Life (Maximum Eclipse — 7 Watts Minimum Power)

Measured Package Wall Temperature with −18° F Margin on Skin	Anticipated Package Wall Temperature in Space
34°F	55°F

* The 18°F margin on the mean skin temperature in (a) is reflected as a 14°F difference in the package wall temperature. In (b), the 21°F temperature difference is a result of the 14°F margin plus a 7°F addition to account for increased absorptivity due to deterioration of surface coatings.

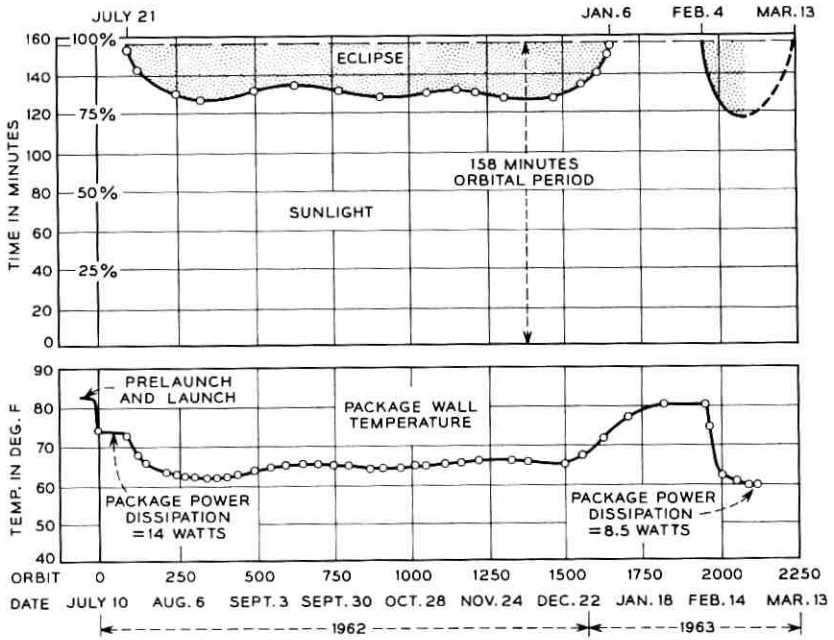

Fig. 9 — Package wall temperature as related to eclipse time.

in the package. The initial temperature in a fully sunlit orbit was 74°F, in comparison to the anticipated 73°F which, of course, had an uncertainty margin of several degrees. At the end of seven and one-half months, the satellite was in the maximum eclipse period of 45 minutes, and the package wall temperature was 60°F with 8.5 watts average orbital power dissipated in the package. At this time the spin axis was nearly normal to the sun. Hence the 60°F temperature encountered in space with 8.5 watts dissipated in the package can be compared to the on-the-ground test figure of 55°F with 7 watts dissipated in the package. The 1.5 watt higher power in space easily accounts for the 5°F higher temperature on the package. It must be emphasized again that these package wall temperatures provide the environment for the electronic components and are not the actual temperatures of the components themselves, which run slightly warmer.[1]

A few over-all observations should be made regarding the package wall temperature in space, shown in Fig. 9. Just prior to launch, the package temperature was 83°F; within nine orbits it dropped to 74°F, where it remained stable for two weeks while the satellite was in a fully sunlit orbit. It will be noted that the variation in package temperature followed very closely the percentage of time that the satellite was in the sun. In January, 1963, the satellite was again in a fully sunlit orbit and the package temperature was about 6°F warmer than in July, 1962. This 6°F change in electronics package temperature can be accounted for by the cumulative effects of the three factors outlined below; figures in parentheses are estimated effects of change on package temperature:

(a) In January the solar constant is 7 per cent higher than it is in July (+6°F),

(b) The absorptivity of the aluminum oxide coating on the satellite skin is presumed to have increased because of ultraviolet and particle radiation effects (+5°F), and

(c) The power dissipated in the electronics package was decreased from 14 watts in July to 11 watts in January (−5°F).

Had the satellite's spin axis precessed from being reasonably perpendicular to the sun rays, there would have been a minimum electronics package wall temperature. Based upon solar simulator tests, the lowest package temperature would be reached with the spin axis parallel to the sun at the end of a two-year life in orbit. In the simulated test, the measured package wall temperature was 14°F with the −18°F safety margin on the skin and the 7 watts expected minimum power in the package. For the reasons outlined previously, the estimated 14°F seems to be unrealistically low: the expected temperature would be 21°F higher, or 35°F.

During the seven months the satellite has been in orbit, the spin axis has remained within 10° of being normal to the sun rays.[12] Hence, no space confirmation of this minimum figure has been possible.

V. CONCLUSIONS

The important features of the Telstar spacecraft structural and thermal design have been presented. In addition, the details of the comprehensive development and environmental test programs have been reviewed.

All mechanical and thermal objectives were achieved, as confirmed by several spacecraft having passed the rigorous environmental tests and the satellite's seven-month performance in space at the time of writing.

The over-all structure and method of support for the electronics package have isolated the vital electronics components from the rigors of launch. Other components, associated with the shell structure, have been designed and proven to withstand qualification level testing.

The active temperature control system has provided a near room temperature environment for the electronic components. Telemetered data from the Telstar satellite have shown that the electronics package wall temperature (component environment) has been maintained between 60°F and 80°F during seven months in orbit. Conditions during this period included fully sunlit orbits, maximum 45-minute eclipse orbits, variation of 7 per cent in the solar constant, and a variable package power of 14 watts to 8.5 watts. When the satellite's spin axis has been normal to the sun, the solar cell temperatures have been maintained close to the 30°F objective.

VI. ACKNOWLEDGMENTS

The writers are indebted to L. Rongved and J. W. West, whose advice, valuable ideas, and over-all guidance contributed so much to the success of the spacecraft structural and thermal design.

APPENDIX

Description and Calibration of Space Simulator

A.1 *Description*

The space simulation facility shown in Figs. 10 and 11 consists of a vacuum chamber with an operating pressure in the low 10^{-6} torr range;

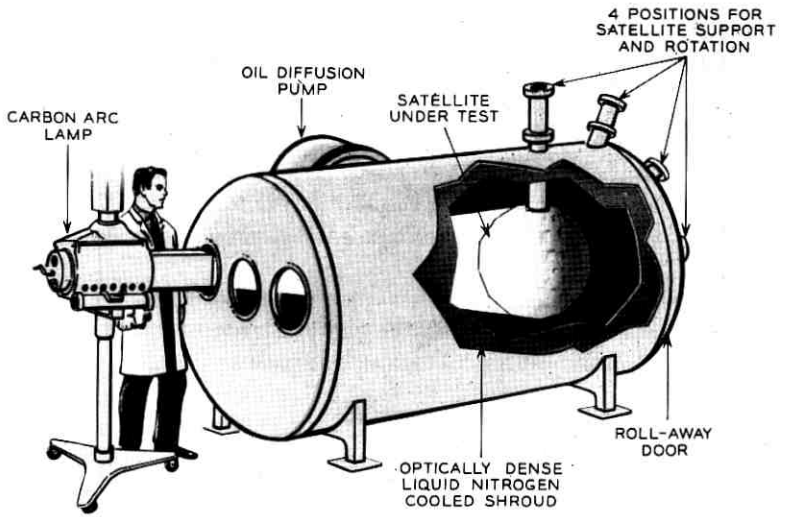

Fig. 10 — Space simulation test facility.

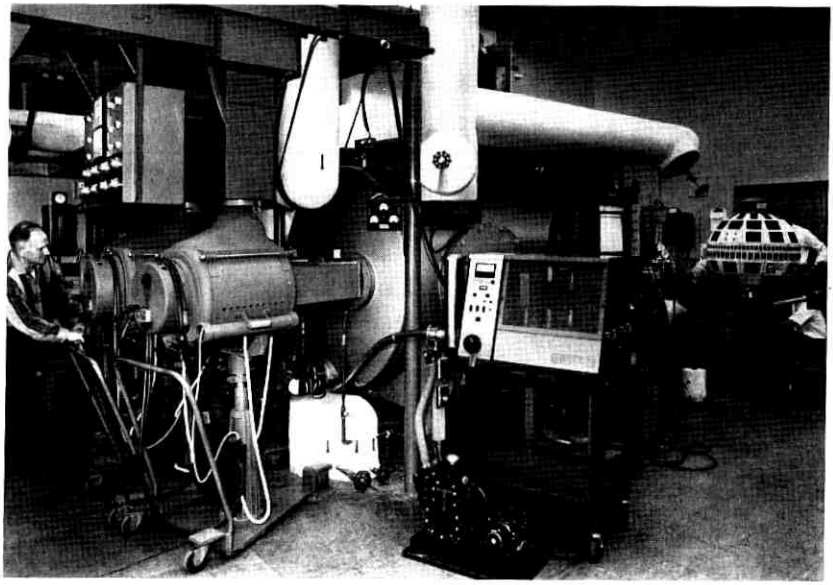

Fig. 11 — Space simulation test facility, showing three carbon arc lamps in place and spacecraft being prepared for test.

a high-absorptivity, liquid nitrogen cooled shroud surrounding the work space; and carbon arc lamps to provide simulated solar energy. The useful working volume in the interior of the chamber is approximately 4.5 feet in diameter by 7 feet long. The solar simulator arc lamps illuminate the spacecraft through three glass ports at the rear of the chamber. Four support positions are provided on the chamber, to permit testing of the satellite with the spin axis at angles of 0°, 30°, 60° and 90°, with respect to the symmetry axis of the chamber.

During the tests, the spacecraft was suspended on a hollow rotating shaft extending into the chamber through a vacuum-tight seal. All electrical leads and instrument connections were brought through the shaft to vacuum-tight feedthroughs at the shaft end. During a test, the spacecraft was rotated about its spin axis; the direction of rotation was reversed about every six revolutions. All external wire connections were installed with enough slack to allow the wires to twist around themselves during rotation, thereby eliminating the need for slip-rings. The rate of rotation was sufficient to avoid any noticeable temperature fluctuations on the skin as a particular portion of the surface rotated in and out of the beam. The point of reversal was staggered during each cycle to eliminate nonuniform illumination of the surface. The test vehicle was insulated from the shaft to minimize conductive heat loss through the shaft.

The radiation from each arc lamp was collected and focused by four glass lenses, and the intensity of each beam was roughly fixed by adjusting the relative positions of these lenses. Each arc emits over 1300 BTU/hr of simulated solar radiation. No attempt was made to collimate the radiation from the lamps, since lack of collimation has a negligible effect on the determination of the $\bar{\alpha}/\bar{\epsilon}$ ratio for an isotropic spherical spacecraft.

For test purposes, the beam cones of the three arcs were adjusted to extend about two inches past the spacecraft cross section, so that the nonuniform beam edge did not influence the tests. The intensity was found to change with time because of variations in supply voltage, differences in electrodes, etc. However, it was possible to compensate for these intensity changes, without appreciably affecting other characteristics of the radiation, by making small adjustments in the spacing between the positive and negative carbons. This was found to be sufficient to control the intensity variations encountered during any run. Solar cells, which are described below, were suspended in the beam inside the chamber to act as intensity monitors for the arc lamp radiation. The electrode spacing was manually trimmed to maintain predetermined short-circuit current outputs on the solar cell monitors.

In all the tests, the intensity of the individual arc lamps was kept constant, and changes in the time-averaged intensity were accomplished by turning the lamps on and off in a suitably scheduled manner. Each arc lamp could be operated for over an hour before its electrodes were consumed. It was a relatively simple matter at this point to remove the spent lamp and replace it with a freshly carboned one.

Three 1 × 2 cm solar cells were suspended in the chamber in front of the spacecraft and were used as arc intensity monitors. The short-circuit current from these cells was calibrated against the intensity of the arc lamps and provided a reference for carbon electrode adjustments. During a test, the short-circuit current from banks of solar cells on the spacecraft surface was also recorded. This provided an additional check on the control of the over-all intensity of arc radiation, although these cells were not specifically calibrated for that purpose. While the short-circuit current from the spacecraft solar plant was not used as a standard for adjusting the arc lamp intensity, it was useful in observing changes in the characteristics of the individual solar cell strings.

The spectral characteristics of the radiation from the carbon arc lamp match quite closely the spectrum of the sun's radiation outside the earth's atmosphere (Johnson curve).[13] The glass lenses in the facility prevent all radiation below 0.35 micron from entering the chamber; however, this small loss in the ultraviolet region does not have a significant effect on the thermal measurements discussed here.

A.2 Arc Lamp Calibration

The arc lamps were positioned to face the center of the test region and were equidistant from it. The centers of the arc beams were all projected along the same horizontal plane, and the areas illuminated by each arc were equal.

The radiation from the arc lamps in the region near the specimen acts as if it were emitted by a point source: i.e., the relationship between intensity and distance is closely represented by an inverse square function. When the power density at the location of the center of the satellite is set equal to some value, I, the average power density on the surface of the spherical satellite from a collimated source also has an intensity I.[15]

Each arc lamp was adjusted to give approximately $\frac{1}{3}$ S at the center of the satellite, where S is the solar constant. This was found to provide sufficient radiative input to the test vehicle to produce the maximum energy condition — i.e., a fully sunlit orbit plus appropriate margins. The lamps were then placed in position, and, with the chamber at am-

bient conditions, the three monitoring solar cells were illuminated by the lamps and their output was compared to a calibrated Eppley pyrheliometer at the point corresponding to the center of the test specimen.

A.3 *Calibration of Space Simulator*

A.3.1 *Thermal Balance Equation*

The total net power stored in a test specimen in the space simulation chamber can be described by a thermal balance equation of the form

$$Q_T = Q_S + Q_R + Q_{IR} - Q_E \tag{6}$$

where the first three terms on the right represent power absorbed by the specimen from, respectively, the simulated solar source, simulated solar power reflected from the surroundings, and infrared power from the surroundings. The last term in (6) describes the power radiated by the test specimen. Here, we have assumed that all thermal energy exchange is by radiation, and that there is no heat dissipation within the specimen.

At thermal equilibrium, (6) can be set equal to zero and rewritten as:

$$\bar{\alpha}A_1 I + \bar{\rho}\bar{\alpha}A_2 I + \bar{\alpha}'A_1 I_w - \bar{\epsilon}\sigma A_2 \bar{T}_S^4 = 0 \tag{7}$$

where

$\bar{\alpha}$ = average absorptivity of specimen to carbon arc radiation
A_1 = cross-sectional area of specimen
I = time-averaged intensity of carbon arc radiation
$\bar{\rho}$ = fraction of I received by the specimen by reflection from the surroundings, averaged over the surface of the specimen
A_2 = surface area of specimen; for a spherical specimen, $A_2 = 4A_1$
$\bar{\alpha}'$ = average absorptivity of specimen for radiation emitted and reflected by the surroundings in the infrared region
σ = Stefan-Boltzmann constant
I_w = intensity of total equivalent collimated infrared flux emitted and reflected by the surroundings
$\bar{\epsilon}$ = average emissivity of the specimen, and
$\bar{T}_S$ = average temperature of the specimen.

Now, making the simplifying assumption that $\bar{\alpha}' = \bar{\epsilon}$ and substituting the appropriate area factors for a spherical specimen, (7), after a slight rearrangement, becomes

$$\frac{\bar{\alpha}}{\bar{\epsilon}} = \frac{4\sigma \bar{T}_S^4 - I_w}{I(1 + 4\bar{\rho})} \tag{8}$$

A.3.2 *Determination of Total Energy Flux in Chamber*

The total energy that a satellite receives in the chamber at a particular lamp intensity has been determined in a test on a "black satellite." The black satellite is a dummy satellite shell of the same dimensions as the Telstar satellite, but covered on the entire exterior with Parson's black lacquer. This paint has an absorptivity and emissivity both approximately equal to 0.98. In the center of the hollow black satellite, a small ball was suspended with nonconducting supports and instrumented with thermocouples. The ball and the interior of the black satellite were also painted black. The steady-state temperature that this ball assumes may be shown mathematically to be the mean shell temperature of the black satellite.

The arc lamp energy reflected from the walls with the black and other satellites in the chamber was measured with a calibrated solar cell. The average reflected flux $\bar{\rho}$ with the black satellite was 0.003. Similar measurements were carried out with an actual satellite installed in the chamber, and $\bar{\rho}$ was determined to be 0.007.

The black satellite was installed in the chamber and the test conducted with the walls at liquid nitrogen temperature and the pressure in the 10^{-6} torr range. The arc lamps were turned on, and the equilibrium temperature of the black satellite was recorded at three different lamp intensities, I. Table V gives the results of these tests. The quantity q_c, which represents the total collimated intensity of radiation incident

TABLE V—CALIBRATION OF ENVIRONMENTAL CHAMBER USING PARSON'S BLACK COATED SPHERE

I BTU/hr-ft²	$\bar{T}_S$ °R	$\bar{\alpha}/\bar{\epsilon}$	I_w BTU/hr-ft²	q_c BTU/hr-ft²
443	526	1	83	530
307	482	1	64	374
189	429	1	44	235
0	215	1	15	15

TABLE VI—DETERMINATION OF $\bar{\alpha}/\bar{\epsilon}$ FOR A *Telstar* SATELLITE SKIN

I BTU/hr-ft²	q_c BTU/hr-ft²	I_w BTU/hr-ft²	$\bar{T}_S$ °R	$\bar{\alpha}/\bar{\epsilon}$
443	529	73	486	0.68
307	372	56	448	0.70
189	234	39	399	0.70

on the surface of the test specimen, has been computed from the relationship

$$q_c = I(1 + 4\bar{\rho}) + I_w \tag{9}$$

where the first term on the right is the radiation from the arc lamps (direct plus reflected), and the second term is the thermal infrared radiation.

The quantity q_c was also determined in a similar manner in a test on a jet-sprayed aluminum oxide (Al_2O_3) covered satellite with known α/ϵ ratio. The values of q_c for both tests showed good agreement.

Table VI gives an example of the calculation of $\bar{\alpha}/\bar{\epsilon}$ for one of the actual spacecraft shells measured in the environmental chamber. The temperature $\bar{T}_s$ was determined with a black ball centrally located in the interior of the spacecraft, as in the previous cases. The interior surface of the skin had a high-emissivity finish and no electronics package was used. The $\bar{\alpha}/\bar{\epsilon}$ ratio in the table was determined from (8). With this ratio known, it is now possible to simulate the extreme orbital conditions by adjusting the time-averaged lamp intensity to produce the calculated mean shell temperature from (2).

REFERENCES

1. Shennum, R. H., and Haury, P. T., A General Description of the *Telstar* Satellite, B.S.T.J., this issue, p. 801.
2. Smith, K. D., Gummel, H. K., Bode, J. D., Cuttriss, D. B., Nielsen, R. J., and Rosenzweig, W., The Solar Cells and Their Mounting, B.S.T.J., this issue, Part 3.
3. Yu, E. Y., Spin Decay, Spin Precession Damping, and Spin-Axis Drift of the *Telstar* Satellite, to be published.
4. Bangert, J. T., Engelbrecht, R. S., Harkless, E. T., Sperry, R. V., and Walsh, E. J., The Spacecraft Antennas, B.S.T.J., this issue, p. 869.
5. Delchamps, T. B., Jonasson, G. C., and Swift, R. A., The Spacecraft Test and Evaluation Program, B.S.T.J., this issue, p. 1007.
6. Heller, G., Thermal Control of the Explorer Satellites, ARS Journal, **30**, Apr., 1960, pp. 344–352.
7. Hanel, R. A., Thermostatic Temperature Control of Satellites and Space Vehicles, ARS Journal, **29**, May, 1959, pp. 358–361.
8. Acker, R. M., Lipkis, R. P., and Vehrencamp, J. E., Temperature Control System for the Atlas Able-4 Lunar Satellite, ASME Paper No. 60-AV-46, June, 1960.
9. Hrycak, P., Effects of Secondary Radiation on an Orbiting Satellite, ARS Journal, **32**, Aug., 1962, pp. 1294–1295.
10. Hrycak, P., Temperature Distribution in a Spinning Space Vehicle, AIAA Journal, **1**, Jan., 1963, pp. 96–99.
11. Hrycak, P., Calculation of Satellite Surface Temperature Distribution, to be published.
12. Hutchison, P. T., and Swift, R. A., Results of the *Telstar* Satellite Space Experiments, B.S.T.J., this issue, Part 2.
13. Hrycak, P., Unger, B. A., and Wittenberg, A. M., Thermal Testing of the *Telstar* Satellite, Proc. Inst. Environmental Sci., 1963, pp. 477–484.

The Spacecraft Test and Evaluation Program

By T. B. DELCHAMPS, G. C. JONASSON and R. A. SWIFT

(Manuscript received January 21, 1963)

Considerations guiding the planning and execution of environmental tests in the development, design qualification and flight acceptance phases of the Telstar satellite program are discussed. Specific test procedures are covered and highlights of test results involving mechanical, thermal and magnetic properties of the spacecraft are reviewed.

I. INTRODUCTION

Essential to the success of any development program are: (a) sound basic design; (b) discriminate selection of materials and components; and (c) careful fabrication. The function of test evaluation, as a fourth phase in the development plan, is to determine the degree to which the three basic requirements listed have been satisfied. It might be suggested that a unique feature of the Telstar satellite program has been the joint achievement of *depth* and *concurrency* in all four development phases. Such an approach has been dictated both by program urgency and the extraordinary cost of failure in an undertaking of this nature. In the process, each phase of the spacecraft development effort has served to reinforce collaterally every other phase, to a degree not normally realized in a sequentially structured program.

The spacecraft design is largely derived from existing systems of proven reliability. Maximum safety margins permitted by size and weight limitations have been utilized. Components and materials have been selected wherever possible on the basis of successful prior use in related applications. Manufacture and assembly operations have been carried out under carefully controlled conditions. The spacecraft test evaluation has served to demonstrate the effectiveness of these measures in providing a design which would survive the launch and operate satisfactorily in the orbital environment. This article will cover both general and detailed aspects of the spacecraft test evaluation, as the

program progressed through the basic-development, design-qualification and flight-acceptance phases.

In the development phase, testing effort was directed toward the evaluation and qualification of spacecraft components and subassemblies, and the study of full-scale models. These tests were conducted under the mechanical and thermal conditions associated with launch and operation in orbit. It was during this phase, through a process of selection and elimination involving available alternatives, that the final design was crystallized. This was followed by design-qualification tests on the prototype spacecraft. In this phase, the controlling philosophy was to achieve maximum assurance, in the limited time available, that the design was capable of surviving launch and performing the intended function under conditions anticipated in orbit. To fulfil this objective, test conditions were selected in a manner which introduced a margin of severity beyond the specific environments predicted for the operational satellite. Finally, flight-acceptance tests performed on operational models were designed to reveal defects which may have been introduced in the manufacturing process. In this phase, the selected test conditions reflected the best estimate of the actual launch environment, but retained, in the thermal-vacuum portion, the added margin previously included in the prototype evaluation. This latter consideration recognized an element of uncertainty in predicting long-term thermal response of the satellite in space.

II. PRELIMINARY MODEL AND SUBASSEMBLY TESTING

The purpose of the preliminary test program was to evaluate the mechanical and electrical design of parts and subassemblies prior to their installation into an actual spacecraft. The tests on structural models with dummy electronics packages provided the necessary data to formulate the subassembly vibration test levels and durations. The levels for temperature tests were based on design objectives and calculated values expected in the space environment.[1] Once a subassembly design had been successfully qualified, there was reasonable assurance that it would survive the dynamic environment of powered flight on the launch vehicle and that it would operate properly in the temperature range predicted for orbital flight.

2.1 *Tests Performed on Development Models*

To conserve time and allow parallel testing, five satellite development models were assembled and used to provide data on system responses to

environmental conditions. The use of models provided information required for subassembly design and pinpointed the possible trouble areas prior to the prototype phase of the project. This allowed any necessary changes to be made before assembly of the prototype. The models used were two structural models (referred to as the vibration and mechanical models), two thermal models, and one electrical development model. The latter, as the name implies, was assembled primarily to evaluate the spacecraft electronics as a complete system, but it also served to provide data on electrical performance under certain environmental conditions. A tabulation of the test models appears in Table I.

2.1.1 *Vibration and Shock Tests*

Vibration tests were performed on the two structural models to evaluate the mechanical design. Vibration levels were determined at various points in the structure when the entire system was subjected to sinusoidal and random vibration over a wide band of frequencies. The areas to which the most attention was directed were the nylon lacing supporting the electronics canister, the solar cells and their method of attachment, and the structure itself. Results of these early tests proved that from the standpoint of vibration: (a) the mechanical design was basically sound, (b) the solar cells would survive a vibration environment more severe than that expected during launch, and (c) that the nylon lacing provided sufficient isolation of the electronics canister for the anticipated environment. On the basis of these results, it was possible to predict the vibration levels which would be experienced by any of the various subassemblies located either inside the electronics canister or on the outer structure of the spacecraft. The vibration response of the electronics canister is shown in Fig. 1. It is evident that

TABLE I — SPACECRAFT TEST MODELS

Model	Panels	Antennas	Electronic Chassis
Vibration	Brass modules to simulate solar cells	No VHF antenna. Brass dummy for microwave	Dummy-weighted to simulate actual chassis
Mechanical	Full complement of actual solar cells	All antennas installed	Dummy-weighted to simulate actual chassis
Thermal model 1	Full complement of actual solar cells	All antennas installed	Dummy—not weighted
Thermal model 2	No solar cells	Microwave only	Dummy—not weighted
Electrical development	Full complement of actual solar cells	All antennas installed	Actual chassis, but not foamed

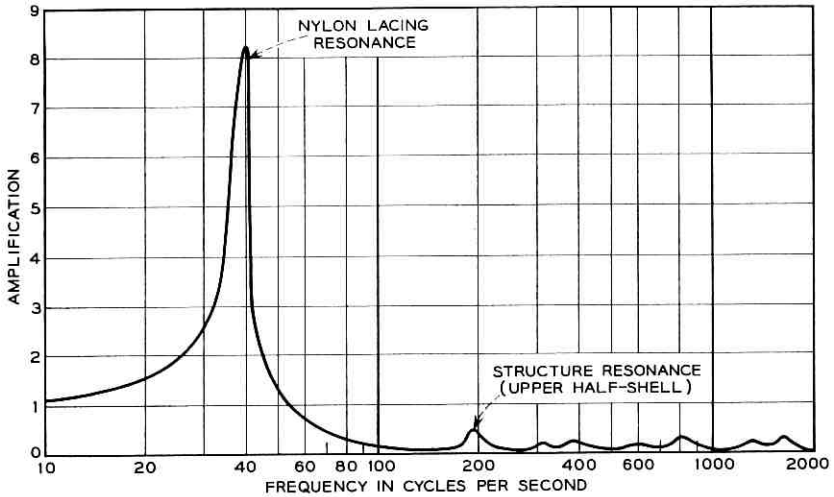

Fig. 1 — Amplification vs frequency, electronics chassis.

at frequencies between 54 and 2000 cycles per second the isolation provided by the lacing is very good.

Figs. 2 and 3 illustrate typical responses at two points on the outer structure. The peaks on these curves represent the resonant frequencies of various parts of the spacecraft. The frequency and amplification factor

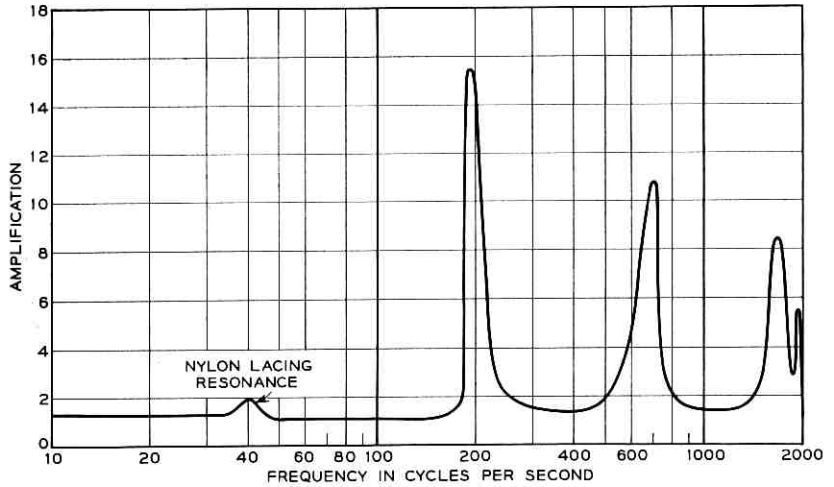

Fig. 2 — Amplification vs frequency, typical solar cell panel.

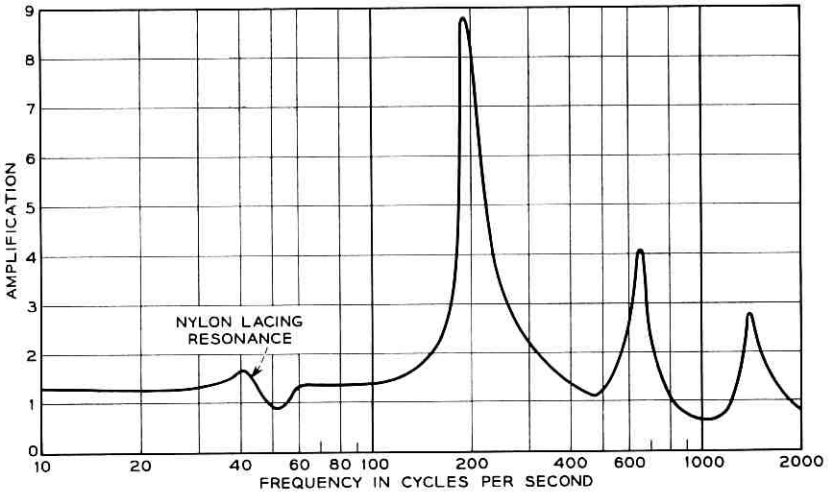

Fig. 3 — Amplication vs frequency, typical structural member (upper half-shell).

associated with each response provided the data necessary to determine the levels for qualification and acceptance vibration of subassemblies, prior to their installation in the spacecraft.

The vibration model was also subjected to several shock tests for the purpose of calibrating the shock test machine and determining the effect of shock on the satellite structure. These tests are summarized in Table II. Pulse shapes from four tests are presented in Fig. 4. The pulse shown in Fig. 4(a) was chosen for the subsequent prototype shock test. No deterioration of the structure occurred as a result of this test.

TABLE II — PRELIMINARY SHOCK TESTS

Drop Number	Drop Height (Inches)	Pulse Time (Milliseconds)	Maximum Acceleration (g's)
1	6.5	—	—
2	6.5	20	21
3	7.5	20	22.7
4	8.25	20	27
5	8.5	19.2	29.4
6	8.0	16.8	33.6
7	7.5	14.4	34.2
8	7.0	15.2	34.5
9	6.0	15.2	31.5

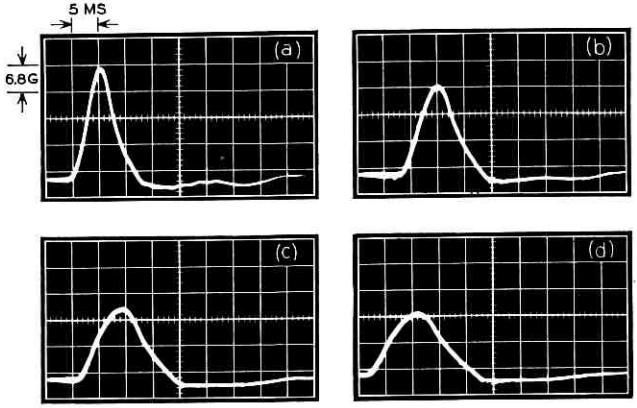

Fig. 4 — Pulse shapes formed using various arrestor rubber thicknesses with Barry 15000 vertical-drop machine: (a) 30-g peak — 13-millisecond pulse obtained with 1-inch rubber arrestor; (b) 24-g peak — 14-millisecond pulse obtained with 1.5-inch rubber arrestor; (c) 20-g peak — 18-millisecond pulse obtained with 2-inch rubber arrestor; (d) 17-g peak — 19-millisecond pulse obtained with 2.5-inch rubber arrestor.

2.1.2 *Preliminary Thermal-Vacuum Tests*

Several tests were performed with the two thermal models in the space simulator for calibration purposes and for verification of the predicted satellite temperatures under extreme orbital conditions. The results of these tests are summarized in Table III. The data obtained from the thermal models show that the chassis temperatures were between 15°F and 90°F. Further tests were performed to observe the thermal-shutter operation and the consequence of a failure of one or both shutter mechanisms. The results of these tests indicated that with the shutters closed in a fully sunlit orbit or open in a maximum eclipse orbit, canister temperatures of 92°F and −20°F, respectively, would prevail. The latter type of failure is the most critical with respect to the operation of the electronic circuits, but, by virtue of the fail-safe nature of the shutter mechanism design, this failure is also the least likely to occur. The shutters have been designed to avoid bearing surfaces which might seize. This leaves loss of fluid in the bellows assembly as the most likely mode of failure. Should this occur, spring loading will force the shutter to return to the closed position.

2.2 *Subassembly Qualification and Acceptance*

Each spacecraft subassembly was subjected to several vibration and temperature cycles prior to installation in the spacecraft. These tests

TABLE III — THERMAL-VACUUM TEST RESULTS

Spin Axis Parallel to Arc Lamps		
Chassis Power	Simulated Orbital Condition	Canister Wall Temperature
16.0 watts	Fully sunlit (plus 18°F margin on skin)	74°F
7.0 watts	Maximum eclipse (minus 18°F margin on skin)	14°F
Spin Axis Perpendicular to Arc Lamps		
Chassis Power	Simulated Orbital Condition	Canister Wall Temperature
16.0 watts	Fully sunlit (plus 18°F margin on skin)	87°F
7.0 watts	Maximum eclipse (minus 18°F margin on skin)	32°F

were performed to detect marginal components which may have slipped by quality control and to pinpoint manufacturing defects. A prototype of each subassembly was vibrated at qualification levels, determined from the results of the vibration tests performed on the structural models. Once a particular design was so qualified, the subsequent flyable units were subjected to acceptance level tests which were somewhat less stringent than those required for initial qualification. The vibration test levels and durations for qualification and acceptance of subassemblies located either inside the electronics canister or on the outer structure, are given in Table IV.

Most flyable subassemblies were temperature cycled over the range of 0°F to 125°F, stabilized at each extreme for a period of six hours and electrically tested at the maximum and minimum conditions. This test represented an extension of 15°F below and 35°F above the temperature range expected during the satellite lifetime.

III. PROTOTYPE QUALIFICATION TESTS

The design qualification program included a complete sequence of tests intended to subject the prototype model to environmental rigors more stringent than those expected from transportation, handling, test, pre-launch, launch, injection, and orbit. The prototype was deliberately over-tested to assure that the basic design possessed a margin of safety which would allow for variations in subsequent systems. The purpose of the design qualification tests was to demonstrate the ability of the design to meet all performance requirements without degradation due

TABLE IV

(a) Vibration Inputs for Inside-the-Canister Assemblies: Qualification Levels

Vibration Axis	Frequency Range (cps)	Sweep Duration (Minutes)	Acceleration (g's Vector)
Thrust	10–30	1.00	2.3*
	30–60	1.00	21.0
	60–2000	2.7	14.0
	550–650	0.5	21.0
Lateral	5–30	1.25	0.9*
	30–60	1.00	4.8
	60–2000	2.7	2.8
	550–650	0.5	4.8

(b) Vibration Inputs for Inside-the-Canister Assemblies: Acceptance Levels

Vibration Axis	Frequency Range (cps)	Sweep Duration (Minutes)	Acceleration (g's Vector)
Thrust	5–30	1.2	1.5*
	30–60	0.5	14.0
	60–2000	1.1	7.1
	550–650	0.5	14.0
Lateral	5–30	1.2	0.6*
	30–60	0.5	4.2
	60–2000	1.1	1.5
	550–650	0.5	4.2

(c) Vibration Inputs for On-the-Frame Assemblies: Qualification Levels (Typical)

Vibration Axis	Frequency Range (cps)	Sweep Duration (Minutes)	Acceleration (g's Vector)
Thrust	10–2000	1.7	2.3†
	150–300	0.5	46.0
	300–2000	1.5	20.0
	550–650	0.5	27.0

(d) Vibration Inputs for On-the-Frame Assemblies Acceptance Levels (Typical)

Vibration Axis	Frequency Range (cps)	Sweep Duration (Minutes)	Acceleration (g's Vector)
Thrust	10–2000	1.7	2.3
	150–300	0.5	28.0
	300–2000	1.5	14.0
	550–650	0.5	21.0

* Maximum table excursion — 0.5 inch double amplitude.
† This run was to observe possible fixture resonances.

to exposure to these more stringent environments. The spacecraft test sequence is tabulated in Table V, and the levels required for design qualification in Table VI. The specific test requirements were jointly agreed upon by Bell Telephone Laboratories, Incorporated, and the National Aeronautics and Space Administration.

3.1 *Balance, Moments of Inertia and Center of Gravity Determination*

To insure correct performance during launch and orbit, the mechanical parameters of weight, center of gravity location, moments of inertia, and degree of unbalance must be accurately measured, and corrected if out of established limits. Briefly, the part each parameter plays in the over-all performance of the satellite is as follows: The permissible weight is determined by the desired orbit and the type of launch vehicle used; for the Telstar satellite, the chosen orbit and Thor-Delta vehicle limited the final weight to a maximum of 175 pounds. The center of gravity location and moments of inertia affect the satellite attitude stabilization in orbit, and also influence corrections required during the guided portion of powered flight. The moments of inertia also determine the size of the rocket motors to provide spin for stabilization of the third stage. The static and dynamic balance of the satellite determine the degree of stability during third-stage flight and orbit.

Since the Telstar satellite is spin-stabilized, it is necessary that the major moment of inertia: (a) be greater than the remaining principal moments of inertia, and (b) have its axis coincident with the desired spin axis. The first requirement may be met by designing for correct

TABLE V — SPACECRAFT TEST SEQUENCE

Qualification Tests	Acceptance Tests
Leak	Leak
Electrical Acceptance	Electrical Acceptance
Static Balance	Static Balance
Spin	
Dynamic Balance	Dynamic Balance
Weight	Weight
Moments of Inertia	Moments of Inertia
Temperature	
Humidity	
Sustained Acceleration	
Shock	
Vibration	Vibration
Dynamic Balance	Dynamic Balance
Thermal Vacuum	Thermal Vacuum
Leak	Leak
System Check	System Check
Electrical Acceptance	Electrical Acceptance

TABLE VI — SPACECRAFT QUALIFICATION TEST LEVELS

Test	Levels		Total Time
	Thrust	Transverse	
Vibration			
5–50 cps	2.3 g peak	0.9 g peak	3.3 min.
50–500 cps	10.7 g peak	2.1 g peak	3.3 min.
500–2000 cps	21.0 g peak	4.2 g peak	2.0 min.
550–650 cps	40.0 g peak	14.0 g peak	1.0 min.
Random (20–2000 cps)	11.5 g rms	11.5 g rms	8.0 min.
Temperature			
Low temperature soak	0°F		6 hours
High temperature soak	140°F		6 hours
Low temperature operate	15°F		6 hours
High temperature operate	90°F		6 hours
Humidity	86°F–95%		24 hours
Thermal vacuum	pressure $<10^{-5}$ mm Hg		
High temperature	max. predicted MRT +18°F		6 days
Low temperature	min. predicted MRT −18°F		3 days
Sustained acceleration			
Thrust	+25 g		3 min.
Transverse (4 orientations)	±3 g		4 min.
Shock			
Thrust (3 drops)	30-g 10–15 millisec half-sine pulse		—
Spin	225 rpm		3 hours

mass distribution and the second by fine adjustment of the static and dynamic balance of the satellite. The design objective for the ratio of maximum transverse moment to the major moment of inertia was a ratio of less than 0.95.

The balance requirements imposed on the satellite by the launch vehicle were a center of gravity offset of less than 0.005 inch and a principal axis shift of less than 0.008 radian.

The prototype spacecraft was balanced to achieve a center of gravity offset of less than 0.003 inch and a principal axis shift of less than 0.002 radian. The moment of inertia ratio was found to be 0.956, which was slightly above the design objective; however, it was known at the time that the flyable satellites would have lower ratios, so no effort was made to optimize the prototype.

3.2 *Temperature and Humidity Tests*

The purpose of the temperature and humidity tests was to show that the spacecraft would survive temperature and humidity extremes that

might be encountered during storage or operation in an uncontrolled environment for short periods. The levels employed for these tests were those which might result from a failure of either heating or air-conditioning equipment in the satellite storage and testing areas.

The tests were performed as follows: storage for a period of six hours at an ambient temperature of 140°F; storage for six hours at a temperature of 0°F; operation at a chassis temperature of 15°F; and operation at a chassis temperature of 90°F. The humidity test consisted of a 24-hour storage period at a temperature of 86°F and a relative humidity of 95 per cent.

During the temperature test, it was found that the telemetry failed to operate below 60°F. The failure was isolated to a switching transistor in the voltage-controlled oscillator and the circuit was redesigned for later spacecraft.

Following the temperature and humidity tests, physical examination of the spacecraft revealed that the oxide coating had flaked off in some areas, and it was noted that several gray stains, which were later found to be caused by oil, had appeared during the test. As a result of these findings, steps were taken to prevent exposure of subsequent satellites to an oil-contaminated atmosphere.

3.3 *Vibration Tests*

The prototype model was subjected to the series of vibration tests outlined in Table VI. The following failures were noted during the vibration tests: (a) radiation detectors P1, P2, E1 became inoperative, (b) one of the static balance weights was torn loose from the framework and damaged a solar cell panel, (c) two helix wires on the VHF antenna were broken, and (d) several short circuits developed in the solar power plant.

It was found that two of the radiation detector failures had been caused by broken wiring at the canister header and the third by a defective diode. In order to prevent failures of the same type, the wiring harness was modified and a more severe diode screening process was instituted. The improved wiring harness and more reliable diodes were installed in all subsequent spacecraft.

The loss of the static balance weight was attributed to local stress concentrations in the satellite frame at the point of attachment. The stress was relieved by distributing the weight over a larger area, allowing more space between the screws used to attach each weight, and by providing some degree of mechanical damping through the use of epoxy between the frame member and the balance weight. As a result of these

modifications, no further difficulty has been encountered with the balance weight mounting.

Close inspection of the breaks in the helix antenna revealed that in both cases the fracture had been started during fabrication. In subsequent units the possibility of breakage was minimized by increasing the radii of the various bends, inspecting the wire more closely before forming, and inspecting the completed antenna assembly for cracks by means of a dye penetrant.

Inspection of the solar power plant wiring revealed that the insulation had ruptured at points where it crossed sharp corners of the spacecraft framework and at cable tie points, resulting in short circuits. The wire was replaced with a wire having a higher density insulation and wrapped with Mylar tape at tie points and areas where the cabling crossed the framework.

3.4 *Shock Test*

The shock test consisted of four half-sine pulses, 30 g's in amplitude and 13 milliseconds in duration, applied along the thrust axis of the spacecraft. Performance of the satellite following the test was satisfactory and gave no evidence of deterioration as a result of the test. During impacts, however, the telemetry dropped out of synchronization on the second, third and fourth shocks. Investigation failed to indicate any reason for the loss of synchronization, and it did not recur during any of the later environmental tests.

3.5 *Thermal-Vacuum Tests*[1]

The thermal-vacuum tests were a simulation of the extreme thermal conditions expected in orbit.[1] For the qualification test, it was required that the satellite be exposed to simulated solar illumination at a pressure of less than 1.0×10^{-5} mm Hg, with a chamber-wall temperature of less than $-280°$F, for a period of nine days. A fully sunlit orbit was simulated for six days with power dissipation within the electronics canister corresponding to maximum efficiency of the solar power plant. This was immediately followed by simulation of the maximum eclipse orbit for three days with a dissipation within the canister corresponding to a solar plant efficiency of 68 per cent of its initial value, the condition expected near the end of Telstar's two-year life. During the six-day test, the simulated solar input was controlled to give a mean radiant temperature[1] 18°F above the value predicted for the fully sunlit orbit, and the power input to the electronics chassis was maintained at 16 watts. The mean radiant temperature during the three-day test was

maintained 18°F below that expected in the maximum eclipse orbit and the power input was limited to 7 watts.

Electrical operation represented maximum use of the satellite in the two extreme conditions and was conducted on the following schedule: the communications experiment and telemetry was turned on for three half-hour periods each day, beginning at approximately 0900, 1200 and 1500 hours, and the telemetry was operated for the first five minutes of each remaining half-hour period.

Shortly after the start of the prototype test, telemetry data showed that the canister pressure had decreased, indicating that a leak had developed. An electrical check indicated that a failure had occurred in the microwave circuitry. The test was terminated at that time and the satellite returned to the Hillside laboratory for disassembly and inspection.

It was discovered that the material around the top shutter mounting stud had failed, causing a leak in the dome of the canister. Since the failure had apparently occurred during either the vibration or shock tests, it served to emphasize the importance of performing the thermal-vacuum test after completion of the mechanical tests. Further investigation revealed the cause of the microwave failure to be destruction of the output transistors in the 255 and 277-mc transistor multipliers caused by voltage breakdown in the power supply resulting from loss of canister pressure. Laboratory experiment confirmed that the failure was a direct result of the corona effect present in the power supply when operated at reduced pressures.

The prototype unit was repaired and returned to the Whippany environmental test laboratory for completion of the qualification tests. The thermal-vacuum test was completed without further incident. The test results are shown in Table VII.

3.6 *Leak Tests*

Since the spacecraft electronics are contained within a hermetically-sealed canister and are designed to operate at a pressure of approximately 10 psia, it was necessary that the canister leak rate be evaluated. The

TABLE VII — THERMAL-VACUUM QUALIFICATION TEST RESULTS

Test	Canister Temperature		Mean Skin Temperature
	Predicted	Actual	
Full sunlight	73°F	73.3°F	21°F
Maximum eclipse	14°F	17.3°F	−47°F

leak test also served as a means of determining if the canister had ruptured or if a weld had failed since sealing. The canister was backfilled with argon gas and the leak rate determined in an evacuated chamber, using a mass spectrometer. Leak tests were performed in this manner prior to and after the environmental test series.

Before testing, the prototype leak rate was less than the measurement capability of the detector. Following the test program, a leak rate of 5×10^{-4} std cc/sec of argon was indicated. Investigation revealed that the chamber, the Mylar insulating blankets around the canister, and the satellite itself, had become contaminated with argon at the time canister pressure was lost during the initial thermal-vacuum test. These findings raised serious doubt as to the significance of this final leak reading. Subsequent tests on flyable spacecraft have revealed that the leak rates are well below the specified 8×10^{-5} std cc/sec of argon.

3.7 *Spin Test*

The prototype was subjected to a spin rate of 225 rpm for a period of three hours, the last hour of which was under electrical load simulating operation in orbit. The 225 rpm spin rate was a 25 per cent increase over that expected in actual flight (the satellite was injected into orbit with an initial spin rate of 177.7 rpm). There were no spacecraft malfunctions during this test.

3.8 *Sustained Acceleration*

The prototype was mounted on a horizontal centrifuge and sustained acceleration, measured at the spacecraft center of gravity, was applied along each of its three coordinate axes. The first test consisted of one run with 25 g's applied in the thrust direction for a period of three minutes. The second test consisted of four runs in the lateral plane, with the prototype spacecraft being rotated 90 degrees after each run. The levels during the latter runs were 3 g's, maintained for a period of one minute in each position. The electrical performance of the spacecraft was monitored during the periods of constant acceleration, and electrical checks were performed following each run. There was no evidence that satellite performance was in any way degraded either during or as a result of the applied accelerations.

3.9 *Magnetic Drag and Moment Measurements*

Since the Telstar satellite is spin-stabilized and orbits within the magnetic field of the earth, it was necessary that the effect of that field

on the spin rate and precession of the satellite be determined. For this reason, the torque due to eddy currents, and the residual magnetic moment along the spin axis of the spacecraft were measured. The former effect is the cause of spin decay and the latter causes precession.

The magnetic drag constant was found to be 1355 ± 15 per cent meters^4 per ohm. The drag torque due to a given field strength was calculated from the relationship $T_0 = p\omega B^2$, where p is the magnetic drag constant, ω the angular velocity of the satellite and B the field strength normal to the satellite spin axis. The flyable spacecraft were essentially the same as the prototype with respect to eddy current generation, and subsequent models were not drag tested.

The magnetic moment of the prototype was measured, and a coarse correction was made to investigate the feasibility of compensating for the effect of the traveling-wave-tube field.

IV. SPACECRAFT ACCEPTANCE TESTS

The spacecraft acceptance test program, illustrated in Table VIII, was similar to the qualification program but consisted of only vibration, thermal-vacuum, balancing, and measurement of weight, center of gravity and the principle moments of inertia. The vibration levels and durations closely approximated those expected during launch. The thermal-vacuum test was shortened to three days maximum sunlight and two days maximum eclipse, at the same levels required for qualification. The same requirements and objectives were met for balance, weight, center of gravity and moments of inertia as for the prototype. The remaining tests (spin, temperature, humidity, sustained acceleration and shock) which had been performed on the prototype model were for

TABLE VIII — SPACECRAFT ACCEPTANCE TESTS

Test	Levels		Total Time
Vibration	Thrust	Transverse	
5–50 cps	1.5 g peak	0.6 g peak	1.7 min.
50–500 cps	7.1 g peak	1.4 g peak	1.7 min.
500–2000 cps	14.0 g peak	2.8 g peak	1.0 min.
550–650 cps	40.0 g peak	9.4 g peak	0.5 min.
Random (20–2000 cps)	7.7 g rms	7.7 g rms	4.0 min.
Thermal Vacuum	Pressure 10^{-5} mm Hg		
High Temperature	max. predicted MRT + 18°F		3 days
Low Temperature	min. predicted MRT − 18°F		2 days

the purpose of design qualification and were not required for flyable spacecraft.

4.1 *Balance, Moments of Inertia and Center of Gravity Determination*

The flyable model spacecraft were subject to the same requirements for static and dynamic balance, moments of inertia, and center of gravity as the prototype model. The results of these measurements are shown in Table IX. All five spacecraft were well within all specification requirements and design objectives.

4.2 *Vibration Tests*

The vibration levels for acceptance testing of flyable spacecraft are shown in Table VIII. The acceptance tests for five flyable spacecraft were completed with no failures of in-line systems or serious malfunction of secondary systems. The two malfunctions which did occur were: flyable 2 — the radiation damage data assigned to telemetry channel 49 gave faulty information following sinusoidal vibration in the thrust direction (the same data are carried on channel 47, so no effort

TABLE IX — BALANCE, WEIGHT, C.G. DETERMINATION, AND MOMENTS OF INERTIA MEASUREMENTS

Parameter	NASA Requirement	Design Objective	Fly 1	Fly 2	Fly 3	Fly 4	Fly 5
Weight (lbs)	None	175.0 max	172.00	170.94	172.30	173.81	174.28
Spin-axis moment of inertia, slug-ft²	None	Not specified	4.164	4.141	4.207	4.202	4.1961
Maximum transverse moments of inertia, slug-ft²	None	Not specified	3.822	3.825	3.872	3.888	3.9184
Moment of inertia ratio	None	0.95	0.918	0.924	0.920	0.925	0.934
C.G. location (inches)							
From separation plane	None	16.5	16.48	16.46	16.36	16.4	16.26
Spin-axis offset	Less than 0.005	—	Less than 0.003*	Less than 0.003*	Less than 0.003*	Less than 0.003*	Less than 0.003*
Principle axis shift (radius)	Less than 0.008	—	Less than 0.002*	Less than 0.002*	Less than 0.002*	Less than 0.002*	Less than 0.002*

* Lower limit of reliable measurement.

was made to isolate the trouble); flyable 5 — following sinusoidal vibration in the thrust direction, telemetry channels 63 and 64 had no output, indicating a failure in one of the radiation detectors located on the skin of the spacecraft. It was agreed that the remaining two channels provided adequate coverage for the radiation experiment. Since complete isolation or repair would have been impossible without opening the canister, no corrective action was taken.

4.3 *Thermal-Vacuum Tests*

The flyable model spacecraft were exposed to the same thermal-vacuum conditions as the prototype, but for a shorter duration. The acceptance tests ran for five days (three days under maximum sunlight conditions and two days under maximum eclipse conditions). The flyable satellites were operated on the same duty cycle as outlined for the prototype.

Performance of the flyable spacecraft during thermal-vacuum tests was satisfactory in all respects. A tabulation of temperatures attained and chamber pressures for each test is presented in Table X. A graph illustrating the range of electronics chassis temperatures for five flyable satellites is shown on Fig. 5. Results from flyable model 2, which is the Telstar satellite, have been plotted for reference.

4.4 *Leak Tests*

The sealed electronics canister of each flyable model spacecraft was leak tested in the same manner as the prototype, before and after the acceptance test program. The results of these tests are shown in Table XI.

TABLE X — THERMAL-VACUUM ACCEPTANCE TEST RESULTS

Satellite	Canister Temperature*		Mean Skin Temperature†		Chamber Pressure	
	Maximum Eclipse	Full Sunlight	Maximum Eclipse	Full Sunlight	Minimum	Maximum
Fly 1	43°F	88.5°F	−34°F	35°F	1.4×10^{-6} mm Hg	2.5×10^{-6} mm Hg
Fly 2	34°F	80.5°F	−40°F	27°F	1.0×10^{-6} mm Hg	2.1×10^{-6} mm Hg
Fly 3	43°F	83°F	−40°F	32°F	1.4×10^{-6} mm Hg	2.7×10^{-6} mm Hg
Fly 4	35°F	83°F	−35°F	36°F	4.8×10^{-7} mm Hg	9.1×10^{-7} mm Hg
Fly 5	38°F	78°F	−41°F	28°F	7.7×10^{-7} mm Hg	1.2×10^{-6} mm Hg

* Average temperature of four battery groups.
† Average of six points on skin.

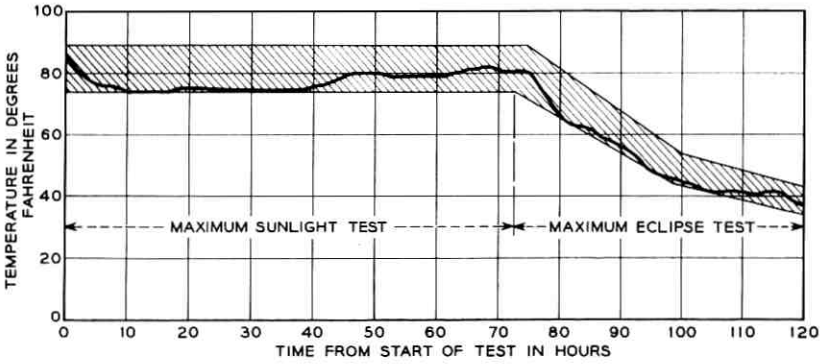

Fig. 5 — Electronic chassis temperature for five flyable satellites; flyable model 2 plotted for reference.

4.5 *Magnetic Moment Measurement*

The magnetic moment along the spin axis of the flyable spacecraft was measured and compensated to achieve the values indicated in Table XII. The plus and minus signs refer to the direction of the magnetic moment vector, the positive direction being toward the top of the satellite.

TABLE XI — LEAK TEST RESULTS

	Before Test	After Test
Fly 1	1×10^{-7} cc/sec argon	2×10^{-6} cc/sec argon
Fly 2	2×10^{-6} cc/sec argon	3×10^{-6} cc/sec argon
Fly 3	2.3×10^{-7} cc/sec argon	1.25×10^{-5} cc/sec argon
Fly 4	2.5×10^{-7} cc/sec argon	1.8×10^{-6} cc/sec argon
Fly 5	3×10^{-7} cc/sec argon	4×10^{-5} cc/sec argon

TABLE XII — MAGNETIC MOMENT MEASUREMENT
(FLYABLE SPACECRAFT)

Satellite	Equivalent Torque in a 0.01-Oersted Field
Fly 1	1.9×10^{-6} ft-lbs
Fly 2	-3.3×10^{-6} ft-lbs
Fly 3	Less than measurement accuracy
Fly 4	-2.0×10^{-6} ft-lbs
Fly 5	Less than measurement accuracy

V. CONCLUSION

Components and materials selected for use in the Telstar satellite program were those which reflected a history of reliable usage in previous

successful programs. The system design included the maximum practical margin of safety, commensurate with weight and space limitations of satellite systems. In addition to designing with a maximum safety factor, all manufacturing was accomplished under the closest possible control. Extensive testing of subassemblies and satellite models, carried out in parallel with the design and assembly of actual spacecraft, enhanced reliability of the finished product, and permitted timely modifications where required.

The environmental test program was designed to provide the most comprehensive evaluation of the spacecraft design in the time available. The qualification tests performed on the prototype provided assurance that the Telstar satellite was compatible with the environments expected during powered and orbital flight. The acceptance tests served to uncover manufacturing defects which may have developed during assembly of the various subassemblies into a completed system. Five flyable spacecraft have successfully completed the acceptance test program with no major failures or malfunctions in the in-line systems.

REFERENCE

1. Hrycak, P,. Koontz, D., Maggs, C., Stafford, J. W., Unger, B., and Wittenburg, A. M., The Spacecraft Structure and Thermal Design Considerations, B.S.T.J., this issue, p. 973.

Command and Telemetry Systems

By R. C. CHAPMAN, JR., G. F. CRITCHLOW and H. MANN

(Manuscript received March 22, 1963)

The command and telemetry portions of the Telstar system provide necessary support functions for the basic communications experiment and the radiation experiment. By means of the command system, the states of 9 magnetic latching relays in the satellite are controlled from the ground. Commands are sent to the satellite by coded signals modulated on a carrier in the VHF band. The telemetry system also uses a VHF carrier to transmit encoded information from the satellite. Data on 112 items are provided once each minute. This paper discusses the over-all command and telemetry systems and considers the general objectives, system aspects and detailed implementation.

I. INTRODUCTION

The Telstar satellite includes circuits designed to perform two basic experiments: (*i*) a communications experiment using a wideband, active repeater and (*ii*) a radiation experiment designed to provide information on the environment in outer space and the effects of this environment on devices used in communication circuits. The command and telemetry portions of the Telstar system provide a very necessary support function for these experiments. This paper discusses the over-all command and telemetry systems; it considers first the need and general objectives and then the systems aspects of the design. Finally it gives a detailed discussion of the implementation of each system.

The need for a command system for the Telstar project arises primarily because of power considerations associated with the satellite repeater: the communications circuits consume more power than the solar plant is capable of supplying.[1] To be able to operate under full load, batteries are provided which supply the additional power needed during operation of the communications circuits. During those intervals when the communications circuits are not on, the batteries are recharged by the solar plant. Hence a command system is necessary to turn the high-power communications circuits on and off. Having provided a

command system, it is then convenient to turn other circuits on and off and provide some other functions which can only be available with a command system. These functions include changing telemetry encoders, testing the two command receivers, and activating a torquing coil for attitude control, as well as turning on and off the traveling-wave tube, the IF amplifiers, the microwave carrier supply, telemetry and the radiation experiments. The command receiver circuits must always be energized so that commands may be acted upon to turn on other circuits. The VHF beacon, used for wide-angle acquisition and tracking, is also left on; however, it can be turned off under special conditions.

The telemetry carried aboard the Telstar satellite provides information on 112 different quantities at a rate of one full frame per minute. These quantities fall in four major categories. One type of data relayed from the satellite consists of status information: for example, the state of control relays, some critical temperatures, the solar plant output, and the battery voltage. These data must be decoded and displayed in real time so that the satellite can be operated with the least chance of damage. The second class of data includes those items which pertain to the general condition of the satellite. Such items include internal and external temperatures, pressure, and solar aspect angle. These data are normally monitored and recorded to be analyzed at a later time. They provide a continuous record of the condition of the satellite and some of the effects of its environment. The third main category of telemetry data is that which monitors parameters pertinent to the communications repeater. These data are monitored and recorded to provide correlation data for the communications experiments. Such items as satellite receiver AGC voltage, transmitted power levels, and certain temperatures are necessary for correlating test data. The fourth category of telemetry information is that which provides data from the radiation damage experiments and those channels which contain the radiation counter information. About one fourth of all the telemetry channels are used in the radiation experiment, one third are used to measure various temperatures, and the remaining channels are used to measure a variety of relay states, currents, voltages, biases and calibrations.

II. SYSTEMS DESCRIPTION

The command and telemetry systems are each one-link transmission systems. The command system has its transmitting terminal on the ground and the receiver in the satellite. The telemetry system, on the other hand, transmits from the satellite and the signals are received on the ground. Fig. 1 shows a block diagram of each system and those por-

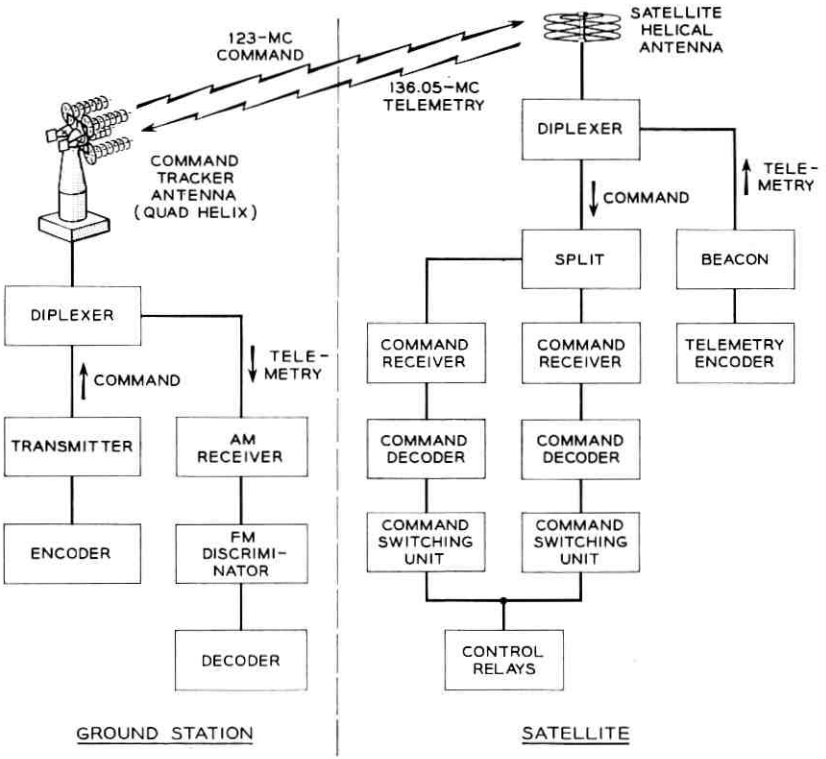

Fig. 1 — Block diagram of command and telemetry systems.

tions of the equipment which are common to the two systems, such as the diplexers and the antennas.

The command system transmits signals to the satellite at approximately 123 mc. The transmitting terminal consists of a command encoder which generates the specified code and a VHF command transmitter which is amplitude modulated by the command signal. The output of the command transmitter goes through the ground diplexer to the command tracker antenna and is radiated to the satellite. The signal picked up by the satellite helical antenna goes through the satellite diplexer and a splitting arrangement into two command receivers. The baseband pulses out of each receiver drive a decoder which activates the proper relay through the action of the switching unit.

The telemetry system transmits information from the satellite back to ground. The transmitting equipment in the satellite consists of a telemetry encoder whose output modulates the 136-mc beacon. The

signal then goes through the satellite diplexer to the helical antenna where it is radiated. The telemetry signal is picked up on the ground by the command tracker antenna and then goes through the ground diplexer to the telemetry receiver. The output of the telemetry receiver drives the decommutator, which presents the information in printouts and displays.

The details of each of these systems will be discussed separately in later portions of this paper. The nature of the signals and the over-all system design considerations will be covered in the following sections.

III. GENERAL DESCRIPTION OF TRANSMISSION SIGNALS

3.1 *Command Signals*

The commands are transmitted to the satellite in the VHF band. The 123-mc carrier is amplitude modulated with a keyed subcarrier. The subcarrier, a 5.451-kc signal, is keyed on and off to generate a code made up of bursts of subcarrier of different widths. A command word is composed of a guard space, a start pulse and six code bits, each occupying a time slot equal in length to 72 cycles of subcarrier. A guard space is no pulse (a blank time slot), and a start pulse is a burst of subcarrier for three fourths of the time slot. The six code bits are made up of three ones (50 per cent duty cycle, burst of subcarrier for half a time slot) and three zeros (25 per cent duty cycle, burst for one fourth of the time slot). This three-out-of-six code permits 20 unique commands, of which 15 are used in the Telstar system. The transmission of a command consists of sending the desired code word five times in succession. This repetition is strictly redundant since each word is decoded and acted upon independently in the satellite. Fig. 2 shows the baseband waveform of a typical word (110100), the keyed subcarrier, and the carrier modulated by this subcarrier. This particular code structure, the carrier, and the subcarrier frequencies were chosen to be compatible with existing command facilities at the NASA Minitrack stations. The command and telemetry signals were thus chosen to provide the greatest flexibility and compatibility with these existing facilities.

The code signal, as described above, is generated in the command encoder. This signal 100 per cent amplitude modulates the command transmitter. The command signal is transmitted from the command tracker antenna and is received at the satellite by the helical VHF antenna situated at one of the poles of the satellite. The command receiver in the satellite shifts the carrier to a 5-mc IF, amplifies it, and detects the code to produce a baseband pulse train which is decoded and which

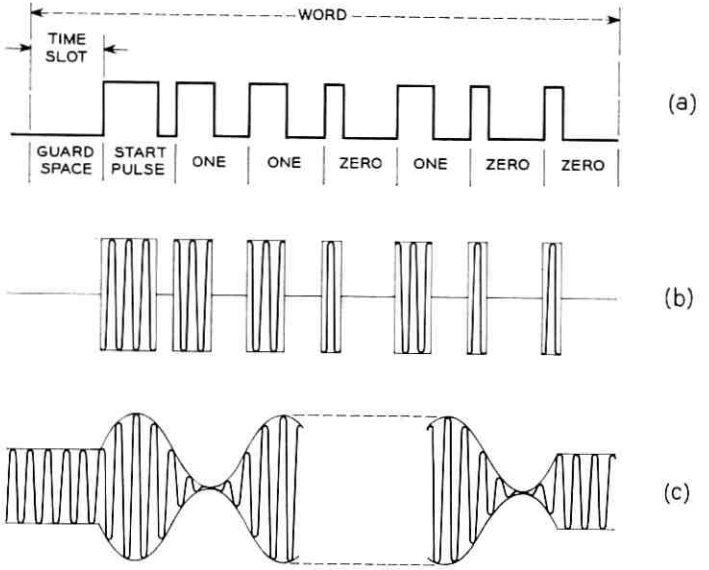

Fig. 2 — Command signal waveforms: (a) baseband code, (b) gated subcarrier (c) modulated carrier (expanded time scale).

causes the proper relay switching to accomplish the function designated by the command being sent.

3.2 *Telemetry Signal*

The telemetry signal is transmitted from the satellite to the ground telemetry receiver, also in the VHF band. The same antennas are used: the satellite helix transmits the 136-mc beacon signal and the command tracker antenna receives it. The telemetry encoder within the satellite generates a PCM signal made up of 120 eight-bit words. Each eight-bit word is made up of a seven-bit binary code with an eighth bit used for word synchronization. Of the 120 words there are 118 data words, and two words (119 and 120) are used for frame synchronization. The baseband PCM signal frequency modulates a 3-kc subcarrier with a deviation of ± 7.5 per cent (± 225 cps). The modulating signal is two-level, so the output of the FM modulator is a signal alternating between two frequencies, 2775 and 3225 cps. This signal in turn 50 per cent amplitude modulates the beacon. Fig. 3 shows a typical telemetry word (level 90, on a 7-bit binary scale from 0 to 127), the corresponding plot of frequency versus time of the subcarrier, and the modulated

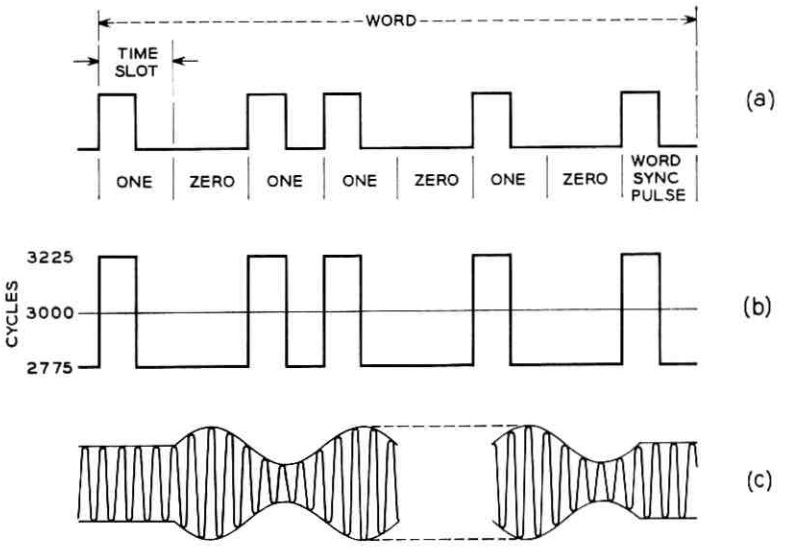

Fig. 3 — Telemetry signal waveforms: (a) baseband code (bit level 90); (b) subcarrier frequency deviation; (c) modulated carrier (expanded time scale).

carrier. This PCM/FM/AM signal is transmitted from the satellite helical antenna and is received by the command tracker antenna. After amplification, the carrier is shifted to a 10-mc IF, and an amplitude detector retrieves the frequency modulated 3-kc subcarrier. A frequency discriminator extracts the baseband PCM signal, which is then decoded to provide the corresponding output for each of the telemetry channels.

3.3 *Command and Telemetry Interaction*

The command and telemetry systems are essentially independent systems. Certain commands are interlocked in such a way that their use depends on what commands have been sent and upon the status indicated by the received telemetry. The telemetry circuits in the satellite can be turned on and off, and some of the telemetry channels monitor parameters in the command circuits. To this extent the two systems interact. Since the two directions of transmission use the same antennas, diplexers are used at each terminal, and there will be some leakage of each transmitter into the other receiver. The frequency separation is large enough so that the leakage problem is not severe. The details of this effect will be discussed under System Performance, Section V.

IV. SIGNAL LEVELS

4.1 *Command*

The command transmitter has an output capability of 200 watts of average unmodulated carrier power. At the Andover, Maine, ground station the cabling distance from the command transmitter to the command tracker antenna is about 150 feet. The signal then goes through the diplexer before being radiated from the antenna. Cabling and diplexer losses are 2.5 db, and the antenna provides a gain of 17.5 db at 123 mc, for a net gain of 15 db.

Loss from transmitting antenna on the ground to the receiving antenna on the satellite may be calculated from the theoretical free-space path loss. Since the range (distance from transmitting to receiving antenna) is constantly changing in a satellite system, the path loss is a variable. For the Telstar satellite launched July 10, 1962, the range may vary from as much as 6500 miles (looking at apogee on the horizon) to as little as 500 miles (perigee directly overhead). These variations in range will result in a path loss variation of 22 db (from 155 to 133 db).

The radiation pattern of the satellite helical antenna is described in detail elsewhere in this issue.[2] Ideally, the antenna would be isotropic. The antenna pattern is essentially a surface of revolution; that is, the gain at any angle does not change as the satellite spins on its axis. However, the gain is not constant as a function of the angle between the satellite spin axis and the direction from which the satellite is viewed. This angle, when measured from the end of the spin axis away from the helical antenna, is called the spin angle. Fig. 4(a) shows the antenna gain (including cabling and matching network losses) as a function of the spin angle. Near the poles the antenna has considerable loss and is difficult to measure; however, if we consider only those angles between 5 and 165 degrees, we see a range in antenna gain of 16 db. Combining this variation with the variation due to range as given by Fig. 4(b), the signal level at the command receiver may vary as much as 38 db over all combinations of range and spin angle. It is possible on a given pass to see a wide range of spin angles; however, to see the full variations in range requires that the apsides advance through half a cycle, which in this case takes about 3 months. The command receiver in the satellite is designed to handle a signal level range of 30 db. This AGC range, while not adequate to cover all cases, is adequate to cover the range of signal levels that result during any pass or group of passes.

In addition to the path loss and the loss in the satellite helical antenna.

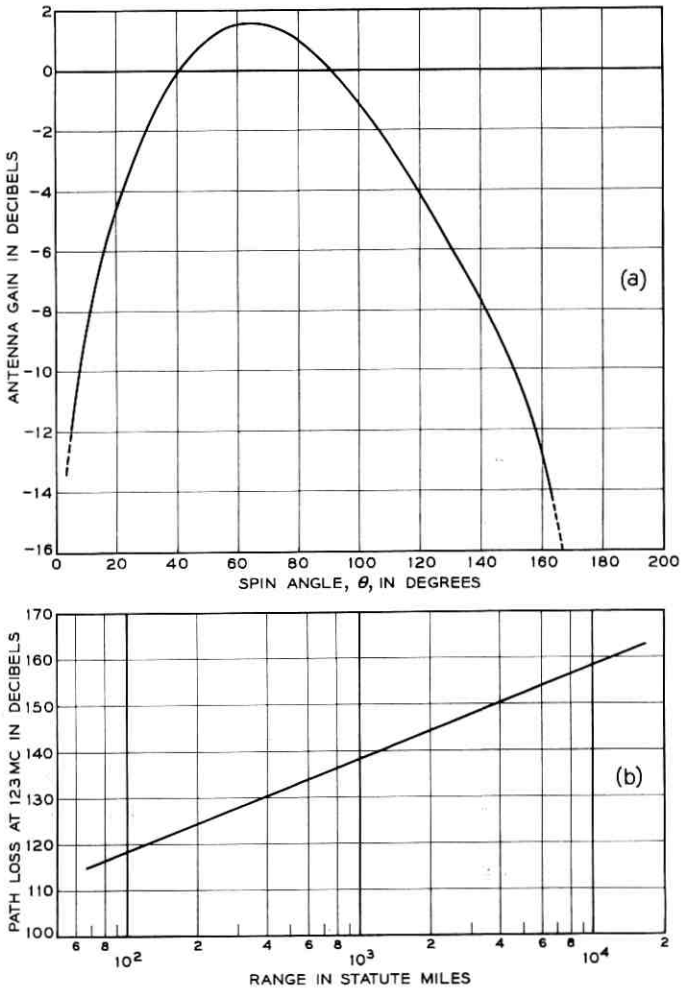

Fig. 4 — (a) Satellite antenna gain as a function of spin angle, (b) free-space path loss at 123 mc as a function of range.

there is a 3-db polarization loss. The helical antenna on the satellite has an essentially linear polarization, and the command tracker antenna quad-helix has a right-hand circular polarization. To get from the antenna to the command receiver, the signal loses 2.5 db in the diplexer and another 3 db in a splitting pad (two receivers operating in parallel for redundancy). The AGC range of each command receiver is such that it can handle signals at its input of -100 to -70 dbm.

4.2 *Telemetry*

The down link of the command and telemetry system consists primarily of the satellite beacon transmitter, the transmission medium, and the RF and telemetry receivers. The beacon puts out 200 milliwatts (+23 dbm) of average unmodulated carrier power. The satellite antenna pattern at 136 mc has approximately the same shape as at 123 mc, but the gain is down about 1 db due to cabling and matching network losses. Free-space path loss at 136 mc is about 0.8 db greater than at 123 mc, and the net gain associated with the command tracker antenna is about 18 db rather than the 15 db at 123 mc. The command tracker antenna is 3 db better at the telemetry frequency than at the command frequency for two reasons. First, the beam is narrower at 136 mc, giving a gain increase of about 1.5 db, and secondly, the 1.5 db of cabling loss is avoided by placing the RF preamplifier in the antenna pedestal instead of in the control room 150 feet away.

There is again a loss of 3 db due to polarization, and the range of received signal levels as before is 38 db. The limitation on the signal level received at the ground is that it be strong enough to produce a detectable signal. The next section will show that a detectable signal will be received if the command link is workable.

V. SYSTEM PERFORMANCE

5.1 *The Command System*

The performance of the command and telemetry systems can best be described by first considering the parameters of the command system. From noise considerations, the minimum allowable received signal level can be determined. Then, knowing the properties of the ground transmitter and of the satellite receiver, the worst combinations of spin angle and range can be determined. The performance of the telemetry system will then be determined, based on the poorest combination of range and spin angle allowed by the command system.

Contributors to the noise performance of the command receiver are (*i*) thermal noise, (*ii*) galactic or cosmic noise, and (*iii*) leakage of the beacon signal into the command system. The effective bandwidth of the command receiver is less than 60 kc. The thermal noise power available in a 60-kc band referred to the input of a 5-db noise figure amplifier is −122.8 dbm. Cosmic noise available in a 60-kc band at 123 mc is taken to be −121 dbm (1000°K)[3]. The leakage of the 136-mc beacon into the command receiver results in an interfering signal at the

output of the receiver. The off-frequency rejection in the receiver referred to −100 dbm at the input is 64 db; the diplexer has 80 db rejection against the +24-dbm, 136-mc signal getting into the command system; and taking the 3-db splitting pad loss, the leakage signal referred to the input of the command receiver is −123 dbm. Adding these three interferences on a power basis results in an interference level at the input to the command receiver of −117.5 dbm. With a −100-dbm input signal, the resulting signal-to-noise ratio of 17.5 db will provide essentially error-free performance in the command decoder.

The minimum signal level within the AGC range of the receiver, as stated earlier, is −100 dbm. Since this also results in a signal-to-noise ratio corresponding to error-free operation, it will be taken as the threshold of commandability. In practice it has been found that a received signal level of −100 dbm is 3 to 5 db above the point where commands will be recognized but with an occasional error.

The received power equation for the command system is

$$P_R = P_T + G_1 - PL + G_2 - 8.5 \text{ db} \tag{1}$$

where P_R = received signal level at the input to each command receiver in dbm

P_T = ground transmitter output power (+53 dbm)

G_1 = command tracker antenna gain at command frequency minus cable and diplexer loss (+15 dbm)

PL = path loss at command frequency (db)

G_2 = satellite helical antenna gain at command frequency (db).

The 8.5 db is made up of 3 db polarization loss, 2.5 db satellite diplexer loss, and 3 db splitting pad loss for driving the two command receivers in parallel. To keep the minimum signal at the command receiver input at −100 dbm requires that the path loss minus the satellite antenna gain shall not exceed 159 db. The path loss at the command frequency is given by

$$PL = 78.4 + 20 \log R \text{ (db)} \tag{2}$$

where R is the range from transmitter to satellite in statute miles. Fig. 4 shows path loss as a function of range and the satellite antenna gain as a function of spin angle. Fig. 5 shows the relationship between range and spin angle such that the minimum workable signal is assured. The contour plotted is for $P_R = -100$ dbm. The received signal level anywhere to the left of the curve will exceed −100 dbm; to the right of the curve the level will be less than −100 dbm and commanding should not be attempted. For an isotropic antenna (the actual antenna has unity

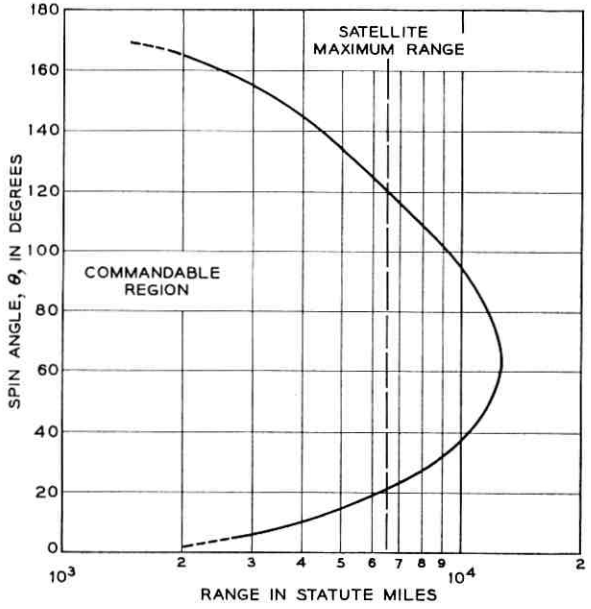

Fig. 5 — Commandability contour for received signal level of −100 dbm.

gain at 90 and 40 degrees) the maximum workable range is 10,700 miles. For the actual antenna, the maximum range which will be safe for any spin angle between 5 and 165 degrees is 2000 miles, and the maximum range for the best spin angle (65 degrees) is 12,900 miles. For the Telstar satellite orbit with its maximum slant range of 6500 miles, the command system will be workable as long as the spin angle stays within 20 to 120 degrees.

5.2 *The Telemetry System*

If the command system is within range, then the path loss minus satellite antenna gain is less than 159 db at the command frequency. Under the same conditions, the path loss minus satellite antenna gain at the telemetry frequency will be less than 161 db (the difference in path loss and antenna gains were pointed out previously) and the received signal level at the input to the telemetry receiver will be at least −120 dbm: satellite transmitted beacon power of +23 dbm, minus 161 db for path loss and antenna gain, plus 18 db for the ground antenna, results in a received signal level of −120 dbm. The noise level referred

to the input of a 3.5-db noise figure receiver with a 20-kc band is −130 dbm. The minimum carrier-to-noise ratio (C/N) for the AM detection is then 10 db. With a C/N ratio of 10 db, the AM detector will not enhance the noise appreciably and the signal-to-noise ratio (S/N) for the FM detector may be calculated directly. The signal power in each sideband for a 50 per cent amplitude modulated carrier is 12 db below the carrier level. With double-sideband detection and a 600-cps bandwidth, the S/N at the input to the FM detector is 16 db: power in each sideband is −132 dbm; noise in a 600-cps band is −145 dbm. Single-sideband detection would give S/N = 13 db, and double-sideband detection results in S/N = 16 db. This signal-to-noise ratio at the input to the FM detector will result in output performance which is essentially error free. To keep a S/N ratio of at least 10 db at the FM detector, the signal level might be allowed to drop another 4 db to −124 dbm. At this point the C/N ratio at the AM detector would be 6 db and the full 3-db advantage of double-sideband detection could not be realized. Hence, the S/N ratio at the input to the FM detector would be about 10 db, and this should be near the breaking point of the system. This has been borne out in practice since the telemetry system has been found to break at input levels of −122 to −124 dbm.

As seen from the above discussion, the command and telemetry systems are both workable under just about the same conditions. In the Telstar satellite orbit (maximum range 6500 miles) both systems are operable with 2- to 4-db margin for spin angles between 20 and 120 degrees. To date the spin angle from the Andover station has not been less than 20 degrees, but it has been as high as 165 degrees. At the command and telemetry station at Cape Canaveral the spin angle has been much greater; in fact spin angles very near 180 degrees have been encountered. Under these conditions both the command and telemetry systems were unworkable as expected. The times of these "spin outages" are predictable and can be avoided by appropriate scheduling.

VI. COMMAND SYSTEM

Previous sections stated the purpose of the command system, gave a brief over-all system description, and discussed signal levels and noise performance. We now proceed to a more detailed description of the command system. First the entire system will be given a general description to functionally relate the major portions. This will be followed by still more detailed descriptions of the major blocks.

6.1 *General Description*

The command system employs fifteen different commands as given in Table I. These are listed here as a matter of general interest and for convenience in understanding subsequent sections.

A functional block diagram of the command system is shown in Fig. 6. A command can be originated in the ground station at the telemetry and operating panel or remotely at the ground station control console. The command encoder translates the specific command to a preselected code and sends this code via the ground station command transmitter to the satellite.

Upon initiation of a command, a control signal is sent over one out of 20 lines to the encoding circuit. This signal is translated to an individual 6-bit parallel code consisting of three ones and three zeros.

A decoding circuit converts the code back to a signal suitable for lighting indicators to show that the proper command has been encoded. Thus, when the command button is pressed it lights up, and another group of six indicator lights shows the actual binary code.

The encoder output is also applied to the word assembly and to "parity and lockout" circuits. The word assembly unit transforms the 6-bit parallel word to an 8-bit serial word consisting of a start bit, the 6-bit code, and a guard space. The 8-bit word is applied to the "parity and lockout" circuit where the code is checked for an odd parity of three

TABLE I — COMMANDS

Command	Function
A	turns on TWT filament voltage
B	turns on TWT helix and collector voltages, energizes circuits associated with the communications experiment
C	turns on TWT anode voltage
CC	turns off TWT anode voltage
AA	turns off TWT helix, collector, and filament voltages; de-energizes circuits used in the communications experiment
D	turns on telemetry and radiation experiment circuits
DD	turns off telemetry and radiation experiment circuits
E	turns on current orientation loop
EE	turns off current orientation loop
F	connects telemetry encoder No. 1
FF	connects telemetry encoder No. 2; F and FF also control direction of current through the orientation loop
SS	initiates CC, AA, DD, and EE and disconnects battery and VHF beacon
S	connects battery back into circuit and turns on VHF beacon
T-1	turns off command decoder No. 2 for 15 seconds
T-2	turns off command decoder No. 1 for 15 seconds

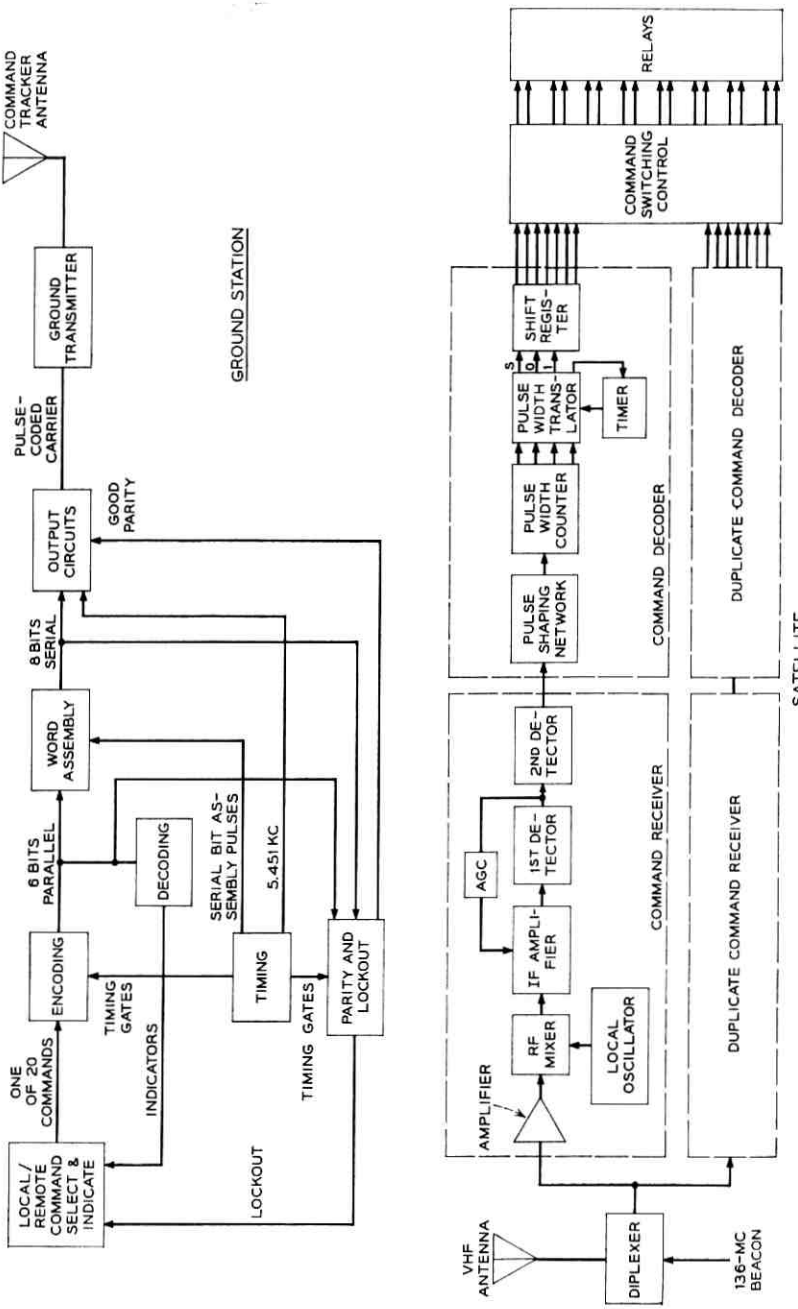

Fig. 6 — Command system block diagram.

ones. If an improper code is detected, a parity relay operates which in turn actuates the lockout circuit. The lockout circuit prevents transmission of the invalid code and selection of a new command until a reset button is depressed.

The word assembly output, if found to be proper, is applied to the output circuit five times in succession. In the output circuit the 8-bit word 100 per cent modulates a 5.451-kc carrier. This amplitude-modulated subcarrier signal is sent to the command transmitter where it 100 per cent amplitude modulates the 123-mc carrier and is then transmitted to the satellite via the quad-helix command tracker antenna.

For reliability, the command portion of the satellite (except for relays) is duplicated and is powered continuously. The two halves of the command system are nearly independent except for some interconnections made to insure proper operations under unusual circumstances. The signal from the diplexer is transformer-coupled to the two command receivers.

The command receiver is of the superheterodyne type and consists of an RF mixer, local oscillator, IF amplifier, AGC, and a two-stage detector. The receiver AGC obviates the need for a variable threshold in the command decoder.

The command receiver output is detected in the shaping network, which has a threshold level fixed at half the average signal amplitude.

The command decoder translates the baseband train of pulses which the receiver has recovered into a pulse on the appropriate one-out-of-fourteen output leads. The decoder consists of a pulse shaping network, pulse width counter, pulse width translator, timer, and shift register.

The one-out-of-fourteen outputs of the decoder are amplified and stretched in the switching units, and the resultant outputs trigger magnetic latching relays. Sensitive magnetic latching relays are employed to conserve power.

To prevent damage to the TWT and the battery of the satellite, a number of safety interlock features are incorporated in the command encoder on the ground and in the switching unit in the satellite.

The TWT anode turn-on (C command) cannot be sent unless three minutes have elapsed since the TWT filament was turned on (A command) and unless telemetry indicates that the filaments are actually on, except when an override push-button is depressed. The override feature is used to permit rapid turn-on of the tube when the 3-minute warm-up time is unnecessary (i.e., if the tube had just been turned off).

Whenever the A relay in the satellite transfers (TWT heater on or TWT off), the B relay (TWT helix and collector) is reset. This obviates the need for a BB command and prevents turning on the TWT helix and collector voltages prior to the TWT heater. The A and C relays are interlocked to assure that the TWT anode voltage (C relay) will be

turned off before the heater, helix and collector voltages are removed. These features prevent damage to the TWT.

A low-voltage trigger circuit removes all loads (except for the command system) and disconnects the battery by resetting the S relay. With the S relay reset, the 136-mc beacon is inoperative and no telemetry is available. The S relay reset state also inhibits the commands A, B, and C, thus preventing turn-on of the TWT with low battery voltage. If the S relay is reset by the low-voltage trigger, it cannot be set by a ground command (S) until the low-voltage condition subsides. This safety feature prevents damage to the battery and to the TWT due to a low-voltage condition which, for example, might be caused by leaving the TWT on for an excessive period.

6.2 *Ground Command System*

6.2.1 *Command Encoder*

A detailed diagram of the encoder is shown in Fig. 7. Operation of a command switch momentarily energizes a command select relay. The matrix input register stores this information temporarily until it is transferred (in the form of a parallel 6-bit code) to the matrix output registers. The use of two stores permits a new command to be selected without interfering with the transmission of the previous command.

The heart of the encoder is the crystal oscillator which furnishes the basic 5.451-kc subcarrier frequency to be used for code transmission. All of the encoder timing is generated from this frequency with countdown circuits. To insure proper timing accuracy in the frequency divider circuits, the oscillator output is applied to a Schmitt Trigger circuit

The N/3 countdown circuit of the cycle counter is of the relaxation divider type, whereas the N/2 countdown circuits consist of binary counter stages. The primary and secondary outputs from the final two binary counters, representing the zero and the one respectively of the ternary code, are applied to the logic I unit to obtain the start pulse and the bit duration. The one and zero are also applied to the parity counter gate. A parity count can be taken in AND gates since, as shown in Fig. 8, the coincidence of the eight code (excluding start) with ones and zeros can have three outputs if and only if the code contains only three ones and three zeros. (The parity enable eliminates the start pulse.) The start, zero, and one outputs control the duration of the outputs of the word timing gate.

A three-stage binary bit counter counts out the 8-bit code word, and feeds the logic II gate whose outputs are used for timing and for the

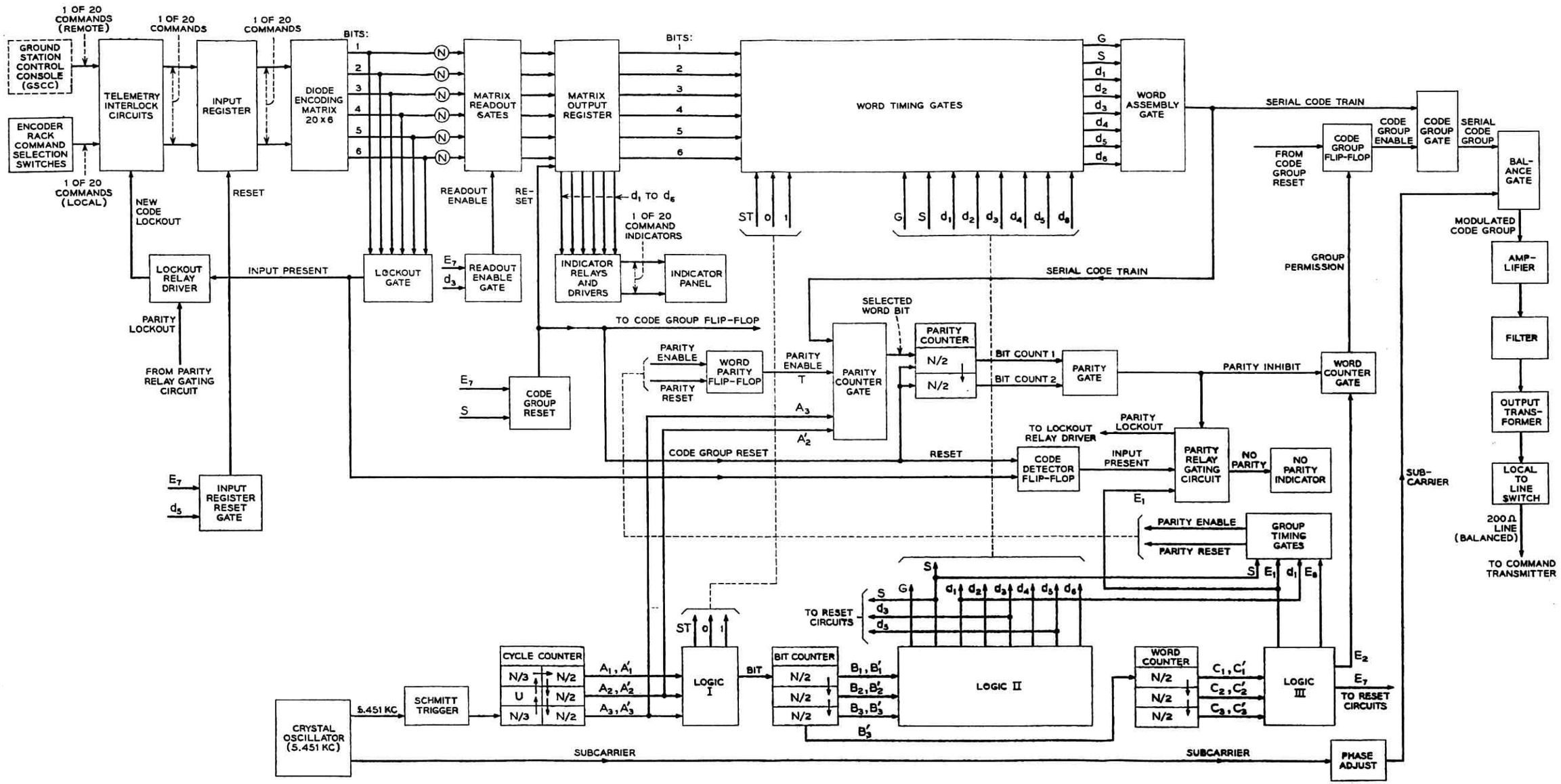

Fig. 7 — Command encoder.

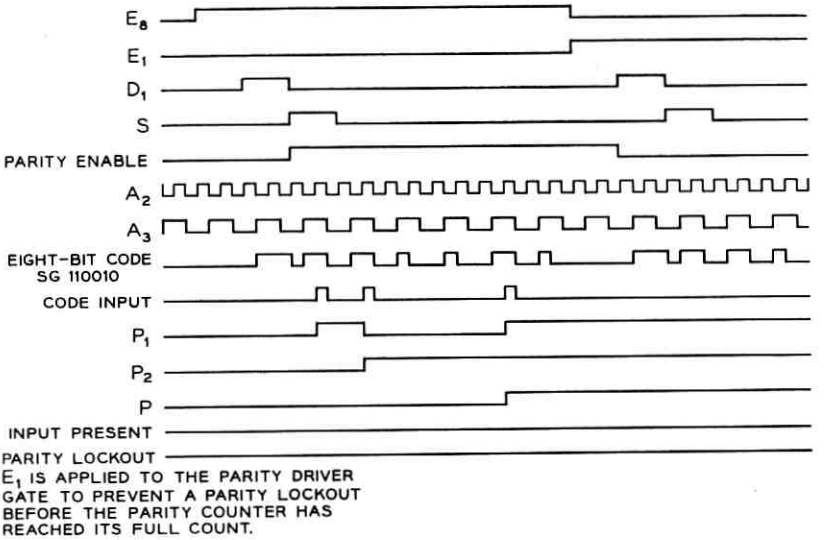

Fig. 8 — Parity count timing sequence.

parallel code to serial code conversion. The output of the third stage of the bit counter feeds the word counter, which in conjunction with logic III permits the code to be generated five times in succession. By the nature of the circuits, a gap of three word intervals follows the generation of the five code groups. Since the timing block of the encoder operates continuously, there can be a delay of about $\frac{1}{2}$ second in transmission of a command if a command is selected just after a word counter cycle has started. Partial code transmission is prevented by the parity and lockout, which can only operate once during a code group (five codes) and is initiated with the third code (dead interval).

6.2.2 *Command Transmitter*

The command transmitter consists of an RF exciter, intermediate power amplifier, modulator, RF power amplifier and an output section. The exciter generates the 123-mc crystal-controlled carrier which drives the intermediate power amplifier. The RF power amplifier then provides the power gain necessary to radiate 200 watts. The output stage is push-pull and is plate-modulated by the signal out of the modulator. The modulator is flat to ± 1 db from 200 cps to 10 kc and is capable of providing 100 per cent modulation of the 200-watt output. The output section provides coupling into the load, and matching trimmers and filters. The equipment is housed in two bays and was designed and man-

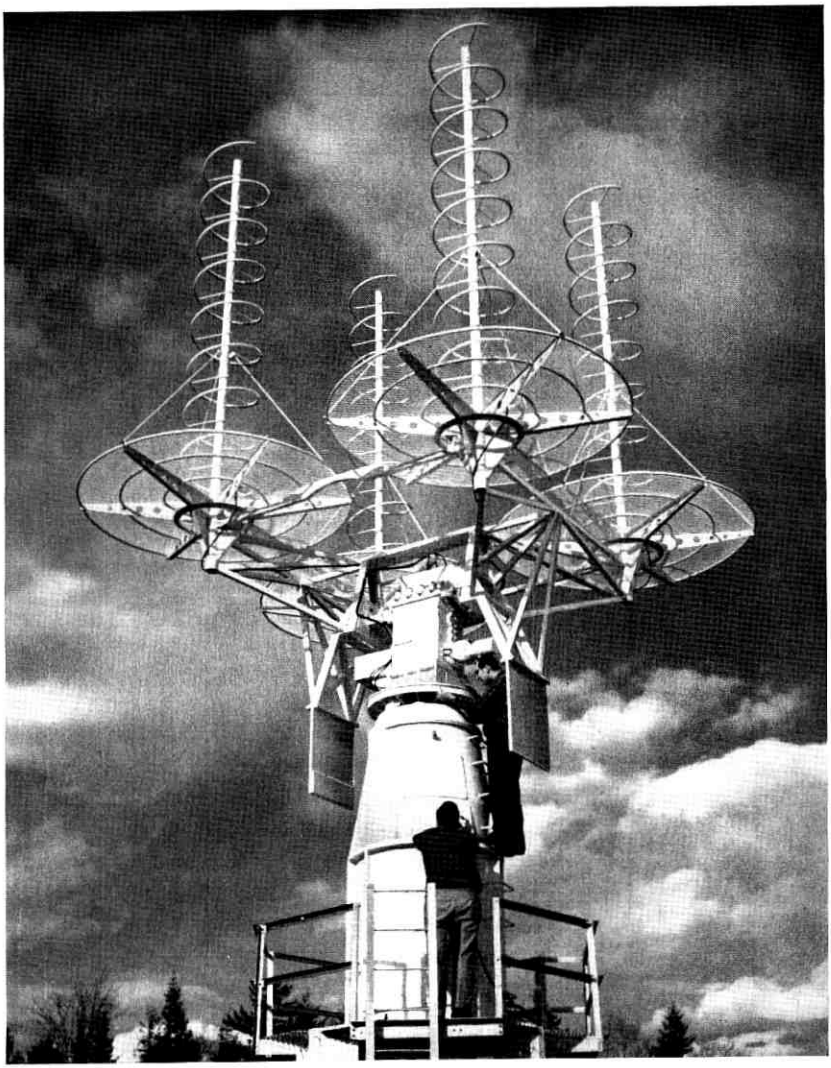

Fig. 9 — Command tracker antenna.

ufactured to Bell Telephone Laboratories specifications by Lockheed Electronics Company, a division of Lockheed Aircraft Corporation.

6.2.3 *Command Tracker Antenna*

The command tracker antenna shown in Fig. 9 is a quad-helix VHF antenna used to transmit the command signals, receive the telemetry

signals, and track the VHF beacon. The antenna has full autotrack capabilities, so the command and telemetry operation can be completely independent of other satellite operations. It can, however, serve as an acquisition aid by providing pointing information to other antennas, such as the precision tracker.[4] It uses phase-sensitive monopulse tracking employing a 4-element helix array and giving over-all pointing accuracy of approximately ± 1 degree.

As a transmitting antenna (123 mc) it has a gain of 17.5 db with right-hand circular polarization, and its side lobe levels do not exceed -11 db. For receiving at 136 mc, the gain is 19 db and the polarization and side lobe performance are the same as at 123 mc. The command tracker antenna was designed and built to Bell Telephone Laboratories specifications by Radiation, Incorporated, of Melbourne, Florida.

6.3 *Satellite Command System*

6.3.1 *Command Receiver*

Each of the two command receivers consists of an RF section, mixer, local oscillator, amplifier and detector. The two command receivers (See Fig. 10) are transformer coupled to the diplexer. The manner of making the connection places the loads in series, permits the use of ground for all returns, and provides the proper generator impedance for optimum noise figure.

The RF section provides 18 to 20 db of gain at 123 mc and has an over-all bandwidth of 3 mc (3 db points). This section consists of two stages separated by a low-Q parallel tuned circuit while the second stage has connected to its emitter a high-Q tuned series circuit. This combination provides a low over-all noise figure with at least 10 db image frequency rejection. The mixer is a single-stage amplifier employing emitter injection of the local oscillator while the RF signal is applied to the base. The conversion gain of the stage is approximately 4 db and the IF signal is at 5 mc. A temperature-stabilized crystal oscillator followed by two diode doubler circuits provides the local oscillator signal of 128 mc for the mixer.

A 4-stage IF amplifier provides 50-80 db of gain, depending upon the AGC control. AGC control is maintained on the first three IF stages and provides a constant detected output level over a 30 db range of receiver input signals. Primary-tuned interstage coupling transformers provide an IF bandwidth of approximately 50 kc (3 db points), which allows for Doppler shifts and transmitter and receiver frequency drifts.

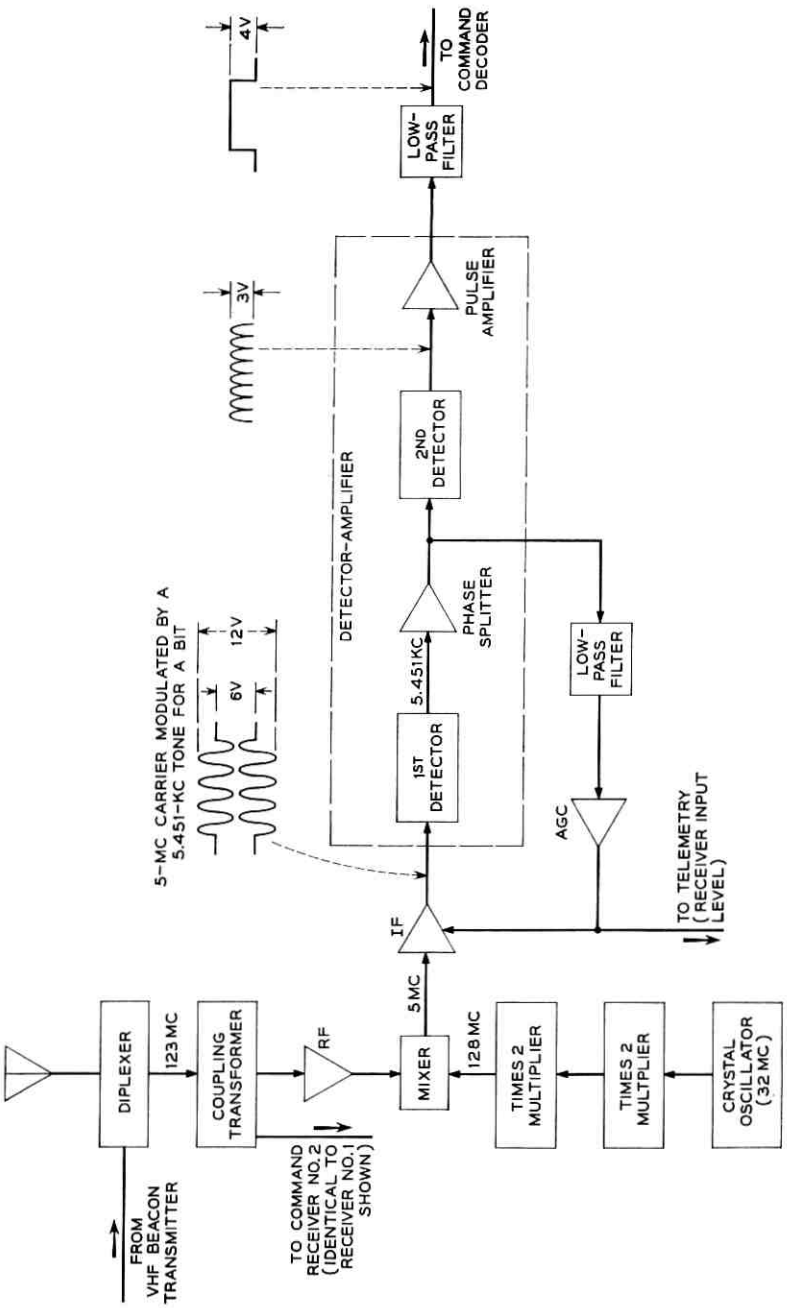

Fig. 10 — Command receiver.

Because of the use of a subcarrier, double detection is necessary. The first detector recovers the 5.451-kc subcarrier. An amplifier supplies a signal to the AGC loop and to the second detector, which consists of a full-wave rectifier followed by an amplifier and a low-pass filter, having a 500-cps cutoff with a 6 db per octave slope. The output signal is a train of pulses having an amplitude between 4 and 4.5 volts and containing less than 1 db of ripple.

6.3.2 *Command Decoder*

A simplified block diagram of the command decoder is shown in Fig. 11 and the timing relationships are shown in Fig. 12. The command receiver output signal is detected in the shaping network. Because the receiver has AGC, the shaping network threshold level is fixed at the average-signal, half-amplitude value. The detected signal permits the gated multivibrator pulse generator to free run for the length of time that the signal exceeds the threshold level. The pulse generator will generate three, two, or one pulse(s) for a start, one, and zero input respectively. The output of the shaping network is also used for readout and reset functions. The pulse width counter and digit gates (zero, one and reset) translate the ternary code to a pulse on one of three output leads. The counter and gates are "reset" by the detected signal. To prevent the inadvertent joining of two code fragments, a consecutive pulse timer controls the one and zero gate outputs. The loss of a word bit resets the timer, thus preventing further one and zero gate outputs. Because of the positive feedback aspects of this circuit, the timer inputs are controlled by the shaping network output.

A detected start pulse at the R gate output is used to reset the flip-flop stores and the digit counter. It also starts the consecutive pulse timer. The combined zero and one outputs drive the digit counter. The digit counter and the counting gates form a series-to-parallel converter for the detected ones. With the inclusion of the flip-flop stores, the combination forms a shift register. The output gates translate the stored binary code to an output pulse on one-of-fourteen leads. To restrict power consumption and to control the output gate readout time, a strobe unit applies power to these gates. The strobe, in turn, is controlled by the digit counter and will generate an output when the digit counter has counted to six. Since the strobe is internally ac coupled, the power to the gates is applied for only a few milliseconds.

To permit disabling of a decoder, the strobe ground can be removed by sending a ground command through its companion decoder. Each decoder can be disabled for approximately 15 seconds by sending the

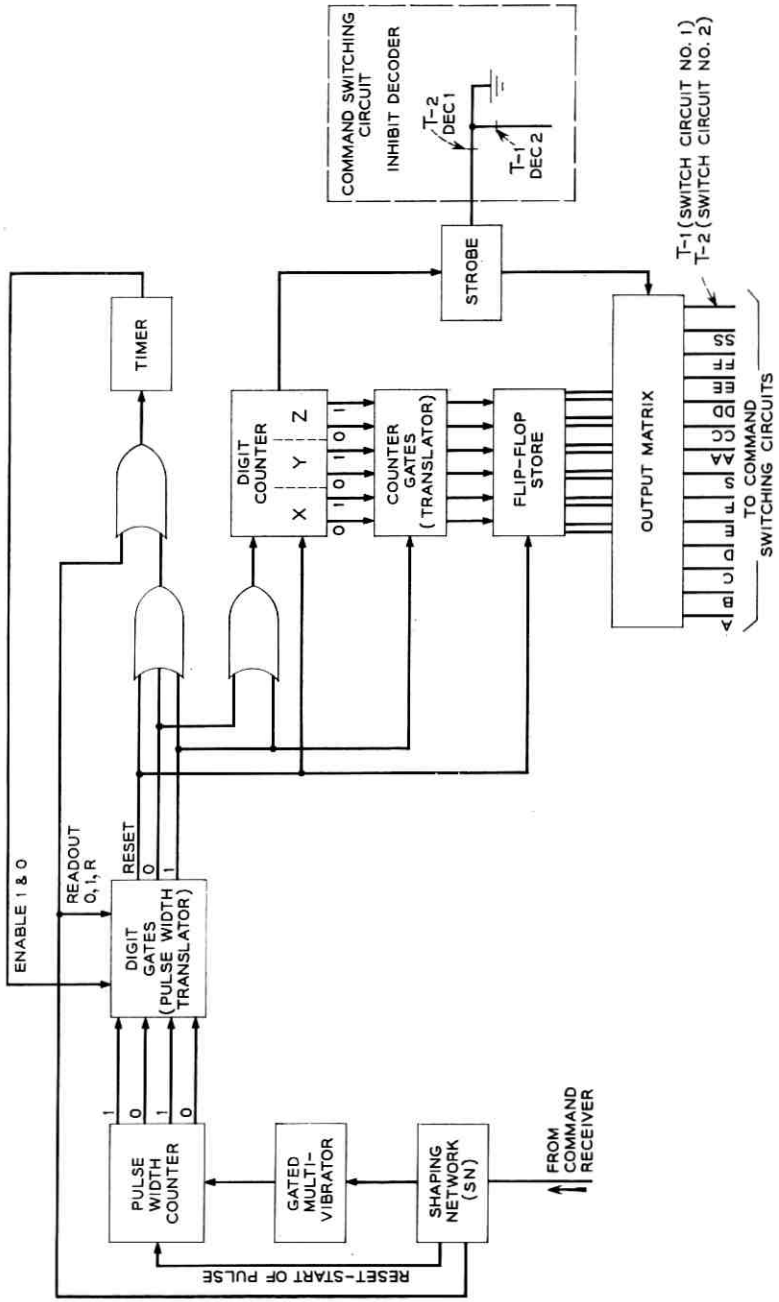

Fig. 11 — Command decoder.

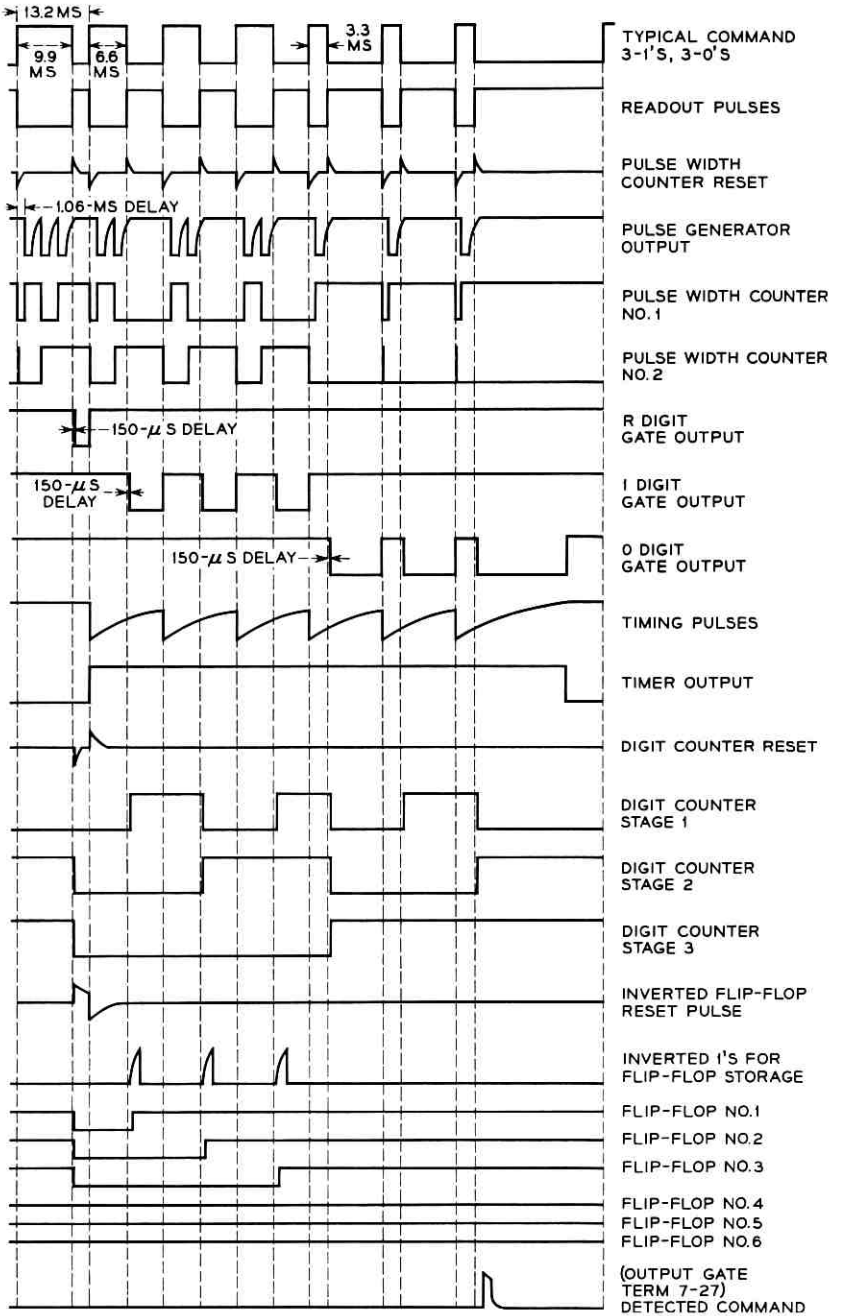

Fig. 12 — Command decoder waveforms.

appropriate (T) command to the other decoder. Thus, if a decoder is detecting a command falsely, it can temporarily be removed from service.

6.3.3 *Command Switching Unit*

The switching unit (Fig. 13) is subdivided into two parts. Each channel performs the same function, thereby providing two separate paths for command execution (except for the T-1 and T-2 commands). Monostable multivibrators provide the necessary amplification and pulse stretching. Driver outputs are combined in OR gates to activate each relay. Single letters designate "set" operations while double letters designate "reset" operations.

As mentioned previously, the S relay is a safety device. Although it can be set and reset by ground command, it can also be reset by the low-voltage trigger circuit. Whenever the battery supply reaches 19.6 volts $\pm$ 0.4 volt, the low-voltage trigger circuit responds, thereby triggering the SS driver. Resetting of the S relay resets all other relays except the F (choice of telemetry encoders) and removes ground command control from the A, B, and C relays. The S relay cannot be prematurely reset while the low-voltage condition persists. These features are incorporated to avoid damage to the battery and the TWT.

To avoid permanently disabling the satellite because of failure of a single low-voltage trigger circuit, an override feature is incorporated. The T-1 and T-2 relays inhibit the operation of the SS-2 and SS-1 drivers, respectively, thus permitting the S relay to be set by command during the 15 seconds deactivation of the faulty trigger circuit. Since T-1 and T-2 cannot be transmitted simultaneously, overriding of a legitimate low-voltage condition cannot occur.

VII. TELEMETRY SYSTEM

7.1 *Over-All Description of Telemetry System*

In the satellite, the signals to be telemetered are time multiplexed by sampling gates, encoded into PCM, frequency modulated on a 3-kc subcarrier, amplitude modulated on the 136-mc beacon, and radiated to the earth by the VHF antenna. On the ground, the signal is picked up by the VHF command-tracker antenna, amplified, and amplitude detected; then frequency discriminated to recover the PCM, decoded, and decommutated; and fed to a printout, punch-out, and various displays.

Figs. 14 and 15 show in block diagram form the principal functional

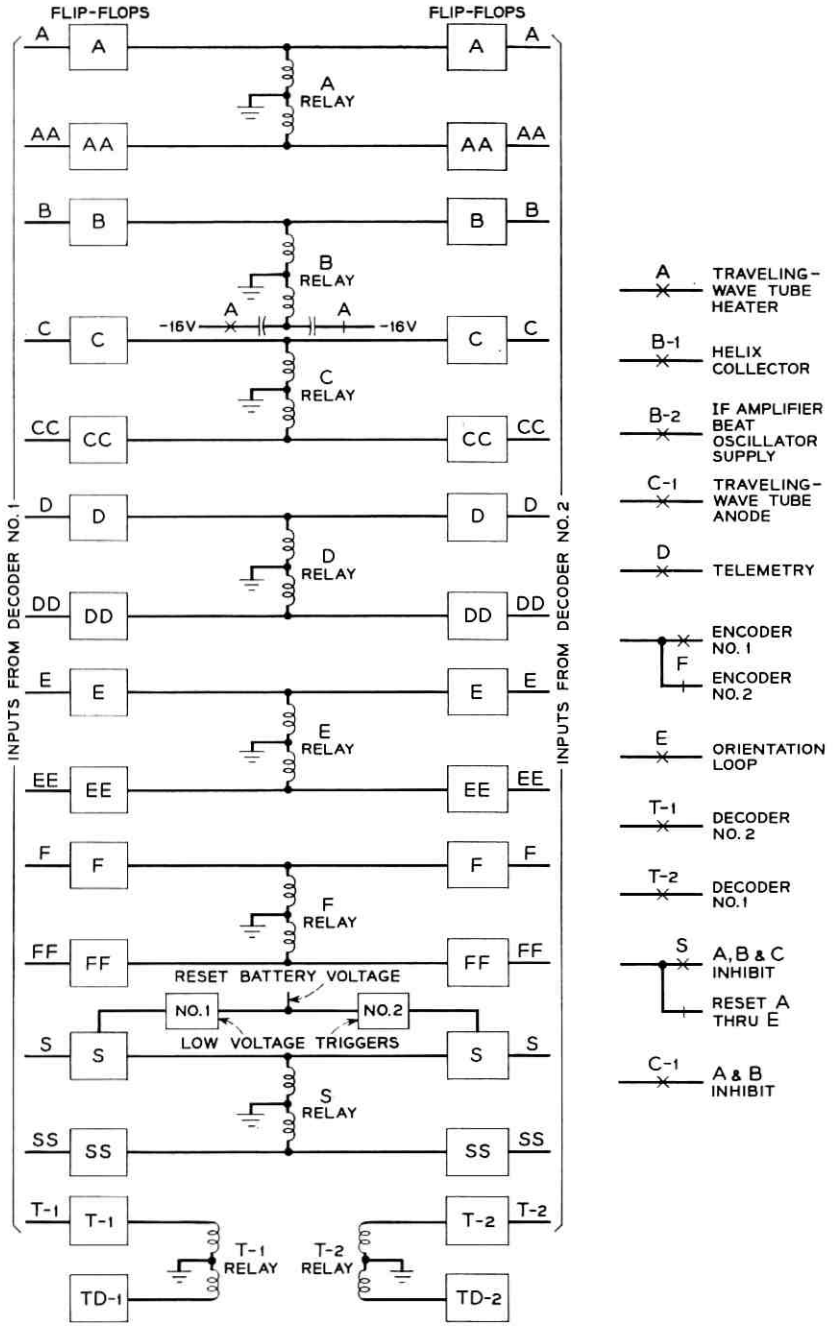

Fig. 13 — Command switching unit.

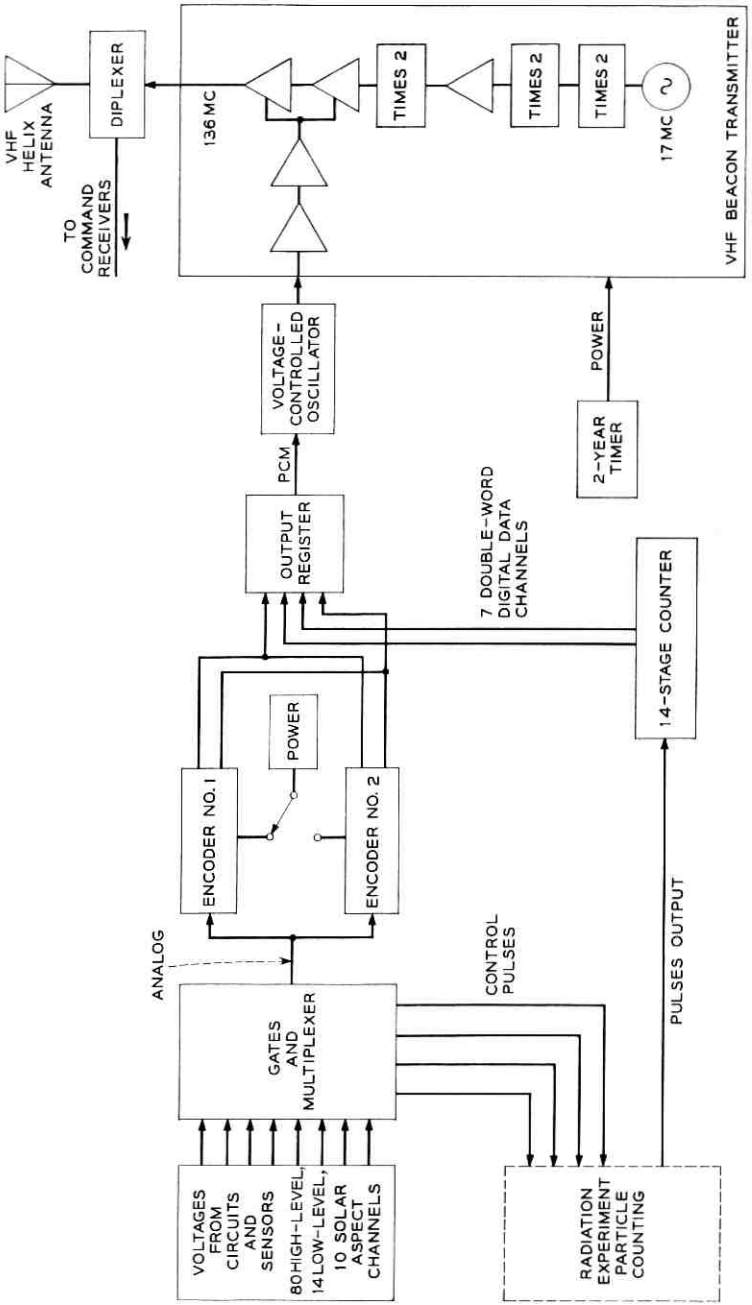

Fig. 14 — Satellite telemetry system.

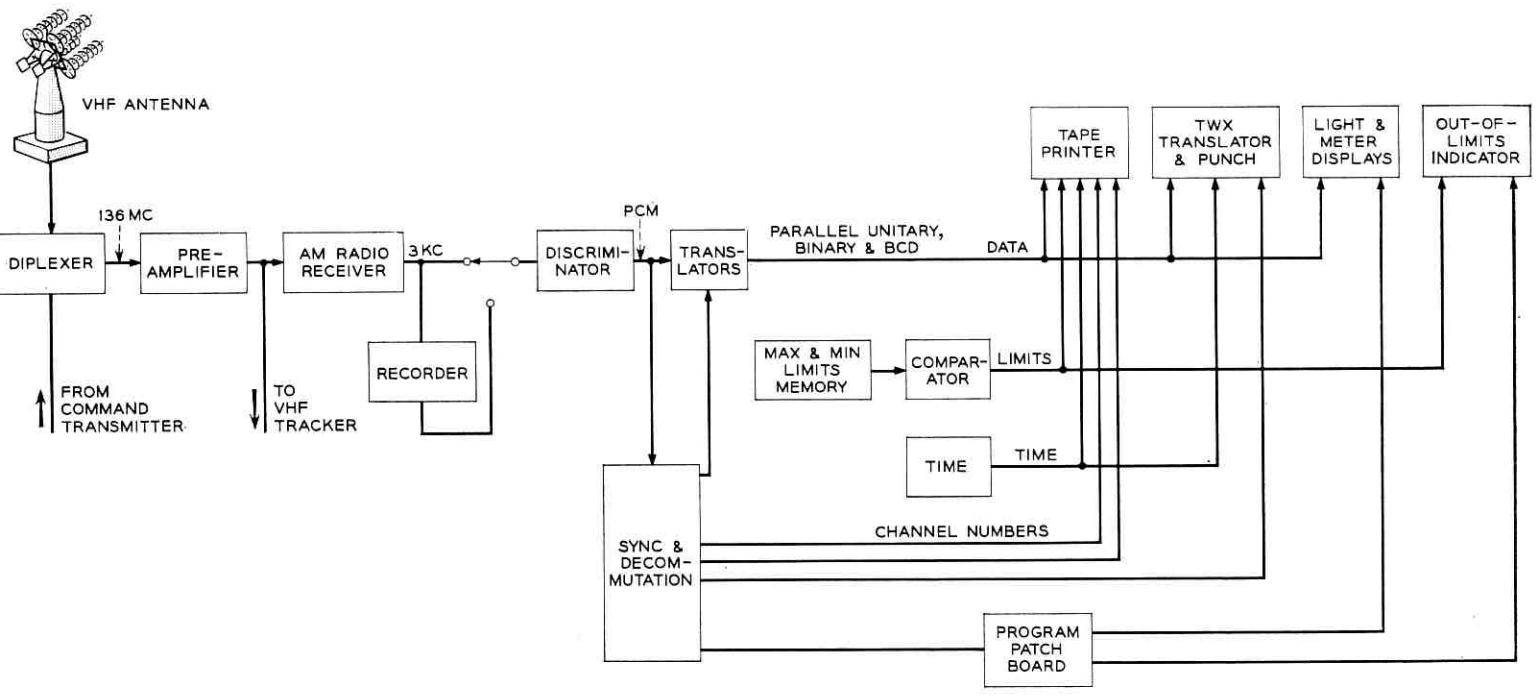

Fig. 15 — Ground telemetry system.

portions of the satellite and ground telemetry systems, respectively. For the satellite system, the portion of the circuit including multiplexer, redundant coders, registers, and voltage-controlled oscillator was developed and constructed for Bell Laboratories by Radiation, Incorporated, of Melbourne, Florida. The ground telemetry, except for the antenna and preamplifiers which are part of the VHF tracker, was supplied by Electro-Mechanical Research, Incorporated, of Sarasota, Florida.

7.2 *Types of Information Telemetered*

The information telemetered falls into several categories as listed in Table II.

The radiation experiment is discussed in detail in another article in this issue.[5] Of the telemetry channels, 16 are used for electron and proton energetic particle counts, 4 for bias of counting detectors, 7 for transistor damage, 4 for solar cell damage, and 6 for solar aspect. In addition to handling the count or measured values of the radiation experiment, the telemetry circuit also provides synchronized pulses for gating on and off the particle-counting circuits and for shifting their thresholds.

Internal temperatures are measured at a number of points in the electronics canister. These are distributed throughout the structure to give both a general temperature picture and to follow certain items of special interest such as battery and traveling-wave tube temperatures. External temperatures are measured at strategic points just under the outer skin and at points associated with the radiation experiment.

TABLE II — TELEMETERED INFORMATION

	Number of Channels
Radiation experiment	37
Internal temperatures	24
External temperatures	16
Microwave circuit	13
Power supply	9
Relay states	4
Command system	6
Canister pressure	2
Calibration	1
Frame synchronization	2
Unassigned	6
Total	120

Various items of the microwave circuit that are monitored via telemetry include the traveling-wave tube accelerator, collector and helix currents, the TWT heater voltage, converter biases, and the IF amplifier AGC. These are of special interest both for the operational control and for the monitoring of performance of the communications repeater. Of the power supply items monitored, perhaps the most important are the solar plant current and the battery voltages. Also monitored are key voltages of the regulator.

Command relay state monitoring is important from an operational standpoint in checking the turn-on and turn-off steps for the traveling-wave tube, the status of the torquing loop, and monitoring the responses to two special commands, T-1 and T-2. Both input and output signals of the command receiver pairs are monitored.

Canister pressure is checked to see whether it is above or below discrete levels of 5 and 1 psia.

7.3 *Types of Telemetry Channels*

To handle the various items to be telemetered, several ranges and types of channels have been employed as listed in Table III.

Where possible, high-level channels were employed. Low-level channels were employed for small signals and differential inputs. The solar aspect channels, in addition to being still more sensitive, are sampled quasi-simultaneously. The digital data channels are for the radiation experiment energetic particle count where the input consists of pulses to be counted. In all cases, the channels are sampled once every minute and converted to binary PCM for transmission.

7.4 *Satellite Telemetry Sending System*

7.4.1 *Sensors*

Except for the so-called digital data channels of the radiation experiment, all the items to be telemetered are first converted to voltages

TABLE III — TYPES OF CHANNELS

Number	Type of Channel	Input
80	High-level	0 to −5 volts analog
14	Low-level	0 to −0.5 volt analog
10	Solar aspect	0 to −0.1 volt analog
14	Digital data (7 pairs)	0 to 16,383 pulses
2	Frame synchronization	

which are subsequently converted to PCM by the encoder. In some cases the analog signal is simply an existing voltage, such as a bias, or a rectified wave, derived directly from the circuit to be monitored. In other cases, transducers or sensors such as thermistors or pressure switches and auxiliary circuits are used to convert the physical quantity to be measured, such as temperature or pressure, to a dc analog signal.

7.4.2 *Multiplexer*

Each analog signal to be telemetered is sampled through sampling gates once every minute and its value encoded into a seven-bit binary code. Channel gates are matched pairs of transistors that are pulsed on in proper channel sequence by transformers of the multiplexer matrix. The 8 × 14 matrix of square-loop magnetic core transformers is driven by horizontal and vertical shift registers and control counters which, in turn, are driven at the word rate. Basic timing at word and bit rate is obtained from a 32-cps oscillator and counters.

In addition to controlling the channel sampling gates, the multiplex matrix also provides timing pulses for the control of the radiation experiment, synchronized with particular word positions. Internal telemetry circuit commands tied to the channel format are also derived from the matrix.

Multiplexing of the solar aspect channels is accomplished by a separate multiplexer operating at high speed in order to effect quasi-simultaneous acquisition of the data. For this, a blocking oscillator, triggered by the main multiplexer, drives a counter and diode matrix which, in turn, drives the transformer-coupled transistor gates.

High-level channel output of the matrix is fed directly to the encoder. Low-level channel output is fed through a 10:1 amplifier and solar aspect channel output is fed through a 50:1 amplifier before going to the encoder. Thus, in all cases, the analog input signals leaving the multiplexer are adjusted to a common 0 to −5 volt range for the encoder to handle.

7.4.3 *Encoders*

To improve reliability, two encoders have been incorporated in the system. Either encoder can be put in operation by ground command (F or FF). The timing circuit oscillators, which are closely linked to the encoders, are also redundant.

For normal high- and low-level channels, each analog signal is sampled once per minute at a rate of one channel each half second. The encoding of each analog signal is accomplished in approximately 50 μsec.

Through consecutive half-amplitude comparisons, the signal is encoded into a 7-bit binary code representing the input signal to an accuracy of ± 1 per cent of full scale range for high-level channels and ± 2 per cent for low-level channels. Thus, each channel input signal is quantized into a code representing one of 127 levels. The binary-coded information is stored in the output register for readout. A word sync pulse is added at the end of the 7 information slots, resulting in an 8-bit word which is then read out at the normal transmitting rate of 16 bits per second.

To conserve power, the encoders are energized in a pulsed-power mode for approximately 170 μsec during each word time.

For solar aspect and solar cell damage measurement, however, essentially simultaneous sampling of ten channels is required. Practically, this has been accomplished by sampling and encoding all ten of these channels in 1100 μsec, during which time the satellite will have rotated approximately one degree. The ten encoded signals are stored in the output register matrix until they are read out at the uniform output rate of 16 bits per second, or one word per half second.

7.4.4 *Digital Data Channels for Radiation Experiment*

Another article[5] in this issue discusses the radiation experiment particle count circuitry. The telemetry system is linked with that circuitry by supplying to it timed control pulses for turning on and turning off various gates and biases at the appropriate times relative to the telemetry frame progression. The result of this is that the particle experiment pulse groups to be counted and telemetered are time multiplexed into seven different time intervals and are fed to a 14-stage counter. Seven times in the course of each frame, corresponding to the seven digital data channel pairs, the 14-bit digital data counter is read in parallel form into the output register, from which the data are read out sequentially as two adjacent channel words. Each pair of these digital data channels can handle pulse counts ranging from 0 to 16,383.

7.4.5 *Output Register*

The sampling, encoding or counting of channel data takes place at several different rates. In order to transmit it at a uniform rate, an output storage register is used. This register has 10 rows and 7 columns of square loop magnetic cores appropriately interconnected with read-in, set, shift and read-out windings. In all cases the final serial read-out for transmission is taken from the top row (row 10). High-level and low-level

data are read into the top row on the completion of encoding. The ten solar aspect channels are read into the bottom row (row 1) one word at a time and shifted upward, filling the register in approximately 1100 μsec. The data are then read out of the top row at the normal read-out rate, shifting the stored words up at word rate. Digital data counts from the 14-bit register are read into rows 8 and 9, which are subsequently shifted up for read-out.

Synchronization information is introduced into the format in the output register. A word sync pulse is added at the end of each group of seven information bit time slots, giving an 8-bit word length in which the most significant bit comes first. Frame synchronization is introduced by putting out an invariant train of pulses in the 16 time slots of the last two word slots of each frame. This pattern of frame sync pulses is read into rows 8 and 9 of the output register by energizing set windings on the appropriate cores. The frame sync words are then shifted up and read out in the normal fashion.

7.4.6 *Voltage-Controlled Oscillator*

The resulting output train of pulses from the output register is sent to the voltage-controlled oscillator (VCO) where it is converted into a frequency modulated signal. The voltage-controlled oscillator is a 3-kc oscillator in which frequency is changed by switching in and out an incremental capacitance in the tank circuit. For a zero bit the frequency stays at 2775 cps for the full one-sixteenth of a second. For a one bit, the frequency is shifted up to 3225 cps for one thirty-second of a second and returned to 2775 cps for the remaining half of the bit time slot.

7.4.7 *VHF Beacon*

The 136-mc beacon has the dual functions of providing a signal for tracking at VHF and serving as the RF carrier for the telemetry 3-kc subcarrier. The beacon can be turned off and on by ground command (S), but it is normally kept on at all times, regardless of the state of telemetry. The beacon will also be shut off automatically if the satellite battery voltage drops below a predetermined low-voltage danger point. Power for the beacon is drawn through contacts of a precision timer which will automatically and irrevocably shut off the VHF beacon at the end of two years. This latter feature is to keep the satellite from indefinitely occupying this spot in the radio frequency spectrum.

The 136-mc frequency is produced by starting with a crystal oscillator

at 17 mc and multiplying successively by factors of two. The crystal is a third-overtone AT-cut quartz unit having a ruggedized mount and is used in a Pierce oscillator circuit using the transistor in a common emitter configuration and operating the crystal as a positive reactance at a frequency slightly above series resonance. Initial frequency adjustment was within ± 1 part per million. Frequency variation with temperature over the anticipated range is less than $\pm \frac{1}{4}$ part per million, and aging is expected not to exceed 1 part per million.

The oscillator is followed immediately by two stages of doublers in which the transistors in common emitter mode are operated as class C amplifiers into collector tank circuits tuned to the second harmonics. Following this is a buffer amplifier and the last stage of multiplication, in which a transistor with common emitter is operated class C into a second harmonic tuned tank, thus producing the final desired frequency of 136 mc. Next, the power level is raised by a driver stage using a common base transistor. Final amplification is obtained in a power amplifier using a transistor in a common base configuration. All stages of the circuit are transformer coupled.

The frequency modulated 3-kc subcarrier from the telemetry VCO is fed to a driver stage and thence to a power amplifier using a pair of transistors in common emitter push-pull. This signal is fed to the collectors of the driver and power amplifier stages of the beacon, producing 50 per cent modulation of the carrier. The signal is then fed to the diplexer which connects the VHF helix antenna to both the beacon and the command receiver while providing isolation between them. The signal is radiated approximately isotropically and linearly polarized from the antenna at a level of 250 milliwatts.

7.5 *Ground Telemetry Receiving System*

7.5.1 *Antenna and Diplexer*

On the ground, the 136-mc signal is picked up by the command tracker antenna. This is a circularly polarized antenna; hence, effective signal strength is not dependent on the orientation of the linearly polarized wave from the satellite. From the antenna the signal goes to the diplexer which permits the use of the single antenna for simultaneous transmitting and receiving purposes without interference. From there, the incoming signal goes to a preamplifier with a noise figure of 3.5 db. The total effective gain of the ground system to this point, including antenna gain, diplexer, and cable losses, is 18 db.

7.5.2 *Preamplifier, Receiver, Discriminator, and Recorder*

After preamplification, the signal goes from the antenna pedestal to the telemetry radio receiver, which recovers the 3-kc subcarrier by AM detection. The 3-kc signal is then fed to a phaselock discriminator which recovers the original pulse train PCM signal. The subcarrier is also fed to a magnetic tape recorder which serves as a back-up to make possible the recovery of telemetry data at a later time in the event of a failure in the ground system beyond this point. The tape can be played back into the discriminator and processing continued in the normal fashion should this be necessary.

7.5.3 *Synchronizer, Translator, and Decommutator*

From the discriminator, the pulse train goes to the synchronizing, translating, and decommutation equipment. Bit rate, word sync, and frame sync are sought and recovered, synchronizing the rest of the equipment. This takes place automatically, progressing from a search mode to a tentative sync or check mode, to a full sync mode. In the event of loss of sync, the circuit automatically reverts to the next lower mode in order to effect recovery. Adjustable controls permit presetting of sync error rate limits at which this reversion takes place. Thus, if desired, the equipment can, in effect, be programmed to accept limited numbers of errors and tide synchronization over temporary fading or interference. After synchronization, the signal is decoded or translated into forms suitable for the several read-out options. Channel numbers are generated in step with the data, and strobing pulses are made available to decommutate the data into selected channel readouts.

7.5.4 *Print-out*

All channels are printed out sequentially with data and corresponding channel number by a Hewlett Packard tape printer. Time is also printed on this record at the spot where the frame sync words would appear (channels 119 and 120). The data read-out is virtually a real time read-out, being delayed by approximately one and one-half seconds. It serves as the primary source of information on all channels.

7.5.5 *Data Limits*

When a channel value is either above or below preset limit values, an out-of-limits mark is printed next to the data. Both maximum and mini-

mum limit values can be set up in a plug board memory for each of the 118 channels individually. The values are set in binary code with plug-in diodes.

7.5.6 *Teletypewriter Punch*

All channel values are also punched in teletypewriter tape, along with appropriate format information to give a page print-out. The teletypewriter tape can be read out and transmitted to other locations either immediately or at a later time.

7.5.7 *Light and Meter Displays*

In addition to the all-channels printed displays, there are also a limited number of binary light displays, analog meter displays, and decimal light displays which can be connected to any of the channels. The choice of channels to be displayed is set up on a program patch board. Out-of-limits relays for remote indicators and command interlock are also connected to the desired channels by means of this program board.

7.5.8 *Operational Considerations*

In the normal mode of operation, the numeric print-out tape is used by an operator to monitor all channels. Commands are marked on the tape at the channel times corresponding to their transmittal by the operator. Remote indicators at the ground station console display the states of the TWT (A, B and C commands) relays as deduced by telemetry. Operating decisions are made with the help of telemetry data thus supplied.

In addition to the VHF ground facilities at the Andover, Maine, station the command and telemetry ground equipment is duplicated at the Bell Laboratories station at Cape Canaveral. The Cape facilities were, of course, used for prelaunch and launch operations and are now used for monitoring of passes. A third telemetry bay, located in New Jersey, was used for satellite manufacturing testing. This bay has modifications which permit it to decommutate magnetic tape recordings at speeds four and eight times real time, and this facility is used to process telemetry subcarrier recordings made by Minitrack stations.

By means of audio tie-lines and teletypewriter lines, the telemetry facilities at these three locations may be interconnected in various ways to provide mutual back-up.

7.6 *Performance*

The telemetry system has been used in the satellites at all stages of its life: during manufacturing tests, launch operations, and in orbit. Thus far, it has been performing normally and is supplying the desired data.

VIII. ACKNOWLEDGMENTS

As is usual on a project of this magnitude, the work represents the combined efforts of a large number of people, with key roles played by so many as to make individual listings difficult. The authors of this article have been fortunate in being a part of the team and wish to thank all who have had any part in making this work successful.

REFERENCES

1. Bomberger, D. C., Feldman, D., Trucksess, D. E., Brolin, S. J., and Ussery, P. W., The Spacecraft Power Supply System, B.S.T.J., this issue, p. 943.
2. Bangert, J. T., Englebrecht, R. S., Harkless, E. T., Sperry, R. V., and Walsh, E. J., The Spacecraft Antennas, B.S.T.J., this issue, p. 869.
3. Hogg, D. C., and Mumford, W. W., The Effective Noise Temperature of the Sky, The Microwave Journal, **3**, Number 3, March, 1960, pp. 80–84.
4. Githens, J. A., Kelly, H. P., Lozier, J. C., and Lundstrom, A. A., Antenna-Pointing System: Organization and Performance, B.S.T.J., this issue, Part 2.
5. Brown, W. L., Buck, T. M., Medford, L. V., Thomas, E. W., Gummel, H. K., Miller, G. L., and Smits, F. M., The Spacecraft Radiation Experiment, B.S.T.J., this issue, p. 899.

The Ground Transmitter and Receiver

By A. J. GIGER, S. PARDEE, JR. and P. R. WICKLIFFE, JR.

(Manuscript received March 22, 1963)

Ground station equipment for the Telstar experiment includes a 6-kmc transmitter and a 4-kmc receiver used for television and telephone channels. This paper describes the over-all transmitting and receiving arrangements and presents detailed accounts of the RF and power-supply subsystems. Information is also presented on protection, control and equipment features, and on receiver noise performance.

I. TRANSMITTER

1.1 *General*

The Telstar ground transmitter is designed to produce a 2-kw frequency-modulated signal in the 6-kmc band, suitable for the transmission of television or multiplex telephony. Fig. 1 is a simplified block diagram which shows the basic features of the four sections of the transmitter: FM deviator, modulator-amplifier, transmitter carrier supply, and power amplifier. The Telstar transmission objectives[1,2] are similar in many respects to those established for domestic microwave radio relay systems. As a result, it has been possible to use in the Telstar transmitter many pieces of equipment designed for that service. The FM deviator, modulator-amplifier and transmitter carrier supply are direct adaptations of units currently being manufactured for the 6-kmc TH radio relay system.[3,4,5] The power amplifier is designed around a 2-kw traveling-wave tube[6] developed at Bell Telephone Laboratories.

1.2 *Design Considerations*

Table I summarizes the transmission objectives established for the ground transmitter. These are derived from system objectives based, primarily, on one-way transmission of monochrome television and 600-channel multiplex telephone. Simultaneous two-way transmission through the satellite, together with its restricted AGC range, deter-

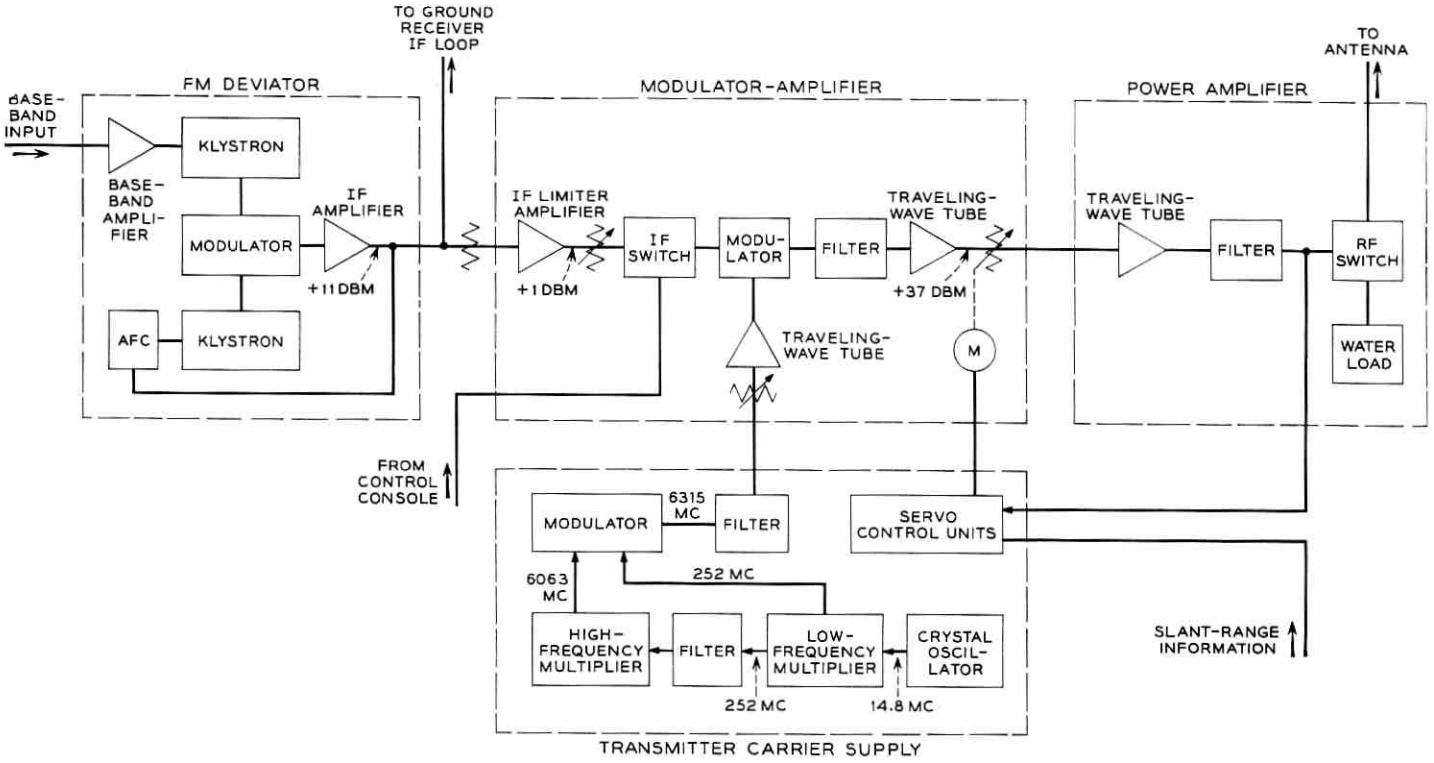

Fig. 1 — Block diagram of the ground transmitter.

TABLE I—TRANSMISSION OBJECTIVES, GROUND TRANSMITTER

Baseband response	2 cps to 5 mc
Peak frequency deviation	10 mc
RF and IF bandwidth	32 mc at 1-db points
Output power	2 kw, continuously variable from 2 kw to 0.02 kw
Center frequency:	
TV and 600-channel telephone	6389.58 mc
12-channel two-way telephone	6384.58 or 6394.58 mc
Frequency stability:	
FM deviator	
without modulation	±50 kc
with modulation	± [50 kc + 0.1 (rms frequency deviation)]
Transmitter carrier supply	±60 kc

mined the need to control the transmitter output. For 12-channel two-way telephony,* it is particularly desirable that the 6-kmc signals at the satellite be independent of slant range.

Operating practices are patterned after those established for domestic radio relay systems. Maintenance procedures, based on the use of standard Bell System test equipment,[7] enable all testing to be performed with the transmitter disconnected from the antenna. In addition, extensive alarm and control circuits have been incorporated in the transmitter to permit continuous, unattended operation.

1.3 *Description*

1.3.1 *General*

In this section the signal is traced through the transmitter; the following sections discuss the individual units of the transmitter in greater detail. Referring to Fig. 1, frequency modulation is generated by applying the television or multiplex telephone signal to the repeller of a reflex klystron. A 1-volt peak-to-peak signal at the 124-ohm balanced input to the baseband amplifier produces a peak deviation of 10 mc. The resulting frequency-modulated microwave signal is translated to the required intermediate frequency by combining it with the output of a second reflex klystron in a modulator. The output of the modulator, corresponding to the frequency difference of the two inputs, is the desired frequency-modulated IF signal. For television or 600-channel multiplex the center frequency is 74.13 mc; for 12-channel two-way multiplex it is 69.13 or 79.13 mc. Shifting the center frequency of the

* Twelve two-way channels is the number selected for this experiment and does not necessarily represent the capacity of the system.

FM deviator plus or minus 5 mc is a convenient means of obtaining either of the two transmitter frequencies required for two-way telephony. At the output of the wideband IF amplifier that follows the modulator, the signal power is +11 dbm. The automatic frequency control circuit samples the output and adjusts the repeller voltage of the second klystron to maintain a constant average output frequency.

In the modulator-amplifier the FM signal initially passes through an IF limiter, which removes any amplitude modulation, and then through an IF switch to the transmitter modulator. The controls of this high-speed switch are connected to the protective circuits in the power amplifier as well as to local and remote operating positions. In the modulator the IF signal is translated to the required RF frequency. The filter following the modulator permits only the signal corresponding to the sum of the frequencies of the IF signal and the 6315-mc output of the transmitter carrier supply to be amplified in the medium-power traveling-wave tube (TWT). At the output of this TWT the signal power is +37 dbm. The motor-driven waveguide attenuator at the output of the modulator-amplifier determines the input to the 2-kw traveling-wave tube in the power amplifier. The attenuator is part of the servo loop that varies the output of the ground transmitter to compensate for the changes in free-space path loss with satellite range. The filter following the 2-kw traveling-wave tube offers approximately 50 db suppression to second harmonic signals in the output. The waveguide switch and water load are part of the test facilities built into the power amplifier.

1.3.2 *FM Deviator*

The FM deviator is an adaptation of the FM terminal transmitter[5] designed for the TH radio relay system. The TH terminal transmitter is characterized by a 4-mc peak deviation capability, a 10-mc baseband response, excellent linearity, and an IF bandwidth of 32 mc. Increasing the gain of the original baseband amplifier was the only change required in the signal path to extend the peak deviation capability to 10 mc. Even at this increased deviation, the linearity of the Western Electric 450A reflex klystron, designed especially as a deviation oscillator for the TH FM terminal transmitter, is more than adequate to meet Telstar objectives. With a required baseband response of only 5 mc, it was possible to realize the additional baseband gain by simply increasing the interstage impedances in that amplifier.

While the basic method of automatic frequency control used in the TH equipment has been retained, increasing the peak deviation to 10

mc has necessitated extensive modifications in the AFC circuits. Requiring the FM deviator to operate satisfactorily with television signals for 405-, 525-, and 625-line systems further complicated the problem.

Referring to Fig. 2, the average frequency of the deviator output is compared with the frequency of a crystal-controlled oscillator. The AFC IF amplifier and the reference oscillator are alternately gated off-and-on at an $18\frac{1}{3}$ cps rate. (The reason for selecting this particular frequency will be discussed later in this section.) During one half of the gating period only the deviator output is effectively connected to the AFC discriminator; the dc output of the discriminator is proportional to the difference between the average frequency of the deviator and the center frequency of the discriminator. During the other half the reference oscillator is connected to the discriminator, and the dc output is then proportional

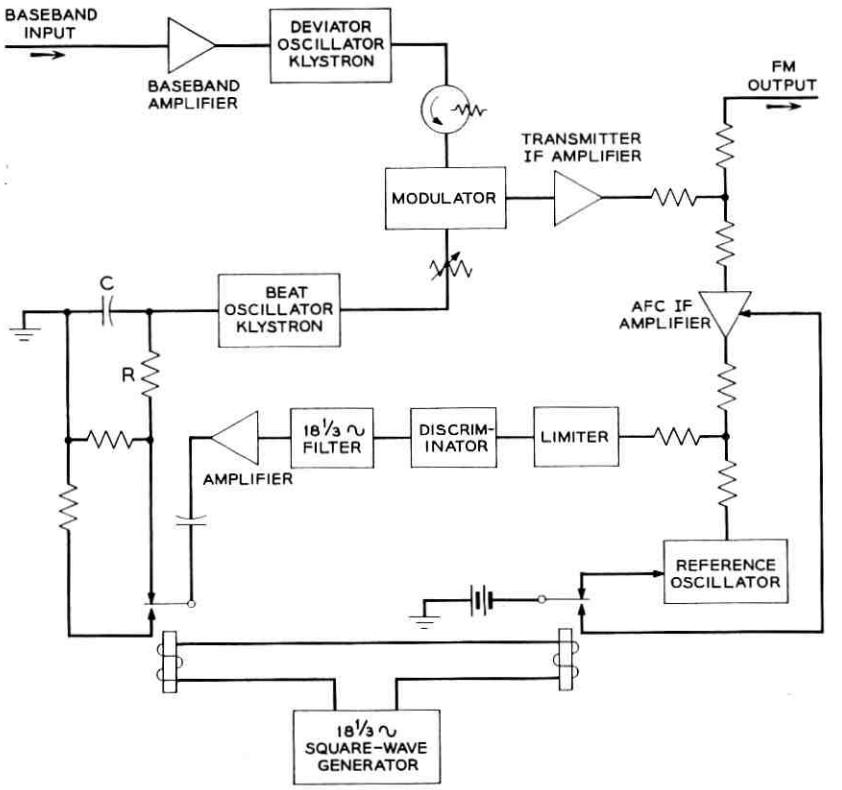

Fig. 2 — Block diagram of the FM deviator.

to the difference between the oscillator frequency and the discriminator center frequency. As a result, the AFC discriminator output contains an $18\frac{1}{3}$ cps square wave whose peak-to-peak average amplitude is proportional to the frequency difference between the reference oscillator and the average frequency of the deviator output. The function of the AFC limiter is to equalize signal amplitudes at the input to the discriminator. The bandpass filter following the discriminator effectively allows only the fundamental component of the $18\frac{1}{3}$ cps square wave to be amplified. At the output of the audio amplifier, the $18\frac{1}{3}$ cps sine wave is rectified in a synchronous detector and filtered. The dc signal is applied to the repeller of the beat-oscillator klystron with the proper polarity to reduce the frequency difference between the reference oscillator and the deviator output. Gating of the AFC IF amplifier and reference oscillator and the use of synchronous rectification eliminate the need for dc amplification and make the AFC loop insensitive to small drifts in the center frequency of the AFC discriminator. The open-loop gain of the AFC system is, typically, 36 db.

In the absence of modulation, frequency errors are in general the result of drifts in the klystron center frequencies. With modulation, the instantaneous frequency of the FM signal is continuously changing, and nonlinearities in the AFC discriminator characteristic will contribute terms to the average discriminator output that are not linearly related to the average frequency of the FM signal. To achieve comparable linearity at the increased peak deviation, the original AFC limiter-discriminator was replaced with the wideband limiter and discriminator of the TH FM terminal receiver.[5] Between 64 and 84 mc the first-order nonlinearity of the wideband discriminator is less than 2 per cent.

In gated AFC systems, objectionable "flicker" interference often arises as the result of beats between the harmonics of the gating frequency and low-frequency components of the television signal or power supply ripple. To make the FM deviator compatible with the 50-cps field rate of European television and the 60-cps U.S. standard, a gating frequency of $18\frac{1}{3}$ cps was chosen. Five-cps beats, developed between the 55-cps third harmonic of the gating frequency and either field rate, are effectively suppressed by the RC filter at the output of the synchronous detector. In addition, the bandpass filter at the output of the discriminator provides more than 20 db of attenuation to 50- and 60-cps signals before rectification At maximum deviation the 5-cps interference is more than 60 db below the 50- or 60-cps modulating frequency.

The wideband characteristics of the IF amplifier, limiter, and discriminator in the AFC loop make possible a simple method of shifting the deviator frequency for two-way telephone transmission. It is only

necessary to substitute a 69.13- or 79.13-mc crystal in the reference oscillator, retune the oscillator, and adjust the beat-oscillator repeller supply so that the output of the synchronous detector is zero. The rest frequency of the beat-oscillator klystron is then 69 or 79 mc different from that of the deviation oscillator klystron.

1.3.3 *Modulator-Amplifier and Transmitter Carrier Supply*

The TH radio relay system provides the basic elements of the modulator-amplifier and the transmitter carrier supply. Detailed descriptions of this equipment and its performance are published elsewhere.[3,4] Modifications that affect operations are limited to the addition of the IF switch and the output power control system.

1.3.4 *Power Amplifier*

The power amplifier, including the power supplies and the TWT itself, is contained in five cabinets. Two of these are on the lower level of the antenna structure and contain the high-voltage rectifier and its controls. The other three are on the upper level and contain the high-voltage regulator, intermediate- and low-voltage supplies, and the TWT and RF equipment. This arrangement imposes the minimum space and weight requirements on the upper level of the antenna structure. In addition to the TWT heater and accelerator supplies, the intermediate- and low-voltage units include supplies for the solenoid focusing magnet, ion pumps, arc detector, and control and protective circuits. Water is supplied for cooling the TWT and also the dummy load. Air under pressure is brought into the cabinets for general cooling, supplemented where necessary by auxiliary blowers.

1.3.4.1 *The RF Circuit.* The M4040 TWT is described elsewhere in this issue.[6] Fig. 3 shows additional elements required in the RF path. Interposed between the modulator-amplifier and the TWT is the input circulator, the principal function of which is to provide isolation between the two for better impedance matching over the frequency band. In particular, as the input signal to the TWT passes through the tube, some small amount will be reflected at the sever (which is not a perfect match over the whole band). This power will reappear at the TWT input port with about 14 db amplification due to its passage through this first section of the TWT. If it undergoes a further reflection due to a mismatch at the modulator-amplifier output, a buildup will occur leading to oscillation and tube damage. A termination at the input circulator absorbs this reflected power, preventing regeneration.

At the output window of the TWT, a photomultiplier tube is mounted

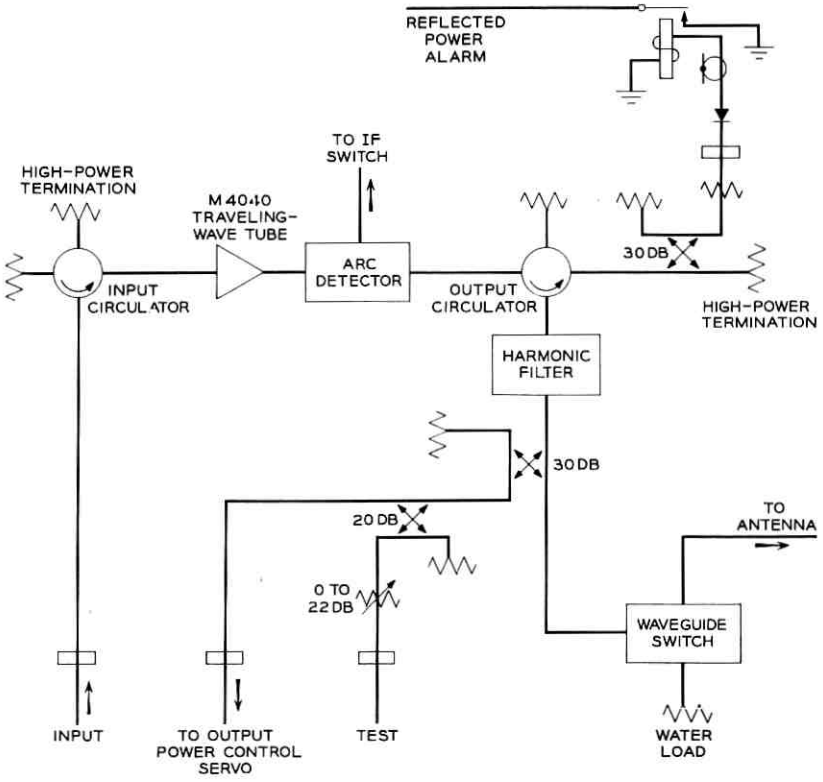

Fig. 3 — Block diagram of the power amplifier.

next to a small hole in the broad wall of the waveguide to detect any arcs that may develop in this region. Associated circuitry operates the IF switch, which removes drive from the tube, thus interrupting the arc.

A high-powered circulator is used in the output waveguide, again providing a minimum return loss of 14 db over the band to prevent oscillations in the output section due to excessive reflected power. In addition, one of the branches is connected through a 30-db directional coupler and an RF attenuator to a detector which monitors reflected power. If this exceeds 50 watts, the detector output operates a meter relay which opens the IF switch and removes the drive.

Following the output circulator, a harmonic filter reduces the second harmonic output of the transmitter, which may be only 25 db below the fundamental. To meet interference objectives, the filter is designed for 50-db minimum harmonic discrimination. To meet transmission

objectives, the filter has 0.5-db maximum insertion loss and 30-db minimum return loss over the band of 5925 to 6425 mc

Following the filter is a directional coupler and a waveguide switch and water load. The coupler is part of the output power control system, described in Section 1.3.5. The switch and water load permit all transmitter tests to be performed with the output disconnected from the antenna.

1.3.4.2 *DC Power Supplies*

(*i*) *TWT Heater Supply.* AC heater operation tends to cause small but measurable amounts of amplitude and phase modulation of the M4040 RF output. To eliminate these effects, a simple dc heater supply, consisting of a transformer, bridge rectifier and filter capacitor, is provided. A variable autotransformer on the power amplifier control panel determines the ac input to the power supply, and hence, the heater voltage. Normally, the heater supply is operated continuously to extend tube life and promote efficient outgassing. Meter relays connected to the primary of the heater supply cause high voltages to be turned off if the TWT heater current falls below a preset value.

(*ii*) *High-Voltage Beam Supply.* This supply, shown in Fig. 4, furnishes a regulated output of 0 to 20 kv at up to 1.5 amperes from 3-phase ac power at 50 or 60 cps. Its regulation for load changes from 1 to 1.5 amps, up or down, and/or line changes of ± 15 per cent, is better than 0.1 per cent peak-to-peak. Ripple and noise at rated load is less than 0.1 per cent peak-to-peak. The supply was designed with depressed collector operation of the TWT in mind for the future, so both plus and minus leads may be isolated from ground. Because of the requirement for regulated operation over the whole range of voltage from 0 to 20 kv, the supply was built with a motor-driven variable autotransformer to control the high-voltage applied to the rectifier, the output of which is further regulated by an electronically controlled series regulator tube. A limited degree of tracking between the autotransformer and the series tube control voltage is provided automatically.

The negative lead of this supply is fed to the TWT cathode at about 17 kv. The positive side, or ground end of the supply, is fed over separate leads to the collector and through the body-current sensing circuit to the body of the TWT. Regulated output voltage and collector and body current are monitored by meters on the control panel.

There are certain trouble conditions affecting the traveling-wave tube which might cause its destruction unless the high voltage is removed

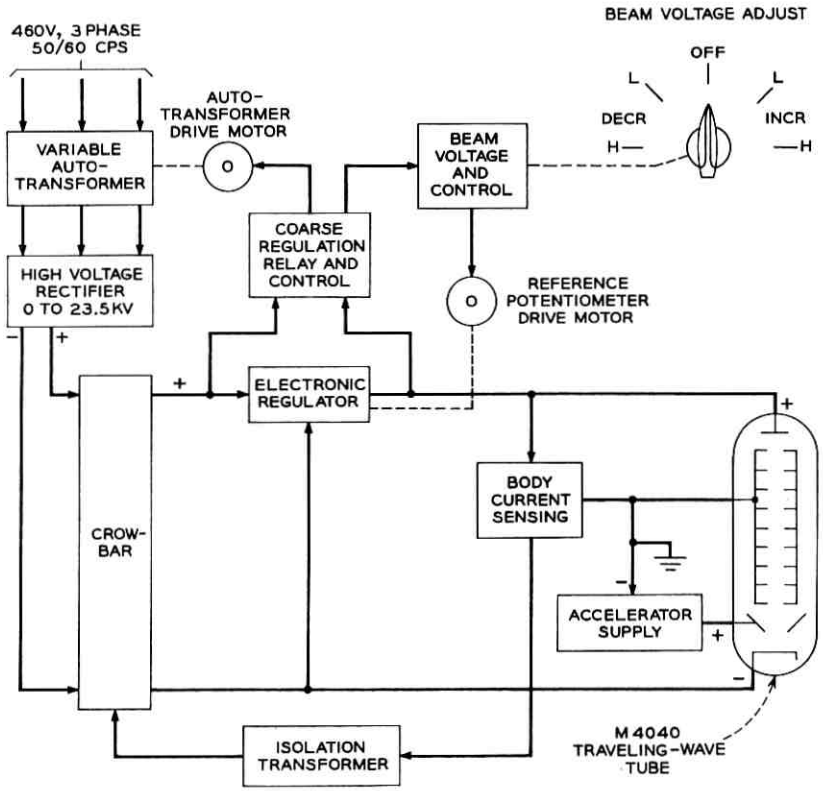

Fig. 4 — Block diagram of the high-voltage beam supply.

within a fraction of a millisecond. Protection of this sort is provided by the "crowbar" circuit, which can be operated by excessive TWT cathode current or body current. The crowbar tube is a type 5563A mercury vapor thyratron. This particular tube can be controlled by a grid voltage change of only 100 volts; the more usual hydrogen thyratrons or ignitrons require control voltages of several thousand volts. Thus, a simple and fast-firing circuit can be used. When fired, the crowbar puts a short circuit across the high-voltage rectifier, reducing the output voltage of the regulator to a few hundred volts in about 20 microseconds. After a few milliseconds delay due to relay operate time, the excessive current drain on the high-voltage rectifier causes its own protective circuits to shut it down.

(*iii*) *The Accelerator Supply.* The accelerator supply consists of a solid-state bridge rectifier and two stages of regulation. The first stage is a

ferroresonant type of circuit, and the second stage is an electronic regulator. Line and load regulation and ripple measure less than 0.03 per cent. Variation of output voltage is controlled by a potentiometer across a voltage regulator tube reference supply. The ferroresonant first stage has a voltage control on the same shaft so that the two stages can be made to track. Under normal operating conditions the output voltage is adjusted to 600 volts. The output current monitor in the supply is part of the protective circuitry in the power amplifier. If the accelerator current becomes excessive, the beam supply and all intermediate-voltage supplies, except those for the ion pumps, are disabled.

1.3.4.3 *Cooling.* Deionized and filtered water is supplied to cool the M4040 TWT and the dummy load. Flow is set at about 18 gallons per minute and valved to the various using areas. Pressure switches are used as part of the protective system as an indication of proper flow in the TWT, the high-powered circulators, and the solenoid focusing magnet. If one or more of these flows are below a minimum, interlocks prevent the application of all but TWT heater voltage and the ion pump supplies.

In addition to the normal flow of filtered air through the cabinets, a spot blower is used to keep the TWT waveguide flanges cool, and another blower is used for the series tube in the beam regulator. A vane switch in the air stream of this latter blower is in the interlock circuit, again preventing the application of all but the heater, ion pump and solenoid voltages.

1.3.4.4 *Operating Interlocks, Controls, and Monitoring Devices.* Because of the experimental nature of the Telstar program, a greater ability to control voltages is necessary than would be expected of a commercial system. The manner of applying dc power to the TWT requires that the heater voltage be raised and lowered by carefully controlled amounts and that accelerator voltage and high voltage be applied in steps. Furthermore, the tube must be protected against arcs in the waveguide; excessive feedback or return power in the tube itself; overheating of the body, sever or collector; inadequate water flow to the body or the solenoid; and various over- or under-voltage or current conditions. The following sections describe some of these features.

(*i*) *Control Panel.* Operating controls for the power amplifier portion of the ground transmitter are located on a panel of the control bay. This control panel contains the power switches, the visual monitoring meters, status indicating lamps, alarm lamps and adjustment controls.

The status lamps indicate upper-level and lower-level standby power, heater on, plate ready, plate on, beam ready, beam on, beam adjust disable, and antenna/dummy load switch positions. The alarm lamps

indicate such conditions as open circuit breakers, open interlock circuits, TWT water on or off, TWT over-temperature, over-current and under-current and over-voltage in certain circuits, high reflected RF power and RF drive disable. An audible alarm rings if the RF drive to the TWT is removed during normal operation. In addition to overload relays, additional protection is provided for the TWT by meter relays which will operate on out-of-limit readings to open the interlock protection circuit. Operation of the interlock protection circuit will remove power from the TWT.

(*ii*) *Circuit Protection and Operations Monitoring.* Individual circuits and functions are protected by 32 circuit breakers on a panel in the power bay in the upper level (there are additional circuit breakers in the beam rectifier control bay in the lower level). Elapsed time meters and operations counters are provided for heater, plate, and high-voltage monitoring.

1.3.4.5 *Mounting Arrangements and Maintenance Philosophy.* The equipment layout was planned with two particular considerations in mind: maintainability and personnel safety.

As much preventive maintenance and trouble analysis as possible is to be done in place, since bench maintenance facilities in the rotating structure are limited. To accommodate the objective of in-cabinet maintenance, sub-units in the control bay (20-kv regulator) are designed with test points of interest accessible from one side of the chassis, which is then mounted so that this side faces the front (or back) of the cabinet. Metal doors provide access to front and back of this cabinet and of the power bay (miscellaneous rectifiers), and inner plexi-glass panels prevent accidental contact with dangerous voltages. Small holes in these panels permit screwdriver adjustment to be made, or the insertion of a probe to some test points. In the case of the 20-kv regulator cabinet, opening these plexi-glass doors will operate interlocks, dropping the system back to the heaters-only condition, and will ground all high-voltage points with gravity-operated shorting bars. Most of the circuitry in this cabinet can be tested without high voltage being turned on, and in almost every case, troubles can be localized to the component requiring replacement without exposing maintenance personnel to undue risk.

The cabinets have been designed with RF shielding at the front and rear doors and some other openings, in order to keep the possibility of interference to the lowest possible level. Consideration of corona from high-voltage leads resulted in rounded corners and large-radius bends for potential corona sources. The cabinet containing the traveling-wave tube and its associated water-cooling, waveguide and RF measuring and monitoring gear was designed to isolate that part of the equipment

which might "leak" RF. The TWT and the leads going to it which carry much of the high voltage, and the arc-detector and photomultiplier, are all in a metal-enclosed box, with the customary shorting bar for the 20-kv supply. Water valves and gauges are in a compartment to the rear of this, and temperature-monitoring pyrometers and RF-monitoring equipment in a compartment next to it. The doors to these two compartments are not interlocked. The traveling-wave tube bay, the control bay (20-kv regulator) and the power bay (intermediate voltage supplies) are of aluminum and are mounted in the upper structure near the end of the horn; the beam rectifier control bay and the beam rectifier bay are of steel, and are mounted below on the rotating platform.

1.3.5 *Transmitter Control*

Off-on control of the ground transmitter output centers around the IF switch. The switch consists of an IF diode gate[8] and a switch control circuit. In the off state the insertion loss of the switch is more than 85 db; there is essentially no input to the power amplifier. In the on state the insertion loss is 1.5 db, and the motor-driven attenuator in the modulator-amplifier effectively determines the output of the transmitter. In order to protect both equipment and personnel from hazardous operating conditions, the IF switch control circuit is inhibited by an extensive chain of relay and switch contacts. The chain encompasses the local and remote operating positions, the waveguide switch and protective circuitry associated with the power amplifier, and the motor-driven attenuator in the modulator-amplifier, as well as the antenna elevation indicators. An auxiliary connection exists between the arc detector in the power amplifier and the IF switch control circuit. It enables the switch control circuit to open the IF gate in less than 5 microseconds after an arc in the 2-kw TWT.

Fig. 5 shows a diagram of the output power control system. The arc detector, output circulator and harmonic filter have been omitted for simplicity. In loop 1 the input power to the RF detector remains essentially constant. Any change at this point unbalances the input to the difference amplifier, operates the polar relay and causes the shaded-pole servo motor to increase or decrease the attenuation of the AGC attenuator until the output of the M4040 TWT changes sufficiently to restore the RF detector input to its nominal value. As a result, the loop automatically compensates for compression in the input-output characteristic of the M4040 TWT and for changes in the RF output of the 5-watt TWT. The output of the transmitter is directly related to the attenuation of the reference attenuator and the manual attenuator.

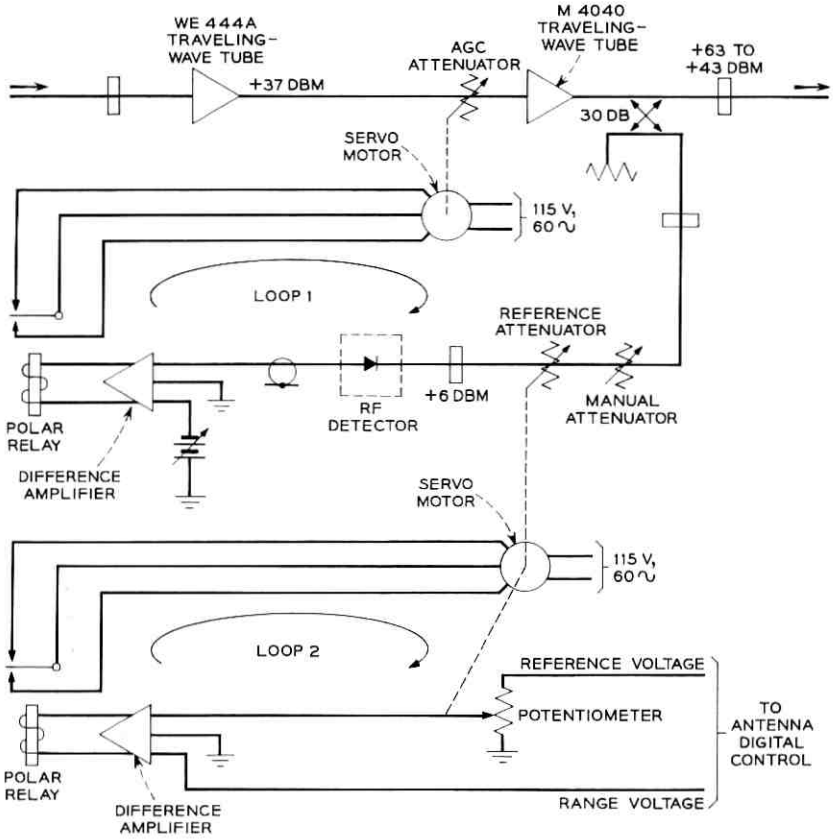

Fig. 5 — Output power control servo.

The control limits of loop 1 are 2 kw and 0.02 kw, equivalent to a 20-db variation in free-space path loss or a 10:1 variation of slant range.

The reference attenuator and hence the transmitter output are controlled by loop 2. The method of generating the two analog inputs to loop 2 is described elsewhere.[9] One is a fixed reference voltage; the second is proportional to the logarithm of the slant range or, in other words, free-space path loss. Expressed mathematically,

$$V_{\text{RANGE}} = 0, \qquad R < 0.1R_{\text{MAX}} \tag{1}$$

$$= V_{\text{REF}} \log_{10}\left(\frac{R}{0.1R_{\text{MAX}}}\right), \qquad 0.1R_{\text{MAX}} < R < R_{\text{MAX}} \tag{2}$$

$$= V_{\text{REF}}, \qquad R_{\text{MAX}} < R, \tag{3}$$

where R is the actual slant range and R_{MAX} is the maximum slant range at which it is possible to achieve a particular input power to the satellite. Since the transmitter is limited to 2 kw, the maximum slant range corresponding to a particular satellite input is determined by free-space path loss and transmitting and receiving antenna gains. For slant ranges equal to or greater than the maximum defined above, the voltage representing range is equal to the reference voltage; the reference attenuator in loop 1 and the potentiometer in loop 2 are set for maximum attenuation and resistance, respectively. As the slant range decreases, the voltage representing slant range also decreases. The inputs to the difference amplifier in loop 2 are no longer equal, and the servo motor adjusts the potentiometer to restore the equality. In so doing the attenuation in loop 1 and, consequently, the transmitter output are reduced. Since the loss in db of the reference attenuator and the resistance of the potentiometer are essentially linear functions of mechanical rotation, the decrease in transmitter output just equals the reduction in free-space path loss. As a result, the power incident on the satellite remains constant. In operation, a small second-order term is added to (2) to compensate for a slight nonlinearity in the attenuation vs mechanical rotation characteristic of the reference attenuator. With this addition, it is possible to maintain the signal incident on the satellite constant to within ± 0.5 db. The major portion of this error can be attributed to the dead space associated with the polar relays.

The IF switch and the output power control servo are interconnected with the ground station control console (GSCC) to permit remote operation of the transmitter from that location. Between passes, the transmitter output is connected to the water load and an out-of-service indication is displayed at the GSCC. Upon completion of pre-pass checks, the transmitter output is switched to the antenna and control is transferred from the local operating position to the GSCC. By activating appropriate switches, the console operator may choose any one of three operating conditions, provided the antenna elevation exceeds 5 degrees. These conditions are carrier off, standby, and carrier on. As long as the antenna is pointing below the horizon, however, the IF switch cannot be closed. The AGC attenuator is automatically positioned for maximum attenuation, independent of the output power control servo, and a carrier off indication is displayed on the GSCC. For antenna elevations above the horizon but less than 5 degrees, the choice is restricted to carrier off or standby. In the latter case, the IF switch is closed. However, the AGC attenuator is still positioned for maximum attenuation so that the radiated power is limited to approximately 0.2 watt. The standby condition is normally used during the pre-pass system checks

with the satellite simulator at the test tower. For antenna elevations above 5 degrees, no restrictions exist. In the carrier on condition, the IF switch is closed and the AGC attenuator is under control of the servo system.

1.4 *Equipment Features*

As stated earlier, the high-voltage beam rectifier and associated controls are located on the lower level of the antenna structure. Fig. 6 shows the arrangement of the units of the transmitter mounted on the upper level. Cabinet doors have been temporarily removed. The transmitter carrier supply and modulator amplifier are located in the two pull-out bays on the left. To the right of the modulator-amplifier are the three remaining units of the power amplifier. The first cabinet contains the M4040 TWT and RF circuitry; the second cabinet contains the series tube regulator and crowbar circuits and the power amplifier control panel; and the third contains the circuit breaker panel and intermediate- and low-voltage supplies. The FM deviator is mounted in the cabinet on the extreme right. Each of the cabinets is 6 feet high and 3 feet deep. The combined width of the four cabinets and the two pull-out bays is $18\frac{1}{2}$ feet. The weight of the six units is approximately 6000 pounds.

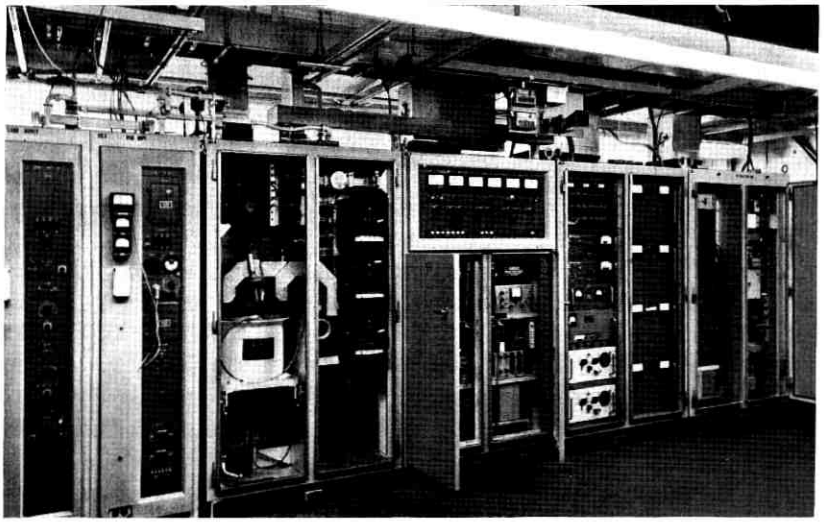

Fig. 6 — The ground transmitter.

II. THE RECEIVING SYSTEM

2.1 *General*

One of the major differences between a conventional microwave receiver — as used, for instance, in such ground-based microwave systems as TD2 and TH — and the ground receiver of the Telstar system, lies in the tremendously improved noise behavior of the latter. By the use of low-noise antennas and masers, the total noise temperature of satellite ground receivers can be made 100 to 200 times lower than for conventional receivers. The noise characteristics of the Telstar receiver are superior in still another respect. Present thinking calls for the use of wideband transmission methods, such as high-index FM, in order to keep the transmitter power in the satellite at a realistically low level. Such high-index systems necessarily work close to the threshold of detection. By the use of the FM with feedback (FMFB) principle, it is possible to extend the threshold of noise improvement in the Telstar system by about 4 to 5 db compared with the standard method of FM demodulation. This allows operation of the transmitter in the satellite with only one third the power otherwise required.

This part of the paper emphasizes the low-noise features of the receiver and describes the circuits responsible for such operation. An overall description of the receiver is given in Section 2.2. The pertinent operational characteristics of the maser, the parametric amplifier, and the FMFB receiver are described in Section 2.3. A description of the diplexer and other waveguide equipment required to connect the transmitter and receiver to the same antenna is found in Section 2.4. Various system noise measurements are presented in Section 2.5. Circuits of a more conventional type and those taken from the TH or TD2 microwave system, such as converters, IF amplifiers, and carrier supplies, are not described.

2.2 *Receiver Description*

2.2.1 *The Transmission Circuits*

A block diagram of the ground receiver is shown in Fig. 7. This equipment is located in the upper equipment room on the horn antenna structure. The received 4-kmc, left-hand circularly polarized signal from the satellite, after being picked up by the horn-reflector antenna, is guided toward the maser by a low-loss waveguide diplexer. The diplexer

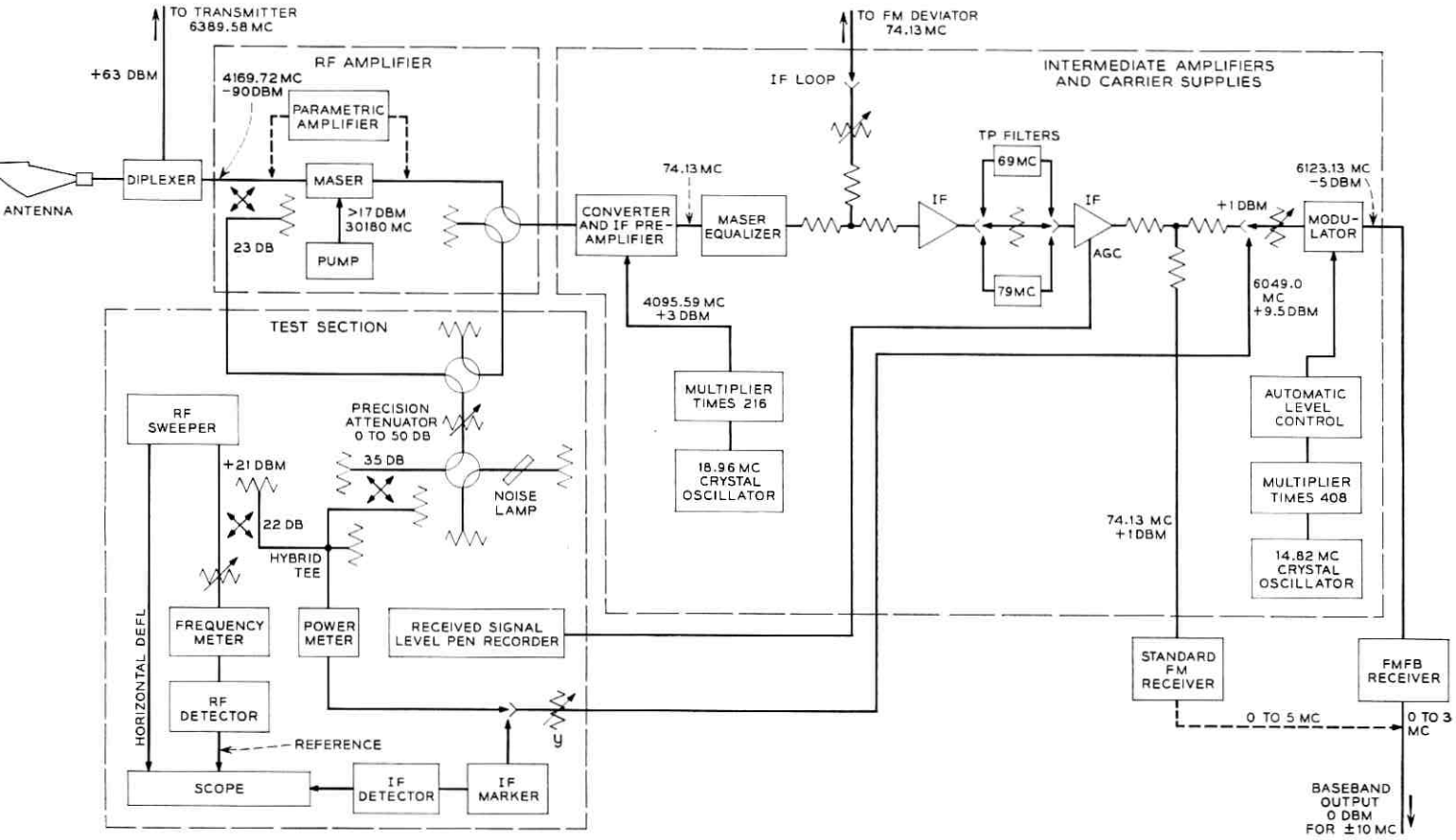

Fig. 7 — Block diagram of the ground receiver.

also accepts the high-power 6-kmc signal from the transmitter and feeds it to the same horn-reflector antenna, from where it is launched right-hand circularly polarized. The maser, operating at the temperature of liquid helium (4.2° Kelvin), has a gain of 42 db and a 3-db bandwidth of 16 mc. The receiver bandwidth is widened to the necessary 25 mc by the insertion of a maser equalizer at IF directly after the frequency converter. The 42-db gain of the maser is high enough to make the noise contribution of the following frequency converter negligible. Total noise temperature of the receiver measured at the input of the maser with the antenna pointed toward zenith is 32°K on a clear day. The maser requires for its operation a "pump" which supplies a frequency-stabilized microwave carrier of 30,180 mc at a power greater than 17 dbm.

It is also possible to use a broadband (60-mc) low-noise parametric amplifier instead of the maser for evaluation in the system.

The signal from the maser is changed to an intermediate frequency of 74.13 mc in a frequency converter. A crystal-derived carrier of 4095.59 mc serves as the local oscillator signal. A low-noise preamplifier and two more IF amplifiers bring the signal power up to a level of +1 dbm, which is held constant by an automatic gain control circuit in the second amplifier.

The transmission characteristic of the converter and IF circuits combined is flat and drops only 0.25 db at the edges of the 25-mc band. Except for the case where the parametric amplifier is used, the over-all transmission is limited by the combination of maser and maser equalizer. For TV transmission this bandwidth is 25 mc at the half-power points, and for two-way telephony it is reduced to 3 mc by the insertion of a special filter ahead of the last IF amplifier. This telephone filter is centered either 5 mc above or below the normal IF frequency of 74.13 mc, depending on the transmitting frequencies chosen in the two participating satellite ground stations. The insertion of the telephone filter is the only step necessary for changing the receiver from television to two-way telephone operation.

To the output of the last IF amplifier can be connected either a standard (conventional) FM receiver or an FMFB receiver after suitable frequency translation. The input frequency of the FMFB receiver is at 6123.13 mc for reasons explained under Section 2.3.3. A balanced diode modulator, together with a crystal-derived carrier of 6049.0 mc, translate the 74.13 mc signal to the required 6123.13 mc.

2.2.2 *The Test Equipment*

In addition to the basic transmission circuits just described, the Telstar ground receiver contains special test equipment for fast and precise measurements of noise temperature, transmission characteristics, gain and received signal level. This equipment is shown in the block called test-section of Fig. 7. It includes an RF sweeper which can be swept over 60 mc anywhere in the 3700- to 4200-mc range, a power meter for 4 kmc and 74 mc with an accuracy of a few tenths of a db, a waveguide noise lamp, a precision waveguide attenuator, an oscilloscope, and a pen recorder. A number of waveguide switches allow the distribution of either the 4-kmc carrier or the noise signal to either the input of the maser or the input of the converter. The output, for test purposes, is taken at the +1 dbm IF point.

The AGC voltage of the IF amplifier is a function of the received 4-kmc signal level and is recorded on a pen recorder. A wealth of information can be obtained from such recordings. Several examples of received level recordings are given in a companion paper.[10] The recorder is calibrated before each pass with a 4170-mc signal from the RF sweeper, which is applied to the input of the maser at the levels of −80 and −90 dbm. Absolute accuracy of the recording is about ±1 db. A second recorder of received level is located on the ground station control console in the control building. Its expanded range, going as low as −110 dbm, allows the personnel tracking the satellite to check whether the autotrack system has locked on the main beam and not on a sidelobe of the horn-reflector antenna. The recording also helps an experienced operator to easily discover troubles in the communications part of the system.

Whereas it is possible to test the entire receiver at Andover by means of an "RF loop" which includes the transmitter and the transponder on the test tower, it is often simpler to test important parts of the receiver in the "IF loop" (Fig. 7) which interconnects transmitter and receiver at intermediate frequencies. In this case, random noise from the input of the receiver can be injected into the communications channel for noise and threshold tests. For such tests the antenna should be pointed at the zenith to ensure stable noise power.

In addition to the integrated test equipment shown in Fig. 7, other specialized test sets are used to maintain all the circuits of the receiver on a routine basis. Tests to be performed include the measurement of IF-to-IF and baseband-to-baseband transmission characteristics, discriminator sensitivity and linearity, and IF and RF return loss. The

receiver can also be left in continuous and unattended operation due to the provision of alarm circuits with remote indication.

2.3 *Circuits for Low-Noise Amplification and Demodulation*

2.3.1 *The Maser*

The heart of the receiver is the low-noise maser amplifier which is described in detail in a companion paper.[11] The single-tuned (or equalized) maser, as described in this reference, was used in the receiver rather than the low-gain stagger-tuned version. This choice resulted in a substantial saving of equipment by eliminating a low-noise second-stage RF amplifier. The single-tuned maser has a gain of 42 db and a half-power bandwidth of 16 mc. At a bandwidth of 25 mc, the maser gain is still 35 db. The noise contribution of the converter with its 12-db noise figure or 4300°K noise temperature, referred to the input of the maser, amounts to a negligible 0.27°K at midband and to 1.36°K at the band edges. The stagger-tuned maser, on the other hand, has a flat gain of about 27 db, and the frequency converter would contribute 8.6°K unless the maser were followed by a low-noise second-stage RF amplifier, such as a traveling-wave tube or a parametric amplifier. The terminal noise temperature of the maser alone is 3.5°K.

The relatively low level at which a maser begins to saturate fortunately does not pose a problem in a satellite communications system, as can be seen from the following. The ruby maser shows a one-db drop from its small signal gain at an output level of about −40 dbm. The single-tuned maser, therefore, will begin to saturate at a single-carrier input level of −82 dbm. The highest expected received signal level is about −75 dbm, at which the gain of this maser is 3.5 db below the maximum. If, instead of a single carrier, a signal with the same power but a flat spectrum of 25 mc, resembling an actual communications signal, were applied to the maser, the saturation effects would be smaller. The automatic gain control circuit of the IF amplifier compensates not only for the variations in received signal level but also for the changes of maser gain due to saturation. Saturation also causes a widening of the maser transmission characteristic. This effect changes the transmission by only a few tenths of a db up to input levels of −75 dbm and can therefore be neglected for all practical purposes.

The saturated maser, unlike an electron tube or transistor amplifier, does not show signs of instantaneous nonlinearity, which would give rise to intermodulation or signal clipping. The maser acts much like an

extremely linear amplifier followed by a voltage divider containing a thermistor whose resistance is changed by the power in the amplified signal. As in this thermistor circuit, the maser gain reacts to a change in level very slowly, with a time constant of about 0.1 second.

The extremely low instantaneous nonlinearity predicted by maser theory was also confirmed experimentally. For this purpose, two strong signals of equal power at frequencies f_1 and f_2 were applied within the passband of the maser, and the third-order intermodulation products $2f_1 - f_2$ and $2f_2 - f_1$, falling again into the maser passband, were measured. If both signals f_1 and f_2 were at the level of -85 dbm, which is possible during two-way telephony operation, the intermodulation terms would be about 180 db lower. It is clear that such low distortion levels are completely negligible. One is also led to the conclusion that the maser is the most linear amplifier in existence.

For the design of the waveguide diplexer, it was necessary to determine how much of the 6390-mc transmitting signal could reach the input of the maser without causing saturation or other effects. Whereas saturation is evident around -82 dbm for signals in the passband (4170 mc), signal levels as high as 2.5 watts (34 dbm) can be applied to the (impedance-matched) maser input at 6390 mc without causing intolerable distortions of the transmission characteristic. In the latter situation, however, the helium boil-off rate will be increased considerably. Because we have no control over the impedance match of the maser at 6 kmc, it is not advisable to apply interfering signal levels in excess of a few hundred milliwatts.

It is possible to saturate the maser from the output side as well. Due to balancing and filtering in the converter, the leakage of the 4095.59-mc local oscillator signal is low enough not to cause saturation of the maser.

The over-all receiver bandwidth is widened to the required 25 mc at the half-power points by inserting an equalizing filter at IF. A simple bridged T single-pole filter is used with a loss of 7 db at midband and 3 db at the 25-mc bandwidth. The resulting transmission characteristic has two peaks of about 0.3 db, 5 mc away from the center frequency.

The magnetic field of 3300 gauss which tunes the maser to a frequency of 4170 mc is provided by a permanent magnet. Because of the high tuning sensitivity of 2.4 mc per gauss, it is necessary to avoid large temperature variations of the magnet, which will change the magnetic field at a rate of 0.4 gauss per degree centigrade and will therefore lead to a temperature sensitivity of 0.96 mc/°C. It is very helpful in this respect that the temperature of the upper equipment room in which the

receiver is located is kept within a few degrees. It has further been found important that magnetic material like metal chairs should not be brought close to the maser to avoid detuning. It is even possible to notice the effect of the earth magnetic field, which amounts to about 0.16 gauss at Andover, Maine. When the horn antenna is turned in azimuth, the earth field will add or subtract from the maser field, and a slight tilting of the transmission characteristic can be observed. (See Fig. 19 of Ref. 10.)

The operation of the maser requires a supply of liquid helium and nitrogen. The handling of these cryogenic fluids has been simplified considerably over standard laboratory procedures by the availability of new 100-liter containers and transfer tubes. The maser accepts 10 liters each of liquid helium and nitrogen, and boil-off occurs in about 20 and 50 hours, respectively. No attempts were made to recover the expended helium gas because this was considered to be an interim situation which would be changed in time by the installation of a closed-cycle helium liquifier.

A ruby maser operating at a frequency of 4170 mc must be pumped with a signal at 30,180 mc. The pump power at the maser terminals should be greater than 50 milliwatts if the maser gain is not to drop more than about 2 db from its maximum. The pump frequency should remain within a few mc of the correct value to ensure maximum pumping efficiency and to avoid loss of gain. A reflex klystron serves as the source of pump power. Good long-term frequency stability is provided by the AFC circuit shown in Fig. 8, which has the following features: (*i*) the reference cavity is made low Q in order to produce a peak-to-peak separation of 30 mc in the Foster-Sealey type waveguide discriminator, (*ii*) a wideband (100 kc) dc amplifier stabilized by a mechanical chopper is used, and (*iii*) the repeller of the klystron is operated at about ground potential. The so-often unreliable voltage translation from ground potential to the high dc potential of the repeller is therefore avoided. This requires operation of the klystron shell at a high potential and makes the use of a high-voltage waveguide choke necessary. The RC circuit between the dc amplifier and the klystron repeller determines the stability of the feedback loop.

2.3.2 *The Parametric Amplifier*

A parametric amplifier[12] can be inserted into the system instead of the maser for evaluation of its performance in a satellite system or as a back-up for the maser. The amplifier consists of two cascaded stages of

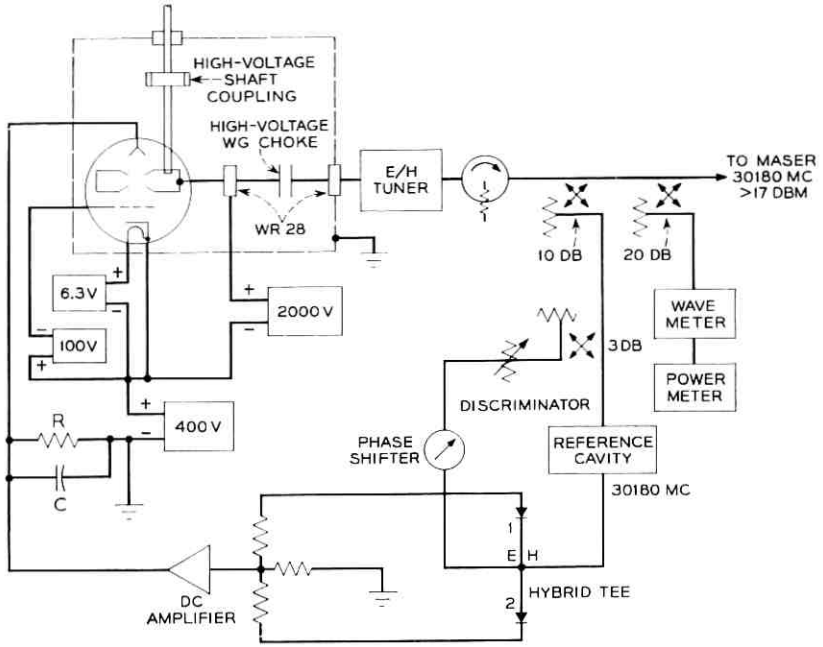

Fig. 8 — Circuit diagram of the maser pump.

similar design. The first amplifier is operated at liquid nitrogen temperature (77°K) and has a gain of 20 db, while the second works at room temperature with a gain of 18 db. The over-all gain of 38 db is therefore close to the 42 db of the maser. The room temperature parametric amplifier with its noise temperature of about 130°K serves as a buffer against the 4300°K noise of the converter circuit. The total noise temperature of the parametric amplifier, including converter, is about 50°K.

The bandwidth of the amplifier is 60 mc at the half-power points. It is obvious that no equalizing filter is needed at IF as in the case of the narrower maser. The over-all 3 db bandwidth of the ground receiver is then 32 mc as determined by the narrower waveguide filters and IF circuits. Saturation in this parametric amplifier, as expressed by a one-db drop from maximum gain, sets in at an input level of −50 dbm. It has been found that intermodulation is no problem for the typical satellite signals of −85 dbm. If a 6390-mc signal is applied to the input of the amplifier at a level greater than 0 dbm, then its 4-kmc transmission will be affected. A band rejection filter can be built into the first parametric amplifier, which raises the tolerable 6-kmc level to about 17 dbm without causing an increase in the noise temperature of the amplifier.

The good over-all stability of this parametric amplifier is due mainly to the stable design of the 23-kmc pump source. The same source is used to drive both stages of the amplifier. Refilling of the dewar with liquid nitrogen is required only every 10 days.

2.3.3 *The FMFB Receiver*

An FMFB receiver is part of the ground receiver. It serves to extend the threshold of noise improvement by 4 to 5 db over that obtained with a standard FM receiver. The feedback circuit is capable of demodulating high-index FM signals with peak frequency deviations of ± 10 mc. The circuit can be used for the reception of television, telephone multiplex and other types of signals.

An integral part of any FMFB receiver is a voltage-controlled oscillator. Such an oscillator should have good modulation linearity, high modulation sensitivity, small signal delay, and good long-term frequency stability. All these features were found in a 6-kmc reflex klystron. This made it necessary to enter the circuit at a frequency of 6123 mc, as indicated in Fig. 7. No further circuit details will be given here; the reader is referred to a companion paper[13] for a detailed description of the FMFB receiver.

2.4 *Diplexer and Associated Waveguide Circuits*

2.4.1 *The 4 kmc - 6 kmc Diplexer*

The waveguide circuit which allows the connection of the 6-kmc transmitter and the 4-kmc receiver to the same horn-reflector antenna is shown in Fig. 9. Although at present this diplexer is only required to work properly over a 25-mc band around the transmitting frequency of 6390 mc and the receiving frequency of 4170 mc, it was designed to handle a much wider band of frequencies. Several components are capable of operating over the full 4-kmc and 6-kmc common carrier bands, extending from 3700 to 4200 mc and from 5925 to 6425 mc, respectively. Other parts are more narrow-band, but studies are in progress to make the circuit work over the full 500 mc of the two common carrier bands.

Returning to Fig. 9, the 2-kw (63-dbm) signal from the 6-kmc transmitter arrives at the diplexer from the left in a rectangular waveguide and with horizontal polarization. The signal travels essentially unchanged over a waveguide transition and through the polarization coupler. The 6-kmc signal which leaks through the coupler into the arm towards the maser is at least 25 db lower. The polarizer then transforms

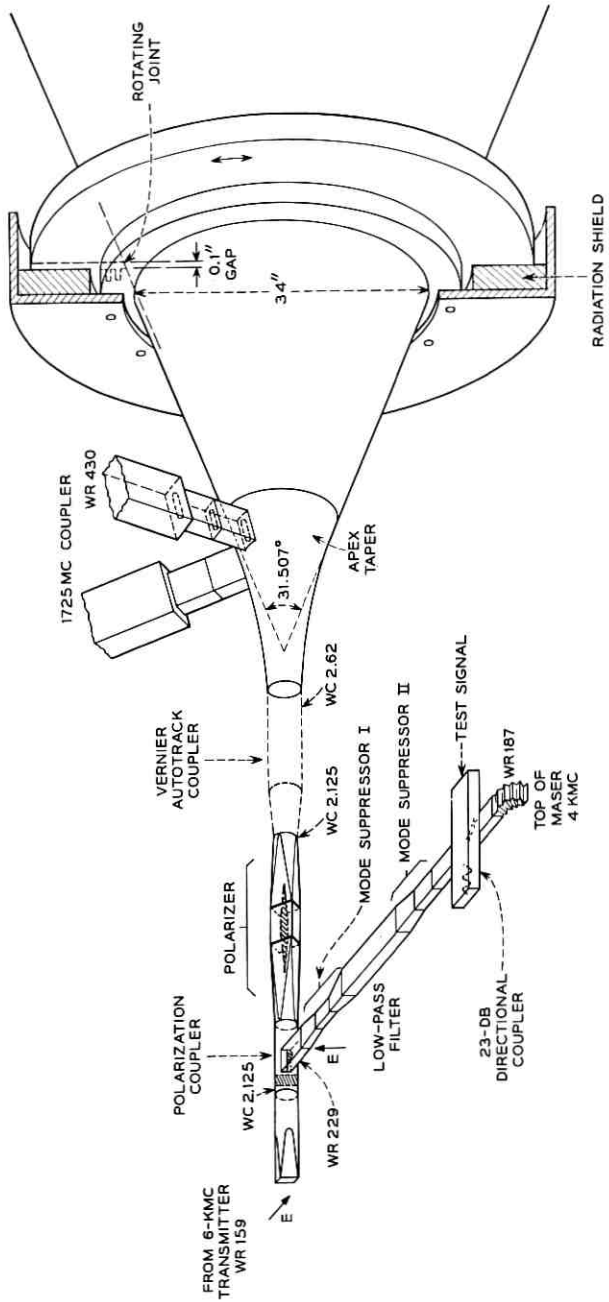

Fig. 9 — Sketch of diplexer and associated waveguide circuits.

the linearly polarized 6-kmc signal into circular polarization for launching by the antenna.

The 4-kmc signal from the antenna, after going through the polarizer, appears as a vertically polarized wave which is guided through the polarization coupler with little loss into the rectangular waveguide leading to the maser. The polarization coupler is of the same type as used in Project Echo, but is designed to work over both the 4- and 6-kmc common carrier bands.[14]

The diplexer was designed under the assumption that the 6-kmc signal level seen at the 4-kmc output terminal shall never exceed 0 dbm. This level is considerably below the value which is acceptable for the maser. It was chosen to allow the use of different types of parametric amplifiers. (See Section 2.3.2.) The diplexer therefore has to provide a total of 63 db of isolation for the 6-kmc signal. With a minimum guaranteed loss of only 25 db in the polarization coupler, additional loss is introduced by a waveguide low-pass filter. This filter was originally designed for the TD2 microwave system, working in the 4-kmc common carrier band, to suppress leakage from the TH system (6-kmc band). The filter has more than 60 db of attenuation for the fundamental mode, but negligible loss for the TE_{20} mode at 6 kmc. It also has an insertion loss of less than 0.09 db over the 4-kmc band. Generators of TE_{20} modes are the polarization coupler and the directional coupler on the maser side. Two mode suppressors were therefore inserted as shown in Fig. 9, consisting of a short piece of narrow-width (1.79-inch) rectangular guide and associated transitions. Each suppressor has little loss at 4170 mc but more than 40 db of attenuation for the TE_{20} mode at 6390 mc. With these precautions, the isolation of the diplexer is found to meet the 63 db isolation with a substantial margin.

The 23.35-db directional coupler at the maser is used for measuring the receiving system noise temperature and for gain and transmission measurements. A short piece of flexible waveguide connects the waveguide circuit to the top flange of the maser.

Because it is necessary to transmit a right-hand circularly polarized wave at 6 kmc and to receive a left-hand circular wave at 4 kmc, a polarizer is inserted between the polarization coupler and the antenna. The polarizer, suitable for operation at 4 and 6 kmc, is shown in Fig. 10 together with a plot of its performance in terms of axial ratio. For pure circular polarization to exist at the output of the polarizer, it is necessary for the field components parallel and normal to the dielectric plate to be equal in magnitude and 90° out of phase. If a differential loss or a deviation from 90° exists, the wave will be elliptically polarized, and

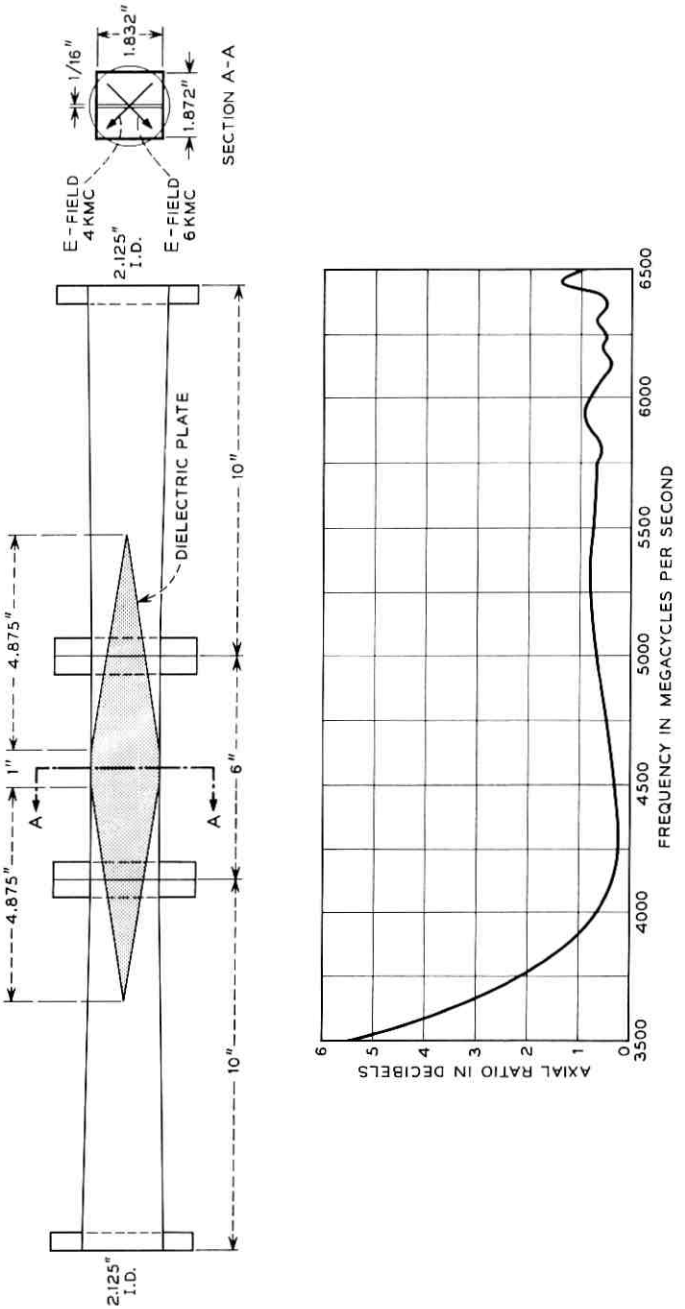

Fig. 10 — The polarizer.

the ratio of major to minor axis, the axial ratio, will be greater than 0 db. Fig. 11 shows how the axial ratio depends on the phase difference and on the differential loss between the two field components. The differential loss was kept below 0.01 db in the polarizer of Fig. 10 by using an extremely low-loss dielectric plate. A phase difference close to 90° is maintained from 4000 to 6500 mc in the polarizer shown. This was made possible by making use of the fact that a dielectric plate in a square waveguide produces a differential phase versus frequency characteristic which is opposite to the one obtained in a nonsquare guide. By locating the dielectric plate in a slightly nonsquare guide, a compensation over a wide frequency range is possible. As a consequence, the axial ratios plotted in Fig. 10 are found to be quite low over a frequency range of 2500 mc.

If imperfect polarizers are used in a system, they will cause a transmission loss. Fortunately, these losses are quite small and amount to only a few tenths of a decibel for the polarizer of Fig. 10 when working with a satellite whose axial ratio is lower than 4 db.

The diplexer is well matched over wide frequency bands at 6390 and

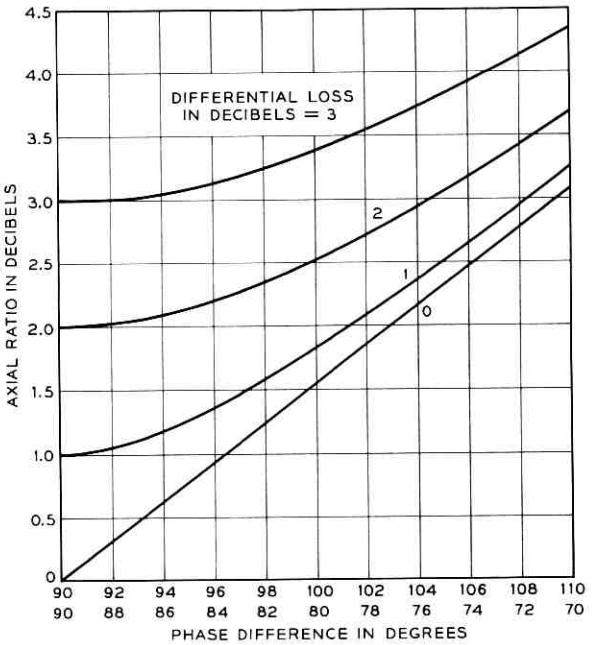

Fig. 11 — Dependence of the axial ratio of a polarizer on differential loss and phase difference.

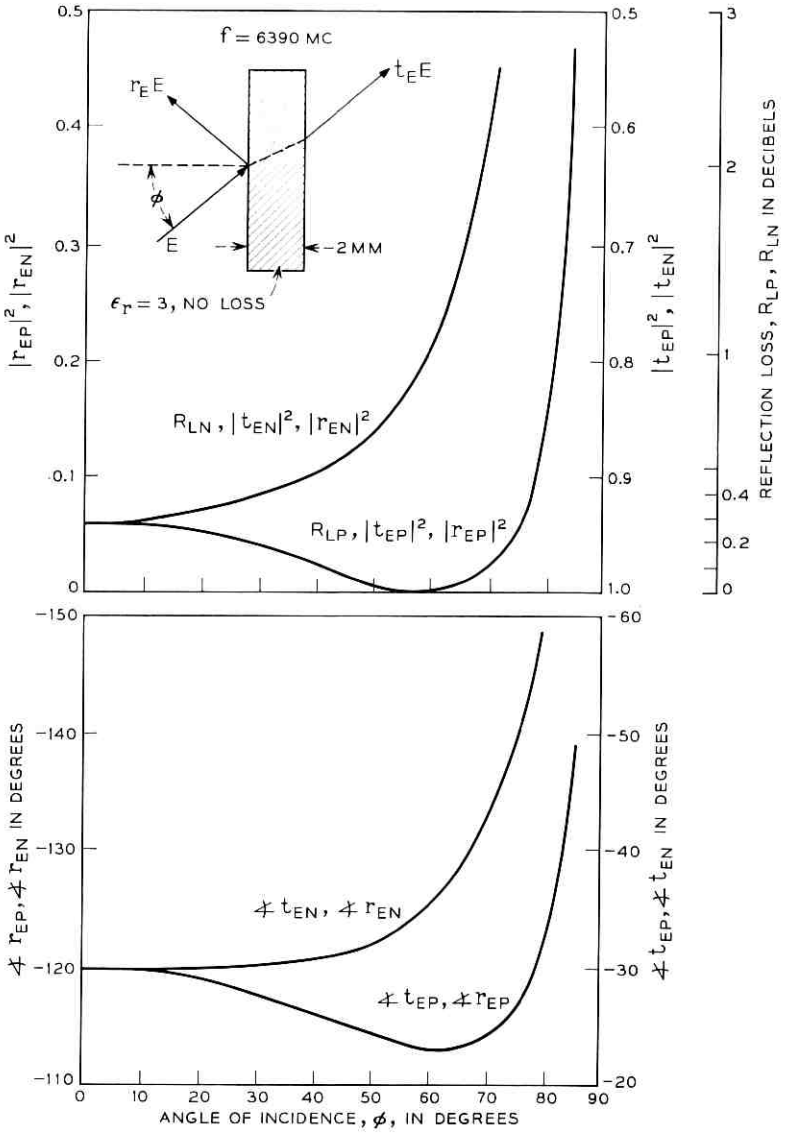

Fig. 12 — Reflection and transmission coefficients of the (lossless) radome at 6390 mc.

4170 mc, and the return losses at the three diplexer terminals are 30 db or higher.

2.4.2 *Effect of the Radome on the Operating Characteristics of the Diplexer*

The 4- and 6-kmc signals are affected in a number of ways by the radome which surrounds the horn-reflector antenna. The possible effects on the operating characteristics of the diplexer will be investigated here. The radome, for instance, will reflect the right-hand circularly polarized transmitted wave as a left-hand circular wave which, after being picked up by the horn antenna, will be directed towards the maser by the polarization coupler. The isolation of the polarization coupler, and in turn the isolation of the diplexer, could be reduced by this reflection. Measurements were made in the laboratory to determine the dielectric constant of the radome material. The power reflection $|r_E|^2$ and transmission $|t_E|^2$ coefficients and their phase angles were then calculated as a function of the angle of incidence Φ. Electric fields parallel (index P) and normal (index N) to the plane of incidence were considered. The results are shown in Figs. 12 and 13 for 6390 and 4170 mc, respectively. According to Fig. 12, the power reflection coefficient of the radome at 6390 mc, averaged over the possible angles of incidence from 8° to 52° and parallel and normal polarization, amounts to about 0.065, which corresponds to a return loss of only 12 db.

Only if all the reflected components from the radome appeared in-phase over the aperture of the antenna could a return loss of 12 db be seen at the apex of the horn. This obviously is impossible. The response of the antenna to reflections from the radome is very similar to its far-field response far away from the main beam. Measurements have indicated that the return loss of the radome as seen from the apex is much greater than 46 db. This figure is considerably higher than the 25 db of isolation provided by the polarization coupler. It can therefore be concluded that the isolation of the diplexer is not affected by the radome.

The radome material can also change the axial ratio of the circularly polarized signals and, therefore, affect the characteristics of the polarizer in the diplexer. The circularly polarized signal arriving at the radome can be decomposed into two linearly polarized waves which can be assumed to be parallel and normal to the plane of incidence. The curves of Figs. 12 and 13 through the voltage transmission coefficients t_{EP} and t_{EN} then tell how much differential loss and phase error is introduced by the radome. For angles of incidence up to 20° for 4170 mc and up to 12° for 6390 mc, no differential effects can be found. At 52°, the highest

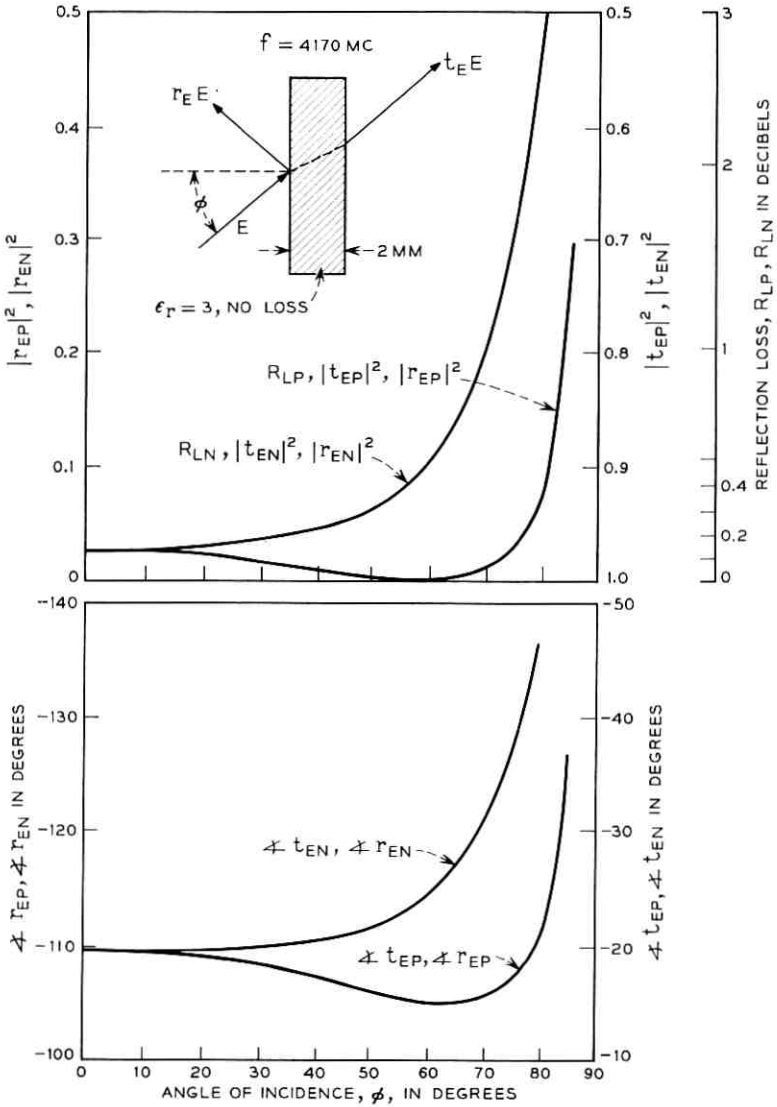

Fig. 13 — Reflection and transmission coefficients of the (lossless) radome at 4170 mc.

possible angle for the Andover horn, the differential losses amount to 0.30 and 0.65 db and the phase errors to 6.50 and 9° for the 4170- and 6390-mc frequencies, respectively. Using Fig. 11, this results in axial ratios of 1.08 db and 1.52 db for the two frequencies. Fortunately, only

a very small part of the energy is radiated (or received) at angles as high as 52°, and no significant loss of signal will result from the degradation of axial ratio by the radome.

2.4.3 *Other Waveguide Circuits*

Following the polarizer shown in Fig. 9, an autotrack coupler is inserted into the line to the antenna. Its purpose is to extract, over narrow-band coupling slots, the TE_{11} and the TM_{01} modes which are generated in the horn antenna by the 4080-mc beacon signal from the satellite. The TM_{01} mode, which propagates freely in the 2.62-inch circular waveguide of the coupler, is completely reflected in the taper leading to the smaller sized polarizer guide. The autotrack coupling section has about 0.01 db of loss for the 4170-mc signal and does not affect transmission of the 6-kmc signal. A complete description of this coupler is contained in a companion paper.[15]

A taper whose impedance varies exponentially with length connects the 2.62-inch circular waveguide to the 31.507° conical apex section of the antenna. The 12.25-inch long taper has a calculated return loss of more than 40 db for the TE_{11} mode and more than 30 db for the TM_{01} mode over the frequency range of 3700 to 6500 mc.[16]

The 1725-mc transmitting signal used in NASA's Project Relay is coupled to the antenna in the conical section directly following the apex taper. Two 1725-mc signals of equal amplitude and 90° phase difference are coupled at right angles into the horn. The phase difference is such as to give a signal right-hand circularly polarized in space. The hybrid Tee and the associated waveguide used to produce the two driving signals are not shown in Fig. 9. The coupling slots are longitudinal and are located at a point where the circumferential wall current at 1725 mc has the first maximum. This maximizes the coupling for the TE_{11} mode and keeps excitation of the TM_{01} mode at a low level. The coupling slots are backed by two-cavity bandpass filters, giving a maximally flat transmission with a 60-mc bandwidth. The filters are built in a small-sized waveguide (4.0 by 0.9 inch) to reduce the number of undesired modes which might be excited at 4 and 6 kmc. Insertion loss at 1725 mc is less than 0.1 db. The filters also act as transformers into the conical section of the antenna and into the larger-sized waveguide WR430, which is used for the rest of the installation. Return loss of the coupler, including the hybrid Tee splitting arrangement, is better than 16 db over a 14-mc band centered at 1725 mc. The coupler has no measurable effect on the transmission of 6390- and 4170-mc signals. The noise introduced into the system by the coupler at 4 kmc is dependent on the

losses in the iris located in the apex taper. By proper mechanical design of this iris, it was possible to reduce this noise contribution to less than 1°K.

A rotating joint is located at a cone diameter of 34 inches. This rather large diameter and a gap width of 0.1 inch simplify the electrical design of a joint which has to work at 6390, 4170, and 1725 mc. A double choke is used and optimized at 4170 mc. Measurements have indicated that for gap widths up to 0.5 inch, and with absorbing material covering the outside of the joint, the 4-kmc noise contribution was still below 1°K. A radiation shield of the form shown in Fig. 9 was put around the outside of the joint in order to keep the radiated energy at 6390 or 1725 mc below the Bell System safety limit for continuous exposure of 1 milliwatt per cm² at all points outside the gap.

2.4.4 *The 4-kmc Waveguide Losses and Noise*

The importance of using low-loss waveguide components in a low-noise system will now be explained. It can be shown that the noise introduced by a matched circuit with a power transmission coefficient a amounts to

$$T = T_R(1 - a) = T_R(1 - 10^{-A/10}),$$

where $A = -10 \log a$, the insertion loss in decibels, and T_R is the temperature of the circuit in degrees Kelvin. With T_R taken to be 290°K, the formula leads to the helpful approximation $T = 66.8$ A, if $A < 0.5$ db. For each tenth of a decibel loss, the noise will therefore increase by about 6.7°K. For a total loss of 1 db, the exact formula gives a temperature of 59.7°K. If one considers that the noise from all the nonwaveguide sources together amounts to about 20 to 30°K in a station like the one at Andover, it becomes clear that the waveguide losses should not exceed a very small fraction of a decibel.

It is enlightening to determine the effect of an additional 0.1 db of loss on the signal-to-noise ratio of a receiver with 26°K over-all noise temperature. We find that the added 6.7°K of noise is equivalent to an increase in the receiver noise power of one db. With the signal down only by 0.1 db the signal-to-noise ratio is degraded by 1.1 db. The effect of the loss is therefore 10 times greater on noise than on signal level. The situation becomes reversed, however, in cases where A is higher than a few db (very lossy waveguide circuits or high rain attenuation). The noise temperature then reaches 290°K asymptotically.

The waveguide components of Fig. 9 were measured with a dual-

TABLE II — LOSS AND NOISE OF THE WAVEGUIDE CIRCUIT AT 4170 MC

Waveguide Unit	Loss (db)	Noise Temperature °Kelvin
Autotrack coupler	0.010	0.67
Polarizer	0.021	1.40
Polarization coupler	0.007	0.47
Mode suppressor I	0.021	1.40
Low-pass filter	0.085	5.67
Mode suppressor II	0.016	1.07
23-db directional coupler, including coupling loss	0.030	2.00
Flexible waveguide	0.023	1.54
Total	0.213	14.22

channel insertion loss test set which gave an accuracy of a few thousandth of a db. Because noise is generated only by the absorptive part of the insertion loss, the loss due to reflections should normally be taken into account. However, the very high return losses (30–40 db) of the components made it possible to neglect the reflection losses for all practical purposes. Table II lists all the waveguide parts which contribute to the noise at 4170 mc.

No contributions from parts to the right of the autotrack coupler in Fig. 9 are shown because they are negligible. The noise temperatures shown in the table were calculated using the above formula. A more direct determination of the over-all waveguide noise temperature was made by using the maser as a low-temperature reference. The result was within 1°K of the above given figure of 14.22°K.

2.5 *System Noise Temperature*

2.5.1 *Method for Measuring Noise*

Those parts of the receiver which are important for the determination of the receiving system noise temperature are shown in Fig. 14. The noise energy coming from the sky, the radome, the antenna, and the waveguide circuits is lumped into a single term $kT_{IN}B$. It is assumed here that B is the receiver noise bandwidth of about 29 mc. Noise from a noise lamp can be injected through a 23.35-db directional coupler into the signal path ahead of the maser. With the noise lamp turned off, we can write for the noise power at the output of the IF amplifier:

$$N_{OFF} = kBg_M g_{IF} (T_{IN} + cT_R + T_M) + kBg_{IF} (f - 1)T_R .$$

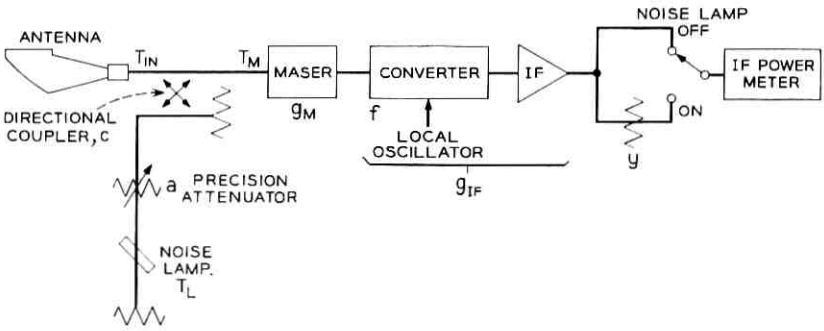

Fig. 14 — Circuit essential for the measurement of the noise temperature of the receiving system.

The g's are power gains, T_R is the room temperature, taken as 290°K, c is the coupling factor of the directional coupler ($=1/216$), and f is the noise factor of the converter ($=15.85$ or 12 db). TM is the temperature of the maser alone, amounting to 3.5°K. Effects like imperfect impedance matches, finite directivity of the directional coupler, and differences in noise bandwidth between the maser and the IF amplifier were neglected because they are very small. If we introduce the new term

$$T_{SYS} = T_{IN} + cT_R + \frac{f-1}{g_M} T_R + T_M,$$

meaning the receiving system noise temperature measured at the input terminals of the maser, the noise power can be written as

$$N_{OFF} = kBg_M g_{IF} T_{SYS}.$$

With the noise lamp turned on, the noise power at the output of the IF amplifier, after going through an attenuator with power loss coefficient y, is found to be

$$N_{ON} = kB \frac{g_M g_{IF}}{y} [T_{SYS} + ac(T_L - T_R)]$$

where T_L is the temperature of the noise lamp, amounting to about 9500°K, and a the power transmission coefficient of the precision attenuator. The noise due to the insertion of attenuator y is neglected because its loss is small and the product $g_M g_{IF}$ is high. In the course of a noise measurement, the two noise powers N_{OFF} and N_{ON} are made equal by adjusting the precision attenuator. The setting of the precision attenua-

tor will depend on, among other variables, the value of attenuator y, which can be changed in one-db steps. We then find for the system temperature:

$$T_{SYS} = \frac{ac}{y - 1}(T_L - T_R).$$

The maximum error of a noise measurement amounts to about ± 0.35 db or ± 8.5 per cent, with T_L contributing 0.2 db; $y - 1$, which includes short-term amplifier gain variations, 0.1 db; and the combination of a and c, 0.05 db. The improved accuracy of the noise lamp temperature over the 0.5 db of the commercial units was obtained by directly measuring the temperature of the lamp with the maser as a low-noise amplifier.

2.5.2 *Results of Noise Measurements*

Measurements of the system noise temperature made at Andover for different elevation angles of the antenna are shown in Fig. 15. The noise at zenith on a clear day is 32°K for the system containing a maser and is about 85°K with the parametric amplifier replacing the maser. The noise increases towards the lower elevation angles due to the higher noise originating in the atmosphere. When the antenna beam hits the ground, the noise increases abruptly to a value of about 235°K. This temperature depends on the actual temperature and the reflection coef-

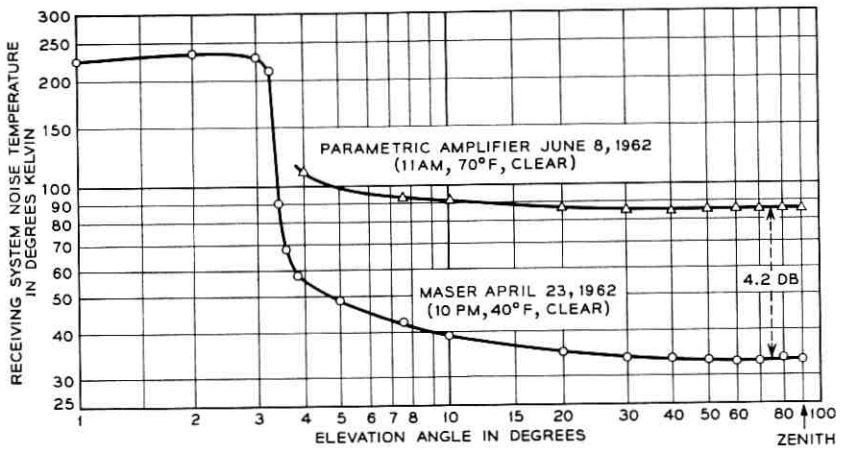

Fig. 15 — Receiving system noise temperature as a function of antenna elevation — clear day data. Azimuth = 142°.

ficient of the ground and on the losses of the signal through the radome and the waveguides. Knowing all these parameters, except the reflection coefficient of the ground, we find for the latter a value of 0.165 at 4170 mc. The sharp increase of the noise at the horizon was used to plot the radio horizon, which then was compared with the far optical horizon. The two coincided within about 0.1° for all regions where the far horizon was not hidden behind nearby obstacles.

The noise distribution shown in Fig. 15 was measured many times and was never found to vary more than one or two degrees on clear or cloudy days. During periods of rain or snow, vastly different noise temperatures were observed. Fig. 16 shows three typical curves. During a heavy rain (curve number 1), high noise values were found, with fast variations occurring in the region from 50° to 90° elevation. Variations at zenith over a period of about 15 minutes ranged from 68° to 126°K. Zenith temperatures between 70°K and 100°K are quite common during periods of moderate rain.

Curve 2 shows a case of light rain, and curve 3 was taken during a light and wet snowfall. The high noise temperatures found near the zenith (curve 3) are clearly due to the presence of the radome on which more snow has accumulated near the top than on the sides. Even curves

CURVE	DATE	LOCAL TIME	WEATHER
1	MAY 24, 1962	10:30 TO 11:30	HEAVY RAIN
2	SEPT 5, 1962	15:00 TO 15:20	LIGHT RAIN
3	OCT 26, 1962	07:10 TO 07:30	LIGHT WET SNOW

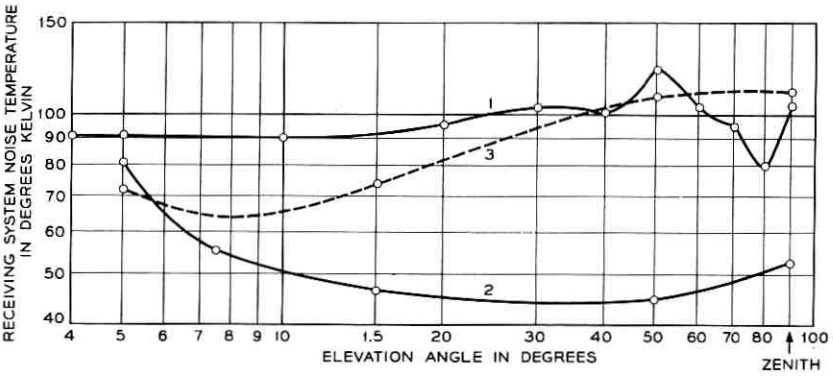

Fig. 16 — Receiving system noise temperature as a function of antenna elevation — rain and snow data. Azimuth = 142°.

1 and 2 show more noise at the higher angles than at, for instance, 15° elevation. This may again be due to some "accumulation" of rain on the top of the radome, but is also due to increased reflection of ground noise into the antenna aperture by the higher portions of the inner radome surface. The latter will become clearer in a moment when the electrical characteristics of the radome are described. The highest zenith system temperature observed to date in Andover due to rain is 135°K and 160°K due to snow. Within about half an hour after the end of a rainfall, noise temperatures close to the dry values of Fig. 15 can be found.

Similar measurements of noise during rain and snow, made at the Holmdel and Whippany, N. J., locations of Bell Laboratories, but without a radome, show a completely different character. Noise temperatures tend to be considerably lower, especially during snow, and they always seem to be lowest at zenith.

2.5.3 *Contributors to System Noise*

Table III gives a breakdown of the system noise into the different contributors. The values for the dry atmosphere were taken from measurements made at Holmdel.[17] The zenith temperature of 2.6°K of this reference appears reduced to 2.4°K by the total loss of 0.36 db in the radome and the waveguides. The contributions of antenna sidelobes, waveguides, maser and second stage are constant and amount to 19.2°K. They were discussed above with the exception of the antenna sidelobes. The horn-reflector antenna is probably the antenna with the lowest possible noise. If operated without a radome, all sidelobes and backlobes

TABLE III — CONTRIBUTORS TO SYSTEM NOISE

	Elevation			
	90°	30°	15°	7.5°
Dry atmosphere	2.4°K	4.8°K	9.2°K	18.4°K
Antenna sidelobes Waveguide circuits Maser Second stage	1.0 14.2 3.5 0.5 } 19.2°K			
Dry (wet) radome absorption	3 (12)	3 (12)	3 (12)	3 (12)
Dry (wet) radome scattering	7.4(18.5)	6.0(15.0)	4.1(10.2)	1.4(3.5)
Total (dry, measured)	32.0 °K	33.0 °K	35.5 °K	42.0 °K

will not contribute more than about 1°K if the antenna is pointed at least one degree above the horizon.

The effect of the radome on system noise is two-fold. First, the absorption of 4170-mc energy by the radome material is a measure of the noise it spontaneously emits at the same frequency; and second, the inner surface of the radome will reflect (scatter) ground noise into the antenna aperture. In order to investigate the first effect, it was necessary to know the loss characteristics of the radome. Laboratory measurements on dry and wet radome samples first gave values for the dielectric constant and the loss tangents. Calculations were then made to determine the power reflection $|r_E|^2$ and power transmission $|t_E|^2$ coefficients and the absorption transmission coefficient $a = |r_E|^2 + |t_E|^2$. The absorption loss in decibels is $A = -10 \log a$ and would amount to 0 db for the lossless material shown in Figs. 12 and 13. The results of the present investigation are shown in Figs. 17 and 18. If we consider again a maximum variation of angle of incidence from 8° to 52°, we find 3° and 12°K as rough averages for the absorptive noise in the dry and the wet case. It should be kept in mind that the data for the wet radome are based on tests made in the laboratory and that they cannot be completely representative of the conditions encountered in the field where the amount of wetness will vary with the rate of rain and possibly the position on the radome. The tests also showed that the dielectric constant and the loss tangent of the wet material decayed rapidly within minutes and later more slowly towards the "dry" values.

The scattering effect of the radome is difficult to determine by calculation. The noise values shown for dry radome scattering in Table III are therefore equal to the amount of noise which could not otherwise be accounted for. The higher scattering at high elevation angles is due to the particular antenna-radome geometry,* and to a certain extent is also dependent on the area surrounding the radome. The ground effects were determined by rotating the antenna 360° in azimuth and observing the change in zenith temperature. Values ranging from 31° to 35°K were found. The data presented in Figs. 15 and 16 and in Table III were taken at an azimuth of 142° (boresight tower).

The scattering effect of the wet radome was found by multiplying the dry values with the ratio of wet-to-dry power reflection coefficients as given in Figs. 17 and 18. This ratio is about 2.5 over a large range of

* Experiments with antennas whose apertures remain always vertical to the diameter of a spherical radome indicate that scatter-noise is minimum at zenith. Such a geometry is impractical for the horn-reflector antenna, however.

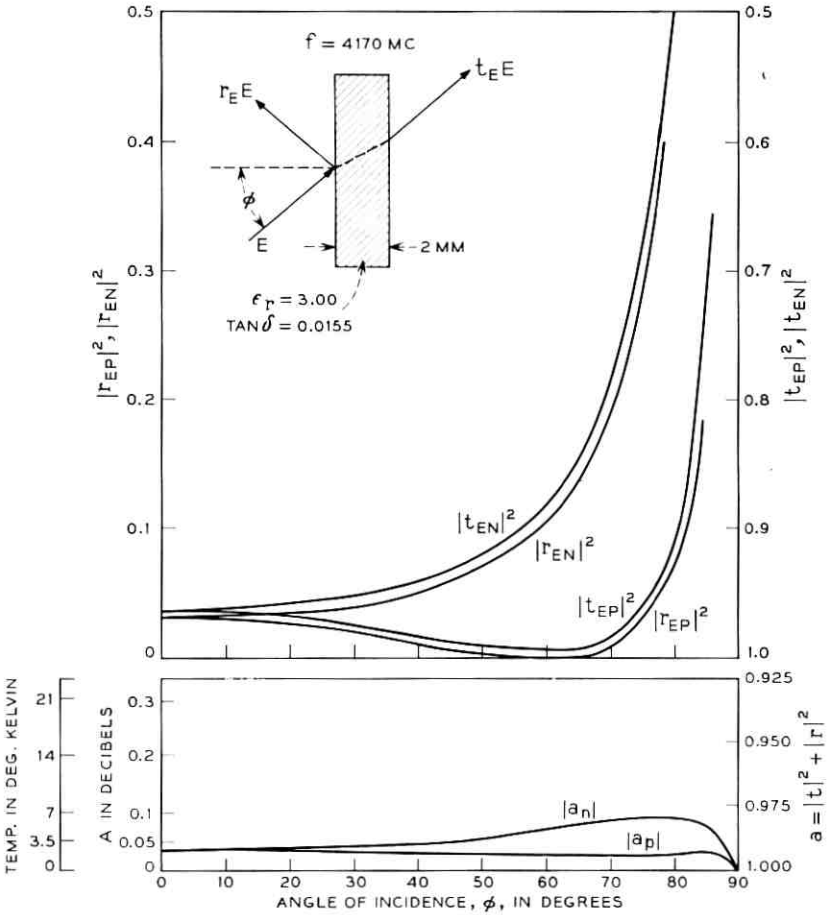

Fig. 17 — Reflection, transmission and absorption transmission coefficients of the dry radome at 4170 mc.

angles of incidence. Wet radome scattering is considerably larger at zenith than at lower angles. This explains the higher noise readings at zenith than at 15° elevation.

Recently, the diplexer of Fig. 9 was operated without the low-pass filter. It was found that one of the polarization couplers built had an isolation peak of 47 db in a narrow band around 6390 mc. This value of isolation allows unperturbed operation of the maser. The system temperature could thereby be reduced by 5°K, or to 27°K at zenith.

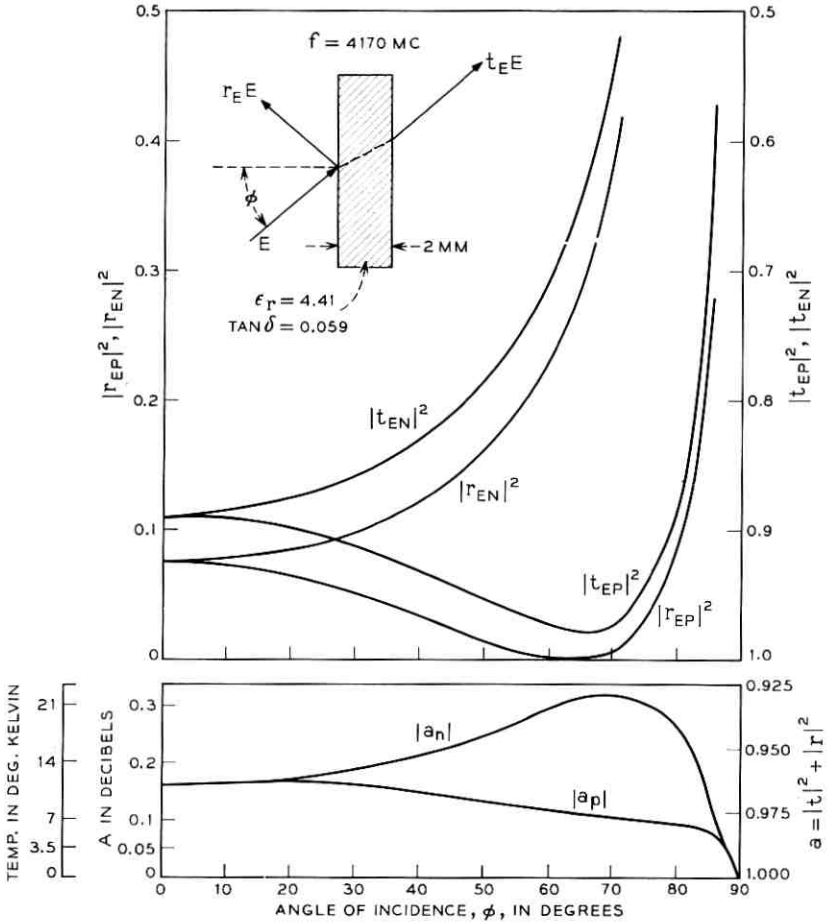

Fig. 18 — Reflection, transmission and absorption transmission coefficients of the wet radome at 4170 mc.

2.5.4 *Other Possible Sources of Noise*

A satellite communications system can be affected by extra-terrestrial noise sources, which is the case on such rare occasions when the satellite passes in front of one of these sources. The strongest source of noise at 4 kmc is the sun, followed by the moon and a number of radio stars. When the antenna is pointed at the center of the galaxy, a few extra degrees of noise will be introduced.

A measurement was made of the receiving system noise at and near

the sun. The antenna was pointed in the path of the sun, which then drifted through the antenna pattern. The result is plotted in Fig. 19. Over an angle of about 0.4°, which is a little less than the 0.5° diameter of the sun, a maximum temperature of 17,000°K is maintained, representing an interfering noise signal of −81 dbm. If we compare this signal with the signal from the satellite, which is in the range of −75 to −100 dbm, it is clear that communications would be disrupted during this time. The drop in noise shown in Fig. 19 is as expected from the radiation diagram of the antenna. Only one degree away from the center of the sun, the noise has dropped to an operationally acceptable 65°K.

The actual temperature of the sun at 4170 mc is higher than the measured 17,000°K by about 1.6 db, or equal to 24,500°K. The 1.6 db is made up of 0.04 db atmospheric loss, 0.15 db radome insertion loss, 0.21 db waveguide loss, and 1.2 db loss due to the finite width of the antenna pattern.

The temperature of the moon was measured on May 10, 1962, 10:00

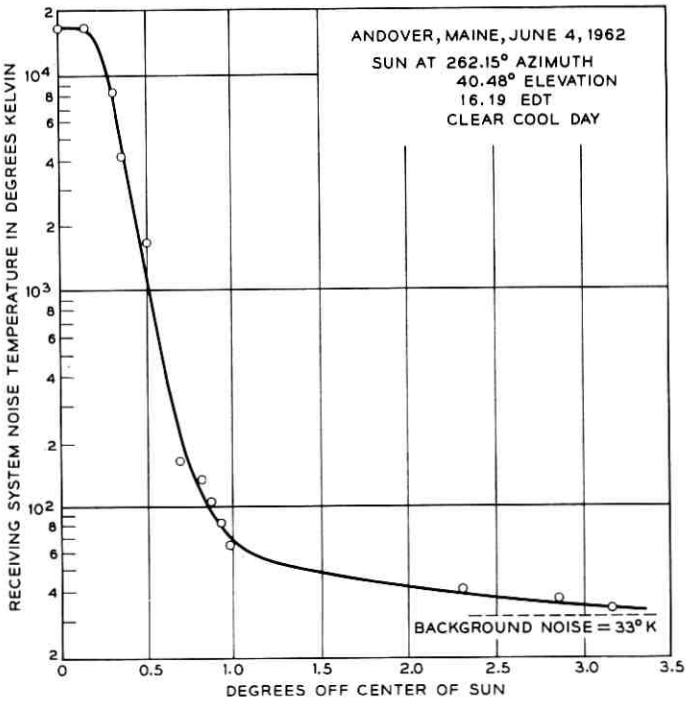

Fig. 19 — Receiving system noise temperature near the sun.

p.m. EDT. The maximum system temperature was found to be 195°K. If we subtract from this figure 34°K of system background noise and add 1.66 db due to the same type of losses mentioned before, we find for the temperature of the moon 236°K. The moon will produce a noise power in the communications channel of −100.5 dbm and therefore can affect the satellite link if the received signal level is lower than −95 dbm.

A search was also made for man-made sources of noise and interference. Such signals would be strongest close to the horizon. The measuring equipment included the receiver followed by a narrow-band IF amplifier which allowed the detection of signals down to −130 dbm. This is about 20 db lower than the normal broadband noise level of the receiver. No noise or other interfering signals could be detected. This is clearly a result of the topography of the Andover site.

III. ACKNOWLEDGMENTS

A number of people have contributed to the development of the transmitter and receiver for the Telstar ground station. The efforts of G. S. Axeling in the design of the receiver waveguide circuits are particularly acknowledged. W. Gabel, G. D. Hohmann and W. S. Irvine contributed to the power amplifier design, and J. Schill was largely responsible for the FM deviator.

REFERENCES

1. Hoth, D. F., O'Neill, E. F., and Welber, I., The *Telstar* Satellite System, B.S.T.J., this issue, p. 765.
2. Shennum, R. H., and Haury, P. T., A General Description of the *Telstar* Spacecraft, B.S.T.J., this issue, p. 801.
3. Sproul, P. T., and Griffiths, H. G., The TH Broadband Radio Transmitter and Receiver, B.S.T.J., **40**, November, 1961, pp. 1521–1568.
4. Susen, C. P., and Degan, J. J., The TH Radio Microwave Carrier Supply System, B.S.T.J., **40**, November, 1961, pp. 1569–1586.
5. Houghton, E. W., and Hatch, R. W., FM Terminal Transmitter and Receiver for the TH Radio System, B.S.T.J., **40**, November, 1961, pp. 1587–1626.
6. Collier, R. J., Laico, J. P., Helm, G. D., and Striny, K. M., The Ground-Station Traveling-Wave Tube, B.S.T.J., this issue, Part 3.
7. Houghton, E. W., and Drazy, E. J., Test Equipment for the TH Radio System, B.S.T.J., **40**, November, 1961, pp. 1717–1743.
8. Giger, A. J., and Low, F. K., The Automatic Protection Switching System of TH Radio, B.S.T.J., **40**, November, 1961, pp. 1665–1715.
9. Githens, J. A., and Peters, T. R., Digital Equipment for the Antenna Pointing System, B.S.T.J., this issue, Part 2.
10. Hatch, R. W., Bennett, S. B., and Kinzer, J. P., Results of the *Telstar* System Communication Tests, B.S.T.J., this issue, Part 2.
11. Tabor, W. J., and Sibilia, J. T., Masers for the *Telstar* Satellite Communications Experiment, B.S.T.J., this issue, Part 3.

12. Uenohara, M., Chruney, M., Eisele, K. M., Hanson, D. C., and Stillwell, A. L., A 4-gc Parametric Amplifier for the *Telstar* Satellite Communication Experiment, B.S.T.J., this issue, Part 3.
13. Giger, A. J., and Chaffee, J. G., The FM Demodulator with Negative Feedback, B.S.T.J., this issue, p. 1109.
14. Ohm, E. A., Project Echo Receiving System, B.S.T.J., **40**, July, 1961, pp. 1065–1094.
15. Cook, J. S., and Lowell, R., The Autotrack System, B.S.T.J., this issue, Part 2.
16. Tang, C., unpublished work.
17. De Grasse, R. W., Hogg, D. C., Ohm, E. A., and Scovil, H. E. D., Ultra-Low-Noise Antenna and Receiver Combination for Satellite or Space Communication, Proc. National Electronics Conference, **15**, October, 1959, pp. 370–379.

The FM Demodulator with Negative Feedback

By A. J. GIGER and J. G. CHAFFEE

(Manuscript received March 22, 1963)

This paper describes the design and theory of operation of the wideband FM demodulator with feedback (FMFB receiver) used at the Andover, Maine, earth station for Telstar satellite communications tests. Performance data for the FMFB receiver indicate a clear advantage over the conventional FM receiver in many cases. The principal advantage lies in the ability of the FMFB receiver to raise the threshold at which "breaking" occurs for TV and other wideband signals.

I. INTRODUCTION

The FM demodulator with negative feedback (FMFB)* is an outgrowth of an FM receiver circuit first described in 1937.[1] A demodulator of this type was used during the communication tests with the Echo I satellite, which started in August, 1960.[2] Compared with a conventional or standard FM demodulator, the principal advantage to be derived from this circuit is its ability to improve the threshold at which "breaking," resulting from excessive noise, will occur.

The receivers mentioned above were capable of demodulating a single 4-kc voice channel. Since it was required that the Telstar system be capable of handling television and other wideband signals, the design of feedback receivers became a problem of much greater complexity as a consequence of the relatively wide baseband.

The FMFB receiver to be described in this paper is used in the Andover ground station for the reception of wideband signals from the Telstar satellite.[3] A different FMFB receiver, described elsewhere,[4] was used in the Holmdel station during Telstar experiments. The basic elements of the feedback receiver are shown in the block diagram of Fig. 1. The incoming RF signal is combined in a mixer with the output of a

* Sometimes called "FM feedback receiver" or "frequency compression demodulator."

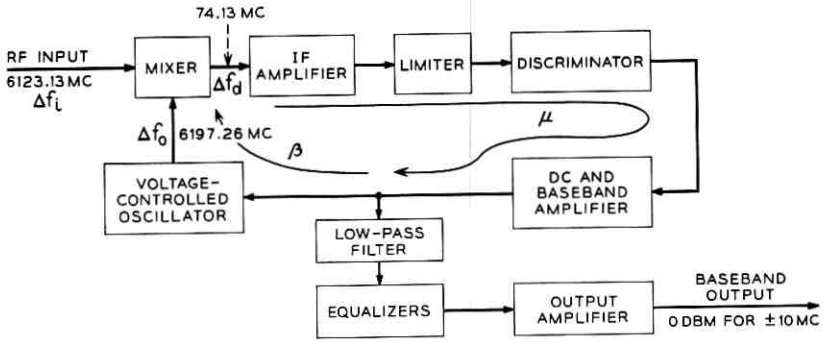

Fig. 1 — Block diagram of FMFB receiver.

voltage-controlled oscillator (VCO) to produce an intermediate-frequency signal. The frequency modulation which has been imparted to this signal, after going through an IF amplifier and a limiter, is then demodulated by the discriminator. The recovered baseband signals are amplified in the dc-and-baseband amplifier and are fed back to the VCO in such a way as to reduce significantly the instantaneous frequency difference between the two signals going into the mixer. The modulation index of the IF signal is thereby diminished. If this reduction is substantial, the resulting FM wave will occupy a much narrower band than the incoming RF signal. This makes it possible to restrict the bandwidth of the IF amplifier. In a sense, the feedback receiver can be considered as a "tracking" filter whose bandwidth is substantially narrower than that required to transmit the complete incoming FM wave; being narrower, the receiver is more immune to incoming noise.

The baseband signal to be fed to the output terminal of the receiver is taken from the input to the VCO and then passed through a low-pass filter, amplitude equalizers, and an output amplifier. The amplitude equalizers correct for deviations in the closed-loop transmission characteristics which are present at low and at high frequencies.

II. THEORY OF THE FMFB RECEIVER

2.1 *Operation above the Breaking Point*

The operation of the FMFB receiver is well understood in the region where the input carrier-to-noise ratio is large, which means well above the breaking point. For analytical purposes, it is convenient to represent the RF and IF circuits in the feedback loop by the baseband analogs

which are valid for FM signals. Simplified analog circuits are normally used which are accurate only for low-index FM signals. Such analogs do not describe the nonlinear distortions of the FM signal which are actually produced in the RF and IF circuits. Nevertheless, they are good enough for a linear analysis above threshold.

The FMFB circuit can then be represented as a conventional feedback circuit with the $\mu(s)$ and the $\beta(s)$ paths defined as in Fig. 1. The mixer is the element which forms the instantaneous difference between the frequencies of the incoming and the fed-back RF signals, i.e., $\Delta f_d = \Delta f_i - \Delta f_o$. The expression $\mu\beta$ is called the open-loop transmission characteristic. It is of fundamental importance in the design of a feedback circuit, since it determines the stability of the loop through its effect on the closed-loop transmission characteristic

$$\frac{\Delta f_o(s)}{\Delta f_i(s)} = \frac{\mu\beta}{1 + \mu\beta} = \frac{\mu\beta}{F}, \tag{1}$$

where $F = 1 + \mu\beta$ = feedback. In any practical wideband FMFB circuit, $\mu\beta$ is a function consisting of many poles and zeros. Analytical methods and actual measurements, together with the optimizing procedures given by Bode,[5] have been used here to design and shape the feedback loop.

The fact that so many stages (or poles) are necessary makes the design of a truly wideband FMFB circuit very difficult. The design problem is reminiscent of the one found in building amplifiers with maximum gain-bandwidth product, to which is added the complicating requirement of holding the over-all phase shift well below 180°. The problem was approached by carefully selecting each part of the FMFB circuit to have as little phase shift and as much gain as possible. In addition, it is advantageous to use high-level signals at the two inputs of the mixer of Fig. 1. This reduces the amount of amplification required inside the loop and can therefore be considered to be the same as obtaining gain without phase shift. This method is limited mainly by the power handling capabilities of the circuits.

In the circuit of Fig. 1 the transmission factor $\beta(s)$ is associated with the VCO alone. In the design to be described in Section III, the VCO consists of a reflex klystron whose transmission characteristic can be assumed to be a constant. The over-all input-output characteristic of the FMFB receiver is therefore obtained by multiplying the closed-loop transmission characteristic with the characteristics of the low-pass filter and the equalizers.

The signal-to-noise ratio (SNR) at baseband for a conventional FM

receiver for carrier-to-noise ratios (CNR) at RF well above breaking is known to be

$$\text{SNR} = \frac{3}{2} m^2 \frac{B}{b} \text{CNR}, \tag{2}$$

where B = RF bandwidth, b = baseband width, and m = modulation index. The RF and baseband transmission characteristics are assumed to be rectangular. It has been shown in Ref. 6 that (2) remains unchanged for an equivalent FMFB receiver. The feedback receiver, therefore, has no noise advantage if operated above the breaking or threshold point. This point, characterized by a certain CNR, is reached when the FM noise improvement given by (2) can no longer be obtained. The breaking point shall be loosely defined here as the CNR where the actual SNR has dropped 1 db below the value given by (2).

2.2 *Operation near the Breaking Point*

No theory is at present available which completely describes the behavior of an FMFB receiver near the threshold of noise improvement. Enloe[6] has introduced a two-threshold concept which has given good results in practical cases. Strictly speaking, the results of Ref. 6 are valid only under the assumption of an unmodulated carrier. We shall use this concept here in order to find simple mathematical expressions for the open-loop and the closed-loop threshold. Relations will then be derived for the optimum amount of feedback and the upper limit of the threshold improvement. These results are then compared with actual measurements taken under various conditions of modulation.

2.2.1 *The Open-Loop Threshold*

Under the assumptions that the incoming carrier is unmodulated and that the VCO generates a steady carrier (open loop), the CNR after the narrow-band IF amplifier (of bandwidth B_{IF}) in the loop will be greater than that at RF (bandwidth $B > B_{\text{IF}}$). Since FM discriminators break at about the same CNR, it can be seen that the insertion of the narrow-band filter results in a threshold improvement over a standard, wide-band FM receiver. The breaking point of a conventional FM receiver varies slightly with the ratio B_{IFN}/b (or B/b). B_{IFN} is the noise bandwidth of the IF filter, and we assume it to be 20 per cent higher than the 3-db bandwidth B_{IF}. B is assumed to be the 3-db bandwidth as well as the noise bandwidth. The empirical formula

$$\mathrm{CNR}_0 = \left[250\left(\frac{B_{\mathrm{IFN}}}{2b} - 1\right)\right]^{\frac{1}{3}} \tag{3}$$

was found to approximate well the breaking points shown in Fig. 9 of Ref. 6. The expression gives good results for B_{IFN}/b as low as 2.5. The threshold, as measured in the RF band B, then appears at

$$\mathrm{CNR}_1 = \mathrm{CNR}_0 \frac{B_{\mathrm{IFN}}}{B} = \frac{B_{\mathrm{IFN}}}{B}\left[\left(250\left(\frac{B_{\mathrm{IFN}}}{2b} - 1\right)\right]^{\frac{1}{3}}\right]. \tag{4}$$

Despite the fact that we consider the threshold under conditions of no modulation, we shall introduce here the modulation index $m = \Delta f/b$, where Δf is the peak frequency deviation caused by full sine-wave modulation at the top baseband frequency b. We can now express B in new terms, employing the so-called Carson's rule

$$B = 2(1 + m)\, b. \tag{5}$$

Under the assumption of uniform feedback F over the band b, the 3-db bandwidth of the IF filter in the loop should be $B_{\mathrm{IF}} = 2[1 + (m/F)]\, b$. Using these relations and $B_{\mathrm{IFN}} = 1.2\, B_{\mathrm{IF}}$, we can rewrite (4) in terms of m and F only

$$\mathrm{CNR}_1 = 1.2\, \frac{1 + (m/F)}{1 + m}\left\{50\,[1 + (6m/F)]\right\}^{\frac{1}{3}}. \tag{6}$$

2.2.2 *The Closed-Loop Threshold*

The CNR at which the closed-loop threshold occurs is directly proportional to B_c, which is equal to twice the closed-loop noise bandwidth at baseband. If we again measure the second threshold in the RF bandwidth B, we find by using equation (1) of Enloe's paper

$$\mathrm{CNR}_2 = 4.8\, \frac{B_c}{B}\left(\frac{F - 1}{F}\right)^2. \tag{7}$$

In order to obtain values for B_c, the open-loop characteristic $\mu(s)\cdot\beta(s)$ has to be specified. The Bode-type open-loop characteristic,[5] which provides constant feedback F up to a baseband frequency b and from there on a constant phase, can be considered to be near optimum for our purposes. It will be used for the following derivation. Although not strictly realizable in practice, this characteristic can be approximated by a technique, also due to Bode, which employs the so-called step and fillet. Fig. 8 of Ref. 6 has curves which give B_c as a function of the phase

margin with F as parameter. A phase margin of 50° is considered to be near optimum, because it minimizes B_c over a wide range of F. The empirical relation $B_c = 2bF^{0.8}$ was found to agree well with these curves for a phase margin of 50°. With this relation and (5), we can write (7) in the following form:

$$\mathrm{CNR}_2 = 4.8 \frac{F^{0.8}}{1 + m} \left(\frac{F - 1}{F} \right)^2 . \tag{8}$$

2.2.3 *Optimum Feedback and Upper Limit for Threshold Improvement*

It can be seen from (8) that an increase in feedback F will increase the closed-loop threshold, mainly due to the increase in B_c. Equation (6), on the other hand, indicates a decrease in threshold with increasing feedback. For a certain value of F, the two thresholds will therefore be equal. Such an operating point will tend to optimize the over-all threshold of the FMFB receiver. Equations (6) and (8) were equated and the result is plotted in Fig. 2 as F_{OPT} in decibels versus the modulation index $m = (B/2b) - 1$. For a practical range of m from 3 to 10, we find feedback values varying over the narrow range from 14.2 to 18.2 db.

We can now determine the improvement I which an FMFB receiver provides over the threshold of a standard FM receiver. The standard

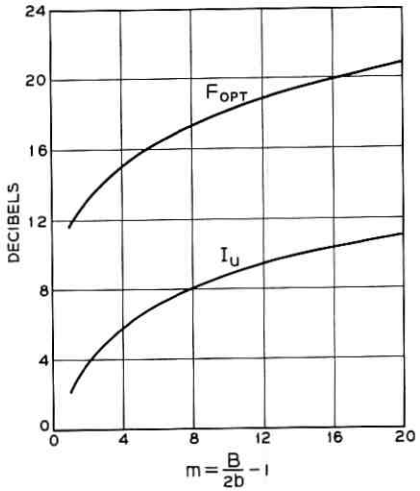

Fig. 2 — Optimum feedback F_{OPT} and upper limit of threshold improvement I_u.

receiver has a threshold given by (3) if B_{IFN} is replaced by B. Using (5), the threshold becomes

$$CNR_3 = \sqrt[3]{250\, m}. \tag{9}$$

Inserting $F_{OPT}(m)$ into either (6) or (8) yields CNR_{OPT}. The improvement is therefore

$$I \leqq \frac{CNR_3}{CNR_{OPT}}. \tag{10}$$

The equals sign indicates an upper limit I_u for the improvement, which could be reached only if the two thresholds occurred abruptly and independently of each other. This will most likely not be the case and the improvement will always be below this upper limit. I_u was calculated using the values of F_{OPT} previously found. The result is plotted as a second curve in Fig. 2. In the range of $m = 3$ to 10, upper bounds for the improvement reach from 4.9 to 8.8 db.

2.2.4 *Comparison with Measured Results*

We shall now compare the formulas derived above with measurements made on the FMFB receiver which are described in Section IV. The pertinent measured quantities are: $B = 25$ mc, $b = 2$ mc, $B_{IFN} = 7$ mc, $F = 15$ db (at 0.5 mc) and $B_c = 15$ mc. Then we find from (4) and (7), $CNR_1 = 2.05$ db and $CNR_2 = 2.90$ db, respectively. Therefore, the closed-loop threshold is governing by the small margin of 0.85 db. This is not quite optimum, and the design could be improved by a slight widening of the IF filter in the loop. Since the over-all threshold of the feedback demodulator is above either of the two thresholds, it must be greater than 2.9 db. It actually occurs at 4.5 db, as indicated by point A on curve 1 of Fig. 12 (Section 4.3.2). It can also be seen from this figure that the threshold is adversely affected by the application of modulation, especially at the higher baseband frequencies. We also wish to compare the measured results with the optimum design. Using (5), we obtain $m = 5.25$, and from Fig. 2 we find an optimum value for the feedback of $F_{OPT} = 16$ db and an upper limit for the threshold improvement of $I_u = 6.65$ db. The optimum setting of F was experimentally found to be the aforementioned 15 db at 0.5 mc. From Fig. 12, the threshold improvement amounts to 4.5 db, equal to the difference between points A and B. It can therefore be concluded that the actual design of the FMFB receiver has come to within 1 db of the calculated F_{OPT} and within 2.15 db of I_u.

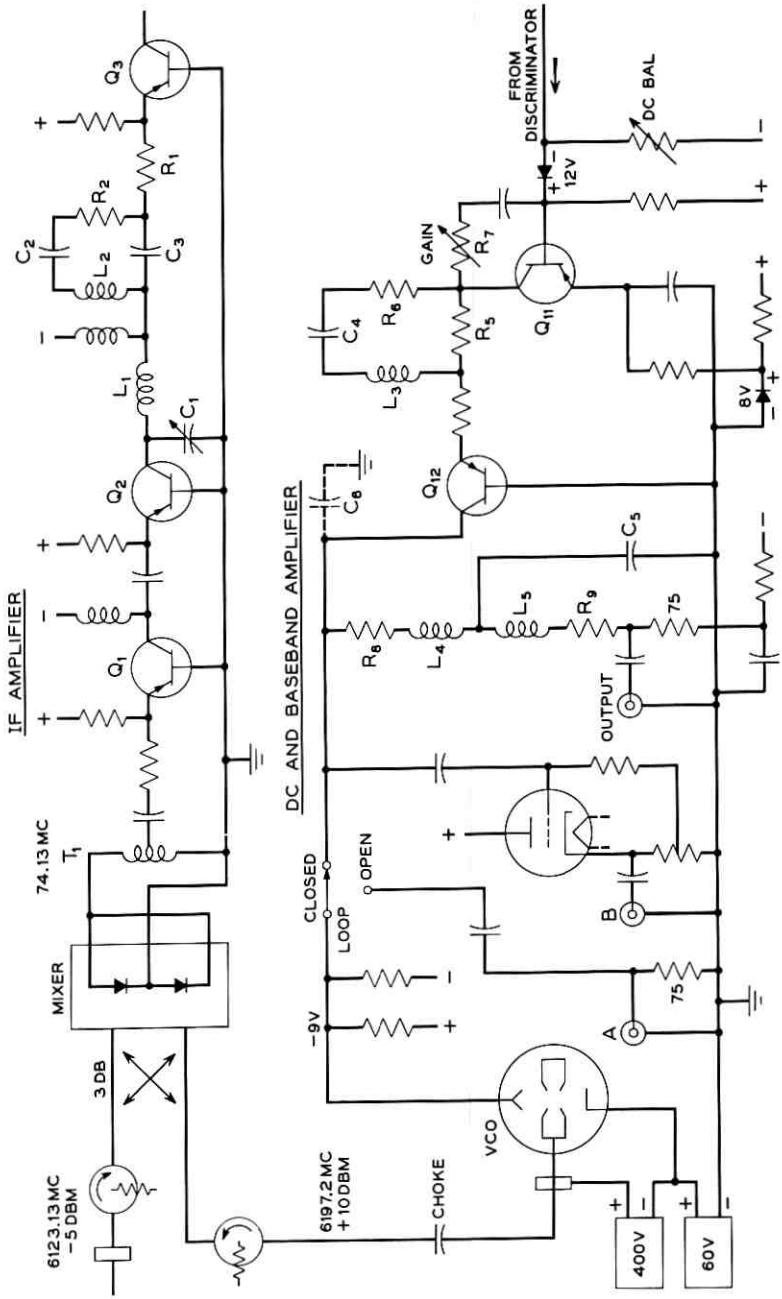

Fig. 3 — Circuit diagram of mixer, IF amplifier, VCO and de-and-baseband amplifier.

III. CIRCUIT DESCRIPTION

Simplified schematic diagrams of the feedback receiver are shown in Figs. 3 and 4. For simplicity, conventional filtering and power supply circuit details have been omitted.

The decision to use a microwave frequency as the input to the feedback circuit was dictated by the choice of a 6-gc reflex klystron for the VCO (Fig. 3). A klystron gives very little signal delay, has good modulation sensitivity, and its linearity is excellent. The klystron used is a modified version of the WE450A tube, in which the modulation sensitivity was increased from 1.5 to 5.0 mc/volt by altering the operation from the 2-3/4 to the 3-3/4 mode, decreasing the loaded Q slightly and changing the repeller geometry.*

The repeller capacitance of only 3 pf tends to keep the delay or phase shift in the driving circuit at a low value. A second, although very small, source of delay is found in the klystron itself. It is estimated that the modulating signal is delayed by the total travel time of the electrons in the repeller field. Since the tube is working in the 3-3/4 mode, this time is about 0.6 ns at the operating frequency of 6197 mc. No delay is produced by the cavity resonator, however. The nonlinearity of the klystron is very low and amounts to a change in modulation sensitivity of less than 4 per cent at a frequency 10 mc away from midband. Since the feedback in the receiver tends to reduce the nonlinear effects of the other circuits, the klystron can be considered the main source of nonlinear distortion. Since this klystron is sensitive to a small degree of mismatch, an isolator is provided between its output and the input to the mixer. The isolator has a signal delay only slightly greater than a straight piece of waveguide of the same length.

In order to maintain the driving transistor circuits at ground potential, the negative terminal of the repeller bias source is grounded. Consequently the cavity of the klystron is at high potential, necessitating the use of an insulating waveguide choke.

The mixer is a version of the receiving modulator used in the TH radio system, modified to operate efficiently at higher local oscillator and input levels. The mixer is designed to deliver the 74-mc IF signal into a 75-ohm unbalanced load. Since the emitter of the grounded-base transistor Q_1 has a much lower impedance, a broadband autotransformer (T_1) having a 2:1 turns ratio[7] is inserted, which partly corrects this mismatch. These transformers have a bandwidth of about 150 mc.

* This modification was carried out at the Allentown Laboratories of Bell Telephone Laboratories.

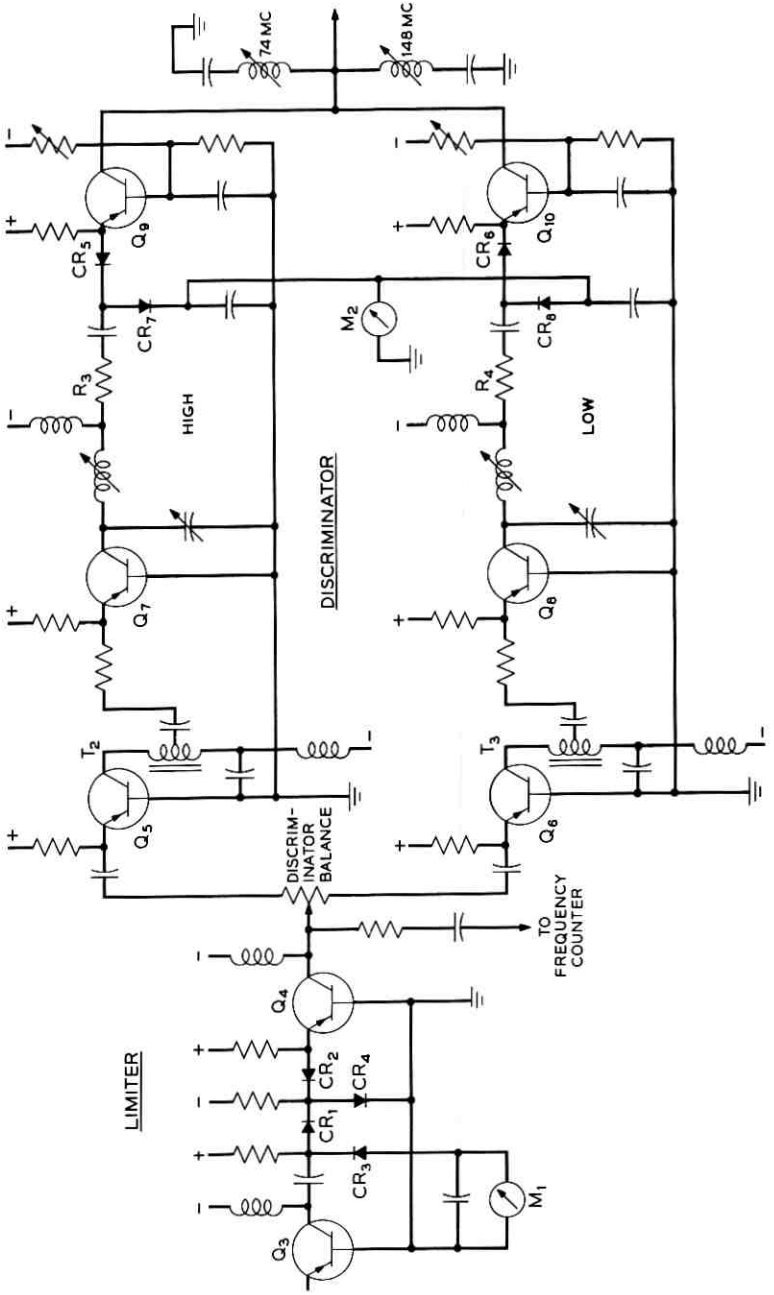

Fig. 4 — Circuit diagram of limiter and discriminator.

Diffused-base germanium transistors with alpha cutoffs above 500 mc were used throughout the circuit.

It was found that the relatively high impedance of the narrow-band IF filter network in the collector circuit of transistor Q_2 produced marked variations in the input impedance of this stage in the vicinity of resonance, even with a transistor having an $r_b'C_c$ product as low as 10 ns. In order to provide a suitable termination for the secondary of autotransformer T_1, it was necessary to introduce a buffer stage, represented by the first transistor, Q_1, to mask this effect.

The network shown in the output of the second transistor (Q_2) provides a bandpass transmission characteristic which limits the noise power delivered to the limiter-discriminator.

In the choice of a filter suitable for use at this point, several factors must be taken into consideration. From the standpoint of noise rejection, the use of a highly selective bandpass structure would be advantageous. However, such a filter would introduce a prohibitive amount of delay into the feedback loop. A simple single-pole network, on the other hand, has a much more favorable phase characteristic, but its effective noise bandwidth is 1.57 times the bandwidth between half-power points. The circuit shown is a compromise between these extremes. The tuned circuit formed by elements C_1, L_1, and R_1 alone would constitute a one-mesh filter circuit adjusted to resonate at the center of the IF band. The addition of a similar tuned circuit formed by elements C_2, L_2, R_2, loosely coupled to the first circuit through the mutual impedance of capacitor C_3, leads to a more nearly flat-topped transmission characteristic, shown in Fig. 5 by solid lines. For comparison, the characteristics of the one-mesh circuit of the same 3-db bandwidth are given by the dashed curves of Fig. 5. Although the two gain curves are superimposed in the figure, the two-mesh circuit produces a current gain which is 3 db greater than that of the one-mesh circuit. Note that the asymptotic phase shift with respect to midband is 90° for both circuits. The noise bandwidth of the two-mesh circuit is 7 mc, which is only 25 per cent higher than its 3-db bandwidth. The current gain is about 24 db. All the current gain in the IF amplifier is achieved by means of stable passive circuitry, with the common-base transistors acting as impedance transformers.

The common-base stage Q_3 feeds the IF signal to the series-type diode limiter which is shown in Fig. 4. Diodes CR_1 and CR_2 are normally conducting except at the peaks of the input wave. Diodes CR_3 and CR_4 normally do not conduct, except when diodes CR_1 and CR_2, respectively, are nonconducting.

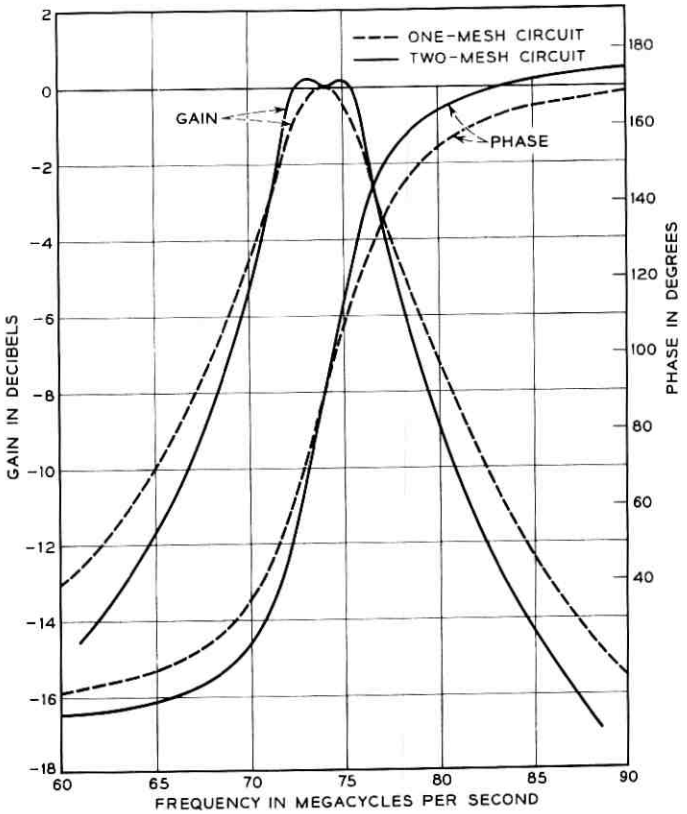

Fig. 5 — Gain and phase characteristics of narrow-band IF filter.

The limiter has no reactive elements and its impedance level is extremely low. This makes it a wideband circuit which exhibits very small signal delay. Envelope variations appearing on the input wave are reduced about 22 db by the circuit.

A dc meter M_1 in series with diode CR_3 serves as a convenient means for adjusting and monitoring the input to the limiter. The level is generally adjusted (by changing the 6123-mc input signal) so that clipping takes place about 3 db below the peaks of the IF signal.

Current delivered by the limiter is divided into two equal parts which are then subjected to 6 db of current gain in transformers T_2 and T_3 before being applied to the two inputs of a balanced discriminator. This discriminator consists of two simple resonant circuits connected to the collectors of transistors Q_7 and Q_8. One circuit is tuned to a frequency

12 mc above and the other a similar amount below the center frequency of the IF band. Damping of each circuit is adjusted by resistors R_3 and R_4 for a bandwidth of about 24 mc, so that the current gain of each branch is equal to 7 db at 74 mc.

When the incoming signal is frequency-modulated, frequency deviations give rise to amplitude variations within the two tuned circuits. These are detected by diodes CR_5 and CR_6. Diodes CR_7 and CR_8 provide a dc return in each case. These dc currents return to ground through a differential meter M_2, which gives a zero indication at midband when the two currents are equal. In order to avoid unequal biasing of diodes CR_5 and CR_6 by the emitter voltages of transistors Q_9 and Q_{10}, a bias is applied to the bases of these two transistors to make the resulting emitter voltages equal to zero.

The output of the discriminator is taken from the collectors of transistors Q_9 and Q_{10} and delivered to the dc-and-baseband amplifier shown in Fig. 3. Amplitude variations occasioned by noise will tend to cancel in the output line, thus supplementing the smoothing action of the amplitude limiter. Series-resonant circuits in the output line shunt to ground the 74- and 148-mc components which remain after the detection process.

The dc-and-baseband amplifier provides gain for the demodulated signal and delivers it to the repeller of the klystron as well as to the outgoing video line. Automatic center frequency control is accomplished by providing dc coupling within the amplifier.

In order to achieve adequate gain and phase margins within the feedback loop, it is necessary to control the open-loop gain characteristic over a wide range of frequencies — a problem common to all feedback amplifiers. This shaping of the loop has in general followed the techniques proposed by Bode.[5] The main correcting network is located in the collector circuit of transistor Q_{12} (Fig. 3). The part of the circuit consisting of C_6, R_8, and L_4, with return to ground over the large capacitor C_5, has a transmission peak at 30 mc which ensures the presence of the correct "Bode step" in the open-loop transmission characteristic. Below 30 mc, the gain of the last stage decreases and eventually rises again to a constant value at about 1 mc because of the presence of another shunt peaking network L_5, R_9, and C_5.

The common-emitter stage Q_{11} provides some minor shaping by means of the local feedback circuit consisting of R_7 together with R_5, R_6, C_4, and L_3. Increased gain is obtained for the "Bode fillet" at 1.25 mc, which is the resonant frequency of the series circuit R_6, C_4, L_3. The gain of Q_{11} otherwise is very flat up to about 40 mc, and can be

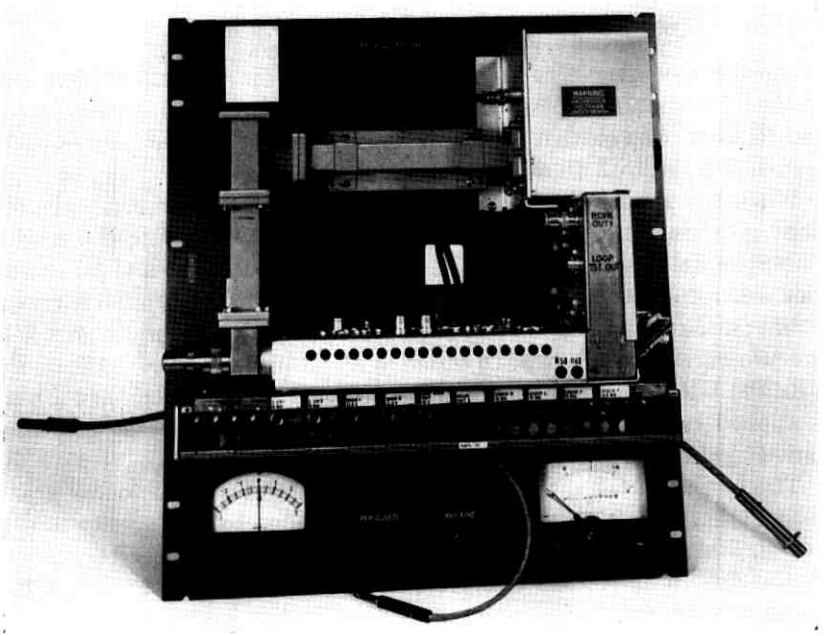

Fig. 6 — Photograph of FMFB receiver.

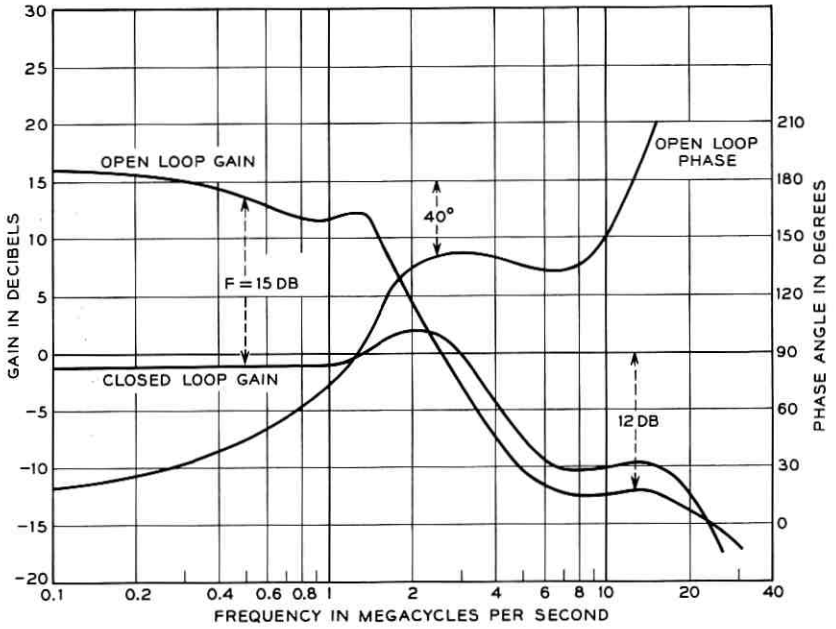

Fig. 7 — Open- and closed-loop transmission characteristics.

varied by R_7 over the range of 2 to 12 db. The normal setting is around 6 db, which results in a feedback of 15 db at 0.5 mc.

The gain characteristic of the loop is also well controlled down to dc by various circuits — not separately described — in the dc-and-baseband amplifier.

Baseband signals to be delivered to the outgoing line are taken from a 75-ohm impedance point within the main equalizing network. Transmission to this point differs markedly from the actual loop characteristic at frequencies above the usual baseband, in that frequencies higher than 3 mc are greatly attenuated. This effect is symbolized by the low-pass filter shown in Fig. 1.

The actual open-loop performance is measured by opening the loop with the switch in Fig. 3, applying baseband signals to the repeller at point A, and observing the voltage which appears at the collector of Q_{12}. Since this is a relatively high-impedance point, a cathode follower is permanently connected to the collector. The cathode impedance of this device is sufficiently low that standard low-impedance measuring devices can be connected at point B. The closed-loop characteristic is likewise measured at point B, with the loop switch in the closed position and a frequency-modulated 6123-mc signal applied to the input of the mixer.

A photograph of the FMFB receiver is shown in Fig. 6. The box housing the klystron (VCO) is shown on the upper right. The mixer on the lower left is attached to the horizontal part of the chassis, which contains the IF amplifier, limiter and discriminator. The dc-and-baseband amplifier is located in the vertical part of the chassis. The equalizers and the output amplifier are not shown in the photo.

IV. MEASUREMENTS

4.1 *Transmission Characteristics*

Gain and phase characteristics of the open loop are shown in Fig. 7. With the feedback F set to 15 db at 0.5 mc, the phase and gain margins are seen to be 40° and 12 db, respectively. Not shown in the figure is the transmission characteristic below 100 kc. Towards the very low frequencies the loop gain is permitted to increase slowly, so as to obtain about 5 db of additional gain at 15.75 kc. This is advantageous from the standpoint of television signals.

The gain with the loop closed is also shown in Fig. 7. In this case, a reflex klystron was used as the source of the 6123-mc FM signal. The closed-loop characteristic exhibits the typical region of gain enhance-

ment in the vicinity of the open-loop gain crossover. This region is strongly affected by the gain in the feedback loop. More gain would increase the transmission bulge around 2 mc, and in turn increase the closed-loop noise bandwidth. Less gain would cause insufficient frequency compression in the loop. With a feedback of 15 db, the closed-loop noise bandwidth at baseband was found to be about 7.5 mc, or $B_c = 15$ mc.

Since the effect of the gain enhancement around 2 mc is also seen at the useful output terminal of Fig. 3, a compensating high-frequency equalizer is included ahead of the output amplifier, as indicated in Fig. 1. The increase of gain in the open loop below 50 kc affects the closed-loop characteristic by about 1.3 db. A low-frequency equalizer makes the transmission flat to about 0.2 db down to a few hundred cycles. Transmission to the output of the output amplifier is shown in Fig. 8.

4.2 *Excess Phase Problems*

The problem of excess phase will now be dealt with in some detail because of its importance to present and future wideband feedback receivers. The term "excess phase" is used to indicate phase shift in excess of the theoretically determined minimum phase associated with the open-loop transmission characteristic. An obvious contribution to excess phase arises from the physical dimensions of the loop structure itself. In the present instance it is estimated that this can account for a delay of about 3.5 ns. In terms of phase, this would introduce a linear phase shift

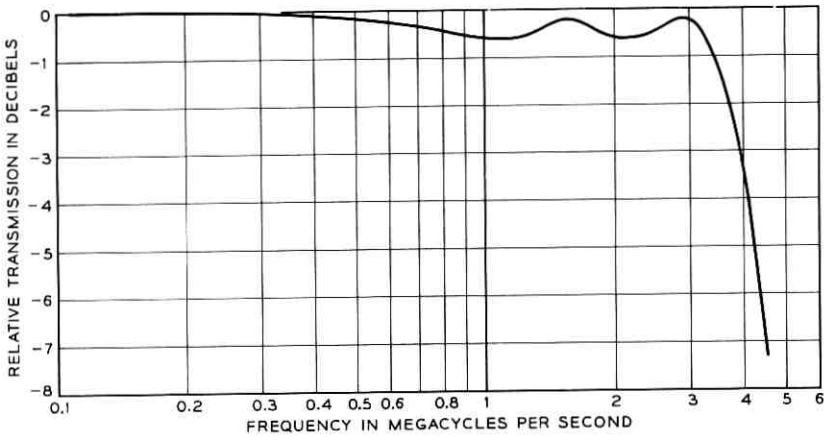

Fig. 8 — Over-all transmission characteristic.

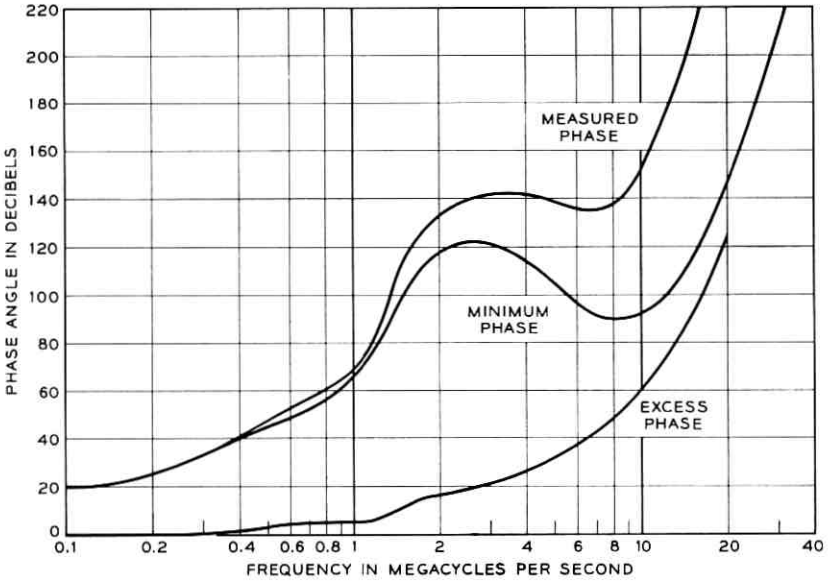

Fig. 9 — Measured and computed minimum phase characteristic of the open loop.

amounting to 1.27 degrees per megacycle. Though not negligible, the restriction thus imposed upon loop performance is rather small. Actually, a much greater amount of excess phase has been observed. This is illustrated in Fig. 9, which shows the computed minimum phase characteristic based upon the measured open-loop transmission. This curve is an approximation because of some degree of uncertainty regarding the cutoff performance at very high frequencies, in the region between 30 and 100 mc. However, conditions at these rather remote frequencies have only a minor influence upon the region of greatest interest.

Shown for comparison is the measured phase characteristic. The difference between these two curves closely follows the linear law of about 6 degrees per megacycle. This is five times as great as that estimated from the physical dimensions of the feedback loop. Several additional sources have been identified. Transistors are known to introduce a measure of excess phase. Measurements made at intermediate frequencies with a single common-base stage, such as is used at many points within the receiver, show excess phase amounting to about 0.2° per megacycle. Since there are in effect eight such stages within the loop, the total contribution of 1.6° per megacycle is not negligible.

TABLE I — SOURCES OF EXCESS PHASE

Source	Estimated Phase
Loop dimensions	1.3°/mc
8 common-base stages	1.6°/mc
Limiter	0.5°/mc
Common-emitter stage	2.0°/mc
Total	5.4°/mc
Measured	6.0°/mc

Considerable excess phase is associated with the common-emitter stage Q_{11} of the baseband amplifier. This amounts to about 2° per megacycle.

The limiter was found to have an essentially linear phase characteristic which, allowing for the input and output transistors, indicated a phase contribution of 0.5° per megacycle. Negligible phase shift is caused by the estimated 0.6 ns of delay in the klystron.

Adding these several contributions, we can account reasonably well for the difference between the minimum phase and the observed open-loop performance as indicated in Table I.

4.3 *Measurements near Threshold*

In order to obtain a better insight into the rather complicated mechanisms responsible for the performance near threshold, several types of measurements were performed on the FMFB receiver and on a conventional or standard FM receiver. The latter was taken from the TH radio system.[8] In order to produce the desired CNR's near threshold, flat thermal noise of 25-mc bandwidth was mixed with the FM signal at the intermediate frequency of 74 mc. This signal was then directly applied to the standard FM receiver, but translated to 6123 mc in a modulator for application to the FMFB receiver.

4.3.1 *Baseband Noise Spectra*

Baseband noise spectra were measured for CNR's ranging from 0 to 22 db. For this purpose, a sensitive analyzer with a 4-kc bandwidth was connected to the output of the receivers and readings were taken over the range from 100 kc to 5 mc. The solid curves of Figs. 10 and 11 show samples of these measurements taken on the standard and the FMFB receivers, respectively, for the case where the carrier is unmodulated. The noise readings were corrected where necessary so as to simu-

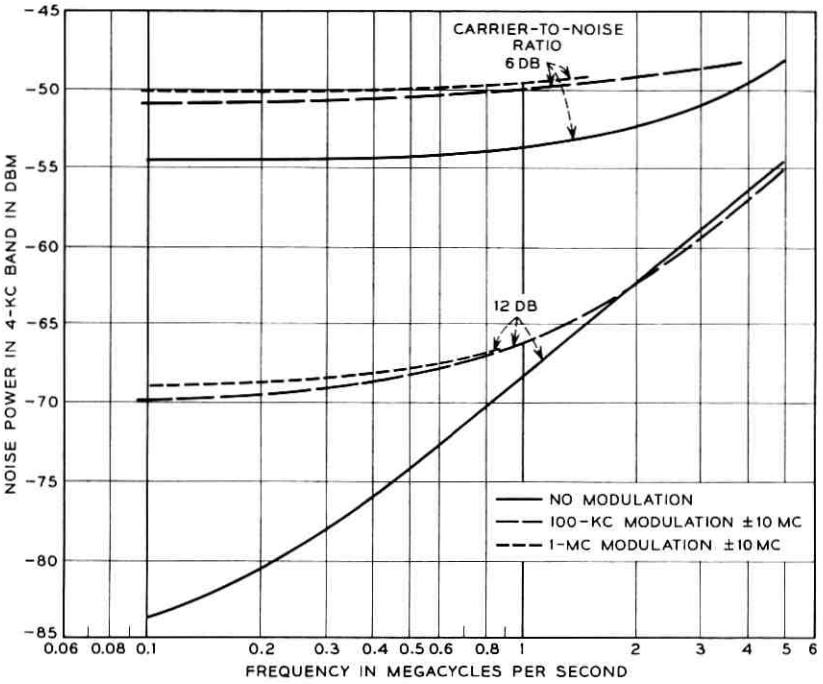

Fig. 10 — Noise spectra for standard FM receiver.

late absolutely flat receiver gain characteristics from 100 kc to 5 mc. At the higher CNR's, and for frequencies above a few hundred kilocycles, the spectra show the typical triangular characteristic of FM noise. When the CNR is decreased, the noise rises much faster at low frequencies, to produce ultimately the fairly flat noise spectra which were calculated by S. O. Rice[9] for the standard FM receiver. It has been known for some time that the baseband noise increases to some extent when modulation is applied to the FM carrier,[10] but the literature on the subject is very sparse. It was therefore decided to measure noise spectra in the presence of full ±10-mc sine-wave modulation. Such measurements are of somewhat limited practical value, because a single tone will only rarely be transmitted with the maximum frequency deviation. This is the case, however, in a number of TV test patterns, especially the "multiburst" pattern. Occasionally, such a situation may also arise in live TV signals for short periods of time. Examples of the results of modulation measurements are also shown in Figs. 10 and 11. A drastic difference exists between the standard and the FMFB re-

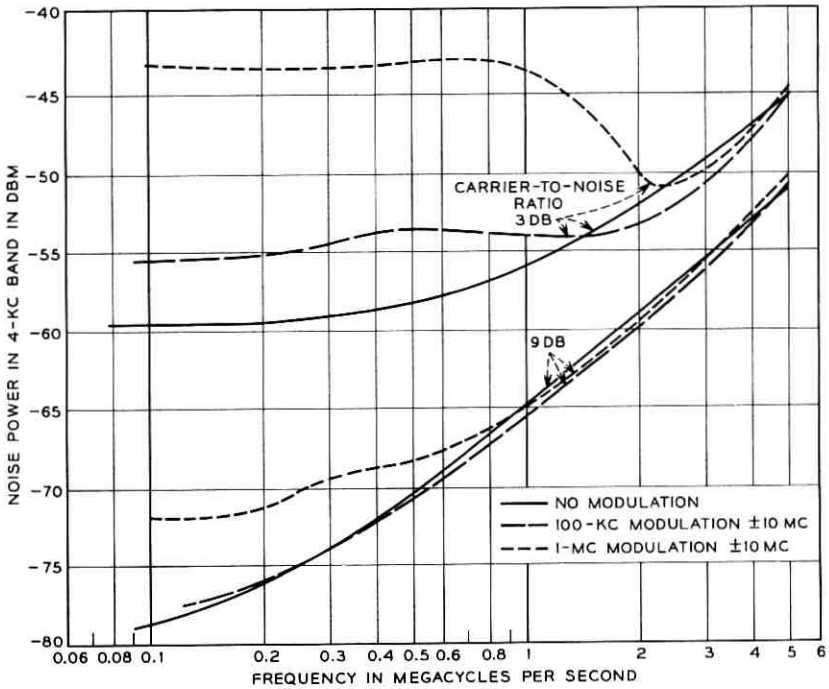

Fig. 11 — Noise spectra for FMFB receiver.

ceiver. The former shows an increase in noise which is nearly independent of the modulating frequency. The FMFB receiver, on the other hand, is little affected by a 100-kc modulating signal but much more so by a 1-mc signal, especially at low CNR's. The strongest effect of the modulation is seen at the low-frequency end of the noise spectrum, particularly in the case of the standard FM receiver at high CNR's.

4.3.2 *Threshold Curves*

The behavior of an FM system above and around the threshold region is often described by plotting the ratio of the signal power to the total noise power (SNR) in a baseband b, as a function of the CNR at RF in the bandwidth B. The total noise power in a 2-mc baseband was first determined for the case of no modulation by integrating a set of curves, of which the solid ones in Figs. 10 and 11 are a part. The result is shown in Fig. 12 as curves 1 and 3.

When modulation is applied, two effects are to be noted. One is the

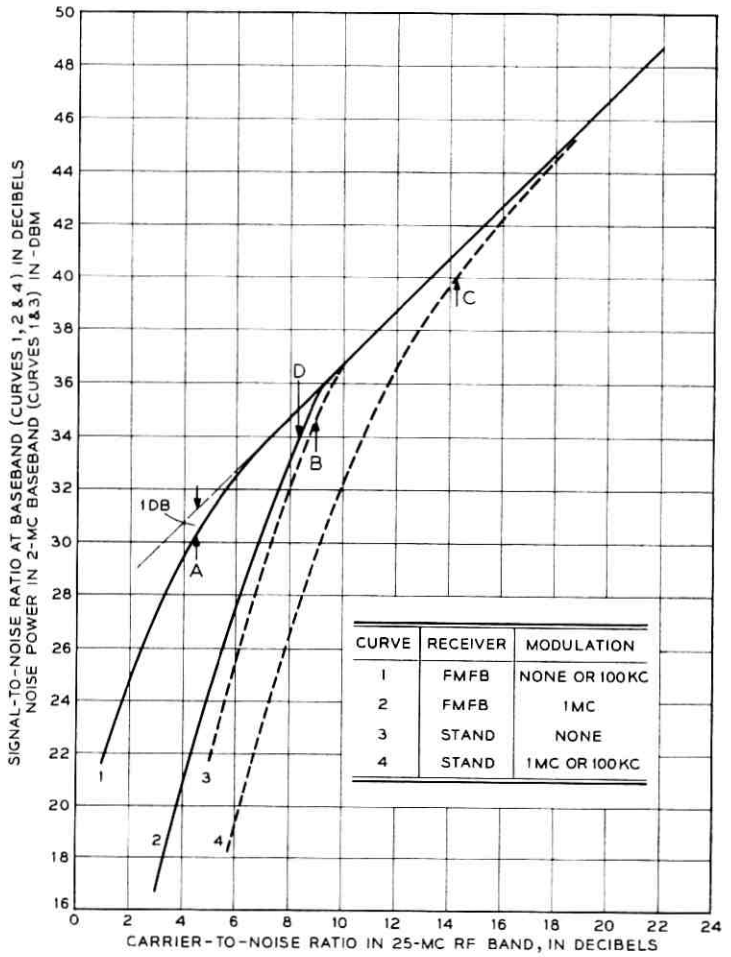

Fig. 12 — Signal-to-noise ratio at baseband.

increase in noise mentioned above. The other is a reduction in recovered signal level when the CNR is rather low. These effects shall be called noise increment and signal reduction, respectively. Noise increments for various CNR's were obtained by integrating spectra such as those shown in Figs. 10 and 11 for the case of full modulation. The results are shown in Fig. 13 for the two types of receivers. The increment is actually negative under some conditions — meaning that the total baseband noise is slightly less than for the case of the unmodulated carrier. This can be seen from the modulation curves of Fig. 11.

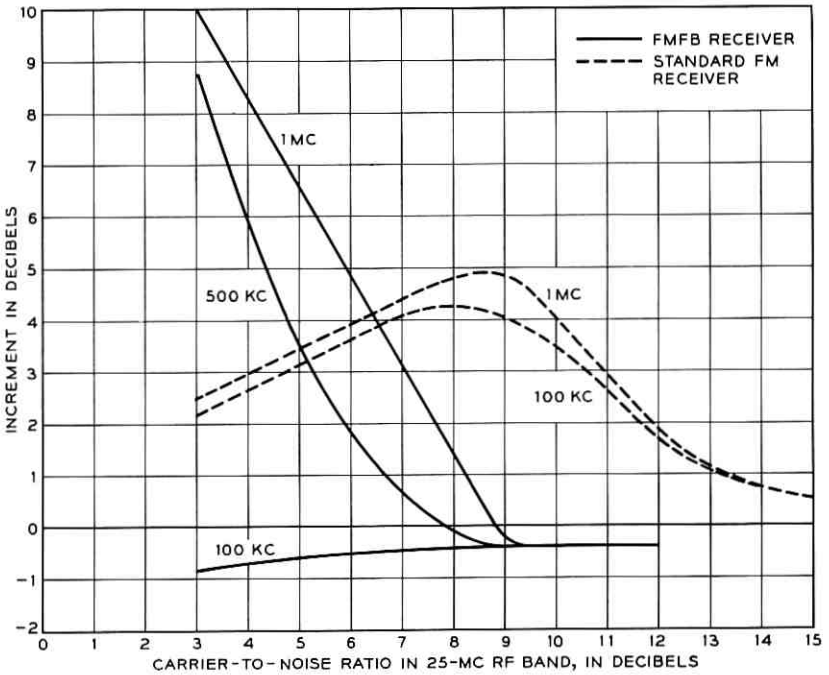

Fig. 13 — Noise increments.

Signal suppression was determined with the aid of a selective analyzer tuned to the signal frequency as the CNR was varied. Fig. 14 shows the performance which was observed.

The actual SNR in the 2-mc baseband can now be determined. The

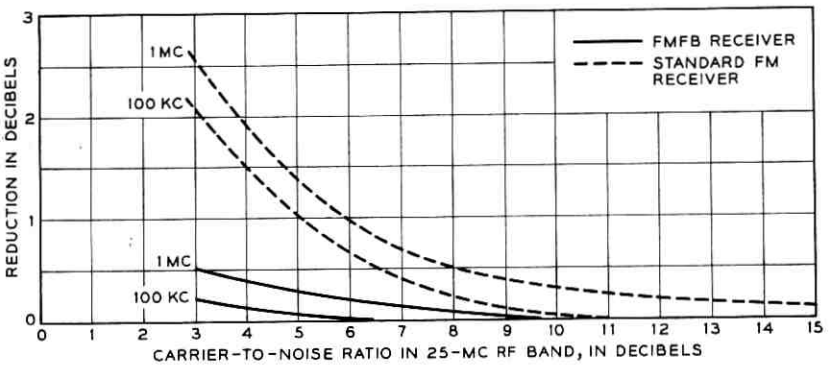

Fig. 14 — Signal reduction.

results are given in Fig. 12 as curves 1, 2, and 4. A few simplifications were made in this figure. Curves 1 and 4 are accurate only for no modulation and 1-mc modulation, respectively, and the 100-kc curves would actually be a few tenths of a db higher. Slight differences of about 0.5 db between the actual curves 1 and 3 and the calculated curve at high CNR's were neglected and made equal to the theoretical value given by equation (2).

The curves of Fig. 12 show clearly the advantage of the FMFB receiver over the standard receiver in the threshold region. An advantage of 4.5 db is obtained for the case of no modulation by taking the difference between the threshold points A and B. For 100-kc modulation the threshold improvement is 9.8 db ($C - A$), and for 1 mc it is 5.9 db ($C - D$). Curves similar to 3 and 4 were calculated by Rice.[10] No theory is yet available which would produce curves 1 or 2 for the FMFB receiver.

The threshold situation for actual signals such as TV and carrier multiplex requires further exploration by subjective tests and noise loading measurements, respectively. Such tests are described in the following two sections.

4.3.3 *Television Threshold Tests*

Fig. 15 shows the results of TV threshold tests. The peak-to-peak deviation produced by the television signal (including the sync pulse) was set to be 14 mc. An aural subcarrier at 4.5 mc, which deviated the main carrier by 2.8 mc peak-to-peak, was also transmitted. The television spectrum was restricted on the transmitting side by the insertion of a well-equalized 3-mc roll-off filter. Fig. 15 shows that the television patterns are still recognizable down to very low CNR's, especially when the FMFB receiver was used. A large number of subjective tests have shown threshold improvements of about 4 to 5 db. These pictures, as well as all the data described above, were taken with the FMFB receiver adjusted for a feedback of 15 db at 500 kc and its discriminator balance set for equal numbers of white and black noise dots. The 15-db figure was found to be a good compromise, giving a small enough closed-loop bandwidth (and therefore low noise) and still enough feedback to make high-frequency breaking due to lack of feedback not too conspicuous. A live TV picture occasionally contains very strong high-frequency components which show up as sharp vertical lines. Since there is not enough feedback available to keep the frequency deviation within the passband of the narrow IF filter, the signal at the discriminator will be below the breaking point at the deviation peaks. Breaking

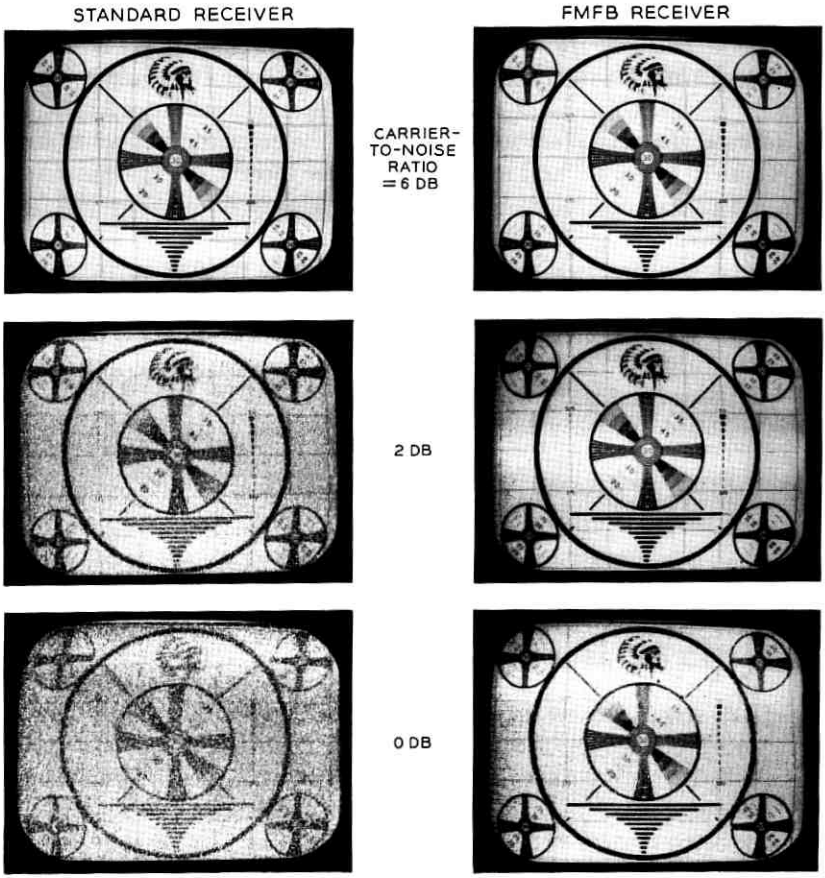

Fig. 15 — TV threshold tests.

which starts at a white peak produces a trailing black dot, and correspondingly a black peak generates a white noise dot. The nonrandomness of this breaking process makes it appear as a characteristic "sparkling" on the screen. It should be mentioned that the sparkling effect is not responsible for the strong increase in noise shown in Fig. 13 for 500 kc and 1 mc. Randomness of the noise in this case is still maintained, as observed on the oscilloscope.

The foregoing description makes it clear that TV pre-emphasis should not be used in a system containing the FMFB receiver of the present design. It is even desirable to insert a baseband roll-off filter in the transmitter in order to restrict the high-frequency components of the picture.

Tests with TV pre-emphasis were made, and it was found that the sparkling effect was strongly enhanced. This is due to the fact that the relatively short bursts of noise which cause the sparkle are integrated or lengthened in the de-emphasis network.

The FMFB receiver has also been tested with color TV signals. The behavior near threshold was found to be excellent if program material was transmitted, but rather poor if the color-bar pattern was used.

4.3.4 *Noise Loading Tests*

Tests were made to describe the behavior of the two types of receivers in the threshold region under conditions of a simulated telephone load. The telephone multiplex signal is simulated for this purpose by a noise signal with a flat spectrum, which in turn frequency modulates the RF carrier. Tests were made with 120, 240, and 600 channels. The noise-power ratio was measured at the receiver outputs in a number of frequency slots as a function of the total rms frequency deviation. The

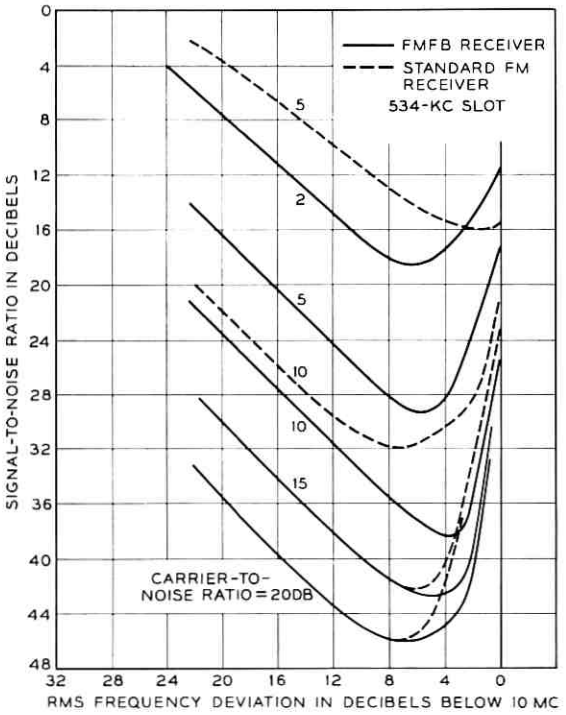

Fig. 16 — 240-channel noise loading.

noise-power ratio is the ratio of signal-plus-noise to noise, with the noise consisting of thermal and intermodulation noise. This ratio is essentially equal to the SNR for values greater than 10 db. Conditions existing in the vicinity of the threshold were established by injecting a 25-mc band of noise into the signal path. The bandwidth of the signal path exceeded the noise bandwidth by about 10 mc. Nonlinear distortions due to band limitations preceding the FM receivers were therefore reduced.

Fig. 16 shows results of 240-channel noise loading tests with a noise spectrum extending from 60 to 1052 kc and the test channel located at 534 kc. The FMFB receiver was found to have slightly more random noise, which is believed to be due to the $1/f$ noise generated in the transistors of the feedback circuit. In Fig. 16 the excess noise effect was subtracted from the original data of the FMFB receiver. Fig. 16 shows a clear advantage of using the FMFB receiver. For 600 channels the SNR should be greater than 31 db, which is consistent with recommendations of CCIR for satellite systems. This corresponds to 40 dbrn at the zero

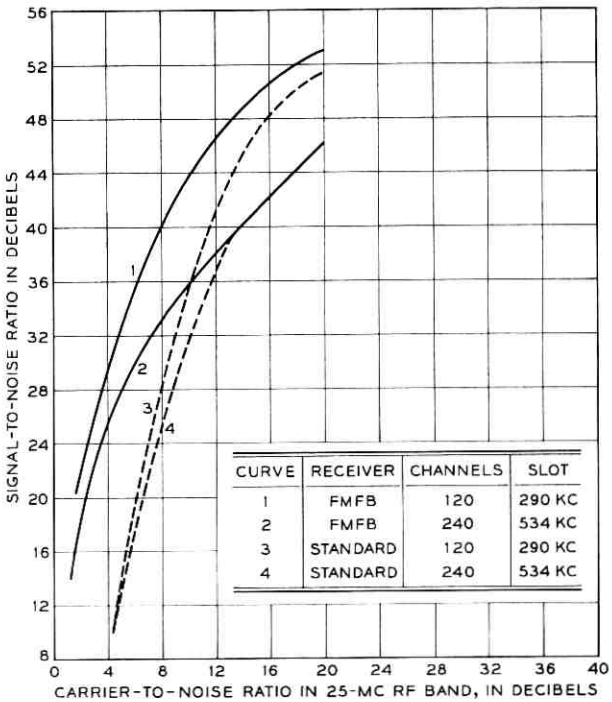

Fig. 17 — Noise loading tests; threshold region.

transmission level point. Curves were also taken at 70 and 1002 kc. They are not different in character, except that the values for SNR are higher for 70 kc and lower for 1002 kc than the ones given in Fig. 16.

With 600-channel noise loading, intermodulation in the feedback receiver begins to appear at lower modulation levels. This is due to the insufficient amount of feedback available in the circuit at higher frequencies. No useful advantage can be obtained from the present FMFB receiver in this case.

In order to show the behavior near threshold more clearly, the curves of Fig. 17 were plotted. They show the SNR in a channel as a function of the CNR at RF. An rms frequency deviation 8 db below 10 mc, or 4 mc, was chosen for these curves. The curves will eventually reach a horizontal asymptote at high CNR's. The noise will then be entirely due to intermodulation. Threshold improvements of about 4 to 5 db can be observed in Fig. 17.

V. ACKNOWLEDGMENT

The authors wish to acknowledge the help of H. A. Gifford in building and testing the FMFB receiver.

REFERENCES

1. Chaffee, J. G., United States patent 2,075,503, granted March 30, 1937; see also Chaffee, J. G., The Application of Negative Feedback to Frequency Modulation Systems, Proc. I.R.E., **27,** May, 1939, pp. 317–331.
2. Ruthroff, C. L., FM Demodulators with Negative Feedback, B.S.T.J., **40,** July, 1961, pp. 1149–1156.
3. Giger, A. J., Pardee, S., Jr., and Wickliffe, P. R., Jr., The Ground Transmitter and Receiver, B.S.T.J., this issue, p. 1063.
4. Ruthroff, C. L., and Bodtman, W. F., Design and Performance of a Broadband FM Demodulator with Frequency Compression, Proc. I.R.E., **50,** December, 1962, pp. 2436–2445.
5. Bode, H. W., *Network Analysis and Feedback Amplifier Design*, D. Van Nostrand Company, Inc., New York, 1945.
6. Enloe, L. H., Decreasing the Threshold in FM by Frequency Feedback, Proc. I.R.E., **50,** January, 1962, pp. 18–30.
7. Ruthroff, C. L., Some Broadband Transformers, Proc. I.R.E., **47,** August, 1959, pp. 1337–1342.
8. Houghton, E. W., and Hatch, R. W., FM Terminal Transmitter and Receiver for the TH Radio System, B.S.T.J., **40,** November, 1961, pp. 1587–1626.
9. Rice, S. O., Statistical Properties of Sine Wave Plus Random Noise, B.S.T.J., **27,** January, 1948, pp. 109–157.
10. Rice, S. O., Noise in FM Receivers, *Time Series Analysis*, ch. 25, ed. H. Rosenblatt, John Wiley & Sons, New York, 1963.

The Mechanical Design of the Horn-Reflector Antenna and Radome

By J. C. DOLLING, R. W. BLACKMORE, W. J. KINDERMANN and K. B. WOODARD

(Manuscript received March 15, 1963)

This paper describes the mechanical design of the horn-reflector antenna and the associated radome. The mechanical considerations dictating the final configuration of the antenna structure are discussed, along with the engineering aspects of the design, fabrication, and erection of the structure. The mechanical features of the data take-off and antenna drive systems are given in detail. The final section presents an account of the requirements, manufacture, and installation of the radome and its accessory equipment.

I. INTRODUCTION

The ground-based communication antenna of the Telstar project must figuratively project a needle of energy toward a 3-foot satellite at a distance of several thousand miles and listen for a whisper in return. It must perform in this fashion while moving about both azimuth and elevation axes. Furthermore, it must provide service in all weather conditions.

Many weeks of study preceded the determination of a general configuration for the structure, its support, and the method of control. The mechanical problems involved in achieving the required antenna performance are discussed in this article.*

The first part (Section II) describes the system requirements and the early design concepts. It also outlines the major factors governing the over-all design and points out the necessary compromises. The next part (Section III) describes the mechanical structure which evolved as the final design and tells of a number of the problems encountered during manufacture and erection.

* The information on concept consideration was provided by Mr. Dolling; that on the mechanical structure by Mr. Blackmore. Mr. Kindermann was concerned with the position data devices and the power drives, and Mr. Woodard with the radome.

The angles which define the pointing of the antenna must be accurately known at all times. The position data devices are among the most precise components in the entire Telstar system. The accuracy requirements for the data take-offs and their mechanical construction are given in Section IV, which also explains the means for driving the antenna about the two axes of motion.

An air-supported construction shelter provided a controlled environment during erection and alignment of the antenna. Later this was replaced by an air-supported radome which assures all-weather operation of the completed antenna. Section V presents a detailed account of the requirements, manufacture, and installation of the radome and its accessory equipment.

II. CONCEPT CONSIDERATION

2.1 *System Requirements*

The horn-reflector type of antenna was selected for the Telstar project because of its broadband and low-noise properties. It provides an offset feed arrangement with very good shielding between focus and reflector. This configuration also permits placement of the receiver at the focal point, thus minimizing line loss.

The velocities and accelerations necessary for tracking the Telstar satellite imposed the need for azimuth and elevation drives capable of operating over a very wide range of velocities, starting from zero. Fig. 1 shows the azimuth velocity requirements for two angles of peak elevation, φ. Accuracy, rigidity and mass inertia are the three basic parameters which determine the quality of the antenna:

2.1.1. A high order of accuracy is called for in the manufacture of all reflecting, rolling, or sliding surfaces. Accuracy of the reflecting surfaces determines the electrical efficiency of the antenna. Furthermore, provision must be made to let fixed and moving parts of the antenna rotate against one another about perpendicular axes and at very accurately controlled tracking speeds.

2.1.2. The antenna structure must present considerable rigidity against both external and internal forces. It is necessary to maintain true focal point-reflector orientation for all elevation and azimuth angles under the influences of gravity, driving acceleration, and thermal expansion forces. The structure also must exhibit high-frequency response to servo control.

2.1.3. The problem of mass inertia about the rotational axes not only calls for a compact design of short over-all dimensions and small radii

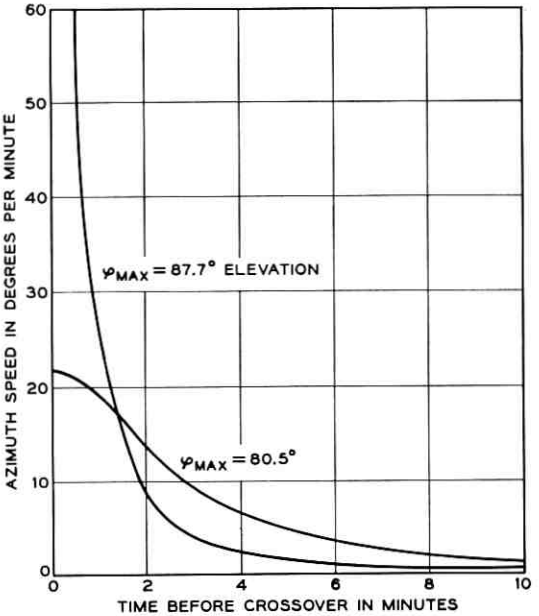

Fig. 1 — Antenna rotational speed for 2200-mile-high satellite in circular orbit.

about the axes but also imposes a very stringent requirement of light weight for every piece that moves with respect to the ground.

Finally, a reliable communication system requires that the antenna be operable under all weather conditions, and that provisions be made for survival in the event of loss of the radome.

2.2 *Investigation of Concepts*

Several antenna design concepts were investigated to find the one design that would best meet the stated requirements. Although the investigation narrowed down to studies of horn-reflector type antennas, early studies included paraboloidal and hemispherical dishes, and sectional sphere-type antennas. Consideration was given to the designs of the hemispherical dish and sectional sphere-type antennas because of the small mass inertia of those parts which require the most precise positioning, the high structural rigidity and compact design. Some of the major reasons for rejecting these types were feed shadow and long transmission lines, each of which contribute excessive noise.

Of the many horn-reflector antenna concepts investigated, the six

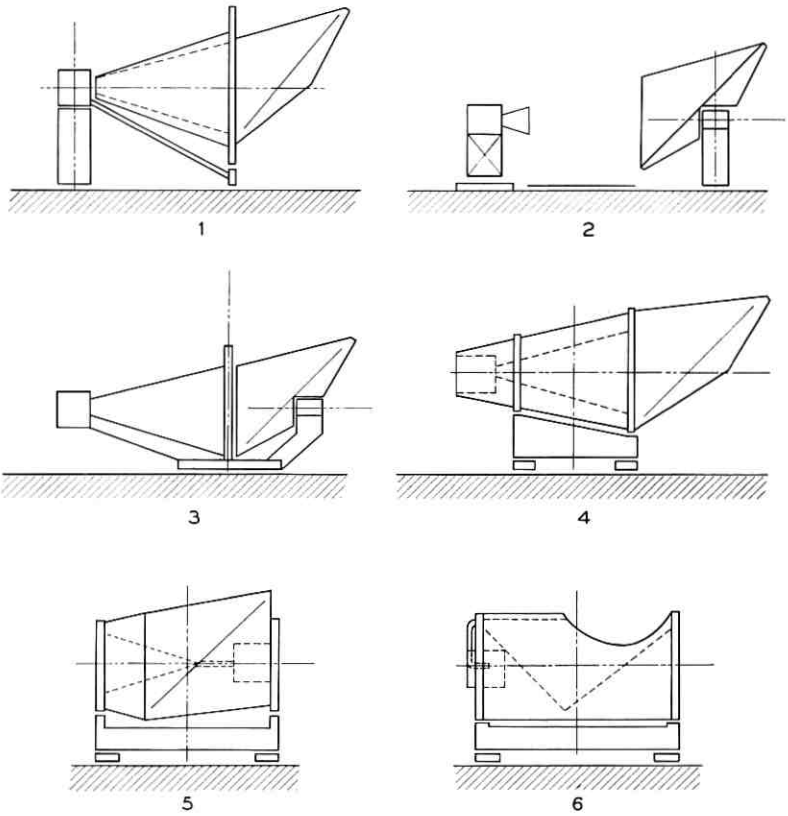

Fig. 2 — Horn-reflector antenna concepts.

that exhibited characteristics falling within system requirements are shown in Fig. 2. The main features of these concepts, the motives that warranted their consideration, and the major reasons for eliminating five of them, are discussed briefly in the following paragraphs.

Concept 1 is a four-sided pyramidal horn-reflector antenna with the horn's symmetry line horizontal and coinciding with the elevation axis. Rotation in azimuth takes place about the horn apex, which is identical with the paraboloid's focal point, so as to avoid translational motions of the equipment room. After study, this concept was abandoned, mainly because of the large turning circles in azimuth and elevation which would result in excessive wind torques and preclude the possibility of a radome because of the very large size.

Concept 2 does away with most of the horn while maintaining the geometry of the paraboloid. A metallic ground plane substitutes in part

for the shielding effect of the horn. The axis of azimuth rotation is coincident with the reflector center. Both measures aim at minimizing wind and mass inertia torques. Uncertainties about effective noise temperature and synchronization of azimuth motions of reflector and feed excluded this scheme from further consideration.

Concept 3 is an attempt to reduce turning circles by using a conical horn and placing the azimuth axis at the largest diameter of the cone. Only the reflector rotates in elevation, but the entire antenna turns in azimuth on a small-diameter platform. Reasons for not following this layout were the excessive weight of the shell structure, lack of rigidity in the reflector structure, and restriction in the elevation motion.

Concept 4 maintains the advantages of a conical horn and a mid-way location of the azimuth axis but adds full elevating rotation, highest stiffness by one-piece design of the horn and reflector plus equipment room, optimum support against gravitational deflection by a cradle-like azimuth carriage, and lightweight space frame design. This concept incorporated most of the desired features.

Concept 5 essentially takes the elements of No. 4, introduces a plane mirror perpendicular to the horn axis and places equipment room and cradle under the reflector, thereby reducing the antenna's length by 40 per cent and improving the contour stability of the sectional paraboloid reflector. Unknowns about the noise temperature of this shortened horn arrangement precluded its adoption.

Concept 6, for the sake of minimum size and ultimate rigidness. opens the flare angle of the conical horn and tilts its symmetry axis, enclosing the horn-reflector antenna in an elevating structure of cylindrical outer shape. The length reduces by about 30 per cent, height by 35 per cent, compared with the antenna actually built. The necessity of a transmission line between horn apex and equipment room was the reason for rejection of this concept.

In the selection of the final antenna concept, an evaluation was made of each on the basis of its ability to meet system and design requirements. Table I illustrates the method employed of comparing and determining the compatibility of the above antenna concepts with the requirements. The concept numbers correspond to those described above, above, and the check marks indicate where the stated requirement is fully met.

It can be seen by examining the columns of Table I that only concept 4 appears to meet all of the basic requirements. Thus concept 4 was selected as the most suitable design for present use in the Telstar program.

TABLE I—EVALUATION OF ANTENNA CONCEPTS

Basic Requirements	Concept					
	1	2	3	4	5	6
System:						
Rotating equipment rooms	√	√	√	√	√	√
Minimum of 180° elevation coverage	√	√	—	√	√	√
Tracking velocity and acceleration	—	√	√	√	√	√
Pointing accuracy	—	—	—	√	√	√
Beam spread stability	—	—	√	√	√	√
Electrical shielding	√	—	√	√	—	√
Minimum wind torques	—	√	√	√	√	√
Thermal differential expansion:						
Ambient temperature	—	√	√	√	√	√
Radiation heat	—	√	—	√	√	√
Operation in extreme precipitation	√	√	√	√	√	√
Survival (hurricane winds & ice)	√	√	√	√	√	√
Life expectancy	√	√	√	√	√	√
Design:						
No feed shadow	√	√	√	√	√	√
Horizontal RF feed	√	√	√	√	√	√
Short, straight transmission line	√	√	√	√	√	—
Minimum mass inertia about azimuth axis	—	√	√	√	√	√
Torsional and mounting rigidity of drive	√	—	—	√	√	√
Rigid structure	—	—	—	√	√	√
Thermal expansion restraint	—	√	√	√	√	√
Minimum deflection suspension	√	√	—	√	√	√
Stable foundation	√	√	—	√	√	√
Stow position	√	—	—	√	√	√
Accessibility of equipment room	√	√	√	√	√	√
Protective radome adaptability	—	—	√	√	√	√

2.3 *Basic Design Considerations*

With the selection of concept 4 as the most desirable antenna, several fundamental questions had to be answered before detailed design could start. They are discussed in the following paragraphs.

2.3.1. What is the best length-to-height ratio of the entire antenna structure? It had been decided that the effective aperture area for the radio beam should be 3600 square feet,[1,2] that the reflector should be a section of a paraboloid, and that the cone axis should coincide with the horizontal elevation axis. Consideration of the location of the center of gravity, the azimuth turning diameter, and the preferred flare angle influenced the choice of the length-to-diameter ratio.

2.3.2. What kind of structural pattern should be chosen for the skeleton of the horn enclosure? A polygonal pyramid of approximately round cross section requires an elevation turning circle 30 per cent smaller than the elevation circle of a horn with a square cross section. Furthermore, it

can be made much more rigid against bending, shear, torsion, differential thermal expansion, and cross-sectional deformation. Also, deflection of the polygonal structure in the vertical plane remains constant with all elevation angles, and finally a round horn is more suitable electrically. The spiral pattern of the structural members has no parts that are idle at any time and thereby provides the most efficient configuration for a high rigidity-to-weight ratio. The lengths of the members were chosen in accordance with resonance and buckling requirements. A shell design would necessarily become prohibitively heavy to prevent skin buckling.

2.3.3. What is the most suitable type of configuration for the cradle structure? To achieve the highest rigidity-to-weight ratio of the entire structure, lattice-box girders are used for the cradle. The structure has the shortest and most direct load-carrying connections between the elevation assembly and the foundation. Minimum deflection support is provided for the elevation structure in two planes. Stability against overturning moments is achieved by use of a sufficiently large base frame. The least amount of material is required and a high natural frequency of structural members is obtained.

2.3.4. Which structural shapes should be used for building the horn enclosure? Structural tubes are three times lighter than any other structural shape for the same static deflection, and their resonant frequency between joints is about 70 per cent higher than that of other shapes of the same weight.

2.3.5. What material is appropriate as structural building material? Light weight and high rigidity are desirable in view of deflections due to gravity and high-frequency response to servo forces in the structure. Steel was selected because of its high modulus of elasticity. The rigidity of an aluminum structure of the same volume would be intolerably low when attached dead loads are considered, even though the resonant frequencies of the load-bearing skeletons may be equal. Increasing the volume of aluminum for stiffening would cancel the effects of savings in weight and mass inertia. Under a radome, an aluminum horn enclosure could at best save 20 per cent by weight of the present antenna and increase the natural frequency by about 10 per cent. Differential thermal expansions, due to sunlight in the open or because of air stratification in a radome, would double with aluminum. An all-aluminum structure of equal static and dynamic but worse thermal properties would cost about 10 per cent more than a steel structure.

2.3.6. Is damping feasible and needed to limit the amplitude of vibrations? Since the structure is designed to have no play in any of the joints, damping can be expected only from the material. This damping decre-

ment is known to be no more than 0.05. With servo impulses applied directly, the structure may resonate, causing erroneous reactions of the servo. Many of the devices investigated for increasing internal damping proved to be either excessively heavy or ineffective because the permissible vibrational amplitudes were too small. External damping devices were also considered but were found to add drag to the rotational torques, thereby increasing the pointing error. Due to the autotrack's minimizing effect on directional corrections, and due to the need for converting digital information into analog, the torque changes originated at the drives are small. These changes are smoothed by gear and wheel friction so that little of this energy is converted to structural vibration. With the antenna in a radome enclosure, no wind forces are present to excite structural resonance. The relatively high natural frequency of the antenna, 2.2 cps, and the coupling of several antenna components with different higher frequencies, eliminate oscillations at resonance.

2.3.7. How should manufacturing and deflection tolerances be distributed among the structural components and foundation? Tolerance accumulation in an antenna system starts deep in the ground and is traced all the way up through the foundation, rails, trucks, azimuth carriage, elevation structure, and reflector suspension to the last panel surface. The distribution of the total allowable antenna pointing error for each part of the mechanical system has to be accomplished in accordance with the limitations of structural geometry, physical properties of materials, resonant frequency requirements, and currently available manufacturing techniques. Consideration also must be given to directions of errors and the probability of their occurrence.

Equations (1) and (2) below represent the total pointing errors about azimuth and elevation axes. Angular errors about the third axis, perpendicular to both azimuth and elevation axes, can be expressed in azimuth measure. Rotations about the nominal pointing vector result in equivalent elevation errors.

$$
\begin{aligned}
A = {} & 2\left\{\left[\beta_{GE} + \beta_{TE} - \left(\frac{c}{l}\right)_{GE} + \left(\frac{c}{l}\right)_{TE}\right]\tan\varphi \pm \beta_{ME}/\cos\varphi\right\} \\
& + (\delta_{GA} - \delta_{TE})\sin\varphi + (\epsilon_{GA} + \epsilon_{TE})\cos\varphi \pm \delta_{MA}\tan\varphi \\
& + \delta_{GE}\sin 2\varphi\tan\varphi + \epsilon_{GE}(1 - \cos 2\varphi) \\
& \pm \left\{\epsilon_{MF}^{\,2} + \epsilon_{MA}^{\,2} + \epsilon_{ME}^{\,2} + \epsilon_{GF}^{\,2} + \epsilon_{TF}^{\,2} + \epsilon_{TA}^{\,2}\right. \\
& + (\delta_{MF}^{\,2} + \delta_{ME}^{\,2} + \delta_{GF}^{\,2} + \delta_{TA}^{\,2} + \delta_{TF}^{\,2})\tan^2\varphi \\
& \left. + 4\left(\beta_{MEr}^{\,2} + \left(\frac{c}{l}\right)_{ME}^{2}\Big/\cos^2\varphi\right)\right\}^{1/2}
\end{aligned}
\tag{1}
$$

$$E = \left[\alpha_{GA} + \alpha_{GE} + \alpha_{TE} - \gamma_{GE} - \gamma_{TE} + \left(\frac{b}{l}\right)_{GE}\right] \cos\varphi$$
$$\pm \left[\alpha_{MF}{}^2 + \alpha_{MA}{}^2 + \alpha_{ME}{}^2 + \alpha_{GF}{}^2 + \alpha_{TF}{}^2 + \alpha_{TA}{}^2 \right. \tag{2}$$
$$\left. + \gamma_{ME}{}^2 + \left(\frac{b}{l}\right)_{ME}^2 + \left(\frac{b}{l}\right)_{TE}^2 \cos^2\varphi\right]^{1/2}.$$

In these expressions, note that (*i*) the equations describe electrical pointing deviations with respect to ground due to structural imperfections and varying deformations; (*ii*) β_{ME} is usually chosen negative to compensate for β_{GE} at the zenith position, which is readily measurable at the time of alignment; (*iii*) δ_{MA}, even though preferably a residual value (r) after adjustment, has a permanent great influence so that its direction must be known for + or −; (*iv*) the equations contain signs for 0 to 90° elevation φ only; and (*v*) the temperature is assumed stratified in the radome for the elevation structure, random for the remaining structure. It is also assumed that there are no wind forces and that operational forces are negligible.

Fig. 3 shows the coordinate systems on which the above equations are based. With the help of this theory, it became possible to generate a tolerance budget for designers, manufacturers and erectors, as presented in Table II. Data for deflections due to servo or wind forces were left out as being negligibly small and zero, respectively. After the antenna design had been completed, the expected total pointing errors were calculated, in part compensated for by mechanical bias against gravitational deflection, and later compared with measurements from radio star tracking, Fig. 4. Agreement between calculations and measurements of variable errors was found to be excellent. The shaded areas in Fig. 4 indicate data scatter, due essentially to the influence of the rolling surfaces. The variable errors then were counteracted by data corrections as functions of elevation angle, so that predictable errors are entirely eliminated. Reflector panels were to be manufactured to within 0.03 inch in contour, and total accumulated deviation from the desired paraboloid was to be kept under $\pm\frac{1}{8}$ inch, so as to insure the least distortion to the beam.

2.4 *Additions to Basic Concept*

After the basic design concept had been selected, some features were added to the antenna to increase its performance and reliability. A radome excludes all influences by the elements such as wind, ice, snow and rain. To obtain the smallest possible azimuth turning clearance, the azimuth axis was shifted closer to the reflector. The four cradle sup-

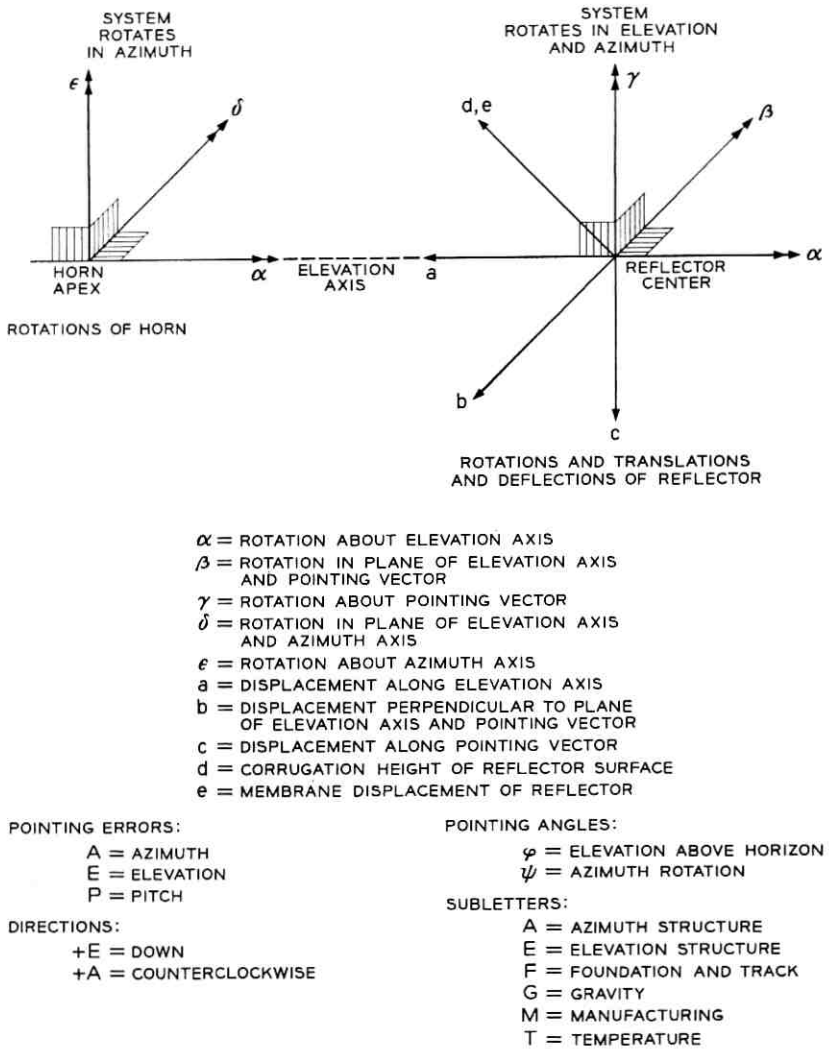

Fig. 3 — Tolerance coordinate systems.

port trucks no longer ride on one common double track but on two individual rails, each mounted on one of two concentric ring foundations. The trucks became two-wheeled and non-self-aligning. Therefore, both a pintle bearing on a central foundation and an extra structure inside the four structural planes of the azimuth carriage had to be added to keep the trucks on the rails against considerable friction forces. More struc-

TABLE II—STRUCTURAL TOLERANCES FOR POINTING ACCURACY

Symbol of Rotation	Tolerances[a] for			Influences[b] on pointing					
				Azimuth			Elevation		
	Mfg. (M)	Grav. (G)	Temp. (T)	A_M	A_G	A_T	E_M	E_G	E_T
Foundation and track (F)									
α	0.10	0.05	0	0	0	0	$\pm 1^c$	± 1	± 1
δ	0.10	0.05	0	$\pm 1u^d$	$\pm 1u$	$\pm 1u$	0	0	0
ϵ	0.10	0.05	0	± 1	± 1	± 1	0	0	0
Azimuth structure (A)									
α	0	0.05	0.05	0	0	0	± 1	$\pm 1w$	± 1
δ	0.05	0.10	0.05	$\pm 1u$	$+1v^e$	$\pm 1u$	0	0	0
ϵ	0	0.10	0	± 1	$+1w^f$	± 1	0	0	0
Elevation structure (E)									
α	0	0.15	0	0	0	0	± 1	$+1w$	$+1w$
β	0.05	0.30	0.15	$-2x^g$	$+2y^h$	$+2y$	0	0	0
γ	0.15	0.50	0.15	0	0	0	± 1	$-1w$	$-1w$
δ	0.15	0.05	0.05	$\pm 1u$	$\pm 1u$	$-1w$	0	0	0
ϵ	0.10	0.05	0	± 1	± 1	$+1w$	0	0	0
b/l^i	0.15	0.30	0	0	0	0	± 1	$+1w$	$\pm 1w$
c/l	0.05	0.10	0	$\pm 2x$	$-2y$	$+2y$	0	0	0

(a) Angular deviations in milliradians; (b) factors of magnification; (c) $+A$ counterclockwise, $+E$ down; (d) $u = \tan \varphi$; (e) $v = \sin \varphi$; (f) $w = \cos \varphi$; (g) $x = 1/\cos \varphi$; (h) $y = (1 - \sin \varphi)/\cos \varphi$; (i) l = horizontal distance between focus and reflector.

ture was added for the transmission of horizontal forces from the rear elevation bearing to the pintle bearing, because the elevation bearing was fixed axially. To allow for expansion at a later date, the equipment room at the apex of the horn was not enclosed within the elevation structure but was placed directly on the azimuth cradle. A lower equipment room located on the azimuth cradle had not been anticipated in the original design but was found to be a necessary addition. Both equipment rooms represent dead loads and therefore impose considerable penalties to the antenna in terms of weight and inertia. Structure-mounted positive drives were employed instead of truck-mounted friction drives to insure slip-free operation under all conceivable conditions, thus imposing high accuracy requirements on the location of the center of azimuth rotation. A view of the antenna model, showing most of the above features, is seen as Fig. 5.

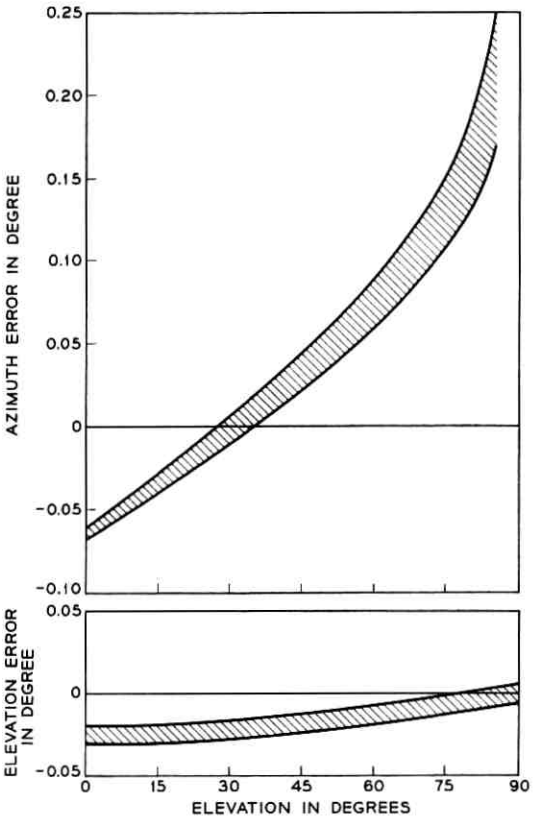

Fig. 4 — Calculated structural variable pointing errors.

III. MECHANICAL STRUCTURE

3.1 *General Configuration*

Fig. 6 is an outline drawing of the horn-reflector antenna. This antenna, which is a greatly enlarged version of the horn-reflector antennas employed in the Bell System's transcontinental microwave relay network, can best be visualized as two separate structures — an elevation structure rotating about a horizontal axis and an azimuth structure rotating about a vertical axis. The elevation structure is an extremely rigid framework which houses a conical horn some 90 feet long and supports a reflecting surface measuring approximately 100 by 70 feet. The horn terminates at its apex in an enclosed room housing the transmitting

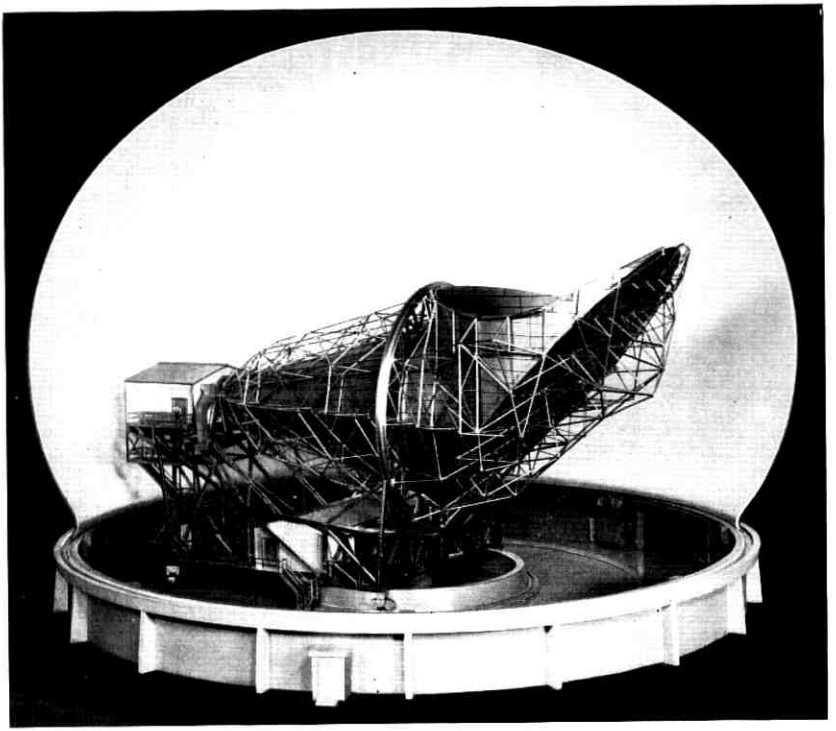

Fig. 5 — Model of Telstar horn-reflector antenna.

and low-noise receiving equipment. At its large end the horn terminates in the reflector, which is a sector of a paraboloid of revolution set at an angle of 45 degrees with the cone axis. The space between horn and reflector is occupied by a cylindrical structure which serves as a shield for the 67.7-foot diameter aperture of the antenna. Fig. 7 illustrates the relation between the conical, cylindrical, and paraboloidal surfaces comprising the horn, shield, and reflector.

The entire antenna structure is 177 feet long, stands some 95 feet above the azimuth rails at maximum elevation angle, and weighs about 380 tons with all equipment installed. The McKiernan-Terry Corporation of Dover and Harrison, New Jersey, were the prime contractors responsible for the detailed design, fabrication, and erection of the structure, guided by the basic design developed by Bell Laboratories. Subcontractors responsible to McKiernan-Terry, and working in close cooperation with Bell Laboratories engineers, included Burns & Roe, Inc., of New York City, responsible for the antenna and radome founda-

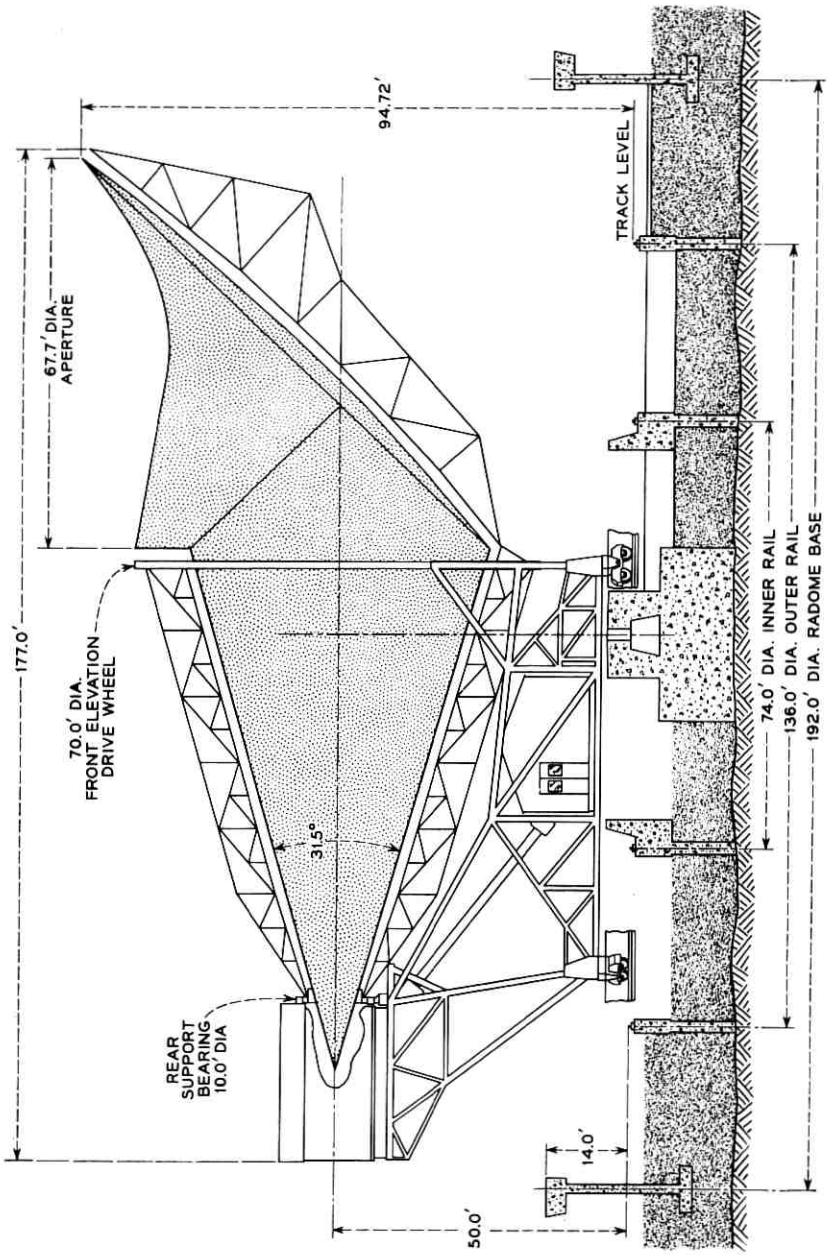

Fig. 6 — Outline drawing of horn-reflector antenna.

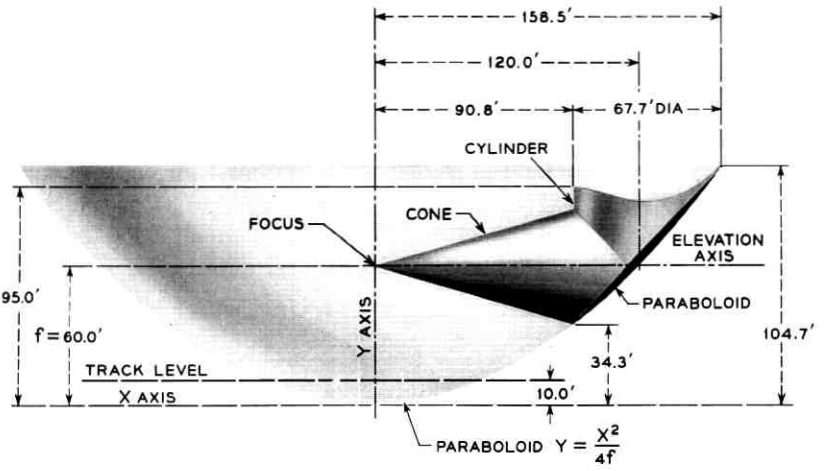

Fig. 7 — Relationship between horn, shield, and reflector surfaces.

tions; Radio Construction Corporation of Pittsburgh, Pennsylvania, erectors of the structure; and Advanced Structures of La Mesa, California, who fabricated and aligned the cone, shield, and reflector surfaces of the elevation structure.

3.1.1 *Elevation Structure*

The elevation structure is supported at two diameters and is provided with a choke joint near the cone apex to permit continuous rotation about the horizontal axis of the conical horn. At the large end of the cone, this support is provided by a circular track ring, integral with the structure. Near the apex, the support, as well as the axial restraint, is provided by a self-aligning ball bearing 10 feet in diameter. The wheels of the two trucks supporting the 70-foot diameter elevation track ring are provided with ball splines to accommodate any breathing of the elevation structure brought about by temperature differences between it and the supporting structure.

3.1.2 *Azimuth Structure*

The azimuth structure serves as the cradle to support the elevation structure. Rotation about a vertical axis is provided for by four trucks supporting the entire weight of both structures and running on two circular and concentric tracks. All horizontal reactions associated with azimuth rotation are assumed by a self-aligning roller bearing three feet

in diameter and located at the center of the concentric tracks. This pintle bearing is isolated from vertical reactions by means of a flexible diaphragm that forms the connection between the outer race of the bearing and the rotating structure. Continuous azimuth rotation is afforded by a slip ring assembly for electrical power and signal circuits, and by a rotary joint for the chilled water required for cooling equipment on the structure. The slip ring assembly, which is an adaptation of a previous design, accommodates 295 electrical circuits: 28 for heavy power, 21 for signal circuits and 246 for general purpose.

3.1.3 *Equipment Rooms*

Two equipment rooms are mounted on the azimuth structure. One, commonly called the upper room, is at the cone apex. Its floor area is 900 square feet, and it houses the Telstar communication transmitters and receivers as well as associated electronic gear and the elevation angle indicating devices. The other room, commonly called the lower room, is located beneath the horn section of the antenna and just to the rear of the pintle bearing. Its floor area is 1600 square feet, and it houses the alarm and signaling equipment, the antenna digital control system, the antenna servo system, the station monitor system, the autotrack system, a transmitter for use in the NASA project Relay experiment, and various items of auxiliary equipment.

3.1.4 *Antenna Foundation*

The antenna foundation consists of three main elements. At the center of azimuth rotation is the massive reinforced concrete pintle block keyed into granite bedrock some 15 feet below grade to enable it to withstand a horizontal reaction of 300,000 pounds which could develop if, in the event of a hurricane, the protective radome were lost and the structure were subjected directly to the full force of a 100-mph wind. The two concentric reinforced concrete rings for the azimuth tracks are also supported directly on bedrock to minimize localized vertical deflections that would result in antenna pointing errors. These foundations are designed so as to contribute no more than 0.005-inch differential vertical deflection between any two azimuth trucks as the 380-ton antenna rotates in azimuth. The two track rings are tied to each other and to the pintle block by eight radial concrete beams to further increase the stability of the entire foundation. The inner ring has associated with it a wall supporting the azimuth bull gear. Fig. 8 shows the completed antenna

foundation. The outer wall, which the photograph shows still under construction, is the foundation to which the radome was attached.

3.1.5 *Azimuth Rail System*

The outer azimuth track, 136 feet in diameter, is made up of 24 segments of heavy-duty crane rail weighing 171 pounds per yard, and the 74-foot diameter inner track contains twelve segments of the same weight rail. These segments were rolled to the proper curvature by the fabricator, Bethlehem Steel, ground to produce a flat and horizontal upper surface in another shop, and then butt-welded to produce a continuous ring after installation at the site. Jacks were interposed between the rails and the foundation sole plates to permit leveling of the entire track system to within $\frac{1}{32}$ inch. The excess weld material at the butt joints was faired into the adjacent ground surface of the rail head with a rail grinder developed specifically for this task. After this operation, each rail weld was checked for proper hardness with a portable hardness tester, and was subjected to a dye penetrant test to disclose cracks and porosity.

Fig. 8 — Completed antenna foundation and partially constructed foundation for attachment of radome.

The inner rail is the most heavily loaded and deflects approximately 0.018 inch between jacks when subjected to the wheel load. However, because of the relative spacing between wheels and jacks and the equalizing action of the truck, a total vertical movement of only half this amount is realized by the corner of the cradle structure.

3.2 *Azimuth Structure Considerations*

3.2.1 *Structural Details*

The principal members comprising the azimuth structure are steel box girders having a cross section one foot square. These girders were fabricated of four common angle sections laced together by welding smaller angle sections between them in a diagonal pattern. The girders were shop-assembled, where practicable, into subassemblies, but these shop subassemblies had to be limited in size so they could be transported by truck. On-site assembly of these members, as well as those of the elevation structure, was accomplished by bolted connections. High tensile strength bolts, which develop highly efficient and rigid joints by virtue of the clamping action on the bolted members, were used for all critical connections. Every high tensile strength bolt was hand-torqued to a predetermined value to insure that the required clamping forces were developed.

3.2.2 *Truck Alignment*

The design and alignment of the azimuth trucks and wheels were engineered to provide, as nearly as possible, pure rolling contact between wheel and rail. Because the only geometric shape capable of providing pure rolling contact along a circular path on a flat surface is a cone, the azimuth wheels were designed as frustrums of cones, and each wheel was aligned at assembly so that the projected cone apex coincided with the point of intersection of the azimuth axis and the plane formed by the top of the azimuth rails. To accomplish this alignment, a mirror mounted on the inboard end of the wheel axle was used to collimate a transit located at the center of azimuth rotation and at the level of the rail heads. The wheel being adjusted was raised off the track by a few thousands of an inch so that it could be rotated during the alignment procedure to verify orthogonality of the mirror and the wheel axis.

3.3 *Elevation Structure Considerations*

3.3.1 *Elevation Wheel Fabrication*

With the installation of the large elevation bearing assembly at the rear and the elevation trucks at the front, the azimuth structure was essentially complete and ready to receive the elevation structure. The first member of the elevation structure to be erected was the 70-foot diameter elevation wheel. This wheel had been fabricated in six separate segments to facilitate truck shipment to the site. Upon arrival at the site, the segments were placed on wooden cribbing some ten feet above the radome arena floor and assembled to form a complete wheel, the plane of which was horizontal. The elevation track, consisting of twelve sections of 104-pound crane rail previously rolled to the proper curvature, was next installed and the twelve rail joints butt-welded to form a continuous track ring. The entire 220-foot circumference of this ring was then ground to produce a smooth and concentric supporting track for the elevation structure. For this operation a grinding rig was devised, consisting of a precision grinding head mounted on a radius arm pivoted about the wheel center from a pintle anchored to the floor. The radius arm was supported near the wheel circumference by a track provided on the upper face of the wheel. The arm was motor-driven to make one circuit of the wheel in about four minutes, and carried a platform at the outer end to accommodate the operator. After some 136 hours of grinding, a continuous track having the required surface finish and width was attained. With the installation of the elevation bull gear segments and a "strongback" to reinforce the wheel during the lifting operation, the complete assembly, weighing close to 50 tons, was then ready for erection.

3.3.2 *Elevation Wheel Erection*

The lifting of this huge assembly, first to a vertical attitude and then up onto the elevation trucks, was the most spectacular and critical phase of the antenna erection sequence. Because of space limitations imposed by the presence of the radome wall and a temporary construction shelter (see below), the cranes involved in this lift could not be deployed to their best advantage and, consequently, the combined lifting capacity of three large cranes, one 90 ton and two 60 ton, had to be employed. Extreme caution was necessary throughout the entire 8 hours required for the two operations to insure that the lifting efforts of the three cranes were carefully synchronized. Any tendency for one of the cranes

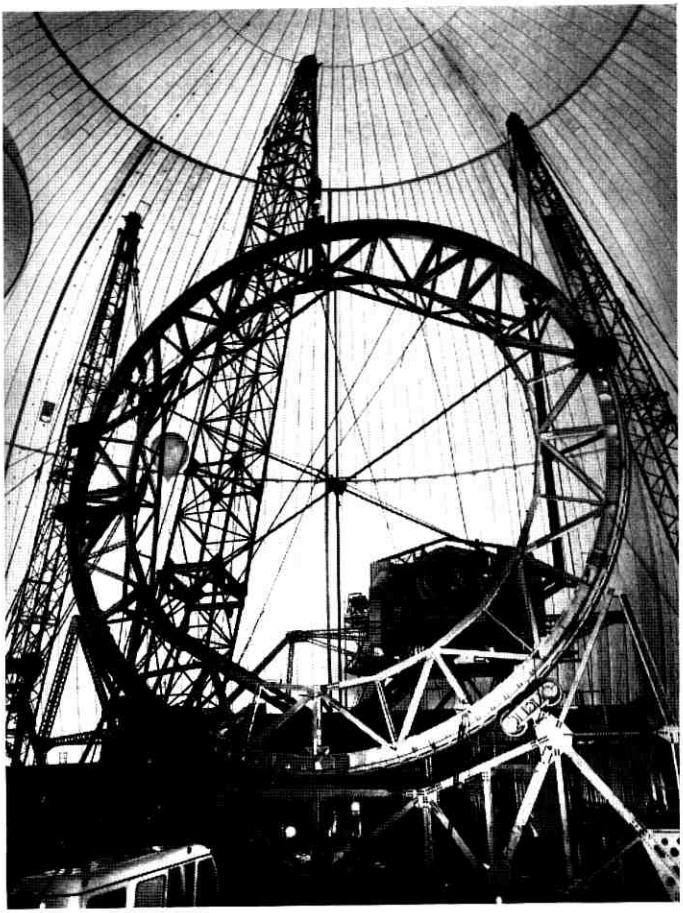

Fig. 9 — Final phase of installation of elevation wheel.

to assume more or less of its proper share of the total load could cause an imbalance, which would have resulted in an overloaded crane and would have led to disaster. Fig. 9 shows the final phase of the operation. The rear elevation bearing can be seen in the background.

3.3.3 *Cone Structure*

The next operation was the installation of the twelve cone rafters connecting the rotating race of the elevation bearing with the elevation wheel and forming the primary support structure for the cone as well as the

means for keeping the wheel erect. These rafters, some 75 feet long by 8 feet deep, had been fabricated as weldments of steel tubing and had been jig-assembled at the shop to insure uniformity of all critical dimensions. Each rafter was made in two sections with a field-bolted joint between the two units to facilitate shipment by truck and passage through the vehicular air lock of the radome.

3.3.4 *Cone Structure Alignment and Panel Installation*

When the cone structure was complete, but before the panels comprising the cone surface could be installed, it was necessary to rotate the cone structure about the elevation axis to establish the center of rotation of the elevation wheel. Because of size and weight considerations it was not feasible to design this wheel to have negligible deflections. Furthermore, the cross section of the wheel had to vary from sector to sector to accommodate the nonsymmetrical loading the reflector structure would impose on it. Consequently, it was necessary to find the actual center of the wheel as it rotated in order to establish the nominal axis for the cone surface. To accomplish this, a theodolite mounted at the theoretical location of the cone apex was used to observe a target suspended in the plane of the wheel. The position of the target was then adjusted to produce a minimum orbit as the wheel rotated. The centroid of this irregular orbit was the desired center of rotation, and the required cone surface was centered about a line connecting this point and the cone apex. For adjusting the cone panels to conform to the desired surface, an optical instrument located at the cone apex and aligned to this centerline was provided with an angle attachment enabling it to sweep the required cone angle. The tolerance on the cone surface is $\pm\frac{1}{32}$ inch at the rear panels and increases linearly to ± 1 inch at the large end of the horn.

3.3.5 *RF Surface Considerations*

The panels comprising the cone, shield, and reflector surfaces were fabricated of aluminum honeycomb. Averaging 3 by 12 feet in area and weighing about 1 pound per square foot, these panels could be readily handled by two men but were strong enough to support safely the weight of the workmen during the installation procedure. To make these panels, two 0.020-inch sheets of aluminum separated by a 1- to $1\frac{1}{2}$-inch thick lightweight aluminum honeycomb core were form molded to conform to the desired curvature to within 0.030 inch. With the curing of the adhesive used to bond the three elements together, this curvature was

"locked in," producing a panel having the required curvature plus an excellent compromise between weight and rigidity.

3.3.6 *Reflector Back-Up Structure*

Erection of the reflector back-up structure was performed with the structure oriented in elevation to point upward toward the zenith because, for this attitude, the nominal 45-degree angle between the reflector plane and elevation axis could be readily monitored by vertical measurements to a horizontal reference plane. Since this structure rotates about the elevation axis, and consequently with respect to the gravitational vector, its asymmetry results in a departure from the normal 45-degree relationship. This departure had been calculated and found to be within allowable limits. Pointing errors resulting from it could be compensated for by azimuth and elevation motions for any pointing angle except the zenith, where no amount of azimuth or elevation correction could overcome an outward or inward sag of the reflector surface. Hence, the zenith orientation was the most critical (as well as the most convenient) for monitoring the erection of this structure.

3.3.7 *Reflector Panel Installation and Alignment*

Upon completion of the reflector back-up structure, the entire elevation assembly was again rotated about the elevation axis, this time to determine the average center of rotation of the back-up structure. The centroid of the minimum orbit thus determined would become the starting point for the paneling of the reflector surface.

These panels, like the cone and shield panels, were provided with six threaded studs for attachment to the secondary support structure. The mounting nuts were appropriately positioned on these studs, and slotted clearance holes were used in the supporting members so that adjustment of the panel in three coordinates was possible. The panels, already curved in two directions by the fabrication process, were positioned to conform to the theoretical paraboloid of revolution to within 0.060 inch on a one-sigma basis by an alignment method developed jointly by Advanced Structures and Bell Telephone Laboratories. Paper targets, cemented to the front surface of each panel in locations corresponding to the support points, were observed from two theodolites located on a predetermined base line established on the radome floor. For this procedure the elevation structure had been rotated to the nadir position and the entire reflector was therefore readily observable from the floor-mounted instruments. The angles observed from the two theodolite positions were fed to

a computer located within the construction shelter and programmed to produce numerical values indicating the departure, in a direction normal to the surface, of each observed target from the theoretical paraboloidal surface. These values could be used directly to move the target points of the panels in or out until they coincided with the desired reflector surface. Corrections for gravitationally induced deflections of the back-up structure and for dimensional changes due to temperature variations were incorporated in the computer program. Fig. 10 is a contour plot of the

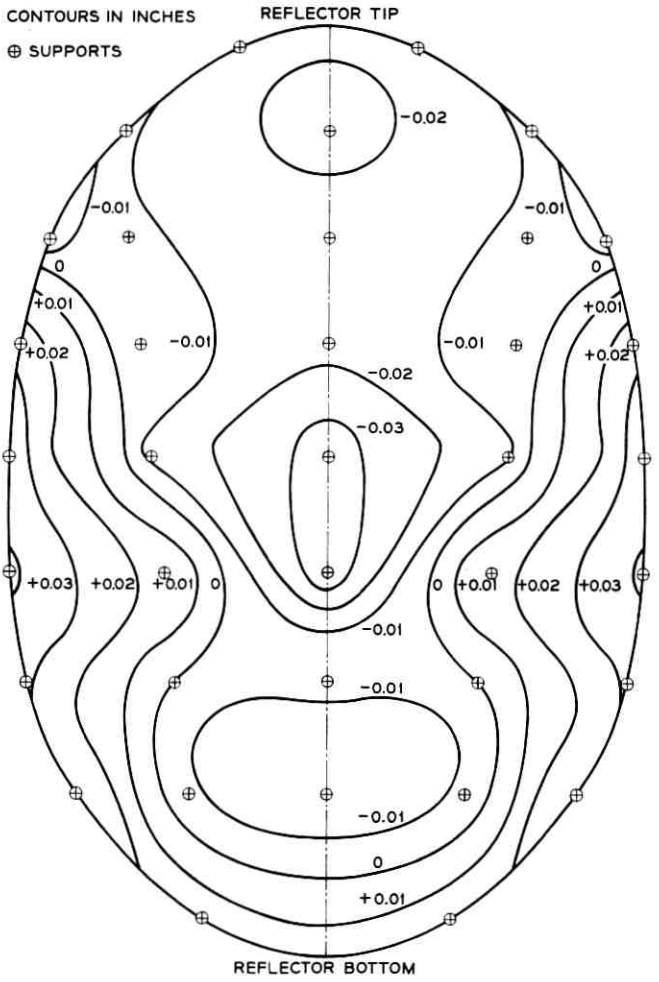

Fig. 10 — Elastic reflector contours.

local deflections compensated in this manner. The downward sag of the plane of the entire reflector frame from the nominal 45° angle also had to be included in the correction, since the effect of the gravitational vector was reversed as the structure was rotated from the zenith position in which it had been aligned to the nadir position employed for panel alignment. Actually, only three-fourths of the full correction was applied. This resulted in a nominally correct reflector surface at 30° elevation angle instead of at 90°. This represented a departure from the original intention to produce an optimum reflector surface at the zenith pointing angle. The compromise was dictated by the consideration that the antenna would never be required to track through the zenith and would spend comparatively little time tracking at the higher elevation angles. Only every other panel was observed, computed, and adjusted. The intervening panels were then faired to the adjusted panels. Shield panel adjustment was a much more simple procedure, the only requirement being that the cylindrical shield not encroach on the radiating aperture of the reflector surface.

With the adjustment of the shield panels and the taping of the joints between horn, shield, and reflector panels with aluminum-faced tape, the antenna structure was essentially complete.

IV. POSITION DATA DEVICES AND ANTENNA DRIVES

Important contributors to the successful performance of the horn-reflector antenna are the precise data take-off devices and the highly responsive hydraulic transmissions with associated low-compliance gearing in the servo drives. This equipment, operating under control of the antenna pointing system, must meet the antenna beam pointing tolerance of ± 0.019 degree under satellite tracking conditions.

4.1 *Data Take-Off Devices*

The narrow beamwidth and stringent pointing error requirements for the antenna dictated the use of extremely accurate data take-off devices on both axes of rotation.

The large primary reference data gears were produced by the Westinghouse Corporation, Lester, Pennsylvania. Type 410 stainless steel $\frac{3}{4}$-inch thick plate stock was used for the gear blanks, and the standard $14\frac{1}{2}$-degree pressure angle, full depth involute tooth forms were produced by hobbing. Table III lists pertinent data applicable to these gears as mounted on the hobbing machine after the final finishing cuts were made.

In addition, very precise reference diameters were machined on the gears just below the root diameter of the teeth. The reference diameters

TABLE III—GEAR DATA

	Azimuth	Elevation
Pitch diameter	40 inches	132 inches
Diametral pitch	32	16
Number of teeth	1280	2112
Tolerance, tooth to any other tooth	10 seconds	12 seconds
Tolerance, tooth-to-tooth	4 seconds	1½ seconds

were later used to accurately center the gears on the antenna axes for final installation.

The final inspection of the gears was conducted by Bell Telephone Laboratories personnel at the manufacturing plant with the aid of rather specialized instrumentation. Precise measurement of angles subtended by groups of teeth were made by means of autocollimation techniques used in conjunction with an optical polygon mounted on the hobber table axis. At each test position, a mechanical probe engaged a gear tooth at the pitch line. Errors in tooth flank angular position as evidenced by probe displacement were detected by an electronic indicator mounted on the probe support.

Gear tooth-to-tooth error and pitch circle eccentricity checks were made with a certified master gear mounted on a precision slide and rolling in engagement with the gear under test. An electronic indicator sensed radial movement of the master gear slide resulting from variations in pitch circle or tooth contours, and the indicator output was connected to a rectilinear recorder to produce a permanent chart record of the test. In correlation with this test, electronic indicator checks were made on the datum circle runout. Figs. 11 and 12 are photographs of the setups for these tests.

On the horn-reflector antenna, the azimuth data gear is mounted and centered on the stationary pintle post, and the data take-off devices are located on the adjacent rotating structure. The elevation data gear is secured to the rotating inner race of the ten-foot elevation bearing, and the data units are mounted on the face of the large pillow block weldment that secures the bearing to the azimuth structure. Thus the synchros and resolvers, comprising the data take-off units, are part of and revolve with the azimuth cradle of the horn. The associated signal leads can therefore run directly to terminal bays in the lower equipment room without passing through slip rings.

The elevation data take-off devices, driven by the rotating gear through anti-backlash pinions, are as follows:

(a) *Precision resolvers* at 1:1 and 64:1 antenna speed. These outputs

Fig. 11 — Test equipment for checking errors in gear tooth flank angular position.

are time-sequence sampled and translated to digital form for antenna position data input to the antenna pointing system.[3,4]

(b) *Synchros*: torque transmitters at 1:1 and 36:1 speeds are used for remote operation of slaved antenna position dials; control transformers at 1:1 and 64:1 speeds are used for manual servo loop control in position or velocity modes. These are used for off-line operation of the antenna.[5]

(c) *Boresight synchro* at 360:1 for initial boresighting and antenna pattern measurements.[2]

(d) *Autotrack coordinate converter*. This is a 1:1 speed synchro and potentiometer assembly used in conjunction with the autotrack system.[6]

Except for the omission of item (d), a similar arrangement is used for the azimuth data devices.

Fig. 13 is a photograph of the horn apex showing four data units clustered around one side of the 132-inch data gear. Fig. 14 shows two typical data units.

4.2 *Antenna Gear Drives and Hydraulic Transmission Systems*

The antenna utilizes hydraulic servo transmissions made by Vickers, Incorporated, and intermediate speed gear boxes made by the Western Gear Co. Two 25-horsepower and two 10-horsepower hydraulic trans-

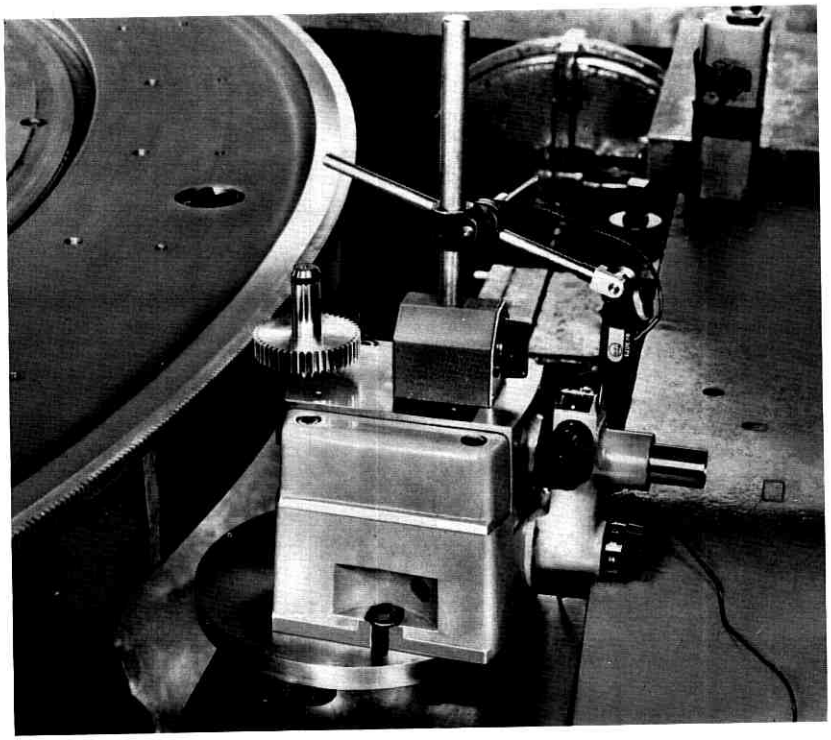

Fig. 12 — Test equipment for checking gear tooth-to-tooth error and pitch circle runout.

missions are used for driving, respectively, in azimuth and in elevation. Each transmission has two motor output shafts — one to drive and the other to provide a reverse torque for anti-backlash purposes as described below. Consequently, four complete gear trains are required for the drives on each axis.

4.2.1 *Drive Gearing*

The two azimuth drives are mounted at diametrically opposite locations on the horizontal framework of the azimuth structure. Fig. 15 depicts the arrangement of one azimuth drive. Fig. 16 shows the schematic of the gear trains.

It is noted that each transmission output shaft drives into the 11.32:1 input gear box which, in turn, drives the 22.59:1 output gear box. The 13-inch pitch diameter pinions engage the 64-foot pitch diameter bull

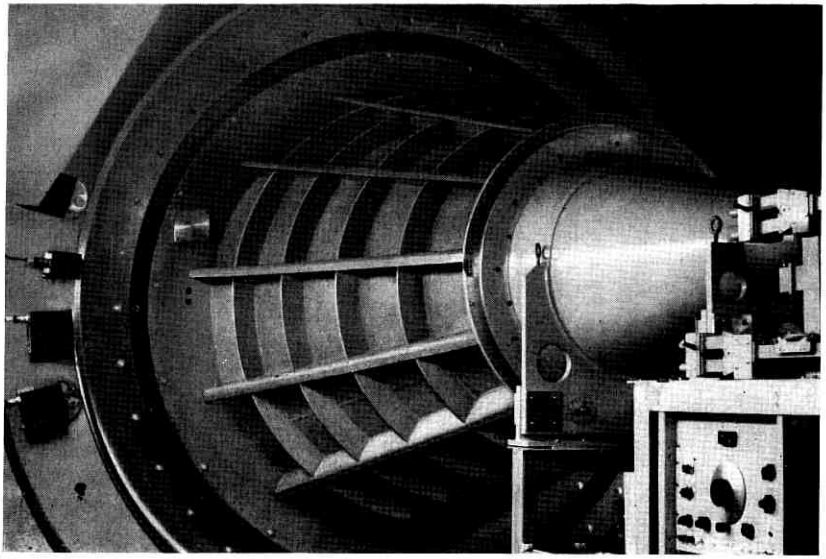

Fig. 13 — Horn apex showing four data units clustered on periphery of 132-inch data gear.

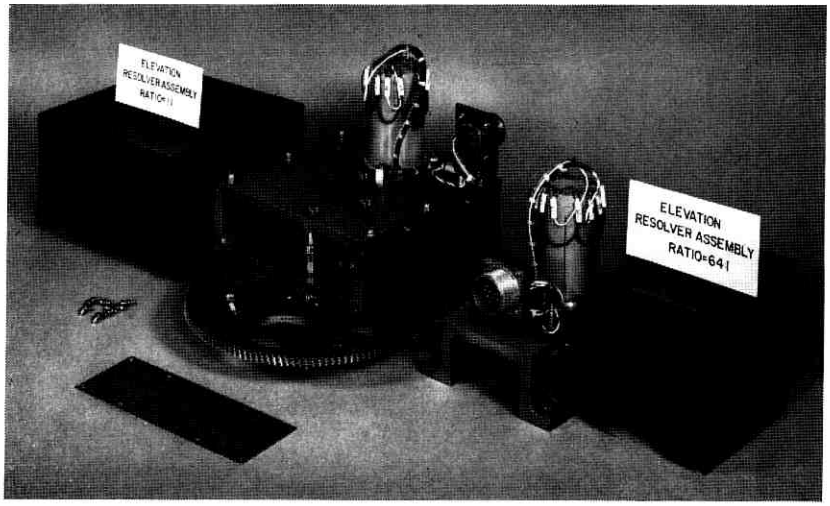

Fig. 14 — Two typical data units.

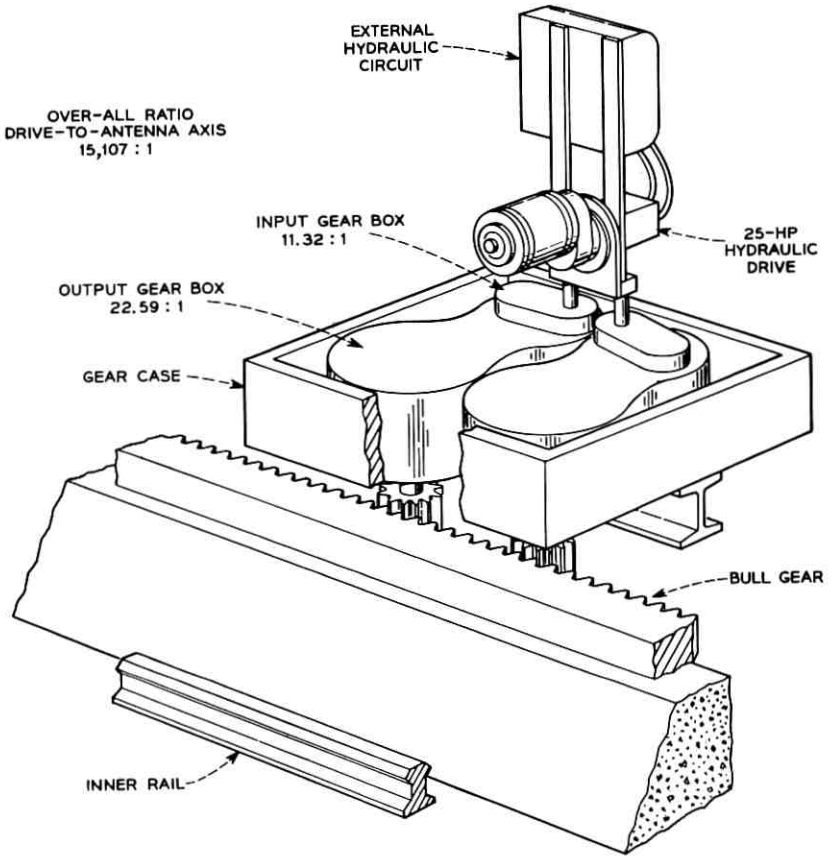

Fig. 15 — Schematic showing arrangement of one azimuth drive.

gear for an over-all drive ratio of 15,107:1; the 13-tooth pinions literally "walk" around the 768-tooth bull gear in rotating the structure.

The azimuth gearing is rather large. The output gear box is 54 inches long, 35 inches wide, and 22 inches high. A pair of boxes mount in a gear case that is 70 by 80 by 28 inches. A complete drive assembly, including the gear boxes and hydraulic unit, weighs $5\frac{1}{2}$ tons. Figs. 17 and 18 are photographs of an azimuth drive mounted on the antenna structure.

The azimuth bull gear is an internal gear of 64-foot pitch diameter and 6-inch face width, and is composed of 32 equal segments. To bring the gear as close as possible to the underside of the horn azimuth framework, the segments are bolted to the top of a five-foot high parapet that is part

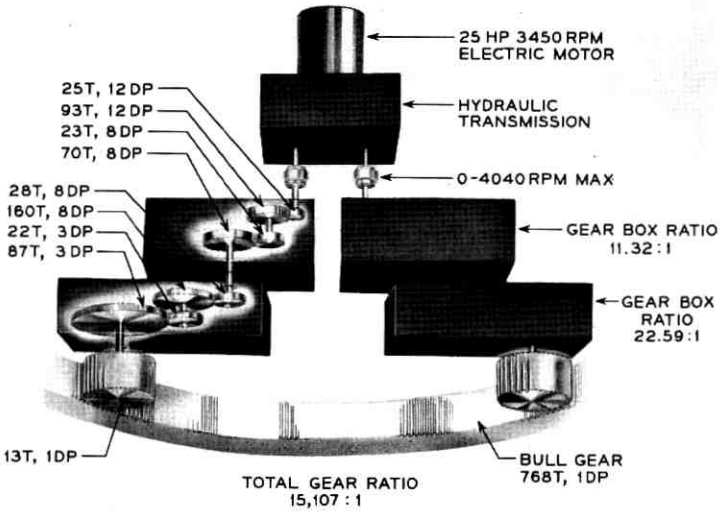

Fig. 16 — Schematic of azimuth gear train.

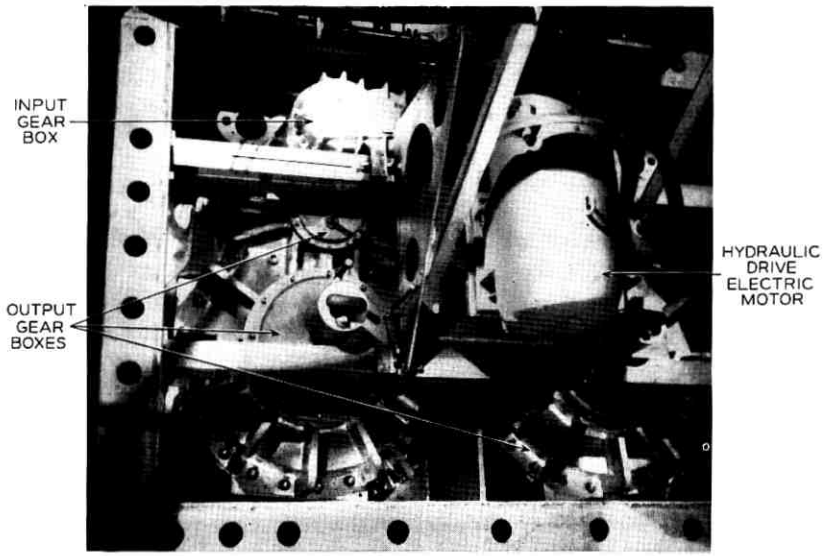

Fig. 17 — Azimuth drive mounted on antenna structure (top view).

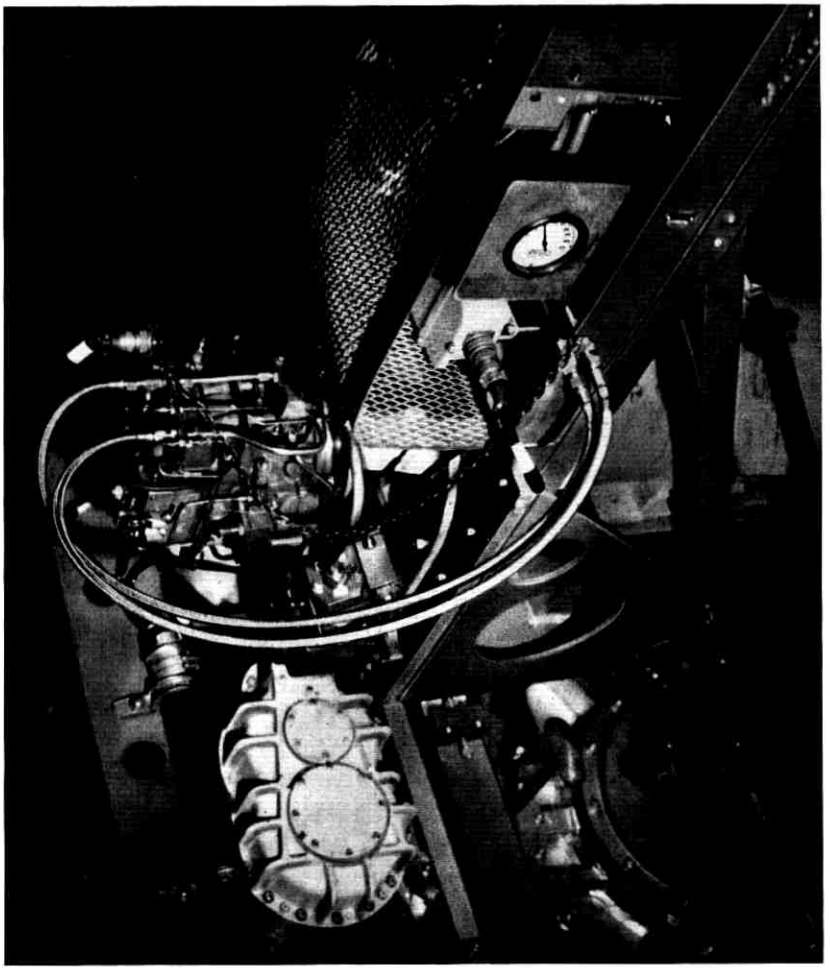

Fig. 18 — Azimuth drive mounted on antenna structure (side view).

of the foundation structure. By this means, the cantilever moment of the gear box and pinion and the resulting azimuth structure compliance are minimized.

Fig. 19 is a photograph of the azimuth drive pinions and a section of the bull gear.

The two elevation drives are mounted on the forward truss of the azimuth structure adjacent to the trucks that support the elevation wheel. Each assembly of the pair consists of the 10-horsepower hydraulic

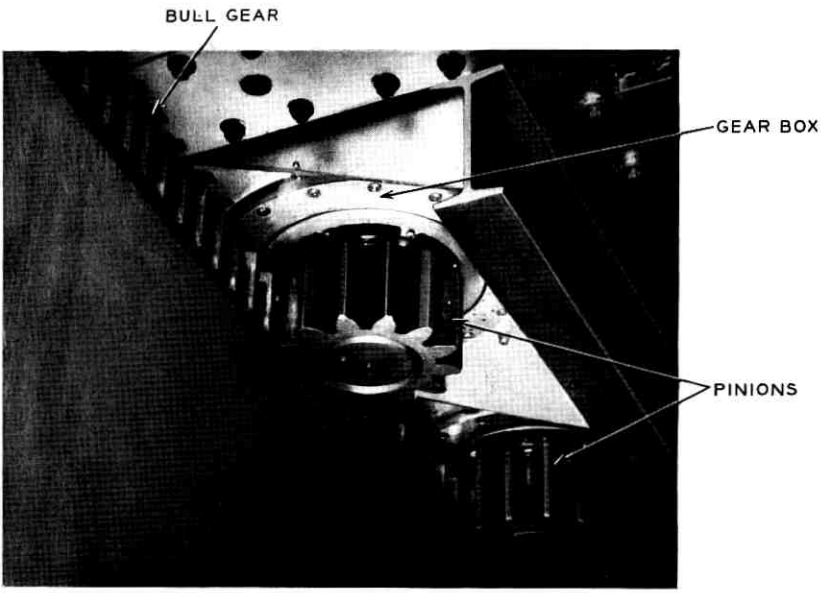

Fig. 19 — Azimuth drive pinions and section of bull gear.

unit which drives the 9.28:1 input gear box. This is the input to the final gear drive box of 23.52:1 ratio. The fifteen-tooth, 10-inch pitch diameter output pinions engage the $1\frac{1}{2}$ diametral pitch, 70-foot pitch diameter bull gear to yield an over-all elevation drive ratio of 18,334:1. The bull gear consists of 36 segments bolted and doweled to the periphery of the elevation wheel. The elevation drive gear schematic is shown in Fig. 20.

Fig. 21 is a photograph of the left-hand elevation drive mounted on the structure. Each gear box measures 48 by 38 by 18 inches, and the pair of boxes are mounted in the gear case of 88 by 90 inches. One complete drive assembly, including the hydraulic package, weighs approximately 3 tons.

4.2.2 *Hydraulic Drives*

The hydraulic drives are the prime movers for the antenna.

The 25-horsepower azimuth drive unit is shown in Fig. 22. The 10-horsepower elevation unit is quite similar in appearance and functioning but is slightly smaller.

The basic hydraulic circuit in somewhat simplified form is shown in Fig. 23. The power input to the system is a three-phase induction motor

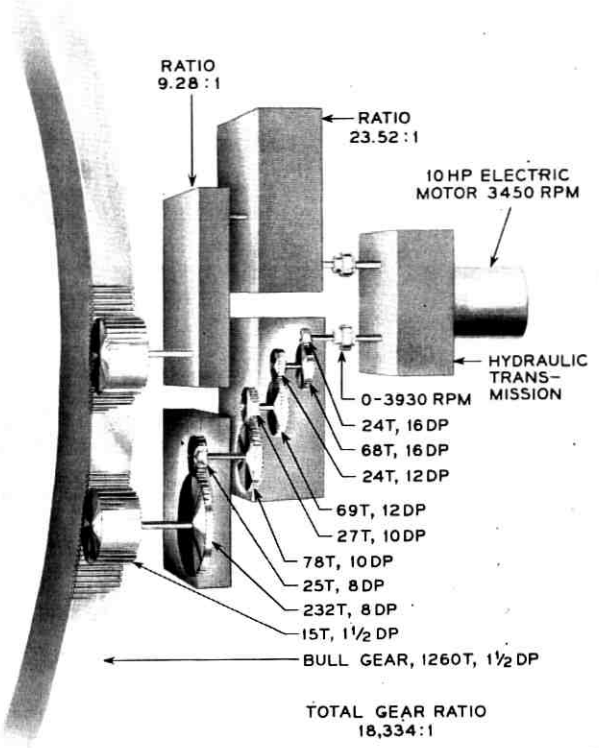

Fig. 20 — Elevation drive gear schematic.

that drives the servo-controlled main pump and two gear-type pumps for control and replenishing fluid pressure. The main pump is a nine-cylinder, variable flow, positive displacement type. As shown in Fig. 24, fluid is displaced when the shaft drives the pistons and cylinder barrel contained within the yoke housing. The yoke is mounted to swing 30 degrees either side of center about a pintle bearing, under control of the stroking cylinder. The flow is directed through ports in the stationary valve plate, and thence through passages in the yoke to the hollow pintle, where connections are made to the hydraulic motor circuit (see Fig. 23). The yoke angular position determines the displacement of the pistons and the direction of output flow.

The pump is connected in a series circuit with the two nine-cylinder hydraulic motors with intermediate connections through relief or di-

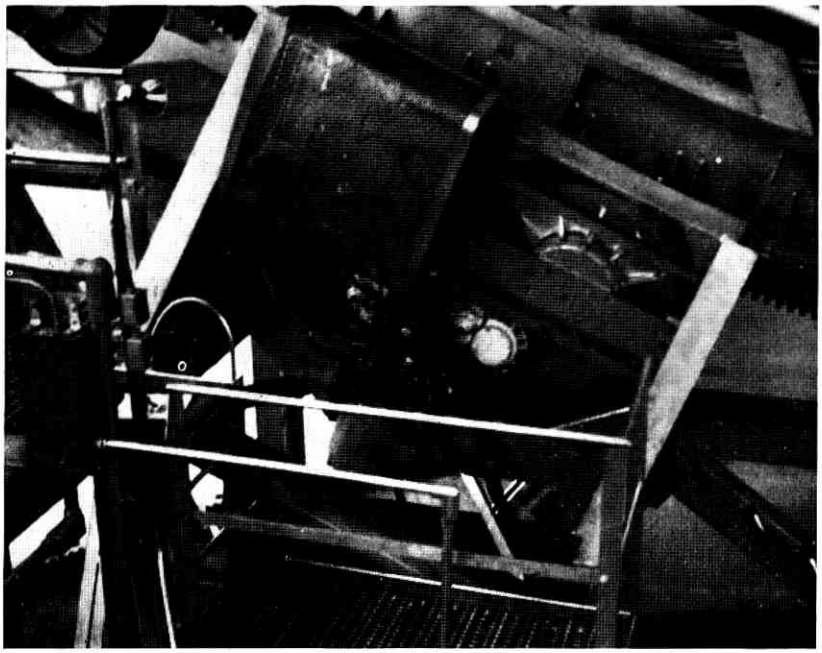

Fig. 21 — Left-hand elevation drive mounted on antenna structure.

rectional valves to the replenishing pump and sump. The hydraulic motors are similar in construction to the pump except that the stroke angle is fixed at 25 degrees. Fluid under pressure acting upon the pistons causes the cylinder barrel assembly to revolve and drive the output shaft. With the fixed angle between the cylinder barrel and shaft, the displacement per stroke is constant. Hence, motor speed is related to fluid flow rate.

For zero input signal, the servo valve, stroking cylinder, and main-pump yoke self adjust to the null or neutral position, and no flow occurs. However, the replenishing pump produces a differential pressure of approximately 60 psi across the two motors, tending to drive them in opposite directions with equal torque. The effect is that clearances in the gear trains are taken up in the direction that the motors normally drive. Because the pressure acting on both motors is equal, net driving torque applied to the bull gear is zero. This arrangement of the replenishing pump in the circuit effectively eliminates backlash in the gearing.

When an input signal actuates the torque motor, the directly coupled servo valve meters fluid at control-pump pressure to the stroking cylinder, causing it to move in magnitude proportional to the signal ampli-

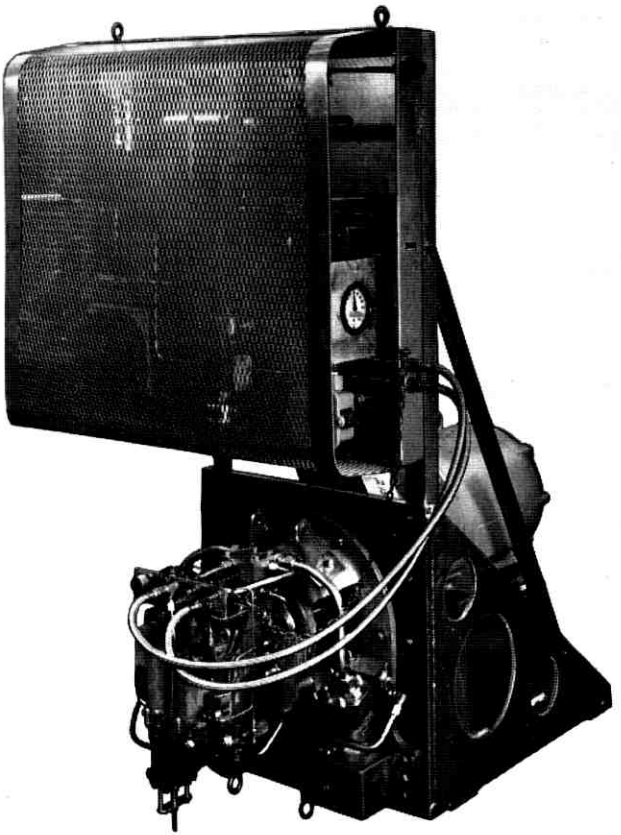

Fig. 22 — Vickers 25-horsepower azimuth drive unit.

tude and in direction in accord with signal polarity. By mechanical connection, the stroking-cylinder piston rod adjusts the position of the main-pump yoke to control a proportional pump output rate in the desired direction of flow.

If it is assumed that the flow is directed to motor 1, the increased pressure closes the directional check valve on the upper side of the replenishing pump connection and acts in the motor to produce driving torque. As antenna rotation occurs, the spent fluid passes to motor 2, which is driven by its gear train as a pump discharging fluid against the 60-psi replenishing pump pressure differential. The resulting light load on the gear train eliminates backlash.

When the input signal amplitude is increased, the pump yoke angle

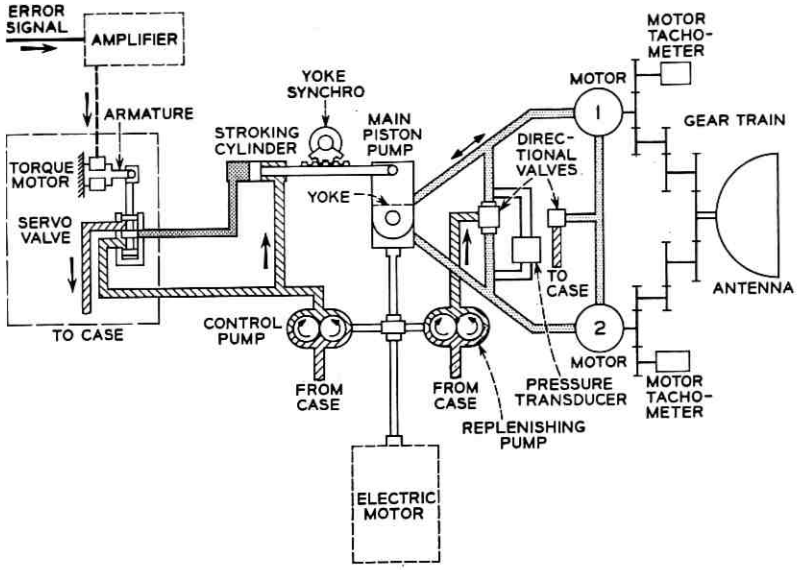

Fig. 23 — Simplified schematic of basic hydraulic drive circuit.

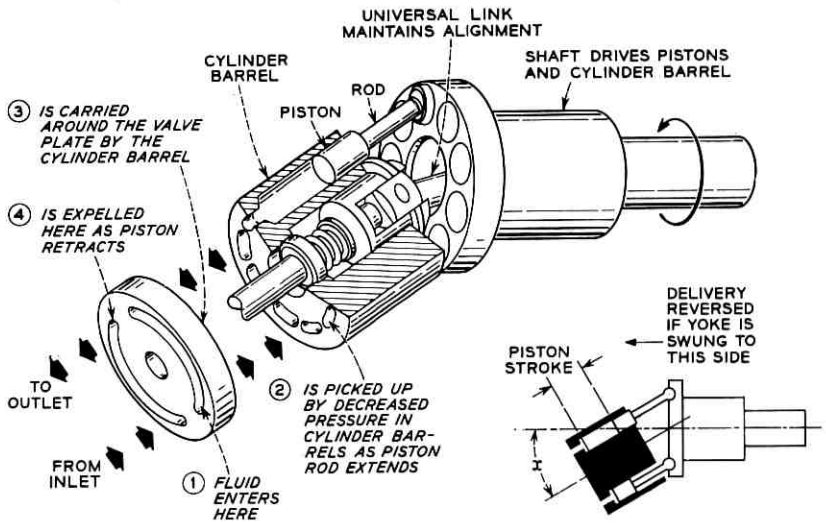

Fig. 24 — Mechanical schematic of piston pump.

increases correspondingly. Motor 1 operates at a higher output, but the retarding torque of motor 2 remains constant.

If a signal of opposite polarity is applied to the torque motor, the same sequence of operations drives the pump yoke to a position on the opposite side of center, direction of flow is reversed, and the two motors interchange their roles, reversing antenna rotation. Because the retarding torque is maintained at all times, reversal is smooth.

The pressure transducer (see Fig. 23) provides an electrical signal proportional to the pressure drop across the main pump, which is proportional to the work load on the hydraulic motor. This signal, as an input to the servo system, is used to equalize the output of the two hydraulic transmissions and to provide system damping. The yoke synchro and motor tachometers are also feedback inputs to the servo system for operational control.

The combination of the Vickers transmission and drive gearing provides remarkable responsiveness and antenna tracking capability. Speeds may vary from zero to maximum antenna slew rates of 1.5 degrees per second in azimuth and 1.4 degrees per second in elevation. As an indication of the acceleration capabilities, it should be noted that at slew speed the drives complete a full reverse command in an interval of less than three teeth on the bull gear. At the other extreme, as in tracking radio stars or under certain conditions during satellite tracking, rotation of one axis may be imperceptible. Particularly impressive is the response to sinusoidal servo input signals as high as 2 cps in frequency.

V. RADOME

5.1 *Need for Radome Coverage*

Early studies at Bell Laboratories and past experience based on tests of military antenna systems have proven that, despite the added system noise, a radome is essential to protect the horn-reflector antenna from the effects of enviornmental conditions. Some of the considerations and the advantages afforded by radome protection are discussed herein.

Without radome coverage, the antenna would be subject to the effects of the common elemental conditions of the area, such as solar heat, wind, snow, ice, rain, and dust. These conditions can seriously affect antenna performance.

(a) Direct solar heat, for example, can disturb the antenna reflecting surface contour accuracy so that the required patterns and gain are not achieved. Furthermore, differential solar thermal distortion can adversely affect beam pointing accuracy.

(b) The influences of wind on an exposed antenna are even more pronounced than those of solar heat. An antenna structure and high-gain antenna servo drive system can become unstable under buffeting winds as low as 30 miles per hour. Excitation or distortion under high wind loading also can jeopardize its tracking performance.

(c) Accumulations of ice, snow, and possibly rain, if suitable drainage is not provided, can substantially interfere with antenna performance. Such accumulations sometimes necessitate limiting the range of antenna motion about its axis; otherwise, there is the risk of introducing too great a turning moment for the servo drives to counteract. This hazard makes disposal of the accumulation difficult, as indicated by a recent experience at a large installation in New England. An attempt to dump a heavy snowfall by tilting the dish caused an excessive moment, resulting in complete lack of control of the moved axis. The snow had to be removed by hand-shoveling and sweeping—a hazardous and time-consuming task that encroached on vital test time.

Under radome protection, however, the antenna is nearly independent of ambient weather conditions and can be scheduled on an optimum basis. Not only does this protection avert the direct adverse effects of the elements on antenna performance, but it also retards physical deterioration. Maintenance requirements are drastically reduced when an antenna is housed in a radome. Moreover, within a radome, antenna maintenance can be conducted with a higher degree of confidence and reliability.

Other less obvious advantages are also derived. If the antenna is to be radome-housed, its structure and servo systems can be built for lighter duty than if it is to be exposed. When no direct provisions are needed to counter the effects of exposure, a greater latitude in design approach is permissible.

5.2 *Selection of Structure*

When the need for a radome was established, it became necessary to choose the type of protective structure that would meet all requirements. Rigid-foam, space-frame, and air-supported structures were considered on the basis of: (a) state of the art, (b) electrical performance, (c) cost, and (d) effect on the schedule. The air-supported structure won by a sizable margin on all counts.

At that time, the largest radome built, either rigid or air-supported, was 150 feet in diameter. The diameter of the protective radome structure for the horn-reflector antenna is 210 feet, which obviously called

TABLE IV — PERTINENT LOAD FIGURES FOR 210-FT DIAMETER TRUNCATED SPHERE

Inflation lift at 0.175 lb/in²	= 730,000 lbs
Aerodynamic lift in a 100-mph wind	= 844,000 lbs
Total lift	= 1,574,000 lbs
Aerodynamic drag	= 221,000 lbs
Aerodynamic moment	= 8,700,000 lb-ft
Fabric tension due to above loads	= 463 lbs/linear in

for a major step beyond the state of the art at that time for any kind of radome structure.

5.3 *Radome Design*

The principal loads imposed on the radome fabric under the most severe weather conditions are due to the internal pressure of the supporting air and the effects of the wind. These loads in a 100-mph wind, which requires an internal pressure of 0.175 lb/in², are listed in Table IV.

Fig. 25 is a good illustration of the aerodynamic load factors encountered on a truncated sphere supported on a base and placed in a free wind stream. The contour lines are on the surface of the sphere and

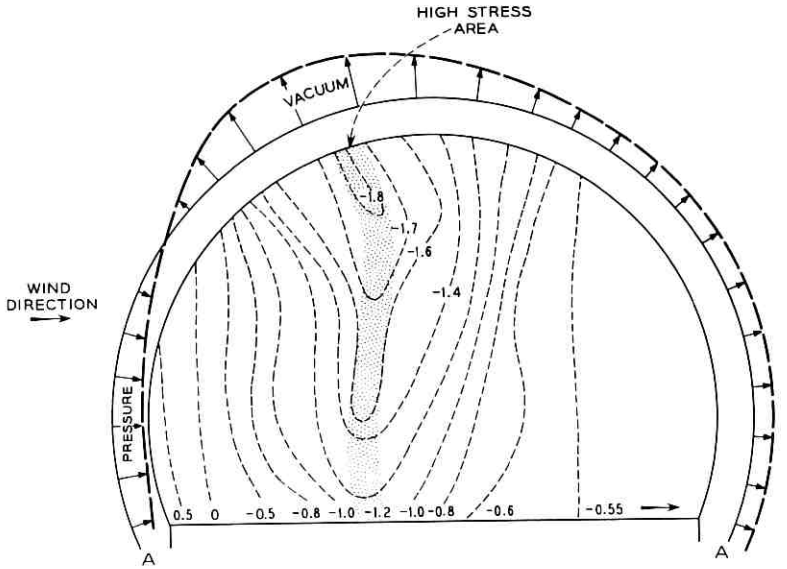

Fig. 25 — Aerodynamic loads on a truncated sphere in a free wind stream.

represent equal aerodynamic pressure of the values shown in the area contoured. A value of 1.0 is equal to the dynamic pressure of the wind for a given air velocity. Plus figures represent inward forces or pressure; minus values stand for outward forces or vacuum.

Fig. 25 reveals that, for a moderately high wind velocity, the aerodynamic suction forces about the sphere add to the internal pressure loading, becoming highest in a circumferential band perpendicular to the wind direction, as shown by the shaded area of high stress. The contour numbers in the figure also reveal that the particular area of highest stress is near the pole or crown. For the sake of clarity, the pressure values in a plane through the center of the radome and parallel to the wind have been plotted from an arc of a circle (A-A) used as a baseline (see Fig. 25). The directions of the arrows from the baseline indicate the direction of the reaction, depending on whether it is pressure or vacuum. The figure also pictorially shows that the aerodynamic drag force and moment about the base are high because of the additive impact pressure on the windward side and the vacuum on the leeward side.

The computations of aerodynamic and inflation pressure loads are straightforward and are all contained in a report by Cornell Aeronautical Laboratory.[7] Therefore, they are not repeated in this paper.

5.4 *Material Development*

The common pneumatic automobile tire could be considered a very distant relative of a large inflatable radome. Since it is a pressure-rigidized structure, it can serve to illustrate just one of the many difficulties in the design of a 210-foot diameter air-supported structure.

At an inflation of 28 pounds per square inch, a passenger automobile tire must withstand a tensile loading of approximately 100 pounds per inch. The tire carcass, of course, is designed to withstand puncturing bruises and road shock; therefore, it is made with a large safety margin of thickness above that required for the tensile load.

Unlike the tire, however, the radome must pass RF energy with minimum loss and pattern distortion. In this case, an undue safety margin of thickness would cause serious degradation of electrical performance. For a given pressure, as the diameter of a spherical pressure vessel increases, the tensile loading per inch of skin increases in direct proportion to the diameter. In the case of the radome, its required inflation pressure is a function of its wind environment. For the Telstar radome, the maximum wind environment capability is 100 miles per hour, and the corresponding inflation pressure is 0.175 pound per square inch (roughly $\frac{1}{100}$ of the tire pressure).

This low pressure might appear to be an insignificant problem in comparison to the 28 pounds per square inch required for the automobile tire. However, with very little calculation it can be shown that, when the 210-foot diameter radome is inflated, its skin is under a tensile loading of 150 pounds per inch, which is 50 per cent higher than the tensile load on the tire. To this load must be added the aerodynamic force of 300 pounds per inch, bringing the total radome skin tension to 450 pounds per inch (based on a 100-mph wind), or about $4\frac{1}{2}$ times the tensile load on the tire.

This load in itself does not appear to be a formidable problem; however, it becomes more drastic in view of the other requirements that are placed on the material. Besides sustaining the tension load, the material must also have the following characteristics:

(a) The base fabric must be stable, little affected by constant exposure to solar ultraviolet radiation, and must be highly rip resistant, with a sufficient margin of safety to allow for factory handling, erection, and anticipated life expectancy under load.

(b) Any protective coating for the base material must be tough, durable, and resistant to both abrasion and erosion from weathering. It must have good adherence to the base material and be capable of being bonded or cemented into joints that will exhibit characteristics equal to or better than the base material. For RF transmission, its moisture absorption must be low.

(c) For electrical reasons, the finished material must have a dielectric constant as low as possible (3.0 in the case of the Telstar system) and a thickness of no more than 0.071 inch, and must be held to an over-all thickness tolerance of ± 0.002 inch. The material must be light in weight to permit transportation and erection with a minimum of difficulty. To equalize stress and to preserve the aerodynamic shape, strength and stretch properties of the material in the warp and fill directions must be as close to equal as possible.

With these specifications to be met, the selection and development of the material obviously was a formidable problem. Because no off-the-shelf commercial material was available, the problem was solved by producing a special radome skin from the best raw materials obtainable. The base yarn, selected for high strength and ultraviolet resistance, was Dacron polyester fiber, hot-stretched and heat-stabilized. Investigation of loom capacity revealed that, to meet strength, rip resistance, and elongation requirements, the radome fabric had to be specially woven to the heaviest gauge within loom capacity. After coating, two such fabric layers were laminated. To distribute loads equally, the two

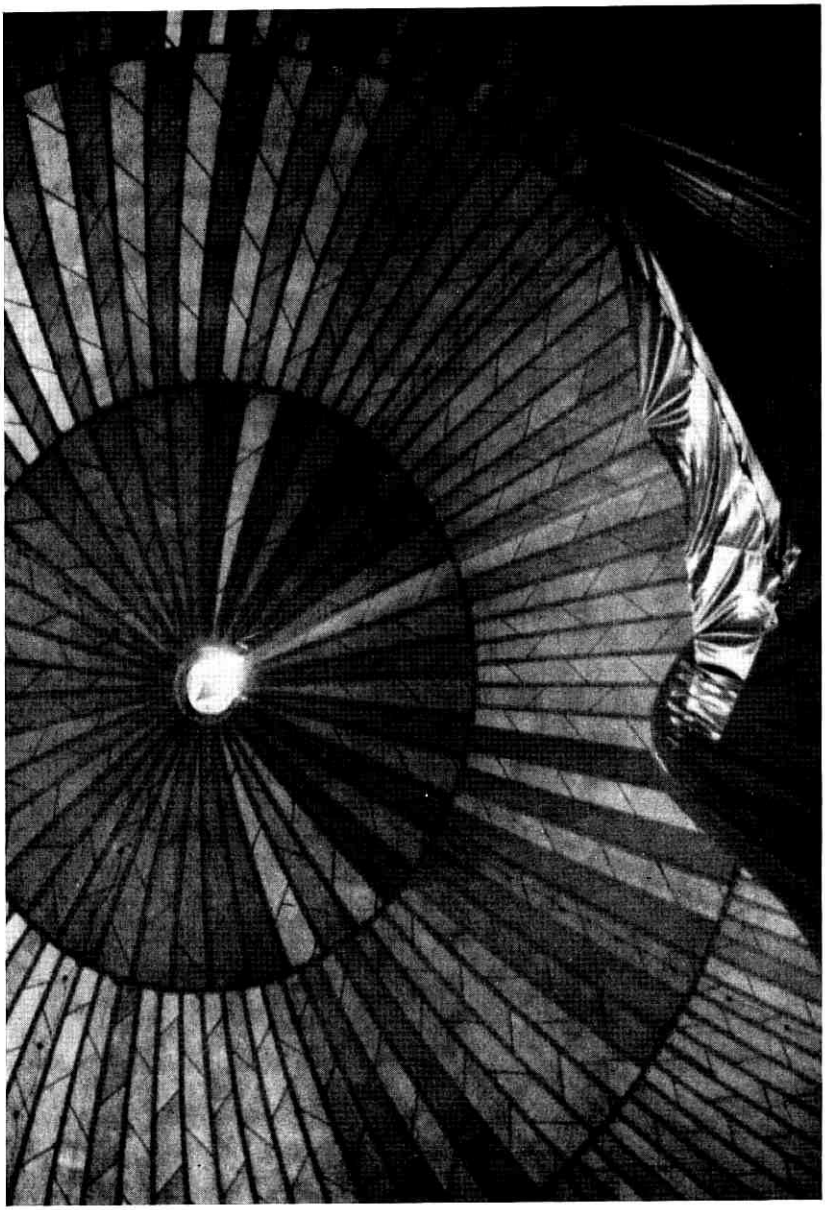

Fig. 26 — Upward view showing herringbone pattern inside Andover radome.

plies were bias-laminated to form a herringbone pattern (see Fig. 26). This laminate was then bonded, piece by piece, to make the full shaped radome shell.

The coating material selected was a synthetic rubber (based on Hypalon, a DuPont proprietary material) specially formulated to minimize RF loss and moisture permeability. This coating, together with commercially available Hypalon air-curing cements, was capable of developing the necessary inter-laminar and joint-bonded strengths, in addition to meeting all the requirements stated above.

To assure quality and uniformity in the finished product, checking was required throughout the entire process — i.e., checks of the yarn, the woven material, the coating material, the coating process, the thickness and quality control of the coated material, the ply laminating process, and the joints. All had to be continuously checked and double checked.

Quality control was a major undertaking because the inflated structure is composed of 6 acres of single-ply material laminated to make 3 acres of 2-ply patterned panels and contains 31,600 feet of hand-cemented joints which bond the patterned panels one to another to produce the final single-piece radome.

5.5 *Radome Fabrication*

The double-ply material, coated and laminated in the materials processing plant in Beacon, New York, was shipped to the radome fabricating plant of Birdair Structures, Inc., Buffalo, New York. The coated fabric was processed so that a single batch operation produced a continuous roll of a length in excess of that required to fabricate two of the 168 major gores, each 154 feet long. The length which was selected permitted sampling of material for quality-control purposes from each end and the middle of the roll. The samples thus represented the full range of curing-heat history. Quality control included warp-and-fill strength tests, coating-adhesion tests, and tests for elongation under load.

When the material was received at the radome fabricating plant, test samples were cut from the prescribed locations on the roll and forwarded to the receiving inspection laboratory for testing to confirm the prior tests and to check the weight, gauge, tear resistance, ply adhesion, and water permeability. Lap-joint specimens were also made and subjected to dead loads at 160 degrees Fahrenheit to determine the hot-ply adhesion and cementability of the coatings.

Material passing all tests, including 100 per cent visual inspection, was then ready for the next step, the cutting of gores according to templates. Patterning the gores took place on a flat table. The templates, therefore, included compensation factors to adjust the shape of the gore for transition from a plane surface to a spherical sector. Other factors took into account the differential elongation between the straight and alternating bias plies and that between the warp and fill of each ply under load. All of these compensations were made to insure the sphericity, under the required inflation pressure, which must be attained in the radome to realize adequate stress distribution and utilization of fabric strength.

The gore edges were next processed for stress relief at lap-joint terminations by subjecting them to a proprietary slitting process.

A sufficient number of gores was produced to cover the entire range of gauge and weight within the tolerance specified. To maintain uniformity of electrical characteristics, each gore produced was selectively assigned to various sections of the radome.

Bonding of gores commenced when an optimum number of gores was available for suitable dispersal in the radome and for consecutive cementing of adjacent panels sequenced in accordance with the folding scheme, which anticipated the eventual unfolding and deployment of the radome about the foundation at the erection site.

The edges to be bonded were buffed with a power buffer to expose a virgin surface of the Hypalon coating for manual application of two separate precoats of Hypalon cement. Mating edges of the precoated gores were then laid up on a form especially designed for holding and aligning the adjacent panel edges for application of bonding cement and curing in the desired panel-to-panel relationship to produce sphericity in the finished radome under inflation pressure.

The bonding cement was applied manually and the joints were rolled with a power-roller, the weight and speed of which were designed specifically for the Telstar radome. Joints remained in tension on the form for 3 to 4 hours for final room-temperature cure. Each long meridianal joint required 3 moves or positions on the form to complete bonding of the entire length.

Each move on and off the form had to be made without jeopardizing the anticipated sequence of folding the finished radome for placement in the 8 × 10 × 40-foot crate for delivery. This latter point was important since the complete radome weighs 60,000 pounds and is difficult to move when bonded into one piece. The upper edge of the main panels

was bonded to the crown, the lower edge to the roped clamping bead. The crown, like the main gores, was made up of numerous bonded pieces.

Sample joints were made daily with each batch of cement, using production materials, and processed by production cleaning and curing methods. Samples were identified with each joint made and with each day's production. After cure, the samples were subjected to strength and peel tests for assurance that no unknown factors had inadvertently affected the uniformly high quality of the unit. To meet acceptance requirements, the strength of the joint had to exceed that of the material.

After final cure of each cemented joint, every inch of each side was visually inspected and "prodded" with a peel tester to ascertain that it was properly and securely bonded. The minutest area exhibiting the slightest indication of being questionable for any reason whatsoever was immediately reprocessed.

A precoated tape was cemented over the outer seam of each finished lap joint. The tape adds nothing to the joint strength, but it protects the exposed edge from invasion of the elements and improves the appearance.

A final inspection of all seams was made again while the radome was being folded into the shipping crate.

5.6 *Erection*

Program schedules did not allow sufficient time for the material development and manufacture of the radome prior to assembly of the antenna structure. To provide environmental protection during the antenna construction period and while development and manufacture of the radome material proceeded, a temporary air-supported structure (construction shelter), also 210 feet in diameter, was designed and fabricated. This structure could be provided relatively quickly and inexpensively because the wind requirements were lower than for the radome, and electrical specifications and long life span were not required. This intermediate structure provided protection for antenna construction and also was used in erecting the final radome.

Use of the construction shelter as an erection aid necessitated the addition of a bulge or blister to the fabric envelope, as seen in Fig. 27. This blister provided clearance for the upper equipment room when the construction shelter was lowered to the position required for radome installation, shown in Fig. 28. Erection of the one-piece, 60,000-pound inflatable radome over the pre-erected 95-foot high antenna and con-

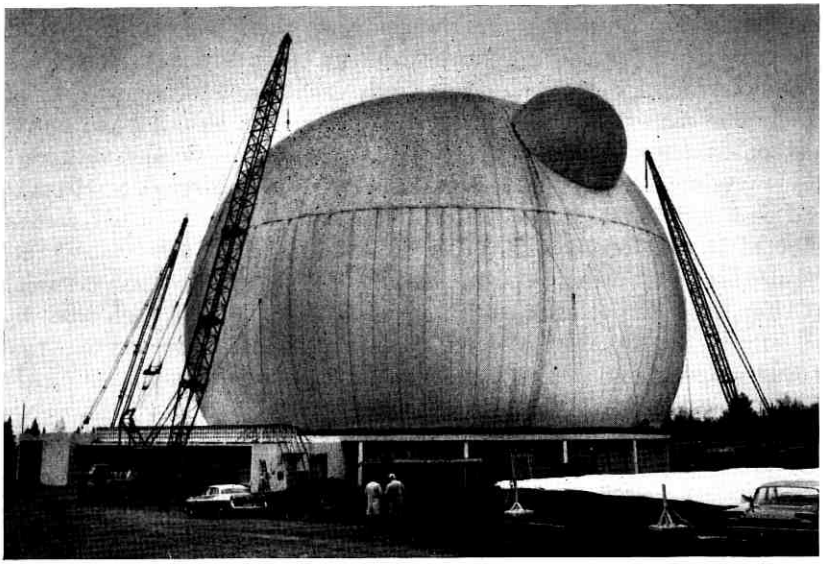

Fig. 27 — Preparing the construction shelter for deflation; permanent radome being unfolded at lower right.

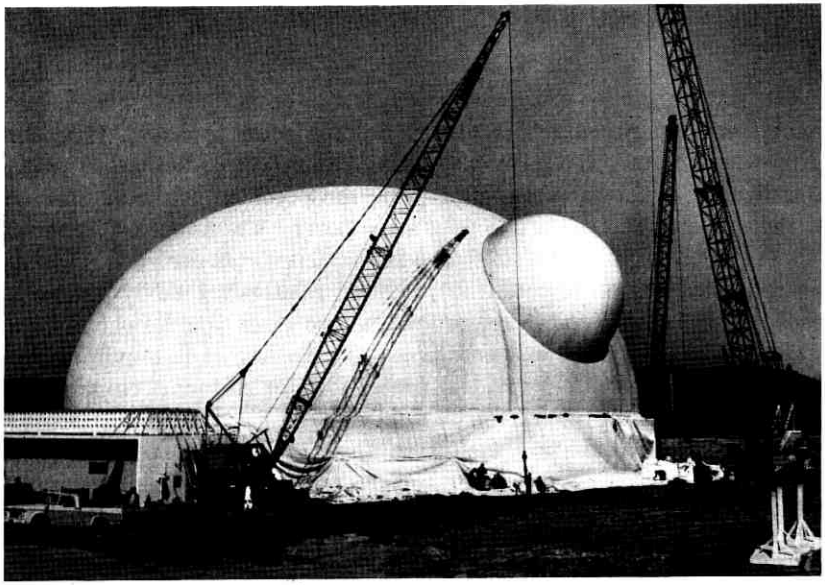

Fig. 28 — Construction shelter lowered and reattached to foundation ring; 160° of the radome is attached to the clamping ring.

struction shelter was a herculean task. Many schemes were considered; some of them included the use of towers, or helicopters or helium bags. Each method considered appeared to be hazardous and expensive or, in many cases, impractical. Strangely enough, the final method utilized air pressure as the main motive force to place the radome over the antenna and construction shelter. The method used is shown in Figs. 27 through 30.

Fig. 27 shows the air-supported construction shelter. The completed antenna has been placed in the stow position inside the construction shelter. In Fig. 28 the temporary construction shelter has been lowered, reattached to its foundation, and reinflated. The radome has been attached to the foundation around 160 degrees of its periphery and has been folded in preparation for lifting the leading edge. In Fig. 29 the leading edge has been lifted over the "blister," and tension is exerted on the leading edge bead by winches at the foundation. Fig. 30 shows

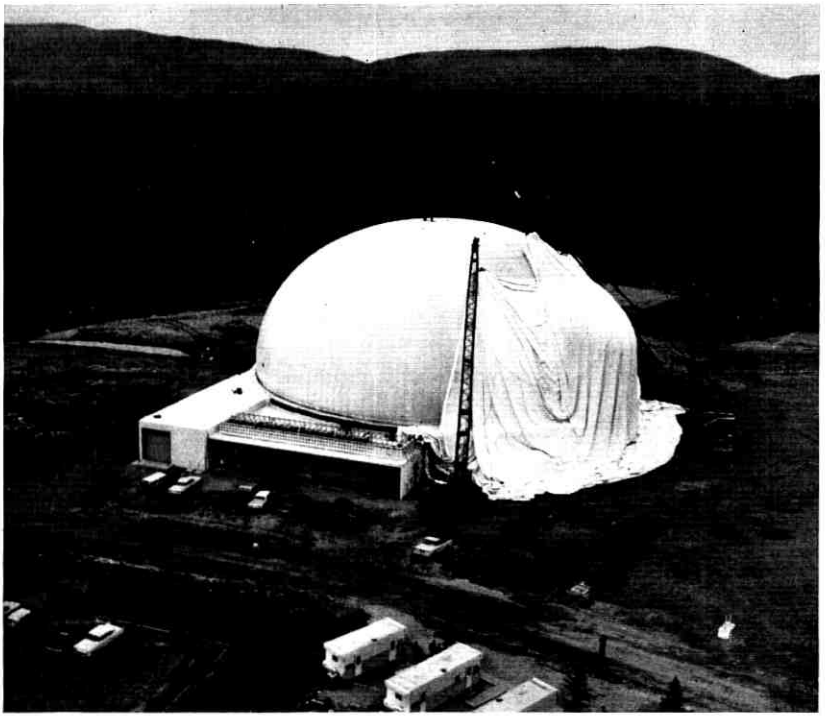

Fig. 29 — Initial raising of the radome over the blister of the construction shelter.

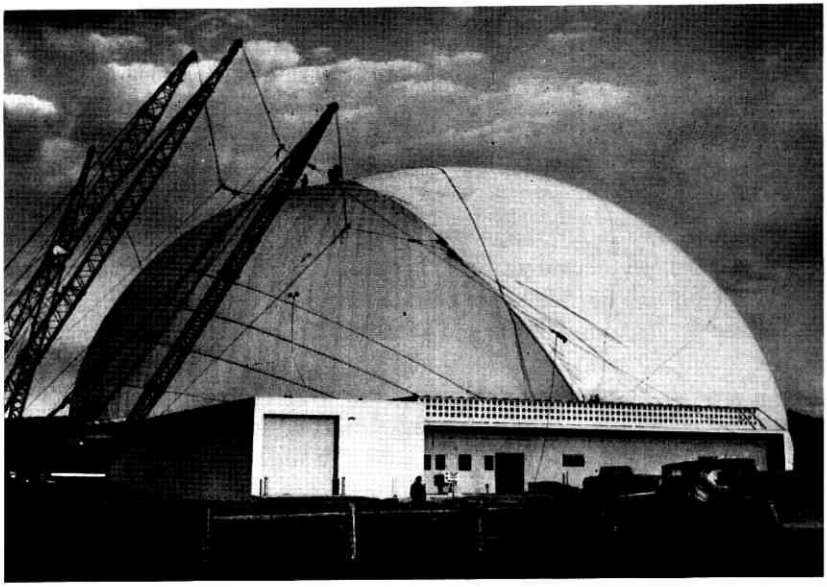

Fig. 30 — Radome being pressurized to allow sliding it over the construction shelter.

crane lines attached to the leading edge of the radome and the radome being pressurized. The pressure reaction on the upper free portion of the radome delivers a net force to the radome toward the cranes and slides the leading edge up and over the inflated construction shelter to engulf it. The radome bead is attached completely and the radome is inflated; the shelter is then removed from within. Fig. 31 shows the final installation with the radome fully inflated.

5.7 *Pressurization System*

The pressurization system is completely automatic and functions always to keep the radome internally pressurized to a level in excess of the dynamic pressure of the wind.

The system is designed to maintain any one of three pressure levels: $1\frac{1}{2}$ inches of water (0.054 psi) by use of two low-pressure blowers for winds from 0 to 45 miles per hour, 3 inches of water (0.108 psi) by use of one intermediate-pressure blower for winds from 45 to 70 miles per hour, and $5\frac{1}{2}$ inches of water (0.20 psi) by use of two high-pressure blowers for winds from 70 to 100 miles per hour. All blowers operate as

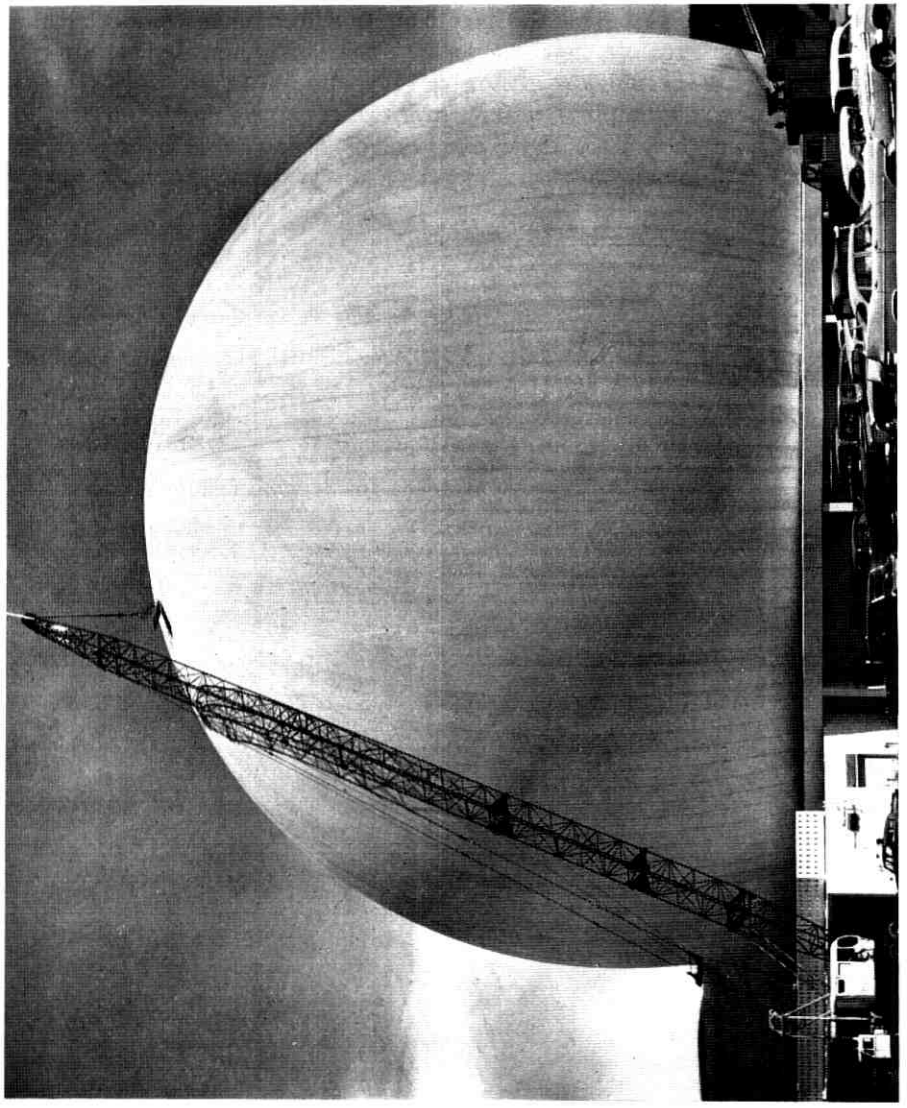

Fig. 31 — Radome installation complete and fully inflated.

a function of the output of an external anemometer and the internal radome pressure. Should a blower fail for any reason, the system is designed so that the next pressure-stage blowers will automatically come on to maintain pressure. For emergency situations, manual remotely controlled vents are provided. Also, high-pressure valves are installed, which will prevent the pressure from ever exceeding the maximum design pressure. All blowers, with the exception of the low-pressure blower, will function automatically from an emergency generator provided at the site.

REFERENCES

1. Hoth, D. F., O'Neill, E. F., and Welber, I., The *Telstar* Satellite System, B.S.T.J., this issue, p. 765.
2. Hines, J. N., Li, Tingye, and Turrin, R. H., The Electrical Characteristics of the Conical Horn-Reflector Antenna, B.S.T.J., this issue, p. 1187.
3. Githens, J. A., Kelly, H. P., Lozier, J. C., and Lundstrom, A. A., Antenna Pointing System: Organization and Performance, B.S.T.J., this issue, p. 1213.
4. Githens, J. A., and Peters, T. R., Digital Equipment for the Antenna Pointing System, B.S.T.J., this issue, p. 1223.
5. Lozier, J. C., Norton, J. A., and Iwama, M., The Servo System for Antenna Positioning, B.S.T.J., this issue, p. 1253.
6. Cook, J. S., and Lowell, R., The Autotrack System, B.S.T.J., this issue, p. 1283.
7. Cornell Aeronautical Laboratory Report, number UB-909-D-2, issued by Rome Air Development Center, March, 1956.

Antenna Pointing System: Organization and Performance

By J. A. GITHENS, H. P. KELLY, J. C. LOZIER and A. A. LUNDSTROM

(Manuscript received February 27, 1963)

This paper is a description of the antenna pointing system used in the satellite ground station at Andover, Maine. It is an introduction to the following five papers in this issue, which describe and discuss in some detail the various major parts and features of the antenna pointing system. In order that the antenna have sufficient gain for the Telstar experiment, it was necessary that it have a "pencil" beam of about $\frac{1}{5}$ degree in diameter. This requires an antenna pointing system of high accuracy. The equipment and methods required to achieve this accuracy are outlined.

I. OBJECTIVES

At the Andover, Maine, satellite ground station the 3600-square-foot aperture horn-reflector antenna[1,2] concentrates the microwave energy in a very narrow beam. This is needed to achieve adequate signal-to-noise ratio in the broadband communications channel provided by the system. Accordingly, it is necessary to provide means for pointing the antenna at the Telstar satellite. The guiding objectives used in engineering and constructing the antenna pointing system are briefly described here.

A demonstration of reliable satellite communications was a primary goal. This required acquisition and tracking of the satellite to an accuracy which would hold the resulting maximum loss in antenna gain to values acceptable to the communication link. It required a system with versatility sufficient to cope with a combination of unfavorable conditions such as deviations of the satellite from the expected orbit, variations in refraction effects, antenna misalignments, and equipment malfunction.

A basic objective of a communications satellite system is reliability. In the current state of the art (weight limitations, etc.) this can be best

realized by designing the satellite so that it will be as rugged as possible and therefore relatively simple. The ground station, on the other hand, may have considerable complexity since it can be maintained and improved.

It was decided that the system must have sufficient flexibility for experiments to evaluate different methods of acquiring and tracking satellites. This required facilities for the recording, reduction, and evaluation of large amounts of pointing data.

1.1 *System Description*

The Telstar antenna pointing system performs two primary functions: (*i*) it establishes the communication connection by causing the horn-reflector communication antenna to acquire and continuously track the satellite throughout a communications pass, and (*ii*) it provides means for determining the satellite orbit so that pointing instructions may be generated for future passes to help meet the requirements of the first function. The most difficult problem encountered in providing these functions is one of accuracy due to the needle-like antenna patterns of the 3600-square-foot aperture of the communications antenna. The beam is nearly circular, with an angular diameter of 0.165° at the transmitting frequency of 6390 mc and 0.225° at the receiving frequency of 4170 mc when measured 3 db down from the beam pattern maximum. Furthermore, the requirement placed on the antenna pointing system is that mispointing of the antenna should contribute no more than 1 db of loss in carrier-to-noise ratio in the communications path. A 1-db decrease in carrier-to-noise ratio would be produced by pointing errors which produce approximately 1-db decrease in the 4170-mc down path transmission. A 1-db contour on the antenna pattern at 4170 mc would approximate a circle of 0.06° radius. Therefore, the maximum tolerable pointing error in antenna azimuth or elevation angle is $\pm 0.06°$. To meet this requirement, one must first know where the satellite is with commensurate accuracy and be able to calibrate and control the horn antenna precisely.

A block diagram of the antenna pointing system is shown in Fig. 1. Before a discussion of the operation of this system is undertaken, consider the characteristics of each block. All of the frequencies shown are approximate.

Satellite:[3] The satellite is not part of the pointing system, but it plays an important role in antenna pointing by radiating two CW beacons for tracking purposes, one at 136 mc and the other at 4080 mc. The 136-mc beacon is radiated continuously, but the 4080-mc beacon is

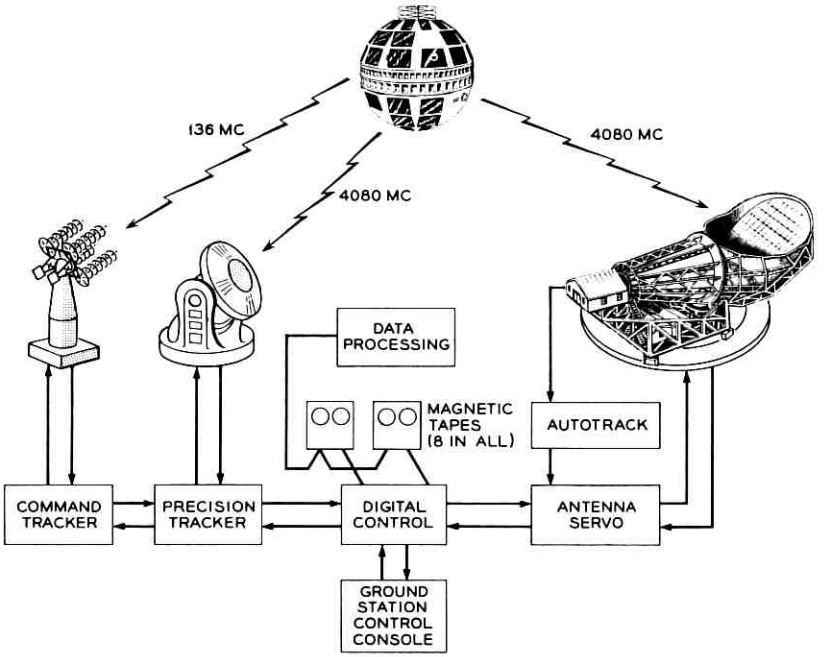

Fig. 1 — Block diagram of pointing system.

transmitted only when the traveling-wave tube amplifier in the satellite is turned on. In addition to its function in the antenna pointing system, the 136-mc beacon also permits the satellite to be tracked by the world-wide NASA Minitrack network. The 4080-mc microwave beacon provides a means of tracking using frequencies in the common-carrier band.

Command Tracker:[4] Tracking of the 136-mc beacon in the satellite is accomplished by the command tracker, a quad-helix antenna having autotrack capabilities. It has a 20° beam diameter and is capable of tracking with an accuracy of about ±1°. In addition to its tracking role, the command tracker also receives telemetry information, which appears as modulation on the 136-mc signal, and transmits commands to the satellite at 120 mc.

Precision Tracker:[5] The 4080-mc beacon is tracked by the precision tracker, a tracking system using an 8-foot Cassegrain dish antenna with a 2° beam. This antenna is capable of autotracking the microwave beacon with an accuracy of about 0.01°. The precision tracker provides the basic data from which the orbital position of the satellite is calculated.

Either of the two trackers, precision or command, can be slaved to the other. This feature is important during initial acquisition, when the position of the satellite is not well known, and will be discussed in more detail later.

Autotrack: The horn-reflector antenna is also capable of tracking the 4080-mc beacon in the satellite by means of its autotrack system.[6] Operating on the nature of the propagation of the received 4080-mc beacon signal in the horn and using a principle similar to the monopulse radar technique, this system produces error signals which indicate the satellite's position relative to the center of the antenna beam. This error signal is used to correct the position of the antenna automatically.

Antenna Servo: The antenna servo[7] controls the hydraulic drive system of the horn antenna. It does this on the basis of commands received from the digital control and/or the error signals received from the autotrack. The servo feedback loop may be closed in the digital control section, where a digital comparison is made between the commanded position and the actual position. An alternative mode of operation is available whereby the servo loop is closed through the autotrack system. This is an autotracking mode and digital control is not involved. These two modes can also be combined so that the autotrack serves to correct any errors in the commanded position.

Data Processing: The data-processing portion of the system consists of two general purpose computers.[8] These facilities perform two primary functions in the antenna pointing system: (*i*) they enable the system to keep track of the satellite by periodically up-dating the basic orbital parameters on the basis of track information derived from the precision tracker and the horn; and (*ii*) they predict future positions of the satellite and generate pointing instructions for both the precision tracker and the horn for future passes. The facilities are also used to record and process data for performance analysis.

Digital Control: The digital control[9] interconnects the various elements of the system and provides a variety of functions. It takes the pointing instructions, which were stored on magnetic tape by the data-processing section, and develops the "program commands" which point the horn-reflector antenna. Similarly, it generates position commands which provide the precision tracker with an acquisition track about which it can search for the satellite. Since, in both instances, these commands must be given at a much higher rate than the rate at which they are recorded on tape, the digital control incorporates interpolation circuits which yield commands at a 128-per-second rate. A second important function is the recording of track information for subsequent use by the

data-processing section in up-dating the orbital elements. The digital control encodes the precision tracker and horn positions and records them on magnetic tape along with the time of each sample. Because of the accuracy requirements in positioning the horn antenna, the digital control also performs the major servo summing operation digitally. That is, the commanded position is compared with the encoded horn position digitally, and only after the error signals are thus derived, and the need for accuracy reduced, is this signal decoded to an analog quantity and used as an input to the antenna servo. The digital control contains the basic time reference in the system and synchronizes the whole operation with real time. Finally, this portion of the system incorporates a number of functions to permit manual supervision and control of the operation and to provide means for establishing the various operational modes and system configurations.

Magnetic Tape Units:[8] The magnetic tape units appear as a separate item on the block diagram because they are shared between the data-processing and digital control sections. These tape units contain a switching feature that permits connection to either the data processing units or the digital control. Thus, tapes which have been connected to digital control and on which track information is recorded during a pass may be switched following the pass to the computers for processing. Similarly, tapes containing pointing instructions prepared by the computers in the data-processing section can be switched onto the digital control to control the antennas during a pass.

Ground Station Control Console:[10] The ground station control console provides facilities for centralized monitoring and control of all antenna pointing operations. The positions of the antennas are displayed, along with the signals necessary to allow the ground station controller to make an instantaneous and continuous appraisal of the tracking performance. Means are provided for remote control of the antenna positions and operating modes, as well as for commanding the satellite itself. The provision of these facilities at a central position permits the operations performed in establishing the communications connection to be closely coordinated.

II. OPERATION

Now that the functions of the components have been briefly described, consider the operation of the system. In preparation for an upcoming communications pass, the data-processing section, using its latest orbital elements, generates the pointing instructions and stores them on mag-

netic tape. The pointing instructions consist of time information, azimuth and elevation position, velocity and acceleration information, and range information. In addition, compensation factors, derived from the horn-reflector antenna calibration curves, are included to correct beam deflections caused by structural deformations which are functions of horn position. Such a set of information is called a data point, and data points are recorded for each four seconds of the pass. For error-correcting purposes, the data points are recorded in triplicate.

In preparation for the upcoming pass, this tape containing pointing instructions is switched to the digital control. Connections within the digital control are made so that these pointing instructions command both the horn antenna and the precision tracker. In addition, the command tracker is slaved to the precision tracker through a synchro connection. Thus, the tape pointing instructions bring all three antennas to the satellite rise point on the horizon. At the predicted rise time, the pointing instructions cause the three antennas to commence moving at the predicted rate along the satellite track.

At this point the satellite is radiating the 136-mc beacon only. In a typical pass, the command tracker acquires and tracks the satellite's 136-mc beacon and then transmits the command at 120 mc to turn on the telemetry and energize the radiation experiment circuits. The received telemetry is examined to determine the "health" of the satellite. The command tracker then transmits a sequence of commands that apply voltage to the traveling-wave tube (TWT) filament, turns on the TWT helix and collector voltages, and energizes the transistor circuits, and, finally, applies voltage to the TWT anode. This enables the 4080-mc beacon, and the precision tracker and autotrack system can then acquire and track its signal. At this point any one of the following modes of operation may be put into effect: (*i*) normal, (*ii*) autotrack, (*iii*) programmed command, (*iv*) precision tracker command, (*v*) initial, or (*vi*) search.

2.1 *Normal Mode*

As soon as autotrack acquires, the communications antenna is locked on the satellite and the communications connection is established. In this mode of operation the function of the pointing instructions (program command) is to place the horn antenna beam on the satellite to within the $\pm 0.15°$ acquisition range of the autotrack. The autotrack system will then center the beam on the satellite. This is considered the normal mode of operation and in the antenna servo, the program command loop has about twice the gain of the autotrack loop.

2.2 *Autotrack Mode*

Other modes are possible and have been used. A full autotrack operation is possible in which, after acquisition, the program command is removed and the autotrack loop has complete control. In this autotrack mode, the autotrack loop can and does have a higher gain than it does in the combined mode. The tracking, therefore, is accurate as long as the velocities required to track are within the maximum system capability of 1.5° per second. As an alternative to using programmed command for acquisition, the antenna may be positioned manually and acquisition effected as the satellite passes through the beam.

2.3 *Programmed Command Mode*

Similarly, a full programmed command can be obtained by removing the autotrack error signals. In this mode the tracking performance is entirely dependent on accurate orbit prediction and on a precise knowledge of antenna calibration. Experience indicates that the accuracy of prediction is sufficient to make this mode feasible. This mode has proven most useful in tracking radio stars or in deliberately offsetting the antenna for experimental purposes, as in measuring antenna patterns using the satellite. It is also useful as a back-up method in the event of an autotrack failure. In this case the full command mode can be supplemented by manual offsets to improve tracking.

2.4 *Precision Tracker Command Mode*

In the normal and autotrack modes described above, it was assumed that the orbit prediction was accurate enough to allow the horn antenna to acquire the satellite with the autotrack, from the pointing instructions, without assistance from the precision tracker or command tracker. That is, it was assumed that the pointing instructions were sufficiently accurate to place the beam center within an angular circle of 0.15° radius of satellite position. In general this is true. However, in unusual cases, as on the first few passes after launch, the orbit may not be accurately known, and the antenna pointing system incorporates a number of features to permit acquisition under these conditions. The command tracker gives a "broad brush" acquisition means with its 20° beam. The slave connection described above can be reversed so that the precision tracker is slaved to the command tracker. Then, the 1° tracking accuracy of the command tracker is sufficient to allow acquisition by the precision tracker with its 2° beam. The horn antenna may be slaved to the precision tracker by use of what is called the "precision tracker com-

mand" mode. In this mode the encoded precision tracker positions are transmitted directly to the antenna servo by the digital control, and these positions are used as the command input to the antenna servo. Thus, the 0.01° tracking accuracy of the precision tracker is more than adequate to enable acquisition by the autotrack. This mode of acquisition was used on the early passes of the Telstar satellite.

2.5 *Initial Mode*

A second form of slave-type operation is possible with this system in what is known as the "initial mode" type of operation. In this mode, the computer is put on line. The precision tracker positions are read directly into the computer, which smooths the positions and does a short-term prediction to produce pointing instructions with which it commands the antenna servo directly. This mode is designed to yield smoother operation than the precision tracker command mode, since the precision tracker jitter is averaged out and the antenna servo is supplied with rate information as well as the positional information.

2.6 *Search Modes*

In addition, to aid in acquisition, the precision tracker has a search mode in which it can search about the acquisition track provided by the digital control. Similarly, the horn antenna servo has a spiral scan capability which causes it to spiral scan about the programmed track. Actuation of a spiral scan causes the horn-reflector antenna to perform a ten-turn spiral out to about 2.5° from the programmed track. Two spiraling rates are available.

In the operational experience to date it has not been necessary to use either the spiral scan or the initial mode operation, and they have been used for experimental purposes only.

At the conclusion of the pass, the command tracker transmits a sequence of commands to turn off the transmission channel. Throughout the pass, the precision tracker and horn positions are measured at twice and once per second, respectively, and recorded on magnetic tape. At the conclusion of the pass these tape units are switched from the digital control to the data-processing section so that the information may be used to up-date the orbital elements. Note that the function of the data-processing section is an off-line operation and that the computers are not directly involved in pointing the antennas.

For calibrating the horn antenna, radiometry equipment and the communication maser are used to track the known positions of radio

stars. In addition, a boresight tower on nearby Black Mountain provides a microwave beacon and satellite electronics for routine calibration of pointing and for autotrack adjustments.

III. CONCLUSIONS

The program objectives were met and successful communication performance achieved, beginning with the first visible pass on July 10, 1962. In no case did antenna pointing performance detectably degrade the communication demonstrations and tests. For the first four months after launch, satisfactory acquisition and tracking were accomplished for all scheduled passes.

All of the modes of operation described were successfully tried. They made possible the high level of system reliability achieved.

Full horn autotrack with predicted pointing information for acquisition was found to be the most accurate mode of operation. It is the most economical and holds promise for application in operational systems. The full tape command system has proven useful for making radio star calibrations of the horn-reflector antenna.

Accurate tracking at azimuth velocities of 1.5°/sec has been achieved. This will permit tracking within a degree or two of the zenith for satellites with 5,000-mile circular orbits.

REFERENCES

1. Dolling, J. C., Blackmore, R. W., Kindermann, W. J., and Woodard, K. B., The Mechanical Design of the Horn-Reflector Antenna and Radome, B.S.T.J., this issue, p. 1137.
2. Hines, J. N., Li, Tingye, and Turrin, R. H., The Electrical Characteristics of the Conical Horn-Reflector Antenna, B.S.T.J., this issue, p. 1187.
3. Shennum, R. H., and Haury, P. T., A General Description of the *Telstar* Spacecraft, B.S.T.J., this issue, p. 801.
4. Chapman, R. C., Jr., Critchlow, G. F., and Mann, H., Command and Telemetry Systems, B.S.T.J., this issue, p. 1027.
5. Anders, J. V., Higgins, E. F., Murray, J. L., and Schaefer, F. J., The Precision Tracker, B.S.T.J., this issue, p. 1309.
6. Cook, J. S., and Lowell, R., The Autotrack System, B.S.T.J., this issue, p. 1283.
7. Lozier, J. C., Norton, J. A., and Iwama, M., The Servo System for Antenna Positioning, B.S.T.J., this issue, p. 1253.
8. Claus, A. J., Blackman, R. B., Halline, E. G., and Ridgway, W. C., Orbit Determination and Prediction, and Computer Programs, B.S.T.J., this issue, p. 1357.
9. Githens, J. A., and Peters, T. R., Digital Equipment for the Antenna Pointing System, B.S.T.J., this issue, p. 1223.
10. Smith, D. H., Carlson, C. P., McCune, R. J., Elicker, R. E., and Sageman, R. E., Planning, Operation and External Communications of the Andover Earth Station, B.S.T.J., this issue, p. 1383.

Digital Equipment for the Antenna Pointing System

By J. A. GITHENS and T. R. PETERS

(Manuscript received February 26, 1963)

This paper describes the digital control and data processing portions of the antenna pointing system used to track the Telstar satellite. The description is functional in nature, giving the form of the inputs, the functions performed, and the outputs produced. A general description of the digital equipment is followed by a discussion of the functions performed by the subsystems, the operational modes provided, the equipment features, and the operating experience.

I. INTRODUCTION

The primary function of the digital equipment in the Telstar antenna pointing system[1] is to generate pointing information for the horn-reflector antenna. The performance of this function requires the prediction of the ephemeris from previously acquired information on the satellite orbit. Together with the precision tracker[2] and the horn antenna,[3] the digital equipment provides means for the acquisition, recording, and storage of the track information in each pass. These data are used to periodically up-date the parameters which describe the satellite's orbit. These updated parameters are the basis for the generation of the pointing instructions which are stored and used to control the horn antenna and precision tracker during future passes. During a pass the pointing instructions are synchronized with real time, interpolated to provide a smooth flow of data and then compared with the actual antenna postion. To insure accuracy in the conversion of the digital pointing instructions to the analog inputs required by the antenna servo,[4] the input comparison is performed digitally. The conversion to analog voltages is performed on the difference, or error, signals for which the accuracy requirements are not extreme. In addition, the digital equipment performs a variety of other functions which will be described in this paper.

In Section II a general description of the seven functional units mak-

ing up the digital equipment will be given. Sections III through X contain detailed descriptions of the operations performed by these functional units. The paper then discusses the configurations of these functional units as they are used to provide the various operational modes of the system (Section XI). The implementation of these functions and the equipment features are described (Section XII) and, in conclusion, operational experience is discussed in Section XIII.

II. GENERAL DESCRIPTION

The digital equipment is made up of seven functional units, or subsystems, as shown in the block diagram of Fig. 1.

2.1 *Data Processors*

The data processors are two general-purpose digital computer systems capable of performing the complex programs[5] necessary to define the satellite orbit from track information, predict future passes, and generate the ephemeris for each pass of interest. Normally, the data processors, having completed their function prior to a pass, take no active part in the pointing during a pass.

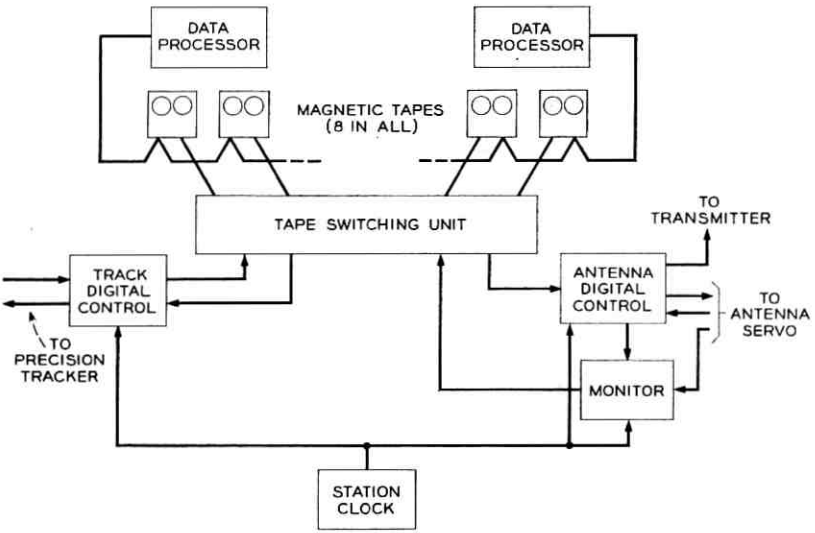

Fig. 1 — Digital equipment block diagram.

2.2 *Magnetic Tape Units*

The magnetic tape units together with the tape switching unit provide for storage and transfer of tracking data and ephemerides within the digital control and data processing system.

2.3 *Antenna Digital Control*

The antenna digital control (ADC) is closely integrated with the antenna servo, which is the actuator of the horn-reflector communications antenna. The ADC, reading pointing instructions from a magnetic tape, synchronizes the pointing operation with time, interprets the pointing instructions in the form and at the rate required by the antenna servo, and closes the servo position loop digitally so that the pointing is achieved with adequate accuracy. In reading the pointing instructions, it performs a variety of tests to check the validity of the data. Careful checking is necessary, because the information is transmitted 1600 feet from the control building and through a slip-ring assembly to the ADC equipment on the antenna structure. Pointing instructions are recorded on tape for each four seconds of the pass, and the ADC provides an interpolator which, using this information, produces position commands at the 128 per second rate required by the antenna servo. Experience has shown that the predominant orbit prediction error is usually in time, and the ADC incorporates means for manually offsetting the predicted pointing instructions in time. This allows the operator to reduce these prediction errors. The ADC also includes features which allow the antenna to be manually offset in position from the predicted track. To meet the system accuracy requirements, the ADC performs the servo position summing operation by comparing the commanded position, as determined from the pointing instructions and the offsets, with the actual antenna position. The actual antenna position is determined from data pick-off units in both axes whose outputs are digitally encoded by the ADC with a precision of 0.003. Only after the position differences, or errors, have thereby been determined, and the need for extreme accuracy reduced, are the ADC outputs converted to analog voltages as inputs to the antenna servo. The output of the ADC may be used in three ways by the antenna pointing system: (a) as the sole source of pointing information; (b) with the autotrack[6] system to provide a combined source of control, in which the autotrack tends to correct for errors in the pointing instructions from the magnetic tapes; and (c) as a means for acquisition of the satellite beacon by the autotrack system, after which autotrack has complete control and the ADC outputs are used only as back-up.

2.4 *Monitor*

The monitor records on tape all the pertinent information on tracking performance from the antenna digital control and the antenna servo. The data processors use the monitor tapes as one source of track data and as a means of performance analysis.

2.5 *Track Digital Control*

The track digital control (TDC) records on tape the precision tracker positions during the pass and provides the data processors another source of track information. These positions are also available in real time as a source of pointing instructions for the horn antenna. This provides a means of slaving the horn antenna to the precision tracker. The TDC also performs a pointing function for the precision tracker similar to that which the antenna digital control performs for the antenna servo and the horn antenna. It provides means for controlling the precision tracker from pointing information stored on magnetic tape. Though the command tracker[7] is not controlled directly by the TDC, it can be slaved to the precision tracker and thereby pointed indirectly by the TDC for acquisition purposes.

2.6 *Tape Switching Unit*

The tape switching unit provides facilities for connecting any of the eight tape units to the antenna digital control, monitor, or track digital control.

2.7 *Clock*

The station clock provides the basic time reference for the system, so that operation may be accurately synchronized with Universal Time.

2.8 *Acquisition Aids*

The digital equipment provides several features to aid in acquisition when the orbit is not precisely known. Since the precision tracker has a relatively broad beam (2°) compared to the beam of the horn-reflector antenna, (0.2°), it can be used as an acquisition aid. This is accomplished by slaving the horn antenna to the precision tracker and performing the initial acquisition of the satellite beacon with the precision tracker. This is called the "PT command" mode. The encoded precision tracker positions produced in the track digital control are used as the command input

in the antenna digital control. The accuracy of the tracker is such that this places the horn antenna well within the acquisition range of the horn autotrack system. A second form of slave operation, initial mode, is possible, in which the data processors are used in real time. In this mode, position information from the track digital control is read directly into the data processors. They smooth the data, perform a short-term prediction and drive the antenna digital control directly with pointing information. This mode yields smoother operation than the PT command mode, since the precision tracker tracking jitter is removed and rate information is supplied.

To aid in acquisition, the antenna servo includes facilities for generating a spiral scan pattern for the horn antenna. The outputs of the spiral scan generator are spiral velocities which are integrated in the antenna digital control and used to offset the programmed position.

In the sections which follow, the functions performed by the seven digital subsystems are described.

III. DATA PROCESSORS

The data processing portion of the antenna pointing system consists of two IBM 1620 Computer systems. Each computer system consists of an IBM 1620 central processing unit, an IBM 1623 core storage unit, an IBM 1622 card reader-punch, and an IBM 1921 tape adapter unit. The 1620 is a desk-sized, solid-state, decimal machine with 20,000 characters of internal magnetic core storage. These units have been equipped with the floating point and automatic divide options. The 1623 core storage unit adds 40,000 characters of core storage, giving each computer a storage capacity of 60,000 characters. The 1921 unit adapts each system for magnetic tape operation and is capable of handling six tape units. The 1622 units provide the systems with card input and output capabilities. The computing systems are pictured in Fig. 2.

The on-site facilities include an IBM 407 printer and an IBM 026 punch. In addition, IBM 7701 magnetic tape transmission terminals working into DATA-PHONE links to the Whippany and Murray Hill Laboratories permit the IBM 7090 computing facilities at these locations to be used as back-up for the on-site facilities.

The primary function of the data processors is to keep an accurate, up-to-date record of the satellite's orbit from which it can predict future passes and generate precise pointing instructions for the site antennas. The orbit is described by a set of basic orbital elements. These elements, or orbit parameters, are periodically refined and updated by the data

Fig. 2 — Two computing systems with four tape units each; three cabinets between tape units contain tape switching equipment.

processors using track information recorded during previous passes by the track digital control and the monitor. The updated orbital elements then are used to predict the upcoming pass and to prepare the mission tape, which contains the pointing instructions. In addition to these functions, the data processors are used for data reduction and performance analysis.

IV. MAGNETIC TAPE UNITS

The Andover installation uses eight IBM 729-II magnetic tape units, shown in Fig. 2. These units are equipped with a switching option which permits each unit to be connected to either the data processors or the digital control. Four units are assigned to each of the data processors. When connected to the digital control, any one of the eight units may be connected by the tape switching unit to the antenna digital control, monitor, or the track digital control input or output. When so connected the tape units operate under the control of these units; the antenna digital control and track digital control input can read tapes and the monitor and track digital control output can write tapes. The low-density mode is always used on these tape units, so that the tape information rate is 15,000 characters per second.

V. MISSION TAPES

The end product of the data processors' efforts is the mission tape for each communications pass. The mission tape, with its pointing instruc-

tions, is the primary input to the antenna digital control and the track digital control. The mission tape consists of data points containing time, pointing angle, and rate information. Normally, a data point is recorded for each four seconds during a pass. To provide for error correction, the information in each data point is recorded redundantly as three separate tape records called blocks. Thus, each data point consists of three redundant blocks of information.

The time information in each block specifies, with a precision of 1/256 second, the time at which the pointing information in that block is to be used. The time information is called tape time. The pointing information consists of azimuth and elevation position, velocity, and acceleration commands. Range information also is given in each block. In addition, compensation factors, somewhat inappropriately called predistortion information, are included in each block. These are correction factors to be added to the pointing information to compensate for mechanical distortions in the horn antenna that cause the electrical axis to differ from the mechanical axis. The use of these factors is discussed further in a later section.

In addition to the time and pointing information, each data block includes a number of unique tape characters called tags. One of these tags identifies the block as the first, second, or third block of a data point. Another tag indicates the checking mode to be used. There are a number of other tags which identify the different types of information and are used to control the disposition of the information by the input circuits.

VI. ANTENNA DIGITAL CONTROL

The antenna digital control equipment is shown in Fig. 3 and is represented by the simplified block diagram of Fig. 4. In this diagram, the antenna digital control (ADC) is shown as three blocks: the input circuits, the ephemeris interpolator, and the output circuits. When a mission tape is connected to the ADC by the tape switching unit, the magnetic tape unit operates under the control of the ADC input circuits. As data blocks are read, the input circuits perform the following functions.

6.1 *Data Checking*

Before a data block is accepted, it is carefully inspected to determine its validity. The following checks are performed.

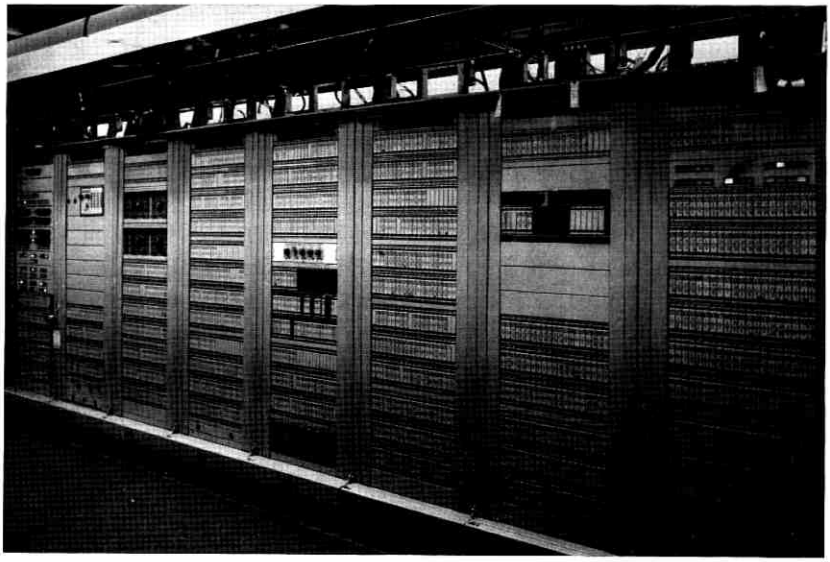

Fig. 3 — Antenna digital control equipment: seven racks at left house ADC equipment; right-hand rack houses monitor equipment.

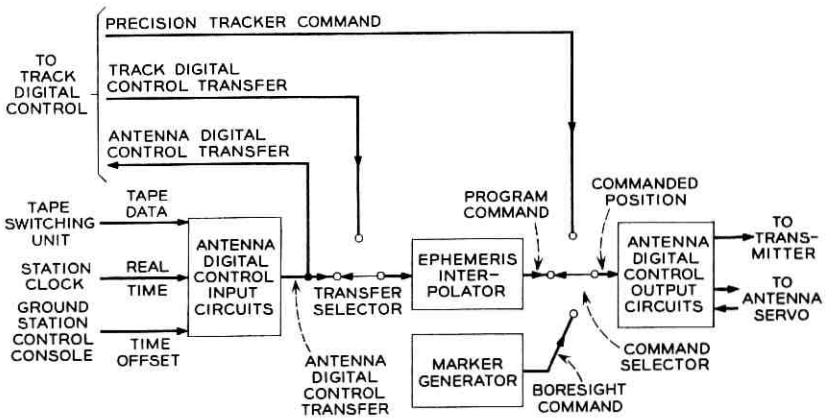

Fig. 4 — Antenna digital control block diagram.

6.1.1 *Parity Checks*

Since the tapes being read in this operation have been written on IBM equipment, the IBM parity checking conventions are used. Each data block is recorded with two forms of parity check bits, the "vertical" check bits and the "longitudinal" check bits. In the vertical parity check

each tape character is recorded with a parity bit which makes the number of ones in that character even. In the longitudinal parity check, an additional tape character is recorded at the end of each tape record (each data point block in this case). A tape record consists of a sequence of seven-bit tape characters recorded on tape in seven channels. Each bit in the longitudinal check character is chosen to make the number of ones in each channel of the record even. The longitudinal check character thus serves as a check on the block as a whole.

In the reading operation, each character and each channel are inspected to determine that the number of ones is indeed even. As a block is read it is written into buffer storage. As the block is read from the buffer memory, the parity of each character is again inspected to check on the storage operation.

6.1.2 *Time Checks*

As data are read in, the time information in each data block (tape time) is checked against Universal Time. Two checks are performed. In the unconditional time check, the tape time is examined to see that it is later than Universal Time. If tape time were earlier than Universal Time it would represent an impossible situation, since time always advances, and data blocks containing such information are rejected. The second check is called the conditional time check, in which the tape time is inspected to see that it is not later than Universal Time by more than 20 seconds.

6.1.3 *Reasonableness Check*

To check the validity of the commanded data in each data block, the change in position commanded is compared with the previously ordered velocity. This check is performed by subtracting the new position command from the previously accepted position command and comparing this difference with the previously accepted velocity command. If the difference exceeds the maximum acceleration to be expected with the orbits under consideration, the data block is rejected as unreasonable.

6.1.4 *Checking Modes*

Each data block contains a tag character specifying the checking mode to be used by the ADC in checking the data. Two checking modes are used: in the first mode all of the above checks are performed, and in the second the results of the reasonableness and conditional time checks are ignored. The second checking mode is used for data points immedi-

ately following track discontinuities, such as are encountered in shifting between stars in star-tracking routines, where the discontinuities would cause good data points to be rejected due to the reasonableness criterion. This checking mode also can be used for data points following initial pointing commands by which the antenna is brought to the initial pointing angles more than 20 seconds before the start of a pass. This makes it unnecessary to program data points for every four seconds to command the same position until the start of the pass. This second checking mode also makes possible the use of lower data rates.

Data blocks are always rejected if there are parity errors or unconditional time errors. When operating in the first checking mode, rejection of two successive data points (six blocks) causes cancellation of the reasonableness and conditional time checks until a data block is accepted. In other words, after rejection of two successive data points, the checking operation reverts automatically to the second checking mode until a data block is accepted.

6.2 *Compensation Factors*

The most critical surface on the horn-reflector communications antenna is the reflector surface. During construction, the panels making up this surface were very carefully aligned to about 0.06 inch. Yet this is a very large surface, about 70 feet by 100 feet, and as the antenna is rotated in elevation the force of gravity acts on the structure at different angles, causing minute distortions in the surface. These distortions cause the electrical axis of the antenna beam to differ from the mechanical axis, and it was necessary to calibrate the antenna so that these deflections could be compensated for in pointing the antenna. The calibration was measured by tracking radio stars of known positions using radiometry techniques.[8] The calibration thus determined is stored in the data processors as an empirical function of antenna elevation angle. As data points are recorded on the mission tape, the data processors add this calibration information. With only a single communications antenna, as in the present installation, these factors could be added directly to the pointing commands. However, when more than one antenna is in operation at a site, the data processors in preparing the mission tapes have no way of knowing which antenna will be used. Anticipating this requirement, the data point format provides for the transmission of the calibration factors as separate items tagged for each antenna. As the data are read by the ADC input circuits, the calibration factors for the particular antenna controlled by that ADC are selected and added to the

pointing commands. Since these factors can be significantly large at high elevations, velocity and acceleration factors, as well as position factors, are necessary if a smooth track is to be obtained.

6.3 *Time Offsets*

The ADC input circuits provide the facility for offsetting Universal Time received from the station clock a total of plus or minus 1 minute, 59 seconds in one-second steps. This facility is provided because experience indicates that the predominant orbit prediction error is usually in time. The time offset is under the control of the ground station control console.

6.4 *Time Synchronization*

The ADC input circuits perform the important function of synchronizing the operation with time. As a good data block is read by the ADC input circuits, it is stored in memory and the tape time is examined 256 times per second and compared with the offset Universal Time. When an exact comparison is obtained, the command data are transferred to the ephemeris interpolator.

6.5 *Ephemeris Interpolator*

While data points are received generally once every four seconds, the antenna servo requires information at a rate of 128 per second. The function of interpolating the command data between data points is performed by the ephemeris interpolator. The ephemeris interpolator performs a quadratic interpolation, using incremental or digital differential analyzer techniques, and produces azimuth and elevation position and velocity commands 128 times per second. The interpolation is performed with a precision of 0.003° in position as long as the velocity does not exceed 0.49°/sec. For higher velocities, the interpolation is performed with 4 times the granularity, or with a precision of about 0.01°. The use of a quadratic interpolation permits several consecutive data points to be rejected without affecting system accuracy.

As shown in the block diagram of Fig. 4, the input to the ephemeris interpolator can come from one of two sources, depending on the position of the transfer selector. With the selector in the position shown, the interpolator receives command data from the ADC input circuits. In the other position the command data are received from the track digital control input circuits. Similarly, command data are transmitted to a transfer

selector in the track digital control. The use of these selectors will be discussed further in the section on operating modes.

The output of the ephemeris interpolator is called the program command. It is one input to the command selector.

6.6 *Manual Position Offsets*

The command selector provides the command input to the ADC output circuits (Fig. 4). One of three inputs can be selected. The switch position shown is considered the normal position with the ephemeris interpolator providing the program command as input. With the selector in the PT command position, precision tracker encoded positions from the track digital control provide the commands. In the boresight command position, the selector provides position commands from memory which serve to bring the horn antenna to the boresight tower coordinates for testing and calibration routines.

The input provided by the command selector is called the "commanded position." The ADC output circuits provide a means for manually offsetting this commanded position in either axis. Two offsets are provided. One offset can be controlled from the ground station control console and either offset may be operated from the antenna control test position. The offsets can be inserted at two fixed rates of 0.01° and 0.75° per second. A control is provided to reset either offset in either axis to zero.

6.7 *Digital Integrator Offsets*

The ADC output circuits provide a digital integrator for each axis for use by the antenna servo in the spiral scan and autotrack. A digital integration is used to provide a drift-free integrator, and is performed by a simple accumulation technique. The integrators can be shared between the spiral scan and autotrack because these functions are never performed simultaneously. The switching between the two inputs to the integrators is performed in the antenna servo equipment. Thus, when the input is the spiral scan velocities, the integrator yields the spiral scan position offsets to the program command. When the input is the autotrack system instantaneous error, the integrator output is the integrated autotrack corrections, or offsets, to the commanded positions. The digital integrator thus develops and remembers the long-term difference between the predicted track and the actual track of the satellite as determined by the autotrack. When the manual offsets are zero, this long-term difference provides a measure of the accuracy of the track prediction.

The integration is performed by encoding the input provided by the antenna servo and simply adding the encoded quantity to the accumulated sum held in memory. The encoding and summing is performed 128 times per second. The smallest value encoded (the least significant bit) corresponds to 0.0000215° ($2^{-24} \times 360°$). However, the smallest value considered in determining the position error is 0.00275° ($2^{-17} \times 360°$) and, therefore, the smallest digital integrator offset must persist for 128 encodings, or 1 second, for it to have an effect on the position difference. The maximum encoded input corresponds to 0.00135°, and this value must persist for only two encodings, or 1/64 second, to be effective. Maximum input errors result in position corrections at a rate of 0.175° per second.

6.8 *Position Encoding*

The ADC output circuits provide the facilities for encoding the horn antenna azimuth and elevation positions. The data pickoff units, which are a part of the antenna servo, produce pulse-position-modulated pulses from a two-speed resolver pickoff on the data gears. The position of the "stop" pulses relative to a reference "start" pulse is proportional to the angular rotation of the data gears and, hence, the position of the antenna. The digitizing of these time intervals is performed by high-speed counting (approx. 2 mc) in two counters, one for fine and one for coarse.[9] The two counts are combined to give a 17-bit binary representation of antenna position. The precision of encoding is 0.00275° ($2^{-17} \times 360°$) and the resultant accuracy is ±0.005°.

6.9 *Servo Summing Node*

One of the most important functions performed by the ADC output circuits is the implementation of the major servo position summing node for the antenna servo. This operation is performed digitally for accuracy reasons 128 times per second for each axis; it is performed with a precision of 1 part in 131,072 (17 bits).

The servo summing node is illustrated diagrammatically in Fig. 5. The first input is the position command from the command selector. Remember that this input may be the program command, PT command, or boresight command. To the position command is added the sum of the two manual position offsets to produce what is called the offset position. To the offset position is added the output of the digital integrator, the digital integrator offset, to produce what is known as the corrected position. Thus, the corrected position is the offset position corrected by the long-term difference determined by the autotrack and

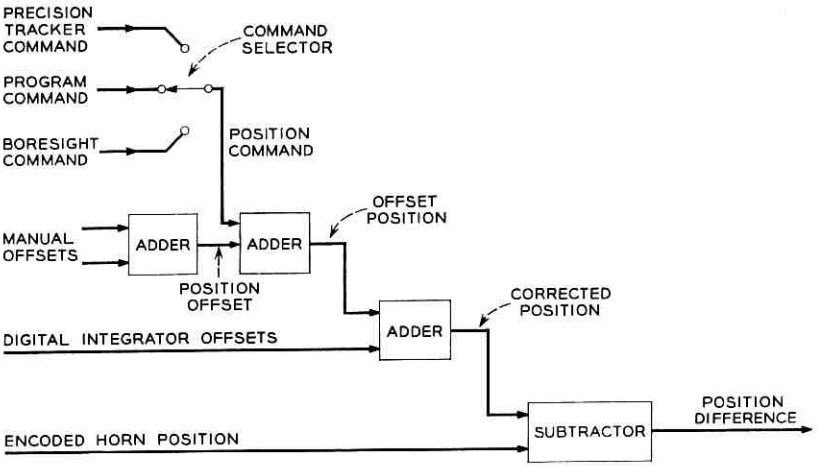

Fig. 5 — Digital servo summing node.

accumulated by the digital integrator. The corrected position, therefore, represents the system's best estimate of the satellite's actual position. Finally, the encoded horn position is subtracted from the corrected position to produce the position difference, the error in the position of the horn. Once the position difference is derived, the need for high precision is removed since the errors are small and they may now be stored and decoded to analog voltages for use by the antenna servo.

6.10 *Velocity Error*

The ADC output circuits determine the velocity error by comparing the actual antenna velocity in each axis with the commanded velocity. The actual velocity is determined by differencing the encoded horn positions 32 times per second, and the velocity error is produced with the same frequency. It is made zero unless the position error is coarse (greater than 0.35°). It is used by the antenna servo to eliminate overshoot as the horn slews to a commanded position.

6.11 *Servo Difference*

Under normal circumstances, if the ephemeris interpolator is working properly, the interpolated commands should agree closely with the new values brought in as each data point is transferred. The difference should not be more than one bit (0.00275°). However, if for some reason several

consecutive data points are rejected, when a new data point is finally accepted a significant difference may exist between the last interpolated point and the new accepted point since the quadratic interpolation may not perfectly describe the actual track. This difference has been termed the servo difference.

If the autotrack is inserted and in phase-lock when this happens, the variation of the interpolated command from the actual track will be compensated by an offset from the digital integrator. It would not be desirable, under these conditions, for the acceptance of a new data point to cause an abrupt jump in the position difference. Therefore, whenever autotrack is inserted and in phase-lock, any difference between the last interpolated point and a new data point is subtracted from the digital integrator contents and the new data point used as the program command. There is no net change in position difference. The result is the same as if the jump were allowed to occur and the autotrack then corrected by making a compensating change in the digital integrator offset. However, the possibility that the step change in position difference would cause the autotrack to drop track is avoided.

6.12 *Error Registers and Digital-to-Analog Conversion*

The ADC outputs to the antenna servo are fine and coarse position differences, and velocity errors in both axes. These signals are delivered as voltages. To produce voltages proportional to these digital quantities, the ADC output circuits provide storage and digital-to-analog conversion circuits. The storage is provided by flip-flop registers. The conversion is performed by constant-current, ladder-type resistance networks which provide a decoding accuracy of 1 per cent. To decode each quantity, two decoding networks, one for positive values and one for negative values, are used to avoid difficulties with zero drift.

6.12.1 *Position Errors*

The fine position error decoders in each axis produce a voltage output of the form shown in Fig. 6(a). As can be seen in this figure, errors less than 0.7° produce a voltage proportional to the error. For errors greater than 0.7°, the output is saturated at 5 volts. As is characteristic of digital-to-analog converters, the voltage produced is actually a staircase where the granularity is 0.02 volt, corresponding to error quanta of 0.00275°.

The coarse decoder output is shown in Fig. 6(b). This output is made zero until the error equals 0.35°. The voltage is then proportional to the

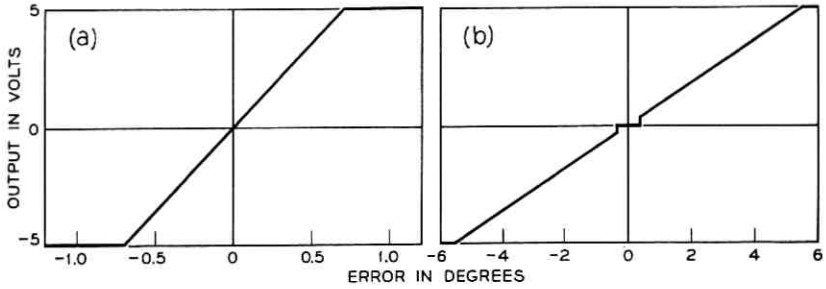

Fig. 6 — (a) Fine position error output; (b) coarse position error output.

error until it saturates at 5 volts for errors greater than 5.6°. In this decoding the 0.02-volt granularity corresponds to steps of 0.02° in error.

6.12.2 *Velocity Errors*

The outputs of the azimuth and elevation velocity error decoders are made zero until the position errors exceed 0.35°. Thereafter, the voltage outputs are proportional to the velocity errors. The maximum voltage of 5 volts corresponds to a velocity error of 2.8° per second. The granularity of decoding is 0.08 volt, corresponding to error quanta of 0.04° per second.

6.12.3 *Range Decoding*

In addition to the outputs to the antenna servo, the ADC output circuits provide a voltage proportional to the range information to the transmitter equipment in the antenna upper room. The range information is proportional to the ratio of the predicted slant range to a fixed range whose value depends on the type of transmission to be used. This output is used to program the transmitted power so that the input signal to the satellite remains essentially constant. The range information is supplied as a part of each data point. The range information is not interpolated but is set into the range register each time a new data point is transferred to the ephemeris interpolator. Thus, in general, the range register is updated once every four seconds.

VII. MONITOR

The function of the monitor is to record on magnetic tape all information on the horn antenna pointing operation that will be useful in orbit

determination and post-run performance analysis. Three types of information are recorded: digital information from the antenna digital control; analog information from the antenna servo, autotrack, and the communication equipment; and telemetry information from the satellite as received and decommutated by the telemetry equipment. The analog information is digitized for recording purposes by an analog-to-digital converter which provides facilities for converting and multiplexing as many as eight channels of analog information.

The digital information recorded includes the time, time offset, and the horn position in both axes. In addition, the acceleration, velocity, and position commands in both axes are included, as are the digital integrator offsets and the two manual offsets. The position differences, the range information, and the checking mode in use by the antenna digital control also are recorded. In other words, everything of interest is recorded.

Eight analog quantities may be recorded. While the quantities to be recorded are easily changed for testing purposes, the autotrack instantaneous errors, the receiver AGC voltage, an indication of autotrack phase-lock status, and the radiometry output (used in star tracking routines) are regularly recorded. The other three channels can be used for test voltages.

The telemetry information from the satellite is received, decommutated, printed, and punched on teletypewriter tape by the telemetry equipment in the control room. This same information is recorded on the monitor tape because the magnetic tape recording provides a more convenient input for computers than does the teletypewriter tape.

In its normal operating mode the monitor samples and records the digital information once per second as a separate tape record. The analog information is sampled seven times per second and the data recorded as two separate tape records. Since there is no synchronization between the monitor operation and the telemetry information, each channel of telemetry data is appropriately tagged and recorded at the end of the next digital or analog record to be recorded.

The monitor has facility for several other modes of operation at different sampling rates that are useful in testing and system checking routines. The monitor equipment is shown in Fig. 3.

VIII. TRACK DIGITAL CONTROL

The track digital control performs functions for the precision tracker similar to those performed by the antenna digital control and monitor

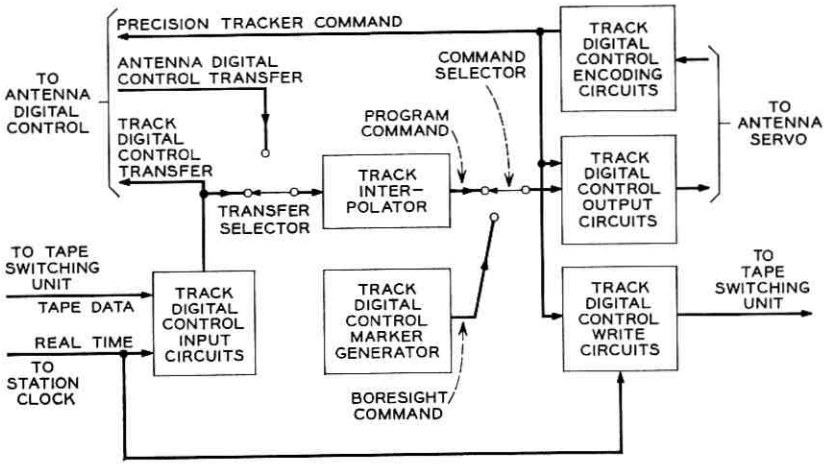

Fig. 7 — Track digital control block diagram.

for the horn antenna. The track digital control is considerably simpler, however, since it serves only as an acquisition aid to the precision tracker.

A block diagram of the track digital control (TDC) is shown in Fig. 7. It is quite similar to the block diagram of the antenna digital control except that the position encoding circuits are shown as a separate entity rather than as part of the output circuits. Also, there is an additional block, the write circuits, which performs a function similar to that of the monitor.

8.1 *Data Checking*

The TDC input circuits are similar to the antenna digital control input circuits except that the TDC input circuits perform no reasonableness check. The parity and time checks performed are identical to those performed by the antenna digital control input circuits. Similarly, there are two checking modes but, in this case, the second checking operation cancels only the conditional time check since the reasonableness check is never performed in any event.

8.2 *Time Synchronization*

The TDC input circuits do not make use of the predistortion information in the data points and do not have any provision for adding time offsets. The time synchronization operation, however, is identical to that

performed by the antenna digital control input circuits. Thus, the output of the TDC input circuits is the command data at the tape time specified in the data point. The data are not predistorted and the time of transfer cannot be offset.

Like the antenna digital control, the TDC input circuits output feeds a transfer selector. The other input to the selector is the output of the antenna digital control input circuits.

8.3 *Track Interpolator*

The track digital control interpolator performs a linear interpolation. That is, unlike the ephemeris interpolator, it makes no use of the acceleration information in providing position commands 128 times per second. The track interpolation is performed with a precision of 0.01°.

The output of the track interpolator feeds one input of the command selector.

8.4 *Position Encoding*

The position encoding performed in the TDC is identical with that performed in the antenna digital control. The result is a 17-bit encoding of the position in each axis 128 times per second. The position encoding circuits are shown as a separate block in the TDC block diagram because, in addition to feeding the summing node in the output circuits, the output feeds the write circuits and also is sent to the antenna digital control as the PT command.

8.5 *Summing Node*

One input to the TDC output circuits is the output of the command selector. The TDC command selector has only two positions and may select either the commanded positions from the track interpolator or the precision tracker boresight coordinates from the marker generator. The TDC command selector is under the control of the precision tracker operator.

The TDC output circuits are quite simple compared to the antenna digital control output circuits. No provision is made for manually offsetting the commanded position, and there is no feedback from the precision tracker equivalent to the horn-reflector autotrack. The summing node consists of a single subtractor which subtracts the precision tracker encoded position from the commanded position.

8.6 *Error Registers and Digital-to-Analog Conversion*

The position error output of the summing node is stored and decoded to provide voltage error signals in each axis to the precision tracker. The voltages are proportional to the errors for errors less than 5.6°. For errors greater than 5.6°, the voltage saturates at 5 volts. The granularity of the decoding is 0.02 volt for error quanta of 0.02°.

8.6.1 *Range Decoding*

The TDC output circuits decode the range information in the data points in exactly the same manner as the antenna digital control output circuits. The decoded range information is used by the precision tracker to estimate the signal-to-noise ratio.

8.7 *Track Write Circuits*

The TDC write circuits perform a track recording function for the precision tracker similar to that performed for the horn antenna by the monitor. The write circuits include a tape write control capable of controlling the recording on a magnetic tape unit connected to it by the tape switching unit. Time, azimuth position, and elevation positions are sampled and recorded as a tape record along with four binary control indications. Samples can be taken at 1, 2, or 4 per second with 2 per second being considered the normal rate. Two of the control bits define the precision tracker status by indicating when it is in autotrack and when the signal-to-noise ratio equals or exceeds 5 db. The third indicator is used in precision tracker optical star tracking routines, and the fourth is used as a control in the initial mode operation described in a later section.

IX. TAPE SWITCHING UNIT

The tape switching unit (pictured in Fig. 2) provides the facility for selectively assigning control of any of the eight magnetic tape units to antenna digital control input circuits, track digital control input circuits, monitor, or track digital control write circuits. To make this possible, the tape switching unit also performs the important function of level shifting to make the tape unit signals compatible with the digital control circuit levels and vice versa. The tape switching unit also makes provision for connecting two tape units simultaneously to the antenna digital control input circuits or the track digital control input circuits; one unit is designated as primary source and the other as the alternate source. The input circuits control both units but only the primary source sup-

plies data. Thus, the alternate source is kept in step with the other tape unit, and a source selector switch under control of the ground station control console permits the alternate tape to be selected to supply data if there is evidence of trouble with the primary source.

The tape switching unit also provides the facility for placing the data processors on line in the digital control system. In this operation, the output of the track digital control write circuits is delivered directly to the data processors as well as written on tape. The outputs of the data processors can be sent directly to either of the input circuits. One data processor serves as the primary source and the other as the alternate, and source selection may be used just as with tape units. These connections are used in the initial mode operation to be discussed in a later section.

X. STATION CLOCK

The station clock provides the basic time reference for the antenna pointing system. Its primary output is a digital representation of the hours, minutes, and seconds of Universal Time (UT_2) to a precision of 1/256 second. This output is supplied to the antenna digital control and track digital input circuits for synchronizing the transfer of command data to the interpolators. The pointing operations are thereby synchronized with Universal Time. The time output is also supplied to the monitor and the track digital control write circuits for recording on the track tapes so that the position samples may be accurately correlated with Universal Time.

The heart of the station clock is a pair of crystal-controlled, temperature-stabilized oscillators operating in duplex at a frequency of 2^{23} cycles per second (8.388608 mc). These oscillators have a specified stability of better than 1 part in 10^9 per day (drift rates of 2 parts in 10^{10} per day have been measured). To permit the adjustment of these oscillators and to phase the output, the station clock produces a one pulse per second output which, after allowing for the transmission delay, is compared with the 1-pps VLF signal transmitted by NBA,[10] Canal Zone. Using photographic oscilloscope techniques, the time output can be set with an accuracy of about 1 millisecond.

The station also supplies a number of time displays in the control room and lower room for operator convenience and an encoded time output for use on strip chart timing channels. Many submultiples of the oscillator frequency are supplied in the form of square waves to the other units in the digital control for local timing operations.

XI. OPERATING MODES

Now that the functions performed by the subsystems have been described, the operation of the digital equipment can be discussed. The tape switching features, the transfer selectors, and the command selector permit the system to be operated in a variety of configurations and modes. One form of the normal mode of operation is illustrated in Fig. 8. Prior to the start of the pass, two tape units containing identical mission tapes prepared by the data processors are assigned to the antenna digital control (ADC): one tape as primary and the other as alternate source. The ADC input circuits read the first block of data and, if it checks, store it in memory and begin to compare the tape time with real time. When a comparison is achieved, the command data are transferred to both the ephemeris and track interpolators by way of the transfer selectors. The interpolators begin producing the program commands at a 128 per second

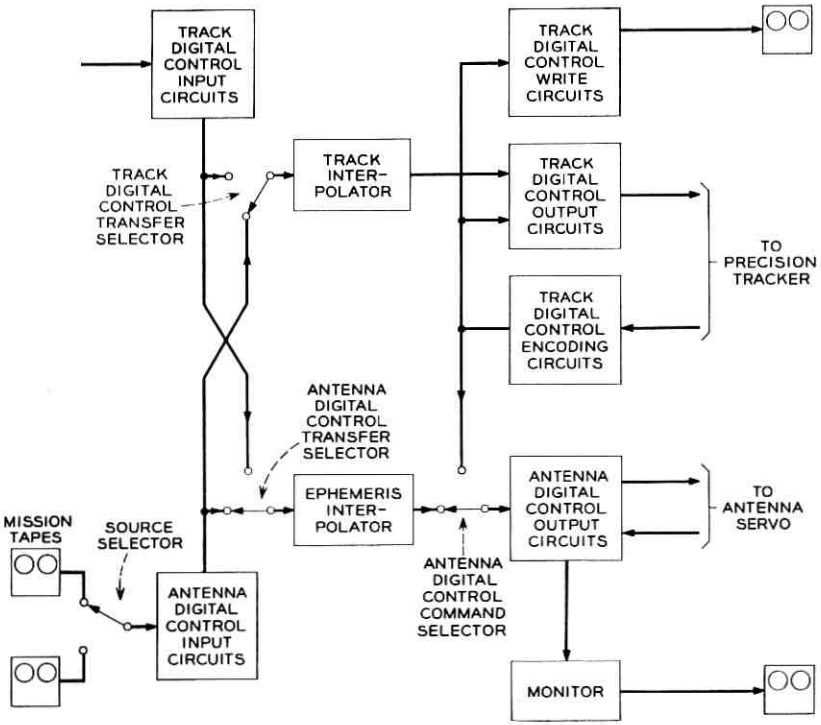

Fig. 8 — Normal mode operation block diagram.

rate and the output circuits cause the horn and precision tracker to come to the proper pointing angle.

At the predicted rise time of the satellite, incoming data points bring in velocity and acceleration commands that cause the horn and precision tracker to begin moving along the satellite's track. If the prediction and pointing accuracy is within $\pm 0.2°$, as is usually the case, the autotrack and precision tracker acquire the microwave beacon within seconds after the satellite traveling-wave tube has been turned on by the command tracker. The communications connection is then established. Operation of the antenna servo may then proceed, with the control shared between the program commands and the autotrack; or the control may be placed entirely in the autotrack loop. Throughout the pass the track information is recorded on tapes by the monitor and the track digital control write circuits.

As the pass proceeds, the antenna digital control continues to process data blocks from the mission tape. After a good block is read, the other blocks of that data point are discarded. If a bad block is encountered, it is rejected and the next block inspected. If a number of data blocks are rejected, the ground station control console operator may decide, from observing the history of data point rejections displayed for that purpose, that the alternate source tape should be selected by actuating the source selector switch. Though no data were read from the alternate tape, the tape received control signals from the antenna digital control and was thereby kept in step with the primary tape and ready to assume the task of supplying data points.

If there appears to be difficulty in the ADC input circuits, the mission tapes may be switched by the tape switching unit to the track digital control input circuits and both transfer selectors switched so that the track digital control input circuits transfer the data to both interpolators. The advantage of using the ADC input circuits is that the precision tracker receives data that have been reasonableness checked and that can be offset in time. It has the disadvantage that the track digital control (TDC) receives data that are predistorted with the horn compensation factors. However, these factors are small compared with the precision tracker beamwidth, and the function of the TDC is to provide only an acquisition track. Conversely, the use of the TDC input circuits to provide data to the ephemeris interpolator has the distinct disadvantages that no reasonableness checks are made, the time offset has no effect, and the data cannot be predistorted. This connection is used only in event of equipment failure.

Alternately, one might connect one mission tape to the ADC and the

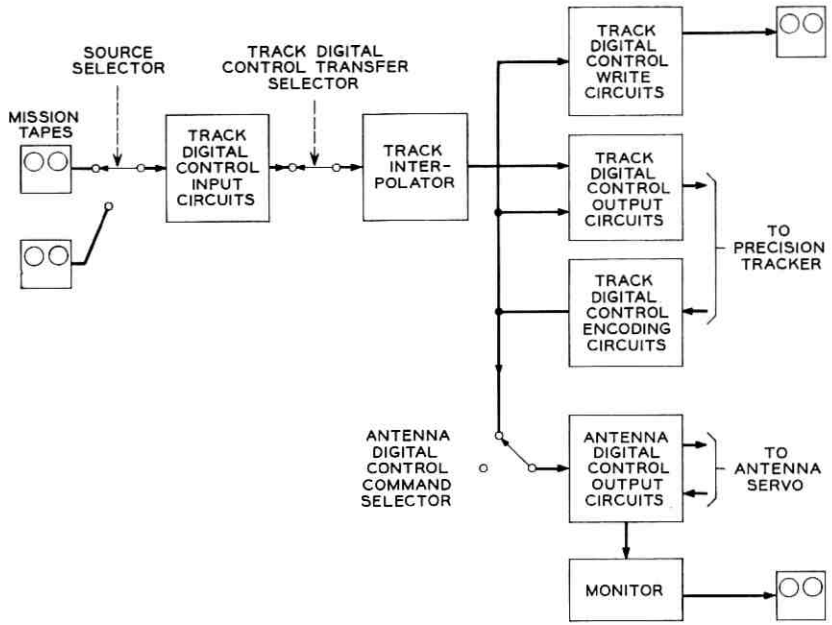

Fig. 9 — PT command mode operation block diagram.

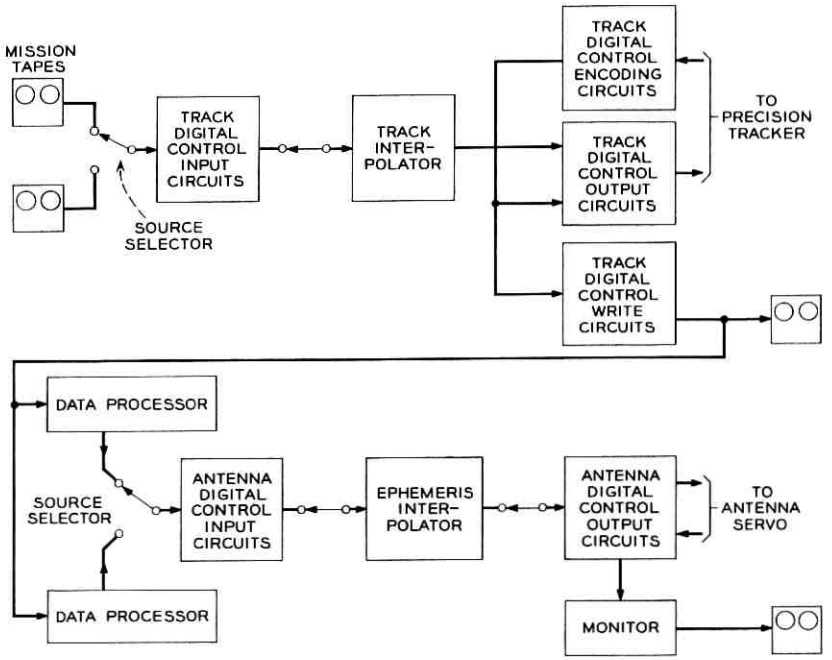

Fig. 10 — Initial mode operation block diagram.

other to the TDC. The ADC and TDC would then operate independently and, in event of failure of either input circuit, the equivalent of source selection could be achieved by use of the transfer selectors. This method of operation suffers from the fact that the source selection in the present equipment arrangement cannot be performed from the ground station control console.

In the above discussion it was assumed that the horn and precision tracker were tracking the same satellite. This is usually the case, especially in the present experimental system with only one satellite in orbit. With a number of satellites in orbit there may be frequent occasions when the antennas may track different satellites. This operation is possible and is the reason, of course, that two input circuits are provided.

When the satellite orbit is not accurately known, the system operation is somewhat different. A mission tape containing the best estimate of the pass is used to drive the TDC and point the precision tracker. The command tracker is slaved to the precision tracker by a synchro connection. The precision tracker and command tracker thus are pointed to the best available estimate of the satellite's position. The command tracker begins searching about this track with its 20° beam. When the command tracker acquires, the slave connection is reversed, bringing the precision tracker to the command tracker pointing angles and, after the command tracker has turned on the satellite, the precision tracker can acquire. The digital equipment provides two methods of slaving the horn antenna to the precision tracker so that the autotrack may acquire. The first of these is called the "PT command" mode and is illustrated in Fig. 9. In this mode the ADC command selector is switched to the PT command position and the output of the TDC encoding circuits, the precision tracker azimuth and elevation positions, is supplied as the commanded position input to the ADC output circuits. Thus, the precision tracker positions are supplied directly without smoothing, and the command positions are subject to the precision tracker tracking jitter. Also, no rate information is available to the antenna servo, and the horn antenna pointing is not compensated for distortion.

The second form of the slave mode, called the "initial mode," is designed to yield smoother performance. In this mode, which is illustrated in Fig. 10, the data processors are placed on line in the pointing operation. The output of the TDC write circuits feeds the two data processors as well as the usual tape unit through connections established in the tape switching unit. This input, consisting of time and position information twice a second, is read and smoothed by the data processors. This smoothed information is then used by the data processors as the basis

for a short-term prediction of the next data point. The data processors operate in duplex with the source selector providing the ground station control console operator with the facility of selecting the output of the secondary processor if his displays indicate that the primary processor is producing doubtful results. The output of the selected data processor drives the ADC input circuits through level-shifting circuits provided by the tape switching unit. The form of the data processor's output is identical to the data points normally recorded on the mission tapes and includes position, velocity, acceleration and range information and compensation factors. The ADC, in fact, operates as if it were reading a mission tape. Thus, the operation in this mode can be as smooth as that in the normal mode.

Throughout a PT command or initial mode pass, the monitor and TDC record the horn antenna and precision tracker tracks on tape in the usual manner. These recordings take on added significance in these slave-type modes because this track information can be used to refine the orbit prediction and permit the system operation to graduate to the normal mode on future passes.

XII. EQUIPMENT ASPECTS

The digital control is implemented using solid-state switching techniques for the most part. The majority of the functions are performed by transistor logic circuits. The digit rate required in performing most of the functions is a comfortably low 32 kc. For these speeds, a form of saturating transistor-resistor NOR logic (TRL) is used. In those few functions requiring significantly higher speeds, such as the encoding counting at 2 mc, a form of resistance-capacitor coupled transistor logic (RCTL) is used.

These circuits are mounted in multicircuit plug-in packages. A total of 29 different types of packages are used in the system to provide the various logic functions, cable drivers, and assorted circuit functions required. A typical logic package is shown in Fig. 11. The packages plug into mounting cages which can mount up to 20 packages. Subassemblies may use as many as four of these cages, or a total of 80 packages. The subassemblies are mounted in open-face racks with conventional back panel wiring. Subsystems may contain up to 5 racks. Interconnections between subassemblies within the same subsystem are made with open-wire runs, while interconnections between subsystems are made by coaxial cable. All wiring terminations, both those used in connecting components within the packages and those used in making the interconnections in the back

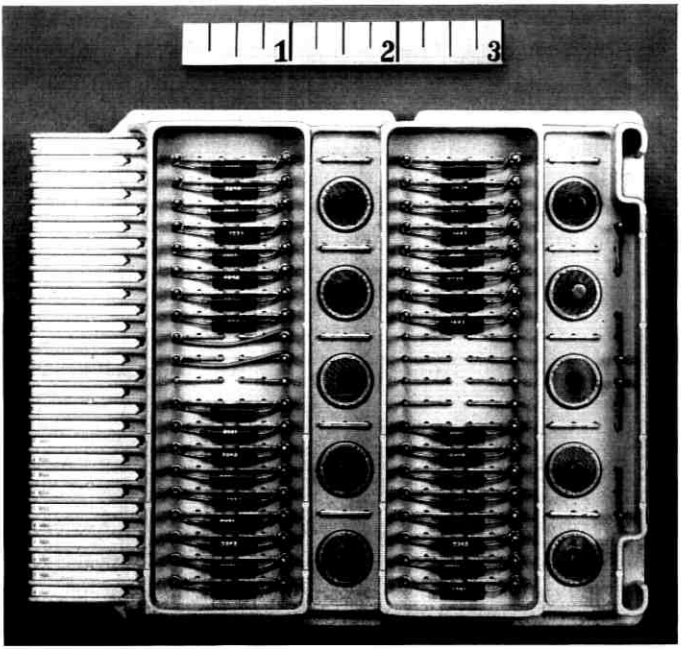

Fig. 11 — Logic package containing eight TRL gates.

panel wiring, are made with solderless-wrap connections for reliability. The racks contain an air ducting arrangement that allows cooling air to be blown over the transistors in each package in a subassembly. Auxiliary equipment, such as power supplies, is mounted in cabinets with swinging door access to both front and back.

With the bulk storage requirements met by magnetic tape units, the requirements for internal storage in the system are modest. Four magnetic core buffer memories are used in the tape read and write control units. These units each have a capacity of 144 characters. In addition, the antenna digital control and track digital control each use a 2048-bit magnetic core memory with sequential access for internal memory requirements.

The information within the digital equipment is handled in serial form, least significant bit first, with negative values represented by two's complement notation. While the use of binary is very convenient for the equipment, the interpretation of binary information by the operators would be difficult. The antenna digital control and track digital control perform the important function of converting the critical position in-

formation from binary to binary-coded-decimal and arranging for its display in decimal form. The antenna digital control provides for the simultaneous display of four two-axis positions selectively chosen from a total of 12 quantities that can be displayed. These quantities are displayed at the antenna control test position with a precision of six digits. Arrangements are made also to display three quantities on the ground station control console with a precision of five digits.

In addition to display functions, the antenna digital control also incorporates a number of features to permit operational control of the horn antenna from the ground station control console. This is not a simple function, because this console is located in the control room of the control building and is 1600 feet from the antenna. The same separation applies to the digital equipment, since the data processors, magnetic tape units, track digital control, station clock, and tape switching unit are in the control room, and the antenna digital control and monitor are in the lower room of the horn antenna. Information between the two areas must be transmitted 1600 feet and pass through the slip-ring assembly which brings all signals and power into and out of the antenna. In general, data signals are transmitted over 75-ohm coaxial cables, and manual control and indication signals are transmitted via a multiplex telegraph system, used to minimize the number of slip rings required. These considerations had considerable influence on the system design.

The dc power for the equipment is supplied by conventional commercially available 60-cycle rectifiers. Since during critical passes the 60-cycle prime power is supplied by diesel powered generators on the site, no precautions against intermittent power failures were taken except in the case of the power supply for the station clock. In this case, even a short power interruption at any time can upset the clock oscillator stability and, by disrupting the countdown process, change the time setting. Therefore, the clock power supply uses duplexed inverters, operating from independent 24-volt battery sources, which supply 60-cycle power to two sets of rectifiers. The outputs of these rectifiers are monitored by an automatic switching circuit which, in event of a failure of one source or one rectifier, switches the load without interruption to the other set of rectifiers. The clock oscillators and the clock countdown chain are thus protected from power failures. For the other parts of the digital control, each voltage also is supplied by two rectifiers which normally share the load but are capable of assuming the entire load. However, in this case, the switching of the loads to the good supply must be performed manually in the event of rectifier failure.

The station clock, track digital control, and tape switching unit oc-

cupy 8 racks, 8 cabinets, and a console in the control room. The antenna digital control and monitor utilize 8 racks and 2 cabinets in the antenna lower room. These racks and cabinets mount a total of 2085 packages and 1000 relays. The packages use over 11,000 transistors.

XIII. OPERATING EXPERIENCE

On the early passes following the July 10, 1962, launch of the satellite, acquisition was achieved using the PT command mode and tracking was performed in the autotrack mode. By the second day, the orbital elements had been refined sufficiently to permit autotrack acquisition from the pointing commands alone. Since that time, the normal mode of acquisition has been from the program command and the use of the precision tracker for acquisition generally has not been necessary. In tracking experiments, all conceivable variations of the acquisition and tracking modes were attempted and, in all cases, operation was satisfactory.[11]

The smoothest tracking performance is achieved with the vernier autotrack in full control. In this mode the antenna follows the autotrack null with peak errors seldom exceeding 0.005°. With the control shared between the program command and the autotrack, these errors can reach 0.008° when the velocities are very low. The program-command-only mode yields tracking performance which meets the design objective. However, the high-quality performance of the autotrack has relegated the program-command-only mode to calibration and testing roles, such as star tracking and measuring the antenna patterns using the satellite.

The operating experience has shown the antenna pointing system to be a very flexible and accurate facility for satellite communications experiments. This operating experience also has demonstrated that the antenna pointing for an operational commercial satellite system can be much simpler and the role of the digital equipment greatly reduced. In such a system, the normal mode of operation would be full autotrack, and the digital equipment would provide acquisition only.

XIV. ACKNOWLEDGMENTS

A system of this size and complexity is not conceived, designed, fabricated and made operational in eighteen months without the full cooperation and extraordinary efforts of many people. The authors are indebted to all these people, and wish to acknowledge in particular the help of M. J. Gilmartin, E. Gomez, and W. T. Hartwell, who contributed heavily to the logical design; G. E. Saltus and W. L. Zweig, who struggled with the circuit problems; and H. Garber and J. O. Whyte, who handled

the equipment design and shepherded the equipment through fabrication, wiring, and installation.

REFERENCES

1. Githens, J. A., Kelly, H. P., Lozier, J. C., and Lundstrom, A. A., Antenna Pointing System: Organization and Performance, B.S.T.J., this issue, p. 1213.
2. Anders, J. V., Higgins, E. F., Murray, J. L., and Schaefer, F. J., The Precision Tracker, B.S.T.J., this issue, p. 1309.
3. Dolling, J. C., Blackmore, R. W., Kindermann, W. J., and Woodard, K. B., The Mechanical Design of the Horn-Reflector Antenna and Radome, B.S.T.J., this issue, p. 1137.
4. Iwama, M., Norton, J. A., and Lozier, J. C., The Servo System for Antenna Positioning, B.S.T.J., this issue, p. 1253.
5. Claus, A. J., Blackman, R. B., Halline, E. G., and Ridgway, W. C., III, Orbit Determination and Prediction, and Computer Programs, B.S.T.J., this issue, p. 1357.
6. Cook, J. S. and Lowell, R., The Autotrack System, B.S.T.J., this issue, p. 1283.
7. Chapman, R. C., Jr., Critchlow, G. F., and Mann, H., Command and Telemetry Systems, B.S.T.J., this issue, p. 1027.
8. Westerman, H. R., Padgitt, R. D., and Penzias, A. A., Antenna Calibration with Radio Stars, to be published.
9. Kronacher, G., Design, Performance, and Application of the Vernier Resolver B.S.T.J., **36**, Nov., 1957, p. 1487.
10. Stone, R. R., Jr., Markowitz, W., and Hall, R. G., Time and Frequency Synchronization of Navy VLF Transmissions, I.R.E. Trans. Instr., **I-9**, No. 2, Sept. 1960, pp. 155–161.
11. Smith, D. H., Carlson, C. P., McCune, R. J., Elicker, R. E., and Sageman, R. E., Planning, Operation and External Communications of the Andover Earth Station, B.S.T.J., this issue, p. 1383.

The Servo System for Antenna Positioning

By J. C. LOZIER, J. A. NORTON and M. IWAMA

(Manuscript received January 22, 1963)

This paper describes the servo system for pointing the horn-reflector antenna. It presents the general considerations which dictated the design and also describes the resulting system in some detail, giving the characteristics of the various parts of the system. Finally, the over-all performance of the servo system is discussed.

I. INTRODUCTION

The needs of broadband satellite communications systems for a high-gain, low-noise antenna led to the choice of the horn type structure. High gain and low noise inherently mean a narrow-beam antenna and, therefore, an antenna with a large reflector which has to be pointed very accurately. In this case, the beamwidth is such that at 4 kmc, the strength of the received signal is 3 db down when the antenna is pointed 0.11° off center. However, in order to conserve signal-to-noise ratio, maximum reduction in received signal strength of 1 db was alloted to errors in pointing.[1] This places an over-all accuracy requirement of 0.06 degree maximum error on the antenna pointing system.

The dynamic requirements on the control system are generated by the orbits of the satellites to be tracked and by the nature of the antenna mount. With an azimuth-elevation mount, it takes a very high azimuth velocity to track a low-altitude satellite passing close to the zenith, and a very low azimuth velocity to track a satellite pass as it comes up over the horizon. The compromise objective set for the system was that it be able to track smoothly and accurately all satellite passes with maximum azimuth velocities up to 0.5 degree per second. For a satellite with a 2500-mile altitude, typical of the first Telstar satellite orbits, the 0.5 degree per second velocity would limit the tracking to passes having maximum angle of elevation less than 81 degrees. However, for satellites with altitudes of 6000 miles and above, the maximum trackable angles of elevation would be 86°.

Two methods of pointing the antenna at the satellite were considered. In one method, the antenna is driven by pointing information derived in advance from the predicted path of the satellite.[2] This is called the "program command" mode. In this mode, pointing information from the digital part of the antenna control system[3] is compared with the encoded outputs of position pick-offs on the mechanical axes to derive the actuating signals for the antenna drive. This mode of operation is subject to errors in prediction and in the calibration of the electrical vs mechanical axes of the antenna, as well as servo errors. A maximum of $\pm 0.2°$ of the total maximum $0.06°$ error was allocated to the servo in this mode; this amounts to $0.014°$ in each axis.

In another method, the antenna is driven by pointing information provided by an autotrack system.[4] In this autotrack mode, the autotrack system generates tracking error signals from a microwave beacon on the satellite, and these signals are used for aligning the electrical axes of the horn antenna with the satellite. The autotrack mode is not subject to the errors of orbital prediction or antenna calibration inherent in the program command mode. However, initial pointing information aid is required, because the acquisition range of the autotrack system is only $\pm 0.02°$ about the satellite position.

Since the system is experimental and the two methods are compatible, provisions are made so that either of these methods alone or a combination of the two can be used to control antenna pointing. When the two modes are combined, tape commands are used to place the antenna beam on the satellite, and the autotrack is used as a vernier to center the beam precisely. This tracking mode, called the "combined mode," unites the accuracy of the autotrack mode with the acquisition capabilities of the program command mode.

II. GENERAL DESIGN CONSIDERATIONS

For a satellite in a circular orbit with a maximum azimuth velocity of $0.5°$/sec, the maximum azimuth acceleration is $0.003°/\text{sec}^2$. These maxima define the input signal spectrum that the azimuth axis must follow in tracking a satellite. The spectrum and accuracy requirements determine the open-loop gain and phase requirements for azimuth. A system using two integrations was selected in order to meet the open loop gain requirement. This resulted in the open-loop gain vs frequency characteristic shown in Fig. 1. Shaping near the gain crossover frequency is necessary for stability reasons. To track with a maximum acceleration of $0.003°/\text{sec}^2$ with an accuracy of $0.014°$ means that the gain crossover

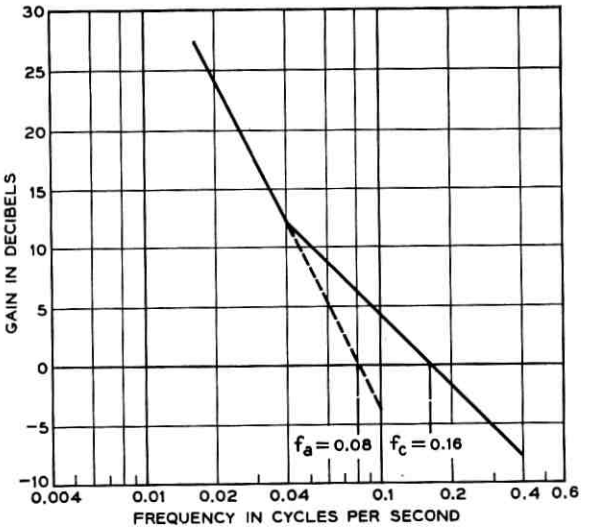

Fig. 1 — Open-loop gain vs frequency characteristic meeting system design objectives.

frequency (f_a) of the projected −12 db per octave asymptote must be at least 0.08 cps, as shown in Fig. 1. In order to realize this frequency with adequate phase margin, the lowest resonant frequency of the combined antenna and drive system must be over 0.64 cps.

Since the antenna and control system were designed and built at one time, it was not clear that the above requirements could be met. Therefore the program command mode was designed to provide and utilize velocity as well as position commands. Velocity command would have been needed if the servo bandwidth could not have been made large enough. However, this proved to be unnecessary, since the primary structural resonance in azimuth was found to be 1.8 cps.[5] Furthermore, the low Q of the antenna structure plus damping at the resonant frequency provided by a pressure feedback loop around the hydraulic motor drives resulted in an effective Q for the system of approximately 3. As a result, an open-loop gain vs frequency characteristic having a gain crossover frequency f_c of 0.4 cps has been achieved, as shown in Fig. 13 of Section 4.1. This gave the ability to track satisfactorily any satellite pass up to the maximum antenna velocity in azimuth of 1.5°/sec.

Other design considerations arise from the need to track accurately at very low speeds. The antenna is supported on rails by four two-

wheeled trucks[5] which develop large discontinuous torques about the azimuth axis at very low turning velocities. Accurate tracking at these speeds requires minimization of the system response to these torques. A peak response of less than 0.014° for a step change of 50,000 ft-lbs applied to the azimuth turntable was the design objective. System responses to these torques are determined by the position feedback loop, antenna inertia, and drive system stiffness. The position feedback loop increases system stiffness at low frequencies; the two integrations in the loop reduce the error due to a constant friction torque to essentially zero. The inertia of the antenna is effective in minimizing the response of the system to the disturbance torques at high frequencies. Hydraulic motor drives were chosen because of their high stiffness, large bandwidth and high acceleration capability. The drive stiffness was further increased by the use of velocity feedback. Compliance of the 15,107:1 gear reduction in azimuth was minimized by the use of a 64-ft diameter bull gear mounted on the antenna foundation and driven by large gear boxes mounted rigidly to the azimuth turntable. The effect of backlash in the gear trains was eliminated by the use in each drive of two opposing hydraulic motors coupled to the bull gear through individual gear trains. As a result of these precautions, a step change in torque of 200,000 ft-lbs rather than 50,000 ft-lbs is required to get a peak error response of 0.014°.

On account of the very large torques that high wind velocities could exert on the horn structure (10^6 ft-lbs at 30 mph), it was clear very early in the project that a radome would be required if the system was to operate reliably under all weather conditions.[5]

Because of the complexity of the servo system and the various nonlinearities present, analog computer simulations have been used extensively for the synthesis and analysis of the proposed configurations. As one of the significant results obtained from the analog computer studies, it was learned that a pressure feedback loop from hydraulic transmissions is not only effective, but essential, for damping out the oscillatory motion of the antenna. The simulations also provided a convenient means for determining the gains of the various minor feedback loops and their effects on the over-all performance. Completely analytical approach would not have been practical because of small as well as large signal nonlinearities present. The final modifications and adjustments of the gains were made on the basis of performance of the actual antenna servo.

III. DRIVE SYSTEM

This section describes the hydraulic transmissions and the associated minor feedback loops, including yoke position, pressure difference, pres-

sure and velocity loops. A functional diagram of the over-all drive system is shown in Fig. 2.

1.3 *Hydraulic Transmission*

Each hydraulic drive system contains a pair of hydraulic transmissions.[5] Each hydraulic transmission is composed of one constant-speed, variable-displacement pump and a pair of constant-displacement motors with output pinions connected to the bull gear through individual gear trains. Pump displacement is controlled by the yoke position.

The two hydraulic transmissions used in the azimuth axis are rated at 25 HP each, and those used in the elevation axis are rated at 10 HP each. The 25-HP unit is capable of developing a maximum output torque of 38 ft-lbs, while a 10-HP unit is capable of delivering 15 ft-lbs. These values correspond to 0.55×10^6 ft-lbs and 0.27×10^6 ft-lbs of torque, respectively, at the bull gear. The actual torques available at the bull gears are reduced by about 10 per cent in overcoming the friction torques. The gear ratios are 15,107:1 for the azimuth axis and 18,344:1 for the elevation axis. Since the inertias (including those of the motors and gear trains) for the two axes are 41×10^6 slug-ft^2 for azimuth and 7.4×10^6 slug-ft^2 for elevation, the maximum accelerations attainable are 1.3 degrees per second squared for the azimuth and 3.0 degrees per second squared for the elevation. The maximum motor velocity is 4200 rpm for both axes. The maximum antenna velocities are 1.5 degrees per second for the azimuth and 1.4 degrees per second for the elevation.

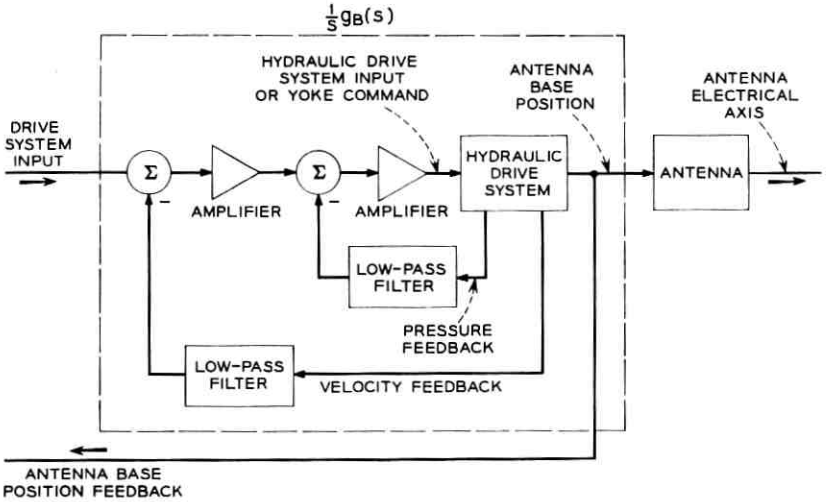

Fig. 2 — Functional diagram of drive system.

A linearized differential equation of the 25-HP unit is:

$$K_L P + K_C(dp/dt) + (d\theta_M/dt) = K_Y Y$$

where

$K_L = 4 \times 10^{-3}$ (radians/second)/(psi)
$K_C = 3.7 \times 10^{-3}$ (radians/second)/(psi/second)
$K_Y = 15$ (radians/second)/(degrees).

Here, Y is the yoke position in degrees, P is the pump pressure in psi, and θ_M is the motor pinion position in radians. The saturation values of Y and P are 30 degrees and 2200 psi respectively. The conversion factor from the pressure to torque is 0.017 ft-lb per psi.

The torque required to overcome friction in the system is a highly nonlinear function of the velocity. This is illustrated in Fig. 3, which shows the average torque required to drive the azimuth axis as a function of velocity.

The friction characteristics in the elevation axis are similar.

This discontinuity of the torque required to overcome friction around zero velocity produces a corresponding nonlinearity in the antenna velocity versus yoke position characteristic shown in Fig. 4. Since the slope of antenna velocity versus yoke position is a measure of the effective gain in the drive system, the small signal gain is highly nonlinear when the average velocity is low.

The hydraulic transmission also has large signal nonlinearities due to such factors as the velocity and amplitude limitations on the motion of the hydraulic yoke, and the hydraulic pressure limitations on the drive motors. However, these large signal nonlinearities are not as difficult to handle as the small signal nonlinearities discussed above.

3.2 *Yoke Position Loop*

The yoke position loop is the innermost of the minor feedback loops in the drive system, as shown on Fig. 5. As the name implies, this loop is designed to control the position of the pump yoke, which in turn controls the motor velocity.

The yoke mechanism is subject to both velocity and position limitations. Position limiting decreases the loop gain but does not degrade the phase characteristics. However, velocity limiting does introduce an additional phase lag which can be as large as 90 degrees. The closed-loop gain versus frequency response characteristics for three different input

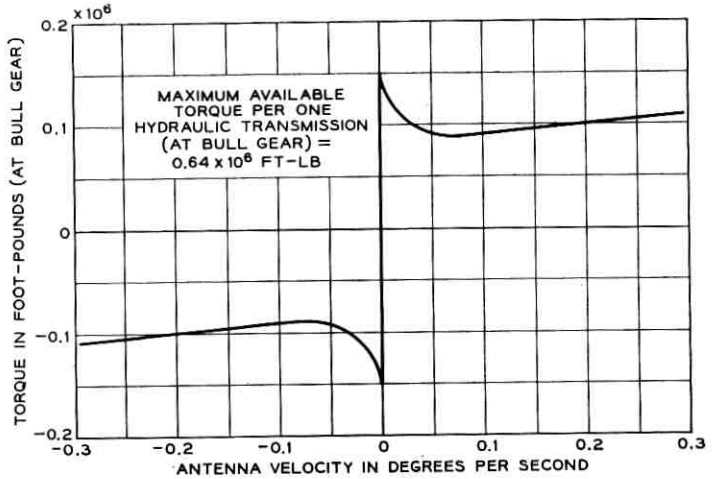

Fig. 3 — Average friction torque at constant velocity — azimuth.

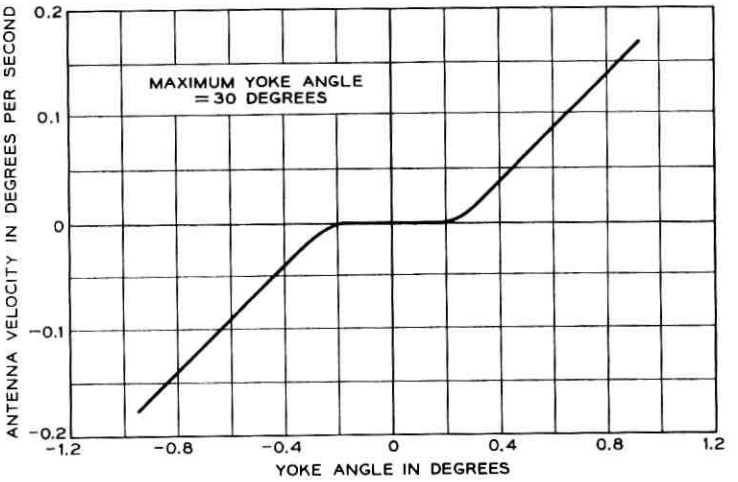

Fig. 4 — Antenna velocity vs yoke position characteristic for one hydraulic transmission — azimuth.

levels are shown on Fig. 6 to illustrate the degradation of the phase characteristic with load.

Allowance was made in designing the rest of the hydraulic drive system for this additional phase shift, so that the system is absolutely stable for large signals.

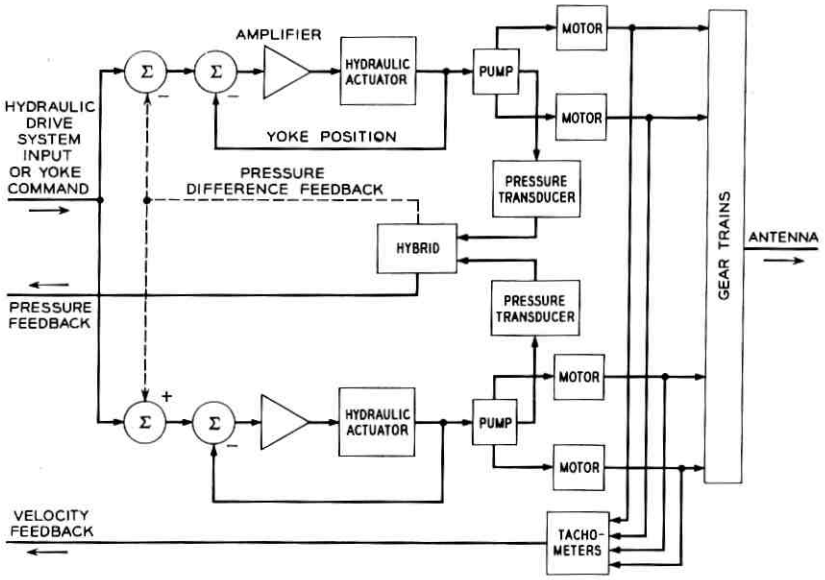

Fig. 5 — Functional diagram of hydraulic drive system.

3.3 *Pressure Difference Loop*

Since two hydraulic transmissions are used per axis to position the antenna, some means for equalizing the load on the two units is necessary. The pressure difference loop performs this function. A voltage proportional to the pressure difference is developed and fed back so as to reduce the yoke position of one unit and increase the other. In this way, the pressures, and consequently the output torques of the two transmissions, are equalized. The pressure difference loop is shown in dashed lines in Fig. 5.

3.4 *Pressure Loop*

It is the function of the pressure feedback loop to minimize the effects of the primary resonance of the combined antenna structure and hydraulic drive system, and this is accomplished by damping the system near its resonant frequency.

The way that the pressure feedback provides damping is easily shown on the electrical analog of the drive system presented in Fig. 7. The equivalent circuit of the antenna is derived from a simplified two-mass-

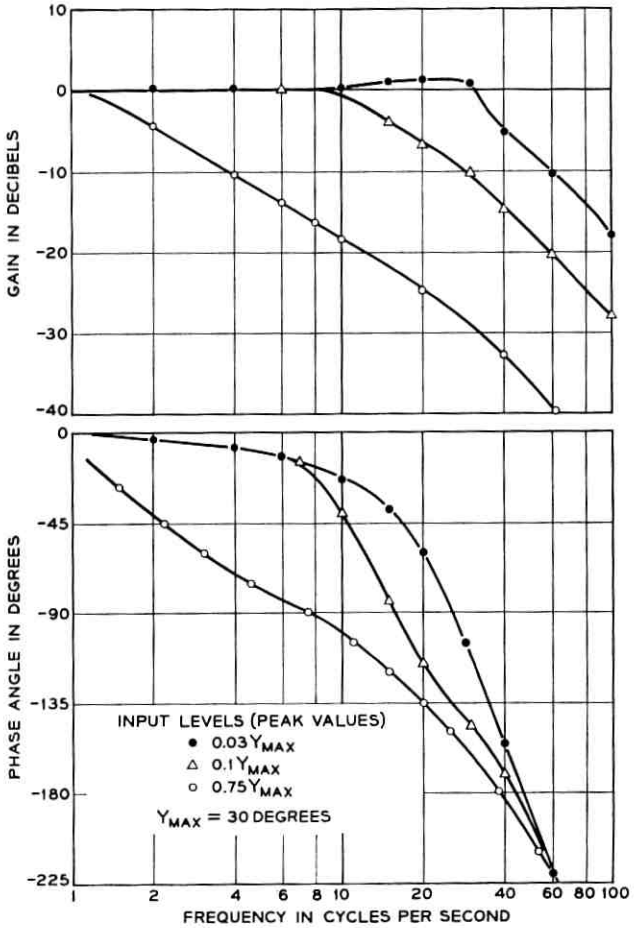

Fig. 6 — Closed-loop frequency response of yoke position — azimuth.

and-spring model, but this simplification does not affect the discussion here. The important point here is that the application of pressure feedback to the system is equivalent to adding a resistance, R_P, in the first mesh of the equivalent circuit. R_P is proportional to the gain of the pressure feedback loop.

It is clear that at resonance the equivalent circuit presents a low impedance to the driving voltage e_Y. R_P will be most effective in reducing the driving current i_M that can flow in the network at resonance

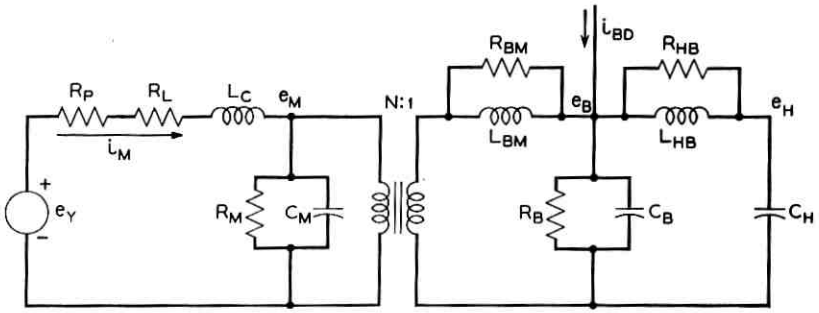

RELATION BETWEEN ORIGINAL AND ANALOGUE QUANTITIES

ELECTRICAL	MECHANICAL
e_Y	YOKE ANGLE
e_M, e_B, AND e_H	VELOCITIES OF MOTOR, ANTENNA BASE, ANTENNA HORN OR ELECTRICAL AXIS
i_M	HYDRAULIC TORQUE
i_{BD}	TORQUE DISTURBANCE AT BASE
R_L AND L_C	HYDRAULIC TRANSMISSION LEAKAGE AND COMPLIANCE
C_M, C_B AND C_H	INERTIAS OF MOTOR, ANTENNA BASE, AND ANTENNA HORN
L_{BM} AND L_{HB}	COMPLIANCES
R_M, R_{BM}, R_B, AND R_{HB}	MECHANICAL FRICTIONS
N	GEAR RATIO
R_P	EFFECT OF PRESSURE FEEDBACK

Fig. 7 — Electrical analog of hydraulic drive system and antenna.

when the impedance of the load is low. In addition to this, R_P helps to damp out transients that might be set up in the system by the torque disturbance, i_{BD} .

Thus the pressure feedback reduces the driving torques that the hydraulic drive system can deliver to the antenna structure at resonance, and it also helps to damp out transients set up in the system by disturbance torques.

The increase in the driving impedance that the antenna sees as a result of pressure feedback reduces the effective stiffness of the driving system. However, the driving system with pressure feedback allows

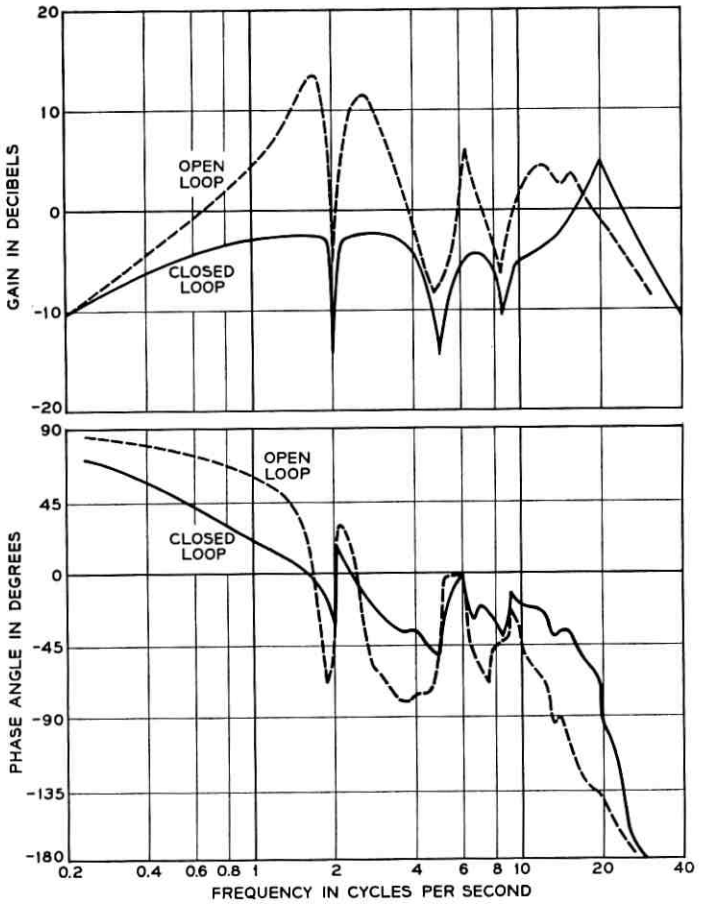

Fig. 8 — Open- and closed-loop frequency response of hydraulic pressure — azimuth.

higher gains in the velocity and position feedback loops at frequencies below resonance so that the effective hydraulic drive system stiffness is maintained at lower frequencies. It is important to keep the hydraulic drive system as stiff as possible to minimize the effects of friction at very low tracking velocities.

The effects of the pressure feedback loop on the characteristics of the combined antenna and hydraulic drive system are shown in Figs. 8 and 9. Here, the input is the driving voltage applied to the hydraulic drive

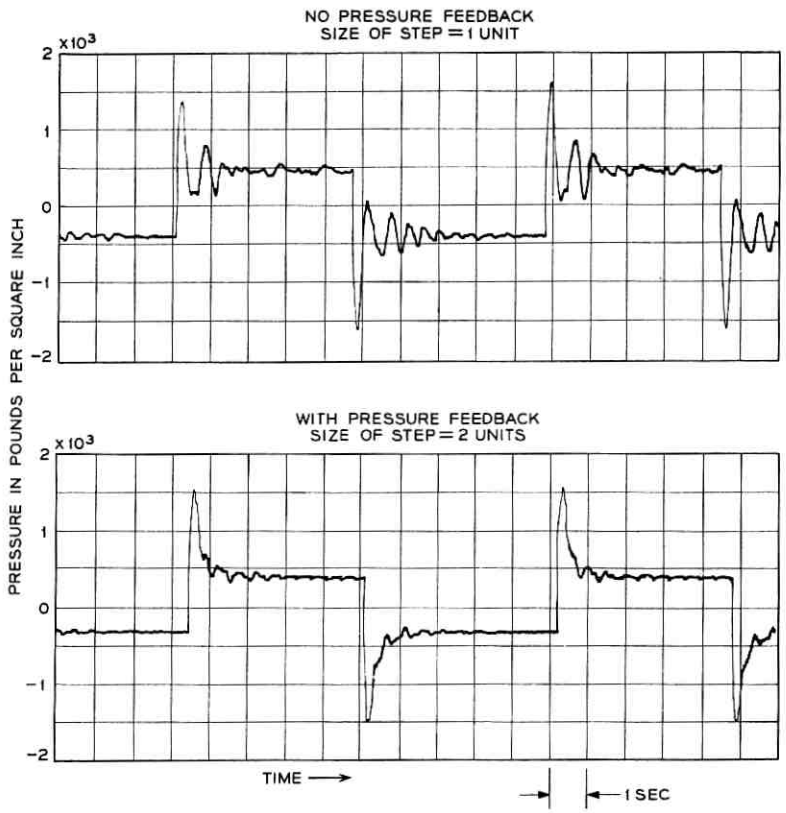

Fig. 9 — Pressure response to a step input with and without pressure feedback — azimuth.

system, and the gain is defined as the ratio of the pressure transducer output to the driving voltage. The gain versus frequency characteristics show that the closing of the pressure loop lowers the driving torque some 16 db at 1.8 cps where the combined antenna and drive system has its primary resonance. The pressure feedback also serves to suppress other resonances in the system all the way out to 15 cps. These curves also show that as far as the gains of the other loops are concerned, the effect of the pressure feedback is negligible at 0.2 cps and below. It should be noted also that the pressure feedback improves the phase versus frequency characteristics at 1 cps. This permits the use of a high-velocity loop gain and ultimately serves to improve the bandwidth and stability of the entire tracking system.

The damping effect is clearly illustrated in the step responses shown in Fig. 9. It is worth noting that two different input step sizes are used, although the peaks in the transient response with and without feedback are comparable in magnitude. It is apparent that the oscillations in pressure are greatly reduced by the use of the pressure feedback. The steady state pressure is equal to the pressure required to overcome the friction torque.

3.5 *Velocity Loop*

The outermost of the minor feedback loops is the velocity feedback loop. Velocity feedback is effectively shunt feedback, and it lowers the impedance of the driving system, in contrast to the effect of pressure feedback discussed above. Its primary function is consequently to increase the stiffness of the driving system at low frequencies. This is important in minimizing the effects of torque disturbances on the system. The other function of the velocity feedback loop is to reduce the system sensitivity to changes in leakage and compliance of the hydraulic transmissions.

The open- and closed-loop frequency characteristics presented on Fig. 10 show how velocity feedback improves the phase and gain characteristics at frequencies below the primary resonance. The improvement in phase margin in the frequency range between 0.2 and 0.8 cps, where the over-all position control loop will have its gain crossover, is as much as 32°. The reduction in gain is 7 db or more at 0.4 cps and below, thereby increasing the effective stiffness of the system to torque disturbances by some 2 to 1 in this critical frequency range. A low-pass network cuts the high-frequency gain of the velocity loop and makes the effect of velocity feedback negligible at higher frequencies.

The hydraulic drive system with all the minor feedback loops closed will be referred to simply as "the drive system" in subsequent sections. A functional diagram of the drive system is shown in Fig. 2. The transfer function $(1/s)g_B(s)$ relates the antenna base position to the drive input system.

IV. ANTENNA POSITION CONTROLS

Two different methods of pointing the antenna at the satellite are incorporated in the system. From the servo standpoint this means that there are two different ways of deriving error signals for closing the position control loop. One way is to use position pick-offs on the me-

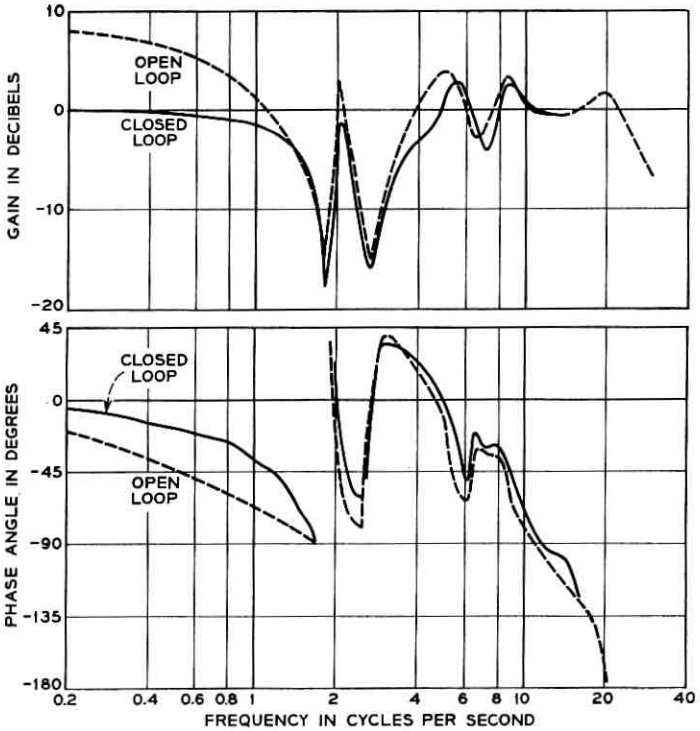

Fig. 10 — Open- and closed-loop frequency response of motor velocity — azimuth.

chanical axes of the antenna structure and compare the measured positions with program-predicted commands. This is the so-called program command mode. The other way is to derive the error signal directly from the 4-kmc beacon signal received from the satellite, using an autotrack technique. This is called the autotrack mode. A third operating mode, the so-called combined mode, operates on a combination of the error signals generated from each of the two methods discussed above.

In order to avoid repetition of the same subject matter, each topic is discussed just once as it is introduced. As a result, the section on the program command mode becomes lengthy, while the other two are relatively short.

A functional diagram of the over-all servo system, showing the interconnections of the various individual units and subsystems, is given in Fig. 11. A brief discussion of the system configuration, responses to test

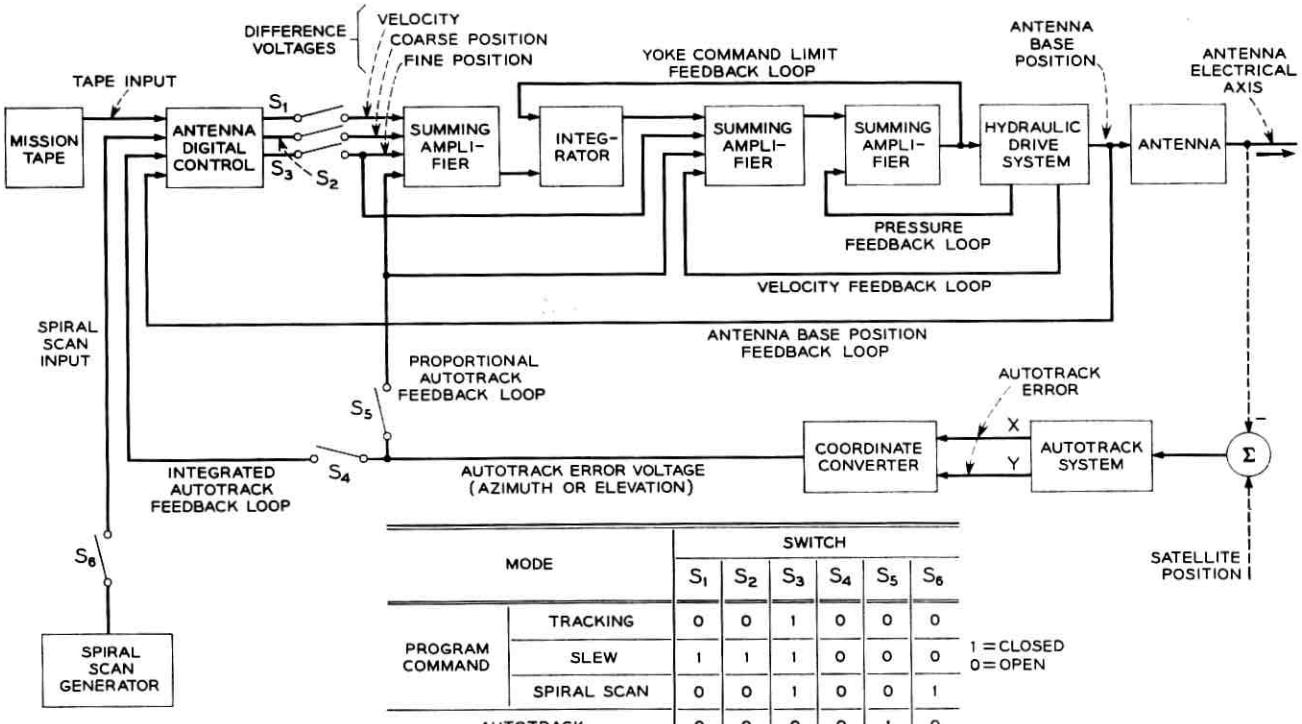

MODE		SWITCH					
		S_1	S_2	S_3	S_4	S_5	S_6
PROGRAM COMMAND	TRACKING	0	0	1	0	0	0
	SLEW	1	1	1	0	0	0
	SPIRAL SCAN	0	0	1	0	0	1
AUTOTRACK		0	0	0	0	1	0
COMBINED		0	0	1	1	1	0

1 = CLOSED
0 = OPEN

Fig. 11 — Over-all functional diagram of the servo system.

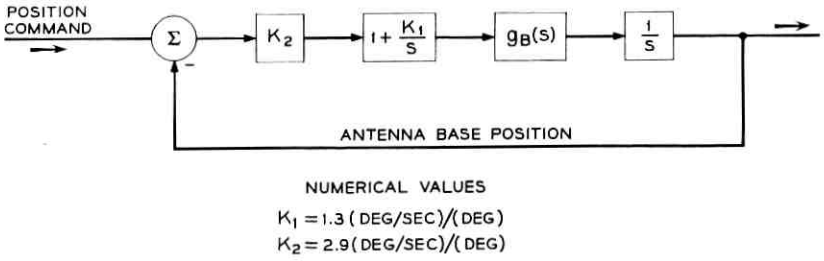

Fig. 12 — Block diagram of servo system in program command mode.

inputs, and the actual tracking performance for each operating mode are presented in the following sections.

4.1 *Program Command Mode*

In the program command mode of operation, the antenna base position is made to follow the program position command provided by the antenna digital control.[3] The block diagram of the system is shown in Fig. 12.

The antenna digital control receives, for a time increment of four seconds, data points from the tape and constructs the position commands. Each data point contains the predicted satellite position, velocity, acceleration, and the time for which it is valid. The position commands are offset to compensate for the differences between the electrical and mechanical axes of the antenna, as measured by star tracking.

The digital unit interpolates between these calibrated data points to provide new pointing information 128 times per second. The antenna digital control also receives the antenna base position information in digital form, compares it with the position command, and decodes the difference to provide a position difference voltage in analog form to the servo drive system.

The position difference voltage is quantized both in amplitude and time. However, the amplitude quantization is so fine (0.00274 degree) and the time quantization is so frequent (128 times per second) that the position difference analog voltage can be treated as a continuous voltage. The position difference voltage saturates at 0.7 degree.

As Fig. 12 shows, the position difference voltage is precompensated by $[1 + (K_1/s)]$, where s is the Laplace transform variable, before it is fed to the drive system. The transfer function $g_B(s)$ relates the antenna base velocity to the drive system input. For all practical purposes, $g_B(s)$ has unity gain in the low frequency region.

The numerical value of K_1 is 1.3°/sec per degree and that of K_2 is 2.9°/sec per degree. The acceleration constant of the system is K_1K_2, or 3.8°/sec² per degree.

The open-loop gain and phase characteristics for the program command mode are shown by Fig. 13. The gain crossover frequency for this

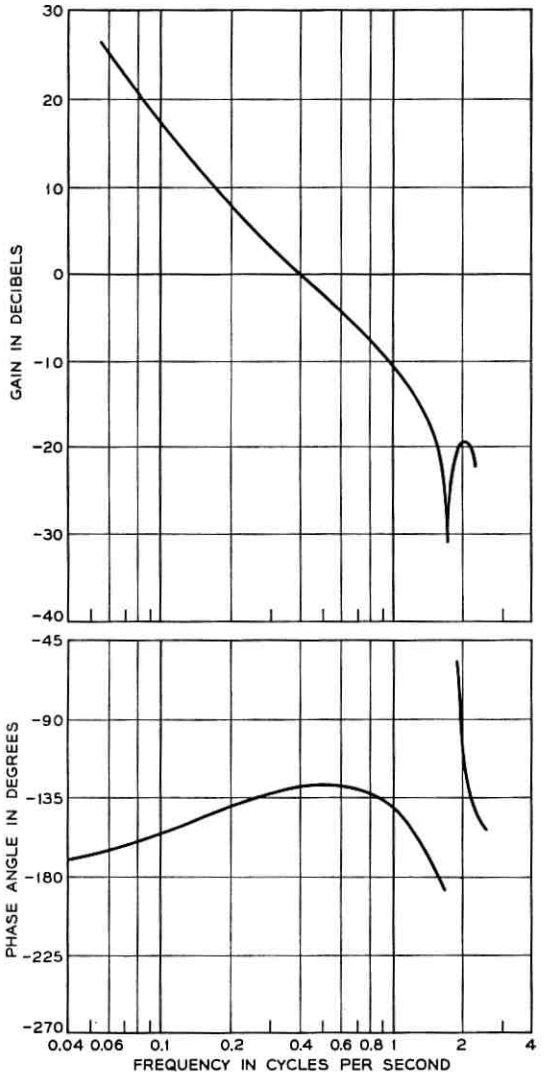

Fig. 13 — Open-loop frequency response of antenna base position — azimuth.

position control loop is 0.4 cps, and the phase margin at gain crossover is 52 degrees. Comparison with the minimum acceptable design objectives illustrated in Fig. 1 shows that the gain versus frequency characteristic realized for the system had the desired shape and that its crossover frequency exceeds the minimum acceptable design objective by 2.5:1. As a direct consequence, it was possible to realize an acceleration constant about 6 times larger than the design objective.

These improvements in loop gain and bandwidth over the minimum acceptable design objectives are due in large part to the increase in fundamental resonant frequency of the antenna structure and drive system from the 0.64 minimum required to the 1.8 cps actually achieved.

The closed-loop frequency response of the system is shown in Fig. 14, and the transient response to a triangular input is presented in Fig. 15. Although these responses are for the azimuth axis only, those for the elevation axis are similar. Input signal magnitudes were chosen to be as

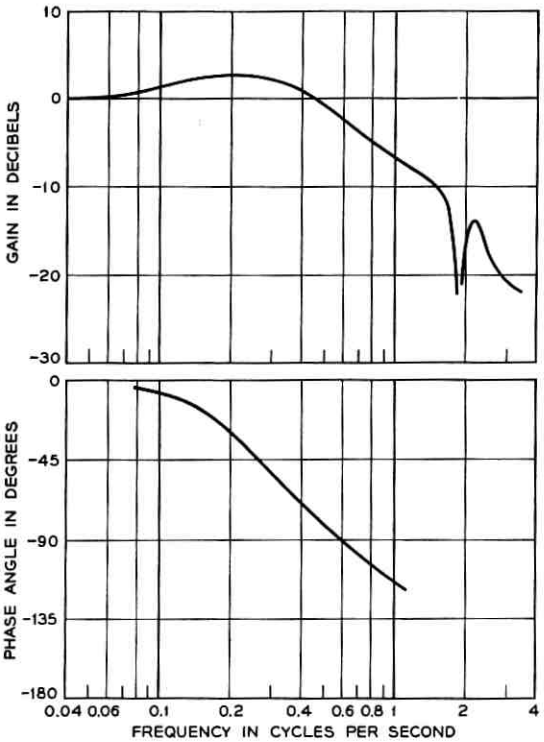

Fig. 14 — Closed-loop frequency response of antenna base position — azimuth.

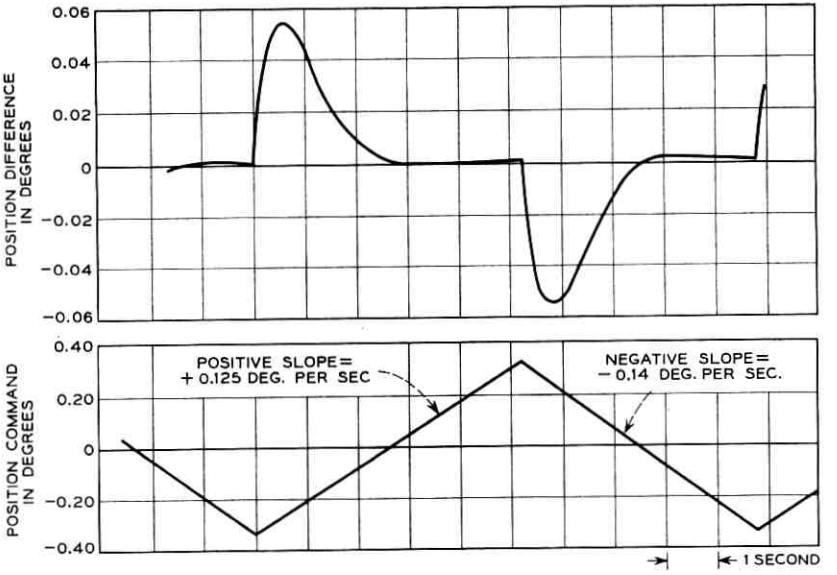

Fig. 15 — Ramp response of program command mode — azimuth.

large as possible but short of saturating the motor torque and velocity. The frequency response curves show that the gain is approximately unity out to 0.4 cps, where the phase lag reaches 60 degrees. Referring to the transient response, the peak position difference in following the position command representing a step velocity change of 0.275 degree per second is 0.055 degree, and the position difference is reduced to zero in less than 3 seconds following each step change in input velocity.

As this is a type 2 servo, the system theoretically follows a constant velocity input with no steady-state error. The acceleration constant for the final system is 3.8°/sec² per degree. This means the position error will not exceed the maximum allowable error of 0.014° for accelerations of less than 0.05°/sec². Since the maximum azimuth acceleration is only 0.026°/sec² for a satellite pass with a maximum velocity of 1.5°/sec, this means that the system can track right up to its maximum slew velocity with an acceleration error of only 0.007°.

The tracking response at low velocities also exceeds the minimum acceptable design objective. The effects of friction have been substantially reduced below the design objectives, since a step in torque of 200,000 ft-lbs applied to the base of the antenna produces a peak position error of less than 0.014°.

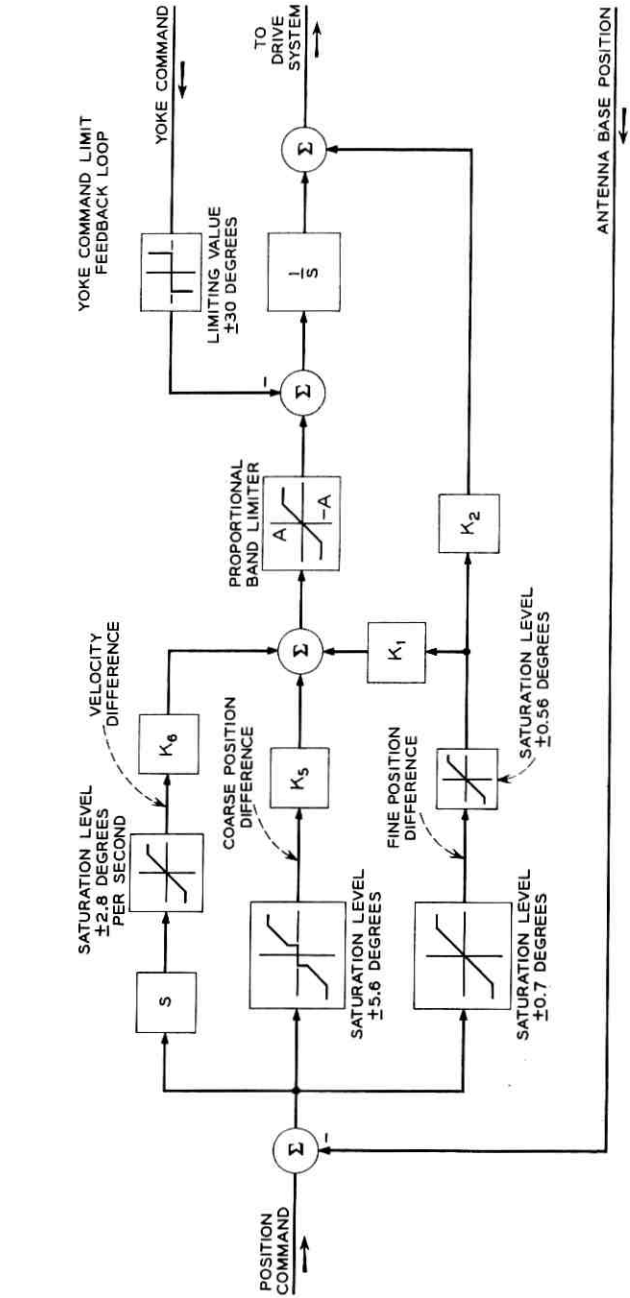

Fig. 16 — Block diagram of the servo system in the program command slew mode.

4.2 *Program Command Slewing*

Program command mode slewing required special attention. Initially, it is necessary to slew the antenna from any arbitrary position to acquire a moving satellite for the start of tracking. The block diagram of the servo system in the program command slew mode shown in Fig. 16 supplements the subsequent discussion.

The tracking servo in the program command mode is actuated by the output of the fine position difference decoder, which produces a proportional difference voltage up to $\pm 0.7°$, but saturates beyond this value. With only this narrow-proportional range the antenna would overshoot several times and suffer rather violent acceleration changes in coming out of slew. These sudden and repeated reversals of drive torque applied to the structure are undesirable because the antenna structure carries both personnel and a large amount of electronic equipment. In order to eliminate this difficulty, the antenna digital control unit also provides a coarse position difference signal with $\pm 5.6°$ proportional range, and a velocity difference signal with 2.8°/sec proportional range. These outputs are both inhibited automatically when the position difference is less than 0.35° in order not to interfere with the normal tracking characteristics of this mode. The coarse and fine position difference signals and the velocity difference signals are combined to form an activating signal for the drive system.

At the start of a slew the antenna is accelerated by the maximum motor torque up to the velocity limit of the drives. This phase takes less than 1.2 seconds in azimuth, and about 0.5 second in elevation. The constant-speed portion of slew takes the major part of the slewing time. A 90-degree slew takes one minute in azimuth, and a little longer in elevation. During the deceleration phase the applied torque is always less than one-third of the maximum in order to limit the amount of energy stored in the compliance of the horn support structure. The position and velocity differences are reduced simultaneously; (see Fig. 17). When the position difference decreases to 0.35° the control system reverts to a tracking mode of operation; at that time the velocity difference is small enough for the tracking servo to terminate the slew without overshoot (see Fig. 18).

4.3 *Spiral Scan*

The spiral scan facility provides a systematic scan that can be used in conjunction with the program command mode of operation to search for a satellite in an increasing spiral about the commanded position. The pitch of the spiral is 0.2 degree per turn, so that successive scans

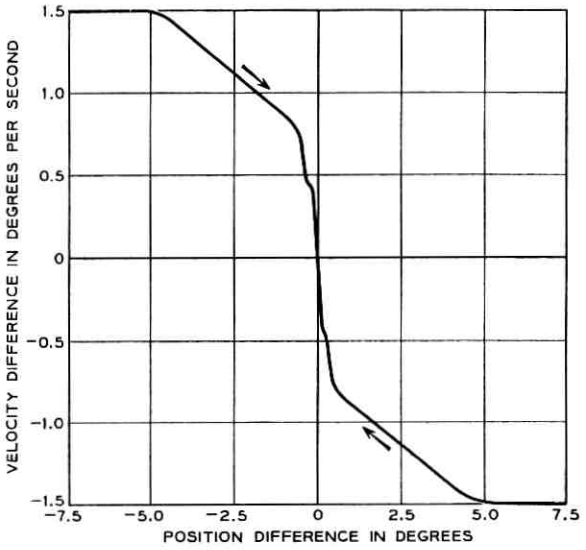

Fig. 17 — Phase plane trajectories of servo system in slew mode — azimuth.

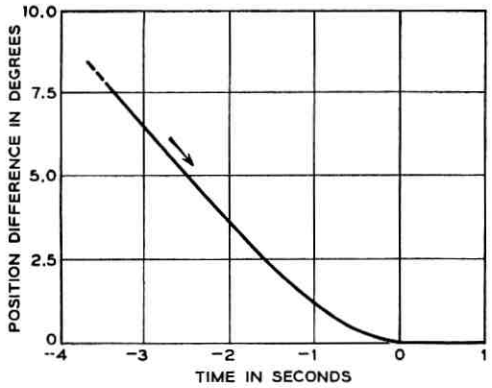

Fig. 18 — Servo system response in slew mode — azimuth.

overlap at the 3-db down point of the antenna beam. In order to scan equal areas in equal times, the angular velocity of the scan is made to decrease as the radius of the scan increases.

Two scanning speeds are provided for fast and slow searching. The fast scan sweeps out a circle with a 1-degree radius in 100 seconds. The slow scan takes 400 seconds to cover the same area. Provisions are made so that the fast scan can be stopped at any time during its scan and a

new slow-speed scan initiated, the center of which is offset from the commanded position by the position of the fast scan at the time the slow scan was initiated.

This spiral scan feature has been used in Telstar tests to search for and acquire the satellite. In a typical test, the high-speed scan was used until indication was received that the antenna had just swept by the satellite. Then the low-speed scan was initiated and the autotrack receiving system was able to achieve phase lock, acquire the satellite, and transfer control to the autotrack mode.

4.4 *Autotrack Mode*

In the autotrack mode, the autotrack error voltages are used to control the antenna position. In other respects the system configuration is essentially the same as that of the program command mode. The block diagram of the system is shown in Fig. 19. The new transfer function $g_E(s)$ relates the antenna electrical axis velocity to the compensated hydraulic drive system input. Here $g_E(s)$ can be considered unity at frequencies below 1 cps.

The value of K_1 is 1.3°/sec per degree and that of K_2 is 1.9°/sec per degree, for both axes. The value of K_2 has been reduced from that used in the program command mode for two reasons. One is to allow for the additional phase lag between the base position and the electrical axis, and the other is to minimize the system transient at the time the autotrack is engaged. The acceleration constant of the system is 2.5°/sec² per degree.

Fig. 20 shows the relation between the autotrack error voltage and corresponding position error for the azimuth axis. The one for elevation is similar. As Fig. 20 shows, for small position errors the slope of the error voltage is very nearly 65 volts per degree. However, the relation is quite nonlinear and the polarity even reverses for angular errors above

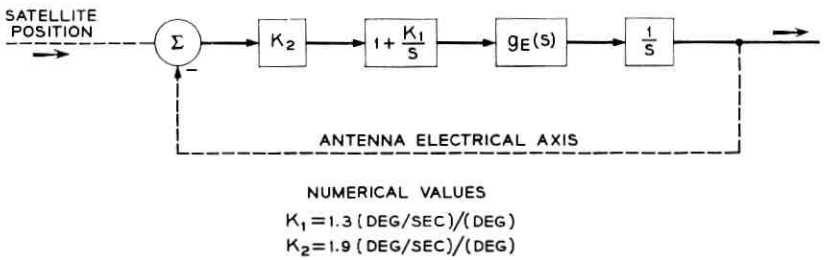

Fig. 19 — Block diagram of servo system in autotrack mode.

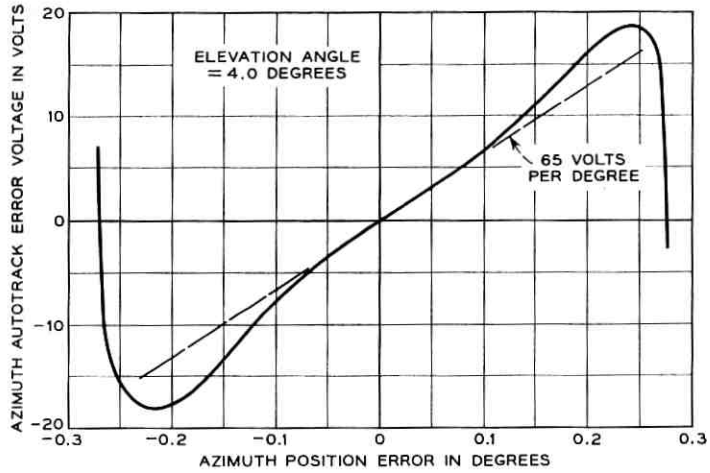

Fig. 20 — Autotrack error voltage versus position error characteristic — azimuth.

0.2 degree. Because of this, the autotrack mode cannot be engaged when the initial pointing error is greater than about 0.15 degree in each axis.

The original autotrack error voltages provided by the autotrack receiving system are in the X and Y coordinate system fixed with respect to the coupler, which does not rotate with the antenna in elevation. These error voltages are converted to elevation and traverse components, and the traverse error voltage is multiplied by the secant of the elevation angle to form the azimuth error voltage.[4]

Fig. 21 shows the transient response characteristics in the autotrack mode when the autotrack loop is closed with an initial error of about 0.1 degree in each axis. These characteristics show that the resulting transients damp out in 4 seconds. Since only the error voltage is available, it is not feasible to measure the open-loop gain and phase characteristics in the autotrack mode.

As in the previous mode, the position error in following a constant velocity is zero, and the position error in following a constant acceleration is proportional to the acceleration. Since the acceleration constant of the system is 2.5 degrees per second squared per degree, this means that the error for the maximum acceleration condition is 0.026 degree per second squared — approximately 0.01 degree.

4.5 *Combined Mode*

The combined mode is a combination of the two previously discussed modes. In this case, the program command and autotrack loops are

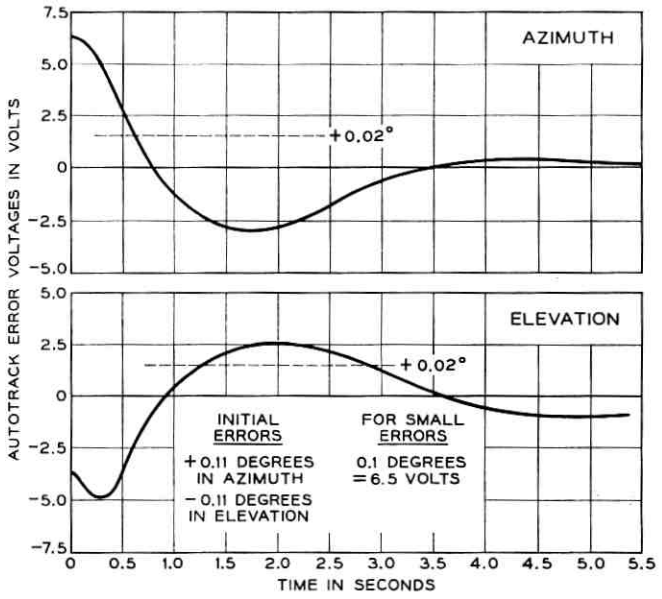

Fig. 21 — Response of servo system in autotrack mode to initial pointing error.

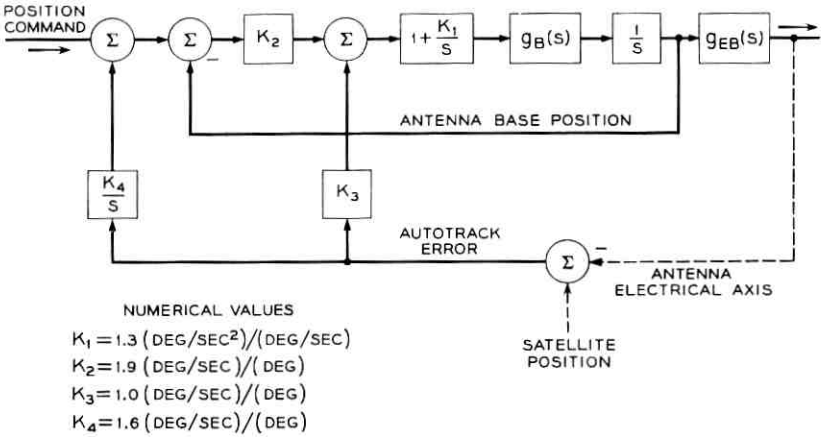

Fig. 22 — Block diagram of servo system in combined mode.

individually closed using the same configurations as before, but with different gains. In addition the autotrack errors are encoded, digitally integrated, and then added to the position command. The configuration is shown on Fig. 22. It is the function of the integrated autotrack error signal to buck out the low-frequency errors in the position command.

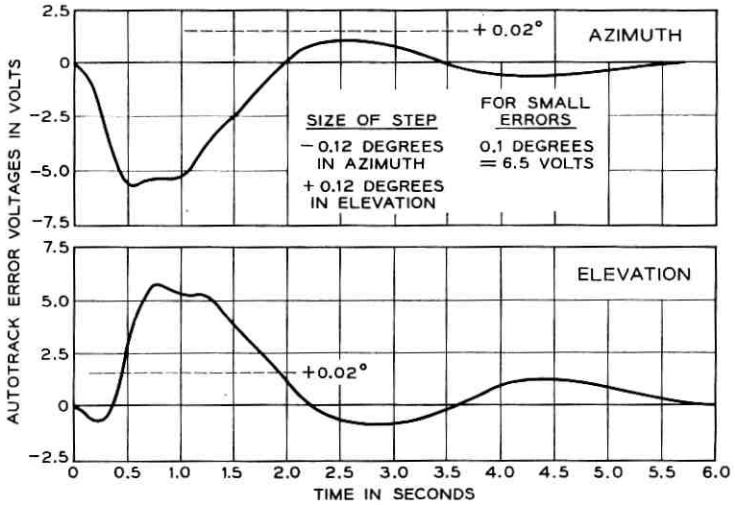

Fig. 23 — Response of servo system in combined mode to step change in program position command.

The relative weights of the program command, proportional autotrack and integrated autotrack loops can be adjusted by changing K_2, K_3, and K_4, respectively. The numerical values of the various gain constants used in the system are 1.3°/sec per degree for K_1, 1.9°/sec per degree for K_2, 1.0°/sec per degree for K_3 and 1.6°/sec per degree for K_4.

In theory, the performance in this combined mode should be comparable to that of the full autotrack mode as long as the errors in the predicted position commands vary slowly as a function of time. However, the higher autotrack loop gain realized in the autotrack mode makes its performance superior to that of the combined mode.

Various step response characteristics for the combined mode are shown in Figs. 23 and 24. Fig. 23 shows the transient response characteristics as measured by the autotrack voltages in response to a step program position command change of 0.12 degree in both axes. The results show that the program position errors are integrated out in less than 6 seconds.

Fig. 24 shows the transients in autotrack error voltages that result from closing the autotrack loop after errors in the program position command had offset the pointing by 0.12 degree both axes. In this case, the pointing errors are reduced to less than 0.01 degree in 5 seconds.

Fig. 25 shows a typical tracking record of the servo system tracking at moderate velocities in the combined mode. Here, the autotrack error

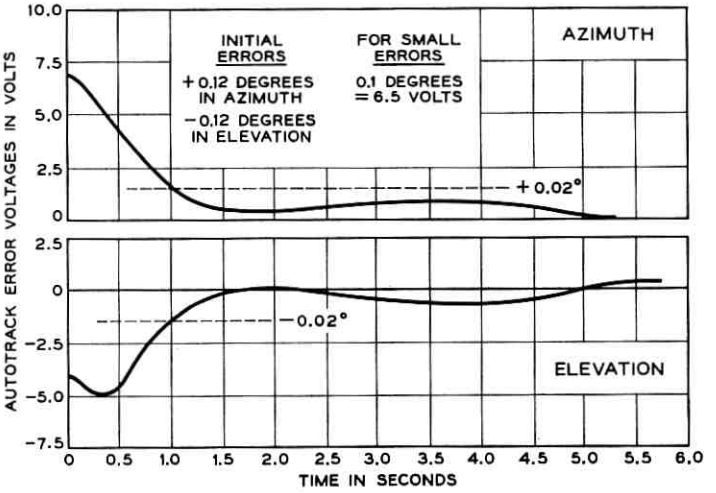

Fig. 24 — Response of servo system in combined mode to initial error in program position command.

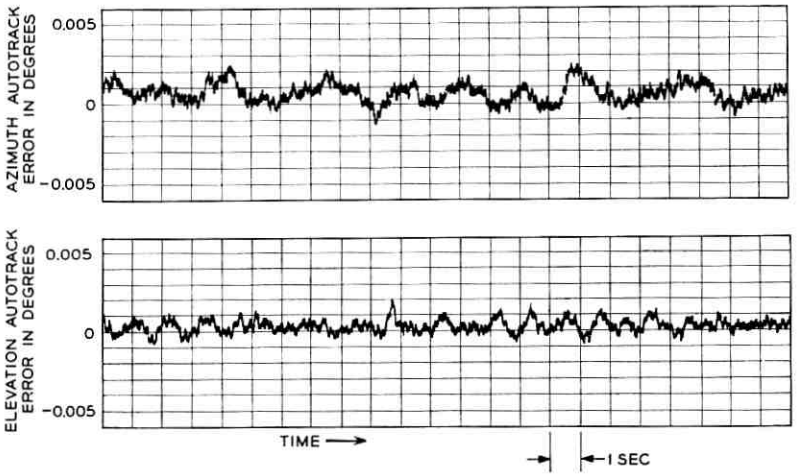

Fig. 25 — Typical tracking record of servo system in combined mode.

voltages are recorded as a function of time. The record shows that the autotrack tracking error voltages in the two axes are less than 0.003 degree. Slowly changing errors in the predicted satellite orbit, distortion of the antenna structure due to gravity, or the effects of quantization

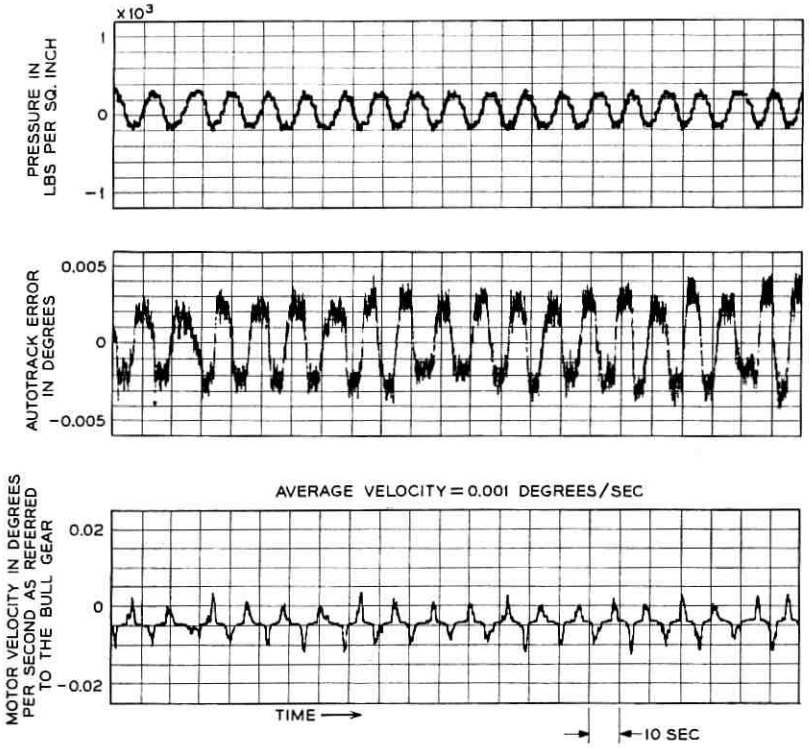

Fig. 26 — Small amplitude hunting in combined mode — azimuth.

in the encoded antenna position do not affect the tracking accuracy in this mode.

The combined mode of operation is subject to a low-amplitude, low-frequency hunting when the tracking velocity in either axis is very low (less than 0.002 degree per second). Hunting about the azimuth axis is shown in Fig. 26. The frequency of the hunting is about 0.17 cps and the corresponding autotrack error can be as large as 0.008 degree.

The hunting phenomenon described above is caused by two factors. One is the extra stage of integration inserted in the autotrack loop to make the autotrack error dominant over the program position command at very low frequencies. The extra integrator makes the combined mode a type 3 servo and, therefore, one which is conditionally stable. The other factor is the reduction in gain of the drive system for small tracking velocities, as discussed previously. This condition is not considered detrimental, because the maximum tracking error is less than 0.008

degree and because the condition disappears when the tracking velocity exceeds 0.002 degree per second.

V. CONCLUSIONS

The design objective called for tracking with a pointing error less than 0.02 degree for all satellite passes where the azimuth velocity is less than 0.5 degree per second. This objective corresponds to tracking a 2500-mile-high satellite up to an elevation angle of 81°.

The relatively high frequency of the first structural resonance and the use of pressure feedback to provide damping of this resonance made it possible to obtain a 2.5:1 increase in bandwidth and a 16-db increase in gain of the position loop over and above the system objectives. The resulting improvement in dynamic performance permits tracking of a 2500-mile satellite up to an elevation angle of 87° rather than the 81° objective.

The servo system has consistently positioned the antenna on the satellite track with an accuracy sufficient to give less than 1-db degradation in antenna gain.

VI. ACKNOWLEDGMENTS

Although it is not possible to give credit to everyone who contributed to the success of this project, the authors wish to acknowledge the work of G. A. Colom, L. Gingerich, W. Lawson, R. Klahn, M. Peak, G. L. Ruzicka, and F. C. Young.

REFERENCES

1. Githens, J. A., Kelly, H. P., Lozier, J. C., and Lundstrom, A. A., Antenna Pointing System: Organization and Performance, B.S.T.J., this issue, p. 1213.
2. Claus, A. J., Blackman, R. B., Halline, E. G., and Ridgway, W. C., III, Orbit Determination and Prediction, and Computer Programs, B.S.T.J., this issue, p. 1357.
3. Githens, J. A., and Peters, T. R., Digital Equipment for the Antenna Pointing System, B.S.T.J., this issue, p. 1223.
4. Cook, J. S., and Lowell, R., The Autotrack System, B.S.T.J., this issue, p. 1283.
5. Dolling, J. C., Blackmore, R. W., Kindermann, W. J., and Woodard, K. B., The Mechanical Design of the Horn-Reflector Antenna and Radome, B.S.T.J., this issue, p. 1137.

The Autotrack System

By J. S. COOK and R. LOWELL

(Manuscript received February 25, 1963)

The autotrack system accurately senses the direction of arrival, at the horn-reflector antenna, of the microwave beacon signal from the communications satellite. When this direction does not coincide with the horn-reflector pointing direction, error correcting voltages are automatically generated to enable the antenna direction system to steer the antenna toward the satellite.

This paper presents a simple analysis of error voltage generation, a description of the system, and a brief discussion of system performance. Measurements at Andover, Maine, have shown that an angular pointing error of less than 0.005 degree is maintained by the antenna when using the autotrack system to follow the Telstar communications satellite.

I. GENERAL

The autotrack system (originally designated and often referred to as the "vernier autotrack," or "VAT") is a pointing-error sensing and processing system for the horn-reflector antenna. It receives the circularly polarized 4080-mc CW beacon signal entering the antenna from the satellite, and, by examining the nature of the propagation of this signal through the antenna feed line, determines the discrepancy between the direction the antenna is pointing and the actual direction of the satellite. This discrepancy is reduced to a set of pointing-error signals to be used by the antenna pointing system to provide either a vernier correction of the programmed antenna pointing instructions, or fully automatic tracking, as shown in the block diagram of Fig. 1.

II. PRINCIPLE OF OPERATION

2.1 *Received Tracking Signals*

As a help to understanding the principle of operation of the autotrack, it is useful to think of the conical horn-reflector antenna as consisting of a conical transition from conventional cylindrical waveguide to a

very large open-end waveguide of circular cross section, having a reflective 90° bend.

Thus, if a particular mode is excited in the feed to the horn reflector, the energy propagated appears in essentially the same modal configuration in the large open cylinder that forms the antenna aperture. Only slight distortion is brought about by the asymmetry of the parabolic reflector which comprises the 90° bend. In all essential characteristics, then, the pattern of radiation from the antenna generated by exciting a particular waveguide mode in the throat of the horn will be like that radiated from a large open-ended circular waveguide excited in the same mode. It is to be recognized that the antenna is a reciprocal device, and that its radiation characteristics hold for transmission and reception alike. Hence, nothing is lost in treating the antenna from a radiating point of view, even though the scheme here described operates on a received CW signal.

In this discussion our interest will be confined to the two lowest-order modes in cylindrical guide: namely the TE_{11}, or dominant, mode and the TM_{01} mode. In fact, the waveguide feed to the horn-reflector antenna at Andover is of such diameter as to cut off all higher modes of propagation at the beacon frequency. The field configurations of the two admitted modes are shown in Fig. 2. Solid lines depict electric fields; dotted lines, magnetic.

Chu[1] has worked out general expressions for the far-field radiation patterns for open-ended circular guides. Though the expressions neglect the discontinuity at the waveguide opening, and are therefore of questionable validity near cutoff frequency, their validity from that point of view is unquestionable for a very large waveguide diameter $\approx 280\ \lambda$.

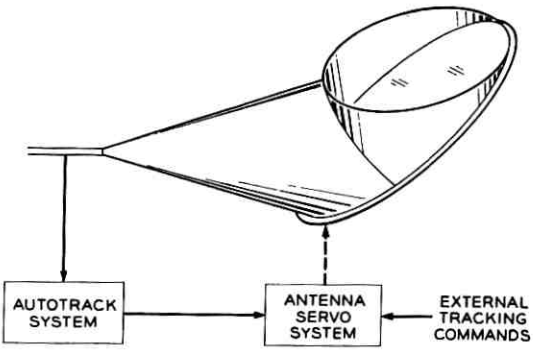

Fig. 1 — Autotrack connection with the antenna servo system.

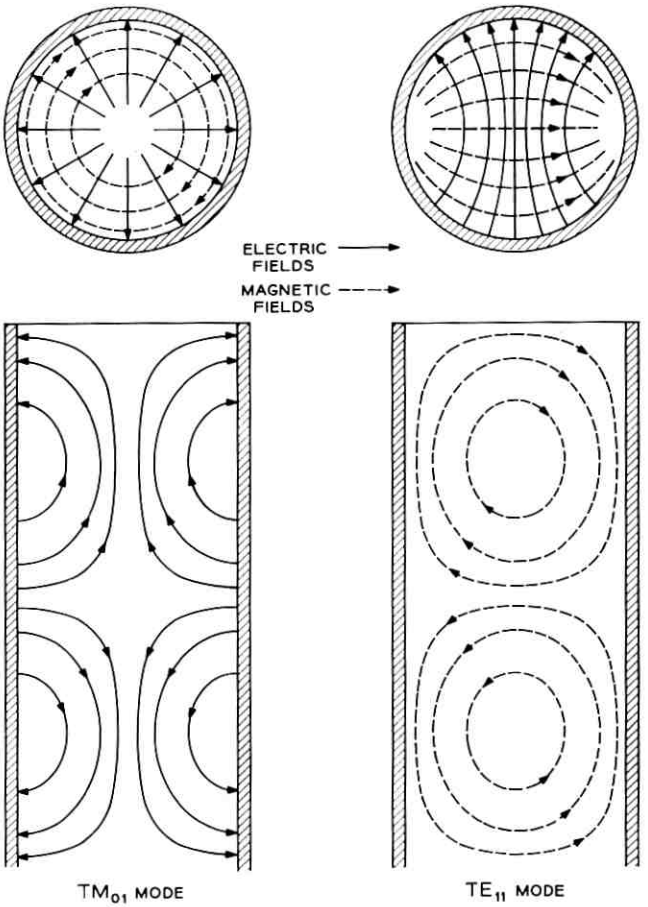

Fig. 2 — Circular waveguide mode field configurations.

The relative amplitude of the far electric fields excited by the radiation of the TM_{01} mode from a large open waveguide is:

$$E_\theta = \frac{E_0}{kR} \frac{J_0(ka\theta)}{\theta\left[\left(\frac{2.405}{ka\theta}\right)^2 - 1\right]} \qquad (1)$$

$$E_\phi = 0$$

$$E_R = 0.$$

For the vertically polarized TE_{11} mode, the far field is characterized by

$$E_\theta = \frac{E_1}{kR}\left[\frac{J_1(ka\theta)\sin\phi}{\theta}\right]$$

$$E_\phi = \frac{E_1 a}{R}\left[\frac{J_1'(ka\theta)\cos\phi}{1-\left(\frac{ka\theta}{1.84}\right)^2}\right] \qquad (2)$$

$$E_R = 0$$

where k is the free-space propagation constant, J_0 and J_1 are the zero and first-order Bessel functions, a is the waveguide (hence aperture) radius, and E_0 and E_1 are arbitrary field constants which may be rationalized in terms of the total power radiated by each mode. It turns out that $E_0 \approx E_1$. The θ, ϕ, R coordinate system is shown in Fig. 4. Both (1) and (2) assume $\theta \ll 1$; i.e., $\cos\theta \approx 1$, $\sin\theta \approx \theta$. The vertical cross sections of the patterns represented by (1) and (2) are shown in Fig. 3. The actual radiation patterns for both the TM_{01} and TE_{11}

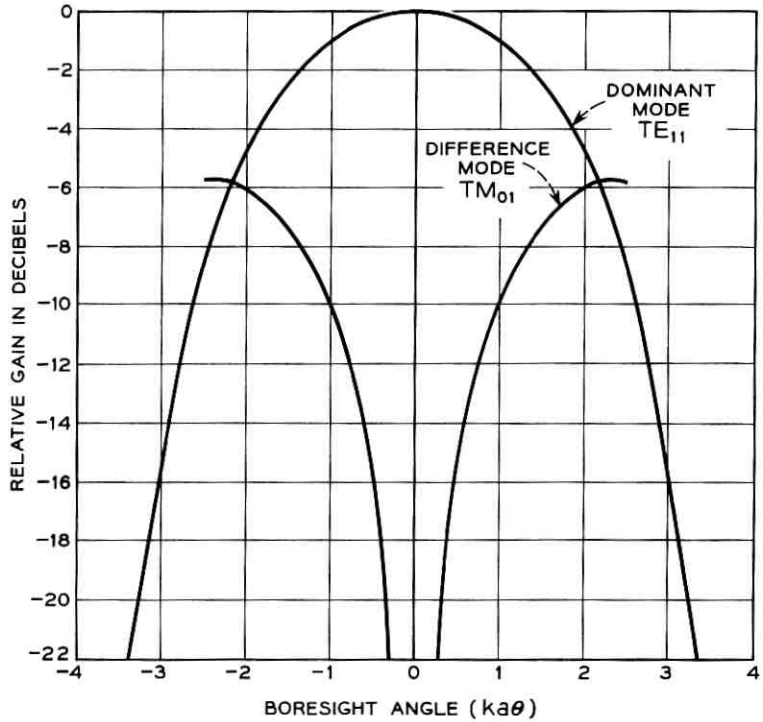

Fig. 3 — Radiation patterns for an open-end circular waveguide.

excitation of the conical horn reflector have been computed by T. G. Li and measured by J. N. Hines[2] and are, indeed, very similar to the corresponding open waveguide patterns.

The significance of the radiation patterns and their associated equations (1) and (2) becomes clear when the reciprocal condition of signal reception is considered. Fig. 4 depicts a source near the waveguide axis at the coordinate position $[\theta, \phi, R]$, where θ and ϕ describe the antenna pointing error. It is assumed that this source is, in general, elliptically polarized. The TM_{01} field-pattern shows that a TM_{01} signal will be excited only by the θ component of incident field, E_θ, and not by the ϕ component. The phase and magnitude of the TM_{01} signal at some reference point in the waveguide will therefore be determined by the phase and magnitude of the E_θ, or ϕ plane component. The magnitude of TM_{01} mode is dependent upon pointing error. For zero error, when the source lies on the waveguide axis, the pattern shows a deep null, indicating that no TM_{01} signal will be excited. However, when the source moves off

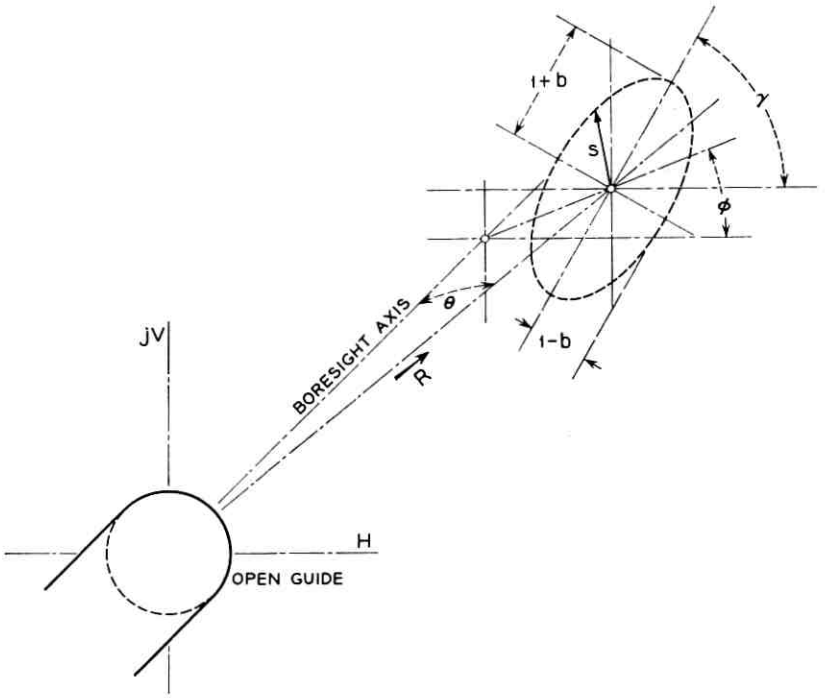

Fig. 4 — Elliptically polarized signal source and space coordinates as used in the analysis.

the waveguide axis, the TM_{01} mode will be strongly excited. When θ is small ($ka\theta < \frac{1}{2}$), (1) may be simplified to

$$\begin{aligned} E_\theta &= \frac{E_0 k a^2 \theta}{2.405R} \\ E_\phi &= 0 \\ E_R &= 0 \end{aligned} \tag{3}$$

which shows that the amplitude of the TM_{01} signal in the waveguide is directly proportional to small pointing error. It will be shown below that these characteristics, an amplitude proportional to pointing error and a phase determined by the θ component of field (that is, the component in the ϕ plane or R-θ plane), allow the TM_{01} signal to be used as an indication of the magnitude (θ) and direction (ϕ) of the pointing error.

The TE_{11} signal provides a reference against which the phase and amplitude of the TM_{01} signal are measured. Its utility for this purpose arises from two properties inherent in (2). First, the magnitude is approximately invariant with pointing error, θ, when θ is small, thus providing a magnitude reference to extract the effects of range. Second, for small θ, the TE_{11} mode is excited by both the θ and ϕ components of field in such a way that the polarization of the incoming signal is preserved; and the measurement of any two orthogonal components of the TE_{11} mode will determine this polarization. This property enables the TE_{11} signal to function as a phase reference.

The TE_{11} and TM_{01} radiation patterns resemble in form and function the "sum" and "difference" patterns, respectively, of conventional simultaneous lobing tracking systems. The conventional designations, "sum" for TE_{11} and "difference" for TM_{01}, will henceforth be used in this paper. The phase and amplitude relationships for these signals will now be derived.

2.2 *The Sum and Difference Signals*

The beacon wave expected from the satellite will be circularly polarized, though sometimes imperfectly. For generality, it will be assumed that the source, S, generates an elliptically polarized wave. Referring again to Fig. 4 for definitions of coordinates, the rotating field vector thus generated in the aperture can be simply expressed in terms of two counter rotating vectors: a positively rotating vector of amplitude, e_0/R, and a negatively rotating vector of amplitude, $b(e_0/R)$. The constant e_0 represents effective radiated power and propagation factors. The R represents range and accounts for the $1/R$ attenuation

of the wave as it radiates from the source. The two vectors rotate at an angular velocity ω. In order to permit the use of complex vector notation, the H-V plane (transverse to the guide axis) is pictured in Fig. 4 as a complex plane with the vertical axis designated as imaginary. The incident wave can then be expressed as

$$E_S = \frac{e_0}{R} (e^{j\omega t} + be^{-j\omega t}) e^{j\gamma} \tag{4}$$

where b determines the signal ellipticity, and γ determines the inclination of the major axis of the ellipse in the complex plane. As seen in the figure, the source is located at a small error angle, θ, off the open waveguide axis, and lies in a plane through the axis which is inclined an angle ϕ counterclockwise from the horizontal plane.

In the autotrack system, the horizontal and vertical components of the dominant mode are sampled and amplified separately. These two sum signals, together with the sampled difference mode, constitute the three autotrack signals derived from the elliptically polarized incident wave. As discussed above, the horizontal sum signal, e_H, responds only to the horizontally polarized component of the incident wave, the vertical sum signal, e_V, only to the vertical component, and the difference signal, e_D, only to the ϕ-plane component (E_θ).

For the sum signals, the response is invariant with small error angle, θ. If the conversion of incident field to the sampled sum signals is represented by a determinable constant, c_1, the sum-signals become

$$\begin{aligned} e_H &= c_1 \operatorname{Re} [E_s] \\ e_V &= c_1 \operatorname{Im} [E_s]. \end{aligned} \tag{5}$$

For the difference signal, the response is proportional to the ϕ-plane component of E_s, Re $[E_s e^{-j\phi}]$, and to the small error angle, θ. Thus

$$e_D = c_2 \theta \operatorname{Re} [E_s e^{-j\phi}] \tag{6}$$

where c_2 is the constant of proportionality between the incident field and the sampled difference signal.

Equations (4), (5), and (6) combine to yield

$$\begin{aligned} e_H &= \frac{c_1 e_0}{R} [\cos (wt + \gamma) + b \cos (wt - \gamma)] \\ e_V &= \frac{c_1 e_0}{R} [\sin (wt + \gamma) - b \sin (wt - \gamma)] \\ e_D &= \frac{c_2 e_0}{R} \theta [\cos (wt + \gamma - \phi) + b \cos (wt - \gamma + \phi)]. \end{aligned} \tag{7}$$

These relationships do not contain the fixed differential phase shifts in the system, which will be calibrated out.

If the polarization is indeed circular, $b = 0$, it is evident that the error, θ, and error direction, ϕ, can be extracted from (7) by a straightforward comparison of phase and amplitude between e_D and e_H or e_V. If the polarization is elliptical, these quantities cannot be precisely determined unless the polarization parameters, b and γ, are known. In practice they will not be known, but the polarization will be close to circular. The sum and difference signals will therefore be processed as if polarization were truly circular, and the anomalies introduced by ellipticity will be examined below. The analysis applies only to small error angles for which the assumptions that (a) incident polarization is preserved, and (b) the difference signal is proportional to error angle, are valid. For the 67-foot aperture of the horn-reflector antenna, this linear approximation holds to about 0.035 degree. Large-error performance will be discussed later.

2.3 *Signal Processing*

It is necessary to process the sum and difference signals (7) to produce error signals proportional to the horizontal and vertical pointing errors, ϵ_H and ϵ_V,

$$\begin{aligned} \epsilon_H &= \theta \cos \phi \\ \epsilon_V &= \theta \sin \phi. \end{aligned} \tag{8}$$

The arrangement used is shown in Fig. 5. Techniques similar to simultaneous lobing, such as used in the precision tracker,[3] are involved. Taking each horizontal or vertical coordinate separately, the difference signal is first normalized with respect to the sum signal in automatic-gain-controlled amplifiers to remove common amplitude variations, such as path loss effects. The resulting normalized difference signal is then phase-compared, or multiplied, with the normalized sum signal, and then filtered to remove RF components. The process, which requires four separate IF channels combined in a horizontal-axis pair and a vertical-axis pair, yields angle-error output voltages, E_H and E_V, represented by

$$\begin{bmatrix} E_H \\ E_V \end{bmatrix} = A \begin{bmatrix} 1 & \dfrac{4b \cos \gamma \sin \gamma}{(1+b)^2 \cos^2 \gamma + (1-b)^2 \sin^2 \gamma} \\ \dfrac{4b \cos \gamma \sin \gamma}{(1+b)^2 \sin^2 \gamma + (1-b)^2 \cos^2 \gamma} & 1 \end{bmatrix} \begin{bmatrix} \epsilon_H \\ \epsilon_V \end{bmatrix} \tag{9}$$

where A is an arbitrary gain constant.

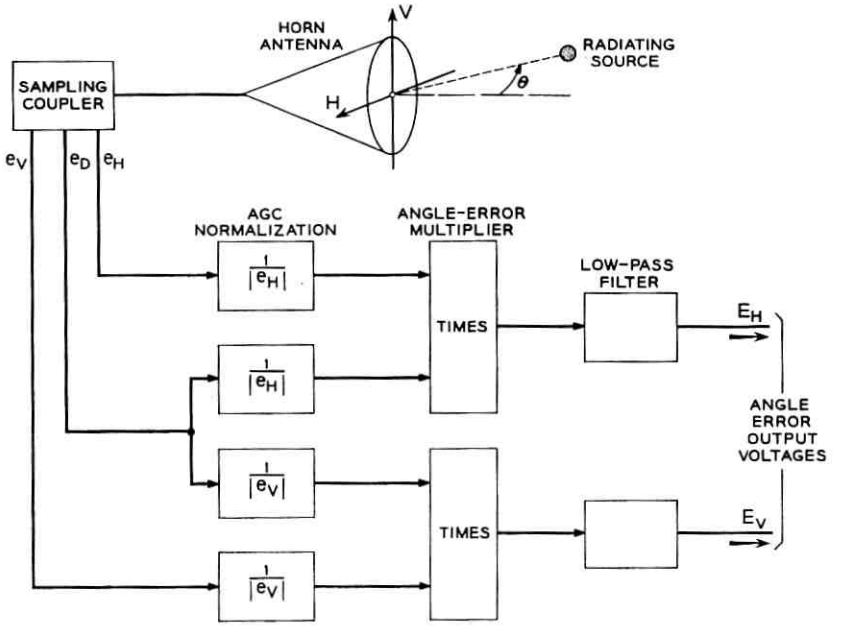

Fig. 5 — Autotrack system block diagram.

This equation shows the existence of cross coupling between the vertical and horizontal axes. The cross coupling is a function of both the ellipticity (determined by b) and the inclination of the major axis. For circular polarization ($b = 0$), the cross coupling vanishes and the error voltages become proportional to the pointing-error angles. Cross coupling also vanishes for any nonlinear polarization ($b \neq 1$) when the major axis of the ellipse coincides with the H or V axes ($\gamma = 0, \pi/2$).

The cross coupling is a consequence of the fact that, with elliptical polarization, the incident field is not a uniformly rotating, constant-amplitude vector. This is reflected in the numerator of the coupling terms, $4b \cos \gamma \sin \gamma$. The denominator results from the particular form of AGC normalization that has been used, and is not fundamental to the basic concept. The AGC system was designed to maintain constant angle-error gain in the diagonal terms of (9). Under conditions of extreme ellipticity, it magnifies the cross coupling terms when γ approaches $n\pi/2$, ($n = 0, 1, 2 \cdots$). It is therefore not the optimum technique for highly elliptical signals.

The cross-coupling coefficients of (9) vary with γ and axial ratio as shown in Fig. 6. For axial ratios less than 3 or 4 db (the maximum expected values for the Telstar satellite) the cross coupling is moderate.

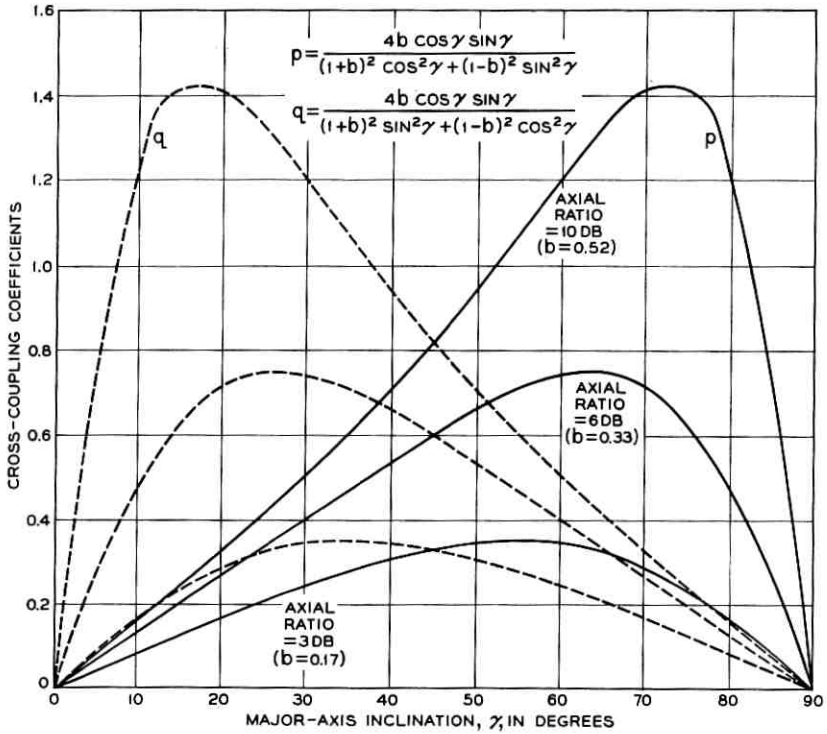

Fig. 6 — Vertical to horizontal pointing error cross coupling due to noncircular polarization of the beacon signal.

To illustrate the effects of cross coupling, (9) was used in a simple iterative error-correcting loop defined by

$$\begin{bmatrix} \epsilon_H \\ \epsilon_V \end{bmatrix}_n = [I - \delta M]^n \begin{bmatrix} \epsilon_H \\ \epsilon_V \end{bmatrix}_0 \tag{10}$$

where $[\epsilon_H , \epsilon_V]_0$ is an initial error, [M] is the error-sensing matrix of equation (9), and $[\epsilon_H , \epsilon_V]_n$ is the resulting pointing error after n iterations. The results of applying this process to two cases of different major-axis inclination and axial ratios are shown in Figs. 7 and 8. Here the arbitrary constant, δ, is chosen small enough (0.1) to plot out a smooth curve whose slope is proportional to E_V/E_H, thus illustrating the direction of the corrective influence at each point. These curves show that, in general, noncircular polarization causes correction to occur in a curvilinear path rather than in a straight line. The end-game appears to be asymptotic to

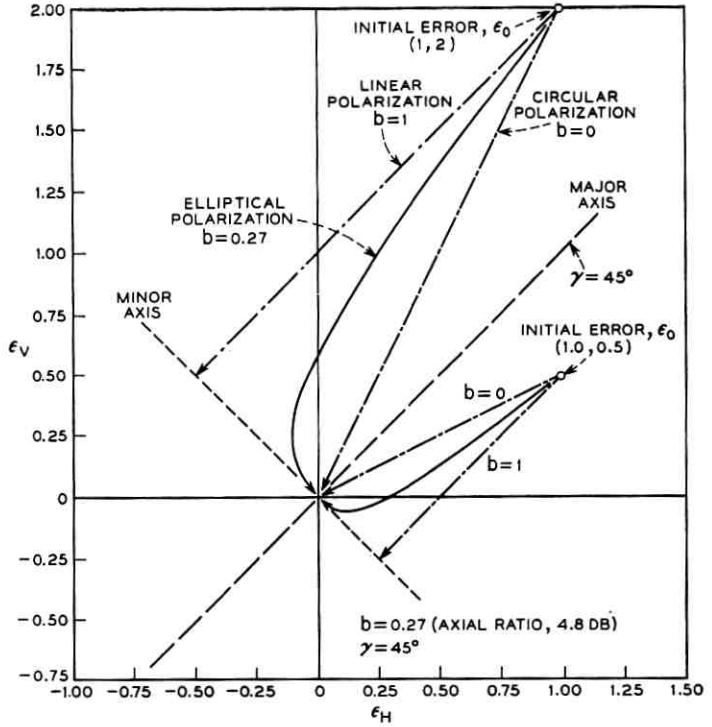

Fig. 7 — Pointing correction path of a weightless antenna in the presence of elliptic cross coupling (b = 0.27, γ = 45°).

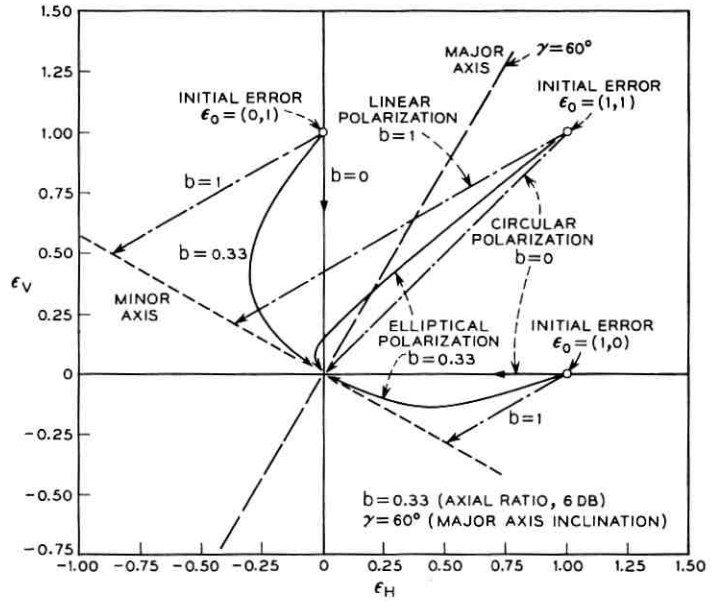

Fig. 8 — Pointing correction path of a weightless antenna in the presence of elliptic cross coupling (b = 0.33, γ = 60°).

the minor axis, implying that the coordinates could perhaps be effectively decoupled along this path. This, however, is strictly true only for $\gamma = 45°$. In general, the cross coupling must be considered in the design of a servo system. The special case of linear polarization is considered in Section 2.4.

The error correcting performance of the actual system in the full autotrack mode is shown in Fig. 9. The tracking target was the Black Mountain boresight antenna,[2] which radiates a slightly elliptically polarized signal of 2 db axial ratio ($b = 0.115$) with a major-axis inclination $\gamma \approx 10°$. A small amount of cross coupling effect is evident in these curves.

2.4 *Linear Polarization*

When the polarization is linear ($b = 1$), an error orthogonal to the plane of polarization will not excite radially symmetric electric fields in

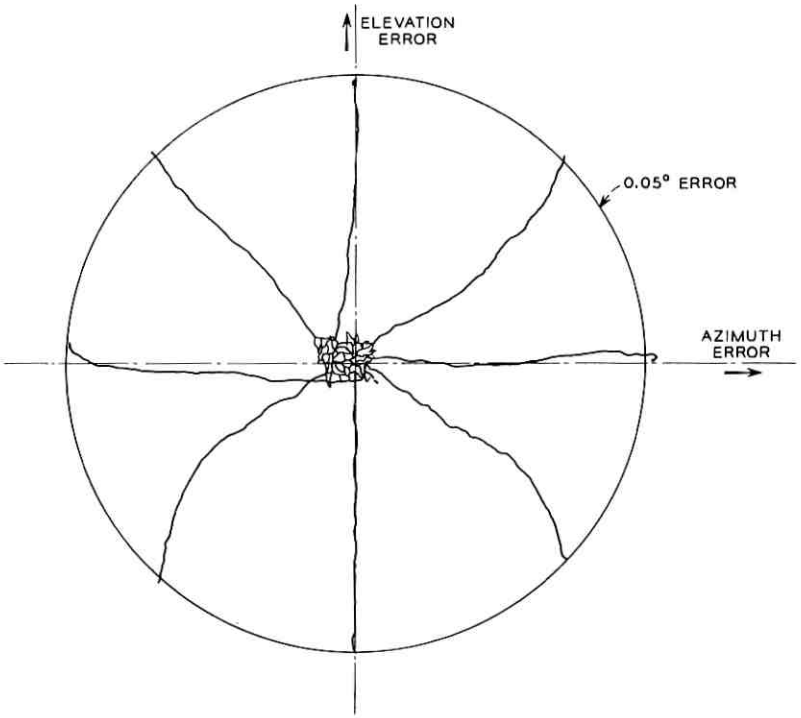

Fig. 9 — Recorded motion of the antenna, using the autotrack system to zero in on the boresight beacon.

the antenna aperture. Hence, the difference mode will not be excited, and no error indication will be generated. This may be seen from (7) and (9) by setting $\phi = \gamma + \pi/2$, to find $e_D = 0$; hence

$$\begin{bmatrix} E_H \\ E_V \end{bmatrix} = 0. \tag{11}$$

Thus, whereas for circular polarization the difference pattern has a null point on the antenna axis, for linear polarization there is a null *plane* orthogonal to the axis of polarization. Fig. 7 shows that attempts at correcting the pointing error with linear polarization result in straight-line motion terminating on the null plane. The target would then tend to slip away along this plane. Target loss of this type has been observed in tracking helicopters equipped with linearly polarized antennas. In theory, however, even a small cross-polarization component will permit full error correction, though with reduced response time.

2.5 *Two-Channel Processing*

For a satellite tracking signal that is near circular in polarization, it is possible to simplify the processing by receiving only one orthogonal component of the TE_{11} mode and generating the other with a $\pi/2$ phase shift. It is presumed here, as before, that the receiving antenna preserves polarization. Two IF channels are required, as shown in Fig. 10. The horizontal error component is obtained using the difference signal, e_D, and the horizontal sum component, e_H. The vertical error component is derived from these, as shown in the figure. The resulting error voltages are

$$\begin{bmatrix} E_H \\ \\ E_V \end{bmatrix} = A \begin{bmatrix} 1 & \dfrac{4b \sin\gamma \cos\gamma}{(1+b)^2 \cos^2\gamma + (1-b)^2 \sin^2\gamma} \\ \\ 0 & \dfrac{1-b^2}{(1+b)^2 \cos^2\gamma + (1-b)^2 \sin^2\gamma} \end{bmatrix} \begin{bmatrix} \epsilon_H \\ \\ \epsilon_V \end{bmatrix}. \tag{12}$$

For circular polarization, $b = 0$, and direct error indications without cross coupling result, as expected. For elliptical polarization with low axial ratio, cross coupling occurs, but the net effect in an error correcting loop is not much different than the four-channel scheme of (9). There is, however, one significant difference. True error sensing in the two-channel system requires prior knowledge of the sense of polarization, while in the four-channel system no prior knowledge is necessary. This may be seen by letting $b \to \infty$. A sign reversal will occur in (12) but not in (9).

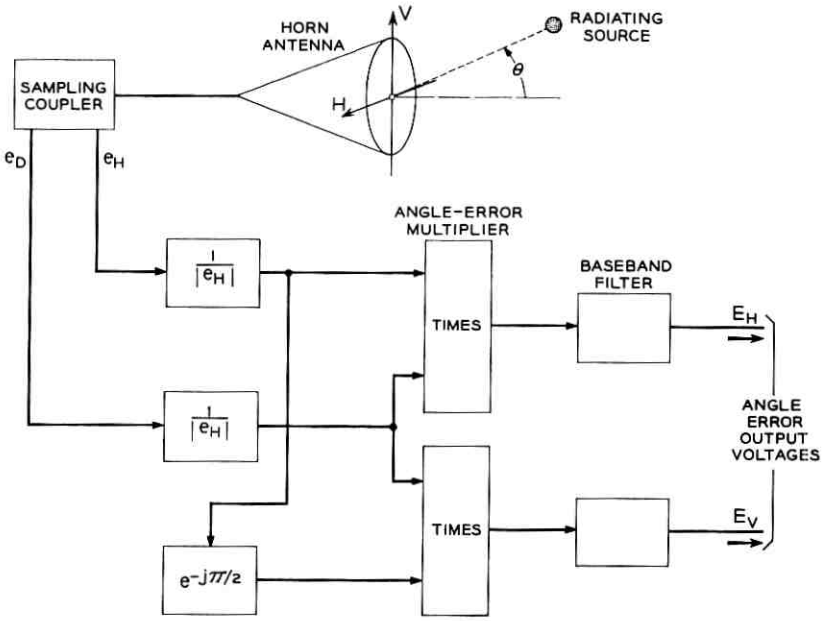

Fig. 10 — Two-channel autotrack arrangement.

The autotrack receiver was implemented for either four- or two-channel processing to permit comparison of the two techniques. The four-channel system offers some advantage in being able to handle signals of either sense of circular polarization. It also permits positive tracking on randomly polarized signals (noise). The two-channel system, on the other hand, requires less equipment.

2.6 *Large Pointing-Errors; Pull-In*

When the pointing error is large, the error voltage response is nonlinear and the receiving antenna introduces cross-polarized signals, so that the foregoing analysis is no longer valid. The resulting distortion in error-indication shows up as additional cross-coupling and effective variation in the tracking loop gain. These anomalies that accompany large error angles affect the pull-in, or angle acquisition limits, of the tracking system. Such behavior does not permit simple analysis, but experimental results show that the pull-in range is almost as large as would theoretically be obtained if circular polarization were preserved. Theoretically, the autotrack system should zero in from error angles up

to the first null in the dominant mode radiation pattern. Reliable acquisition to about 80 per cent of this angle is actually achieved. The pull-in ranges of the four-channel and two-channel systems, furthermore, are about equal.

2.7 *Coordinate Conversion*

Thus far, the analysis has been based on an open waveguide antenna in a simple H-V coordinate system lying in the aperture plane. In the actual horn-reflector antenna, the mode sampling coupler does not rotate with the horn in elevation. The error signals generated by the autotrack, designated E_x and E_y, refer to the coordinates of the mode coupler, not the aperture. The aperture-plane error signals, E_H and E_V, must be derived from these signals by a simple coordinate rotation.

Let the longitudinal and transverse (elevation) coordinates of the aperture plane be, respectively, H and V; and let the elevation angle be β. The three mode signals, referred to the aperture plane, are as given in (7). E_H and E_V are found by suitable operations on e_H, e_V, and e_D as already shown. These may be expressed in terms of transverse and longitudinally polarized modes whose coordinates are indicated in Fig. 11. Transverse fields are reversed upon reflection from the parabolic

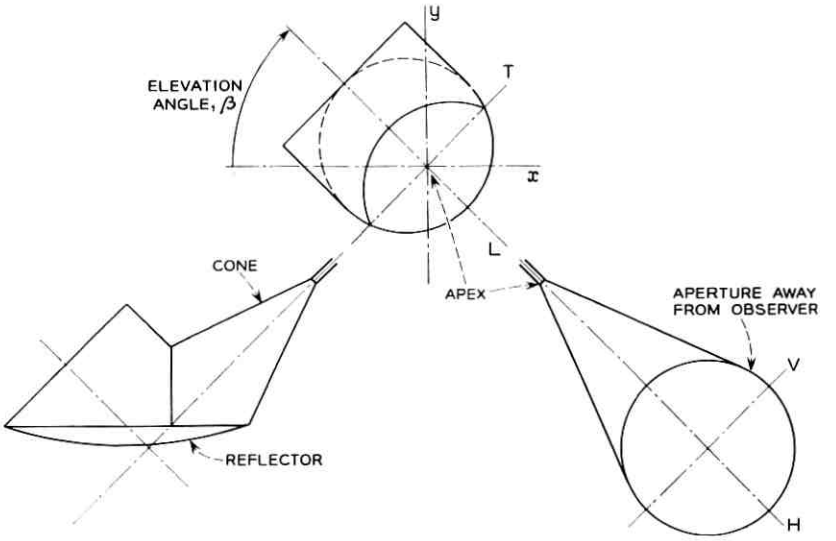

Fig. 11 — Coordinates used in determining the coordinate correction required when the horn rotates in elevation.

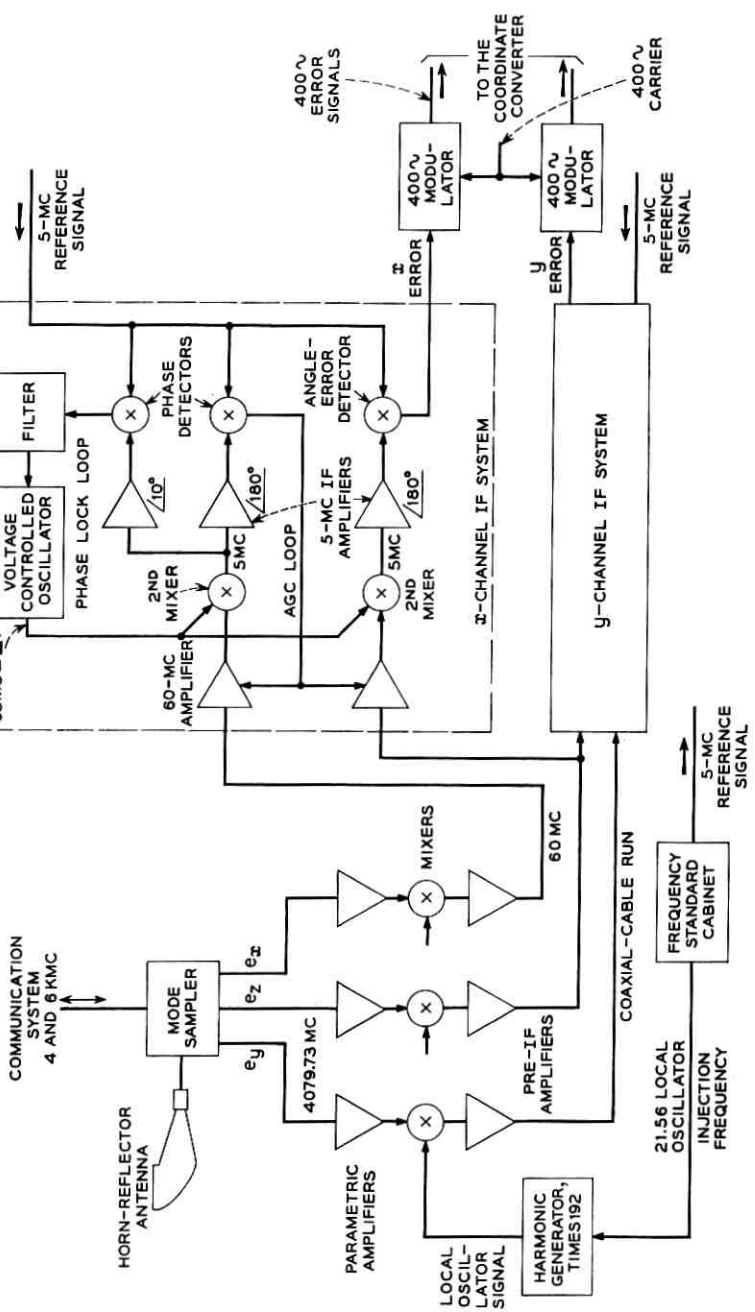

Fig. 12 — Standard four-channel autotrack system arrangement.

surface; longitudinal fields are not. Thus,

$$e_H = e_L \tag{13}$$

$$e_V = -e_T \tag{14}$$

$$e_D = -e_z \tag{15}$$

where e_z is the difference signal propagated in the z-direction.

From the figure,

$$e_L = e_x \cos \beta - e_y \sin \beta \tag{16}$$

$$-e_T = -e_x \sin \beta - e_y \cos \beta. \tag{17}$$

Then

$$e_H = e_x \cos \beta - e_y \sin \beta \tag{18}$$

$$e_V = -e_x \sin \beta - e_y \cos \beta. \tag{19}$$

Since

$$E_n = e_D e_n \tag{20}$$

equations (15), (18), (19) and (20) may now be combined to derive the required coordinate conversion. In doing this, it is necessary to invert the sign of e_x so that, for $\beta = 0$, positive x-coordinate errors will result in positive H-coordinate errors. This is done as a matter of course when the system is calibrated. The resulting transformation from error voltages referred to the mode sampler coordinates to error voltages referred to the aperture coordinates is

$$\begin{bmatrix} E_H \\ E_V \end{bmatrix} = \begin{bmatrix} \cos \beta & \sin \beta \\ -\sin \beta & \cos \beta \end{bmatrix} \begin{bmatrix} E_x \\ E_y \end{bmatrix}. \tag{21}$$

The coordinate conversion is performed on the output signals by the coordinate converter, which is part of the antenna servo system.[4] The necessity for coordinate conversion could have been avoided by rotating the coupler with the antenna in elevation. This, however, would have complicated the mechanical designs of the rotary joint and the autotrack RF circuitry.

III. SYSTEM DESCRIPTION

3.1 *General*

The block diagram of Fig. 12 shows the autotrack system hookup for four-channel signal processing. A special circular waveguide coupler

(the sampling coupler) samples the horizontal and vertical dominant modes and the difference mode excited by the 4079.73-mc beacon signal at the throat of the horn reflector. The resulting signals, e_x, e_y, and e_z, are separately amplified and down-converted in three amplifier chains. Each chain consists of a varactor parametric amplifier, a balanced mixer, and a 60-mc preamplifier. These units are located at the apex of the antenna in close proximity to the mode coupler. The three 60-mc IF signals are then transmitted, via coaxial cables, to the IF signal processing equipment located in the lower equipment room on the antenna structure. It is here that the signals are paired off for four-channel processing. Only one of these pairs, the horizontal error channel, or x channel, is depicted in detail. The other channel is identical. The signal processing for each pair consists first of IF amplification and AGC normalization in a pair of 60-mc main IF amplifiers. The signal is then down-converted to a 5-mc second intermediate frequency. At this point, the sum channel includes a phase-lock loop that works against a stable 5-mc reference signal. The phase-lock loop provides automatic Doppler tracking and permits operation with extremely weak signals. In addition, the phase coherence established by the phase-lock loop is used to advantage by performing AGC and angle-error detection coherently.[6,7] Noncoherent detection, however, is available at the turn of a switch so that the system can track on noise emitting targets such as the sun. After angle-error detection, the resulting dc horizontal and vertical angle-error signals modulate a 400-cycle carrier. They are sent to the coordinate converter in this form.

A comparison of this block diagram and that of the precision tracker[3] reveals a great functional similarity in their circuits. This fact was used to advantage to minimize the over-all development and fabrication effort. Wherever possible, the circuits and equipment were designed to be suitable for both the PT and autotrack systems. The RF and IF amplifiers, and the angle detection and frequency generation circuitry, for instance, are identical to their PT counterparts. Differences exist in the interconnection of these "building block" components to the extent that the autotrack signal processing differs from the PT processing. The autotrack also differs in (a) using dissimilar packaging of the RF "front-end" circuitry; (b) requiring a dc power supply cabinet that operates from 60-cycle, 120-volt, three-phase power; and (c) having a display and control cabinet (in place of a console) to house the 400-cycle angle modulators, status indicators, angle-error indicators, and phase-lock loop tuning controls. For circuit details of common units, the reader is referred to the precision tracker system.[3] The sampling coupler, how-

ever, is unique to the autotrack, and therefore deserves a brief description.

3.2 *Sampling Coupler*

Fig. 13 shows the autotrack RF unit in place at the apex of the horn-reflector. The sampling coupler itself is pictured in Fig. 14. Its function is to separately sample the difference mode and the vertically and horizontally polarized dominant modes excited in the antenna by the satellite microwave beacon. As an energy coupling device, the coupler is not optimum. It was designed to meet the specific needs of the satellite system, including:

(a) minimum attenuation and reflection of the 4-kmc communication signals,

(b) minimum coupling of the transmitted 6-kmc signal into the autotrack paramps, and

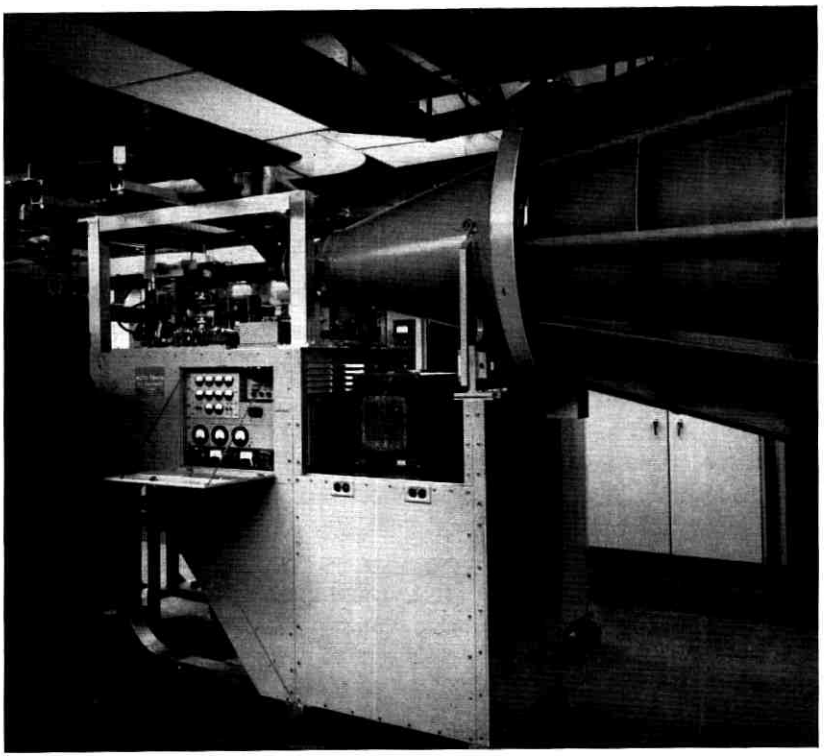

Fig. 13 — Autotrack RF unit in place at the horn apex, Andover, Maine.

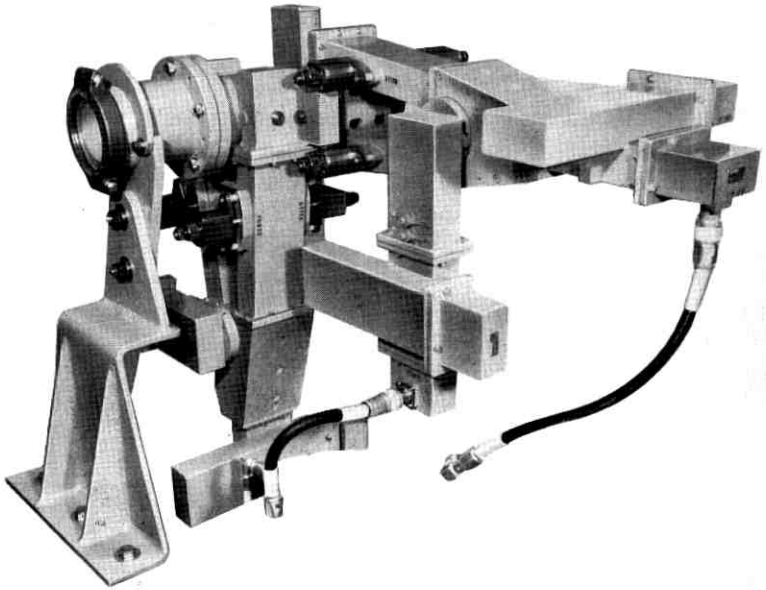

Fig. 14 — Autotrack sampling coupler.

(c) the expeditious use of existing waveguide components where possible.

The coupler takes advantage of the particular symmetry of the circular waveguide modes to separate them from one another. Fig. 2 shows that there exists a circumferential magnetic field at the cylinder walls for both types of mode — at the upper and lower surfaces for the vertically polarized dominant mode, at the side walls for the horizontally polarized mode, and all the way around for the difference mode. Because of the high gain of the large antenna, the ultimate in coupling efficiency is not necessary. It is therefore practical to magnetically couple both modes through the same holes and to separate them after coupling. The magnetic fields for the dominant modes are oppositely directed on opposite guide walls: e.g., clockwise on one side and counterclockwise on the other. By contrast, the difference mode magnetic field is continuous around the guide circumference. If balanced signals are coupled from holes on opposite sides of the guide and combined in a hybrid junction through a balanced filter and waveguide system as shown in Fig. 15, symmetry requires that energy carried by the ap-

propriate dominant mode, and that carried by the difference mode, will be separated in the hybrid.

A two-cavity filter was used to increase the coupling coefficient and provide high rejection of both transmitted and received communication signals.

Since the dominant mode components are geometrically orthogonal, they must be separately sampled using orthogonal sets of coupling holes, and they therefore require the two hybrids seen in Fig. 14. Due to the circular symmetry of the difference mode, it couples out through both sets of holes. To enhance the difference signal, the second hybrid difference arm is shorted at a point that optimizes the difference output of the first hybrid. Coupling of the difference mode is further enhanced by the fact that the waveguide at the coupler output is below cut off for that mode. The signal is reflected from the output transition, and the coupler holes are positioned to take advantage of the resulting standing wave.

The output of the coupler gives a sampling of the dominant mode beacon signal, which is about 7 db down from that received by the horn reflector; the difference mode signal is about 3 db down.

It is important to prevent coupling of the dominant modes into the tracking difference channel. This cross coupling is held about 35 db below the direct coupling level by tuning the filter cavities for a careful

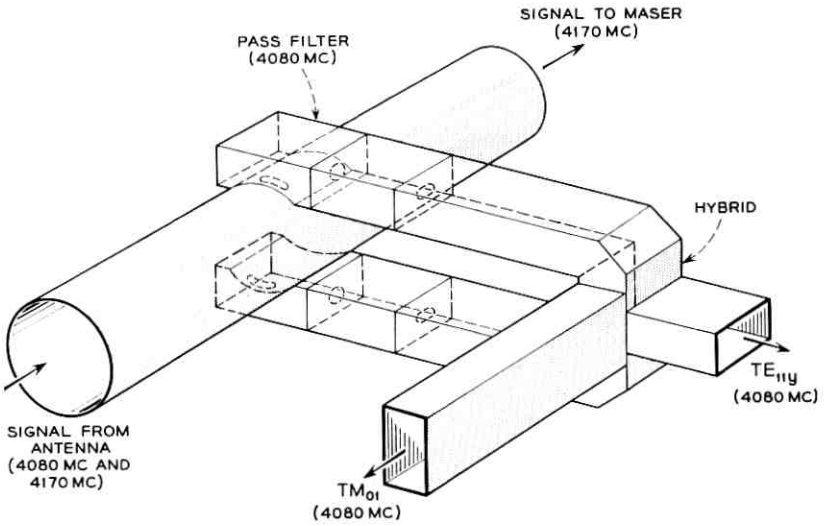

Fig. 15 — Conceptual version of the sampling coupler.

balance coincident with maximum dominant mode sampling. Additional phase and attenuation trimmers in each input arm of the hybrids provide final balance adjustment.

IV. SYSTEM PERFORMANCE

In the design of circuits for common use in both the autotrack and the precision tracker, the system gains, dynamic range, bandwidths and noise thresholds were chosen to meet the requirements of the less sensitive system, the precision tracker. Consequently, the autotrack receiver always operates well above its threshold capabilities. This threshold is determined by the ability of the phase-lock loop to remain locked in phase to the received signal despite the presence of both random phase modulation of the beacon oscillator and thermal noise. The effect of thermal noise is held to a minimum by the use of low-noise parametric amplifiers and a narrow threshold bandwidth phase-lock loop. The random phase noise is kept low by using crystal-controlled devices of high spectral purity for the satellite beacon oscillator and for the receiver beating oscillators. A practical threshold level has been experimentally determined to be about -130 dbm at the input to the sampling coupler for the horizontal and vertical dominant mode signals. Tracking accuracy is adequate for communication purposes for signals of several decibels below this value, but the angle-error gain deteriorates rapidly from its nominal value of about 100 volts/degree. The autotrack signals in normal Telstar system operation range from -90 dbm to -120 dbm.

Closed-loop tracking performance has been measured by Iwama and Norton and is discussed in more detail in their paper.[4] The acquisition angle has been found to be 0.2° in all directions, as shown by the pull-in pattern of Fig. 16. These curves show the paths taken by the antenna in zeroing in on the Black Mountain boresight antenna from an initial error angle of 0.2°. The large-angle coupling factors due to antenna-induced cross-polarization (which are not present in the small-angle pull-in patterns of Fig. 9) are evident here. These are apparent in the circumferential motion that occurs at large initial error angles, particularly in the first and fourth quadrants. The antenna motion is rather complex; it represents the combined effects of the autotrack angle-detection anomalies and the response of the servo system. The major portion of each curve is traced out in about one second.

Iwama's measurements of tracking errors show that the autotrack system maintains the null axis of the antenna within 0.005 degrees of the actual satellite direction, limited only by the tracking rate capa-

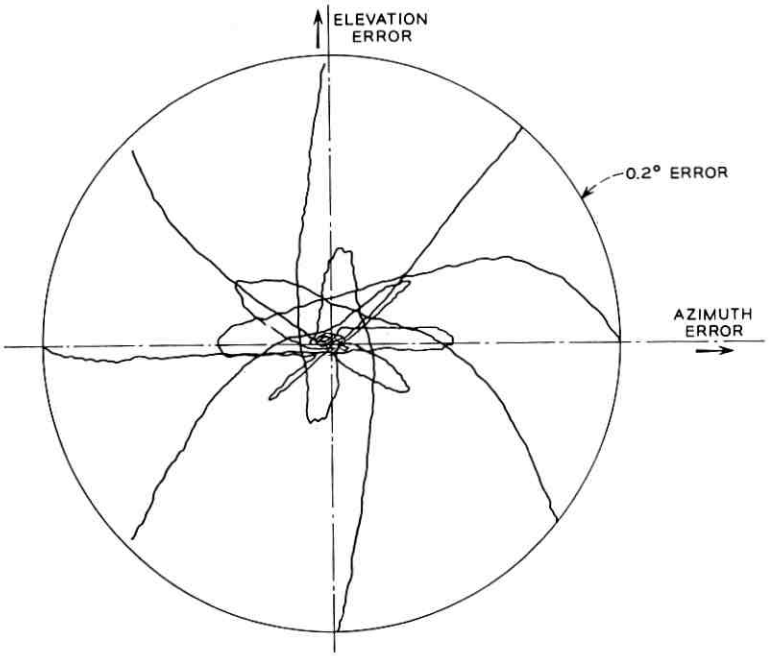

Fig. 16 — Antenna corrective motion from 0.2° initial pointing error.

bilities of the drive motors. The null axis coincides with the geometrical axis of the antenna. In the reception of circularly polarized communication signals, it is possible to obtain a small increase in gain by pointing off-axis in elevation by about 0.02°. Although it is theoretically possible to bias the error signals so as to achieve off-axis tracking by this amount, it is not done, because the gain enhancement is not significant.

The signal levels received in the autotrack system during the first Telstar communication pass are compared with predicted levels in Fig. 17. The received signal data represents points taken from a continuous recording of AGC voltage at about 0.5-minute intervals. The predicted values were based on measured satellite antenna gain patterns (shown as a smoothed curve), predicted range (also plotted), and predicted spin angle (not shown). The spread between the upper and lower predicted signal bounds, S_{MAX} and S_{MIN}, represents two factors: the ellipticity of polarization as a function of spin angle, and a variation in satellite transmitter power from 17 dbm to 19 dbm. This is the maximum power variation expected when the ground transmitter is turned on and off. As may be seen by the 2-db drop in received power at approximately 23:25

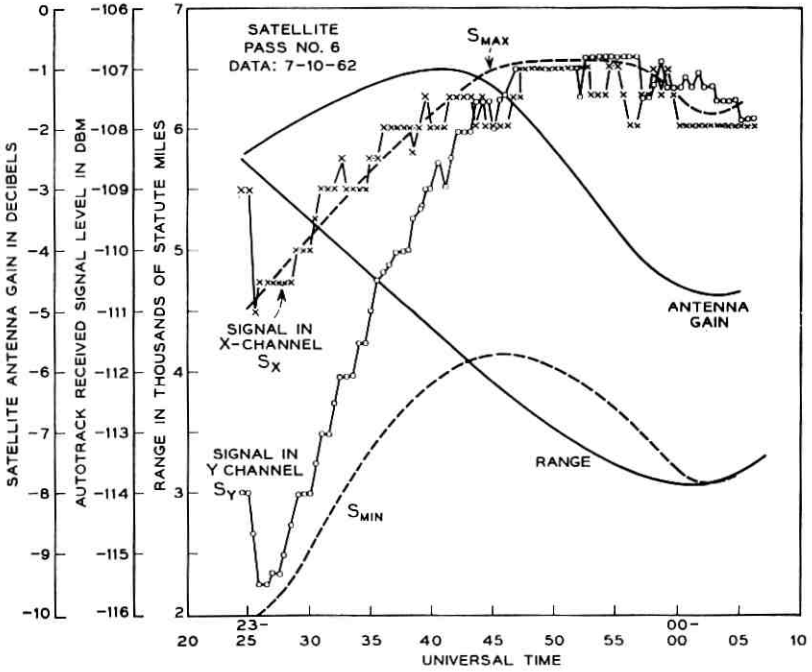

Fig. 17 — Received signal levels for Telstar satellite pass 6.

to 23:26 hours, the ground transmitter was turned on at this time and remained on for most of the pass. The 17-dbm value of satellite transmitter power should therefore have been used for prediction from that time on. Thus, after 23:26 hours, the S_{MAX} curve should have been displaced downward by 2 db in order to represent true conditions. From these considerations, it may be seen that the measured signals differed from predicted values by about +2 db. The accuracy of receiver calibration and of prediction are each about ±1 db.

The high tracking accuracy made possible by the autotrack system eliminates antenna tracking error as a limiting factor in the performance of the ground station. The basic techniques are applicable not only to the horn-reflector antenna, but also to a wide class of more conventional reflector antennas.

V. ACKNOWLEDGMENTS

The multimode sampling technique on which the autotrack system is based was jointly worked out by J. N. Hines and the authors. It was

found to be closely related to S. E. Miller's earlier work.[5] The evolution from first concept to a smoothly operating, reliable system came about through the cooperative efforts and suggestions of many, many people. We feel particularly indebted to R. V. Lohmiller and his department for detailed design and fabrication of a major portion of the equipment; to K. B. Woodard and his group for detailed mechanical design of much of the RF equipment; to E. M. Elam for final design, coordination, assembly, installation, and testing of the complete autotrack RF unit; and to E. C. Snyder, Jr. for coordinating much of the assembly, installation, calibration, testing, and operation of the autotrack system both at Andover, Maine, and Pleumeur-Bodou, France.

REFERENCES

1. Chu, L. J., Calculation of the Radiation Properties of Hollow Pipes and Horns, J. Appl. Phys., **11,** Sept., 1940, p. 603.
2. Hines, J. N., Li, T., and Turrin, R. H., The Electrical Characteristics of the Conical Horn-Reflector Antenna, B.S.T.J., this issue, p. 1187.
3. Anders, J. V., Higgins, E. F., Murray, J. L., and Schaefer, F. J., The Precision Tracker, B.S.T.J., this issue, p. 1309.
4. Lozier, J. C., Norton, J. A., and Iwama, M., The Servo System for Antenna Positioning, B.S.T.J., this issue, p. 1253.
5. Miller, S.E., Multimode Automatic Tracking Antenna System, U.S. Patent 2931033, March 29, 1960. Patent applied for July 19, 1955.
6. Nelson, W. L., Phase-Lock Loop Design for Coherent Angle-Error Detection in the *Telstar* Satellite Tracking System, to be published.
7. Ball, W. H. W., Analysis and Digital Simulation of the *Telstar* Precision Tracker, Paper No. CP-63-368, presented at the IEEE Winter General Meeting, New York, 1963.

The Precision Tracker

By J. V. ANDERS, E. F. HIGGINS, JR., J. L. MURRAY and F. J. SCHAEFER, JR.

(Manuscript received February 25, 1963)

The precision tracker, a simultaneous lobing, amplitude-comparison, passive, continuous-wave tracker based in principle and design upon a monopulse tracking radar, is employed at the Andover, Maine, and Pleumeur-Bodou, France, stations to find the satellite and direct the horn-reflector antennas when required and, at regular intervals during subsequent passes, to provide the precise tracking data required for prediction of future orbital parameters.

I. INTRODUCTION

The Telstar satellite radiates a 4079.73-mc continuous-wave (CW) carrier 90 mc below the frequency of the communications carrier.[1] This signal is designed as a beacon for the processes of tracking and initial acquisition. The design of the precision tracker receiver is thus based on the characteristics of this beacon signal as modified by the dynamic orbital parameters: these are listed briefly in Table I.

The system application — the manner in which the tracker is integrated into the Telstar ground system operations — is described in Ref. 2. Section II of this paper is a brief description of the precision tracker system; sections III through IX cover the several subsystems in greater detail.

II. SYSTEM DESCRIPTION

The precision tracker (hereafter referred to as the PT) is essentially a radio theodolite. From the viewpoint of the over-all Telstar system, it has one simply defined task: to provide the antenna pointing system with the real-time, locally referenced azimuth and elevation angles of the satellite.

TABLE I — NOMINAL DESIGN CHARACTERISTICS OF THE BEACON AND ORBIT

Apogee	3000 nm
Perigee	600 nm
Inclination	45 deg
Tangential velocity	302 nm/min
Beacon frequency	4079.73 mc
Doppler rate, maximum	575 cps[2]
Doppler shift, maximum	±65 kc
Precision	±4 kc
Stability	±12 kc/day
Thermal variation	±40 kc
Effective radiated power	+13 dbm

2.1 *Data Take-Off*

To provide the required angle data, the PT antenna rotates in two axes — azimuth and elevation. A multispeed gear box is associated with each axis; mechanical angle is converted by precision 1-speed and 64-speed resolvers to ac analog voltage, which in turn is converted to pulse time modulation for transmission to the track digital control unit of the antenna pointing system.

2.2 *Automatic Tracking*

The PT is a *simultaneous lobing, amplitude-comparison, passive, CW* tracker. The antenna, with its four-horn feed system, the microwave comparator, and the three-channel tracking receiver, develops output voltages proportional to the azimuth pointing error and the elevation pointing error. These error signals are passed through equalizers, modulators, and amplifiers to the azimuth and elevation drive motors, thus closing two servo loops that continuously serve to minimize the angular errors between the antenna's boresight axis and the line-of-sight to the satellite.

2.3 *Simultaneous Lobing — Amplitude Comparison*

The microwave energy received by the four feedhorns is processed by the comparator to develop three different antenna pattern response characteristics: the *sum* pattern, corresponding to a conventional antenna pattern; the *elevation difference* pattern, having two main lobes in the elevation plane with a deep null on the boresight axis; and the *azimuth difference* pattern, having two main lobes in a plane perpendicular to the elevation plane with a deep null on the boresight axis. (Strictly

speaking, this should be called the traverse difference pattern; however, the error signal is applied to the azimuth axis of the mount.)

The difference signals are developed in the comparator by amplitude summations in hybrids. The system is phase-sensitive in that the phase of the error signals relative to the phase of the sum signal is employed as an indication of the sense of the error signals, i.e., left-right and up-down.

The three-channel tracking receiver employs two stages of conversion to bring the sum, azimuth, and elevation signals down to 5 mc prior to demodulation. An AGC voltage is developed from the sum channel and applied to all three channels; thus, the demodulator outputs are proportional to D/S, the difference pattern response divided by the sum pattern response. This has two important effects. First, the angle-error function is linearized with respect to off-axis angle: the two-lobe difference pattern function is converted to a nearly linear function. Second, the output scale factor is rendered insensitive to changes in absolute received signal level within the frequency response of the AGC system and the dynamic range of the receiver.

2.4 *Signal-to-Noise Ratio*

A high probability of detection with a low false-alarm rate is required for the acquisition process; a low standard deviation in tracking error is required by the orbital prediction program. These two requirements imply certain minimum signal-to-noise objectives.

Both the tracking noise (jitter) and bias vary in a complex way with the signal-to-noise ratio (SNR) available to the signal processing circuits. Generally the bias decreases with increased SNR, while tracking jitter increases rapidly as the SNR decreases below values of about +3 db at the intermediate frequency output. The available satellite beacon power, the space transmission path, the receiver "front end" design, and the signal-processing equipment all affect the degree to which these objectives are met. The deviation in the radiation pattern of the satellite from isotropic results in variation of about 5 db; the changes in its beacon power due to communication loading result in about 2 db variation. The transmission path length change is the most significant variable, accounting for about 12 db variation over the portion of the orbit tracked. As a result, the dynamic range of input signals is expected to be in the order of 20 db, a relatively small range. Since the SNR and tracking properties vary with path length, the slant path at apogee (about 5700 statute miles) sets the most stringent requirements.

Because orbital tracking requires the tracking antenna to be directed through a wide variety of space regions, the effects of noise sources, both spot and distributed, also contribute to the over-all received signal. The sun, which could contribute some 1500°K additional to the receiver temperature if it were viewed directly, is an example of a potent spot noise source; but the most important noise source in the field of view of the system is the atmosphere. At the receiver frequency of 4079.73 mc, the atmospheric noise contribution for the PT receiver can vary from about 14°K at the zenith to 170°K at the horizon, increasing rapidly for angles below 5 degrees. Normally the system operates over elevation angles of from 7.5 to 82.5 degrees and thus never experiences the maximum noise and SNR degradation condition except during test operations.

The loss effects for the 5700-statute-mile path, including an antenna polarization loss factor, are tabulated in Table II at a reference elevation angle of 10 degrees.

A practical optimum in system noise reduction at the front end of the receiver is attained through the use of room-temperature parametric amplifiers, located in the moving antenna support structure along with the first converters and the 60-mc IF preamplifiers. The resulting system operating noise temperature (about 340° K) and received signal level (as low as −138 dbm) place severe requirements on the signal detection schemes.

2.5 *Acquisition Receiver*

The PT was designed for rapid acquisition after a few spacecraft orbits. The maximum expected uncertainties in time, angles, and frequency were used as boundary conditions for design.

Enhancement of signal-to-noise ratio by a narrow-bandwidth filter was defeated, for the initial-orbit acquisition process, by *time*: to the

TABLE II — LOSSES

Loss Type	Loss Value (db)
Divergence (path loss)	184.20
Oxygen	0.25
Water vapor	0.15
Ozone and other particles	0.10
Polarization loss, vertically polarized antenna, nearly circularly polarized signal (includes axial ratio effects)	3.00
Total	187.70

finite time required to search the volume of space expected to contain the satellite must be added, for each beamwidth increment, the time per beamwidth necessary to sweep a narrow filter across the frequency band within which the beacon frequency will lie. It was not possible to develop an efficient and simple search strategy in which the necessary search time was compatible with the rate of motion of the search volume. The solution employed in the PT is to reduce the frequency-search time essentially to zero by a stationary search conducted with a comb filter.

The equipment associated with the comb filter has been designated the acquisition receiver. As may be seen from the block diagram (Fig. 1), the acquisition receiver serves as an initial tuning control to preset the frequency of the narrow band tracking receiver. Upon sensing the presence of a signal in the sum channel, it also stops the antenna's angular search at the point where the signal was detected. Thus, at the expense of 300 channels of signal processing, the frequency-search time per unit beamwidth has been reduced from 30 seconds to the $\frac{1}{4}$-second response time of the acquisition receiver's post-detection filters and threshold detectors.

The acquisition receiver was used to advantage on July 10, 1962, at 7:25 p.m. when it set the PT to a condition of fully automatic tracking within 6 seconds after the satellite repeater had been ordered to turn on.

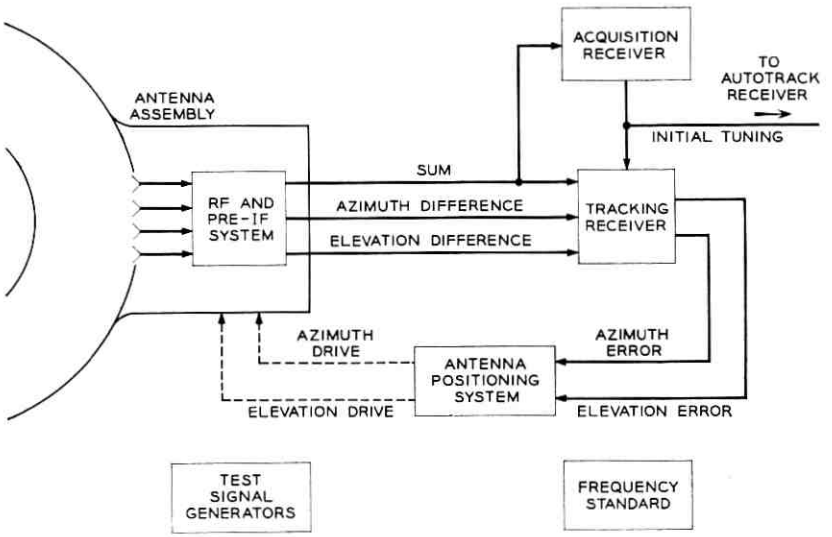

Fig. 1 — Precision tracker, block diagram.

2.6 *Tracking Receiver*

In the tracking receiver, which can develop usable angle-error signals with a signal-to-noise ratio 10 db or more below signal detection threshold, the need for maximizing the signal-to-noise ratio is based on reducing tracking jitter to the levels required by the orbital prediction program. It is also necessary to hold the jitter to levels which will damage neither the horn-reflector antenna and its associated electronic equipment nor the operating personnel when the horn-reflector is slaved to the PT. Since it is essential to recover the phase of the error signals relative to the phase of the sum signal, the demodulation technique offering the greatest noise rejection is coherent detection. The sum signal is kept in phase coherence with a noise-free 5-mc reference by a phase-lock loop or tracking filter discussed in Section IV. The 59.98-mc azimuth difference and elevation difference IF signals are converted to 5 mc by the 64.98-mc local oscillator signal developed in the phase-lock loop; thus, all three channels are maintained in phase coherence with the 5-mc reference, and coherent detection is effected in the angle error and AGC demodulators.

As a test option, the demodulation scheme may be converted to correlation detection for tracking the sun or other sources of wideband, random-phase radiation. To effect this conversion, the 5-mc demodulating reference is replaced by the 5-mc sum signal.

Under normal tracking conditions, when the tracking receiver is employing coherent detection with the phase-lock loop locked to a received CW signal with less than ± 10 degrees of phase jitter, the angular tracking jitter of the antenna is controlled by the bandlimiting effect of the servo system upon the effective receiver noise power. The nominal one-sided servo bandwidth varies from 0.2 cps to 1 cps under control of the received signal level. Thus, the narrower bandwidth reduces tracking jitter when the satellite is at longer range and the signal is weaker; the wider bandwidth reduces acceleration lag at shorter ranges where the signal is strong but the angular velocity and acceleration are greater.

The salient characteristics of the PT are listed in Table III. The following sections will describe the various subsystems of the PT in greater detail.

III. ANTENNA, RF PROCESSING, AND PREAMPLIFIERS

3.1 *Introduction*

The RF system used in the PT is composed of a low-noise antenna and comparator,[3] a high-gain, low-noise parametric amplifier, and a

TABLE III — SALIENT PARAMETERS OF THE PRECISION TRACKER

Effective receiver input temperature	315°K
Equivalent noise power in 3-kc bandwidth	−139 dbm
Received signal power at feedhorns for range of 5700 statute miles, satellite beacon power +13 dbm, PT line-of-sight to satellite's equator	−137 dbm
Received signal power at feedhorns for range of 5700 statute miles, satellite beacon power +13 dbm, PT line-of-sight 40 degrees off satellite's equator	−142 dbm
Over-all mechanical precision of antenna assembly, azimuth and elevation (1 sigma), including effects of wind loading and thermal variation on both antenna and boresight tower	0.005 deg
Tracking jitter, azimuth and elevation — standard deviation objective	0.015 deg
Slew rates	45 deg/sec
Servo bandwidth, autotracking mode	0.2, 0.5, and 1.0 cps
Acquisition time	
Angle search	0–24 sec
Acquisition receiver response	0.25 sec
Tracking receiver preset	0.45 sec
Tracking receiver frequency search	0–4 sec
Most probable time lapse from signal presence to autotrack	2.7 sec

well matched mixer-preamplifier transmission system. (See the block diagram in Fig. 2 and associated Table IV.) This arrangement ensures an adequately low receiver noise contribution.

3.2 *Antenna*

The 8-foot Cassegrainian reflector, shown in Fig. 3, provides a 2-degree beamwidth, which represents a nearly optimum compromise between the wide beam needed for acquisition and the antenna gain required for tracking accuracy. The antenna system is a unique embodiment of the Cassegrainian configuration; it consists of a parabolic main reflector, a hyperbolic subreflector, and a four-horn feed system which illuminates the subreflector from the rear through a hole at the axis of the main reflector. It is designed to process an impinging wave front polarized vertically. For any other polarization it may be considered as accepting only the vertical vector component; thus, for the nominally circularly polarized Telstar spacecraft beacon signal, a 3-db effective loss is entailed.

3.2.1 *Reflector Assembly*

Fiberglas honeycomb is the main structural material employed in the reflector assembly, as shown in Fig. 3. The subreflector and its conical support constitute an integral structure of molded Fiberglas honeycomb core overlaid on both sides with a Fiberglas skin. The conducting hyper-

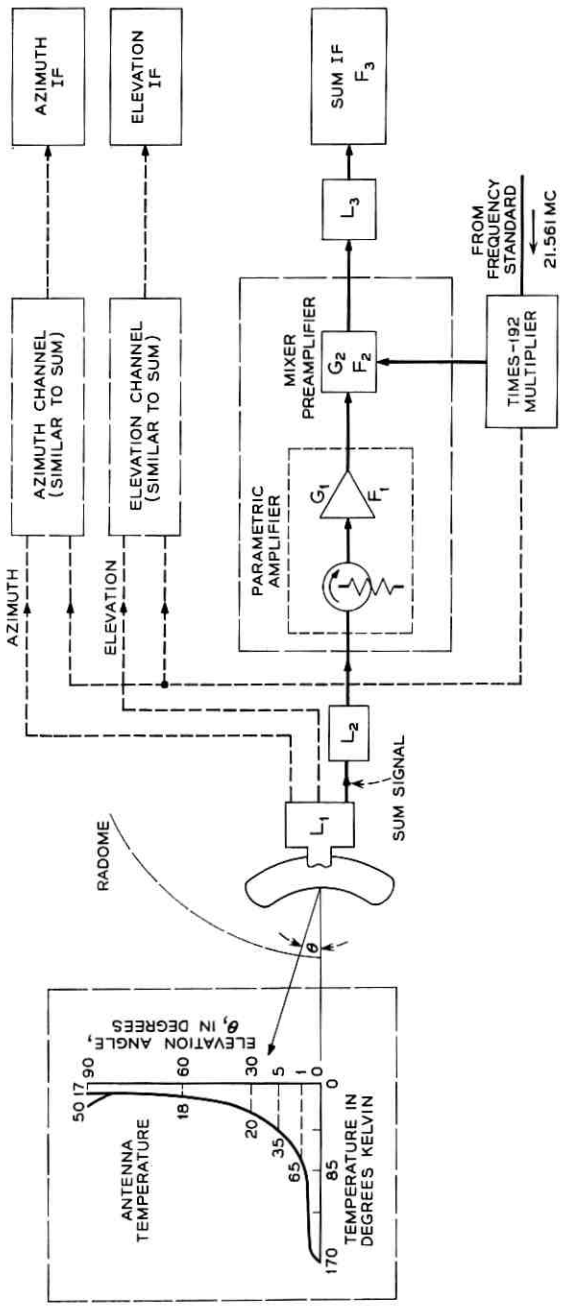

Fig. 2 — Over-all RF block diagram.

TABLE IV

Antenna and Radome Temperature	Comparator Loss	Coupling Losses, Semi-Rigid Line	Parametric Amplifier, Mixer-Preamplifier and Harmonic Multiplier	Slip Rings and Coax Cables	Main IF Amplifier
Radome $\approx 9°K$ System input temperature (T_e) $T_e = \sum_{1}^{n} \frac{(T_a)n}{\prod_{n}^{(1-n)} G(n-1)} = 315°K$ System operating temperature (T_{op}) $T_{op} = T_{ant} + T_e$ $= 340°K$ at $\Theta = 10°$	Dissipative and mismatch loss $L_1 \approx 0.2$ db $T \approx 290°K$ Connector loss = 0.1 db Total $L_1 = 0.3$ db	Rigid cable loss at 4079.73 mc $L_2 = 0.2$ db	Over-all unit noise figure 2.7 db Circulator loss 0.2 db $G_1 = 23$ db, including circulator $G_2 = 25$ db $F_1 = 2.5$ db $F_2 = 9$ db max.	Ring loss 0.4 db Cable loss 4.2 db Connectors 0.2 db Total 4.8 db	$F_3 = 9$ db $T = 290°K$

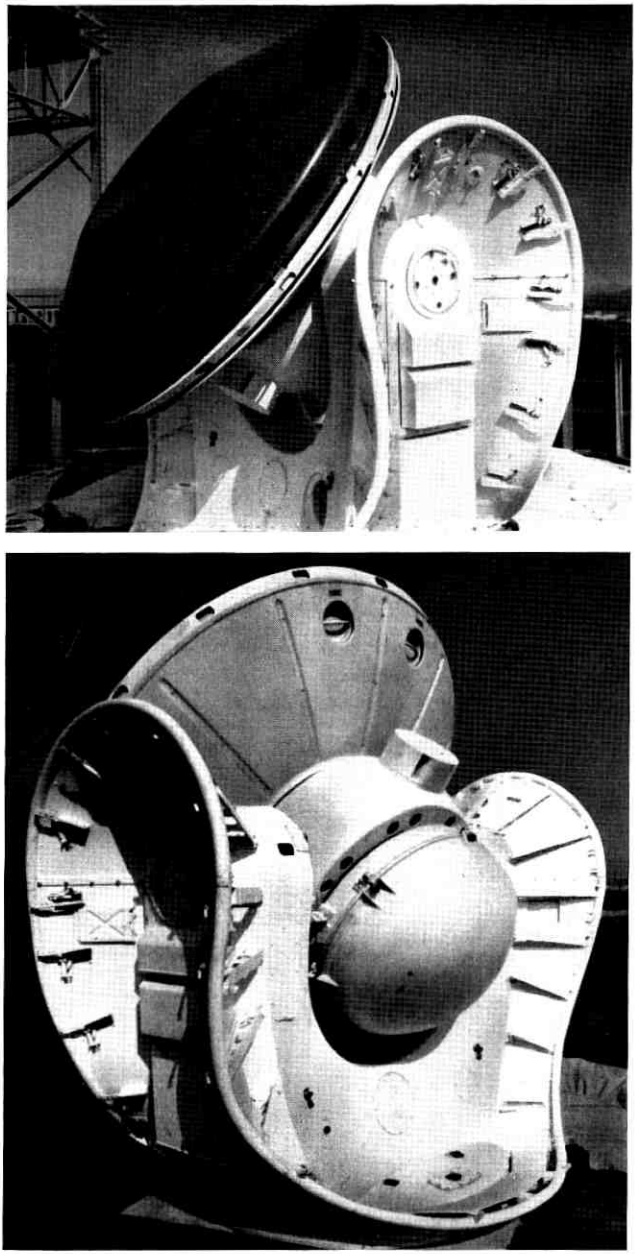

Fig. 3 — Precision tracker antenna, front and rear views.

bolic surface of the 36-inch diameter subreflector is composed of a horizontal array of aluminum wires of 0.01-inch diameter embedded in both the inner and outer skins. The subreflector is transparent to impinging vertically polarized signal components (see Fig. 4). The periphery of the area containing the wires is serrated rather than circular, to cause cancellation of the major effects of diffraction at the wire ends. The subreflector is 26.6 inches in front of the main reflector along the boresight axis.

The 92-inch diameter main reflector is made up of an aluminum parabolic reflector surface on which is overlaid a Fiberglas honeycomb core. The Fiberglas skin affixed to the core contains an aluminum wire grid embedded at an angle of 45 degrees to the vertical. The structure is called a twist-reflector: a vertically polarized signal component impinging upon the surface of the 45-degree wires may be resolved into two vector components, one normal to the wires and the other parallel to the wires. The parallel component is reflected by the wires; the normal component passes through the wires and honeycomb core and is reflected from the aluminum reflector to pass back through the core and the wires. The delay through the core is such that the two components recombine, at the wire surface after reflection, to result in a horizontally polarized signal at the subreflector.

The subreflector, whose wire structure is opaque to horizontal polarization, refocuses the signal to the four feedhorns projecting through the center of the main reflector.

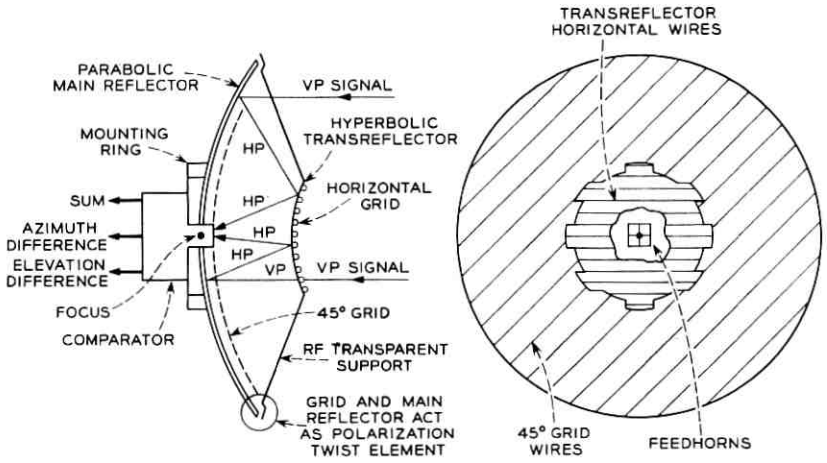

Fig. 4 — Cassegrainian antenna and twist reflector.

3.2.2 *Comparator-Feed Assembly*

Four individual patterns, each "squinted" symmetrically away from the central boresight axis of the antenna system, are created by the four horns and reflectors. The feedhorns are an integral part of the comparator-feed assembly, illustrated in Fig. 5, which shows the assembly, the microwave absorber ring which surrounds the feed, and the Fiberglas dust cover.

The assembly is made from aluminum stock in which the horns, four waveguide hybrid junctions, and waveguide phasing sections are precisely machined. The signals received by the horns are processed by vector additions and subtractions in the hybrids to form the three antenna response functions[4] required for tracking. The sum pattern is formed by the summation of all signals propagating in the four horns; the azimuth difference and elevation difference patterns are formed by obtaining the difference between the sums of signals in adjacent vertical pairs and horizontal pairs, respectively.

Connections from the signal output ports of the comparator to the parametric amplifiers are made by waveguide-to-coaxial transitions and through semirigid, low-loss coaxial line.

3.2.3 *Advantages of the Antenna System*

The Cassegrainian antenna as employed in the PT has the following advantages:

(a) It possesses the high gain associated with parabolic structures.

(b) Secondary radiation patterns having excellent sum pattern symmetry and difference patterns with high slope factors and deep boresight nulls are achieved.

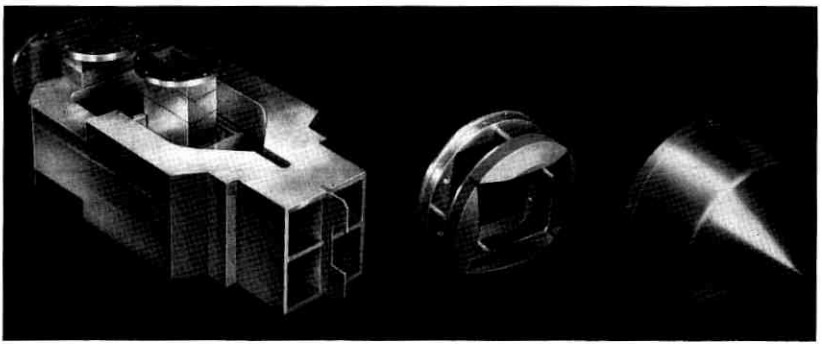

Fig. 5 — Microwave comparator (photo courtesy Wheeler Laboratories, Inc.).

(c) Shadow effects are minimized by the subreflector design, and therefore the effective area is essentially the same as that of an equivalent-sized parabolic system.

(d) Since the focal point is in the parabolic contour, the comparator can be located near the RF amplifier, thus minimizing coupling loss noise; the effective receiver temperature is lowered over that of antenna-receiver types having forward feeds and feed-support schemes.

(e) Since tracking angles are above the horizon, the primary patterns are coupled to the low-temperature sky rather than to the high-temperature earth; therefore, the effect of increased noise due to the primary radiation pattern coupling is lessened.

(f) Side lobes, back radiation, and spillover lobes are well below peak response (see Fig. 6 and associated Table V).

(g) A structure of relatively low moment of inertia is obtained, since the heavy receiving components are located near the rotational axis.

3.3 *Parametric Amplifiers*

Three low-noise parametric amplifiers amplify the sum and difference signals prior to mixing. These amplifiers are of the nondegenerative negative-resistance type. The input signal is fed through an input circulator, an impedance transformer, and a low-pass filter, so as to match the impedance at the varactor element and minimize coupling between the idler, pump, and signal circuits. The varactor element is mounted in a cavity resonant at both the pump frequency (16 kmc) and the idler frequency (12 kmc). The pump signal is produced by a reflex klystron which is immersed in a temperature-controlled oil bath and coupled to the parametric amplifier via K-band waveguide sections. The specifications for the PT parametric amplifiers are given in Table VI.

The parametric amplifier outputs for the three channels are fed to a balanced mixer-preamplifier unit. These units have an over-all gain of 25 db and a maximum noise figure of 9.0 db (double channel). The preamplifier utilizes a cascade circuit to minimize the over-all noise figure of the mixer-preamplifier assembly. The preamplifier has a center frequency of 59.98 mc and a bandwidth, at a -3 db response, of 6 mc.

Local oscillator drive is supplied to all three mixers by a common solid-state harmonic multiplier. This unit produces a minimum of 3 mw of RF power for each mixer at a frequency above the signal input. The output signals from the preamplifier are matched to 50-ohm coaxial cables and supplied to the slip rings for transmission from the rotating portion of the antenna assembly to the stationary tracking mount.

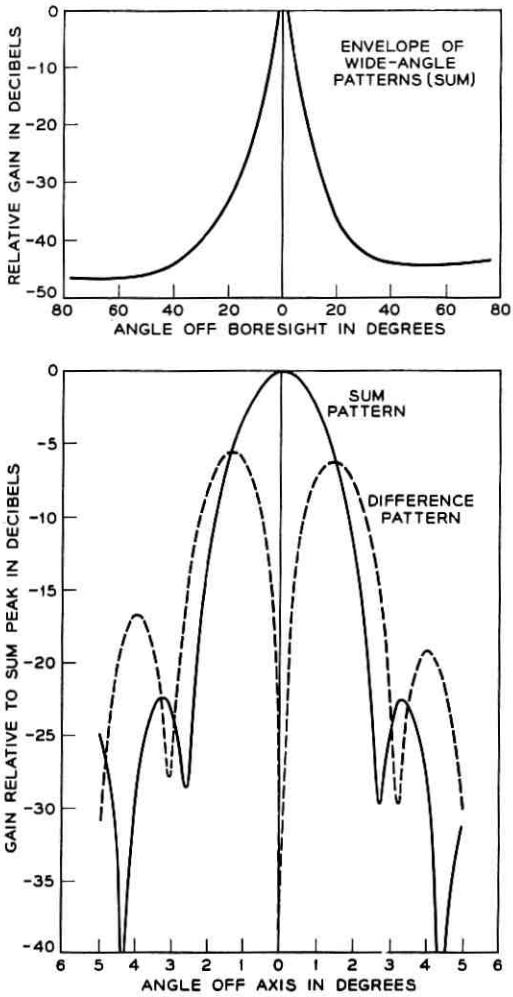

Fig. 6 — Secondary radiation pattern of precision tracker antenna system.

TABLE V — NOTES FOR FIG. 6

Antenna Characteristic	Value
Frequency	4079.73 mc
Polarization	vertical
Sum gain	37.2 db
3-db beamwidth, sum mode	2.1°
Suppression of first side lobe, sum mode	22.3 db
Difference gain, average of EL and AZ	30.6 db
Difference peak separation, average of EL and AZ difference modes	2.8°
Suppression of first difference side lobe, average of EL and AZ difference modes	12.6 db
Difference slope, normalized to an isotropic radiator	43.5v ratio/deg.

TABLE VI — PARAMETRIC AMPLIFIERS

Parameter	Value
Center frequency	4079.73 mc
Gain	23 db nominal
Bandwidth, instantaneous	20 mc nominal
Pump frequency	16,037 ± 2 mc
Pump power	60 mw nominal
Noise figure, excluding coupling losses	2.5 db max.
Gain stability, channel to channel	3 db max. fluctuation
Phase stability, channel to channel	12° max. fluctuation

The 50-ohm coaxial preamplifier lines are matched to the rings by a shorted stub element attached to each of the three signal rings. A 50-ohm double-shielded coaxial cable transmits the IF signals to the main IF amplifier.

3.4 *Signal-to-Noise Ratio*

A determination can be made of the SNR achieved for the system, taking into account the added noise components due to the atmosphere and the properties of the receiver components. The noise producing elements are defined as those up through and including the slip-ring assembly (see the block diagram of the RF system, Fig. 2, and associated Table IV). The receiver's effective input temperature, obtained from the component values shown here, is determined to be 315°K. Adding the antenna temperature to this value gives the system effective operating noise temperature (T_{op}). The effective input noise power ($P_n = KT_{op}B$) can then be obtained for each elevation angle. The results are shown in Fig. 7, together with the expected received signal power (P_s) for the 5700-statute-mile path. The SNR is the difference in ordinates between the two functions. It can be seen that the receiver and antenna noise contribution over the operational range of angles reduces the SNR value, based on the noise power associated with an input termination in thermal contribution over the operational range of angles reduces the SNR value, equilibrium at 290°K, by some 0.7 db. The average SNR over the operational elevations for maximum slant range is +3 db for a beacon signal at +15 dbm, or +5 dbm for a beacon signal power of +17 dbm.

IV. TRACKING RECEIVER

The precision tracker's tracking receiver (fifth bay of Fig. 8) functions to extract azimuth and elevation pointing error information from noise-laden IF signals produced in the tracking antenna and RF assembly by

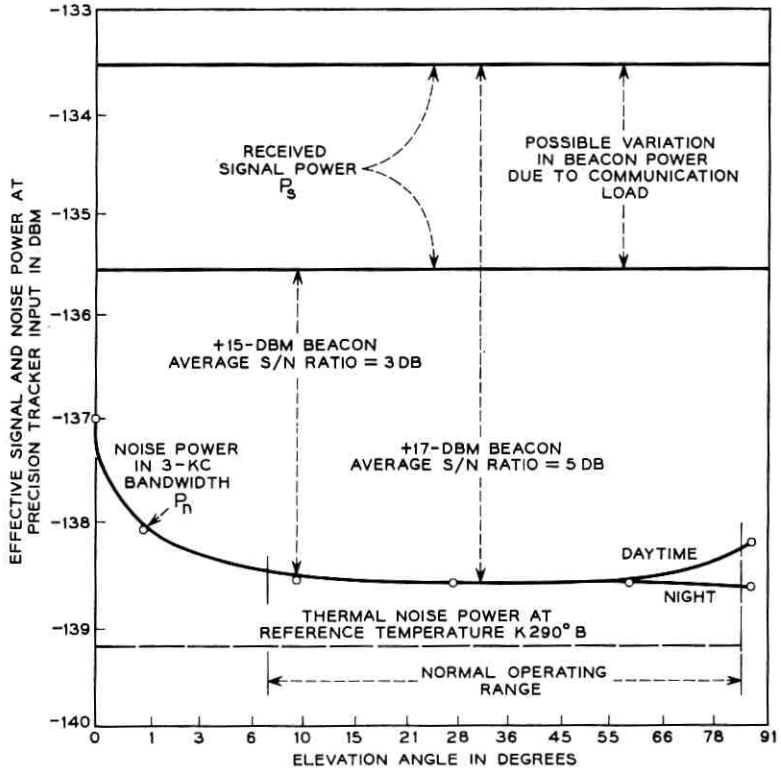

Fig. 7 — System noise power.

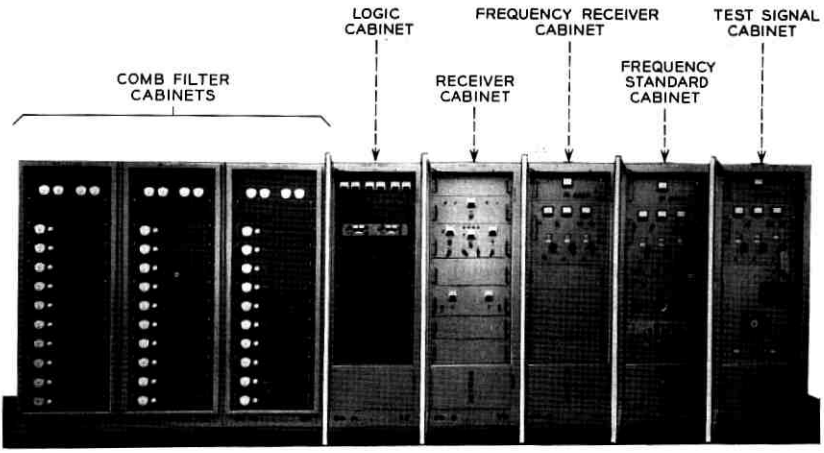

Fig. 8 — PT equipment cabinets.

a 4079.73-mc CW tracking beacon in the satellite. Because of the combined effects of Doppler shift and satellite frequency drift, the received IF signal frequency may differ from a nominal center frequency of 59.98 mc by as much as ±120 kc. A narrow-band adaptive tracking filter provides a phase-locked second local oscillator signal to permit coherent signal detection over a frequency range of ±150 kc.

4.1 *Block Diagram Description*

A simplified block diagram of the complete tracking receiver is shown in Fig. 9. The nominal 59.98-mc IF signals from the three IF preamplifiers in the antenna RF equipment enclosure are transmitted through matched slip rings and 250 feet of triple coaxial cable to the inputs of the sum, azimuth, and elevation main IF amplifiers. These matched amplifiers, under automatic gain control (AGC), provide a large portion of the 151-db receiver gain necessary to amplify the received signals to detector level. Each main IF amplifier is divided into two sections, with a bandpass filter of 1-mc bandwidth located between the sections to reduce the total noise and interference imposed on the amplifiers following.

The signal frequency is reduced to 5 mc at the three second converters by mixing with a nominal 64.98 mc derived from a voltage-controlled crystal oscillator (VCXO) and multiplier chain. The frequency and phase of this oscillator are determined by phase comparison of the 5-mc sum IF signal with a local phase-stable 5-mc reference signal in a somewhat sophisticated phase-lock loop. As shown on the block diagram, this loop also contains 5-mc IF amplifiers, a limiter, a 3-kc bandwidth crystal filter, a phase detector, and the loop filter.

The three remaining 5-mc channels are similar in that they contain 5-mc IF amplifiers, 3-kc bandwidth crystal filters, and phase detectors, all supplied by the same 5-mc reference signal. The phase-lock loop establishes and maintains a constant phase relationship between the received signals and the 5-mc reference signal, and permits coherent detection of the IF signals in these three channels. The detected sum signal provides an indication of phase lock and a measure of the received signal amplitude for operation of the AGC loop. The detected azimuth and elevation signals provide both sense and magnitude of antenna pointing errors for application to the respective antenna-positioning servos.

Biases that might occur in the pointing information because of detector unbalance or dc amplifier drift are eliminated by commutating the phase of the 5-mc IF error signals prior to detection and then synchronously demodulating the ac-coupled detector outputs.

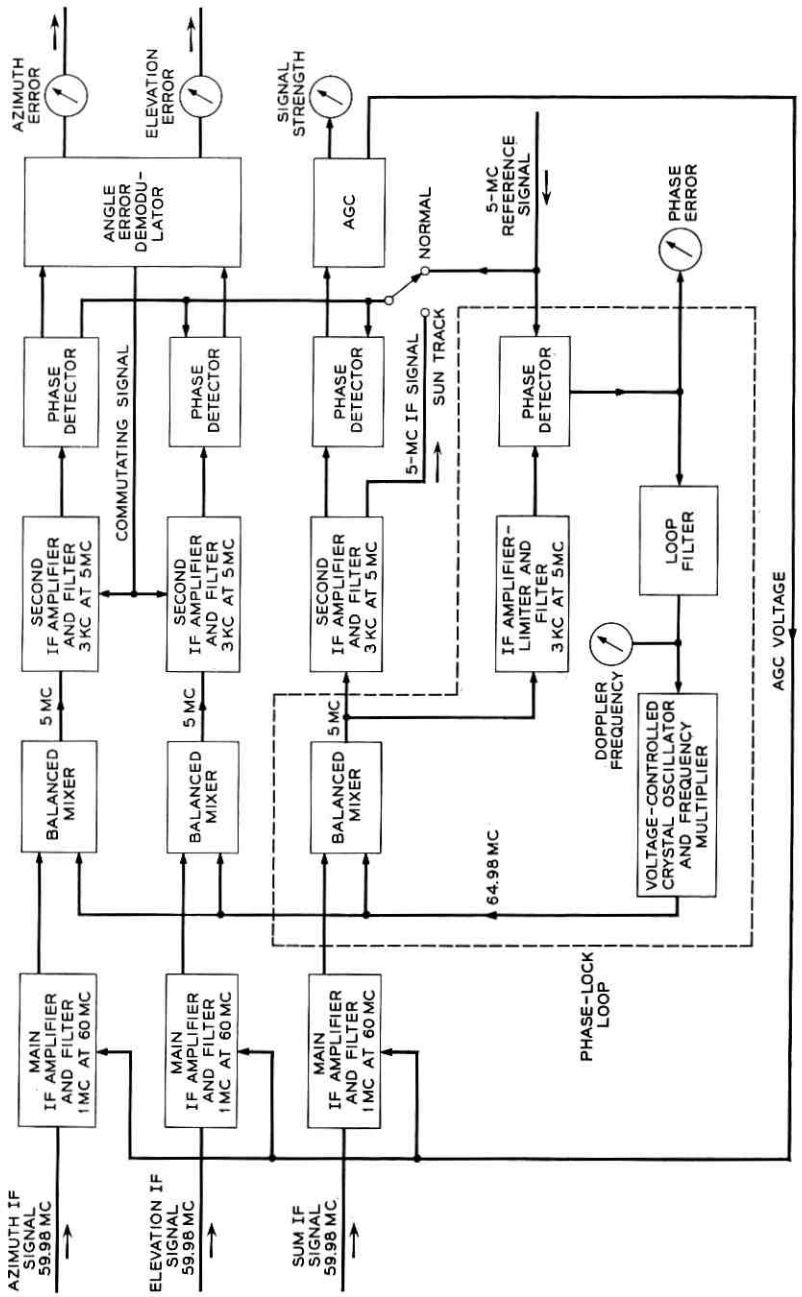

Fig. 9 — Tracking receiver, block diagram.

The mechanism for the correlation detection test option is indicated on the diagram as a "sun track" switch. The switch controls the substitution of a properly phased 5-mc sum IF signal for the 5-mc reference supplying the AGC and angle-error detectors.

A more detailed discussion of the key features of the tracking receiver follows.

4.2 *Main IF Amplifiers*

The two sections of each main IF amplifier include a total of ten transitionally coupled, synchronously tuned amplifier stages utilizing Western Electric 5847 electron tubes at a center frequency of 60 mc and an over-all bandwidth of 8 mc. The first two stages, which employ fixed gain, are followed by an adjustable phase-control network that provides approximately 150 degrees of receiver phasing adjustment per channel. The IF signal for the PT acquisition receiver is tapped off the sum channel at this point. Manual gain adjustment of the first two stages of the azimuth and elevation channels provides ±4 db of receiver gain equalization.

The remaining eight amplifier stages of each channel are gain controlled by the AGC. The stability of the amplifiers is such that the differential gain and phase of the three channels do not exceed 1 db and 3 degrees, respectively, when controlled over a 60-db range of gain from a common gain-control voltage.

A passive LC filter of 1-mc bandwidth separates the two sections of each channel for intermediate reduction of noise bandwidth.

Insertion pads are included at the input of each channel for the connection of a common IF test signal originating in the PT frequency standard and test signal cabinets.

4.3 *Second Converters*

The 59.98-mc IF signals from the three main IF amplifiers are converted to 5 mc by mixing with a common 64.98-mc local oscillator signal in three balanced passive mixers. Each input signal is terminated in a 50-ohm impedance provided by a broadband toroidal transformer hybrid. Mixing is accomplished in a matched pair of 1N35S germanium diodes.

4.4 *5-mc IF Amplifiers*

Conventional single-tuned amplifiers utilizing Western Electric 403B and 404A electron tubes follow mixer impedance matching networks

in the three channels. A 5-mc crystal lattice filter with a 3-kc noise bandwidth and a 180-degree phase delay is located, with appropriate input and output matching networks, between the first and second amplifier stages of the azimuth and elevation channels and the AGC branch of the sum channel. In the third stage of the azimuth and elevation channels, signal impedance is lowered to 50 ohms to drive a phase-commutating transformer, the operation of which will be detailed later. A fourth stage drives the 50-ohm phase-detector transformer. Following the second stage the AGC channel is split into two 50-ohm output stages, one driving the AGC detector transformer and the other providing 5-mc sum IF signals for correlation detection. The net gain of all three channels from mixer input to detector transformer is fixed at 45 db. The level of the signal appearing at all detector transformers is +13 dbm when the azimuth and elevation error signals equal the sum signal.

4.5 *Phase-Lock Loop*

The phase-lock loop is the heart of the tracking receiver. It embodies a form of adaptive tracking filter that approaches an optimum filter under all conditions of SNR, Doppler change, and rate of change expected in the PT environment.[6]

A block diagram of the phase-lock loop is shown in Fig. 10. The 5-mc IF input signal obtained from the second mixer in the sum channel is amplified approximately 75 db at a bandwidth of 200 kc by three single-tuned amplifier stages and is "hard" limited by a type 6BN6 limiter. The gain is sufficient to ensure at least 20 db of signal limiting at all times. A crystal filter with associated matching networks follows the limiter.

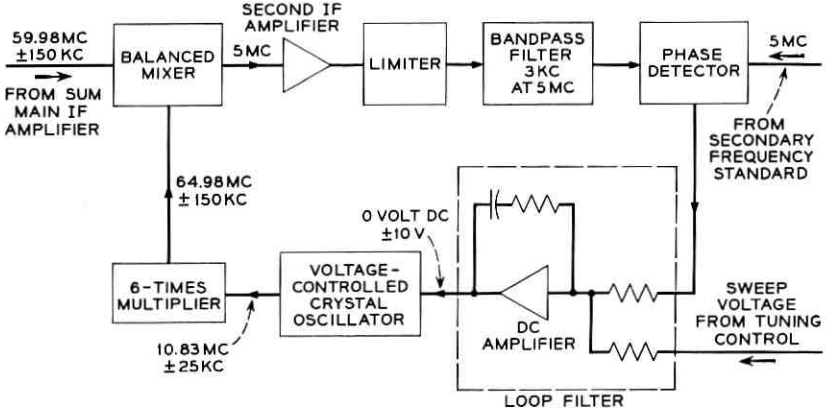

Fig. 10 — Phase-lock loop, block diagram.

This filter is similar to those in the other 5-mc IF channels in that it has a 3-kc bandwidth, but it has only a 90-degree phase delay. The requirement for a 90-degree phase difference between the reference for the phase detector in the phase-lock loop and the reference for all the other phase detectors is thus satisfied by the relative phase delays of the filters used in the 5-mc IF circuits.

A single amplifier stage matches the filter output to the 50-ohm phase-detector transformer. The signal power reaching the detector is a function of the SNR in the limiter. Because the total signal-plus-noise power in the output of the limiter is constant, the signal power at the detector will be suppressed as the direct ratio of noise-to-signal appearing at the limiter input for the ratios above approximately unity in the 200-kc bandwidth at this point. A direct consequence of this action is a reduction of phase-lock loop gain with decreasing received signal strength.

The phase detector (Fig. 11) consists of a carefully balanced and shielded broadband transformer hybrid driving a matched pair of silicon diode detectors. A high-gain dc operational amplifier accepts the two detector outputs in a differential connection to provide a low-impedance, single-ended output. Amplifier gain, and thus the phase detector gain constant, is determined by the ratio between input and feedback resistors. The 5-mc reference signal is applied to the phase detector at a much higher level than the IF signal, resulting in a sinusoidal output

$$e = \alpha K \sin \theta$$

where

α = limiter suppression factor
K = 5.75 = detector gain constant
θ = loop phase error.

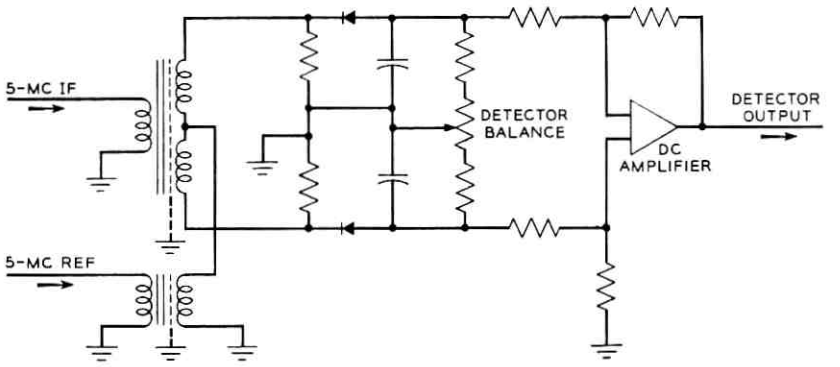

Fig. 11 — Phase detector.

The detector parameters given produce an output of 0.1 volt/degree for $\theta \leqq \pm 10$ degrees and a suppression factor of unity (strong signal).

The phase detectors of the azimuth, elevation, and AGC channels differ from this configuration only in differential amplifier gain.

The loop filter takes a form approaching that of an ideal integrator modified for loop stability. A high-gain, chopper-stabilized, dc operational amplifier with a capacitor in the feedback loop provides a dc gain of 30×10^7, falling off at 6 db/octave above 0.032 cps. This, combined with the inherent 6 db/octave slope of the VCXO/phase-detector combination, causes gain crossover to be approached at 12 db/octave. A resistor in the integrator feedback provides a lead corner at approximately 10 cps to stabilize the phase-lock loop. Because of limiter suppression, with the attendant change of loop gain, both loop bandwith and damping factor change with received SNR in a manner that optimizes the loop characteristics for minimum phase error. A plot of loop bandwidth and damping factor versus SNR is shown in Fig. 12. The use of an integrator as the loop filter results in negligible accumulated phase error at the extremes of the ± 150-kc tracking range.

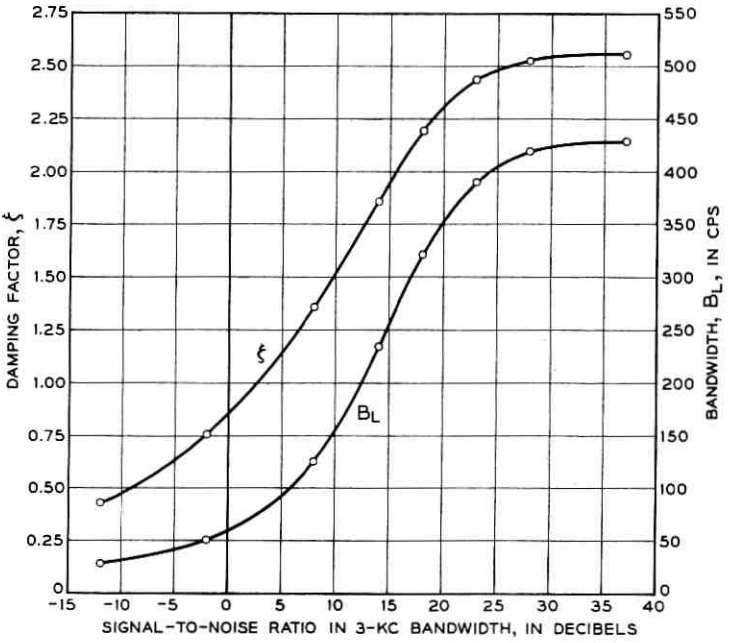

Fig. 12 — Loop bandwidth and damping factor vs signal-to-noise ratio.

During frequency acquisition the integrator is automatically preset to a voltage equivalent of 3 kc below the frequency indicated by the acquisition receiver and swept, by means of a dc voltage applied to the integrator through a separate input resistor, to the equivalent of 3 kc above indicated frequency. When phase lock occurs, the sweep is automatically disabled. The choice of one of four sweep rates is based on predicted signal strength. Manual preset and sweep controls are also provided.

The variable frequency element in the phase-lock loop is a voltage-controlled crystal oscillator (VCXO) with a stable center frequency of 10.83 mc. To permit accurate transfer of frequency acquisition information from an independent source, the voltage-frequency linearity is held to ±1 per cent of a straight line function having a slope of 2.5 kc/volt over a ±25-kc range. The unit is a commercially obtained solid-state device packaged in an oven.

The 10.83-mc (±25 kc) oscillator output is multiplied to 64.98 mc ± 150 kc by a tripler and a doubler. Three separate output stages are provided to drive the three balanced mixers at +20 dbm.

Performance of the phase-lock loop has demonstrated a capability of holding peak phase errors to a level of less than ±10 degrees over the full dynamic range of tracking conditions encountered in the PT. Good coherent detection of azimuth and elevation error signals, with the associated benefits accrued in the low SNR region, is thus assured.

4.6 *Automatic Gain Control*

Because of the phase relationships established by the crystal filters in the 5-mc IF amplifiers, the AGC phase detector provides coherent detection of the peak amplitude of the sum IF signal. The gain of the detector differential amplifier is such that a +13 dbm IF signal produces +25 volts output.

A simplified version of the AGC amplifier and loop filter is shown in Fig. 13. A dc operational amplifier, with current booster, is operated as an integrator. An adjustable limiter is provided to limit the maximum positive output voltage, thus limiting the maximum receiver gain. The +25-volt AGC detector output is compared with a nominal −25 volts in the input summing network to provide the necessary error signal for loop operation. The diodes in the capacitor feedback circuit switch an additional capacitor into the loop during signal increase to equalize loop response times for increasing and decreasing signals. Integrator time constants result in a closed-loop cutoff frequency of approximately 3 cps. Because of the extremely high dc loop gain provided by the opera-

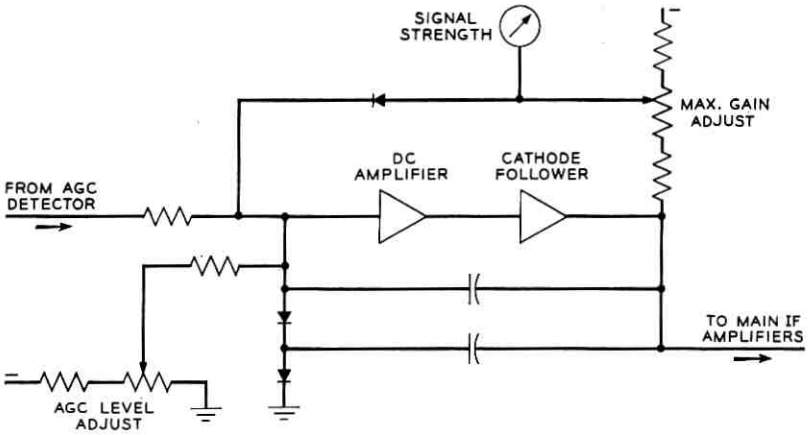

Fig. 13 — AGC amplifier and loop filter.

tional amplifier, there is negligible change in detected signal level over the entire range of gain control.

4.7 *Angle-Error Detectors*

As in the AGC detector, the azimuth and elevation phase detectors provide coherent amplitude detection of the 5-mc IF signals. The polarity of the detector output depends upon the direction of the antenna pointing error.

The prediction program, which employs the PT data, is particularly sensitive to bias errors in the angular position data obtained in the process of tracking. Bias errors of large magnitude could occur in angle-error detectors and dc circuits associated with the detectors. A commutation technique used in the tracking receiver to eliminate these errors is shown in Fig. 14. The phase of the 5-mc IF error signal is periodically reversed by the switching action of diodes in the secondary of a balanced transformer, initiated by a square wave generated at about 50 cps. As a result, the detector output becomes a square wave containing the angle error information in its amplitude. A capacitor blocks any dc bias content and couples the square wave for amplification and synchronous demodulation in a carefully balanced ring demodulator, using the same switching square wave as reference.

Detector and demodulator gain constants, together with the antenna difference pattern slope factor, result in a nominal 7.14-volt/degree pointing error scale factor at the antenna servo input. Some gain adjust-

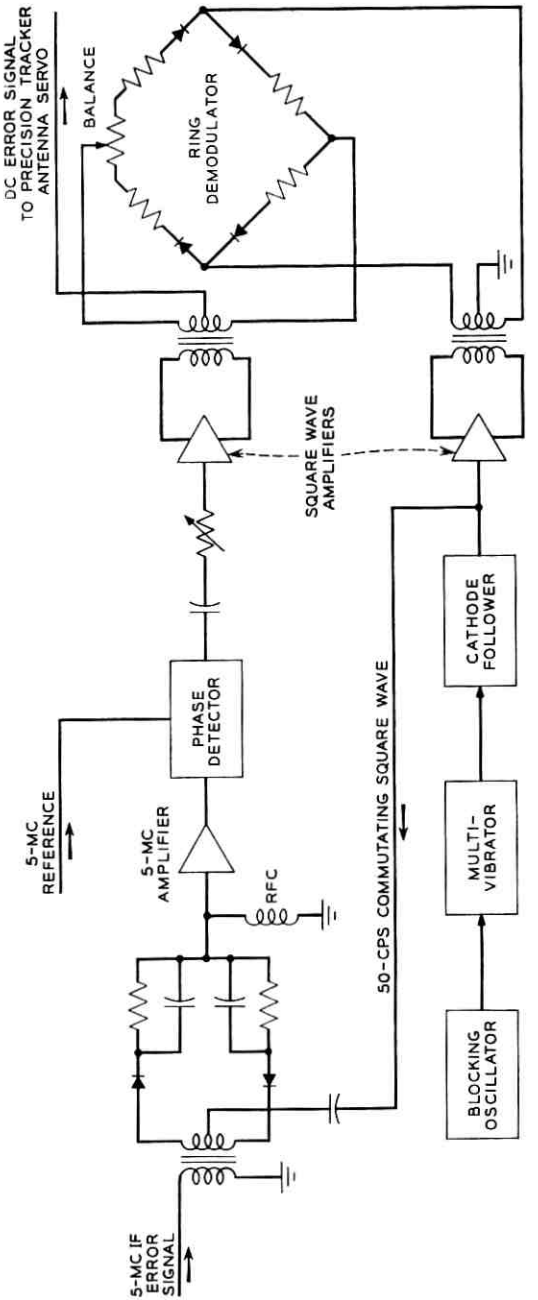

Fig. 14 — Angle-error detector commutation.

ment is provided at the demodulator input for over-all antenna servo loop gain adjustment.

V. ANTENNA POSITIONING SYSTEM

5.1 *General Description*

The antenna positioning circuits permit automatic, manual, or test control of the PT antenna. The positioning circuits consist basically of similar azimuth and elevation servo loops, which operate antenna drive motors.

In the automatic tracking mode of the precision tracker, antenna positioning data for the servo loops are in the form of azimuth and elevation error signals from the tracking receiver. Before these signals can be generated, however, the precision tracker must acquire the 4079.73-mc beacon signals from the Telstar spacecraft. To do this, input data from the track digital control or the command tracker drive the antenna positioning circuits.

During the initial stage of satellite acquisition, azimuth and elevation error signals from the track digital control point the PT antenna to the predicted position of the satellite, as described in Ref. 2. When the 4079.73-mc beacon signal is acquired by the precision tracker, the scan program is automatically stopped, the antenna positioning circuits of the precision tracker switch to the automatic tracking mode, and pointing signals from the command tracker are automatically removed.

During its acquisition and tracking operations, the precision tracker uses data on the predicted range of the satellite to optimize the frequency search rate in the tracking receiver and the bandwidths in the antenna positioning circuits. Normally, the range data are supplied in printed form by the on-site data processing system prior to the pass.

Once the 4079.73-mc beacon signal from the satellite has been acquired and the antenna positioning circuits are operating in the automatic tracking mode, the precision tracker can supply precise azimuth and elevation data to the antenna pointing system and to the data processors via the track digital control.

If because of some external or local disturbance, the precision tracker should lose autotrack, the 4079.73-mc signals may be reacquired in several ways. The precision tracker again may be slaved to the command tracker (if the CT itself is still in autotrack); the PT antenna may be repointed with predicted satellite position data from the track digital control; or the precision tracker may be placed in the manual tracking

mode. During reacquisition by any of the above means, manual or automatic scanning may be employed.

The antenna positioning circuits can be operated in any one of the following six modes:

(1) manual (test and backup acquisition mode)
(2) aided (test mode)
(3) track digital control (acquisition mode)
(4) autotrack (operational mode)
(5) command tracker (acquisition mode)
(6) remote (test and maintenance mode).

5.2 *Servo Drive Circuits*

Basically, each of the antenna positioning circuits comprises a main servo drive circuit and several servo control circuits, as shown in Fig. 15. Since the antenna positioning circuits for azimuth and elevation are electrically similar, Fig. 15 is applicable to both circuits. The main servo drive circuit is shown outlined in heavy brackets. All other circuits, outlined in light brackets, are a part of the servo control circuits.

The main servo drive circuit amplifies relatively low-level control signals to the higher power levels required to position the PT antenna mechanically. The circuit consists essentially of an input network, preamplifier, four magnetic amplifiers, four drive motors, and four tachometers.

The input network consists of three low-pass filters. One of these 0-6-0-6 db/octave filters is selected for insertion in the track loop, depending upon the range between the tracker and satellite. The widest bandwidth filter is used for the low-range, fast-moving portion of the pass, while the lowest bandwidth is used during the early, long-range portion of the pass. An additional 6-db/octave roll-off is present because of the servo closed-loop motor-tachometer combination. The 6-db/octave roll-off causes the servo to be of the velocity type 1 variety. Table VII shows a plot of open-loop gain versus frequency, and lists some of the associated parameters of the servo system.

5.3 *Manual and Aided Modes*

The manner in which the control signals are generated depends on the PT mode of operation. During either the manual or the aided mode, the control signal is generated by means of a handwheel mounted on the PT control console. During the manual mode, rotation of the handwheel generates a drive signal, which represents desired speed and direction

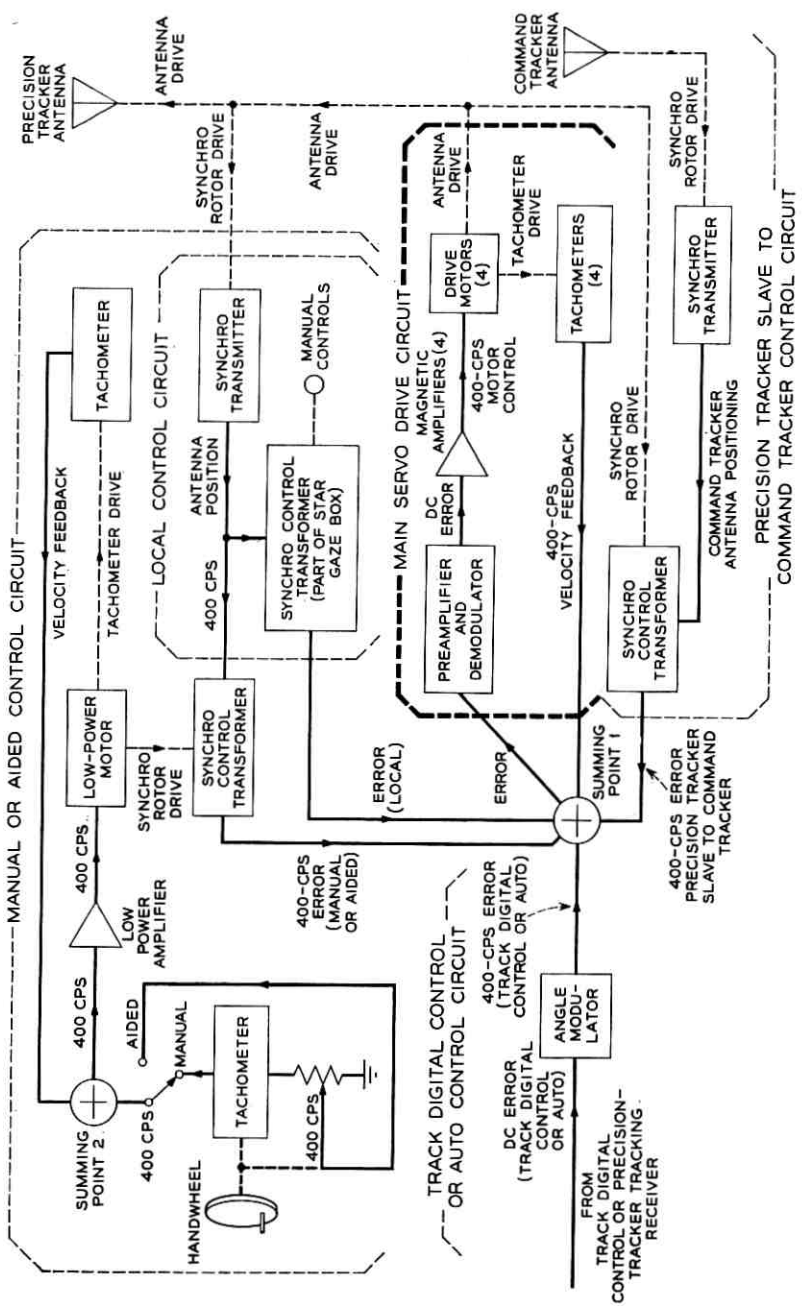

Fig. 15 — Antenna positioning circuits, azimuth or elevation.

TABLE VII — SERVO TRANSFER FUNCTION AND CONSTANTS

Open-Loop Transfer Function

$$G = \frac{\left(\frac{S}{\omega_2} + 1\right)}{\left(\frac{S}{\omega_0}\right)\left(\frac{S}{\omega_1} + 1\right)\left(\frac{S}{\omega_3} + 1\right)}$$

Closed-Loop Transfer Function

$$K = \frac{\left(\frac{S}{\omega_2} + 1\right)}{\left(\frac{S}{\omega_2} + 1\right) + \frac{S}{\omega_0}\left(\frac{S}{\omega_1} + 1\right)\left(\frac{S}{\omega_3} + 1\right)}$$

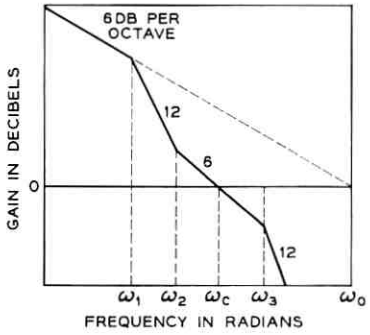

Constants

	Range (miles)			
	400–800	800–1700	1700–3500	3500–7000
Scan Rate (sec/revolution)	2	3	4	6
ω_1	0.046	0.012	0.0021	0.0021
ω_2	1.5	0.76	0.31	0.31
ω_3	150	150	150	150
ω_0	200	200	200	200

Scan Radii

Step	Degrees
0	0
1	1.4
2	2.8
3	4.2

of antenna movement. During the aided mode, an angular displacement of the same handwheel generates a constant-rate signal, which represents desired rate and direction of antenna movement. Either signal (depending on the selected mode) is amplified and applied to a low-power motor. The motor, in turn, physically positions the rotor of a synchro transformer. The position of the rotor of the control transformer represents desired antenna position. A second input to the same control transformer is an electrical input to its stator, representing actual antenna position as sensed and transmitted by a synchro transmitter that is geared to the PT antenna. The output of the control transformer represents an error between the desired antenna position and the actual

antenna position. This error signal, called "error (manual or aided)" on Fig. 15, is injected into summing point 1, where it becomes the error signal in the main servo drive circuit.

5.4 *Track Digital Control and Autotrack Modes*

During either the track digital control or the autotrack mode, the control signal is generated by circuits external to the antenna positioning circuits. The track digital control signal originates in the track digital control portion of the antenna direction system, and the autotrack signal is developed within the PT tracking receiver. Each is a dc voltage representing an error in desired antenna position. The dc voltage is converted into ac voltage by the angle modulator and is inserted into summing point 1, where it becomes the error signal within the main servo drive circuit.

5.5 *Command Tracker Mode*

During the command tracker mode, a synchro link between the precision tracker and the command tracker is used to control the main servo drive circuit of the PT. A synchro transmitter within the command tracker senses the position of the command tracker antenna and transmits this information to a synchro control transformer within the PT. The output of the synchro control transformer, representing the error between the PT and command tracker antenna shafts, is injected into summing point 1 as the error signal within the main servo drive circuit.

5.6 *Remote Control Mode*

In the remote mode, the antenna can be positioned by use of a portable control unit called the "star gaze box," which is connected by cable to the antenna base. Manual controls mounted on the star gaze box enable the operator to choose two types of control: (a) He can rapidly slew the antenna by means of switches that introduce a constant error signal into the main servo drive circuit via summing point 1. The error persists as long as the slew switch is depressed. (b) He can gently position the antenna by means of a control knob that controls the rotor of a synchro control transformer mounted in the star gaze box. A second input to the same control transformer senses actual antenna position as given by a synchro transmitter geared to the antenna. Any difference between desired antenna position, as represented by the position of the manually controlled rotor of this control transformer, and actual antenna position,

as received from the synchro transmitter, generates an error, which is fed into summing point 1 and then into the main servo drive circuit. The error persists until the antenna moves to the desired position.

5.7 *Search Scan*

In order to enhance the satellite acquisition capability of the precision tracker, the PT antenna beam can be caused to search about the mean azimuth and elevation angle to which it is pointed. The search is the result of a circular motion of the PT antenna and is controlled (either manually or automatically) by the scan control circuits located in the PT control console.

The PT antenna, as mentioned above, is positioned by two independent servo systems, one for the azimuth angle and one for the elevation angle. A separate error signal within each servo system controls antenna position in each angle. Since the PT antenna is a two-axis system, simultaneous motion in both axes is necessary if a circular pattern is to be traced about the mean angle. This is achieved by the superimposing of small offset (or bias) errors onto the main error signal in each servo system. The biasing errors are developed by the rotating rotor of a resolver, which is the key component in the scan control circuits.

Both the radius and the frequency (or period) of the circular search must also be controlled. The radius is controlled by the amplitude of the bias signals applied to the two servo systems. A choice of one of four different preset radii is available to the console operator. The desired radius is selected by means of the scan step control indicator mounted on the console. The period is established by the rate of rotation of the rotor of the resolver, which depends on the scan mode of operation.

During manual scan, the period of the PT antenna circular search is controlled by the scan handwheel drive (refer to Fig. 16). Rotation of the handwheel causes a generator to produce a voltage proportional to the speed of rotation of the handwheel. This voltage is combined with velocity feedback voltage and sent to the low-power amplifier as a motor control voltage. The motor drives the rotor of resolver B_2 at a speed proportional to the original speed of handwheel rotation and thus establishes the period of circular search. The two quadrature voltages taken from the rotor of the resolver are sent to the switch assembly, where their amplitude is regulated by the radius of scan selected by the console operator.

During the automatic scan mode, the period of the PT antenna's circular search is controlled as a function of range to ensure a good probability of beacon signal detection. At short ranges, when the satellite

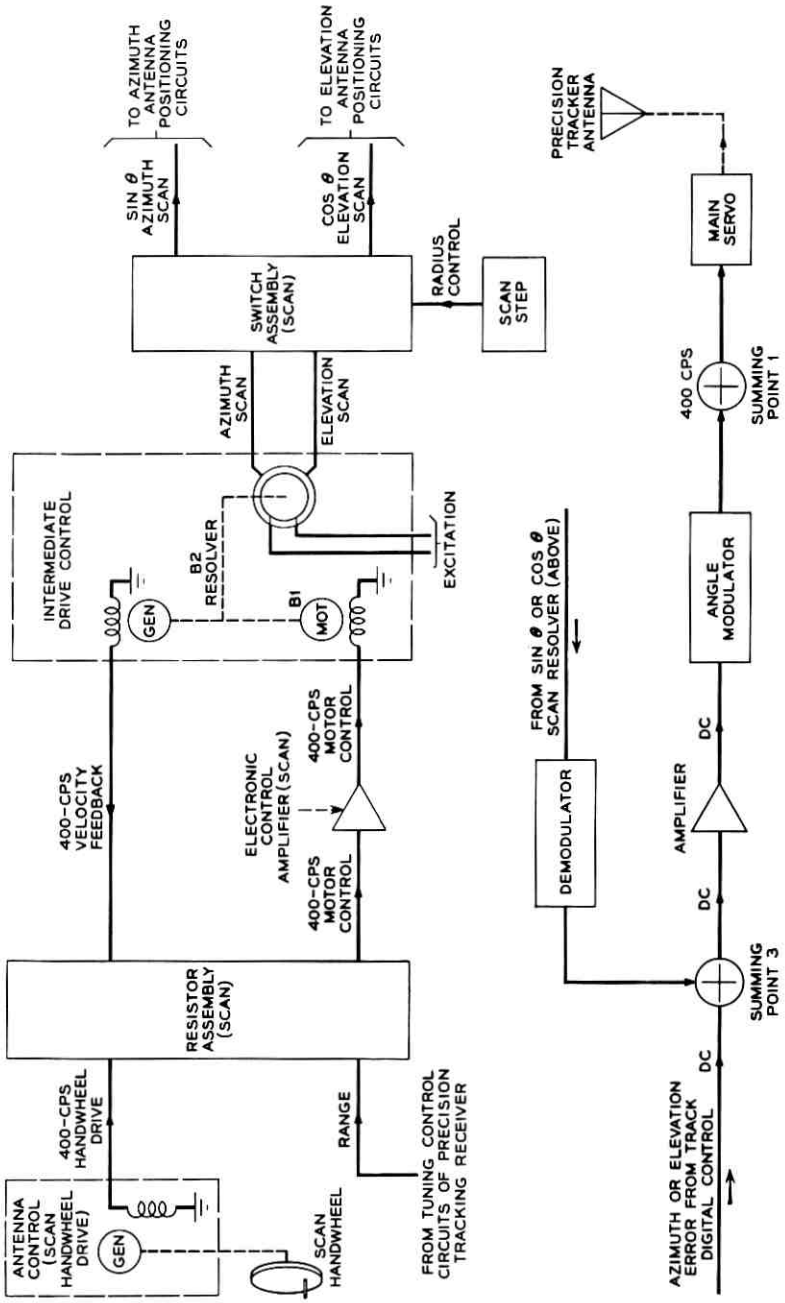

Fig. 16 — Scan control circuits.

has a high angular velocity, the antenna scans rapidly in order to search the area around the satellite. However, at longer ranges, when the angular velocity of the satellite is slower but the beacon signal strength is weaker, the antenna must search more slowly to ensure the same probability of detection.

When the track digital control mode is utilized, the orthogonal resolver rotor outputs are sent to a demodulator for conversion to a dc voltage. The automatic scan signal is then combined at summing point 3 with the track digital control error signal and converted to an ac signal in the angle modulator. This error signal is sent to the main servo drive circuit for use in positioning the antenna.

If the manual or command tracker mode has been selected, the resolver rotor output is sent directly to azimuth and elevation summing point 1.

5.8 *Data Take-Off*

The precise readout of PT azimuth and elevation angles is accomplished by 1-speed and 64-speed resolvers and analog-to-digital encoders contained in data transmitter gear boxes geared to the PT's precision data gears. These resolvers and encoders are essentially a remote extension of the track digital control and are described in another paper.[7]

VI. ACQUISITION RECEIVER

6.1 *General Description*

Owing to such factors as Doppler frequency shift and satellite oscillator drift, the frequency of the beacon signals from the Telstar spacecraft may deviate by as much as ± 150 kc about the 4079.73-mc design center frequency. The acquisition receiver (bays 1, 2, 3, 4, and 6 of Fig. 8) is employed to detect the actual received frequency and to provide an analog of this frequency for initial tuning of the phase-lock tracking receiver.

The requirement of tuning to the Doppler shifting received frequency within the period of time that the narrow antenna beam is crossing the satellite demands a rapid determination of received frequency. This is accomplished with a stationary search by use of a comb filter bank conducting a parallel observation of the frequency spectrum.

In the acquisition receiver, the sum IF signal is amplified, converted to 2.15 mc, and applied to a comb filter bank. This frequency-detection circuit consists of 300 channels housed in three cabinets, 100 in each

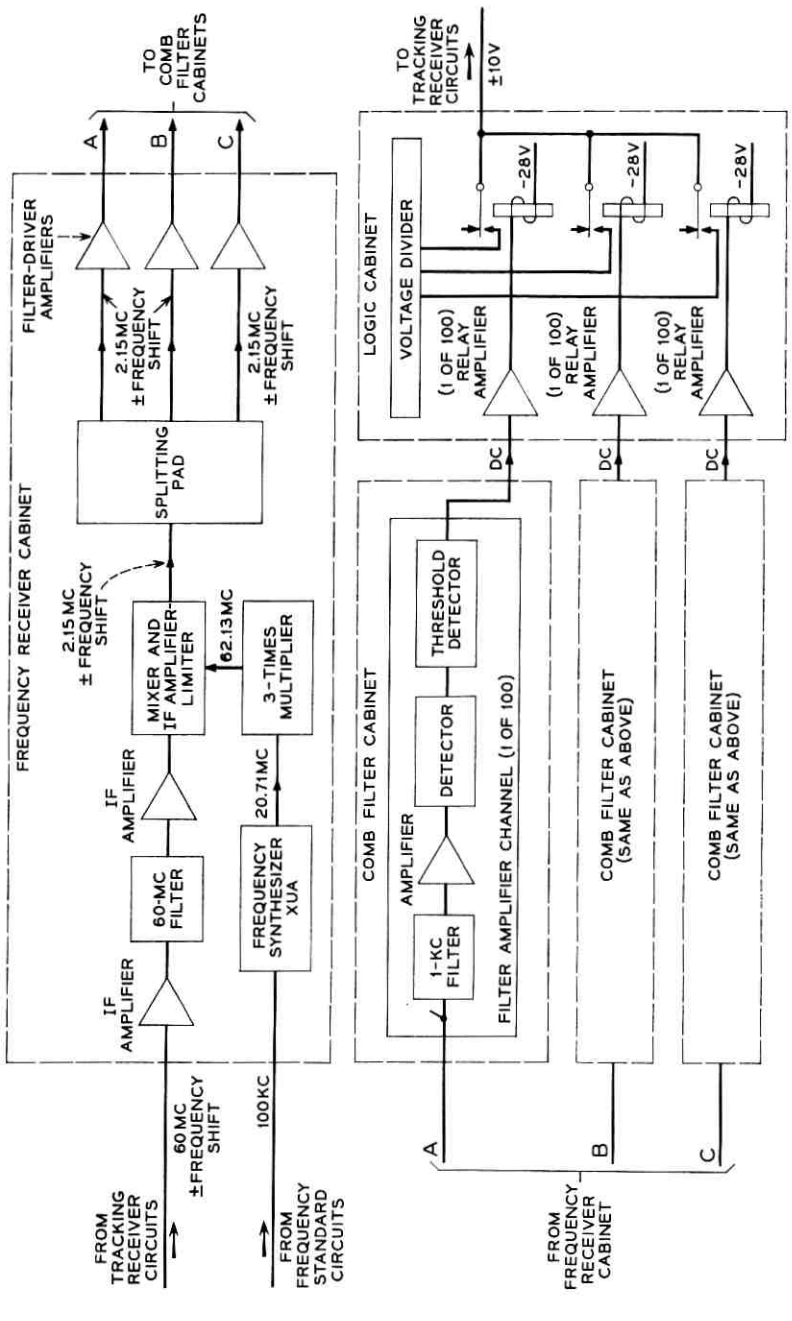

Fig. 17 — Acquisition receiver, block diagram.

cabinet. Each channel includes a narrow-band (1 kc at −1 db) crystal filter, an amplifier, a detector, a low-pass filter and a threshold circuit. All 300 detection channels are identical except that the crystal filters are cut to different center frequencies. (Filters are arranged to give a continuous coverage across the band.)

An incoming signal at the PT antenna that is within the range of 4079.73 mc ± 150 kc and is equal to or greater than noise in a 1-kc band will activate one of the comb filter channels. Overlap of the filter band-pass characteristics may cause two adjacent channels simultaneously to energize the associated threshold indicators. Normally, no more than two channels will pass a signal simultaneously. The operated channel will feed a signal to an associated relay amplifier located in the logic cabinet.

Logic circuitry determines which channel contains the received signal, disables all channels except this one and the two adjacent, and provides an analog output voltage proportional to signal frequency deviation. This voltage is supplied to the tuning control operational amplifier in the tracking receiver in order to bring a voltage-controlled crystal oscillator within the pull-in range of an automatic phase-lock loop. Once the phase-lock loop of the tracking receiver is locked, the logic input is disconnected and the frequency acquisition receiver performs no active function in the tracking. However, the acquisition circuitry is still active and can be utilized if tracking is lost. The output voltage from the acquisition receiver circuits also is sent, as an indication of received frequency, to the autotrack equipment.

6.2 *59.98-mc Amplification and Conversion*

Fig. 17 is a block diagram of the acquisition receiver. The acquisition receiver accepts 59.98-mc intermediate frequency signals and noise from the tracking receiver circuits. The two 59.98-mc IF amplifiers amplify the IF signal and noise from the sum IF amplifier in the tracking receiver circuit. The 59.98-mc narrow-band filter band limits noise to prevent overloading of the second IF amplifier.

The frequency synthesizer, synchronized to the 100-kc frequency standard, produces a signal of 20.71 mc. This signal is tripled by the 3× multiplier, which feeds a 62.13-mc signal to the mixer. The mixer produces a nominal frequency difference signal of 2.15 mc. Because of the Doppler shift in the beacon signal, the 2.15-mc signal will shift by a like amount. However, this shift will not exceed ±150 kc, which defines the limits of the comb filters.

TABLE VIII — ACQUISITION RECEIVER LEVELS

Unit	Gain (db)	Nominal Bandwidth (mc)	Minimum Signal Level (dbm)
Parametric amplifier	+18	20	−139
Mixer preamplifier	+25	8	−119
Cable	−5		−94
59.98-mc IF amplifier	+70	10	−99
59.98-mc filter with pads	−15	1	−29
59.98-mc IF amplifier	+45	10	−44
Mixer, amplifier, limiter	+50	600 kc	+1
Driver			3v rms
Comb filter			22v rms

6.3 *2.15-mc Amplification and Limiting*

The mixer output is amplified to a power level sufficient to "hard" limit the noise. In effect, the zero crossings are preserved but the peaks are clipped. The limiter output, consisting of signal plus noise, is fed to three filter driver amplifiers, which, in turn, drive the remainder of the acquisition receiver circuits.

The limiter is incorporated to establish a uniform noise threshold across the 300-kc filter bank, resulting in a constant false-alarm rate. This permits signal detection close to threshold in all channels, thus improving detection probability and simplifying logic design. After limiting, additional amplification is necessary to provide a suitable level of output to the filter driver amplifiers. A noise level set potentiometer sets the gain between the limiter and output to the comb filters. The bandwidth of each stage between the mixer and limiter is 1 mc with an over-all bandwidth of 600 kc at 3 db.

Further amplification is necessary to supply noise at the proper level for the comb filters. This is accomplished by the three filter driver amplifiers, each of which feeds the 100 filters contained in one cabinet.

6.4 *Comb Filter Channels*

Each filter-amplifier channel in the system contains a crystal filter, a two-stage amplifier, a detector, a post-detection filter, an amplifier, and a threshold circuit. The signal plus noise is filtered, amplified, and sent to the envelope detector. At this point the signal plus noise enters a 10-cps post-detection filter, after which it is amplified and compared with the threshold voltage. If its level exceeds that of the threshold voltage, the detected and amplified signal drives saturated solid-state amplifiers to provide a "signal present" dc output of −10 volts.

6.5 *Logic Circuits*

Each of the 300 comb filter channels terminates in the logic cabinet at a relay channel consisting of a transistor amplifier and relay. The relays, when operated, provide a contact closure which ties the precision voltage divider to the phase-lock loop in the track receivers of both the PT and the autotrack. In addition, the logic cabinet locks out all comb filter channels except the channel indicating a signal present and those adjacent to it. The logic circuits will follow a Doppler shifting signal and progressively lock out past adjacent channels and unlock new adjacent channels. A third feature provides a scan freeze indication to the servo scan circuits when a signal is present, in order to stop angular search.

Tests have indicated a reliable detection threshold better than -143 dbm, with a usable limit around -147 dbm, as observed during a moon bounce experiment between Holmdel and Andover.

VII. FREQUENCY STANDARD AND TEST SIGNAL

7.1 *General Description*

The frequency standard cabinet (bay 7, Fig. 8) contains circuits designed to provide stable frequencies to the precision tracker for use as local oscillator injection and testing signals. In addition, this cabinet generates the primary and secondary frequency and time references used throughout the satellite communications ground station. These references are used to adjust the station clock to the Naval Research Laboratory cesium standard at Bethesda, Maryland.

7.2 *Basic Standard*

The basic 100-kc frequency is generated in a standard master oscillator, which is in turn referenced to the VLF 18-kc Naval Station NBA. A VLF phase comparator (see Fig. 18) accepts the standard master oscillator 100-kc output and compares this frequency with an 18-kc signal received from NBA. The resultant phase difference is recorded on a strip-chart recorder. The VLF receiver also develops an audio 1-second time tick for use in the station clock. The standard master oscillator uses a highly accurate, comparator-controlled, quartz oscillator to generate a 1-mc signal. Other circuitry within the standard master oscillator utilizes the 1-mc signal in the generation of the standard 100-kc and 5-mc signals. These two signals are applied to the dis-

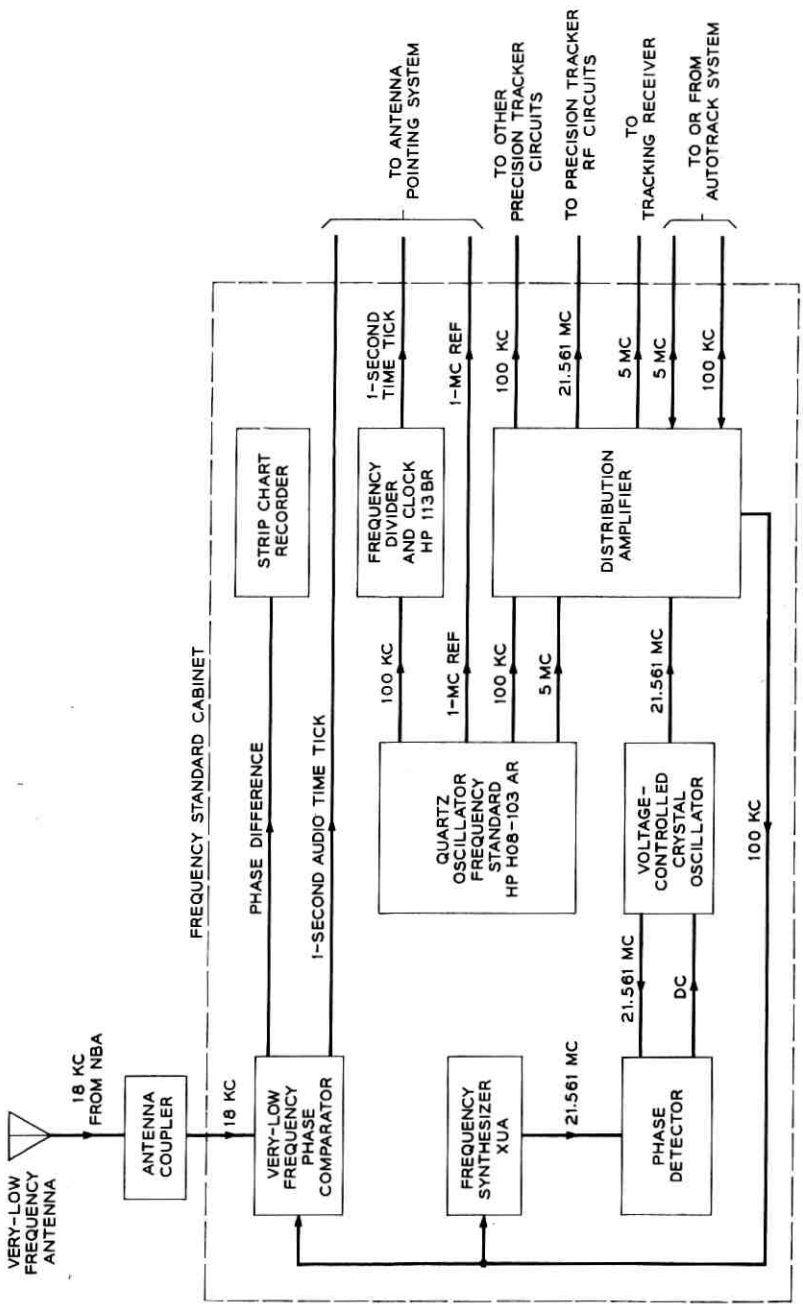

Fig. 18 — Frequency standard circuits, block diagram.

tribution amplifier, which provides amplification necessary to distribute the standard frequencies as needed throughout the PT. The 100-kc signal is also applied directly to the frequency divider and clock.

The frequency divider and clock utilizes the 100-kc signal from the standard master oscillator in the generation of a 1-second time tick. This signal is fed out of the precision tracker to the antenna pointing system along with the 1-second time tick from the VLF phase comparator for comparison purposes. An adjustment within the frequency divider and clock corrects any time deviations from NBA time. A time readout located in the unit is also driven by the 100-kc input signal.

7.3 *Local Oscillator Signals*

A 21.561-mc signal from the frequency standard cabinet is sent to a harmonic generator, which multiplies this signal 192 times to give a 4139.71-mc local oscillator frequency for use in mixing the incoming beacon frequency (4079.73 mc), to give an IF frequency of 59.98 mc. Any variation in the initial 21.561-mc signal will be multiplied 192 times, directly affecting the stability of the track and frequency acquisition receivers. A phase-lock loop is used to minimize the variation; it consists of a frequency synthesizer, a phase detector, and a short-term, stable voltage-controlled crystal oscillator (VCXO). The frequency synthesizer derives a 21.561-mc signal from the basic standard master oscillator 100-kc output. This 21.561-mc signal is compared in the phase detector circuit with the 21.561-mc output of the VCXO.

The frequency multiplier which converts the 21.561-mc signal to 4139.71 mc is a solid-state harmonic generator consisting of two 2× multipliers, a power amplifier, a low-frequency 4× multiplier using a varactor diode in shunt configuration, a quadrupler using a self-biased diode operated in a series configuration, and a microwave tripler. The harmonic generator is designed for an input from a 50-ohm source of from 3 to 5 mw at 21.561 mc and delivers 15 mw at 4139.71 mc into a 50-ohm load.

The frequency receiver cabinet receives the 100-kc standard master oscillator signal for use in deriving the frequency acquisition receiver local oscillator injection signal. A frequency synthesizer receives the 100-kc signal and develops a 20.71-mc signal. The 20.71-mc signal is tripled to a frequency of 62.13 mc and then inserted in the local oscillator port of the frequency acquisition mixer.

Table IX shows the output levels and accuracy of each frequency discussed above.

TABLE IX — FREQUENCY GENERATION

Frequency (mc)	Cabinet	Level	Accuracy	Application
18 kc	Frequency standard	>0.1 μv	$1:10^{11}$	NBA reference
100 kc	Frequency standard	1v rms	$5\ 10^{10}$	Second LO injection frequency acquisition IF test
5	Frequency standard	1v rms		Coherent phase detection
20	Test signal	0–1v rms (0.4v nom)	Short term $1:10^{10}$ Long term $5:10^{10}$	IF test
20.71	Frequency receiver	0–1v rms (0.4v nom)		Second LO injection for frequency acquisition
21.561	Frequency standard	50 mw in 50 ohms	Long term $5:10^{10}$ Short term $1:10^{7}$	First LO injection for track receiver
60	Receiver	1–2.8v rms in 50 ohms		IF test
62.13	Frequency receiver	1–2.8v rms in 50 ohms	Long term $5:10^{10}$ Short term $1:10^{10}$	Second LO injection for frequency acquisition
4079.73	Test signal	0 dbm	$\pm 0.001\%$/day	RF test
4139.71	RF assembly	5 mv in 50 ohms	Long term $5:10^{10}$ Short term $1:10^{7}$	First LO injection for track receiver
Time				
1-sec audio tick	Frequency standard	1v in 600 ohms 450 msec	Same as NBA	Coarse time for station clock
1-sec tick	Frequency standard	2v in 50 ohms 200 μsec	Same as NBA	Reference time for station clock

7.4 *RF Test Signals*

The test signal cabinet contains circuits designed to provide a 4079.73-mc frequency for use as a simulated satellite beacon signal. This signal is sent through a pressurized semirigid Heliax coaxial cable to a boresight tower test horn antenna located 300 feet from the PT track mount and 600 feet from the test signal cabinet. A TD2 harmonic generator is used to generate the microwave CW test signal. The generator may be turned on and off locally at the test signal cabinet or remotely at the PT control console. A directional coupler (see Fig. 19) provides a sampling take-off for a power meter. This measurement is made to validate receiver sensitivity checks made by use of the test tower.

A phase-coherent 20-mc test signal is also developed in the test signal cabinet (Fig. 20). A 100-kc input from the standard master oscillator is

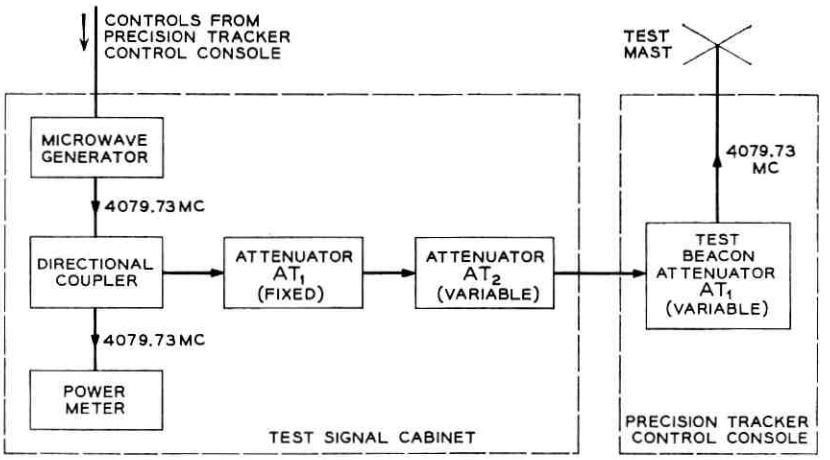

Fig. 19 — 4-kmc test signal circuits, block diagram.

multiplied to 20 mc in a frequency synthesizer. The 20-mc signal is fed to the track receiver cabinet and frequency tripled for use as a 60-mc IF test signal. A motor-driven chain drive is coupled to the frequency synthesizer to simulate Doppler shift for testing purposes.

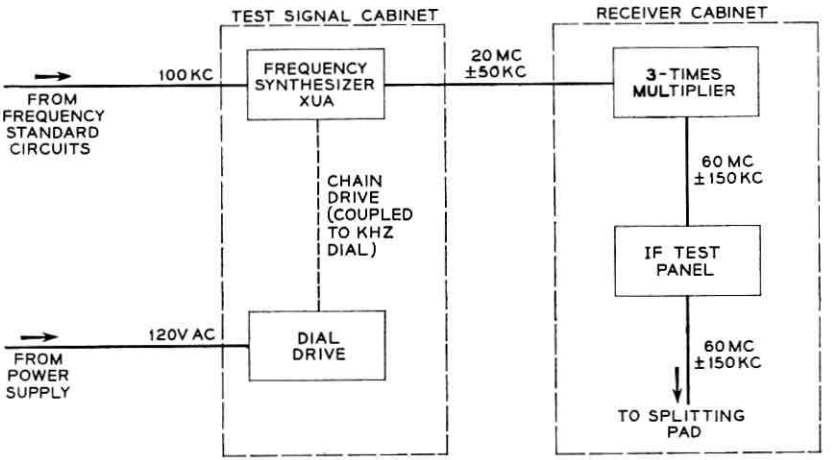

Fig. 20 — 60-mc IF test signal circuits, block diagram.

VIII. CONTROL CONSOLE

8.1 *Controls and Indicators*

Operating controls and indicators for the precision tracker are mounted on the PT control console (Fig. 21). Among the controls on the console are switches used to select mode of operation and input data source, handwheels used to point the antenna and scan the beam manually, and controls used to search in frequency. Indicators on the console include lamps showing PT and system status; meters showing azimuth error, elevation error, range, signal strength, and frequency deviation; and decimal readouts of station time and PT antenna angle data. In addition, an array of test function switching controls is located behind the upper right-hand door.

The various acquisition modes, discussed in Section V, are controlled at the console. The three operational groupings include elevation at the left, azimuth in the center, and frequency at the right. Experience has shown that only one operator, seated centrally before the azimuth position, is required. His duties are mainly to precondition the system before a pass and monitor the acquisition and tracking processes during the

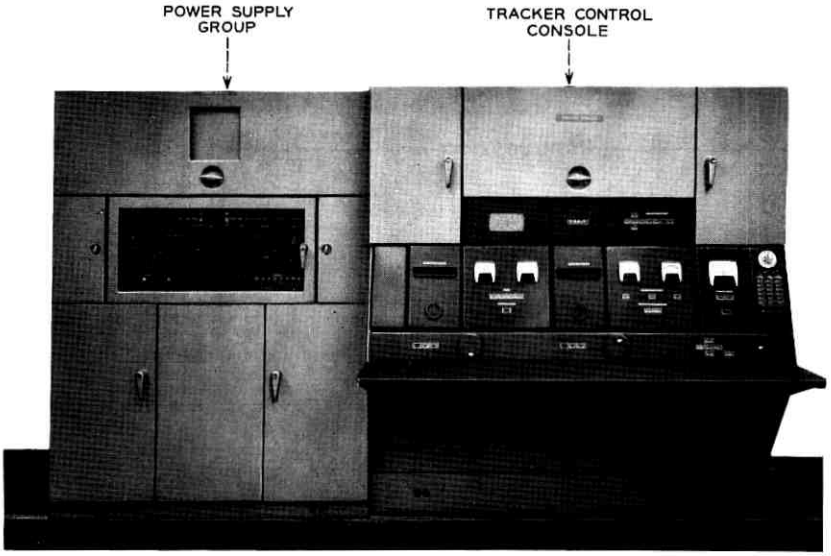

Fig. 21 — Console and power supply group.

pass. He can intervene to change modes or manually search in angle and frequency. The operator can read out Doppler shift, received signal strength, and tracking perturbations if requested by the tracking director.

8.2 *Power System*

The precision tracker uses both 120/208-volt, 400-cycle, 3-phase power and 120-volt, 60-cycle, single-phase power in its operation. The 400-cycle power is fed directly to the PT power control cabinet (Fig. 22) for operation of power supplies in the cabinet and for distribution to the antenna positioning circuits. "Technical" 60-cycle power is distributed from a wall panel to the acquisition and tracking receivers and to the frequency standard, VLF, and test circuits. "Utility" 60-cycle power is distributed from another wall panel to outlets in the PT equipment cabinets.

IX. ANTENNA ASSEMBLY AND TOWER

The physical specifications associated with the major structures of the precision tracker system are listed below.

(1) Antenna Assembly	
Weight	7000 pounds
Height, jack pads to elevation axis	11 feet 9 inches
Torques:	
Overturning, 60-mph wind	8700 ft-lbs
Overturning, 120-mph wind	27,200 ft-lbs
Rotational in horizontal plane	650 ft-lbs max.
(2) Antenna Tower (Fig. 22)	
Concrete with hexagonal cross section	
Height, base to elevation axis	35 feet 8 inches
Twist at 650 ft-lbs torque	0.05 milliradian max.
Sway	0.05 milliradian max.
Settling:	
Per day	0.03 milliradian max.
Limit	45 milliradians, total
(3) Test Tower	
Distance from antenna tower	300 feet
Height	60 feet
Twist in 40-mph wind	± 3 minutes max.
Sway at top in 40-mph wind	± 0.06 inch max.

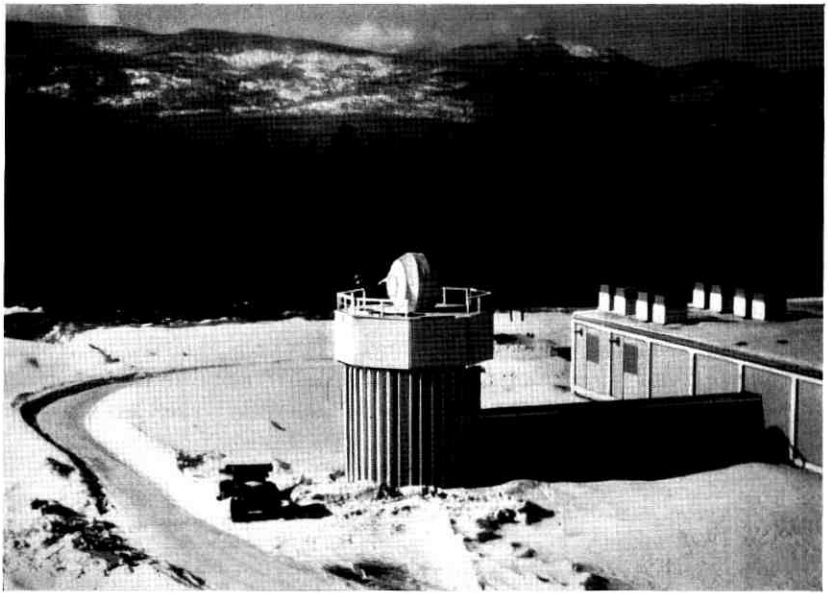

Fig. 22 — PT antenna tower at Andover, Maine, radome deflated.

X. TEST DATA AND OPERATING EXPERIENCE

10.1 *Operating Noise Temperature*

The input noise power from all sources including antenna, sky, and radome as measured by the CW signal substitution method is −138 dbm at an elevation of 0 degree. The measurement was made in the 3-kc bandwidth of the tracking receiver's sum channel to an accuracy of 0.9 db. The receiver noise figure, which was also measured, was found to be 3.1 db corresponding to a noise temperature of 315°K. The total effective noise temperature, for an elevation angle of 10 degrees, is estimated as follows:

Sky	13.5°K
Side lobes	2.5°K
Radome	9°K
Input temperature of receiver including comparator and fittings	315°K
Total at 10° elevation	340°K

The variation in system noise with elevation angle was also meas-

ured. This is shown in Fig. 7. The slight increase at the zenith is typical of a daytime measurement and is caused by coupling to the sun. Similar measurements made at night reveal the expected minimum at the zenith. −139 dbm is taken as a receiver signal power reference for a 0-db signal-to-noise ratio in the 3-kc bandwidth of the sum channel.

A careful measurement was made of the degradation in sensitivity with the parametric amplifiers bypassed. The increase in effective system input noise was measured as 7 db. This figure was obtained by relation of the signal-to-noise ratios obtained in each condition for the same fixed input signal level.

10.2 *Received Signal Levels*

Received signal levels for six typical passes of the Telstar spacecraft are plotted in Fig. 23. In this figure, signal level is plotted as a function of slant range, a technique adopted during the first days of tracking to enable on-the-spot checks of beacon transmitter and PT performance. The reference line is plotted as a 6-db per octave slope to account for variation in path loss with range; it assumes +17 dbm radiated beacon power and a truly isotropic antenna on the satellite. The 0-db SNR is based on the −139 dbm effective input noise power of the PT. The data were plotted point by point during each pass, taking slant range from the mission printout at the time of measurement; SNR was read from the calibrated signal strength meter on the PT console.

The measured SNR may generally be expected to fall below the reference slope. Variations in communications power from none to maximum may cause the beacon power to vary from the nominal +17 dbm to +15 dbm with full power in the communication channel. These variations appear on the measured SNR curves as the minor fluctuations departing from the generally smooth curve; they were correlated in time with the changing power levels indicated by the accompanying communication experiments during the first several passes.

The general trend of departure from the 6 db/octave slope is a function of the satellite's antenna pattern and the changing spin angle. Reference to the spin angle predictions and the antenna pattern showed a correlation within 1 db.

10.3 *Tracking Jitter*

The variation of angle tracking jitter with signal-to-noise ratio is shown in Fig. 24. The test consisted of tracking the RF test signal from the boresight tower. The data shown are for the azimuth coordi-

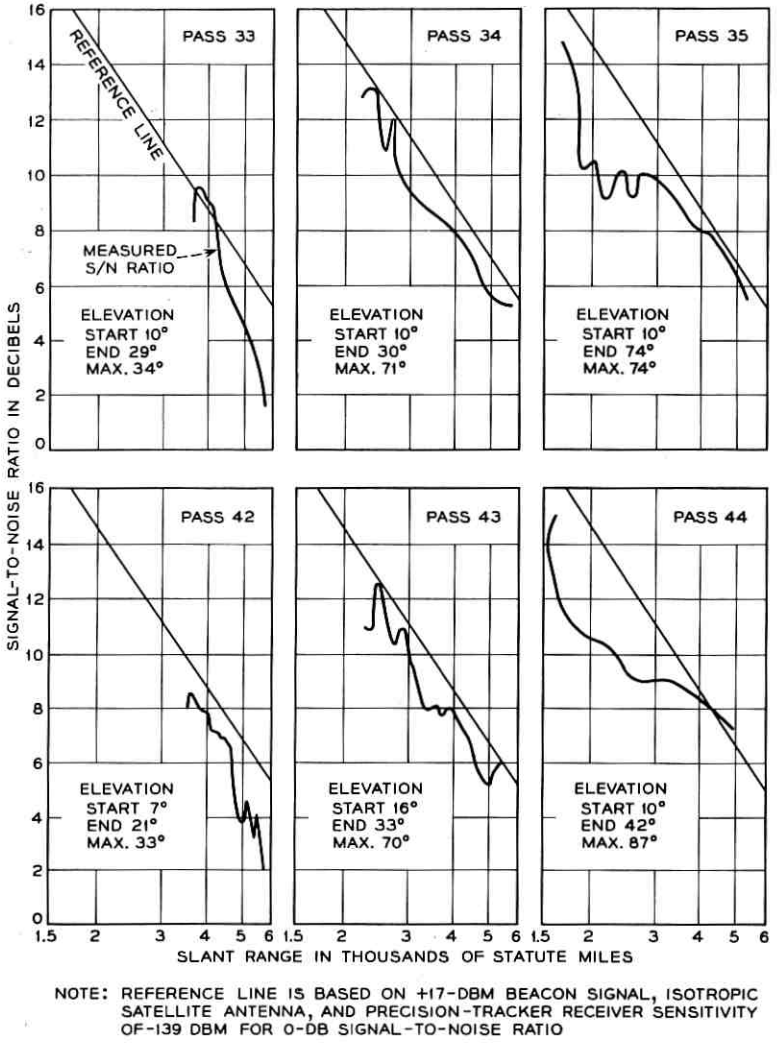

Fig. 23 — Received signal levels.

nate; the elevation data agreed more closely with the theoretical performance.[8]

10.4 *Phase Jitter and Frequency Measurements*

The coherence time, or phase jitter, of the beacon signal is a critical parameter in the performance of the PT and the autotrack. The phase-

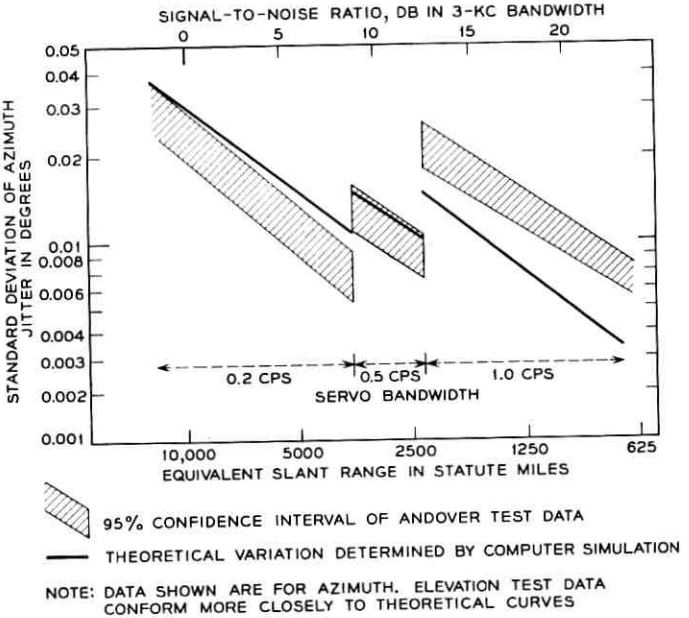

Fig. 24 — Angle tracking jitter.

lock loop of the PT tracking receiver has been employed to measure this parameter of different beacon sources, including models of the Relay and Telstar satellites and the Holmdel, N.J., 4079.73-mc transmitter employed to illuminate Echo I for tracking tests. In all cases, the jitter of the beacon signals made a negligible contribution to the total jitter in the phase-lock loop.

XI. ACKNOWLEDGMENTS

Credit for the successful completion of the precision tracker is due to many individuals and organizations. The staff of Wheeler Laboratories, Incorporated, designed and tested the Cassegrainian twist-reflector antenna and the microwave comparator/feedhorn assembly and provided valuable consultation throughout the program. Itek Corporation designed and produced the 300-channel comb filter. Mr. K. B. Woodard and members of his group were responsible for the mechanical design of the antenna, the RF assembly, and data units, and for testing the mechanical accuracy of the antenna assembly. Messrs. W. L. Nelson, R. W. Hatch, R. Lowell, L. H. Enloe, and R. H. Turrin made important

analysis and design contributions in the development of the phase-lock loop and coherent angle-error detectors.

REFERENCES

1. Davis, C. G., Hutchison, P. T., Witt, F. J., and Maunsell, H. I., The Spacecraft Communications Repeater, B.S.T.J., this issue, p. 831.
2. Githens, J. A., Kelly, H. P., Lozier, J. C., and Lundstrom, A. A., Antenna Pointing System: Organization and Performance, B.S.T.J., this issue, p. 1213.
3. Hannan, P. W., Optimum Feeds for All Three Modes of a Monopulse Antenna I and II, Trans., I.R.E., **AP-9,** 1961.
4. Rhodes, D. R., *Introduction to Monopulse*, McGraw-Hill, New York, 1959.
5. Reed, E. D., Diode Parametric Amplifiers — Principles and Experiments, Semiconductor Products, **4,** Jan., 1961, pp. 25–30, and Feb., 1961, pp. 35–42.
6. Nelson, W. L., Analysis of the Angle-Error Detection System for Automatic Tracking of *Telstar* Satellites, to be published.
7. Githens, J. A., and Peters, T. R., Digital Equipment for the Antenna Pointing System, B.S.T.J., this issue, p. 1223.
8. Ball, W. H. W., Analysis and Digital Simulation of the *Telstar* Precision Tracker, Paper No. CP-63-368, presented at the IEEE Winter General Meeting, New York, 1963.

Orbit Determination and Prediction, and Computer Programs

By A. J. CLAUS, R. B. BLACKMAN, E. G. HALLINE and W. C. RIDGWAY, III

(Manuscript received March 15, 1963)

Orbit determination and prediction programs are needed to generate ephemerides for the satellite. Orbit determination is from tracking data consisting of angles only, and is based on a modified version of a method by R. E. Briggs and J. W. Slowey of the Smithsonian Institution. Trends in the data due to perturbations from a Keplerian orbit are removed before this process, and estimates of the orbital elements from individual passes are combined statistically to produce refined estimates. Ephemeris calculation is by a semi-analytic method in which deviations from a Keplerian orbit are obtained by integrating the perturbing forces. The programs to implement these procedures have been written for both the IBM 7090 and the IBM 1620 computers.

I. INTRODUCTION

The following paper describes the methods and programs used in the Telstar project for the purposes of orbit determination and ephemeris calculation. The orbit determination process involves the computation of orbital elements from tracking data obtained during each pass, and subsequent refinement by combining such single-pass estimates. The tracking data are in terms of angular observations only. The ephemeris calculations involve standard procedures for computation of Keplerian orbits and perturbations due to the earth's oblateness.

It is well known that in the problem of orbit determination from angular data only, three observations (each observation consisting of two angles and a time) are not sufficient to determine an orbit if the three sightlines are coplanar. If the three sightlines are nearly coplanar, the computed orbital elements may reflect large uncertainties which are not necessarily due to observational errors. Hence, the method used is based on the determination of a set of orbital elements from four observations.

This method is a modified form of the method described in Ref. 1. In the modified form, initial estimates of the orbital elements are computed from the first and last of the four observations, supplemented by estimates of the ranges corresponding to them (Section 2.1). By a method of successive approximations the two ranges are adjusted until an agreement with the second and third observations is secured in a least-squares sense (Section 2.2).

With typically many more than four observations in one pass through the visibility zone of an angular tracker, the observations are divided into four nonoverlapping blocks, each block containing the same number of observations, N. Taking one observation at a time from each block, in serial order, N sets of orbital elements are computed. These N sets are combined into a single set of intrapass average orbital elements and an associated covariance matrix (Section III).

Trends in the data due to perturbations induced by the earth's oblateness are removed by a method which is essentially the same as that described in Ref. 2 (Section IV).

Sets of intrapass average orbital elements, and their associated covariance matrices, from two or more passes, are combined into a set of interpass average orbital elements and an associated covariance matrix (Section V). The method used is similar to the method described in Refs. 3 and 4, inasmuch as it was motivated by the desire to avoid the necessity of pooling all of the observational data from two or more passes in order to derive refined estimates of the orbital elements, as would have to be done in the classical "differential corrections" method commonly ascribed to K. F. Gauss (1777–1855). However, the method used differs from the referenced method in two respects, viz., (a) the covariance matrix associated with each set of intrapass average orbital elements is related to the actual observational data for the pass, and (b) the necessity of computing the partial derivatives of all of the observed angles (numbering $8N$ in each pass) with respect to each of the orbital elements is avoided. On the other hand, this method gives single-pass estimates of the orbital elements which are biased even when the observational errors are not biased. These biases may be appreciable for short passes associated with low altitudes of the satellite near perigee. Methods for removing or reducing these biases have been under study but were not ready for use before the launching of the Telstar satellite on July 10, 1962.

This orbit determination method was designed to permit effective antenna pointing operations with the use of a modest computing facility. The program implementation (Section VI) consists of two major

program subsystems. The first of these is the orbit determination program (Section VIII), which determines the characteristics of the satellite orbit from tracking information. The second program (Section IX) computes orbit predictions from a knowledge of these orbit characteristics. The operational results obtained in using these methods and programs are discussed (Section X).

II. ORBIT DETERMINATION FROM ANGLE-ONLY DATA

2.1 *Orbit Determination from Two Observations and Estimated Ranges*

Two observations (each observation consisting of two angles and a time) and estimates of the ranges (i.e., topocentric distances) along the two sightlines are sufficient to establish two points P_1 and P_2 through which an orbit can be passed at the times of observation by only one set of orbital elements. Denoting the geocentric distances by r_1 and r_2, and the geocentric angular difference by θ_{12}, we have

$$r_1 = \frac{a(1 - l^2 - m^2)}{1 + l}, \tag{1}$$

$$r_2 = \frac{a(1 - l^2 - m^2)}{1 + l \cos \theta_{12} + m \sin \theta_{12}}, \tag{2}$$

where

$$\begin{aligned} l &= e \cos \omega, \\ m &= e \sin \omega, \end{aligned} \tag{3}$$

a is the semi-major axis, e is the eccentricity, and ω is the argument of perigee referred to the first sightline. From (1) and (2), we have

$$\alpha_1 l + \alpha_2 m = \alpha_3 \tag{4}$$

where

$$\alpha_1 = \cos \theta_{12} - \frac{r_1}{r_2},$$

$$\alpha_2 = \sin \theta_{12},$$

$$\alpha_3 = \frac{r_1 - r_2}{r_2}.$$

It is convenient to regard either l or m as an independent variable. Actually, in order to avoid an indeterminacy and to improve accuracy,

preference is given to l if $|\alpha_1| \leqq |\alpha_2|$, and to m if $|\alpha_1| > |\alpha_2|$. In either case, the other two of the three quantities l, m, and a are determined by (1) and (4). These, in turn, through Kepler's equation, determine a travel time between P_1 and P_2. A search is then made for the value of l which gives the observed travel time. For bounded orbits (the only ones of interest for ground-to-ground communications) the search is confined to the interval (l_-, l_+), where

$$l_\pm = \frac{1}{\alpha_1^2 + \alpha_2^2}(\alpha_1\alpha_3 \pm |\alpha_2| \sqrt{\alpha_1^2 + \alpha_2^2 - \alpha_3^2}).$$

With a, l, m (hence also e and ω) determined, the time of perigee passage, τ, is determined through Kepler's equation.

2.2 *Orbit Determination from Four Observations*

The two observations involved in the procedure described in the preceding section are the first and last of a set of four observations. Subsequent to that procedure, the four angles corresponding to the times of the second and third observations are computed and compared with the observed angles. The sum, Φ, of the squares of the differences between the computed and observed angles is regarded as a function of the estimated ranges D_1 and D_4 associated with the first and last of the four observations. The quantity Φ is next minimized with respect to D_1 and D_4 by a method which is analogous to the classical "differential corrections" method. (With only three observations corresponding to coplanar sightlines there would be only one angular difference, and therefore D_1 and D_3 would be indeterminate.) This method involves the solution of two simultaneous equations which are linear in the corrections to D_1 and D_4, with coefficients which are quadratic in the first-order partial derivatives of the computed angles with respect to D_1 and D_4. The terms which do not involve the corrections to D_1 and D_4 are products of the first-order partial derivatives and the angular differences. Since the partial derivatives are functions of D_1 and D_4, the minimization of Φ is an iterative procedure which is terminated when the values of a, e, ω, and τ are sufficiently stabilized. Detailed formulas are given in Ref. 5.

With a, e, ω, and τ determined, the orientation of the plane through P_1, P_2, and the center of the earth gives the values of Ω and i, where Ω is the longitude of the ascending node and i is the inclination of the orbital plane.

III. ORBIT DETERMINATION FROM $4N$ OBSERVATIONS IN ONE PASS

The combined procedures described in Sections 2.1 and 2.2 are applied to as many sets of four observations as may be drawn from all of the reliable observations for each pass in accordance with the method of selection indicated in the third paragraph of Section I. The N sets of orbital elements are then combined into a single set of intrapass average orbital elements. In addition, an associated covariance matrix (an estimate of the variability of the mean in a sample of size N drawn from a correlated multivariate population) is computed in accordance with the standard formulas

$$\bar{C}_{\alpha\alpha} = \frac{\sum_{i=1}^{N} (\alpha_i - \bar{\alpha})^2}{N(N-1)}, \qquad \bar{C}_{\alpha\beta} = \frac{\sum_{i=1}^{N} (\alpha_i - \bar{\alpha})(\beta_i - \bar{\beta})}{N(N-1)},$$

where α stands for each of the six orbital elements (with average $\bar{\alpha}$), and β for each of the other five (with average $\bar{\beta}$).

A typical result of the single-pass routine, as described up to this point, is shown in Tables I and II. The orbital elements listed as "exact value" were used to generate tracking angles. These angles, combined with random errors from a normal population with a standard deviation of 0.2 milliradian, were processed. It may be noted that were it not for the strong correlation between some of the orbital elements, errors in

TABLE I

	Ω, degrees	i, degrees	a, feet	e	ω, degrees	τ, seconds
Exact value	144.4462	46.9190	31,567,194	0.240764	171.6756	47,953.227
Sample mean	144.4455	46.9184	31,573,342	0.240688	171.6349	47,950.120
Standard deviation of sample mean	0.0018	0.0018	6,212	0.000120	0.0374	2.852

TABLE II — CORRELATION COEFFICIENTS

	Ω	i	a	e	ω	τ
Ω	1	0.13189	0.64082	−0.57898	−0.67162	−0.64998
i	0.13189	1	−0.49292	0.52030	0.44004	0.47260
a	0.64082	−0.49292	1	−0.96559	−0.99058	−0.99680
e	−0.57898	0.52030	−0.96559	1	0.92798	0.94376
ω	−0.67162	0.44004	−0.99058	0.92798	1	0.99797
τ	−0.64998	0.47260	−0.99680	0.94376	0.99797	1

the elements of the order of the standard deviations shown could result in pointing angles for the same pass with errors as large as 10 times the standard deviation of the original tracking errors.

A caveat should also be noted with respect to the precision of computation of the covariance matrix. Any matrix which purports to be a covariance matrix must have a nonnegative determinant. Due to the high correlation among the elements a, e, ω, and τ, however, values of 10^{-8} for the determinant of the correlation matrix are common. Errors of the order of 0.1 per cent in some covariances could result in a matrix with a negative determinant. Such a matrix can still serve as a guide in judging the reliability of the orbital elements obtained, but the use of this matrix for interpass orbit refinement would very likely lead to absurd results, such as negative variances.

IV. TREND REMOVAL

Since the procedures described in Sections 2.1 and 2.2 are based on the assumption that the orbit is Keplerian, it is important to determine the extent to which it is necessary and sufficient to correct for deviations from that assumption. Such deviations, usually called perturbations, are induced by the asphericity of the earth, drag, radiation pressure, etc. Preliminary computations, confirmed by tests with artificial data, indicated that for the orbit and satellite under consideration here it would be necessary and sufficient to correct only for the earth's oblateness. The corrections are made to the observational data. Detailed formulas for the corrections are given in Ref. 5. These formulas involve the orbital elements which, however, do not need to be known to high accuracy for the purposes of trend removal. If sufficiently accurate values of the orbital elements are not available for trend removal, they may be obtained by including trend removal in the iterative routine of Sections 2.1 and 2.2 after the first values of the orbital elements have been obtained without trend removal.

Table III shows the importance of trend removal for the effects of oblateness. The same input data, which included the effects of oblateness, were used in both runs. The errors in the second run (without trend removal) are not acceptable. In particular, the error in the semi-major axis could lead to an error in predicted pointing angles of as much as 1.5° after only one period.

Table IV shows the speed of convergence, with trend removal, in the absence of initial estimates of the orbital elements. After only one iteration (one-half minute additional computing time for 200 observa-

TABLE III

	Ω, degrees	i, degrees	a, feet	e	ω, degrees	τ, seconds
Exact osculating elements at the center of the pass	144.4439	46.9170	31,566,742	0.240879	171.6124	47,950.421
Results of run no. 1 (with trend removal)	144.4439	46.9169	31,566,884	0.240875	171.6118	47,950.365
Results of run no. 2 (without trend removal)	144.4372	46.9152	31,542,821	0.241313	171.7500	47,961.173

TABLE IV

	Ω, degrees	i, degrees	a, feet	e	ω, degrees	τ, seconds
Exact osculating elements at the center of the pass	144.4439	46.9170	31,566,742	0.240879	171.6124	47,950.421
Results of run no. 1	144.4377	46.9149	31,543,423	0.241311	171.7487	47,960.978
Results of run no. 2	144.4439	46.9169	31,566,909	0.240874	171.6117	47,950.352
Results of run no. 3	144.4439	46.9169	31,566,886	0.240875	171.6118	47,950.362

tions, on an IBM-7090 computer), acceptable orbital elements were obtained.

V. COMBINATION OF SINGLE-PASS ORBITAL ELEMENTS

The method of combining single-pass estimates of the orbital elements is based on a matrix formula derived briefly as follows. Let $\bar{x}$ be a vector (i.e. a one-column matrix) estimate of the vector z, with ave $\{\bar{x} - z\} = 0$ and cov $\{\bar{x} - z\} = A$, where A is a covariance matrix. Similarly, let $\bar{y}$ be another estimate of z, with ave $\{\bar{y} - z\} = 0$ and cov $\{\bar{y} - z\} = B$. If $\bar{x}$ and $\bar{y}$ obey independent multivariate normal probability distributions, the "maximum likelihood" estimate of z is the $\bar{z}$ which minimizes the quadratic form

$$\bar{Q} = (\bar{z} - \bar{x})' \cdot A^{-1} \cdot (\bar{z} - \bar{x}) + (\bar{z} - \bar{y})' \cdot B^{-1} \cdot (\bar{z} - \bar{y})$$

where the primes denote transposition. Thus,

$$A^{-1} \cdot (\bar{z} - \bar{x}) + B^{-1} \cdot (\bar{z} - \bar{y}) = 0.$$

whence,

$$\bar{z} = (A^{-1} + B^{-1})^{-1} \cdot (A^{-1}\bar{x} + B^{-1}\bar{y}) \tag{5}$$

with covariance matrix

$$C = (A^{-1} + B^{-1})^{-1}. \tag{6}$$

In fact, it may be easily verified that

$$\bar{Q} = [\bar{z} - C\cdot(A^{-1}\bar{x} + B^{-1}\bar{y})]'\cdot C^{-1}\cdot[\bar{z} - C\cdot(A^{-1}\bar{x} + B^{-1}\bar{y})] + \text{terms independent of } \bar{z}.$$

A somewhat longer derivation without the normality assumption, in which the main diagonal (variance) elements of C are minimized, leads to the same results.

Formulas (5) and (6) require three matrix inversions which result in an intolerable loss of accuracy in cases of highly correlated estimates of the orbital elements. This difficulty is relieved to a very large extent by using the equivalent formulas

$$\bar{z} = w_1\bar{x} + w_2\bar{y} - (w_1P - w_2Q)(P + Q)^{-1}(\bar{x} - \bar{y}), \tag{7}$$

$$C = \tfrac{1}{2}[w_1A + w_2B - (w_1P - w_2Q)(P + Q)^{-1}(A - B)] \tag{8}$$

where $P = AG$, $Q = BG$, G is an arbitrary six-by-six matrix, and w_1, w_2 are any two six by six matrices whose sum is a unity matrix (see Appendix A). Formulas (7) and (8) require only one matrix inversion. The matrix G can be constructed so that the matrix $(P + Q)$ is well suited for inversion.

As a matter of additional necessity, formulas (7) and (8) were further transformed by the introduction of matrices U, V, defined by $U = SAS$, $V = SBS$, where S is a diagonal matrix whose elements are

$$S_{ii} = (A_{ii} + B_{ii})^{-\frac{1}{2}},$$

so that the diagonal elements of the matrix $(U + V)$ are unity. Restricting w_1, w_2 to diagonal matrices, then,

$$\bar{z} = w_1\bar{x} + w_2\bar{y} - R(\bar{x} - \bar{y}), \tag{9}$$

$$C = \tfrac{1}{2}[w_1A + w_2B - R(A - B)], \tag{10}$$

where

$$R = S^{-1}(w_1\hat{P} - w_2\hat{Q})(\hat{P} + \hat{Q})^{-1}S, \tag{11}$$

$\hat{P} = UH$, $\hat{Q} = VH$, and $H = S^{-1}G$. The formal construction of the arbitrary matrix H is not necessary. The matrices $\hat{P}$, $\hat{Q}$, and $\hat{P} + \hat{Q}$ are obtained by linear combinations of rows and/or of columns of the matrices U, V, and $U + V$ according to rules which are easily programmed for a digital computer.

Two details must be noted in the use of these formulas for combining

sets of orbital elements. The first detail is that the orbital elements are actually "osculatory" orbital elements which vary with time; therefore, each set is necessarily referred to a specific "epoch." Hence, before combining two sets, the set referred to the earlier epoch must be "updated" to the later epoch. In updating a set of orbital elements, it must also be noted that the "time of perigee passage" is actually the "time of mth perigee passage," where m is a specific number, usually different from the one for the set referred to the later epoch. The second detail to be noted is that the covariance matrix for the set referred to the earlier epoch must also be updated.

If $\tilde{C}_1$ is the covariance matrix to be updated, the updated covariance matrix is given by the formula

$$C_1 = J\tilde{C}_1 J',$$

where J is the Jacobian of the updated orbital elements with respect to the orbital elements from which they were predicted. Even in the hypothetical case of Keplerian orbits, in which all of the orbital elements, with the possible exception of τ, are constants, the Jacobian may differ from a unity matrix. For example, if the updating is through m times the period $2\pi\sqrt{\tilde{a}_1^3/k}$, so that

$$\tau_1 = \tilde{\tau}_1 + 2\pi m\sqrt{\tilde{a}_1^3/k},$$

then,

$$\partial\tau_1/\partial\tilde{a}_1 = 3\pi m\sqrt{\tilde{a}_1/k}.$$

The results of a test problem of this hypothetical sort are shown in Table V, in which the updating was through one period. The standard deviation of the improved estimate of the semi-major axis is approximately $\frac{1}{150}$ times the average of the corresponding standard deviations for the two runs. The improved estimate is in error by only 52 feet.

Table VI shows the results of a more realistic test problem in which the input data included perturbations due to the earth's oblateness. With "no updating" of the orbital elements and the covariance matrix from the earlier pass, except only to the extent required in the hypothetical case of Keplerian orbits, the "improved" semi-major axis is in error by 5094 feet, which is inconsistent with the standard deviation of only 73 feet. However, with updating of the orbital elements, taking account of the effects of the earth's oblateness, the error is only 72 feet.

VI. PROGRAM DESCRIPTION

The computer program system required to track a satellite and generate steering information for the communications antenna is divided into

TABLE V

		Ω, degrees	i, degrees	a, feet	e	ω, degrees	τ, seconds
Exact Values		144.5662	47.5190	32,107,194	0.253364	175.2756	49,218.920 or 58,853.603
Pass No. 1	Single-pass estimates	144.5638	47.5181	32,102,870	0.253387	175.3081	49,221.250
	Standard deviations	0.0017	0.0014	5,884	0.000124	0.0318	2.609
Pass No. 2	Single-pass estimates	144.5688	47.5196	32,116,970	0.253228	175.2114	58,848.774
	Standard deviations	0.0017	0.0006	8,683	0.000100	0.0543	4.325
Combination of passes No. 1 and No. 2	Combined estimates	144.5667	47.5193	32,107,246	0.253340	175.2741	58,853.608
	Standard deviations	0.0010	0.0005	46	0.000023	0.0026	0.128

TABLE VI

		Ω, degrees	i, degrees	a, feet	e	ω, degrees	τ, seconds
Exact values at t = 54,046 sec.		144.4439	46.9170	31,566,742	0.240879	171.6124	47,950.422
Exact values at t = 64,081 sec.		144.2383	46.9111	31,562,512	0.241047	171.8311	57,341.533
Pass No. 1 (center of the pass ≈ 54,046 sec.)	Single-pass estimates (t = 54,046 sec.)	144.4461	46.9183	31,562,047	0.241027	171.6318	47,952.202
	Standard deviations	0.0038	0.0024	11,077	0.000227	0.0638	4.936
Pass No. 2 (center of the pass ≈ 64,081 sec.)	Single-pass estimates (t = 64,081 sec.)	144.2410	46.9111	31,557,704	0.241211	171.8561	57,343.464
	Standard deviations	0.0025	0.0014	13,931	0.000176	0.0932	6.946
Combination of the passes No. 1 and No. 2; no updating	Combined estimates	144.3523	46.9400	31,557,418	0.240653	171.7592	57,344.864
	Standard deviations	0.0018	0.0010	73	0.000030	0.0044	0.186
Combination of the passes No. 1 and No. 2; updating included	Combined estimates (t = 64,081 sec.)	144.2412	46.9110	31,562,440	0.241105	171.8262	57,341.304
	Standard deviations	0.0018	0.0010	73	0.000030	0.0044	0.186

two major subsystems. The first of these is the orbit determination program, TELETRACK, which determines the characteristics of the satellite orbit from tracking information. The second major program, TELEPATH, computes orbit predictions from a knowledge of these orbital characteristics.

The division of the program system into these two parts is not only natural, but is also dictated by systems considerations. One of the requirements on the system was to minimize the amount of data transmissions. Ephemeris data to steer the communications antenna can be generated from the six orbital elements, and a division of the program system into two components linked together only by these six numbers achieves this requirement if each ground station is provided with suitable computational facilities. Stations having communications antennas require the program TELEPATH and updated sets of the orbital parameters. Stations having tracking antennas process the tracking data with TELETRACK and broadcast the updated elements to other stations as they become available.

The IBM 1620 computer was chosen to provide on-site computations. The IBM 7090 computer was used, however, for the initial development of the program systems. This was done for two reasons. First of all it was desirable to take advantage of the more powerful facilities and speed of the larger computer to facilitate the development and testing of the methods employed in the program system. Secondly, it was desirable to have the complete program system available at the Whippany, N. J., location of Bell Telephone Laboratories as a back-up to the on-site computer centers. Experience has shown that it is absolutely essential to have these duplicate programs available for testing and checking of the on-site operations.

By the nature of the 7090 and 1620 computers, different operating philosophies are required for each. The speed of the 7090 and turnaround times inherent in a large computation center are such that the programs must be as automatic as possible. However, they must also be flexible enough to allow selected programs from the system to be performed when necessary. Towards this end the following system evolved. The entire set of 7090 programs can be run consecutively as a single automatic chain job. Each program communicates to the following program through a magnetic tape, but as far as the computation center is concerned each program is a separate job. As a consequence, each program can also be run independently (with input provided by cards) since it is an entity in itself. The hidden gain in this system is the fact that there is only the one flexible version of each program, thus eliminating confusion and mistakes.

For the 1620, which is devoted entirely to this problem, and which is a slower machine, such completely automatic operation is not necessary. The system can be run automatically, but is usually run with more direct operator intervention. This allows greater flexibility and the ability to monitor intermediate results. On the 1620 the two major program systems are broken down conveniently into several program components. Each of these programs runs independently of the others, receiving input data generated by one of them and preparing output data for another. Operation of the program systems is achieved by loading and running one of the program components at a time. The various program components are stored on magnetic tape, and each program in the system loads the next program into the computer from this tape. Transfer of data between the programs is accomplished by punched cards, magnetic tapes and common memory storage. The method of data transfer in a particular instance depends upon the nature and quantity of the data.

Numerous error conditions were anticipated while the programs were being written. Many of these are handled automatically by the programs themselves. Some must be taken care of by manual intervention.

VII. INERTIAL COORDINATES AND ORBITAL ELEMENTS

All orbital calculations must, of course, be referenced to an inertial (or near inertial) coordinate system. The basic system used in these programs is the usual earth-centered, right-handed rectangular system. The X-Y plane coincides with the earth's equatorial plane, the X-axis is parallel with the line of equinoxes, and the Z-axis passes through the North pole. The orientation of the earth in this system at the time of an observation is obtained from UT_2 at time of observation and the Greenwich Mean Sidereal Time at 0 hours UT of date. Conversion from Mean Sidereal Time to Apparent Sidereal Time is made using the Equation of Equinoxes at 0 hours UT of date; interpolation of this number to the time of observation was deemed unnecessary.

The satellite orbit is described by means of the osculating orbital elements, consisting of

(a) semi-major axis
(b) eccentricity
(c) right ascension of ascending mode
(d) inclination angle
(e) argument of perigee, and
(f) time of perigee passage.

These elements specify the ellipse osculatory to the satellite orbit at some instant in time. These six numbers are therefore accompanied by an epoch specifying the time of osculation. The time of perigee passage specifies the perigee passage immediately preceding the epoch and is stated in seconds relative to the epoch.

The following paragraphs describe in some detail the two program systems, TELETRACK and TELEPATH.

VIII. TELETRACK PROGRAM SYSTEM

The TELETRACK program system processes tracking data in terms of azimuth and elevation to produce estimates of the six orbital elements describing the satellite orbit. It processes tracking data from one pass over the tracking station at a time to produce a "single-pass estimate." Single-pass estimates are combined to provide "combined estimates." The combining of several single-pass estimates provides a statistical averaging of the several independent estimates and a refinement based on the separation in time of the various independent estimates.

A flow chart of TELETRACK is shown in Fig. 1. Each of the major program components and the modes of data transfer between them are shown. A few of the program switches which control the mode of operation of the system are also shown.

8.1 *TELED*

TELED is the input/edit section of TELETRACK. Inputs to this program are

(a) tracking data consisting of time, azimuth and elevation for one pass, and

(b) data cards containing date and number of pass, identification of the tracking station and satellite, meteorological conditions during the pass, GMST at 0^h of date, estimates of the orbital elements, number of data sets to be selected (N), and values of the mode control switches for TELETRACK.

TELED reads the tracking data from tape and performs format and units conversion. Data points for which the precision tracker was not in autotrack or for which the signal-to-noise ratio level was not above a predetermined level (usually 4 or 5 db) are rejected. Furthermore, data points for which the elevation is below 7.5° or above 82.5° are rejected. The specified number ($4N$) of data points is selected from the group satisfying these criteria. The set of data so selected is distributed as uniformly as possible over the available set.

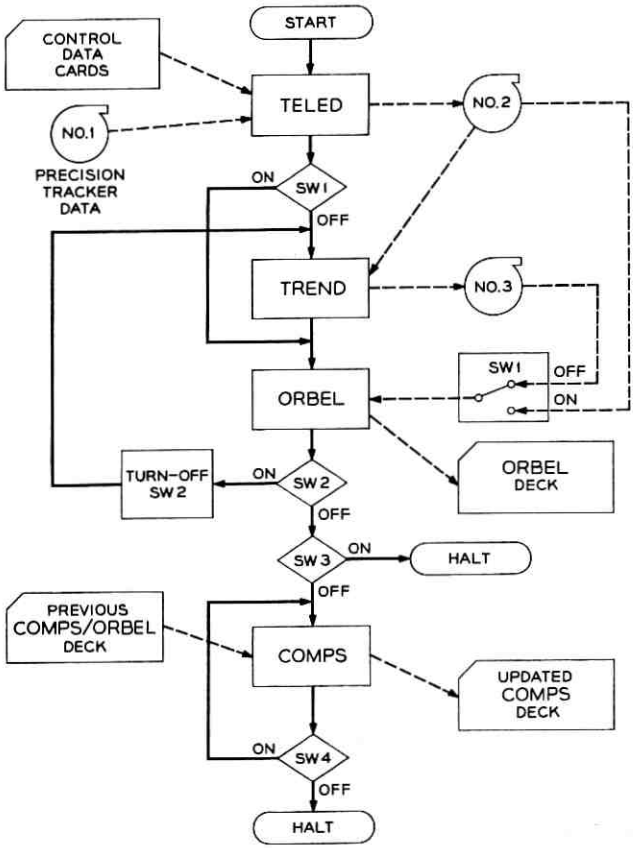

Fig. 1 — TELETRACK flow chart.

Boresight and refraction corrections are then applied to the selected data points. Following this, coordinate conversions are performed to transform the data from the topocentric azimuth-elevation system to the inertial coordinate system. Deviations of the vertical from the normal to the geodetic spheroid are accounted for in this process. Since range data are not available, the results of the coordinate conversion are in terms of the direction cosines relative to the inertial system of the observed sight lines. Also computed are the coordinates in inertial space of the tracker at the time of each observation.

Outputs from TELED are stored on magnetic tape for subsequent

programs. The primary output consists of $4N$ data points. Each data point contains time of observation, the three direction cosines of the observed sight line, sine and cosine of the right ascension of the tracker at the time of the observation, and the inertial coordinates of the tracker at the time of the observation. Various other data are also stored on this tape for subsequent programs.

8.2 *TREND*

The direction cosines produced by TELED are adjusted by TREND to produce the set which would have been obtained had the satellite been moving in an unperturbed, elliptical orbit throughout the pass. These adjustments are described in detail in Section IV above. The time of osculation (t_c) between the perturbed and unperturbed orbits was selected by TELED to correspond to the center of the pass and is passed on to TREND via tape.

As noted above, an estimate of the orbital elements at time t_c is needed. These are obtained by updating to time t_c the elements supplied on the input cards to TELED. Program ORBFIX is used for this purpose, details of which are given below.

The output from TREND consists primarily of the adjusted direction cosines for each observation. These are stored on a tape which is identical in format with the TELED output tape. By making these formats identical it is possible under one of the modes of operation to bypass TREND if estimates of the orbital parameters are not available.

8.3 *ORBFIX*

As mentioned above, ORBFIX updates a set of osculating orbital elements valid at one epoch to another epoch. The program essentially makes use of the subroutine OBLATE with only minor additional bookkeeping operations. The subroutine OBLATE is a numerical integration routine in true anomaly which integrates in steps of 0.08 radian the first-order oblateness perturbation equations to provide the desired corrections. The equations also include sufficient second-order terms to allow taking steps of 2π, so that in actual use steps of 2π are taken until a value π or closer to the desired point is reached. The program then integrates either forward or backward in small steps to reach the desired point exactly. It is also possible to go only in 2π steps in cases where only limited accuracy is required. This results in a large time saving.

8.4 *ORBEL*

Calculation of the orbital parameters is performed by the program ORBEL. The input data normally consist of the adjusted direction cosines from TREND. In the absence of initial estimates of the orbital elements, however, ORBEL can process the unadjusted data from TELED. The $4N$ observations are divided into four nonoverlapping groups. A set of four observations is obtained by selecting one observation from each group. N independent estimates of the orbital elements are calculated from the resultant N sets of observations. Averages, variances and covariances of the six elements for one pass are calculated from these. Details on the methods are given in Sections II and III.

The estimates of the ranges required in producing the first set of elements are normally produced by TREND during the trend removal procedure. In the absence of trend removal these estimates must be supplied on the input data cards to TELED. Subsequent estimates of range are derived by ORBEL itself from its previous estimates of the elements.

The output from ORBEL consists of a set of cards (an "ORBEL deck") containing the single-pass estimates of the orbital elements, the standard deviations of those elements, and the correlation coefficient matrix. Pass number and the corresponding epoch are also stored on these cards. These cards are filed away for possible future use.

The information on these cards is also retained in memory for use by the combination of passes program, COMPS.

8.5 *COMPS*

Combination of the estimates from the various passes is accomplished by the program COMPS. The method employed is described in Section V above. The inputs consist of two sets of orbital elements, standard deviations and correlation coefficient matrices. The first set, obtained from input cards, is either from a single ORBEL run or from an earlier COMPS run. The second set is from the current ORBEL run and is usually supplied directly by ORBEL through common memory storage. Under some modes of operation, however, the second set is supplied by cards.

The output from COMPS is a set of cards (the "COMPS deck") identical in content and format with the ORBEL deck. These cards are filed to maintain a permanent record of the combined orbital elements. The output data also replace the data from the first input set in memory in case certain operating modes are selected.

8.6 *Modes of Operation*

Several mode-control switches are provided to permit selection of one of a number of possible operating modes. The more significant of these switches are shown in Fig. 1. Each switch is identified by a number and consists of a one-bit variable which is read from an input data card and stored in memory.

In the normal mode of operation it is assumed that some estimate of the orbital elements is available for trend removal and that a combination of the ORBEL output with an earlier COMPS output is wanted. All switches are set in the "off" condition and the sequence of operations is TELED, TREND, ORBEL and COMPS in that order. The first set of inputs to COMPS is determined by the operator, who selects the proper COMPS deck, and the second set is supplied directly by ORBEL.

An alternative mode of operation is to stop the program after the single-pass estimate is produced by ORBEL and then combine a number of such estimates in a "batch combination" at a later time. This is accomplished by turning switches 3 and 4 on and accumulating a number of ORBEL decks. These decks are fed to COMPS in order by time, with the earliest deck first. COMPS reads the first two decks and combines them, producing a combined estimate valid at the time of the second set. This in turn is combined with the third set to produce a combination of the first three decks valid at the time of the third. This process continues until all decks have been combined into a single estimate valid at the time of the last set.

Another mode of operation is available in case estimates of the orbital elements are poor or unavailable. By turning switch 1 on, trend removal is skipped initially, and ORBEL is given unadjusted data with which to estimate the elements. If switch 2 is also on, ORBEL will call on TREND after computing this initial estimate of the orbital elements. This estimate is passed on to TREND for use in adjusting the data. Switch 2 is turned off, the data are adjusted, and then ORBEL is called upon a second time, this time to process data with trend due to perturbations removed.

IX. TELEPATH PROGRAM SYSTEM

The ephemeris generation for the Telstar satellite is carried out by a trio of programs collectively known as the TELEPATH program. The three individual programs are called MUVIS, COKE, and ACEXP, and are complete entities in themselves, solving distinctly separate

portions of the problem. The MUVIS program is solely concerned with finding times of future visibility or mutual visibility and updating the orbital elements to these time periods. Its output is a listing of future passes which is in itself useful, and a set of cards which serves as input to the COKE program. The COKE program generates a theoretical ephemeris for each pass as determined by the input cards, and outputs it on tape. The COKE program can also be used by itself to re-create any pass for which orbital elements are available. Both programs exist in almost identical form both for the IBM 7090 and the IBM 1620. The only differences in the programs are due to storage limitations in the 1620. This results in some extra tape manipulations in the 1620 programs which are unnecessary on the 7090. The final program, ACEXP, exists only on the 1620 and is used for adding predistortion and refraction corrections to the theoretical ephemeris.

Fig. 2 shows the flow chart of the 1620 program with its various operating options. A more detailed description of the program follows, without reference to machine.

9.1 *MUVIS*

This program takes a set of osculating orbital elements at an epoch and using them predicts when the satellite will be visible at a designated site, and when it will be mutually visible with a second designated site. The emphasis in this program is speed with only a limited amount of accuracy. It is envisaged that this program will be used for planning and general information, and thus the methods used were chosen with this in mind.

Basically, the program steps time by some increment, predicts the satellite's position in inertial coordinates for the new time, checks for visibility and mutual visibility, and continues. There is naturally a fair amount of bookkeeping associated with executing these steps, but they are essentially the heart of the program.

Since the program consists of many iterations through the basic loop outlined above, it was felt worthwhile to streamline it as much as was possible. Towards this end the following steps were taken.

(*i*) The program takes variable time steps. A coarse step is used until visibility is determined, and at this point a finer step is used for a more refined estimate. This feature is carried one step further by permitting a time step of close to a full period after visibility ends, or when the satellite appears to be moving away from visibility.

(*ii*) When the satellite's position is calculated at some time, osculat-

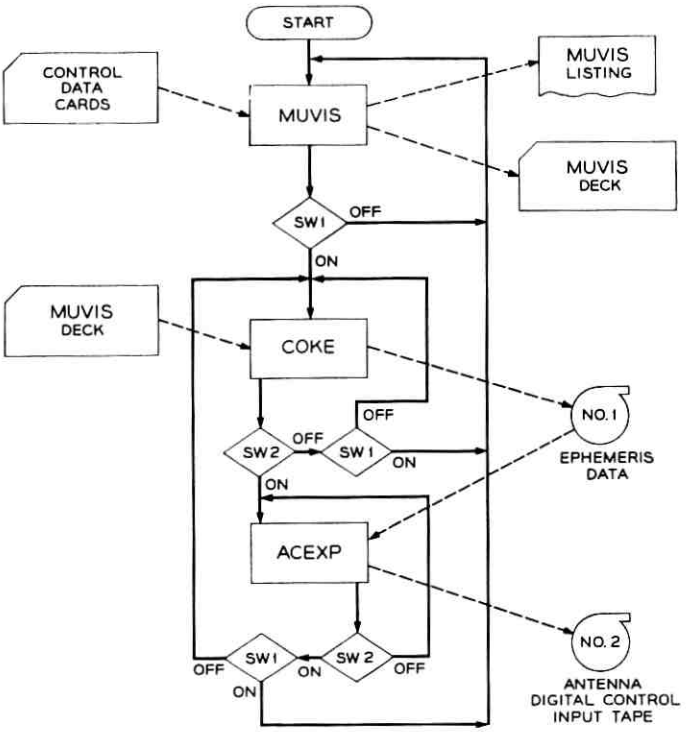

Fig. 2 — TELEPATH flow chart.

ing orbital elements are used which are valid at most one-half a period away. This enables the program to update the elements in steps of 2π, which results in a large time saving. The errors introduced by not completely updating the orbital elements are far less than the accuracy desired.

(*iii*) The determination of visibility at a site is not done by the obvious method of computing elevation and checking for a positive angle. The reason for this is that once the satellite's coordinates have been obtained, this method requires at least a square root, an arc tangent, and approximately thirteen multiplications. The method used instead requires only seven multiplications with the resultant saving in time. Instead of computing elevation, the program passes a plane through the site tangent to the earth. This plane, which can be considered a ground plane at the site, has the equation

$$\alpha X_s + \beta Y_s + \gamma Z_s - R_e = 0$$

where X_s, Y_s, Z_s are the inertial coordinates of the site, and R_e is the distance from the center of the earth to the site. If, however, the coordinates of the satellite are substituted in the equation, then a value other than zero is usually obtained. If this value is minus, then the satellite lies on the same side of plane as the center of the earth and is therefore below the horizon, but if the value is positive, then the satellite is on the opposite side of the plane which is above the horizon and is therefore visible. The determination of visibility is thus reduced to evaluating α and β, which are time varying due to the rotation of the earth, evaluating the four-term expression, and testing the sign of the result. The evaluation of α and β can be done using the previous values of α and β with only four multiplications. It should again be noted that the price for this increase of speed is the loss of some accuracy. This method does not fully take into account the earth's oblateness. The result is that the plane is not exactly tangent to the earth, and a small amount of inaccuracy is to be expected. (About 140 feet of error in placing the site.) This method is also limited in that it cannot predict rise and set at any angle other than 0°, but this information can always be obtained later from the COKE program.

When the program has determined a period of visibility, it updates the orbital elements to either the center of the mutual visibility if any exists or otherwise simply the center of visibility, and punches out the elements plus other pertinent data on the pass. The program also prints out the pass number, rise and set times at the ground station, start and end of mutual visibility, and the maximum elevation seen at the site.

This procedure is continued until a final time is reached. At this point the program finishes any pass it may be working on and then stops.

9.2 *COKE*

The COKE program uses the MUVIS results to generate an ephemeris that is exact but omits physical effects such as refraction and antenna distortion. Thus the tape can be generated ahead of time and just before the pass corrected for both meteorological conditions and the boresight corrections of the antenna to be used (there is only one antenna at each site at present).

The program uses an Encke type method (see Ref. 6, p. 176) to solve for the satellite's position at four-second intervals. These are computed both forward and backward from the center of the pass or the center of mutual visibility, whichever the orbital elements have been updated to. Thus some rearrangement of data must be done to output the

ephemeris in time order. The heart of the program is the same integration program used in the trend-removal portion of TELETRACK. Therefore only the peripheral programming needed to convert the results to pointing angles, to rearrange and output the results, and to control the direction and length of integration had to be written from scratch.

9.3 *ACEXP3*

The ephemeris tape required as input to the antenna digital control during a pass is generated by the expander program, ACEXP. In addition to generating this tape, this program also produces the "mission printout," a listing of pertinent data regarding a pass over the ground station. The main input to this program is the data tape from COKE, containing time, azimuth, elevation and range at four-second intervals.

One data point on the ephemeris tape contains the following information:

(a) time
(b) azimuth and elevation positions
(c) azimuth and elevation first differences
(d) azimuth and elevation second differences
(e) azimuth and elevation predistortions, and
(f) gain factor.

Azimuth and elevation first differences for the ith data point are computed according to

$$D^1 = \tfrac{1}{2}(P_{i+1} - P_{i-1})$$

where P_i represents azimuth or elevation position. The second differences are computed according to

$$D^2 = P_{i+1} - 2P_i + P_{i-1}\,.$$

Azimuth and elevation predistortions, which are discussed in Ref. 7, are estimated to be functions of elevation only and to be of the form

$$PD_A = (a + bE)/\cos E$$

$$PD_E = c + dE.$$

Current values for the parameters are

$a = 0.015$ degree
$b = -0.000786$
$c = 0.057$ degree
$d = -0.000712$.

The ground station transmitter gain factor, discussed more fully in Ref. 8, is computed as a function of range as follows

$$\gamma = \frac{127}{128}\alpha[1 + 0.0791(\alpha - 1)]$$

$$\begin{aligned} \text{where } \alpha &= \log_{10} S/S_{\min} && \text{for} && S_{\min} < S < 10\ S_{\min} \\ &= 0 && \text{for} && S \leqq S_{\min} \\ &= 1 && \text{for} && 10\ S_{\min} < S. \end{aligned}$$

$S_{\min}$ is chosen according to the characteristics of the pass over the site.

Elevations are corrected for refraction as follows. Index of refraction is computed according to

$$n - 1 = (0.776 \times 10^{-4}\, p + 0.372\, e/T)/T$$

where T is temperature in degrees K, p is air pressure in millibars, and e is water vapor pressure in millibars (Ref. 9, pp. 13–15). The correction

$$\Delta E = (n - 1) \cot E$$

is added to the elevation, E, before putting it on the ephemeris tape.

The mission printout is generated to aid the operating personnel during a satellite pass. Tabular data at one-minute intervals specify time, azimuth, elevation, range, one-second increments in azimuth, elevation and range, and Doppler shift. From a knowledge of the azimuth rates the program predicts when (if at all) the horn antenna will lose autotrack due to excessive azimuth rates. The angular distances between the satellite and the sun are also computed, and if they come within 2° of each other an appropriate warning is included in the mission printout.

X. OPERATIONAL RESULTS

These programs have been a part of the Bell System satellite communications ground station operational system since the July 10, 1962, launch. Initial predictions were based on the launch and injection data, corrected by the few observations possible in the first six orbits. From the sixth orbit on, predictions were based entirely on track data acquired at the Andover site. By the seventeenth orbit (the second day), the orbital elements had been refined sufficiently so that the horn-reflector antenna autotrack could acquire the satellite using the predicted angles. From that point on the normal mode of acquisition was from the

predicted angles, and the use of the auxiliary antennas as acquisition aids was generally not required. This means that predictions have generally been within $\pm 0.2°$, at least at the horizon where acquisition is usually achieved.

The launch of the Telstar satellite was carefully planned to put the apogee in the northern hemisphere to maximize the periods of mutual visibility in the early phases of the experiment. During the first few weeks following the launch, the prediction accuracy was very good. Samples of the results of orbit determination and prediction during this period are shown in Table VII. The predicted angles, extending five days ahead, were generated from orbital elements computed from precision angular tracking data obtained during the preceding five days. The observed angles were obtained from the precision tracker. It should be noted that errors in azimuth should be multiplied by the cosine of the elevation in order to convert them to errors in sightline angle on a par with the errors in elevation.

With apogee in the northern hemisphere, the tracking periods were long (over 30 minutes). As perigee precessed toward the northern hemisphere and the tracking periods became shorter, a gradual degradation in prediction accuracy was noted. While the prediction accuracies were sufficient for the daily antenna pointing operations at Andover, they proved inadequate for providing pointing information for the optical experiment at Holmdel[10] and for determining satellite positions for the radiation effects study.[11] These uses of the predictions require accuracies of 0.1° and both require that the satellite positions be related to geographical sites other than that at which the track data are acquired.

This prompted a renewed study of the orbit determination method and the program implementation. This investigation revealed that this method is quite sensitive to observational bias, particularly when the track data are obtained from short passes rising to high elevations. This sensitivity can be reduced by using only tracking passes of 30 minutes or more in which the maximum elevations do not exceed 50°. However, that is a severe restriction to place on a single tracking site with a highly eccentric orbit such as that under consideration here. In addition, it was found that the approximate methods used to account for the perturbations due to the earth's oblateness were inadequate except when the line of apsides is nearly parallel (as in July, 1962) or nearly perpendicular to the line of the nodes. Programs providing more complete perturbation calculations have been written and are presently undergoing tests.

From this study it was concluded that to achieve prediction accura-

TABLE VII

Date and Pass Number	Time (hrs-min, UT)	Azimuth (degrees)		Elevation (degrees)	
		Observed	Predicted	Observed	Predicted
7/23	21 35	195.16	195.20	20.50	20.48
#124	21 41	188.83	188.86	29.37	29.38
	21 47	179.58	179.60	38.28	38.29
	21 53	165.12	165.14	46.35	46.37
	21 59	142.81	142.80	51.28	51.29
	22 05	115.18	115.21	49.24	49.22
	22 11	92.13	92.15	39.03	39.04
	22 17	77.19	77.19	24.08	24.08
7/24	21 17	187.80	187.81	25.73	25.72
#133	21 23	179.40	179.40	34.40	34.40
	21 29	166.95	166.97	42.47	42.44
	21 35	148.30	148.32	48.26	48.26
	21 41	123.75	123.75	48.91	48.88
	21 47	99.92	99.93	42.22	42.20
	21 53	82.60	82.60	29.77	29.77
7/25	23 43	238.23	238.24	22.01	22.03
#143	23 49	237.62	237.61	32.26	32.29
	23 55	235.99	236.00	44.29	44.29
7/26	00 01	231.28	231.31	58.89	58.94
#143	00 07	207.91	207.83	76.43	76.44
	00 13	99.76	99.82	72.91	72.91
	00 19	80.65	80.65	46.23	46.22
7/26	20 31	183.69	183.68	21.11	21.12
#151	20 37	175.55	175.59	29.39	29.42
	20 43	164.51	164.54	37.05	37.04
	20 49	149.13	149.17	42.90	42.91
	20 55	129.16	129.21	45.17	45.18
	21 01	107.72	107.77	41.98	42.02
	21 07	89.57	89.59	33.43	33.44
	21 13	76.29	76.29	21.36	21.35
7/27	20 08	181.81	181.84	18.66	18.67
#160	20 14	173.80	173.85	26.84	26.84
	20 20	163.25	163.30	34.25	34.31
	20 26	149.03	149.11	40.15	40.19
	20 32	130.89	130.95	42.99	42.98
	20 38	110.85	110.93	41.09	41.09
	20 44	92.90	92.93	34.18	34.20
	20 50	78.98	79.01	23.62	23.63

cies of 0.1° or better, the angular observations must be taken from more than one geographical point or, if from a single tracking site, the angular observations must be supplemented by an additional independent track measurement, such as slant range to the satellite. A program system avoiding the shortcomings of the present method is now under active development. This system uses a modified method of combining

passes and improved perturbation calculations, and has the ability of including slant range measurements and data from several tracker sites.

The orbit determination method described meets the objective of minimizing the computer requirements by eliminating the mass storage requirements and time-consuming iterative procedures inherent in the classical differential corrections technique. As described, the method and programs are adequate for providing acquisition information for autotracking communications antennas if the tracking restrictions can be met. For a single tracking site, these restrictions imply a perigee of 1000 nautical miles or more. If lower orbits must be handled or greater accuracies are required, the improvements mentioned above should be considered.

APPENDIX A

Derivation of Equations (7) and (8)

Since $A^{-1}\bar{x} = (A^{-1} + B^{-1})\bar{x} - B^{-1}\bar{x}$, (5) may be written in the form

$$\bar{z} = \bar{x} - (A^{-1} + B^{-1})^{-1} B^{-1}(\bar{x} - \bar{y}).$$

Now,

$$\begin{aligned}(A^{-1} + B^{-1})^{-1} B^{-1} &= [B(A^{-1} + B^{-1})]^{-1} \\ &= [1 + BA^{-1}]^{-1} \\ &= [(A + B)A^{-1}]^{-1} \\ &= A(A + B)^{-1}.\end{aligned}$$

Hence,

$$\bar{z} = \bar{x} - A(A + B)^{-1}(\bar{x} - \bar{y}).$$

Since, by (5), we may interchange $\bar{x}$ and $\bar{y}$ provided that A and B are also interchanged, we have

$$\bar{z} = \bar{y} + B(A + B)^{-1}(\bar{x} - \bar{y}).$$

Thus, if w_1 and w_2 are any two six-by-six matrices whose sum is a unity matrix,

$$\bar{z} = w_1\bar{x} + w_2\bar{y} - (w_1A - w_2B)(A + B)^{-1}(\bar{x} - \bar{y}).$$

Substituting $A = PG^{-1}$ and $B = QG^{-1}$, and noting that

$$(A + B)^{-1} = G(P + Q)^{-1}$$

$$w_1A - w_2B = (w_1P - w_2Q)\, G^{-1}$$

we get (7).

Noting that the right-hand member of (6) is a half of that of (5) if we replace $\bar{x}$ by A and $\bar{y}$ by B, (8) follows from (7).

REFERENCES

1. Briggs, R. E., and Slowey, J. W., An Iterative Method of Orbit Determination from Three Observations of a Nearby Satellite, Special Report No. 27, Astrophysical Observatory, Smithsonian Institute, June 30, 1959.
2. Shapiro, I. I., *The Prediction of Ballistic Missile Trajectories from Radar Observations*, New York, McGraw-Hill Book Company, Inc., 1959, Part III, Chapter IV.
3. Swerling, P., A Proposed Stagewise Differential Correction Procedure for Satellite Tracking and Prediction, Rand Corporation Report P-1292, January 8, 1958.
4. Swerling, P., First Order Error Propagation in a Stagewise Smoothing Procedure for Satellite Observations, Journal of Astronautical Sciences, **6**, No. 3, Autumn, 1959.
5. Claus, A. J., Orbit Determination for Communication Satellites from Angular Data Only, to be published.
6. Brouwer, D., and Clemence, G. M., *Methods of Celestial Mechanics*, New York, Academic Press, 1961.
7. Githens, J. A., and Peters, T. R., Digital Equipment for the Antenna Pointing System, B.S.T.J., this issue, p. 1213.
8. Giger, A. J., Wickliffe, P. R., Jr., and Pardee, S., Jr., The Ground Transmitter and Receiver, B.S.T.J., this issue, p. 1063.
9. *Handbook of Geophysics for 1960*, U.S. Air Force Air Research and Development Command.
10. Jakes, W. C., Jr., Participation of the Holmdel Station in the *Telstar* Project, B.S.T.J., this issue, p. 1421.
11. Brown, W. L., Gabbe, J., and Rosenzweig, W., Results of the *Telstar* Radiation Experiments, B.S.T.J., this issue.

Planning, Operation and External Communications of the Andover Earth Station

By D. H. SMITH, C. P. CARLSON, R. J. McCUNE, R. E. ELICKER and R. E. SAGEMAN

(Manuscript received February 25, 1963)

This paper relates some of the considerations in the planning of the Andover, Maine, earth station. It describes the station layout, the operating plan and the Long Lines interconnections. Power facilities, air conditioning, heating and dehumidification arrangements are also covered.

I. INTRODUCTION

The purpose of this paper is to describe the layout, operation, and external communications links of the Andover, Maine, earth station. This station was designed to provide the terminal facilities required for communications via artificial earth satellites. Complete facilities for orbit determination, tracking, and broadband microwave communications were included in order to obtain data which would be useful in the evaluation of designs for future operational systems. Experimental verification of the feasibility of communicating via satellites was, however, the primary goal.

In this paper, various aspects of the Andover station are described in detail under the following headings: II. Site Planning, III. Operating Plan, IV. Power Facilities, V. Air Conditioning and Heating, VI. External Communications Requirements, and VII. Experimental Demonstrations

II. SITE PLANNING

The Andover ground station is situated in a 1000-acre tract surrounded by mountains. The site is nearly ideal since the mountains are high enough to protect against interference from overland microwave systems but low enough to permit proper operation when the satellite is near the horizon.

Fig. 1 — Site plan for Andover

Aerial surveys of the site were used to assist in locating the control building, antennas and boresight towers. Anticipating the possibility of more extensive experimentation or of eventual commercial systems, a sufficiently large site was obtained such that a control building could be located on relatively high ground, surrounded by five horn antennas. One possible commercial system would require a multiplicity of satellites and a minimum of two antennas at each terminal for efficient operation. One antenna at each terminal point would follow a satellite as long as that satellite is mutually visible. As the end of a period of mutual visibility is approached, continuity of service could be provided by switching to a second, or handover, antenna which would be tracking another satellite in the early part of its period of mutual visibility. A third antenna might be provided as an active spare. On this basis, it was estimated that five antennas would be sufficient to provide three broadband radio channels, with one antenna always available for handover and another as a spare.

2.1 *Antenna Spacings*

On the Andover site, five antennas could be located, as shown in Fig. 1, in such a manner as to prevent masking of the microwave signals by each other at elevation angles above 7.5 degrees. The most practical arrangement would be to cluster the antennas about the control building. At the potential locations the antennas would be at varying distances from the control building and from each other because of the contours of the land. The antenna location for the Telstar experiment was selected because of its proximity to the approach highway.

Trees were cleared to avoid interference at low angles. For the same reason the commercial power line was placed underground as it approached the control building. Masking of the precision tracker and command tracker antennas by the control building was avoided by elevating them on concrete pedestals and locating them at opposite sides of the control building so that their beams would clear the building and each other for elevation angles above 7.5 degrees.

2.2 *Control Building*

A cutaway view of the control building and its facilities is shown in Fig. 2. The building is a windowless one-story structure, and it may be considered as being made up of three areas. One area contains the heating, power and utility equipment, not only for the control building itself but also for the horn antenna and its radome. Another area contains

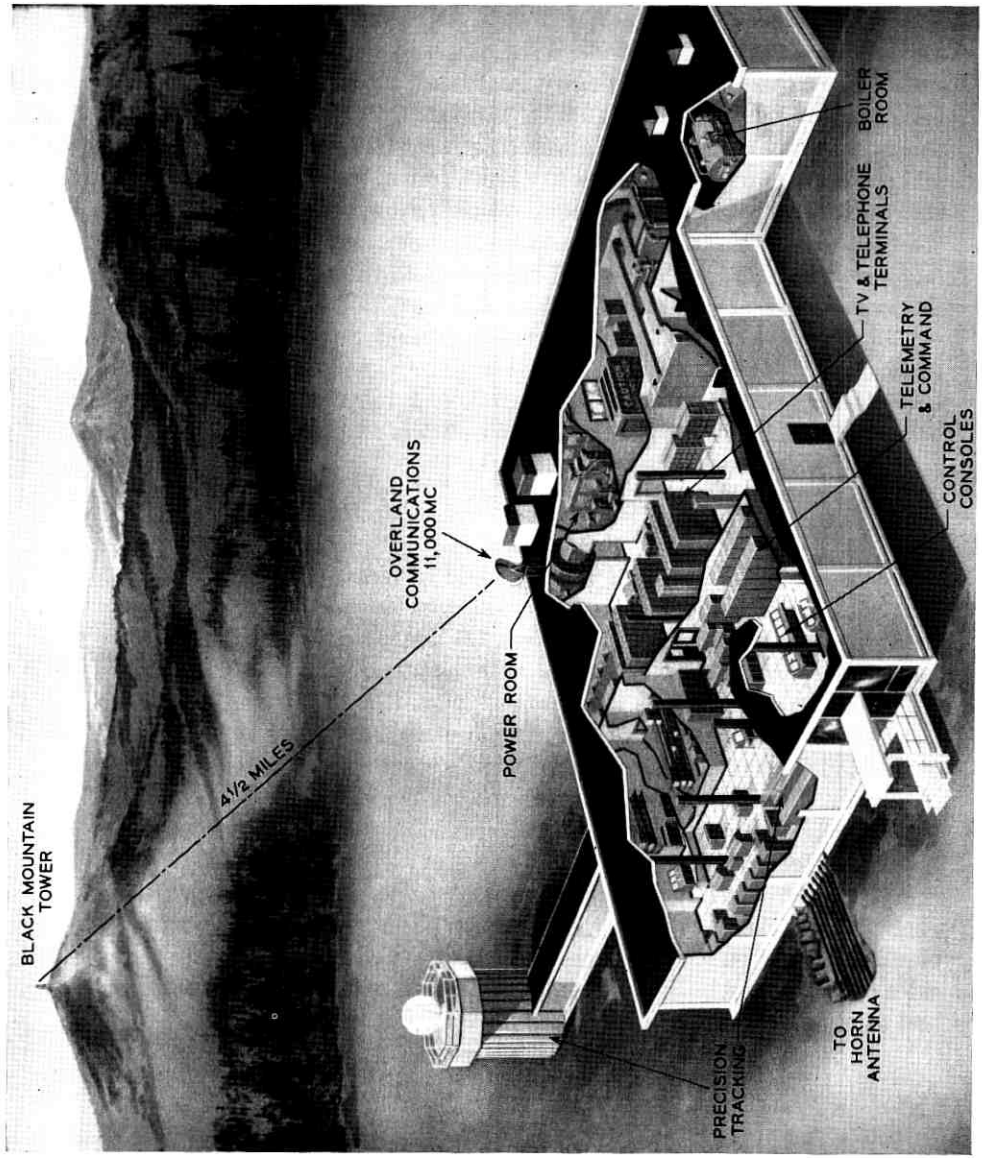
BLACK MOUNTAIN TOWER
4½ MILES
OVERLAND COMMUNICATIONS 11,000 MC
POWER ROOM
PRECISION TRACKING
TO HORN ANTENNA
CONTROL CONSOLES
TELEMETRY & COMMAND
TV & TELEPHONE TERMINALS
BOILER ROOM

the telephone terminal equipment, microwave terminal, television operating center and distributing frames. Most of the equipment in this area is made up of standard Bell System items.

The third area contains equipment quite special for the Telstar project. This consists of the ground station control and other consoles, antenna pointing equipment, computers, precision tracker, command, telemetry and sundry testing equipment.

2.3 *Main Antenna Building*

It was considered desirable to concentrate as much of the transmission and antenna guidance equipment as possible in the control building. This would obviate dispersal of maintenance personnel and equipment. However, to avoid expenditure of considerable development time, it was necessary to locate much of this equipment on the horn-reflector antenna structure or in the utility building at the periphery of its radome. The horn antenna structure design included two rooms for equipment and personnel. One room, located at and behind the apex of the horn feed, is called the "upper" room. The other room, located on the floor of the azimuth near the pintle area, is called the "lower" room. The apportionment of equipment among the utility building and the lower and upper rooms of the rotating antenna structure was given serious consideration. In order to achieve optimum servo performance it was essential that the nonstructural weight on the movable structure be minimized. It was not only the weight of the equipment that had to be considered, but also the flooring and housing for it. Furthermore, of the equipment that was to be placed on the antenna structure, as much as possible was located in the lower room close to the center of rotation. Figs. 3 and 4 show the arrangement of equipment in the upper and lower rooms, respectively.

In the interest of weight saving, the cabinets, unit frameworks and overhead cable rack and framing supports were made of aluminum. Closed cabinets permitted the use of local air cooling as required. The air for cooling equipment in some of the cabinets is provided from outside the room and is exhausted outside the room through a closed system over a chilled water heat exchanger. In other cabinets where the heat generated is moderate, room air is used for cooling.

2.4 *Slip Ring Assembly*

Electrical connections between the equipment on the moving part of the antenna and the remainder of the system are made through slip

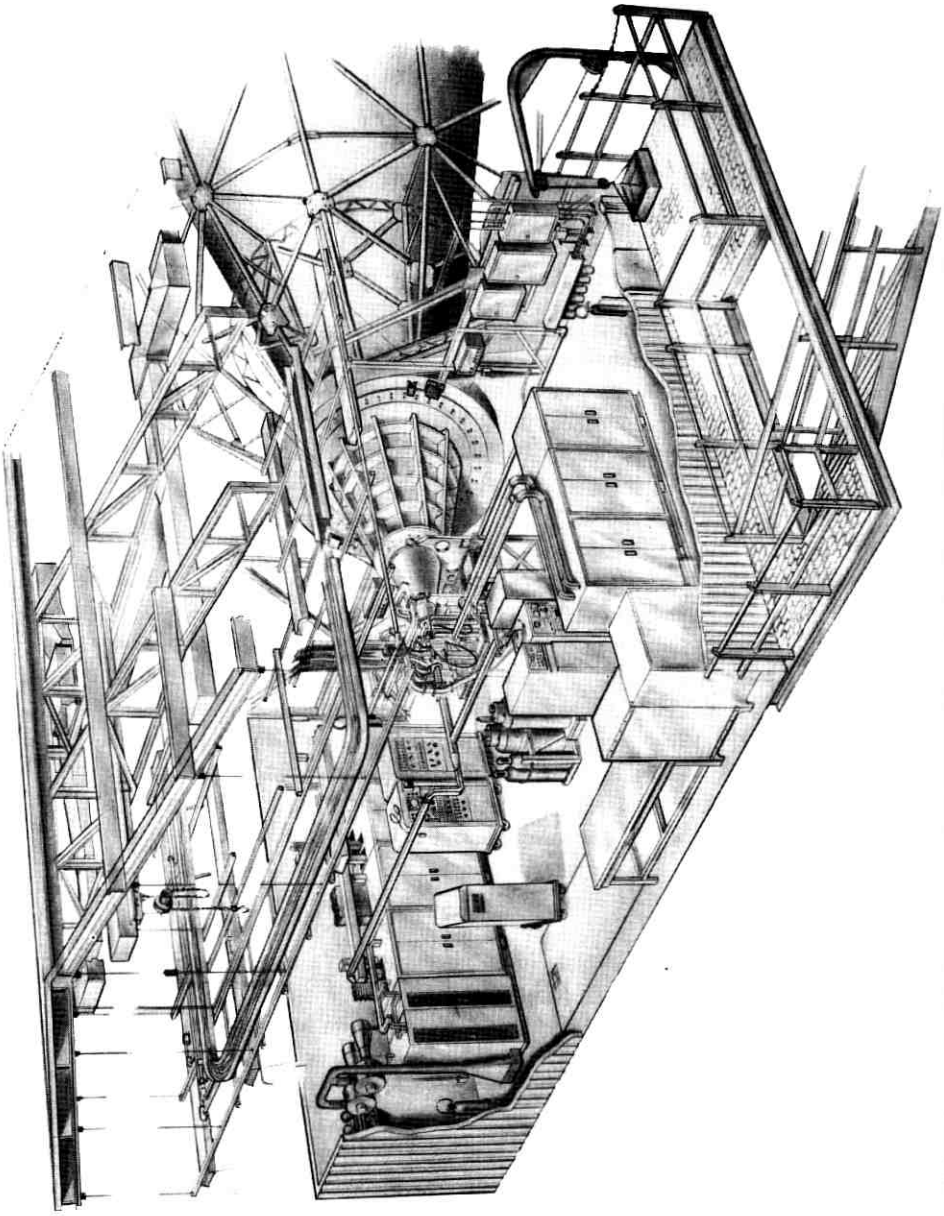

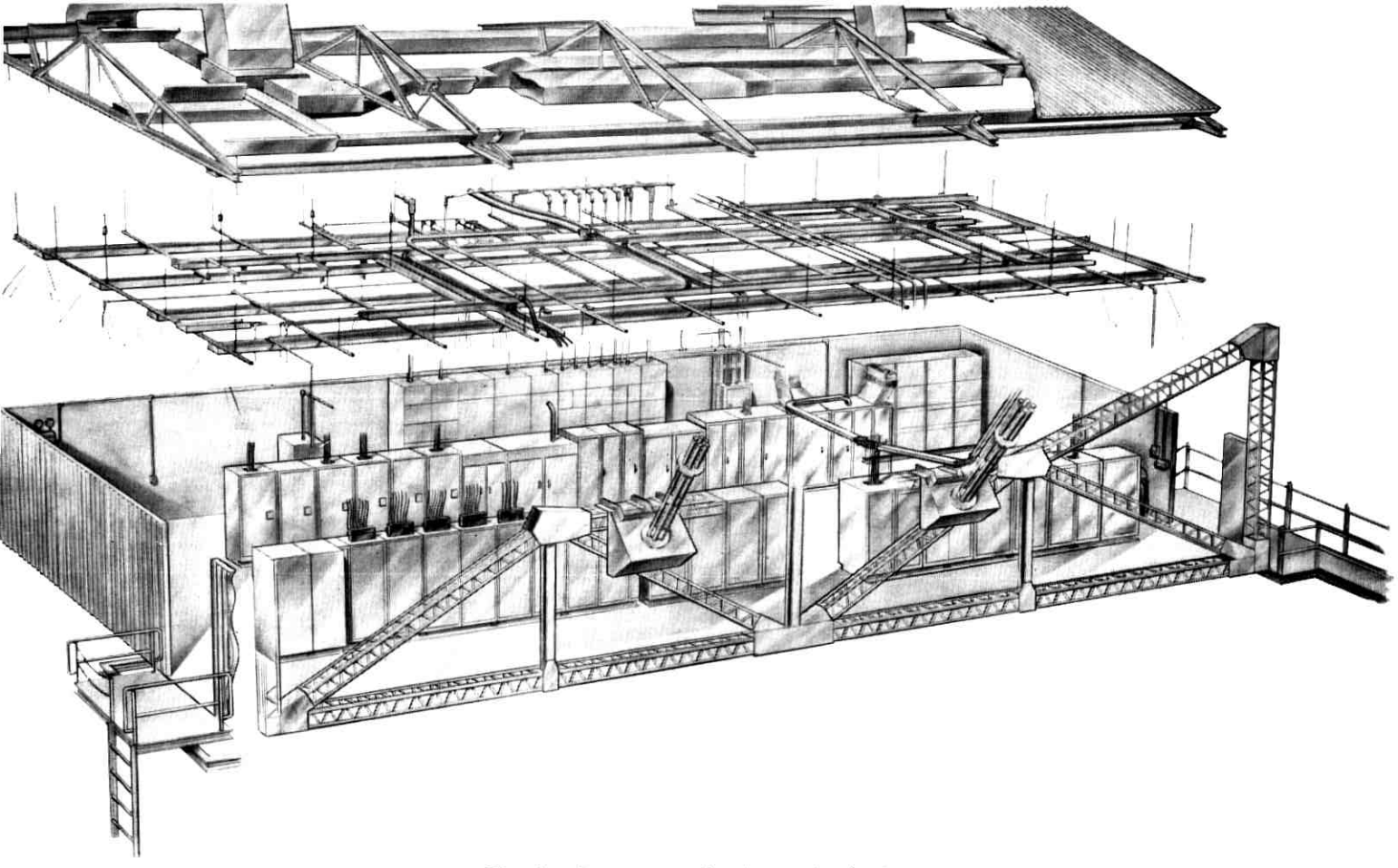

Fig. 4 — Lower room of antenna structure.

rings. A slip ring assembly previously designed for another project was modified to satisfy the requirements of the Telstar installation. The previous design was for 12 power rings, 300 general-purpose rings and seven unbalanced video circuits. The modifications permitted 28 power rings, 246 general-purpose rings and three balanced video circuits of very good quality.

The bulk of the power requirements for the rotating structure are satisfied by 340 KVA 440-volts 3-phase 60-cycles. It was deemed desirable to bring 440 volts instead of lower voltages into the rotating structure in order to minimize the current requirements for the slip rings. Where 208/120-volt power is needed, this is obtained from transformers on the antenna structure.

It is now believed that a cable-wrap system would be more practical than a slip ring assembly. The slip ring assembly would be essential for an antenna that has to revolve continually but is not of great value for a communications satellite ground station antenna that requires only a partial revolution for any one pass. With a cable-wrap system a fair amount of equipment would be eliminated.

III. OPERATING PLAN

An early step in system planning for the Andover ground station was the development of an operating philosophy. Analytic studies were made to determine the sequence of activities that could occur during the interval commencing with preparation for a satellite pass and ending with release of all systems at the termination of a mission. From these studies, operator decision points were defined and assigned as functional responsibilities at logical operator positions. Control and display requirements were then established and incorporated in the design of operating consoles. Also, an operations plan was prepared to set forth the specific procedures that would be used when operating various systems in concert. Training exercises and evaluation tests were carried out for the system as a whole to: (a) calibrate the interconnecting equipments, (b) determine system response times and other necessary operations data, (c) verify operations procedures, and (d) develop an efficient operator team. The last step in operations "prove-in" came through the experience obtained once the Telstar satellite was in orbit.

3.1 *Concept of Operations*

Centralized control was considered essential for coordinated operations involving many interrelated but independent subsystems—particularly

in view of the experimental nature of the project, the time constraints imposed upon design and installation, and the objective of insuring highest probability of success. Of secondary importance, but still significant, was a desire to minimize manpower requirements once standardized routines were validated.

The central control functions for ground operations very naturally group into two areas of responsibility: (*i*) satellite acquisition and tracking, and (*ii*) broadband experimental communication. The purpose of the first area is to establish and maintain a usable broadband communication path, while that of the latter is to carry out the various transmission experiments and obtain resulting test data. The two areas are assigned, respectively, to a ground station controller and a communications controller. Over-all supervision of operations during a mission is accomplished by a mission director or by one of the two controllers, dependent upon the complexity of the scheduled experiments and degree of external coordination required. Operating positions for the two controllers are adjacent to each other, with the director's monitoring position located behind the controllers as shown in Fig. 5.

The ground station controller has specific responsibility for:

1. Coordinating the pre-mission calibration and testing activities.
2. Verifying operability of the tracking and command complex before each pass.
3. Locating the satellite.
4. Activating the satellite in an appropriate sequence.
5. Positioning the horn-reflector communication antenna to excite the satellite repeater with broadband signals from the ground, and to receive its 4-kmc signal outputs.
6. Keeping the horn-reflector antenna properly positioned throughout the satellite pass so that experiments can be conducted.
7. Deactivating the satellite functions in an appropriate sequence before the satellite goes outside of command coverage.

The communications controller has specific responsibility for:

1. Calibrating the communication transmitter and receiver systems before and after each pass.
2. Setting up and verifying readiness of all scheduled communications experiments.
3. Carrying out such experiments and coordinating with external participating sites so that valid useful data are obtained.

Assisting the controllers are operators at a few vital equipment positions. Their duties are: (*i*) to monitor the performance of a subsystem or major equipment group, (*ii*) to make operating adjustments or con-

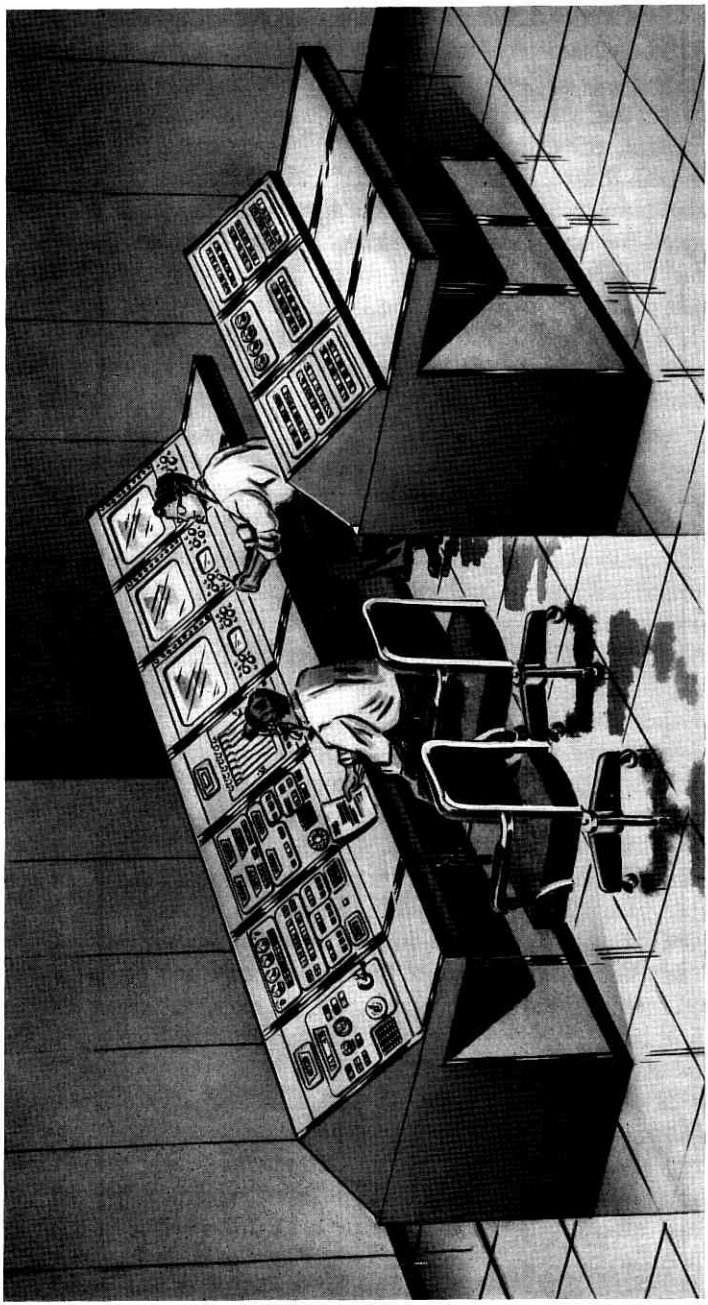

Fig. 5 — Director and control consoles.

TABLE I — BASIC OPERATIONS MANNING

Mission Operator Designation	Operator Position
Director	Director console
Ground controller	Ground station control console
Communication controller	Communication console
Command operator	Command encoder cabinet
Command track (1)	Command tracker equipment
Data operator	Tape switching console
ACE	Antenna digital control group
SERVO (2)	Antenna servo group
VAT	(Vernier) autotrack equipment
Receiver	4-kmc receiver equipment
Transmitter	6-kmc transmitter equipment
Test operator	Communications test center
TEG (3)	Track digital control group
Precision track (4)	Precision tracker console
Recorder (5)	Intercom and video recorders
Satellite (6)	Telemetry equipment bay

Notes:
(1) Manned only for initial operations, usually covered by command operator.
(2) Manned separately when needed, otherwise covered by ACE.
(3) Manned only when ranging data are scheduled.
(4) Manned separately when needed for orbit determination data.
(5) Manned only when video recordings are scheduled.
(6) Manned during first weeks of operation, for real-time assessment of satellite operating performance.

figuration changes when directed, and/or (*iii*) to perform manual control actions assigned to the local position. Table I presents the positional manning that was used during the first three weeks of operation after launching of the Telstar satellite. As indicated on the table, several of the positions are not manned during normal, routine missions.

Fig. 6 shows the basic control configuration of the ground station and the primary flow of status and control signals during a satellite pass. Briefly stated, normal operations proceed according to the general plan outlined below, assuming that the horn-reflector, command tracker and precision tracker antennas are all active. The plan is simplified for approximately 50 per cent of the passes by the deletion of the precision tracker and associated track digital control group when data for orbit determination are not required.

All systems are activated, tested and calibrated individually; they are then turned over to the two controllers who establish the integrated configuration and verify its operability by use of the satellite replica located on the test tower several miles from the station. The mission tape, with the pointing ephemeris and related data for the satellite pass, includes a set pattern of pointing and ranging data necessary for dynamic verification using the test tower. This tape is generated and

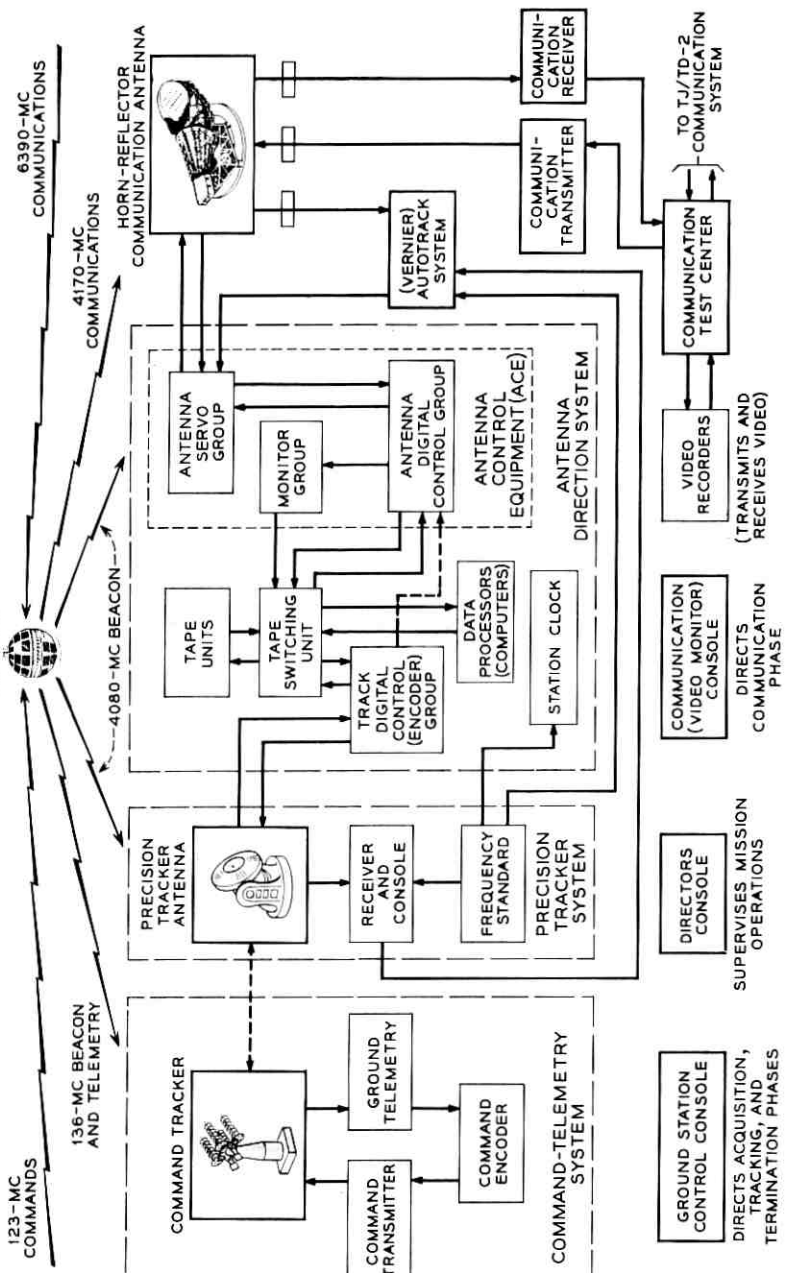

Fig. 6 — Basic control configuration.

checked by one of the local computers prior to the system testing interval. Concurrent with generating the tape data points, the computer produces a print-out of information about the pass for use by the operators; this print-out includes, among other things, pointing angles and rates for every whole minute during the passage. The print-out provides the operations team with a convenient reference for anticipating actions that will be necessary during the pass; it also serves as a back-up, for manually positioning any of the antennas to acquire the satellite, in case of loss of the automatic pointing data coming from the mission tape or other antennas.

Upon completion of the verification tests, and several minutes prior to expected satellite rise time, all three antennas are positioned to the angles for expected acquisition, using the mission tape as a common pointing source. When the command tracker begins receiving 136-mc beacon signals from the satellite and obtains a frequency phase-lock, its autotracking mode is selected. As soon as the strength of the received signal permits, commands are transmitted in a prescribed sequence to energize operating circuits in the satellite that activate telemetry and later turn on the broadband repeater. During this interval of several minutes, all vital conditions for safe operation of the satellite are verified by the received telemetry data. The mission tape keeps the horn-reflector communication antenna and the precision tracker pointed toward the satellite as it rises, or, optionally, the precision tracker can be slaved to the command tracker if desired.

As soon as the satellite repeater is ON, its 4080-mc beacon signal is radiated. At that time, both the autotrack system (sometimes referred to as vernier autotrack or VAT) and the precision tracker commence frequency search and obtain phase-lock for tracking. Concurrently, the communication transmitter may radiate 6390-mc carrier at normal power, and the broadband FM signals from the satellite repeater will usually be detected through the communication receiver, confirming satisfactory pointing by the horn-reflector antenna. When phase-lock is established, the autotrack system outputs are inserted into the tracking loop for the main antenna; similarly, the precision tracker begins autotracking. If difficulties are experienced in acquisition by either antenna, outputs from the other system may be used to assist in completing the process.

When the autotrack system error loop has been completed and the signal strengths in the 6390-mc and 4170-mc paths have been confirmed to be at expected levels, the communications controller uses the link for scheduled experimental transmissions. At a predetermined time during

satellite descent, or if a critical condition should occur in its operation, the ground station controller sends a sequence of commands that shut down the satellite repeater and restore other operating circuits to their secured state. Tracking is terminated at this time, and any necessary post-mission calibration data are obtained prior to release of the ground systems.

3.2 *Operational Performance*

The first several days of operation after the Telstar satellite launching established that command tracking acquisition normally can be accomplished slightly before the satellite rises to the optical horizon, that command of the satellite is reliable as soon as the acquisition is completed, and that usable telemetry data can be obtained before 5 degrees elevation except in the presence of severe noise from electrical storms or man-made interference. Acquisition by the horn-reflector antenna was found to be considerably more rapid than had been anticipated, usually being completed in less than ten seconds after full activation of the satellite repeater. Similarly, precision tracker acquisition was usually swift and was no problem. Some of the contingency capabilities that had been provided in the tracking systems were therefore of lesser importance than had been expected. These capabilities did give a great deal of flexibility for handling any troubles that might arise, and for probing for the marginal performance limits of tracking — quite appropriate characteristics for an experimental facility. During the first three weeks after the launch, all possible acquisition and tracking modes and configurations were attempted and all were successful. This even extended to slaving the horn-reflector antenna to the command tracker for acquisition. Of particular interest was the capability for manual acquisition by the horn-reflector antenna — that is, manually positioning to angles in advance of the satellite along its expected path and then achieving a full autotrack state during the interval that the satellite moved through the 0.22-degree beamwidth of the antenna's main receiving lobe. It was found that this technique could be used even at high elevation angles: At a satellite angular rate of movement of 0.3 degree/sec or less, the acquisition was relatively easy; at an angular rate of 0.45 degree/sec the acquisition required good operators, particularly at the autotrack position, but could be effected. Also of interest was the capability for minimizing disruptions of the communications link when the satellite passed very close to the site's zenith. By alert operation at the ground station control console, the link outage could be kept to within 10 seconds of the calculated interval for azimuth slew at the maximum rate

of 1.5 degrees/sec. Finally, horn-reflector antenna tracking up to elevation angles of 85 degrees was eminently satisfactory: The autotrack system nearly always held the pointing to within 0.005 degree of its null when its servo-loop was closed, or with the autotrack loop open the indicated pointing error could be kept under 0.01 degree by manually inserted offsets. Even with the autotrack system outputs turned off, a usable communications link could be maintained by keeping the 4170-mc received carrier AGC maximized through manual offset insertions, admittedly an arduous monitoring task for the ground station controller.

3.3 *Console Design Considerations*

3.3.1 *Ground Station Control Console (GSCC)*

An important objective in designing the operating position for the ground station controller was to achieve a minimum over-all manpower requirement for supervision, operation and maintenance at the ground station; consequently, design philosophy was based on performing as much of the acquisition and tracking control from this one console as was practical. This meant that the ground station control console or GSCC would interconnect with nearly all systems on the station (see Fig. 7). At the same time, the experimental nature of the project dictated that the design be flexible enough to accommodate development changes. Therefore, displays and controls were organized so that console activities could be handled by a single operator or apportioned between two, or even three, operators if necessary during training and early experiments. Also, features were included in the mechanical and wiring design so that functional changes could be made quickly after the console was installed, with minimum interference to its operational use.

Controls for the entire tracking and command complex were provided in the GSCC except for the precision tracker, data processors and their associated equipments. These were excluded for three reasons:

1. The primary real-time tracking complex does not require control changes involving these subsystems during normal operations.

2. If operating controls for these subsystems were included, the GSCC size and complexity would be such that a single operator, or possibly even two operators, might not handle the work load.

3. The excluded subsystem might be used for other operations during certain active passes in which they were not a part of the real-time horn-reflector antenna pointing complex. In particular, the data processors would be used for data reduction or generation of future predictions,

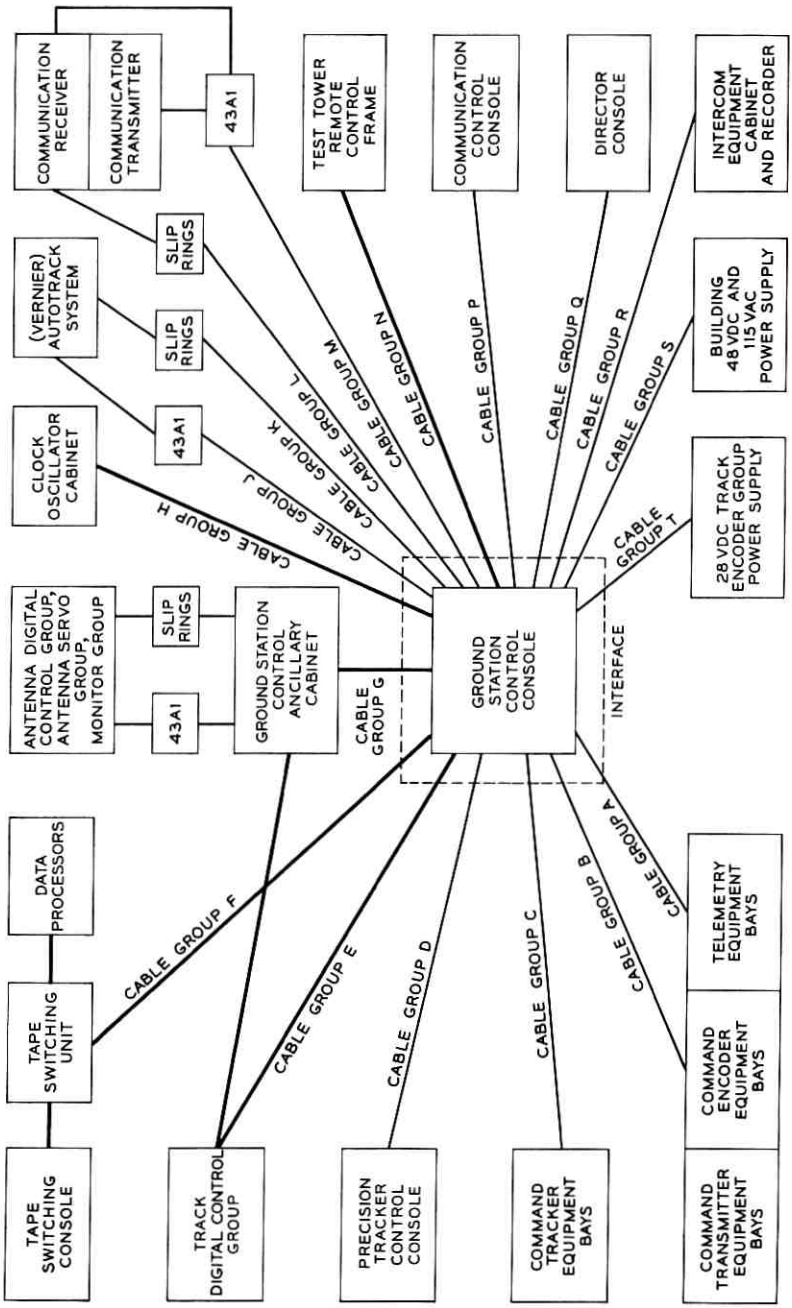

Fig. 7 — Connections to ground station control console (GSCC).

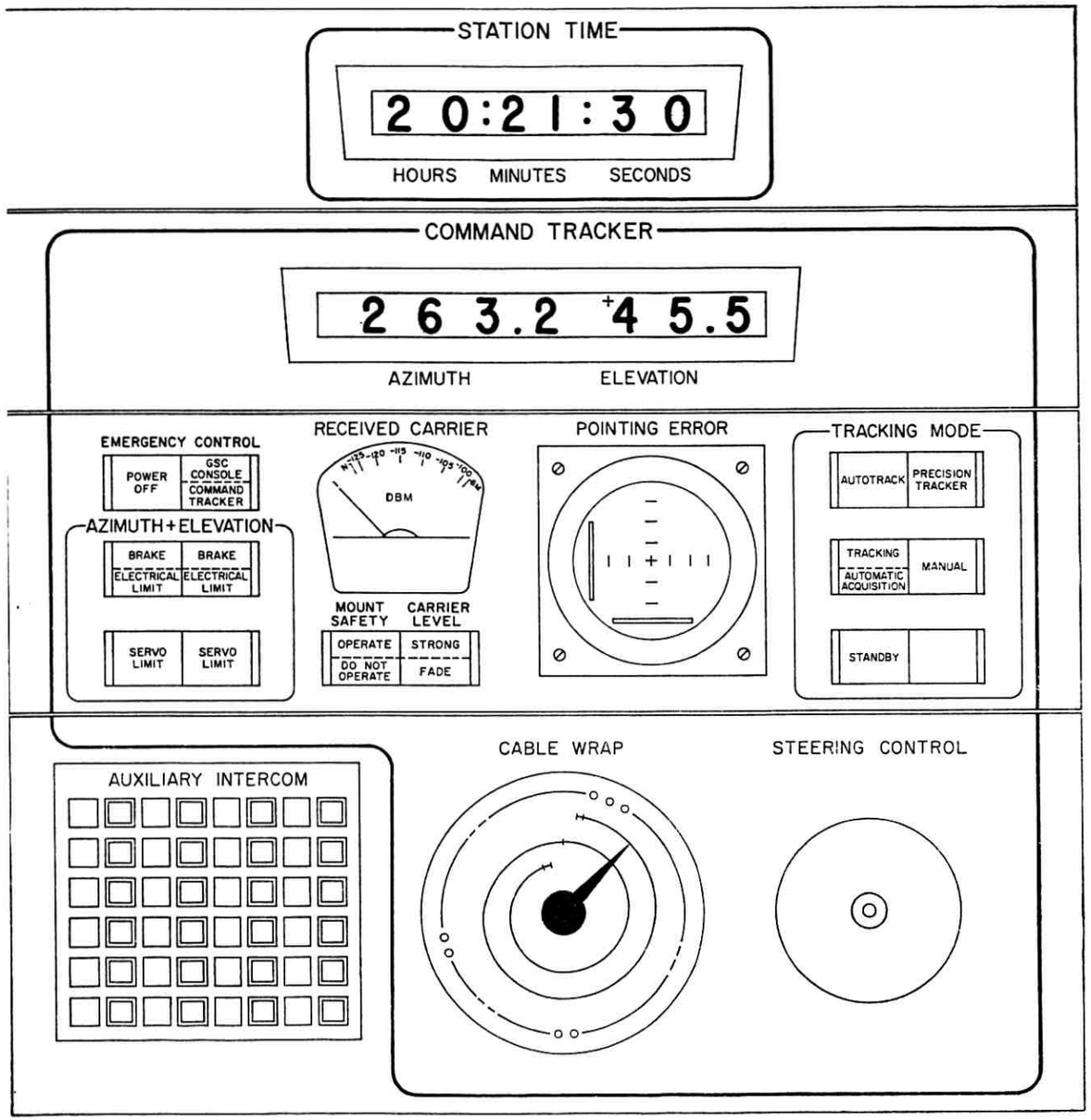

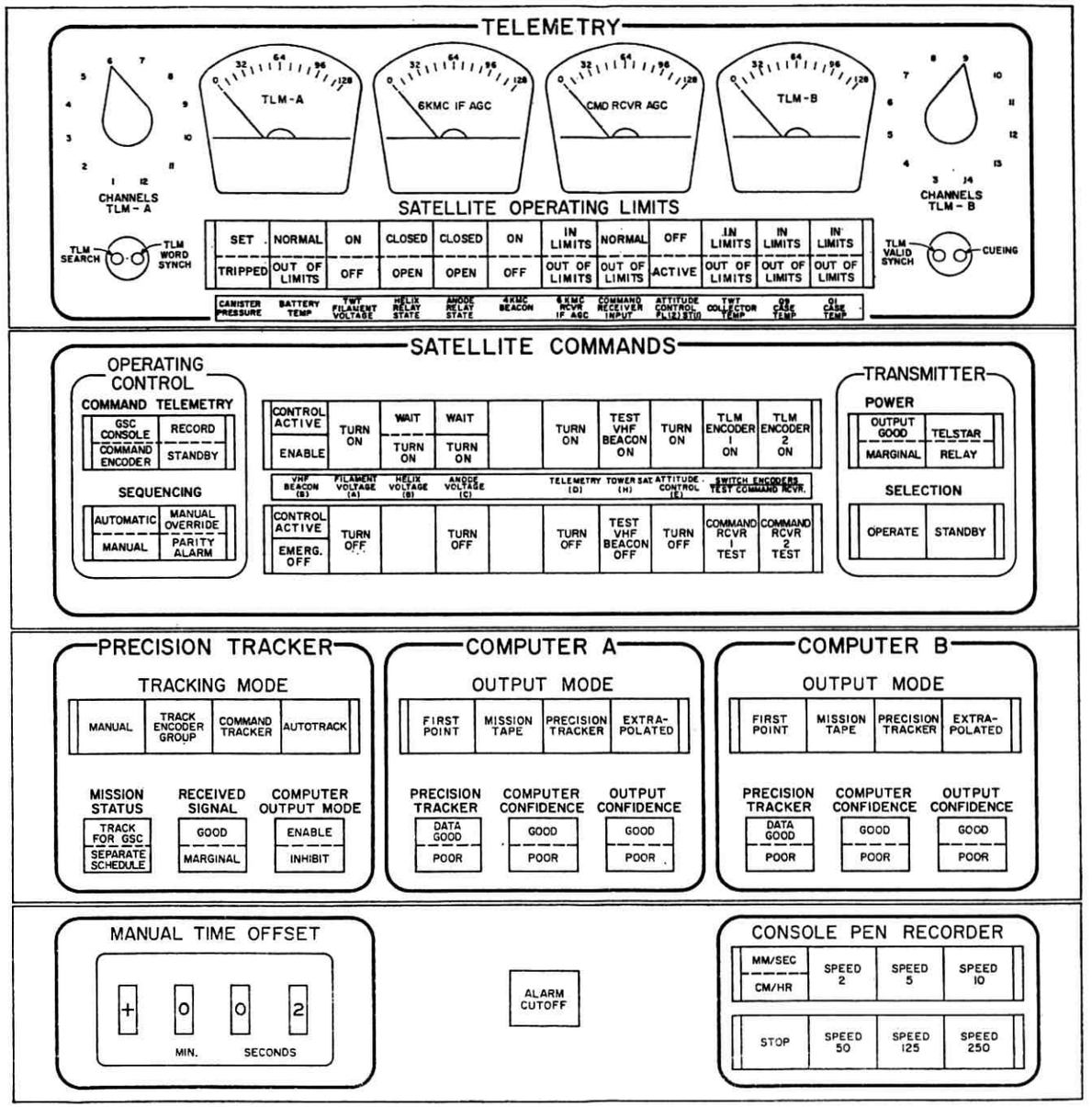

Fig. 8 (This page and overleaf)—Front panel layout of ground station control console.

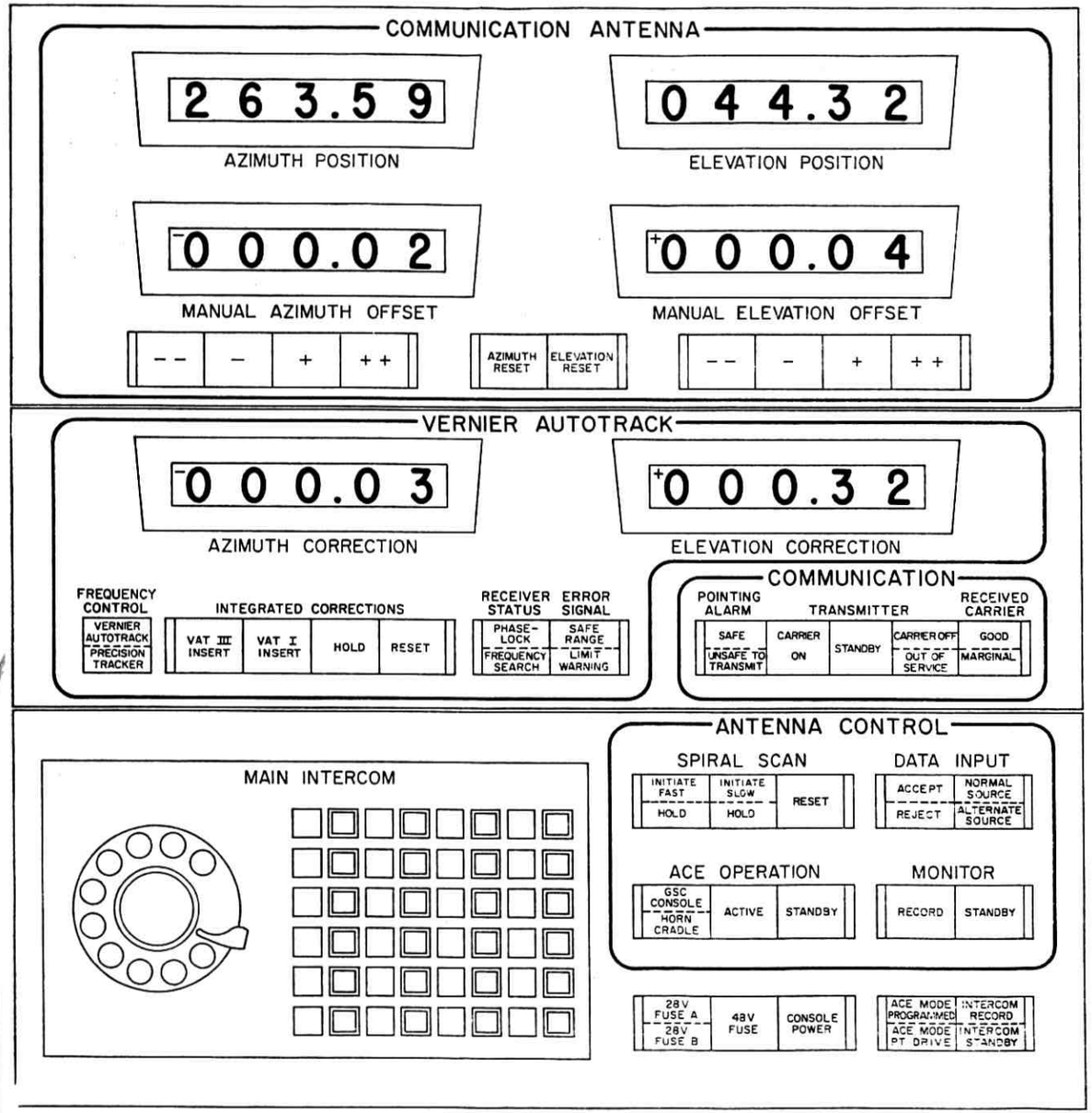
COMMUNICATION ANTENNA
263.59
AZIMUTH POSITION
044.32
ELEVATION POSITION
-000.02
MANUAL AZIMUTH OFFSET
+000.04
MANUAL ELEVATION OFFSET
-- - + ++
AZIMUTH RESET
ELEVATION RESET
-- - + ++
VERNIER AUTOTRACK
-000.03
AZIMUTH CORRECTION
+000.32
ELEVATION CORRECTION
FREQUENCY CONTROL
VERNIER AUTOTRACK
PRECISION TRACKER
INTEGRATED CORRECTIONS
VAT III INSERT
VAT I INSERT
HOLD
RESET
RECEIVER STATUS
PHASE-LOCK
FREQUENCY SEARCH
ERROR SIGNAL
SAFE RANGE
LIMIT WARNING
COMMUNICATION
POINTING ALARM
SAFE
UNSAFE TO TRANSMIT
TRANSMITTER
CARRIER ON
STANDBY
CARRIER OFF
OUT OF SERVICE
RECEIVED CARRIER
GOOD
MARGINAL
MAIN INTERCOM
ANTENNA CONTROL
SPIRAL SCAN
INITIATE FAST
HOLD
INITIATE SLOW
HOLD
RESET
DATA INPUT
ACCEPT
REJECT
NORMAL SOURCE
ALTERNATE SOURCE
ACE OPERATION
GSC CONSOLE
HORN CRADLE
ACTIVE
STANDBY
MONITOR
RECORD
STANDBY
28V FUSE A
28V FUSE B
48V FUSE
CONSOLE POWER
ACE MODE PROGRAMMED
ACE MODE PT DRIVE
INTERCOM RECORD
INTERCOM STANDBY

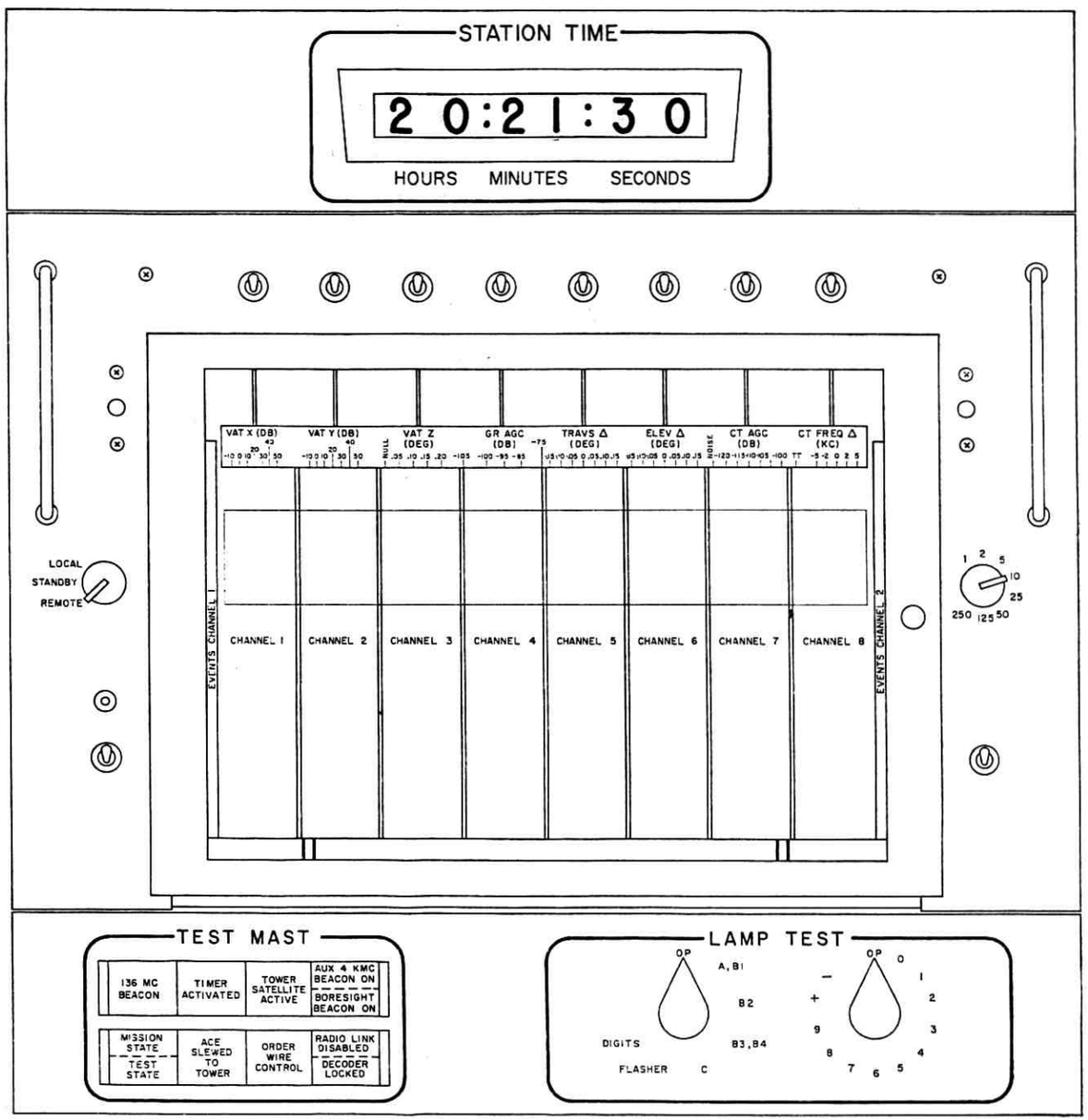
STATION TIME
20:21:30
HOURS MINUTES SECONDS
VAT X (DB)
VAT Y (DB)
VAT Z (DEG)
GR AGC (DB)
TRAVS Δ (DEG)
ELEV Δ (DEG)
CT AGC (DB)
CT FREQ Δ (KC)
LOCAL
STANDBY
REMOTE
EVENTS CHANNEL 1
EVENTS CHANNEL 2
CHANNEL 1
CHANNEL 2
CHANNEL 3
CHANNEL 4
CHANNEL 5
CHANNEL 6
CHANNEL 7
CHANNEL 8
TEST MAST
136 MC BEACON
TIMER ACTIVATED
TOWER SATELLITE ACTIVE
AUX 4 KMC BEACON ON
BORESIGHT BEACON ON
MISSION STATE
TEST STATE
ACE SLEWED TO TOWER
ORDER WIRE CONTROL
RADIO LINK DISABLED
DECODER LOCKED
LAMP TEST
OP
A, B1
B2
B3, B4
DIGITS
FLASHER
C

and the precision tracker might eventually be used for concurrent tracking of a second satellite.

Several of the GSCC controls and displays were included to allow full manual operation if required or desired during early experiments. In some instances, this capability was essentially a back-up for a mechanized feature or a hedge against operating problems that could but probably wouldn't arise; in others, it was an interim measure used for operations procedures that might eventually be automated after experience was gained with the first satellite. Thus, it was anticipated that the console and the operator's job would simplify as the system evolved after first experiments.

Fig. 8 shows the front panel layout of the console. Controls and displays were arranged in logical functional groupings and were located in the general order that the groupings are needed during acquisition and tracking; thus, operator activities start from the left and proceed to the right, going from top to bottom of each section. In so far as was practicable, the usual human engineering rules of uniformity, legibility, compatibility and operability were followed in the over-all design.

Components for display of magnitude quantities were selected on the basis of the dimensionality of the quantity and total range or precision required. Unidimensional quantities were presented on meter movements if no better than 2 per cent of full-scale accuracy was required; when greater precision was needed for such quantities, co-planar, projection-type decimal-digital displays were used. Important quantities whose history of variation over an interval of time was significant were presented on an eight-channel strip chart recorder in the section furthest to the right.

The digital nature of a substantial portion of the circuits in the tracking systems required that magnitude controls be in a digital form. An exception to this was the manual pointing control for the command tracker, which was in analog form. For uniformity in control and display configurations, magnitude inputs were decimal-digital wherever practicable. For quantities whose rate of change had to be limited, control from the GSCC was effected through increase/decrease switches associated with a decimal-digital display feeding back the present magnitude of the quantity stored in the associated subsystem.

Self-illuminated placard displays were used for binary event and for status information displays. Labels were engraved directly on the placards so that they would be visible even when the placard was dark. If a display was associated with a binary control function, the control and status displays were combined in a single pushbutton placard assembly.

This afforded visual confirmation by illumination of the control when an action was effected. All status indicators were arranged to be lighted by contact closures at the applicable system so that only confirmed status would be displayed. Wherever possible, a satisfactory condition would be shown by positive information (a lighted indicator), rather than by the lack of a warning signal.

Color coding for indicators was assigned on the following bases:

1. *White* was used for display of active equipment status or to confirm the execution of a simple, mutually exclusive GSCC command.

2. *Green* was used to signify that operation is normal and within limits or, on a control, that a binary command which is necessary in the acquisition-tracking process has been executed by the interconnected subsystem.

3. *Amber* was used to indicate that a function necessary to the acquisition-tracking process remains to be executed or requires attention by the controller. When flashing, the amber indicator was to denote a mild warning that a function of some urgency requires attention.

4. *Red*, when steady, was used to warn the operator that a control action is prohibited or that a vital function is in an unsatisfactory, nearly critical condition. Flashing red was reserved for emergency and alarm situations that required immediate action by the controller. Flashing red indicators were arranged also to trigger an audible alarm and to remain ON until acknowledged by the controller. When warranted, steady red controls were provided automatic interlocks to prevent effecting the prohibited action until the improper status had been cleared.

The color-coded status displays were selected so that they (*i*) prevented overlooking any essential steps in the acquisition, activation and tracking processes and (*ii*) gave the ground station controller confirmation at a glance (only green and white displays showing) that all conditions were normal once the communications link was established. This made it possible for the controller to direct primary attention during transmission experiments to the recorded traces on the strip chart or to specific satellite operating parameters.

Operational experience, after the Telstar launch, confirmed that for normal passes all necessary ground station controller responsibilities could be carried out by a single competent operator at the GSCC. Two operators could adequately handle the position under even the most unusual command or tracking experiments that were scheduled. It was also demonstrated that the position could be shared by three operators in a quite satisfactory manner, which was very convenient for collecting specific data on tracking performance during early operations and for training new controllers.

3.3.2 *Communication and Director Consoles*

In conducting transmission experiments via the satellite, it is necessary that close coordination be maintained with the ground controller and with participating external stations while concurrently monitoring the test signals sent and received. The communication console was therefore located adjacent to the GSCC so that key displays could be shared and critical interactions could be accomplished expeditiously and efficiently. A separate test center was provided as well, instrumented essentially as both a television operating center and a toll test board. Duplicate facilities were provided so that either the communication console or the test center could control, through a video and an audio crossbar switch, the connection of baseband inputs to the communication transmitter and outputs from the communication receiver.

For dynamic evaluation of the working outputs at the video switch, the communication console was instrumented with three commercial-type picture and waveform video monitors. One of these displays the selected outputs for transmission on the satellite up-path, another the received picture on the satellite down-path, and the third any available picture input such as that received over land-line circuits from the Holmdel station. For control of the video, a pushbutton matrix was installed on the console whereby any one of 10 transmission and test input signal channels may be applied to any one of 10 output channels. Associated audio, where applicable, was made available to the operator's headphones via a separate group of 10 pushbuttons on the console. In addition, several auxiliary control and status features were provided, such as those for interposition and external communication and those for selecting between the three available video standards for display generation.

The director console was designed to give a general view of the progress of operations and to provide flexibility in communicating with external participating stations prior to, during, and upon completion of a mutual experiment. For convenience, many of the individual status displays at the GSCC were provided to the director console in multiple. The only controls provided to this position were those associated with the intercom system and a mission time counter. This counter provided a display of time relative to the expected rise of the satellite, in minutes, from up to 99 minutes before the epoch until 99 minutes after the epoch had occurred. This display was used by the controllers and operators as the main reference for cueing during operations in that it was a more convenient display for the purpose than conventional station time.

The consoles for the controllers and the director were each provided

with direct access to the voice telephone circuits interconnecting external participating stations for operational coordination purposes. Also, the consoles were given access to the local PBX, intercom and paging systems. This arrangement allowed nearly complete freedom among the three positions for exercising supervisory responsibilities and for preventing overloads or coordination delays. The local intercom was designed to include two conference loops with appearances at all operating positions, and four maintenance loops with appearances at certain operating and related maintenance points. The conference loops were engineered for monitoring by each operator at all times desired, with freedom to talk simultaneously over this or another selected circuit. During operational missions, one conference loop is normally monitored by all operators as the primary coordination channel, and the other is used to handle any lengthy interchanges that may become necessary between two or three positions during the mission. Standardized station designations, push-to-talk, and a modest set of rules are imposed as circuit discipline for the conference loops.

IV. POWER FACILITIES

The Andover earth station, fully equipped with several communication systems, would require about 1000 kw of 60-cycle alternating current to energize rectifiers in the technical equipment and loads such as motors, lights and other utilities. Present load at the station is about one half the anticipated maximum load. There are two sources of this current. One source is commercial service from the local public utility company. The second source is a self-contained prime power plant equipped with diesel engine-generator sets.

The earth station loads are divided into the categories of technical loads and utility loads. Among the technical loads, examples include power for electronic equipment: rectifiers for tracking equipment, antenna control equipment, computers, receivers, transmitters, video monitors, tape recorders, and 60-cycle servomechanisms; and for primary essential services: motors for the main antenna drive, motor generators for 400-cycle servomechanisms, compressors for the maser cryostat, air conditioning and lighting for movable rooms on the main antenna structure, and blowers for equipment cabinets. Among the utility loads, examples include power for various secondary essential services: lighting circuits and convenience outlets in the control building and for stationary rooms in the main radome, motors and controls for building heating and air conditioning equipment, blowers for pressurizing the main radome

(see below), and dc power plants with battery stand-by for alarms and carrier telephone facilities.

The general plan for distribution of current to these loads is shown in Fig. 9. The service reliability criterion influenced greatly the choice of power switching circuits, the choice of the engines, the plant operating procedures, and the switchgear operating sequences.

The Andover plant is presently operated as a hybrid prime power installation with commercial service used for both the technical and utility busses during stand-by periods. During an experiment, even a brief interruption on the technical bus is unacceptable. A short interruption on the utility bus is undesirable, but tolerable.

The power-plan circuit in Fig. 9 is shown in the normal operating condition which obtains during a satellite communications experiment. Generators A and B are in parallel, delivering energy through the generator circuit breakers A and B, and the tie breaker AB to the technical bus. The utility bus is energized from the commercial service through circuit breaker K1B. When an interruption occurs in the commercial service, breaker K1B is opened and breaker 2B is closed, so that the engines feed both busses. If one engine fails during normal operations, the other engine can carry the load on the technical bus. If an engine

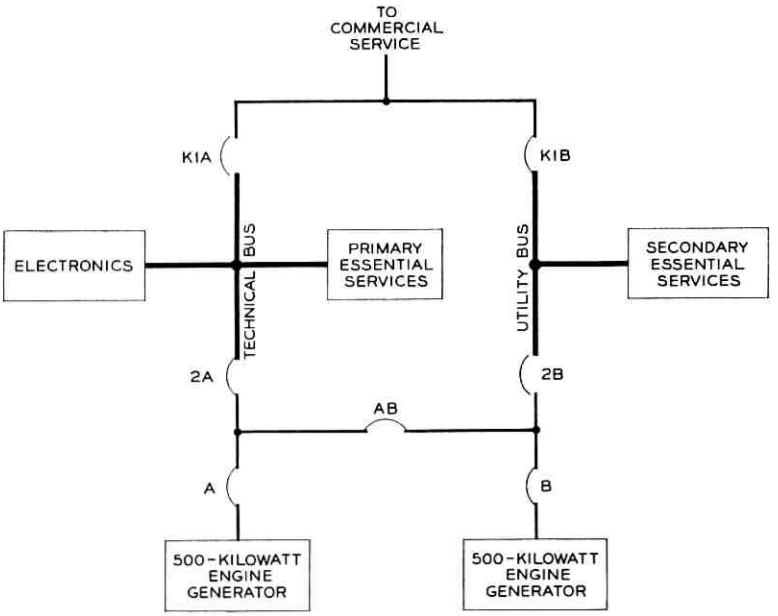

Fig. 9 — General plan for distribution of power.

fails during a commercial failure, the remaining engine will carry the entire load on the technical bus plus part of the load on the utility bus.

The engine-generators are rated at 500 kilowatts, 900 rpm, and are of the type procured by the Bell System for stand-by service in central and toll offices. The choice of this particular machine was dictated primarily by load demand, although a single larger engine could have been used to carry the total station load. The use of two 500-kilowatt machines gives greater flexibility for growth, and for higher reliability than would be obtainable with a single machine. Also, a considerable backlog of experience has been built up with this particular set, and its proven performance in other prime power applications makes it a preferred choice.

An axiom derived from Bell System power plant experience is that the probability of occurrence of operator error is highest during the first few minutes of an emergency such as a power failure. Therefore, power plant operator procedures are arranged so that most failures of the types expected to be encountered do not require immediate action on the part of the operator. Thus, if commercial service fails, the operator is relieved of pressure to restore utility bus voltage by the fact that immediate restoration is not necessary, by definition, on the utility bus. Similarly, if one of the engines fails, the operator is relieved from pressure by the fact that one engine can carry the technical bus load indefinitely. Of course, engine circuit breakers are depended upon to clear overloads due to faults or current reversals.

It will be noted that the blowers for pressurizing the main radome are fed from the utility bus. This is the one load on the utility bus for which a power failure of a few minutes duration could be a hazard. Consequently, the motor control center for the blowers can be energized from a small 30-kilowatt, automatic-start diesel generator, located at the radome, as well as from the utility bus. This arrangement gives protection against failure of the utility bus or any of the switchgear associated with the bus, for more than a few minutes.

The reliability features in the power system have proved to be well worth-while. Operating records show that there were six interruptions in the commercial service in 1962, four of which occurred after the Telstar satellite was launched. One of these interruptions caused a loss of system power long enough to disturb seriously a communications experiment. In addition, there have been partial and full power failures due to operator errors and training sequences, but these failures were anticipated as an unescapable part of the installation and familiarization program. Analysis of the causes of these failures has confirmed the sound-

ness of the plan to minimize pressure on the operator during an emergency.

V. AIR CONDITIONING AND HEATING

The Andover site, located in a remote section of Maine, experiences some of the most severe environmental conditions in the United States. In order to communicate with a satellite orbiting in space, precise control of the 380-ton antenna[1] is essential at all times. To reduce mechanical deviations which might be expected from snow, ice, wind and large fluctuations in temperature, the entire antenna is housed in a large air-inflated plastic radome. The inside of the radome requires heating to prevent the accumulation of ice and snow on the outside surface of the radome. It also requires dehumidification to avoid damage to equipment through rain, fog or condensation within the radome.

In addition to the radome, the two rooms which house transmitting, receiving and tracking equipment are part of the rotating antenna structure and require heating and cooling for both equipment and personnel.

Heating and cooling for the utility building adjacent to the radome foundation and the control building presented no unusual problems and will not be discussed in this paper.

5.1 *Radome Heating and Deicing*

The use of a protective radome created a number of engineering problems. Controlled heating of the inside air is needed to prevent ice and snow accumulation on the radome which might impair system transmission. The heating system must be capable of maintaining temperatures suitable for both personnel and equipment.

Fig. 10 is a schematic diagram of the closed hot water system used to heat the utility building and to heat and deice the radome. This system originates at the control building where two oil-fired boilers, each with an output rating of 10 million BTU per hour, supply 200°-225°F hot water. The complete output of these boilers is not used at the radome, however, since some 4 million BTU per hour are used at the control building itself. The hot water is piped one quarter mile underground to the radome and utility building where it is distributed by branch piping to the heating coil, room space heaters, and the radome heating-deicing units. The discharge water from these units is directed into return water lines which eventually return the water to the boilers for reheating.

Radome heating and deicing represent two different heat problems.

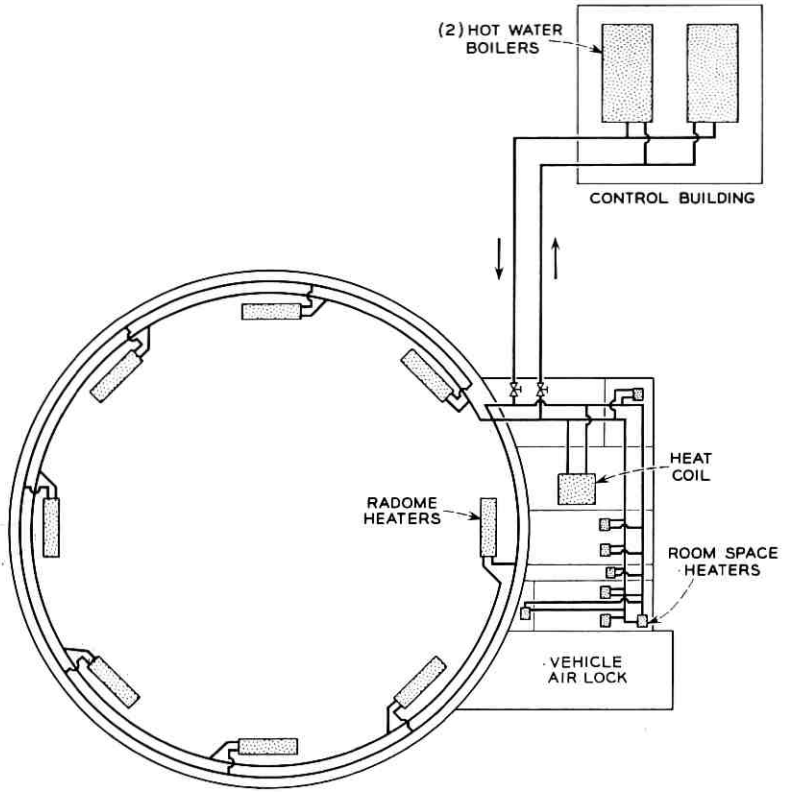

Fig. 10 — Schematic diagram of closed hot water system.

For interior heating it is desirable to direct the bulk of the heat near the equipment and working areas and to minimize heat losses through the plastic type radome. For snow melting and deicing, heat concentration should be at the top and sides of the radome with a maximum heat flow through the radome material being desirable.

In order to design an adequate heating-deicing system for the radome, it was necessary to calculate heating requirements for both heating and deicing. Calculations indicate that 13,551,000 BTU/hr is required for radome heating and that 10,250,000 BTU/hr is required to melt the snow and any ice film on the outside surface. Therefore, radome heating determines the maximum amount of heat to be supplied to the radome.

Although heating is the governing criterion in determining the amount of heat to be supplied to the radome, the distribution of heat is another

problem. The air temperature in the upper portion of the radome must be 107°F to melt snow, and an air temperature of 62°F is required to keep water from freezing on the lower portion. To accomplish this heat distribution, eight radome deicers spaced 45 degrees apart discharge warm air into a plenum chamber through a transition section and into flexible plastic wall ducts. Tap-off ducts, with damper-controlled flow, were designed for scrubbing the lower radome wall. Eight circular plastic ducts were provided; four were designed to extend 50 feet above the radome heaters and four designed to extend eighty feet. The duct openings are directed to provide a scrubbing action over the inner radome surface.

5.2 *Radome Dehumidification*

In addition to radome heating, another problem encountered in using a protective enclosure was radome dehumidification. Provisions for this had to be made in order to avoid damage to equipment through rain, fog or flooding of the concrete base by condensation. Condensation occurs when saturated air is cooled. During the cooling process, the heat losses of the saturated air represent the sum of sensible heat of air and the latent heat of the condensed water.

Considering the radome conditions, if it is assumed that the outside dry bulb temperature is less than the inside dew point temperature, the following conditions can occur:

1. When the inner radome surface temperature is greater than the inside dew point temperature, no condensation will occur.
2. When the inner radome surface temperature is less than the inside dew point temperature, condensation will occur on the radome skin.
3. When the inside dry bulb temperature is equal to the inside dew point temperature, the air will be saturated and condensation in the form of fog or rain will occur within the radome.

In order to prevent the formation of condensation within the radome enclosure, it is necessary to keep the dew point temperature lower than the dry bulb temperature. This can be accomplished by using a dehumidifying coil. The coil can be placed in the incoming air stream and by circulating cold water through the coil, most of the moisture contained in the incoming air can be condensed out. With a chilled water system supplying 40°F water, incoming air can easily be cooled to 45°F. 38.7 tons of refrigeration are required to maintain the proper conditions during the summer.

For winter operation, a thermostatically controlled heat coil, located on the input side of the dehumidifying coil, is used to heat incoming air

above freezing. The heat coil selected is a 2-row Aerofin Coil having the required heat capacity when circulating 13 GPM of 225°F water.

5.3 *Temperature Control in the Equipment Rooms*

The two house-sized rooms, built as part of the rotating structure, require heating and cooling for both equipment and personnel. The upper room, measuring approximately 26 feet by 34 feet by 9 feet high at the walls, is located about 60 feet above the radome floor. This room contains the radio transmitting and receiving equipment. The lower room, located about 10 feet above the floor of the radome, is approximately 24 feet by 68 feet by 9 feet high at the walls. This room contains the antenna drive and control equipment and the power distribution equipment.

Electronic equipment, transistorized and otherwise, operates very efficiently in a stabilized ambient of 60° to 85°F with a relatively low humidity; the majority of people are comfortable at 70°F and approximately 50 per cent relative humidity. Fortunately, these conditions are not contradictory, and the latter condition was established as the ambient design condition inside both rooms on the antenna structure.

Chilled air is transmitted through a system of ducts for both equipment and personnel cooling. The duct system is split into two parts, one for distributing chilled air to plenum chambers running under each row of equipment cabinets for equipment cooling, and the second for supplying chilled air to outlets in the head space of the room for personnel cooling. Resistance heaters in the personnel supply ducts permit the use of these ducts for heating purposes. Air-handling units mounted beneath the floor of each room, upper and lower, contain the blowers and chilled water cooling units required to supply chilled air to the duct systems.

A source of chilled water was required for the air-handling units and for the water-cooled traveling-wave tube in the transmitter for the Telstar satellite, and also for the klystron used in the transmitter used for experiments with the Relay satellite.

5.3.1. *Equipment Cooling and Personnel Air Conditioning*

The first step in the solution of the equipment cooling and personnel air conditioning problem was to determine the expected climatic conditions from synoptic meteorological records. Expected heat loads and their distribution were established and were categorized as to whether they were sensible or latent Finally, it was necessary to determine the most

efficient means to dissipate the heat, i.e., by forced cooled air or chilled water, and whether the equipment and personnel cooling systems should be in series, parallel or a combination of both.

Investigation indicated that one of the following three systems for providing over-all cooling and heating would be feasible.

1. A chilled water system for water cooling plus radome air-cooled, self-contained air conditioning units for forced air cooling plus electrical resistance heating.

2. A chilled water system for water cooling plus chilled water air handling units for air cooling plus electrical resistance heating.

3. A chilled water system for water cooling plus water-cooled, self-contained air conditioning units for air cooling plus electrical resistance heating.

Using as an evaluation criterion the basic philosophy of requiring (*i*) the least weight on the rotating structure, (*ii*) the least power required, and (*iii*) the least expense from the standpoint of maintenance as well as first cost, system No. 2 was selected for the Telstar project.

To insure that the heat-transfer surfaces of the traveling-wave tube in the 6-kmc transmitter[2] did not suffer degradation from contamination, the water used in the chilled water system had to be very pure. Copper piping, which has a tendency to kill bacteria and does not add impurities such as rust to the water, was selected for use in the chilled water system. To further insure that the water passing over these heat transfer surfaces was pure, all minerals found in ordinary drinking water in the form of ions and cations had to be removed. This was accomplished by installing a deionizer with a bed of nuclear grade resin in series with a microfilter. The microfilter is capable of removing particles as small as 1 micron. The water obtained by using the copper piping, the microfilter and the deionizer is purer and cleaner than normal drinking water and has an electrical resistance of between 12 and 20 million ohm-centimeters.

Specifying the size and physical requirements of the equipment to be designed or modified requires that a summation of the heat gains and losses be determined for all equipment and personnel locations. Using established design criteria, the heat gains and losses had to be correlated with the existing outside ambient conditions for Andover, as well as for the predicted inside ambient radome conditions. After accumulating this information, a heat balance was made to determine the amount of refrigeration required in the summer and the heating required in conjunction with cooling during the winter. The requirements for refrigeration are summarized in Table II.

TABLE II — REFRIGERATION AND CHILLED WATER FOR UPPER AND LOWER ROOMS

	Gal/min Water	Tons
Lower room		
Air handler	35	25.2
Klystron for Project Relay	25	11.44
Upper room		
Air handler	24	17
TWT tube	25	7.10
	109	60.74
Dehumidification	60	38
Total	169	98.74

Air handlers having the following characteristics based on the use of 42°F cooling water were selected:

	Lower Room	*Upper Room*
Cooling capacity	25.2 tons	17 tons
Quantity chilled water required	25 gal/min	24 gal/min
Air temperature drop	20°F	20°F
Air flow capacity	14,000 CF/M	10,000 CF/M

5.3.2 *Refrigeration System*

To insure reliability in this system, multiple smaller-sized refrigeration components are used instead of one large unit. The main components of the water system are two chillers, each having four compressors, two centrifugal water pumps, four condensers, a deionizing unit, two air handlers, four receivers, and a dehumidifying coil. The majority of these components are installed in the utility rooms at the base of the radome, external to the pressurized area.

The refrigeration system uses four refrigeration circuits. If one circuit fails, maintenance can be completed without affecting the other three circuits. Each refrigeration circuit consists of two compressors, one air-cooled condenser, a liquid freon receiver, and associated refrigerant valves. The nominal capacity of the four circuits is 100 tons of refrigeration.

Integral with each refrigeration circuit is an air-cooled condenser located on the roof of the utility building. Again reliability was a contributing factor in the selection of this type condenser. The severe winter

conditions in the Andover area made it necessary to pick a unit with simple controls requiring a minimum of maintenance. The air-cooled condenser is preferred over the evaporative type of condenser or cooling tower because air instead of water is used to dissipate heat.

5.3.3 *Chilled Water System*

The requirement for reliability indicated the need for more than one high-pressure pump for circulating chilled water. Failure of the operating pump requires that the standby pump must start automatically and immediately. As a result, the pumps were supplied with automatic back-flow check valves at the supply end of each pump. This insured no loss of pressure due to flow through the idle pump but of course increased the flow pressure on the output of the other pump. The requirement that the traveling-wave tube, inherently a high-flow resistance device, be used in parallel with a low-flow resistance unit such as an air handler, required special valves in conjunction with regular valves, which increased the over-all flow resistance of the system.

Two high-pressure pumps, each having a flow capacity of 230 gallons per minute when pumping against a head pressure of 231 feet of water (93 psi), were installed. The chilled water flow path starts at the operating pump and passes through the two chillers operating in parallel. These chillers cool the return water to 40°F. The water is then forced through a 4-inch, cork-insulated copper pipe. At the center of the antenna, the pipe size is reduced to 2 inches prior to passing through the rotary joint. (Water flowing from a stationary component onto a rotating structure, such as the antenna, requires a leakproof rotary joint, illustrated in Fig. 11.) The chilled water then passes through one cavity of the rotary joint onto the antenna, where it is diverted to several branches of fiberglass insulated pipe which carry it to the upper and lower rooms. At these rooms the chilled water is distributed to the TWT, klystron tube and air-handling units.

The requirement for very pure water also dictated that the chilled water system be a closed one. Therefore, the return water passes through the second cavity of the rotary joint and back to the pumps. A portion of the chilled water is used to dehumidify the air used to inflate the radome.

The selection of a deionizer was based upon an established standard that a deionizer have sufficient capacity to handle at least one per cent per minute of the total gallonage in the system. A deionizer with a capacity of 6 to 20 gallons per minute was selected.

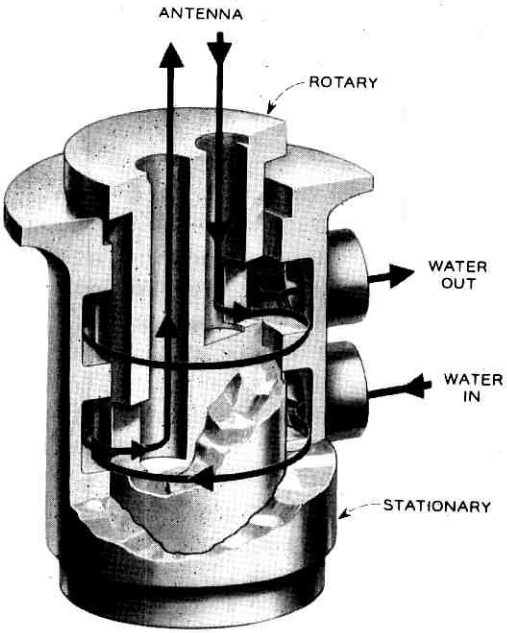

Fig. 11 — Rotary joint for chilled water system.

5.3.4 *Heating of Equipment and Personnel Areas*

To establish a stabilized air conditioned area for personnel in both the upper and lower room requires that heat be added when the radome temperature is between 40° and 50°F. Since both the rooms are on the rotating structure, a great advantage can be derived in using an electrical resistance type of heat, as no storage tanks are required and the heat is "clean." Assuming that the radome temperature surrounding the lower equipment rooms is 45° and knowing that the personnel area is to be maintained at 70°F, there will be a loss of heat from the room to the radome. Part of this heat loss is offset by warm air discharged from the equipment and by heat radiated from the lights and personnel. Additional heat, however, must be added to the air being supplied directly to the personnel area in order to maintain the desired 70°F room temperature. A summary of the heat losses indicates that 19.7 kw is required in the lower room and 15 kw is required in the upper room to maintain design temperature of 70°F.

5.3.5 *Duct and Control System for Equipment Rooms*

The duct system used for both upper and lower rooms is made of aluminum. In these rooms, it was desirable to keep background noise levels as low as possible. In order to achieve this with the air flow required, the ducts had to be not only thermally insulated but also insulated acoustically with all ninety-degree duct turns vaned. This was accomplished by using a 1-inch fiberglass thermal insulation in conjunction with a simulated horse hair acoustical absorbing material, both of which were attached to the inside of the ducts. Control of the air distribution was accomplished by using strategically located manual dampers, along with adjustable air diffusers and registers. Due to the limited space available in both the upper and lower equipment rooms, the associated air handlers were suspended in a centrally located area under each room. This also helped to reduce the noise level inside the rooms. A system of catwalks and platforms provides access to the air handlers for maintenance purposes. Transmission of vibration to the antenna structure and rooms was reduced by mounting the air handler units on vibration isolators. To further reduce noise and vibration transmission through the ducts, canvas boots were used to attach both supply and return ducts to the air-handling units.

The duct system was designed so that the air handler associated with a specific room cools both the personnel area and equipment. This meant that the unit had a common return and supply duct. The supply duct was branched under the room floor to feed cool air to distribution ducts and equipment plenum chambers running under each row of equipment cabinets.

The personnel area branch duct feeds a portion of the cooled air to the distribution duct system located in the head space of the rooms. The temperature of all cool air leaving the air conditioning unit is controlled by a by-pass damper box. This box is located on the return side of the air handler and is controlled by a thermostat in the supply duct in front of the unit. This adjustable thermostat, usually set for 60°F air, modulates the flow of air across the cooling coil of the unit. If the outgoing air is too warm, the dampers direct more return air across the coil; if the air is too cold, most of the air by-passes the cooling coil.

The air temperature in the personnel space is controlled by a thermostat. This instrument is located in the personnel return air duct in the room just prior to the point where the equipment and personnel return air ducts combine into a common return duct. The thermostat controls the resistance heaters, which can add heat in increments of 2.5 kw in the

upper room and 3.3 kw in the lower room up to totals of 15 kw and 20 kw, respectively.

VI. EXTERNAL COMMUNICATIONS REQUIREMENTS

An extensive communications network involving some 86 circuits was provided between the Andover earth station and various U. S. and European locations by the Long Lines Department of the American Telephone and Telegraph Company. Its purpose is to provide operations control and coordination, tracking and telemetry data exchange, and interconnection for remotely originated tests and demonstrations. The facilities used include voice, teletypewriter, data and video channels.

Access by the Andover station to the nationwide radio relay network was attained by the construction of four links of microwave radio relay between Andover and Portland, Maine. In addition, a 150-pair cable was placed between Andover and Rumford, Maine, where it connected with existing cable facilities.

On July 10, 1962, all connecting circuits with Andover were involved in the initial tests and demonstrations. For the first four months after launch, these facilities were used regularly for nearly 400 demonstrations and remote tests.

6.1 *Support Communications*

Control and information circuits were provided to coordinate station operations and to exchange tracking and telemetry data between Andover and other Bell Laboratories, NASA, A.T.&T. Co., and overseas locations. Figs. 12 and 13 show these circuits, consisting of 7 full-period voice circuits, 5 order wires, 3 DATA-PHONE and 5 teletypewriter circuits.

The voice circuits interconnect Andover with the several Bell Laboratories locations in New Jersey and at Cape Canaveral, as well as with the French and British earth stations at Pleumeur-Bodou and Goonhilly. The order wires interconnect with A.T.&T. Co. Long Lines Department plant operating centers for the coordination of carrier telephone, radio relay and television channel usage to and from Andover.

DATA-PHONE circuits between Andover and the Murray Hill and Whippany Laboratories and the French station were established to transmit antenna pointing data to Andover and Pleumeur-Bodou and to return satellite telemetry information from Andover. These circuits transmit digital data at 1200 bits per second between commercial magnetic tape data terminals.

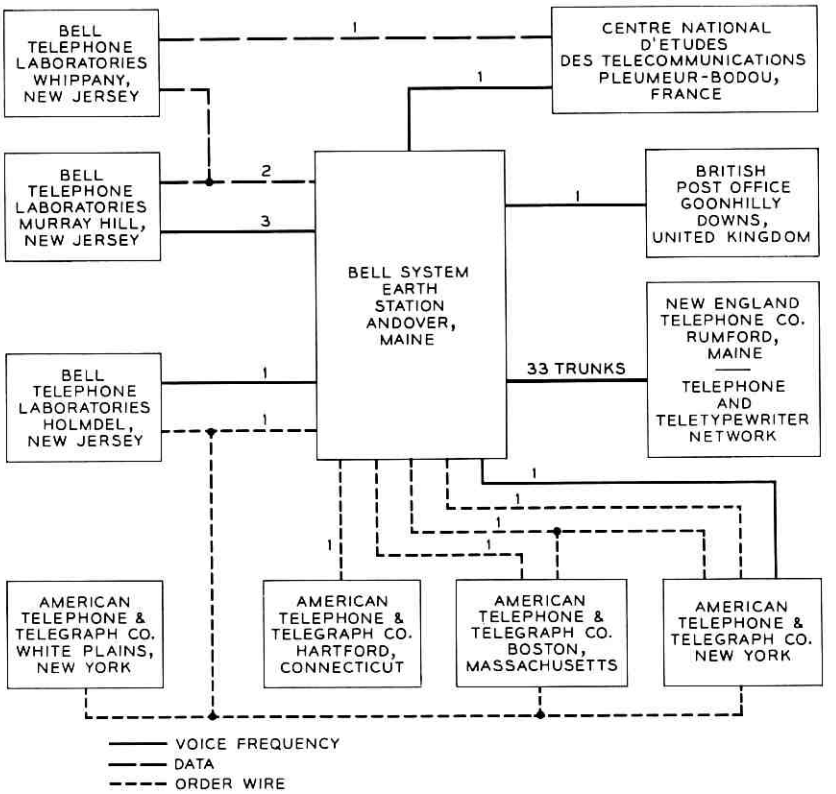

Fig. 12 — Voice-frequency, data and order wire connections with Andover.

Teletypewriter circuits to carry scheduling information, operations messages, orbital tracking data and administrative traffic were installed between the Andover station and NASA Goddard Space Flight Center, Bell Laboratories computing center and operations offices in New Jersey, and the British and French stations.

As shown in Fig. 12, local trunks from the Andover station interconnect with the message telephone network at Rumford, Maine. These serve the local administrative needs of the station and include 10 inward and 10 outward dial trunks through the station PBX, a TWX trunk, 2 public coin box lines and 10 miscellaneous local trunks.

The basic test and demonstration network, consisting of 24 voice-grade channels, 2 telephoto circuits and 2 video channels in each direction, is shown in Fig. 14. These facilities were used for demonstrations

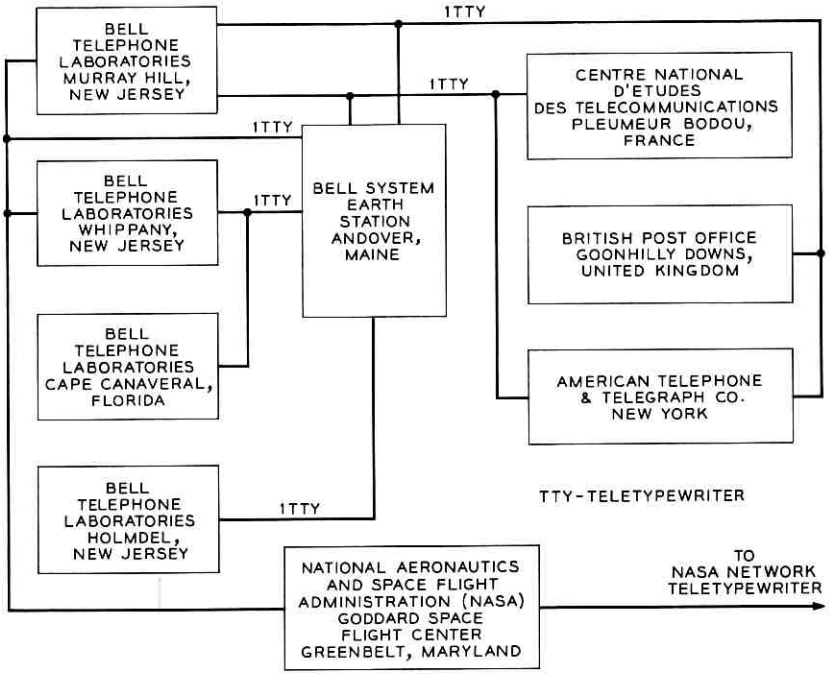

Fig. 13 — Teletypewriter connections with Andover.

and for conducting data transmission tests at the A.T.&T. Co. Long Lines Department headquarters in New York City. In addition, a pair of video channels and a telephoto circuit were provided from the Bell Laboratories Holmdel, New Jersey, receiving station to New York for test and demonstration use.

6.2 *Radio Relay and Cable Access Links*

New broadband facilities were required to link the Andover station with the existing Bell System radio relay network to handle video and multiplex telephone channels. The nearest junction point was Portland, Maine, approximately 90 miles south of Andover. Microwave radio relay links of TD2 (4 kmc) and TJ (11 kmc) were constructed in tandem between Portland and Andover. Since the satellite-to-ground signal is at 4170 mc and the ground-to-satellite signal is at 6390 mc, it was decided not to employ either TD2 (4 kmc) or TH (6 kmc) systems for the first external microwave links out of Andover. Therefore, a TJ (11 kmc)

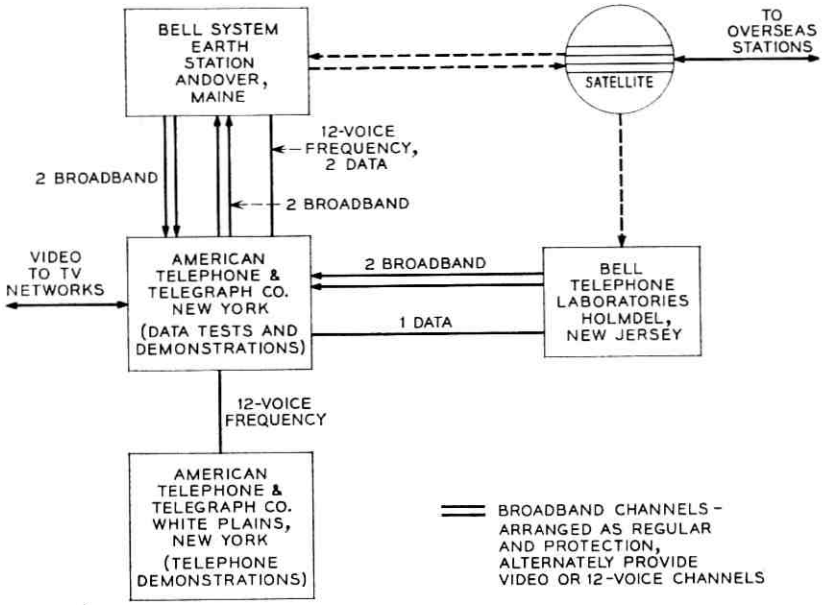

Fig. 14 — Test and demonstration network.

system was selected for the first two links. A coaxial cable system would have been free of interference but was economically impractical because of the mountainous terrain. The first microwave repeater station was located 4.5 miles south of the Andover station atop Black Mountain, on the rim of the "Andover bowl." Beyond the second link a TD2 system was used. The combination of the ring of mountains forming the bowl, the physical distance, and the bearing of the paths reduce to inconsequential levels any stray signals between the repeater stations and the Andover site. From this point to Portland, Maine, where connection was made to the existing TD2 microwave network, normal engineering criteria were used. The over-all route is shown in Fig. 15.

Two radio channels, one regular and one protection in each direction, were provided between Andover and Portland. They were each equipped to handle a 4-mc video signal with the corresponding audio signal provided by a diplexing arrangement using a subcarrier inserted above the video band. Channelizing equipment to permit transmission of 12 two-way telephone circuits instead of the video signals was also installed.

In addition to wideband facilities, voice-frequency cable circuits were provided to handle the support communications requirements. Sixty-one

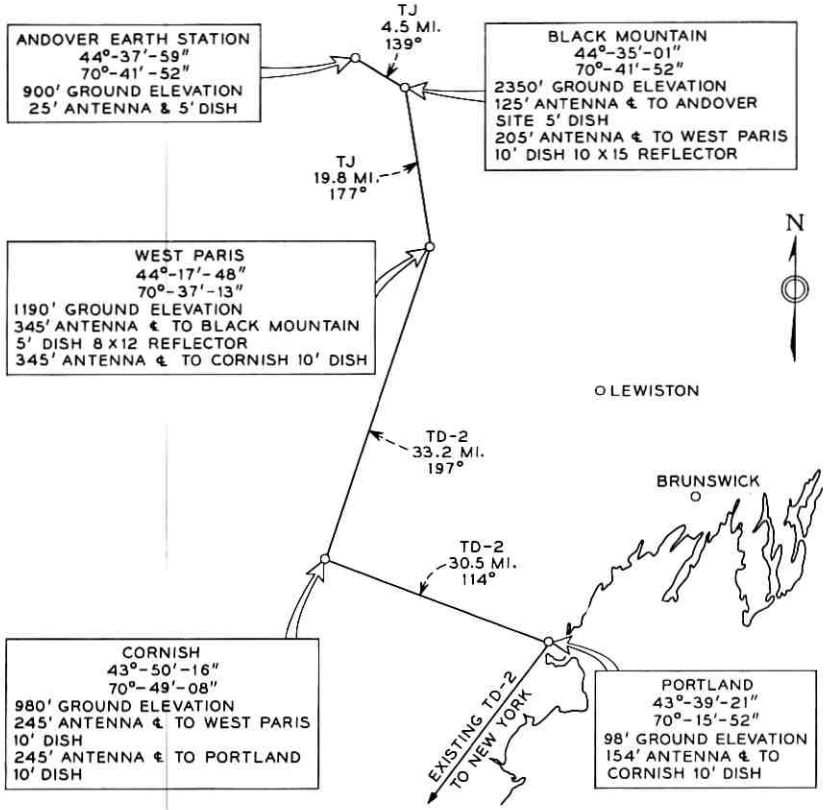

Fig. 15 — Overland route to Portland.

pairs of a 150-pair 19-gauge cable, planned to serve the area north of Rumford, Maine, were extended into the Andover site by the New England Telephone and Telegraph Company. Voice-frequency circuits over this cable were interconnected at Rumford with existing ON carrier circuits to Portland. Later, the ON carrier system was extended directly to Andover to provide 24 direct Andover-Portland circuits.

VII. EXPERIMENTAL DEMONSTRATIONS

Eight special networks were established for the first demonstrations on July 10, 1962, using the support communication facilities shown in Fig. 14.

A closed-circuit video network was established between Andover, Boston, New York, Holmdel and Washington. The pickup equipment

located at Andover and Washington was provided by Theatre Network Television, Inc., monitors provided in the Andover, Boston, Washington and New York areas made it possible for several thousand people to view the closed-circuit program. In addition, a feed was provided from Andover to New York to feed the program to the ABC, CBS, and NBC television networks.

Vice President Lyndon B. Johnson and Mr. F. R. Kappel, Chairman of the Board of the A.T.&T. Co., spoke between Washington and Andover on the first telephone call using the Telstar satellite. Mr. Kappel spoke via the satellite and the diplexed audio channel. Special program facilities were used to transmit Vice President Johnson's voice to Andover.

Special facsimile, data and telephone circuits also were established for the several initial transmissions. The first facsimile test, a picture of the Telstar satellite, was transmitted during the latter portion of the first usable pass (during the 6th orbit) from the auditorium of the Long Lines

TABLE III — SUMMARY OF *Telstar* DEMONSTRATIONS AND TESTS: July 10, 1962, to November 22, 1962

Telephone calls		117
Black-and-white TV (to and from Europe) including simultaneous 2-way TV, Andover/France		42
Color TV		5
Facsimile		9
International carriers (6)		126
Telegraph	68	
Data	26	
Facsimile	31	
Telephone	1	
Data		66
42,000 bits/sec (52,000 wpm)	1	
62,500 char/sec computer to computer	1	
875,000 bits/sec (1.4 million wpm)	1	
1,000 wpm—punched tape	3	
Data speed—magnetic tape (1,200 bits/sec)	1	
1,000 wpm—teletypesetter	3	
Clock synchronization to UK	3	
66 wpm—teletypewriter to UK	9	
EKG—recording over DATA-PHONE	1	
Other data tests	43	
Business machine manufacturers (11)		14
Radio broadcast programs		6
Satellite light-route equipment tests and demonstrations—Holmdel/Andover and Holmdel/Holmdel		5
Total		390

headquarters building in New York via the satellite to press locations in New York, Andover, Holmdel and Washington. A press release was prepared on punched paper tape and transmitted at 1050 words per minute during the second usable pass (the 7th orbit) from the visitors' building at Andover via the satellite to the Long Lines headquarters in New York using Bell System DATA-PHONE sets. The message was converted to page copy by a tape reader and printer in New York. Six telephone channels were also established via the satellite during this pass, including circuits connecting via the regular message telephone network to points throughout the United States. Calls were made by government and Bell System officials and members of the press.

Between July 10, 1962, and November 22, 1962, some 390 demonstrations and tests were conducted using the connecting communications facilities to Andover. A summary of the demonstrations is shown in Table III.

VIII. ACKNOWLEDGMENTS

The authors acknowledge with thanks the contributions of Mr. J. L. White and Mr. D. L. Schwemmer of the Long Lines Department of the American Telephone and Telegraph Company and of Mr. W. E. Peterson, Mr. Dona Cauchon, Mr. John Sturm, and Mr. John Cloutier of Bell Telephone Laboratories in the preparation of this paper.

REFERENCES

1. Dolling, J. C., Blackmore, R. W., Kinderman, W. J., and Woodward, K. B., The Mechanical Design of the Horn-Reflector Antenna and Radome, B.S.T.J., this issue p. 1137.
2. Giger, A. J., Pardee, S., Jr., and Wickliffe, P. R., Jr., The Ground Transmitter and Receiver, B.S.T.J., this issue, p. 1063.

Participation of the Holmdel Station in the *Telstar* Project

By WILLIAM C. JAKES, JR.

(Manuscript received January 21, 1963)

The facility for satellite communication studies at Holmdel, New Jersey, was originally established to take part in Project Echo. This paper describes the modifications required to participate in the Telstar experiments and the results obtained during operations from July 10 to November 9, 1962. Reception of television from the satellite was successfully accomplished, studies were made of the signal levels, and the changes with time of the satellite spin rate and spin axis orientation were determined.

I. INTRODUCTION

1.1 *Objectives*

The Holmdel station was originally established in 1959–1960 to carry out communication tests with the passive earth satellite Echo I. A complete description of the station and results obtained during Project Echo are given in Ref. 1. In the summer of 1961 it was decided to take part in the Project Telstar program, and the necessary modifications to the station were begun at that time.

The main objective for Holmdel was to receive an acceptable television picture from the Telstar satellite and relay it back to Andover by land routes for comparison with the original picture transmitted from Andover. The Andover station was also expected to receive a television signal, but it was felt that a demonstration of transmission between two separated points would be meaningful. It was not anticipated at the time that the European stations would be ready by the expected launch date. In addition, having two receiving stations would increase the probability of successful operation.

Secondary objectives for Holmdel operation were:

(a) Measure the 4-gc signal levels to check the satellite transmitted power.

(b) Determine the location of the spin axis of the satellite and the spin rate.
(c) Carry out any other scientific experiments of value.

1.2 *Preliminary Tests*

Before the Telstar launch a number of transmissions were made at 4079.73 mc from Holmdel to Andover via reflections from Echo I and the moon. A 200-watt transmitter was connected to the Holmdel horn-reflector antenna for this purpose. These tests made it possible for Andover to check their tracking capabilities under actual operating conditions. The 961-mc "Project Echo" radar system was used to point the Holmdel horn at the target.

II. SYSTEM DESCRIPTION

The facilities used in Project Telstar were essentially those used for receiving in the Project Echo experiment. The 20-foot horn-reflector antenna was used for reception and modifications were made in the receiving equipment for use at 4170 mc instead of the 2390 mc used in Project Echo. The 18-foot tracking antenna from the radar system was also modified to permit operation with the 4080-mc beacon signal from the satellite. A simplified block diagram of the system is shown in Fig. 1, and the system is briefly described in the following four sections, covering the functions of reception, tracking, optics, and data recording.

2.1 *Receiving System*

2.1.1 *Antenna and Waveguide*

The properties of the horn-reflector antenna are described in detail in Ref. 1. Additional tests were made at 4170 mc before the spacecraft launch, and the resulting characteristics are:

Gain	48.0 db
3-db beamwidth	0.78° (circular polarization)
Projected area	380 square feet
Effective area	274 square feet

As anticipated,[1] a difference in elevation boresighting was noted for CW and CCW circular polarization. The measured value was 0.09°, which compares favorably with the calculated value of 0.10°. Final boresighting was done with CCW polarization, which would actually be transmitted by the satellite.

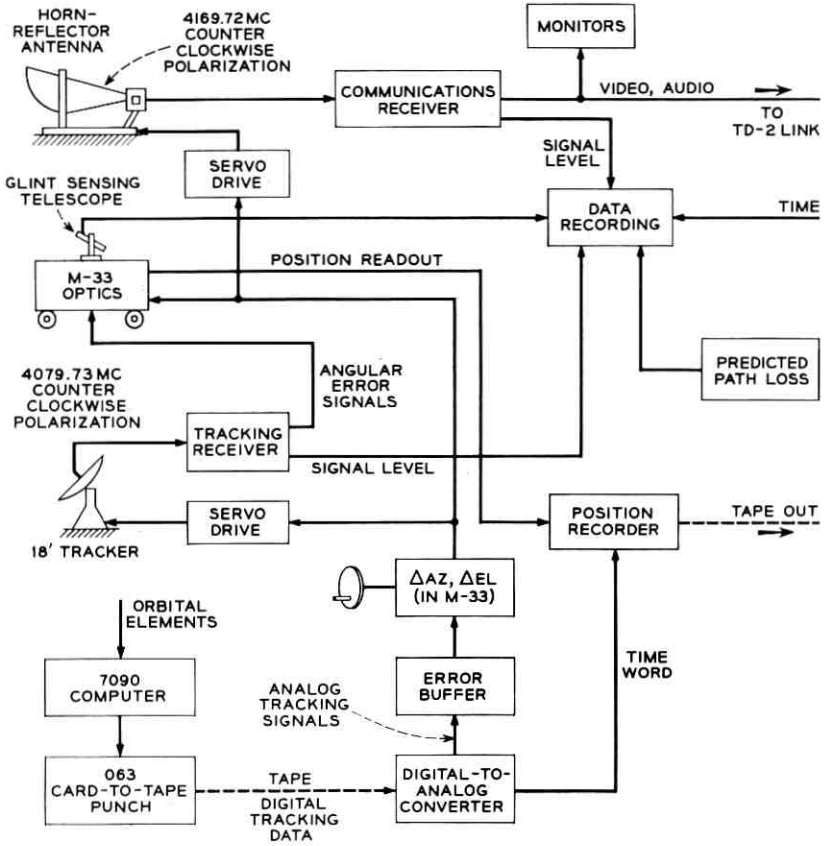

Fig. 1 — General block diagram of Holmdel facilities for Telstar satellite communications experiment.

The horn throat tapered down to round waveguide inside the antenna cab. A low-loss rotating joint was provided between the horn and the waveguide system, which included a 90° phase shifter to convert to linear polarization, a transducer to couple to the maser, and a directional coupler for the introduction of either a noise source or signal source for calibration purposes.

2.1.2 *Low-Noise Amplifiers*

The first stage of RF amplification was a maser operating at 4.2°K in liquid helium. This was followed by a parametric amplifier cooled with liquid nitrogen, and then by a traveling-wave tube amplifier. The maser

would operate for about 20 hours on one filling of liquid helium, and the paramp for about 10 days on one filling of liquid nitrogen. A certain amount of equalization was provided between the paramp and TWT amplifier to achieve an RF band flat to within ± 1 db over 20 mc. This rather elaborate array of low-noise amplifiers was felt necessary in order to achieve a system with the lowest possible noise temperature and capable of operating over the wide band necessary for television reception. Calculations indicated that if all system objectives were realized a good quality picture could be obtained from the satellite out to a range of 5,000 statute miles. In addition, a certain amount of flexibility was provided in that operations could still be carried on at reduced ranges in the event of failure of any one amplifier. The characteristics of the amplifiers are listed in Table I.

The over-all system noise temperature was measured to be somewhat less than 17°K pointing at the zenith, which included about 4.5°K for waveguide losses, 2.5°K sky noise, 2.5°K for antenna side lobes and heat losses, and 5°K for the maser.

The TWT amplifier was followed by a filter to remove the undesired noise sideband, and then a balanced crystal mixer with 70-mc cascode IF preamplifier. The mixer-preamp noise figure was about 11 db. The IF signal was then brought from the antenna to the main control building via a wrap-around coaxial cable for distribution to the various receivers located there.

2.1.3 *Television Receiver*

The heart of the television receiver was the frequency compression demodulator which was used to obtain an improvement in the S/N threshold. This unit and underlying design principles are described in detail in Refs. 2 and 3 and will be only briefly discussed here. As shown by the block diagram in Fig. 2, the incoming 70-mc IF was up-converted to 263 mc and then mixed with a voltage-controlled oscillator (VCO) to give a 70-mc IF. This signal was then amplified, filtered, limited, and demodulated in a frequency discriminator. The baseband signal was

TABLE I

	Maser	Paramp	TWT
Gain, db	27	31	20
3-db bandwidth, mc	20	30	>50
Noise temperature, °K	≈5	70	625

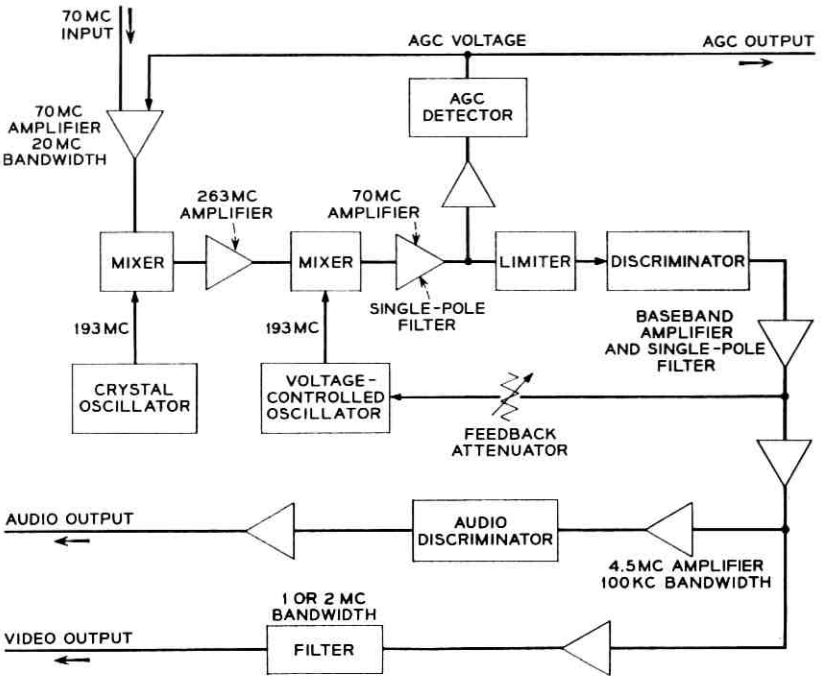

Fig. 2 — Block diagram of frequency compression demodulator.

then amplified, filtered, and applied to the VCO in the proper sense to cause a reduction in the FM index. The baseband signal was also passed on to television monitors for local viewing and to the Bell System microwave relay terminal for transmission to New York City and Andover. The audio portion of the signal was carried on a 4.5-mc FM subcarrier in the baseband, and was separated from the video signal by a filter of 100-kc bandwidth. AGC was supplied by a separate amplifier and detector, and also made available for recording signal strength. The system specifications were:

Video frequency deviation	±7 mc
Audio channel deviation	±0.7 mc
Audio subcarrier deviation	±0.05 mc
Open loop bandwidth	1.0 mc
Closed loop bandwidth	6.7 mc
Feedback factor	12 db
Threshold improvement	5–6 db.

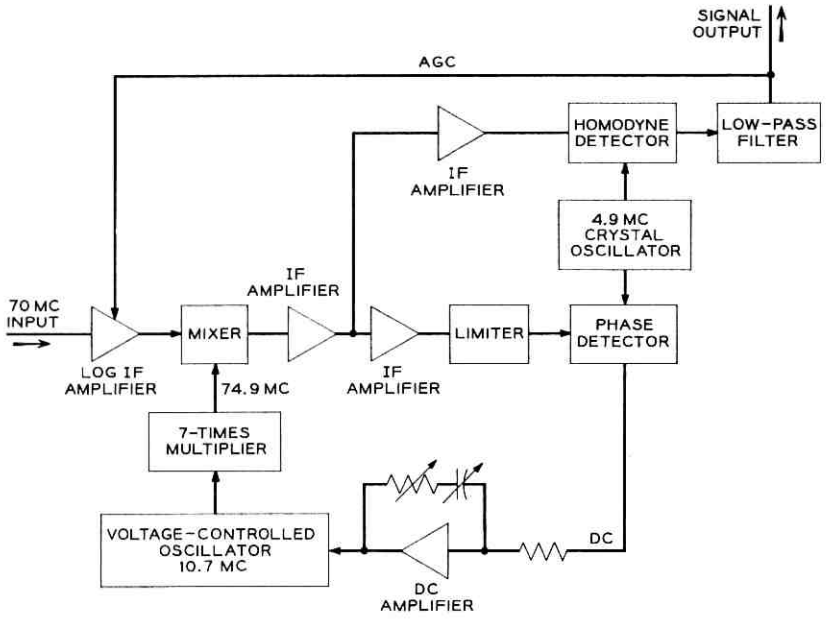

Fig. 3 — Block diagram of phase-locked loop.

2.1.4 *Phase-Lock Receiver*

In order to obtain signal level measurements at times when the signal might be below the threshold of the frequency compression demodulator, a phase-lock receiver was provided with a much narrower bandwidth. Because of the narrow band it was expected that for these tests it would be necessary for Andover to transmit a crystal-controlled, unmodulated carrier.

A block diagram of the receiver is shown in Fig. 3. The 70-mc input was passed through a logarithmic IF amplifier, and then converted to 4.9 mc by mixing with a 74.9-mc signal from the VCO. This IF was amplified, limited, and then phase-detected by comparison with a 4.9-mc crystal oscillator. The output of the phase detector was then passed through a filter to the VCO in the proper sense to cause the VCO frequency to lock in to the incoming frequency. The 4.9-mc IF was also separately detected in a homodyne detector with a low-pass output filter. The output voltage was then recorded for signal level determinations.

Receiver characteristics:

Closed-loop bandwidth	$\approx$100 cps

Maximum tracking rate	20 kc/sec² for large signal
Signal channel bandwidth	2 kc
Tuning range	±200 kc.

2.1.5 *Video Relay*

The video baseband signals were connected to standard Bell System video relay equipment in the control building, passed by cable to a microwave relay transmitter connected to a small paraboloid antenna, and transmitted to a nearby TD-2 microwave relay tower for transmission to New York City. The audio portion of the signal was sent by regular land-line circuits.

2.1.6 *Expected Signal Levels*

Ignoring effects such as atmospheric attenuation and tracking errors, the received signal level may be calculated from

$$P_r = P_t G_t G_r \left(\frac{\lambda}{4\pi r}\right)^2$$

where
P_t = satellite transmitted power
G_t = satellite transmitting antenna gain
G_r = receiving antenna gain
λ = wavelength
r = slant range.

Two cases were of importance at Holmdel: reception of the 4079.73-mc beacon signal on the tracking antenna, and reception of the 4169.72-mc communications signal on the horn-reflector antenna. For the nominal transmitted power, the expected received levels and S/N ratios are summarized in Table II for a maximum practical operating range of 5,000 statute miles. The receiving system temperature is specified at an antenna elevation of 15°.

The values of S/N ratio given are the worst that would be encountered, since at higher elevation angles the system temperature and slant range both decrease. Taking into account the acceptable operational

TABLE II

Frequency mc	G_t db	G_r db	P_t dbm	P_r dbm	Bandwidth kc	Rec. Temp. °K	S/N Ratio db
4079.73	0	38.9*	13	−130.9	0.1	≈420	21
4169.72	0	48.0	33	−102.0	2000	≈30	19

* Includes cable and scanning loss.

S/N thresholds of 14 db for the television receiver and 6 db for the tracker it is evident that both systems would operate satisfactorily over the major portion of every satellite pass with some margin.

2.2 *Tracking at Holmdel*

As shown in Fig. 4, the tracking information was principally derived from the predicted satellite trajectory. Corrections were then manually applied during the pass by using the angular error information provided by the beacon tracker. At times when the satellite was close enough to be seen optically the corrections could also be provided by means of the tracking telescope. As a last resort the corrections could be determined by scanning the horn-reflector antenna manually in azimuth and elevation to maximize the signal.

2.2.1 *Determination of Predicted Position*

The local azimuth, elevation, and corresponding rates of change of these quantities as a function of time were computed from the "modified orbital elements" of the Telstar satellite orbit for each pass. Details of the

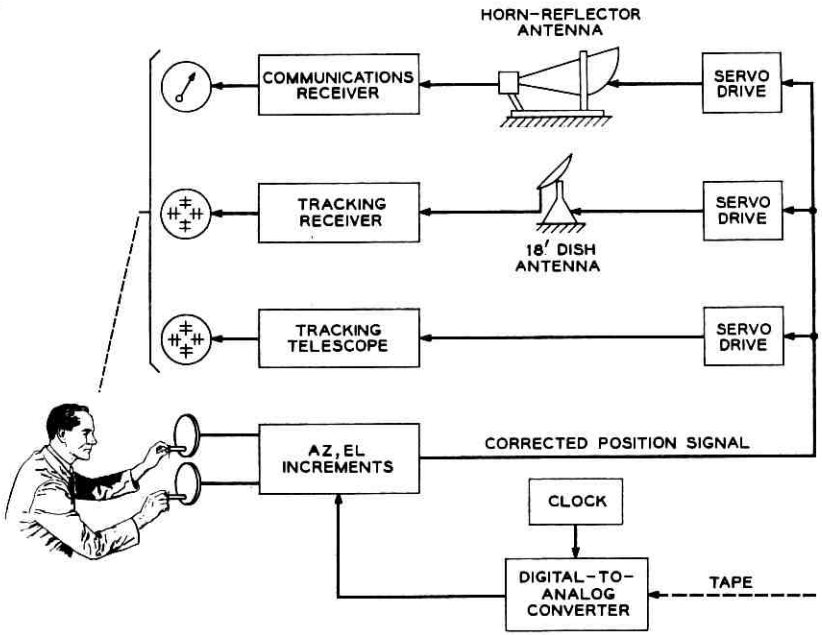

Fig. 4 — Block diagram of tracking modes at Holmdel.

method are given in Ref. 4, and hence will be only briefly summarized here. It was assumed that the orbit could be defined at a given time (epoch), T_0, by six parameters unchanging with time: eccentricity, e, and focal distance, f (perigee), of the ellipse and its inclination, i, to the earth's equator; the angle of perigee ω_0 (measured from the equator in the plane of the ellipse), the ascending node longitude, Ω_0, (determined by the intersection of the orbital plane with the equator), and the perigee-perigee period, P_0. In addition, the two main precessions, apsidal and nodal, were assumed to vary linearly with time. From this description of the orbit it was possible to calculate local "look-angles" by first solving Kepler's equation and then using simple geometric transformations. The Telstar satellite orbit proved to be so stable that predictions accurate to a few tenths of a degree for more than a month could be made using this method and an accurate set of orbital parameters.

Following determination of the azimuth and elevation of the satellite referred to the Holmdel station for a given pass by the 7090 computer, the data were transferred to a standard five-hole paper tape along with the corresponding time for each point. The tape was then read automatically in real time by the digital-to-analog converter[1] (DAC) which provided appropriate analog output signals for positioning the various elements of the system. An error buffer unit, which stored the current azimuth rate, was also provided in the azimuth channel. If an obvious error occurred in the azimuth signal from the DAC (caused possibly by an erroneous punch in the tape) the error buffer sensed the fact and switched the drives to the stored rate, which would then keep the antennas moving along an approximately correct path until remedial steps could be taken. It was the intent to provide a similar unit for the elevation channel, but time did not permit.

Before the analog position signals were transmitted to the antennas and optics, they were finally passed through the manually controlled device for inserting differential corrections in azimuth and elevation.

2.2.2 *Beacon Tracker*

The beacon tracker was essentially a modification of the Echo radar receiver.[1] Briefly, the original 961-mc receiver consisted of an 18-foot diameter paraboloid with a conically scanned beam for angular error determination, a low-noise RF amplifier and down-converter, AFC and gated narrow-band IF amplifier circuitry, quadrature phase detectors for extracting voltages proportional to azimuth and elevation errors, and appropriate error displays. The 4-cps conical scanning feature was preserved for angular error determination, but gating the receiver off and

on was no longer necessary since the tracker worked on the CW signal from the Telstar spacecraft beacon.

The RF portion of the system had to be converted from 961 mc to 4080 mc, and for this purpose a new circularly polarized turnstile feed for the 18-foot paraboloid was provided, along with a parametric amplifier for the new frequency. The dish surface was lined with window screening to render it more opaque to the higher frequency. As shown in Fig. 4 the angular error was presented to the operator by the position of the spot on a CR tube, and by introducing offsets he could zero the indicated errors. Since the horn-reflector antenna and the tracking antenna had been previously boresighted together, the horn antenna would then also point at the target.

In order to measure the received signal level at 4080 mc the tracker AGC voltage was calibrated in terms of input signal power and recorded. A determination of the apparent beacon power output from the satellite could then be made. The beacon tracker system parameters were:

Antenna gain	42.4 db
Cable loss	1.2 db
Radius of conical scan	0.4°
Scanning loss	2.3 db
Antenna 3-db beamwidth	0.8° × 1.0°
System noise figure	4 db
System threshold	−145 dbm
System pointing sensitivity	±0.03°
Tracking IF bandwidth	500 cps.

2.2.3 *Optical Tracking*

The telescope used on Project Echo[1] was also used for Project Telstar. It was part of an M-33 surplus fire-control radar, and was characterized more by convenience of operation than by high sensitivity. The field of view was 6° with a magnification of 8x and a 2-inch diameter objective lens. On a clear night stars of magnitude +6 to +7 could be seen, comparable to the magnitude of Telstar when it approached to 1000 miles or less.

In addition to the M-33 telescope a spotting telescope, mounted on the glint telescope, was available for checking the tracking optically. It had a 3-inch diameter objective lens and thus could see much fainter objects than the M-33 telescope. On the few occasions when the satellite was observed, the spotting telescope was used to check on the beacon tracker.

2.3 *Glint Telescope*

In order to maintain a favorable aspect of the satellite antenna patterns with respect to the earth and to insure that all solar cells received an equal amount of sunlight the satellite was given an initial spin of 178 rpm about an axis normal to the ecliptic plane. The interaction of a spinning conductor with the earth's magnetic field, however, introduced a force which tended to move the spin axis away from its preferred orientation. To follow this motion, and to check on the effectiveness of corrective measures when they were applied, three mirrors were mounted on the satellite's surface in order to reflect flashes ("glints") of sunlight to earth. Two mirrors were mounted tangent to the sphere at an angle of 95° from the spin axis spaced 120° apart in longitude, and a third mirror at 68°. For a given location of the spin axis there was then a unique time during a given pass when the sun-satellite-observer angle was such that the observer could see a glint from one of the two sets of mirrors. Conversely, knowing the time of the glint and the satellite position (given by the orbital parameters), a cone could be determined on which the spin axis must lie. Another such observation determined a second cone, and the spin axis must then lie along one of the two intersection lines of these two cones. A third glint observation, of course, would remove the ambiguity; however, solar aspect information from solar cells on the satellite was generally available at the same time, and was sufficiently accurate to eliminate the wrong intersection line. The position of the spin axis was usually specified in terms of the right ascension and declination of the intersection of the axis with the celestial sphere.

The glint telescope itself was a 12-inch Cassegrain with a 0.5° field of view seen by a photomultiplier at the focus. Sensitivity was such that the glints could be detected out to a slant range of 3,000 miles or more, depending on viewing conditions. (Of course, the glints could only be seen at night.) The telescope was mounted on the M-33 optical tracker, and was pointed at the target by the methods described above to an accuracy well within the angular field of view. Because of the finite size of the sun, a glint event usually consisted of a train of flashes occurring at the spin rate of the satellite and lasting from ten to thirty seconds. The mid-point of the train was taken as the time of the glint. By using a precise crystal oscillator for time comparison it was also possible to determine the spin rate of the satellite by measuring the interval between successive flashes. A more detailed description of the telescope and associated electronics is given in Ref. 5.

2.4 *Data Recording*

A variety of recording means was provided in order to insure that no significant information during a Telstar satellite pass was lost. The areas of interest may be grouped as follows:

(a) Signal levels
(b) Glint telescope
(c) Spin rate
(d) Audio portion of the television signal
(e) Comments of operating personnel during a pass
(f) Tracking data
(g) Time synchronization of all recordings.

A block diagram of the recording system is shown in Fig. 5.

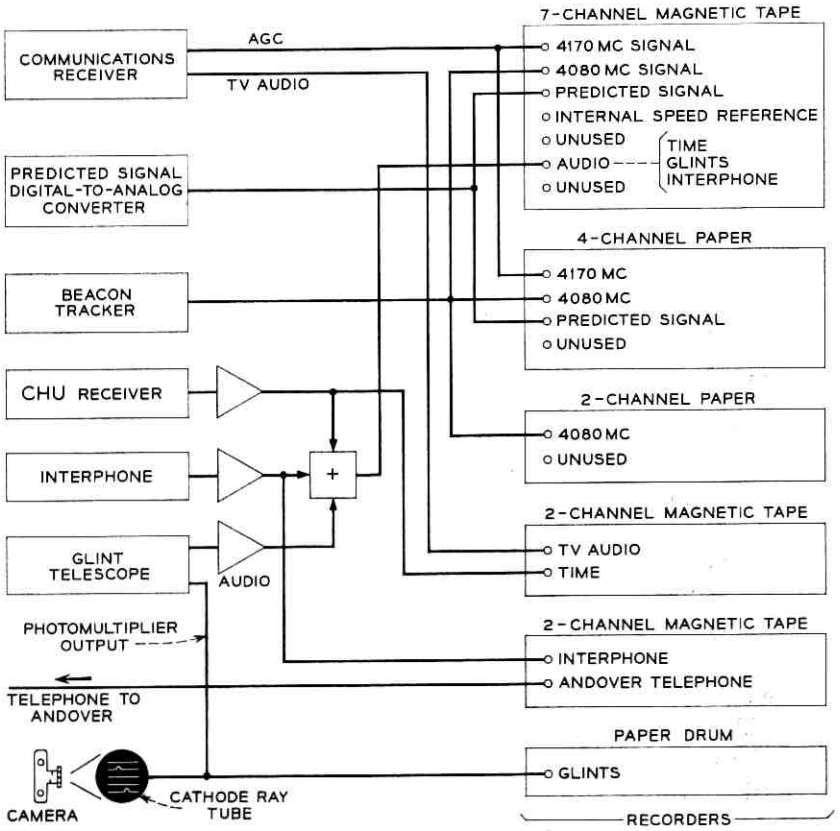

Fig. 5 — Block diagram of data recording facilities.

2.4.1 *Signal Level Recording*

The AGC voltage from the beacon tracker receiver was recorded on a paper recorder at the tracker location, and also in the main control building on the 7-channel magnetic tape recorder and the 4-channel paper recorder. This voltage was calibrated in terms of signal level before and after every pass.

A voltage from the communications receiver was also recorded by the magnetic and paper recorders in the control building. This voltage was obtained either from the frequency compression demodulator AGC during video transmission, or from the phase-lock receiver when a crystal-controlled carrier was transmitted. Signal level calibrations were also made before and after every pass.

Knowing the slant range to the satellite, frequency, and gain of the antennas, it was possible to calculate the received power as a function of time for a given transmitter power. This calculation was included in the computer program used for making the tracking tapes, making it possible to provide another punched paper tape containing the predicted received power level at four-second intervals. This tape was fed into a fairly simple digital-to-analog converter and read in real time during a Telstar satellite pass. The output voltage was proportional to the received signal in dbm, and was recorded in the control building on the magnetic and paper recorders. It was thus possible to compare predicted signal levels with those actually being observed during the pass.

2.4.2 *Glint Telescope Recording*

The pulses of light incident on the glint telescope photomultiplier during a glint event were recorded in three ways:

(a) Photographs of a CR tube with the pulses on the vertical plates and a linear time raster on the horizontal plates.
(b) Pen deflections of a paper drum recorder.
(c) Tone bursts on the audio recording channel of the 7-channel magnetic recorder. Audio time signals from radio station CHU were also recorded on this channel.

This variety of methods for glint recording facilitated the determination of the exact time of the glints and the flash spacing for spin rate determination.

2.4.3 *Spin Rate Recording*

The signal level voltage from the communications receiver contained a number of Fourier components due to the satellite rotation and the

slight nonuniformity of the azimuthal antenna radiation pattern. The fundamental component occurred at the spin rate, approximately 3 cps, and was selectively amplified by a high-Q ($\approx$25) amplifier tuned to the actual spin frequency. The amplifier output was a close approximation to a sine wave whose period was then measured with a standard counting instrument by manually recording the time required for ten periods. An average of 500 periods was actually used to determine the spin rate, achieving an accuracy of about $\pm$0.05 rpm.

The spin rate was also independently determined on passes when the glints were observed by comparing the time between glints to the period of an accurate, crystal-controlled oscillator. An accuracy of about $\pm$0.02 rpm could be achieved.

2.4.4 *Audio Recording*

The audio portion of the television signal was recorded on one channel of a 2-channel magnetic tape recorder, with time signals recorded on the other channel.

2.4.5 *Personnel Comments*

All operating personnel at Holmdel were in communication with each other by a common telephone circuit. This circuit was recorded on one channel of another 2-channel magnetic recorder. The comments obtained in this way occasionally proved very helpful in subsequent data reduction, since it was impossible to keep a written log of all the last-minute changes in system performance or operation that occurred on various passes.

The Holmdel station was also in constant communication with Andover by means of a private telephone circuit for purposes of coordinating operations. This circuit was recorded on the other channel of the 2-channel recorder mentioned above, and served the same purpose as the local interphone recording.

2.4.6 *Recording of Tracking Data*

During a pass the azimuth and elevation offsets required to track the satellite accurately were recorded at approximately one-minute intervals in a written log. The true azimuth and elevation could then be determined later by adding the offsets to the predicted positions during the pass. The true angles were used to make slight corrections in the orbital

elements so that more accurate determination of the satellite position could be made for use in other studies concerned with the satellite.

Towards the end of the Holmdel experiments with the Telstar satellite an analog-digital converter unit was acquired which encoded the true azimuth-elevation angles into punched paper tape, along with time, at selectable intervals of 1, 2, 4, or 8 seconds. This unit made the task of improving the orbital elements considerably easier

2.4.7 *Time Synchronization of Recordings*

The station clocks were generally set to the correct time by referring to the time signals broadcast by the Canadian station CHU on 3.33 mc, 7.335 mc, or 14.670 mc. As mentioned above, the magnetic tapes were time referenced by actually recording CHU on one audio channel. The 4-channel paper recorder included an auxiliary time marking pen which was actuated by a pulse every 10 seconds from the clock chain in the DAC. The paper recorder for the beacon tracker also contained a time marking pen which was supplied with 1-second and 1-minute pulses generated locally by synchronous motors. These were initially synchronized with the station clocks. The paper drum recorder for the glint telescope was manually time-tagged by referring to the station clocks.

III. EXPERIMENTAL RESULTS

3.1 *Preliminary Tests*

During the period from April 11–July 6, 1962, transmissions were attempted to Andover via reflection from Echo I on 36 passes, with increasingly successful results culminating in the demonstration of satisfactory operation at Andover of all the various tracking modes. These tests helped to confirm, among other things, that it was possible to predict a satellite trajectory for Andover and have the horn properly follow the predictions, that the sense of polarization of the microwave signals was correct, and that the system thresholds at Andover were as expected. The Echo tests were challenging, since the signal levels were marginal and had large, rapid fluctuations due to the wrinkled nature of the balloon.

During the same period of time mentioned above, transmissions were made to Andover via reflections from the moon at 4080 mc on a total of five separate occasions, again with increasing success. Although these tests were not as demanding as the Echo tests, they did serve a useful purpose in checking system performance. The average value of signal

received from the moon indicated its scattering cross-section at this frequency to be about 20 db below a perfect sphere of the same size.

3.2 *Television Reception*

Starting with the first possible pass (No. 6) television was received at Holmdel on a total of 23 passes with excellent results. A brief summary of the more noteworthy demonstrations seen at Holmdel is given in Table III.

Fig. 6 shows pictures of the Holmdel monitor during scenes from the earlier passes. These are reproductions of selected frames from a 16-mm movie camera using a high-speed film, which accounts for a certain amount of graininess in the photographs. The streaks of light are reflections of room lights in the monitor glass surface. Also shown is a photograph of the picture seen at Andover after being relayed from Holmdel by land routes. The 1.0-mc filter was in the output circuit of the Holmdel receiver when these pictures were taken. The general impression was that a 1-mc bandwidth provided a picture of quite acceptable quality. On a few occasions the 2.0-mc filter was tried, and resulted in somewhat improved definition. It is evident from the photograph of the multiburst test pattern that the 1.0-mc filter had a fairly slow cutoff characteristic, which probably accounts for the qualitative appraisal of picture mentioned above.

The predicted threshold of the television receiving system was verified during operations with the Telstar satellite, as the picture showed essentially no noise out to maximum range. On a few occasions, however, a signal from a nearby microwave relay transmitter operating at 4165 and 4175 mc produced interference either by direct propagation or by scatter from thunderstorms. This caused a noticeable deterioration in the S/N ratio.

The audio portion of the television signal was received with acceptable quality.

TABLE III

Date	Pass	Test
July 10	6	First transmission from satellite
July 11	15	First television from France
July 12	16	First television from England
July 23	123	Special program to Europe
	124	Special program from Europe
July 24	133	Special program from France
	134	Special program from England
July 31	196	Special program from Sweden

FIRST PICTURE RECEIVED AT HOLMDEL
PASS NO. 6, JULY 10, 1962

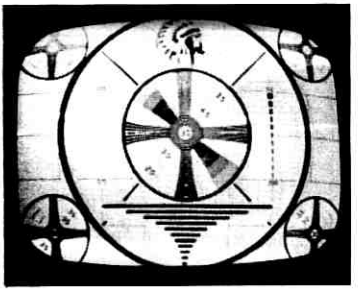

INDIAN HEAD TEST PATTERN

LIVE VIDEO ON PASS NO. 6

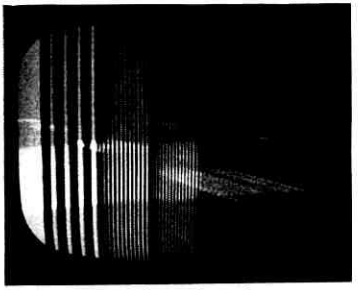

0.5 MC 1.5 MC 2.0MC 3.2MC
MULTIBURST TEST PATTERN

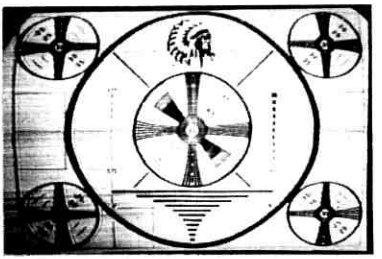

PICTURE SEEN AT ANDOVER AFTER
RELAY FROM HOLMDEL

Fig. 6 — Television received at Holmdel from Telstar spacecraft repeater.

3.3 *Data Reception*

On pass 270, August 8, 1962, transmission of high-speed data was demonstrated at Holmdel. The data were sent at a rate of approximately 40 kilobits/sec from a computer at the Murray Hill, New Jersey, location of the Bell Laboratories to Andover for transmission to the Telstar satellite. From the satellite it was relayed to the Holmdel station, and then

sent by microwave relay to the computer in the new laboratory building at Holmdel, some 2 miles from Crawford Hill. The accuracy of data transmission was found to be as good as that obtained over the usual land line route from Murray Hill to Holmdel.

3.4 *Received Signal Levels*

Using the expression for received power given in Section 2.1.6, a comparison between predicted level and observed level was made for one point on every pass worked for both the beacon signal and communication signal. The point used on each pass was chosen to fulfill the following conditions as nearly as possible:

(a) Angle between the spin axis and observer-satellite line within $90° \pm 30°$. This insured that the gain of the spacecraft transmitting antenna could be assumed to be 0 ± 1 db
(b) Tracking satisfactory at the time
(c) System operation normal.

Assuming the system parameters given in Section 2.1.6, the following expressions were used to calculate signal levels:

$$\text{Beacon signal: } P_r = -116.9 - 20 \log \left(\frac{r}{1000}\right), \text{ dbm}$$

$$\text{Communications signal: } P_r = -88.0 - 20 \log \left(\frac{r}{1000}\right), \text{ dbm,}$$

where r is the slant range in miles.

Any differences between calculated and observed signal levels may be interpreted in terms of departures of the satellite communications repeater transmitted power from nominal values. Points calculated on this basis are plotted in Fig. 7. The gap in the data for the beacon signal between pass 198 and 762 is due to the use of the tracker antenna in the skinny route terminal project (see Section 3.8). After pass 606 the horn antenna receiver was used for measuring the beacon signal and reception at 4170 mc was discontinued.

The data show that the power transmitted by the Telstar satellite repeater was 2 watts at 4170 mc within a measurement accuracy of ± 2 db and at least 20 mw at the beacon frequency. These were the design objective values for the satellite. No significant changes with time were observed.

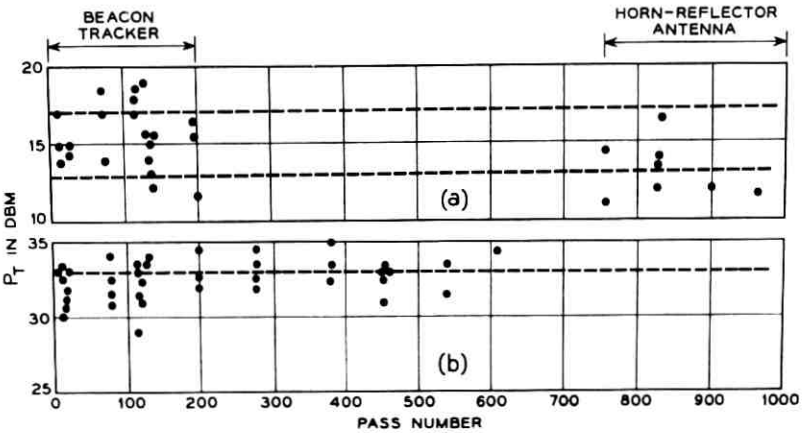

Fig. 7 — Telstar spacecraft radiated power inferred from signal level measurements at Holmdel. (a) Apparent beacon power radiated at 4080 mc. The dashed lines define the nominal tolerance of +13 to +17 dbm. (b) Apparent power radiated on the communications channel at 4170 mc. The dashed line represents the nominal power of 2 watts. Reception on horn-reflector antenna.

3.5 *Tracking*

The beacon tracker was operated on 29 passes of the Telstar satellite, and was able to acquire and hold the beacon signal through the Doppler shift of as much as ±100 kc with no difficulty. The achieved tracking accuracy was on the order of ±0.05°, shown by comparison with the 3-inch spotting telescope on a few passes.

The satellite was seen optically in the M-33 tracking telescope on four passes out to a maximum range of 1700 miles. With care, a tracking accuracy of about ±0.05° could be achieved.

Scanning the receiving horn antenna in azimuth and elevation proved to be a surprisingly accurate method of correcting errors in prediction, with tracking accuracies of ±0.1° being typically obtained. There were certain drawbacks to this method, however, which made a more sophisticated system desirable. For example, during the time that the antenna was being scanned the signal level data were essentially useless. A typical scanning procedure took about 15 seconds and was usually repeated every one or two minutes, depending on the accuracy of the predictions. Thus for predictions seriously in error the method would become increasingly poor due to the necessity of more frequent scanning, whereas the beacon tracker did not have this limitation. It was also essential to have a predicted drive tape to use this method, whereas the tracker could follow the satellite by manually steering the antenna to zero the error, as demonstrated on a few passes.

3.6 *Spin Rate*

The spin rate was measured on almost every pass worked, using either signal analysis or the optical "glints". It was found that an exponential function could be determined which agreed with the measured data to within ± 0.5 rpm from pass 6 to 1114 (or 122 days after launch):

$$R = 178.2 \exp(-t/333), \text{ rpm}$$

where t is the number of days since launch. The spin has a "half-life" of 333 days, which is in the range of 300–400 days estimated by a rough calculation prior to launch by E. Y. Yu of Bell Laboratories. If this expression continues to be valid, the spin will be reduced to a minimum useful value of 20 rpm in two years. A plot of the spin decay is given in Fig. 8.

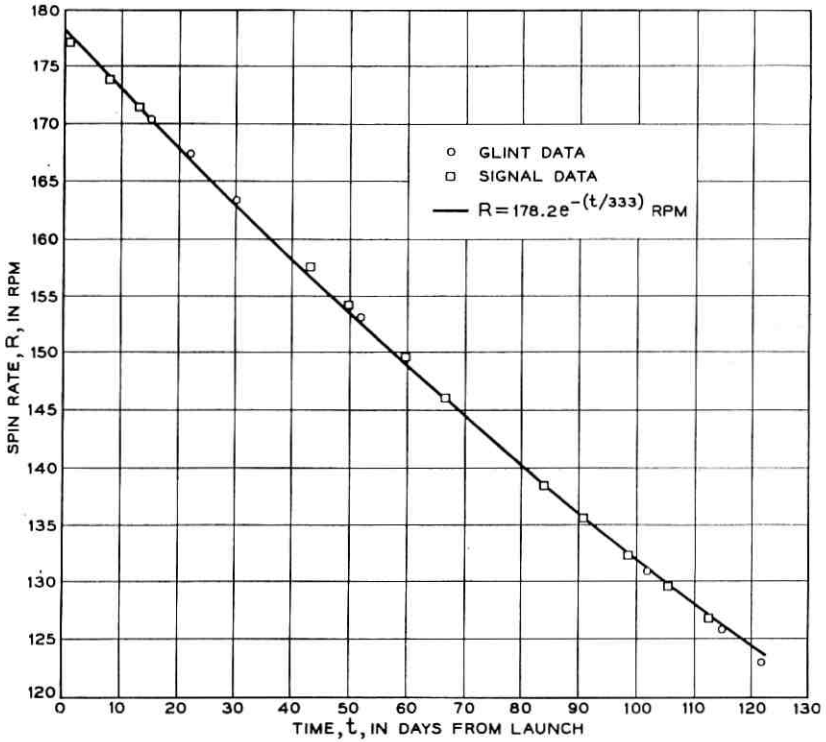

Fig. 8 — Change of satellite spin rate with time.

3.7 *Spin Axis Orientation*

3.7.1 *Determination of the Axis Using Glint Data*

During the period from the launch on July 10, 1962, to November 9, 1962, a total of 17 separate glint events were observed at Holmdel. These made it possible* to determine 11 different locations of the spin axis, as summarized in Table IV.

These points are plotted in Fig. 9, along with a theoretical curve derived by L. C. Thomas for an assumed satellite magnetic dipole moment of -1.0 ampere-turn-meter^2. From pass 16 to 472 the agreement is quite good, but pass 931 falls more closely on a -1.1 ampere-turn-meter^2 curve. Some discrepancies were expected, of course, due to lack of complete knowledge of the earth's magnetic field and to the elliptical shape of the satellite orbit. In order to test the effectiveness of the torque coil in the satellite it was turned on in the positive sense for 18 hours between passes 1052 and 1069, and in the negative sense for about the same length of time between passes 1069 and 1114. The changes caused by these tests were apparent, and demonstrated the ability to take corrective action whenever necessary.

Also shown in Fig. 9 is the design objective location of the spin axis, corresponding to a line normal to the ecliptic plane. The achieved orientation was well within tolerance.

TABLE IV

Pass	Date	Mirror Observed	Right Ascension	Declination
7	7/11	68°		
7	7/11	68°	These passes were averaged	
8	7/11	68°	together to give one fix:	
8	7/11	68°	81.96°	−65.57°
9	7/11	68°		
9	7/11	95°		
16	7/12	68°	84.39°	−65.81°
72	7/18	68°	86.86°	−66.10°
135	7/25	68°	91.22°	−65.86°
136	7/25	68°		
199	8/1	68°	95.4°	−65.4°
272	8/9	68°	100.08°	−64.51°
472	8/31	68°	104.44°	−59.92°
931	10/20	95°	98.04°	−50.69°
1051	11/2	95°	95.8°	−50.3°
1069	11/4	95°	98.48°	−49.36°
1114	11/9	95°	94.05°	−51.91°

* The data reduction was carried out by D. W. Hill[6] and L. C. Thomas of Bell Laboratories along lines laid out by the former.

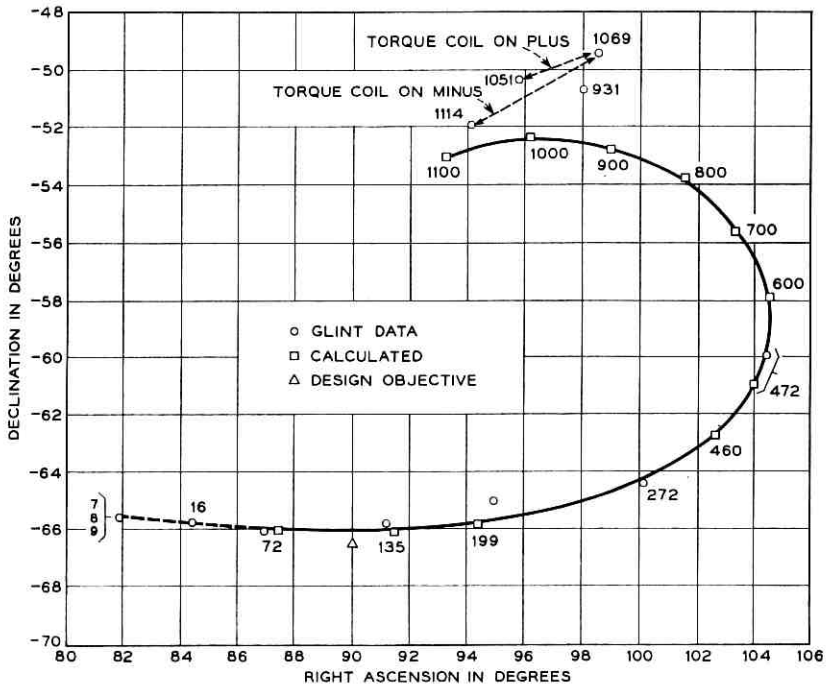

Fig. 9 — Change of spin axis location as determined by glint data; numbers refer to pass number.

3.7.2 *Determination of the Axis Using Signal Level Data*

The transmitting antenna pattern of the satellite at 4 gc was very nearly uniform in longitude,* and also in latitude* for angles within $\pm 30°$ of the equator. (The satellite transmitting antenna belt was approximately on the equator, and the satellite spun about an axis normal to its equatorial plane.) For values of latitude progressively nearer the poles, however, the pattern contained maxima and minima of increasing range. Thus during a pass when the observer-satellite line made an angle of about 45° or less with respect to the spin axis the received signal level showed corresponding fluctuations with time. If the angular location of the maxima and minima of the satellite latitude pattern were known with respect to the spin axis, it would be possible to determine values of the spin angle (defined as the latitude of the observer, measured in the satellite co-ordinates) as a function of time during a pass. Two such values

* These are satellite-centered coordinates.

would then be enough to determine a "fix" on the spin axis location. In order to determine the satellite pattern, the process was reversed on one or two passes for which the spin axis location had been determined from the glint data. Knowing the axis orientation it was a simple matter to compute the spin angle for a number of times during the pass corresponding to the observed maxima and minima, and thus obtain a pattern calibration. Curves obtained by this method are shown in Fig. 10 for the two frequencies of measurement, 4080 mc and 4170 mc. As one would expect, the minima are somewhat closer together in angle at the higher frequency. In the plots the maxima have all been set to the same level, revealing that all minima have different values so that there is the possibility of unambiguously determining spin angles from the received signal level variations. An expanded replica of the signals received during pass 117 is shown in Fig. 11, including both the 4170-mc and 4080-mc signals. By measuring the depth of a minimum referred to the midpoint of a line joining two adjacent maxima for all minima, a list of minima depths was determined. This list was then compared to that given by the appropriate reference pattern calibration (Fig. 10) and correspondence of minima and maxima thereby established. Knowing the times associated with the minima and maxima it was then possible to determine the apparent variation of spin angle with time during the pass. Such a plot for pass 117 is shown in Fig. 12, where data determined from both frequencies are included. It can be seen that the points for both frequencies lie on the same curve, as they should.

In order to determine the orientation of the spin axis from the spin

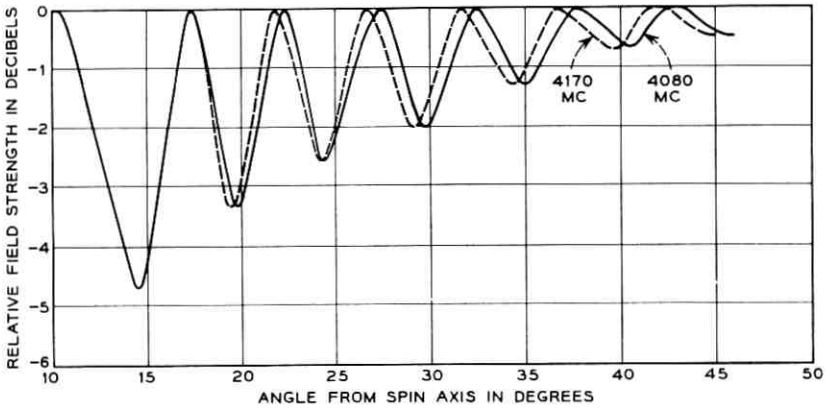

Fig. 10 — Measured latitude radiation patterns of spacecraft while in orbit.

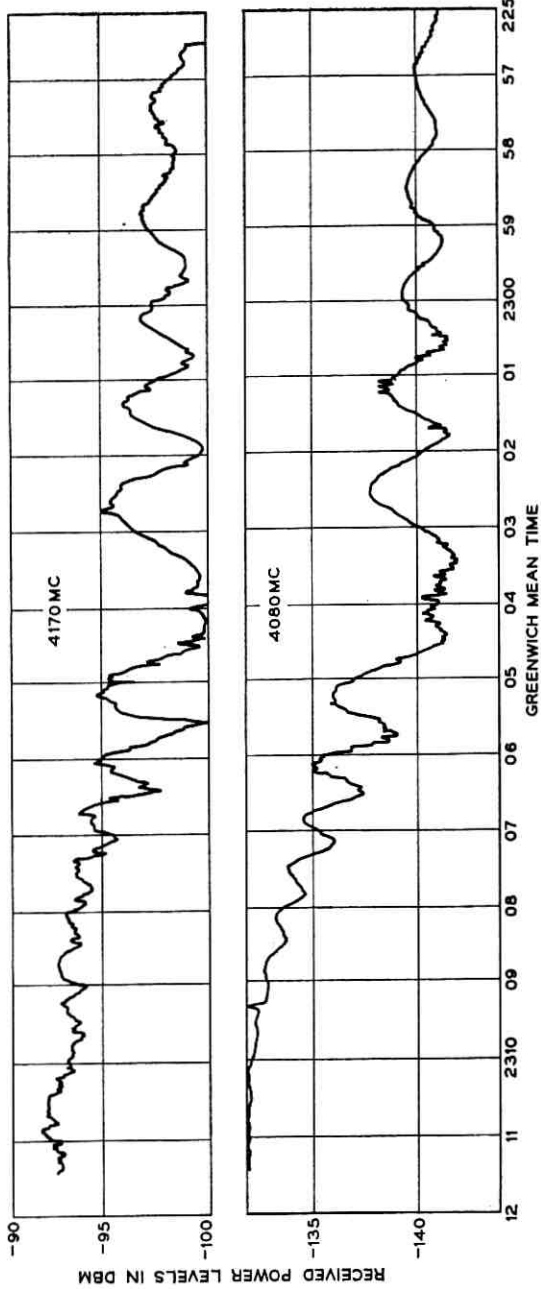

Fig. 11 — Expanded replica of received signal recordings at 4080 mc and 4170 mc showing variations caused by Telstar spacecraft antenna pattern lobes on pass 117, July 23, 1962.

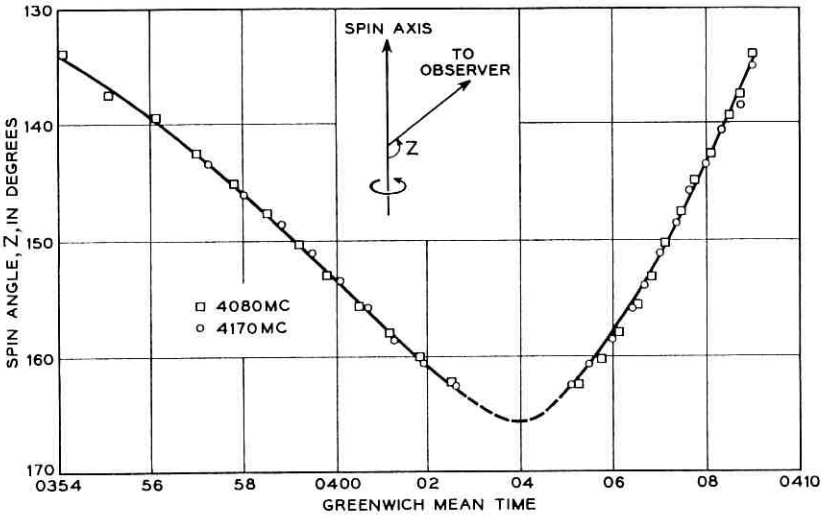

Fig. 12 — Measured variation of spin angle with time for pass 117 on July 23, 1962.

angle information, a computer program was prepared which computed the axis location from two selected data points from the set of given spin angles and corresponding times, and then computed spin angles from this value of spin axis location and compared them to the remaining given data points. Examination of the differences then revealed any gross errors, such as a slip of one adjacent minimum in achieving a correspondence between the pattern calibration and measured signal variations. Generally the spin angle differences did not exceed 1°. It was found that in choosing the two points from which to compute the axis, it was better to use two with the largest difference in spin angle, rather than the largest difference in time.

A more elegant approach, of course, would be to utilize all of the data points (spin angles with their corresponding times) and make a least-squares fit to determine the best value of spin axis orientation. It was felt, however, that the accuracy of measurement was insufficient to warrant this approach.

The coordinates of the spin axis determined from the pattern data are plotted in Fig. 13 for passes 7-271 and the agreement is seen to be within $\pm 1°$ of the values determined from the glint data. After pass 271 the line-of-sight to the satellite did not come close enough to the spin axis to yield any more data, due to a combination of orbital precessions and movement of the spin axis.

3.8 *Skinny Route Terminal*

After the Telstar spacecraft was successfully launched and proved to be operating as planned, it seemed desirable to demonstrate a minimal-type ground station that would provide one voice channel over the satellite. An inexpensive, compact station would be useful for remote locations in the world. It was decided to adapt the 18-foot tracker antenna at Holmdel for both transmission and reception, and modify the tracking mode to make it independent of a predicted drive tape. The effort was started on a crash basis in late July, 1962, by members of the Military Research Laboratory at Whippany, and culminated in successful demonstrations of a two-way voice circuit to Andover less than three weeks later. A description of the system and tests conducted may be found in Ref. 7.

IV. CONCLUSIONS

The general objectives outlined in Section 1.1 were accomplished during the Telstar experiments. In addition, it was clearly demonstrated that a relatively modest ground station utilizing a 20-foot horn-reflector antenna can do a creditable job of receiving a television picture across the Atlantic Ocean from an active satellite.

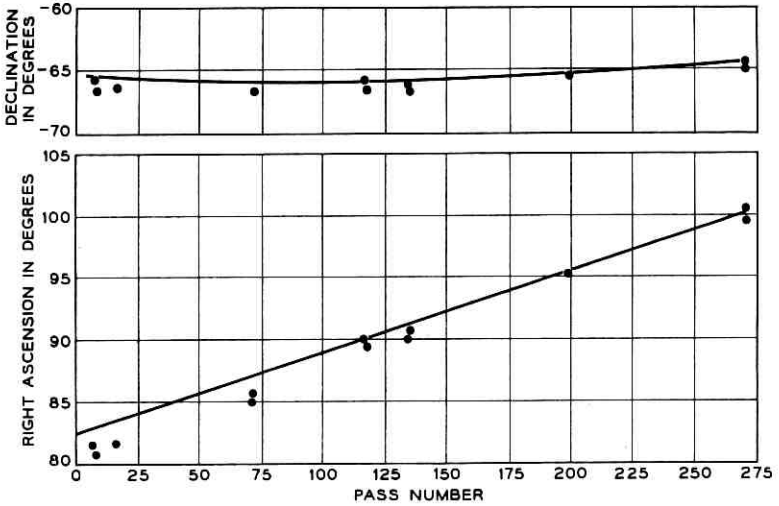

Fig. 13 — Plotted points: spin axis determination from signal level analysis. Solid curve: average of glint data.

V. ACKNOWLEDGMENTS

The Holmdel station could not have taken a successful part in the Telstar experiments without the efforts of a great many individuals. In particular, the author wishes to acknowledge the work of D. C. Hogg, R. A. Semplak, and R. A. Desmond in carrying out the conversion of the horn antenna to 4 gc and installing, testing, and operating the low-noise amplifiers; C. L. Ruthroff, W. F. Bodtmann, J. P. Schafer, and H. E. Keller for providing and operating the frequency compression demodulator; R. H. Turrin, H. A. Gorenflo, and R. H. Brandt for their part in the phase-lock receiver program and other areas; O. E. DeLange, J. T. Ruscio, and H. E. Groener for conversion of the tracker system to 4 gc and operational help; L. R. Lowry for his help with operations management and in providing many of the necessary communication facilities; E. L. Frantsvog, J. W. Barto, W. E. Legg and F. W. Radcliffe for their assistance with many of the details of conducting operations and reducing data. J. S. Courtney-Pratt and his associates planned the glint experiments, and provided and operated the equipment.

The work was carried out under the general direction of C. C. Cutler, and his continued guidance and active participation are gratefully acknowledged.

REFERENCES

1. B.S.T.J., Project Echo Issue, **40**, July, 1961.
2. Ruthroff, C. L., and Bodtmann, W. F., Design and Performance of a Broad-band FM Demodulator with Frequency Compression, Proc. I.R.E., **50**, December, 1962, p. 2436.
3. Enloe, L. H., The Synthesis of Frequency Feedback Demodulators, Proc. Nat. Elec. Conf., Vol. **18**, 1962, p. 477.
4. Ossanna, J. F., Jr., The Generation of Look-Angles from Regularly Available Mean Orbital Elements for 1960 Iota One, Photographic Science and Eng., Nov.–Dec., 1962.
5. Courtney-Pratt, J. S., McLaughlin, J. W., and Hett, J. H., Optical Measurements on the *Telestar* satellite to Determine the Orientation of the Spin Axis and the Spin Rate, to be published.
6. Hill, D. W., Optical Attitude Determination for the *Telestar* satellite, to be published.
7. Two-Way Voice Channel via Telstar Established with Compact Ground Station, Bell Labs. Record, **40**, October, 1962, p. 342.

Launching of the *Telstar* Satellite

By H. N. UPTHEGROVE, J. B. D'ALBORA, JR., A. R. KOLDING and B. A. McLEOD

(Manuscript received March 20, 1963)

The launching of the Telstar satellite from Cape Canaveral is described, with emphasis on the pre-launch testing and test facilities.

I. INTRODUCTION

The Telstar satellite was launched on July 10, 1962, from Cape Canaveral by a Delta launch vehicle. The pre-launch and launch operations were carried out jointly by the National Aeronautics and Space Administration (NASA) and Bell Telephone Laboratories. NASA had responsibility for procurement, checkout, and launch of the Delta vehicle and for mating of the Telstar spacecraft with the launch vehicle. Bell Telephone Laboratories was responsible for delivery, checkout and monitoring of the spacecraft, and observed and participated in the launch vehicle preparation and spacecraft-to-vehicle mating operation. Bell Telephone Laboratories provided radio command guidance for the Telstar launch, as for all Delta launches.

At Cape Canaveral the principal test locations for the Telstar launch operations are:

(1) Launch Complex 17, consisting of two launch pads, 17A and 17B, and supporting facilities; the Telstar satellite was launched from 17B.

(2) Guided Missile Control Facility No. 3, the Laboratories-operated command guidance ground station; Telstar launch operations facilities were located here.

(3) Spin Test Building, operated by Douglas Aircraft Company for NASA; here, the Telstar spacecraft was mated to the Delta third-stage motor and the combination was spin-balanced prior to installation on the launch vehicle.

II. LAUNCH PREPARATIONS AND FACILITIES

2.1 *Summary*

Following the final tests and inspections at the Hillside, N. J., Bell Telephone Laboratories, the spacecraft used in the launch operations

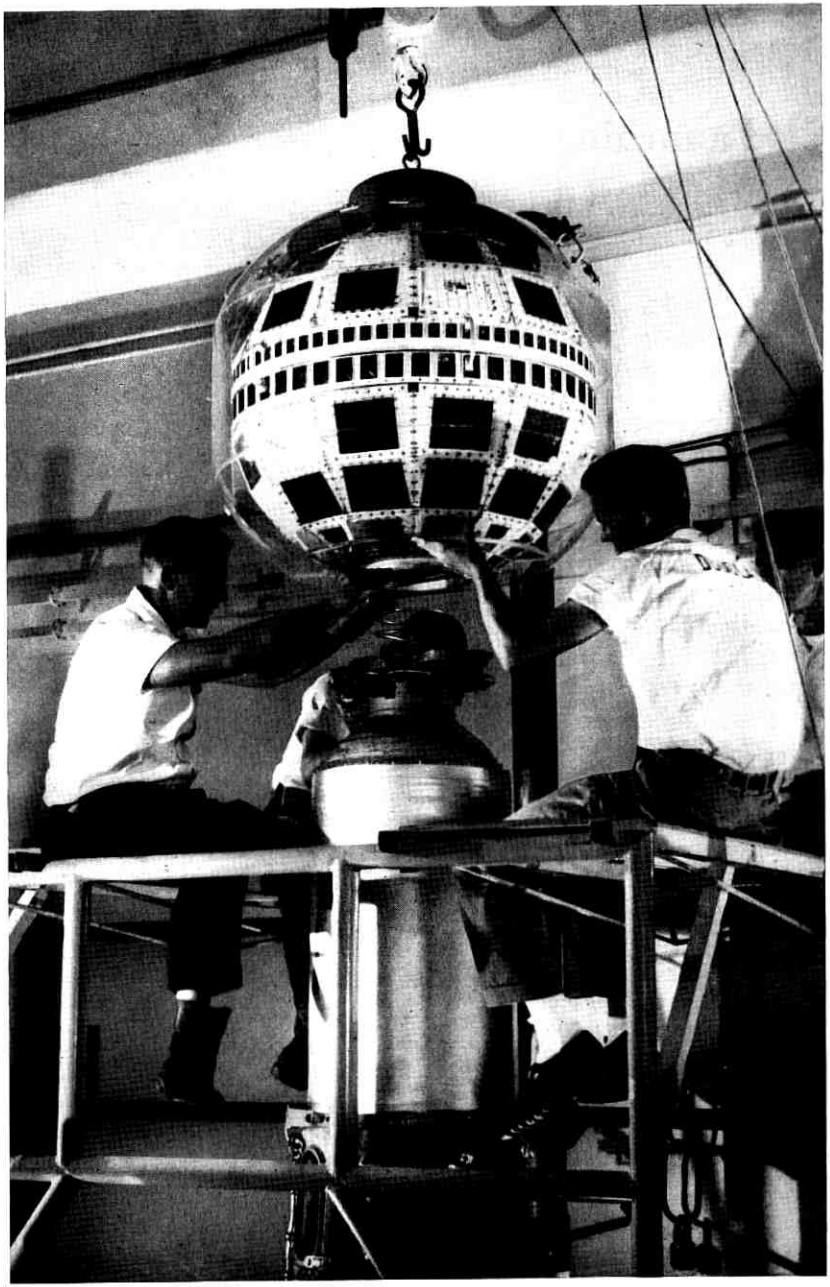

Fig. 1 — Mating the spacecraft to the Delta third stage.

were shipped by special truck to Cape Canaveral for the subsequent series of pre-launch tests and the mechanical operations involved in mating the satellite to the Delta launch vehicle.

The electrical testing required the establishment of new facilities at Cape Canaveral in three locations. The base location at the Laboratories' missile guidance area provides test equipment and spacecraft storage facilities in three air-conditioned 40-foot vans. In addition, there are an autotracking VHF antenna system for command and telemetry and several microwave antennas used for tests when the spacecraft is at either of the other two locations.

A second test location is in the spin test building. In this building, the spacecraft is mated to the third stage of the rocket as shown on Fig. 1, and the combination is dynamically balanced at spin rates it will have in flight. The special installation for the Telstar project consists primarily of three antennas mounted on a tower outside the building and coupled to the satellite to permit remote testing from the base location.

The third test location is the launch stand, where test equipment was installed in an existing test room on the seventh level. This was used together with the test equipment at the base location for tests of the satellite.

Before the flight models were available, the prototype model of the spacecraft was sent to Cape Canaveral and used to check out all of the testing and handling procedures at the three locations. It was also used in the radio-frequency compatibility test which is required by the missile range. Two spacecraft were provided to serve as the flight model and the back-up model. These were designated Fly 2 and Fly 3; Fly 2 was to be launched unless trouble developed requiring the substitution of Fly 3.

The first operation with the Fly 2 spacecraft after arrival at the Cape was the comprehensive arrival check to verify that all of its systems were intact after the trip from Hillside. Subsequent to this, the spacecraft was given a daily routine check during the period of time it remained in the satellite van prior to delivery to the spin building. The back-up spacecraft, Fly 3, was tested in the same way and then remained in the spacecraft van receiving daily checks until it was shipped back to Hillside after the launch.

On F − 9 day (9 days before launch), Fly 2 was moved from the spacecraft van to the spin building for mating to the live third stage.* This operation consists of coupling the spacecraft to the third stage. The combination of spacecraft and third stage was tested for eccentricity before the dynamic spin balancing operation. A remote electrical performance

* Discussed later in this paper. The live stage contained approximately 500 pounds of solid propellant.

test was then made from the vans at the base location to make sure that the spacecraft had not been damaged.

Following this test, the spacecraft and third-stage assembly was moved to the spin test fixture. In the balancing operation, the assembly was rotated at its flight rate and the imbalance measured with accelerometers. Following the balancing operation, another remote check was made to verify that no damage was done during the spin operation.

The mated third stage and spacecraft were then transported to the launch stand in a special carrying canister on F − 4 day. After attachment to the second stage of the rocket, the spacecraft and the live third stage were encased in a clear plastic enclosure which was continuously supplied with dust-free, dry, cool air.

Prior to roll-back of the gantry, the spacecraft was tested daily using test consoles on the seventh level of the gantry. After the gantry was rolled back the testing was done by direct radio coupling from the Telstar spacecraft antennas to the base location antennas. In the final minutes of the terminal count immediately preceding the launch, the spacecraft microwave repeater was again tested. Telemetry monitoring was continued through lift-off and until the satellite disappeared below the horizon.

2.2 *Transportation to Cape Canaveral*

A one-ton truck equipped for the special requirements of spacecraft transportation was procured. The body is insulated and contains a heater (independent of the cab heater) and a cooling device which uses solid carbon dioxide. The spacecraft carrying case contained a shock mounting to which the spacecraft was clamped. Additional shock suspension of the carrying case within the truck was found to be undesirable.

Road tests with a dummy spacecraft load verified that the truck and carrying case would provide safe transportation for the actual spacecraft.

The carrying case was filled with dry nitrogen before it left the Hillside Laboratories, and a small positive pressure was provided by a low-pressure feed of nitrogen from tanks in the truck.

2.3 *Satellite Test Facilities at Base Location*

The base location at the Bell Laboratories guidance area, GMCF-3, is far removed from the industrial area and vehicle traffic. Because of the unobstructed radio paths from this location to the spin building and to launch area 17, antennas could be mounted on low supporting structures. The arrangement of the vans and antennas at the base location is shown in Fig. 2.

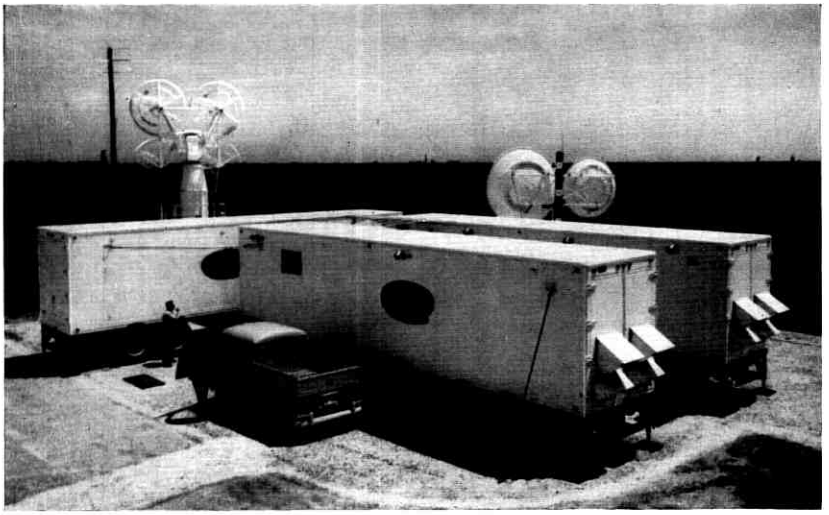

Fig. 2 — Launch operations — base location.

2.3.1 *Description of Vans*

The vans were designed for the particular requirements of the Telstar base location. The three vans are designated "spacecraft van," "telemetry van" and "command tracker van," where the names are those of the principal function of the van. Each van is 40 feet long and 8 feet wide and has about 7 feet of head room. All features required for long-distance road travel were provided to permit relocating the base.

The air-conditioning system provides air filtering and limits the maximum relative humidity. The spacecraft van has additional dust filtering which removes particles larger than 2 microns. The ac power is taken from the power supply of the missile guidance system. For launch operations and other critical operations, the power circuit is switched to two large diesel-driven generators.

The interior arrangements of the three vans are illustrated in Fig. 3. The spacecraft van is divided into three compartments. The central area contains mounting pedestals for two spacecraft. The end compartment is an unpacking area where the spacecraft in its carrying case is unloaded from the truck. In this area, the three-piece carrying case is removed and the spacecraft lifted off the base with a traveling electric hoist which carries the spacecraft to the mounting pedestal. After the arrival tests on each spacecraft, the daily routine tests were conducted remotely through cables to the telemetry van.

The limitation of traffic by the provision of a separate van for the

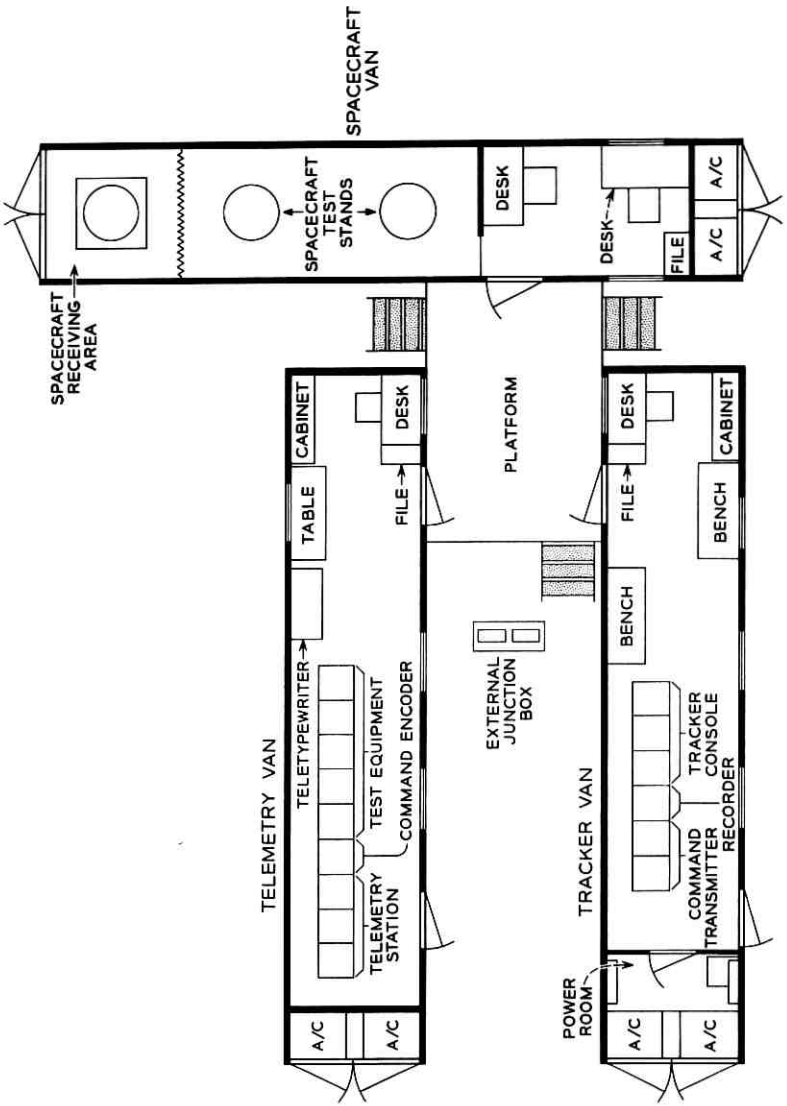

Fig. 3 — Van layout — base location.

Fig. 4 — Interior view of telemetry van.

spacecraft minimizes exposure to contamination, humidity, and fluctuations in temperature.

The telemetry van provides the principal working area for pre-launch testing, countdown tests at launch, and telemetry and command activities in post-launch orbits.

This van contains a lineup of 9 cabinets, as shown in Fig. 4. Three of these house the telemetry receiver and decommutating circuits. The next cabinet contains the command encoder, whose output modulates either a low-power 123-mc* command transmitter for pre-launch testing or the 200-watt transmitter in the command tracker van. The remaining five cabinets contain a variety of test equipment. This van also contains an arrangement of teletypewriter instruments, primarily for the transmis-

* This value, as well as all other frequencies given in this paper, is approximate, but is within 1 per cent of actual.

sion of telemetry information from the Cape to Andover, Murray Hill, and Hillside. The telemetry decommutating system provides a punched tape for sending the data to other locations.

Provisions were made to use the identical telemetry reduction systems at the Cape and at the Hillside Laboratories as back-ups for each other. This allowed tests on two spacecraft to be conducted at the same time at the Hillside Laboratories during periods when the Cape telemetry was not in use. It also provided a back-up during critical operations against failure of the Cape telemetry system. The means for doing this required only the addition of a two-way audio-frequency data channel between the two locations to carry the 3-kc telemetry subcarrier and its sidebands. The teletypewriter circuit returned the output to the distant station in either case. Since the 136-mc receiver of the telemetry system was not included in the back-up, the 136-mc receiver of the command tracking antenna system was arranged to be used as a spare.

A full-period telephone line from the telemetry van to the Andover earth station was used to coordinate activities during launch and in subsequent tracking operations.

Telephone communication among all locations involved in launch and pre-launch operations was provided at Cape Canaveral by the Missile Operations Phone System (MOPS).

The command tracker van contains the equipment used for all tracking operations, sending of commands, and receiving telemetry. The 200-watt command transmitter and the control console for the command tracking antenna system are the principal items.

2.3.2 *Antennas*

Antennas at the base location were needed for remote testing by radio coupling to the spacecraft at the spin building, for terminal countdown tests on the launch stand and for the monitoring of telemetry during the ascent trajectory and subsequent orbits.

The same type quad-helix autotracking antenna designed for use at the Andover earth station was provided for command and telemetry. This antenna system provides autotracking of the 136-mc beacon to a precision of about $\pm 1°$ in both azimuth and elevation. The 136-mc signal received by the antenna is amplified and sent to the telemetry receiver for detection and decommutation.

The 123-mc command signal from either the 200-watt or the 2-mw transmitter may be multiplexed to the antenna.

A boresight antenna for periodic alignment of the command tracker is located 100 feet away on a 50-foot wood pole. A low-level 136-mc signal

is sent from the command tracker van to this antenna over a coaxial cable.

Two parabolic dish antennas were installed at the base location for remote testing of the spacecraft at the spin building and on the gantry. The 6390-mc transmitting antenna is 8 feet in diameter, and the 4170-mc receiving antenna is 10 feet in diameter. Both antennas were attached to a rigid framework mounted on a 25-foot telephone pole embedded in concrete and well braced with guy wires. The framework is manually steerable to permit aiming at either of the two remote locations. A low-power optical telescope is used to aim the antenna.

2.4 *Test Facilities at the Spin Building*

At the spin building, two 4-foot diameter parabolic antennas were mounted facing the base location on a 40-foot steel tower. Waveguide runs connect these antennas to one port of each of the spacecraft's antennas. The same tower also supports a VHF corner reflector antenna for telemetry and command use. The only other test equipment at the spin building is a rectifier for supplying power to the spacecraft during electrical tests.

2.5 *Spacecraft Facilities on the Launch Stand*

Upon completion of spin balancing, the spacecraft–third-stage combination was enclosed in a carrying canister for transportation to the launch stand. The carrying canister was lifted up to the top level of the service tower and lowered to mate with the Delta second stage. After removal of the canister, the spacecraft and the third stage of the rocket were each enclosed in plastic shrouds continuously supplied with dry, cool air. The working area on this level was also enclosed in an air-conditioned tent.

Because of the presence of the live third stage, it was decided to put the test equipment consoles in an existing room on a lower level and connect to the spacecraft through waveguide and coaxial cable runs. Thus, the testing prior to removal of the gantry was done in a manner similar to the testing at the base location.

III. SPACECRAFT TESTING

3.1 *Summary*

Two types of tests were made on the spacecraft. The first was a comprehensive test which was made three times — after the spacecraft was

received from Hillside, again after mating to the third stage and balancing, and again after the spacecraft was moved into launch position. The second type of test was a daily routine which determined that all major systems continued to function properly.

The comprehensive test included: physical inspection; checks on the radiation package, microwave antennas, solar cells, and two-year timer; and the complete daily routine. The daily routine included VHF beacon measurements, telemetry encoder comparisons, and checks on the command receiver, command decoder, power plant, microwave repeater, transistor damage experiment, and temperature and pressure sensors.

The spacecraft was tested at the base of operations, at the spin building and at the gantry tower, using the test arrangements previously described. During the final hours of the terminal countdown, testing and monitoring continued via radio through the fairing to the antennas at the base location.

During the launch the command tracking antenna tracked the satellite to the horizon, so continuous communication was maintained until that time. Telemetry was closely watched during this period, so that in the event that any relays should change state due to shock, they could be corrected by sending the appropriate command.

3.2 *Specific Test Procedures*

In preparation for all tests in the vans the spacecraft circuits were coupled to the test equipment in the following manner:

(1) The spacecraft helical antenna was disconnected near the canister and was replaced by a cable to the test equipment. This connection made possible precise measurements on the VHF systems without having to use the spacecraft antenna. It also permitted testing of the satellite without radiating power at the VHF beacon frequency or at the command frequency. The latter consideration is especially important at Cape Canaveral, where all radio-frequency radiation is carefully scrutinized and frequently prohibited for the sake of range safety.

(2) A single port of each microwave antenna was connected through a special coupling device to the equipment in the telemetry van. The remainder of the ports were girded by RF absorbing bands which reduced radiation and provided a termination for the antennas.

(3) A rectifier which supplied current required by the circuitry plus a small amount required for charging of the nickel-cadmium cells was connected through the battery jack.

The command and telemetry connections are shown in Fig. 5. A 20-db

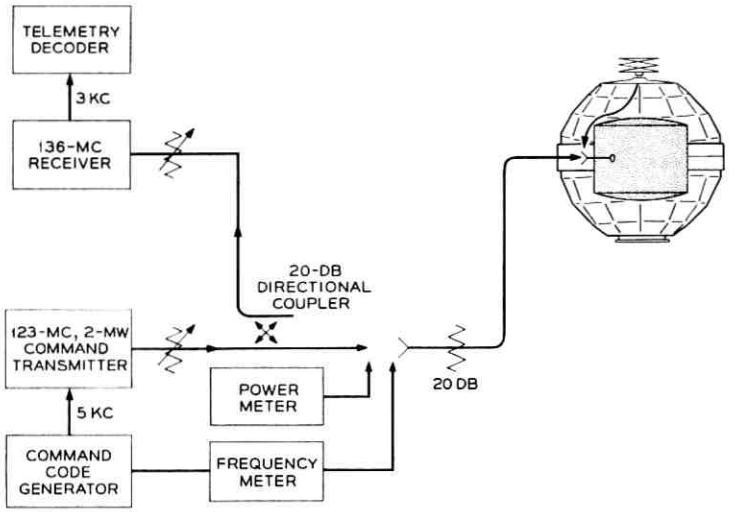

Fig. 5 — Command and telemetry test connections.

directional coupler was used to pick off the 136-mc signal for telemetry and to minimize the 123-mc command signal at the telemetry receiver input. The 20-db fixed pad was introduced to prevent the spacecraft from ever being subjected to the full power of the small command transmitter. It also attenuated the 136-mc signal down to the range of the power meter. The variable attenuators were used to set independently the desired power levels for both the 123-mc command and 136-mc beacon.

The microwave test connections are shown in Fig. 6. The 6-gc path contains only a variable attenuator. The 4-gc path has switching and filtering so that the composite 4-gc signal could be viewed on the spectrum analyzer and the 4170 and 4080-mc signals could be measured separately.

Figs. 7 and 8 show connections used to communicate with the spacecraft after it has left the van area. The test procedures in these locations were nearly the same as the van tests.

A description of each part of the daily test routine is given below

3.2.1 *VHF Beacon*

The power output and frequency of the unmodulated 136-mc beacon were measured.

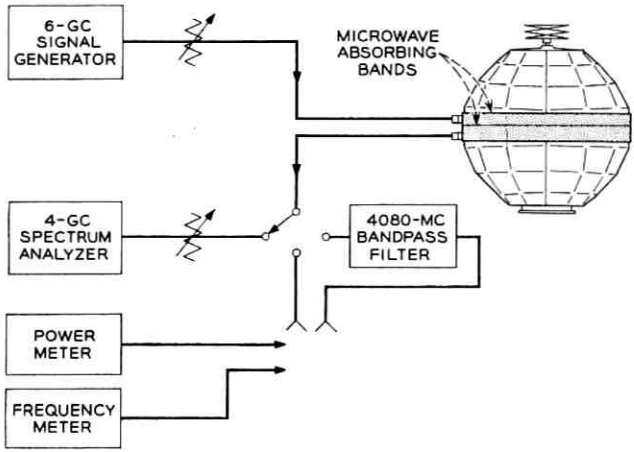

Fig. 6 — Microwave test connections.

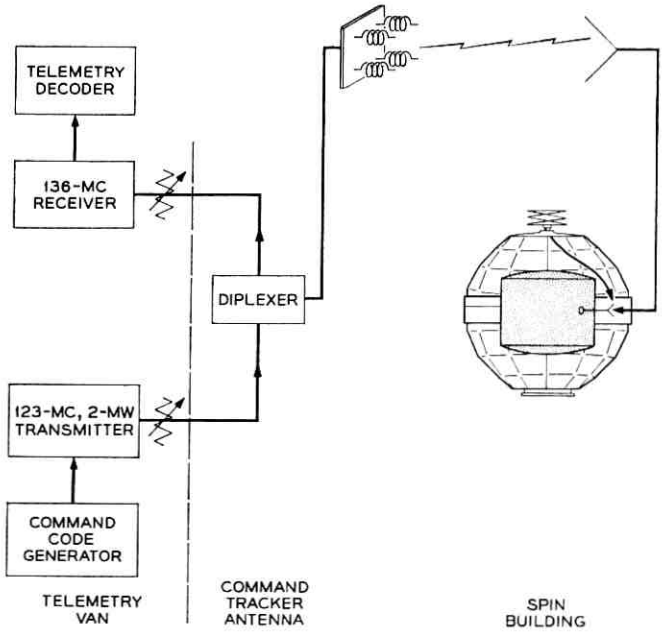

Fig. 7 — Command and telemetry connections for testing spacecraft in spin building.

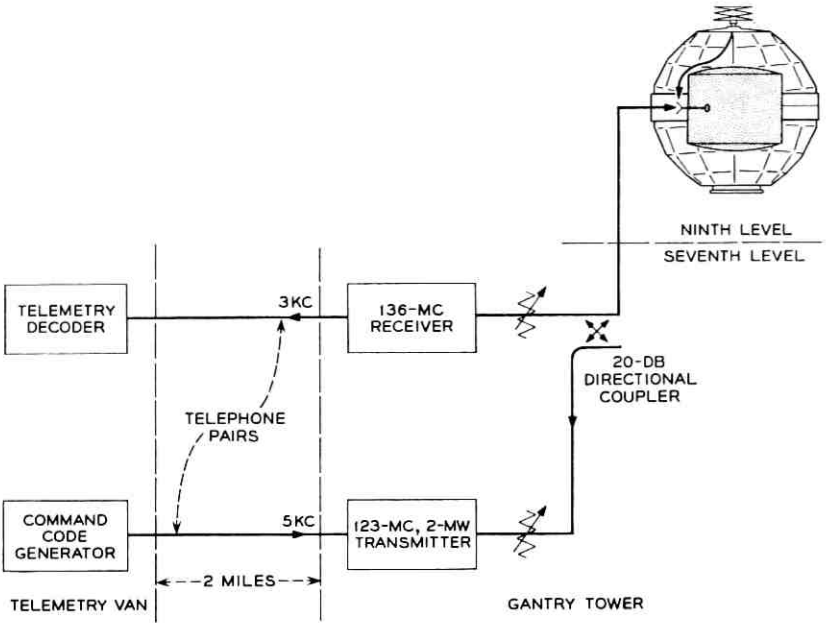

Fig. 8 — Command and telemetry connections from F − 5 day to F − 0 day.

3.2.2 *Telemetry Encoder Comparisons*

One complete frame of telemetry was taken from each of the two telemetry encoders and the readings compared.

3.2.3 *Command Systems*

The sensitivities of the two command receivers were checked with unmodulated signals. Following this, the commandability of each command receiver was verified.

3.2.4 *Power Plant*

The power plant test was an observation of 22 telemetered values of voltages, currents, and temperatures. Included were voltages and temperatures of the nickel-cadmium batteries and temperatures of key transistors in the regulators and dc-to-dc converters.

3.2.5 *Temperatures and Pressures*

Telemetry reads out 40 temperatures and 2 pressures. All values were checked and where possible were compared with external thermometers.

3.2.6 *Transistor Damage Experiment*

Six transistors with various degrees of shielding were placed in circuits which measured common-base short-circuit current gain. The values were checked via telemetry and compared with the known value of gain.

3.2.7 *Microwave Repeater*

The microwave repeater was checked using the following steps:

(a) check all related telemetry channels,

(b) with no signal input, measure 4-gc noise output,

(c) with no signal input, measure 4080-mc beacon frequency and power,

(d) with midrange signal input, measure beacon power,

(e) with midrange signal input, measure signal output power,

(f) view the spectrum of output signal for spurious sidebands, and

(g) measure point-by-point frequency characteristic of repeater.

The following tests were made in addition to the daily routine for the comprehensive test:

3.2.8 *Microwave Antenna*

As a check of the 4-gc transmitting antenna, a power measurement was made at each of the 48 ports. This test was made in lieu of a pattern measurement, which could not be made with the existing facilities. As a check of the 6-gc receiving antenna, a low-level 6390-mc signal was sent separately to each of the 72 antenna ports while the 4170-mc signal was observed at a single 4-gc port. The level was chosen to be below the automatic gain control range of the repeater so that amplitude differences in 6390-mc signal reaching the repeater would cause differences in level of the 4170-mc output.

3.2.9 *Solar Cell Check*

The output of all 50 banks of solar cells in the power plant and all of the individual cells in the solar aspect circuit was read as each cell or bank of cells was illuminated with a low-intensity light source. For the solar power plant, short circuit current was read with a milliammeter, and the solar aspect circuits outputs were read by telemetry.

3.2.10 *Radiation Package Checks*

Each of the four radiation sensing circuits was tested by bypassing the actual sensing element and delivering pulses directly to the inputs of

the preamplifier circuits. The thresholds of all of the detectors were verified by changing the pulse amplitudes once per minute and observing the telemetered data.

3.2.11 *Two-year Timer Check*

This test involved temporary powering of the two-year timer, applying a start signal, and verifying that the timer had started. After verification, the timer was stopped by removing power.

3.3 *Testing of the Spacecraft at Remote Locations*

All testing of the spacecraft in the spin building was done remotely by radio from the base location. All of the tests described above were made, but some techniques had to be changed to accommodate the lower signal levels available over the radio link to the base location.

When the spacecraft was at the launch stand, daily tests continued. To reduce radiation at all working frequencies and to eliminate the variability of the path losses in the measurements, all of the spacecraft radio systems were terminated in test equipment on the seventh level of the gantry tower. From that point to the base location, telephone pairs were used to carry the 3-kc telemetry and the 5-kc command subcarriers. Microwave tests were made on the seventh level. All tests made on the gantry were under the direction of the test conductor in the telemetry van, so voice communication was maintained at all times.

IV. FROM F — 15 DAY TO F — 0 DAY

On F — 15 day (15 working days before launch) the prototype spacecraft was taken from the van to the spin building, where it was mated to a dummy third stage. This event was in preparation for the RF compatibility test on F — 11 day, but it also gave personnel of the Douglas Aircraft Company and of the Laboratories an opportunity to rehearse their procedures a few days in advance of the arrival of the flight model at the spin building.

On F — 12 day the prototype and dummy third stage were transferred to the launch stand and were attached to the second stage of the Delta vehicle. The RF compatibility test on F — 11 day showed that all the range radars, the guidance system, the destruct system, vehicle beacons, and the spacecraft systems were mutually compatible.

On F — 9 day the Fly 2 spacecraft was transferred to the spin building to be mated to the live third stage. Daily checks continued at the

spin building until F − 5 day, when the spacecraft was transferred to the launch stand.

From F − 5 to F − 1, daily checks continued on the spacecraft and the Delta vehicle.

The F − 0 countdown was started at 5:40 p.m., July 9, on the evening before the launch. The first check of the day, ending at 7:00 p.m., was a complete daily routine. After completion of the routine, telemetry was left on and the spacecraft battery was charged until 8:15 p.m. At approximately 10 p.m. preparation for fairing installation began. For this it was necessary to: (1) disconnect all test cables, (2) remove air-conditioning and shroud, (3) remove the plastic protective cover, (4) remove microwave absorption bands, (5) remove spacecraft access panel, (6) connect helix antenna, (7) verify two-year timer operation, (8) install access panel, (9) remove protective covers from radiation sensors and mirrors, and (10) inspect. After these preparations were made, the fairing was installed, leaving one access hole open for insertion of the umbilical plug, which was the final link between the spacecraft battery plant and the rectifier in the blockhouse.

By midnight the fairing was installed and all umbilical connections were made and checked. Once again, before the gantry tower was rolled away, the spacecraft was turned on for the purpose of making a test with commands going through the fairing to the helical antenna, as they would during the early part of the ascent trajectory. This task was completed successfully by 30 minutes after midnight, and the spacecraft was turned off again as a period of "no radiation — no switching" began.

At 1:10 a.m. checks of the van equipment were started as the gantry tower removal began. The command tracker was aligned with the boresight; the command transmitter was measured for proper VSWR, modulation percentage, and power output. Another command routine was made and completed at 2:10 a.m. For the next 50 minutes, batteries were charged and telemetry was watched very closely.

At the end of the 50 minutes, the time was 3 a.m. or T − 35 minutes. The terminal count began. Between T − 35 and T − 10 a brief command routine test was performed, and the microwave repeater was given a last test. At T − 10 all commandable circuits were in launch condition: i.e., all were turned off except for the 136-mc beacon and the telemetry modulating the beacon.

Lift-off occurred at 3:35 a.m. (0835 GMT) on schedule. The command tracking antenna autotracked the VHF beacon from lift-off to horizon. Small variations appeared in the signal level due to ground reflections and attenuation, but otherwise the track was routine. Until the satellite dropped below the radio horizon, telemetry was watched very closely

with particular emphasis on relay states, battery temperature and voltage, solar plant current, AGC level from command receivers and the low-level calibration channel.

To ensure that good command capability was maintained during the launch, the telemetered AGC levels of the spacecraft command receivers were watched, and at a predetermined level, the 123-mc carrier power was increased 20 db to the full 200 watts.

Other telemetry channels bore interesting information on several aspects of the ascent. Fig. 9 shows skin temperatures on two different facets of the satellite. One of the two was illuminated by the sun continually for approximately 10 minutes — from the time the spacecraft emerged from the earth's shadow until the spin rockets were fired, causing the satellite to spin and thereby putting the facet into the shadow of the satellite part of the time. The other facet shown was in complete darkness until spin-up, when it began to receive some solar radiation.

Fig. 10 shows on one trace the amount of current supplied to the satellite either by the blockhouse rectifier or by the solar plant. Between 0840 GMT and 0849 GMT the current showed a steady decrease because that part of the solar plant which was delivering the current was being warmed (see Fig. 9) and was becoming less efficient. After spin-up some of the cooler portions came into sunlight and the average current increased.

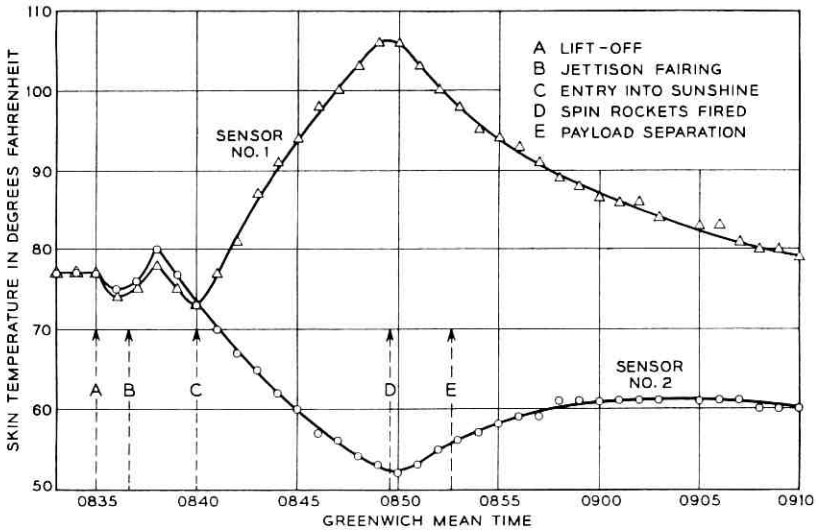

Fig. 9 — Skin temperature variation after lift-off

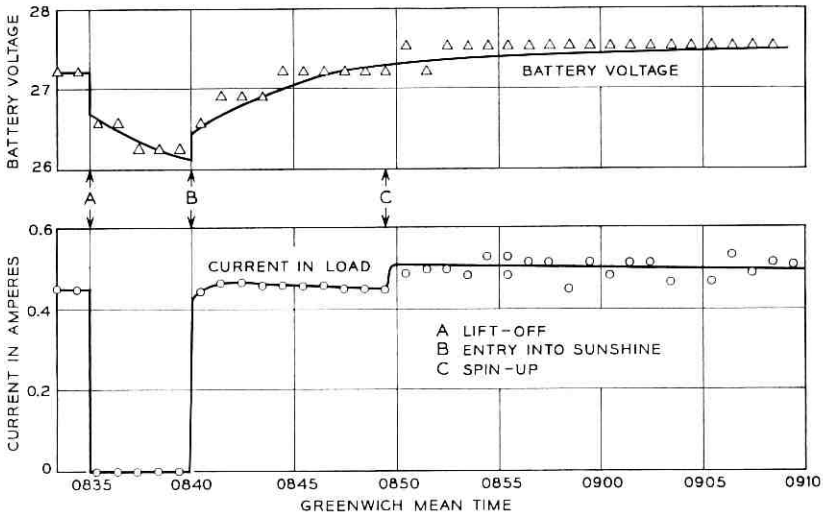

Fig. 10 — Ni-Cd battery voltage and current delivered to canister during launch.

The voltage of the battery plant is shown in the other trace of Fig. 10. The abrupt drop in the battery voltage at lift-off is attributable to the fact that when the rectifier in the blockhouse was disconnected, the current in the battery changed from a 0.3-ampere charge to a 0.2-ampere discharge. The battery continued to discharge until the satellite emerged into the sunlight, at which time the voltage began to increase.

The spacecraft went below the Cape Canaveral radio horizon at 0848 GMT (0348 EST), so all information shown beyond this time was taken from magnetic tape recordings made by the NASA Minitrack stations. Coverage by Cape Canaveral and by these stations was as follows:

Cape Canaveral from lift-off to 0848 GMT
Antigua from 0839 to 0853 GMT
Ascension from 0845 to 0902 GMT
Johannesburg from 0904 to 0917 GMT.

V. LAUNCH VEHICLE AND ORBIT

5.1 *Description of the Delta Launch Vehicle*

Fig. 11 is a cutaway view of the Delta vehicle as used for the Telstar launch. It is a three-stage rocket, with ground-guided, liquid-fueled first

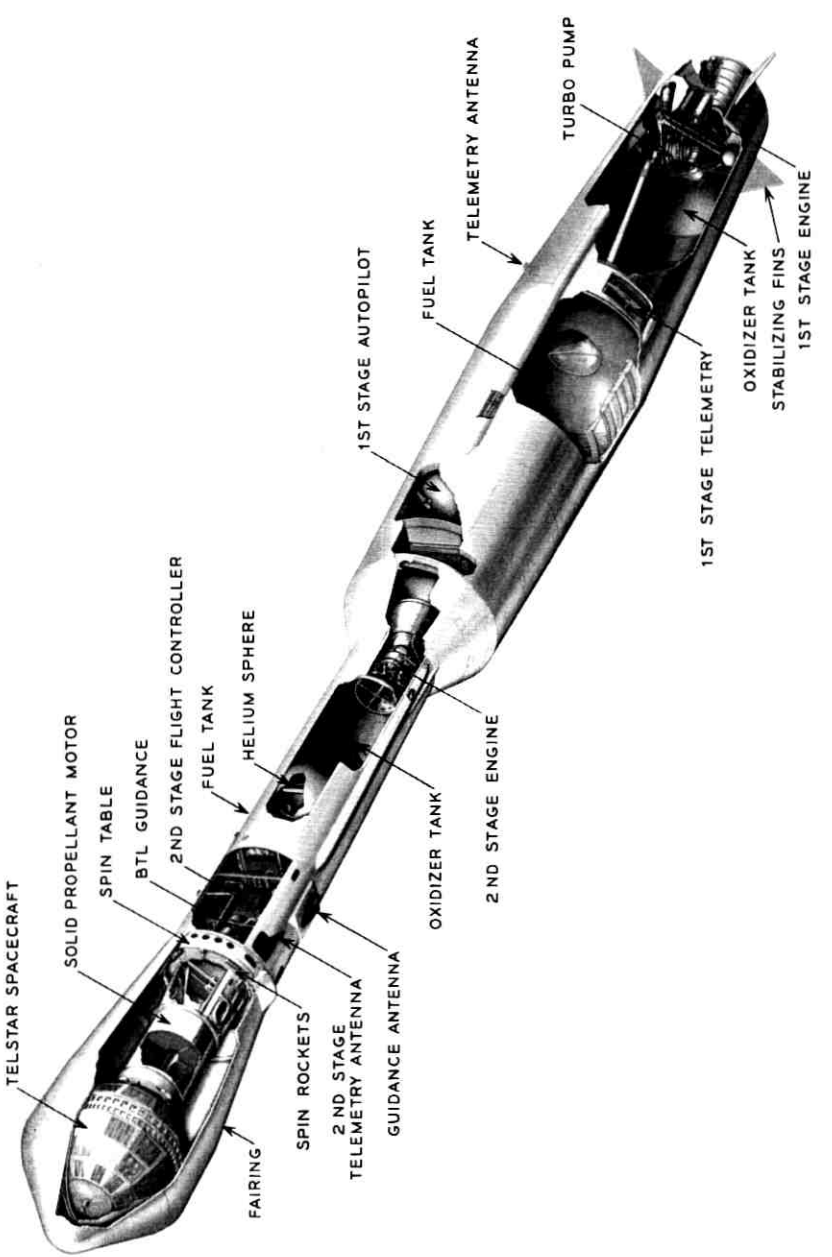

Fig. 11 — Delta vehicle-Telstar spacecraft.

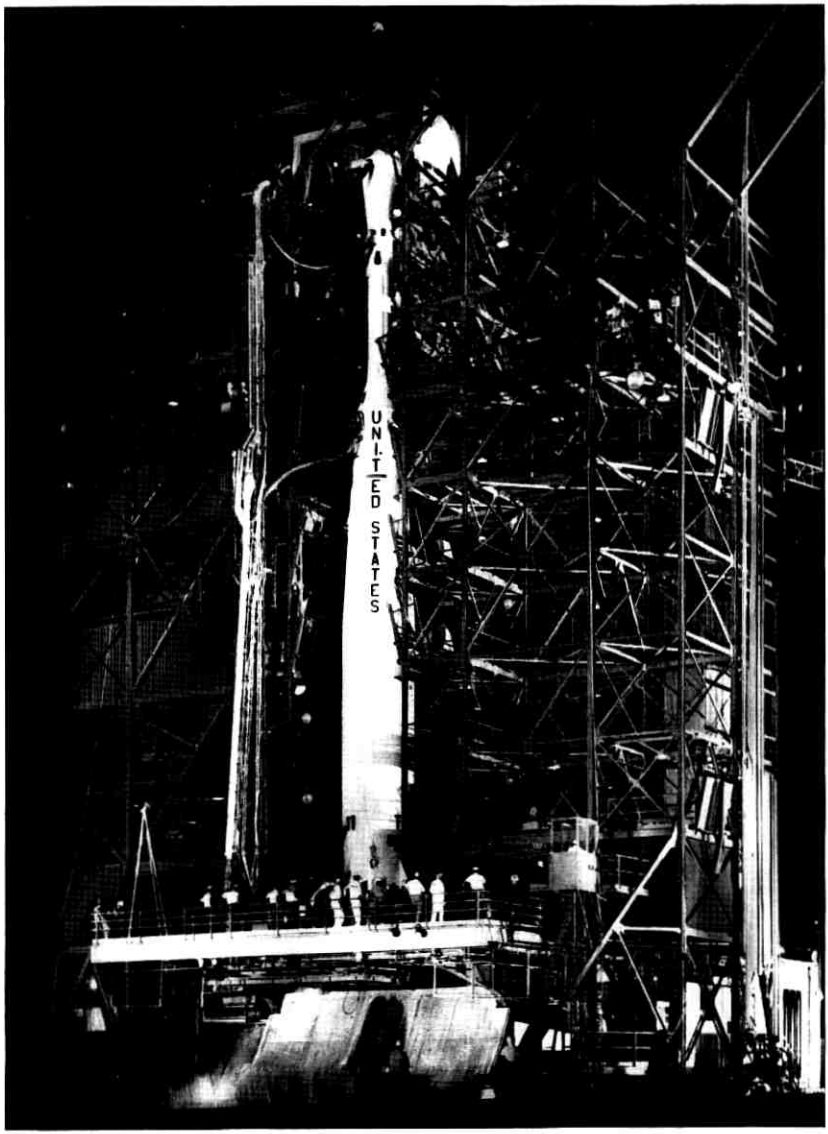

Fig. 12 — Delta vehicle and Telstar spacecraft in gantry.

and second stages, and a spin-stabilized, solid propellant third stage. A bulbous fiber glass fairing surrounds the third stage and the Telstar spacecraft mounted on it in the launch configuration. Fig. 12 shows Delta No. 11 in the service tower about three hours before launch. It is approximately 90 feet high and weighs about 57 tons, fueled and ready for launch.

The first stage is an operational-type Thor missile modified for the Delta use. Its engine uses RP-1 (kerosene) fuel with liquid oxygen (lox) as the oxidizer. Vehicle performance is based on use of at least 99 per cent of the propellants. A flight controller employing three integrating gyros, three rate gyros, and a programmer is used to provide open-loop control until the ground guidance system takes control at about 90 seconds after lift-off. Control is achieved by a combination of the gimballed main engine nozzle and two small vernier engines.

The second stage is a propulsion system which uses unsymmetrical dimethyl hydrazene fuel (UDMH) and inhibited white-fuming nitric acid as the oxidizer. A gaseous nitrogen retro system is used on the second stage to provide reverse thrust to get the required separation distance between the second and third stages at third-stage ignition.

Second-stage in-flight steering control is achieved by hydraulic gimballing of the second stage engine thrust chamber. Roll control is accomplished by discharging helium gas through four roll jets, two of which react in a clockwise direction, and two of which react in a counterclockwise direction. Both pitch and yaw control systems respond to commands from the Laboratories guidance system.

During the coast period, starting at second-stage burnout and ending at second/third-stage separation, the vehicle was turned to its proper spatial orientation by means of a second-stage coast phase control system. The gyros used to control the second stage during the powered portion of flight supply the attitude reference used to control the gas jet system during the coast phase. An on-off type of gas jet operation was used. To provide range safety destruct capability, the Delta vehicle carries radio receivers in the first and second stages. The flight termination system in each stage consists of the receiver and decoder, antenna system, safety and arming mechanism, detonating cord strand to rupture propellant tanks, and a power supply independent of vehicle power. Prior to first/second-stage separation, either system would destruct both stages. A large-diameter (approximately 22 inches) ball bearing mounted at the forward end of the second stage supports the spin table, which in turn supports the third-stage motor and spacecraft. Prior to third-stage ignition, the third stage and spacecraft were spin stabilized at approximately

180 rpm by small rocket motors attached to the spin table. The third-stage propulsion system had a solid propellant motor.

The separation of the third stage was delayed approximately 2 minutes after nominal fuel depletion to allow time for afterburning and outgassing of the third-stage motor and thus prevent contamination of the satellite. The third-stage motor was tumbled by an asymmetrical weight after separation to prevent impact with the satellite.

A bulbous fairing was provided to decrease aerodynamic drag and to protect the spacecraft and third-stage motor from aerodynamic heating during flight through the atmosphere. This fairing was jettisoned at an altitude of 85 nautical miles, where protection from aerodynamic heating was no longer required.

5.2 *Spacecraft/Launch Vehicle Integration*

The Delta vehicle for the Telstar project placed limits and requirements on the spacecraft to ensure compatibility. The dimensions of the standard bulbous fairing fixed the maximum diameter of a spherical spacecraft at slightly over 35 inches. A standard Delta payload attach fitting was incorporated as an integral part of the spacecraft structure, to mate with the corresponding fitting on the Delta. The compatibility of the spacecraft design was confirmed at a fit-check mating at Douglas Aircraft Company, Santa Monica, California, in December, 1961, when a full-scale, accurate mockup of the spacecraft was assembled with the appropriate launch vehicle components. The Fly 2 spacecraft weight, when delivered to Cape Canaveral, was 170.325 pounds. General environmental capabilities for temperature, humidity, shock, vibration, acceleration and thermal vacuum were established by qualification and acceptance tests at the Laboratories. Possible contamination from fairing outgassing due to aerodynamic heating was investigated and found to be of no concern.

5.3 *Orbit Determination and Guidance*

The desired Telstar satellite orbit resulted from a sequence of activities taking more than a year and involving several organizations. In 1960 and 1961, the Laboratories made parametric studies to relate Telstar transmission requirements to Delta capabilities in terms of achievable orbits and spacecraft weight and size. When the weight had been set at approximately 170 pounds, more detailed studies were made to precisely define the desired orbit. This study indicated that the Delta vehicle could place 170 pounds in an orbit of the following characteristics:

Apogee: 3000 nautical miles
Perigee: 500 nautical miles
Inclination of orbit to the earth's equator: 45°
Spin-axis azimuth at injection: $\geqq 155°$

A Delta trajectory to achieve this orbit was generated and its feasibility confirmed. This trajectory became part of the detailed test objectives (DTO) for Delta No. 11. The necessary guidance equations to represent the desired trajectory were developed. After translation into a punched guidance tape, these results were checked by simulation testing in the command guidance system at Cape Canaveral.

Because of range safety considerations, when a Delta vehicle is launched from Cape Canaveral the launch azimuth may not exceed 108°. This establishes a path which crosses the equator at an angle of about 33°. The orbital inclination will have this value if all three stages are fixed in the initial flight plane, as they would be for maximum energy use. The desired higher inclination of 45° was attained by yawing the second and third stages to the south of the initially established ascent trajectory plane when the vehicle had arrived at a point where the range was clear to the south. Since the energy imparted to a spacecraft is reduced by such yawing, the final apogee or perigee or both will be reduced.

In developing the ascent trajectory it is necessary to ensure that the command guidance system at the launch site maintains contact with the vehicle during first and second-stage burning. The vehicle must stay well above the launch site horizon, and certain limitations are imposed on the orientation of the axis of the vehicle so that its antenna pattern will properly receive guidance signals from the launch site. Several calculations are required for the determination of the optimum ascent trajectory.

After the second-stage engine cutoff (SECO), the vehicle is allowed to coast upward, losing speed, until finally it reaches the apogee of the ascent trajectory established by the first and second stages. At this point the third stage is ignited. The third-stage axis is maintained in the local horizontal plane at the time of firing, in order that no more energy be wasted than necessary, and so that the final perigee position will coincide with the ascent trajectory apogee. For the final Telstar satellite orbit, perigee was about 5° latitude north of the equator and apogee about 5° south.

Within this framework, various possible orbits were calculated. First, a particular spacecraft weight and perigee height were selected and a series of ascent trajectories was calculated with the object of finding ones

whose ascent trajectory apogees were equal to the specified final perigee height. One was chosen which had the maximum velocity at ascent trajectory apogee and still met the requirements that command guidance contact be maintained during the burning of first and second stages and that a certain amount of yawing to the south be accomplished during second-stage burning in order to increase inclination. When such an optimum ascent trajectory had been determined, possible final orbits were calculated, assuming the third stage to be yawed southward by increasing amounts, resulting in increasing inclinations and decreasing apogee heights. The result was a family of orbits where apogee height is a function of inclination. Iteration of this process produced a family of feasible orbits from which one was selected for the Telstar satellite.

The Telstar launch vehicle was guided by the command guidance system designed by the Laboratories. The command guidance system consists of a precision tracking ground radar, a digital computer and a missile-borne system in the second stage of the rocket, consisting of a radio receiver, decoder and transmitter. The ground guidance facility, GMCF-3, which is located about two miles from the launch pad, houses the radar and the computer. In the command guidance system the launch vehicle position is continuously determined by the precise ground-based automatic tracking radar. The computer accepts the position data and derives appropriate vehicle velocities. The missile position and velocity data are compared with precalculated values, representing the desired trajectory, which have been stored in the computer prior to flight. Coded steering commands, based on deviations between the actual and desired values, are transmitted to the missile on the radar beam.

An engine cutoff command is sent to the vehicle when the ground-based computer is satisfied that appropriate terminal conditions have been met. The high degree of accuracy of the command guidance system results primarily from the combination of reliable communications to the vehicle, precise radar tracking, and a unique computation process involving radio inertial guidance principles for determination of velocity.

TABLE I — *Telstar* ORBIT PARAMETERS

	Orbit Computed Preflight	Orbit Predicted From Burn-Out Parameters	Actual Orbit (NASA Minitrack)
Apogee (nm)	3000	2990	3043.2
Perigee (nm)	503	513.14	511.9
Period (min)	156.48	156.55	157.6
Inclination to equator (deg)	44.97	44.99	44.78

5.4 *Actual Orbit Achieved*

The Delta No. 11 second-stage burnout parameters obtained from the guidance computer at the conclusion of the second-stage guidance were used to predict the final orbit. The predicted orbit parameters obtained are shown on Table I, with the preflight computed orbit and the actual orbit obtained by tracking shown for comparison. Differences among the three are small.

VI. CONCLUSION

The testing methods and facilities developed by the Laboratories for the pre-launch and launch operations at Cape Canaveral were used successfully on the first Telstar launch, and only minor changes will be made for the second Telstar launch.

The excellent cooperation between all of the people of the Laboratories involved in the launch and the members of the National Aeronautics and Space Administration and its supporting agencies at Cape Canaveral contributed immeasurably to the successful launch.

Results of the *Telstar* Satellite Space Experiments

By P. T. HUTCHISON and R. A. SWIFT

(Manuscript received March 1, 1963)

This paper describes how the Telstar satellite has performed in space. Included is information on changes in the temperature, spin rate, spin-axis precession, orbital parameters and power levels of the satellite signals, and comments on the behavior of the electrical circuits in the space environment.

I. INTRODUCTION

This paper describes the initial performance and changes in the electrical characteristics of the communications repeater, command system, and telemetry system and changes in the temperatures, spin rate, spin-axis precession, and other physical phenomena occurring in the Telstar spacecraft during the first months of operation.

One of the objectives of the Telstar experiment was to obtain information on the performance of an active communications satellite repeater over an extended time interval and to obtain data that would be applicable in the design of a commercial communications satellite. To this end, the Telstar spacecraft has been closely monitored since it was launched. The satellite is monitored by measurements of signals received at the ground stations and by telemetry. Observations at ground stations give orbital, satellite-orientation, antenna-pattern, and signal-level data. Telemetry gives satellite orientation, solar plant output, satellite temperature, and electrical performance data.

The spacecraft was spin-stabilized and injected into orbit with its spin axis nearly perpendicular to the ecliptic plane. This insured the most favorable coverage of the earth by the Telstar antennas, the maximum output power of its solar cells, and the most favorable skin temperature distribution. The value of the spacecraft as a communications satellite is a function of how well it retains this orientation as it orbits the earth. Measurements of the changes in this orientation indicate an average precessional torque of 3×10^{-6} pound foot due to the residual

magnetic moment of the satellite. This type of information is helpful in developing orientation schemes for future satellites.

The spacecraft was designed and tested to withstand the environmental conditions it would see throughout launch and its life in orbit, based on the known and assumed aspects of its environment. By placing the spacecraft in orbit, the assumptions made could be evaluated.

The most meaningful test of a communications satellite is the test of how well its electronics circuitry operates under actual space conditions. The results of the successful communications experiments are discussed in a separate paper[1] in this issue. In this paper, the emphasis is placed on changes that may have occurred since launch on July 10, 1962.

When the Telstar satellite was launched, it was injected in the predicted orbit with the spin axis favorably orientated with respect to the sun at a time of day which resulted in 14 full sunlit days before the satellite entered periods of eclipse. The initial orbit parameters were as follows:

Apogee	3047 nautical miles
Perigee	515 nautical miles
Inclination	44.79 degrees
Spin rate	177.7 rpm
Solar aspect	90.5 degrees

During the period from launch on July 10, 1962, to the time of interruption of the VHF command system on November 23, 1962, there were only minor variations in the power levels and the operating characteristics of the communications repeater in the satellite. The satellite temperature, attitude, visibility times, and eclipse times have varied as anticipated. It is the purpose of this paper to discuss qualitatively the causes and effects of the expected and unexpected variations in satellite performance.

II. SOLAR ASPECT

Solar aspect is defined as the angle between the sun-satellite line and the satellite spin axis, measured from the telemetry antenna. This angle is determined by sampling the currents from (each of) six solar cells mounted at the ends of three mutually perpendicular axes on the satellite skin. The output currents of the six cells, together with their known geometric arrangements, uniquely define the solar aspect angle[2] with an accuracy of $\pm 0.5°$. The curve shown in Fig. 1 indicates the spacecraft orientation for the twelve-week period following launch.

The reasons for the shape of this curve are twofold. First, the satellite spin axis at injection was not quite normal to the plane of the ecliptic.

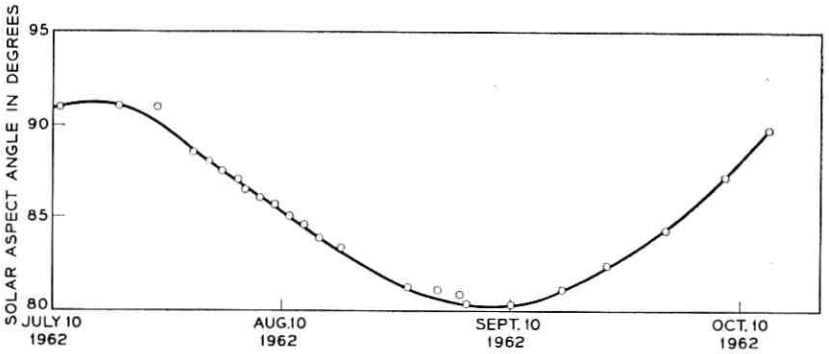

Fig. 1 — Telstar spacecraft — solar aspect angle versus time.

As both the earth and the orbit rotate with respect to the sun, the spin-axis projection alternately decreases and increases. Second, the attitude of the spin axis in inertial space is varying due to a precessional torque. This will be discussed later. The main effects of solar aspect deviations from 90° on the satellite's performance are to reduce the available power from the solar cells and to change the skin temperature distribution. This occurs because the solar-cell distribution is not isotropic over the satellite surface; however, the small deviations noted to date have not resulted in a significant change in output from the power supply.

III. ATTITUDE

Changes in the solar aspect angle are due in part to attitude changes in inertial space. Attitude is expressed in the spatial coordinates of declination and right ascension. In terms of an infinite sphere with the earth's lines of latitude and longitude projected upon it, declination corresponds to the latitude and right ascension to the longitude measured eastward from the vernal equinox. The coordinates of the attitude indicate the intersection of a line coinciding with the spin axis that starts at the center of the satellite and goes through the telemetry antenna and the infinite sphere.

The analysis of three sets of data serves to determine the attitude of the satellite. As previously mentioned, solar sensors indicate the angle between the satellite spin axis and the sun. Another angle is obtained from a series of light flashes observed from mirrors mounted on the satellite.[3] The time of the flash occurrence yields an indication of the angle between the spin axis and the satellite-ground station line, sometimes denoted as the earth aspect angle of the satellite. These two angles form tangent cones with a common apex. The intersection is a straight

line whose direction is determined from the knowledge of initial launch conditions. Fig. 2 is a plot of satellite attitude during the first three months, equivalent to approximately 800 orbits.

Changes in satellite attitude are caused by a torque generated by the interaction of the satellite magnetic moment and the earth's magnetic field. Prior to launch, a compensating magnet was mounted on the satellite to reduce the effect of the TWT magnetic field. However, a residual moment causing torques on the order of 10^{-6} pound feet remained. Owing to the nodal regression of the Telstar satellite orbit, the precessional torque rotates with respect to the satellite. The torque induces a continuously changing attitude of the satellite moment of momentum and a rapid precession about the momentum vector. Precession dampers within the satellite effectively eliminate this rapid precessional motion. As seen in Fig. 2, attitude changes increase from orbit to orbit as the satellite spin decreases; that is, the satellite tendency to rotate due to torques increases with spin decay.

The satellite is equipped with a coil of wire around its equator and a direct-current supply which, when activated, either reinforces or reverses the axial magnetic moment, thereby providing a means for attitude correction.

IV. SPIN RATE

The effect of the precessional torque is heightened by the steady decrease in the satellite spin rate. The major retarding torque causing this

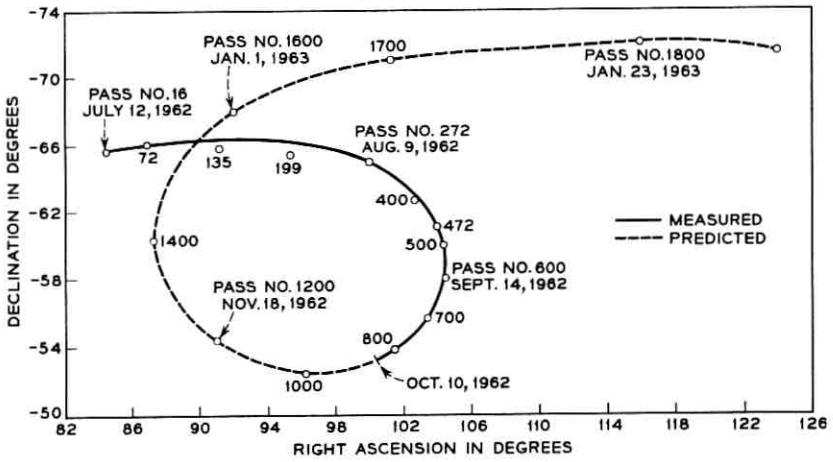

Fig. 2 — Telstar satellite attitude.

spin decay is produced by eddy currents generated in the satellite as it rotates in the earth's magnetic field. Since the instantaneous torque is dependent on the spin rate, the satellite would undergo a pure exponential decay if it were rotating in a uniform field. However, the effective magnetic vector, which is the component normal to the spin axis, is a function of both satellite attitude and altitude, geomagnetic field along the orbit, the regression of the orbit plane, and the advance of perigee. Satellite attitude and nodal regression are considered to be secondary effects. Fig. 3 is a sketch of field variation and satellite latitude versus orbital period. The dashed line indicates the satellite latitude. Shortly after injection, the perigee occurred near the equator. As the orbit precessed, the perigee moved toward the region of higher field strength. The net effect is to continuously alter the slope of the exponential decay curve, resulting in an initial decay that was almost linear, as shown in Fig. 4.

On the basis of this curve, it is calculated that the spin rate will be

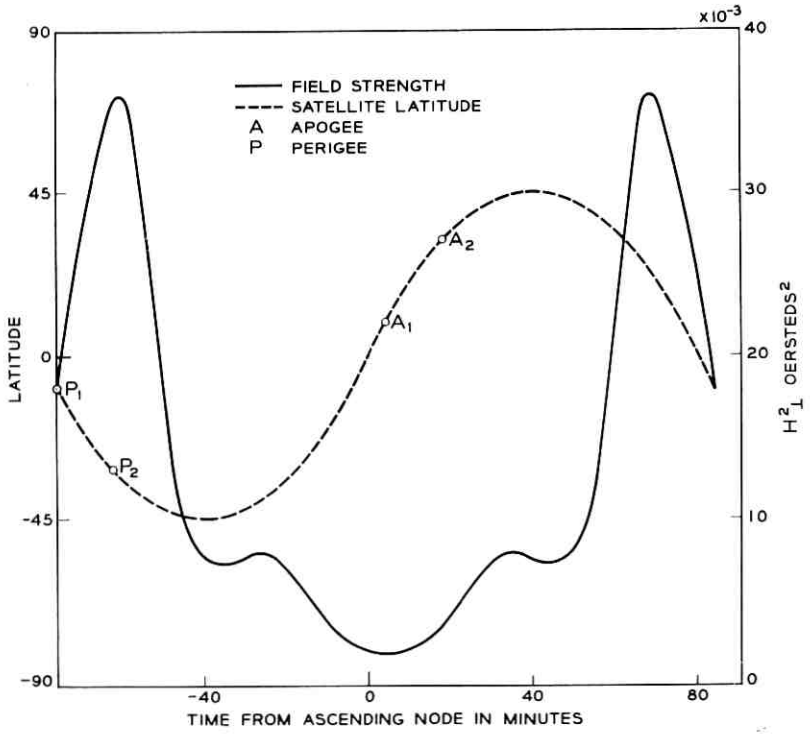

Fig. 3 — Field strength and satellite latitude versus time from ascending node.

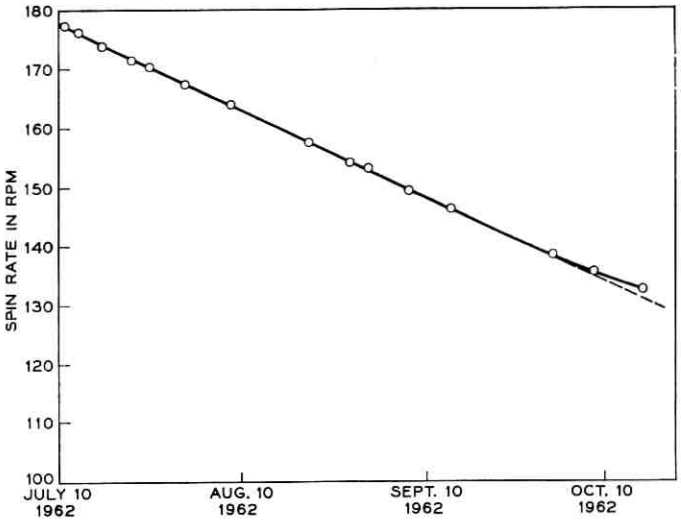

Fig. 4 — Telstar satellite — spin rate versus time.

reduced from an initial rate of 177.7 rpm to 66 rpm in about 330 days,[4] and the spin rate will therefore stabilize the Telstar satellite for about two years.

V. VISIBILITY TIME

It has been shown that the motion of the perigee within the orbit plane affects the satellite spin rate and attitude. Owing to the ellipticity of the orbit, the perigee motion also affects the minimum usable time per day. Usable time is defined as the time the satellite remains at least 7.5° above the horizon. The higher the satellite is during a pass, the longer it will be visible to a particular ground station. As the perigee moves to its most southern latitude (−45°), the apogee is almost over the Maine ground station; and as shown in Fig. 5, the usable time reaches a maximum. Maximum visibility occurs when apogee is over the ground station for two reasons. This is the time when the greatest portion of the orbit is visible and also the time in orbit when the satellite velocity is a minimum.

VI. ECLIPSE DURATION

Satellite eclipse duration is important insofar as it affects the satellite temperatures and the ability of the solar cells to recharge the batteries. A curve of satellite eclipse time per orbit is shown in Fig. 6.

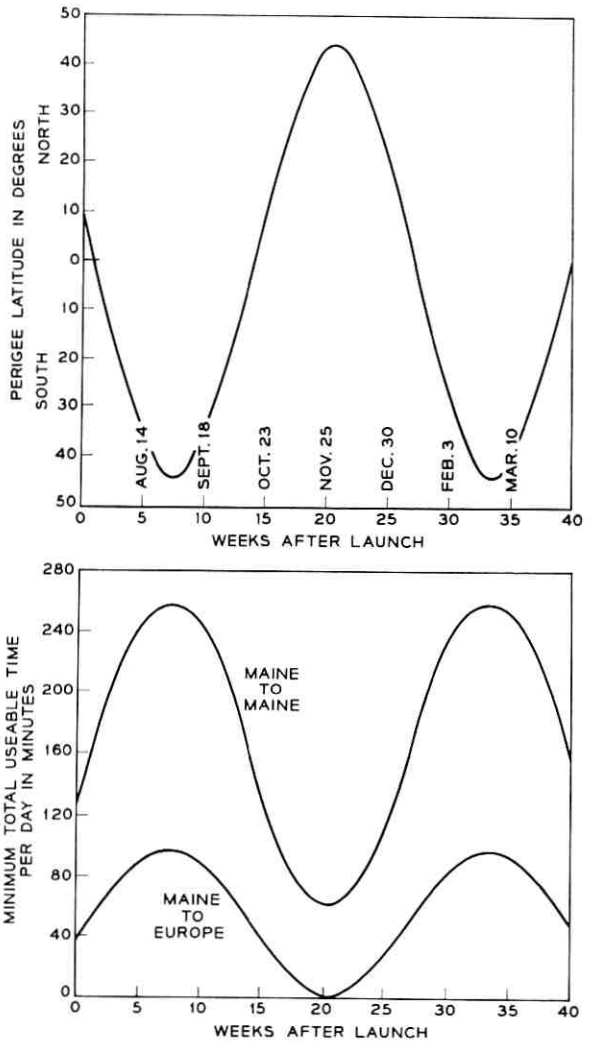

Fig. 5 — Telstar satellite — perigee latitude and minimum usable time per day.

Between July 21, 1962, and January 8, 1963, the satellite was to be in shadow for a period of about 30 minutes per orbit on the average. The shape of this curve is principally a result of three motions·

(1) The motion of the earth and the orbital plane about the sun.

(2) The regression of the orbital plane.

(3) The advance of the apogee and perigee within the orbital plane.

The effect of these motions on the orbit-earth-sun orientation is shown

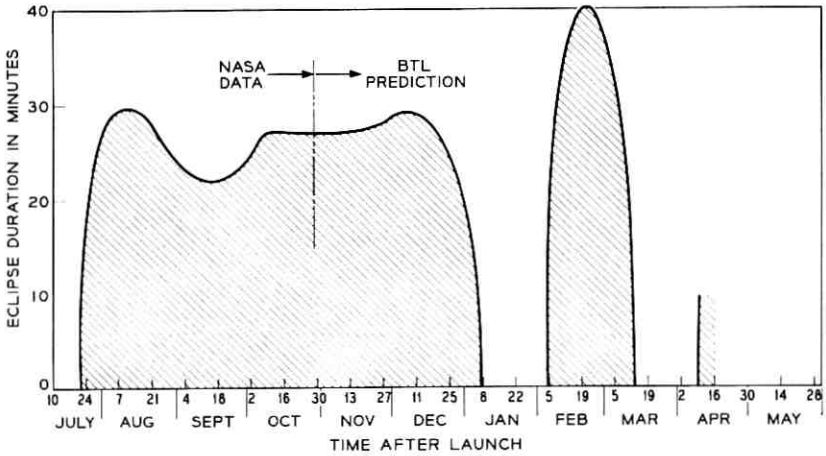

Fig. 6 — Predicted satellite eclipse duration.

pictorially in Fig. 7. It is seen that the orbit rotates clockwise in the direction opposite to the earth's spin as the earth moves counterclockwise about the sun. The perigee moves in the direction of the satellite motion within the plane of the orbit. The perturbing influence causing these motions is due principally to the attractive forces associated with the earth's equatorial bulge.

Shortly after the Telstar satellite first went into eclipse, July 21, 1962, the perigee was in shadow. Each day the satellite goes into eclipse approximately two minutes later than on the previous day. This is shown in Fig. 8, where eclipse occurrence time after ascending mode is plotted against calendar time and orbit number. The vertical height of the gray area on any particular day represents the eclipse time. This curve was made for passes occurring near midnight EDT.

VII. SATELLITE TEMPERATURES

The satellite temperatures of major interest are those of the electronics canister and the solar cells. The energy transfer paths determining these temperatures are shown schematically in Fig. 9.

It is important that the solar-cell temperatures be kept low for two reasons: first, the conversion efficiency of the solar cell plant decreases with increasing temperature; second, the solar cell life decreases with sustained high temperatures. Temperatures within the canister must be kept within certain ranges to ensure optimum system operation.* It will

* In the satellite, the nickel-cadmium battery is the component most sensitive to temperature variations.

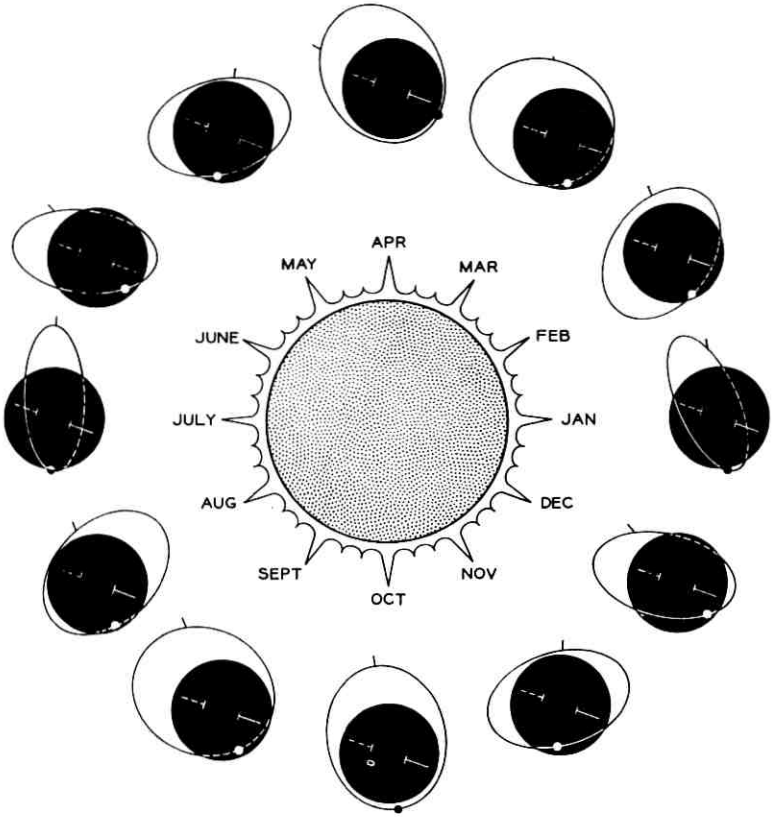

Fig. 7 — Orbital motion of spacecraft.

be seen in the following how solar aspect, in addition to periods of eclipse, influences satellite temperatures and power-plant efficiency.

The Telstar spacecraft geometry and the near isotropic distribution of solar cells makes the total energy absorbed nearly insensitive to the satellite orientation or attitude. Therefore, the mean radiant temperature, T,* depends chiefly on the energy incident on the satellite and the

* The mean radiant temperature, T, is determined by equating the incident energy to the radiated energy.

$$\text{heat in} = \text{heat out}$$

$$\pi R^2 \alpha (S + A + I) = 4\pi R^2 \epsilon \sigma T^4$$

$$T^4 = \frac{1}{4} \frac{\alpha}{\epsilon} \frac{1}{\sigma} (S + A + I)$$

where

α = absorptivity
ϵ = emissivity
σ = Stefan Boltzmann constant
R = radius.

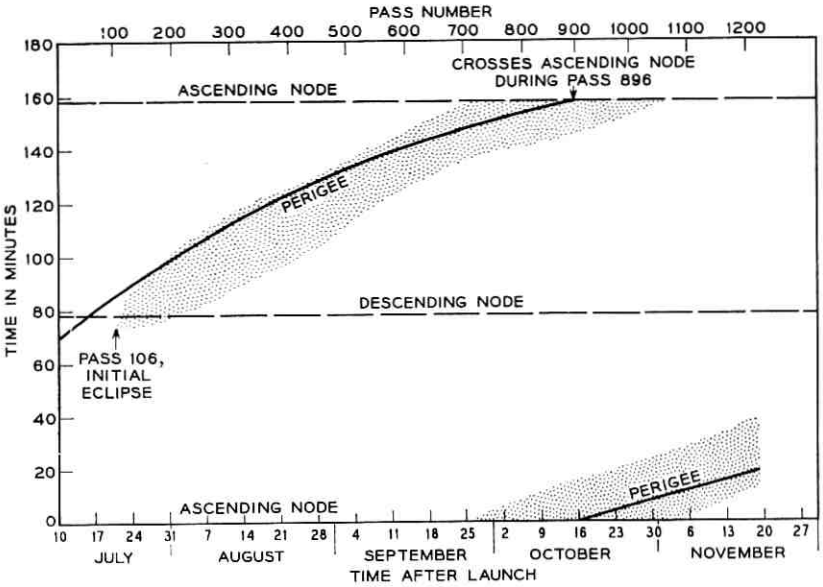

Fig. 8 — Telstar spacecraft orbital events.

satellite's surface characteristics. Both the skin temperature distribution and the temperatures within the electronics canister are related to the mean radiant temperature and the energy dissipated within the chassis, Q. However, the nature of the skin temperature distribution affects the solar plant; large temperature extremes over the satellite surface result in lower net power.

Since the spacecraft is spinning, the most favorable skin temperature distribution occurs when the sun rays are normal to the spin axis.

7.1 *Satellite Skin Temperatures versus Time*

Typical satellite skin temperatures for the first three months after launch are plotted in Fig. 10. During this period the solar aspect has varied over a range of 10°. The effect of the changing aspect has been to increase the temperature of the pole inclined toward the sun. The period of temperature variation closely corresponds to that of the variation in solar aspect. The difference is accounted for by the effects of secondary radiation, infrared energy radiated from the earth, and solar energy reflected from the earth. These data were recorded when the satellite was well out of eclipse. It is evident that the average of these skin tempera-

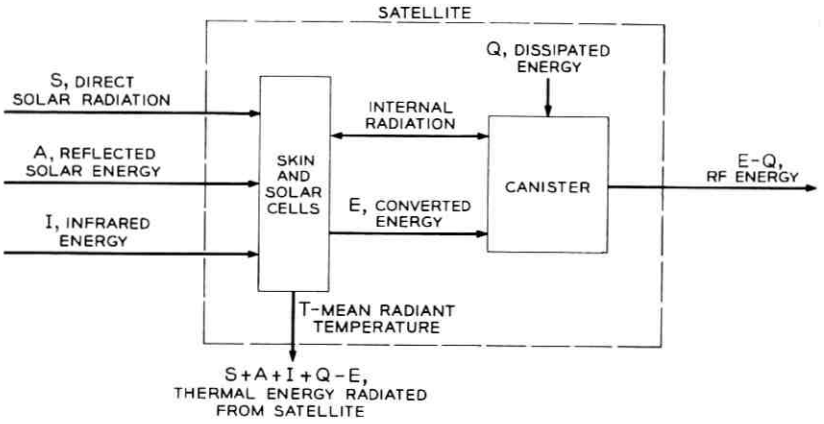

Fig. 9 — Spacecraft energy transfer.

tures has decreased, even though the solar flux density is increasing as the earth moves closer to the sun. This indicates that the effect of eclipse is greater than the effect of the increasing solar flux density.

7.1.1 *Skin Temperatures During a Typical Orbit*

Fig. 11 indicates how the skin temperatures vary as a function of time from perigee. These data were recorded August 16, 1962, and are repre-

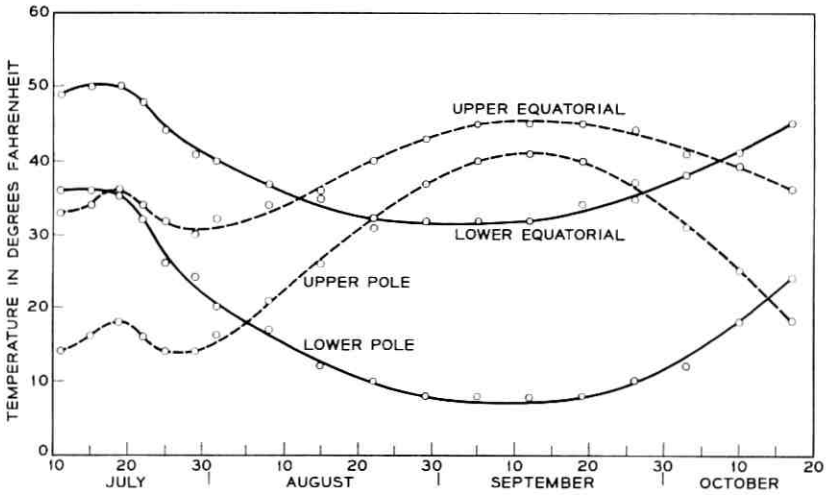

Fig. 10 — Skin temperature versus time.

sentative of a few orbits on that day. The effect of solar aspect is clearly seen during the period 60 minutes to 130 minutes. After 130 minutes the satellite went into eclipse. During eclipse the upper pole temperature was lower than the lower pole temperature. This temperature difference is a result of energy reflected and energy radiated from the earth. While in eclipse, the lower hemisphere was favorably inclined with respect to the earth for heat transfer from these secondary sources.

7.1.2 *Skin Temperatures During Eclipse*

The Telstar satellite first went into eclipse on July 21, 1962, and by August 16, 1962, the perigee was in shadow for 30 minutes. As shown in

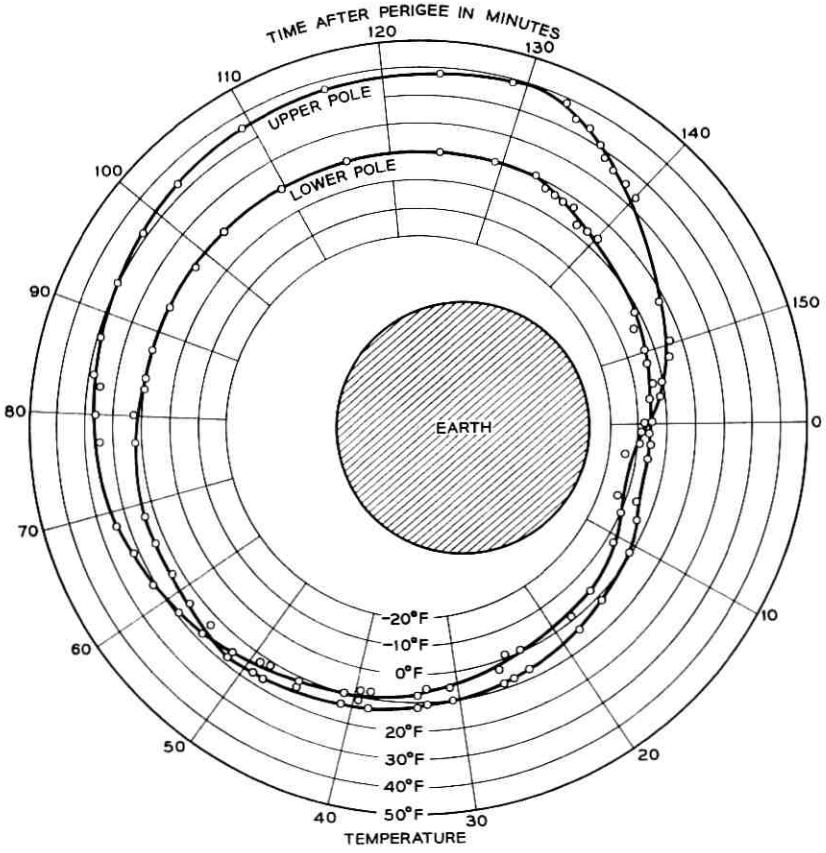

Fig. 11 — Skin temperature versus orbital position.

Fig. 12, the skin temperatures dropped sharply as the satellite went into eclipse, but were slow to return as the satellite emerged from shadow. This is best explained in terms of the skin surface properties. Since the average value of the absorptivity to emissivity ratio, α/ϵ, is about 0.65, the spacecraft emits energy faster than it will absorb.

7.1.3 *Skin Temperatures During Launch*

The satellite was designed to operate satisfactorily over wide temperature variations during both orbit and launch. During the launch

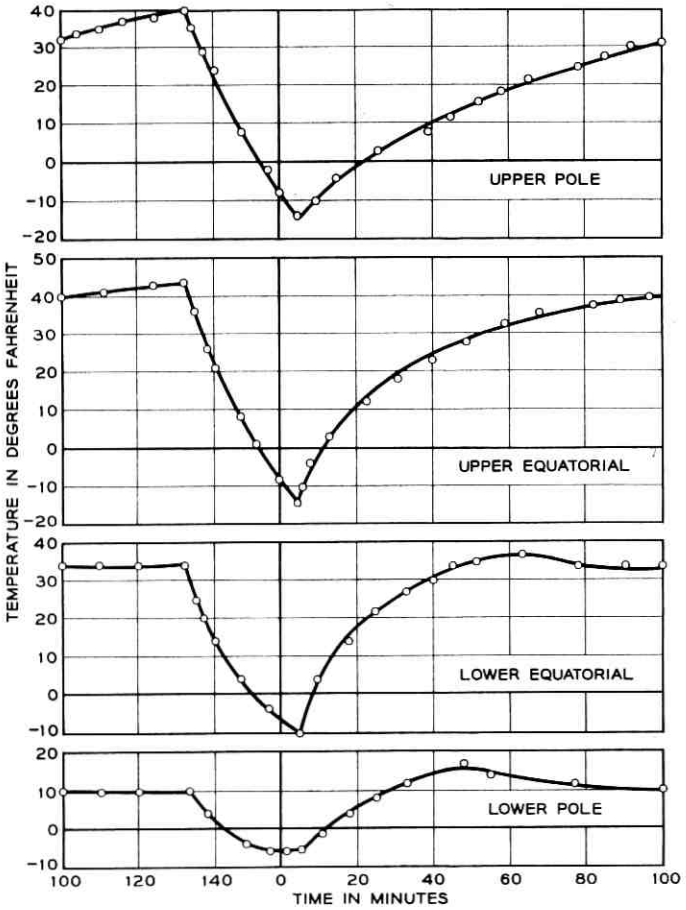

Fig. 12 — Satellite skin temperature during typical orbit with eclipse.

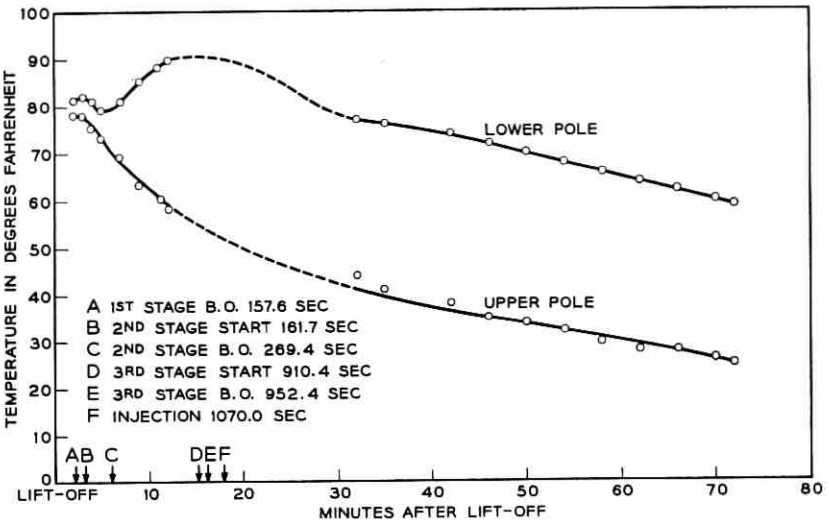

Fig. 13 — Skin temperature during launch.

phase, the satellite was protected from aerodynamic heating by a fiberglass shroud which separated from the second stage prior to third-stage ignition. As seen in Fig. 13, the shroud was effective in maintaining reasonable skin temperatures on the satellite. Initially, the lower pole temperature rose slightly; it is believed that energy conducted from the missile was responsible for this temperature increase.

7.2 *Temperatures Inside the Electronics Canister*

The electronics canister is a hermetically sealed unit which houses 95 per cent of the electronics circuitry of the satellite. The canister is completely covered with an aluminized Mylar "blanket" when the bellows-actuated shutters, which cover the upper and lower domes, are closed.[5] When the shutters are open, the emissivity of the domes is increased, so the shutters control the canister temperatures. The solar plant furnishes, when new, a power of about 14 watts continuously except when the satellite is in eclipse. This primary source of power energizes the electronics equipment, charges the battery, and heats the canister.

Telemetry information from 21 thermistors located inside the electronics canister gives the temperatures of various components and sub-

assemblies from which rough temperature gradients can be found. Nine of these sensors are located in the switching regulator, in the dc-to-dc converter, and near the collector of the traveling-wave tube (TWT). These sensors are located at expected local hot spots, so the TWT can be turned off before the temperature exceeds the safe limit at these points. The remaining 12 sensors are located on various subassemblies where the temperature affects the calibration of a telemetry channel, or near points of special interest such as the Ni-Cd cells.

The temperature of the Ni-Cd cells is important, so this temperature is one of two chosen as representative for discussion. Maximum and minimum telemetry readings of the Ni-Cd cells are plotted as a function of time in Fig. 14(a). The general wavy nature of these curves does not mean that the temperature extremes vary this much from week to week, but is a result of the fact that telemetry data are taken only during certain times in each orbit and the temperatures of all parts of the satellite are dependent on satellite position as shown in Fig. 11. Also, the variation of temperature over one day depends partially on how much the TWT is used. During the time the TWT is used, the battery is discharging, so stored energy is furnished by the battery to the tube and other circuits which convert most of the electrical energy to heat energy. After long use of the TWT, the battery is discharged, and energy from the solar plant goes into chemical energy in the battery instead of going into heat energy, as it does when the battery is fully charged. Thus, there is a short time after TWT use when there is a slight drop in battery temperature. The TWT was operated more in August than at other times because of longer visibility from Andover, Maine, during this period.

The temperature of the waveguide used as part of the up converter is plotted as a function of time in Fig. 14(b). This plot shows much less temperature variation than the plot of battery temperature because the waveguide is a good heat sink.

VIII. RADIO-FREQUENCY POWER LEVELS

In this section, telemetry readings are presented to show that there have been no appreciable changes in the power levels of the three signals radiated from the satellite, the local oscillator signals used for the modulators in the satellite, or the signals associated with the microwave carrier supply (MCS). In order to prove the invariance of some of these power levels, it is necessary to show that the characteristics of the TWT and the beat-oscillator (BO) modulator have not changed. Microwave

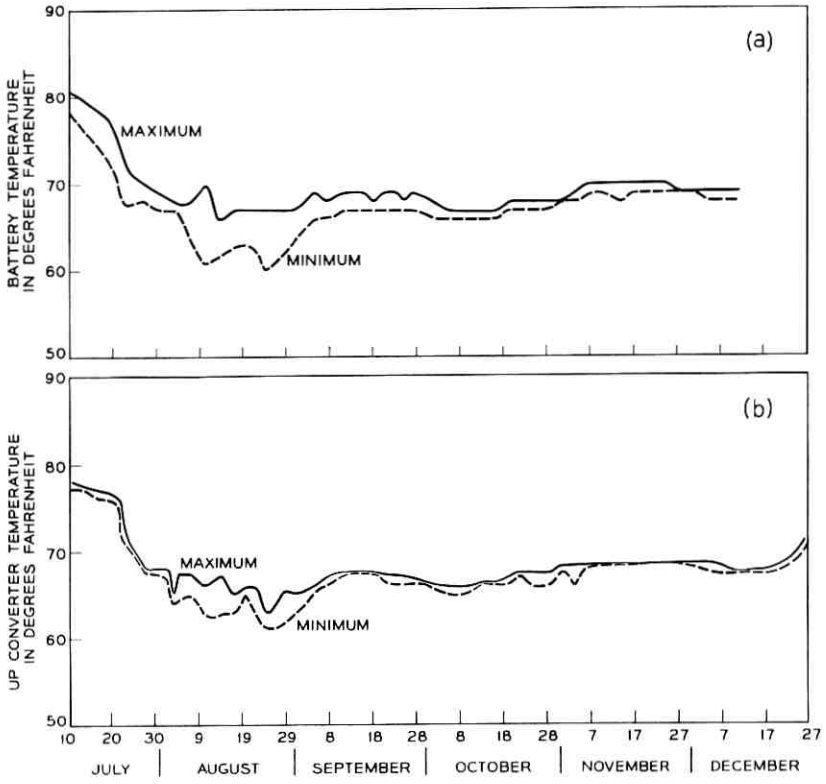

Fig. 14 — (a) Battery temperatures since launch; (b) up-converter temperature since launch.

power levels and their associated telemetry channels are shown in Fig. 15, which gives a simplified block diagram of the communications repeater. Fig. 16 is a block diagram which shows the VHF beacon and other VHF circuitry. Both figures show frequencies accurate to two decimal places, but for simplicity approximate values will be used in the discussion. Throughout this and the following sections, reference is made to Table I, which gives voltages, currents, powers, and temperatures for important telemetry channels. The purpose of these representative data is to show changes in these quantities, and not the actual values. In particular, some of the power monitors are inaccurate in determining absolute values, but changes in readings are significant. The telemetry channel numbers used in the discussion are for conven-

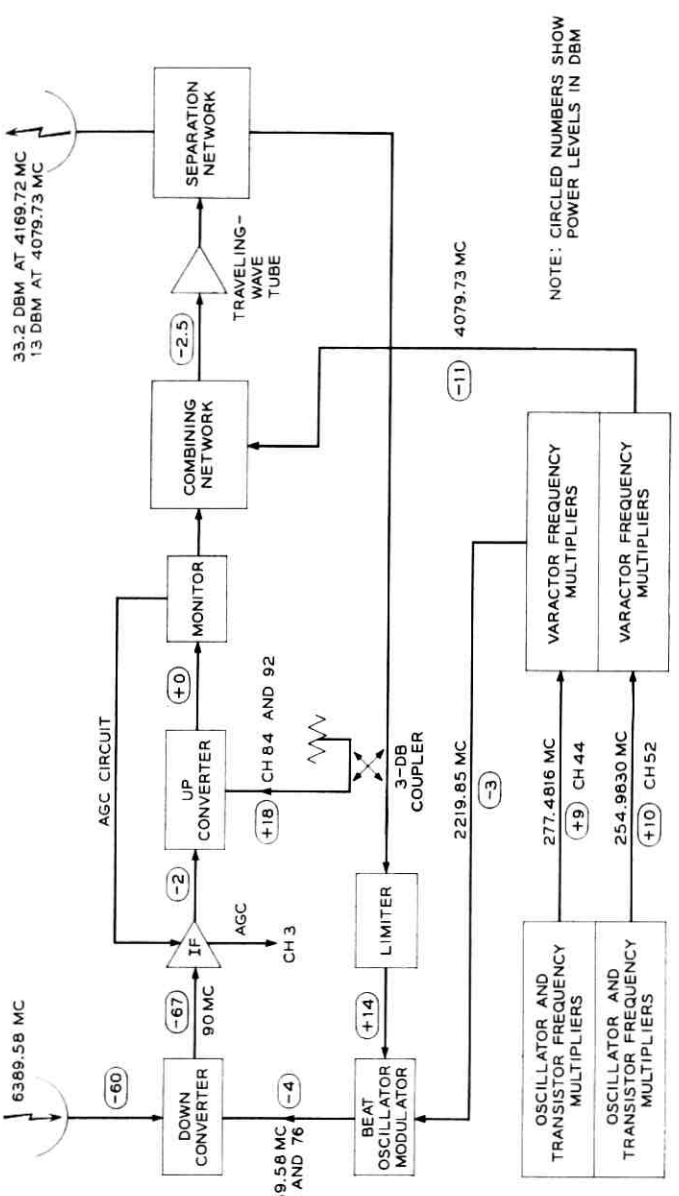

Fig. 15 — Communications repeater.

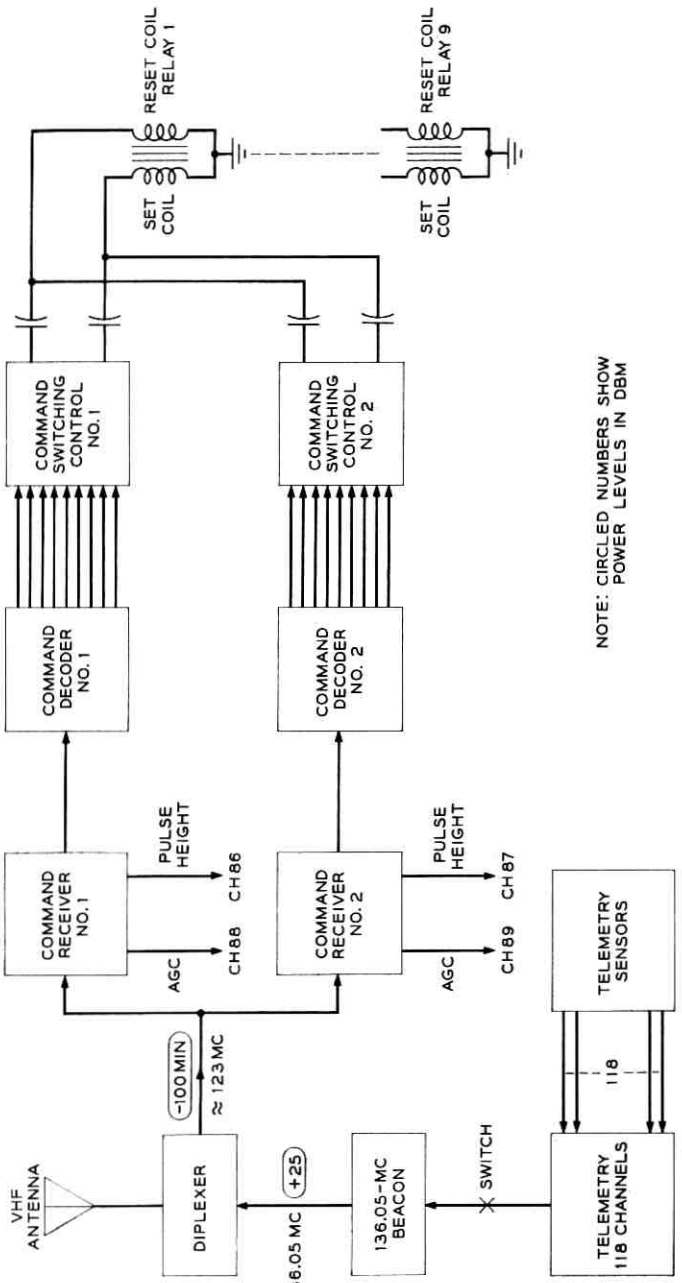

Fig. 16 — Command and telemetry systems.

ience only; the assignment of the actual channel numbers was to a large degree arbitrary.

8.1 *Microwave Beacon*

As Fig. 15 shows, the same 4080-mc frequency is used to provide the microwave beacon signal and to pump the varactor diodes in the up converter and BO modulator. The reflex circuit which provides sufficient power at this frequency is discussed by another paper[6] in this issue. Since the insertion losses of all the filters in the satellite are known, the 4080-mc power levels at any point can easily be calculated if the level at one point is known. The 4080-mc signal is used to pump the self-biased varactor diodes in the up converter, so the bias voltages on these diodes, monitored by telemetry channels 84 and 92, are used to measure the power levels at this part of the circuit. The IF signal level into the up converter is small (−2 dbm) so the bias voltages on these diodes are due almost entirely to the 18-dbm pump at 4080 mc. Figs. 17(a) and 17(b) show the relationships between the bias voltages and the pump

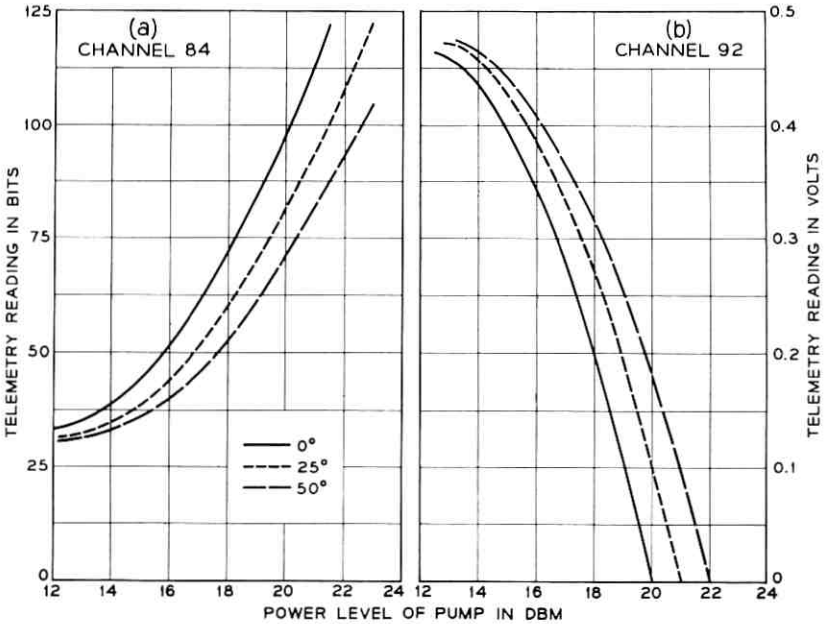

Fig. 17 — Telemetry readings versus pump level for the up converter.

input.* A normal power level of 18 dbm at the input to the up converter corresponds to a power of 18.6 dbm to the antenna feed system. Insertion loss of the antenna and feed is approximately 1.6 db, so the normal radiated microwave beacon power is 17 dbm.† The exact insertion loss of the antenna and feed system is not known over the temperature range experienced by the satellite, but the variation is known to be less than 0.1 db.

The data for channels 84 and 92 in Table I show about a ½-db disagreement in the measured pump level, but the change in power since launch, as shown by both channels, is very small. Powers are calculated to three significant figures in an effort to show changes in level, but obviously no such absolute accuracy is claimed by this method of monitoring the power.

When no power at 6390 mc is transmitted to the satellite, only noise (about −6 dbm) drives the TWT, and the power output of the tube at 4080 mc increases[6] about 2 db, as shown in Fig. 18. This results in an increase in the radiated power at 4080 mc, but this is normal circuit behavior and does not represent any change in the satellite circuitry.

8.2 *The Communications Signal*

The power output of the satellite in the 4170-mc band is not monitored, but the approximate output can be calculated by using known values of satellite antenna gain and path loss and the measured values of received signals on the ground. However, changes in the power output can be more accurately determined by another method. As Fig. 15 shows, the TWT in the satellite amplifies signals at both 4080 and 4170 mc. Because the tube is driven into partial saturation by the signal at 4170 mc (see Fig. 18), changes in the output level at this frequency are accompanied by greater changes in the level of the signal at 4080 mc. The power at 4080 mc is monitored, so changes in the power level at 4170 mc can be measured indirectly if the characteristics of the TWT do not change and if the input signal to the TWT is constant. The drive to the TWT is constant when the signal at 6390 mc is within the AGC range. The data in Table I show that the helix and accelerator currents have increased from 135 and 115 microamperes prior to launch to 185 and 155 microamperes, respectively, in four months. However, the tube charac-

* The output of the diode monitored by channel 92 is positive, so its output is combined with a fixed negative voltage to give a net negative voltage needed by the telemetry circuit.

† The required radiated power at this frequency is only +13 dbm.

TABLE I—CURRENTS, VOLTAGES, POWERS AND TEMPERATURES IN THE ELECTRONICS CANISTER

Channel No.	Function	Universal Time of Telemetry Readings				
		18:11 July 9, 1962	23:03* July 11, 1962	23:15 July 11, 1962	11:51* Nov. 6, 1962	12:03 Nov. 6, 1962
		Readings in bits and units				
1	TWT heater	50 bits	50	50	49	50
		4.7 volts	4.7	4.7	4.75	4.7
3	6390-mc input power	21 bits	11	16	33	11
		−62 dbm	−66.5	−64.5	−60	−66.5
41	IF amplifier temperature	70 bits	64	65	57	59
		86°F	79	81	71	74
4	TWT accelerator	24 bits	24	22	34	32
		115 μa	115	110	163	155
12	TWT collector current	86 bits	85	85	85	85
		17.8 ma	17.6	17.6	17.6	17.6
60	TWT helix current	14 bits	17	16	21	19
		135μa	165	155	200	185
36	Calibration voltage	69 bits	69	70	69	70
		0.23 volt/ bit				
44	277-mc power	102 bits	103	102	104	104
52	255-mc power	109 bits	110	109	112	111
68	Down converter bias 1	43 bits	44	43	43	43
		−4 dbm	−4.1	−4	−4	−4
76	Down converter bias 2	66 bits	66	66	66	66
		−3.9 dbm	−3.9	−3.9	−3.9	−3.9
13	Down converter temperature	74 bits	70	70	64	64
		80°F	77	77	70	70
84	Up converter bias 1	50 bits	55	54	56	55
		17 dbm	+17.45	+17.4	17.45	17.4
92	Up converter bias 2	79 bits	70	70	68	68
		+17.4 dbm	+17.9	+17.9	+17.9	+17.9
29	Up converter temperature	68 bits	64	64	57	57
		82°F	77	77	69	69
99	Reference diode	105 bits	105	105	105	105
		8.4	8.4	8.4	8.4	8.4

* Time when the TWT was turned on. Launch time was 08:35 Universal Time, July 10, 1962.

teristics do not change even when these currents increase to 500 microamperes. The input signals for comparative power measurements must be within the AGC range of −70 to −55 dbm or the 4170-mc drive to the tube will not be the same, and obviously this will cause a change in output at both 4080 and 4170 mc. Since launch there has been almost no change in the 4080-mc output of the tube, so the change in output at 4170 mc from the normal output of 35 dbm has been negligible. The insertion loss of the antenna and feed system is 1.6 db at room temperature, and this loss decreases less than 0.1 db at the low temperatures

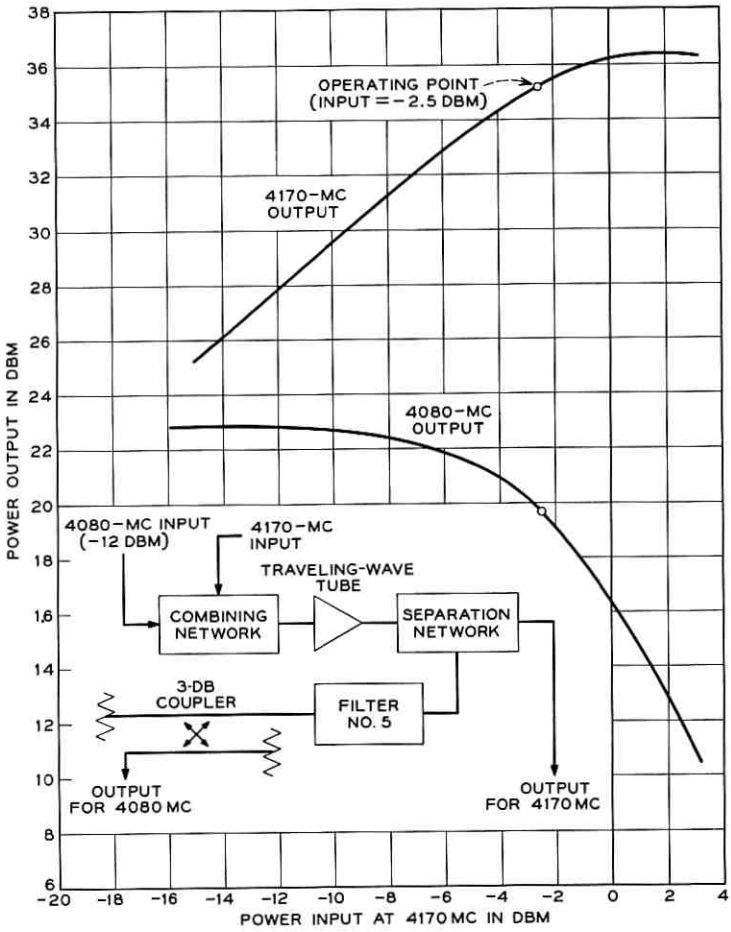

Fig. 18 — Operating characteristics of the traveling-wave amplifier.

encountered in space. At 4170 mc the uncertainty of the antenna insertion loss and the inaccuracies of monitoring 4080 mc by telemetry may give a combined error of ¼ db when calculating the power level, but the radiated power at 4170 mc (33.2 dbm) has not changed appreciably since the satellite was assembled.

8.3 *The Local Oscillator for the Down Converter*

The 6300-mc local oscillator signal for the down converter is obtained from the BO modulator, which combines a signal at 2220 mc from the

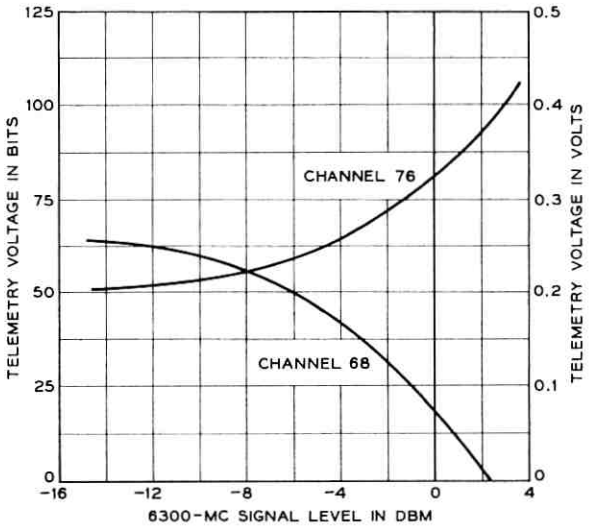

Fig. 19 — Telemetry readings versus local oscillation level for the down converter.

MCS with a portion of the pump signal at 4080 mc. The direct currents in the silicon diodes in the down converter are caused by the RF signal at 6300 mc and by small external dc voltages that forward bias the diodes. Fig. 19 shows the relationship between the telemetry readings of channels 68 and 76 and the level of the local oscillator signal. As is the case with channel 92, used to monitor one of the up-converter currents, the positive output voltage from the down converter is added to an external negative voltage to give a net negative voltage for telemetry. The data in Table I show that the 6300-mc signal has since pre-launch measurements changed only one bit according to channel 68 and no bits according to channel 76. At the operating point, a change of one bit on telemetry corresponds to a change in 6300-mc power level of less than $\frac{1}{4}$ dbm, so this power has remained almost constant for four months.

8.4 *Power Levels in the Microwave Carrier Supply*

The microwave carrier supply furnishes signals at 2220 and 4080 mc which are used to provide the local oscillator signals for the up and down converters. Each signal is obtained by feeding the output of a crystal oscillator into a transistor frequency multiplier section, which in turn feeds a varactor frequency multiplier section.

8.4.1 *The Transistor Sections*

Each transistor frequency multiplier section in the MCS contains a pseudo AGC system which in all tests prior to installation in the Telstar spacecraft held the VHF power drive to the varactor section constant to within ±0.15 db over a temperature range from 25 to 125°F. The telemetry readings, channels 44 and 52, associated with these powers do not give an accurate measure of power output because changes in transistor characteristics change the calibration. However, if the telemetry reading at a known temperature corresponds to a value taken during bench tests when the power was measured, there is a strong indication that the power is normal. The readings of channels 44 and 52, as shown in Table I, have since launch varied only 3 and 2 bits, respectively. Pre-launch measurements on the completed satellite showed that the readings of these two channels increased with a decrease in temperature. On November 6 the average canister temperature was 7°F below the temperature the day after launch, so the slight increase in the readings of channels 44 and 52 on this date is normal and indicates that the transistor sections of the MCS were normal.

8.4.2 *The Varactor Sections*

The output powers of the varactor multipler sections are not monitored, but these powers can be checked indirectly.

The output power at 2220 mc can be checked indirectly by noting the changes in channels 68 and 76, which measure the level of the power at 6300 mc. A change of 1 db in the 2220-mc signal into the BO modulator, when operating normally, changes the output at 6300 mc by ¾ db, and the BO modulator conversion gain does not change rapidly with temperature. Since the level of the 6300-mc signal has remained essentially constant, the level of the 2220-mc signal could not have changed appreciably.

As is the case with the output of the 2220-mc varactor section, the output of the 4080-mc varactor section is checked indirectly. The 4080-mc power from the MCS is amplified by the TWT and is fed to the pump arm of the up converter. Since any change in the output of the MCS at 4080 mc is translated as an equal change in power to the up converter, channels 84 and 92 indirectly give a measure of the power from the MCS if the tube characteristics and RF power drive are unchanged, as discussed earlier. The measurements made since launch do not show the actual power level of the 4080-mc output of the MCS, but they do show that this power level has not changed appreciably.

8.5 *The VHF Beacon*

Under normal conditions the satellite radiates continuously a 23-dbm signal at 136 mc, used for tracking purposes by the command tracker on the ground. This tracker is completely separate from the tracking equipment associated with the microwave beacon, which is radiated only when the TWT is turned on. When telemetry is turned on, the 136-mc signal is amplitude modulated. This VHF beacon is not monitored by telemetry, so the only check on this power is made by measuring the received ground power and by calculating the transmitted power from known values of path loss and known gains of the satellite and ground antennas. This method is accurate to within ± 1 db when many readings are averaged. Accurate measurements can be made only when the weather is clear and the satellite is above elevation angles of 10°. At low elevation angles, this signal is subject to selective fading.

Measurements of the 136-mc beacon made on the ground prior to launch and in orbit on a weekly basis since launch show that the power has not changed, but day-by-day fluctuations of 1 db, if they existed, could not be detected by these measurements.

IX. CIRCUIT PERFORMANCE CHANGES

In the preceding section, telemetry readings were used to show that power levels of the 255, 277.5, 2220, 4080, 4170, and 6300-mc signals inside the electronics canister had not changed appreciably since launch. Also the method of calculating the transmitted power levels at 136, 4080, and 4170 mc using antenna gains, path loss, and received signal level was discussed. In order to show the invariance of 6300 and 4170-mc signals, it was necessary to show by telemetry that the characteristics of the TWT, MCS, and BO modulator have not changed. In this section, the remaining parts of the satellite circuitry, excluding the radiation experiment circuits, will be discussed from the viewpoint of changes in their operating characteristics.

9.1 *The Down Converter, IF Amplifier, and Up Converter*

In Section 8.2 the methods of checking the output of the tube at 4170 mc were described. The conclusion of this section is that the output power of the TWT, and thus the input power to the TWT at 4170 mc, has remained essentially constant when the input at 6390 mc falls in the AGC range. However, the conversion loss of the down converter, the gain of some stage in the IF amplifier, or the conversion gain of the up

converter could change, and the power drive at 4170 mc to the TWT would remain constant, because the AGC system keeps the power input to the TWT constant by changing the gain of the IF amplifier. If changes occur in the up or down converters or in some part of the IF amplifier, the current through variolossers in the IF amplifier changes to keep the TWT input constant. Channel 3 in the telemetry circuit gives the variolosser current as a function of the input signal to the satellite. Calculations using ground transmitted power, antenna gains, and path loss show that channel 3 readings in space are consistent with readings made before launch. However, the accuracy of this method is no better than 2 db, so the gain of some unit between the input and the TWT could have changed by this amount and it would not have been detected.

9.2 *Nickel-Cadmium Cells*

Since (1) there is no simple way of telling when the Ni-Cd cells are fully charged, (2) the cells may be damaged by excessive discharge and (3) the charging efficiency is a function of state-of-charge, charging current, temperature and past history of the cells, the operating procedure for the Telstar satellite has been very conservative. Graphs are plotted daily showing the state-of-charge of the battery on the basis of a conservative 60 per cent average charging efficiency. Each time the TWT is used, a continuous plot is kept of battery voltage versus time. These plots are compared in an attempt to find changes in the battery, either gradual or otherwise. Two battery discharge curves will be the same only if the battery temperature, the solar-plant current, TWT operate time, and initial battery charge are the same for the two passes compared. The aging of the solar plant due to radiation damage and the variation of eclipse period and its time relative to visibility from Andover, Maine, make exact duplication of conditions for battery comparisons at widely separated intervals impossible. Since these conditions cannot be duplicated, corrections are made in order to get a meaningful comparison. The corrected discharge curves are so similar that they indicate no measurable change in the battery.

9.3 *The Solar Cells*

The solar power plant consists of 50 parallel-connected groups of 72 series-connected silicon n-on-p solar cells covered with sapphire shields 32 mils thick. Fig. 20 shows the average solar plant current from the time the satellite was launched until early January, 1963. These data were taken while the TWT was on, so there is a period of about a month

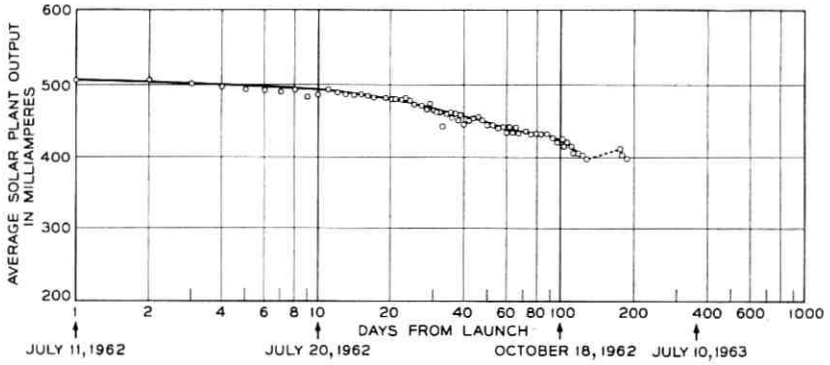

Fig. 20 — Solar plant output.

(December, 1962) when data were not available because of the command malfunction. The points on this graph do not give a perfectly smooth curve because there are, at different times, temperature differences in the solar cells which affect their output. The general shape of the curve shows a degradation due to radiation which by July, 1964, should result in a 32 per cent reduction in capacity.[2]

9.4 *The Voltage Regulator and the dc-to-dc Converter*

The voltage regulator receives power at a varying voltage from the Ni-Cd battery and provides a regulated output of negative 16 volts to power all the transistor circuits and the dc-to-dc converter. When the regulator was first installed in the electronics package, the output voltage of the regulator, as measured by telemetry, remained constant at 96 bits as the load current changed from 0.3 ampere to 1.5 amperes. One telemetry bit corresponds to 0.167 volt. After approximately five months in orbit, the regulated output for all load currents has changed only one bit. It was estimated before launch that radiation damage plus aging might cause the output voltage of the regulator to vary as much as ± 3 per cent, although present data indicate this prediction was pessimistic.

The dc-to-dc converter chops the 16-volt direct voltage from the regulator and steps up the resulting ac voltage with transformers to higher voltages which can be rectified, filtered and applied to the helix, accelerator, and collector electrodes of the TWT. The TWT heater voltage is also obtained by transformer action, but it is only about 4.5 volts. Telemetry is used to monitor the heater voltage and the helix, accelerator, and collector currents for the TWT. Since launch, as Table I

shows, the heater voltage after transients have died out has varied only one bit or 0.08 volt. Increases in accelerator and helix currents shown in Table I result from aging and a slight defocusing of the electron beam in the tube, and are not necessarily caused by increases in voltages. The best proof of the constancy of the TWT voltages is the measure of the output power at 4080 mc, a point discussed earlier. Changes of only 10 volts in the helix voltage (1520 volts is normal) will cause a change of about ½ db in the output of the TWT at 4080 mc. Telemetry readings which monitor this 4080-mc power level indicate a change much less than ¼ db, so the helix voltage has changed very little. The accelerator and collector voltages are derived from the same source as the helix voltage, so they should not have changed either, but there is no direct proof of these voltages remaining constant.

9.5 *Pressure Switches*

The electronics package is hermetically sealed to keep the pressure inside the package at a level of 10 psia. In the event of a leak, the high voltages associated with the TWT would cause corona at critical pressures. One 5-pound and one 1-pound pressure switch (monitored by telemetry) are inside the electronics canister to show the presence of leaks. Since neither pressure switch has operated after six months of operation, even if a small leak exists, no corona problems would exist for several years.

9.6 *The Telemetry System*

While the telemetry does not have a self-check, there are ways to tell something about the unit if some readings are suspicious. The power supply has a reference diode which is monitored by telemetry channel 99, and the telemetry circuit has its own reference diode. Any general error in telemetry readings would show up in channel 99 unless both reference diodes change the same amount. Also, the 16-volt regulated supply is monitored in two places, so differences in these channels could show telemetry troubles. Troubles in the telemetry would probably be first detected by bad readings on many channels. There have been isolated telemetry errors due to external noise pulses in the telemetry receiver on the ground, but in each case an error that occurs in a particular channel on one frame of telemetry information has been corrected on the following frame.

Channels 119 and 120 are used to send out a Barker code[7] and its complement to synchronize the ground telemetry system. It has been

found that when the telemetry is first turned on, the synchronizing signals on channels 119 and 120 are incorrect during the first minute. After one minute, the synchronizing information on these channels is correct.

9.7 *The Command System*

The Telstar command system, as shown in Fig. 16, has redundancy from the diplexer to the relay driver circuits. The output pulse heights of the command receivers are monitored by telemetry channels 86 and 87, and the AGC voltages of the receivers, calibrated to give received RF power levels, are monitored by channels 88 and 89. The receivers can be tested by comparing the output voltages as measured on channels 86 and 87 with similar data taken prior to launch and by comparing the received power levels. The tests on the receiver have been made on a daily basis since launch, and they indicate that there has been no apparent damage to the command receivers.

The T1 and T2 commands are used to test the command receivers and decoders. The T1 command disables decoder 2 for 15 seconds so that command receiver 1 and decoder 1 can be tested; T2 is a similar command which disables decoder 1 for 15 seconds. It was decoder 2 that first gave trouble in the Telstar satellite. This decoder became intermittent on August 8, 1962, became inoperative a few days later, and except for one short intermittent period in mid-October was inoperative until December 21, 1962. On November 23, 1962, after five days of sluggish operation, decoder 1 became inoperative. The cause of the malfunction of the command systems and the measures taken to correct the problem are discussed in a separate paper in this issue.[8]

X. CONCLUSIONS

The launch of the Telstar satellite was highly successful, so the initial orbit, attitude, solar aspect, and spin rate agreed very closely with the predicted values. Most of the data in this report cover the first three months of operation. Subsequent information obtained through January 4, 1963 proves that, except for the command system, the satellite behavior has been normal and predictable. The temperature sensors on the shell show that these temperatures have not exceeded 79°F, which is slightly less than the predicted value. While the electronics equipment operates satisfactorily over a wide temperature range, it is important to see that the average canister temperature has been held at near 70°F throughout the first 1400 orbits. Data from telemetry and from ground

measurements give no indication of any deterioration of the communications repeater or the telemetry system. The command system has obviously been damaged by radiation, but the extent of the present damage after the recovery is not known. The pressure in the electronics canister, as proved by the pressure switches, is at least 5 psi; even if a very small leak does exist, no corona problem associated with the TWT high voltages will exist for several years.

REFERENCES

1. Hatch, R. W., Bennett, S. B., and Kinzer, J. P., Results of the *Telstar* System Communication Tests, B.S.T.J., this issue, p. 1561.
2. Brown, W. L., Buck, T. M., Medford, L., Thomas, E. W., Gummel, H. K., Miller, G. L., and Smits, F. M., The Spacecraft Radiation Experiments, B.S.T.J., this issue, p. 899.
3. Courtney-Pratt, J. S., Hett, J. H., and McLaughlin, J. W., Optical Measurements on *Telstar* Satellite to Determine the Orientation of the Spin Axis and the Spin Rate, to be published.
4. Yu, E. Y., Spin Decay, Spin Precession Damping, and Spin-Axis Drift of the *Telstar* Satellite, to be published.
5. Hrycak, P., Koontz, D. E., Maggs, C., Stafford, J. W., Unger, B. A., and Wittenberg, A. M., Spacecraft Structure and Thermal Design Considerations, B.S.T.J., this issue, p. 973.
6. Davis, C. G., Hutchison, P. T., Witt, F. J., and Maunsell, H. I., The Spacecraft Communications Repeater, B.S.T.J., this issue, p. 831.
7. Chapmann, R. C., Critchlow, G. F., and Mann, H., Command and Telemetry System, B.S.T.J., this issue, p. 1027.
8. Mayo, J. S., Mann, H., Witt, F. J., Peck, D. S., Gummel, H. K., and Brown, W. L., The Command System Malfunction of the *Telstar* Satellite, B.S.T.J., this issue, p. 1631.

Results of the *Telstar* Radiation Experiments

By W. L. BROWN, J. D. GABBE and W. ROSENZWEIG

(Manuscript received June 7, 1963)

The data from the particle experiments of the Telstar satellite have been analyzed to provide maps of the distribution of electrons and protons as measured in three of the Telstar detectors during the period from July through October, 1962. For the protons between 26 and 34 Mev and >50 Mev, the particle distributions are stable in time, but for the electron distribution there is a time decay of the electron flux over most of the region explored by the Telstar orbit. The connection of these observations to the high-altitude nuclear explosion of July 9, 1962, is discussed. The introduction of additional electrons by Russian tests at the end of October was also observed. The particle maps have been used to derive the integral particle exposure of the satellite, which is found to account quantitatively quite well for the radiation damage observed in the main solar power plant and in the radiation damage experiments on solar cells and special damage transistors carried by the satellite. In the main power plant the proton and electron contributions to damage are found to be equal. The integral particle exposure has also been used to compute the level of ionization in different depths of material in order to evaluate the degradation of semiconductor devices in the Telstar canister.

I. INTRODUCTION

This article presents some of the results obtained from the radiation experiments on the Telstar satellite. It describes the distribution of several classes of energetic charged particles mapped out by these experiments, and the integral radiation exposure of the satellite in orbit which has been calculated from these distributions. It also describes the radiation damage effects observed directly on semiconductor devices carried by the satellite and compares the damage with that to be expected on the basis of the orbital integrals.

1.1 *Charged Particle Experiment*

As described in detail in an accompanying article,[1] there are four silicon p-n junction charged particle detectors on the Telstar satellite, three that measure the distribution of protons in space at different energies and one that measures the electron distribution and some simple properties of the electron energy spectrum. All four detectors are energy proportional devices, giving an electrical pulse-height response proportional to the energy deposited by a charged particle in the active volume of the detector. By adjustment of the active volume, the levels of pulse height examined, and the amount of absorbing material which must be penetrated by a particle in reaching the detector, it is possible to distinguish protons from electrons and put bounds on the particle energies.

In the electron detector, particle pulses are sorted into four channels corresponding to deposition of different amounts of energy between 250 and 1000 Kev in the detector. Because of the nature of the energy loss processes for electrons, this detector primarily responds to electrons below 1 Mev but also responds to electrons of much higher energy with decreasing sensitivity. The efficiency of the four pulse-height channels of this detector for monoenergetic electrons in the region of primary sensitivity is shown in Fig. 1. The time and spatial variations of the electrons as observed by this detector will be discussed in considerable detail in Section 2.2. Electrons are of major importance in the radiation surface effects observed in the Telstar command decoder and also contribute about half of the radiation damage in the main solar power plant.

The highest-energy proton detector of the three carried by the satellite measures protons above 50 Mev. The medium-energy detector measures in a well defined energy interval between 26 and 34 Mev. The results for these two detectors are simpler than the electron case because of the relative time stability of the proton distributions that they measure and the simplicity of their detection sensitivity. The spatial distribution of these protons and the energy spectrum that can be derived from them will be discussed in Section 2.3. The remaining half of the damage to the Telstar solar power plant is caused by protons. The fourth detector in the satellite measures low-energy protons between 2.5 and 25 Mev and provides rather detailed information on the spectrum, particularly below 12 Mev. The analysis of these data is not yet complete and the results from this detector are not included in this paper.

The period between July 10, when the Telstar spacecraft was launched, and the end of October, 1962, has been of special interest. This period begins just after the United States high-altitude nuclear test (Starfish)

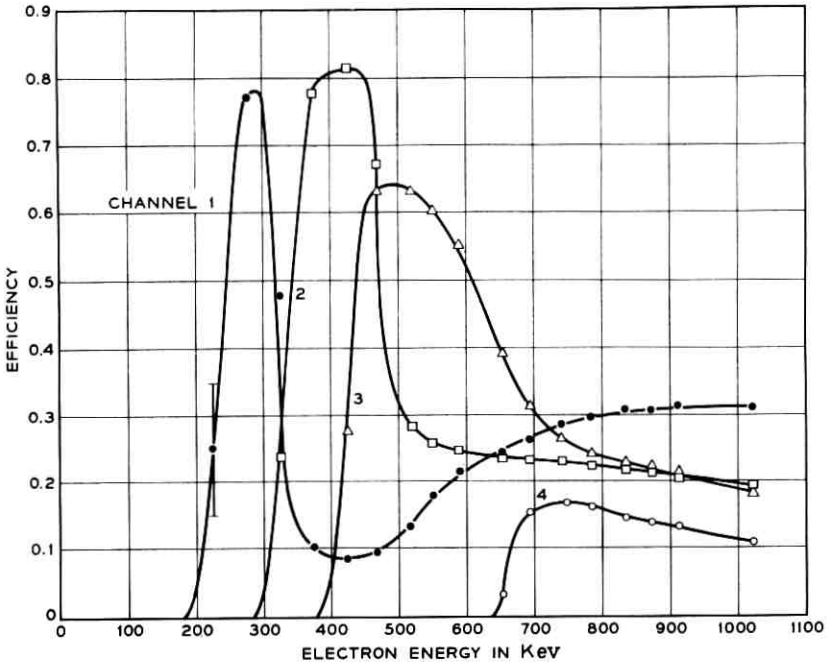

Fig. 1 — Electron detection efficiency as a function of incident electron energy.

of July 9 and ends with the first two Russian high-altitude nuclear tests on October 22 and 28. During most of this time, the Telstar satellite was the only intermediate-altitude radiation monitor in space. In these months, 770 hours of usable telemetry was acquired by the NASA tracking network and the Bell System telemetry stations at Andover, Maine, and Cape Canaveral, Florida. Although some later data are used, it is the 180,000 data points which represent the output of the electron and the two higher-energy proton detectors for the first 104 days in orbit that form the basis of the charged particle distributions that follow.

1.2 *Radiation Damage Experiments*

Radiation damage effects on the bulk properties of silicon are directly observed in the short-circuit current of four solar cells and in the common-base direct current gain of six specially fabricated silicon transistors. The details of these devices and the type of information they provide are described in an accompanying paper.[1] In addition to these special experiments, the main solar power plant provides a large statistical study of damage to several thousand essentially identical devices

measured together. The present paper will describe the results from all three of these sources and will relate the damage observed to the radiation exposure of the satellite as calculated from the particle experiments. Particular attention will be centered on the first 104 days in orbit because the particle distribution has been studied in detail during this time.

II. PARTICLE EXPERIMENTS

2.1 *General*

2.1.1 *Motion of Geomagnetically Trapped Particles*

The basic motion of a charged particle trapped in the earth's magnetic field is a spiral around a magnetic line of force; see Fig. 2. As the

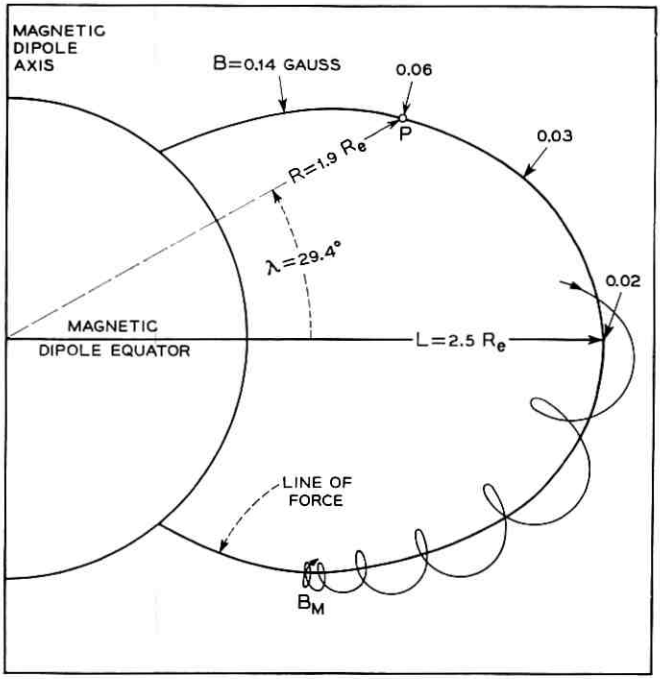

Fig. 2 — The motion of a charged particle trapped in a dipole magnetic field. The particle is confined near the magnetic shell $L = 2.5\ R_e$ and is mirroring at field strength B_m. The B-L coordinates of the point P are $B = 0.06$ gauss and $L = 2.5\ R_e$. The R-λ coordinates of the point P are $R = 1.9\ R_e$ and $\lambda = 29.4°$. Distances are measured in units of earth radii, R_e.

particle gets nearer to the earth and into regions of higher magnetic field strength, the spiral becomes flatter until eventually the particle is reflected and goes back out along the line of force. A given particle is always reflected at the same value of the field strength, B_m (B_{mirror}). The mirror point depends upon the angle between the particle velocity vector and the magnetic field vector at the magnetic equator. Particles moving very nearly parallel to the field line at the equator mirror close to the earth, at large values of B_m, while particles moving nearly perpendicular to the field line at the equator mirror close to the equator, at nearly equatorial values of the field. Superimposed on the back and forth motion in the magnetic field is a small but important longitudinal drift, westward for protons and eastward for electrons. These motions, their stability and various injection and loss mechanisms have been treated in considerable detail in the literature.[2-14] The longitudinal drift shifts the particles so that they spiral about longitudinally adjacent lines of force which are equivalent. The set of equivalent lines of force is called a magnetic shell. Thus, a particle is constrained to move so that the locus of the center of its spiral always lies near the same magnetic shell, and is confined to regions on the shell with magnetic fields equal to or less than B_m. A natural coordinate system in which to consider this motion is one which identifies the magnetic shell appropriate to the particle and then measures position in the shell in terms of the magnetic field strength. Such a coordinate system has been developed and is described below.

2.1.2 *Coordinate Systems*

A transformation developed by McIlwain[15] maps the earth's magnetic field onto a dipole field having the same first moment. In the axially symmetric dipole field, a magnetic shell is defined simply as the surface generated by rotating a line of force about the dipole axis. The magnetic shell is labeled by L, the distance from the dipole axis in the equatorial plane of the dipole. Position in the magnetic shell is given by the field strength, B, Fig. 2. Because of the additional symmetry of the dipole field, a quarter of a meridian plane is a complete representation. The B-L coordinate system is well suited to many theoretical calculations, and we have done most calculations and present some results in this system. However, the geometrical distortions inherent in the transformations make it difficult to get an intuitive picture of the spatial distribution of the particles in B-L coordinates. For this reason, we present many results in the magnetic dipole polar coordinates R and λ,

Fig. 2, which give a pseudo-geographic representation. Both R and L will be measured in units of earth radii, R_e, in what follows. As a result of the anomalies in the real field, the surface of the earth is very wrinkled in R-λ coordinates. Some of the wrinkles exceed 0.1 R_e in extent.

The magnetic field used to calculate the coordinates is a 48-term spherical harmonic expansion with the Jensen and Cain[16] coefficients for 1960. The coordinates are only as good as the expression for the magnetic field, $\pm\approx 2$ per cent.[53] In addition, the magnetic field is assumed to remain fixed, whereas the field in space is known to vary as a result of fluctuations in the earth's magnetization, currents in the ionosphere, currents due to circulating magnetically trapped particles, and other perturbations connected with solar activity. The coordinate system as used here acts as a fixed grid against which changes in both the magnetic field and the particle population are measured. The two effects are not separable, but in the part of the magnetosphere covered by the Telstar satellite the magnetic variations are small compared to the changes in the particle population.

2.1.3 *Treatment of the Data*

The counting rates of the various channels of particle information are deduced from readings of the 14-bit binary register in the telemetry,[17] modified in the case of register overflow in accordance with analog readings of log ratemeters in those channels to which the ratemeter information applies.[1] It is convenient to report the distribution of a particular class of particles in space in terms of its omnidirectional flux, defined as the number of particles passing through a sphere of unit cross-sectional area per unit time. Deducing this quantity requires a knowledge of the efficiency of the detector, which in turn depends on the energy spectrum of the particles being measured. To obtain a number which expresses the data more directly, we have chosen to define an omnidirectional counting rate (OCR) which contains all the geometrical factors required to specify an omnidirectional flux, but which does not contain a factor for the detector efficiency. The efficiency can be specified for an assumed particle spectrum by integration over curves of the type shown in Fig. 1. For example, if the electron spectrum is that corresponding to equilibrium beta decay from fission fragments, channel 3 of the electron detector has an efficiency of 0.2, and a flux can be deduced from its OCR by multiplying by 5. In principle, several parameters of an approximate spectrum and the corresponding detector efficiency can both be deduced by iteration, using the efficiency curves for monoenergetic particles. This process has not yet been carried out in detail.

The angular distribution of particles at any particular point in space is far from isotropic, and the omnidirectional flux (or omnidirectional counting rate) is the average over all directions. The two proton detectors whose results will be described in Section 2.3 are essentially omnidirectional detectors in their construction; that is, they measure an approximately equally weighted average of the proton flux from all directions. The electron detector, however, is highly directional. Its axis is normal to the spin axis of the satellite and hence, over a number of satellite rotations, it measures an average directional intensity that depends on the angle between the satellite spin axis and the local magnetic field. The average directional counting rate has been converted to an omnidirectional counting rate (*OCR*), using an approximate expression for the influence of the aspect of the satellite.

$$OCR = \frac{C/G}{1 + 0.4 \cos 2A}, \tag{1}$$

where C is the average directional counting rate, G is the geometrical factor of the detector, and A is the angle between the spin axis and the local magnetic field. A more exact expression would take into account the anisotropy of the angular distribution of the particles at the particular location at which the measurement is being made and hence would vary from one place to another in space. Expression (1), however, is a good approximation over most of the space investigated. For the omnidirectional proton detectors, the *OCR* involves only the counting rate and the geometrical factor of the detector. Note that the *OCR* has the same units as omnidirectional flux ($1/\text{cm}^2$ sec) throughout the paper. The *OCR* has been written most conveniently in terms of the variable Φ defined by

$$\Phi \equiv \log_{10} (OCR). \tag{2}$$

From a knowledge of the satellite ephemeris and the orientation of the satellite spin axis, the coordinates B-L or R-λ and the angle A are calculated and associated with the *OCR* as defined above. The data have then been machine plotted in a number of different forms:

Plot 1. *Constant* OCR *contours in* R-λ *space.* The plotting coordinates are R and λ. For a given detector, a point is plotted if Φ and the time, T, at which the datum point was taken fall within specified intervals. Fig. 3 is a plot of all the points for which data are available in electron channel 3 between days 263 and 267, 1962. Fig. 4 is a plot of all the points in Fig. 3 for Φ-range 2 (contour 2), Table I. The inner-belt contour stands out clearly. These plots give the flux distributions in space.

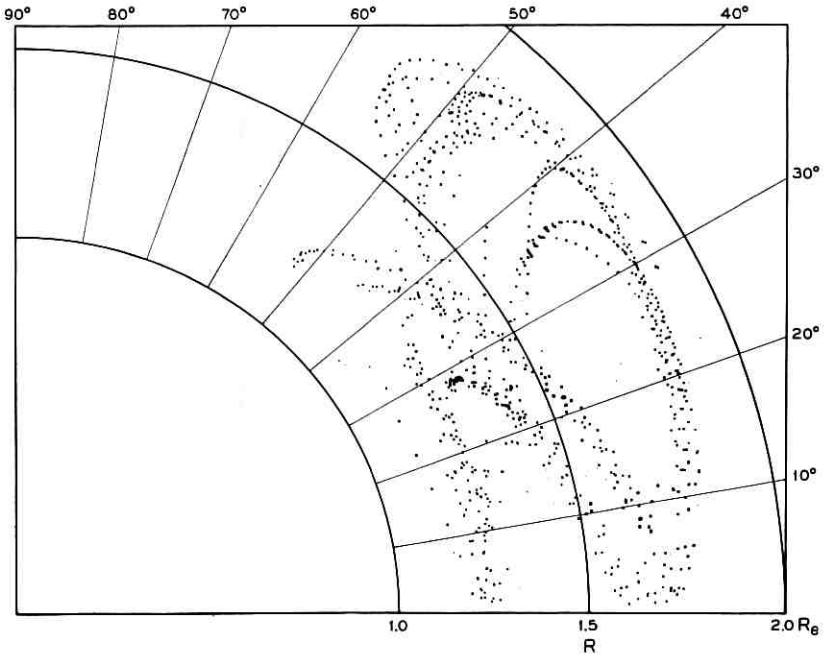

Fig. 3 — Points at which data were acquired in electron channel 3 for days 263 to 267, 1962, plotted in R-λ coordinates. The surface of the earth occurs at $R = 1.0 \pm 0.1\ R_e$.

Plot 2. *Constant* OCR *ratios in* R-λ *space.* These plots are analogous to plot 1, except that a range of $\Phi_a - \Phi_b$, where a and b indicate different channels, is selected instead of a range of Φ_a . These plots give an indication of the energy spectrum.

Plot 3. *Constant* OCR *contours in* B-L *space.* The difference between plots 1 and 3 is that B and L are used as plotting coordinates for plot 3 instead of R and λ. The geometry of the two coordinate systems is very different and they are appropriate to different calculations.

Plot 4. *Constant* OCR *ratios in* B-L *space.* The remarks under plot 3 apply.

Plot 5. Φ *vs* T. Under strict constraints, Φ values separated in time by not more than two minutes are interpolated to find Φ at given values of L. Φ is then plotted against T in days for the given value of L and a small range of B. The resultant plots give a time history of the radiation in almost 200 limited regions of space.

Plot 6. Φ *vs* B. Φ is interpolated to specific values of L, as in plot 5,

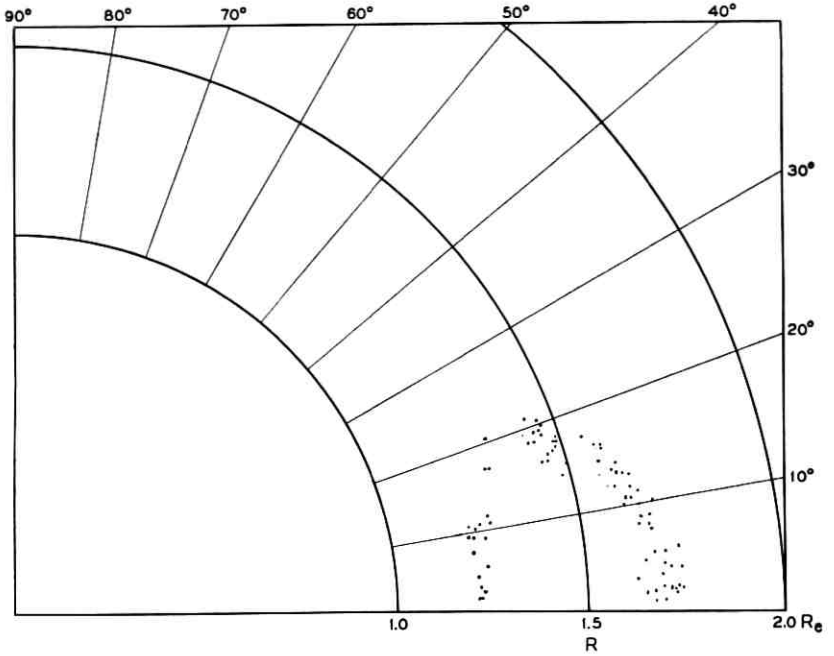

Fig. 4 — Points in Φ-range 2 (contour 2), electron channel 3, days 263 to 267, 1962, plotted in R-λ coordinates. The inner-belt contour is well defined. Φ ranges are defined in Table I.

TABLE I — VALUES FOR THE ELECTRON CONTOURS [OCR has the units counts/cm^2 sec; $\Phi \equiv \log_{10}(OCR)$]

Contour	Φ min	Φ max	Average OCR
1	8.0	≈8.4	1.5×10^8
2	7.5	8.0	6.6×10^7
3	7.0	7.5	2.1×10^7
4	6.5	7.0	6.6×10^6
5	6.0	6.5	2.1×10^6
6	5.5	6.0	6.6×10^5
7	5.0	5.5	2.1×10^5
8	4.5	5.0	6.6×10^4
9	4.0	4.5	2.1×10^4
10	3.5	4.0	6.6×10^3
11	3.0	3.5	2.1×10^3
12	2.5	3.0	6.6×10^2
13	$-\infty$	2.5	$<10^2$

and plotted against B. Only data taken within a given interval of days are included. These plots indicate the distribution of mirror points within a given magnetic shell.

Plot 7. Φ *vs* T. Φ is plotted against T in minutes for each pass. A pass is a single passage within range of a telemetry station. By examining the data in this context, spurious points may be identified. This is most important when the data are sparse.

The material presented in the next section has been selected and synthesized from the seven kinds of cross-referenced plots just described.

2.2 *Results of the Electron Measurements*

2.2.1 *Flux Maps*

Contours of constant *OCR* for electron channel 3 have been drawn through collections of points like those of Fig. 4. Data from the other electron channels have been treated as spectral rather than intensity information. Five of the contour maps thus produced in R-λ space are presented in Figs. 5 through 9. In four cases, the maps cover five-day

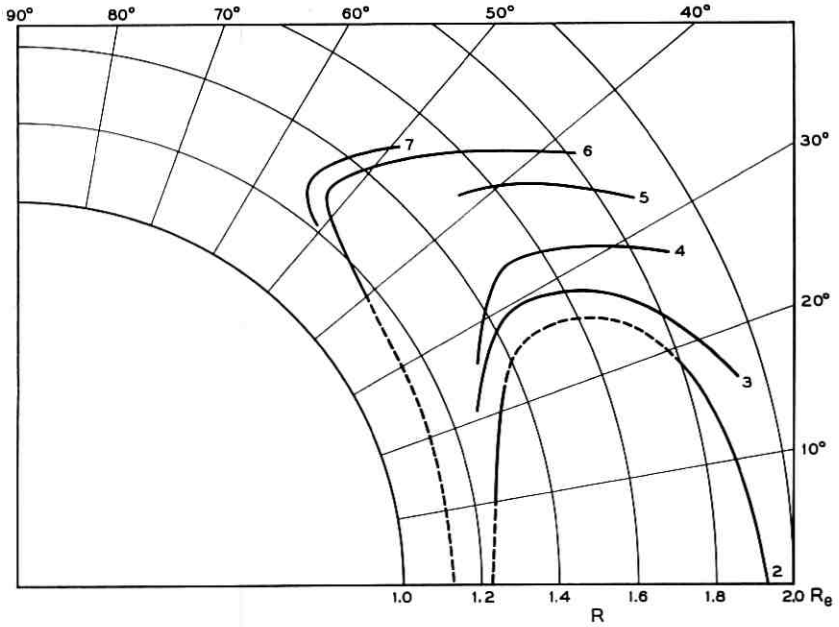

Fig. 5 — Contours of constant *OCR*, electron channel 3, days 193 to 197, 1962, plotted in R-λ coordinates. Dashed lines indicate interpolations and extrapolations. Φ ranges are defined in Table I.

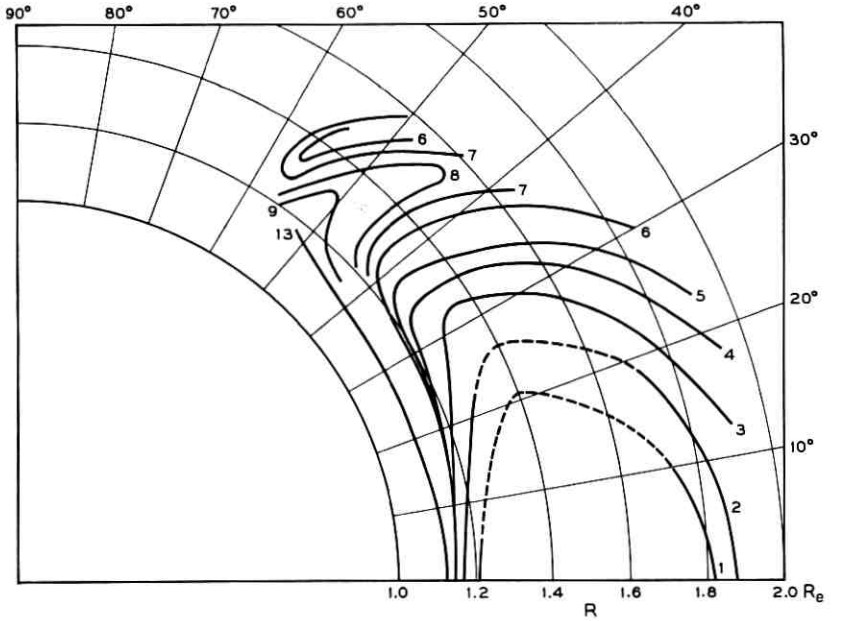

Fig. 6 — Contours of constant *OCR*, electron channel 3, days 203 to 207, 1962, plotted in R-λ coordinates. Dashed lines indicate interpolations and extrapolations. Φ ranges are defined in Table I.

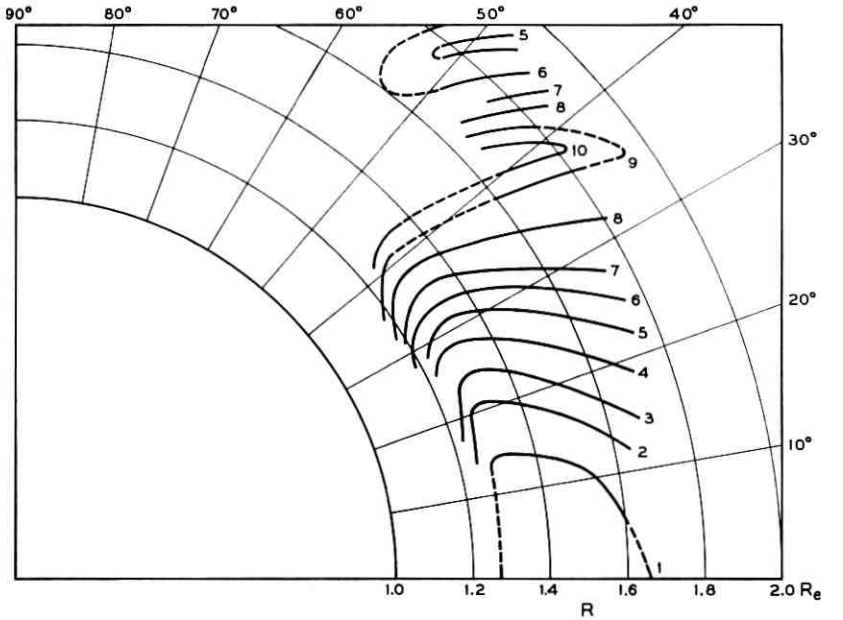

Fig. 7 — Contours of constant *OCR*, electron channel 3, days 238 to 242, 1962, plotted in R-λ coordinates. Dashed lines indicate interpolations and extrapolations. Φ ranges are defined in Table I.

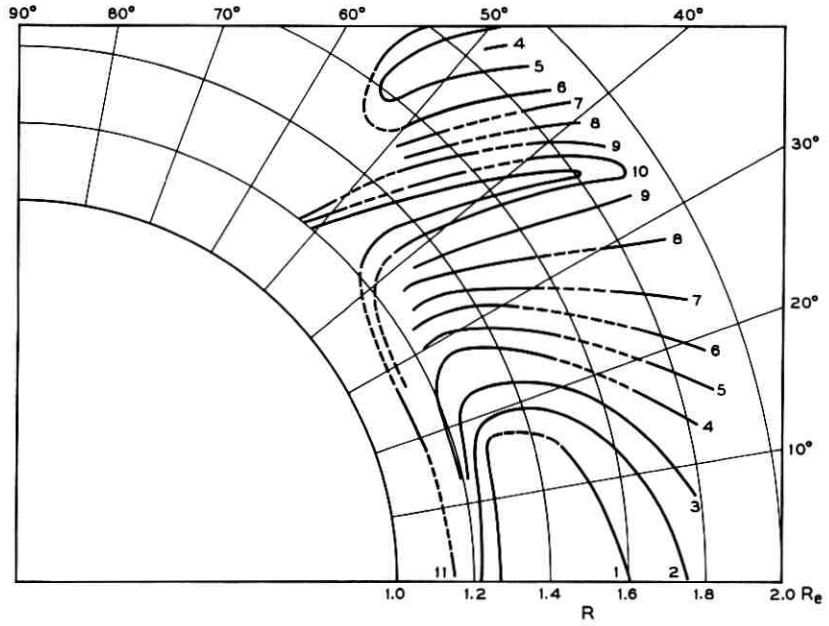

Fig. 8 — Contours of constant *OCR*, electron channel 3, days 263 to 267, 1962, plotted in R-λ coordinates. Dashed lines indicate interpolations and extrapolations. Φ ranges are defined in Table I.

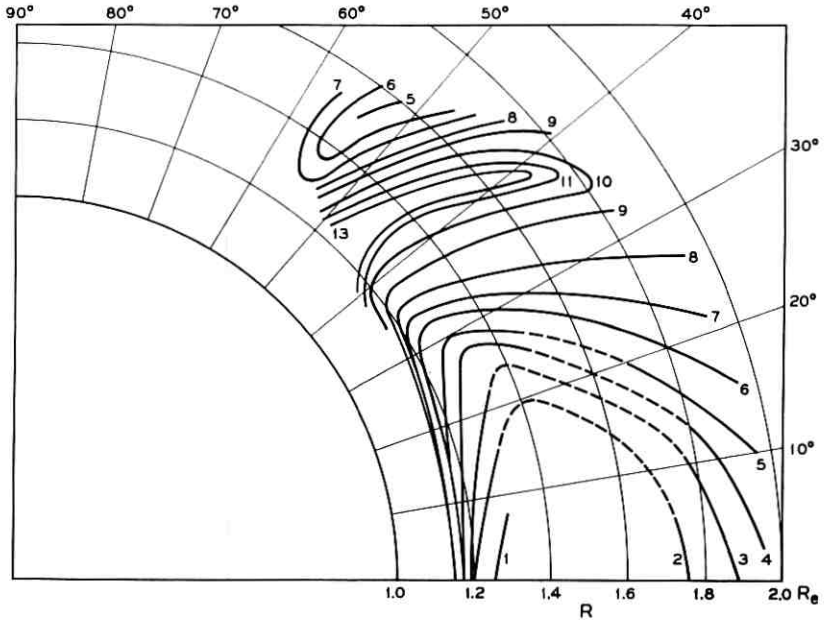

Fig. 9 — Contours of constant *OCR*, electron channel 3, days 288 to 294, 1962, plotted in R-λ coordinates. Dashed lines indicate interpolations and extrapolations. Φ ranges are defined in Table I.

intervals, the earliest containing the data for days 193–197, starting two days after the Telstar launch and three days after the Starfish nuclear test. The latest map, covering the seven-day period, days 288–294, is for the week immediately preceding the first of the Russian high-altitude nuclear tests on October 22. The counting rates of adjacent contours on these plots are separated by $\sqrt{10}$ in *OCR* or by 0.5 in Φ, as indicated in Table I. An exception is contour 1, for which the actual data do not uniformly cover the half decade counting rate range that would be assigned to this contour in the normal progression. A second exception is contour 13, which indicates the limit beyond which the counting rate is not measurably different from 0. The contour maps for each five-day interval have been drawn by hand essentially independent of one another, and there are minor changes in contour shapes and positions which do not represent the optimum contour fitting to the data taken as a whole. A more comprehensive processing of the data is in progress. Dashed lines on the contour maps indicate extensions of the contours into regions devoid of data. Such regions shift with time as the orbit of the satellite precesses, a feature which will be discussed more fully in Section 2.4.1.

The highest electron fluxes lie on the equator in a region centered at a radial distance of about 1.45 R_e. This is the general region of the inner Van Allen belt. The contours lie increasingly close together as one proceeds to lower altitudes from this maximum because of the removal of particles from trapped orbits by the increasingly dense atmosphere. In Figs. 6 through 9 the tip or horn of the outer Van Allen belt is also clearly evident in the secondary maximum at $\lambda \approx 50°$ and $R \approx 1.5\ R_e$. The separation into two belts is not apparent on days 193-197, partly because the orbit stops short of the outer belt maximum, but even more importantly, because the region between the two belts on those early days is filled with electrons, presumably from the Starfish explosion. Through the sequence of five figures a minimum-intensity slot between the inner and outer belts continually develops until on days 288-294 it contains a counting rate immeasurably different from 0 in the Telstar electron detector. During this period, all the contours around the inner belt peak are contracting. This occurs more rapidly on the lower-intensity contours and at larger values of R and λ than in the low-R nearly equatorial region, but nowhere as dramatically as in the region of the slot. This time decay will be discussed in more detail in Section 2.2.3.

Figs. 10 and 11 show contours of constant *OCR* in the *B-L* representation, corresponding to the contours in R-λ space shown in Figs. 6 and 9, respectively. The distortions introduced by the *B-L* coordinates show

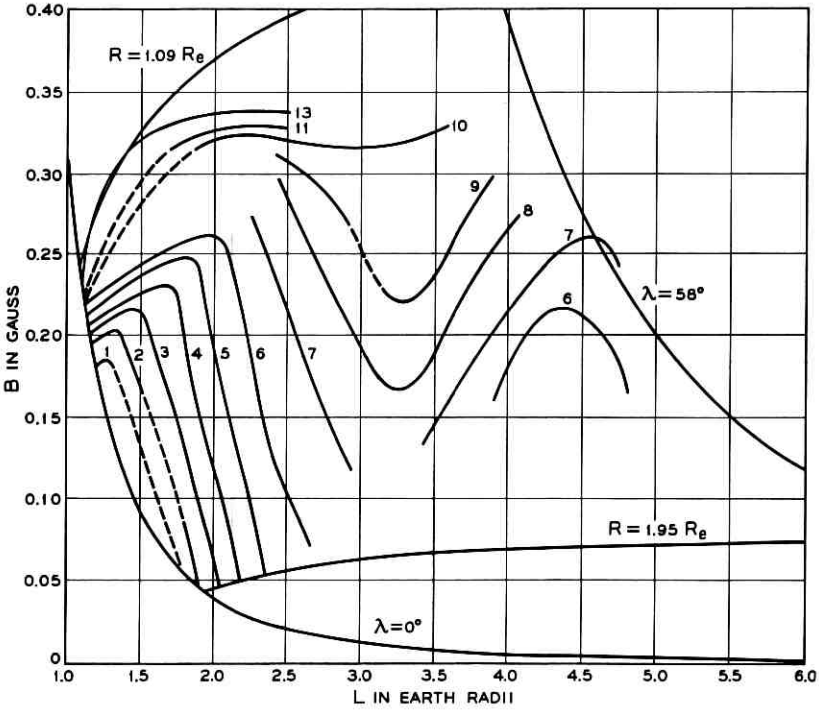

Fig. 10 — Contours of constant OCR, electron channel 3, days 203 to 207, 1962, plotted in B-L coordinates. Dashed lines indicate extrapolations and interpolations. The lines $R = 1.09\ R_e$, $R = 1.95\ R_e$ and $\lambda = 58°$ define the approximate boundaries of the space swept out by the Telstar orbit. Φ ranges are defined in Table I.

graphically in contour 1 and in the appearance of the horn of the outer belt. The B-L diagrams contain three lines that approximately bound the Telstar orbit: $R = 1.09\ R_e$, the lowest altitude limit; $\lambda = 58°$, its extreme in equivalent dipole latitude; and $R = 1.95\ R_e$, the upper altitude extreme. All of the space more distant from the earth than the Telstar satellite can observe is compressed between the $R = 1.95\ R_e$ line and the $\lambda = 0°$ line, the trace of the equatorial plane of the magnetic dipole in this space. The orbital integrals which will be described in Section 2.4 have been conveniently carried out in B-L space.

2.2.2 *The Energy Spectrum*

As discussed in Section 1.1, the major sensitivity of the electron detector is to electron energies between 0.25 and 1 Mev. The detector

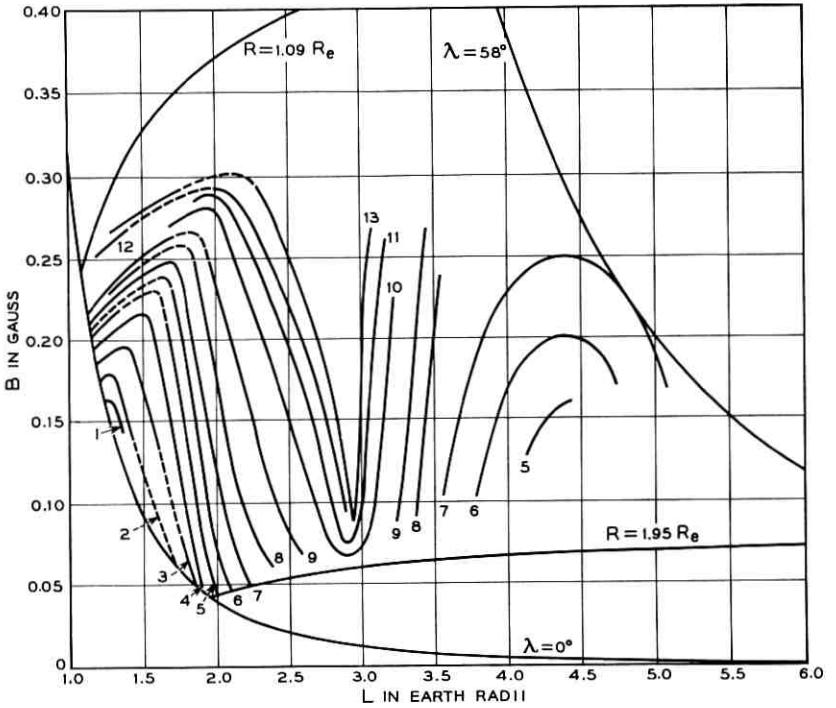

Fig. 11 — Contours of constant *OCR*, electron channel 3, days 288 to 294, 1962, plotted in *B*-*L* coordinates. Dashed lines indicate extrapolations and interpolations. The lines $R = 1.09\ R_e$, $R = 1.95\ R_e$, and $\lambda = 58°$ define the approximate boundaries of the space swept out by the Telstar orbit. Φ ranges are defined in Table I.

gives only an indirect indication of the spectrum above 1 Mev, an energy region which contributes heavily to radiation effects. The ratios, ρ_{34}, of channels 3 to 4 for two five-day periods are indicated in Figs. 12 and 13. Unfortunately, channel 4 has no log ratemeter and ratios cannot be taken in the high-intensity region inside contour 3, where the register begins to overflow. During mid-July, ρ_{34} had a value of approximately 3 over much of the space accessible to the instruments. This is exemplified by the region marked C in Fig. 12. A ratio of 3 is consistent with an electron spectrum appropriate to fission fragment beta decay.[18,19] Such consistency does not, however, constitute a unique determination of such a spectrum. Without postulating an extremely complex spectrum with a maximum intensity at about 700 Kev, a ρ_{34} equal to 3 cannot be produced unless there is a significant population of electrons in excess of 1 Mev. It is not possible, however, to assert that the fraction of electrons

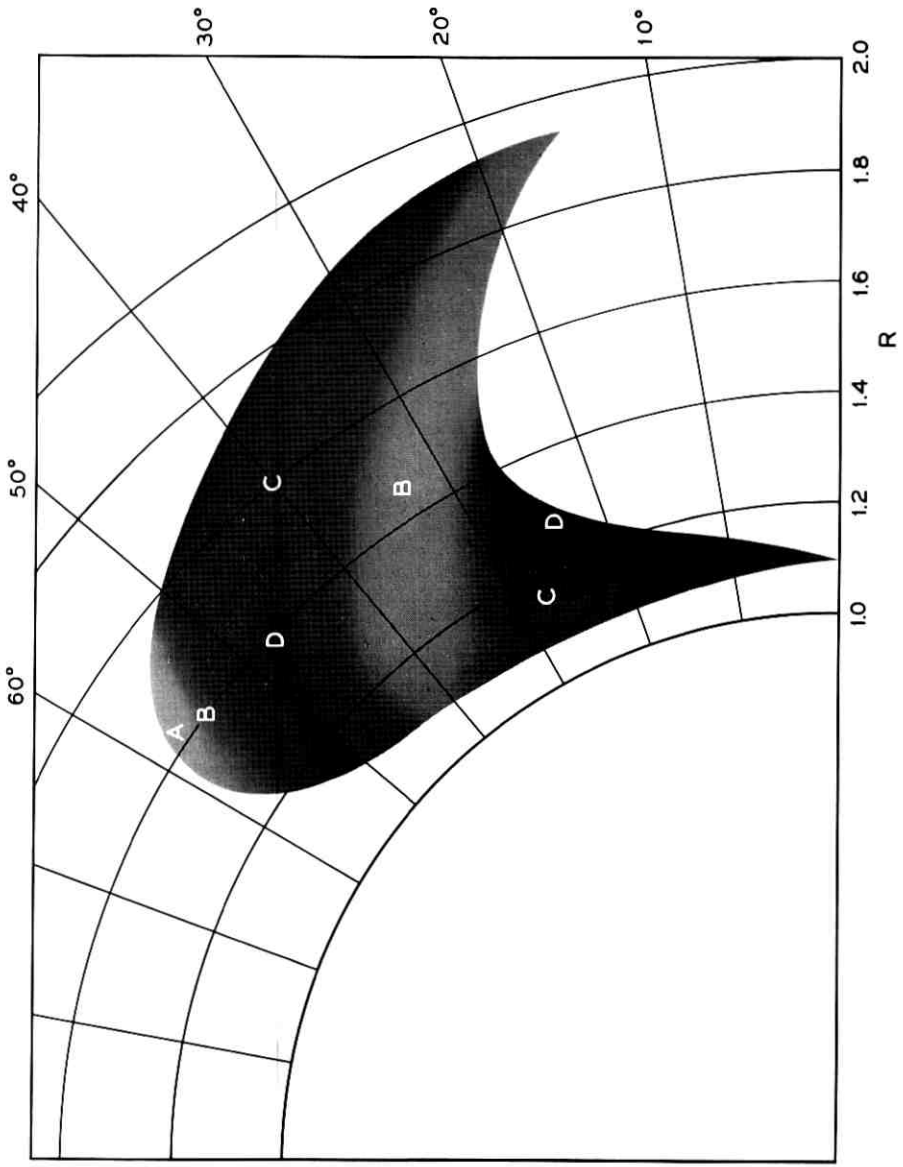

Fig. 12 — Ratio of *OCR* electron channel 3 to *OCR* electron channel 4 (ρ_{34}), days 203 to 207, 1962, displayed in R-λ coordinates.

Label	Range of ρ_{34}	Comment
A	>8	very soft
B	4–8	soft
C	2–4	fission-like
D	1–2	hard

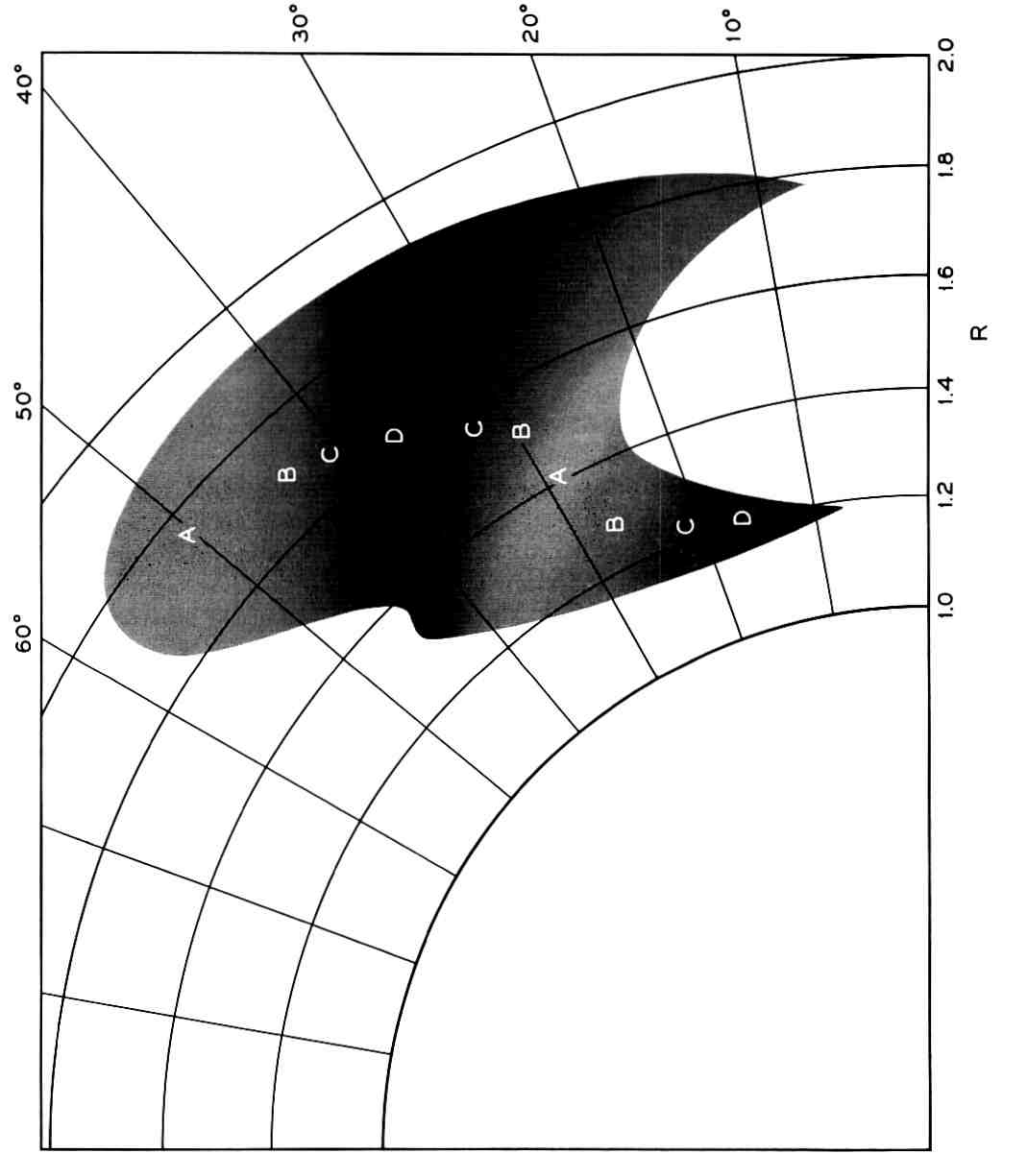

Fig. 13 — Ratio of *OCR* electron channel 3 to *OCR* electron channel 4 (ρ_{34}), days 263 to 267, 1962, displayed in R-λ coordinates. Labels are identified in the legend of Fig. 12.

above about 1.5 Mev is 0.2 of the total electron spectrum, as would be the case in the fission spectrum.[19]

Van Allen, Frank, and O'Brien[20] have reported on measurements from an instrument in the Injun I satellite that effectively measures electrons above 1.5 Mev.[21] They have concluded that the spatial distribution of the energetic electrons injected by Starfish had a maximum at $L \approx 1.2$ R_e, and they have inferred that the flux is 10 per cent of this maximum at an equatorial L of about 1.8 R_e. From the Telstar data shown in Fig. 6, the electron flux at $L = 1.8$ R_e on the equator is essentially the same as that at $L = 1.2$ R_e, and contour 3, which is 10 per cent of the maximum measured value, apparently has an upper crossing of the equator at $L \approx 2.1$ R_e. When these two sets of observations are translated into R-λ space, they give high-intensity regions very different in extent and will, if one asserts that the electrons seen by the Telstar detector are a result of Starfish, give rise to quite different values of the total number of electrons injected into trapped orbits by that explosion. Since the two detectors measure electrons at quite different energies, the apparent conflict between these two sets of results is easily resolved by proper treatment of the electron energy spectrum. The higher flux of electrons for $L > 1.6$ R_e as seen by the Telstar detector do not have associated with them the proportion of high-energy electrons to be expected in a fission electron spectrum. The possibility has been considered that most of the lower-energy electrons (the Telstar data) on these higher-L lines may be of natural origin. However, the time-dependence of the measured flux, which will be discussed in Section 2.2.3, strongly suggests that a major fraction of these electrons was connected with the explosion. A mechanism is thus required by which a high-altitude explosion can introduce a spectrum of electrons which varies in space and can be appreciably different from that of fission beta decay. Although the details of such a process are not yet understood,[22] direct observation of this effect on a less extensive scale was made by Explorer XV[23,24] on electrons injected by the second Russian high-altitude explosion on October 28. Several mechanisms for degrading the electron energy spectrum from a fission electron source have been suggested.[25,26] It also seems possible that low-energy electrons (<0.25 Mev) normally present in space might be accelerated as a result of the shock front of the expanding bomb debris to energies where they would be counted by the Telstar electron detector. A quantitative determination of the spatial variation in the electron spectrum which will satisfy the July measurements of the Telstar and Injun satellites has not yet been made, but with recognition of a softer spectrum on higher-L lines there seems

little doubt that a large part of all the electrons measured by the Telstar satellite in July were a result of the Starfish test.

In the tip of the outer belt, region A of Fig. 12, the spectrum softens appreciably, $\rho_{34} > 8$, and a similar but less pronounced softening occurs in region B. In the small regions D, the spectrum was apparently harder, $2 > \rho_{34} > 1$, than a fission beta spectrum. It is very difficult to see how a ratio smaller than 2 can be obtained for any electron spectrum in the light of the efficiency curves of Fig. 1, and the low ratios seem to arise from two other effects. In the lower-intensity of the two regions marked D (at high λ), ratios of <2 arise from statistical fluctuations in the number of counts in the register. In the high-intensity D region, these anomalous ratios arise from fluctuations in the log ratemeter measurement of the counting rate of channel 3, which is modulated as the spin of the satellite sweeps the acceptance cone of the detector through the nonisotropic particle distribution.

The temporal changes in the electron belts are heavily energy dependent. By late September, Fig. 13, the configuration is still fissionlike, as indicated by ρ_{34} only in the areas marked C. The spectrum is soft on the high-altitude slope of the inner belt, very hard in the slot, and soft again in the tip of the outer belt. The higher-energy electrons appear (surprisingly) to decay faster on the high-altitude slope of the inner zone, while the lower-energy electrons seem to disappear more rapidly in the center of the slot, at $L = 3\ R_e$.

Until about September 23, the ratio, ρ_{13}, of channel 1 to channel 3 on the Telstar detector indicates that between 0.25 and 0.6 Mev the spectrum is very soft, $\rho_{13} > 8$, in the slot and contains appreciably more low-energy electrons than a fission beta-decay spectrum except at very low altitudes and the center of the inner belt. Beginning on September 23, there is a very extensive and complex change in the electron population for $L > 1.8\ R_e$ and particularly for lower-energy electrons. The changes are small in channels 3 and 4, but are sufficiently large in channels 1 and 2 to have a profound influence on the ρ_{13} ratio in some places. These effects are apparently of natural origin. They have not yet been studied in sufficient detail to permit discussion in this paper.

2.2.3 *Time Variation*

The time variation of the electron flux will be discussed in terms of the omnidirectional counting rates of channel 3. The other channels show generally similar time decays, but there are differences in detail which give rise to the changes in the spectrum discussed above. Figs. 14

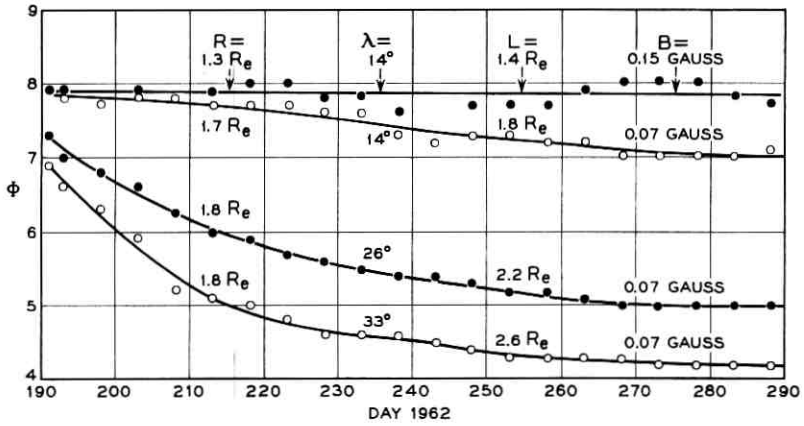

Fig. 14 — Temporal behavior of Φ for electron channel 3 at various positions in the radiation belts.

and 15 have been constructed from type 5 and 6 plots and show the long-term time dependence in representative regions of the belts.

The *OCR* in the high-intensity zone of the inner belt, typified by the point $L = 1.4\ R_e$ and $B = 0.15$ gauss ($R = 1.3\ R_e$, $\lambda = 14°$), shows no net long-term variation. There is some scatter in the points which may be real but which seems more likely to be a result of systematic differences introduced by the interpolations required to remove the B, L, and A dependence of the data. At $L = 1.8\ R_e$ and $B = 0.07$ gauss ($R = 1.7\ R_e$, $\lambda = 14°$) the *OCR* has decayed by somewhat less than a factor of 10 between July and the middle of October, and the rate of

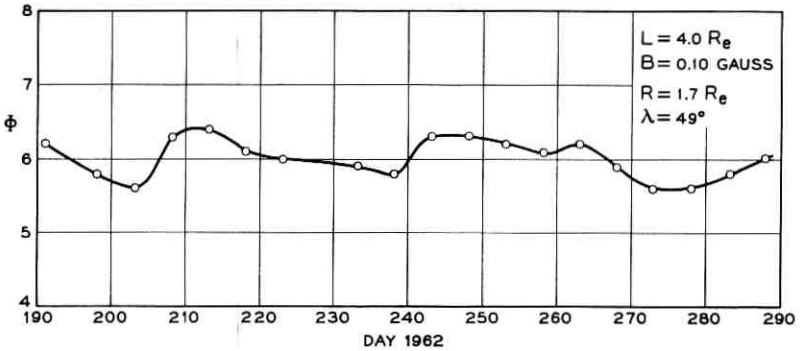

Fig. 15 — Typical temporal behavior of Φ for electron channel 3 in the tip of the outer belt.

decay seems to be slowing. Closer to the center of the slot $B = 0.07$ gauss and $L = 2.2$ and 2.6 R_e ($R \approx 1.8$ R_e and $\lambda = 26°$ and 33°) the decay is faster and greater, and the *OCR* levels off after day 260 at a value 50 times less than it had in early July. The outer-belt horn is characterized by the fluctuations apparent in Fig. 15, at $L = 4.0$ R_e, $B = 0.10$ gauss ($R = 1.7$ R_e and $\lambda = 49°$). The short-term fluctuations are much sharper than those shown in Fig. 15, which have been smoothed over five-day intervals. There is no doubt that the variations here are real, but in these data there appears to be no trend.

In the region below $L = 1.4$ R_e there is general agreement that the bulk of the electrons present were injected by Starfish. This was directly observed as a sudden change by Injun I[20] and TRAAC,[27] both of which had a record of the high-energy electron distribution in this region for many months prior to July. Furthermore, Telstar and Injun measurements in this region have subsequently been verified by other satellites — Explorer XIV,[21] Explorer XV,[23,24] and several Air Force satellites[28-31] — that show the spectra in this region are far too hard to be of natural origin. Since the Telstar satellite was launched a day after Starfish, such a direct statement cannot be made for near equatorial regions with $L > 1.4$ R_e. However, the observation of continuous monotonic decay over the months from July to October, and verification of the absolute intensities observed by the Telstar satellite with measurements by Explorer XV, make it almost impossible to conclude that electrons beyond $L = 1.4$ R_e were not also a result of that test. Electrons were introduced by Starfish even as far out as $L = 3.5$ or 4 R_e. If one adds up the electrons in space as shown on days 203-207, and if the detector efficiency of channel 3 were unity above the threshold, approximately 1.2×10^{25} electrons must have been introduced with energies above 440 Kev. Using the average efficiency (0.38) between 440 Kev and 1 Mev as shown in Fig. 1, the data require at least 3×10^{25} electrons with energies between 440 Kev and 1 Mev. If one uses an efficiency for a fission electron spectrum of 0.2, the number of electrons of all energies was 6×10^{25}. This is something like 10 per cent of all the fission electrons produced in the explosion, although some nonfission source associated with the bomb cannot yet be ruled out.

Fig. 16 presents some preliminary results of observations made during the Russian high-altitude test series. The first two tests, days 295 and 301, injected electrons into the slot region between L values of about 1.8 and 4.0 R_e. After the initial surge we again observe a rapid decay near the center of the slot, and a slow decay near the slopes of the inner and outer belts.

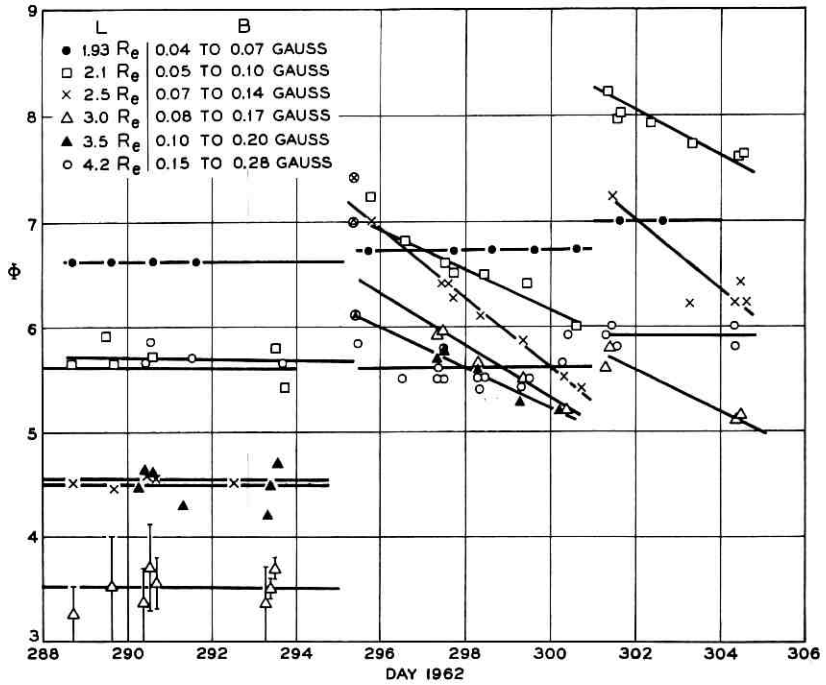

Fig. 16 — Temporal behavior of Φ for electron channel 3 during the first two Russian high-altitude nuclear tests. Circled points on day 295 are probably initial transients.

2.3 *Results of the Proton Measurements*

The *OCR* of the omnidirectional proton detectors have proven very stable in time. This stability has greatly simplified the analysis of the results. Figs. 17 and 18 are maps of the *OCR*, which apply to the entire 15-week period covered. There are five contours per decade in the proton plots, rather than two as in the electron maps previously described. No shift of as much as half a contour (25 per cent) has been observed. The measurements agree well with previous measurements in the inner zone,[32,33] and it seems unlikely that the Starfish test had any appreciable effect on protons in these energy ranges. The maximum intensity occurs at a lower altitude for the higher-energy protons in agreement with theory[10] and other observations.[23,24,34] Both detectors exhibit a well-defined cutoff, beyond which no counts are recorded in the region accessible to the spacecraft. The efficiency of the detectors is high, and

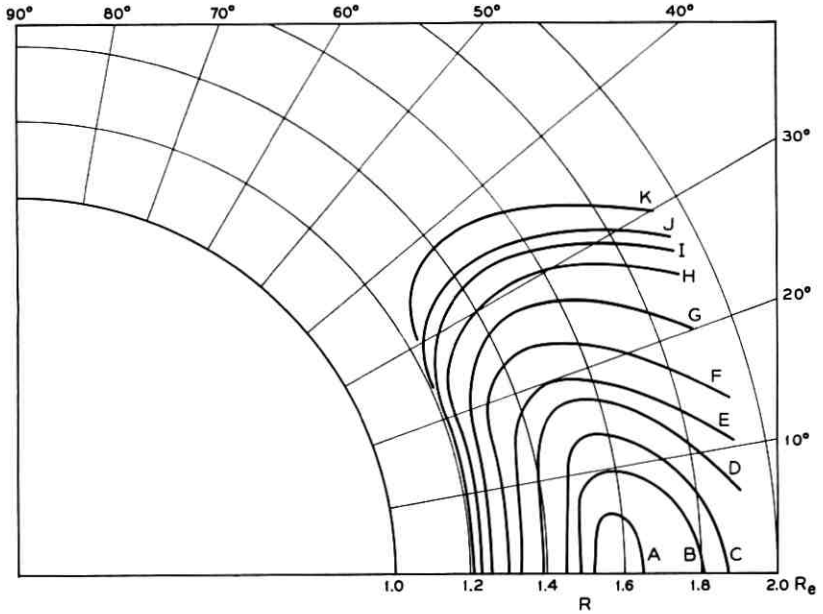

Fig. 17 — Contours of constant *OCR*, protons in the energy range 26 to 34 Mev, days 191 to 294, 1962, plotted in R-λ coordinates. To convert *OCR* to omnidirectional flux (1/cm² sec), add 0.32 to Φ. The range of Φ associated with the contours is: A, 4.0-4.2; B, 3.8-4.0; C, 3.6-3.8; D, 3.4-3.6; E, 3.2-3.4; F, 3.0-3.2; G, 2.8-3.0; H, 2.6-2.8; I, 2.4-2.6; J, 2.2-2.4; K, 2.0-2.2.

using the average efficiency in their regions of sensitivity, the flux is approximately 2.1 *OCR* for the 26 to 34 Mev detector, and 2.6 *OCR* for the >50 Mev detector.

2.3.2 *Energy Spectrum*

The contours for the two detectors have different shapes, which show that the energy spectrum in this range of energies is not constant with position. This is clearly indicated in the equatorial flux plot of Fig. 19. The equatorial omnidirectional *fluxes* for the two detectors are graphed as a function of L. (On the dipole equator $L = R$.) Plotted in the same figure are the quantities N_{26} and n from the expression for the differential spectrum

$$N(E) = N_{26}(E/E_0)^{-n}, \tag{3}$$

where $N(E)$ is the flux of electrons in the energy range dE at E, and

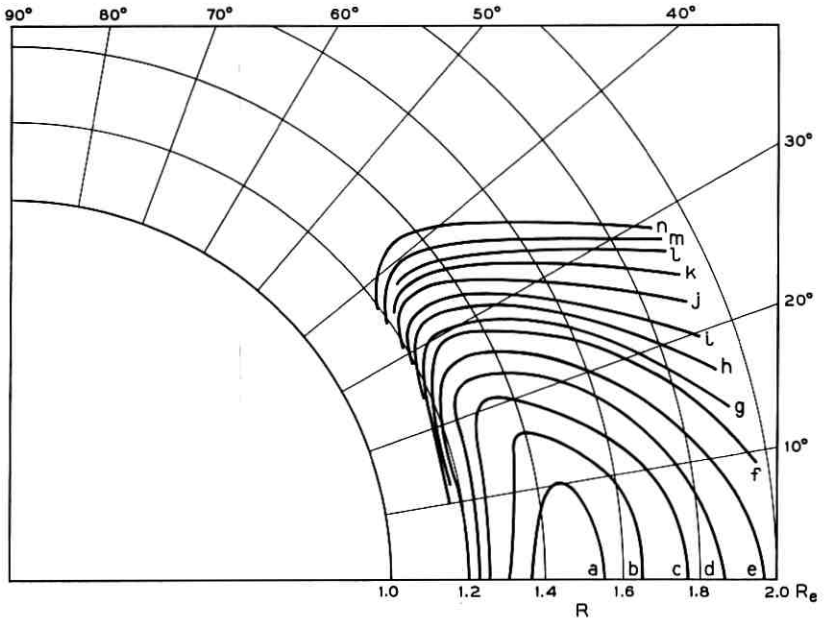

Fig. 18 — Contours of contant *OCR*, protons with energies >50 Mev, days 191 to 294, 1962, plotted in R-λ coordinates. To convert *OCR* to omnidirectional flux (1/cm² sec), add 0.42 to Φ. The range of Φ associated with the contours is: a, 3.2-3.4; b, 3.0-3.2; c, 2.8-3.0; d, 2.6-2.8; e, 2.4-2.6; f, 2.2-2.4; g, 2.0-2.2; h, 1.8-2.0; i, 1.6-1.8; j, 1.4-1.6; k, 1.2-1.4; l, 1.0-1.2; m, 0.8-1.0; n, 0.4-0.6.

$E_0 = 26$ Mev. A fit to the data could have been made with an exponential spectrum of the form[33]

$$N(E) = N_0 \exp(-E/E_c), \tag{4}$$

where N_0 and E_c are constants. However, such a spectrum extrapolates in a very unreasonable way to lower energies, giving far fewer low-energy protons than observed either by the Telstar low-energy proton detector or by detectors on Explorer XV.[24]

With the power law spectrum the value of $n \approx 4.5$ applies over a considerable part of the region beyond the 50-Mev proton maximum, but at smaller L values the spectrum is very much harder and n decreases to a value of about 2. Such a power law variation at low equatorial altitudes seems to be in reasonable agreement with the observations of Freden and White[35] and Naugle and Kniffen.[36]

Using the constants of the spectra as given in Fig. 19, the maximum integral flux of protons with energies >40 Mev is found to be approxi-

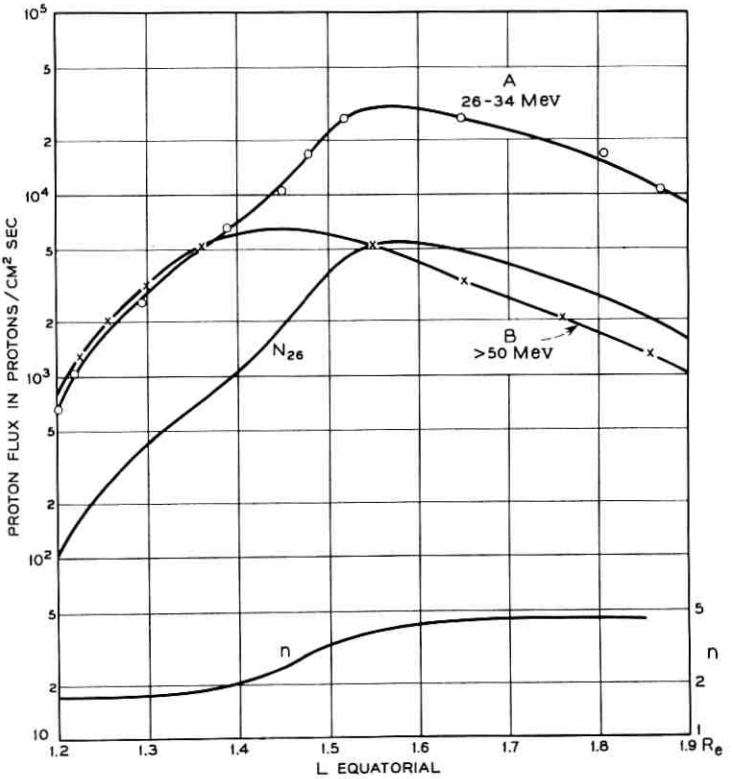

Fig. 19 — Equatorial proton flux. Curve A is for protons in the energy range 26 to 34 Mev, and curve B for protons with energies >50 Mev. n and N_{26} are defined in the text.

mately 1.5×10^4 protons/cm^2 sec, quite close to the historical value of 2×10^4 quoted by Van Allen in 1958[32] for the peak flux in the inner belt.

2.4 *Radiation Exposure of the Satellite*

2.4.1 *Orbital Effects and Method of Calculation*

The radiation exposure of a satellite is an integral along the satellite orbit of the particle flux weighted in accordance with its energy spectrum. The Telstar satellite spends a considerable part of its time in the inner Van Allen belt and thus experiences an unusually rigorous radiation environment. The radiation exposure is far from constant in time, however. The instantaneous exposure varies enormously as the

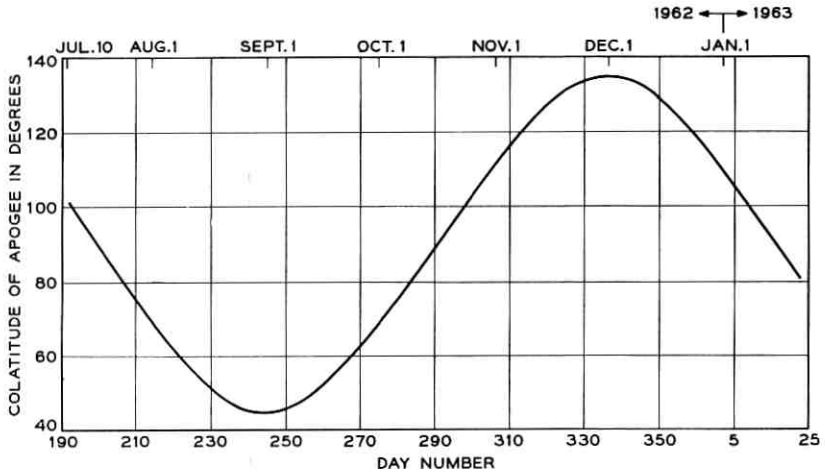

Fig. 20 — The position of apogee colatitude for the Telstar satellite as a function of time.

satellite enters and leaves the region of high intensity in the inner belt. Furthermore, the average exposure over an orbit varies throughout a day because of the geographical asymmetry of the magnetic field that controls the trapped particle distribution. And finally, the average exposure over a period of several days varies as the position of apogee in the orbit precesses. This latter orbital change is shown in Fig. 20, which is a plot of the colatitude of apogee, θ_A, of the Telstar orbit as a function of time. The period of this precession is 181 days, and the maximum and minimum colatitudes are 45 and 135 degrees, corresponding to the 45-degree inclination of the orbit.

To illustrate the wide differences between orbits on a single day, orbits 1 and 6 for day 205 are shown in Fig. 21 in the R-λ space used in displaying the electron and proton distributions. The particles by definition have north-south symmetry in this equivalent dipole representation, but the northern and southern parts of the satellite orbit are far from the same. The differences between the two orbits of the figure near $\lambda = \pm 45°$ are caused primarily by the 11-degree offset of the earth's geomagnetic axis. Near $\lambda = 0°$ and especially at low altitudes, the differences arise from the Brazilian magnetic anomaly. On day 205 of Fig. 21, apogee is near the equator, $\theta_A = 81°$. In contrast, two orbits for day 335, when apogee is at its most southern point, $\theta_A = 135°$, are shown in Fig. 22. These orbital variations from week to week were

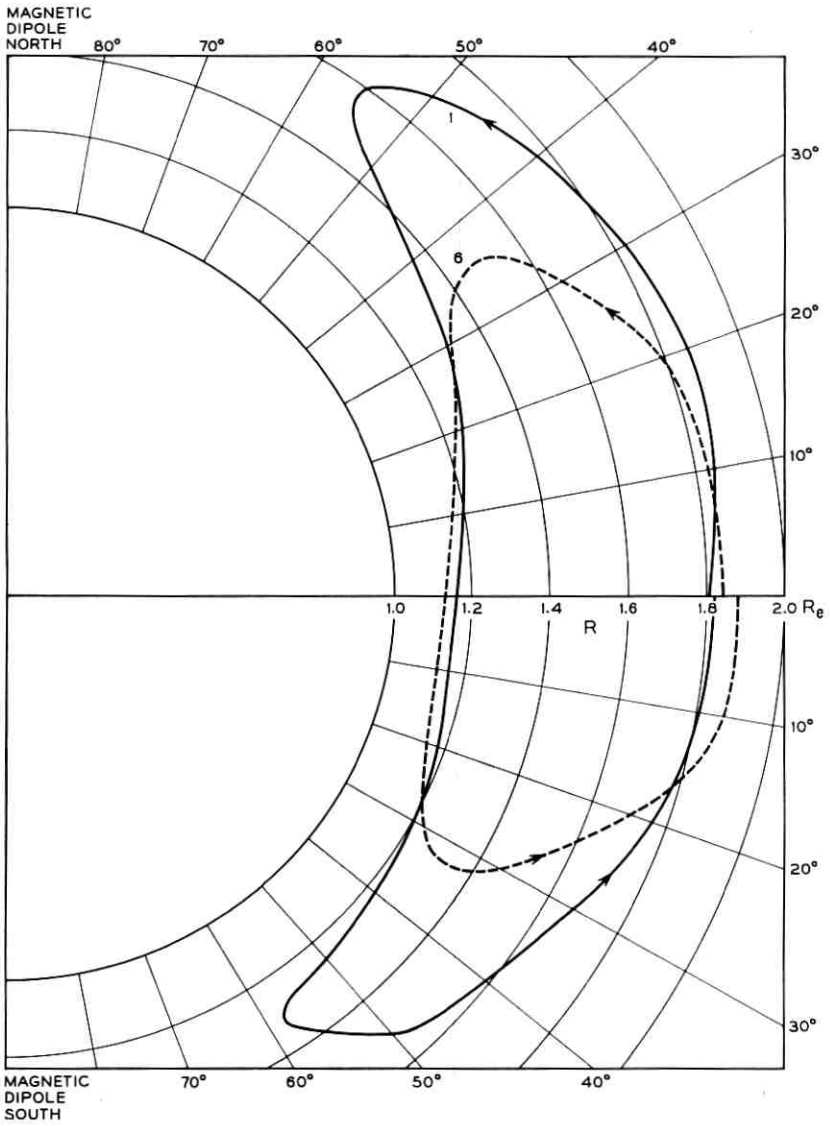

Fig. 21 — Orbits 1 and 6 for day 205, 1962, plotted in R-λ coordinates. Apogee is near the geographic equator.

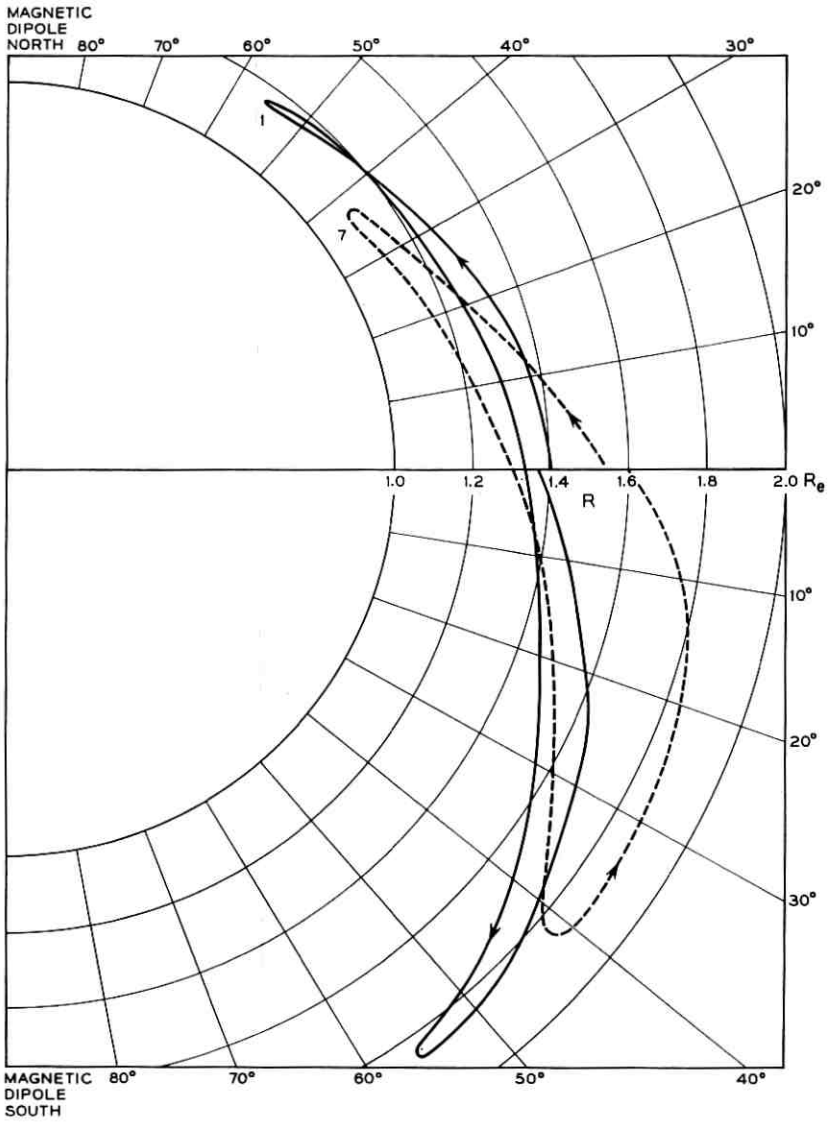

Fig. 22 — Orbits 1 and 7 for day 335, 1962, plotted in R-λ coordinates. Geographically, apogee is at the most southern point in the orbit.

previously noted in connection with regions in B-L space for which data are missing; see Figs. 5-9. The orbital picture is further complicated in computing an integral radiation exposure by the variation in satellite speed along the orbital path, a factor not shown in Figs.

21 and 22. The vehicle spends much more time close to apogee than to perigee. The complex motion of the satellite with respect to the trapped particles makes it necessary to undertake fairly detailed calculations, including transformations to a magnetic coordinate system, in order to find the integrated radiation exposure of the satellite.

The following method has been used. The part of B-L space to which the Telstar satellite is confined has been divided into 620 areas by a grid that is spaced so that the areas are small in the important regions. Thirteen colatitudes of apogee, at 7.5-day intervals, have been selected. For each position of apogee, eighteen equally spaced ascending-node longitudes have been chosen. The fraction of time, T_{ik}, spent in each B-L box has been computed and averaged over the eighteen nodal positions associated with each apogee position, using a Keplerian orbit very close to the Telstar orbit. The step size along the orbit is varied so that the computation is done most accurately in the most critical places. The results of the calculation for $\theta_A = 79.48°$ are shown in Table II. By examining the OCR maps in B-L space, values, OCR_{ik}, appropriate to the days when θ_A had a given value are assigned to the B-L boxes. When necessary a similar procedure is followed for the spectrum, S_{ik}. The operation

$$F = \sum_{i,k} T_{ik} OCR_{ik} S_{ik} \tag{5}$$

is performed. F is now approximately the average flux of all electrons incident on the spacecraft during a one-day period. The calculation is approximate in the sense that the actual orbit, with its continuously varying apogee colatitude and with ascending node longitudes that do not shift by a simple fraction of 360°, has been replaced by a set of closely spaced but discrete orbits. One does not calculate in this way an instantaneous radiation intensity but only an intensity that is very nearly correct over a period of a day or several days. Actually, a more serious inaccuracy is contributed by a lack of detailed knowledge of the particle energy spectrum. This will be described in more detail in connection with specific applications in Sections 3.2 and 3.3.

2.4.2 *Integrated Electron Flux*

Using the method outlined above, the average and cumulative omnidirectional electron flux to which the Telstar spacecraft was exposed have been calculated. The electron flux is obtained from the OCR contours for channel 3 of the electron detector, e.g., those shown in Figs. 10 and 11. These counting rates are multiplied by a factor of 5 to yield the total flux (above 0 energy) under the assumption that the

TABLE II — AVERAGE TIME SPENT BY THE *TELSTAR* SATELLITE IN VARIOUS B-L REGIONS FOR AN APOGEE COLATITUDE OF 79.48°

B_{MIN} gauss. B_{MAX} gauss.	.04 .06	.06 .08	.08 .10	.10 .12	.12 .13	.13 .14	.14 .15	.15 .16	.16 .17	.17 .18	.18 .19	.19 .20	.20 .22	.22 .24	.24 .26	.26 .28	.28 .32	.32 .36	.36 .40	.40 .50
L_{MIN} R_e	L_{MAX} R_e	(Entries are in 0.1 Per cent)																		
1.00	1.05	0	0	0	0	0	0	0	0	0	0	0	0	0	0	0	0	0	0	0
1.05	1.10	0	0	0	0	0	0	0	0	0	0	0	0	1	2	0	0	0	0	0
1.10	1.15	0	0	0	0	0	0	0	0	0	0	0	6	9	3	1	0	0	0	0
1.15	1.20	0	0	0	0	0	0	0	0	0	2	3	13	4	1	2	1	0	0	0
1.20	1.25	0	0	0	0	0	0	0	1	3	5	3	7	3	1	1	1	0	0	0
1.25	1.30	0	0	0	0	0	0	0	1	1	1	4	4	2	1	0	2	0	0	0
1.30	1.35	0	0	0	0	0	0	0	1	1	0	3	5	2	0	1	1	0	0	0
1.35	1.40	0	0	0	0	0	0	0	1	0	0	3	2	2	1	1	1	0	0	0
1.40	1.45	0	0	0	0	0	0	0	1	0	0	3	4	2	0	0	2	1	0	0
1.45	1.50	0	0	0	0	0	0	0	1	0	1	2	4	2	0	0	1	0	0	0
1.50	1.60	0	0	0	0	0	0	0	1	0	3	3	2	3	1	1	2	1	0	0
1.60	1.70	0	0	0	0	0	0	0	1	1	2	1	6	2	2	0	1	2	0	0
1.70	1.80	0	7	0	0	0	0	0	2	1	1	3	3	2	2	0	2	1	0	0
1.80	1.90	102	17	5	0	0	1	2	1	0	2	3	3	2	1	1	0	0	0	0
1.90	2.00	65	27	5	4	3	2	2	0	1	3	3	0	3	0	1	1	0	2	0
2.00	2.10	26	29	4	3	1	1	0	1	4	5	1	1	2	2	3	0	2	1	0
2.10	2.20	12	18	12	3	1	1	0	2	4	2	1	0	0	0	0	0	0	1	0
2.20	2.30	3	17	16	1	1	1	4	4	2	1	1	1	2	1	0	0	0	0	0
2.30	2.40	6	8	9	9	5	4	2	4	1	0	0	1	2	1	1	0	1	0	0
2.40	2.50	3	11	7	4	3	2	1	1	0	0	0	0	0	0	0	0	0	0	0
2.50	2.70	0	7	10	20	3	7	1	2	3	2	1	1	1	4	0	1	0	3	0
2.70	2.90	0	10	8	6	3	0	1	1	1	1	0	0	4	2	0	1	1	1	0
2.90	3.10	0	3	0	4	3	8	1	3	1	1	2	2	0	1	0	0	2	0	0
3.10	3.30	0	4	0	5	0	3	0	1	1	0	2	0	2	0	0	0	0	0	0
3.30	3.50	0	0	3	2	2	0	5	2	2	0	1	0	1	2	0	0	2	0	0
3.50	3.80	0	0	3	0	0	0	0	2	7	1	0	4	0	0	1	2	0	0	0
3.80	4.10	0	0	7	6	0	2	0	0	0	2	0	2	4	0	2	0	4	0	0
4.10	4.40	0	0	0	0	2	0	2	0	0	2	2	4	0	2	0	0	0	0	0
4.40	4.70	0	0	0	3	0	0	0	0	0	0	0	0	0	1	3	0	0	0	0
4.70	5.00	0	0	0	0	3	2	4	0	0	2	0	0	0	0	0	0	0	0	0
5.00	9.99	0	0	0	0	0	0	0	2	0	0	0	0	0	0	0	0	0	0	0

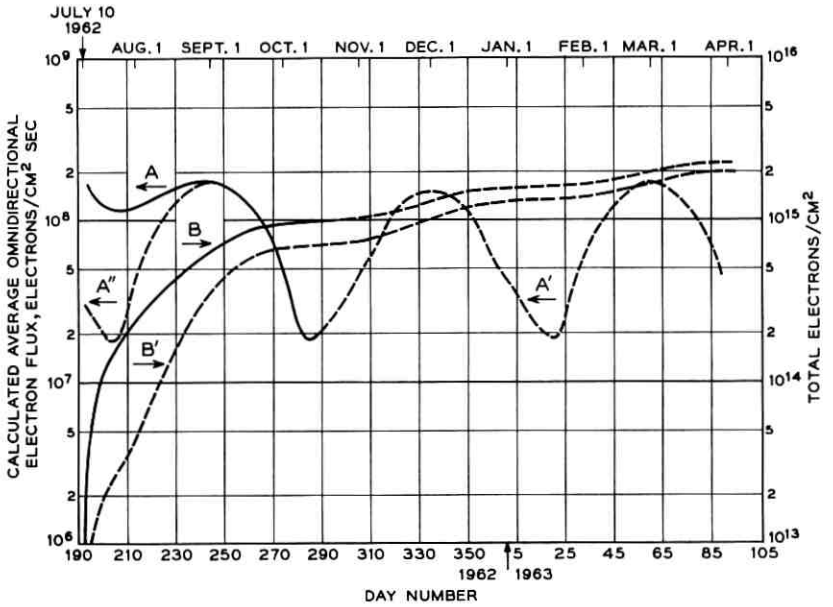

Fig. 23 — The exposure of the Telstar satellite to electrons. A fission beta-decay spectrum is assumed throughout space. The various curves are discussed in Section 2.4.2.

spectrum is everywhere that of fission fragment beta decay. The results are plotted in Fig. 23. When apogee is near the equator, the principal contribution comes from the high-intensity zone above $R = 1.7\ R_e$ and within 15 degrees of the magnetic dipole equator. When apogee is far north and south, the principal contribution comes from the higher-altitude portion of the passage through the equatorial region. In both cases, major contributions are made by regions on the high-altitude slope-off of the inner belt, where the spectrum definitely is softer than a fission spectrum, at least in later months. The total electron exposure as calculated is not substantially in error as far as electrons of 0.5 to 1 Mev are concerned. The total as plotted is probably too low to represent all electrons above 0 energy (or even 100 Kev) because of extra lower-energy electrons that are not shown in channel 3, but on the other hand it overestimates the flux of 1.5- or 2-Mev electrons if one applies to Fig. 23 the fraction of the fission beta spectrum that is appropriate to these higher energies.

The curves A and B represent the observed data from channel 3 with the assumed spectrum. From curve B we deduce that the Telstar

satellite experienced an average omnidirectional flux of 1.2×10^8 electron/cm^2 sec during its first 104 days in orbit. However, we point out that the instantaneous peak flux was 1.2×10^9 electrons/cm^2 sec and that the minimum instantaneous flux was substantially zero.

The curves A′, A″, and B′ make the additional assumption that the situation in mid-October prevailed between launch and March, 1963. The difference between curves A and A″ is due to those electrons which were observed to decay between July and October and hence seem certainly associated with the Starfish test. A large but still ill determined part of the remaining exposure, shown as curves A′, A″ and B′, is also attributable to Starfish electrons which are decaying much more slowly than those on the high-altitude side of the inner belt or in the slot between the inner and outer belts.

Substantial perturbations of the electron distribution were produced by a series of three Russian high-altitude nuclear tests on October 22, 28 and November 1. These additional electrons contributed significantly to the exposure of the satellite during late October and early November, when the exposure due to the natural electrons and those residual from Starfish, as indicated by curve A′, is relatively small. However, the effects of these electrons soon after they were produced were small in comparison with the peak exposure, such as shown by curve A′ for December 1. Furthermore, the Russian electrons disappeared relatively rapidly. The study of the detailed time dependence of the contributions of these three tests has not yet been completed.

2.4.3 *Integrated Proton Flux*

The *OCR* of the omnidirectional proton detectors have also been integrated. The results for protons between 26 and 34 Mev are presented in Fig. 24. Because the proton fluxes displayed so little temporal variation, the extrapolation to April, 1963, is more likely to be valid for protons than for electrons. The average *OCR* for this detector is 1.1×10^3 counts/cm^2 sec. The instantaneous *OCR* has a peak value of 1.5×10^4 counts/cm^2 sec and a minimum of zero. The curve A in this figure best displays the effect of the Brazilian anomaly. When apogee gets sufficiently far north, the orbit begins to go under the most intense region inside contour A of Fig. 17; this causes the dip in the average *OCR* centered at day 244. Owing to the Brazilian anomaly, the average position of the magnetic dipole equator is somewhat south of the geographic equator, and apogee does not get far enough south to make the dip pronounced on day 331. The asymmetry in the curve for the >50-

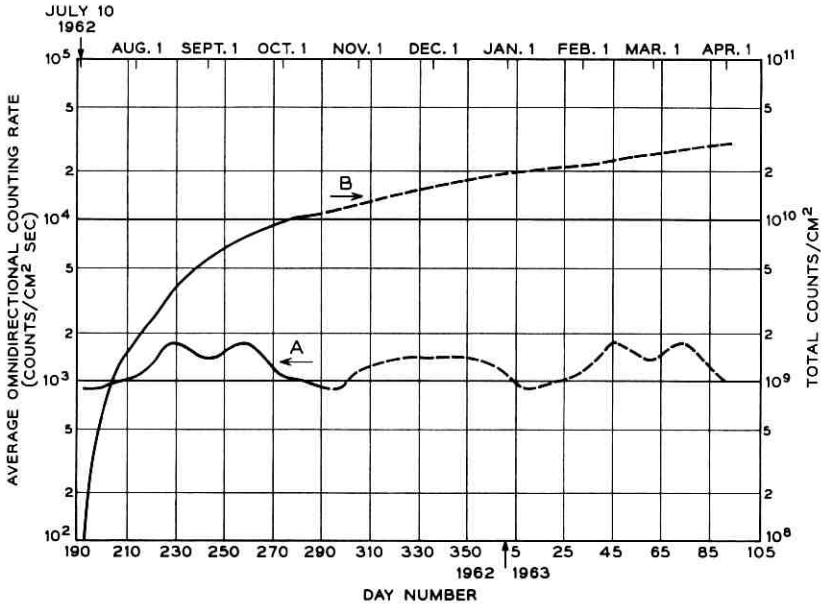

Fig. 24 — The exposure of the Telstar satellite to protons in the energy range 26 to 34 Mev. To convert to flux, multiply scales by 2.1. The curves are discussed in Section 2.4.3.

Mev proton detector is not as noticeable because here, as in the electron case, the central *OCR* contour extends to lower altitudes. The average *OCR* for protons above 50 Mev is 190 counts/cm^2 sec, as may be seen in Fig. 25. The range of observed instantaneous *OCR* is from 0 to 2500 counts/cm^2 sec. The conversion from *OCR* to flux is given in Section 2.3.

III. RADIATION DAMAGE AND SATELLITE COMPONENT EXPOSURE

The effects of radiation on the satellite fall into two broad classes. First, there are effects which arise from collisions of high-energy particles with the atoms of a solid in which sufficient energy may be transferred to create defects in the bulk of the solid. Immediately after a collision, the defects consist of vacancies where atoms are missing from normally occupied positions in the crystal and of interstitial atoms which occupy positions between the normal lattice sites. These defects are often highly mobile in the crystal and may recombine to restore the local crystal perfection or may become associated with one another or with other chemical or structural imperfections in the crystal. It is these combined

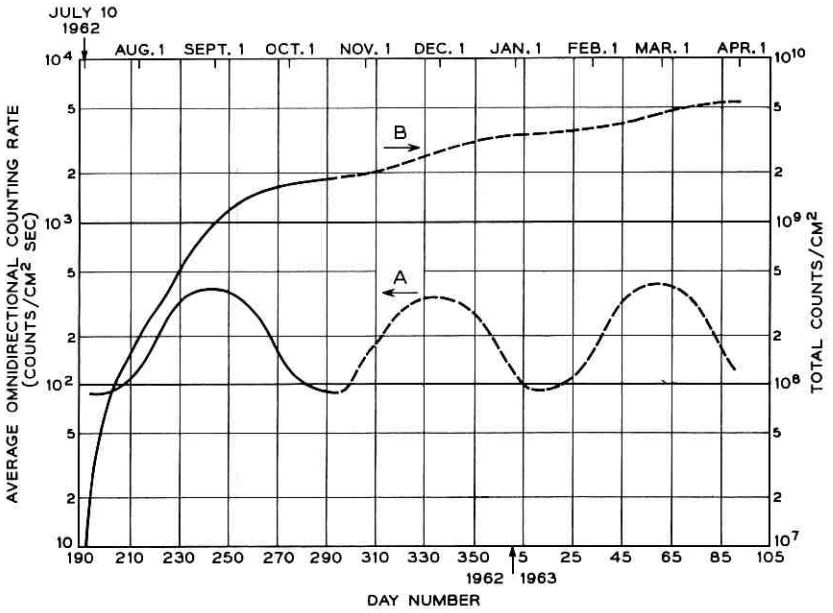

Fig. 25 — The exposure of the Telstar satellite to protons with energies above 50 Mev. To convert to flux, multiply scales by 2.6. The curves are discussed in Section 2.4.3.

centers that are in general stable at room temperature and give rise to radiation damage effects on the electrical, optical and structural properties of the material.[37,38] Such effects are produced in all solids. However, for semiconductor devices to operate, a high degree of perfection is required of semiconductor materials, and therefore radiation damage is usually much more important in semiconductor than in other solid-state materials.

The second broad class of radiation effects is produced by ionization due to high-energy charged particles. The ionization may be in the bulk of a solid and give rise to transient currents or provide electrons or holes that may be trapped at existing chemical or structural defects. The latter case is responsible for much of the coloration of transparent solids by radiation, an effect of negligible importance in the sapphire chosen for shielding the solar cells on the Telstar satellite. The ionization may cause chemical changes in organic plastics with resultant changes in their electrical and mechanical properties, and in the oil of capacitors with a resultant pressure build-up. By choice of materials, these effects have

been reduced to minor significance in the Telstar satellite. The ionization may also occur in gases, where it has been found to be of substantial importance if the gases are closely associated with semiconductor surfaces, as is often the case in encapsulated semiconductor devices. This latter effect, ionization damage to semiconductor devices, was recognized[39] and has proven to be of major importance in the performance of the satellite in space.

In this section of the paper, radiation damage (bulk effects) as observed in the semiconductor devices of the Telstar satellite will be considered in detail. The last parts of this section will discuss ionization to be expected at components in the canister of the satellite. The effects of this ionization on the component performance of the Telstar command decoder are discussed in another paper.[40]

3.1 *Measurements of Radiation Damage in the Satellite*

Radiation damage is measured directly in the solar power plant of the satellite, and in solar cells and specially fabricated transistors carried by the satellite for this experimental purpose. Solar cell results all depend upon the orientation of the sun with respect to the satellite, and thus the measurements of damage will be preceded by a description of the solar aspect determination made by the satellite.

3.1.1 *Solar Aspect*

As described in detail in a preceding paper,[1] the sun's orientation with respect to the satellite is determined by essentially simultaneous measurement of the output of six pre-irradiated silicon solar cells placed with their normals mutually perpendicular. The orientation can be described in terms of two angles: φ, the rotational angle or longitude of the sun in the coordinates of the satellite, and α, the colatitude of the sun measured with respect to the spin axis. Fig. 26 shows a sequence of measurements with the six aspect cells during an orbit on July 17, 1962. Because the spin rate of the satellite is not in general commensurate with the frame time of the telemetry, the particular cells which see the sun most directly change from frame to frame of the telemetry. In the case shown in Fig. 26, during each telemetry frame (approximately one minute), the satellite rotated by a number of complete rotations plus approximately 36 degrees. Thus, from frame to frame the readings gradually work through a sequence of rotational angles. Since the spin rate of the satellite gradually decreases (from its initial rate of approximately 180

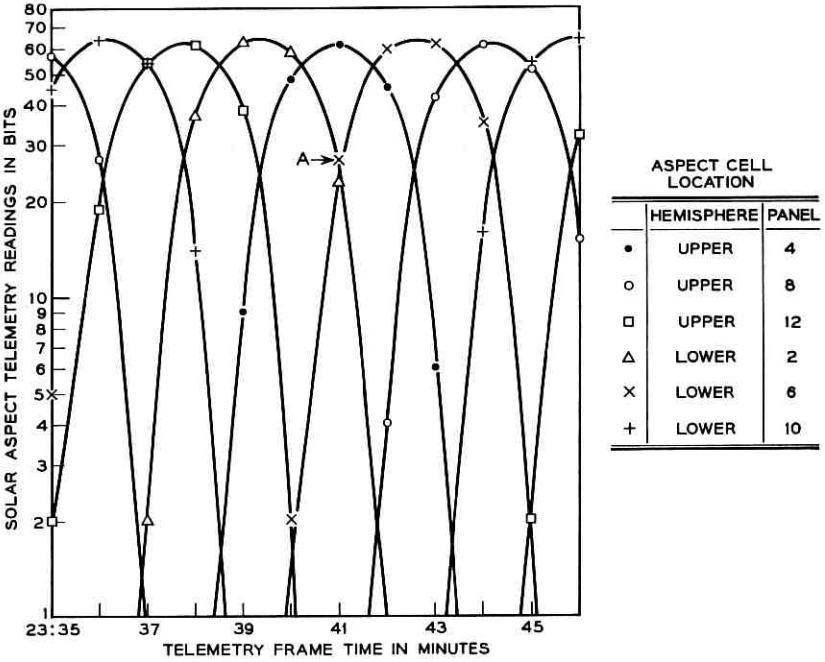

Fig. 26 — Telemetry bit readings of the six solar aspect cells on twelve successive frames of pass 70, July 17, 1962.

rpm at launch), this change in φ from frame to frame also changes. Furthermore, since this change in φ is measured at the end of a large number of complete rotations, the strobing of the solar aspect measurement gives a vernier measure on the rate of decay of the spin of the satellite. The accuracy of the measurement is limited by the accuracy of the telemetry frame time and by the accuracy of the determination of φ in a particular sequence of frames. No further discussion of this facet of the measurement will be included in the present paper.

The accuracy of the determination of the sun's position varies as the satellite rotates. At points such as A in Fig. 26, where three cells are prominently illuminated, α and φ can both readily be determined to within ± 0.5 degree. The data of the figure indicate that the sun is nearly on the equator of the satellite, since the peak outputs of the cells on the upper and lower hemispheres are nearly equal. The lower-hemisphere cells are reproducibly higher, however, and when calculated from these data, α is found to be 91.5 ± 0.5 degrees, measuring from the telemetry antenna end of the satellite.

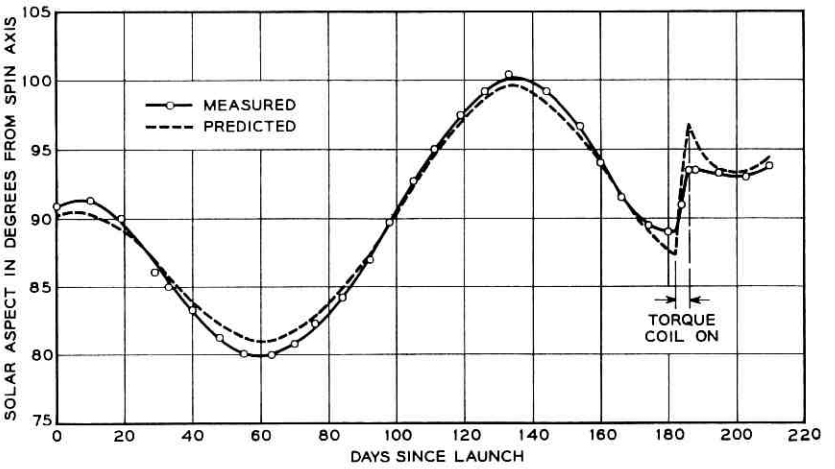

Fig. 27 — The time variation of α, the angle between the spin axis of the satellite and the satellite-sun line, from launch until February 5, 1963. The angle is measured from the telemetry antenna end of the satellite.

The history of the solar aspect of the satellite from launch to February, 1963, is shown in Fig. 27. The sun has been within ± 10 degrees of the equator at all times, a desirable position from the standpoint of temperature uniformity of the satellite and maximum capability of the solar power plant. The predicted curve illustrated here is discussed in an accompanying paper[41] dealing in more detail with satellite performance.

3.1.2 *Solar Power Plant*

Fig. 28 shows the output of the solar power plant of the satellite.[42] Since the distribution of solar cells is not uniform over the surface of the satellite, the telemetry reading which gives a momentary snapshot of the current from the power plant varies with φ and α. The data points of Fig. 28 have been derived from averages over a sequence of readings which, judging from the solar aspect measurements described in Section 3.1.1, represent a complete sampling over all values of φ. In cases for which the spin rate and telemetry frame rate are more nearly commensurate than in Fig. 26, a long sequence of readings will produce a cluster of points near some one or some several rotational angles. These cases have not been used in Fig. 28. Because small changes in the spin rate are reflected as large changes in φ at one-minute intervals, successive passes on the same day will exhibit quite different sampling characteristics. Data have also been selected for a particular battery voltage,

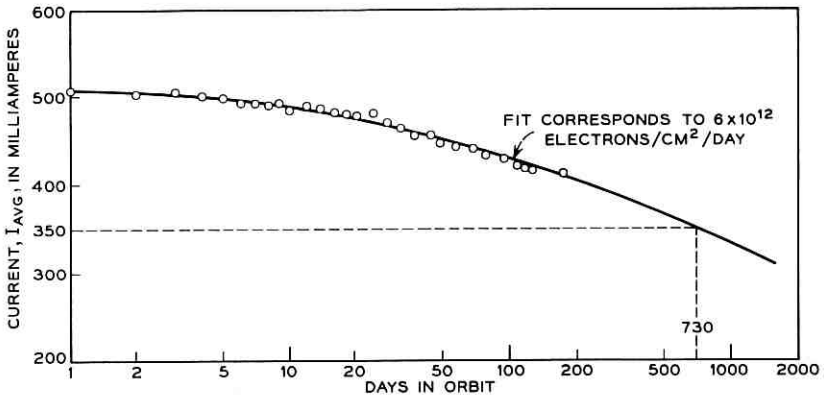

Fig. 28 — The average over the angle φ of the output current of the solar power plant from launch until February, 1963. Corrections have been made for mean solar distance. No detailed temperature corrections or corrections for solar aspect angle have been made in these data. Such corrections are expected to reduce the scatter of the points.

since the current which the power plant supplies depends on the load into which it is working. The chosen voltage corresponds to 0.36 volt/cell in the series solar-cell strings. The solar power plant current, selected in this way and averaged over φ, has been corrected for mean solar distance to give the points plotted.*

The solar power plant output will decrease due to radiation damage of silicon by energetic particles capable of penetrating the 0.3 gram/cm^2 sapphire shielding which covers the solar cells. The observed damage can be expressed in terms of an equivalent flux of 1-Mev electrons which would have produced this damage in the laboratory under conditions of normal incidence and zero shielding. The term "1-Mev equivalent flux" will be used for this measure of damage. The curve fitted through the points of Fig. 28 corresponds to a 1-Mev equivalent flux of 6×10^{12}/cm^2 day. This fitting implies that the damage flux encountered by the satellite is constant in time, in contrast to the oscillatory radiation exposure of the satellite discussed in Section 2.4. The accuracy of the solar cell data does not permit such a conclusion to be drawn, however, and the fit of Fig. 28 represents an equivalent flux averaged over 100 or more days in orbit. The choice of 6×10^{12} in this fit is at least accurate to within a factor of 1.5. The extrapolation of the curve indicates, as shown in the figure, that after two years the solar power plant will have degraded to 68 per cent of its initial performance.

* These considerations are discussed in more detail in Ref. 42.

3.1.3 *Solar Cell Damage*

Three solar cells with different shielding thicknesses were flown to measure radiation damage. Their outputs are sampled at the same time as the outputs of the solar aspect cells, Section 3.1.1, and the damage cells have the same orientation with respect to the sun as the aspect cell on panel 12 of the upper hemisphere of the satellite. Thus, no corrections for angle of illumination are required in recognizing the presence of damage. The ratio of the output currents of the damage-measuring cells to that of the pre-irradiated aspect cell on panel U-12 are shown in Fig. 29. The initial ratios are within ±2 per cent of those anticipated from laboratory calibrations of the spectral response of the cells and calculation of their performance under outer space illumination.

The currents of the initially unirradiated cells degrade with time in orbit and after a few days are ordered in accordance with their shielding thicknesses. The lack of order in the earliest days is due entirely to the slightly different initial outputs of the three individual devices. The shapes of the three curves are very similar, although there is some scatter in the data due in large measure to the approximately ±1 per cent digitizing accuracy of the telemetry. The shapes of the curves are not what would be expected from a constant particle exposure and indicate a minimum in the damage rate between approximately 70 and 110 days after launch. This corresponds reasonably well with the minima in radiation exposure shown on Figs. 23 to 25. The damage sensitivity

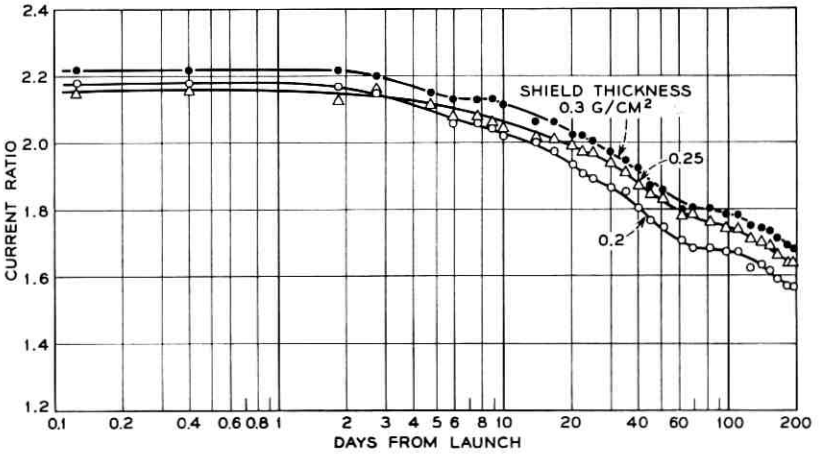

Fig. 29 — The ratios of the output currents of the radiation damage solar cells to the pre-irradiated aspect cell on satellite panel upper 12.

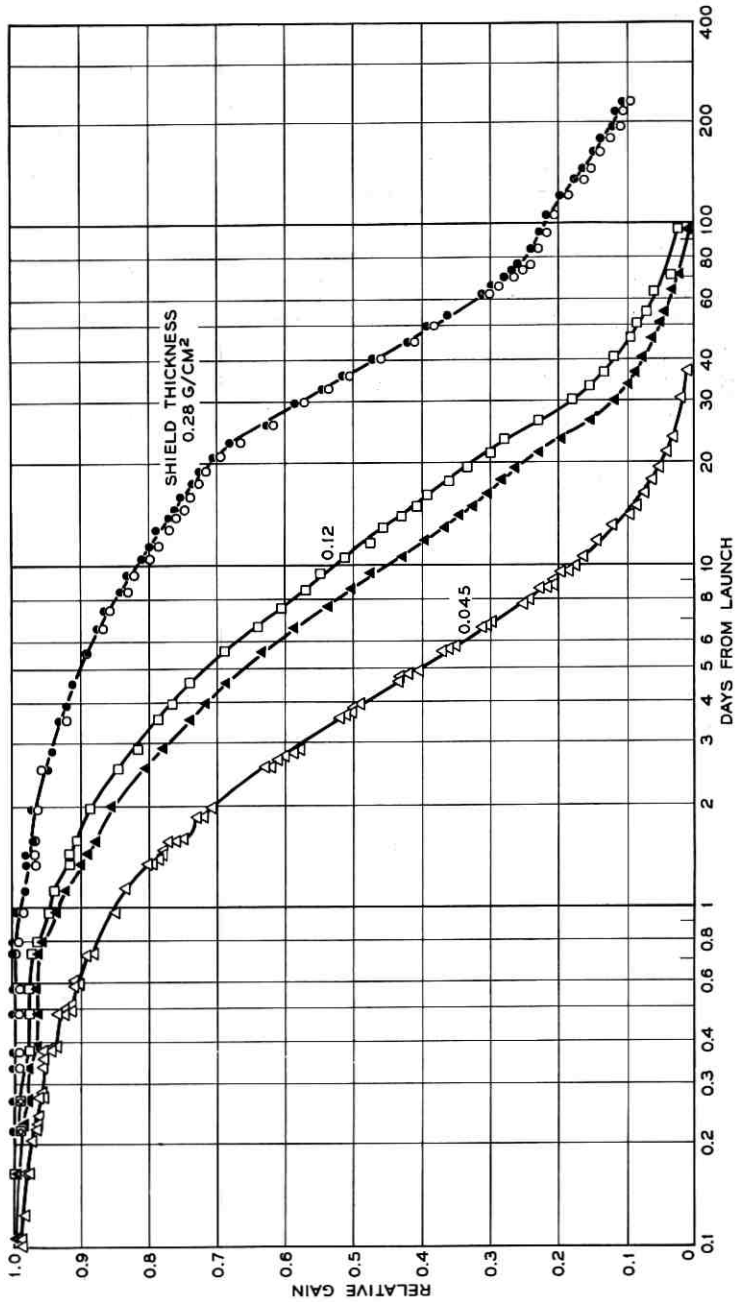

Fig. 30 — The relative gains of the radiation damage transistors as a function of time.

of the 0.20 and 0.30 gram/cm² shielded devices differs by approximately a factor of 2, with the 0.25 gram/cm² shielded cell falling between these extremes.

3.1.4 *Damage Transistors*

A group of specially fabricated n-p-n transistors with unusually wide base regions provides an independent measure of radiation damage to silicon with advantages in comparison to solar cells that light is non-essential and that sensitivity to damage is quite high. These devices are described in a previous paper.[1] The common-base current gain of these transistors is directly related to the lifetime of holes in the p-type base region and thus to the additional recombination centers added by radiation damage. This is the same property which is of major importance to damage in solar cells.

Fig. 30 shows the current gain of the transistors, normalized by their initial gain values. The initial gain ranged for this group of devices between 0.40 and 0.48, but examination of the theory indicates that a normalized gain scale retains very little sensitivity to the actual initial gain values. Five devices provide the essential data of Fig. 30, two each at two shield thicknesses and one at a third. The shield of these transistors is made up partly (and in the most lightly shielded case, totally) of the 3-mil Kovar lid of an encapsulating can and partly of additional aluminum. The thickness indicated on the curves is the aluminum shielding which would be equivalent to the sum of these, taking into account the relative mass stopping power of the two materials for protons.

All of the curves of Fig. 30 have similar S-shapes. If the devices followed a simple form of the theory, the curves should be closely related to the hyperbolic secant of the square root of the damaging flux, or if the flux is constant in time, to the square root of the abscissa of Fig. 30. This is only very roughly the case. In the 0.045 gram/cm² shielded device, the decrease observed during the first two days in orbit exhibits some clear downward steps. These steps are larger than those to be expected from changes of the telemetry reading by a single bit. They are associated with passages of the satellite through the inner radiation belt. The separation of the steps is a minimum of about 0.1 day, or approximately the orbital period of the satellite. Similar changes cannot be discerned beyond two days in orbit for this transistor or at any time for the more heavily shielded devices. This is a result in both cases of too low a sensitivity to detect such behavior, although it must occur. On the most heavily shielded pair of transistors there is a definite indica-

tion that the damage rate increases in the region between 25 and 70 days, decreases between 80 and 110 days, and increases again at longer times. This is suggestive of the oscillations in radiation exposure illustrated in Figs. 23 to 25. The more lightly shielded devices have been so severely degraded by these times that it is not possible to draw similar conclusions from their data. The relative damage sensitivity of the devices, as represented by their separation on the log time scale, varies only a small amount for relative gains between 0.9 and 0.2. Comparing the least and most heavily shielded devices, these ratios range from approximately 9 to 12, with the larger number being clearly too high because of the jog in the curve between 80 and 110 days. The average response of the intermediate-shielded transistors, compared with the heavily shielded pair, shows a relative sensitivity to radiation of between a factor of 3.5 and 4.5 over this same range in normalized gain. The effective damaging flux versus time could be deduced for each of the devices essentially by differentiation of the plotted curves. The data do not seem to be capable of providing this detailed a result, however, and although the variations in slope of the curves are evident as noted above, the magnitude of these variations cannot be deduced with any significant accuracy. The data have been used to specify the relative effectiveness of shielding or the relative sensitivity of differently shielded devices to radiation damage in the Telstar orbit.

3.1.5 *Composite Damage vs Shielding*

The results of the solar cell damage and transistor damage experiments have been combined in Fig. 31. The damage rate for the 0.30 gram/cm^2 shielded solar cell has been selected as unity and the other solar cells referred to it. The most heavily shielded transistors (0.28 gram/cm^2) have been placed at an ordinate interpolated between the 0.30 and 0.25 gram/cm^2 solar cell results. The other transistors have been placed by reference to the most heavily shielded pair. The increase in damage rate with decreasing shielding in the Telstar orbit is more than a factor of 10 over the range examined. This range extends from the sapphire shield of the Telstar power plant to shielding approximately equivalent to the 6-mil glass microsheet often used in the solar power supplies of lower-altitude satellites. If very thin solar cell shields had been used on the Telstar satellite, the two-year extrapolated performance of the power plant would have been realized in about 2.5 months. Furthermore, if p-on-n rather than n-on-p solar cells had been used in the power plant, this extrapolated end-of-life power would have been reached

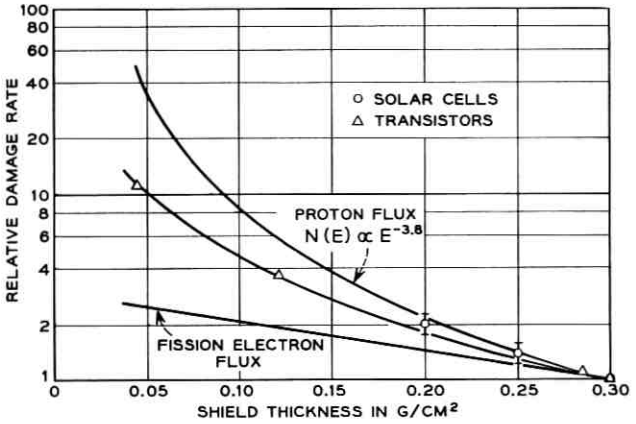

Fig. 31 — The composite results for radiation damage rate vs shielding thickness as determined from the solar cell and transistor damage experiments.

after about two or three weeks in space. The increase in damage with decrease in shielding can arise from either the proton or the electron component of the radiation environment. The two remaining curves of Fig. 31 bear on this question and will be discussed in detail in Section 3.2.3.

3.2 *Correlation of Particle Exposure and Observed Damage*

In this section the effects of the Van Allen belt particles on damaging n-on-p silicon solar cells will be considered, first in general and finally specifically in terms of the radiation exposure of the Telstar satellite as mapped out by its particle detectors and computed by integrating over the satellite orbit.

3.2.1 *Proton Damage vs Energy and Shielding*

A great deal of experimental data has been obtained on the changes in characteristics of n-on-p solar cells under bombardment by electrons and protons of different energies.[43-46] The experiments have generally been carried out with particles brought in at normal incidence to unshielded solar cells. These data, together with an understanding of the penetration characteristics of particles through shield materials, provide the basis for constructing the equivalent damage flux in the sense of Section 3.1.2 for any particle energy distribution and shielding configuration of a solar cell array.

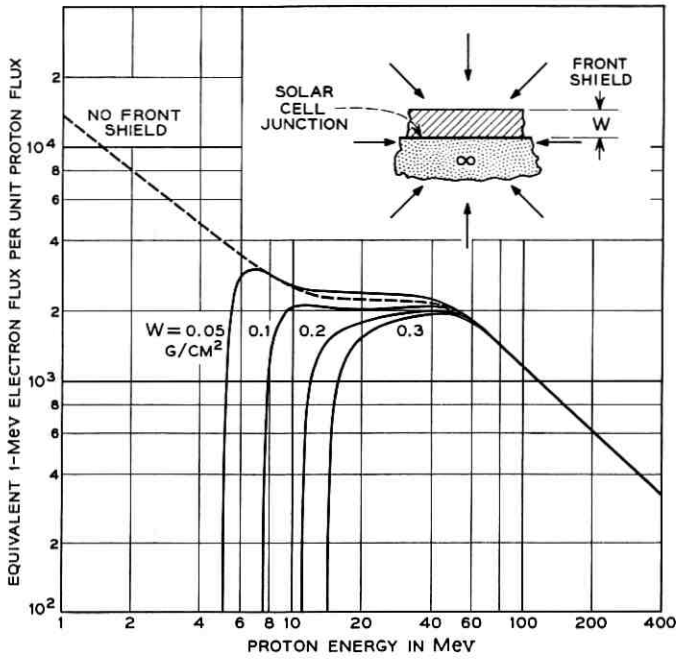

Fig. 32 — The damage-equivalent 1-Mev electron flux as a function of the energy of a monoenergetic isotropic flux of protons incident on n-on-p solar cells with various front shielding. The back shield is assumed to be infinitely thick.

Fig. 32 shows the 1-Mev electron flux equivalent in damage to a monoenergetic isotropic proton flux at different energies and for different shielding thicknesses. The curve for "no front shield" is a smooth curve with a shape determined by data obtained at four different proton particle accelerators and at seventeen different energies over the energy range between 1.4 and 135 Mev. It has been extrapolated with only minor uncertainty at both ends, although particles in the extrapolated extremes have a negligible effect on damage in the Telstar satellite case. The absolute ordinate scale for this curve differs from the data by exactly a factor of 2. As noted in the inset to the figure, the incident flux is assumed to be omnidirectional and uniform, and in all cases the solar cell is considered to have effectively infinite shielding on the back. This represents the actual situation in the Telstar solar power plant quite well. In this case, only one-half of all the protons in the incident flux can reach the solar cell, hence the factor of 2. The simplicity of this factor involves another approximation. Particles arriving at non-normal

incidence have longer paths in the solar cell and as a result create proportionately more defects in the radiation-sensitive thickness of the device. This introduces a $1/\cos\theta$ factor, where θ is the angle of particle incidence, which just cancels the $\cos\theta$ factor that reduces the proton flux because of the change in projected area of the device at an angle θ. As long as the sensitive thickness, t, is small enough so that $t/\cos\theta$ is small compared with the proton range, this approximation is good. At very low proton energies and at large angles of incidence, however, this approximation breaks down. For the sensitive thickness of the n-on-p solar cells used in the Telstar power plant, this approximation begins to be poor below about 5 Mev. One final reservation needs to be made concerning these data. The solar cell property that is being affected by the radiation damage in these experiments is the diffusion length for electrons in the p-type silicon base of the solar cell. This property controls the efficiency with which hole-electron pairs created by light in the base material can reach the p-n junction and contribute current to an external load.[44] This property change exhibits itself directly in a decrease in the short-circuit current of solar cells as a result of radiation. This effect is the primary cause of degradation in solar cell performance in the Telstar satellite. It is not, however, the only effect that occurs. There is a change in junction impedance that shows up as a decrease in open-circuit voltage, and there is a change in the temperature coefficient of the solar cell because of the introduction of new recombination centers. Although these are of minor importance in the Telstar case, they are not always of minor importance for other solar power plant designs. In particular, recent experiments have shown very severe damage to the junction impedance by very low energy, <1-Mev protons.[46] For unshielded solar power plants and possibly for very lightly shielded cases as well, this effect could be of major significance. Furthermore, if the power plant has not been designed for maximum power after radiation damage, including the modified temperature coefficient of the solar cells, the particular operating point may emphasize the changes in junction voltage.[42]

The shape of the basic proton energy dependence of damage, as illustrated by the upper curve of Fig. 32, is still not quantitatively understood. The straight line portions at low and high energies have slopes that agree very well with the theory of atomic displacements[47] by heavy charged particles. The offset in these two line segments, produced by the nearly energy-independent portion between about 10 and 40 Mev is, however, still a subject of discussion.[45,48,49] The same energy dependence, but with a difference in absolute magnitude, is also found for

proton damage in p-on-n solar cells. The shape seems most likely to be determined by details of the short-range interaction of energetic protons with atoms of the silicon lattice.

Starting with the upper curve of Fig. 32, the other curves in the figure have been generated by machine computation, taking into account the penetration properties of protons. For each shield thickness, the equivalent damage flux rises sharply with increasing proton energy as the protons are capable of penetrating the shield. The curves then join with the unshielded curve at higher energies. One might expect that because lower-energy protons are more damaging, the introduction of shielding, which would reduce the proton energy for those protons capable of penetrating the shield, might increase rather than decrease the damage. However, because the protons are incident over all angles, the very severe limitation of the solid angle available to protons that go through the shield and have a small residual energy reduces what must be a real effect to relative unimportance. The effect does appear as a small crossing of the equivalent flux curves for the unshielded and most lightly shielded cases. The Telstar radiation damage experiments discussed in Section 3.1 covered just the range of shields illustrated in Fig. 32. The main solar power plant with 0.3 gram/cm^2 sapphire shielding is sensitive only to protons of more than 15 Mev. The most lightly shielded damage transistors respond to protons of more than 5 Mev. Because the damage per particle is high at lower energy, and because there are more protons in the Telstar orbit with lower energies, a reduction in shielding is expected to effect a large increase in damage.

3.2.2 *Electron Damage vs Energy and Shielding*

Fig. 33 shows a set of curves for electron damage having the same significance as those for protons of Fig. 32. These curves are based on measurements made of damage at different angles of incidence and thickness of shielding with electrons up to 3 Mev.[50] The uniformity in variation of the results with the extrapolated range of electrons has permitted extension of the shielding calculations to higher energies. In all cases the damage increases with increasing electron energy in contrast to the decrease with increasing proton energy. For the "no front shield" curve, the rapid fall-off below 1 Mev reflects the fact that electrons are relatively inefficient in moving atoms in the silicon crystal to produce damaging defects and at low energies become nearly incapable of transferring enough energy to the atoms for them to be displaced. The shape of the curve is very roughly in accord with theoretical expectation below

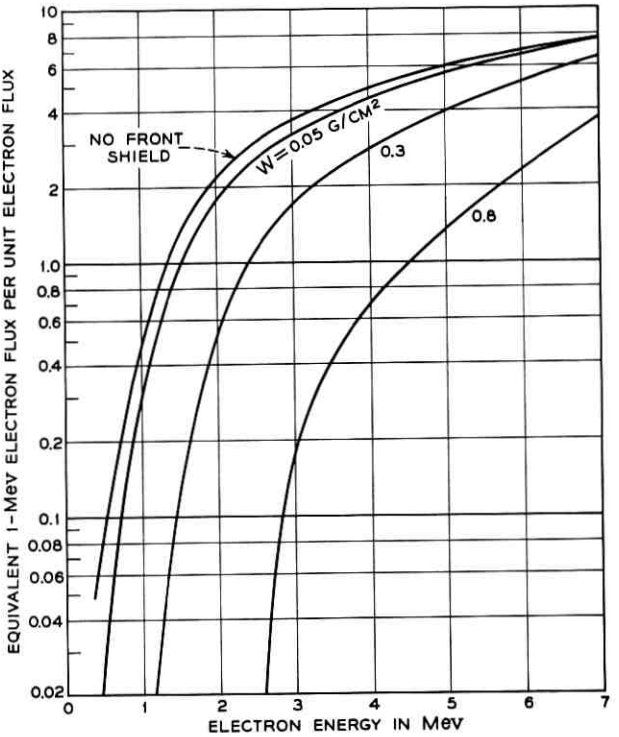

Fig. 33 — The damage-equivalent 1-Mev electron flux as a function of the energy of a monoenergetic isotropic flux of electrons incident on n-on-p solar cells with various front shielding. The back shield is assumed to be infinitely thick.

1 Mev. Above 1 Mev the simple theory of atomic displacement predicts that the curve should flatten out without much further increase at higher energies.[47] The experimental data from which the curve was drawn, however, show more than a factor of 10 increase between 1 and 7 Mev.* The situation for p-on-n solar cell damage is quite different in this respect, the increase above 1 Mev being much more nearly in accord with the simple theory. Apparently the high damage efficiency for high-energy electrons in p-type silicon is due to the formation of a different type of damage defect in the crystal which is very efficient as a recombination center. It is plausible that this new defect is a divacancy.[52]

The equivalent 1-Mev damage flux for 1-Mev electrons is 0.5 in Fig.

* The data above 3 Mev for no front shield are due to J. M. Denney and R. G. Downing, Ref. 51.

33 because of rejection of half of the electrons in an omnidirectional flux by the assumed infinite back shielding. There is an additional effect of reflection of electrons (back scattering) from the surface of the silicon for high angles of incidence that tends to reduce the value to less than 0.5, but this effect is quite small. The Telstar solar power plant, with 0.3 gram/cm^2 shielding, begins to be severely damaged by electrons in the 1- to 2-Mev region, while transistors shielded by 0.045 gram/cm^2 are similarly damaged by electrons of 0.5 to 1.0 Mev energy. Even for these lightest shields, electrons below 0.5 Mev become rapidly insignificant.

3.2.3 *Composite Damage from the Satellite Exposure*

Two factors in the Telstar radiation damage results will be considered in this section: first the damage vs shielding thickness of Fig. 31, and second the absolute magnitude of the damage to the solar power plant as described in Section 3.1.2. It is evident from the curves of Figs. 32 and 33 that the energy spectra of the protons and electrons encountered by the satellite are of enormous importance in both of these respects.

The proton spectrum varies with position in space as discussed in Section 2.3.2, and this spectrum change could have been included in carrying out the initial orbital integrals. However, from the 100-day average exposure of the 26 to 34 Mev protons, Fig. 24, and the >50-Mev protons, Fig. 25, we have instead deduced an average spectrum for the exposure. This average spectrum has the same significance as the spectrum derived for any single point in space. It is characterized by (1) in Section 2.3.2 with $n = 3.8$, a value which is intermediate between the $n \approx 2$ for the heart of the inner belt and $n \approx 4.5$ for the outer side of the inner belt. The average spectrum has been derived over approximately half a period of the precession of the line of apsides, Fig. 20; and since the proton flux is essentially constant in time, the average should reflect the situation for longer times as well.

The spectrum above has been folded through the curves of Fig. 32 to obtain the dependence of the proton damage on shielding thickness. The result is the upper curve of Fig. 31, which has been normalized to the 0.3 gram/cm^2 point. This curve asserts that if the damage at 0.3 gram/cm^2 shielding is due entirely to protons, then the damage should increase at thinner shields as shown. The actual observations lie everywhere below this computed curve, suggesting tentatively that protons may not be responsible for all the damage at 0.3 gram/cm^2. Because of the extrapolation involved in including protons as low as 5 Mev in energy, the calculation for lower shield thicknesses becomes increasingly

uncertain. However, from an as yet incomplete analysis of Telstar and Explorer XV low-energy proton data, the 5-Mev proton exposure derived from the average spectrum seems to be correct to within approximately a factor of 2.

Because of the very important contribution of high-energy electrons to the damage and the inability of the Telstar electron detector to specify their spectrum above 1 Mev, the electron case is more difficult. There is no doubt that a substantial part of the Telstar electron exposure came from regions where the electron spectrum was characteristic of fission beta decay (Section 2.2.2). However, a substantial part of its exposure also came from regions in which there is little doubt that the spectrum contained a smaller fraction of high-energy electrons than the fission spectrum. For lack of more complete knowledge, we have assumed the spectrum is fission-like throughout and recognize that this overestimates the high-energy part of the average electron spectrum. Folding this spectrum through the curve of Fig. 33, the lowest curve of Fig. 31 is obtained. This curve is fitted, as in the proton case above, at the 0.3 gram/cm^2 point under the assumption that at that point all the damage is due to electrons with a fission spectrum. In this case the calculation falls everywhere below the observations. The calculated curve is relatively flat because fission electrons are so energetic. The electron spectrum could, of course, be adjusted to fit the actual observations by adding electrons between 0.5 and 1.0 Mev. However, this is the energy range in which the Telstar electron detector is measuring the flux of particles, and there are altogether too few electrons under the assumption of such a soft spectrum to allow electrons to contribute in a major way to the damage at any thickness of shielding.

The fact that the observations fall between the electron and proton predictions suggests that the actual situation contains important contributions from both types of particles. A half-and-half sharing of the damage at 0.3 gram/cm^2 nearly accounts for the points at lesser shielding. For the thinnest shield, such a computation gives a result a factor of approximately 2 above the point; however, this is the region in which the proton damage is subject to an uncertainty of about this magnitude.

Using the same spectral assumptions discussed above and the computed average of the particle exposure of the satellite, Figs. 23 to 25, the absolute damage to be expected in the solar power plant can be obtained. The damage from the proton exposure averaged over 100 days in orbit is found to be equivalent to that which would be produced by 3×10^{12} 1-Mev electrons/cm^2 day at normal incidence on bare n-on-p solar cells. A similar calculation for electrons gives the same results, although in this case the spectral assumption is such as to overestimate

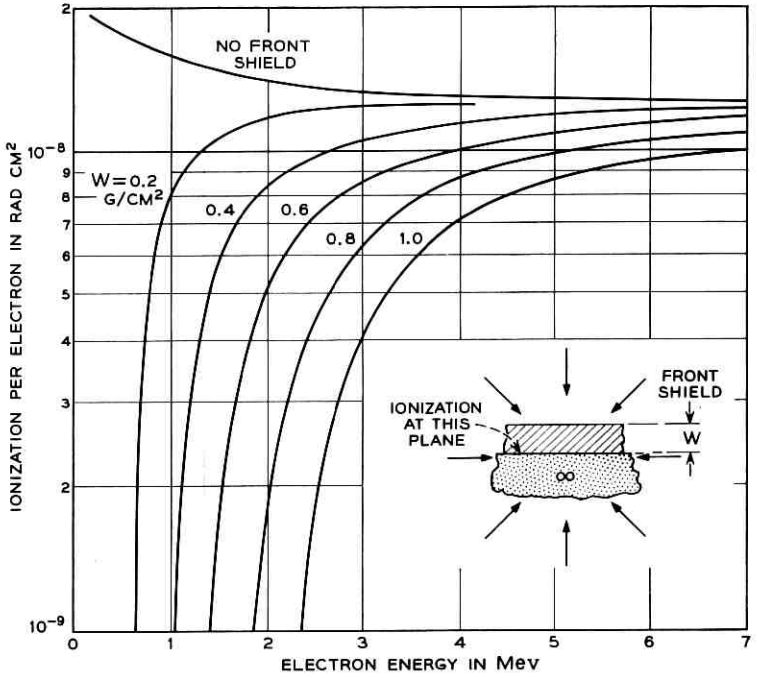

Fig. 34 — Ionization produced by a monoenergetic isotropic flux of electrons behind various thicknesses of front shielding. The back shield is assumed to be infinitely thick.

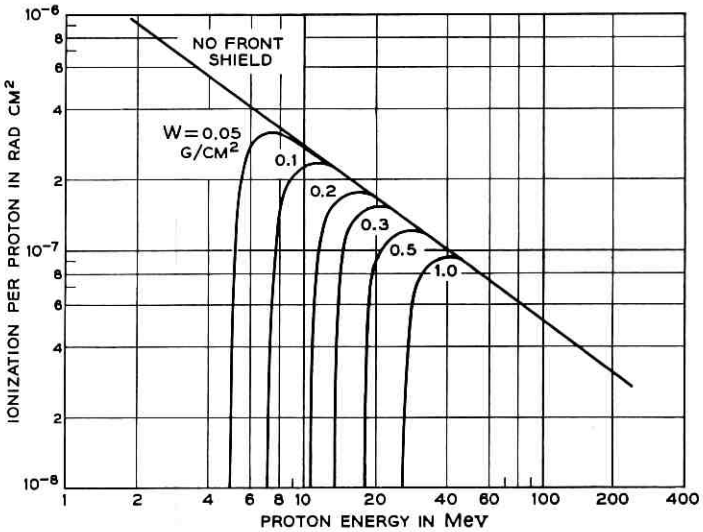

Fig. 35 — Ionization produced by a monoenergetic isotropic flux of protons behind various thicknessess of front shielding. The back shield is assumed to be infinitely thick.

the electron damage. To the accuracy with which this calculation has presently been carried out, it is possible to account for the observed damage by an equivalent 1-Mev electron flux of 6×10^{12}/cm^2 day, half of which is produced by protons and half by electrons. This composite also provides a satisfactory fit to the dependence of damage on shielding thickness. The electron contribution in this calculation is higher than that quoted in an earlier paper[18] because recently measured damage by high-energy electrons to n-on-p solar cells is considerably greater than had been anticipated from measurements at lower energies which were used in the earlier computation.

3.3 *Radiation of Circuit Components in the Satellite Canister*

The calculation of the radiation exposure of the satellite has made it possible to explain the changes in characteristics that have been observed in the silicon solar cells and the closely related damage transistors. In this section we will examine the exposure from the standpoint of the ionization (rather than the bulk semiconductor damage) it produces under different thicknesses of shielding. The results are applicable, for example, to ionization damage in the transistors of the Telstar command decoder.

3.3.1 *Ionization Due to Electrons and Protons*

Fig. 34 shows the ionization as a function of electron energy in an isotropic monoenergetic electron flux. The geometry of the case considered is indicated in the inset to the figure. A typical point on this set of curves is to be interpreted as follows. In an omnidirectional flux of 10^7 2-Mev electrons/cm^2 sec incident on a semi-infinite slab of material, the ionization level would be $5 \times 10^{-9} \times 10^7$ rads/sec or 1.8×10^2 rads/hr at a depth of 0.6 gram/cm^2.

Fig. 35 shows a similar set of curves for protons. There is more ionization per particle in this case because the protons are not minimum-ionizing. Beyond the right-hand extreme of the proton curves, the ionization converges to the same value per particle as for the electrons, the protons now being relativistic in velocity and minimum-ionizing in their interaction with materials.

3.3.2 *Composite Ionization from the Integrated Satellite Exposure*

With the same average particle spectra as used in Section 3.2.3 to compute the radiation damage to solar cells, the ionization due to elec-

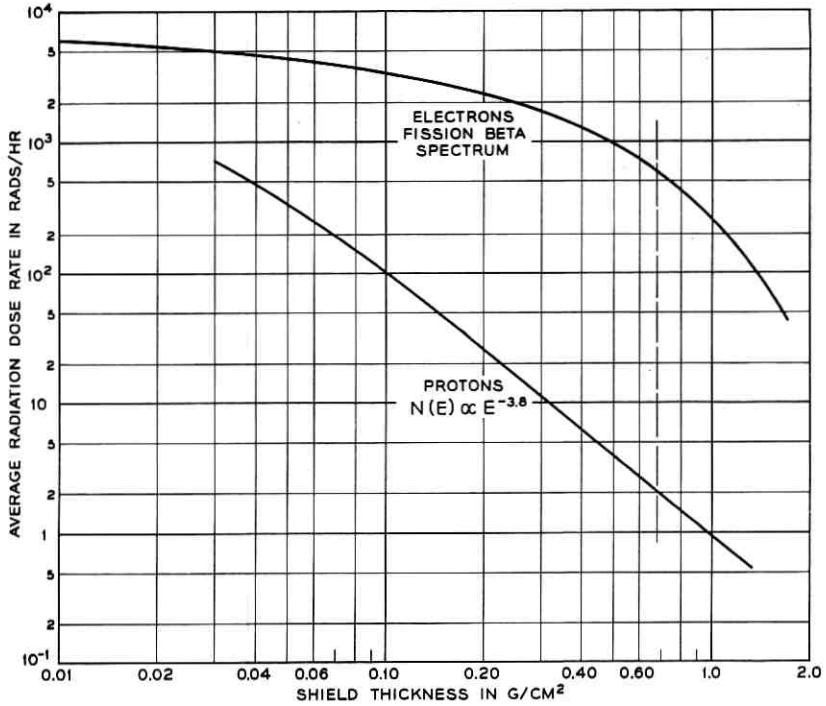

Fig. 36 — Average radiation dose rate vs shielding thickness for the average proton and electron exposure of the satellite.

trons and protons has been derived from the curves of Figs. 34 and 35. The results are shown in Fig. 36. At a shielding thickness of 0.68 gram/cm² (0.1 inch of aluminum, the approximate location of the Telstar decoder transistors) only protons of >20 Mev and electrons of >1.5 Mev are important. At this thickness the electron contribution to the radiation is about 600 rads/hr compared with 2 rads/hr from the protons. The proton-produced intensity is nearly what had been expected before launch, but the more than two orders of magnitude additional ionization contributed by the penetrating electrons were totally unexpected and were responsible for the failure of the Telstar command decoder.[40]

IV. ACKNOWLEDGMENT

We are deeply appreciative of the efforts of many people who have contributed greatly to this work. In particular we are grateful to Miss

E. M. Engert, who had a major role in the data reduction; Mrs. M. F. Robbins, who wrote many of the plot programs; R. L. Stickle, who decommutated the telemetry data, and Mrs. P. L. Gibbs, who edited it; L. C. Thomas, who supplied the satellite spin axis orientation and most of the ephemeris, and F. T. Geyling and G. J. Miron, who supplied the remainder; D. B. Cuttriss, who reduced the solar power plant data; D. W. Hill, who organized the program for reduction of solar aspect data; and L. V. Medford, who carried out this reduction as well as that for the radiation damage solar cells and transistors.

We especially acknowledge the participation of the NASA world-wide tracking network which recorded more than half of the telemetry acquired from the Telstar satellite.

REFERENCES

1. Brown, W. L., Buck, T. M., Medford, L. V., Thomas, E. W., Gummel, H. K., Miller, G. L., and Smits, F. M. The Spacecraft Radiation Experiment, B.S.T.J., this issue, p. 899.
2. Welch, J. A., Jr., and Whitaker, W. A., Theory of Geomagnetically Trapped Electrons from an Artificial Source, J. Geophys. Res., **64,** 1959, p. 909.
3. Northrop, T. G., and Teller, E., Stability of the Adiabatic Motion of Charged Particles in the Earth's Field, Phys. Rev., **117,** 1960, p. 215.
4. Northrop, T. G., The Guiding Center Approximation to Charged Particle Motion, Ann. Phys., **15,** 1961, p. 79, and references therein.
5. Hess, W. N., Canfield, E. H., and Lingenfelter, R. E., Cosmic Ray Neutron Demography, J. Geophys. Res., **66,** 1961, p. 665.
6. Dessler, A. J., and Karplus, R., Some Properties of the Van Allen Radiation, Phys. Rev. Letters, **4,** 1960, p. 271.
7. Walt, M., and MacDonald, W. M., Diffusion of Electrons in the Van Allen Radiation Belt, J. Geophys. Res., **67,** 1962, p. 5013.
8. Welch, J. A., Jr., Kaufmann, R. L., and Hess, W. N., Trapped Electron Time Histories for $L = 1.18$ to $L = 1.30$, J. Geophys. Res., **68,** 1963, p. 685.
9. Ray, E. C., On the Theory of Protons Trapped in the Earth's Magnetic Field, J. Geophys. Res., **65,** 1960, p. 1125.
10. Lenchek, A. M., and Singer, S. F., Geomagnetically Trapped Protons from Cosmic-Ray Albedo Neutrons, J. Geophys. Res., **67,** 1962, p. 1263.
11. Pizzella, G., McIlwain, C. E., and Van Allen, J. A., Time Variations of Intensity in the Earth's Inner Radiation Zone, October 1959 through December 1960, J. Geophys. Res., **67,** 1962, p. 1235.
12. Kaufmann, R., Experimental Tests for the Acceleration of Trapped Particles, J. Geophys. Res., **68,** 1963, p. 371.
13. O'Brien, B. J., A Large Diurnal Variation of the Geomagnetically Trapped Radiation, J. Geophys. Res., **68,** 1963, p. 989.
14. O'Brien, B. J., Direct Observations of Dumping of Electrons at 1000 Kilometer Altitude and High Latitudes, J. Geophys. Res., **67,** 1962, p. 1227.
15. McIlwain, C. E., Coordinates for Mapping the Distribution of Magnetically Trapped Particles, J. Geophys. Res., **66,** 1961, p. 3681.
16. McIlwain, C. E., private communication, June, 1962.
17. Chapman, R. C., Jr., Critchlow, G. F., and Mann, H., Command and Telemetry Systems, B.S.T.J., this issue, p. 1027.
18. Brown, W. L., and Gabbe, J. D., The Electron Distribution in the Earth's Radiation Belts during July 1962 as Measured by Telstar, J. Geophys. Res., **68,** 1963, p. 607.
19. Carter, R. E., Reines, F., Wagner, J. J., and Wyman, M. E., Free Antineutrino

Absorption Cross Section, Expected Cross Section from Measurements of Fission Fragment Electron Spectrum, Phys. Rev., **113,** 1959, p. 280.
20. Van Allen, J. A., Frank, L. A., and O'Brien, B. J., Satellite Observations of the Artificial Radiation Belt of July 1962, J. Geophys. Res., **68,** 1963, p. 619.
21. Van Allen, J. A., Absolute Intensity, Spatial Distribution and Time Decay of Intensities of Artificially Injected Electrons Based on Observations with Injun I, Explorer XIV, Injun 3, and DOD Satellites, Program of the 44th Annual Meeting of the American Geophysical Union (April 17, 1963), p. 76.
22. Brown, W. L., Hess, W. N., and Van Allen, J. A., Collected Papers on the Artificial Radiation Belt from the July 9, 1962 Nuclear Detonation. Introduction, J. Geophys. Res., **68,** 1963, p. 605.
23. McIlwain, C. E., Trapped Electron-Proton Intensities as Functions of Energy, B, L, and Time, Program of the 44th Annual Meeting of the American Geophysical Union (April 17, 1963), p. 76.
24. Brown, W. L., Trapped Particle Population from Telstar and Explorer XV Observations, Program of the 44th Annual Meeting of the American Geophysical Union (April 17, 1963), p. 76.
25. Hess, W. N., Injection and Loss Problems, Program of the 44th Annual Meeting of the American Geophysical Union (April 17, 1963), p. 76.
26. Whitaker, W. A., private communication, April 1963.
27. Pieper, G. F., Williams, D. J., and Frank, L. A., TRAAC Observations of the Artificial Radiation Belt from the July 9, 1962 Nuclear Detonation, J. Geophys. Res., **68,** 1963, p. 635.
28. West, H. I., Jr., Mann, L. G., and Bloom, S. D., Spectra and Fluxes of Electrons Trapped in the Earth's Magnetic Field Following Recent High-Altitude Nuclear Bursts, Program of the 44th Annual Meeting of the American Geophysical Union (April 17, 1963), p. 77.
29. Giacconi, R., Paolini, F. R., and Katz, L., Measurements of Trapped Particles Injected by Nuclear Detonations, Program of the 44th Annual Meeting of the American Geophysical Union (April 17, 1963), p. 77.
30. White, R. S., Freden, S. C., Mihalov, J. D., Mozer, F. S., and Paulikas, G. A., The Artificial Radiation Belts at Low Altitudes, Program of the 44th Annual Meeting of the American Geophysical Union (April 17, 1963), p. 77.
31. Smith, R., Electron Flux Measurements from DOD Satellites During the Period July to November 1962, Program of the 44th Annual Meeting of the American Geophysical Union (April 17, 1963), p. 76.
32. Van Allen, J. A., The Geomagnetically Trapped Corpuscular Radiation, J. Geophys. Res., **64,** 1959, p. 1683.
33. McIlwain, C. E., and Pizzella, G., On the Energy Spectrum of Protons Trapped in the Earth's Inner Van Allen Zone, J. Geophys. Res., **68,** 1963, p. 1811.
34. Davis, L. R., and Williamson, J. M., *Low Energy Trapped Protons,* Space Research, vol. III, edited by W. Priester, Interscience Publishers, Inc., New York, 1963.
35. Freden, S. C., and White, R. S., Particle Fluxes in the Inner Radiation Belt, J. Geophys. Res., **65,** 1960, p. 1377.
36. Naugle, J. E., and Kniffen, D. A., Flux and Energy Spectra of the Protons in the Inner Van Allen Belt, Phys. Rev. Letters, **7,** 1961, p. 3.
37. Conference on Radiation Effects in Semiconductors, J. Appl. Phys. **30,** 1959, p. 1117.
38. Watkins, G. D., and Corbett, J. W., Electron Paramagnetic Resonance of Defects in Irradiated Silicon, Disc. Faraday Soc., **31,** 1961, p. 86.
39. Peck, D. S., Blair, R. R., Brown, W. L., and Smits, F. M., Surface Effects of Radiation on Transistors, B.S.T.J. **42,** January, 1963, p. 95.
40. Mayo, J. S., Mann, H., Witt, F. J., Peck, D. S., Gummel, H. K., and Brown, W. L., The Command System Malfunction of the *Telstar* Satellite, B.S.T.J., this issue, p. 1631.
41. Hutchison, P. T., and Swift, R. A., Results of the *Telstar* Space Experiment, B.S.T.J., this issue, p. 1475.
42. Smith, K. D., Gummel, H. K., Bode, J. D., Cuttriss, D. B., Nielsen, R. J., and Rosenzweig, W., The Solar Power Plant, B.S.T.J., this issue, part 3.

43. Loferski, J. J., and Rappaport, P., The Effect of Radiation on Silicon Solar Energy Converters, RCA Review, **19,** 1958, p. 536.
44. Rosenzweig, W., Gummel, H. K., and Smits, F. M., Solar Cell Degradation under 1-Mev Electron Bombardment, B.S.T.J., **42,** March, 1963, p. 399.
45. Rosenzweig, W., Smits, F. M., and Brown, W. L., Energy Dependence of Proton Irradiation Damage in Silicon, Bull. Am. Phys. Soc., Series II, **7,** 1962.
46. Lodi, E. A., and Crowther, D. L., Some New Results from Low Energy Proton Irradiation of Silicon, Appl. Phys. Letters, **2,** 1963, p. 22.
47. Seitz, T., and Koehler, J. S., *Displacement of Atoms During Irradiation*, Solid State Physics, vol. 2, Academic Press, 1956.
48. Baicker, J. A., Flicker, H., and Vilms, J., Proton Induced Displacement in Silicon, Appl. Phys. Letters, **2,** 1963, p. 104.
49. Denney, J. M., and Downing, R. G., private communication, May, 1962.
50. Rosenzweig, W., Augustyniak, W. M., and Wright, K. A., to be published.
51. Denney, J. M., and Downing, R. G., IEEE-AIAA Photovoltaic Specialists Conference, April 1963.
52. Bemski, G., Szymanski, B., and Wright, K. A., A New Paramagnetic Center in Electron Irradiated Silicon, J. Phys. Chem. Solids, **24,** 1963, p. 1.
53. Heppner, J. P., *The World Magnetic Survey*, Space Science Reviews, D. Reidel Publishing Company, Dordrecht, to be published.

Results of the *Telstar* System Communications Tests

By R. W. HATCH, S. B. BENNETT and J. P. KINZER

(Manuscript received February 29, 1963)

The results of the communications tests on the Telstar satellite system which have been conducted at the Andover earth station are presented. These tests have included successful transmissions of telephone, television, and data signals. In addition, measurements of received carrier power, noise, transmission characteristics, linearity, data system errors, absolute delay, and Doppler shift have been made. The results are in good agreement with the expected performance.

I. INTRODUCTION

Since the launch of the Telstar satellite on July 10, 1962, a large number of communications tests have been conducted at the A.T.&T. earth station at Andover, Maine. These tests have consisted of numerous successful transmissions of monochrome and color television signals, two-way telephone signals, and a variety of data signals. In addition, communications test signals of many types have been transmitted. Most of the television and telephone transmission tests have been conducted between the Andover station and the British Post Office (GPO) and French National Center for Telecommunications Studies (CNET) stations. These stations are respectively located at Goonhilly Downs, England and Pleumeur-Bodou, France. In addition, a number of one-way transmissions were made from the Andover station to the Bell Telephone Laboratories station at Holmdel, New Jersey, described in a companion paper.[1] Communications tests, most of which have been made on a loop basis to the satellite and back to the Andover station, have included measurements of received carrier power, noise, transmission gain and stability, system linearity, data system errors, absolute delay and Doppler shift. A large amount of valuable data has already been obtained; and, as this is written, system tests continue. This paper summarizes the more significant communication test results, most of which have been gathered during the period from July to November, 1962.

Although the companion papers provide detailed descriptions of the various subsystems which make up the Andover-Telstar communications system, it seems advisable to devote a small portion of this paper to a short over-all description. This has been provided in Section II, which also includes a communications system block diagram that will be useful in understanding and interpreting the test results to which most of this paper is devoted.

Section III provides a brief summary of the modulation methods, baseband signals, and the frequency allocation used for both the one-way and two-way tests.

Section IV is devoted to a description of the experiment plan. This section includes a list of the principal experiments which have been conducted and are herein reported. As such it serves as a table of contents for the remainder of the paper, which is devoted almost completely to documentation of test results.

II. COMMUNICATIONS SYSTEM

An over-all block diagram of the Andover communications system is shown in Fig. 1. The major part of the communications equipment, including the ground transmitter and ground receiver, is located on the horn antenna structure. A video transmission system interconnects this communications equipment and the test area, which is located in the control building 1600 feet away. Most of the communications test equipment is located in the test area. The Andover station is connected to the Bell System network via a microwave radio system from Boston which also terminates at the test area.

The over-all layout permits a large amount of flexibility in the way tests are conducted, as indicated in Fig. 1. Most of the tests described in this paper are RF loop tests. In this case, the communications path is from the test area, through the ground transmitter to the satellite, back through the ground receiver, finally terminating in the test area. Transmission to the satellite and back can also be simulated by transmitting to a boresight repeater located on Black Mountain about 4.5 miles from the ground station. This repeater is a bay-mounted duplicate of the Telstar communications repeater and uses waveguide feeds to small tower-mounted horn antennas. Adjustable attenuators are provided in the feeds so that the received power at both the repeater and ground receiver can be adjusted to simulate those in the actual satellite system.

In addition to these two RF loops, provision is also made for IF and baseband loops as shown. In this paper those test results which were

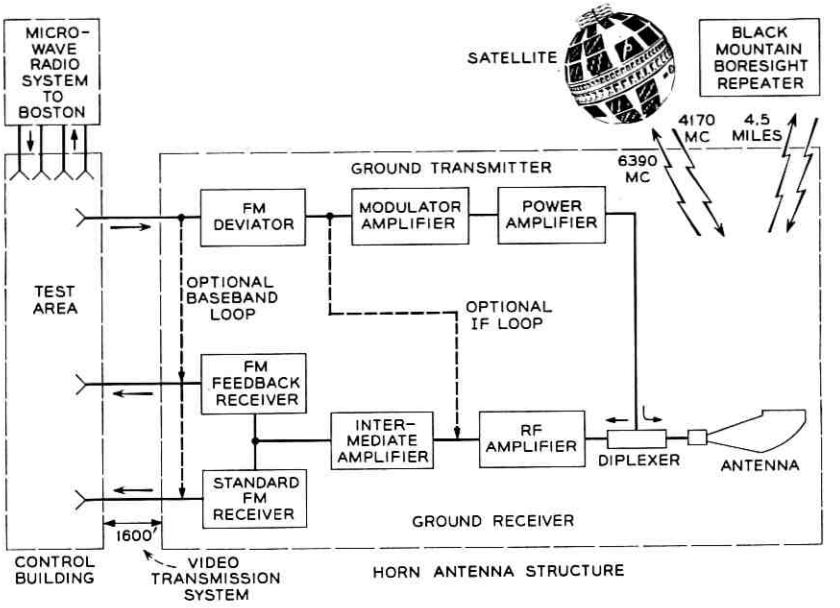

Fig. 1 — Telstar communications system.

taken on loops which do not include the Telstar satellite are identified as boresight, IF, or baseband loop test results.

The baseband transmission characteristic for a loop from the test area to the satellite and back depends on which FM receiver is used. As some of the later data will show, the transmission is essentially flat to well beyond 5 mc with the standard receiver and is flat to about 3 mc with the FM feedback receiver. Additional design and performance information for the individual parts of the communications system are included in the various companion papers.

III. MODULATION METHODS AND BASEBAND SIGNALS

Many of the test signals can be applied directly at baseband in the test area and similarly measured there. Typical examples are baseband transmission measurements such as gain-frequency characteristics and baseband noise spectra. However, other signals such as the combined video and audio signals for television transmission and the frequency-multiplexed telephone signal require additional equipment. In this section the special arrangements used for these signals will be described.

Fig. 2 is a simplified block diagram showing the optional patching arrangements for television and two-way message transmission. For television transmission, the audio signal is applied to the transmitting diplexer, which frequency-modulates the audio signal onto a 4.5-mc subcarrier. The video signal is band-limited by a 2-mc low-pass (roll-off) filter and combined with the 4.5-mc aural subcarrier. The combined signal is then transmitted to the ground transmitter via the video transmission system.

At the receiving end of the system the reverse procedure takes place. The combined signal is received at the ground receiver and transmitted to the control building via the video system, where it is applied to the receiving diplexer. Here, the 4.5-mc aural subcarrier is separated from the video signal and demodulated by a frequency discriminator centered at 4.5 mc. Separate video and audio outputs are provided from the diplexer.

For two-way message operation, standard telephone channel bank equipment replaces the diplexers, as shown in Fig. 2. In this arrangement, 12 individual telephone channels are frequency-multiplexed into the 60 to 108-kc band as shown. However, there is an additional difference between

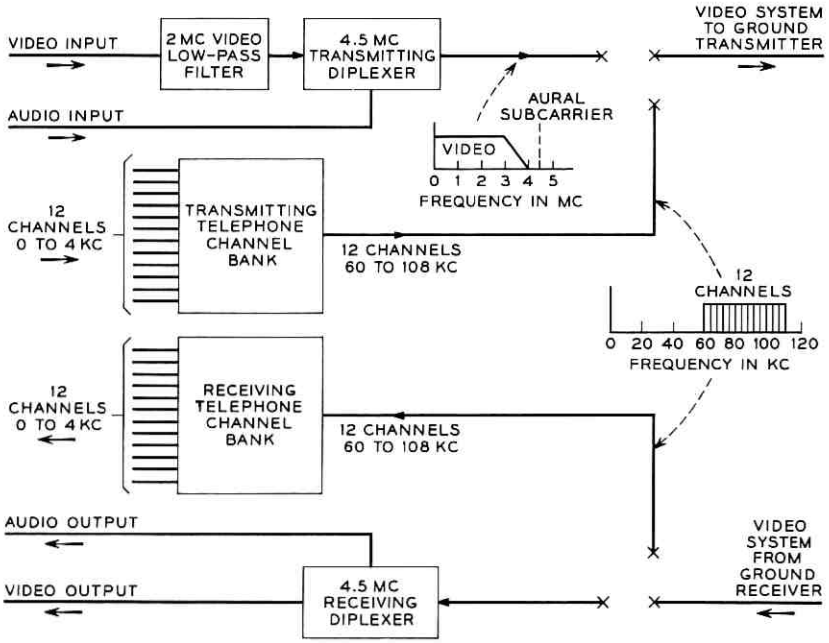

Fig. 2 — Arrangements for television and two-way message transmission.

the television and two-way telephone tests; the television tests are one-way tests which normally use the entire RF bandwidth of the system, whereas the two-way message tests involve simultaneous transmission and reception by two ground stations. This is accomplished by simultaneously using two separate bands for the two directions of transmission. In this case, the individual ground transmitters and receivers are offset by 5 mc from their normal center frequencies, as shown in Fig. 3. Typically, the Andover transmitter and the European receiver are tuned 5 mc above the nominal center band frequency. Similarly, the European transmitter and the Andover receiver are tuned 5 mc below the center of the band. Both signals, separated 10 mc in frequency, are simultaneously received and amplified by the satellite repeater. Since the repeater has only a single wideband channel and a single automatic gain control circuit, the two amplified signals at the satellite output will be unequal in power unless the two input signals are equal. In fact, due to the compression in the traveling-wave tube, any difference in signal power at the input is exaggerated at the output. In order to prevent vastly different signal powers, and hence unequal noise performance for the two directions of transmission, it has been customary for the two participating ground stations to coordinate and control their transmitter power so that approximately equal signals are received at the satellite repeater input.

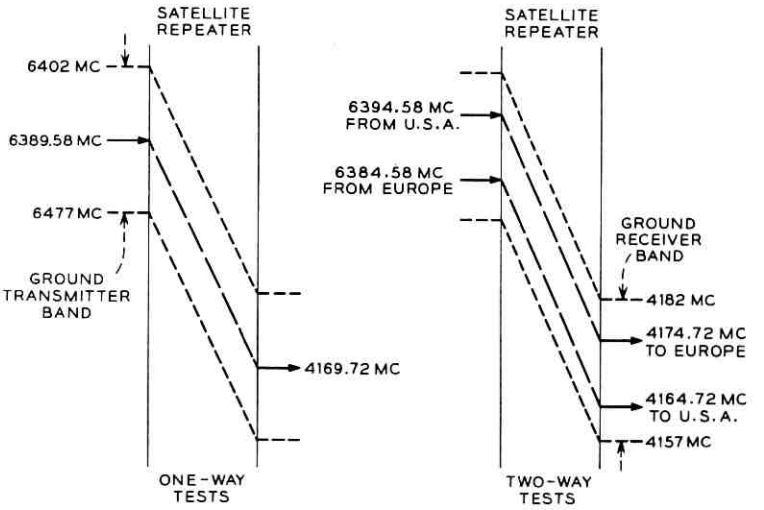

Fig. 3 — Frequency allocation plan.

When two ground stations are conducting two-way tests, both signals are received at a particular ground receiver input. Narrow bandpass filters (3 mc wide at Andover) are inserted at IF to pass the desired signal and reject the unwanted one.

Normal frequency deviations for both television and two-way message transmission are presented in Table I. Television transmission tests have been made both with and without the standard 525-line television pre-emphasis and de-emphasis prescribed by the CCIR.[2] The respective networks, when used, are inserted directly in front of the FM deviator and immediately following the FM receiver. These networks have the effect of increasing the frequency deviation for the high video frequencies by about 3 db and reducing the deviation for the low video frequencies by about 9 db. No pre-emphasis was used for the 12-channel two-way telephone tests.

Table I also shows the nominal frequency deviation used for one-way noise loading tests which simulate 600-channel loading.

TABLE I — NORMAL FREQUENCY DEVIATIONS

Television	
Peak-to-peak deviation by video	14 mc
Peak-to-peak deviation by aural subcarrier	2.8 mc
Nominal peak-to-peak deviation of aural subcarrier by audio signal	100 kc
Two-way message	
Nominal peak-to-peak deviation by 12-channel telephone signal	2 mc
Full load sine wave power at 0 db TL	+16 dbm
One-way message (600-channel noise loading)	
Nominal peak-to-peak deviation by 600-channel telephone signal	20 mc
Full load sine wave power at 0 db TL	+23 dbm

IV. EXPERIMENT PLAN

Prior to the launch of the Telstar satellite it was apparent that special consideration would have to be given to the test procedures because:

(a) the time per day available for tests would be small

(b) significant variations in the system signal-to-noise ratios would occur because the satellite range would change rapidly with time

(c) there would be a time variation in the apparent gain of the satellite antenna due to change in the "spin angle," defined as the angle between spin axis of the satellite* and the line of sight to the satellite from the earth station

(d) Doppler shift might affect some of the tests

* Measured from the south pole (opposite the telemetry antenna) of the satellite.

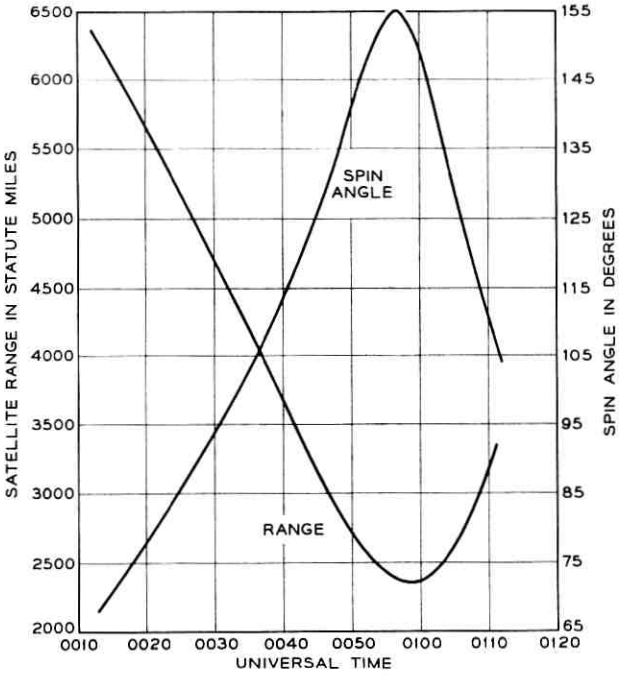

Fig. 4 — Range and spin angle vs time; pass 125, July 24, 1962.

(e) the life of the satellite might be shorter than expected, and it would therefore be essential to gather as much data as possible during the first few weeks.

Of the above considerations, the small amount of available test time has probably been the most important. With a total of about four thirty-minute passes per day and six operating days per week, there is a total of only two hours per day or twelve hours per week to be shared by several earth stations conducting a variety of tests, demonstrations, and special transmissions. This, plus the rapid variation in range and spin angle due to satellite orbital motion (Fig. 4 shows the variation in range and spin angle for a typical pass), made it very important to plan the individual tests to insure rapid and accurate completion. Several steps were taken to make this possible. An experiment plan was developed describing each of the proposed tests in detail, including test equipment requirements, patching arrangements, prepass calibration procedures, data to be recorded, and the recording method. Where possible, several individual tests were combined so that they could be per-

formed simultaneously. In addition, the station itself was arranged so that as many tests as possible could be made from a single test area in the control building. Finally, a video switch was provided so that input and output signals to the satellite system could be rapidly switched during a pass without the need for patch cords.* A portion of the test area is shown in Fig. 5.

The principal experiments described in this paper are listed in Table II. The section numbers are included, so that this table also serves as an index to the experimental results reported in the remainder of the paper.

No tests were made of correction techniques for the effect of Doppler shift on transmission, or on the problem of transferring transmission from one satellite to another without interruption.

V. RECEIVED CARRIER POWER

Received carrier power in the communications channel centered at 4170 mc was continuously measured at the ground receiver by monitoring the voltage in the main IF amplifier's automatic gain control circuit. Similarly, the 6390-mc received carrier power at the satellite was measured by monitoring the automatic gain control voltage in the satellite's IF amplifier; in the latter case, the measurements were taken at one-minute intervals and the quantized readings transmitted to the ground via the telemetry system. The over-all accuracies in these measurements are estimated to be approximately ± 0.5 db at the ground receiver and ± 1 db at the satellite receiver. Large amounts of these data have been obtained and analyzed in various ways. In general, the measured values of received carrier power agree with the predicted values when both range and spin angle effects are included.

5.1 *Received Carrier Power as a Function of Time*

A typical pen recording of the 4170-mc received carrier power at the ground receiver is shown in Fig. 6. This trace, taken with a recorder speed of about 50 cm/hour, covers a period of about 20 minutes during pass 125. The relatively broad width (1 to 3 db) of the trace is due to a rapid jitter of the pen following the variations in the antenna pattern due to the spin of the satellite. The slower variations which are more clearly visible are caused primarily by the variation in the spin angle at the satellite and to a lesser extent by range variations.

---

* Even with these precautions, it has been difficult to obtain completely consistent sets of data; a critical reader can undoubtedly find some evidence of this in the paper.

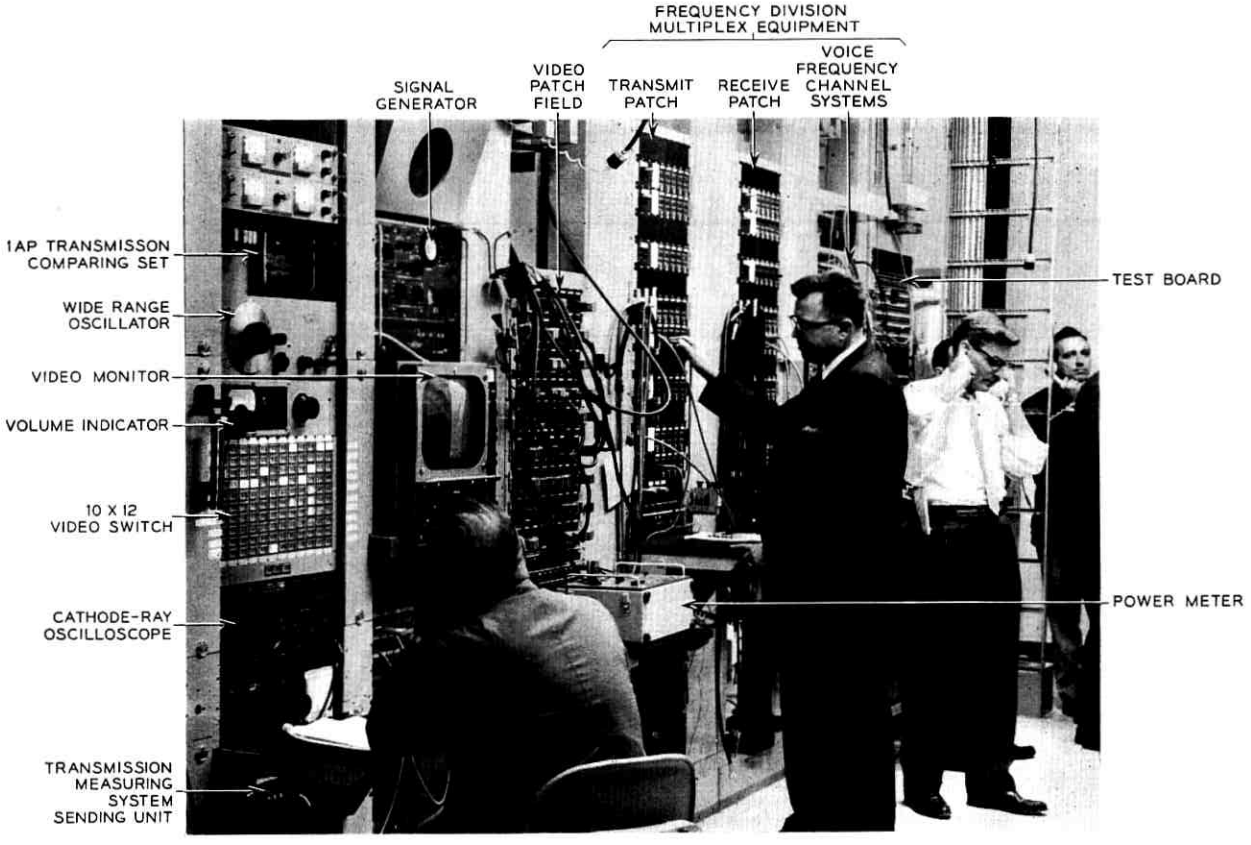

Fig. 5 — Portion of Andover test area.

TABLE II — EXPERIMENT RESULTS INCLUDED IN THIS PAPER

Type of Test	Section
Received Carrier Power	5.0
Received Carrier Power as a Function of Time	5.1
Received Carrier Power vs Range	5.2
Antenna Patterns	5.3
Radio Frequency Transmission Stability	5.4
Linear Transmission	6.0
Baseband Transmission	6.1
IF-RF Transmission	6.2
Baseband Stability	6.3
Noise	7.0
Baseband Noise Spectrum	7.1
Noise at 6 mc	7.2
Television Noise	7.3
Telephone Noise	7.4
Impulse Noise	7.5
IF Noise Spectrum	7.6
Nonlinearity and Cross-Modulation	8.0
Envelope Delay Distortion	8.1
Differential Gain and Phase	8.2
Noise Loading	8.3
Intermodulation: Video to Audio	8.4
Television	9.0
Early Transmissions	9.1
Color Television	9.2
Two-Way Television	9.3
Two-Way Telephony	10.0
Early Transmissions	10.1
Channel Noise	10.2
Crosstalk	10.3
Data Transmission	11.0
Digital Data	11.1
Facsimile	11.2
Miscellaneous	12.0
Doppler Shift	12.1
Absolute Delay	12.2
Time Synchronization	12.3
Interference	12.4

The symmetry of the pattern around 00:57:00 Universal Time occurs at the point of maximum spin angle. This point can be quite accurately determined and, therefore, serves as a check against computer-produced spin angle data.

In Fig. 7, similar but higher-speed pen recordings are shown of the 4170-mc received carrier power. Here, the details of the previously mentioned pen jitter become apparent and show the variations in received carrier as the satellite rotates. These variations correspond to the constant-latitude antenna patterns of the satellite for the three values of spin angle shown. The spin rate of 159 rpm was determined from the periodic nature of the patterns.

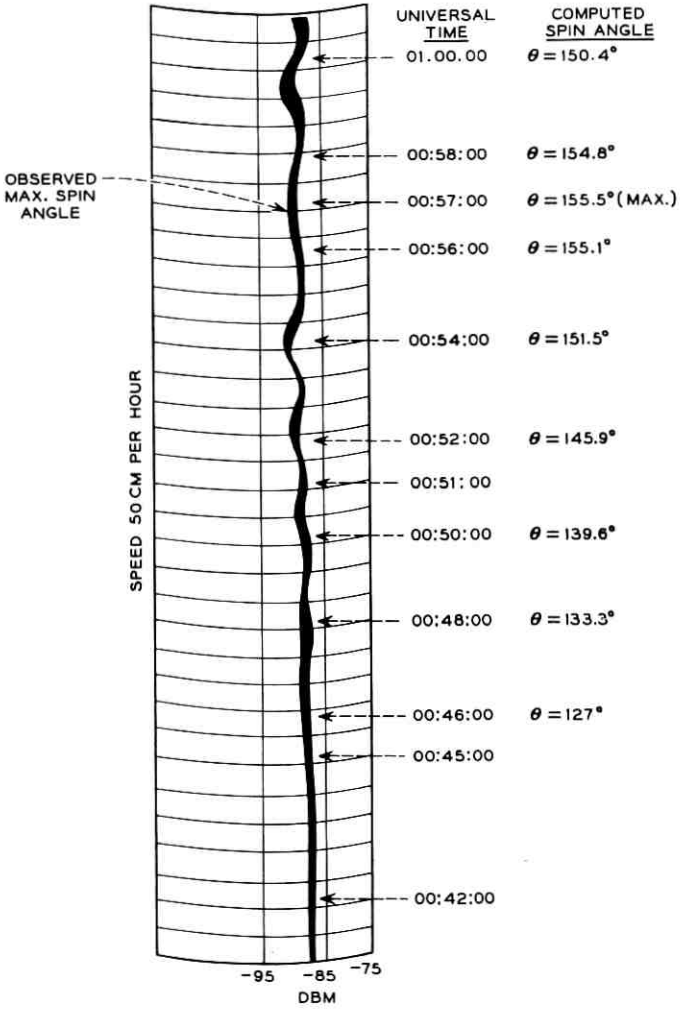

Fig. 6 — Recording of received signal power; pass 125.

Transmission phenomena at low elevation angles are not normally observed at the Andover station because the satellite is commanded on and off well above the horizon. However, on pass 470 the Bell Laboratories command system at Cape Canaveral was instructed to command on the satellite as it rose above the horizon at Andover so that low-elevation effects could be observed. The pen recording shown in Fig. 8 was obtained during this pass. For this test, the horn antenna was slaved

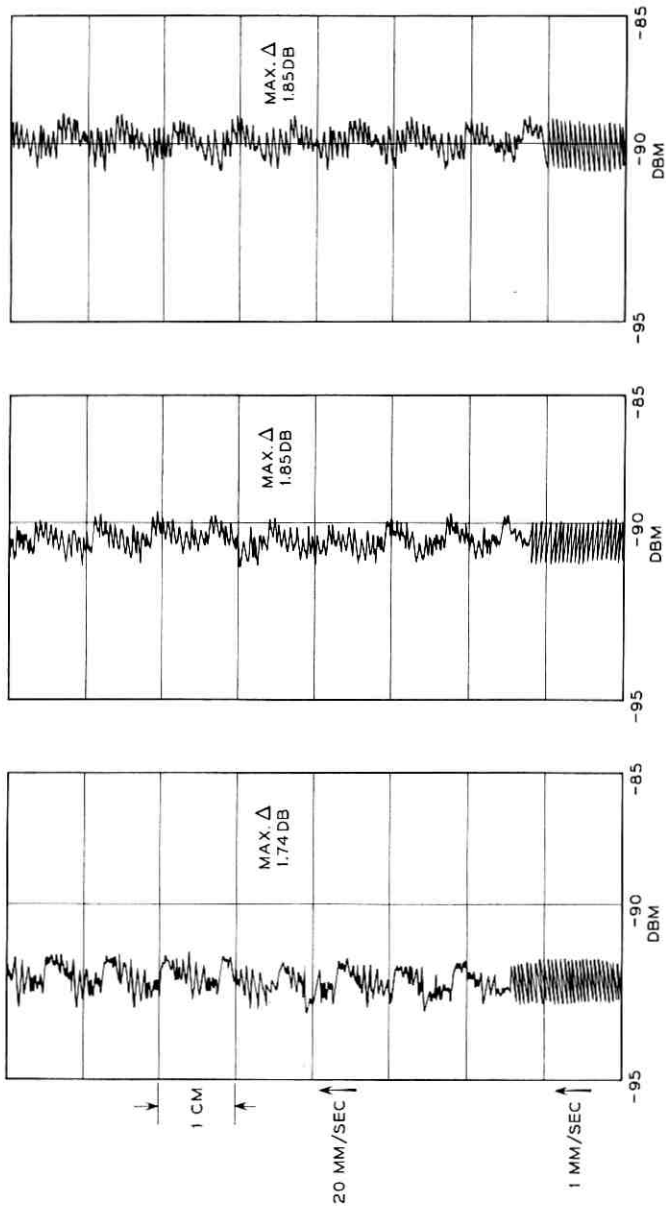

Fig. 7 — Received carrier power recordings showing constant-latitude satellite antenna patterns at 4 kmc; spin rate = 159 rpm; pass 397, Aug. 22, 1962.

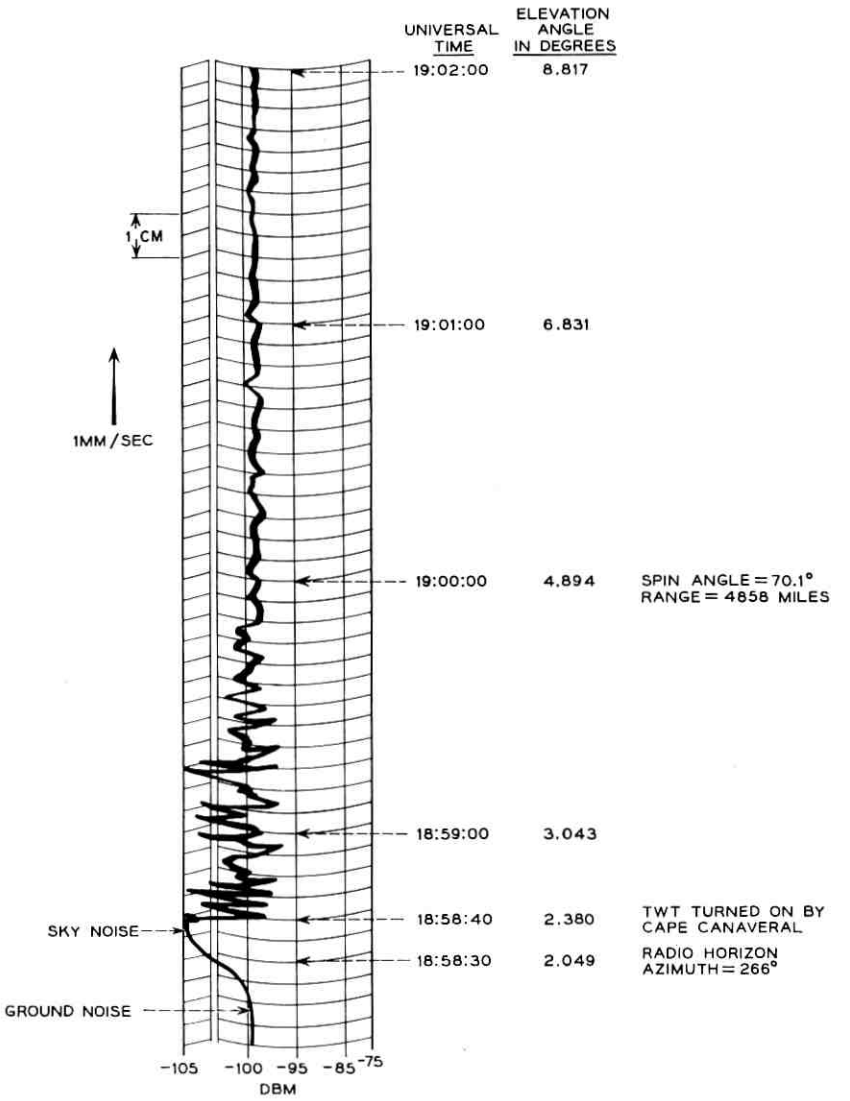

Fig. 8 — Low-angle fading at 4170 mc; pass 470, Aug. 30, 1962.

to a magnetic tape drive with an estimated accuracy of $\pm 0.02°$ (well within the 4-kmc antenna beamwidth). A ground noise level of -99.5 dbm was observed (bottom of Fig. 8) while the horn antenna was pointed below the radio horizon. At 18:58:30 UT the antenna was driven

above the radio horizon at 2.04° elevation (optical horizon 1.95°) and the noise dropped to a level of about −104 dbm. A few seconds later, at 18:58:40 UT, the satellite was commanded on from Cape Canaveral. For a period of about one minute large variations in the signal were observed. Some of these appear to be almost complete fades or cancellations of the signal. Reliable transmission was not attained until an elevation angle of about 4° was reached.

5.2 *Received Carrier Power vs Range*

The received carrier power in db plotted against range is shown in Fig. 9 on a logarithmic scale for pass 125. If range were the only variable

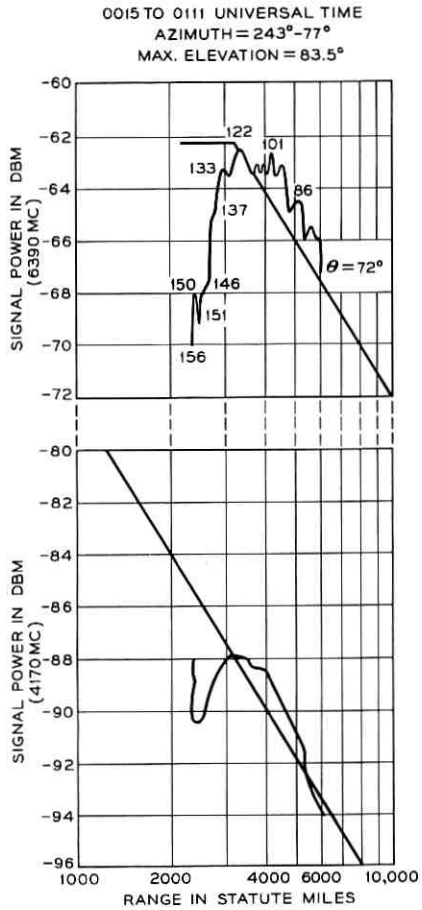

Fig. 9 — Received carrier power vs range; pass 125.

affecting received carrier power, the curves would be straight lines. The straight lines appearing on the graph represent the theoretical results under the assumptions shown in Table III.

5.3 *Antenna Patterns*

At elevation angles well above the horizon, the variation in received carrier power has been found to be primarily a function of range and spin angle. Thus, it is possible to take received carrier power measurements such as those in Fig. 6, compensate them for range variations, and plot them against accurate spin angle data to display the polar patterns of the 4-kmc satellite antenna. Fig. 10 illustrates the received carrier power measurements obtained during pass 125, compensated for range and plotted against spin angle. The resulting curve agrees very well with antenna pattern measurements made in the laboratory prior to launch.[3]

Fig. 11 shows a similar curve for the 6-kmc antenna. In this case, the received carrier power measurements were only obtained once per minute from telemetry, and it is not possible to get the same accuracy and fine detail as is possible for the 4-kmc antenna.

The pointing accuracy of the horn antenna has also been checked by means of the satellite. This has resulted in determination of the 4- and 6-kmc horn reflector antenna patterns shown in Figs. 12 and 13. Known offsets were added to the programmed horn antenna drive tape, and the changes in carrier power were measured and plotted after correction for range and spin angle. In order to obtain the 4-kmc measurements, the French station at Pleumeur-Bodou transmitted a 6-kmc signal to the satellite during pass 132 to insure a constant output as the Andover horn was offset. The 6-kmc pattern was taken during pass 105 and the received carrier measurements were made at the satellite. The measurements confirmed that there was no offset between the 4- and 6-kmc communications patterns or between the patterns and the drive tape. The patterns themselves were comparable to those obtained earlier by means of the boresight tower.

TABLE III — ASSUMED SYSTEM CONSTANTS

	6390 mc	4170 mc
Radiated power	62 dbm	33.5 dbm
Satellite antenna gain at 90° spin angle	1 db	0 db
Earth station antenna gain	60 db	58 db
Loss in satellite antenna cable	2 db	
Radome loss		0.4 db

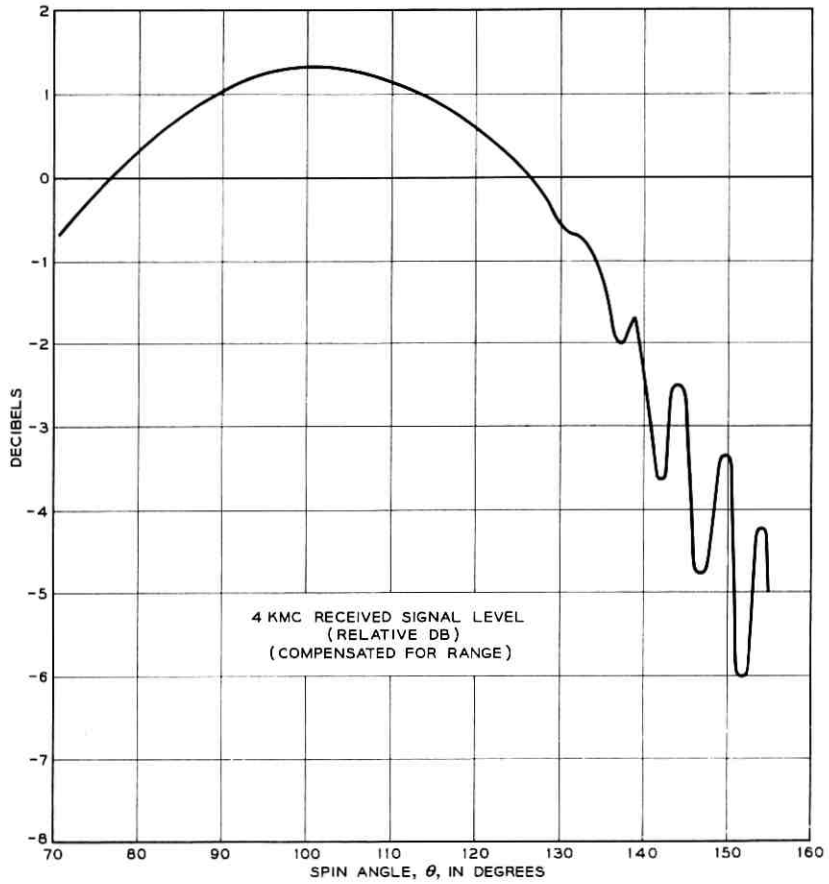

Fig. 10 — 4-kmc satellite antenna pattern; pass 125.

5.4 *Radio Frequency Transmission Stability*

Fading is a common phenomenon in 4- and 6-kmc overland microwave radio systems. In fact, this problem is so severe that in systems where high reliability is required, it is customary to provide spare radio channels and automatic switching equipment to protect the working channels. A fading problem was not anticipated in satellite systems except at very low elevation angles. The performance thus far achieved tends to confirm this expectation.

To study the system stability, received carrier power measurements from a number of passes were compensated for range and plotted against

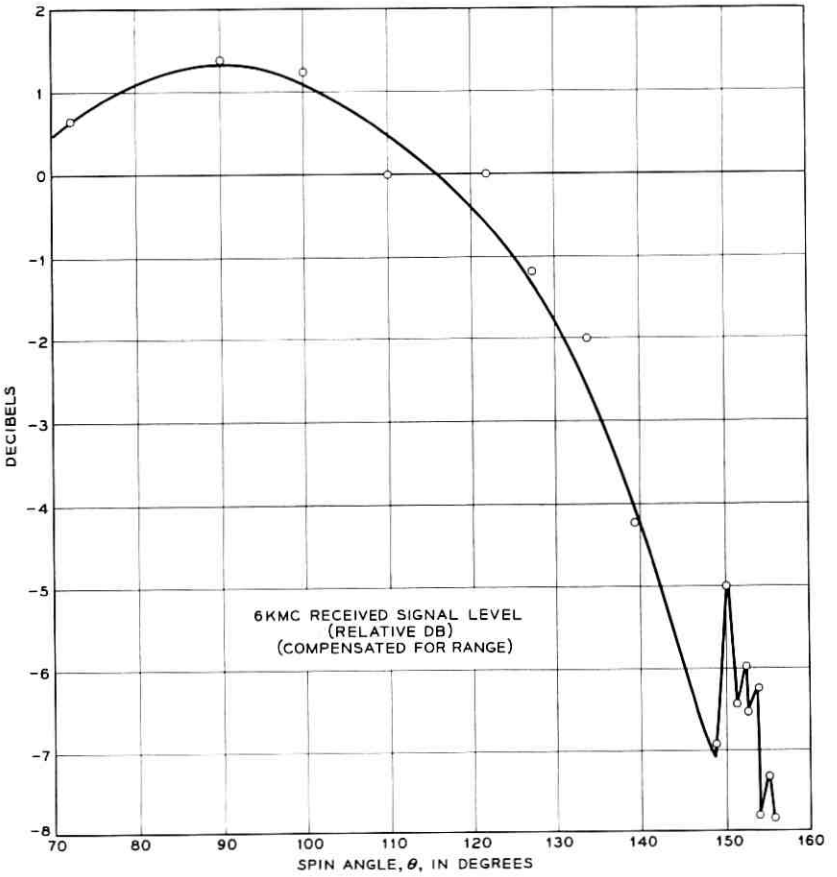

Fig. 11 — 6-kmc satellite antenna pattern; pass 125.

the computed spin angle of the satellite. The scatter diagram which is thus obtained provides a basis for estimating the system stability and the predictability of received carrier power. Two such scatter diagrams are shown here as Figs. 14 and 15.

VI. LINEAR TRANSMISSION

The linear transmission tests define the baseband and IF gain vs frequency characteristics. Due to the many varying parameters, e.g., range, spin angle, and satellite antenna patterns, the stability of these characteristics is of prime concern and is included as part of these tests. The accuracy of the baseband transmission tests is estimated at ± 0.1 db and

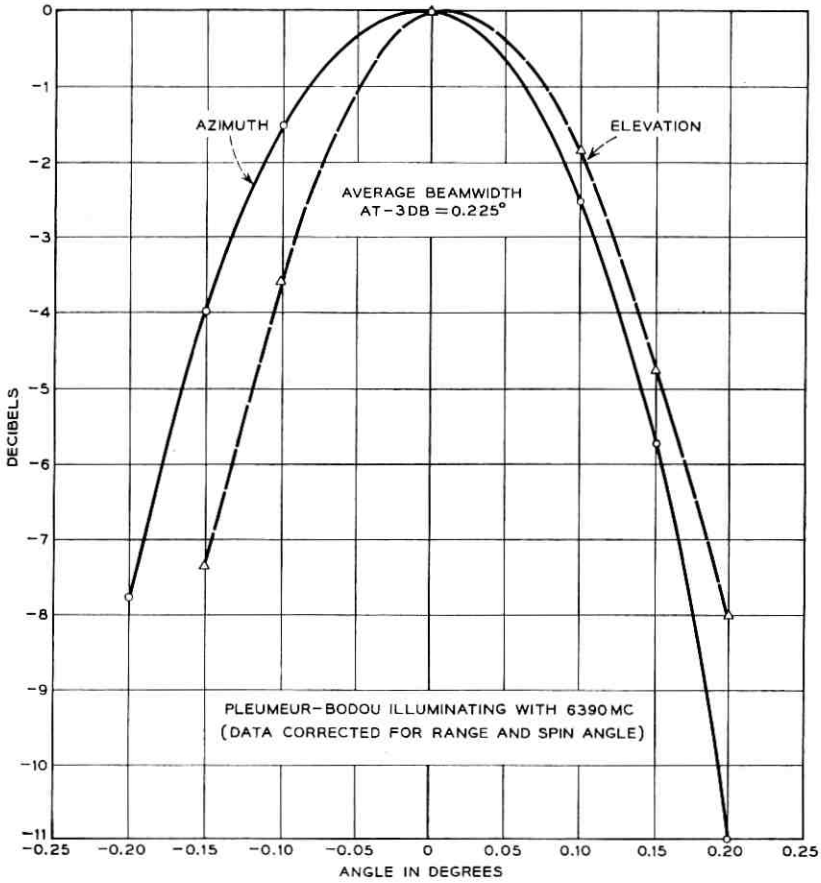

Fig. 12 — 4-kmc horn antenna pattern; pass 132, July 24, 1962.

that of the stability measurements at ±0.05 db. In general, the results of these tests with the Telstar satellite show that the transmission shapes are primarily due to the ground equipment, as expected, and that the baseband transmission is not a function of the varying satellite parameters.

6.1 *Baseband Transmission*

The baseband gain vs frequency characteristic for various transmission loops is shown on Figs. 16 and 17. Fig. 16 shows the baseband frequency response for the baseband loop (A), the IF loop (B), and the

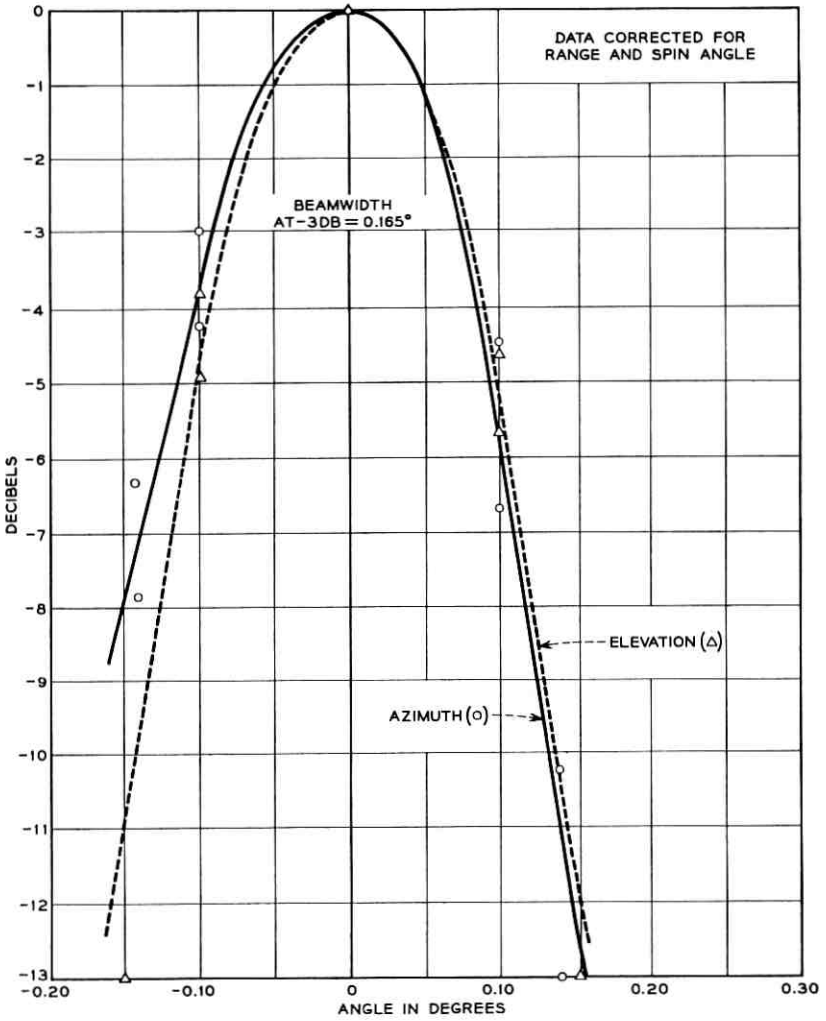

Fig. 13 — 6-kmc horn antenna pattern; pass 105, July 21, 1962.

satellite loop (C). The standard FM receiver was used in determining (B) and (C); no diplexers or roll-off filters were used for any of the three curves.

The gain of the baseband loop appears to be about 0.5 db higher than that of the other loops. However, the baseband loop was measured on a different day than the others, and the difference is probably due to a

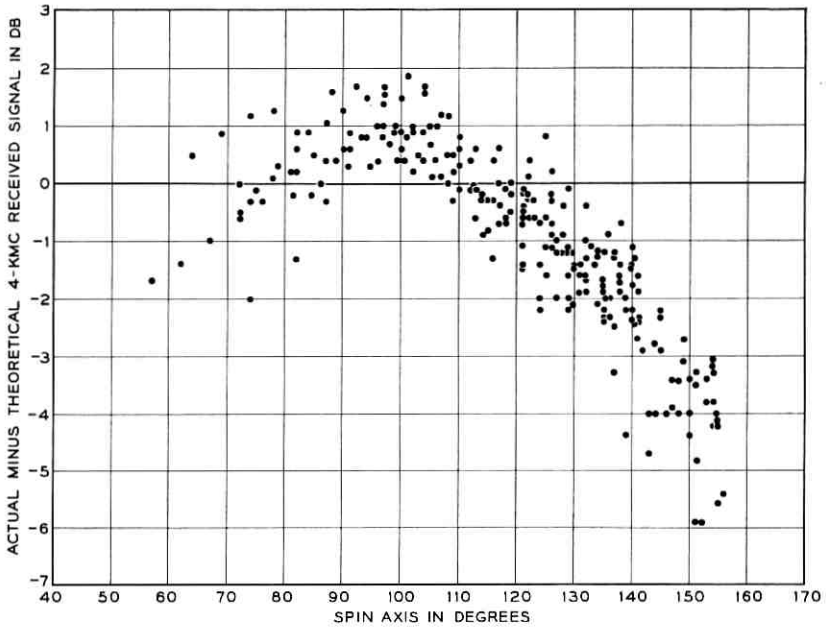

Fig. 14 — 4-kmc received carrier: difference between actual and theoretical power vs spin angle.

slightly different gain adjustment for the various video amplifiers in the transmission path.

The principal difference between the IF and the satellite loops, (B) and (C) of Fig. 16, is the peak of about 0.5 db at 1.7 mc. This is a characteristic of this particular satellite, and was first discovered during pre-launch tests. No noticeable degradation of transmission is caused by this irregularity. It is clear from Fig. 16 that the transmission is essentially flat, up to at least 5 mc, when the standard FM receiver is used. Color television signals were transmitted across the Atlantic, as described in Section 9.2, using such an arrangement.

The effect of the FM feedback receiver (FMFB) on the baseband transmission characteristic is shown on Fig. 17. Curves (A) and (B) show that there is little difference in baseband frequency response between the IF and the satellite loops;* the response is essentially flat to within ± 0.5 db to about 3 mc and approximately 3 db down at 4 mc. Adding the 2-mc roll-off filter and diplexers for video transmissions results in the characteristic shown by curve (C). This transmission shape

* The peak at 1.7 mc is not shown due to the coarseness of this measurement.

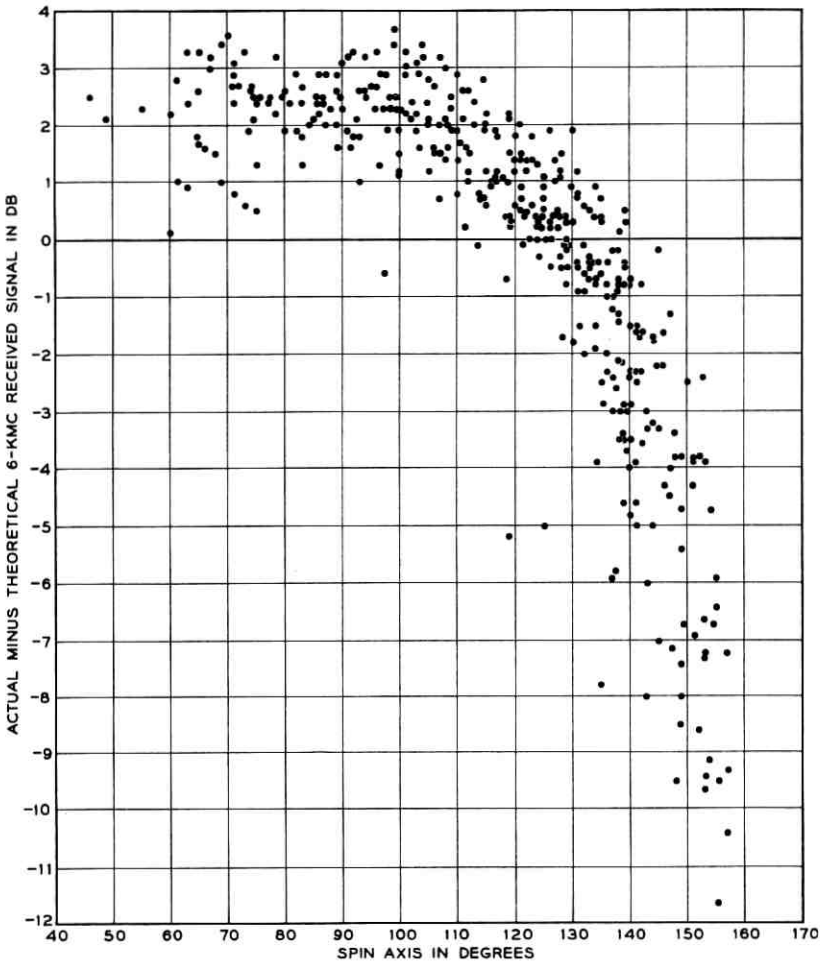

Fig. 15 — 6-kmc received carrier: difference between actual and theoretical power vs spin angle.

is the product of a preliminary design and has been used with satisfactory results for many of the television demonstrations. A substantial improvement is possible by a redesign of the diplexers and the roll-off filter.*

The baseband transmission characteristics, shown in Figs. 16 and 17,

* A roll-off filter is desirable to limit the video spectrum at the aural subcarrier frequency and also to restrict the amount of high-frequency energy entering the FMFB receiver.

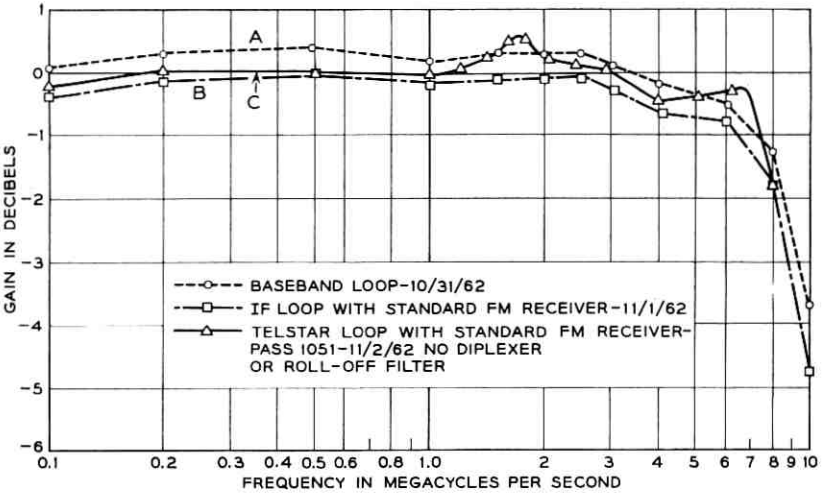

Fig. 16 — Baseband frequency response (standard FM receiver).

determine to a large extent the quality with which black-and-white television pictures are transmitted over the system. The effect of the system with a characteristic as shown on (C) of Fig. 17 on various patterns and signals is illustrated in Fig. 18. The reduction in the high-frequency content is obvious from the "after" pictures.

6.2 *IF-RF Transmission*

A gain-frequency characteristic of the IF and RF equipment, including the satellite repeater, determined during pass 188, is shown in Fig. 19. Before each pass the maser is adjusted to produce a transmission curve similar to the center curve of Fig. 19. When the satellite first appeared on pass 188, the transmission characteristic was that shown at the left of the figure; it then changed gradually over to the middle curve and finally to that shown on the right. The phenomenon can be explained by the interaction of the earth's magnetic field with the field of the maser. The earth's field either adds to or subtracts from the maser field, and thereby shifts the maser frequency at the rate of 2.4 mc per gauss. This shift, superimposed on the maser equalizer characteristic, then introduces the transmission slopes shown. The tilt in the transmission characteristic has not caused any detrimental effects to the system performance. However, this characteristic must be taken into account when analyzing the IF noise measurements of Section 7.6.

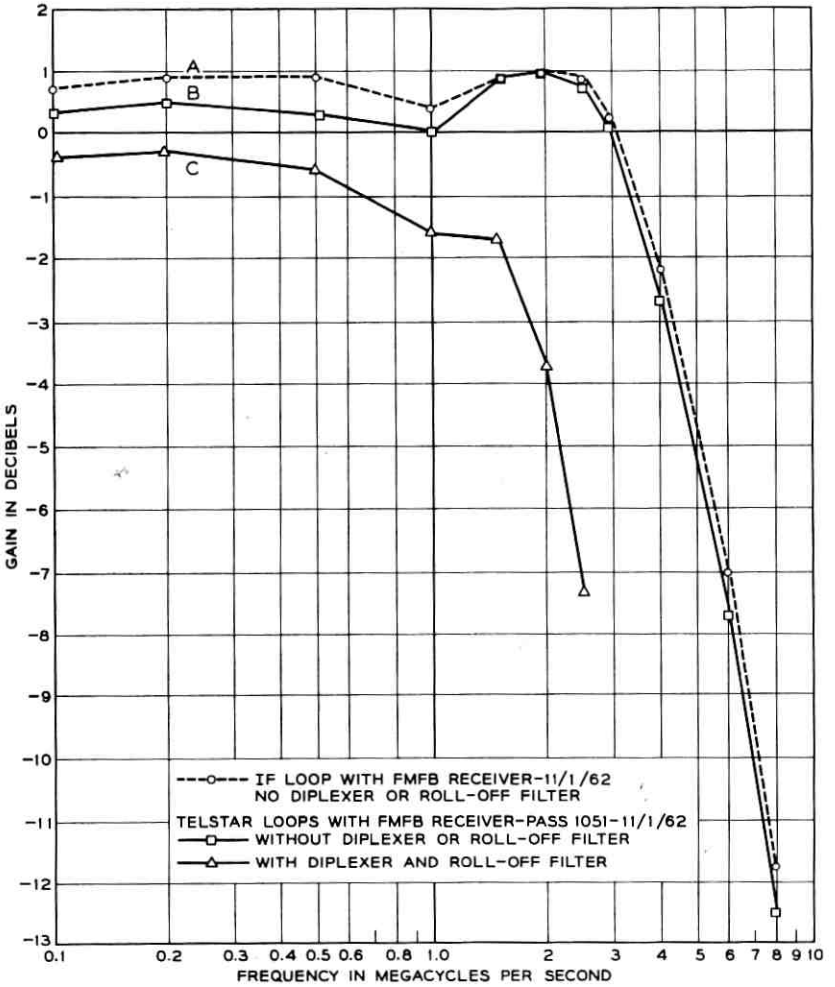

Fig. 17 — Baseband frequency response (FMFB receiver).

6.3 *Baseband Stability*

Stability measurements of the baseband gain-vs-frequency characteristic were made on several passes under conditions of varying slant range (or received carrier powers) and spin angle. The test was made by applying a 450-kc tone to the input of each of the five type "L" supergroups Nos. 2, 4, 6, 8, and 10.[4] The 450-kc tone was then translated to the frequencies 415, 915, 1411, 1907 and 2651 kc, respectively, and trans-

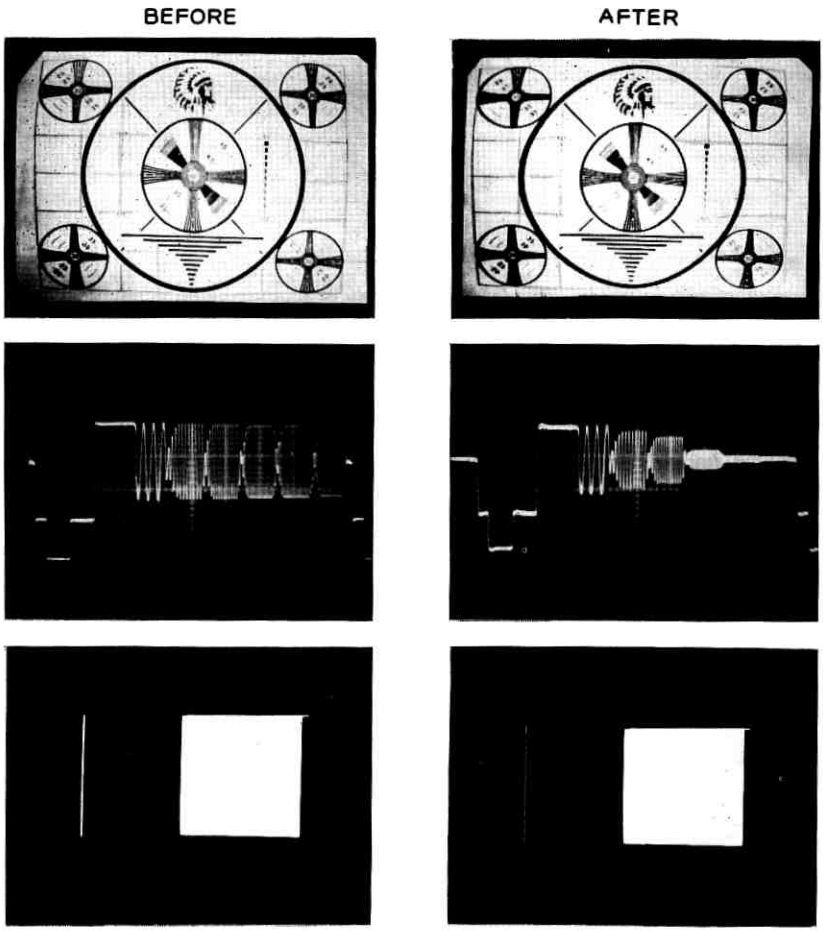

Fig. 18 — Effect of transmission on various test signals.

mitted over the satellite communications repeater. The five received signals were shifted back to 450 kc by means of the receiving supergroup equipment, detected and recorded on a strip chart. An expanded db scale capable of discerning changes of 0.05 db was used. In all cases the stability was better than ± 0.1 db, most of which is attributable to drift in the measuring equipment.

VII. NOISE

Various measurements of baseband and IF noise are described in this section. In view of the many varying parameters affecting the system's

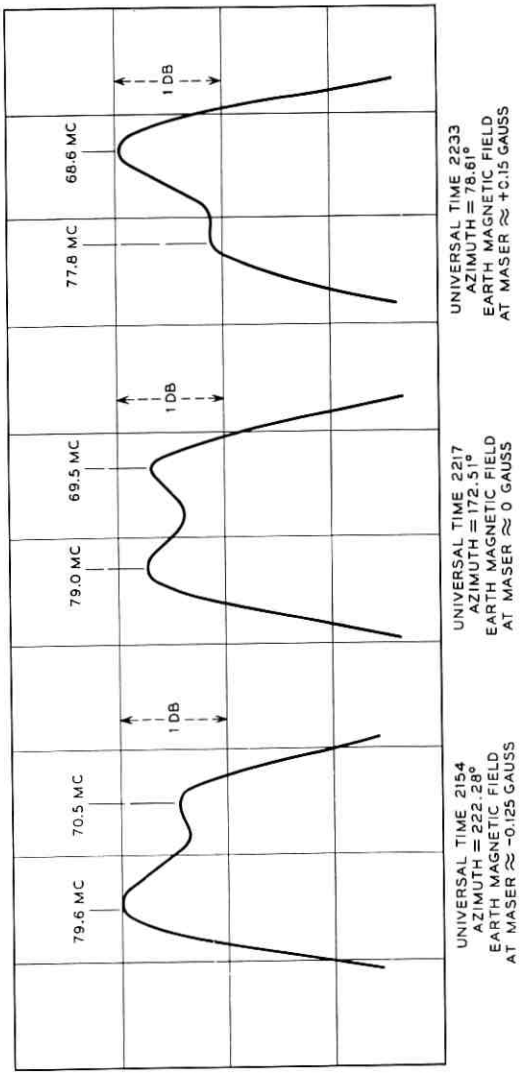

Fig. 19 — IF-RF transmission characteristics; pass 188, July 30, 1962.

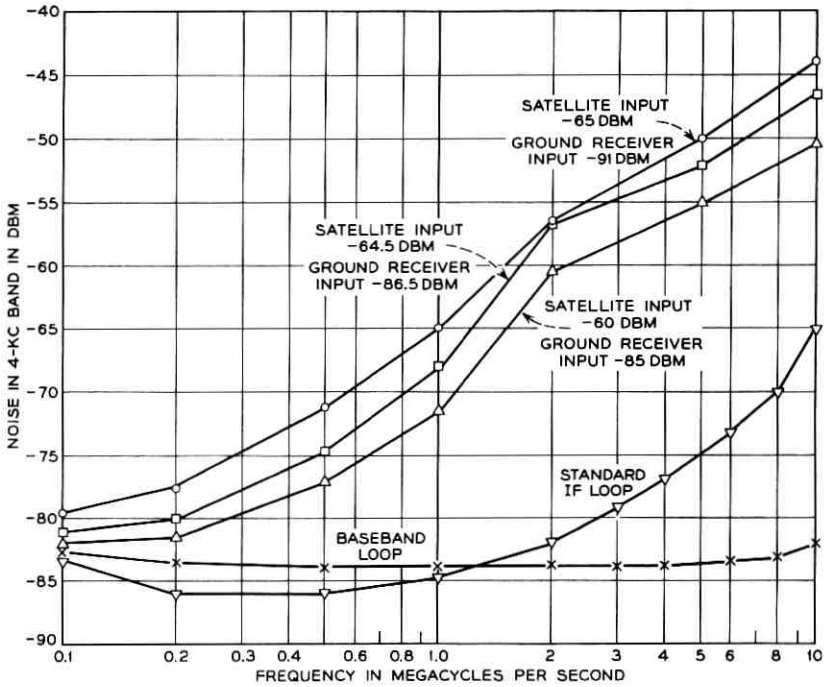

Fig. 20 — Baseband noise spectra: standard FM receiver; no diplexer or clamper; measured at test area; pass 62, July 17, 1962.

baseband noise, i.e., satellite elevation above the horizon, slant range, spin angle, power transmitted to the satellite, and ground receiver used, most noise measurements have been repeated often in order to obtain sufficient data for statistical analysis.

7.1 *Baseband Noise Spectrum*

Typical measurements of the baseband noise spectrum made from the test area* during pass 62 are shown in Fig. 20. These noise measurements, made in a 4-kc band, have been corrected for the transmission characteristic of Fig. 16. The figure clearly exhibits the effect of changing slant range on received carrier power and on the system's noise performance. In addition, noise measurements for the standard IF loop and the baseband loop are also shown. The latter show that significant noise is contributed by the video circuits and FM terminals below 200 kc.

* Fig. 1 shows the system block diagram.

Baseband noise spectrum measurements were repeated often during the first four months after the launch of the Telstar satellite. The results are consistently similar to those of Fig. 20.

To relate baseband noise measurements made at various points in the system to RF signal-to-noise performance, the following constants of the Telstar system must be defined:

(a) A tone (or a one-cycle band of noise) X dbm at the test area is $X - 5$ dbm at the deviator input (or at the FM receiver output).

(b) Zero dbm of a sine wave at the deviator input corresponds to an rms frequency deviation of 7.07 mc.

If the RF noise spectrum is white, the expected baseband noise spectrum is triangular. In practice, the baseband noise is decreased at the high-frequency end due to the IF-RF transmission characteristic (see Fig. 19) and increased at low frequencies due to noise in the terminal and baseband equipment, as well as FM noise from the satellite carrier supplies.

To obtain data under carefully controlled conditions of range and satellite attitude, eleven complete noise spectrum measurements were made at one-minute intervals at the test area during pass 297. The total system noise at each frequency was plotted against time, and smooth curves drawn. The smoothed values obtained at 20:32 UT for a satellite slant range of 4000 miles are shown in Fig. 21, curve A.

To isolate the satellite or up-path contribution to the total noise for comparison with pre-launch measurements, the down-path baseband noise is computed. Assuming a receiving system noise temperature of 35°K and a 4-kmc received carrier of −88.6 dbm, the down-path noise at 10 mc in a 4-kc band is −50.4 dbm at the test area and decreases at 20 db/decade. The calculated down-path noise is shown by the dotted line on Fig. 21. At low frequencies, the noise contribution of the baseband trunks and FM terminals is added in to get the total down-path noise. Subtraction (on a power basis) of the down-path noise from the total system noise gives the up-path noise, shown as curve B of Fig. 21.

Fig. 21, curve C, shows the up-path noise measured in the laboratory prior to launch. The two curves, B and C, agree within the measurement error. It is therefore concluded that the satellite's noise performance has not been changed by the launch or by space environment. This is further substantiated by the IF noise measurements of Section 7.6. Fig. 21 shows that the contribution of the up-path to the total system noise is somewhat greater than the down-path for this pass. The data consistently show that two paths contribute about equally to total noise, with a tendency for the up-path to be the larger contributor.

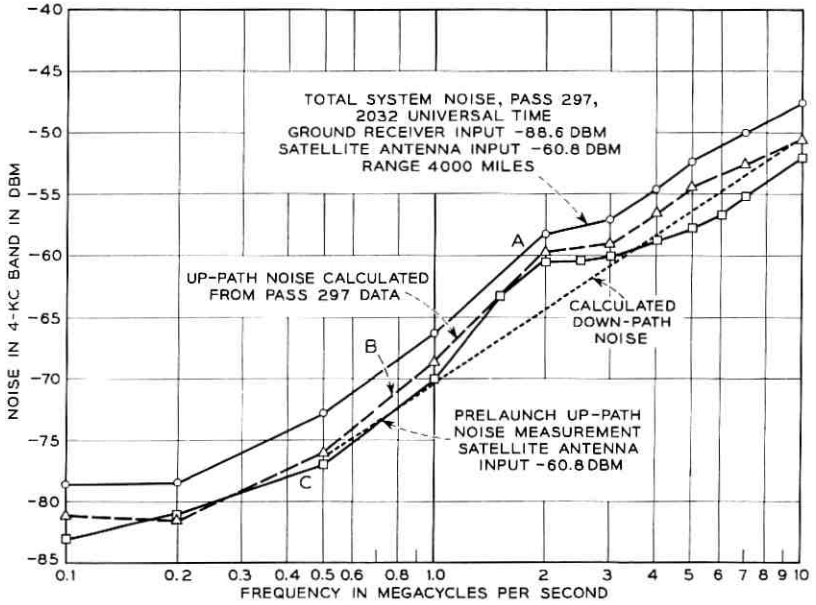

Fig. 21 — Comparison of pre-launch and post-launch baseband noise spectra: post-launch data from pass 297, Aug. 11, 1962.

7.2 *Noise at 6 mc*

Since typical monochrome television signals have negligible energy at 6 mc, the system noise at this frequency serves as a monitor of the system performance during video transmissions and noise tests and is therefore recorded continuously at the test area. Such a recording, made during pass 988, is shown at the top of Fig. 22. This figure clearly exhibits the dependence of the baseband noise on the range and received carrier powers tabulated thereon. Further, it shows that after appropriate adjustments are made for transmission losses (see Figs. 16 and 17), the two FM receivers detect the same noise at 6 mc, everything else being equal.* The 6-mc noise is measured at the same point as the baseband noise spectra of Section 7.1, but in a 6.3-kc band.

Of the several parameters affecting the noise at 6 mc, the slant range and spin angle are both reflected in the 4170-mc carrier power received at the ground receiver. Therefore, Fig. 23, which is the scatter diagram

* At the time of switching between FM receivers, the sensitivity of the measuring equipment was decreased 10 db. This accounts for the apparent decrease in 6-mc noise on Fig. 22.

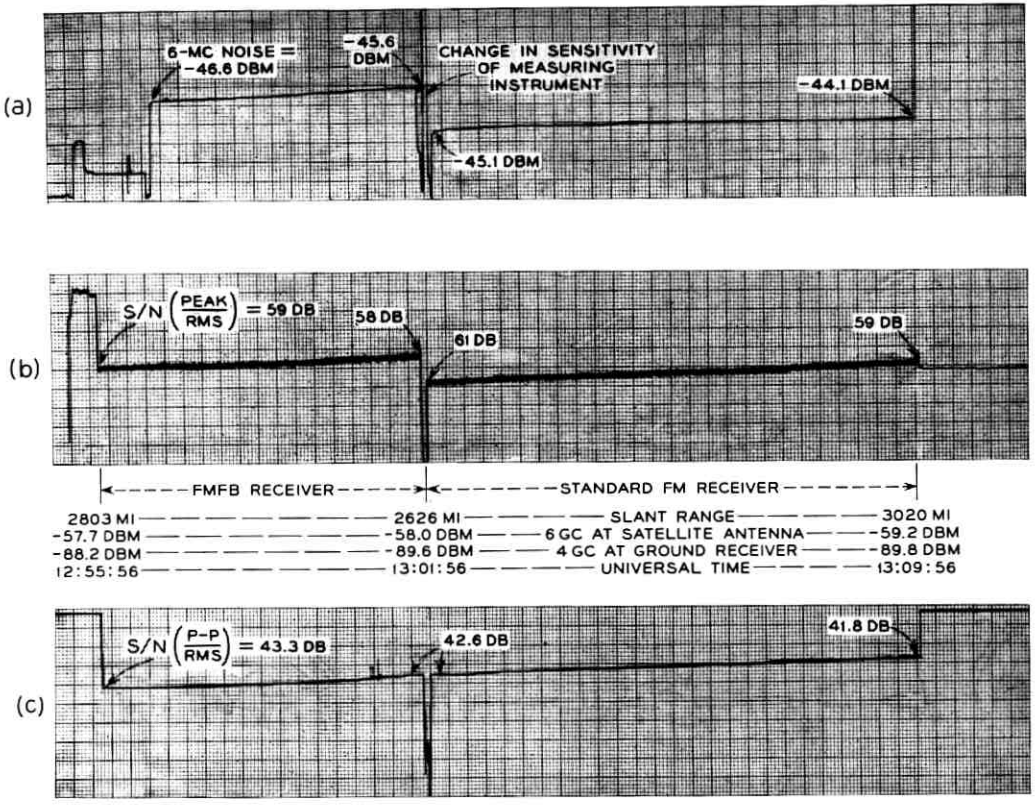

Fig. 22 — Baseband noise recordings; pass 988, Oct. 26, 1962. (a) Noise at 6 mc in 6.3-kc band; (b) weighted audio noise; (c) weighted video noise.

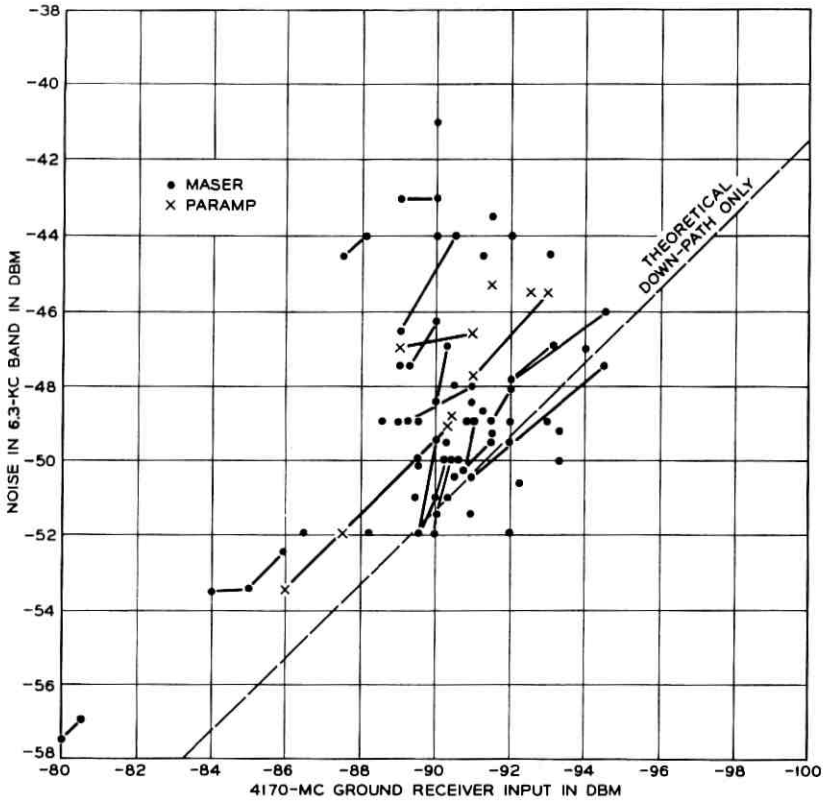

Fig. 23 — 6-mc noise vs received carrier power.

of 6-mc noise vs received carrier power,* shows the effect on the noise of the remaining parameters and of the measurement errors. The principal known parameter is the carrier power transmitted to the satellite. This affects the up-path contribution to the total noise. Since the maximum available power of 2 kw was not always transmitted to the satellite, only noise measurements corresponding to received carrier powers within the satellite's 20-db AGC range were used for this figure. The satellite's elevation angle, which determines the ground receiver's effective noise temperature, is of secondary importance in Fig. 23 since all values used correspond to elevations of 15° or more. The effect of using the parametric amplifier instead of the maser at the ground receiver is also shown explicitly on the figure.

* The straight lines on the figure represent continuous measurements during a pass.

There are two principal sources of measurement error in the data of Fig. 23: human errors and the different system configurations. The human errors are particularly acute, because of the relatively short time available for both measurements and calibrations, and because of inability to reproduce exactly any given set of testing conditions. The use of different system configurations for various tests has resulted in variations of the baseband transmission characteristics which were not always observed and recorded, thus leading to errors.

The large variance of the data on Fig. 23 thus reflects the measurement uncertainties and the increases in noise due to decreases in transmitted power to the satellite. The theoretical line shown on the figure gives the down-path noise alone, based on a 35°K system noise temperature and on the assumption of a triangular noise spectrum. The fact that the mean value of the figure is above the theoretical down-path line substantiates the assertion of the previous section, namely, that the up-path contributes about as much noise to the total as does the down-path.

The contribution of the baseband and IF loops to the 6-mc noise is negligible in every measurement: about −70 dbm for the IF loops and −80 dbm for the baseband loop.

7.3 *Television Noise*

7.3.1 *Video Noise*

The noise in the video channel is weighted using the latest Bell System video noise weighting network ahead of the measuring instrument. The detected video noise is recorded continuously during a pass simultaneously with the 6-mc noise and often with the audio channel noise. A typical recording of these noises is shown on Fig. 22, with the video noise at the bottom.

As expected, the video signal-to-noise ratio (SNR) is the same for both FM receivers, since their transmission characteristics are both essentially flat in the band of interest for video noise, i.e., below 2 mc. This is also evidenced by the scatter diagram of video noise vs received carrier power, Fig. 24, which shows the scattering to be the same for both receivers. The comments on the variance of the 6-mc noise data apply here equally well.

To account for the clampers used in the video circuit between the FM receiver and the test area in the computation of SNR, 1.0 db has been added to noise measured without clampers. Thus, the signal-to-noise ratios shown represent the practical situation for television receptions.

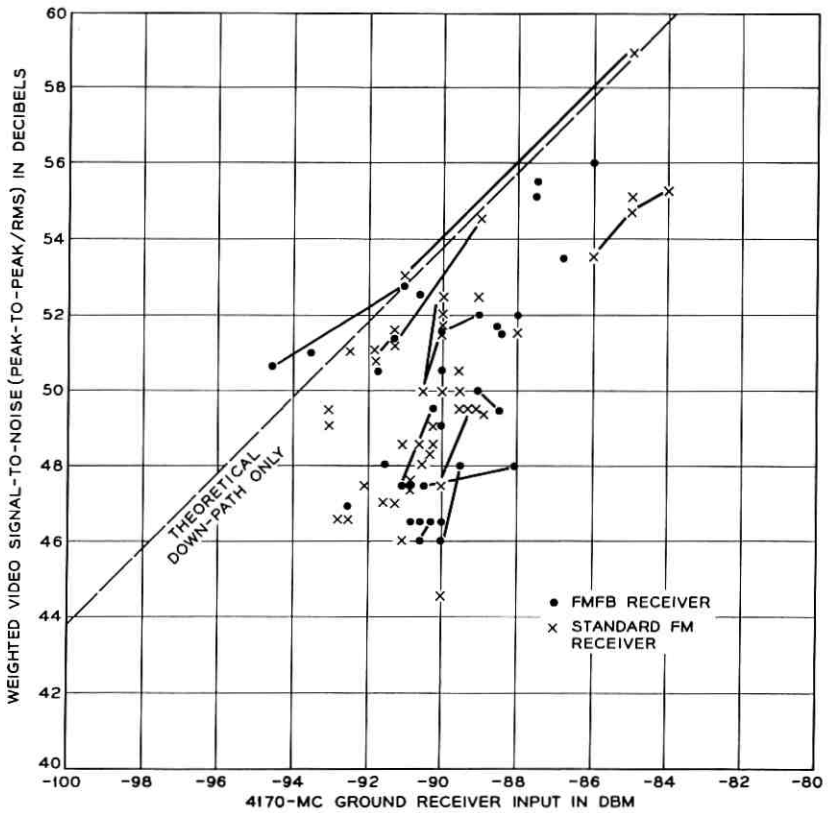

Fig. 24 — Video noise vs received carrier power.

The calculation of the theoretical value of the SNR for the down-path of Fig. 24 again assumes a triangular noise spectrum, plus the effect of the clamper and of the noise weighting. In this case, however, a triangular noise spectrum is too optimistic an assumption, as can be seen from the baseband noise spectra, Figs. 20 and 21. Because the up- and down-path noise contributions are about equal at 1 mc and because of the excess noise in the 1- to 3-mc band, it is not surprising that the average total video noise is about 5 db higher than the theoretical down-path noise.

As can be predicted from the baseband noise spectra measurements of Section 7.1, the IF loop video noise is at least 12 db lower than the satellite loop noise and the baseband loop noise is 2 to 3 db lower than the IF loop noise. The IF loop SNR is about 72 db.

TABLE IV — AUDIO SIGNAL/NOISE RATIO

	Audio SNR
Baseband loop	80 db
IF loop with FMFB receiver	75 db
IF loop with standard FM receiver	77 db
Satellite loop	55-65 db

7.3.2 *Audio Noise*

The Bell System 8-kc program noise-weighting network is used for the measurement of noise in the sound channel of the television signal. A continuous recording of the audio noise using the two FM receivers is also shown on Fig. 22, curve B.

This figure shows that under identical conditions the audio noise measured with the FMFB receiver is about 3 db higher than with the standard FM receiver. For the purpose of computing SNR, the signal is taken to be the peak power of a 1000-cps sine wave, resulting in a peak frequency deviation of the aural subcarrier of ±50 kc.*

The audio SNR measurements range from about 55 db to 65 db for 4-kmc received carrier powers of −95 dbm to −85 dbm. These measurements are not extensive enough to warrant presenting them in the form of a scatter diagram. The audio signal-to-noise ratios for the baseband. IF and RF loops are shown in Table IV.

7.4 *Telephone Noise*

The noise in five telephone channels located across a 3-mc band has been measured using the Telstar repeater. In addition to the circuits of Fig. 1, supergroups 2, 4, 6, 8 and 10 of the type L multiplex system were used for these measurements. The measuring equipment connected at the output of each supergroup consisted of a selective voltmeter† and a six-channel pen recorder. The noise was thus monitored continuously for several complete passes in order to observe the variation in noise with range, spin angle and satellite elevation.

The pen recordings for these measurements are very similar to those made for 6-mc and video noise shown on Fig. 22 and therefore are not reproduced here. However, typical values of noise in dbrn at 0 db TL (transmission level), measured during pass 1088, are shown in Table V.

* The so-called "program level" signal sometimes used for the calculation of SNR is 10 db lower than the signal assumed for the above computations.

† The voltmeters have a noise bandwidth of 6.3 kc and were each tuned to 450 kc. The values of Table V are corrected to a 3-kc bandwidth and for "C" message weighting.

TABLE V — TELEPHONE NOISE — PASS 1088

	11:52:00 UT	12:03:00 UT	12:07:30 UT	12:11:00 UT
Satellite antenna input (dbm)	−58.5	−60	−61	−62
Ground receiver input (dbm)	−88.5*	−92	−93	−94.3
Spin angle (degrees)	63	50	49	50
Range (miles)	2800	3115	3550	3960
Elevation (degrees)	20	27	22	18
Supergroup 2 (450 kc) dbrn at 0 db TL	27	30	31.5	31.5
Supergroup 4 (915 kc) dbrn at 0 db TL	34.5	36	37.5	38
Supergroup 6 (1411 kc) dbrn at 0 db TL	40.5	42	42.5	43
Supergroup 8 (1907 kc) dbrn at 0 db TL	42	45.5	47	47.5
Supergroup 10 (2651 kc) dbrn at 0 db TL	44	46	47.5	48

* This value, although inconsistent with other entries in the table, has been carefully rechecked against the original pen recording.

This table also shows the location of the measured channel in the baseband frequency spectrum.

7.5 *Impulse Noise*

Impulse noise measurements were made on the Telstar system during passes 208, 217, and 226 (August 1–3, 1962). These measurements were made primarily on voice circuits using an impulse counter and an experimental peak noise distribution measuring set. A standard noise measuring set was used to monitor the rms value of the noise.

The distribution of the noise peaks was recorded by the peak noise distribution set on voice circuits at levels of 6 to 10 db above rms value. These data indicate that only random thermal noise was present. The results of counting the noise peaks with the impulse counter also support the conclusion that very little impulse noise is present in the Telstar system.

7.6 *IF Noise Spectrum*

The IF noise spectrum is measured directly in the IF band using a selective analyzer covering the range of 55 to 95 mc. The analyzer used has nominal bandwidths of either 100 or 10 kc, a sensitivity of −100 dbm, and an accuracy and stability in the order of 0.2 db. The analyzer is connected at an intermediate point of the IF amplifier of Fig. 1. This IF amplifier consists of two separate amplifiers in tandem, the first being fixed-gain and the second having AGC. The analyzer is connected at the output of the first amplifier, where the nominal power is −22.5 dbm for a −80-dbm, 4-kmc input carrier to the maser.

Fig. 25 shows the results obtained during pass 1664, January 8, 1963. After the pass, the Andover antenna was pointed at the zenith and the

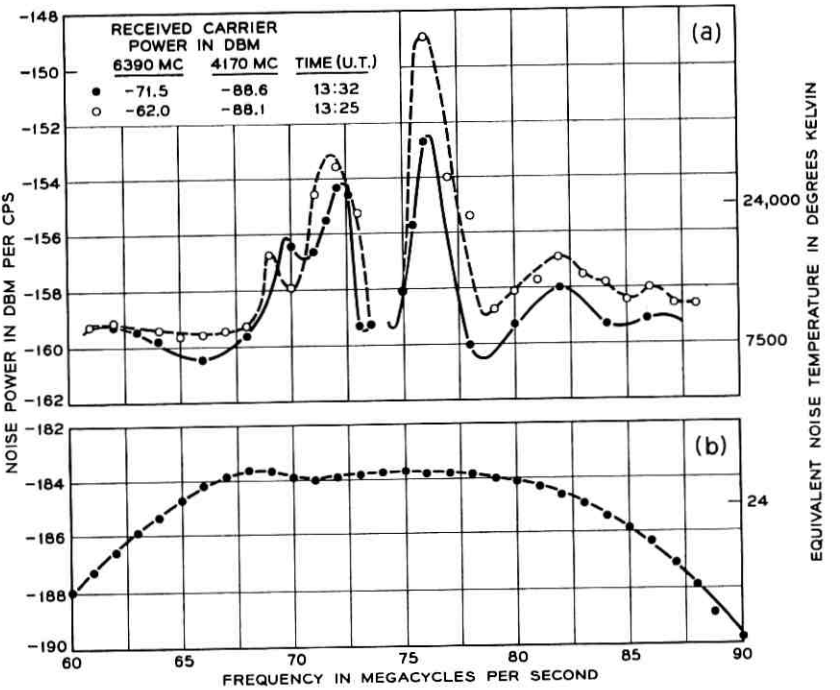

Fig. 25 — IF noise spectra: (a) Telstar satellite noise referred to satellite down-converter input; pass 1664, Jan. 8, 1963; (b) Andover zenith noise referred to maser input.

IF noise was measured. This measurement is referred to the output of the horn-reflector antenna (maser input) by correcting for the gain from this point to the point of measurement.* The bottom curve of Fig. 25 shows this result. The shape of this curve is consistent with the maser's transmission characteristic (see Section 6.2) with a bandwidth of 25 mc at 3-db points. The apparent ground station noise temperature is 30°K, which agrees closely with other observations.

To enhance the accuracy for the noise measurements with the satellite, a technique similar to that described in Section 7.1 was used. Four complete spectrum measurements were first made at about 2-minute intervals with maximum 6-kmc power transmitted to the satellite. The transmitted power was subsequently reduced, in order to increase the satellite's contribution to the total noise, and a detailed spectrum meas-

* This gain was measured only once, at the center frequency, and is therefore taken as fixed and uniform. In addition, the measured gain is increased by 1 db to account for the difference in maser gain when the input is broadband noise as opposed to carrier plus noise.

urement was made. The total noise was plotted as a function of time and smoothed values obtained corresponding to 13:25 UT (for full power transmitted) and 13:32 UT (reduced power). These smoothed values for the total IF noise were corrected on a power basis, for the ground station noise already discussed, to obtain the satellite's noise. Since the 6-kmc input to the satellite is known from telemetry and the 4-kmc input to the ground receiver is known from direct measurement with the selective analyzer,* it is possible to refer the satellite noise to the satellite down-converter input by making the appropriate corrections. The results are shown at the top of Fig. 25.

Several features of these curves are of interest. The humps at 72 and 76 mc, 6 to 10 db above the general noise level, clearly correspond to the hump at about 2 mc in the baseband noise, Figs. 20 and 21, and to the peak at 1.7 mc in the baseband frequency response, Fig. 16. The presence of the two humps suggests that the noise is leaving the satellite as modulation of the carrier.

The general noise level, excluding the humps, is -159 dbm/cps ± 2 db, corresponding to a noise figure of 15 db ± 2 db. The inclusion of the noise humps results in an integrated noise figure of 16.5 db ± 2 db (integrated over a 20-mc band), referred to the satellite's down-converter input. A separate measurement made prior to launch[6] using a noise lamp resulted in a satellite noise figure of 13.5 db ± 1 db, for the region where the noise spectrum is flat.

It was stated in Section 7.1 that the baseband noise attributable to the satellite has not been affected by launch or space environment. The same conclusion is reached from a comparison of Fig. 25, for pass 1664, with Fig. 26, the calculated† pre-launch IF noise spectrum. The exact symmetry of Fig. 26 is due to the fact that these curves were calculated from measurements of baseband noise such as shown on Fig. 21, curve C. As expected, the peaks of the calculated noise of Fig. 26 lie between the levels of the measured, unequal peaks of Fig. 25.

VIII. NONLINEARITY AND CROSS-MODULATION

8.1 *Envelope Delay Distortion*

The envelope delay distortion (EDD) discussed here is that found in in the IF and RF circuitry of the system. It is to be distinguished from

* For this test, the 6-kmc carrier transmitted to the satellite is derived from a crystal-controlled oscillator. The stability of this source is sufficient to enable accurate measurement of the received 4-kmc carrier within the 100-kc band of the selective analyzer used.

† The measurement of noise at IF was not made prior to the launch of the Telstar satellite.

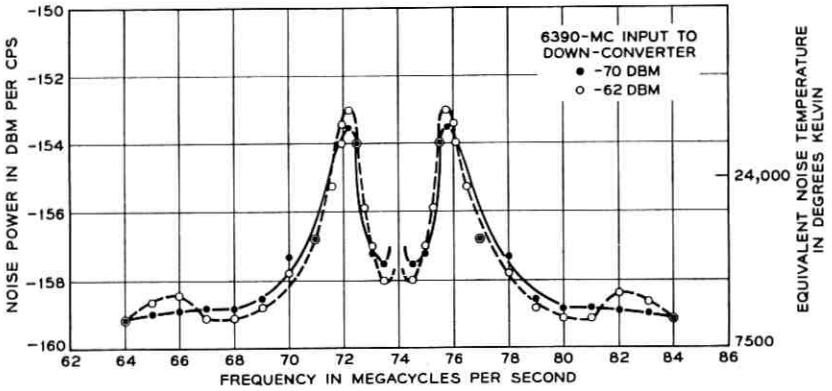

Fig. 26 — Pre-launch IF noise spectra of Telstar satellite referred to satellite down-converter input; calculated from baseband noise measurements.

the over-all baseband delay distortion of the system. This latter, which causes baseband waveform distortion, is of importance in the total baseband when transmitting TV and in individual segments of baseband when data-type signals are transmitted. Measurements of baseband distortion are not presented here for the Telstar satellite because available test equipment does not have adequate resolution in the presence of signal-to-noise ratios typical of those encountered in this experiment. It is inferred that it is satisfactory from examination of television test signal transmissions.

EDD, which causes cross-modulation in FM systems, is measured by the two-frequency sweep method, using the standard test set used on TD-2 and TH radio systems. The test set is located adjacent to the FM terminals, to which it is connected directly.

Briefly, this set operates as follows. A 100-cps sine wave is applied to the BO klystron of the FM deviator[5] so that the output IF sweeps from 62 to 86 mc. Simultaneously, a 278-kc sine wave from a crystal oscillator is applied to the video (baseband) input of the deviator to give a peak deviation of about 200 kc. At the FM receiver video output, the 100-cps and 278-kc signals are recovered and separated. The 100-cps tone is used for horizontal scope deflection. The 278-kc tone is phase-modulated by the transmission delay distortion of the system (at 278 kc, 1° = 10 ns). Its phase is compared with that of a 278-kc crystal oscillator located in the delay receiver. The latter oscillator is phase locked to the long-term average phase of the received 278-mc tone by suitable circuitry. The phase variations are used for vertical scope deflection, with a customary EDD sensitivity of 5 ns per small division (0.2 inch). As may be seen

from the photos presented, the signal-to-noise ratio of this set is really not satisfactory for the Telstar system, but is not so poor as to obscure essential results.

Each of the elements shown in the block diagram of Fig. 1 contributes to the total EDD of the system. The EDD is mostly parabolic and is inherent in the bandpass characteristic of the system. Delay equalization provides the inverse characteristic and improves the cross-modulation performance of the system for telephone operation and the differential phase for TV operation. It is desirable to equalize each element individually, but this is frequently impractical.

On pass 925 (October 19, 1962) the over-all system was equalized. The equalization was in four parts, as shown in Table VI.

In the feedback FM receiver, the IF swing is reduced by the feedback to less than 1 mc, and therefore, its EDD is negligible.

Fig. 27 shows the measured EDD of the IF loop, which includes the equipment and equalizers of the first three items of Table VI. Fig. 28 shows the EDD measured through the boresight repeater and Fig. 29 shows the EDD measured through the satellite on pass 925.

8.2 *Differential Gain and Phase*

The differential gain and phase measurements are similar to the EDD test, but are specifically designed to measure the ability of a video system to transmit color TV. The details are therefore different. The low frequency is 15.75 kc and is adjusted to sweep the IF ±7 mc (67 mc to 81 mc). The high frequency is 3.58 mc and is applied at a power level 14 db below that of the 15.75 kc. The test set is located in the test area where it is connected to the video lines. For this test, the low-pass filter and the diplexers of Fig. 2 are removed from the video lines, and

TABLE VI — EDD EQUALIZATION

Equalization for	Location	Amount of Eqn* (ns)
FM deviator	Output of deviator	†
Intermediate IF amplifier	Input of IF amp.	$-0.25(\Delta F) - 0.07(\Delta F)^2$
Standard FM receiver	Input of FM receiver	$+0.44(\Delta F) - 0.10(\Delta F)^2$
RF circuits, including modulator-amplifier, power amplifier, satellite repeater, and RF amplifier	Output of RF amp.	$+0.95(\Delta F) - 0.13(\Delta F)^2$

* This is expressed as a power series, in which ΔF is the difference in mc from 74 mc.

† This is a gain equalizer for the delay equalizer of the standard FM receiver and has negligible EDD.

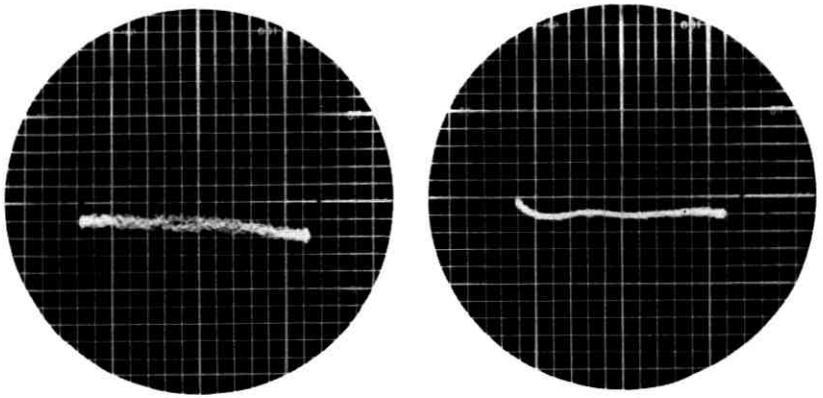

Fig. 27 — Envelope delay distortion of IF loop, Oct. 19, 1962. Left: FMFB receiver. Right: standard FM receiver. Horizontal scale: 1 division = 2 mc (sweep = 62–86 mc). Vertical scale: 1 division = 5 ns.

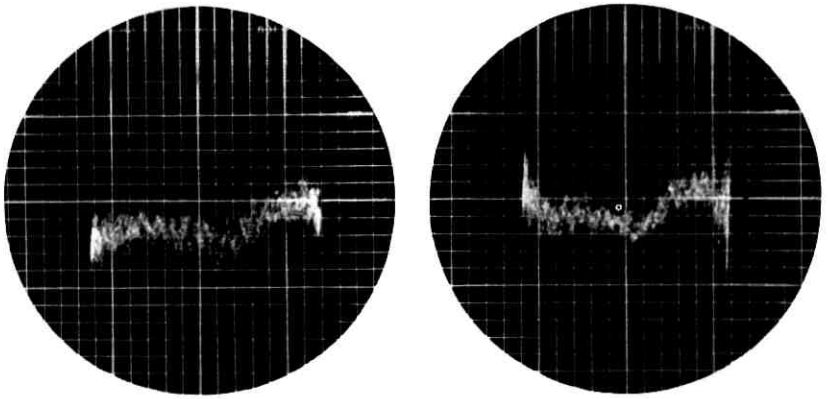

Fig. 28 — Envelope delay distortion of equalized loop through boresight repeater, Oct. 19, 1962. Left: FMFB receiver. Right: standard FM receiver. Scales same as Fig. 27.

only the standard FM receiver is used. At the receiving end, the recovered 15.75-kc tone drives the scope horizontally. Either the gain or phase variations of the 3.58-mc tone can be shown as the vertical deflection. Typically the sensitivity is 0.2 db and 1° per small scope division. The SNR of this test set when used with the satellite system is poor.

On pass 1113 (November 9, 1962) photos were made of the equalized system. Fig. 30 shows the results. The baseband loop has no discernible distortion on this test, and therefore no photo is presented here.

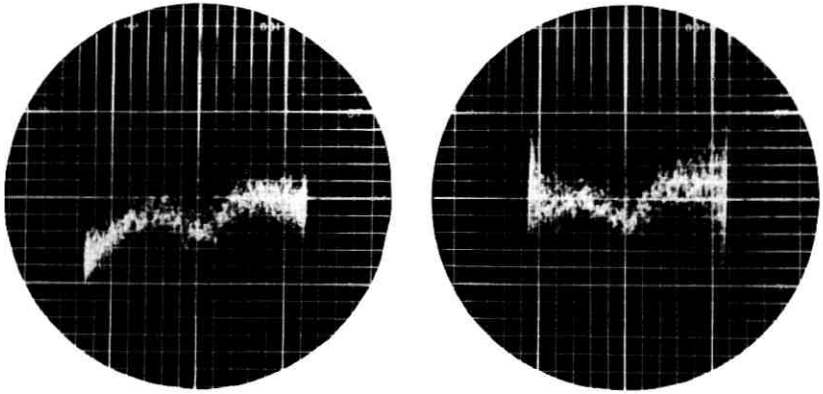

Fig. 29 — Envelope delay distortion of equalized loop through Telstar satellite; pass 925, Oct. 19, 1962. Left: FMFB receiver. Right: standard FM receiver. Scales same as Fig. 27.

8.3 *Noise Loading*

Noise loading simulates the operation of the system with 600 channels of multiplex telephony. The test set used for the noise loading measurements generates white noise in the band of 60 to 2660 kc and has slots cleared of noise at 70, 1248, and 2438 kc. With flat loading, the calculated normal TL at the test point is −18 db TL. The total noise power corresponding to the 600 telephone channels is −7 dbm. The system has an over-all net loss of 0 db, and therefore the receiving TL is the same as the transmitting TL. The noise loading equipment measures the total received noise power (sum of thermal noise and cross-modulation noise) in the noise slots. This is converted, for plotting purposes, into dbrn at the zero db TL point.

There is 5 db loss from the test area to the FM deviator input; hence, at nominal TL, the noise power at the FM deviator is −12 dbm. The deviator sensitivity is set so that 0 dbm of a sine wave gives 20-mc peak-to-peak, or 7.07-mc rms, deviation. Therefore, the rms deviation for nominal TL is 1.77 mc. By varying the applied noise power (the drive on the system) the rms deviation can be changed; this corresponds to changing the assigned TL.

Fig. 31 shows the results obtained on pass 1015.* When circuit noise is controlling, the SNR improves db for db as the drive (rms deviation) is increased. This accounts for the 45° down-sloping line at the left.

* At this time, one of the components of the equalizer for the RF circuit was defective and was removed, so that +0.5 ns/mc of EDD slope equalization was missing from the satellite loop. The measured EDD for this condition (taken on pass 1042, November 1, 1962) is shown in Fig. 32.

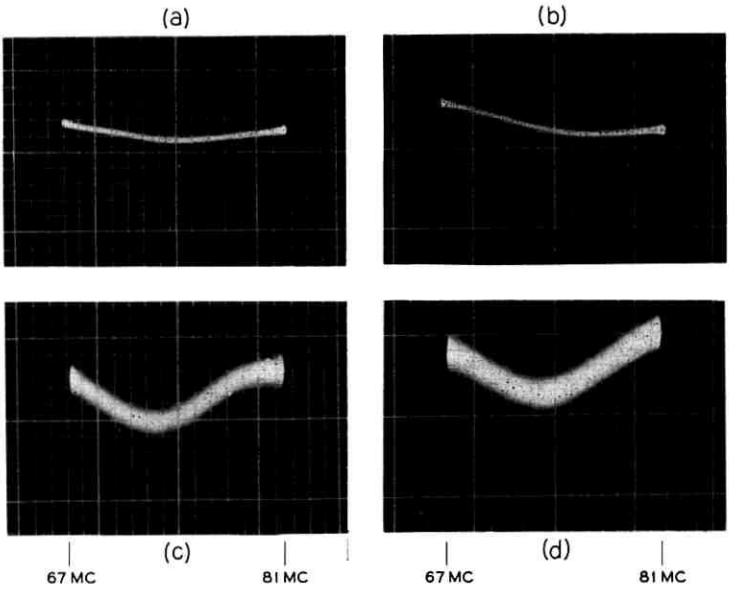

Fig. 30 — Differential gain and phase of equalized loops; standard FM receiver. Sweep: 67–81 mc. (a) Differential gain of IF loop. Vertical scale: 1 division = 0.2 db. (b) Differential phase of IF loop. Vertical scale: 1 division = 1°. (c) Differential gain of Telstar satellite loop; pass 1113, Nov. 9, 1962. Vertical scale: 1 division = 0.4 db. (d) Differential phase of Telstar satellite loop; pass 1113, Nov. 9, 1962. Vertical scale: 1 division = 2°.

However, as the drive is raised, the cross-modulation products increase 2 db per db for second order, 3 db per db for third order, and eventually become controlling. The very sharp upward break at the right shows that very high order modulation products are involved, indicative of severe overload or clipping.

Overloading (or overdrive) occurs when the peaks of the noise substantially exceed the design peak deviation. The peak deviation due to noise is 6 db higher than rms 5 per cent of the time, 9 db higher 0.4 per cent of the time, and 12 db higher 0.01 per cent of the time. For example, with a drive corresponding to an assigned −12 db TL at the test point, or 6 db above normal, the rms deviation is 3.54 mc and the peak deviation exceeds 10 mc 0.4 per cent of the time. At −9 db TL drive, the peak deviation exceeds 10 mc 5 per cent of the time and 20 mc 0.01 per cent of the time. The system bandwidths cannot accomodate such overdrives.

Fig. 33 shows noise loading curves for the IF loop. This shows the modulation break to be generated, to a considerable extent, in the

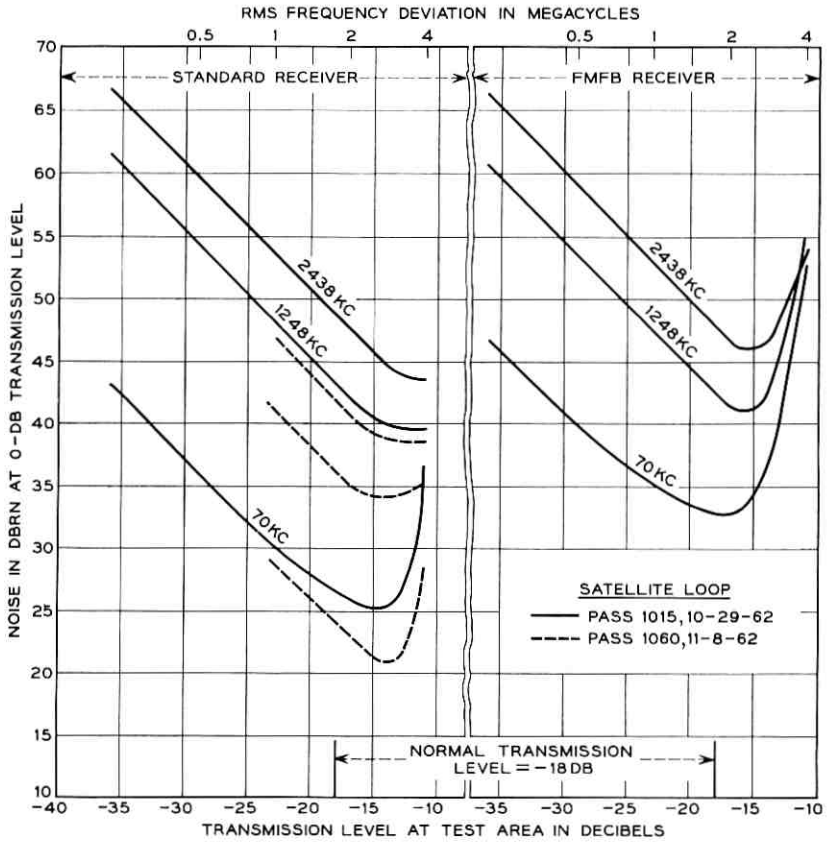

Fig. 31 — Telstar satellite loop noise loading measurement; passes 1015 and 1060.

terminal equipment. The FMFB receiver overloads sooner than the standard FM receiver since its noise performance at normal TL is nearly 10 db poorer than the standard receiver.

Since the video transmission system (Fig. 1) is also included in these tests, Fig. 34 shows noise loading performance of the baseband loop. This graph indicates that the baseband has third-order cross-modulation.

It appears from the noise loading data that for the EDD equalized system carrying 600 telephone channels and using the standard FM receiver, the contribution of cross-modulation to total system noise is small at the normal operating TL. Operation would probably be satisfactory at 3 db higher TL, giving 3 db less noise. The modulation break

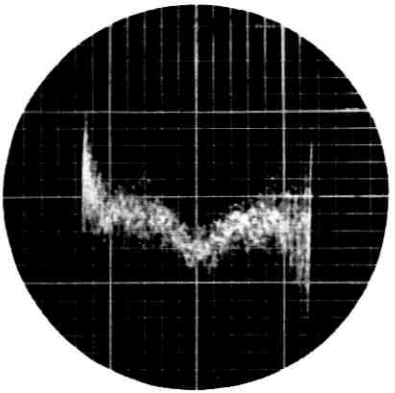

Fig. 32 — Envelope delay distortion of Telstar satellite loop with 0.5 ns/mc EDD equalization missing; pass 1042, Nov. 1, 1962; standard FM receiver. Scales: same as Fig. 27. Compare with Fig. 29, right.

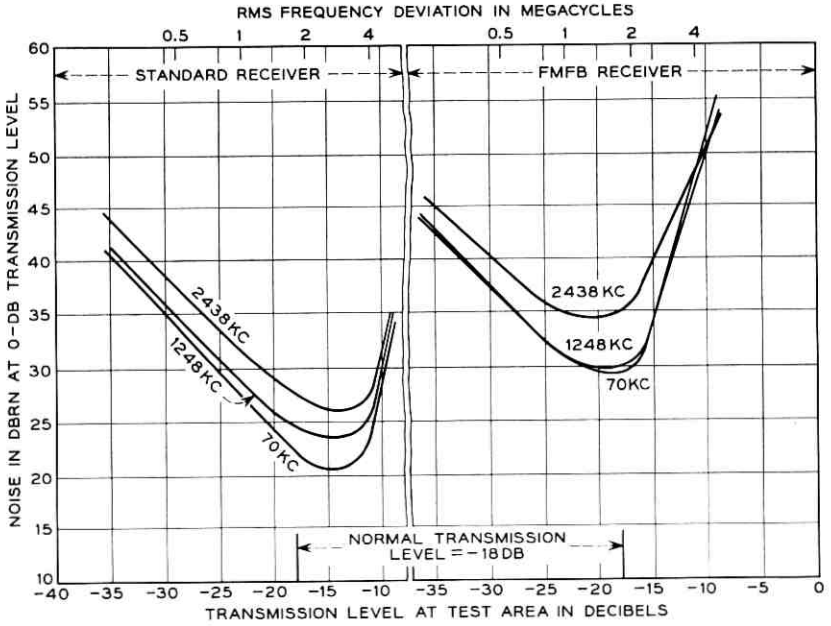

Fig. 33 — IF loop noise loading measurements, Nov. 1, 1962 (no pre-emphasis).

appears to be controlled by the video and IF equipment. However, the tests and calculations are based on telephone loading and take advantage of talker volume distribution and idle time. If a substantial part of baseband is carrying data service, the allowable TL will be reduced.

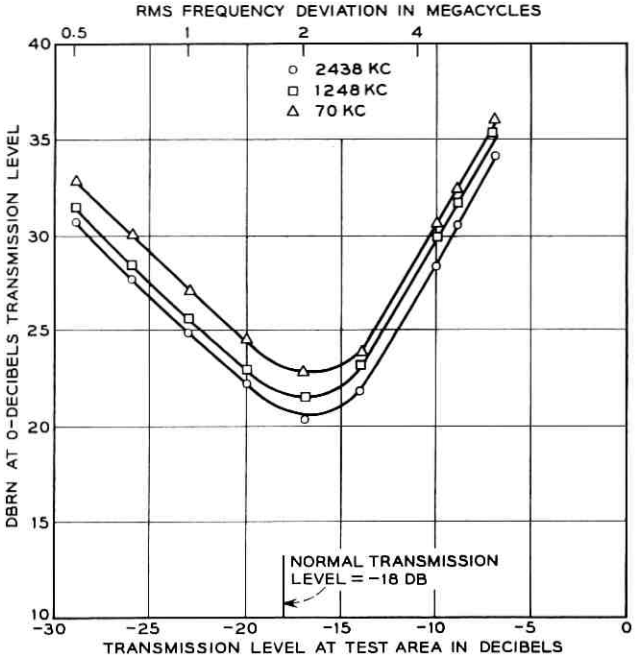

Fig. 34 — Baseband loop noise loading measurements, Sept. 27, 1962.

An acceptable value for channel noise at zero TL is 45 dbrn. Fig. 31 shows this to be exceeded by 3 db at 2438 kc. However, high-frequency noise is determined by the radio path. The dotted lines on Fig. 31 illustrate a noise loading test made during pass 1060 (November 3, 1962) when the range was about 1500 miles instead of the approximately 4000 miles for pass 1015. The channel noise performance therefore is a statistical process, and the data at hand are not sufficient to plot a noise probability distribution curve.

It is clear from Fig. 31 that the noise performance could be equalized across the band by the use of pre-emphasis. Tests have been made using the standard TD-2 pre-emphasis, shown in Fig. 35. The pre-emphasis and de-emphasis networks are patched in ahead of the FM deviator and after the FM receiver (see Fig. 1). Their total loss is a flat 14 db. This was compensated for by removing a 3-db pad in the transmitting line and 11 db of loss in the receiving line. Over the range of 60-2660 kc, the pre-emphasis network reduces the total noise power by 6.5 db with a resulting net power loss of 3.5 db in the transmitting path. Therefore, the normal TL at the test area is −14.5 db TL.

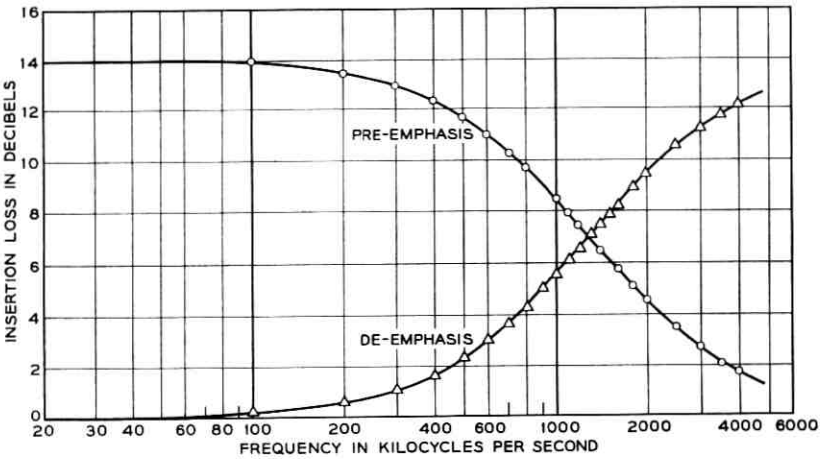

Fig. 35 — Insertion loss for telephony pre- and de-emphasis networks.

Fig. 36 shows noise loading measurements with pre-emphasis. These results show that TD-2 pre-emphasis is not the optimum for this system.

8.4 *Intermodulation: Video to Audio*

The audio noise measurements discussed in Section VII and shown in Fig. 22 are for the condition of no video signal being transmitted. When video material is transmitted, the audio noise increases. Presumably, the additional noise is due to cross-modulation (video-to-audio) due to nonlinearity of the over-all system. Tests of diplexers back-to-back show that direct interference due to power in the video signal at 4.5 mc is not significant, except possibly for the multiburst test signal.

Audio noise was measured repeatedly with no video present and also with a monoscope (Indian Head) signal. The 2-mc roll-off filter was omitted. No EDD equalization or video pre-emphasis was used in the system for this test. Examination of the data shows no clear correlation between audio noise and 6- or 4-kmc received carrier. Accordingly, the data for each pass have been averaged with the results shown in Table VII.

These data show the monoscope signal to give a weighted audio SNR of about 56 db. Tests made on early passes with other types of video test signals (multiburst, stairstep, window) showed the monoscope to have about as much effect as any. No audio to video cross-modulation interference has ever been observed, even under exaggerated laboratory tests.

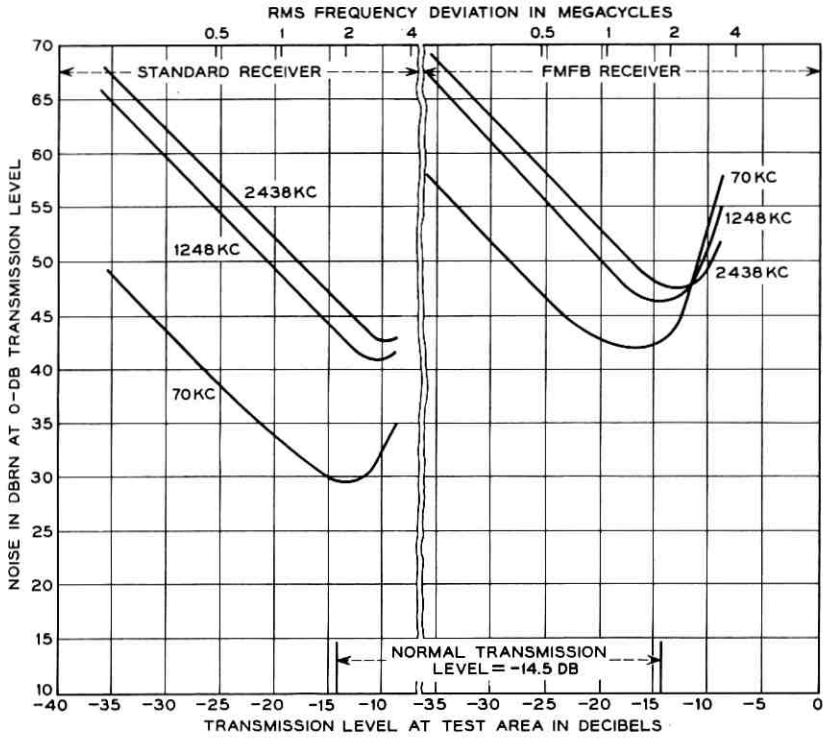

Fig. 36 — Telstar satellite loop noise loading measurements; pass 1016, Oct. 29, 1962 (with pre-emphasis).

IX. TELEVISION

Television transmission over the Telstar system has been highly successful for both monochrome and color signals. Most of the signal impairment which has been observed was expected and is in agreement with calculated performance. One type of impairment which was not anticipated is also reported here.

Probably the most noticeable signal impairment is some loss in picture definition. This is almost entirely attributable to the low-pass characteristics of the ground station equipment. The principal contributors are the 2-mc low-pass filter, the transmission characteristics of the 4.5-mc diplexers, and the roll-off in the FMFB receiver. This impairment was intentionally accepted in order to make possible the transmission of the audio signal as well as the video signal. As indicated by the baseband transmission characteristics presented in Section 6.1, the

TABLE VII — VIDEO-TO-AUDIO INTERMODULATION

Pass	FM Recvr.	Avg. Recd. Carr. (dbm)		Weighted Audio SNR*	
		6 kmc	4 kmc	No Video	Monoscope
316	Std	−61.5	−90	63	56
326	FB	−61	−89	61.5	55
341	FB	−61.5	−88	61.5	56.5
350	FB	−61	−92.5	60.5	56
350	Std	−62.5	−93	62	58
570	Std	−63	−91	60.5	57 (Monoscope) 55 (Multiburst)

* SNR is defined in Section 7.3.2.

removal of the filter and diplexers and the use of the standard FM receiver eliminate this impairment.

A second impairment, also anticipated, was somewhat noticeable noise at maximum range. Under this condition the predicted (and measured) weighted signal-to-noise performance of the system is somewhat less than the normal Bell System objectives for commercial service. Typical values for the weighted signal-to-noise ratio have already been discussed in Section 7.3.

A third impairment, not anticipated, occurred during several of the demonstration transmissions from Andover to Europe. In these demonstrations, the transmitted signal originated in other parts of the country and was transmitted to Andover via the microwave radio system between Boston and Andover. Coincident with switches at the originating studio from one camera pickup to another, there were very annoying bursts of noise occurring in both the video and audio channels received over the satellite system. These noise bursts were not present in the signal applied to the ground transmitter. The difficulty was apparently caused by the transients which accompanied the switch from one signal to the other. In the signal as received for transmission at Andover, these appeared as relatively long (100 milliseconds or greater) negative pulses which were large compared to the normal peak-to-peak value of the video signal. Since the system itself uses a high-index deviation (14 mc peak-to-peak) in a 25-mc system bandwidth, these pulses were apparently large enough to cause the FM deviator to shift momentarily out of the 25-mc band. This resulted in momentary loss of signal at the various ground receivers, and the automatic gain control circuit increased the receiver gains long enough to cause substantial noise bursts in both the video and audio outputs.

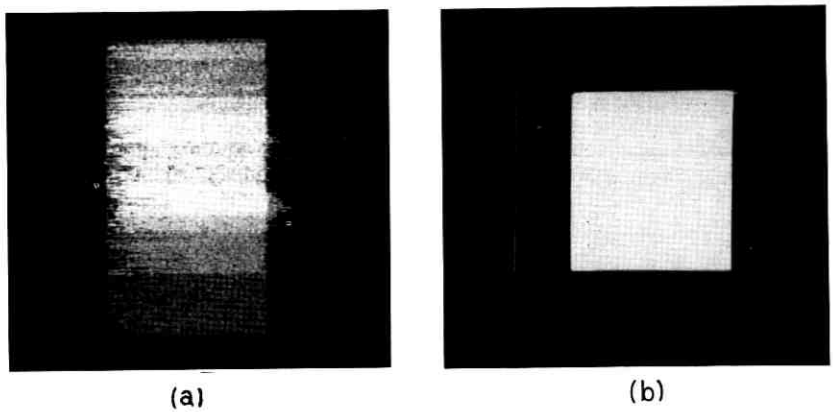

Fig. 37 — First video signals from Telstar satellite; pass 6, July 10, 1962. (a) Noisy pulse and window; (b) clear pulse and window.

9.1 *Early Transmissions*

This section includes samples of some of the early picture material transmitted over the Telstar satellite. In all cases the television signal was a standard 525-line signal. The photographs were all taken at Andover using a standard picture monitor and oscilloscope and a Polaroid camera. A substantial amount of picture degradation has occurred in the reproduction processes, but the results are believed to be of sufficient historical interest to warrant their inclusion here.

Pass 6—July 10, 1962

During this pass the satellite repeater was turned on for the first time following the successful launch earlier in the day. Some of the significant events of this pass are recorded in Table VIII; the table explains the signals shown in Figs. 37 and 38.

Pass 15—July 11, 1962

On the following day the first television pictures were received from Europe. Fig. 39(a) shows the first signal received from France during pass 15 and Figure 39(b) shows a subsequent picture received during the same pass. The French material had been prerecorded on video tape.

Pass 16—July 11, 1962

A little less than three hours later the first transmissions from England took place. The first signal and a subsequent picture received from the

(a)

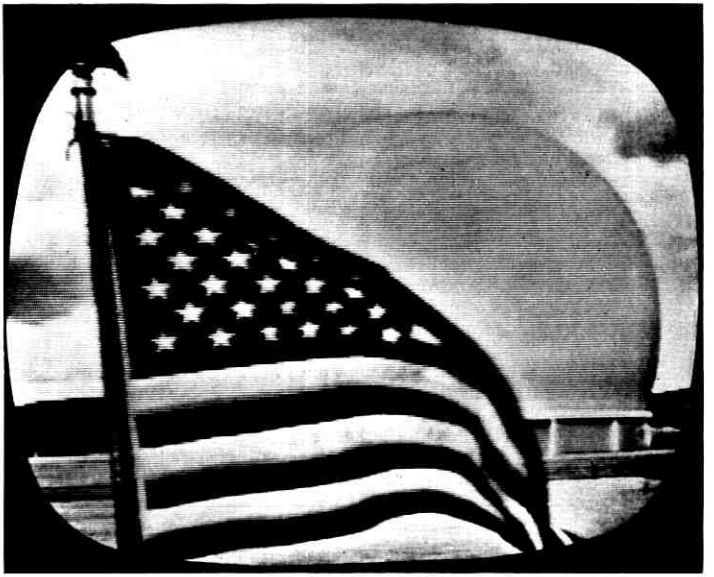

(b)

Fig. 38 — First public demonstration of television via Telstar satellite; pass 6, July 10, 1962. (a) American flag in front of radome; (b) Mr. Frederick R. Kappel.

TABLE VIII — SIGNIFICANT EVENTS — JULY 10, 1962

Time (UT)	Event
23:18	Andover command tracker acquires Telstar satellite.
23:20	Andover telemetry in synchronism. First command sent to turn on traveling-wave tube.
23:21	Second command sent to turn on traveling-wave tube.
23:23:36	Third and final command completed turn on of traveling-wave tube.
23:23:56	Precision tracker in autotrack.
23:24:34	Autotrack system for horn antenna in lock.
23:25:00	First video signal from Telstar satellite, a noisy pulse and window, received at Andover. Transmitter not yet at full power. [Fig. 37 (a)].
23:25:30	A clear pulse and window being received [Fig. 37(b)].
23:30	Start telephone conversation from Mr. Frederick R. Kappel, AT&T Board Chairman, to the Vice President of the United States, Mr. Lyndon Johnson.
23:33	Taped television transmission sent to Telstar satellite. The first received picture is shown in Fig. 38(a). The picture shown in Fig. 38(b) was taken about 2 minutes later.
23:47:30	Television pictures were received in France.

Goonhilly Downs station are shown respectively in Figs. 40(a) and 40(b). The picture material is from a live pickup at the Goonhilly station.

9.2 *Color Television*

Color television signals have been transmitted via the Telstar satellite on several occasions. The first such transmission took place during pass 60 on July 16, 1962, when several color slides were transmitted from the Goonhilly Downs station to the Andover station. A similar transmission took place during pass 88 on July 19. Photographs taken at the Andover station of the Goonhilly signals are shown in Fig. 41 (color plates, opposite p. 1614). In addition, several color slides were originated at the Murray Hill location of Bell Telephone Laboratories and were transmitted from Andover to Goonhilly Downs on this pass. Additional test transmissions in both directions took place during pass 178 on July 29, 1962. For all of these tests the 4.5-mc aural diplexers and low-pass filter were removed from the circuit and the standard FM receiver was used.

9.3 *Two-Way Television*

The first two-way transatlantic television tests were conducted during pass 142 on July 25, 1962, between the Andover station and the Pleumeur-Bodou ground station. Separate FM carriers were used for the two directions. The signal from Andover to Pleumeur-Bodou was trans-

Fig. 39 — First television signals received from France; pass 15, July 11, 1962. (a) First signal received; (b) video tape transmission.

mitted at 6394.58 mc, or 5 mc above the nominal center frequency. The signal in the other direction was transmitted 5 mc below the nominal center frequency, or at 6384.58 mc. Fig. 42 shows a test pattern received from France during this test.

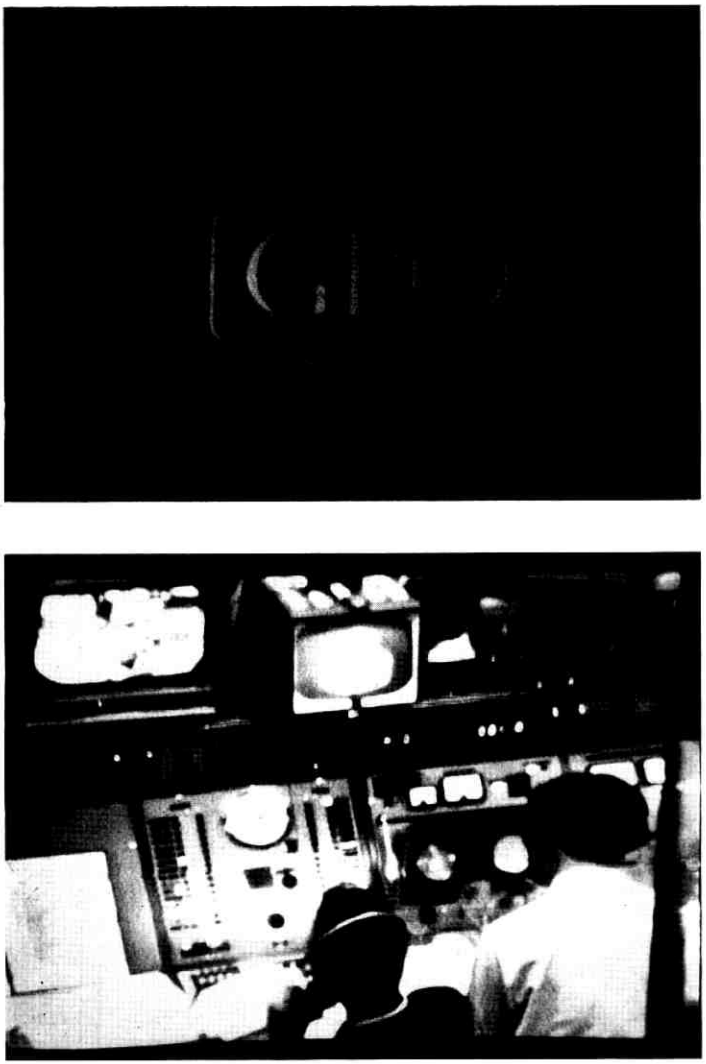

Fig. 40 — First television signals received from England; pass 15, July 11, 1962. (a) First signal received; (b) live video from Goonhilly Downs.

In addition to the simultaneous transmission in two directions, some two-way loop tests were made. Fig. 43 shows a photograph of video tape material after transmission to Pleumeur-Bodou, where the signal was looped and returned to Andover after traveling twice through the satellite repeater.

For these tests, IF bandpass filters 6 mc wide were used in both stations. The frequency deviation was adjusted to be approximately 2 mc peak-to-peak. Audio signals were transmitted in both directions by means of the 4.5-mc diplexers, but with definite degradation in audio quality.

A stabilizing amplifier was used to insert new sync pulses in the received signal. This resulted in definite improvement in the synchronization of the monitors.

In an attempt to optimize signal-to-noise ratios at the ground receivers, the ground transmitter power was programmed at both stations to provide −63 dbm at the satellite converter (assuming an isotropic antenna at the satellite).

The principal degradation to picture quality was noise, which was probably about 20 db poorer than in normal one-way transmissions. About 16 db was due to the reduction in frequency deviations from 14 mc to 2 mc peak-to-peak. The additional degradation was due to the reduced transmitter power per carrier at the satellite output. The ratio of peak-to-peak signal to rms noise was probably between 25 and 30 db. Crosstalk between channels was not noticeable.

X. TWO-WAY TELEPHONY

10.1 *Early Transmissions*

The Andover and Goonhilly Downs stations were arranged for two-way telephone tests for pass 24 on July 12, 1962. Transmission and noise were checked on each of the two-way channels. One of the channels was used as an order wire by technicians in the two stations to coordinate the test procedure. These tests indicated that a successful demonstration of two-way telephony could be expected on the following day.

During pass 33 on July 13, 1962, the first demonstration of two-way telephony took place between Kingston, New York, and Paris, France. The first call was placed by Mr. E. J. McNeely, President of the A.T.&T. Co., to M. Jacques Marette, Minister of Communications, and other French government officials. This was followed by other calls.

10.2 *Channel Noise*

Noise measurements in at least a portion of the telephone channels have been made on nearly all of the many two-way message transmissions. Typically, the channel noise has been in the range between 40 and 48 dbrn at 0 db TL, depending on the satellite range and the relative

power in the two signals at the satellite input. Although range information is available for all of the passes, the determination of the relative input power of the two signals is not possible during a normal transmission test. This is because the AGC circuit in the satellite responds only to the total signal. On pass 706 more complete data were obtained in an Andover and Pleumeur-Bodou test. By alternately turning off the two ground transmitters, their individual contributions to the input power at the satellite was measured and adjusted. In this way, it was possible to determine the noise in telephone channels of both carriers being transmitted by the satellite under known conditions. On pass 1014 a similar test was made, at which time the satellite range was substantially less. The results are shown in Table IX and are in good agreement with expected performance. Just as one would expect, when the power of one of the carriers is reduced at the input to the satellite, the noise increases for the channels on that carrier. At the same time, the other carrier gets an increased portion of the total power at the satellite output and the noise decreases in the telephone channels on the stronger carrier.

10.3 *Crosstalk*

The simultaneous amplification of the FM signals in the single satellite repeater gives rise to some crosstalk from one carrier to the other. No problems have been encountered in actual two-way telephone transmissions. However, the mechanism is such that with reduced circuit noise, intelligible cross-talk would occur from a particular telephone channel on one carrier to the corresponding channel on the other carrier. With sufficient noise, the crosstalk falls below the noise level and is not objectionable.

To evaluate quantitatively the crosstalk loss, specific tests were made such that the crosstalk could be measured above the background noise. The results of one such test made during pass 697 are included in Table X. The 6395-mc carrier transmitted at Andover was modulated with either a 100- or 200-kc sine wave. Peak frequency deviations of 1.0, 0.5 and 0.25 mc were used. A 6385-mc unmodulated carrier was transmitted by the Goonhilly station. At Andover the 100- or 200-kc modulation of the carrier received from Goonhilly was measured and compared with the modulation applied to the Andover carrier. The difference was recorded as the crosstalk loss.

Fig. 41 (Opposite page) — Color test signals from Goonhilly Downs to Andover; pass 88, July 19, 1962. ⟶

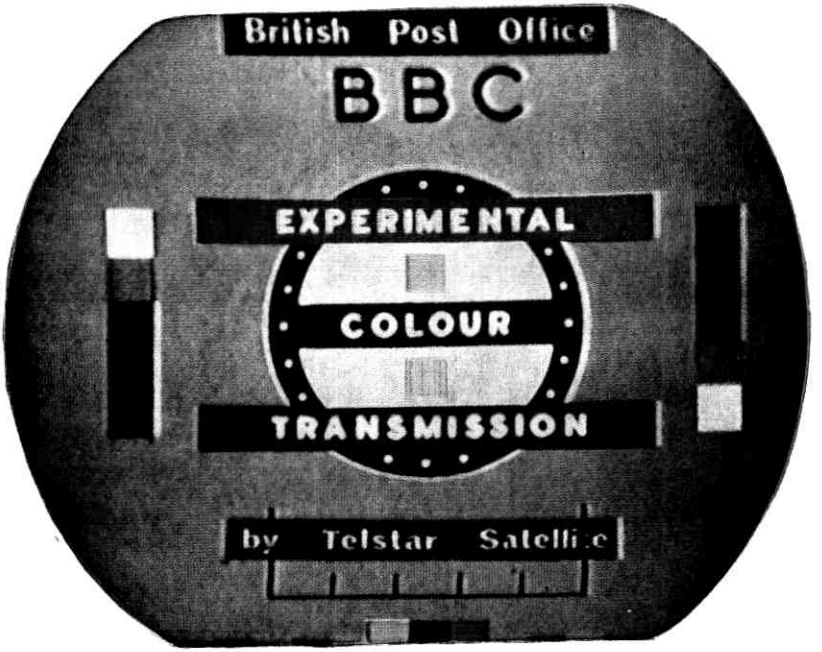
British Post Office
BBC
EXPERIMENTAL
COLOUR
TRANSMISSION
by Telstar Satellite

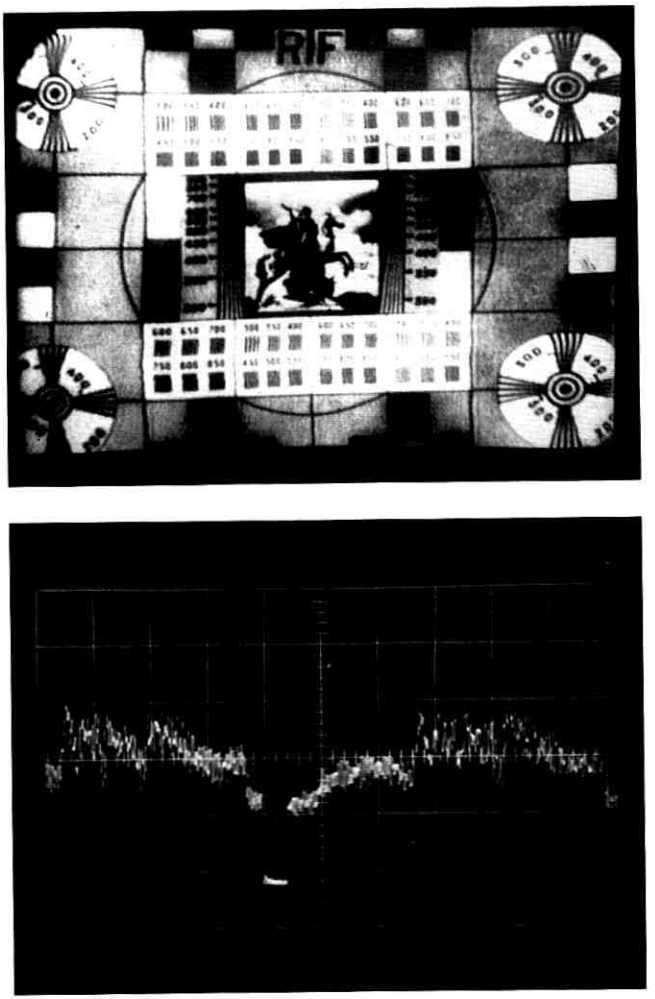

Fig. 42 — Signal received from France during two-way television transmission; pass 142, July 25, 1962. Top: test pattern. Bottom: oscilloscope presentation of individual lines.

XI. DATA TRANSMISSION

The suitability of the Telstar system for handling various types of data signals has been verified by means of tests ranging from the transmission of ordinary 60-wpm teletypewriter signals to 875,000 bit per second serial data, as well as various types of facsimile signals. Bell System data terminals were used for most of these tests. In order to

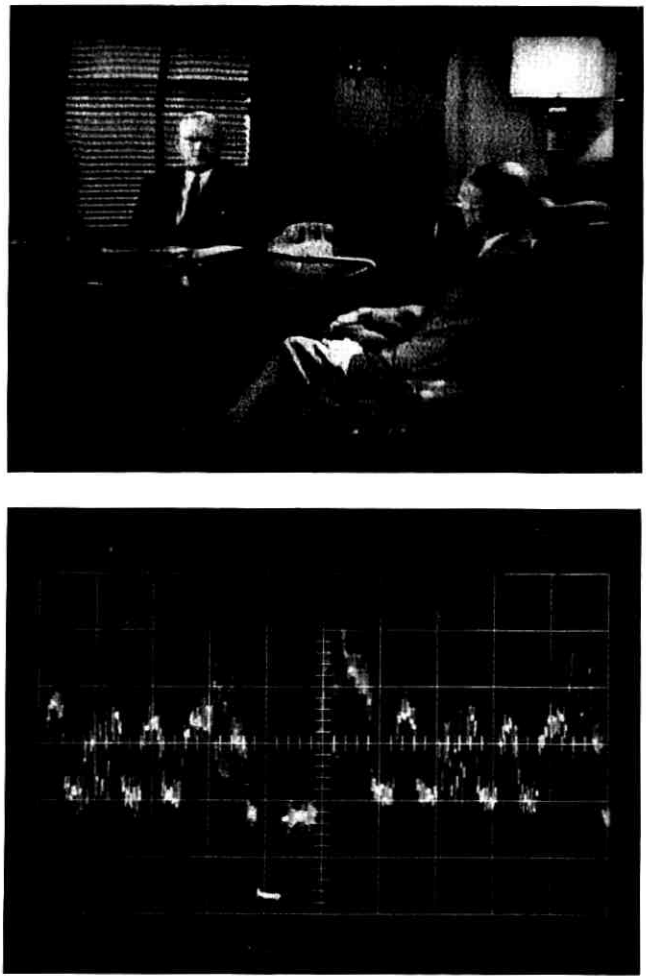

Fig. 43 — Television signal transmitted to France and returned to Andover; pass 142, July 25, 1962. Top: monitor presentation. Bottom: oscilloscope presentation of individual lines.

predict the performance of other signals and data terminals, basic transmission parameters in the voice-frequency band were also measured.

The transmission path for these tests included approximately 800 miles of land telephone circuits* in addition to that shown in Fig. 1,

* Most of the U. S.-based terminal equipment was located at 32 Avenue of the Americas, New York City. The tests described herein were principally conducted by personnel of the Long Lines Dept., A.T.&T. Co., from August 6 to October 18, 1962.

TABLE IX — TWO-WAY TELEPHONE NOISE

Pass No.	Time (UT)	Andover to Satellite Range (SM)	Signal Power at Satellite (dbm)		Telephone Noise (dbrn at 0 db TL)*				Received Carrier Power at Andover (dbm)	
					Andover Carrier		Pleumeur-Bodou Carrier			
			Andover Carrier	Pleumeur-Bodou Carrier	Channel 1	Channel 11	Channel 1	Channel 11	And. Car.	P-B Car.
706	15:54:30	3390	−65	−65	—	—	43.5	43.5†	—	−95
	15:56:30	3490	−65	−65	40.0	42.0†	—	—	−95	—
	15:59:30	3760	−68	−65	47.0	45.2†	—	—	<−95	—
	16:01:30	3850	−68	−65	—	—	43.0	43.0†	—	−94
	16:04:30	4030	−71	−65	—	—	42.0	42.0†	—	<−95
	16:08:30	4420	−71	−65	51.0	52.0†	—	—	<−95	—
	16:09:30	4470	−71	−65	43.0	44.0†	—	—	<−95	—
	16:10:30	4580	−65	−65	—	—	44.0	46.0†	—	<−95
1014	09:17:30	1800	−61	−61	—	—	36.5	36.0	—	−90.0
	09:18:30	1930	−61	−61	35.0	34.0	—	—	−85.8	—
	09:19:30	2070	−64	−61	37.5	36.0	—	—	−89.6	—
	09:21:00	2300	−64	−61	—	—	37.0	36.0	—	−88.4
	09:22:00	2460	−67	−61	—	—	36.0	35.0	—	−88.5
	09:24:00	2790	−67	−61	41.0	39.0	—	—	−96.0	—
	09:26:00	3120	−58	−61	35.0	34.5	—	—	−91.0	—
	09:27:00	3280	−58	−61	—	—	41.0	39.0	—	−101.0

* All measurements are with "C" message weighting except those denoted †, which are with 3-kc flat weighting.

TABLE X — TELEPHONE CHANNEL CROSSTALK LOSS
(Pass 697 — September 24, 1962)

Andover Carrier Power at Satellite (dbm)	Goonhilly Carrier Power at Satellite (dbm)	Frequency Deviation at Andover (mc)	Crosstalk* on Goonhilly Carrier	
			100 kc	200 kc
−70	−70	1.0	51.6	52.8
−70	−70	0.5	52.6	51.6
−70	−70	0.25	49.0†	50.5†
−64	−70	1.0	48.9	51.2
−64	−70	0.5	48.8	47.0
−64	−70	0.25	46.2†	47.2†
−73	−70	1.0	58.0	
−73	−70	0.5	55.4	
−73	−70	0.25	51.0†	

* Defined as the ratio of modulating signal on the modulated carrier to the received signal plus noise on the unmodulated carrier.
† The crosstalk was below the background noise level.

thereby simulating a typical service offering. Analysis of all the results of these extensive tests has not been completed to date. However, the analyses made indicate that the system performance is as predicted — in fact, very similar to a 4000-mile microwave radio relay system except

TABLE XI — SUMMARY OF DATA TESTS

Type of Test	Equipment	Signal or Modulation	Transmission Rate	Results
Low-speed digital	(a) 43A1 VF carrier terminals (b) 101B DATA-PHONE Data Set	Standard teletypewriter FSK	(a) 60 wpm, 5 level (b) 100 wpm, 8 level	Highly satisfactory. See Fig. 44 for per cent distortion on pass 914.
Medium-speed digital	63-bit word generator with either: (a) 202B DATA-PHONE Data Set (b) 201A DATA-PHONE Data Set	(a) FSK (b) Four-phase	(a) 1200 bauds (b) 2000 bauds	(a) See Fig. 45 for eye patterns, pass 542. (b) See Fig. 46 for eye patterns, pass 578. Eye patterns* indicate sufficient margin against errors. Error rates averaged better than generally accepted standards.
High-speed digital	(a) Bell System high-speed data terminal with IBM 729 magnetic tape units, a 1945 data transmission terminal and a 1401 computer	(a) Seven parallel double-sideband AM channels, each using a bandwidth of 480 kc and keyed at 62,500 bauds.	(a) 62,500 characters per second	(a) Some timing problems experienced due to changing absolute delay. Error-free transmission achieved for several minutes on pass 353.
	(b) 301A-X1 data set† using as terminal equipment: (1) 63-bit word generator (2) IBM 729 mag. tape units, 7287 data trans. term., and a 1401 computer	(b) Four-phase	(b) 42,000 bauds	(b1) 69.5 million bits received error-free on pass 270. (b2) 2.8 million characters received error-free on pass 270. See Fig. 47 for eye patterns.
	(c) Experimental high-speed data system‡	(c) Four-phase	(c) 875,000 bauds	(c) On pass 833, 970 million bits transmitted in 18.5 minutes with only one bit in error. Slight signal deterioration observed, probably due to change in slant range.¶ See Fig. 48.

* Eye patterns are formed by overlaying successive demodulated mark and space pulses before reshaping or retiming.
† The signals for these tests originated from Murray Hill, N. J. and were received at Holmdel, N. J.
‡ This test was conducted from Pleumeur-Bodou to New York City.
¶ The slant range to Andover varied from 2996 to 4809 miles during the test.

for the expected frequency shift due to Doppler effect and for the change in absolute time delay due to changing slant range. The test results were satisfactory to excellent. Doppler shift caused some distortion in low-speed data signals; however, transmission results were satisfactory. Changes in absolute time delay caused some degradation in high-speed data and facsimile transmission which can be compensated for in equipment design.

11.1 *Digital Data*

Table XI outlines the digital data tests made and summarizes the results obtained. Some further results are presented in Figs. 44 to 48. The results indicate that digital data can be successfully transmitted over the Telstar system.

11.2 *Facsimile*

Facsimile copy using both voice-band and broadband circuits were transmitted over the satellite repeater via landline facilities between New York and Andover.

Voice-band facsimile* was transmitted on pass 461 at keying frequency rates of 555 cps (60 rpm) and 1110 cps (120 rpm) over ordinary equalized L-type multiplex voice-band channels (nominal 4 kc). Envelope delay distortion was equalized to within 460 microseconds, while amplitude distortion was held to ± 1 db over the band 1000 to 3000 cycles for the system. Fig. 49 shows a typical voice-band reception of an IRE test chart copied at 60 rpm. With the exception of a slight increase in noise evident in mid-gray tones, receptions copied at 60 and 120 rpm are subjectively equivalent to those copied over the facilities looped at Andover.

High-speed, two-tone facsimile,† utilizing a keying frequency rate of 675 kilocycles, was transmitted on pass 352 over the Telstar repeater via unclamped video facilities between New York and Andover. Figs. 50 and 51 are copies of portions of two consecutive transmissions conducted during a single satellite pass. Fig. 50 illustrates the result of employing an out-of-band transmitted synchronizing signal to drive the receiving drum motor. Some jitter is noticeable due to unfiltered low-frequency transients located in the landline facilities. Fig. 51 shows the results obtained when local (separate, stable) synchronization is employed. Here, frame skew due to the change of slant range (absolute

* Muirhead D-628-F, D-700-AM, DSB-AM, 1300-cps carrier.
† Westrex modified CTRT-5, DSB-AM, 2-mc carrier.

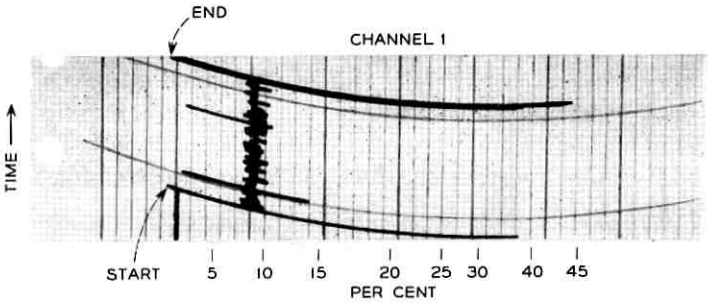

Fig. 44 — Per cent distortion vs time, using 43A1 VF terminals at 60 wpm from London to New York; pass 914, Oct. 18, 1962.

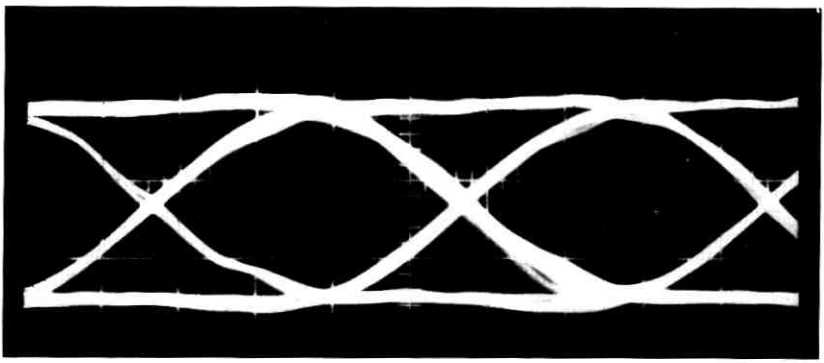

Fig. 45 — Eye pattern; 202B DATA-PHONE Data Set. Satellite loop, pass 542, Sept. 7, 1962.

delay change), is pronounced. This is to be expected at the 3000-rpm scanning rate of 675 linear inches per second.

It is concluded that transmission of facsimile signals via the Telstar satellite repeater, at both voice and video bandwidth rates, is entirely feasible. For wideband, high-speed systems, it will be necessary to utilize a transmitted synchronizing signal to eliminate frame skew in the recorded copy. Voice bandwidth systems require no change in operation.

XII. MISCELLANEOUS

This section includes a few tests not otherwise classified and one test in which the first measurements have been made only very recently and on which testing is still in progress.

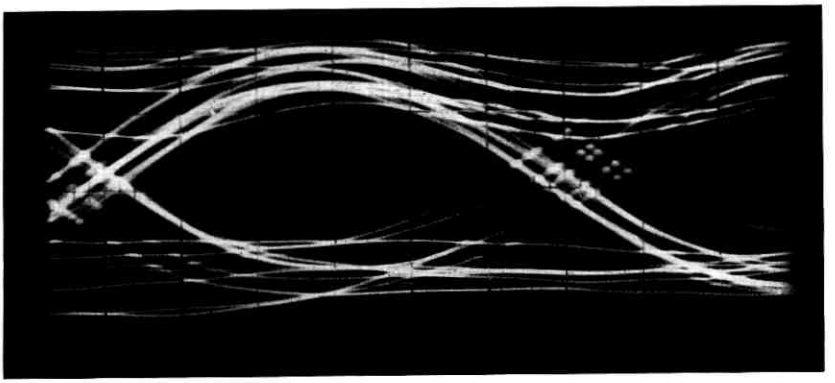

Fig. 46 — Eye pattern; 201A DATA-PHONE Data Set. Satellite loop, pass 578, Sept. 11, 1962.

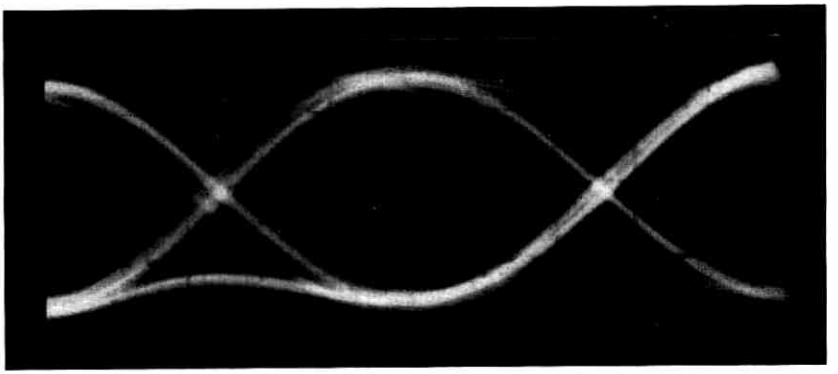

Fig. 47 — Eye pattern; 301A-XI Wideband Data Set. Satellite loop, pass 270, Aug. 8, 1962.

12.1 *Doppler Shift*

Fig. 52 shows measured and calculated Doppler shifts of the communications carrier in Andover and Goonhilly. Andover transmitted a crystal-controlled carrier at 74.13 mc, received it and measured the frequency in a counter connected to the 74-mc output of the IF amplifier. Goonhilly likewise measured the frequency at the output of the 70-mc IF amplifier. The measured frequency values were set to be zero at the same point where the calculated ones cross zero. This was necessary because zero-doppler is not known with this method. The measured and calculated curves agree to within 1 kc, and this occurs over a period of about 45 minutes.

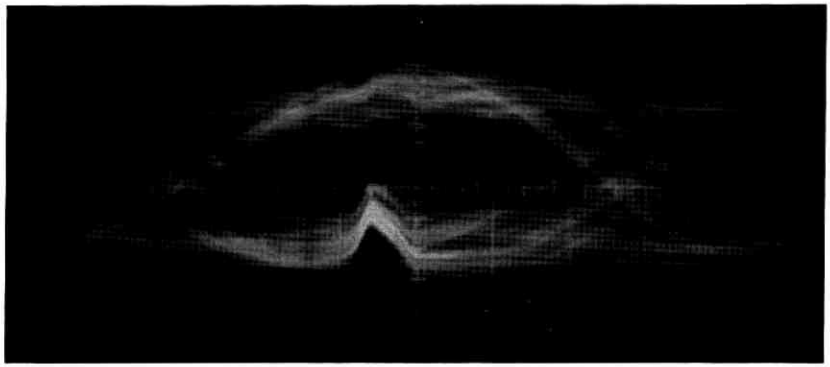

Fig. 48 — Eye pattern; experimental four-phase, high-speed data system. Pleumeur-Bodou to NewYork, pass 833, Oct. 9, 1962.

12.2 *Absolute Delay*

During most of pass 463, the signal delay in an Andover loop was measured. Fig. 53 shows the measured as well as calculated delays based on range information. A maximum error of about 20 microseconds or 2 miles was found.

12.3 *Time Synchronization*

On pass 424, the precision clocks at Andover and Goonhilly were compared by transmitting time pulses simultaneously in both directions. The accuracy of the method was believed to be about 20 microseconds, and a difference in clock time of 2 milliseconds was found. A more detailed description of the experiment is given in Ref. 7.

12.4 *Interference*

Measurements of propagation from potentially interfering TD-2 transmitters were made during October and November, 1962. Special crystal-controlled 4170-mc transmitters were located at the two nearest existing TD-2 stations and were equipped with antennas aimed directly at Andover. Study of the profile between Andover and West Paris, Me., 23.5 miles away, indicated that the controlling mode of propagation would be diffraction over a single obstacle about three miles from Andover. Study of the profile to Cornish, Me., 55 miles away, indicated that the controlling mode of propagation would be tropospheric forward scatter. These expectations were verified by the characteristics of the signal received at Andover. The signal from West Paris was very steady,

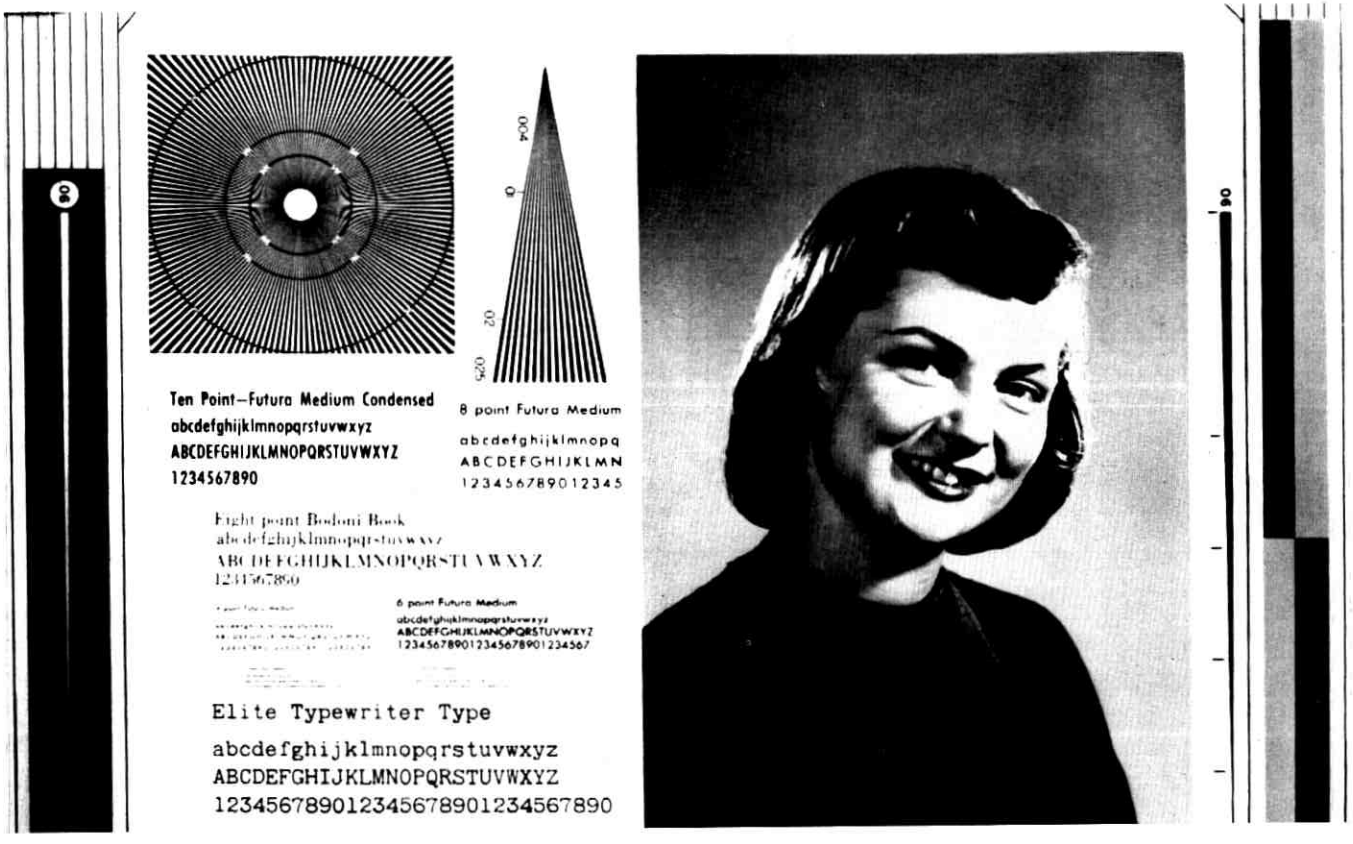

Fig. 49 — Voice-band facsimile transmission; satellite loop, pass 461, Aug. 29, 1962.


The New York Times.

Washington

In The Nation

Letters to The Times

Making Conduit Width Work

A Year of the Alliance

Fig. 50 — High-speed, two-tone facsimile; satellite loop, pass 352, Aug. 17, 1962. (Keying rate is 675 kc. Jitter is due to unfiltered transients in the landline facilities.)

with negligible long-term and short-term variations. The signal from Cornish, on the other hand, showed the very rapid fading characteristic of tropospheric forward scatter. The median signal from Cornish was within about 5 db of what had been predicted, taking into account the "gain loss" of the transmitting and receiving antennas. The signal from West Paris, however, was about 30 db less than had been computed on the basis of knife-edge diffraction. The actual diffracting obstruction was a mountain covered with pine trees.

About 100 hours of measurements of the signal from Cornish were made with the Andover antenna elevated a few degrees above optical horizon. Several short periods of enhancement were noted, usually during the early evening hours, in which the received signal rose as much as 30 db for a few seconds. Several one-hour recordings were made on antenna lobe peaks near elevations of 2, 4, 6, 8 and 10 degrees. No anomalous effects were observed.

During reception from West Paris, elevation sweeps from horizon to zenith were made during moderately heavy rainfall and during dry weather. The rain appeared to augment the received signal when the Andover antenna was elevated more than about 40 degrees, but the augmentation was only about 3–4 db. Several slow-speed azimuth scans

Fig. 51 — High-speed, two-tone facsimile; satellite loop, pass 352. (Frame skew is due to changing absolute time delay for the synchronizing signal.)

were made at several low elevations to define the "hot spot" at the true bearing of the interfering transmitter. At very low elevations the signal was increased in some directions, apparently by reflections from hills surrounding the Andover station.

Analysis of these data is continuing.

XIII. CONCLUSIONS

With economic, administrative, and hardware design considerations set aside and attention confined to technical transmission aspects, the Telstar satellite communication system is closely related to the FM microwave radio relay systems operating in the same frequency bands, i.e., the TD-2 and TH systems. The design parameters are somewhat different and subject perhaps to different state-of-the-art limitations, but the performance is just as predictable.

The communications tests show that the transmission performance of the Telstar satellite system is as good as or better than an equivalent length of the related land lines, when the satellite is visible to the terminal stations. Certain problems of great design importance in the land

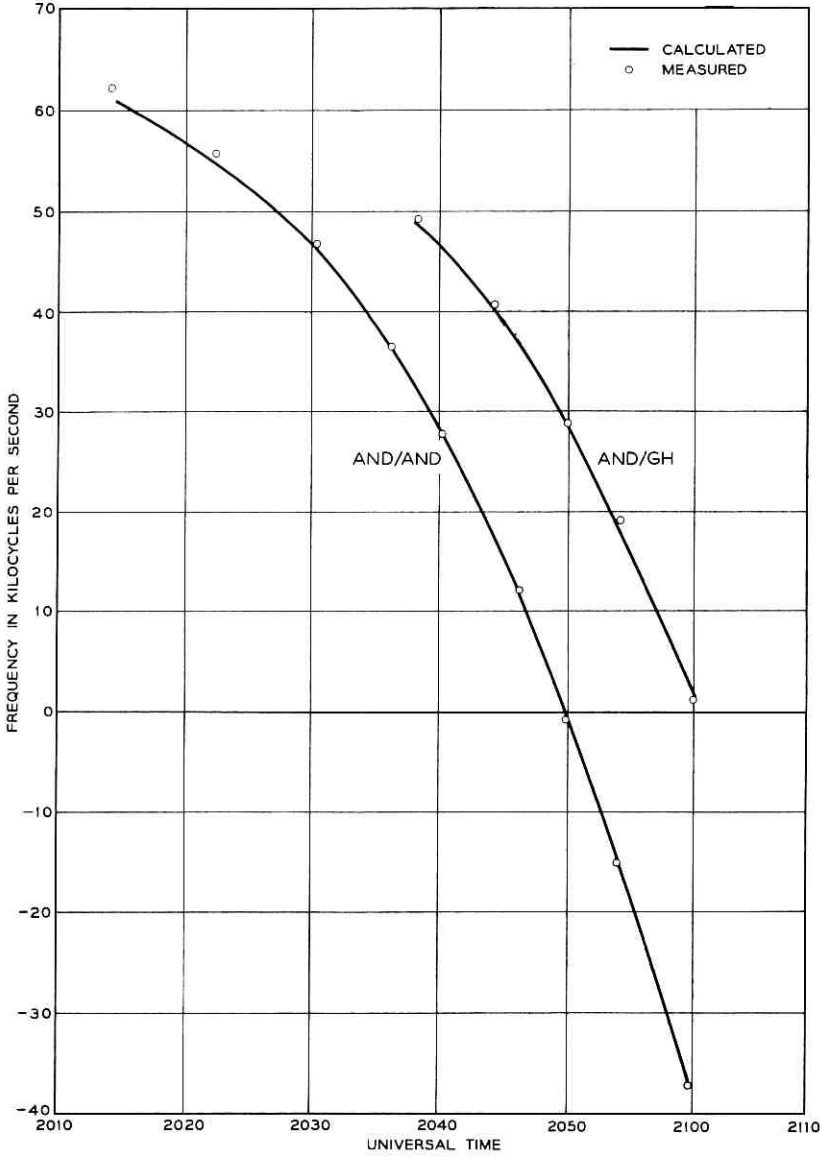

Fig. 52 — Doppler shift of communications carrier; pass 443, Aug. 27, 1962.

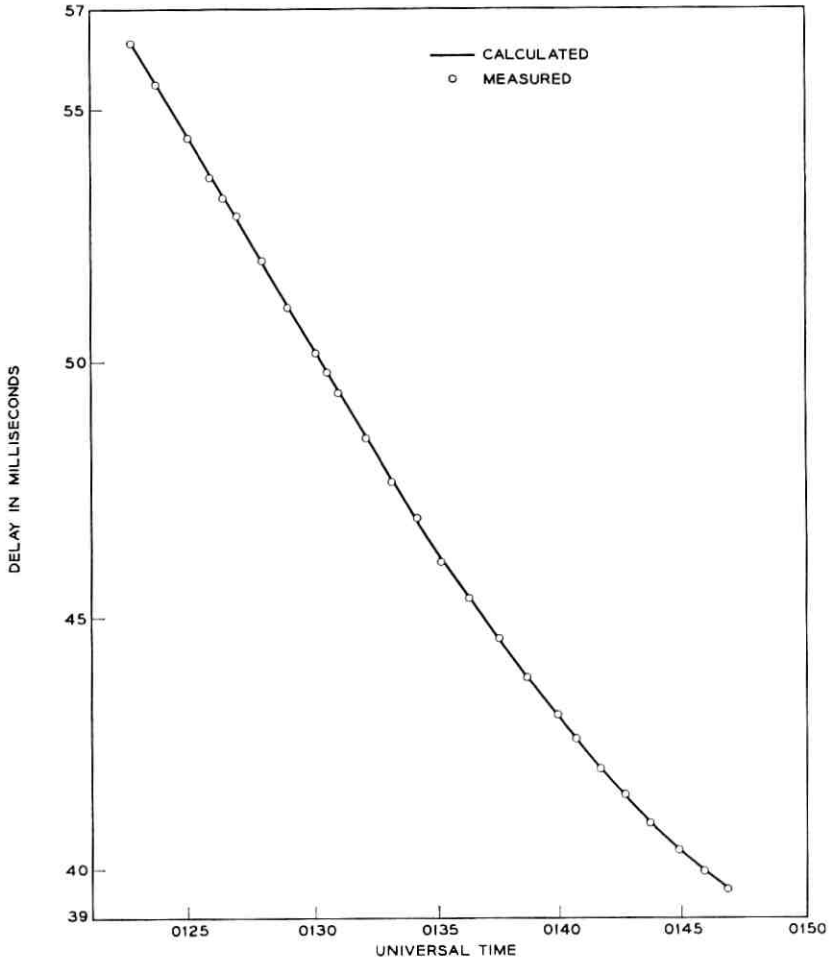

Fig. 53 — Absolute time delay of 5-μs pulse over satellite loop; pass 463, Aug. 30, 1962.

systems mentioned above are not present in the satellite system. These are (a) fading, (b) the need for highly accurate transmission equalization, and (c) the need for extraordinarily good frequency accuracy. The latter two arise from the large number of tandem relay sections in the landline systems.

On the other hand, some problems peculiar to a low-orbit satellite system are a direct result of its orbital nature, and are due to the vary-

ing range and spin angle. Although these variable parameters do not affect the transmission gain or delay distortion shapes, so far as is known, the variations in path loss do affect the noise performance. Although satellite spin (about its axis) is clearly seen on some of the recordings, there is no evidence to date of any effects on signal transmission. In addition, there are the Doppler and variable absolute delay effects to consider, particularly when transmission is transferred from a setting to a rising satellite; no tests were made on these effects.

XIV. ACKNOWLEDGMENTS

The work reported in this paper has been completed with the extensive cooperation of many people in both Bell Telephone Laboratories and the Long Lines Department of A.T.&T. Co. Although a complete list of contributions would be too long to be included here, the authors would like specifically to acknowledge the contributions of Messrs. R. E. Blatz, L. I. Farber and D. B. Seamans for their effort devoted to the collection and reduction of the data; the editorial assistance and data reduction provided by Mr. L. A. Howard; and the work of Mr. L. C. Thomas in preparing computer programs and providing computer printouts of orbital information. The efforts of these people have contributed to the results included in practically all parts of this paper.

In addition, a number of people have made large contributions to specific parts of the test program. These include Mr. R. W. Edmonds, Mr. J. R. Hefele, and Mr. F. W. Kammerer, who gave very valuable assistance in the design and alignment of video test facilities. The authors are also indebted to these people for most of the video photographs included in this paper. Mr. A. J. Giger has kindly provided much of the data and analysis of received carrier power. Messrs. H. A. Ahnemann, T. F. Benewicz, E. A. Gregario, E. H. Kessler, D. F. Schwemmer and C. F. Usher have been principally responsible for the conduction and analysis of the data transmission and facsimile tests reported herein. The material on interference from TD-2 was supplied by Mr. D. K. White.

Finally, none of this would be possible without the tremendous development effort of hundreds of people who created the Telstar satellite and the Andover earth satellite station. Nor could these data have been obtained without the assistance of the many people of both Bell Telephone Laboratories and Long Lines who have devoted many months of long days to operating and maintaining the Andover station. We also acknowledge the invaluable assistance of our foreign partners at Goonhilly Downs, England and Pleumeur-Bodou, France.

REFERENCES

1. Jakes, W. C., Jr., Participation of the Holmdel Station in the *Telstar* Project, B.S.T.J., this issue, p. 1421.
2. Recommendation No. 277, CCIR, 9th Plenary Assembly, Los Angeles, 1959.
3. Bangert, J. T., Engelbrecht, R. S., Harkless, E. T., Sperry, R. V., and Walsh E. J., The Spacecraft Antennas, B.S.T.J., this issue, p. 869.
4. Crane, R. E., Dixon, J. T., Huber, G. H., Frequency Division Techniques for a Coaxial Cable Network, Trans. AIEE, **66**, 1947, pp. 1451–1459.
5. Giger, A. J., Pardee, S., Jr., and Wickliffe, P. R., Jr., The Ground Transmitter and Receiver, B.S.T.J., this issue, p. 1063.
6. Davis, C. G., Hutchison, P. T., Witt, F. J., and Maunsell, H. I., The Spacecraft Communications Repeater, B.S.T.J., this issue, p. 831.
7. International Time Comparison by Telstar, Electronic Engineering, **34**, No. 146, October, 1962, p. 681.

The Command System Malfunction of the *Telstar* Satellite

By J. S. MAYO, H. MANN, F. J. WITT, D. S. PECK, H. K. GUMMEL and W. L. BROWN

(Manuscript received March 22, 1963)

Loss of the command function of the Telstar satellite first occurred on November 24, 1962. There had been earlier indications of degraded performance. Facts are presented which led to the conclusion that the malfunction of the command system was due to surface damage to certain transistors in the redundant command decoders by the enhanced radiation in the inner Van Allen belt.

Correction steps have included laboratory experiments to gain a better understanding of the cause of failure, the use of continuous normal commands, commands transmitted from Johannesburg, South Africa, and specially modified commands to circumvent failure of the more vulnerable transistors. The operations which aided in the gradual rejuvenation of both command decoders are described. Also covered are the subsequent reappearance of the command system malfunction on February 21, 1963, and its correlation with the variation of the average radiation intensity seen by the satellite.

I. INTRODUCTION

After more than four months of successful performance, difficulties were experienced with the Telstar satellite command system. Early in the week of November 18, 1962, the command system became sluggish — the satellite responded only after a long string of continuous commands had been sent. Normally, a command is carried out as soon as it is received. On November 24, after five days of increasingly sluggish performance, the command system failed to respond.

There had been signs of deterioration earlier, which, however, did not affect command system performance. On August 7, about one month after launch, there was an indication that one of the redundant command decoders may have been operating intermittently. By August 21, failure of one decoder appeared to be complete. However, intermittent

operation of that decoder was again possible for a three-day period during October.

A program was initiated to determine the cause of failure and the action to be taken to recover the command function. Several steps were taken as a result of this study and, on December 20, through the use of modified command pulses, certain commands were executed by the satellite. With the command function recovered (in a limited sense), operations were performed on the satellite, and evidence suggests that these operations aided in gradual rejuvenation of both command decoders. On January 3, 1963, with both decoders responding to *normal* commands, the communications-experiment equipment in the satellite was turned on and tests indicated normal performance.

This paper describes the stages of failure and recovery of the command system. An explanation is suggested for both failure and recovery in light of the available evidence.

Complete failure of the command system again occurred on February 22, 1963. The pattern of malfunction in many ways resembled that of late 1962. Detailed treatment is given of only those events which occurred during November, December, and January.

II. COMMAND DECODER

The failure of the command system of the satellite was traced to the command decoders through the examination of telemetry data. Hence, a brief discussion of the command decoders, which are described in detail elsewhere in this issue,[1] is in order here.

There are two virtually identical command decoders in the command system. Each is driven by one of the two command receivers and each drives a command switch unit, as shown in Fig. 1. Each command relay is normally driven by both command switch units in parallel; the design is such that a pulse from either or both command switch units is sufficient to operate a relay. Thus, redundancy exists between the input to the command receivers and the output of the command switch units.

Several checks are available on the health of the redundant command circuits: The AGC and output voltages of the command receivers are telemetered. Also, two commands are used to disable the decoders. T-1 command disables decoder 2 for 15 seconds and permits testing of decoder 1; T-2 command disables decoder 1 for the same length of time and permits testing of decoder 2. These and the 13 other commands are described in Table I of Ref. 1. Information is telemetered, telling whether

or not T-1 or T-2 commands have been executed, as well as indicating the state of the relays in the command switch.

III. MALFUNCTION OF THE COMMAND SYSTEM

3.1 *Failure to Respond to T-2 Command*

The first indication of trouble in the command system of the satellite came on pass 260 on August 7 when there was no response to the T-2 command. On the next visible pass that same day, T-2 command was carried out in a normal manner. Table I shows the erratic response to the T-2 command between August 7 and October 21, when the T-2 command function had apparently failed completely. Note that there is a gap of approximately two months during which no acknowledgement of T-2 command was received.

Failure to respond to the T-2 command is not conclusive evidence that decoder 2 has failed. The same symptom could result from failure of command receiver 2, T-2 relay, or T-2 relay-state telemetry channel

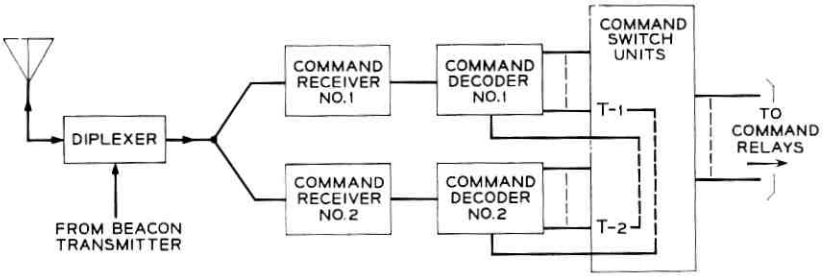

Fig. 1 — Block diagram of command system.

TABLE I — FAILURE OF DECODER 2

Date	Pass	Observation
Aug. 7, 1962	260	No response to T-2 command
	261	Normal operation
Aug. 8	268,9	No response to T-2 command
	270	Intermittent T-2 command response
	271	Normal operation
Aug. 9–20		Intermittent T-2 command response
Aug. 21		Decoder 2 apparently completely failed
Oct. 17–20		Intermittent T-2 command response
Oct. 21		Decoder 2 apparently completely failed

or of the circuits in the command decoders and switch unit associated with T-2 command.

3.2 *Gradual Failure of Command System*

Except for the difficulty described in the previous section, the command function was satisfactory until November 18; the response to commands from the ground appeared to be instantaneous. On November 18, however, it took 8 minutes before the satellite responded to a command. Delay between command and response became gradually greater and, on November 23, complete failure of the command system occurred.

The chronology of events of the week of November 18 is given in Table II. During this week, one important consistency was apparent: After the first command was executed on a pass, other commands were carried out immediately in a normal way, even if the first command took several minutes to go through. One can see from Table II that three different commands were used to bring about recovery (for at least one pass). The duration of continuous pulsing to bring about recovery gen-

TABLE II—THE WEEK OF NOVEMBER 18

Date	Pass	Duration of Commands Before Recovery	Command at Recovery	Successful Commands After Recovery	Final Command of Pass
Nov. 18	1203	8 min	T-1	DD, D, T-1	T-1
	04	0	—	A, AA, B, C, CC	AA
	05	0	—	A, AA, B, C, CC	AA
	06	0	—	T-1	T-1
19	1212	0	—	A, AA, B, C, CC	AA
	13	0	—	A, AA, B, C, CC	AA
	14	0	—	A, AA, B, C, CC	AA
	15	No commands sent	—	—	—
20	1221	No recovery	—	—	T-1
	22	2 min	A	A, AA, B, T-1	T-1
	23	20 sec	T-1	F, FF, T-1	T-1
	24	0	—	F, FF, T-1	T-1
21	1230	No recovery	—	—	T-1
	31	3 min	C	C, CC, F, FF, T-1	C
	32	15 sec	T-1	C, CC, F, FF, T-1	T-1
	33	0	—	C, CC, F, FF, T-1	T-1
22	1239	No recovery	—	—	T-1
	40	No recovery	—	—	C
	41	11 min	T-1	C, CC, F, FF, T-1	F
	42	3 min	T-1	C, CC, F, FF, T-1	T-2
23	1247	No recovery	—	—	—

erally decreased for succeeding passes on a given day. Increased degradation was apparent from day to day. Also, during a period when commands were not executed, several different commands were sent with no response; the failure appeared to be in the part of the decoder which is common to all command channels.

When it was apparent that the command system was deteriorating, care was taken to hold the satellite in the condition which would be most useful in the event of failure of the command function. The communications experiment could not be left on because, under that condition, energy would have been drained from the storage cells faster than it would have been replenished by the solar plant. The resultant dropping battery voltage would have automatically tripped the low-voltage trigger circuit which disconnects the storage cells from the power supply circuit* and turns off all circuits except the switching regulator in the power supply, the command receivers, the command decoders, and the two-year timer. Power restoration to all other circuits can only be accomplished through use of the command system. Incidentally, the action of the low-voltage trigger circuit is the same as that accomplished by sending the SS command; knowledge of the function of this command is essential to the understanding of Section V. The low-voltage trigger circuit and the SS command control the same S relay.

Hence, during the week of November 18, care was taken to assure that the satellite was left with the VHF beacon, radiation experiment and telemetry circuits powered; the command system is permanently connected to the switching regulator and always receives power except when the S relay is open and the satellite is in darkness. Thus, even without an operative command system, valuable information was relayed from the Telstar satellite; radiation field mapping data, battery charging rate (from which solar cell quality could be ascertained), solar aspect data, temperatures throughout the satellite, pressures and the performance of the command receivers were among the useful pieces of information received.

The failure of the command system which began on November 18 suggests that the T-2 command difficulty was indeed a failure of a circuit common to all commands in decoder 2. The later pinpointing of the exact failure in decoder 2 further supports this idea. Hence, most of the time since launch, command signals were probably being interpreted only by decoder 1.

---

* There is an exception; the storage cells can be charged by the solar plant through a diode.

IV. FAILURE MECHANISM

4.1 *Possible Causes of Failure*

The earth satellite environment creates a number of effects which should be suspected as possible causes of failure. The pertinent effects are enumerated and discussed in this section.

4.1.1 *Temperature Variation*

Because of the thermal design of the satellite, the assemblies within the electronics canister are subjected to relatively small temperature excursions. In particular, the temperature of the decoders has been between 22 and 37 degrees C since launch. During a given pass, the temperature of the decoders will vary by only one degree and may go up or down depending on the state of circuits in the satellite, solar aspect and the time of occurrence of an eclipse. The range of temperature is small and is well within the design limits of the decoders. There appears to be no correlation between temperature and the recovery of the command function during a pass.

One can hypothesize the following: The decoder circuit has failed because a component has deteriorated badly but can be made "good enough" if warmed slightly. Further, assume that one can heat the faulty component by means of the application of command signals to the decoder. In practice, the amount by which the temperature of a device can be changed by this method is only a few degrees. If one assumes, however, that the component in question is cool enough at the beginning of a pass so that the circuit has failed, then behavior of the sort listed in Table II might be explained. Final collapse of the command function could be attributed to further deterioration of the component. However, the data show that the deterioration is slow and that it does not correlate with decoder ambient temperature. Hence, one might suppose that the recovery is caused by a temperature variation which has been brought about by application of command signals, but that the damage itself results from some other effect. It is shown below that there is a much more probable cause of recovery.

4.1.2 *Eclipse*

Whether the satellite is in sunlight or the shadow of the earth greatly affects the temperature on the outer surfaces of the satellite. However,

the electronics canister is hardly affected by a single eclipse.* Study of the data has indicated that there is no correlation between the occurrence of an eclipse and the failure of the command system.

4.1.3 *Magnetic Field Variations*

The command switch unit drives nine magnetic latching relays. Satisfactory operation is achieved in the leakage field of the traveling-wave tube, which is as large as 10 gauss at some of the relays. The external magnetic flux density never exceeds 0.44 gauss. No evidence supports magnetic effects as the cause of decoder failure, especially since it would take a very strong magnetic bias to render *all* relays inoperative.

4.1.4 *Noise*

Galactic noise was considered as a possible cause of failure, but was ruled out because there were no indications of a noisy signal entering the decoder. Commanding under extremely noisy conditions usually results in the execution of incorrect commands, but there were no errors during the week of November 18. No unusual noise conditions were detected at the ground station during the period the command system was inoperative. Telemetry signals indicated that normal signals were entering the two decoders and that the command receiver AGC voltage was consistent with the range and aspect of the satellite.

4.1.5 *Aging*

Another possible cause of failure would be aging failure of a component. Even though very reliable components were used, the large numbers in this experimental model do raise the question of the statistical probability of such a failure. On the basis of estimated random failure rates under operating conditions of one in 10^9 component hours for passive components (largely resistors and capacitors), and 10 in 10^9 for semiconductor components, there results a 9 per cent probability of one component failure in the entire system or a 1 per cent probability of failure in each decoder in a four-month life. This is not consistent with the occurrence of two failures, one at even a shorter time, each occurring in the same portion of the system. Furthermore, the failure of the command system was gradual rather than catastrophic. Gradual failure would be expected if one component were undergoing a gradual

* Unless, of course, S relay is in the SS state. For this case, eclipse will turn off all circuits, including the command system.

change in characteristics and thus causing a circuit to become marginal. Since the components used were carefully screened under power aging conditions to eliminate those with drifting characteristics, only a catastrophic equipment failure is reasonable by residual random failure mechanisms. The absence of catastrophic failure points to the presence of a wear-out mechanism distinct from power aging.

4.1.6 *Radiation Damage*

Bulk damage to semiconductor materials by energetic particles, i.e., protons and electrons, is a well known phenomenon which leads primarily to degradation of minority carrier lifetime. This degradation is the failure mechanism for solar cells and must be considered for wide-base, low-frequency transistors. The effect is negligible for the diodes and narrow-base transistors used in the decoder. Therefore, this mechanism can be ruled out as an explanation for the failure.

4.1.7 *Ionization Damage*

Exposure of certain types of transistors to ionizing radiation can cause failure at radiation doses appreciably lower than those necessary to cause bulk damage.[2] Parameters which are dependent on the semiconductor surfaces, such as the collector reverse current or the transistor gain, will degrade gradually under radiation (with considerable variation in degradation rates among different transistors), and will typically recover temporarily to some degree when removed from exposure or when exposed with a reduced (or zero) collector-to-emitter voltage. Issuance of a command to the satellite turns some "off" (V_{CE} high, I_C low) transistors "on" (V_{CE} low, I_C high), and hence could cause recovery of those transistors. Recovery is not instantaneous with either voltage reduction or removal from exposure. Therefore, ionization damage could explain why (*i*) during the failure of decoder 1 during the week of November 18, delayed response to commands was observed, but once commands were obeyed, the command function was operative during at least that pass, and (*ii*) the temporary recovery of decoder 2 in October occurred during an experiment which involved continuous transmission of commands.

Since many transistors in the command decoder are of a type sensitive to ionizing radiation such as that encountered in the Telstar satellite orbit, it is reasonable to consider this phenomenon as a plausible cause of failure. In fact, since the other possible causes of failure do not satisfactorily account for the deterioration observed, ionization damage is

thought to be the most probable cause. The next section describes the evidence which supports this contention.

4.2 *Radiation Effects*

4.2.1 *Ionization Damage to Transistors*

The effect of ionizing radiation on transistors has been described in considerable detail.[2] It appears to result from the interaction of semiconductor surface contaminants with gaseous ions produced in the transistor enclosure by radiation, and with electrical bias applied to the transistor. A few of the features of this effect, pertinent to the immediate consideration, are:

(a) Transistors encapsulated in a gaseous atmosphere are generally most susceptible to surface radiation damage.

(b) Parameters sensitive to surface states are affected; these parameters include I_{CBO}, h_{FE} and noise figure at low frequencies.

(c) Transistors removed from radiation will typically recover usable characteristics.

(d) A degraded transistor will tend to recover when the collector voltage is removed, or even reduced, while either in radiation or out of radiation. This recovery may be quite appreciable even within the first few seconds.

(e) Collector junction degradation rate is dependent upon the magnitude of reverse collector voltage, so that a marginal transistor may be more or less degraded, depending upon its voltage condition.

These effects were recognized while the Telstar circuits were being assembled. Where possible, units of the sensitive types were irradiated and the most resistant ones selected for use. Screening experiments indicated that pre-irradiation up to one tenth of the expected orbital dose could reasonably predict the behavior in orbit. However, test results had also indicated that the reliability of screening predictions decreases with increasing ratio between the actual and screened radiation levels. Because the average dose rate encountered in the Telstar orbit was found to be approximately two orders of magnitude greater than expected at the time of launch (see Section 4.2.2), and because only a part of the transistors in the command decoder were screened, ionization damage remains the prime suspect as the cause of circuit malfunction.

4.2.2 *Radiation Intensity Seen by Telstar Command Circuits in Orbit*

The radiation effects on the devices in the Telstar satellite are produced by the Van Allen belt, which is composed of energetic electrons and

protons trapped in the earth's magnetic field. The surface effects depend only on the ionization caused by these particles inside a transistor's encapsulation. Protons and electrons which actually penetrate the transistor's container contribute directly. In addition, there may be a contribution from the bremsstrahlung, X-rays, created in stopping energetic electrons. It is convenient to express the integrated radiation dose in rads, a unit of energy deposited by the ionizing particle flux per unit mass of material.* In principle, the dose is calculable for any location in the satellite from a knowledge of the energy distribution of the particle flux at the surface of the satellite and the shielding provided by the satellite skin and frame, the wall of the canister housing the electronic circuits, other components, etc. Only approximate calculations are feasible in view of the complex geometry of the shielding in the satellite and the incomplete information concerning the electron energy distribution.

The highest intensity in the inner Van Allen belt is around the magnetic equator of the earth and extends between about 1200 and 2500 statute miles above the earth's surface at the equator. The Telstar satellite's orbit is in the region about 20 per cent of the time. Because the earth's magnetic field which controls the motion of the trapped particles is misaligned with respect to the earth's geographic axis, the particle flux incident on the satellite varies from orbit to orbit. The daily average also varies as the apogee of the orbit precesses between its extremes at 45° north and south latitudes with a period of 181 days. In addition, of course, there are time variations of the radiation belt.

The estimated upper limit of the radiation dose contributed by energetic protons in the region of highest intensity is illustrated in Fig. 2 as a function of aluminum absorber thickness. The radiation dose rate is shown under the assumption of uniform shielding and exposure to a uniform omnidirectional proton flux. For the decoders which are very close to the surface of the electronics canister, the minimum shield thickness is only about 0.1 inch of aluminum, but the solid angle for acceptance of particles through this thickness is between $\frac{1}{4}$ and $\frac{1}{2}$ of the total 4π solid angle. The curve applied to this case gives an orbital average of between 5 and 10 rads per hour. The proton exposure of the satellite has been quite close to the pre-flight estimate.

Trapped electrons can also contribute directly to ionization. For an electron to reach the average component in the canister, it must have an energy of more than 5 Mev, and for a circuit shielded by 0.1 inch of aluminum, such as the decoder, the electron energy must exceed

* One rad equals 100 ergs of absorbed energy per gram of material.

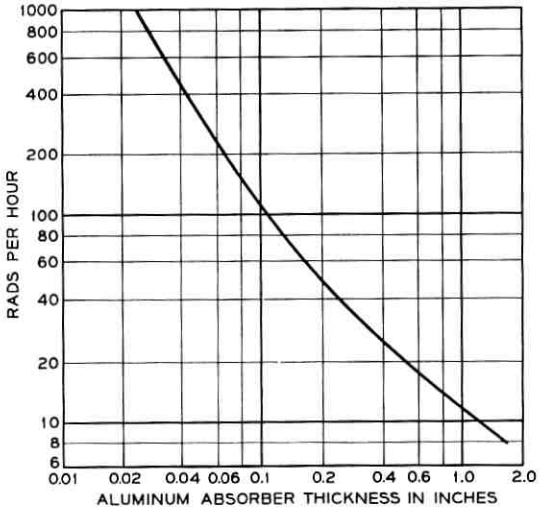

Fig. 2 — The radiation due to high-energy protons in the peak of the inner Van Allen belt.

about 1.5 Mev. It was believed before launch that there were very few electrons with energies this high in the inner Van Allen Belt, and thus it was concluded that direct electrons were of no importance. Consequently, with the expected orbital average flux less than 10 rads/hour, which implied a total dose of 1.8×10^5 rads over the two-year expected useful life of the satellite, the screening dose for sensitive transistors was held to 1.4×10^4 rads.

From measurements by the Telstar and Explorer XV satellites, it has been concluded that a very substantial fraction of the electrons in the inner Van Allen Belt have energies above 1.5 Mev. In parts of the inner belt region, the energy distribution can be reasonably represented by an expression of the form $\exp - E/E_0$ where $E_0 = 1.2$ Mev. A large part of these high-energy electrons are believed to have been introduced by the high-altitude nuclear explosion of July 9, 1962.

The omnidirectional electron flux averaged over the first four months of the Telstar satellite's orbit is about 10^8 electrons/cm^2 sec. The radiation dose rate for electrons with this flux and the above spectrum is shown as a function of shield thickness in Fig. 3. The curve represents the radiation in the Telstar canister for shielding thicknesses small compared to that in the middle of the canister.* For transistors in the

* The curve includes the influence of the solar cells and the canister itself in reducing the effective solid angle for incident electrons. It also contains the effect of nonnormal incidence on the effective shielding.

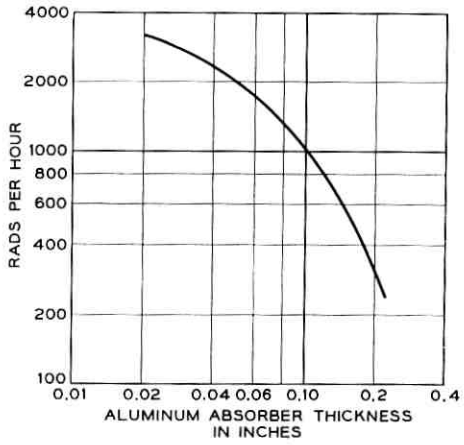

Fig. 3 — The average radiation due to high-energy electrons in the Telstar orbit.

decoder the dose rate due to electrons is approximately 10^3 rads/hour. The estimated dose rate due to protons is only 5 to 10 rads/hour. Hence the components in the Telstar command decoder have been exposed to approximately 100 times the anticipated radiation intensity, and the major contribution is not from protons but from high-energy electrons. It is believed that the peak radiation intensity could be as high as 10^4 rads/hour. The bremsstrahlung is insignificant in comparison with the direct electron effects.

4.2.3 *Transistor Ionization Damage Experiments**

Two kinds of experiments were conducted to evaluate the hypothesis that radiation was the cause of command decoder malfunction and to pinpoint the problem areas in the circuit with the ultimate hope that some corrective action could be taken. Transistors of the same code as those used in the decoders were cycled in a radiation field (gamma rays from a cobalt 60 source) with a period about the same as the Telstar satellite orbital period. Also, complete command decoder circuits were subjected to gamma irradiation. These experiments confirmed what was already known about surface ionization damage, summarized in Section

* The experiments described in this section are a direct extension and application of experience gained in work on surface effects of radiation in semiconductor devices, a part of which was performed under contract with Electron Technological Laboratories, Aeronautical Systems Division of the United States Air Force Systems Command.

4.2.1, but the data obtained were more directly applicable to the Telstar command problem.

Since there is a very large variation in radiation damage for different transistors of the same code and because the experiments did not duplicate the environment of the transistors in orbit,* the conclusions are qualitative or, at most, quasi-quantitative. The following statements can be made regarding the radiation-sensitive transistor type used in the command decoder, which is a nitrogen-filled diffused silicon npn unit.

(*i*) Those units which were heavily degraded in the high-intensity field partially recovered in the low-intensity field. The time constant for I_{CBO} and h_{FE} degradation ranged from 1 to 20 minutes; recovery has logarithmic time dependence. Typical cycles are shown in Fig. 4 for a transistor which had been pre-irradiated to degrade I_{CBO} from a few nanoamperes to several microamperes.

(*ii*) Short-term reciprocity does not hold; i.e., during cycling tests it was apparent that a given total dose applied at a fast rate caused more degradation than the same dose applied at a slower rate. Note from Fig. 5 that 3.6 hours at 4.5 kilorads per hour induce less effect than 1 hour at 16 kilorads per hour, although the total dose is the same for both cases.

(*iii*) Removal of power from the device during cycling resulted in temporary improvement, and the improvement was generally greater if power was removed during the high-intensity interval. The degree of memory of this improvement varied widely from one transistor to another.

Although irradiation tests on an actual command decoder are less useful from a statistical point of view than the experiments conducted with individual devices, they offer the possibility of focusing attention on vulnerable areas in the circuit and can possibly bring to light certain subtleties which might be overlooked in a perusal of circuit diagrams. Two command decoders (referred to here as decoder A and decoder B) were irradiated, both at high intensities (0.68 and 0.34 megarad per hour) to cause early failure; then decoder A was disassembled to study the failed component, and decoder B was placed in a low-intensity field (500 rads per hour) to study various recovery techniques. A summary of the results of these tests follows:

(*i*) Decoder A failed at a total dose of 2.3 megarads. (If reciprocity were to hold between time and dose rates, then this total dose would

* In most of the experiments the units were cycled between a level of 10 kilorads per hour for one hour and 30 rads per hour for one and one-half hours. This high average dose rate (5 kilorads per hour) was used to accelerate deterioration.

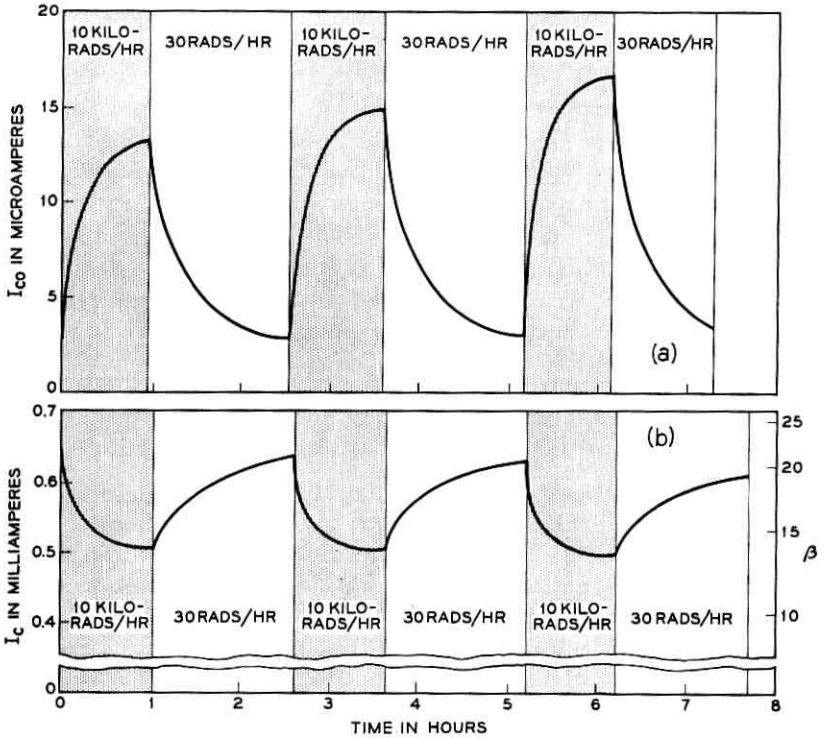

Fig. 4 — Leakage current and gain of a transistor cycled between high and low radiation field intensities.

correspond to 26.5 years at 10 rads per hour or 3.2 months at 1 kilorad per hour.) Up to this dose level, continuous commands had been sent to the decoder and some degradation (but not failure) had been observed. Failure occurred immediately after the continuous commands ceased, which indicates that the commanding had retarded failure.

When the circuit was removed from radiation, it recovered and operated satisfactorily.

The failure was traced to low h_{FE} in the "zero" digit gate transistor, which, because of its load configuration, had a turn-on time which was too slow to advance the digit counter.[1] Measurements on the device confirmed the diagnosis.

(*ii*) For tests on decoder B, commands were sent only intermittently until failure had occurred. The failure occurred at a total dose of 0.62 megarad (7 years at 10 rads per hour; 25 days at 1 kilorad per hour). The decoder did not respond to the first of a continuous train of com-

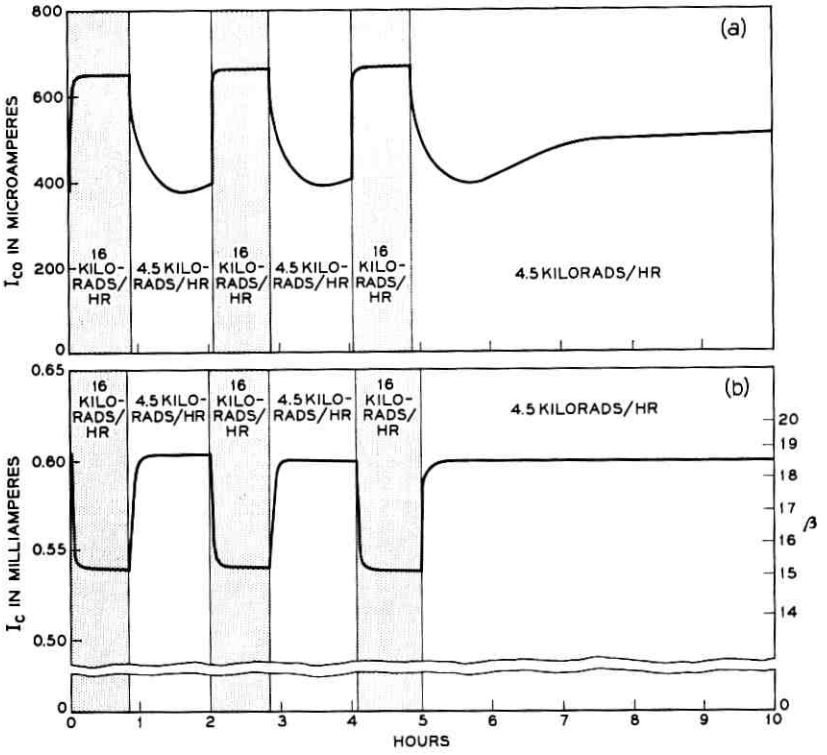

Fig. 5 — Leakage current and gain of a transistor cycled between two high radiation field intensities.

mands, but did react properly to all succeeding commands. (Each command lasts about 0.1 second.)

Deterioration was gradual: Continuous commands caused recovery in 2 seconds at a total dose of 2.4 megarads and in 14 seconds at a total dose of 4.0 megarads.

Even after the command decoder had received a total dosage of 10 megarads, recovery occurred when it was removed from the radiation field.

The failure occurred in the shaping network which controls the pulse generator.[1] The pulse generator, a gated astable circuit, is held off most of the time by the shaping network, but due to increased I_{CBO} of either the first or the second stage of that circuit,* the astable circuit became free-running, independent of the decoder input signal.

* See Appendix Sections A.2 and A.3.

(*iii*) After a total dose of 10 megarads at the high dose rate, decoder B was placed in the low-intensity field (500 rads per hour). Failure again occurred, but the malfunction was not in the shaping network. The trouble, which occurred at an additional exposure of about 0.3 megarad, was traced to the one digit gate, which has several output functions. One of these, which is the resetting of the timer circuit, was not being performed by the digit gate.[1]

Eventually the shaping network did fail in the low-intensity radiation field. However, since the total exposure to cause this failure was much greater for the low-intensity field than for the high one, it is suggested that either an out-of-radiation recovery mechanism exists or that deterioration is rate-sensitive for some transistors.

Continuous commands, power removal or extraction of the circuit from the radiation field could bring about recovery of the circuit.

4.2.4 *Ionization Damage as the Cause of Failure*

Two significant facts which pertain to the failure are apparent from the previous three sections: (*i*) High radiation dose rates were encountered by the satellite prior to the failure of the command system, and (*ii*) the gradual failure with temporary recovery after a successful command is consistent with the kind of failure observed in the laboratory when transistors were irradiated.

In addition to their usefulness in pinning down the cause of failure, the data described above also helped lead to the recovery of the command function. The action which was taken to this end is described in the next section.

V. RECOVERY OF THE COMMAND SYSTEM

5.1 *Corrective Measures*

Since previous tests had provided evidence that either reduced radiation field or voltage removal from certain transistor stages might lead to recovery of the command function, certain corrective steps were taken.

5.1.1 *Turning "Off" Transistors "On"*

The command decoder is basically a digital logic circuit and, as such, contains mostly transistor and diode stages which are normally in either a "conducting" or "nonconducting" state. When a command pulse train is being interpreted by the decoder, its stages alternate one or several times between these states, and the majority of them end up

in a particular state at the end of each command pulse train. There are, however, several circuits whose resting state is a function of the last received command signal. Out of the 34 transistors of the radiation-sensitive type in each decoder, 24 can be controlled to be "off" (high V_{CE}, low I_C) or "on" (low V_{CE}, high I_C). Any of the 24 transistors could have been triggered into the more desirable "on" state (from the standpoint of radiation damage), and, of course, if it had been known that a particular one of these devices was the cause of malfunction, such action would have been taken. Even though response to commands would not be expected initially, the healing effect of reduced V_{CE} might have led ultimately to recovery. Unfortunately, no device could be "tagged" as the most probably faulty one,* and further, acquisition of the more desirable state by one device usually resulted in forcing an adjacent device into the "off" state. Several experiments, which were designed to control the states of the various stages, were carried on over a period of three weeks, but to no avail.

5.1.2 *Continuous Commands*

Although the command function was inoperative, it was felt that some benefit could be gained from sending continuous commands from the ground terminals whenever the satellite was in view.† The probability was high that such action would reduce the average V_{CE} applied to the damaged transistors. Command signals were designed to benefit particular transistors; e.g., a train of signals consisting of "ones" only was sent to exercise optimally the one digit gate. A number of such commands were tried, all with no success, in attempts to "heal" the satellite after the command failure.

5.1.3 *Commands from Johannesburg*

The normal operating procedure called for issuance of commands from Cape Canaveral, Florida, or Andover, Maine. However, at the time of the failure of the command system, the apogee of the orbit, at which the radiation field is at a minimum value, was in the southern hemisphere and was not visible to either normal command station. The NASA command and telemetry station at Johannesburg, South Africa, was selected as a third Telstar satellite command terminal. In addition

* Examination of the data taken during the week of November 18 was carried out to see if any correlation between the last command sent and depth of recovery existed. No conclusive correlation was apparent.

† That recovery can be brought about with continuous commands had been demonstrated in the laboratory. See Section 4.2.3.

to the advantage of apogee visibility, it also had sight of the satellite as it passed through the region where radiation was thought to be a minimum because of the anomalies in the earth's magnetic field.

The tests were begun on December 6. On at least one pass each day, conditions were thought to be favorable from the standpoint of passage through the radiation belt. As many commands as possible were sent during each visible pass on the assumption that the cumulative effect of a large number of commands would increase the probability of response in the reduced radiation field. All results were negative, although telemetry indicated a normal signal at the output of the command receiver. These tests were terminated on December 17.

5.1.4 *Modified Commands*

By far the most fruitful approach to the recovery of the command function was the use of command signals which were designed to circumvent some assumed failed circuit. Such a procedure, if successful, would lead to full use of the satellite for communications experiments and would also locate the exact area of the decoder circuit in which the failure had occurred.

The first procedure was a process of elimination to focus attention on those stages for which the probability of failure was highest. The considerations which greatly reduced the number of suspects are listed below:

1. Only those circuits which had a function common to all command channels were considered, since failure existed for all commands. Also, during the week of November 18, when the circuit recovered, all commands which were issued were carried out.
2. Only stages containing the device-type known to be radiation sensitive were examined in detail.
3. Stages which were normally in the "on" state except during a command pulse train were excluded.
4. First priority in the investigation was given to those devices with especially high V_{CE} and in circuit positions known to have stringent leakage current and gain requirements.

The results of this study suggested that six transistors were most vulnerable. For only one of these, the reset digit gate transistor,[1] was it not possible to design a satisfactory modified command. However, this device could be set into the "on" state by means of the transmission of a start pulse (normally at the beginning of each command) as the last pulse of a pass. This procedure was carried out as soon as its importance

was realized. The other five transistors were the first two stages of the pulse shaping network, the normally "off" transistor of the astable pulse generator, and the zero and one digit gate transistors.[1]

The modified commands were designed either to permit satisfactory circuit operation without the use of the stage under study or to enable circuit operation to occur even after the normal operating margin had been reduced to zero. Refer to the Appendix for a description of each of the modified command procedures.

Prior to use of the modified commands on the orbiting satellite, a laboratory test was carried out on a decoder which had a condition simulating the probable failure. In this way, the reliability of the procedure was evaluated.

An interesting aspect of use of modified commands involved the experiments on irradiated decoders which were described in Section 4.2.3. The failures observed in those experiments were all in regions which were thought to be most vulnerable to radiation damage and which were arrived at through the process of elimination described earlier. Furthermore, in each instance, it was demonstrated that modified commands could restore the command function. This fact is indeed a fortunate coincidence, for one could point to other stages, which are thought to be less vulnerable to radiation damage, where increased leakage or reduced gain would lead to a failure about which nothing could be done.

5.2 *Return to Normal Operation*

On December 19, two different test signals were transmitted to the satellite. They were designed to override high leakage in the first and second stages of the shaping network. Neither test was successful. A third test, which was established to circumvent failure of the zero digit gate, was successfully tried on December 20. The C command was carried out on pass 1492, and during the next pass CC command was properly executed.*

Following the success of the test on December 20, on December 21 it was decided that commands C, CC, T-1 and T-2 would be tried. The C, CC and T-2 commands were successful; T-1 command was not successful but, because of the nature of that command, one could not definitely say that decoder 1 was not functioning (see the Appendix).

* The C command, which normally turns on the traveling-wave tube anode voltage, is not executed unless A and B commands are sent first and, since a telemetry channel indicates the state of the C relay, C and CC commands provide a convenient means for checking the command system.

The significance of execution of the T-2 command was substantial for it meant that the zero digit gate failure was in decoder 2. This decoder was the first to exhibit command system difficulties (one month after launch).

With the failure pinpointed in one decoder, the plan was to increase the size of the list of commands which would be obeyed. For operating convenience, magnetic tape recordings were made of the modified command signals. As outlined in the Appendix, application of the modified command which circumvents the zero digit gate failure is somewhat difficult because of the bandwidth limitations of the satellite command receiver system. Through a gradual increase in confidence in operation of the command system, it was expected that all features of the satellite repeater would be recovered. On December 27, on pass 1555, after a successful C command, CC command was interpreted as an SS command and the S relay opened; this removed the connection between the nickel-cadmium battery and the solar plant and left the command system powered by only the solar plant. This occurrence, which has since been duplicated in the laboratory, was unexpected since it meant that the CC command had been converted into its complement. Within one minute the S relay opened, closed and opened again, and it was left in this state as the satellite disappeared over the horizon.

While out of view of Cape Canaveral and Andover, the satellite went into eclipse for a period of 25 minutes. Thus power was removed from the ailing decoders for that length of time On the next pass the satellite first became visible to Cape Canaveral, which had not yet been equipped to send the modified command signals. With the hope that power removal might have caused enough recovery of the damaged transistors, a continuous normal S command was transmitted from Cape Canaveral for 12 minutes; however, the satellite did not respond. When the satellite came in view of Andover, a modified S command was sent and properly executed. Telemetry, which is automatically turned off through the interpretation of an SS command, was turned on again with a modified D command.

On December 28 and 29, continuous normal command signals were transmitted to the satellite and, during pass 1574, a repetitive *normal* C command was executed after 37 minutes. The time to execute repetitive normal C, CC and T-2 commands gradually decreased, and, during pass 1602 on January 1, 1963, the first nonrepetitive command (C) was executed. Up until that date, there had been no response to T-1; all successful commands had been decoded by decoder 2. On that day, however, T-1 command was also properly interpreted, and it was clear that both decoders were responding to normal commands, although some sluggishness was still apparent.

On the last visible pass of January 1, the SS command was executed erroneously by the satellite during a sequence of normal T-2 commands. The S relay was not closed and the decoders were left powered by only the solar plant; the satellite went through five 20-minute eclipses during which power was removed from the command equipment. On the next visible pass (1609) the following day, normal operation was observed for decoder 1; response to T-2 command was less sluggish. The S relay was deliberately left open on the last pass of January 2 (1613), and on January 3 complete recovery of both decoders had taken place.

The traveling-wave tube was turned on, for the first time since November, on January 3, and normal operation of all systems was reported. Since that time, commands have been successfully carried out through the use of both normal and modified commands. The latter commands do not use the zero digit gates of either decoder. On only four different occasions have the modified commands been misinterpreted by the satellite.

Since January 2, the SS command has been sent intentionally whenever it was operationally convenient to do so to retard radiation damage and hopefully to increase the circuit operating margins. The length of an eclipse varies with time, however, and dropped to zero from January 6 to February 4.[3] Hence, power was applied continuously to both decoders during that period. Nevertheless, normal commands gave satisfactory performance throughout that interval.

5.3 *Cause of Recovery*

There is no conclusive evidence that there is any one cause of recovery of the normal command function. Laboratory experiments have shown that reduction of V_{CE} and/or reduction of the radiation field intensity can bring about recovery, although the degree of improvement varies greatly among devices. The facts related in the previous section show that there is a definite correlation between recovery and V_{CE} reduction through the use of continuous commands and the occurrence of eclipse with the S relay open. However, simultaneous with the efforts to regain the command function, there was a reduction in the radiation flux seen by the Telstar satellite due to decay of the particle density in space and the oscillatory change in the orbital average as the line of apsides of the orbit precessed. On January 1, 1963, the average flux had dropped to less than 20 per cent of the value it had on November 15, and to less than 10 per cent of that measured during the month of July.* The re-

* The temporary recovery of the T-2 command on October 17 occurred at the time of a minimum in the radiation intensity with apogee of the satellite's orbit at the equator.

covery was probably due to a complex combination of the effects described above.

5.4 *Reappearance of Command System Malfunction*

Throughout the month of January, the command system responded normally. On February 5, however, the malfunction of the zero gate in decoder 2 again appeared, and it was necessary to command through that decoder with the use of the modified command signals described in Section A.4. Decoder 1 continued to function normally until February 14, and, to assure reliable operation, taped modified commands were used almost exclusively for commanding the satellite through decoder 2. On February 21, however, the command system apparently misinterpreted a modified T-2 command and the S relay was opened. Thus the storage batteries were disconnected from the solar plant and power was supplied to only the command system. The satellite has failed to respond to further command attempts.

The cyclic behavior of the average radiation intensity to which the Telstar satellite is exposed has a period of approximately three months. It is significant that the February malfunction, like that of November, occurred near the peak of the cycle.

The phenomenon of the conversion of a modified command to the SS command has been demonstrated in the laboratory. It occurs when I_{CBO} of the reset digit gate transistor attains a critical value. Circumstances indicate, therefore, that the problem in decoder 2 might be failure of both the one and reset digit gates.

VI. CONCLUSION

The facts have been presented which led to the conclusion that the malfunction of the command system was due to surface damage to certain transistors by enhanced radiation in the inner Van Allen belt. Correction steps have included laboratory experiments to gain a better understanding of the cause of failure, the use of continuous normal commands, commands transmitted from Johannesburg, South Africa, and specially modified commands to circumvent failure of the more vulnerable transistors.

VII. ACKNOWLEDGMENTS

Other members of the technical staff of Bell Telephone Laboratories were instrumental in planning and conducting the experiments and tests which led to the diagnosis and cure of the command system mal-

function. Contributions were made by R. H. Shennum, R. C. Chapman, H. H. Henning, D. B. Cuttriss, W. Rosenzweig, J. D. Gabbe, E. R. Schmid, and W. Gianopulos.

APPENDIX

Modified Command Signals

A.1 *General*

The five most vulnerable transistor stages, selected in the manner described in Section 5.1.4, require the use of different modified command signal structures to accomplish proper decoding in failed units. The relative location of each of these stages can be determined from the block diagram of the command decoder shown in Fig. 6. A detailed description of the operation of the decoder circuit is given in Ref. 1.

A.2 *First Stage of the Pulse Shaping Network*

This circuit is an emitter follower with a high V_{CE} ; high I_{CBO} (>25 microamperes) will force the base voltage of this stage above a threshold level and will consequently cause the pulse generator to free-run. The input of the emitter follower is coupled to the output of the command

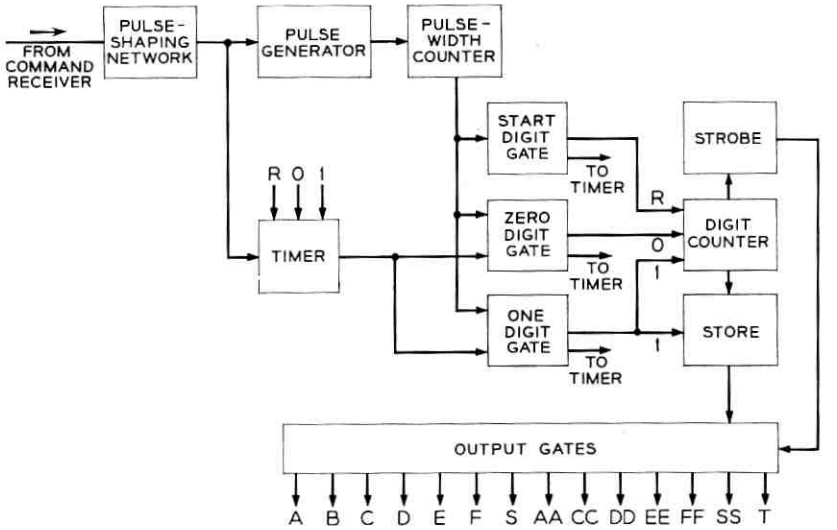

Fig. 6 — Command decoder block diagram.

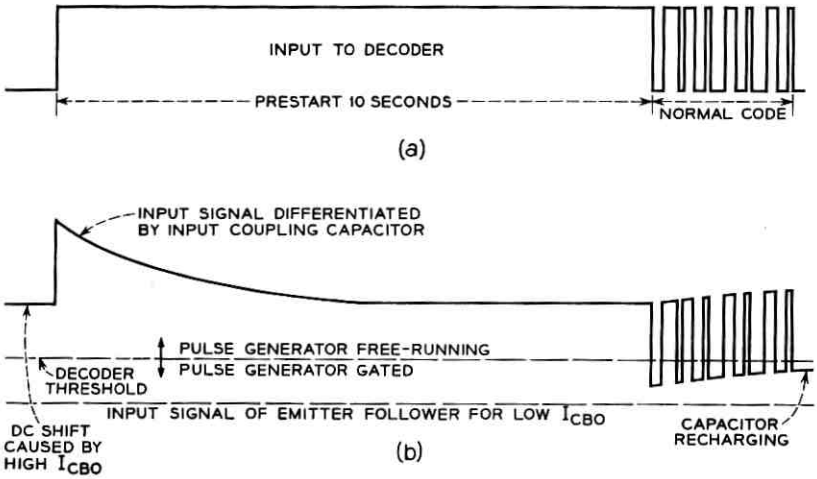

Fig. 7 — Modified command for high I_{CBO} in pulse shaping network first stage.

receiver through a capacitor. By preceding a normal command signal by a long pulse, as shown in Fig. 7(a), the input capacitor is charged to the full pulse amplitude level. When the pulse is removed, the charged capacitor will serve to pull the base of the emitter follower below the threshold level so that a command may be transmitted during the interval that the capacitor is being discharged by the leakage current (see Fig. 7b).

A.3 *Second Stage of the Pulse Shaping Network*

If the leakage current of this stage is above 150 microamperes, the pulse generator will free-run. Leakage currents in excess of 300 microamperes will cause the digit gates to be held off; consequently, the modified command signal described here will be effective only for a leakage current below 300 microamperes. Normally, the pulse generator, a gated astable circuit, is allowed to free-run only when an input pulse is present, as shown in Fig. 8(a). The modified command consists of a near-standard command set up on a shorter time interval basis, so that the input pulses are occasionally "in phase" with the free-running astable circuit, as shown in Fig. 8(b). With the shortened code it is possible to cause spurious decoder response when proper phasing does not exist. Errors can be avoided if the command pulse sequence is very carefully established.

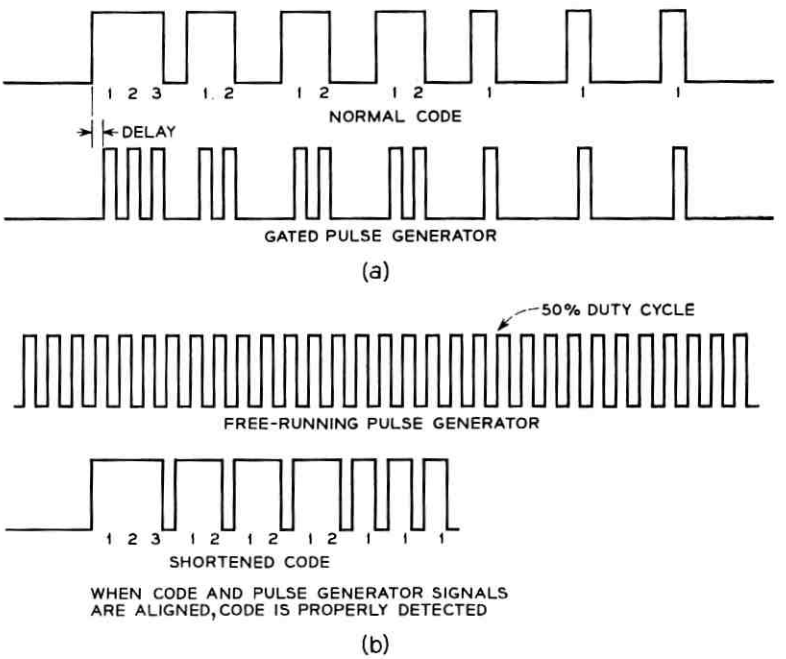

Fig. 8 — Modified command for high I_{CBO} in pulse shaping network second stage.

A.4 *Zero Digit Gate*

If the gain of the zero digit gate transistor becomes sufficiently low in value, that stage will not be capable of driving the digit counter. As one sees from Fig. 6, the zero digit gate drives the digit counter and the timer; the one digit gate drives the digit counter, and, after a small amount of delay, drives the store. The scheme for circumventing the failed zero digit gate is to send in place of a "zero" a modified "one" code in such a way that the one digit gate is turned on and almost immediately turned off again. By use of the notched and shortened pulse in Fig. 9(c), it is possible to advance the digit counter but not to build up sufficient voltage to set a "one" into the store. Thus this notched "one" causes the same response in the digit counter and store as a "zero." Unfortunately, the notched "one" does not fully enable the timer circuit, and it is difficult to handle codes containing three sequential "zeros," unless these "zeros" are at the end of the code.*

* Since the T-1 command contains three "zeros" in sequence, there is uncertainty regarding the reason why a modified T-1 command caused no response on December 21. See Section 5.2.

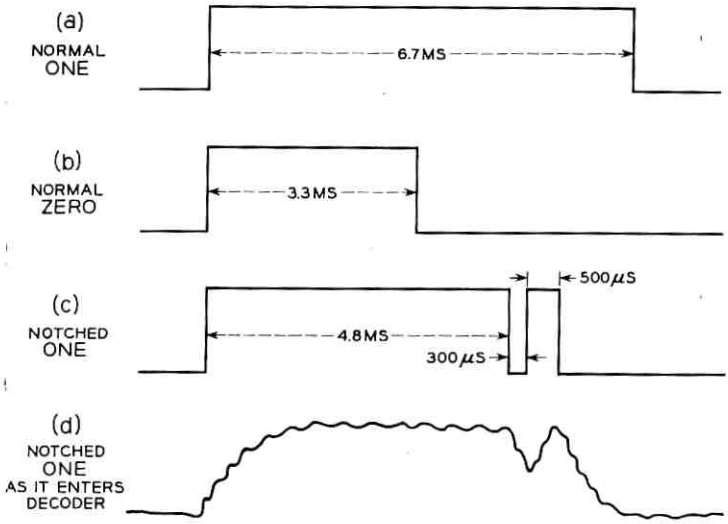

Fig. 9 — Modified "one" to circumvent failed zero digit gate.

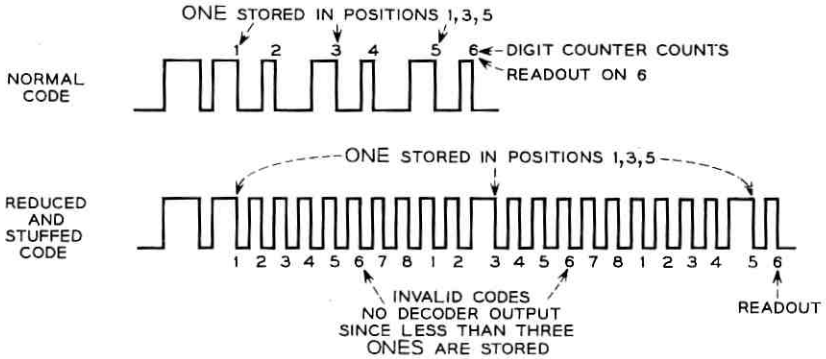

Fig. 10 — Modified command for low gain in one digit gate.

Proper detection of this modified command is difficult (but completely workable) since a code must be transmitted which produces a very marginal "one" out of the one digit gate. The margin involved is of the order of 30 microseconds in a system where the residual ripple from the subcarrier occurs with a period of 100 microseconds. Also, the notch is greatly distorted by the bandwidth limiting which occurs ahead of the decoder (see Fig. 9d). However, through the use of width modulation of the notch, the one digit gate output jitters through the region of un-

certainty. As the notch width decreases, the "one" digit notch provides outputs ranging from a "one" to a "zero." One therefore establishes a reliable mode of operation by randomly modulating the notch widths in a manner such that the desired response of the one digit gate to a notched "one" occurs with finite and acceptable probability. The number of commands that must be transmitted to execute a given order is increased. However, since the normal command time is about one-tenth second, an exchange of command time for operating margin is acceptable.

A.5 *One Digit Gate*

There are two ways in which loss of gain in the one digit gate transistor will most probably first show up. Either the gate will fail to advance the digit counter (but still set the store and reset the timer), or it will fail to fully reset the timer (but still set the store and advance the digit counter). Failure to advance the digit counter is easily overcome by preceding each legitimate "one" by a zero. (The zero advances the counter.) Thus 111000 is transmitted as 010101000.

A failure which prevents full resetting of the timer can be combated by sending a code with shortened pulse widths and pulse intervals. If that method is not satisfactory, extra zeros may be inserted in the code (to reset the timer) so that a "one" is stored in the proper slot each cycle of counter operation. See Fig. 10 for an example of this procedure.

A.6 *Normally "Off" Transistor in Pulse Generator*

The effect of excessive leakage or low gain in this stage is to increase the natural frequency of the astable multivibrator, which is the basic pulse generator circuit. To circumvent this problem it is only necessary to set up standard commands on a contracted time scale. This procedure will work up to the point that degradation is so severe that astable operation is no longer possible.

REFERENCES

1. Chapman, R. C., Jr., Critchlow, G. F., and Mann, F., Command and Telemetry Systems, B.S.T.J., this issue, p. 1027.
2. Peck, D. S., Blair, R. R., Brown, W. L., and Smits, F. M., Surface Effects of Radiation on Transistors, B.S.T.J., **42**, January, 1963, pp. 95–129.
3. Hutchison, P. T., and Swift, R. A., Results of *Telstar* Satellite Space Experiments, B.S.T.J., this issue, p. 1475; see Fig. 6.

Components for the *Telstar* Project

By W. C. HITTINGER

(Manuscript received March 5, 1963)

The Telstar project required a variety of components and structures of high reliability. The program for obtaining these components was essentially that originated for submarine cable devices, in which designs of proven integrity were manufactured under controlled conditions, screened and aged to remove defectives, and then life tested and certified using techniques for selecting the most stable components. This program summary illustrates in principle the techniques described in detail in the body of this components section of the issue.

I. INTRODUCTION

The papers comprising Part 3 of this issue describe the design, performance, and reliability considerations of the major components utilized in the Telstar spacecraft and certain of the unique electronic components of the earth station. Those papers pertaining to components of the spacecraft were presented orally at Bell Telephone Laboratories, Murray Hill, New Jersey, on November 14, 1962, to representatives of the National Aeronautics and Space Administration, Department of Defense, and many electronics and space companies. Particular emphasis was placed on the reliability requirements of spacecraft components and the means taken to ensure satisfactory life of the communications satellite. This issue highlights reliability by describing those steps taken to design, fabricate, test, and certify components to ensure reasonable certainty of operation for the communications satellite experiment. Companion papers presenting descriptions of the Telstar system are contained elsewhere.[1]

This paper is devoted to a broad description of component reliability as related to the design of the system. Consideration is given to the means for obtaining highly reliable components within a time schedule which precluded highly specialized manufacture and long term life testing.

II. COMPONENT RELIABILITY REQUIRED FOR PROJECT TELSTAR

The reliability requirements of components for communication satellites have been stated previously.[2] This earlier study described the three periods of satellite life, namely pre-launch, launch, and orbit, and showed how the orbit period dominates the reliability design. The Telstar experiment was undertaken with an objective of two years operating life in orbit. Because of the large launch cost penalty of increased weight and size, excessive component and circuit redundancy was considered prohibitive. The system therefore depended critically upon the use of highly reliable components which must survive a wide variety and range of thermal, electrical, mechanical, and radiation stresses. These stresses arise in particular during the launch and orbit phases when replacement of defectives is impossible. Certain of the components, such as the traveling-wave tube, are used singly or in small numbers, and thereby present a challenging design and reliability assurance problem. Other components are used in quantity and, to meet the objectives of the system, require maximum failure rates in the range of 1 to 20 failures per 10^9 component hours (0.0001 to 0.002 per cent per 1000 hours). This degree of reliability had been observed in the field and therefore gave confidence that the system objective could be met. When one considers that Project Telstar was accomplished in 15 months from start of the program to launch, and that design changes involving the addition of component types were made during a significant part of this period, the task of assuring this level of reliability became imposing indeed.

The decision was made at the onset that only components of proven integrity could be used. The environmental conditions during the launch phase, involving large mechanical stresses, and the orbit phase, involving Van Allen belt radiation and temperature cycles, were defined. Component designs were evaluated to ensure that they had the capability of meeting environmental conditions with margin. Where time allowed, devices were manufactured under engineering surveillance to ensure the highest possible integrity. All devices were carefully screened to expected environmental conditions and pre-aged to eliminate defectives. The survivors were then life tested under simulated system conditions and then the best were certified using statistical analysis and engineering judgment. Finally, the components were used in circuits of conservative design where they operated well within maximum ratings.

III. COMPONENT RELIABILITY ACHIEVEMENT

The program used to provide Telstar components was essentially that originated for submarine cable devices.[3] The major steps of this program are shown in Fig. 1.

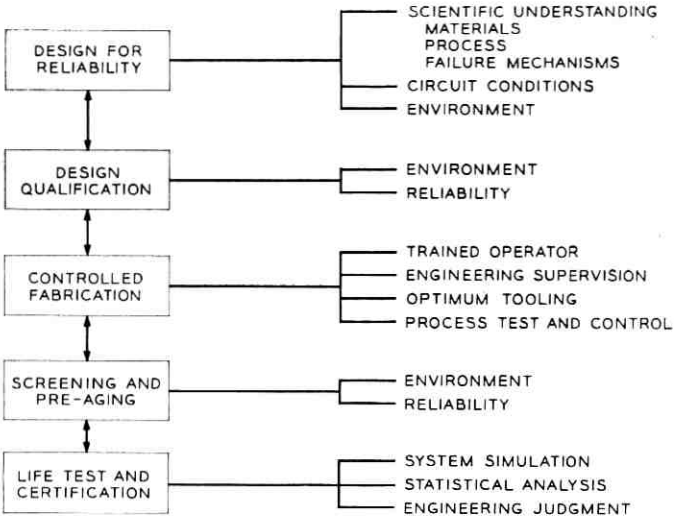

Fig. 1 — Major steps of component reliability program.

3.1 *Design for Reliability*

Satellite components must operate over a wide variety and range of mechanical, electrical, thermal, chemical, and radiation stresses. Device types intended for use were first examined for compatibility with these environments. In general only those which had demonstrated a consistent history of minimum manufacturing difficulty and outstanding field performance were considered. Specific details of design choices, such as diffused silicon semiconductor devices and nonadjustable passive components, are described in the companion papers of this part of issue.

Fig. 2 shows a failure distribution for a manufacturing lot of a component type in which failure rate is plotted as a function of time under expected system conditions. The distribution has two regions of relatively high failure rate, one early in life attributable to manufacturing "freaks," one later in life attributable to "wear-out," separated by a region of low failure rate. Device types were chosen in which the designer, through his knowledge of structure and mechanisms of change, could place the onset of wear-out well beyond the required useful life. Specific instances of wear-out were the deactivation of cathode life in the traveling-wave tube used in the satellite transmitter and the degradation of solar cells by energetic bombardment in the Van Allen belt. In cases like these, lengthening the onset of wear-out could only be achieved by understanding the mechanisms and then designing the devices to minimize or eliminate the effect.

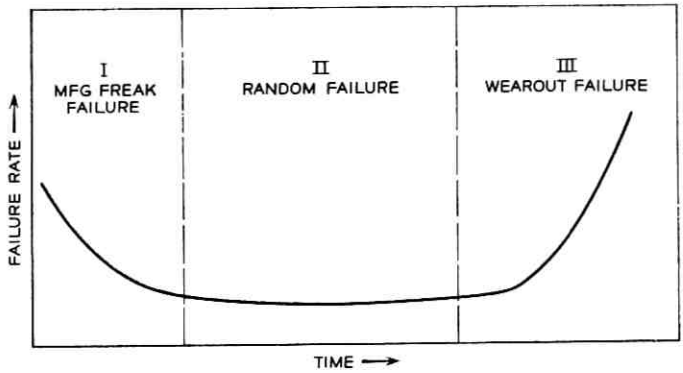

Fig. 2 — Failure distribution curve for components from one manufacturing lot.

3.2 *Design Qualification*

After the question of wear-out was settled, the next step was to ensure that the design was capable of meeting the variety of environmental conditions encountered during launch and orbit. Samples of each device type were subjected to qualification tests, many of which greatly exceeded the expected system conditions. Of particular note were gamma ray bombardment studies designed to simulate long periods of exposure expected in the Van Allen belt. Many tests were extended to destruction to obtain a measure of the design margins obtainable under actual operating conditions.

3.3 *Controlled Fabrication*

Because of the short Telstar program schedule, most of the devices were selected from manufacturing lines already producing standard products; only in a few cases were new lines established for special controlled production runs. In all cases, reliance was placed on the use of trained operators working on stable product lines in which quality control procedures were well established. These lines normally produce product in which the occurrence of manufacturing "freaks" (Fig. 2) is kept to a low level.

3.4 *Screening and Pre-Aging*

Remaining "freaks" were carefully removed from the manufactured product through the use of environmental screening and pre-aging tests. All devices were given environmental tests, many of which exceeded the

expected system levels. For example, short-term aging at highly elevated temperatures was used to eliminate devices that normally would have exhibited early failure. Samples from each manufacturing lot were subjected to step-stress aging,[4] in which the median stress for failure and the failure distribution with stress were compared to previous lot history. This latter test is a rapid means to determine whether the lot is similar to preceding lots.

Controls applied during the manufacturing phase and the screening and pre-aging tests were designed to eliminate the "freaks." The remaining product should then exhibit the low and almost constant failure distribution of the "random failure" portion of Fig. 2.

3.5 *Life Test and Certification*

For this last step, a larger number of devices than needed for the system was put on life test under circuit and temperature conditions expected in service. Every effort was made to continue the life test for the longest possible time. Parameter data were taken periodically using automatic testing and recording techniques. Only those devices were chosen for satellite assembly which showed the minimum change and closest behavior to design predictions. Final certification was done after the use of statistical analysis and engineering knowledge and judgment by experienced personnel.

IV. CONCLUSIONS

The Telstar experiment required a large number and variety of components, the reliability of which, for satellite use, had to be in the range of 1 to 20 failures per 10^9 component hours for success of the mission. This need called for the same approach to component reliability that was first used for submarine cable devices, in which devices of proven integrity are used in a conservative design. Fig. 1 lists the major steps in the program. Devices with proven design were manufactured under controlled conditions, screened and aged to remove manufacturing "freaks," and then life tested and certified using statistical techniques and engineering judgment.

Detailed descriptions of each major class of device used in the Telstar project are given in the papers to follow. Each paper describing components used in the satellite illustrates the application of these reliability principles in detail. Although components used in the earth station did not require the same degree of reliability assurance as those in the satellite, they were also designed for reliable, high performance service.

REFERENCES

1. B.S.T.J., this issue, Parts 1 and 2.
2. Ross, I. M., Reliability of Components for Communication Satellites, B.S.T.J., **41,** March, 1962, p. 635.
3. McNally, J. O., Metson, G. H., Veazie, E. A., and Holmes, M. F., Electron Tubes for the Transatlantic Cable System, B.S.T.J., **36,** January, 1957, p. 163.
4. Dodson, G. A., and Howard, B. T., High Stress Aging to Failure of Semiconductor Devices, Proc. Seventh National Symposium on Reliability and Quality Control, Philadelphia, Pa., Jan., 1961.

Component Design, Construction and Evaluation for Satellites

By D. S. PECK and M. C. WOOLEY

(Manuscript received March 11, 1963)

Components for a high-reliability system such as the Telstar project are obtained by:

(a) design of the component for the required environment,

(b) careful control of manufacturing processes,

(c) elimination of potential early failures by screening tests, and

(d) selection of the most stable components.

For passive components, these methods could be applied by using design parameters, suppliers and screening techniques established in the earlier submarine cable program, with consideration being given to the additional effects of the satellite launch and orbit environments.

Semiconductor component designs were selected by qualification tests using accelerated electrical and environmental stress conditions. Screening tests were applied to eliminate early failures, and resulting components were aged from two to six months before selection for the satellite. The recognition of the effect of ionizing radiation on transistors caused the addition of a radiation qualification test, or a screening to assure selection of the least sensitive devices. Tests have shown this screening to be effective for the radiation intensity expected.

Experience with the passive components, and evaluation of the accelerated test results and aging data of the semiconductor devices, indicate that the reliability objective was obtained.

I. INTRODUCTION

The importance of component reliability in the production of a successful electronic equipment of the complexity and with the reliability requirements of the Telstar satellite is well appreciated. Small systems and those of less complexity can be designed and built with special care, at reasonable cost, to have long life; large systems are subject to the laws of large numbers, which increase the probability of the malfunction-

ing of at least one component part. Normal maintenance of large earth-bound systems may be economical, however, and system performance may be acceptable if malfunctions are not too frequent. In an orbiting satellite, on the other hand, the first failure must be at sufficiently great time to provide an economical system, and the component failures must therefore be sufficiently distant in time, or at a sufficiently low rate, to allow a practical design. This does not ignore the requirement that the circuit and equipment designs use the component characteristics to best advantage, and also protect themselves as much as possible against the probable modes of component failure.

Considerable experience has been built up in the Bell System on the use of parts of high reliability, a most easily recognized example being the long submarine telephone cable systems which at this date have had no failures in over 10^9 passive component hours and 5×10^7 electron tube hours of service.

The submarine cable repeaters, however, use specially designed and manufactured electron tubes and passive components. The design and selection of these were based upon many years of experience and life testing.[1,2] In contrast to this situation, the limited power available in an orbiting satellite and the severe limitation on total weight dictate the use of transistors as the active components, and in this case there is no extensive experience in a system of limited maintainability such as that of the submarine cable. Evidence is rapidly mounting, however, regarding the low failure rates obtainable with transistors in large systems, even without the use of special selection techniques. Transistors in large military systems have recorded replacement rates of 25 to 35 failure units,* and subsequent improvements in manufacturing processes show promise of failure rates appreciably below this figure. The sample calculations by I. M. Ross,[3] however, show that failure rates in the order of 10 failure units would be required even for a satellite system using only 140 transistors and 160 diodes in order to achieve a satisfactory probability of success for times appreciably beyond one year. Since the Telstar satellite circuitry requires a complement of about 1100 transistors and 1500 diodes, it can be recognized that failure rates better than 10 failure units would be desirable even for an experimental system. Similarly, since there are approximately 4700 passive components, capacitors, inductors, resistors and transformers in the satellite, these components must have an over-all failure rate of the order of 1 in 10^9 component hours if there is to be a high probability of success for a two-year experiment.

* A failure unit is defined as one failure per 10^9 component hours.

The immensity of the testing required to measure such low failure rates is difficult to comprehend and all but impossible to achieve in a limited time. For example, to provide 90 per cent confidence that none of the passive components in the satellite would fail in less than two years would have required that components of the same quality be tested until they had accumulated over 2×10^9 component hours without a failure. Even with the use of accelerated tests which, in the extreme case, might compress time by a 1000:1 ratio for some types of components, this amount of testing is prohibitive. Fortunately, other avenues are available which provide a basis for obtaining a high degree of reliability but with less assurance of its numerical value.

1.1 *Principles of Achievement of Satellite Component Reliability*

The principles and techniques originated for submarine cable components and now being applied to some of the complex missile systems were recently reviewed by J. A. Morton at the Eighth National Symposium on Reliability and Quality Control. These are, briefly:

(*a*) *Design of the component for the required environment.* This requires consideration of the possibility of actual "wear-out" of the component because of the environmental or life conditions. Even with the best design knowledge and perfect manufacture there may be fundamental limitations to the usefulness of a given material in its environment. Examples are the eventual evaporation of the oxide cathode in an electron tube and the limitation on the life of silicon solar cells due to radiation bombardment in space. If possible, with a proper knowledge of the operating and environmental requirements and of the capabilities of materials and processes, the designer should place this wear-out point well beyond the required useful life of the component.

(*b*) *Careful control of manufacturing process.* The relationship of quality control in manufacture to resulting uniformity of product and hence uniformity of response to operating environment can be readily acknowledged. This process control should be used to control all three phases of product life response: (1) it should prevent marginal product from extending the period of early failures due to manufacturing defects far into the useful life region, (2) it should assure low failure rates during the useful life, and (3) it should assure that wear-out failures do not occur prematurely, in the region of normally useful life.

(*c*) *Weed-out of potential early failures by screening tests.* It may be recognized that even in a product under careful quality control in manufacture there may be a certain percentage subject to early failure because of some defect not recognizable by the normal testing processes. Such

defective units can usually be eliminated by means of rigorous environmental tests and by operating tests under conditions similar to that expected in use.

(*d*) *Selection of the most stable components of the population.* Even with careful quality control of the manufacturing process and with rejection of defective units through screening tests, there may still be expected a distribution of stability among the remaining units in the product. The state of the art of a given process required to obtain suitable operating characteristics may possibly result in variations of initial electrical parameters or in drifts or variations of these parameters with time. The careful observation of such parameters during the life test period may then allow the use of various selection techniques, more or less sophisticated as the requirements indicate, to obtain for actual satellite use those components least likely to fail in operation or to cause circuit performance changes.

The techniques of application of the principles of achieving reliable components will vary somewhat, depending upon the state of knowledge of design and processing, of testing and life evaluation methods and of circuit application factors. Because of the wide disparity of system experience with passive components and semiconductor devices, the following material will treat each of these separately.

II. PASSIVE COMPONENTS

Experience with passive components in submarine telephone cable repeaters has shown that this philosophy when applied to the selection, construction and testing of those components resulted in a highly reliable product. (Since in the systems made with such tightly controlled components there have been no component failures, for the present we can only say that there is a 70 per cent probability that the failure rate of the passive components does not exceed 1 in 10^9 per hour.) Similarly, experience and performance records with other Bell System and military projects has shown that some other types of components not used in submarine cable repeaters, when carefully manufactured and screened, are capable of this kind of performance. In a satellite these failure rates may be increased by unknown environmental factors, particularly the effects of Van Allen belt radiation and extreme shock or vibration during launch. Another liability for Telstar was a short schedule which required that screening tests, intended to eliminate potential failures, be limited to short-time tests, generally 100 hours or less. A further complication was the wide range of component types and values required.

These liabilities are offset to some extent by the fact that operating

conditions of voltage, power dissipation and temperature are mild for the vast majority of the passive components. Thus the most likely causes of component malfunction are an occasional mishap in construction or some unforeseen effect of the environment or application. Consequently, with adequate derating to minimize the deteriorative processes resulting from load or voltage, the problem becomes primarily one of

(a) careful choice of components to minimize the effects of the environment,

(b) thorough inspection and screening to eliminate all components which may be subnormal in any way and thereby potential failures, and

(c) care in the physical application of the components to avoid compromising their integrity.

2.1 *Selection of Component Types*

The choice of the component types to be used was governed by a number of factors. One of the most basic and restrictive of these was that no new or untried types could be used. In other words, only those types which have been in widespread use for a period long enough and under a sufficient range of conditions to prove by field performance that they were capable of reliable operation, were considered for use. This restriction was also applied to the materials used in the construction of the components and to the details of construction so that both materials and the type of construction were well established and proven by field experience.

It is generally recognized that, especially under conditions of severe vibration or mechanical shock, adjustable components are less stable than their fixed counterparts. Consequently a strenuous effort was made to avoid the use of adjustable types. In most cases this was accomplished by selection from "post office" bins which covered the required range in suitably small fixed steps. Where this was inadequate, the over-all stability was enhanced by limiting the range of adjustable components to cover only the range between closely-spaced fixed steps.

It is easy to visualize the increased hazard of failure when conductors are made very small or dielectrics are unusually thin. Thus for extreme values of resistance the resistive film may be made so tenuous that at some points it is practically nonexistent, or for very low values the heavy deposit required to produce low resistance may be mechanically unstable. Similarly in capacitors, in an effort to crowd the maximum capacitance into a given space, factors of safety may be reduced, clearances may be made smaller, and physical damage to critical parts may even result. In addition to this degradation of reliability at the extremes of compo-

nent values, it is not uncommon to find that characteristics such as temperature coefficient and stability with time or frequency are also degraded at extreme values. For these reasons the range of values, in a given physical size, was severely limited for the satellite components. This affected capacitors and resistors particularly, and in some cases limited the range of usable values to less than 15 per cent of the range of commercially available values.

Although the anticipated cumulative exposure to electron and proton radiation appeared to be well within the acceptable limit for most components, only the most resistant types were used. Thus hermetically sealed components filled with oils or electrolytes were avoided because such materials gas and build up destructive pressures under severe radiation. Structural and housing materials and coatings were also examined and chosen for their resistance to deterioration under radiation. These choices were based on the reported results of many studies, both within and outside Bell Laboratories, and on supplementary tests made in a Co^{60} cell on the specific types of components used in the satellite. Most of these were tests in which the components were subjected to load or voltage during radiation, and they were continued until the exposure exceeded by several times the maximum expected in service. From these tests it was concluded that radiation would not be the limiting factor in the life of the components, at least in a two-year experiment.

It was expected that, because of being sealed in the canister, the majority of the components would not be exposed to the extreme vacuum of space. All of the types, however — resistors, capacitors and power transformers — on which low pressure might have an effect were tested under such conditions. Furthermore, such components were rated so that they would operate under extremely low pressure without abnormal temperature rise or other harmful effects.

Even with these restrictions there were very few instances where suitable standard components were not available.* Table I lists the types of components used and their typical uses.

2.2 *Selection of Components for Specific Applications*

As mentioned above, the most likely causes of malfunction of components are misapplication and deviations from design intent during manufacture of the components. The term "misapplication" in this case

* Approximately 95 per cent of the passive components used were purchased outside the Bell System.

TABLE I—TYPES AND TYPICAL USES OF PASSIVE COMPONENTS

Use	Type	Number Used
Capacitors		
General purpose, temperature compensation	Ceramic	814
Precision in low values	Glass	47
Precision in high values	Mylar*	18
High values, small size	Tantalum solid	444
Precise tuning	Glass and quartz tubular trimmers	20
Resistors		
General purpose, low precision	Carbon composition	1325
General purpose, moderate precision	Pyrolytic carbon film	1414
High precision, high frequency	Metal film	136
High precision	Wire wound	44
Power dissipation	Vitreous enameled wire wound	30
Inductors		
High frequency, general purpose	Nonmagnetic core, fixed Nonmagnetic slug, adjustable	140
Power frequency	Permalloy dust core toroid	2
Memory coils	Ferrite core	230
Transformers		
Narrow-band high frequency (tuned)	Nonmagnetic core, adjustable inductance Magnetic core toroid	43
Broadband high frequency	Closed ferrite core Ferrite cup core Laminated magnetic core	15
Power frequency	Magnetic tape core toroid Permalloy dust core toroid	6

* Registered trademark, E. I. DuPont DeNemours & Co.

is used in a broad sense to include improper voltage, temperature or wattage, or failure to meet circuit or ambient conditions, as well as the actual physical mishandling or incorrect mounting of the component. Since the components used were types known to be capable of reliable operation, the major problems were to assure their reliability by careful handling and use and to eliminate by thorough testing or screening those individuals which were abnormal in any way. An essential ingredient in any project requiring reliability in components is the care and perspicacity with which these factors of selection and use are examined. In these respects Project Telstar differed from other Bell System projects in

degree only. Component engineers recommended types on the basis of circuit engineers' requirements and also prescribed conditions of use (handling, mounting, etc.). Subsequently the application was independently checked by a reliability engineer, who compared operating conditions with component ratings which were established especially for the Telstar program. In general, all components were derated at least 50 per cent from commercial ratings. During fabrication of all development, preproduction and final models of the Telstar spacecraft, all cases of malfunction which were in any way related to the components were examined and appropriate measures taken to avoid future difficulties. This procedure was particularly effective in eliminating misapplications and physical mishandling.

2.3 *Screening and Final Selection*

The testing or screening of components varied from type to type, but in general the bases for the tests were standard Bell System high-reliability specifications, which were supplemented by restrictions on materials and in some instances by additional requirements. In addition the suppliers were asked, and willingly agreed, to apply any additional tests or requirements which in their opinion would enhance the reliability of the product. Several such additions to normal processing were made, ranging from special handling to the imposition of short-time life tests or special electrical tests. Chief of the requirements added to the Bell System specifications was the assignment of an identifying number to each component and the recording of data for each numbered component at various stages of the test program. These data were delivered by the supplier with the components. On receipt of the components they were subjected to additional tests which ranged from a check of electrical characteristics to voltage or power aging supplemented by "before" and "after" measurements of all critical characteristics. All of the data, both the supplier's and the Bell Telephone Laboratories', were then analyzed either manually or by machine. The components to be used were selected by this analysis. Three criteria were used in this selection:

(1) fixed limits on critical attributes,
(2) stability of characteristics throughout the test period, and
(3) conformance with normal behavior.

Many of the requirements applied to conventional components have no direct relation to the performance of the circuits in which the components are used but are instead applied to control the quality, i.e., to insure the integrity of the materials and proper processing of the component. The same is true to an even greater extent when extreme re-

liability is required, so that every property which might have an effect on, or be a measure of, reliability is controlled. Table II lists the major kinds of requirements applied to capacitors and resistors. Some of these were applied only to certain types: for example, the X-ray requirement was used only on hermetically sealed designs where internal clearances and positioning could not be checked visually. Similarly the requirement for change under load was applied only to resistors intended to dissipate significant amounts of power. As shown in this table, the requirements for the Telstar satellite components covered much more than those attributes which were of importance from a circuit performance standpoint. An example of this is the application of requirements for ability to withstand atmospheric moisture. At no time during shipment, assembly into equipment, or use were the components subjected to severe humidity conditions, but tests were made to measure their ability to withstand such conditions. Since the normal product is capable of meeting these requirements, failure of the Telstar satellite components to do so would have indicated that the product was inferior to normal product either in its moisture protection or in contamination with moisture-sensitive materials. Similarly, voltage aging tests on capacitors and power aging tests on resistors were made at stress levels chosen to insure that the component quality was consistent with capability rather than just adequate for the stresses in service. Furthermore, these tests were made on 100 per cent of the product, and entire lots which had more than a few per cent of failures were rejected.

In the final selection of the components to be used the record of each one was scanned. Where there was a large margin between the component capability and operating conditions or requirements, practically all components which met the fixed requirements were considered qualified for use. In other cases where the margin between capability and use was

TABLE II—TYPES OF REQUIREMENTS APPLIED TO CAPACITORS AND RESISTORS

Resistors	Capacitors
Resistance	Capacitance
Aging resulting from load	Power factor
Aging resulting from temperature cycling	Insulation resistance (or leakage current)
Moisture resistance (sampling)	Dielectric strength
Change under load	Capacitance-temperature characteristic
Temperature coefficient of resistance	Voltage aging (100%)
	Life test (sampling)
	X-ray

smaller, only those components with characteristics near the norm and showing a high degree of stability were considered acceptable. Even when deviations from normal behavior were in the direction of better performance, those which showed abnormal deviations were rejected since this might be the compensatory result of two mechanisms, one of which could ultimately cause failure. As a result, the yield of acceptable components ranged from nearly 100 per cent of those received of some types to approximately 50 per cent of other types.

While the foregoing applies specifically to purchased components, the procedure for those few components made by the Bell Telephone Laboratories or Western Electric Company differed mainly in that their construction was under direct engineering supervision and inspection. This close supervision and detailed inspection is particularly important for some types of components, such as inductors and transformers, where tests to accentuate and uncover weaknesses are either destructive or nonexistent. In addition to this factor, manufacture of some components by Bell Telephone Laboratories or Western Electric was undertaken because of the need for special characteristics, unusually close tolerances on electrical parameters or unusual operating conditions. Examples are: very stable inductors with a narrow (2 to 3 per cent) adjustment range, others with inductance tolerances measured in millimicrohenries and unimpregnated capacitors for use at high voltages. The manufacture and testing of many of these were essentially laboratory operations, but even with this close control the components were screened by appropriate tests before being released for use. For example, the high-voltage capacitors used in the dc supply for the traveling-wave tube were screened by applying an overvoltage of 150 per cent of rating for eight weeks.

While these measures do not permit or lead to any quantitative calculation of the reliability of the components, past experience, coupled with engineering judgment of the effect of the special handling, leads to the belief that the passive components will achieve the low failure rate needed for successful conclusion of the Telstar experiment.

III. SEMICONDUCTOR DEVICES

As indicated previously, the number of semiconductors to be used in the Telstar experimental satellite dictated that the failure rate should be in the order of 10 failure units or less to provide assurance of reasonable life even for experimental purposes. The achievement of such reliability would require close attention to the principles outlined previously, and a program was established along these lines for selecting the necessary devices. In contrast to the situation on passive components,

very limited experience was available regarding the specification of suitable procedures for manufacture or selection to the desired reliability. The reliability principles described in Section 1.1 can be applied, however, and the particular techniques of application are indicated in the following description of the semiconductor program.

3.1 *Component Design*

Table III shows the numbers of diodes and transistors required per satellite, the total number required for all satellite models and the number actually processed in the program. The total number of transistors and diodes was divided into 41 different basic types or prototypes, from which a total of 93 individual codes were selected to match the specific requirements of the many circuits. Although two types of diffused germanium transistors and three types of diffused silicon diodes were designed and manufactured for the Telstar satellite, the large number of other types and the total numbers required dictated that existing types in production be used where possible for this system, provided each had the basic design features necessary for reliability[3] and could also qualify for use in the specific intended environment.

A basic requirement of design-for-reliability is that there should not be any feature of the design which contributes the possibility of wear-out failure within the usable lifetime or which prevents the achievement of low failure rate during that time. Most of the types were selected from those previously designed for either military or Bell System use. The designs had already received consideration of possible wear-out failures and they had also met such design requirements as (a) high internal element resonant frequencies, (b) capability of withstanding storage temperature extremes and soldering temperatures and (c) adequate resistance to vibration or shock of typical applications.

Beyond these normal design considerations, it was additionally necessary to review the capability of each candidate type for operation in the satellite environment. This was accomplished by a number of design

TABLE III—*Telstar* SEMICONDUCTOR REQUIREMENTS

	Number per Satellite	Number of Types	Total Number Required	Total Number Processed
Diodes	1,521	18	12,526	28,525
Transistors	1,119	23	9,996	29,644
Total	2,640	41	22,522	58,169

qualification tests, as shown in Table IV. The requirements for these tests were established to exceed the specific conditions resulting from the satellite design or, as with some of the mechanical tests, to reconfirm the normal device design capability. For example, the temperature cycling extremes for the devices to be used in the electronics package were established by typical device capability even though the mechanical design of the package is such as to maintain its internal temperature at or near normal room temperature. The diodes used to isolate groups of solar cells, however, were to be mounted near the outer shell or skin and would be subjected to much more extreme temperatures; the temperature limits were established, therefore, to assure that no feature of the design would prevent proper performance at these temperatures.

Similarly, the vibration tests for most of the designs were established to assure performance in the electronics package at the low frequency of resonance determined by its mounting, using considerable margin in the acceleration level. The blocking diode design, however, was actually tested on a mechanical model of the Telstar satellite design in order to assure achieving the mechanical environment of the exact mounting location. The other conditions of centrifuge, shock and temperature-humidity cycling conform to typical requirements of handling, since the corresponding requirements of the satellite would be very mild.

The qualification of device types for reliability depended heavily upon the step-stress techniques[4,5] which determine the distribution of failures with increasing stress for a given time of application of stress. With this distribution obtained for several different times of application, a plot can be made of a relationship between time and the stress value at

TABLE IV—DESIGN QUALIFICATION TESTS

Mechanical	
Temperature cycling	
−65 C to +85 C for devices in electronics package	
−120 C to +40 C for devices on skin	
Temperature-humidity cycling	
Shock	2,000g, 0.2 msec
Centrifuge	5,000–10,000g
Vibration	100g, 80 cycles for devices in electronics package
	100g, 100–2,000 cycles for devices on skin
Reliability	
Accelerated tests	
Field experience	
Radiation	
Proton, electron and γ-ray exposure	

median failure. Either temperature or power, or both were used as the stress for each transistor or diode type in order to achieve extrapolations to the expected condition of use and to provide estimates of the failure rates to be expected. Generally the results were significant and satisfactory. One diode type was rejected from the program because of the very short median life indicated by the extrapolation of the step-stress data. Some of the microwave diodes, however, were not capable of accelerated stress testing because of their construction, and dependence was therefore placed upon the long history of satisfactory experience with these diode types in other transmission systems.

To qualify the designs for resistance to radiation, samples were exposed to proton and electron radiation, with electrical tests being made before and after exposure. No adverse response was indicated here except for germanium alloy transistors for power regulation, which showed degradation due to permanent damage in the germanium. These tests were augmented with γ-ray exposure (correlated to proton exposure) and sufficient data were obtained to establish the alloy transistor degradation rate. A shielding of about 0.120 inch of aluminum was used to reduce this rate to an acceptable value for the system life.

In addition to the design qualification testing, consideration was given to circuit application factors and to the effect of the environment on device capability as described for passive components in Sections 2.1 and 2.2.

3.2 *Control of the Manufacturing Process*

Most of the semiconductor devices were obtained as early as possible in order to provide a suitable time period for certification life testing. They were therefore taken from product already manufactured under normal quality control and inspection techniques. A sample of each lot of product obtained, however, was subjected to step-stress testing where applicable to assure that the failure pattern would match that expected from the design qualification tests or from previous experience. Some of the diffused germanium high-frequency transistors, however, and three types of special diffused silicon diodes were manufactured specifically for the Telstar program and were made under direct engineering control with careful scrutiny of each step of the processing.

3.3 *Screening and Pre-Aging*

Table V shows the list of the various screening and pre-aging conditions used to eliminate early failures from the product. Each condition was considered for at least one of three reasons: (1) general applicability

TABLE V—SCREENING CONDITIONS

Mechanical
Centrifuge
Temperature-humidity cycle
Tap, shock or vibration
X-ray inspection
Temperature cycle
Reliability
High-temperature processing

of the testing condition for quality control, (2) knowledge of the design which would cause concern about capability of every individual device to withstand the environmental condition or (3) specific requirements of the application. In addition, when prior experience was not available, tests were made to obtain assurance that the environmental screening condition would not induce additional incipient failures into the product and would, in fact, eliminate devices which were distinctly weaker than the normal population. Not all conditions were used for each type, and the choice of conditions for each type was determined, at least in part, by results of the qualification tests.

Results of the mechanical screening operations are presented in Table VI. The low rejection rate of the diffused germanium high-frequency transistors, in comparison to that of the silicon transistors having a generally similar structure, is felt to represent the improvement due to the careful attention given them during fabrication. On the other hand, the high rejection rate of the alloyed germanium types for power use reflects marginal capability of meeting screening conditions for which these particular types were not originally intended.

Reliability screening, or pre-aging by the application of high temperatures, was used only in one case where the qualification testing indicated early failure rates could be improved. In most cases such proc-

TABLE VI—MECHANICAL SCREENING RESULTS

	Number Processed	Per Cent Rejects
Diodes		
Microwave	774	2.3
Rectifier	3,292	3.0
Small Signal	24,109	0.27
Transistors		
Power (Ge)	635	9.5
High Frequency (Ge)	4,780	0.3
Amplifiers (Si)	24,229	2.8

essing was included in the normal production sequence and was not repeated in this program.

In addition to these results of the planned program, additional mechanical screening was required later for two diode types when molded into a module. The molding flash removal operation was apparently causing damaging shocks to be transmitted down the diode leads. Although alteration of the flash-removal process appeared to eliminate the problem, diodes were also given a very severe tap test which caused rejection of 25 per cent of the diodes for that application.

Subsequent to the initial radiation evaluation it was recognized that devices held under electrical bias while being exposed to ionizing radiation could suffer degradation at a much lower dose than that necessary to produce permanent damage in the semiconductor material.[6] This effect occurs in quite varying degrees in transistors of different types and among individuals of a sensitive type. It apparently results from ionization of the gas ambient in the device and the effect of such ionization on the semiconductor surface. All types were therefore exposed to ionizing gamma radiation from a Co^{60} source for short periods at an accelerated dose rate of about 10^6 rads per hour and for long periods at a dose rate of 5 rads per hour, simulating the exposure expected in the Telstar satellite orbit, according to data available prior to launch. Those types showing no degradation under either exposure were considered qualified for this environment. Those types showing degradation were given additional radiation screening, consisting of exposure while under bias in normal transistor operation, for one minute in a γ-ray dose of 8.5×10^5 rads per hour. This provided a total dose of 1.4×10^4 rads, the equivalent in ionization energy to that dose expected in three months in the satellite orbit for devices shielded in the electronics canister. Such screening was necessary for two types of silicon mesa transistors. Fig. 1 shows an example of the distribution (on a normal probability scale) of the increase in collector reverse current (I_{CBO}) of one of the transistor codes after screening, indicating the percentage selectable at any stated screening limit for three months in orbit. (The measurements prior to radiation were in the 10^{-10} to low 10^{-9} ampere range.) Since for these types the I_{CBO} increases beyond this value approximately as the $\frac{1}{2}$ power of total dose, a selection for two-year operation (eight times the equivalent of the screening dose) is made by setting the I_{CBO} limit for screening a factor of 2.8 tighter than the circuit limit. Some additional safety factor is desirable because of the lack of perfect correlation between screening dose and dose in orbit. The knowledge of this response to radiation and the distribution thereof allows careful matching of screening limits and circuit use requirements, if necessary to obtain maximum screening yield.

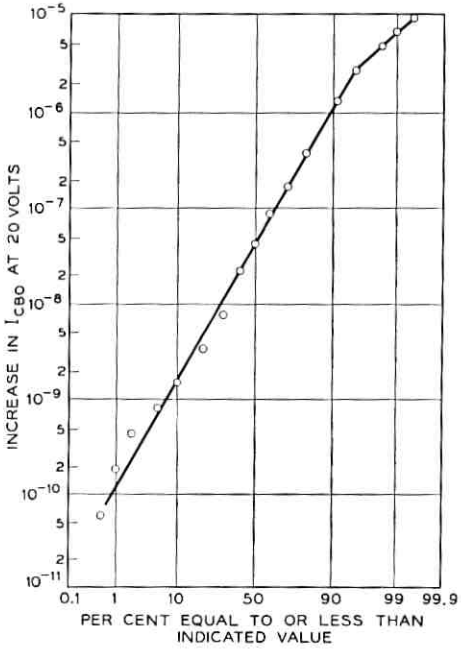

Fig. 1 — Distribution of reverse current degradation resulting from radiation screening.

Suitable selection was made of these types, without allowing more than two orders of magnitude increase for use in the most lenient circuit.

Subsequent low-level exposure tests[6] have confirmed the effectiveness of this screening procedure through equivalence of its results to those expected in orbit. Fig. 2 shows the distribution, on a normal probability scale, of the ratio of h_{FE} of one of the transistors after the screening dose to that before screening. This shows that, in the total population screened, 10 per cent suffered degradation to below 30 per cent of the original measurement. Since increases in gain were not of concern, the screening selection affected most strongly the units degrading most. The units with highest initial gain suffered the greatest percentage of degradation in screening, while those with lower initial gains degraded less or tended to increase, so that the problem of selecting units with sufficiently high gain after radiation was not severe.

3.4 *Selection of the Most Stable Components*

In order to select the best devices from the available product, all devices were subjected to a life testing period of an intended six-month

duration or for as long as possible between the time of availability and the deadline for shipment. (For the devices selected for the Telstar satellite, the average life test was about fifteen weeks.) During this life test period all pertinent parameters were measured on each device at regular intervals, generally of the order of two weeks. Up-to-date listings were kept of the data on each device so that the life history could be examined readily for drifts of characteristics, unusual variations in measurements, proximity to critical circuit limits or the existence of wild and unexplainable readings.

All the devices were operated at electrical conditions close to those at which they would be used in the satellite or close to the most severe condition for those types used in several circuit applications. On this basis, the operating condition was typically in the order of 10 per cent of the normal device rating. Although this does not take advantage of the acceleration of changes which might be induced by higher power levels, it was considered to be the safest approach. Furthermore, this resulted in some of the transistor types operating at quite low currents, at which the gain measurements are more sensitive to changes, and differences in stability between individuals may have tended to show up even more readily than at the higher power levels. Most of the devices were installed in modules which could be inserted into the aging equipment or into the test equipment without additional handling of the device itself.

The selection process consisted of obtaining the most stable units on the basis of the recorded life data and electrical measurements before

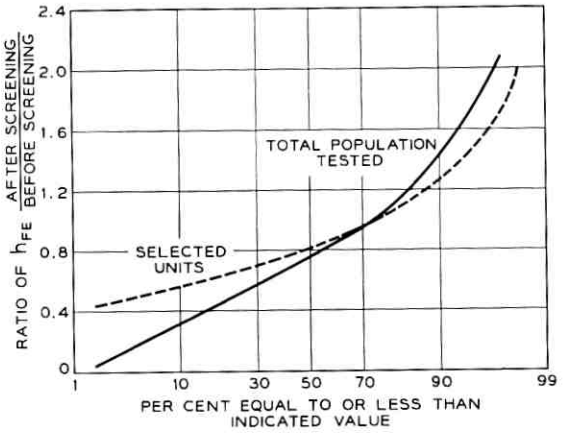

Fig. 2 — Distributions of h_{FE} degradation, of total group screened and of selected units, resulting from radiation screening.

and after the various screening procedures. Whereas many of the lots were sufficiently small that this could be done readily by observation of the data listings, other lots were sufficiently large that the initial selection was done by machine as much as possible. A computer was programmed to estimate the time at which each device would exceed an established limit for any parameter, considering drift, variations, and the initial values. The individuals were then ranked according to these time estimates and a listing was prepared from which selections could readily be made.

The final certification of each device chosen for use consisted of a complete review of all electrical measurements, X-ray photographs and similar data by qualified technical personnel, stamping of the proper code number to identify the circuit application intended and final inspection and electrical test. Many of the general considerations were similar to those described for passive components in Section 2.3.

3.5 *Evaluation of Life Testing and Selection*

It is of interest to review the life testing data and the results of selection, in order to observe the effectiveness and the degree of discrimination of selection and to obtain some estimate, if possible, of the probable reliability of the selected units.

Fig. 3 shows one example of the selection sensitivity for one parameter of a silicon mesa transistor. This plot, on a normal probability scale, shows the distribution of the rate of change of h_{FE}, or transistor current gain, in per cent change per month, averaged over the life test period (six months in this case). Silicon transistors typically experience a slight increase in gain early in life, becoming quite stable thereafter, and the total population on this life test shows, for most of the units, this typical increase. About 4 per cent of the total, however, evidence a negative drift, indicating degradation of the order of 1 to 2 per cent per month or more, this portion of the product also deviating from the Gaussian distribution indicated by the straight line of the rest of the product. The distribution of the selected units shows the complete elimination of the degrading units. Those having the expected increase in gain during life test have stabilized during the latter part of the test and are stable at the time of selection. It is felt important that the life testing period be sufficient to provide the data necessary to distinguish such a distribution and such a deviation from it.

Another means of evaluating life test results consists of assigning "defect" limits to the electrical parameters being measured for each

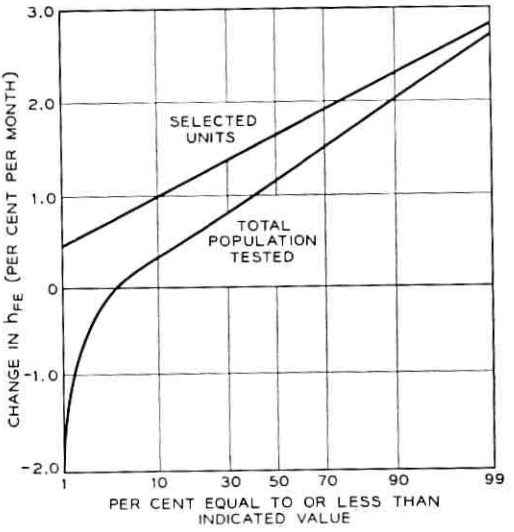

Fig. 3 — Distribution of h_{FE} degradation rate on life test, for total group life tested and for selected units.

transistor or diode type and noting the frequency of occurrence of units exceeding these limits. Such limits were defined for the major types on life test, and Fig. 4 shows the resulting plot of defect rates for a typical transistor and a typical diode. The defect rate, in defects per 10^9 component hours, is calculated for life test intervals and is plotted with time on test, on a log scale, showing the decreasing "failure" rate typically reported for semiconductor life tests. The shape and general position of the curves are also typical of most of the types on life test and show the marked gain which can be achieved in defect rate of the product through such a life test period.

It is also noted that the defect rate of about 1000 defects per 10^9 component hours for transistors, or 100 for diodes, at the selection time of about fifteen weeks is appreciably above the 10 failure units set as the maximum objective for Telstar satellite semiconductors. In order to estimate probable failure rate of Telstar components from the life test data, however, certain factors must be considered. A large factor is that the spacecraft components are selected as the most stable ones, whereas the life defects represent generally the least stable. Most of the defects occur by degradation of a measured parameter to the defect limit, this degradation being recognizable early in life. The certified units are those with no definite degrading trend and hence should not be subject to such

failures. The only indication of possible failures from among the selected units is the frequency of catastrophic life test defects, a measurable rate much below that of the total defect rate. Additionally, since most of such sudden changes occur in units showing some tendencies which would otherwise prevent their selection, the measurable estimate of improvement from total defect rate to estimated catastrophic failure rate of the selected units is considered quite conservative.

Many of the device types are used in several circuits, some of which have requirements for device parameter limits which are relatively severe compared to the majority of circuits using that type. The life defect limits correspond to the most severe requirements, and the calculated defect rate is therefore much greater than that which would be representative of the major portion of that product. The average failure rate is therefore additionally reduced by as much as a factor of ten for some types for this reason. The frequent testing is another factor which may have more bearing on some types than on others, but may always be present. Consideration of all these factors for each type, to the degree measurable, indicates conservative ratios of from 10 to 200 between life defect rates and estimated circuit failure rates.

Table VII shows a summary of the defect rates by device classes taken from such plots as in Fig. 4 for the time of shipment of Models 1 and 2 of the satellite and of Models 3 and 4. These data include over 90 per cent of the types, excepting those for which the numbers on life test were too small to develop meaningful statistics — among these being the germanium alloy types for power control use. Among all types, the lower defect rate for the second shipment time shows the effect of the decreas-

TABLE VII — LIFE TEST AND SELECTION RESULTS

	Number per Satellite	Defect Rate at Shipment Time, Defects per 10^9 Component Hours		Conservative Failure Rate in Satellite, Failures per 10^9 Component Hours	
		Models 1 & 2	Models 3 & 4	Models 1 & 2	Models 3 & 4
Diodes					
Microwave	14	4,500	3,000	45	30
Rectifier	83	30	20	3	2
Small signal	1,424	70	35	3.5	2
Transistors					
High frequency (Ge)	94	550	400	13	10
Amplifiers (Si)	1,011	4,000	3,000	30	20
Weighted average				14.2	9.3

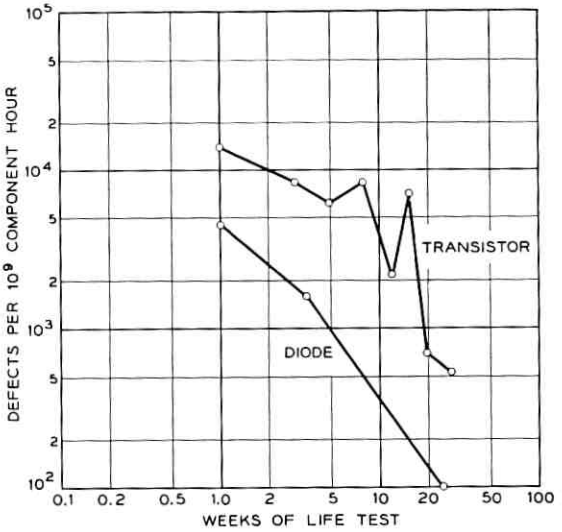

Fig. 4 — Defect rates through life test for typical transistor and diode.

ing defect rate as shown in Fig. 4. The relatively high defect rate of the silicon transistors for general amplifier use comes about largely through the contribution of one type which had a defect limit on collector reverse current, I_{CBO}, of 10^{-8} ampere, a much lower figure than that normally used for life test limits. Also shown for each class of product are the failure rate estimates for the selected devices, taking into account the factors mentioned above.

With these failure rate estimates weighted according to the number of each class of device used per satellite, an over-all average can be calculated, indicating about 14 failure units for the Telstar satellite semiconductors, with an expected improvement to 9 failure units for Models 3 and 4. Since these estimates are conservative, as indicated above, it is felt with considerable confidence that the screening and life testing program has resulted in devices meeting the initial objective of less than 10 failure units.

REFERENCES

1. McNally, J. O., Metson, G. H., Veazie, E. A., and Holmes, M. F., Electron Tubes for the Transatlantic Cable System, B.S.T.J., **36,** January, 1957, p. 163.
2. Gleichmann, T. F., Lince, A. H., Wooley, M. C., and Braga, F. J., Repeater Design for the North Atlantic Link, B.S.T.J., **36,** January, 1957, p. 69.
3. Ross, I. M., Reliability of Components for Communication Satellites, B.S.T.J., **41,** March, 1962, p. 635.

4. Dodson, G. A., and Howard, B. T., High Stress Aging to Failure of Semiconductor Devices, Proc. Seventh National Symposium on Reliability and Quality Control, Philadelphia, Pa., January, 1961.
5. Peck, D. S., The Uses of Semiconductor Life Distributions, *Semiconductor Reliability*, Vol. II, ed. W. Von Alven, Engineering Publishers, Elizabeth, New Jersey, 1962.
6. Peck, D. S., Blair, R. R., Brown, W. L., and Smits, F. M., Surface Effects of Radiation on Transistors, B.S.T.J., **42**, January, 1963, p. 95.

Nickel-Cadmium Cells for the Spacecraft Battery

By D. C. BOMBERGER and L. F. MOOSE

(Manuscript received January 31, 1963)

The storage battery for the Telstar satellite must undergo frequent charge-discharge cycles; in addition, it is subject to overcharge during a substantial portion of its life. Nickel-cadmium cells were chosen as best capable of satisfactory long-time operation under these conditions. A design and selection program was undertaken to ensure that Ni-Cd cores would meet objectives imposed by battery service conditions, and the cell enclosure was designed to minimize electrolyte leakage. Selection, qualification, and life tests indicated that a storage battery using the cell design would perform satisfactorily. To date, the only failures occurring during continuing life tests have been among cells subjected to 100 per cent discharge daily; this operation is far in excess of the expected duty cycle of satellite cells.

I. BATTERY DESIGN OBJECTIVES

Since the peak power required during the communications experiment exceeds that available from the solar cells, the storage battery will undergo many charge-discharge cycles (to depths of discharge as great as 40 per cent of capacity) during the lifetime of the satellite. On the other hand, several times each year the satellite is in continuous sunlight for long periods, during which the daily average solar cell power exceeds the average power used during visible passes. Thus the battery will receive overcharge current for a substantial fraction of its life.

Design objectives for the storage battery thus include high overcharge capability and long cycle life; additionally, high recharge efficiency is of importance in minimizing electrical losses, and a nonfailing hermetic seal is required to prevent the loss of electrolyte. The nickel-cadmium storage cell, in principle, can meet these objectives. It has a theoretical capability of long cycle life; also, if there is an excess of capacity in the negative electrode of the cell, no hydrogen will be evolved during normal overcharge, and the oxygen which does form will recombine at moderate

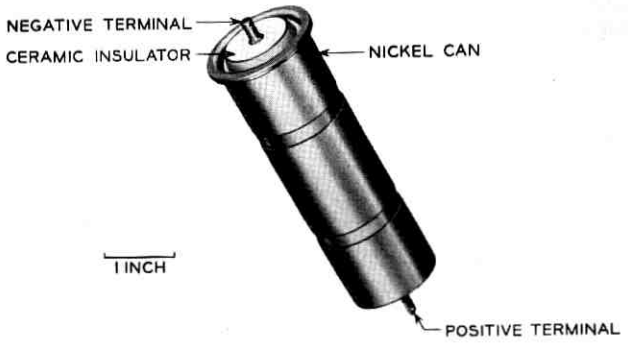

Fig. 1 — Nickel-cadmium cell for spacecraft battery.

ceramic and metal members was made by first metallizing the ceramic with a finely divided mixture of molybdenum and manganese sintered at 1525°C in a wet hydrogen atmosphere. The surfaces were then prepared for brazing by adding approximately 30 milligrams per square inch of electroplated nickel. A nickel-gold alloy requiring a brazing

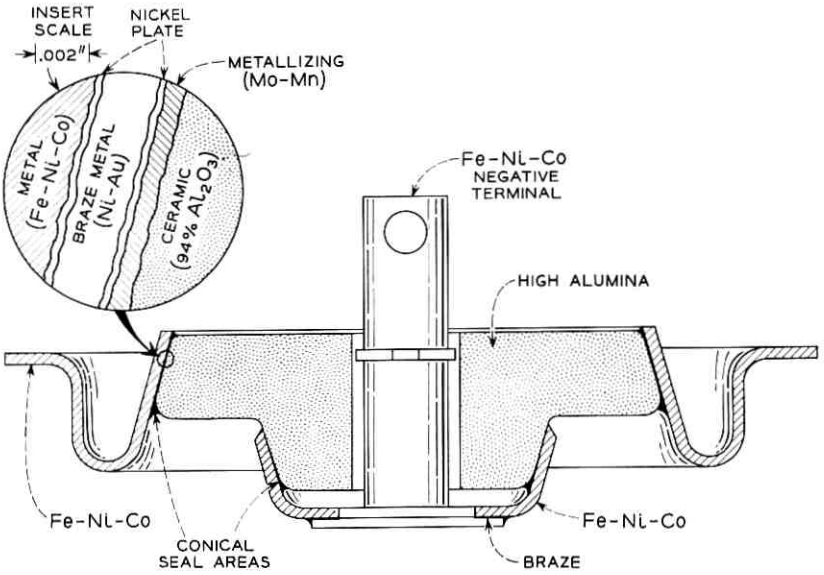

Fig. 2 — Details of ceramic seal.

temperature of approximately 1000°C was used to bond the metallized ceramic to the iron-nickel-cobalt alloy. An additional part later to serve as the negative terminal of the cell was attached to the smaller metal member at the time of the braze. The nickel-gold brazing alloy was chosen in order to avoid copper. Copper, common in other conventional brazing alloys, was considered to be an undesired electrolyte contaminant in cells designed for long life.

The remainder of the container consisted of a cylindrically drawn nickel shell having a flange at the open end with a cylindrical projection coined on the outer surface of the flange. The center of the closed end of the can was pierced to accommodate the tubulation. The tubing was attached to the can by means of a gold braze made in a resistance welder.

The sequence of assembly, as shown in Table II, was initiated by inserting the electrode assembly into the cylindrical can. Then the connector from the positive plate was spot welded to the can as shown in Fig. 3, and the negative connection from the assembly was spot welded to the center terminal of the insulator assembly. The insulator assembly was welded to the flange of the cylindrical can by a resistance weld, using the projection that had been previously formed. A resistance weld was chosen because it provided a positive means of attachment that could be accomplished with a minimum of deformation and with only local heating, thereby eliminating the use of temporary heat sinks and minimizing the chance of damage to the electrode assembly. This weld was performed using a 175-kva welder and a time setting of approximately 1/10 second. If more power had been available, a shorter time cycle would have

TABLE II—SEQUENCE OF ASSEMBLY

Preliminary assembly (a) Fabricate seal assembly (b) Fabricate can and tubulation assembly (c) Fabricate electrode assembly
Insert electrode assembly in can and tubulation assembly
Spot weld electrode connectors to terminals
Projection weld seal assembly to flange of can and tubulation assembly
Add electrolyte through tubulation
Seal tubulation and form positive terminal
Compress can to contact electrode assembly
Charge and selection test

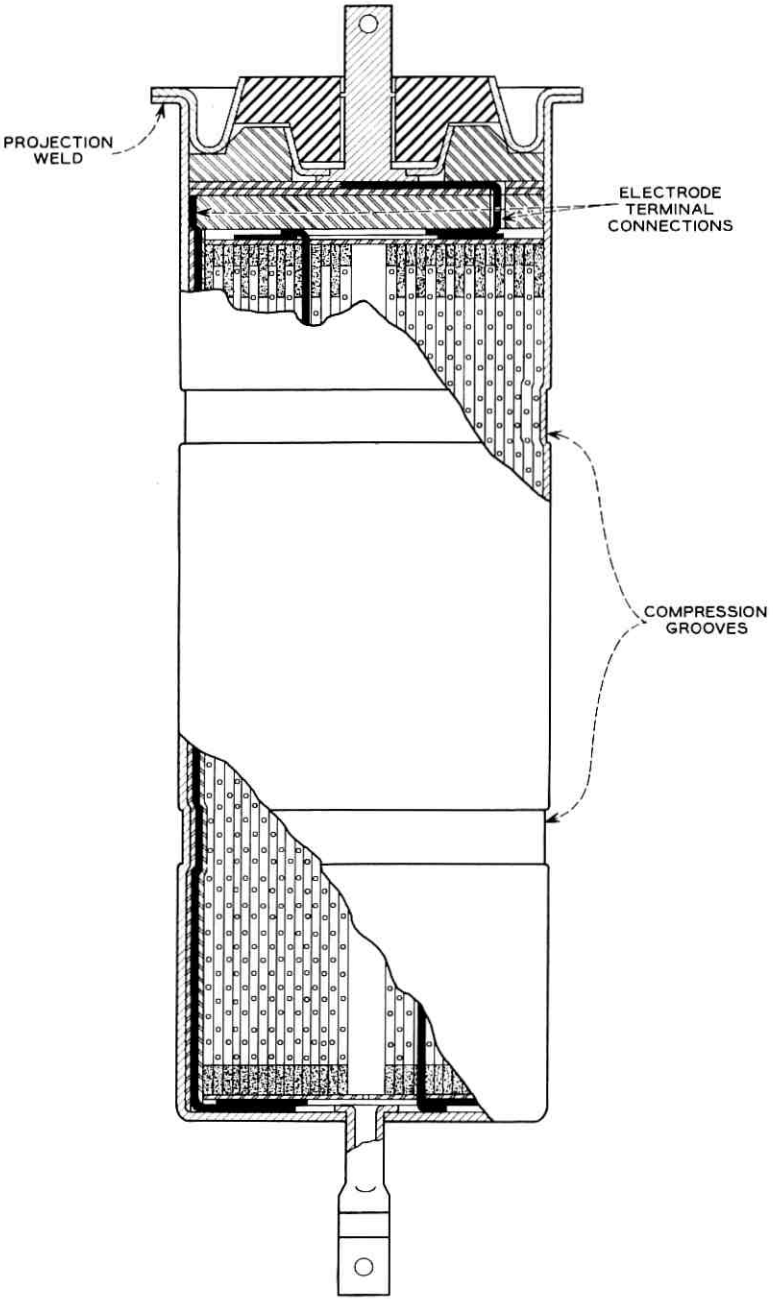

Fig. 3 — Section of completed cell.

been chosen. Cylindrical electrodes were mounted in a die set, and adequate pressure was used to prevent local expulsions.

Next, a carefully metered amount of electrolyte was inserted through the small diameter tubing using a needle type filler. The tubing had an integral gold-clad liner, which was wiped clean after application of electrolyte. Next, the tubing was squeezed flat and sealed by a resistance weld. Thus the final closure was accomplished. By shearing and drilling, the end of the tubulation was formed into a usable positive terminal. Radial compression was applied by a spinning operation to assure a snug fit of the core to the can. The snug fit was used to prevent core motion in the can during the vibration and acceleration of the launch period. Deformation resulting from the compression may be seen as two cylindrical grooves in Fig. 3.

The quality of all closure parts, of the welding operations, and the brazing operations, was evaluated by inspection of metallurgical sections made of sample assemblies. In addition, hydrostatic pressure tests were made to determine the strength of the welds. Each seal assembly and can and tubulation assembly was individually checked for leaks, using helium as a tracer gas and a mass spectrometer as a detector. Similarly, the complete assembly was checked for leaks before the electrolyte was added. The cells were finally sealed with a 50 per cent helium, 50 per cent oxygen atmosphere, with the expectation that tracer techniques could be used on the completed cell. However, after the electrolyte was added, the sensitivity of all types of tracer gas techniques proved to be erratic. It is hypothesized that this behavior is due either to a liquid or solid plug of the electrolyte, or to a compound containing electrolyte that prevented the flow of gas while selectively permitting a seepage of potassium hydroxide liquid. The most sensitive method for detecting leaks after seal-in proved to be the use of hydroxyl ion detectors on external surfaces adjacent to the seal. Tests on the completed container showed that no plastic deformation occurred for internal pressures below 500 pounds per square inch, and that rupture would occur only at appreciably higher pressures. In the event such pressures were generated, no provision was made to prevent destructive rupture.

In life tests of batteries similar to those installed in the satellite, evidence of leakage has been found on some cells. In all cases this leakage appeared to take place in the vicinity of the ceramic-to-metal seal. The design of this seal took into account actual rates of chemical reaction of alkali solutions with the materials used and, while corrosion was expected, the seals were designed so that failure was not anticipated in a two-year interval. Examination of sectional microphotographs of leaking

seals indicated that more rapid attack had taken place in this area than had been anticipated. It was observed that the thickness of the brazing material used in the ceramic-to-metal seal varied from the desired thickness of 2–3 mils to less than 1 mil and to greater than 6 mils. In addition, void areas were found where brazing material was present at both surfaces of the leaking seals. In some instances blisters were discovered between the metallizing and the plating. Leakage observed may have been due to a combination of the expected corrosion of the interface material coupled with fast creepage of electrolyte in void areas internal to the seal. As the voids appreciably reduced the seal length susceptible to corrosion, the time to failure was shorter than anticipated. The completed metal ceramic seals cannot be inspected for continuity of internal interfaces; hence, prevention of internal defects must be established by tolerance control and process inspection.

Experience indicated that when leaks did occur they were small. The dimensions of the material subject to attack were limited by the small circular area of the metal-ceramic interface adjacent to the void, and they were further diminished by the plugs of electrolyte. In most cases the appearance of a carbonate which forms when potassium hydroxide reacts with carbon dioxide in air has been so slight that leaks could not be detected by visual examination even though pH tests of the surface showed the presence of potassium hydroxide. Since the plugging effects observed in the leak-detection experience appeared to limit the flow of gases, it is believed that little gas has been lost from the leaking cells.

V. SELECTION TESTS

The following tests were performed on each completed cell, in the order shown:

(*i*) Capacity test — At an ambient temperature of 77°F, the cells were charged at 0.6 ampere for a period of 16 hours, then discharged at about the one-ampere rate. This cycle was repeated a minimum of 8 times. The end-of-charge voltage, cell temperature, and cell capacity were measured.

(*ii*) Continuous overcharge test — At an ambient temperature of 77°F the discharged cells were charged for a period of 64 hours at 0.6 ampere. The end-of-charge voltage and cell temperature were measured. The cells were then discharged and capacity was determined.

(*iii*) Self-discharge test — At an ambient temperature of 77°F the cells were again charged at 0.6 ampere for 16 hours. At the end of this period the cells were placed on open circuit for a period of 48 hours.

The cell voltage was measured continuously and the cell capacity determined by a discharge at the one-ampere rate.

(*iv*) Internal resistance test — At an ambient temperature of 77°F the cells were again charged at 0.6 ampere for 16 hours. Following this charge the cells were discharged at the one-ampere rate for 2 hours, after which a 2-ampere, 3-second pulse discharge was performed. The cell voltage was monitored on an oscilloscope to observe the instantaneous voltage change.

(*v*) Capacity test — Test (*i*) was repeated for two cycles at an ambient temperature of 30°F.

(*vi*) Vibration test — The cells were vibrated in the axial direction as shown in Table III. Total time for this test was 4.3 minutes.

(*vii*) Capacity test — Test (*i*) was repeated for 4 cycles at an ambient temperature of 77°F.

(*viii*) Leak test — All cells were tested for leakage using pH indicator paper, which was moistened with distilled water and rubbed over seal and weld.

(*ix*) Selection — For each test, distribution curves were plotted of the test variable (i.e., end-of-charge voltage, capacity, etc.) versus the number of cells. Only those cells which fell into a tight grouping around the variable mean were selected for satellite use.

VI. QUALIFICATION TESTS

A small sample of cells which passed the selection tests was given the following qualification tests, and then retested electrically:

(*i*) Vibration tests — Selected cells were subjected to 40g vibration in two planes between 5 and 2000 cps for 1.5 hours.

(*ii*) Acceleration tests — After vibration tests, the cells were subjected to 30-g acceleration in two planes for $\frac{1}{2}$ hour.

VII. CELL CHARACTERISTICS

Of 513 nickel-cadmium cells constructed and tested as described above, only two were found to be defective. One of these had an ob-

TABLE III

Frequency Range, cps	Test Duration, Seconds	Acceleration, g, 0 to Peak
7–25	30	1.5
25–60	40	14.0
60–2000	75	7.0
550–650	30	14.0

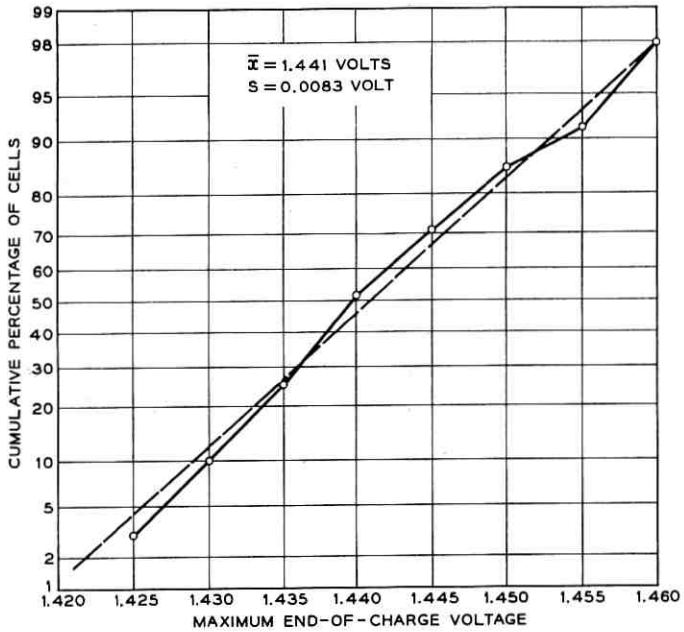

Fig. 4 — End-of-charge voltage distribution, 200 nickel-cadmium cells. Temperature 77°F, 0.6-ampere charge current.

viously cracked seal which caused a leak. The second developed a short circuit during the selection tests, and was considered to be the sole operational failure during selection testing. Only the 391 cells produced in the later stage of seal development were considered suitable for satellite batteries. The first 122 had seals of an earlier design which was considered to be less satisfactory.

Electrically, all cells (except the two noted above) showed adequate uniformity in the important measured quantities. The distribution charts showed normal distribution with satisfactory central values, which changed only slightly from test to test of the selection sequence. An example of a cumulative distribution chart for end-of-charge voltage of 200 cells is shown in Fig. 4. The ordinate scale on this figure is one for which a normal distribution plots a straight line.

A summary of the results of the electrical measurements of all cells at 77°F ambient temperature is as follows:

Capacity	6.2 ± 0.7 ampere hours
End-of-charge voltage at 0.6 ampere	1.45 ± 0.025 volts

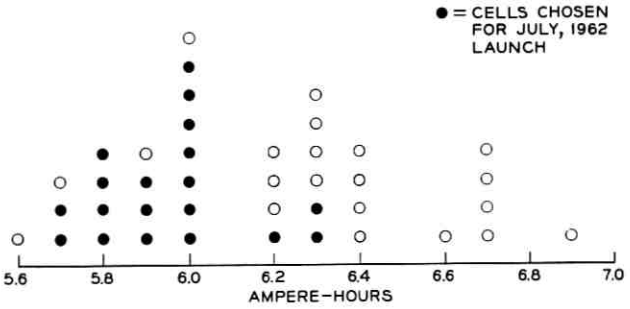

Fig. 5 — Capacity distribution, 40 nickel-cadmium cells.

Capacity loss on open circuit	0.8 ± 0.2 ampere hours (48 hours)
Internal resistance	28.0 ± 4.0 milliohms

Fig. 5 shows a typical chart of capacity measurements for the 40 cells from which the Telstar spacecraft battery was selected. The cells chosen for use were those whose capacities had the tightest grouping around a central value, while also showing reasonably tight grouping around central values of the other electrical quantities measured.

Fig. 6 presents what are commonly known as Tafel curves, for typical cells. These show the end-of-charge voltage as a function of overcharge current at various temperatures between −15°F and 120°F. The curve for 0°F has been extended to show the typical rapid rise of cell voltage which occurs when the overcharge current exceeds the safe value for the temperature at which the cell is operating. The limit to overcharge current is shown, for other temperatures, by the upper ends of the curves. Even at a temperature as low as 30°F the cells can accept the full output current of the solar cell power plant, although they never receive this full amount, nor are they expected to operate at this low temperature.

Ampere-hour charge efficiency of the cells is of general interest for two kinds of operation: (a) charging a completely discharged cell and (b) replacing a partial discharge removed from a fully charged cell. However, only the second of these operations is of importance to spacecraft operation, since the satellite's battery normally is only partially discharged. Representative data from significant efficiency measurements are presented in Table IV.

These data are believed to be descriptive of spacecraft battery performance. The sequence of measurement operations for each test was as follows:

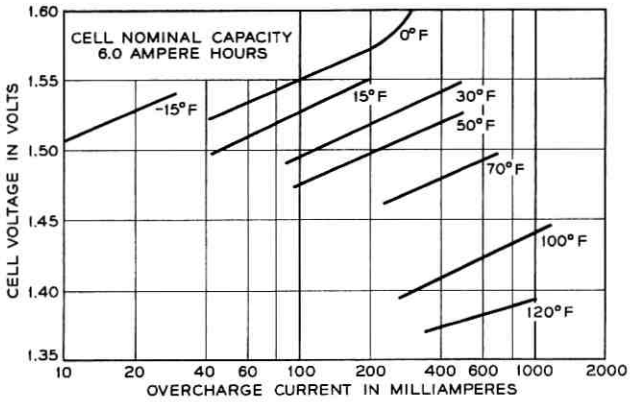

Fig. 6 — Nickel-cadmium cell Tafel characteristics.

(a) Charge, then discharge, all cells to measure normal capacity
(b) Charge all cells fully
(c) Discharge all cells at 1 ampere for 2.5 hours
(d) Recharge all cells at 0.200 ampere for time indicated
(e) Repeat (c), (d) nine times
(f) Discharge all cells to measure remaining capacity.

The above procedure divided capacity-measurement uncertainties among ten charge-discharge cycles, and resulted in efficiency data which had a spread of only a few per cent among all cells measured. Further, the procedure simulated (except for a difference in the time scale) a 2.5-ampere-hour discharge occurring during several successive orbits, followed by recharge during subsequent nonvisible orbits, at about the spacecraft's normal charge current.

The high efficiency noted in the 12-hour charge is actually an incremental efficiency; at the end of this charge-discharge sequence the battery was no longer fully charged. The lower efficiencies of the other tests reflect extra ampere-hours required to recharge the battery more

TABLE IV — AMPERE-HOUR CHARGE EFFICIENCY (REPLACING A PARTIAL DISCHARGE)

Test No.	Temp. °F	Charge, Amperes	Charge Time, Hours	Average Charge Efficiency
1	60	0.200	12	97%
2	60	0.200	14	88%
3	60	0.200	15	82%
4	60	0.200	16	77%

nearly completely. Full charge was obtained only after about 14 hours of recharge time. For this reason, a charge efficiency of 85 per cent is a conservative value to use in calculating the charge-discharge balance of the battery.

VIII. LIFE TESTS

At the time of launch of the Telstar satellite, many thousands of cell-hours of operation had been accumulated as a result of both selection tests of many cells and many experimental studies with a limited number of cells. However, the failure mechanisms of the spacecraft sealed nickel-cadmium cells are not yet known, so that significant life estimates will require data from operation over extended periods of time. Such data will be obtained from several batteries on life test.

One battery of 20 cells was placed on a simulated orbital cycle at room temperature in November, 1961. The cells of this battery had early seals, not used for satellites, but otherwise they were identical with those used for all models of the satellite, including that in orbit. This battery receives approximately 9 charge-discharge cycles per day, as shown in the load profile of Fig. 7. The three deep discharges represent use of the communications equipment during eclipse; the five shallow discharges represent subsequent eclipses when the beacon and telemetry constitute the loads on the power system.

A second battery of 22 cells with later, improved, seals was placed

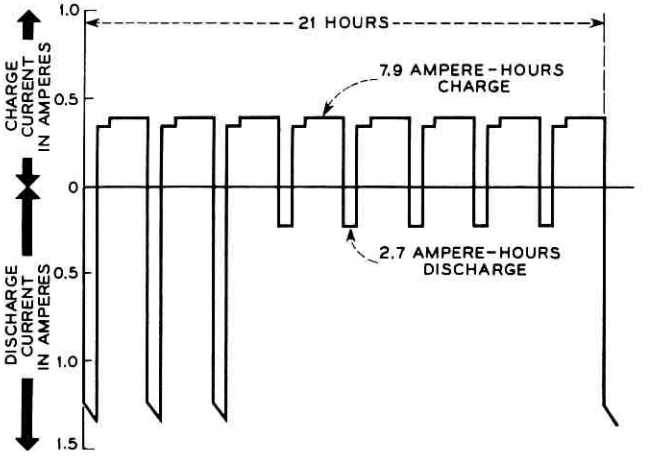

Fig. 7 — Load profile — simulated orbital cycle.

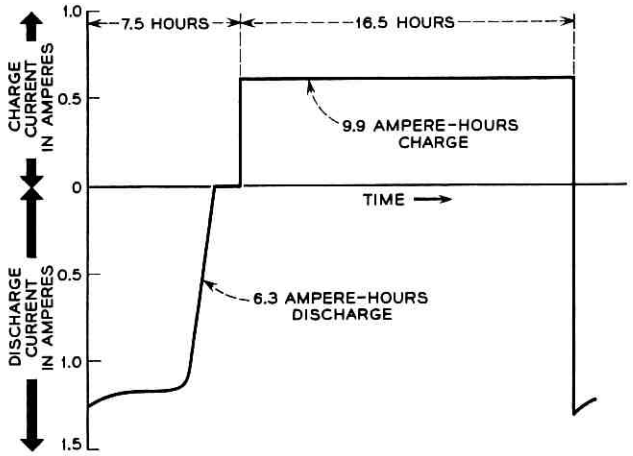

Fig. 8 — Load profile — accelerated life cycle.

on cycle test in April, 1962. This battery receives daily a complete discharge followed by a substantial overcharge, as shown in Fig. 8. This cycle was intended to provide an accelerated life test, and is identical to those of the selection tests; cells of this battery had received 22 selection-test cycles before being placed on life test.

During June, 1962, the battery on the simulated orbital cycle was removed from cycle test for measurements to answer questions raised during the spacecraft tests. Before being returned to the life test cycle all cells were examined for leaks, as had been done periodically since the life test was initiated. An indication of leakage of potassium hydroxide was found around the seals of 5 of the cells. Similar leak tests were made on the cells of the battery on accelerated life test, and two indications of leakage were found. These circumstances are summarized in Table V.

Both batteries were given several deep discharge cycles, after which several other indications of leak were found in cells on orbital life cycle,

TABLE V—JUNE, 1962, RESULTS

20 Cells, Orbital Life cycle		22 Cells, Accelerated Life Cycle
217	Test days	43
1753	Cycles	65
5	No. cells with indication of leak	2

TABLE VI

Group No.	Depth of Discharge	Charge Time, Hours	Discharge Time, Hours*
1	100%	16.5	7.5
2	75%	12	4
3	25%	4	1.5
4	Continuous overcharge at 0.6 ampere		

* Discharge through 1-ohm resistor.

and one other in a cell on the accelerated life cycle. Capacity measurements made during these discharges showed no loss of capacity from that measured on the cells during selection tests.

After the finding of indications of leakage in June, the battery on accelerated life cycle was divided into 4 cell groups, to determine, if possible, the effects of different modes of operation. These 4 groups were operated as shown by Table VI.

New cells previously subjected only to the selection test cycling were added to these groups as shown in Table VII.

In October, 1962, all the above cells were discharged to measure capacity. All yielded the capacity measured during their selection tests. The original cells had 6 months of operation, the new ones four months, all in addition to the selection tests. Eight of the original cells gave a positive indication to leak test, as did seven of the new cells. These seven were distributed among the four groups with no clear correlation between mode of operation and tendency to leak.

Most of the leaks discussed above have not resulted in visual evidence of the effect of potassium hydroxide reaching the open air. Thus the loss of electrolyte by these cells is quite small, although it is enough to cause a blue coloration of the indicator paper used in the leak test. As discussed in connection with the cell enclosure, it is believed that loss of evolved gas is also small.

In December, 1962, after more than one year of operation, all cells on

TABLE VII

Group No.	Depth of Discharge	Original Cells	New Cells	Total
1	100%	5	7	12
2	75%	5	5	10
3	25%	5	5	10
4	Continuous overcharge, 0.6 ampere	5	8	13

simulated orbital cycle, with their early seals, showed indications of leak. Less than half of the cells with later seals showed indications of leak. However, three of the cells in group 1 (Table VI) were found to have distorted seal assemblies, indicating that internal pressure had built up to dangerously high levels. End-of-charge voltages on these, as well as on several nondistorted cells of group 1, had risen to 1.5 volts. It has been determined that these cell failures were coincident with the evolution of hydrogen gas, although the cause of this evolution is not yet known.

Thus the first cell failures have occurred on the accelerated life cycle (100 per cent discharge daily). All cycle tests are being continued, and it is anticipated that useful data on both length of life and mechanism of failure will eventually be acquired. As yet, however, there are no significant data on which to estimate cell life in a satellite environment. Telemetry data from the satellite continued to show normal battery performance through January, 1963.

The Satellite Traveling-Wave Tube

By M. G. BODMER, J. P. LAICO, E. G. OLSEN and A. T. ROSS

(Manuscript received March 5, 1963)

The traveling-wave tube amplifier described provides a minimum output power of 3.5 watts at 4.0 to 4.2 gc. Design aspects that lead to lifetimes in excess of 10 years and to tube efficiencies between 35 to 40 per cent are discussed. The tube is focused by an improved version of the single-reversal magnetic circuit. Performance data pertinent to this particular satellite operation are shown. Highlights from the final production run and the subsequent life test serve to illustrate the care with which this TWT has been built.

I. INTRODUCTION

The output power amplifier in the Telstar spacecraft microwave repeater operates near 4 gc; the amplifier is required to accept a fractional milliwatt signal distributed over approximately 100 megacycles bandwidth and amplify it some 4000 times to provide an output of several watts. In the satellite, this power amplifier is the major power utilizing device, and its efficiency is controlling in the design of the satellite and of the system. Of the possible microwave devices which might be considered, the traveling-wave tube is outstandingly well suited to the application. The broad bandwidth and high gain is such that only a single tube is necessary. The efficiency is as high as or higher than that of competitive devices, and a considerable history exists to suggest that very long life and high reliability can be achieved.

This paper describes the development of the M4041 traveling-wave tube for this application. The design methods for traveling-wave tubes for radio relay applications are well known and can be found in such texts as Ref. 1; therefore, discussion will be limited to those aspects which are peculiar to this application. Since reliability is the most important aspect in the Telstar experiment, considerable attention will be paid to this aspect of the design. The development of the tube was carried on in five phases. Initially, there was a design phase in which close interaction with the systems area produced a final amplifier specification

which was compatible with other parts of the system. This was followed by a qualification period, during which development models of the tube were subjected to extensive electrical and mechanical tests at levels in excess of the environment anticipated in the application. Next, a group of tubes was fabricated under the best available clean-room conditions, which included extensive engineering checks on the details of the fabrication. These tubes were tested and placed on aging racks at the established nominal operating conditions. Finally, from this group of tubes, those showing the most uniform and stable characteristics were selected and married to their final power supplies for incorporation into actual satellites. Each of these phases will be discussed in the text.

In considering the design and qualification phases of the development, it must be remembered that this amplifier is a relatively complex package, and it is therefore not possible to fabricate a sufficient number of models to permit extensive use of statistical methods and stress aging. It was therefore necessary to place great emphasis on design integrity: that is, upon the use of techniques which had been established as reliable in previous devices. While nearly every one of the electron tubes which have been developed by the Laboratories has contributed in some way to our knowledge, three developments are peculiarly related to the Telstar spacecraft application. The earliest of these was the development of the 175HQ, the pentode used in the present submarine cable repeaters. During this development, a large number of controlled laboratory experiments were carried out, some extending to 100,000 hours of real-time testing. These tests have given us a great deal of information concerning the effect of impurities and processing on cathode life. It was during the development of this tube that many of the techniques of building superclean tubes for applications requiring high reliability were developed. In particular, the concepts of aging and selection to avoid manufacturing freaks appeared. There are currently 1608 such tubes in underwater applications, and these have accumulated over 60,000,000 tube hours of operation without failure. The second development which is of specific interest is that of the M1789 traveling-wave tube. This is a 5-watt amplifier developed for a 6-gc transcontinental radio relay. This tube is currently in production, and field experience has given us a great deal of information concerning failure mechanisms in traveling-wave amplifiers. Towards the end of the development, a group of final design tubes were fabricated, under what were then considered clean conditions; and from these, 12 tubes were selected on the basis of cathode activity for a life experiment. After some six years of operation, 11 of these tubes are still operating satisfactorily. (The twelfth tube was accidentally lost during

a modification of the laboratory building.) This experiment suggests that our selection techniques can be successfully applied to a traveling-wave amplifier. These tube developments show that it is possible to develop tubes with extremely long life and with high reliability. The third development relates to the rigors of the launch environment. The M1958 traveling-wave amplifier is a 9-gc tube developed for a missile guidance system. In this system, the tube is mounted in the missile-borne equipment and must not only survive, but also operate satisfactorily, during the shock and vibration of the launch. In more than 100 launches, no failures of this device have been observed. In the design of the M4041 traveling-wave tube, the techniques developed for these previous devices have been employed wherever possible. Where the specialized application required new design approaches, these have been extensively qualified during this development.

II. SYSTEM REQUIREMENTS

Table I lists the final requirements placed upon the performance of the M4041 traveling-wave amplifier. The table lists not only specific maximum or minimum values for parameters, but also indicates other design constraints necessary to the application.

III. TUBE DESIGN PARAMETERS

Previous experience has established the practical range of a number of tube parameters. From this experience in using conventional traveling-wave tube analysis, a three-dimensional set of tube designs was computed using the following three parameter ranges:

$$\gamma a = 1.0\text{–}1.6$$

$$V_{helix} = 1000\text{–}2500 \text{ v}$$

$$I_0 = 5.0\text{–}20 \text{ ma.}$$

In these designs, a number of restrictions were imposed, based on past experience and on engineering judgment. These restrictions are listed in Table II and will be discussed in detail in subsequent sections. From this field of designs, a final set of parameters was chosen as the optimum, and this is summarized in Table III, where γ = radial propagation constant; a = helix radius; $K = 2\pi/\lambda_0$ and λ_0 = free-space wavelength; C = gain parameter from Pierce; and QC = space charge parameter from Pierce.

TABLE I — SYSTEM REQUIREMENTS FOR M4041 TWT

Life (average before failure)	In excess of 10 years
Operating frequency band Beacon at 4.08 gc Signal at 4.17 gc ± 25 mc	4.0–4.2 gc
Output power (saturated)	P_0 = 3.5 w minimum
Input drive available	P_{in} = 0 dbm maximum
Total dc power available	P_{dc} = 16 w

Weight of TWT
To be minimized along with its associated equipment — like the solar plant with its support structure, storage batteries, power supply, etc.

Hot matches at optimized V_{helix} and I_0
Input better than 18-db return loss in band (VSWR = 1.3)
Output better than 10-db return loss in band (VSWR = 1.9)
Output better than 5-db return loss over a 20% band (VSWR = 3.5)

Short circuit stability with V_{helix} reduced 75 volts from operating point*

Tube must operate with all voltages ±3% from set nominal value (because of long time drift in regulated 16-v supply)

Noise figure better than 30 db

AM to PM conversion less than 12°/db

Cooling of collector by conduction to housing and through waveguide to remainder of electronics canister

Completed package to withstand environmental conditions during launch, in orbit, and eclipse

Vibration — tube inoperative; 15-50-15 cps, 0.3-inch displacement 50-2000-50 cps at 20 g in all 3 directions at a sweep rate of one octave per minute

Thermal cycling ±15°F to 90°F to 15°F.

* The operating point for best efficiency was chosen at helix overvoltage ($\Delta V_{helix} \approx 150$ volts) where amplifier gain is considerably reduced from the low-level synchronous condition. Reducing the helix voltage from the operating point automatically increases the over-all gain and reduces short circuit stability.

TABLE II — DESIGN PARAMETERS FOR M4041 TWT

Cathode current density	<85 ma/cm²
Beam area convergence	<25
Beam perveance	<0.3 microperv
Voltages	<2000 volts
Magnetic flux density	<550 gauss
Saturated output power at output flange	>3.5 watts
Computed depressed efficiency (not including heater)	>35%
Intercept currents	<1%

TABLE III — SUMMARY OF M4041 DESIGN

Helix Dimensions

Mean diameter	90 mils
Wire diameter	10 mils
Turns per inch	49
Pitch	20.4 mils
Active length	5.75 inches

Voltages and Currents

	Voltage	Current
At 4.0 watts output cathode	0	17.4 ma
Beam forming electrode	0	0
Accelerator	1800	<0.1 ma
Helix (overvoltage)	1550	<0.15 ma
Collector	750	>17.15 ma
Heater power		1.4 watts (730°C true at cathode)

TWT Parameters at Midband (4.1 gc)

$\gamma a = 1.33$
$Ka = 0.098$
$C = 0.063$
$QC = 0.25$
N (number of λ's on helix) 26
Dielectric loading factor 0.86
Impedance reduction factor 0.4

Electron gun:

Gun type — converging Pierce gun
Cathode type — high purity nickel with 0.1% zirconium; base coating low-density double carbonate
Cathode current density 85 ma/cm² (I_k = 17.4 ma)
Cathode diameter 0.192 inch
Convergence half-angle 12° 45′
Cathode radius of curvature ($\bar{r}_c$) 0.435 inch
Anode radius of curvature ($\bar{r}_a$) 0.176 inch
$\bar{r}_c/\bar{r}_a = 2.48$.

IV. DESIGN OF THE TRAVELING-WAVE TUBE

From the foregoing specification, it is apparent that the M4041 is, as might be expected from the reliability required in the application, a conservative design. On the other hand, if the goals in life and efficiency are met, the tube will represent the state-of-the-art in these parameters.

Fig. 1 shows a photograph of the completed traveling-wave tube amplifier. The functional parts — the TWT, the magnets with their respective pole-pieces, and the RF couplers — are displayed in their relative positions. The magnetic design used is a single-reversal circuit. It consists basically of two cylindrical magnets charged with the same polarity at the center plane and separated by a septum, the field reversal pole-piece. The tube is held in alignment with the magnets through

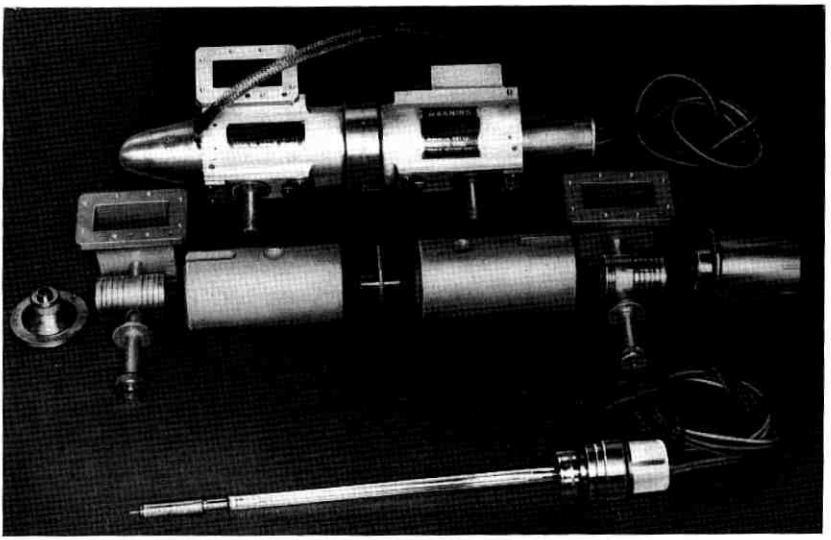

Fig. 1 — Packaged TWT amplifier with a layout of its major functional components.

reference surfaces in both gun and collector pole-pieces. RF connections to the TWT are established by externally tuned reentrant coaxial couplers which, in turn, are matched to the rectangular waveguide.

In this section, the tube is broken down into its individual parts of gun, helix, collector, envelope and focusing circuit, and each part with its major design parameters is discussed separately.

4.1 *The Gun*

The basic Pierce-type gun is characterized by three major parameters: perveance, convergence, and cathode current density. To maintain the concept of "proven integrity," these parameters were limited to the corresponding values of the 6-gc radio relay tube, our main source of life test data. The limiting values are 0.3 microperv for perveance and 25 for the area convergence. The choice of the cathode current density limit warrants a separate discussion which follows this paragraph.

Life tests on 12 M1789, 5-watt TWT's, developed for a 6-gc radio relay, had in 1960 exceeded without failure an individual accumulated life of 35,000 hours at a cathode current density of 210 ma/cm^2. Analyses of the life test data compiled over the past six years showed a slow, but steady, increase in accelerator and helix interception with constant cathode current in the majority of the 12 M1789 TWT's on life test, by a

factor of as much as five. This has been interpreted as a small degradation of the beam profile within the gun, caused by small areas of lowered activity on the cathode. Their effect is an increase of the transverse velocities of the electrons, producing crossovers and consequently an increase of the final beam diameter. This type of beam degradation is aggravated by increasing the area convergence and perveance to higher values. Either increase results in a gun which is inherently less stable and more sensitive to aberration in the beam formation.

The cathode current density chosen has a first-order effect on the life capability of the TWT. From our past life tests on TWT's, we have observed that the average life is highly dependent on the actual cathode temperature; a decrease of 25°C will, in general, double the life of the cathode. Similar data have been obtained with microwave triodes, using a considerably larger universe for testing. The cathode temperature, in turn, is dependent on cathode current density and the work function of the coating. In Fig. 2, these relations are approximated by a line of constant slope; a lower work function moves the line to the right, a higher work function to the left. We cannot measure the work function in completed tubes, but we have a point which represents our tube art of several years ago. In our final life test, all M1789 TWT's had exceeded 35,000 hours in 1960. This point is plotted at the proper cathode current density in Fig. 2 and a line with the proper constant slope drawn through it. This curve was used as our design basis and is quite conservative, since not all tubes will fail at one time. For a ten-year life, the current density should be less than 85 ma/cm^2. Since that time, most of these same tubes have passed 50,000 hours (however, one envelope broke due to an interruption of the cooling air). The graph has been revised accordingly (1962). It must be pointed out that our area of experience is limited and that, in the interest of conservatism, the extrapolations indicated by the dashed part of the line should be used with caution at the present time.

In choosing the cathode base material for the M4041, a number of factors must be considered. Most important in this application are questions of rate of activation, sublimation and coating adherence. Of the 12 M1789 TWT's in the life test mentioned earlier, several exhibited internal arcing, usually between 5000 and 20,000 hours of operating life. This arcing is attributed to a build-up of a conducting film on the electrode insulators. The film is believed to be due in part to sublimation of the additive from the base nickel of the cathode. This problem is distinct from those encountered in gridded tubes like the submarine cable pentode, just as interface resistance does not influence the choice in this case. Several alloys were considered for the cathode base. The final choice was a pure nickel with a single 0.1 per cent Zr additive. It is produced

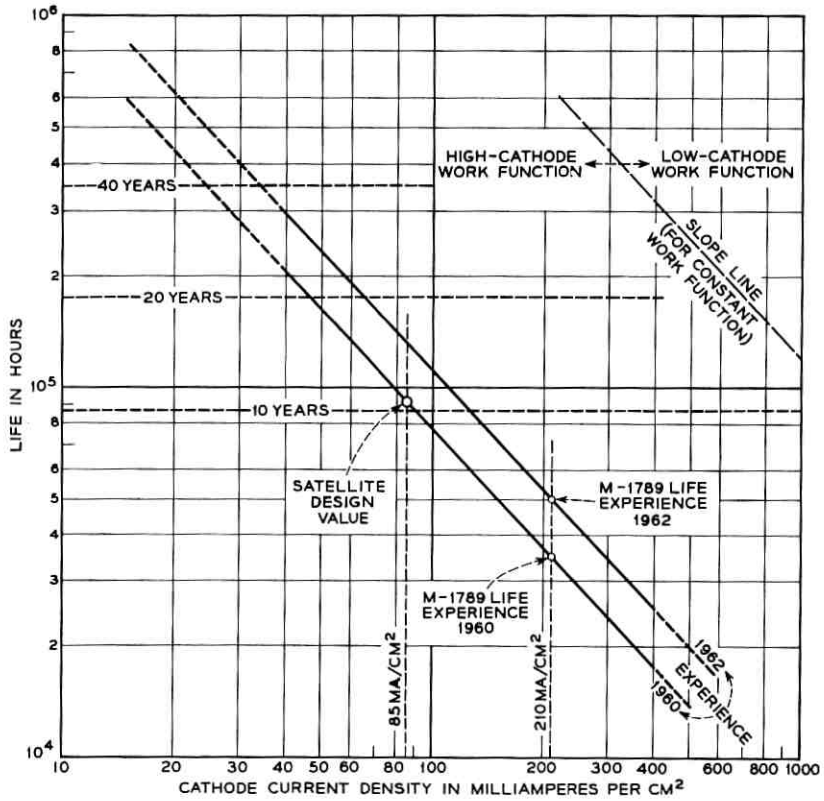

Fig. 2 — Average life expectancy vs cathode current density.

in this Laboratory[2] under conditions in which impurities, particularly carbon, are held to less than 0.005 per cent. The Zr additive as a reducing agent has the advantage of producing little or no sublimation. In addition, the production of donors is not limited by the diffusion of the reducing agent, but by the chemical reaction rate of the coating. The thickness of the alloy was chosen as 0.040 inch, which should give at 730°C a 100 per cent depletion of the coating with an 89 per cent depletion of the Zr after 19 years,[3] as shown in Fig. 3. This represents a safety margin of nine years over the expected tube life, a needed guarantee, since a tube will fail long before complete exhaustion of the cathode coating. As the coating becomes thin, the emission becomes nonuniform and the beam transmission is impaired. This results in excessive heating of the helix and subsequent further deactivation of the cathode through

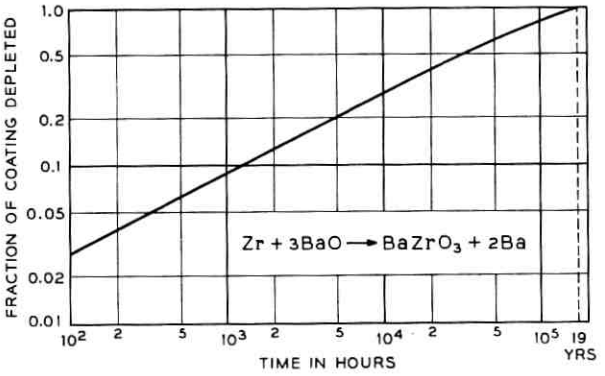

Fig. 3 — Calculated depletion of oxide coating on 0.1 per cent Zr-nickel base. Calculations are based on the following numbers, corresponding to values for M4041 tube:

thickness of nickel base	0.040 inch
thickness of coating	0.0015 inch
density of coating	1.1 gm/cm³
cathode temperature	730°C, true.

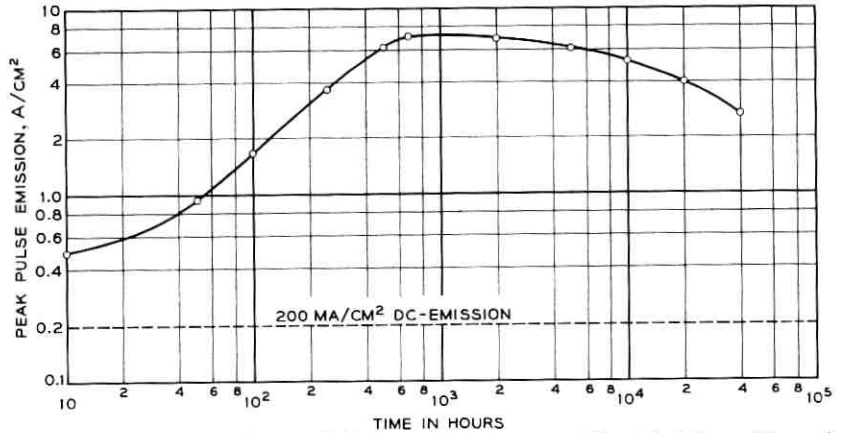

Fig. 4 — Life tests of control diodes with 0.1 per cent Zr-nickel base. Normal operating condition 200 ma/cm² dc, cathode temperature 740°C true. Activity measured by superimposing pulse directly over dc.

the released gases. It is predicted that uniform emission will be maintained at least to the design figure of ten years. This estimate is supported by tests with diodes constructed with this alloy, which have been operating close to six years without noticeable decreases in emission. Fig. 4 gives the average peak pulse emission versus elapsed time which has been

obtained in diode testers with this alloy in recent tests.[2] Beyond choosing a low sublimation rate base nickel, a maximum voltage limit of 2000 volts per electrode was imposed and all possible leakage paths were lengthened and shielded. These steps were taken because some of the leakage may be due to the deposition of barium from the coating.

The emitter is physically in the form of a button, machined precisely to shape. The surface on which the cathode coating is to be applied is liquid-honed with calcium oxide powder to provide a roughened area to facilitate adherence. Calcium oxide is used because it is chemically compatible with the cathode coating materials, should any particles be embedded. A combined coating of barium and strontium carbonates is machine sprayed on the roughened surface. The density of the coating is held to 1.10 ± 0.1 gm/cm^3, equivalent to a thickness of 1.5 ± 0.10 mils.

Structurally, the gun is designed in two sections, as shown in Fig. 5. One section, which might be considered a chassis, consists of two molybdenum focusing electrodes — the beam-forming electrode and the accelerating electrode — plus the molybdenum cathode-support sleeve, all of which are concentrically aligned and supported from a cupped molybdenum base. Support for the focusing electrodes from the base is obtained by glazing to three Alsimag 475 (zircon body) ceramic tubes,

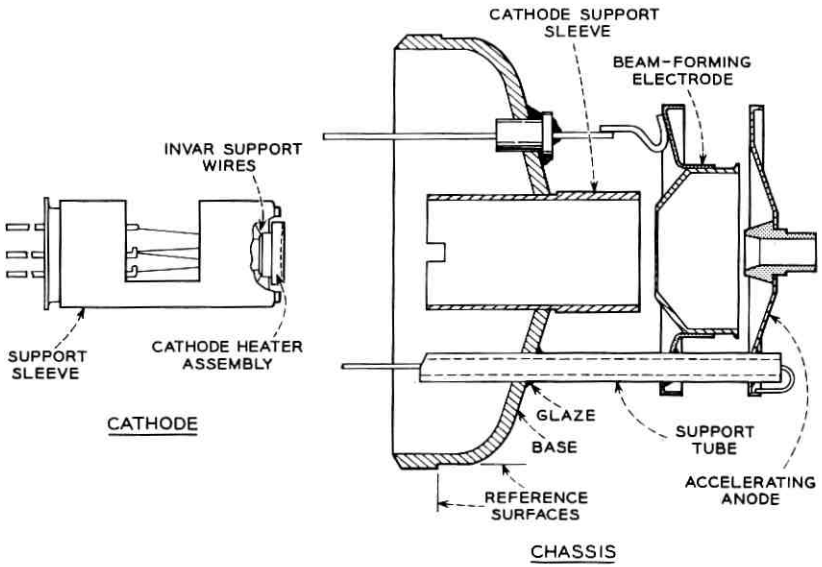

Fig. 5 — Gun assembly.

which also serve to insulate these electrodes. The cathode support sleeve is brazed concentric to the reference surface machined on the base. Tolerances in tenths of mils are readily held in concentricity, squareness and axial dimensions (see Fig. 5). These materials have compatible thermal expansions, are structurally stable, and are capable of withstanding thermal shock, rigorous cleaning, high-temperature outgassing, and vigorous vibrating.

The inner section consists of a cathode and heater mounted in a sleeve. The sleeve serves a double purpose. Its inside diameter encloses and supports the cathode heater assembly by means of fine Invar wires, while its outside diameter is machined to slide snugly, by selection, within the cathode support sleeve of the chassis.

The heater is one of the principal power consuming elements of the tube. It is therefore important to minimize this power, or else the over-all efficiency will be degraded. By virtue of the unique design,* in which the cathode is suspended by fine wires, and a minimized radiating area of the cathode body, a power of 1.4 watts is sufficient to heat the 0.192-inch diameter emitting surface of the cathode to an operating temperature of 730°C.

4.2 *The Helix*

The interaction efficiency of the TWT depends to a large degree on the helix itself, even if the beam parameters are optimized. In early prototypes, the depressed collector efficiency averaged around 27 to 30 per cent. In the final series of tubes, this value had climbed to 36–40 per cent. The only changes made were: the reduction of the cold loss, the increase of the dielectric loading factor and, finally, the optimization of the shape and length of the sprayed loss pattern. The cold loss of the 6-inch helix averaged 4.2 db; this value was reduced to 2.7 db with careful copper plating of the helix and subsequent sintering.

The original helix support was provided by three round F66 steatite rods. They were replaced by grooved rods of the same material, as illustrated in Fig. 6. Most of the dielectric material has been removed from the vicinity of the helix wire, where the RF fields are the strongest. The dielectric loading factor, which is computed from the low-current synchronous helix voltage, increased from 0.81 to 0.86. As a consequence, the helix turns-per-inch (TPI) was increased from 46 to 49 to maintain the same helix voltage.

The original loss section was about 2 inches long, with a 1.5-inch section where no net gain could be obtained, and started 1.5 inches from

* To be described in a subsequent paper.

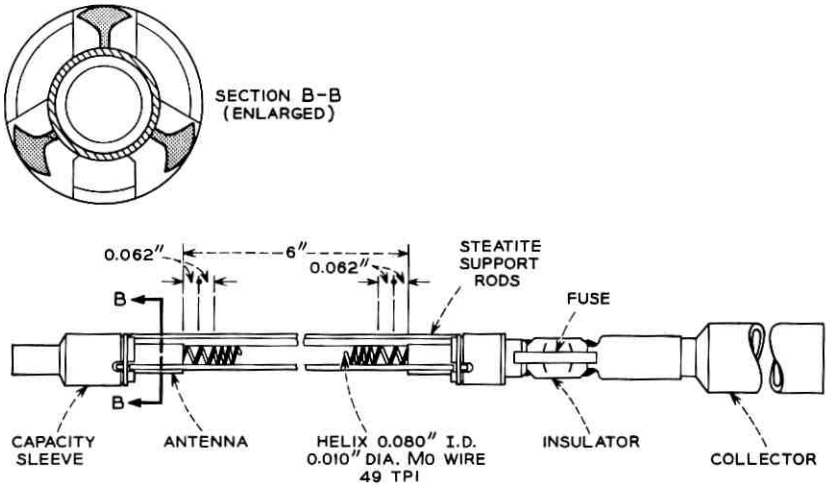

Fig. 6 — Helix assembly, showing cross section with special undercut F66 ceramic support rods.

the input coupler. It was found that the efficiency continued to improve as this section was shortened and moved closer to the input, as long as enough gain was maintained in the input section to establish the slow wave. The final loss pattern, as measured on a completed helix, is shown in Fig. 7. Moving the loss section towards the input and shortening it led to a considerable increase in the gain of the output section, where a maximum low-level gain of 46 to 49 db is produced. Since the tube must be short-circuit stable, this imposes a tremendous requirement on the return loss of the output edge of the loss pattern and the uniformity of the helix near this edge. A return loss of 52 db or more would have been desirable. It proved to be extremely difficult to maintain a return loss of better than 46 db. The short-circuit stability test was the most serious shrinkage factor on otherwise acceptable tubes for flight. Fig. 8 shows the hot and cold output match for an acceptable and a rejected tube, measured when the voltages are adjusted for maximum low-level gain.

The physical embodiment of the helix consists of a winding of 10-mil diameter molybdenum wire, wound with an inside diameter of 80 mils and a length of 6 inches at 49 TPI, except for two turns at each end which are at 66 TPI. Each turn of the winding is glazed to each of the three F66 steatite ceramic rods (spaced 120° apart) and then it is copper plated. After this, attenuation in the form of the aquadag is sprayed on. Fig. 9 shows schematically the means for applying and controlling this deposit.

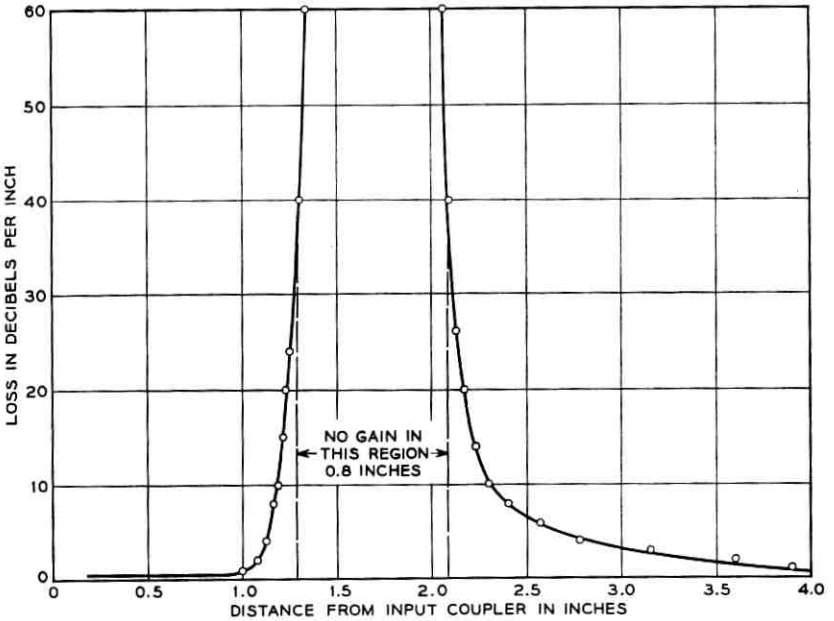

Fig. 7 — Final helix loss patterns of sprayed aquadag (intrinsic loss with Cu plating 2.78 db; total loss 83 db).

The glazed helix structure is shown in Fig. 6. The helix wire is wound to a maximum pitch variation of ±1 per cent (±0.0002 inch). Techniques developed at these Laboratories for fabricating glazed helices[4] make it possible to hold the outside diameter of the helix structure, defined by the outside of the ceramic support rods, to ±0.00075 inch. This is a maximum of 1.4 mils smaller than the inside bore diameter of the glass envelope within which it will be assembled later on. This close fit not only precisely aligns the helix, but also provides a support that enhances its resistance to shock and vibration. The helix structure is capable of withstanding thermal shock, extensive cleaning procedures, and outgassing in vacuum. The outgassing temperature is limited by the vapor pressure of the copper plating to 650°C.

4.3 *The Collector*

The collector in a high-efficiency TWT plays an important part. To improve the efficiency, the collector voltage is depressed below that of the helix until the maximum tolerable helix or accelerator interception is reached. For long-life tubes, it is desirable to keep this interception at

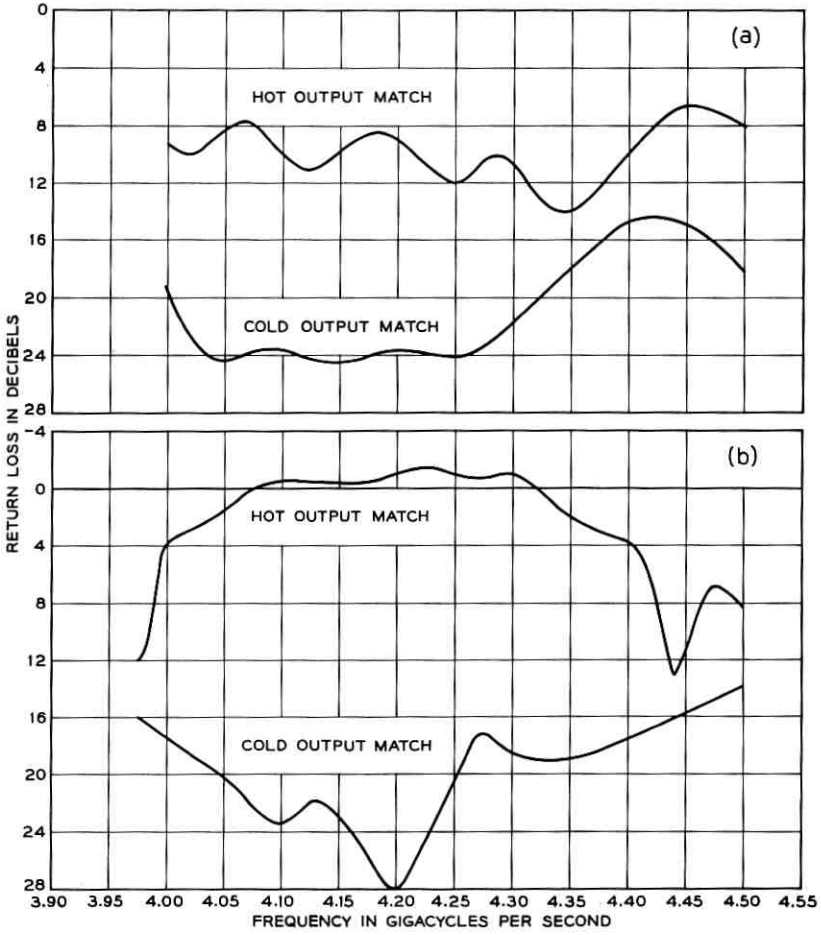

Fig. 8 — M4041, output matches measured at waveguide flange: (a) acceptable tube, (b) rejected tube (note return gain in band center).

the beginning of life to a maximum of 1 per cent of the beam current, since this interception increases slowly but steadily throughout life.

In Fig. 10, the helix current is shown as a function of collector voltage with no RF drive and with a drive to saturate the output power. When the collector voltage is depressed below the helix, the helix interception rises rapidly until it reaches a plateau. This current, called back-streaming, consists largely of secondary or reflected electrons, which finally terminate on the helix or accelerator. In addition, RF feedback that can

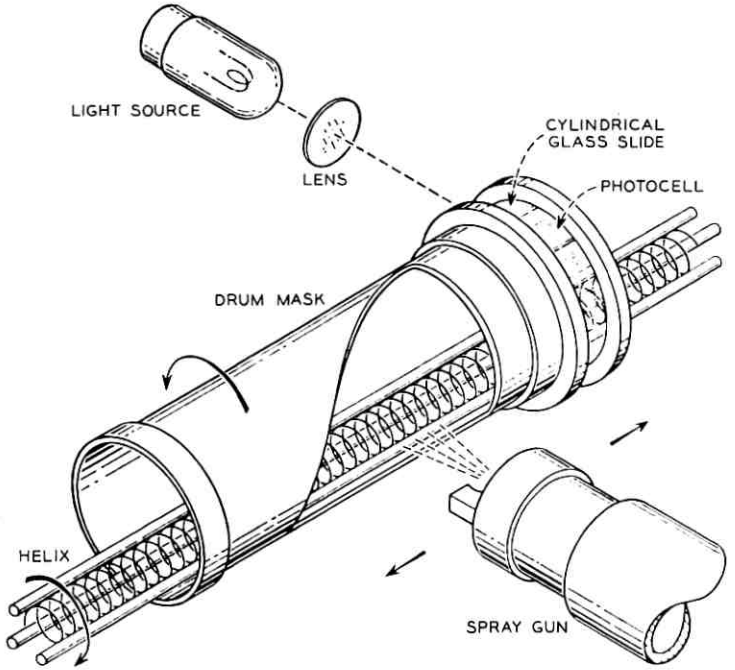

Fig. 9 — Schematic diagram of machine used for spraying aquadag loss section on helix.

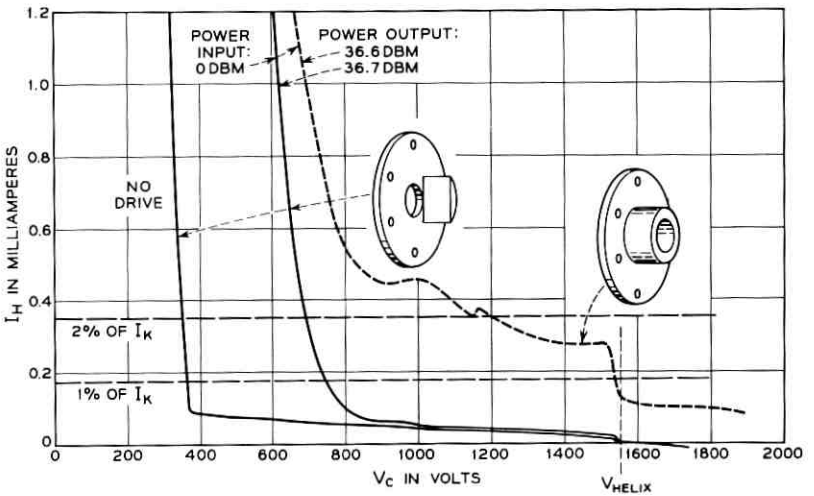

Fig. 10 — Depressed collector operation. Helix current vs collector voltage is shown for symmetrical and asymmetrical output pole-pieces. (Note the suppression of secondary and reflected electrons.) I_k = 17.4 ma, V_{helix} = 1550 v.

lead to internal oscillations is caused by the returning electrons, which provide a small amount of coupling between the output and input of the helix. The secondary and reflected electrons leave the collector on trajectories similar to those of the primaries, but in the reverse direction. The original collector pole-piece was shaped symmetrically, with a spreading magnetic field. To prevent back-streaming from the inside of the collector, a transverse field was produced in the area of the collector chamber by an asymmetry of the pole-piece. The returning electrons now follow different trajectories and are thereby prevented from leaving the collector again.

4.4 *Envelope*

The vacuum envelope in Fig. 11 is made in two sections: the bulb, which consists of concentric details of Corning 7056 glass and Kovar; and the stem, made of the same materials. The stem provides leads and connections to all elements and a tubulation for evacuating the tube, while the bulb provides the surfaces which support the helix and gun assemblies in precise alignment. There are two accurately located reference surfaces. One is the bore of the glass tubing which will enclose the helix; it is held to a diameter tolerance of ± 0.2 mil and a straightness of 3 mils maximum camber. The other surface, which later locates the gun, is machined to the inside of the large Kovar detail and is held with respect to the bore of the glass tubing to a total indicator reading (TIR) of 1 mil. The external reference surfaces, used later to assemble the tube to the circuit, are machined on the outside of the Kovar detail to a concentricity of 1 mil TIR with respect to the inner reference surfaces.

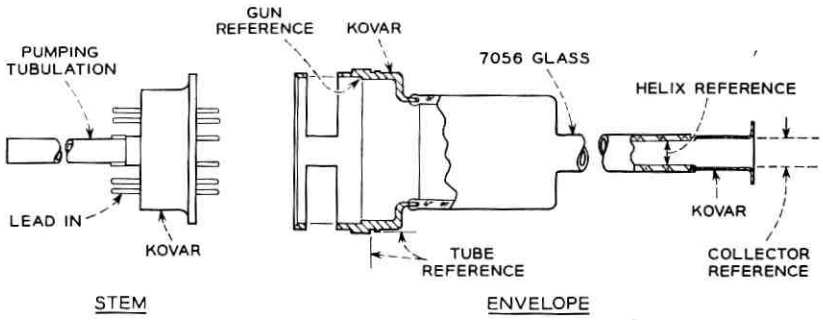

Fig. 11 — Envelope assembly with reference surfaces.

4.5 *The Focusing Circuit*

In a satellite system, weight is the controlling factor. The choice of the magnetic focusing circuit is intimately coupled to the problem of over-all system weight. In this connection, the solar plant with its supporting frame, the storage batteries, the regulator and the tube power supply contribute the majority of the weight. The average duty cycle of the tube is low, but because of long operating periods, the supply must be designed close to CW capacity. The solar plant, shielded for protection from particle radiation, and its support frame also add a considerable weight which is almost proportional to the power required by the TWT. To find the lightest over-all system, it was necessary to consider not only the weight of the tube package, but also the tube power requirements, or the tube efficiency. In the present satellite, several pounds must be allowed per watt of power supplied to the TWT.

The lightest focusing package would be a periodic permanent magnet circuit (PPM) which requires approximately one-half pound of magnetic material. The drawback is that it is relatively more difficult to focus the beam, which tends to scallop to a higher degree than in other magnetic circuits. This leads to higher beam interception and to a slightly higher collector voltage. It was estimated that this type of circuit might require 10 to 15 per cent more dc power than a straight field magnet.

From the viewpoint of life and efficiency, a straight field magnet (PM) would be the most desirable circuit since, with it, significant changes in cathode activity can be tolerated without degradation of the focusing. Its magnet weight of about 25 pounds is, however, prohibitive. A compromise is the single-reversal, permanent magnetic circuit (SRPM). It provides the excellence of focusing and high efficiency inherent in the PM design at a considerably lower weight. In common with the PM design, it has the disadvantage of some external magnetic leakage flux. The use of this design results in a magnet weight of 4 pounds, 3.5 pounds greater than the PPM circuit. On the other hand, the SRPM gives a power saving of about 1.5 watts over the PPM circuit. (See Table IV.)

TABLE IV — COMPARISON OF FOCUSING CIRCUITS

Focusing Circuit, Type	Magnet Weight, Pounds	Focus	Efficiency
PM	25	excellent; large leakage flux.	high
SRPM	4	excellent; some leakage flux.	high
PPM	0.5	more difficult; not for ultra-long life; no leakage flux.	lower

From these considerations, the SRPM was chosen for the Telstar satellite. It is comparatively new and has had little coverage in the literature.[5] In the form fully developed for this application, several objectionable qualities have been eliminated, and its operation is much better understood. A detailed description of this circuit and the improvements follows.

The weight of a magnet increases approximately with the third power of the length over which the field must be maintained if the length-to-diameter ratio is notably larger than one. By dividing the magnet in the middle and magnetizing the two halves so that their fields oppose each other, a weight saving of a factor of four can be realized. This is the result of a volume reduction of the leakage flux. The focusing of a traveling-wave tube in such a field should be a straightforward operation, provided the magnetic field can be reversed instantly. In practice, this is difficult to do unless a tapered reversal pole-piece is used between the two magnets, with a hole diameter only a small fraction of the scallop wavelength of the beam. In the present tube, the maximum diameter of the pencil type envelope is 0.319 inch and the measured scallop wavelength, 0.6 inch. The axial magnetic field of such a circuit is shown in Fig. 12. The reversal pole-piece used has a hole diameter of 0.35 inch; we can see that the reversal requires more than 0.6 inch. This means that a serious degradation of the beam focus will take place — the beam starts to scallop with a considerable increase in over-all diameter. Under these conditions, about 20 per cent of the beam current was intercepted by the helix in the reversal region.

A solution had to be found, since an interception of 20 per cent is intolerable. Before describing the solution, it is necessary to describe the behavior of a laminar beam in a uniform magnetic field which includes a small perturbation, as is shown in Fig. 13(a). The perturbation disturbs the laminar flow and forces the beam into a scallop mode. This is, however, reversible; and again observing Fig. 13(a), going from right to left, we can state: a scalloping beam in a uniform magnetic field can be forced back into laminar flow by a field perturbation of the right magnitude and the right phase with respect to the scallop. In Fig. 13(b), two perturbations of the same magnitude are placed a half-scallop wavelength apart. The beam begins to scallop at the first perturbation and is forced back into laminar flow at the second perturbation. Similarly, the second perturbation could be placed $(n + \frac{1}{2})\lambda_{sc}$ away. (If n is even, the perturbation has the same sign; if n is odd, the opposite sign.)* From now on, we will consider the field reversal as nothing but

* An analog can be found in a transmission line with discontinuities or mismatches, where the beam diameter would correspond to the VSWR and the per-

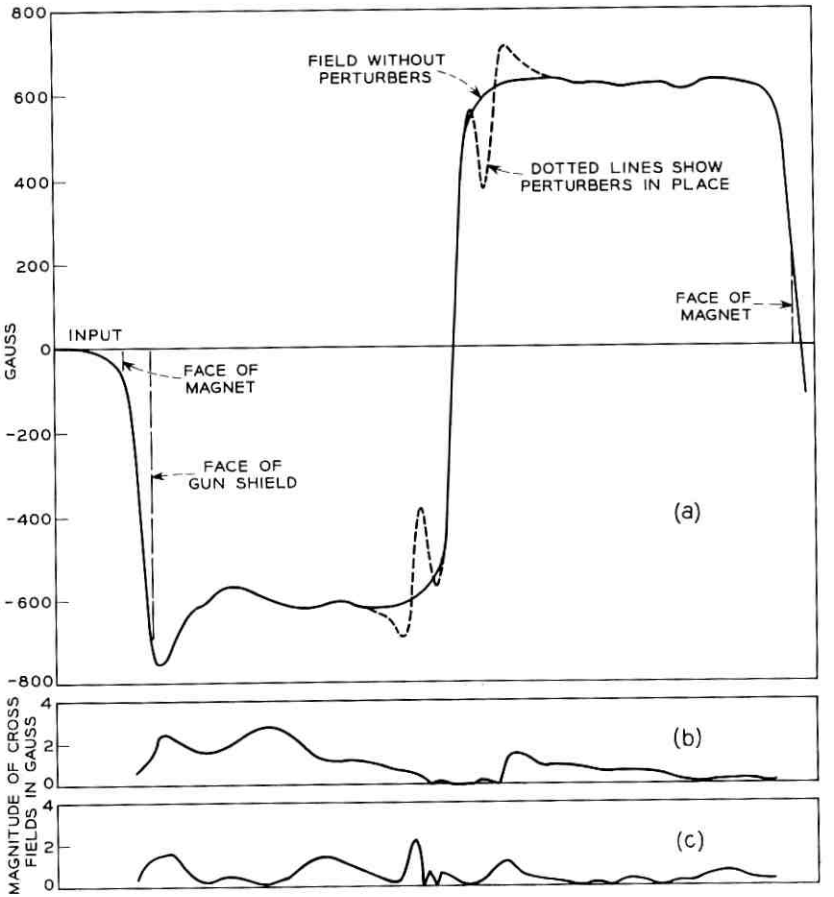

Fig. 12 — Magnetic fields in the single-reversal circuit: (a) axial magnetic field shown without perturbers, and modified field with magnetic perturbers in place; (b) horizontal cross fields; (c) vertical cross fields.

a large perturbation. Earlier SRPM circuits did not use perturbers to counteract the effect of the reversal plane. By mismatching the beam entrance from the gun to the uniform field, one can obtain a scalloping beam, which is shown in Fig. 13(c). If the phasing of the scallop is correct, it can counteract a further beam expansion at the reversal plane. This phasing or phase angle depends on the product of the distance between gun and reversal and the reciprocal of the beam velocity. The

turbations would represent the mismatches. The standing wave produced by one discontinuity can be canceled out by placing a second discontinuity of identical magnitude one-half wavelength away.

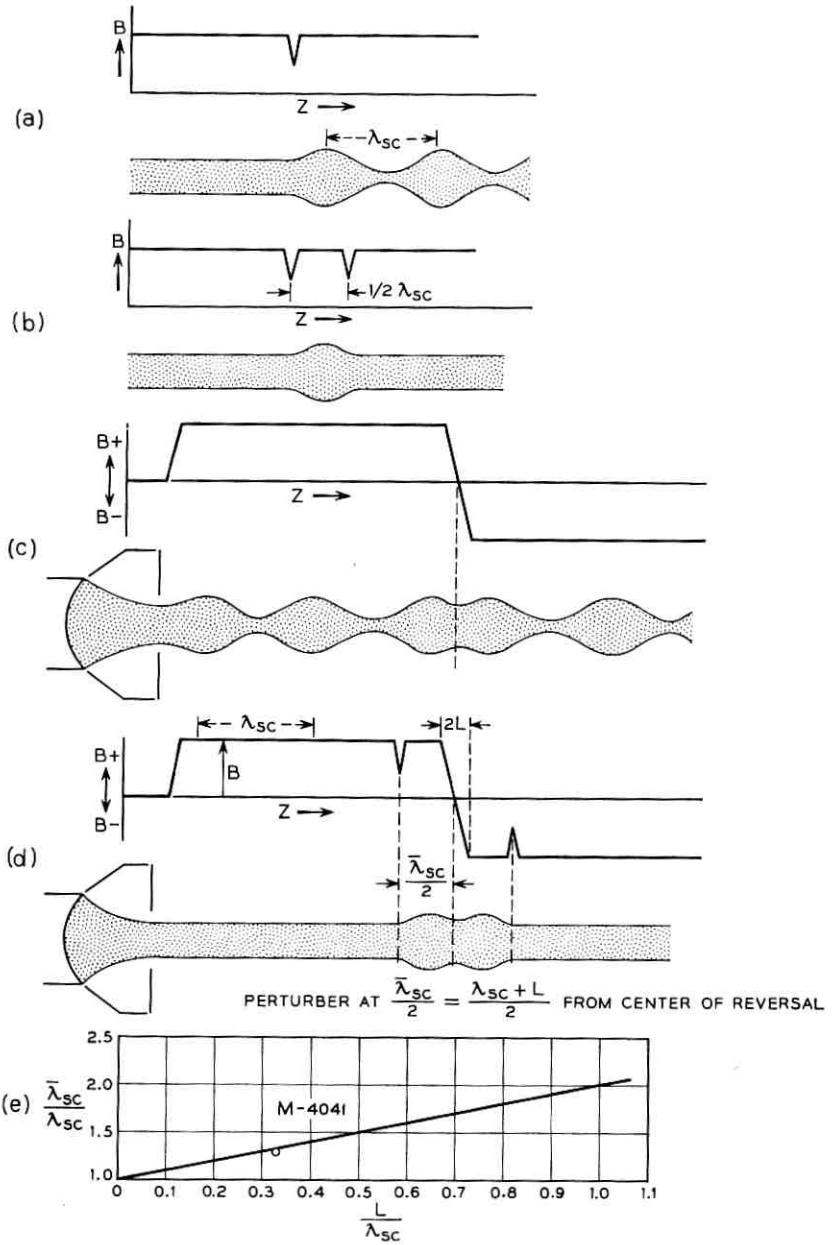

Fig. 13 — Focusing of beam with single-reversal circuit. (a) Laminar beam in uniform magnetic field with single perturbation. (b) Laminar beam in uniform magnetic field with two identical perturbations spaced by a half-scallop wavelength. (c) Focusing of beam through the reversal by pre-scalloping beam at start of magnetic field. (d) Focusing of beam through the reversal, using two magnetic perturbations, each spaced $\bar{\lambda}_{sc}/2$ from center plane. (e) Position of the perturbation computed for a linear field change in the reversal: normalized distance to the reversal plane is plotted vs the normalized length of the reversal. The measured value of the M4041 circuit is indicated and shows excellent agreement.

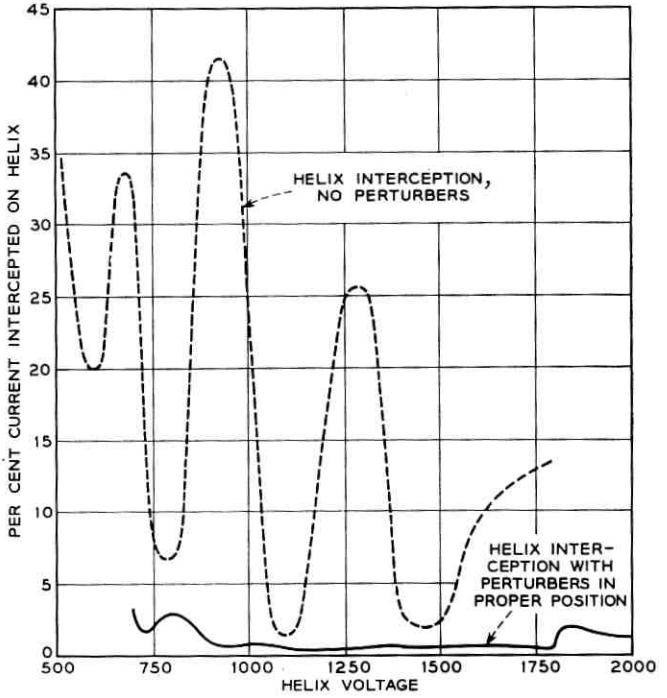

Fig. 14 — Single-reversal circuit, helix interception vs helix voltage.

helix interception measured on such a system is shown in Fig. 14 by the dotted line. The periodicity of the phasing between scallops and reversal is quite pronounced. The voltage passband is only 150 volts. To make the SRPM circuit usable, it is necessary to reduce the voltage dependence. This can be done by reducing the distance between the reversal plane and the point where the beam starts to scallop. For minimum scalloping, proper phasing is achieved with a distance of $(n + \frac{1}{2})\lambda_{cs}$ between perturbation and reversal. It is minimized for $n = -1$, which means that excess field would have to be placed at the reversal plane; this is inconsistent with the basic problem. For $n = 0$ and $n = -2$, we find two possible solutions. To obtain the smallest beam diameter at the reversal and least dependent on voltage, one should place one-half the perturbation, $\frac{1}{2}\lambda_{sc}$, before the reversal and one-half the perturbation, $\frac{1}{2}\lambda_{sc}$, after the reversal. This is shown diagrammatically in Fig. 13(d). In the reversal region, λ_{sc} is no longer constant; it depends on the magnetic field, which changes rapidly. The half-scallop wavelength measured from the center

of the reversal and expressed as $\bar{\lambda}_{sc}/2$ can be calculated by integration. For the special case of a reversal with linear dependence of the magnetic field, $\bar{\lambda}_{sc}/2$ has been computed and the values are plotted versus the normalized length of the reversal in Fig. 13(e). The actual improvement in beam transmission and independence of beam voltage is shown in Fig. 14 with the solid line. If the interpretation is correct that the beam now enters and leaves the extended reversal in a laminar mode, one should be able to stack several of these reversals in succession. This has been demonstrated recently in a three-reversal circuit, where only a small degradation in the beam voltage passband had to be accepted. (The weight of the Alnico V magnets was further reduced from the 4 pounds for the SRPM to less than 1.5 pounds for the three-reversal circuit.)

The physical design of a focusing package depends to a large degree on how the RF connections to the tube are made. Since waveguide outputs were required by the system, RF connections were the first feature considered. Direct coupling of waveguide to helix would have required a penetration of the magnets by the waveguides, making for a bulkier and heavier package, and was therefore rejected. Coupled helix matches were considered, but also rejected, because the additional loss in the outputs would have reduced the over-all efficiency, though it would have been very easy to physically combine the SRPM with coupled helix input and output.

The solution finally adopted consisted of nonresonant coaxial couplers at both input and output. A sketch is shown in Fig. 15. The coaxial coupler has two coaxial lines connected symmetrically to the reentrance: one is a feed; the other is a line with a movable short circuit, the position of which determines the impedance of the coupler. These coaxial couplers have been made small enough in diameter to be inserted into a series of uniformly spaced field straightener rings which are needed to reduce the magnetic cross fields on the axis of the tube. These field straightener disks are made of permalloy 45 and are used throughout the length of the magnetic field. Geometrically, it is important that they be held square to the axis of the beam. The resulting crossfields are shown at the bottom of Fig. 12. Because waveguide inputs and outputs were required, a further transducer had to be provided. It consists of a standard coaxial antenna transducer with a specially shaped dielectric cylinder to support the center conductor and give the necessary impedance transform. The over-all cold match from waveguide to helix was quite good over a 10 per cent band, with a VSWR of less than 1.2.

The focusing circuit described is not magnetically shielded. The field has a rotational symmetry about the axis of the circuit. Some knowledge

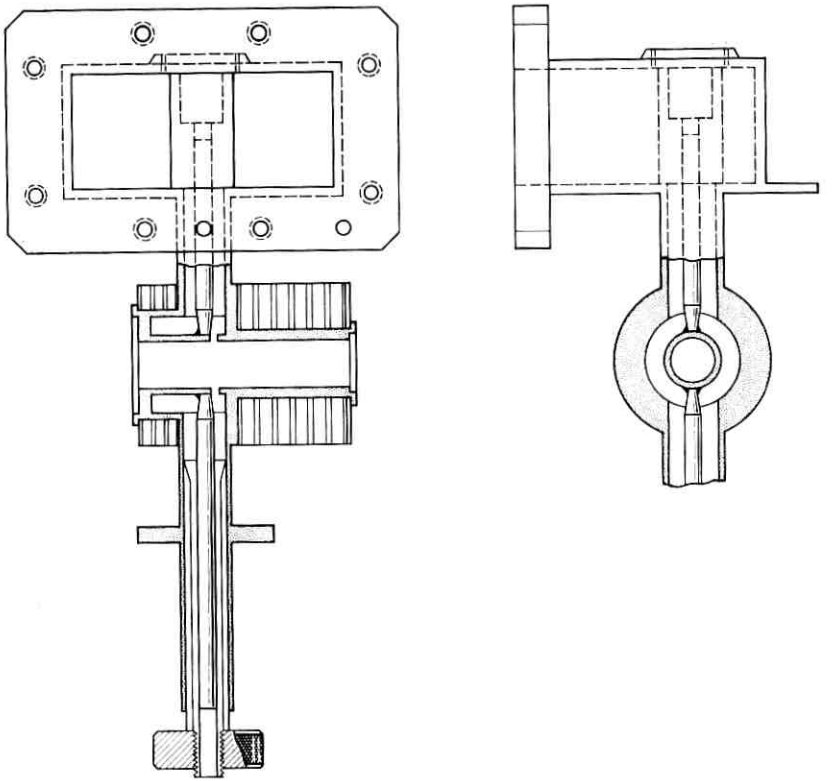

Fig. 15 — Nonresonant coaxial helix coupler with matching stub and transition to waveguide.

of the leakage flux was needed in order to evaluate its effects on other components in the tightly packaged satellite. The external fields are shown in a plane through this axis in Fig. 16. Little interference was experienced, except in the case of the telemetry package, which had to be shielded with permalloy 45.

V. PACKAGED DESIGN

The packaged traveling-wave tube consists of a tube with its magnetic circuit and RF couplers joined together to form a compact unit. This arrangement has many advantages to recommend it for satellite use. One of these is the optimization of tube characteristics by fine-grained adjustment, at the factory, of the relationship of the magnetic

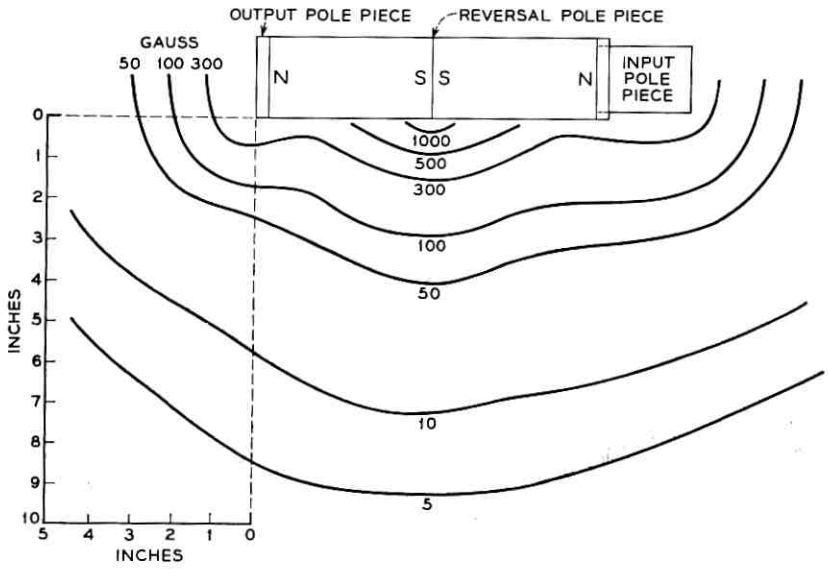

Fig. 16 — External magnetic leakage field of the single-reversal circuit.

field and RF matching sections to the tube. Another is the greater latitude permissible in designing the package to (a) ensure the stability of this relationship for the full life of the unit, (b) provide the ruggedness and support needed to protect the unit against shock and vibration, (c) provide an enclosure as protection against handling and environmental conditions, and finally, (d) provide the most elementary and rugged connections for securing the unit in the repeater.

Fig. 17 shows a graphical cross section of the package. All elements are enclosed by, or mounted on, an aluminum tubular housing which forms the "backbone" of the structure. The tube is a pencil-like figure through the center of the unit. Between it and the inner wall of the housing are two Alnico V magnets and an array of field straighteners. The magnetic circuit is completed by a pole-piece at each end of the magnets and a Permendur septum with its perturber bushings separating the magnets. Mechanical support is given to the tube by means of the pole-pieces at each end, and by contact with two sets of four pins each which cradle the tube at points substantially equidistant between the end supports. Electrical connections are made to the elements by silicone rubber encapsulated leads at the gun end and a single lead at the collector end. Waveguide-to-coaxial transitions are shown at the respective input and output coupling points on the helix. An RF filter

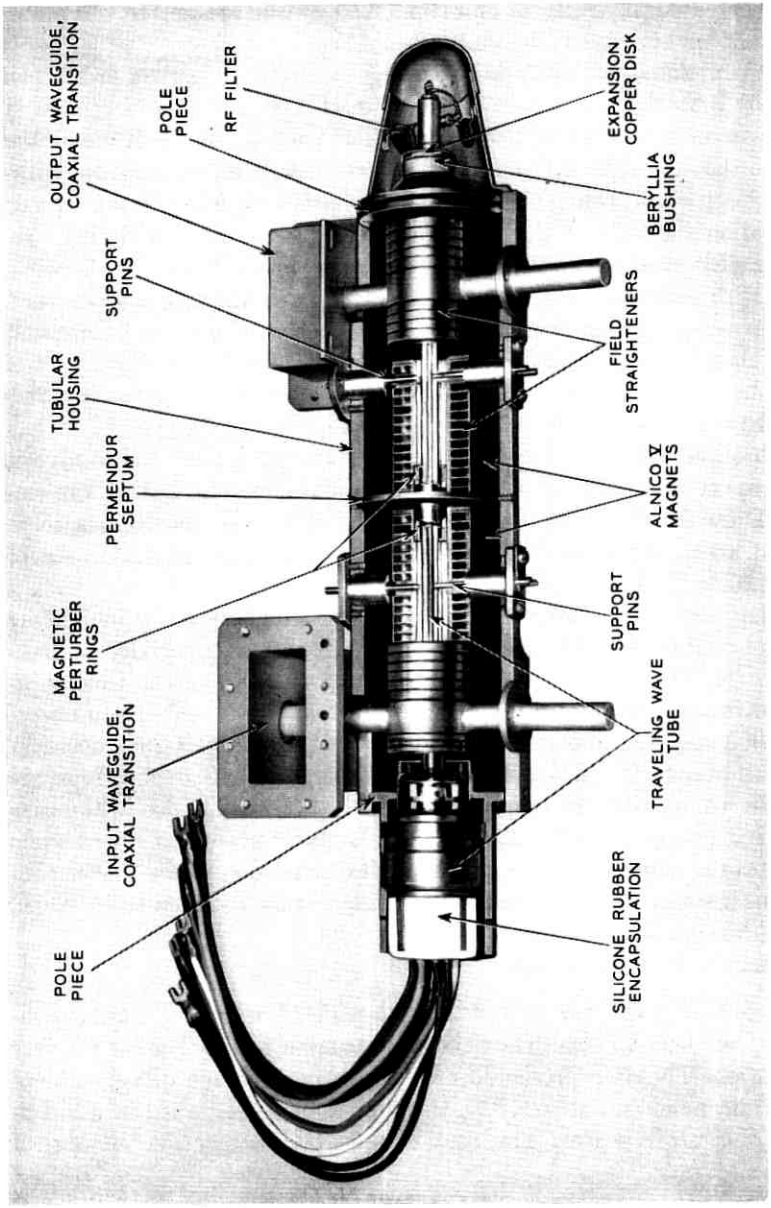

Fig. 17 — Cross-section view of completed amplifier package.

is connected to the collector and supported by the protective aluminum cone that encloses the collector.

The completed amplifier is a package wherein each part is kept in place by a weld or by a screw, and also with cement; the unit cannot be disassembled except by destruction. The package, in effect, floats the tube so that the tube is free to move with changes in temperature without any detectable change in its electrical characteristics. This is achieved by welding the tube to the package at the gun end and soldering to a copper disk at the collector end. The disk, which is 0.005 inch thick, flexes with changes in length brought about by changes in temperature. Furthermore, the disk, which is a part of a subassembly—the other parts of which are a beryllia bushing and a copper cone — also forms part of a thermal path through which some ten watts of collector power is transmitted to the body of the package and dissipated.

Two other constraints are put on the traveling-wave tube to give it the support necessary to resist the vibrations inherent in this application. These are two sets of four aluminum pins, previously identified, located about equidistant between the two end supports. Each set of pins cradles the 0.290-inch diameter glass tubing of the tube in such a way that each pin is deflected laterally approximately 0.002 inch at its point of contact with the glass, to ensure support over a wide temperature range. The result is that the resonant frequency of the tube is increased from an unacceptable value of approximately 700 cps to one of over 3000 cps, well above the specification requirement of 2000 cps.

In installing the package in the repeater, the RF connections are made by connecting the amplifier flanges to the waveguides in the canister giving support to the package. This support is supplemented when the repeater canister is filled with polyurethane foam. Electrical connections are established by flexible insulated leads attached to the tube.

VI. ELECTRICAL PERFORMANCE

The M4041 TWT was tested under a wide variety of operating conditions, but here we shall restrict the discussion to the Telstar satellite application. The data presented are taken from average tubes, some of them from model number KP24, the tube actually installed in the Telstar spacecraft repeater. The best values attained are quoted only if so indicated.

6.1 *The Tube Gain*

The tube gain for KP24 is plotted in Fig. 18 versus helix voltage. The low-level gain is 47 db and occurs at 1380 volts. Here, the maximum

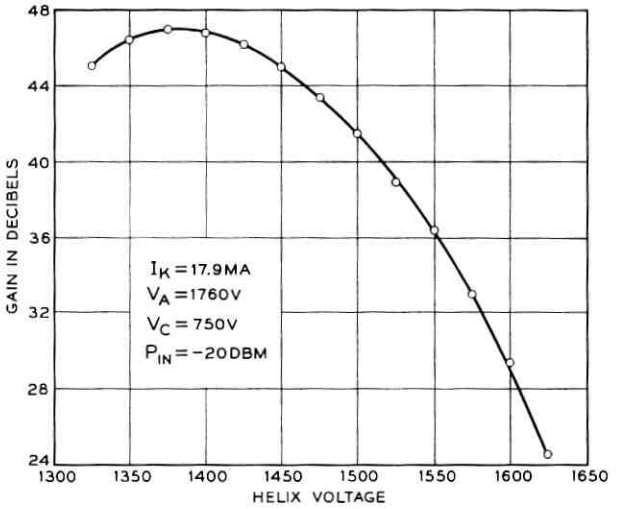

Fig. 18 — Small-signal gain vs helix voltage for KP24 installed in its final circuit.

power output and efficiency are low; to improve both, the tube is run at overvoltage. For the satellite repeater the operating point was chosen at 1520 volts. This point is indicated in the figure and shows a low level gain of 39 db. In Fig. 19 the power output and gain for this same tube are shown for a range of helix overvoltages. The tube was originally designed for an input drive of 0 dbm. Late in the development, a compromise had to be made to permit satisfactory two-signal operation, and to allow for a possible ±3 per cent voltage drift on all dc voltages. The gain versus frequency is shown in Fig. 20 for three different operating conditions. At the voltage for maximum low-level gain, the peak occurs at about 4.1 gc. Raising the voltage to the overvoltage condition lowers the frequency at which the maximum gain occurs, and thereby increases the gain slope; however, when the tube is driven into saturation, the gain drops off but the slope is greatly reduced. With an input level of −3 dbm, the gain slope is 0.5 db over the 4.0–4.2-gc band.

The TWT is not terminated by a well-matched load. The filters and antenna present somewhat of a mismatch. Gain measurements were performed with the tube operating into an attenuator followed by a sliding short circuit. For each attenuator setting, there were periodic positions of the short circuit for which the gain could be enhanced or reduced. In Fig. 21 the maximum and minimum values of the gain are plotted versus twice the attenuator setting, which is equal to the return loss of this load. The gain is not only periodic with the position of the

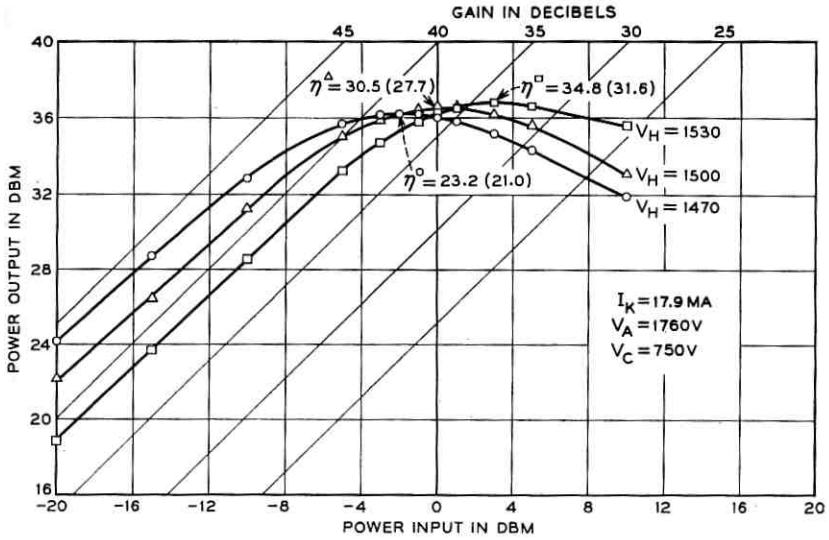

Fig. 19 — Output power vs input power with helix voltage as parameter for KP24. Depressed collector efficiencies are shown at maximum power points; overall efficiencies in brackets include heater power.

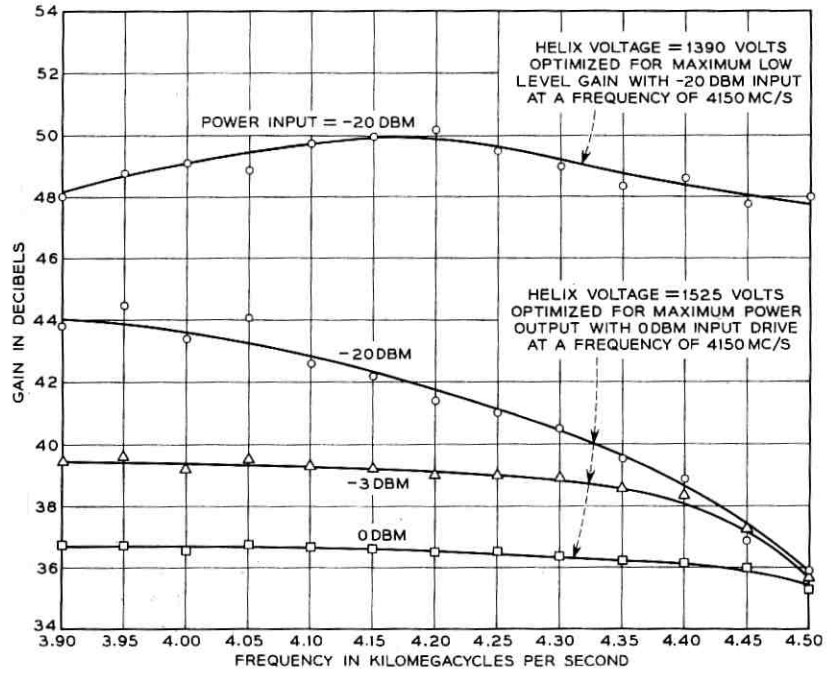

Fig. 20 — Amplifier gain vs frequency for different input power levels.

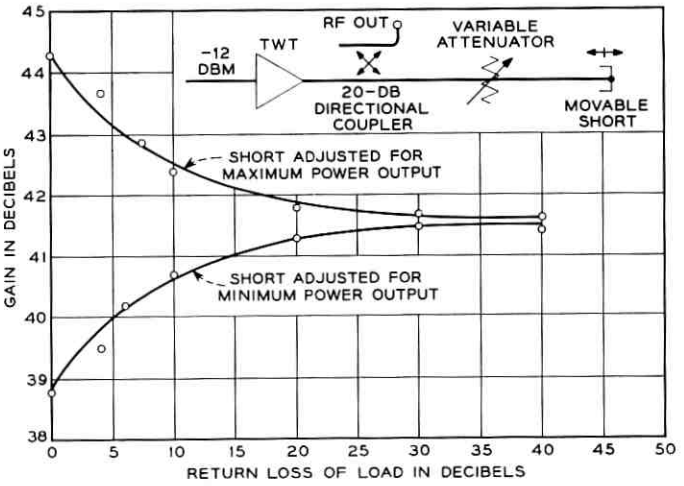

Fig. 21 — Effect of load mismatch on low level amplifier gain.

short circuit, but also with frequency, impressing a ripple on the gain curve. The frequency band between two maxima depends upon the electrical distance between the load and the TWT attenuator. In the region of saturation, these gain variations are considerably reduced.

6.2 *Power Output and Efficiency*

The power output and efficiency at 4.17 gc were studied as a function of the input drive and beam currents. The results are shown in Fig. 22. At each point the helix voltage was optimized and the collector depressed until the highest efficiency was obtained. It is interesting to note that the same TWT can maintain efficiencies of over 30 per cent for output powers from 0.3 to 10 watts. It must be remembered that the efficiency falls off much more rapidly when the helix and collector voltage have been set and only the input drive is varied. A curve of this type is shown for 17 ma as a dotted line in Fig. 22.

The highest efficiency measured with this tube type was 43 per cent at the output power level of 5.4 watts, giving an over-all efficiency of 38.5 per cent. Several other models reached 40 per cent, but most of the tubes gave approximately 38 per cent. These efficiencies look attractive; however, they are not realistic for actual satellite conditions, since they can be achieved only with high helix and accelerator interception not permissible in a long-life tube. From our life tests, we know that throughout the life of TWT's, the helix and accelerator interceptions

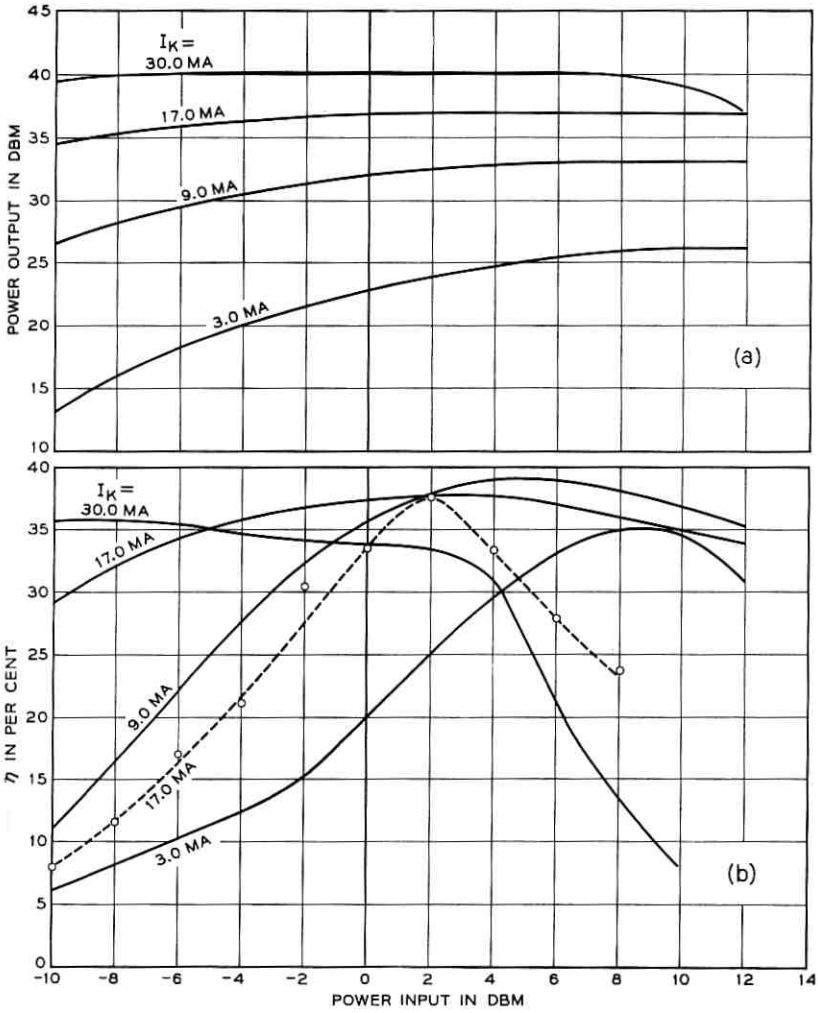

Fig. 22 — (a) Maximum saturated power vs input drive with cathode current as parameter. At each point, the helix voltage is optimized to obtain the maximum power output. (b) For each of the points in (a), the collector voltage is also optimized to achieve the maximum depressed collector efficiency. This efficiency is then plotted vs input drive. Operation with fixed helix and collector voltage is shown for comparison at 17 ma with a dashed line (helix and collector were optimized for highest efficiency with an input drive of +2 dbm).

increase and might eventually be the ultimate cause for tube failure; for this reason, they should be kept as low as possible when the tube is finally installed.

Fig. 23(a) shows both accelerator and helix interception at the oper-

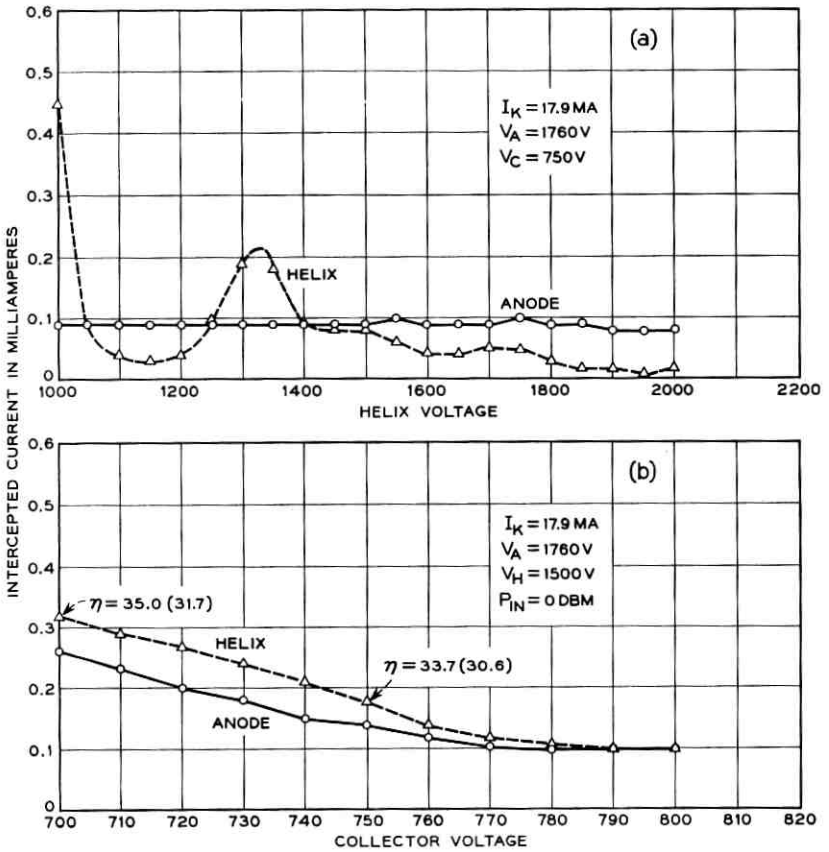

Fig. 23 — Beam current intercepted on helix and anode for KP24 in final package: (a) interception vs helix voltage without RF drive, (b) interception vs collector voltage with RF drive at saturation. Efficiencies, depressed collector and over-all (in brackets), are also shown at two points.

ating point without RF drive as a function of the helix voltage. These data stem from KP24 shortly before delivery for incorporation in the satellite with about 2800 hours of life. The accelerator interception was originally less, but has already climbed from its original value. This has been observed previously with many M1789 tubes on life tests. The hump in the helix interception at 1300 volts is not standard and is most likely caused by residual cross-fields. In Fig. 23(b), helix and accelerator interception is plotted versus collector voltage at full RF drive. Decreasing the collector voltage improves the efficiency, but the interception current exceeds the limit set for long life performance.

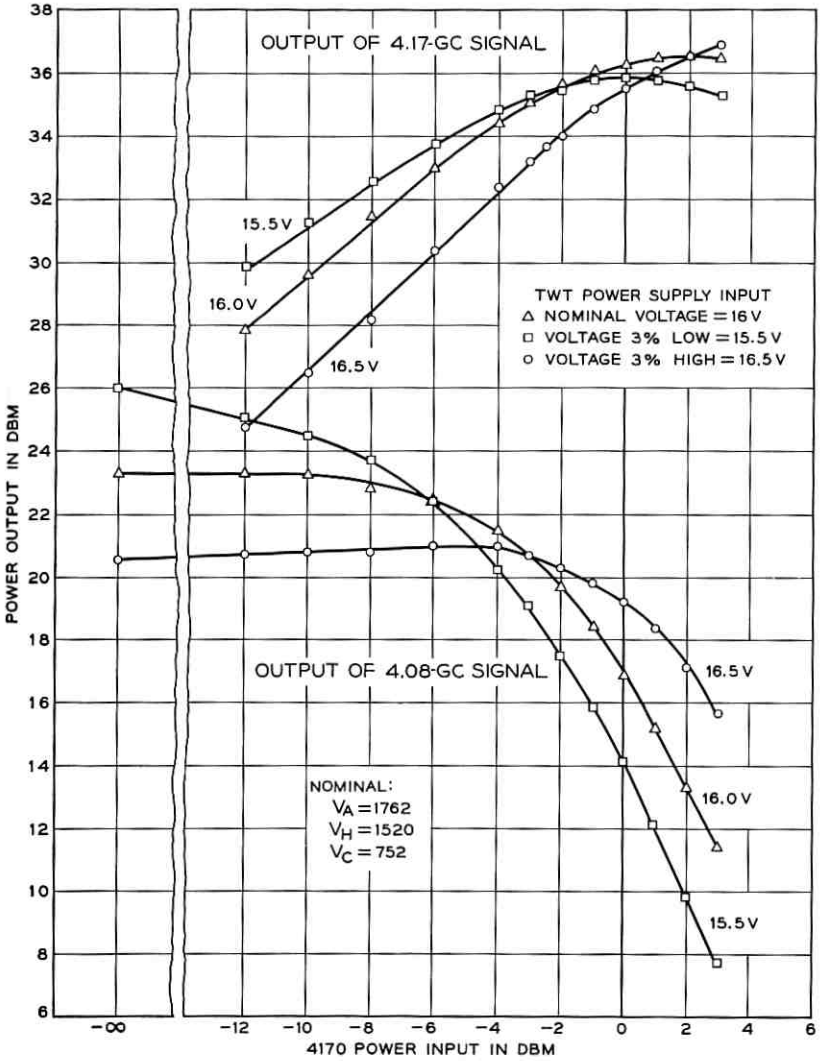

Fig. 24 — Two-signal operation of KP24 in final package. The 4.08-gc beacon input is held constant at −12 dbm as the 4.17-gc signal is varied. Power output is shown for both frequencies with the input voltage to the TWT power supply as a parameter.

6.3 *Two-Signal Operation*

After each tube had been tested and approved for flight, a two-signal test was made to determine the actual operating point (V_{helix}). In the

satellite, the tube simultaneously amplifies the beacon and the communication signal. The beacon input is constant at 4.08 gc and −12 dbm. The signal at 4.17 gc has a variable level from −12 to 0 dbm. As the signal level increases, the output of the beacon drops off because the tube is driven into saturation. The beacon and signal outputs are shown in Fig. 24 as a function of the signal level. System limitations were imposed on the operating point to prevent envelope oscillation within the feedback loop of the converter. The limit imposed was that the beacon could not drop off more than 1 db if the signal level were raised by 1 db; this represents a 45° slope on the beacon output. At the nominal input voltage to the dc-to-dc converter, this occurs at −2.5 dbm. This, then, is the operating point chosen for the TWT. The efficiencies, depressed collector and over-all, have been computed for the −2.5- and 0-dbm input levels for the three cases of undervoltage, nominal and overvoltage. These figures are shown in Table V. To satisfy this late system requirement, a noticeable degradation in efficiency had to be accepted to guarantee a stable two-signal operation.

6.4 *AM-to-PM Conversion*

Instead of measuring the AM-to-PM conversion directly, a method described by Mr. H. L. MacDowell[6] has been used. Two signals of much different amplitude and frequency are amplified in the TWT. The intermodulation products are measured and the AM-to-PM conversion computed. These values are all plotted in Fig. 25 together with the output power against the input drive. The curves are from measurements made with different input voltages to the satellite dc-to-dc converter, for the nominal voltage of 16 volts, and for 16 volts ± 3 per cent. These are estimated limits of regulation throughout the life of the satellite. The maximum of 4°/db measured with 3 per cent overvoltage is less than the value encountered with the TH relay tube under similar drive conditions.

TABLE V — COMPUTED EFFICIENCIES FOR KP24 WITH TWO-SIGNAL OPERATION

Input η	−2.5 dbm		0 dbm	
	Depressed	Over-All	Depressed	Over-All
−3%	28.0	25.2	29.0	26.2
Nominal	27.0	24.4	32.0	29.0
+3%	17.3	15.7	24.2	22.0

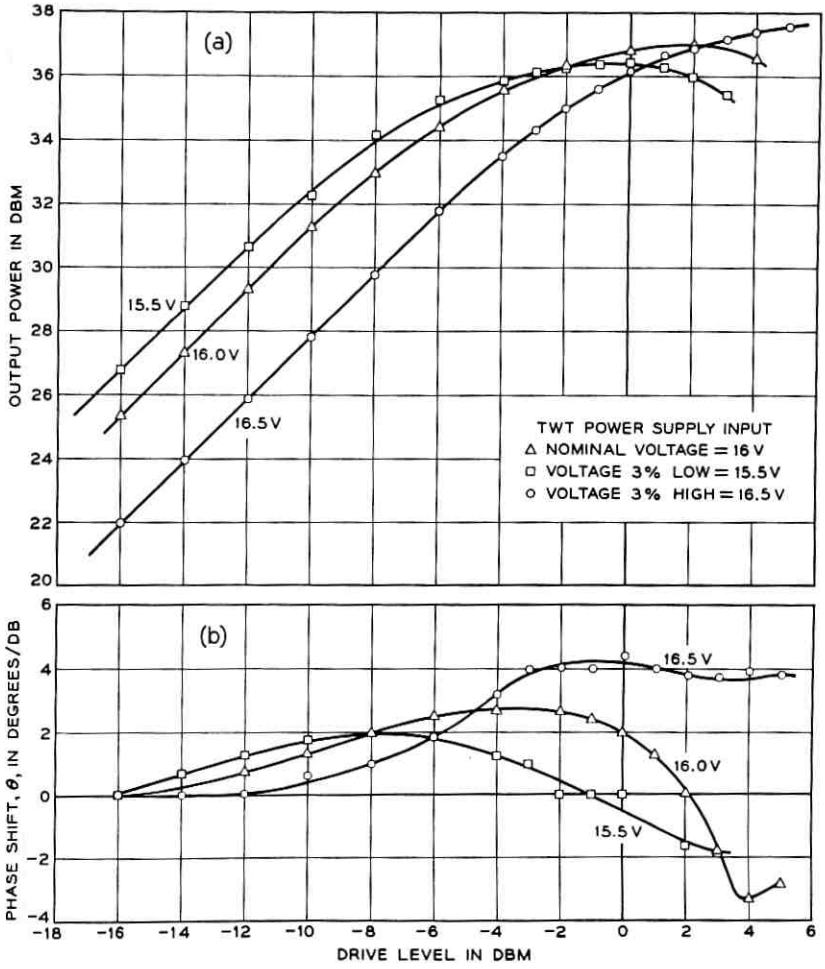

Fig. 25 — AM to PM conversion: (a) power output vs input drive, (b) phase shift vs input drive at 4.1 gc.

VII. MECHANICAL CAPABILITY

Mechanical capability, in the sense used here, is limited to the conditions the amplifier, or its components, have been shown to withstand by actual tests, and not the ultimate that it can withstand. In all cases, tests were defined to impose conditions more severe than were likely to be encountered in preparation for or in actual satellite flight.

Before a unit is passed for satellite use, it is subjected to the following

vibration tests: 15-50-15 cps at 0.3 inch displacement (3.5-38-3.5 g), 50-100-50 cps at 20 g, 100-2000-1000 cps at 10 g.

During development, typical packages were subjected to mechanical and thermal tests as follows:

(1) Thermal cycle, three packages, heater off: −30°F to +105°F to −30°F.

(2) Thermal cycle, one package, heater operated on and off: +15°F to 90°F to 15°F.

(3) Thermal cycle, six guns after 28,000 to 38,000 on-off cycles of heater: −30°F to 150°F to −30°F.

(4) Vibration tested four guns after 11,000 on-off cycles of heater: 15–2000 cps from 4–20 g.

(5) Shock tested four guns after 11,000 on-off cycles of heater: three to 400 g without harm; one to destruction at 1600 g.

(6) Vibration check of five heater-cathode structures: 100-3000 cps at 40 g.

(7) Cycled 31 heaters in guns made exactly as in tube from 4000 to 44,000 on-off cycles with no losses. Fourteen were opened, carefully dissected and examined for deterioration at cathode and heater coatings. None was found. Seventeen still on cycling life.

(8) Two heaters same as item (7) put on continuous life. Satisfactory after 6100 hours and still on.

(9) Vibration (to remove foreign particles) applied to all guns and helices during fabrication: 50-2000-50 cps at 20 g.

VIII. BUILDING THE FINAL TUBES FOR SATELLITE USE

8.1 *General Cleaning and Processing Procedure*

To ensure an end product free of contamination and mechanical defects, procedures and processes are spelled out in great detail. All operations are inspected upon completion, and these inspections are supplemented by inspection of subassemblies. Assembly is done under pressurized hoods in areas where the atmosphere is controlled and personnel traffic is minimized. A general listing of these activities is:

(1) All piece parts and subassemblies are inspected for defects as received and again at several points in the assembly procedure.

(2) All subassemblies are inspected for particles, either airborne or by-products of fabrication, and particles are removed by hand or vacuum.

(3) All parts and subassemblies must pass an atomizer test, which is a very sensitive indicator of surface cleanliness, just prior to assembly.

M-041 TWT PROCESSING RECORD

GUN ASSEMBLY B983596 Qty 4 Ident. no. 146 Date 2-9-62

Parts:

		Iss	Lot	Date
Accelerating anode assem.	B-983597	1	5	2-1-62
Beam-form. electrode assem.	B-983600	1	4	1-29
Cathode support assem.	B-983603	1	Ident. 146	2-3-62
Ceramic tubes	B-983607	1	Lot 1	2-9
Ceramic button	B-983606	2	2	2-9
Glaze, M24-0	B-778137	2	1	2-9
Platinum wire .015 C.P.	as required			

Procedure:

1.	Place parts on tool per B-983969	Iss 1 (#2 FIRST)	by X Yellow 2/9
2.	Apply glaze and polystyrene		XX 2/9
3.	Fire to glaze joints		XX 2/10
4.	Remove glazed structure from tool-if necessary ultra-sonic agitate in methanol then blow dry with N_2		XX 2/10
5.	Break off excess length of ceramic tubes		XX 2/10
6.	Measure assem. on comparator - record below		XX 2/10
7.	Attach anode and B.F.E. leads		XX 2/10
8.	Submit to I. LYONS for vibration		LYL 2/10/62
9.	Atomizer test per BA-286011 then methanol rinse and blow dry with filtered nitrogen.		C.E.Winter 2-16-62
10.	If unsatisfactory, clean per B886498-13.		
11.	Vacuum fire (store sealed until needed)		Bert Tuttle 2-16-62

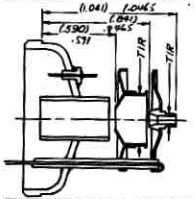

Remarks: Atomizer test grade 3

T.I.R.	Anode B.F.E.	within .0005	✓ ✓	other	

C.E.W. Final approval

	M-041 TWT	
Eng.	EGO	Iss.
Edit.	ALS	1 2-15-62

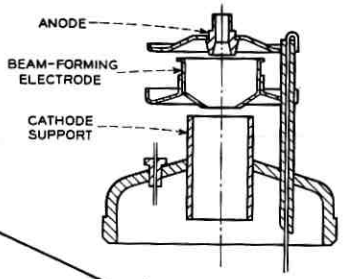

M-041 TWT PROCESSING

MOLYBDENUM CLEANING

1. Place parts in suitable rack providing free access of fluids to all surfaces.
2. Vapor degrease per B-888142-1.
3. Blow dry with nitrogen under hood.
4. Ultrasonic wash per B-888142-2.
5. If use within 2 weeks not anticipated, store at this stage in stoppered glassware cleaned per B-886498-1.
6. Prepare following solution:

   75% by vol. distilled water.

   20% by vol. 30% hydrogen peroxide (H_2O_2) C.P. or reagent grade, A.C.S.

   5% by vol. 30% ammonium hydroxide (NH_4OH) C.P. or reagent grade, A.C.S.

   Immerse parts at room temperature for 10 sec. periods until no further surface change is apparent.
7. Rinse in filtered bottom-fed overflowing tap water 5 min.
8. Rinse in cascading deionized water per B-888142-3.
9. Blow off excess water with nitrogen.
10. Dry in nitrogen fed oven at 110°C for 15 min.
11. Transfer parts to molybdenum rack suitable for subsequent operations and cleaned as above.
12. Reduce in wet hydrogen at 925°C for 15 min.
13. Atomizer test sample parts per BA-286011.
14. Dry samples per steps 9 and 10.
15. If unsatisfactory reprocess batch as follows:

    Oxidize in air at 400°C for 20 min.
    Reduce in dry oxygen-free hydrogen at 700°C for 15 min.
    Reprocess starting with step #13.
16. Store in stoppered glassware cleaned per B-886498-1.
17. If stored beyond 10 days, reprocess starting at step 13.

APPROVALS [illegible] DEPT. 2824 [illegible] DEPT. 2816 [illegible] M-041 TWT

Sheet	Date		TITLE	DRAWING NO.
2	11-15-61	EGO	CLEANING PROCEDURE MOLYBDENUM	B-886498-2
		ALS		

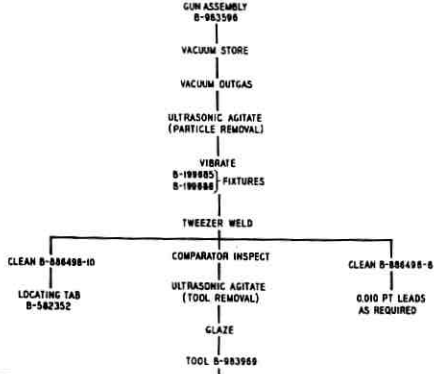

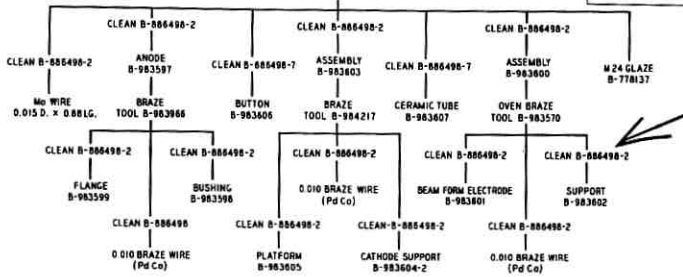

Fig. 26 — Typical flow chart of a subassembly procedure, with detailed specifications for a cleaning operation and the check sheet used to insure careful observation of each step required.

(4) Cleaning operations:
   (a) trichloroethylene wash — liquid or a vapor (all metal parts)
   (b) hydrogen reduction (all metal parts)
   (c) air firing (all ceramics)
   (d) ultrasonic agitation in detergent or solvents (all parts and subassemblies)
   (e) cascade rinsing in deionized water — rinse used after operation (d)
   (f) chemically reactive immersion (some metal parts: i.e., cathode surface, gun parts)
   (g) oxidation-reduction (gun parts)
   (h) liquid honing (glass stem leads, cathode surface)
   (i) vacuum outgassing (all subassemblies)

(5) Storage

All cleaned parts are stored in containers which have passed an atomizer test. The limit of storage is ten days, after which they are automatically recleaned. The coated cathode is the only assembly that departs from this procedure; if held ten days, it is rejected.

(6) All fixtures and tools used in assembly are cleaned to the same standards as the parts.

(7) All vacuum outgassing containers are equipped with filters to entrap airborne particles when the container is open to air.

(8) Extraordinary "clean room" procedures are followed, in that assembly is done under a protective pressure hood in a dust-free temperature- and humidity-controlled room located within a similarly controlled area. The movement of personnel in the inner room is restricted to essentials.

The meticulous cleaning and assembly procedure is guided by a flow chart for the tube as a whole and subordinately for each subassembly. Each cleaning process is separately listed. This system is illustrated in Fig. 26 with a flow chart for the gun subassembly and the cleaning procedure for molybdenum. To prevent omission of any step, check lists are used for each individual component, small or large.

8.2 *Processing on the Pump Station*

To check for subsequent changes, the tube undergoes an additional inspection before it is sealed on the pump station. A similarly designed station was used for the M1789 TWT. This system uses a roughing pump, followed by an oil diffusion pump and two liquid N_2 cold traps. After a vacuum of 1×10^{-5} mm Hg is obtained, the tube is baked at slightly less than 450°C for a minimum of 16 hours. Subsequently, the helix is outgassed at 650°C by passing current through it, and the col-

lector is baked in a small oven to higher temperatures to make sure all surfaces which are directly exposed to the beam have been freed from occluded gases. After the tube is thoroughly outgassed, the Ni-Zr cathode is broken down at a temperature of 1000°C for 4 minutes. Then a maximum of 500 volts is applied and a beam of about 2.3 ma drawn to helix and accelerator. The cathode temperature is gradually lowered, provided space-charge-limited emission can be maintained. The TTW is then sealed off.

8.3 *Preaging*

The TWT is now inserted into a focusing circuit and preaged. The cathode nickel is fairly inactive, and it takes the tube about one-half to one hour until full emission (20 ma) can be drawn with the nominal accelerator voltage, at a temperature of 900°C. For the next few hours the tube is permitted to age in before full RF drive is applied. Most of the tubes remain for about 100 hours on preaging. The tube is now removed from the aging circuit; the leads are attached and based in a silastic rubber cap. Thorough mechanical inspection follows, to eliminate further processing of a defective tube.

8.4 *RF Testing*

The tube is now ready to be checked for its RF performance. Thorough tests are made on all parameters to determine whether the tube passes the limits set for satellite use. At this point a considerable number of tubes are already marked "nonfly." The highest number of rejections are caused by a poor hot output match and an associated tendency to oscillate when the tube is short-circuit terminated. Some of these tubes, however, continue through this testing and are used for life studies.

8.5 *Aging and Life Tests*

All of the care in designing and building this tube is of little value if confidence in its life capability is not established. The aging-in phase is the only period in which the tube can be observed. Various observed characteristics can be used as indications of the later behavior and give confidence in the long-life abilities and reliability by eliminating poor or questionable tubes. An extremely sensitive method, the dip test,[7] was selected to measure relative changes in the average cathode work function, more commonly known as the "activity level." This test is initiated by a precisely timed interruption of the heater power to the tube under study while observing changes in cathode current, particularly the maximum drop which occurs shortly after the heater power is re-

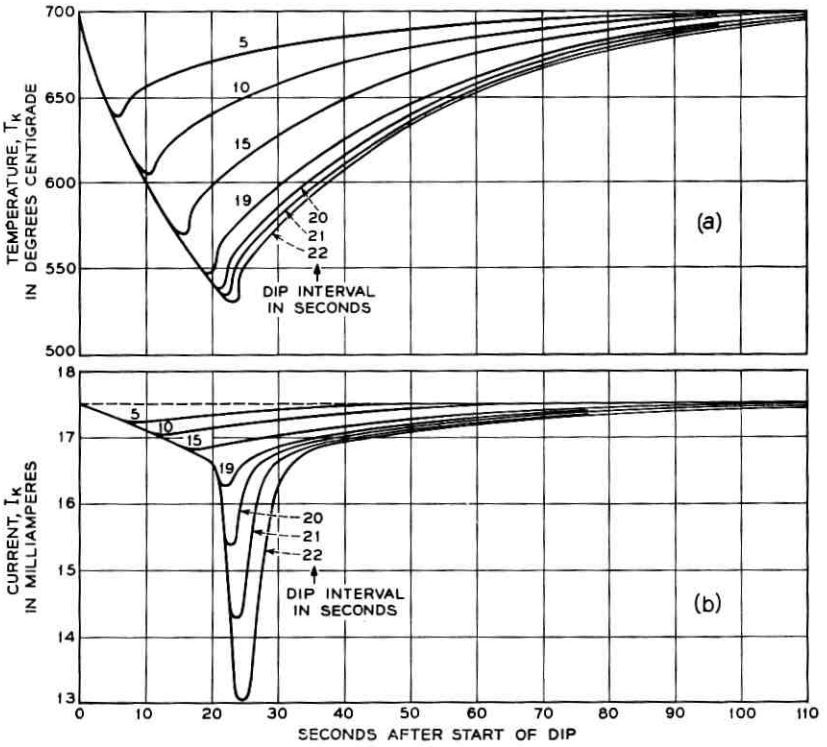

Fig. 27 — Dip test of typical M4041: (a) cathode temperature measured with built-in thermocouple during dip test, with dip interval as parameter; (b) corresponding cathode current.

stored to the tube. Fig. 27 shows composite plots of cathode currents and temperature, as measured with a built-in thermocouple, versus time. The sensitivity of the test can be increased by lengthening the timed dip interval and is shown for several values. This test basically gives a measure of how far below the set operating point the emission of the cathode changes from space charge to temperature limitation. The temperature at which the emission becomes temperature-limited changes downward in early life, reaches a minimum after several thousand hours, and eventually starts to climb again, until at the end of life it reaches the operating temperature of the cathode.

The shape of the dip curve reveals a further quality of the cathode, the uniformity of work function over the surface. A dip which breaks sharply indicates uniformity; one which is well rounded, a geometrical spread of different work function. These two dip curve types are shown in Fig. 28.

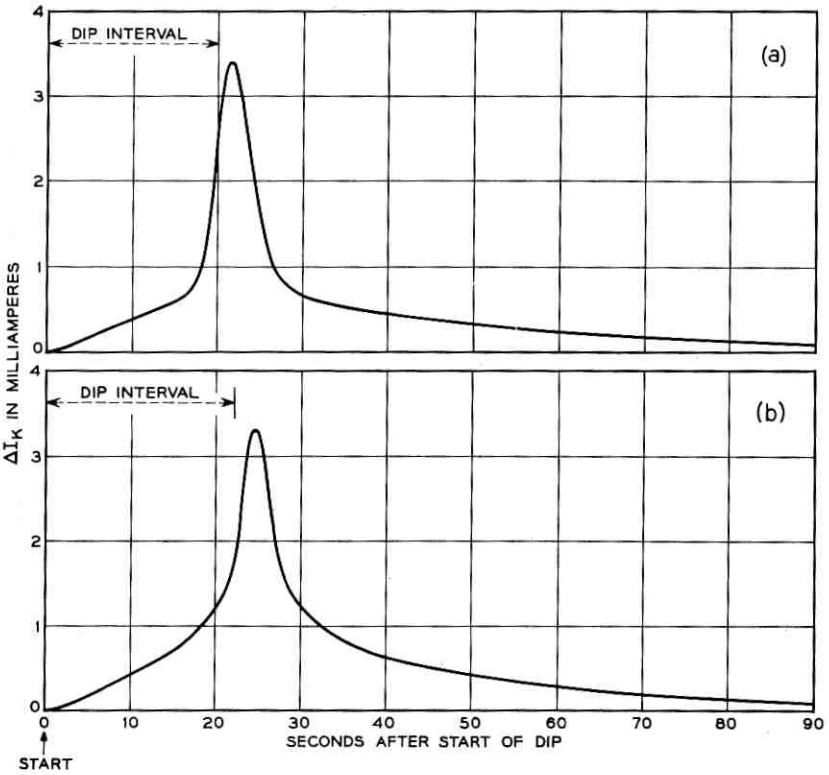

Fig. 28 — Shapes for cathode current dip curves: (a) uniform emission — uniform work function, (b) nonuniform emission caused by work function which is irregular throughout the cathode surface.

The tubes which have gone through the RF testing are now ready for the aging phase. They are installed in an aging rack. Each tube is driven by an individual high-reliability power supply, which has a large number of safety controls to prevent damage to the tube in case of certain failures. The RF drive power to each tube is also individually controlled. The cathode temperature is set at about 750°C and the tubes adjusted for 4 watts output. The tubes are tested daily and their temperature and cathode current dips recorded on a strip chart. When the activity has improved and the 20-second dip no longer exceeds 2 ma, the cathode temperature is lowered. After 1000 hours of aging, the best tubes are selected for possible fly candidates. At this point, the tubes are removed from life test and taken out of their packages to be given the most thorough mechanical inspection. The good tubes are then in-

stalled in selected focusing circuits. A series of electrical tests follows to assure tube performance. The repackaged tubes, with their own circuits, are installed once more in the life area. Activity and stability of interception currents were especially observed. Even at this point it is found that the helix and accelerator interception change slightly with improving activity levels. This phase of the aging period extends over several hundred hours.

So far the tube was approved only for continuous operation. The next phase consisted of a switched life test. The voltages were switched on and off to simulate the actual satellite conditions: 3 minutes heater warmup, 15 minutes operation, and 12 minutes cool-off. At this point, an interesting phenomenon was observed. The cathode current climbed continuously at a very small rate as switching cycles were accumulated. This was first attributed to changes in mechanical tolerances due to the heat cycling, but precise measurements of the gun dimensions discredited this theory. The change had to be attributed to changes of the cathode itself. At the same time, it was discovered that test diodes in an entirely different vehicle displayed a similar behavior. Changes of 2 per cent were observed in cathode current and gun perveance over a period of 1000 switching cycles. For this reason, all fly tubes were cycled for an excess of 1000 cycles, when the time schedule permitted.

8.6 *Final Sealup of Tube and Circuit*

At the point where a tube and its focusing circuit had proven themselves by performance, the two were mated together, a process which is irreversible, since neither tube nor circuit can be recovered. The final steps in this operation are outlined below. First, the tube is rotated and input, as well as output, pole-pieces are slightly readjusted to obtain best focus at an input level of 0 dbm. The waveguide and coaxial transitions are moved longitudinally, and the coaxial plungers trimmed to obtain a match at input and output optimized for satellite performance. The unit is now ready for final packaging. It is positioned so that the central line of the tube is vertical and the gun end is up. The tube is gently lifted off its seat about 0.02 inch and allowed to fall back into position, after which it is lifted and held 1 mil off its seat, at which point it is locked in place by soldering the collector carefully to its collector support. The one-mil gap precludes the possibility of a bend in the tube as a result of pole-piece displacement during adjustment, or by the nonsquareness of the reference surface, either on the tube or on the circuit. A bend would serve to bind the tube in its supports so that it would resist "falling" into place. As a result, the tube is fastened and supported

in a free and unstressed state. All adjustments are pinned or locked. An epoxy resin is used as an additional bond so that all individual parts (housing, magnets, pole-pieces, waveguide tube, etc.) are locked together into an inseparable integrated unit. The resin is cured and the completed package subjected to the final vibration test.

Once more the tube is installed in the life rack to be observed for a few more days. The operating voltages are set accurately to the values which are expected at the beginning of life in the satellite. Interception and activity should now have stabilized. At this point, all the records of the tube are reviewed to make sure no detail or trend in its life history has been missed. The tube is now cleared for satellite use and remains on life until called for.

The final step consists of the marriage between the TWT and its power supply. For optimum performance, the TWT voltages are adjusted individually. For reasons of efficiency of the dc-to-dc converter, this is accomplished by selecting the best taps on the primary side of the transformers. The tube, converter and the assigned microwave network are assembled for tests. Subsequently, the helix voltage is chosen and the dc-to-dc converter completed. Once the taps are set, the converter is embedded in foam: no further changes are possible.

IX. CHOICE OF CATHODE TEMPERATURE

A word is advisable on the choice of the cathode temperature. It was pointed out earlier that the life of the tube is highly dependent on the cathode temperature. To be able to compare this cathode with those of other tubes, we have tried to find a parameter which would be independent of operating temperature and the dip interval chosen for the test. It is possible from the dip curves to obtain for each tube the actual point where the tube goes into temperature-limited operation by correlating the knee of the cathode current curve with the corresponding cathode temperature. On some tubes, estimates had to be made, since they were not dipped all the way into temperature-limited emission. For comparison, a point was chosen in life as a standard time for comparison: specifically, 1000 hours. In Fig. 29, the transition temperature from space charge limited emission to temperature-limited emission is plotted for each tube in chronological order. These values are not steady-state values, since they are taken on a transitional basis; however, they suffice for comparison with other dip tests. We see that these transition temperatures lie at 550° to 600°C. Where was the operating point now chosen? Similar points of the M1789 lie about 50° higher, namely 600° to 650°C. This difference can be attributed to the lower cathode current

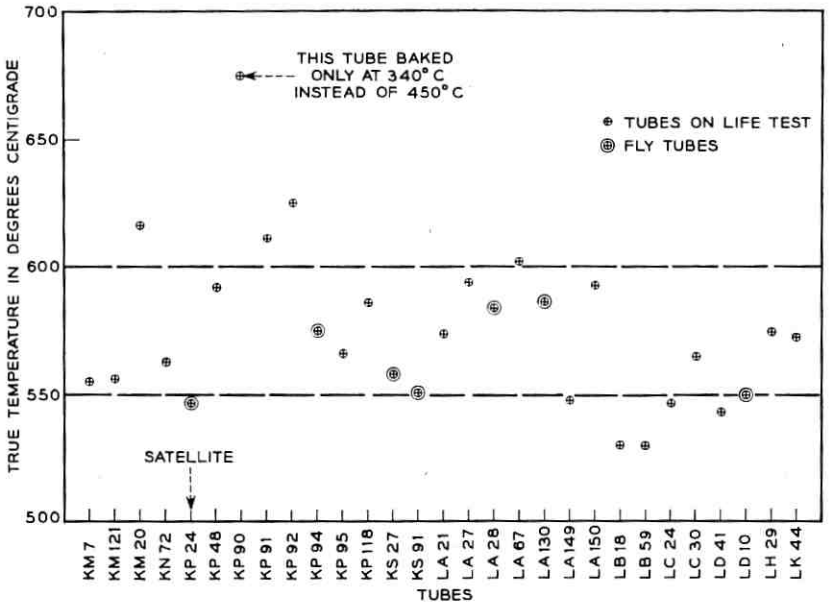

Fig. 29 — Transition temperature of cathodes for the 29 tubes put on life test (space-charge-temperature-limited emission).

loading and to the improvements in tube techniques and cleanliness. The point chosen for the M1789 was 775°, about 150° higher than the transition temperatures. It was found desirable to maintain about the same margin in the satellite tube. A lower cathode temperature would have extended the life but reduced the safety margin towards cathode deactivation; the choice was therefore made to favor reliability.

The data plotted in Fig. 29 are uniform to a high degree with the exception of tube KP90. This tube was accidentally baked at a lower temperature of 340°. This single deviation in processing resulted in an increase of the transition temperature by 100° from the average. No other tube shows such a large deviation. This test illustrates the true uniformity of all the tubes made, since no tubes were eliminated for activity reasons prior to the 1000-hour test. However, in most of the tubes the transition temperature continues to decrease with further aging; usually a minimum value is reached between 3000–10,000 hours.

X. KP24 DATA SINCE ITS INJECTION INTO ORBIT

The telemetry system in the Telstar satellite transmits once every minute the following data concerning the tube: heater voltage, helix

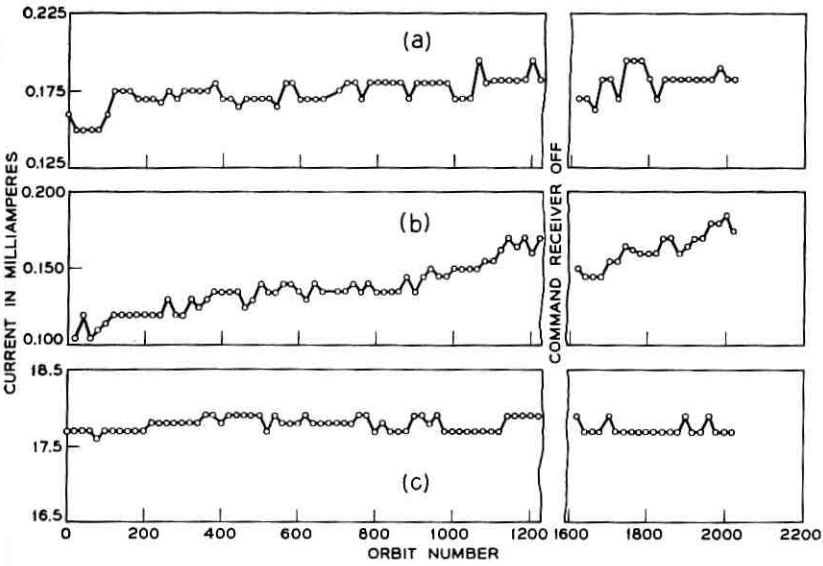

Fig. 30 — Telemetry data for KP24 after injection into orbit: (a) helix current, (b) anode current, (c) collector current.

current, accelerator current, collector current, and finally the temperature of the tube package as measured at the output waveguide flange. The values are transmitted in digital form and are therefore quantized. The smallest increments are: helix, 10 microamperes; accelerator, 5 microamperes; and collector, 200 microamperes.

In Fig. 30, the points represent data selected from active passes during which the TWT was operating under reasonably similar drive conditions. The intercepted currents on helix and accelerator vary to a certain degree; this is caused partly by the telemetry and partly by the varying experiments being performed with the satellite. Nevertheless, some trends can be observed. While the helix current remains steady, the accelerator current shows a slow but gradual increase, similar to that observed in the M1789. The collector or the cathode current (the sum of all three) shows a slight but noticeable increase, such as had been previously discussed under switched life tests. At the moment of writing (January, 1963) the tube has been turned on in excess of 400 times and has accumulated at least 100 hours of operation in orbit. There is no indication that the tube performs differently than if it had remained on the life rack.

XI. CONCLUSIONS

A high-reliability, long-life TWT has been designed, built, tested, and injected into orbit. The basic design philosophy of the conservative approach, based wherever possible on thoroughly proven experience, has paid off. There were only four new concepts used; these, however, had been thoroughly proof tested before incorporation. They are: (a) new cathode nickel (b) on-off operation (c) cathode heater structure (d) SRPM circuit. None has shown any undesirable side effects.

XII. ACKNOWLEDGMENTS

Many members of the Laboratories contributed to the successful development of the satellite traveling-wave tube amplifier. The authors wish to call attention to the excellent performance of all the highly skilled personnel involved in fabrication and assembly of the tube. Mr. C. J. Mataka was responsible for close supervision of the tube assembly line and resolution of the many problems arising from fabrication and assembly of the device. Mr. A. L. Stevens assisted in overseeing the many inspection points incident to ensuring the quality of fabrication. He also conducted tests to evaluate certain mechanical properties of the gun structure.

Mr. J. F. Milkosky undertook the mechanical development of the magnetic circuit and parts related to packaging the tube. In this work he was assisted by Mr. B. Smith. Mr. D. O. Melroy handled the interface problems which were encountered in associating the TWT with the microwave components and power supply in the satellite.

Messrs. A. J. Chick and A. C. Fodor took charge of conducting the life testing experiments. Messrs. H. J. Oudheusden, L. M. Reveron, and D. L. Van Haren were responsible for processing the completed tube on the pump station and for the complex electrical testing which immediately followed. Mr. D. L. Van Haren undertook the final development of the single-reversal magnetic circuit.

REFERENCES

1. Pierce, J. R., *Traveling-Wave Tubes*, D. Van Nostrand, New York, 1950.
2. Olsen, K. M., High Purity Nickel, Metal Progress, **72**, 1957.
3. Kern, H. E., earlier data in Proc. of 6th Nat'l. Conf. on Tube Techniques, Sept. 1962. Test diodes described in *Handbook of Physics*, **XXI**, McGraw-Hill, New York, 1958, pp. 145–146.
4. Olsen, E. G., The Use of Powdered Glass as a Binding Medium in TWT Construction, Third Nat'l. Conf. on Electron Tubes, 1956.

5. Murphy, B. T., and Kelly, J., Reversed Field Focusing, Proc. of Internat'l. Congress on Microwave Tubes, Munich, 1960; see also Winwood, J. M., Permanent Magnet Focusing of Low-Noise TWT's, Proc. of Internat'l. Congress on Microwave Tubes, Munich, 1962.
6. Laico, J. P., McDowell, H. L., and Moster, C. R., Medium Power Traveling-Wave Tube for 6000-mc Radio Relay, B.S.T.J., **35**, November, 1956, p. 1336.
7. Bodmer, M. G., Dip Testing, a New Method for Measuring Cathode Activity, I.R.E. Trans. PGED, **ED-5**, January, 1958, p. 43.

The Design and Construction of the Electronics Package

By R. H. SHENNUM and E. J. REID

(Manuscript received April 1, 1963)

The electronics system of the Telstar satellite is described from the point of view of philosophy of design and construction rather than that of circuit details. The reliability is emphasized, and steps taken to preserve the inherent reliability of the components are discussed. The physical construction of modules, subsystems, and finally the entire system is described, including the foam encapsulation and the eventual hermetic sealing of the canister.

I. INTRODUCTION

The reliability program of the Telstar satellite is based upon three factors: component reliability, conservative circuit design with few innovations, and rugged equipment design with quality construction insured by specially trained craftsmen and extensive inspection. Wherever possible, past experience with proven reliable systems provided a guide when applying these factors. In contrast to the approach used in many other satellite programs, the Telstar spacecraft contains a minimum of redundancy. It is also unusual in that the mechanical design encloses most of the electronic circuitry in a hermetically sealed canister filled with polyurethane foam. This prevents readjustment and unit replacement; however, it provides a very rugged unit which is safe from tampering. To further enhance reliability, "white room" conditions were observed during all construction stages.

II. COMPONENTS[1]

Component reliability, together with redundancy, sets an upper limit on the reliability of the system, for the circuit designer can at best preserve the inherent level of reliability built into the components furnished to him. The selection of semiconductor types was based upon proven reliability in previous systems. A large number of units of a single type

were tested, and those used in the spacecraft were obtained by choosing the best — about 33 per cent of the total number tested. These tests consisted of operating each unit at a controlled power dissipation or exposing each unit to a controlled amount of radiation while observing the degradation against time of such properties as gain, voltage breakdowns and leakage currents. To further improve reliability, deratings of approximately ten to one were typically used with respect to power rating, voltage breakdowns and leakage current.

The types of passive components used were also chosen for their proven reliability in previous systems. In addition, each component was individually tested before use. The passive components used were not a selection of the best of a large group, as with the semiconductor devices, but those components which passed the tests. This provided, in most cases, a better than 90 per cent yield from those tested. Derating factors of at least two to one were used with respect to power ratings and voltage breakdowns to improve reliability. All other special components were carefully examined and tested to insure good over-all component reliability.

The careful screening of components means that the construction program of circuit modules, subassemblies, and entire canisters need not be based on having large numbers from which to select the best units. This results in the electronic circuit tests being utilized chiefly to find design errors and interface incompatibilities.

III. CIRCUIT DESIGN

Reliable circuit operation is obtained by minimizing the need for new inventions; by basing the circuit design on well established methods; and by including in the design as much margin as power consumption, size, and weight will permit. In the case of microwave design, the Bell System has a great fund of knowledge which has been built up over the years with the two transcontinental microwave systems, the TD-2 and TH systems, operating at 4 and 6 gc respectively. Since both of these frequencies are used in the Telstar project, it was possible to follow earlier designs of such equipment as filters and frequency converters. Similarly, years of Bell System experience in designing circuits for operation from dc to very-high-frequency form a basis for development in these areas.

During the circuit development stages, the circuits were temperature cycled between $-20°C$ and $+60°C$. Circuits with components which would be severely affected by these temperature extremes were given as wide a temperature test as their components would allow. The mini-

mum design temperature range is 0°C to +40°C. To be acceptable, a circuit was required to operate completely satisfactorily within the design temperature limits and to operate with little loss in performance between the −20°C to +60°C temperature limits. Groups of circuits were also exposed to these temperature tests to investigate circuit interface problems.

As early as possible the circuit was wired into its first equipment layout form and foamed to assure proper operation in its final environment. It was then given vibration tests with vibration magnitudes equal to or greater than those specified in the satellite qualification test specification.[2] These requirements were more stringent than the conditions expected during handling and launching. Those circuits which would normally operate during the launch were electrically tested during the vibration test. Circuits not expected to be operational during the launch phase, such as the microwave circuits, were electrically tested for survival only.

Following the design of a circuit, a computer analysis was used, time permitting, to investigate the effects of variations in active and passive components which would result from temperature effects, aging, and initial tolerances. A variational study permitted the investigation of "worst-worst" conditions.

IV. EQUIPMENT DESIGN, CONSTRUCTION, AND TEST

The equipment design used in the Telstar satellite is conservative and is based when possible on past experience. No microminiaturization is utilized, but rather the usual methods associated with microwave and lower-frequency circuits have been used. To aid in explaining the equipment design approach, an example of the construction and evaluation process in the form of a regulator will be described in some detail.

The initial step in the production of a unit such as the regulator is the compiling of the necessary components. As described in a companion paper,[1] each component is serialized before being delivered to the assembly area. Clerical personnel assemble all the necessary components for a particular circuit into a kit and record the serial number of each component, together with the location of that component in the circuit. This careful record keeping on devices can be of considerable value in diagnosing failures. A case in point is the command circuit malfunction in the satellite.[3] In this case, once the transistor which caused the malfunction was determined, it was possible to review that transistor's original characteristics.

Certified wiremen with special training then assemble the circuit.

Special precautions were observed when the more delicate components were handled. Operators handling point-contact semiconductor devices wore grounded bracelets, and those handling units with critical finishes wore white nylon gloves. Fig. 1 shows the completed wiring of one of the boards making up the regulator. The miniature magnetic latching relays used for controlling the traveling-wave tube are shown together with a number of passive components. Much thought was put into the type of mechanical structure and the type of electrical connections employed in such boards to assure the necessary mechanical and electrical reliability.[4] Upon completion of wiring, the board shown in Fig. 1 is sent to the inspectors.

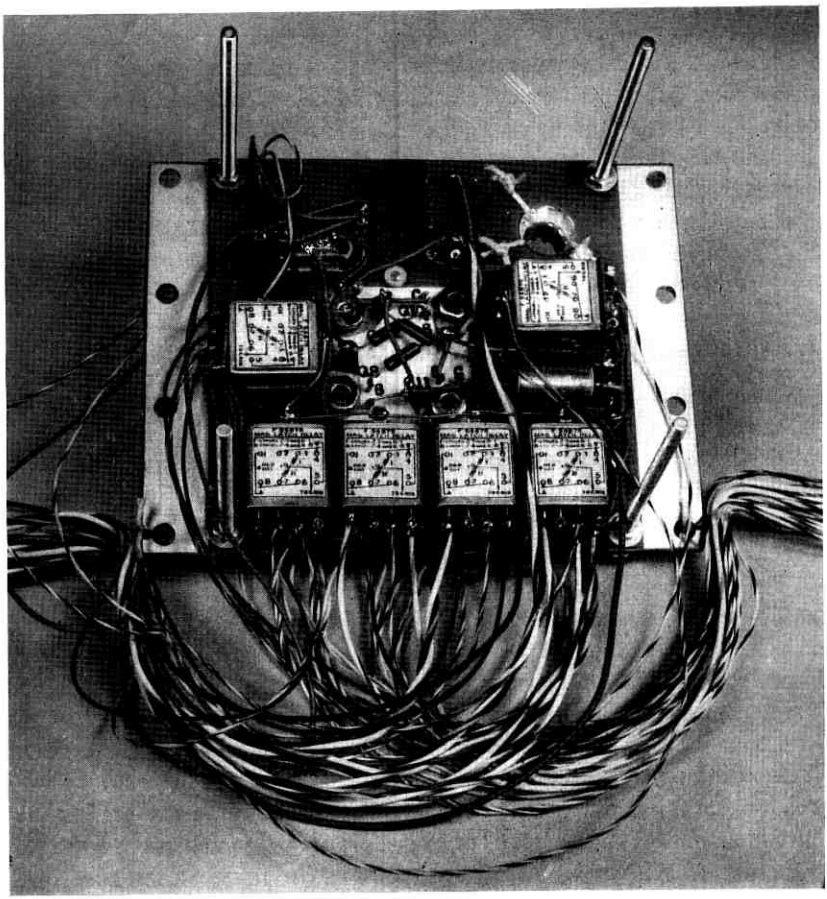

Fig. 1 — First circuit board of regulator.

Visual inspection plays an important part in assuring mechanical reliability. The Bell System's experience in the development of the submarine cable repeaters, where an equal or greater degree of mechanical reliability was necessary, had indicated the need for inspection and developed suitable methods to be used. This function was felt to be important enough to have the inspection group placed under the supervision of the engineering division. The circuits are inspected for correct wiring and every solder joint is examined under a microscope. Each component is examined for correct polarity and value; it is also examined to determine that no harm has been done to it during installation. The trained inspector also observes the over-all circuit to catch any potential trouble conditions. In all cases, a sufficient number of wiring and inspection steps is included to assure that no component is buried beneath another card or component before it has been checked. Fig. 2 shows the result of a number of such steps. The completely wired regulator in this figure is ready for extensive electrical tests.

The initial electrical tests are performed at room temperature and

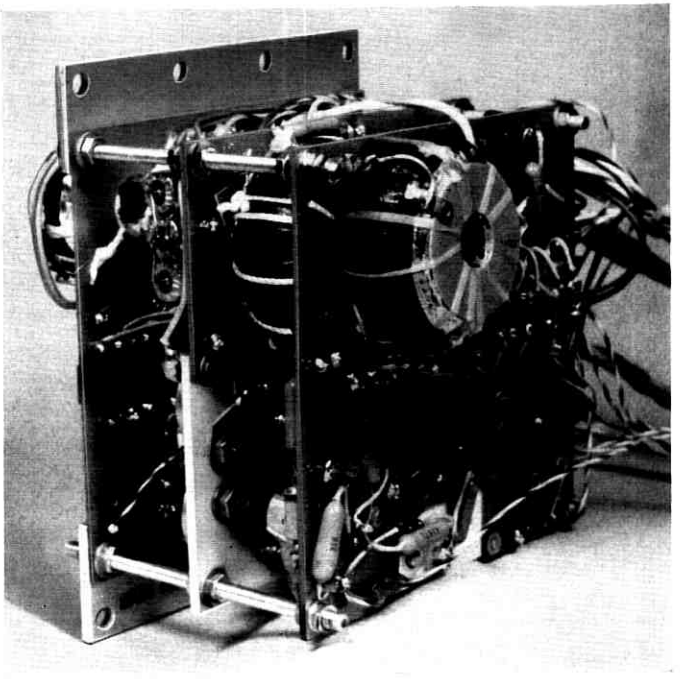

Fig. 2 — Completely wired regulator.

include any adjustments and component selection called for in the normal testing program for proper operation of the circuit. The selected components are then wired in place and inspected as indicated before. At this point, the circuit is rechecked for proper operation while it is exposed to changes in temperature, power supply voltage, and other variable quantities peculiar to that circuit. In the case of the regulator used as the example in this discussion, it is also exposed to the magnetic field of the traveling-wave tube and to a change in input voltage and output load. No vibration tests are included at this time because the unit has not yet been foamed. The foam, which encases every component, provides the necessary strength for the rather light circuit board structure.

Fig. 3 shows the regulator placed in an aluminum mold ready for foam encapsulation, and Fig. 4 shows the same unit upon completion of the encapsulating process. Special attention was given to the selection

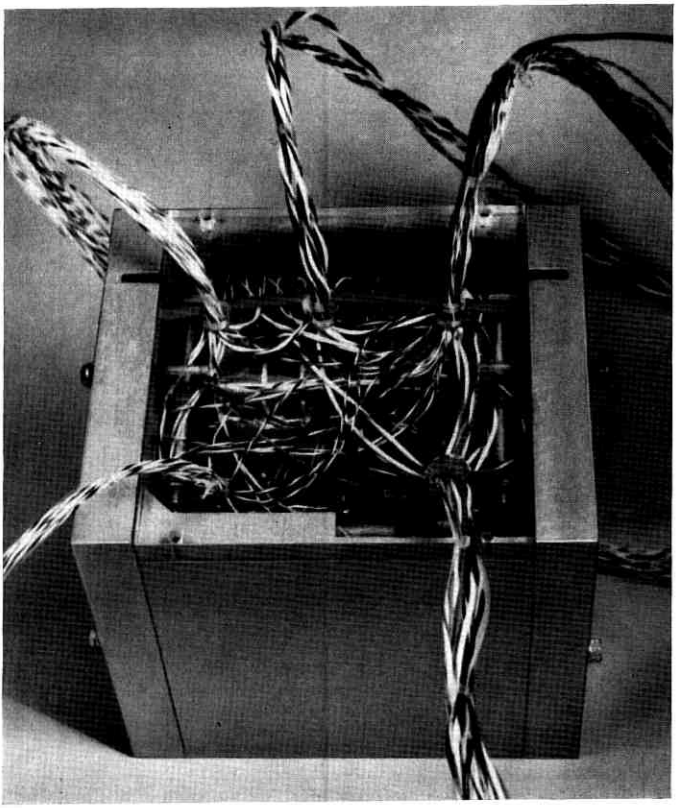

Fig. 3 — Regulator in mold ready for foam encapsulating.

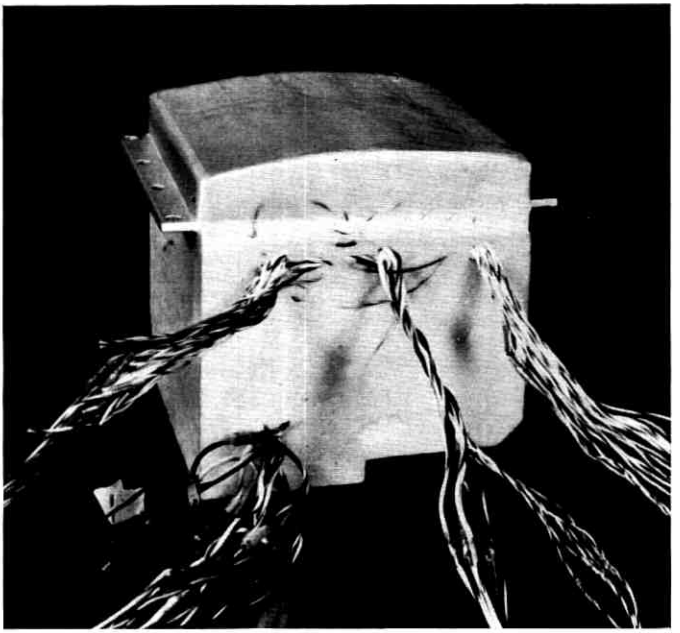

Fig. 4 — Encapsulated regulator.

of foam material and its density, to assure a reasonable compromise between supporting strength and weight.[4] Bell System experience with foam encapsulation in a missile control X-band guidance system had indicated that considerably improved mechanical reliability could be obtained by encapsulating the circuits with foam.

After foaming, the circuit is put through all the electrical tests performed prior to foaming and vibration tests with vibration magnitudes equal to those specified in the satellite acceptance test specification.[2] Because the regulator would normally operate during the launch, it was electrically tested during the vibration test. At this time, the construc tion and evaluation process of the unit is complete.

It can be seen that careful control of the assembly process plays an important part in establishing the high level of reliability which we believe to be incorporated in the Telstar satellite. Fig. 5 is a copy of the first of several control sheets describing the steps through which the regulator progressed on its way to completion. Most circuits have as many as 50 to 60 steps, which have all been recorded on such sheets. In each case, the person involved in a particular step signs his initials and the date, signifying the proper completion of his task. This careful record keeping assures no steps are bypassed, gives a permanent record

ROUTE SHEET POWER SUPPLY REGULATOR
B-890049 Iss. 3 (Schem)

B-133491 Iss. 2 (Assem)
Board 1 of 3

		Date Recv'd.	Date Compl.	Sign.
1.	Assemble board as per above drawings. Serial No. F5-8515	2-8-62	2-9-62	Jaw
2.	Record transistor and diode serial numbers	2-8-62	2-9-62	Jaw
3.	Inspect Step 1	2-10-62	2-10-62	EJM
4.	Inspect Step 2	2-10-62	2-10-62	EJM
5.	Electrical Test and Adjust	2-14-62	2-14-62	AET
6.	Inspect Step 5	2-15-62	2-15-62	EJM

B-133489 Iss. 4 (Assem)
Board 2 of 3

1.	Assemble board as per above drawings. Serial No. F5-8519	2-10-62	2-10-62	DTW
2.	Record transistor and diode serial numbers	2-10-62	2-10-62	DTW
3.	Inspect Step 1	2-12-62	2-12-62	JaF
4.	Inspect Step 2	2-12-62	2-12-62	JaF
5.	Electrical Test and Adjust	2-16-62	2-16-62	AET
6.	Inspect Step 5	2-18-62	2-18-62	JaF

B-133490 Iss. 7 (Assem)
Board 3 of 3

1.	Assemble board as per above drawings. Serial No. F5-8523	2-14-62	2-14-62	Jaw
2.	Record transistor and diode serial numbers	2-14-62	2-14-62	Jaw
3.	Inspect Step 1	2-16-62	2-16-62	EJM
4.	Inspect Step 2	2-16-62	2-16-62	EJM
5.	Electrical Test and Adjustment	2-19-62	2-19-62	AET
6.	Inspect Step 5	2-21-62	2-21-62	EJM

ATTACHED PAPERS: Transistor and diode serial numbers

Fig. 5 — Copy of one of the regulator route sheets.

of who handled the unit, and keeps everyone constantly aware of the need for care and caution. If trouble should develop, the sheets provide a history from which the trouble can be traced and evaluated.

V. CANISTER AND ITS ASSEMBLY INTO THE SPACECRAFT

After every individual unit such as the regulator is completed, the process of mounting in the canister is started. Fig. 6 shows the canister in an early stage of assembly, together with the electronic equipment it will contain when completed. The traveling-wave tube is shown directly below the canister on the rotary table of the stand. Clearly visible are several pieces of silver-plated magnesium waveguide, and near the extreme left is the regulator which has been described in some detail in the previous section. Fig. 7 shows the same canister almost fully as-

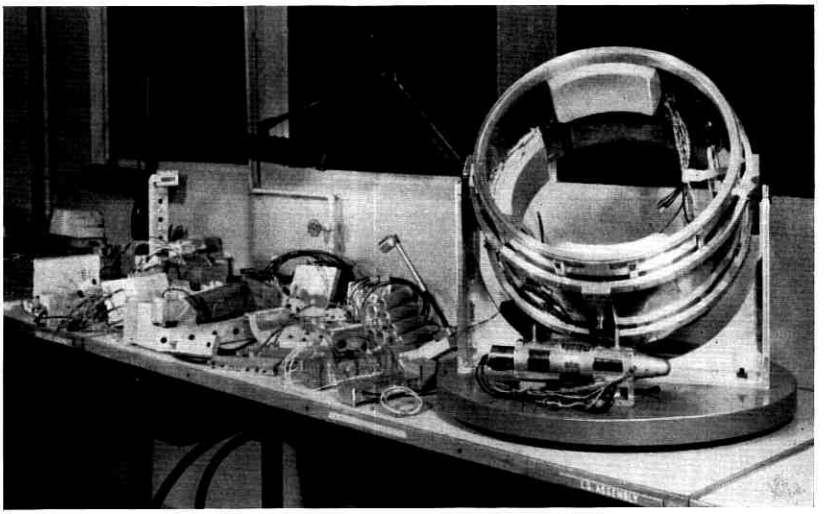

Fig. 6 — Partially assembled canister with subassemblies.

sembled, with the traveling-wave tube mounted in the center and the waveguide surrounding it in a roughly circular arrangement. The digital, low-frequency, and VHF circuits fill in the remaining available space. The units are interconnected in nearly all cases by crimped connections. The use of connectors is kept to a minimum, because of the difficulty in determining whether a good connection has been made by the cable into each of the mating parts and whether the mating parts have been properly seated into each other. The connectors used in the canister are all tested for shorts during various mechanical manipulations of the cable and connector, and most are X-rayed. The X-ray analysis is only partially successful, however, because the inner connection is masked by the massive body of the connector.

Prior to the foaming operation, the completed canister is given an all-feature inclusive electrical test at room temperature. The only parameter changed during this test, other than the radio frequency signals, is the supply voltage. The goal of this test, as well as future tests, is not to establish a level of reliability but rather to uncover design oversights and errors made in the design process. Upon successful completion of this test, the canister is subjected to a +25°F temperature electrical test, and a +95°F* temperature electrical test. These electrical tests are not as inclusive as the initial program; however, they give a complete check of the satellite's operation.

* This value was used rather than the 40°C design value to protect the Ni-Cd cells, as explained in Ref. 5.

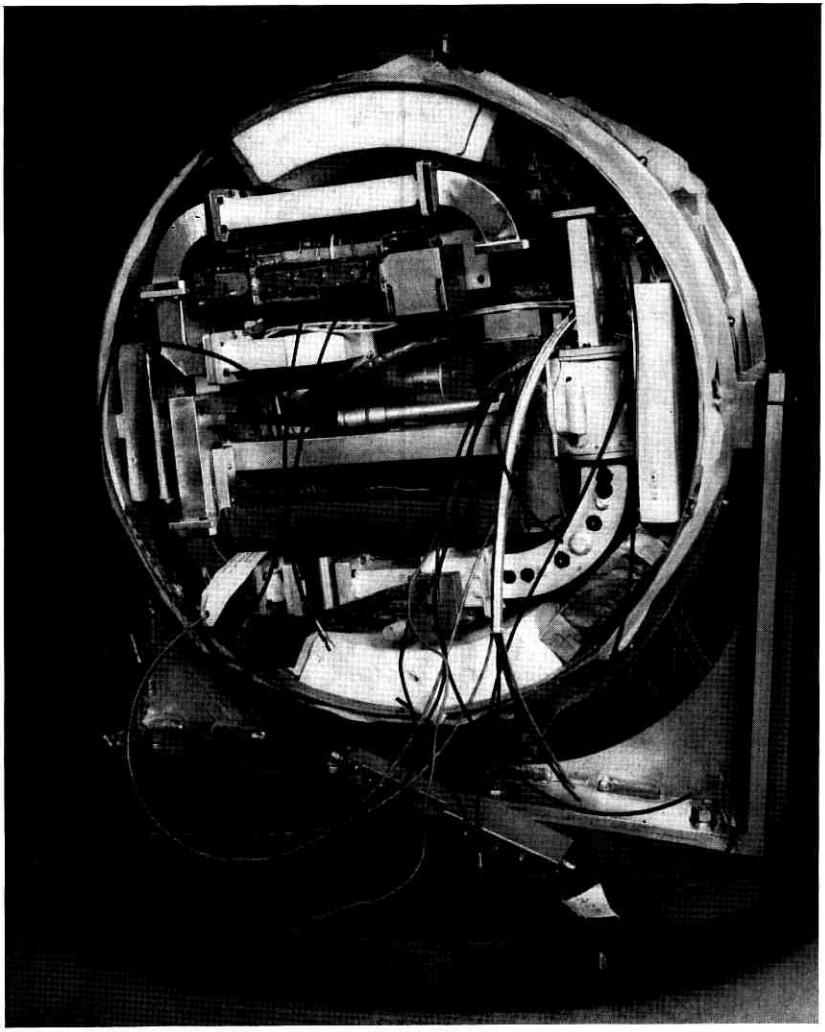

Fig. 7 — The electronics canister.

The next step is the foam encapsulation of the canister. Fig. 8 shows the canister in the last stages of the foaming process. A detailed explanation of the process is given by Shennum and Haury.[4] The properties of foam in a hermetically sealed canister in a radiation environment have been investigated; tests indicate the foam to be a stable material. During the foaming process the chief gaseous material generated is carbon

dioxide with only the slightest traces of potentially corrosive materials. Careful chemical analysis has indicated that these materials are of such small quantity that they represent no threat to the enclosed components for periods of at least several years.

Upon completion of the foaming process, the canister is subjected to a +125°F temperature soak for six hours, a 0°F temperature soak for six hours, a +25°F temperature electrical test, and a +95°F temperature electrical test. These tests are the same as the last complete tests performed on the canister prior to foaming.

Fig. 9 shows the completed canister with the domes welded in place. Before it is installed in the frame, the hermetically sealed canister is

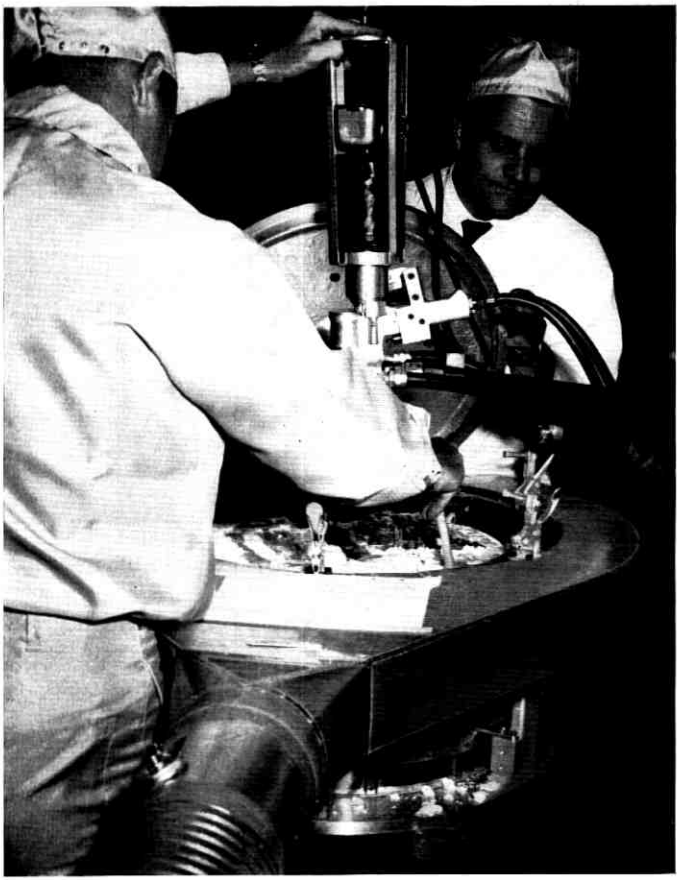

Fig. 8 — Foam encapsulation of the canister.

Fig. 9 — Mounting of electronics canister into the frame.

checked for leaks.[4] There are a number of headers which provide electrical access to the circuitry inside the canister for such things as solar power, antenna feeds, and the radiation experiment. It is important that these headers as well as the canister dome welds be leakproof, for a complete loss of pressure in the canister when in orbit might cause permanent damage to the circuits within. Upon successful completion of the leak test, the canister is wrapped with insulating material and the thermal shutter is attached.[4] A final electrical test at room temperature assures that the canister has not been harmed during performance of the operations described.

The canister is then lowered into the frame and attached to the mounting rings, which are suspended from the frame by nylon lacing.[6] The required electrical connections are made between the external framework and the canister, the top half of the frame is attached, and the aluminum panels which support the 3600 solar cells are electrically connected and screwed into place. This completes the construction of the satellite. Prior to the detailed environmental tests which the complete satellite must undergo, an all-feature electrical test is conducted to assure that the above assembly process was complete and correct.

The detailed environmental tests include vibration on the thrust axis and on the lateral axis, and a thermal-vacuum test.[2] After every stage of the above tests, complete electrical tests are made. Each electrical test is designed to indicate that no harm was done during the environmental test. Upon completion of these tests, a successful leak test and a successful all-feature inclusive electrical test indicate that the spacecraft is of launch quality.

Fig. 9 also illustrates the working conditions which were enforced during the entire construction process. The construction area was air-conditioned; air-conditioning provided triple filtering to remove foreign particles, a 75°F* temperature, and a 35 per cent† relative humidity. In addition to the special mechanical and electrostatic air filtering, stringent controls were imposed to minimize the introduction of contaminants. These included:

1. Providing special lint-free uniforms and caps for all white area operating personnel.
2. Providing lint-free smocks and caps for all occasional personnel and visitors. Visitor entry was minimized.
3. Requiring that all personnel wash their hands and clean their shoes on each entry.
4. Cleaning all equipment to be brought into the white areas with alcohol and lint-free cloths.
5. Using paper, writing implements, and cloths that would not produce lint or dust. For example, ball point pens were used in place of pencils and dust-free crayon boards were used in place of chalk boards.
6. Mopping and dusting all white areas daily.

To monitor the effectiveness of this program, a dust count was made twice weekly and posted on local bulletin boards. The Bell System's experience in the construction of the submarine cable repeaters had

* Temperature was maintained at nominal 75°F, but was always in the range 73 to 77°F.

† Relative humidity was maintained at nominal 35 per cent, but was always in the range 30 to 40 per cent.

established the value of this sort of environment and discipline in the construction of high-reliability equipment.

VI. SUMMARY

The care exercised in assuring a spacecraft of maximum reliability has proven valuable. An unexpected level of radiation inside the canister of two orders of magnitude above the anticipated value caused command decoder circuit operation to become intermittent after four and one-half months in space with over 1100 orbits around the earth. This unexpected radiation caused one command link to become intermittent after one month of operation. The command link is completely redundant, however, so normal operation of the satellite continued. It was not until four and one-half months had passed that the other command link became intermittent and hence operation of the satellite curtailed.

It was after the second command link had failed that it was possible to make meaningful experiments on the satellite in space to determine the source of trouble. Telemetry continued to operate giving indications that the command receiver was operating normally. Exercising the command decoders with a modified command code finally operated the satellite via the command link which had failed first. This isolated the failure in that decoder to a single transistor stage.[7] The cause of the second command link failure has not been so narrowed as yet. Following the removal of power from the decoders for several passes, normal commands operated the satellite via both command links. This recovery characteristic, plus other observations at the original time of failure, indicated that the trouble was associated with a surface ionization effect on the active surfaces of transistors caused by radiation.

The telemetry unit, which has continued to operate satisfactorily, supplies information concerning the health of other parts of the system, including the communications repeater, the battery and the solar plant, and indicates that all units in the satellite are operating normally. By the use of normal commands, the Telstar repeater is again carrying communications information on an operational basis. These tests, carried on from Andover to Andover and from Andover to both England and France, indicated that the communications repeater was operating with no measurable degradation. A second period of loss at command began in late February, 1963.

VII. ACKNOWLEDGMENTS

As in any corporate effort, many people contributed to the work described in this paper. The leadership and advice of Mr. E. F. O'Neill is particularly worthy of acknowledgment.

REFERENCES

1. Peck, D. S., and Wooley, M. C., Component Design, Construction and Evaluation for Satellites, B.S.T.J., this issue, p. 1665.
2. Delchamps, T. B., Jonasson, G. C., and Swift, R. A., The Spacecraft Test and Evaluation Program, B.S.T.J., this issue, p. 1007.
3. Mayo, J. S., Mann, H., Witt, F. J., Peck, D. S., Gummel, H. K., and Brown, W. L., The Command System Malfunction of the *Telstar* Satellite, B.S.T.J., this issue, p. 1631.
4. Shennum, R. H., and Haury, P. T., A General Description of the *Telstar* Spacecraft, B.S.T.J., this issue, p. 801.
5. Moose, L.. F, and Bomberger, D. C., Nickel-Cadmium Cells for the Spacecraft Battery, B.S.T.J., this issue, p. 1687.
6. Hrycak, P., Koontz, D. E., Maggs, C., Stafford, J. W., Unger, B. A., and Wittenberg, A. M., The Spacecraft Structure and Thermal Design Considerations, B.S.T.J., this issue, p. 973.
7. Peck, D. S., Blair, R. R., Brown, W. L., and Smits, F. M., Surface Effects of Radiation on Transistors, B.S.T.J., **42,** January, 1963, p. 95.

The Solar Cells and Their Mounting

By K. D. SMITH, H. K. GUMMEL, J. D. BODE, D. B. CUTTRISS, R. J. NIELSEN and W. ROSENZWEIG

(Manuscript received March 28, 1963)

Objectives in development of the solar plant for the Telstar spacecraft were to provide a power source which would withstand launching stresses and the expected space environment, with optimum end-of-life performance. Radiation damage to the silicon solar cells is the primary factor limiting their useful life; the effect of energetic protons or electrons is the generation of recombination centers in the silicon which reduce the minority-carrier diffusion length and therefore the long-wave response of the cell.

The spacecraft solar cells use the n-on-p structure, in preference to conventional p-on-n structure, to obtain a factor of 3 to 10 increased life expectancy. Response to light in the 0.4 to 0.7 micron range is enhanced by using a thin n-layer (about 0.5 micron) and an antireflection coating with minimum reflectance at 0.55 micron wavelength. Early estimates of electron and proton fluxes in the satellite orbit showed that even the best cells would not give sufficient life without radiation shielding. Therefore the cells are protected against electrons of energy up to 1 Mev by 0.3 gm/cm² sapphire cover plates. The cell mountings are designed to withstand peak vibration stresses of 200 g and repeated temperature cycles from +65°C to −100°C.

The 3600-cell solar power plant is composed of 300 twelve-cell groups of 1 cm × 2 cm cells, yielding a nominal initial power of 14 watts at 28 volts for any spin-axis orientation relative to the sun. Telemetry information on performance of the solar plant indicates degradation of the shielded solar cells equal to that measured in the laboratory on unshielded cells with a 1-Mev normal incidence flux of 6 × 10¹² electrons/(cm² day). From this comparison it is estimated that the plant will degrade to 68 per cent of its initial output after two years in orbit.

I. INTRODUCTION AND BACKGROUND

1.1 *Introduction*

General objectives in design of the solar plant for the Telstar spacecraft were to provide cells and mounting arrangements suitable for

prolonged operation in a radiation environment and, consistent with the state of technology and the program schedules, to optimize the output per cell after some years in orbit. Preliminary estimates clearly indicated that deterioration of cell output through energetic particle radiation damage would be the most serious effect, and that, unless this damage could be held within reasonable bounds, we would be forced to overdesign the initial power considerably, perhaps by a factor greater than two, as compared to end-of-life requirements. Answers to the following questions were urgently needed:

(1) What power must be supplied by the solar plant?

(2) What orbit will be used?

(3) What radiation will be encountered?

(4) What will be the effect of this radiation on the solar cells?

(5) What design choices may be made and how do they interact to affect life?

(6) What other factors are of importance besides radiation effects?

(7) What temperatures and temperature gradients must be designed for?

(8) Can manufacturing feasibility be shown for structures of optimum or near-optimum design?

This report will consider: the radiation effects study; design, fabrication and evaluation of the solar cells; design and engineering of the mounting of solar cells into groups; mounting and arrangement of cell module groups on the satellite; performance estimates and measurements leading to the choice of total number and connection of cells; and measurements of performance. It begins with consideration of the historical background of the solar cell and ends with evaluation of the flight performance.

1.2 *Background*

Silicon photovoltaic converter cells of moderate-to-high solar conversion efficiency were first prepared in 1954.[1] In the following two years, a few cells with 11 per cent conversion efficiency were made, and in the laboratory it became possible to fabricate cells in the 8 per cent to 10 per cent range with good yield.[2] The process was at this time given to Bell System licensees, some of whom continued development through the next several years.

In the early development, cells of both p-on-n and n-on-p structure were made. However, during the greater part of the development program n-type silicon of appropriate resistivity was more readily available

than p-type; also, the p-on-n cells made at that time gave somewhat higher conversion efficiency than n-on-p cells — perhaps because of the low reflectance of the degenerate surface layer characteristically resulting from the boron trichloride diffusion process. The result was that the standard or conventional solar cells made in the U. S. have been of the p-on-n structure. Russian development engineers, and possibly others in Europe, appear to have concentrated on n-on-p cells, perhaps because of material availability or the state of their diffusion technology, or both.

3.1 *Principles of Operation*

A brief discussion of the operation of the solar cell is in order as an introduction to more detailed consideration of the merits of different cell structures and effects of radiation and other environmental factors. The silicon photoelectric energy converter or solar cell, shown schematically in Fig. 1, is representative of a class of devices in which radiant energy is absorbed within a material, thereby upsetting an equilibrium condition and permitting electrical power to be delivered to an external circuit. In the solar cell, the absorbed photons create electron-hole pairs in the silicon. In the frequency range of interest, one pair is produced for each photon.

Referring to Fig. 2, it can be seen that events subsequent to the arrival of photons at the cell surface may be:

(1) Photons are reflected and thus no energy is available.

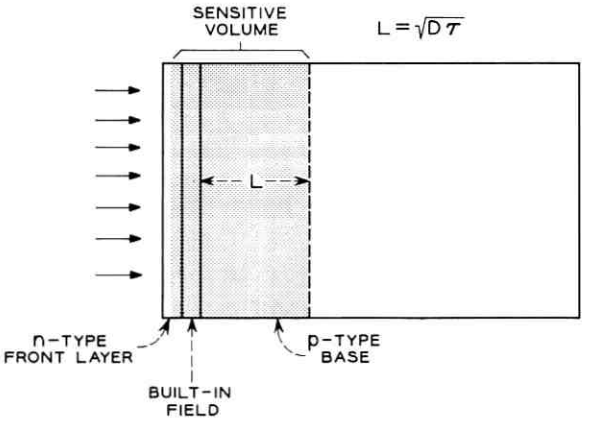

Fig. 1 — Schematic of n-on-p solar cell.

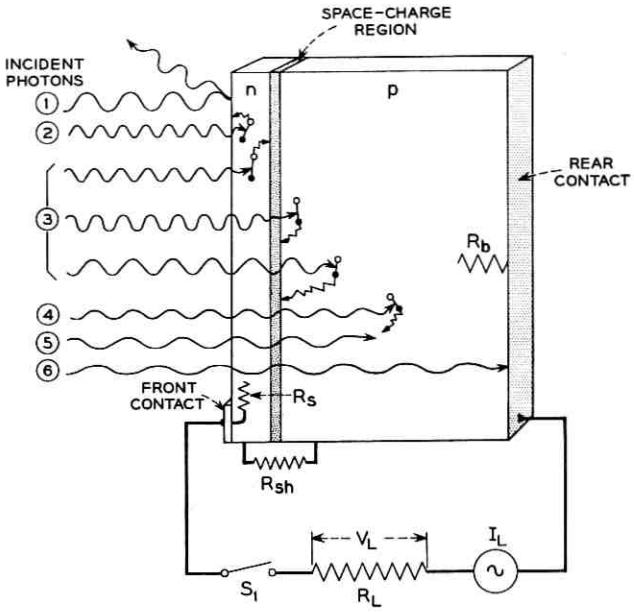

Fig. 2 — Photon and resistive losses.

(2) Photons are absorbed near the cell surface, creating hole-electron pairs, but the holes recombine with electrons without reaching the field region at the p-n junction. No electric energy is available from this reaction; however, thermal energy appears.

(3) Hole-electron pairs are created near enough to the junction for the minority carrier to reach the field region and cross the junction, contributing to the useful output current. Some heat is also generated.

(4) Pairs are created, but too far from the junction to be useful.

(5) Photons are absorbed, but have insufficient energy to create hole-electron pairs. Only heat is generated.

(6) Low-energy photons may not be absorbed in the semiconductor.

Since only the photons of (3) are effective in contributing to the electrical output of the cell, every effort will be made to optimize conditions so as to make use of as many photons as possible.

The external power which can be generated by the charge carriers which reach the junction is affected by the following considerations:

(a) The terminal voltage of the device cannot exceed that value which will drive across the junction a forward current equal to the photon-generated current. If we consider the situation with switch S_1 of

Fig. 2 open, we see that the forward bias current will just equal the generated current; the efficiency will then be zero.

(b) The generated current must flow to the external circuit through the series resistance R_s of the diffused layer and the series resistance of the semiconductor body, R_b. Generally, the body resistance can be made much lower than the surface layer resistance.

(c) There will be some shunt resistance, R_{sh}, effectively in parallel with the p-n junction. Generally this may be neglected in power circuits.

From the above discussion, it becomes evident that performance optimization will require consideration of:

(1) the spectral distribution of solar radiation
(2) the environment
(3) the properties of the semiconductor
(4) reflection losses
(5) recombination losses
(6) parasitic resistive losses
(7) load impedance and
(8) the useful life desired — if the environment is destructive.

1.4 *Significance of Van Allen Belt*

Before 1957, estimates of expected life of satellite solar power plants did not generally include deterioration of performance resulting from energetic particle radiation, since no continued high-intensity source was known and the integrated effects from cosmic rays and solar flares were not expected to be serious. The discovery of the Van Allen belts[3] changed this situation completely. For satellites at altitudes in the 1000–10,000-mile range, particle radiation is the principal cause of solar cell performance loss. Therefore, it became of immediate importance to evaluate the radiation effects and, if possible, design solar cells and solar power plants to be radiation resistant. A development program initiated at U. S. Army Signal Research and Development Laboratories (USASRDL), with the objective of obtaining solar cells of improved conversion efficiency, had resulted in a feasibility demonstration of n-on-p cells comparable in conversion efficiency to the p-on-n cells commercially available in 1960. Also, these cells had a thin n layer, so they were more sensitive in the short-wave end of the visible spectrum and better matched to space sunlight than conventional cells.

In the course of radiation evaluation experiments[4] on USASRDL cells conducted by Radio Corporation of America under NASA contract, these n-on-p cells were found to be significantly more resistant to both

electron and proton radiation than p-on-n cells of equivalent initial performance. On December 8, 1960, USASRDL presented their results, together with a complete description of their laboratory scale fabrication operations for the n-on-p cell, to representatives of the major industrial laboratories.

Bell Telephone Laboratories development effort on the radiation-resistant n-on-p cell was initiated in October, 1960, as a result of the early radiation reports[5,6] and informal discussion with Signal Corps personnel. Some of the Laboratories staff assigned to this development had also engaged in the p-on-n cell feasibility development (1955–56), and so had considerable experience in solar cell technology. Laboratory fabrication of n-on-p cells was undertaken about the end of October, 1960, and the first cells exhibiting satisfactory performance were made about a month later.

1.5 *Solar Cell Requirements for the Telstar Spacecraft*

During the early part of the n-on-p solar cell development, and even into the initial Western Electric Co. fabrication, the satellite power requirements were not firm and the number of cells to be used on each vehicle was not known. The objectives were to achieve the highest end-of-life performance consistent with manufacturing feasibility. Having established this performance level, the total number of cells required for a particular end-of-life power requirement could be determined to the accuracy with which the environmental conditions could be predicted. Coordinated work on evaluation of radiation effects, technology of cell fabrication, environmental studies, and satellite power drain was therefore required. This work is considered in the following sections.

II. RADIATION DAMAGE STUDIES

2.1 *Background*

Proton and electron particle radiation, such as is found in the Van Allen radiation belts, produces permanent damage in silicon by reduction of the minority-carrier lifetime. This degrades the solar cell performance by decreasing the collection efficiency for carriers generated by penetrating light and by increasing the saturation current of the junction. The degradation of lifetime with particle bombardments of the type and energy expected in the Van Allen belts is thus of primary interest, as is the correlation between the performance of a given type of solar cell and its bulk minority-carrier lifetime.

The type of information on radiation damage in semiconductors available at the beginning of the project is quite well summarized in Ref. 7. Work on damage rates for protons had been almost nonexistent (the nature of the defect was considered too complex to allow simple analysis), and the electron damage studies had emphasized the search for the location of energy levels in the forbidden gap. All evaluations of the defect introduction rates had indicated that the results were dependent on the presence of impurities, both controlled and uncontrolled. Electron spin resonance experiments carried out since that time have indicated that the important defects, at least in n-type silicon, arise from complexes of vacancies in association with impurity atoms.

In light of this situation the radiation damage problem was approached with the following objectives:

(1) the evaluation of the outer space solar cell performance on a good statistical sample of cells bombarded by a convenient source of radiation (1-Mev electrons) and the correlation of this performance with the minority-carrier lifetime;

(2) the determination of lifetime degradation rates for protons of various energies and for electrons of various energies and under various shielding thicknesses; and

(3) the synthesis of the above information for the best available Van Allen belt spectrum with the assumption of "equal performance for equal lifetime" for a specific type of cell.

2.2 *Measurement Techniques*

The most important parameter characterizing the outer space performance of the solar cell is its outer space short-circuit current. Once this quantity has been accurately determined, the output characteristics can be measured under any convenient light source whose intensity has been adjusted to produce the predetermined outer space short-circuit current.

Determination of outer space short-circuit current was carried out by measuring the response of the cells at various discrete wavelengths and using this information to synthesize the outer space cell response.[8] The synthesis is achieved by multiplying the response at a given wavelength by an appropriate weighting factor, so that the summation of these products over all wavelengths yields the integral which represents the outer space short-circuit current. This procedure also allows one to assess the contributions to the total current of the various wavelength components, and thus to optimize the design in regard to spectral response.

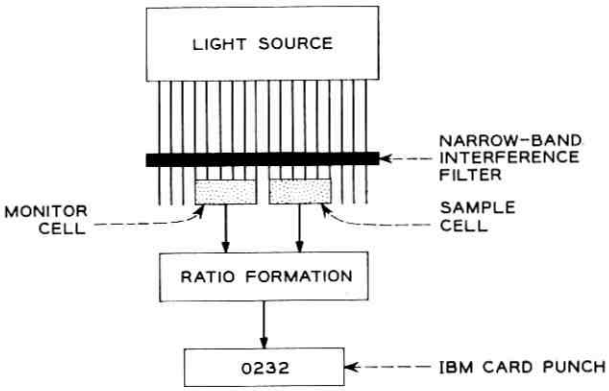

Fig. 3 — Schematic representation of spectral response ratio measuring apparatus.

An automatic test set was developed[9] which carries out spectral response measurements at eight wavelengths, in addition to making five other tests which serve to evaluate the cell junction characteristics. Fig. 3 shows schematically the method used for measuring the spectral response. Electronic ratio formation of the response of the sample relative to the monitor cell is used to eliminate the influence of fluctuations and aging in the light source. All measurements appear in digital form and are punched on IBM cards to permit further processing.

The minority-carrier lifetime was determined by measuring a related parameter, the minority-carrier diffusion length. Diffusion length measurements were carried out by a technique which utilizes the ionizing properties of penetrating radiations such as high-energy electrons, protons, and gamma rays.[10]

2.3 *1-Mev Electron Statistical Experiment*[11]

A statistical evaluation of solar cell performance was carried out with a 1-Mev electron Van de Graaff generator. Groups of 16 or more solar cells of the following types were used:

(1) Blue-sensitive n-on-p cells produced by Western Electric Co.: these cells were randomly selected from a lot of 10,000 cells, from which only those cells having an efficiency less than 7.5 per cent under outer space light had been removed.

(2) Normal p-on-n cells secured from a commercial source and rated as 14 per cent efficient under tungsten light.

(3) Blue-sensitive p-on-n cells secured from a commercial source and rated as 12 per cent efficient under outer space light.

To achieve uniform exposure for all cells, the solar cells were mounted near the perimeter of an aluminum disk, which was continuously rotated during the irradiations in such a way that the cells passed through the center of the beam.

The cells were irradiated in five steps to integrated fluxes of 1.8×10^{13}, 9.0×10^{13}, 5.4×10^{14}, 2.7×10^{15} and 1.8×10^{16} electrons/cm^2. Before the first and after each successive bombardment the cells were subjected to optical and electrical measurements and to measurements of the minority-carrier diffusion length. The results of the experiment are shown in Figs. 4, 5, and 6. Fig. 4 is a plot of the outer space short-

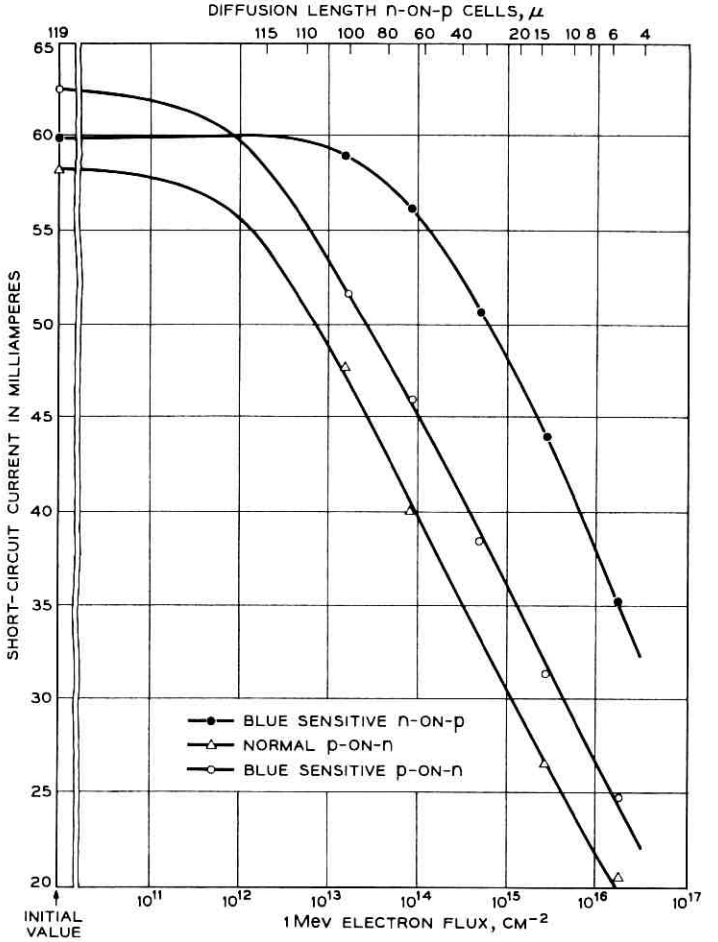

Fig. 4 — Outer space short-circuit current as a function of 1-Mev electron flux.

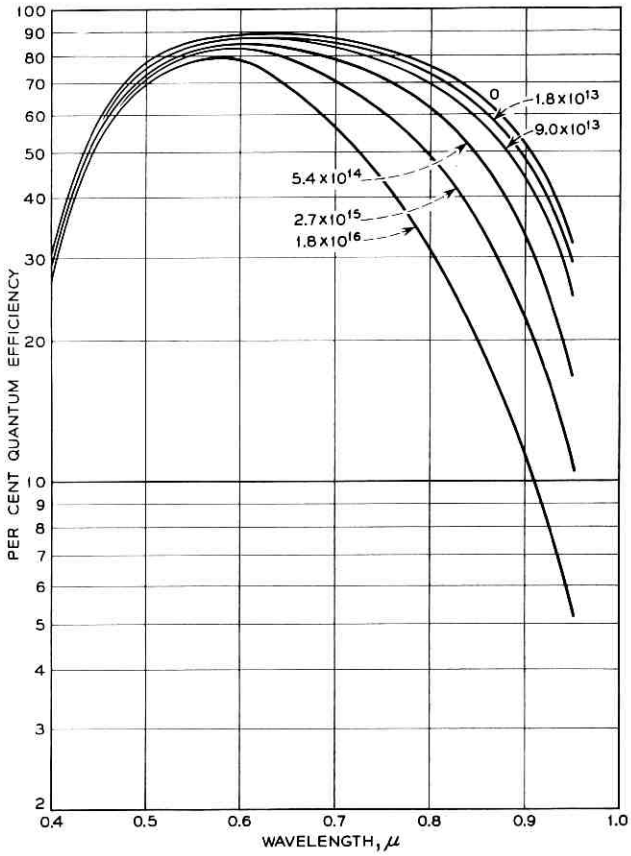

Fig. 5 — Per cent quantum efficiency as a function of wavelength for n-on-p cells, with 1-Mev electron flux as parameter.

circuit current as a function of bombardment flux. A detailed analysis[11] shows that the short-circuit current degradation is consistent with the diffusion length degradation and its effect on the quantum efficiency. Fig. 5 is a plot of the per cent quantum efficiency, defined as the number of carriers collected per 100 incident photons of a given wavelength, as a function of wavelength for various levels of bombardment of the n-on-p cells.

The predicted maximum power for outer space sunlight as a function of flux is given in Fig. 6. The decrease in maximum power with bombardment is caused not only by the decrease in short-circuit current but also by the degradation of the junction characteristics.

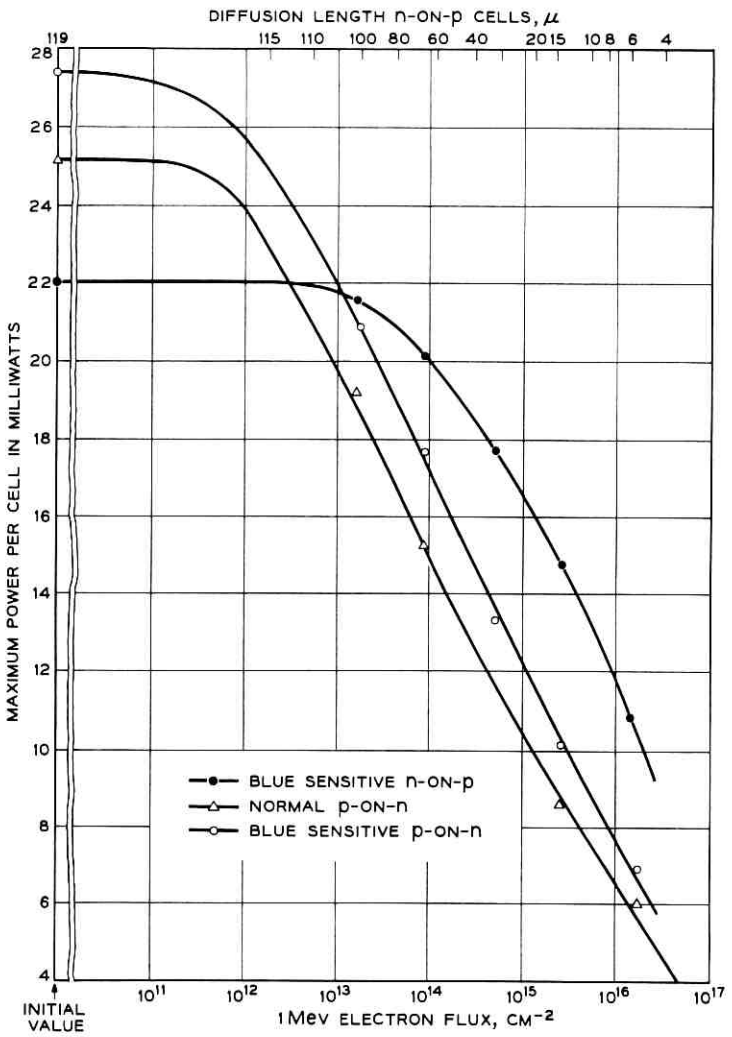

Fig. 6 — Outer space maximum power as a function of 1-Mev electron flux.

2.4 *Proton Bombardments*[12]

The proton bombardment damage study of solar cells required the use of four accelerators for coverage of the energy range of interest. At the higher-energy accelerators, the solar cells were stacked with aluminum absorbers to allow a simultaneous exposure at energies ranging from the initial beam energy down to about 20 per cent of this value.

The ionizing property of the proton beams was used to monitor the radiation-induced diffusion length changes. This change was found to follow quite closely the formula

$$\frac{1}{L^2} = \frac{1}{L_0^2} + K\Phi \tag{1}$$

in which Φ is the bombardment flux in cm^{-2}, L is the diffusion length in cm for that flux, and L_0 is the initial diffusion length. The damage coefficient, K, can thus be determined as a function of proton energy in these experiments. The damage coefficient, K, is a measure of the damage rate for a given type of radiation on the cell. The relative fluxes of two different radiations to produce the same damage may be obtained by forming the inverse ratio of their damage coefficients.

The results are summarized in Fig. 7, which is a plot of K vs proton energy. The K values appearing in the figure are those which are observed after two weeks of room temperature annealing, which results in a recovery of about 15 to 20 per cent in diffusion length. Relative K values were also obtained for one set of 1 ohm-cm p-on-n cells in the energy range 16.8 Mev to 130 Mev, and were found to be greater by a factor of 6.2 ± 2 independent of energy.

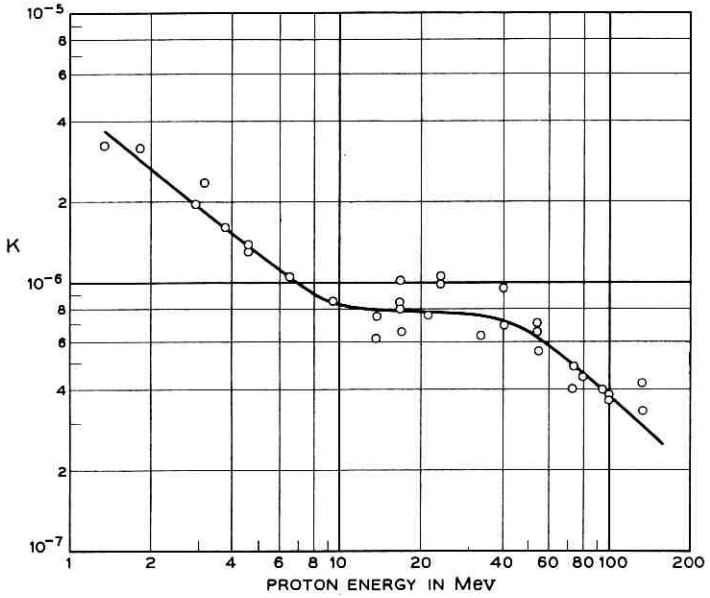

Fig. 7 — Damage rate as a function of proton energy.

2.5 *Original Estimates of Solar Plant Radiation Damage*

During the design phase, the data available for estimating the Van Allen belt radiation fluxes were quite limited. An integral omnidirectional proton spectrum was estimated by constructing a composite curve which above 40 Mev had a slope as determined by Freden and White,[6] and at lower energies as determined by Naugel and Fichtel.[13] Such a curve was made to pass through Van Allen's[3] point, 2×10^4 cm^{-2} sec^{-1} at 40 Mev for the heart of the belt. The resulting omnidirectional integral spectrum is shown in Fig. 8. For protons, the effect of shielding can be taken into account readily by making use of the range-energy relationship to calculate the energy attenuation. The result of shielding calculations is given as the upper curve in Fig. 9. The calculation is based on the proton spectrum of Fig. 8 and expressed in terms of an equivalent 1-Mev electron flux that would cause equal damage when normally incident on unprotected cells. This curve shows that the damage is reduced by a factor of about 10 when the shielding thickness is increased from 0.1 to 0.3 gm/cm^2. The relatively smaller advantage with larger shielding thickness is mainly due to the hardening of the proton spectrum for energies above 40 Mev. The shielding thickness used on the Telstar spacecraft is about 0.3 gm/cm^2, in the form of 30 mils of sapphire.

The electron component was estimated from Van Allen's[3] measurements, which indicated for the heart of the inner belt omnidirectional

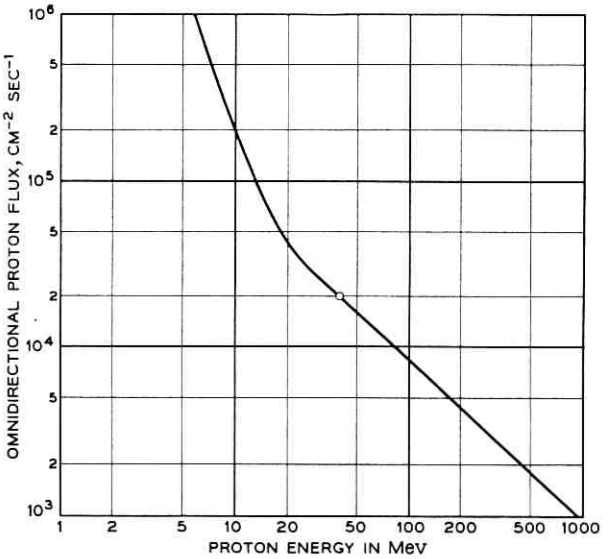

Fig. 8 — Omnidirectional integral proton flux as a function of energy.

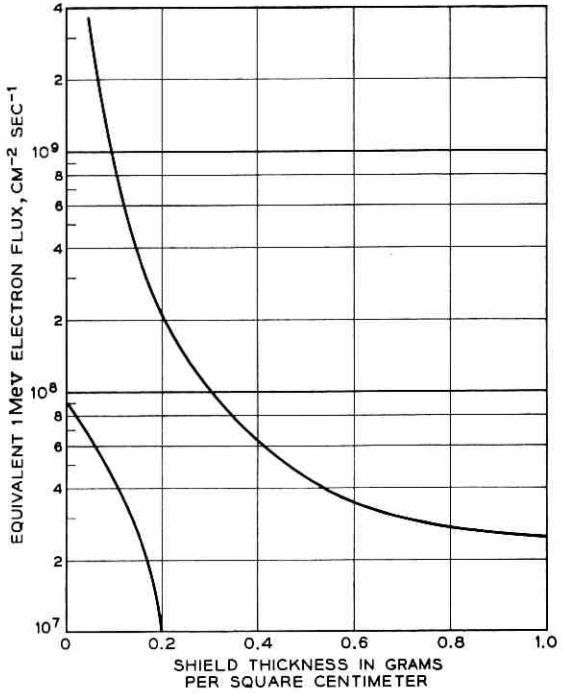

Fig. 9 — Equivalent 1-Mev electron flux as a function of shielding thickness.

intensities of 2.5×10^{10} cm^{-2} sec^{-1} for energies greater than 20 Kev, and 1×10^8 cm^{-2} sec^{-1} for energies greater than 600 Kev. Cells covered with various thicknesses of sapphire were subjected to electron bombardments at a set of energies (0.4, 0.6, 0.8 and 1.0 Mev) with intensities designed to simulate the above spectrum. The resultant equivalent 1-Mev flux as a function of shielding thickness is also shown in Fig. 9. According to these data, the electron damage is small compared to the proton damage. However, in view of data taken after the July 9, 1962, high-altitude nuclear test explosion, the equivalent fluxes of Fig. 9 are not applicable to the satellite which was launched on July 10, 1962. In Section 5.6, the flight performance of the solar plant will be discussed in the light of our present understanding of the radiation belts.

III. CELL DESIGN AND FABRICATION

3.1 *Considerations Leading to Decision to Develop N-on-P Cells*

During the fourth quarter of 1960, the superiority of n-on-p over p-on-n silicon cells in high-level radiation environments was firmly

established. Cells of the n-on-p type are more resistant than p-on-n cells to 1-Mev electron irradiation by a factor of as much as ten. They are also from 3 to 8 times less sensitive to protons than p-on-n cells in current use.

At that time, there were no n-on-p silicon cells in production in commercial quantities. However, experimental n-on-p cells were obtained from several suppliers, and information was made available by the Signal Corps on methods of fabrication of n-on-p cells. This information, combined with our own development studies, led to the conclusion that the n-on-p cells would not be essentially more difficult to manufacture than p-on-n cells of comparable initial performance in space, except that (a) an antireflection coating would be required, which was not necessary as a separate operation on the p-on-n cell, and (b) development effort would be required to obtain a highly manufacturable electrical contact of good integrity and low electrical resistance. We concluded that these problems could be solved and that a suitable cell could be nearly as economical in quantity fabrication as p-on-n cells of comparable initial performance in space. The decision to initiate the n-on-p cell program was based on the two prime considerations: (1) the cells would give longer life in a radiation environment, and (2) they appeared feasible for manufacture.

3.2 *N-on-P Solar Cell Design*

3.2.1 *Material*

Silicon material characteristics usually considered important in semiconductor work are (1) the impurity concentration or doping level, (2) the minority-carrier lifetime, (3) the crystal structure perfection, and (4) the crystallographic orientation. For solar cell fabrication, the size of the crystal may also be a consideration, particularly if cells are to be carried through several fabrication steps as multiple elements.

For n-on-p cells for satellite service, the effects of changes or variations in these characteristics required evaluation. Silicon was obtained from several sources over a range of resistivity for comparative process evaluation. Since the prime effect of the radiation environment on the cell is a reduction in carrier lifetime, there appeared to be no advantage in requiring high initial lifetime in the starting material, or extreme perfection of structure. Therefore, during the period of manufacture, the silicon material used by Western Electric Co. for this project was not held to a stringent lifetime requirement, nor were the imperfections controlled by monitoring the etch pit count. The crystals were sliced parallel to the

[111] crystal plane, and twinned material was rejected for mechanical reasons. It was found feasible to grow crystals of sufficient diameter that one-inch square slices could be cut. These were used as the starting material for cell fabrication. One hundred or more such slices were usually cut from a single crystal.

The impurity concentration in the cell body, which determines the specific resistivity, can affect the cell voltage, the sensitivity to radiation damage, and the effective series resistance of the cell. This last effect is small in the range of resistivity usually used: it would reach 0.1 ohm with a body resistivity of 5 ohm-cm. The envelope of open-circuit voltage measurements vs material resistivity obtained with experimental cells is shown in Fig. 10. As expected from theoretical considerations, better radiation resistance would be obtained with high-resistivity silicon used as starting material. However, the loss in open-circuit voltage obtained with experimental cells of high resistivity silicon led to a decision to use nominal 1 ohm-cm p-type silicon for the initial production, and this was continued through the program.

3.2.2 *Cell Structure*

Early in our development program, a decision was made to keep the physical dimensions of the cells compatible with commercially available p-on-n cells, if this could be done without serious sacrifice in performance. Fig. 11 shows the cell dimensions and front contact arrangement. The cell was made about 5 mils thinner than the conventional product; this resulted in a minor weight saving without serious loss in strength.

An etch-polished front surface was adopted to reduce surface recombination losses and permit application of a smooth antireflection

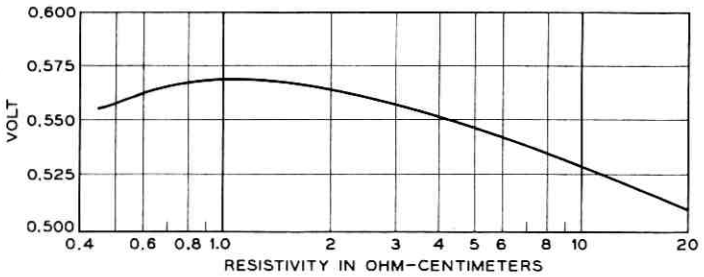

Fig. 10 — Solar cell open-circuit voltage vs resistivity.

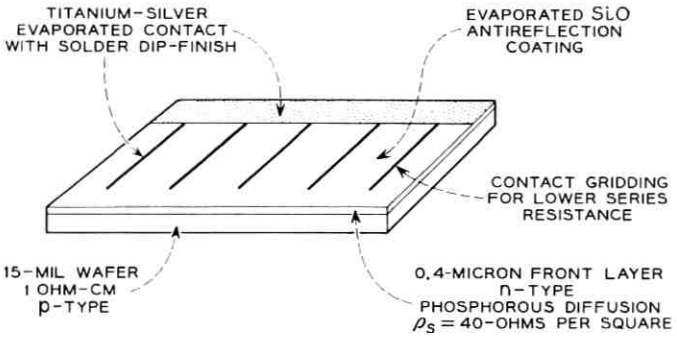

Fig. 11 — Cell structure.

layer of uniform thickness. Good adhesion and integrity of this antireflection coating required coordinated effort on the diffusion process, postdiffusion cleaning, and the contact application process, which is discussed in more detail in Section 3.3.

The diffusion process was selected after a series of diffusion experiments, combined with contact studies and model fabrication. Control of the diffusion operation was used as the principal method of adjusting the spectral response of the cell. The control was exercised by requirements placed on the diffusion environment and temperature, leading to a specified n-layer sheet resistance and desired n-layer thickness.

The cells were designed to be sensitive in the blue-green region of the solar spectrum. No particular efforts were made to obtain good long-wave response since, as discussed in Section II, the long-wave or infrared response is degraded rapidly in a radiation environment. The photon sensitivity peak was chosen to be near the wavelength for maximum incident photon flux from the sun. Fig. 12 shows calculated short-circuit current response, initial quantum efficiency, and relative response for equal energy input vs wavelength for a typical n-on-p cell after antireflection coating.

At the start of the development program, it was realized that improved cell contacts would be required. Intensive work was initiated, leading to the titanium-silver evaporated contact used on all Western Electric Co. n-on-p cells. This in turn required special attention to the solder used for cell tinning and assembly. Many experiments were made to determine optimum methods for assembling the cells in series groups, as will be considered in Section IV.

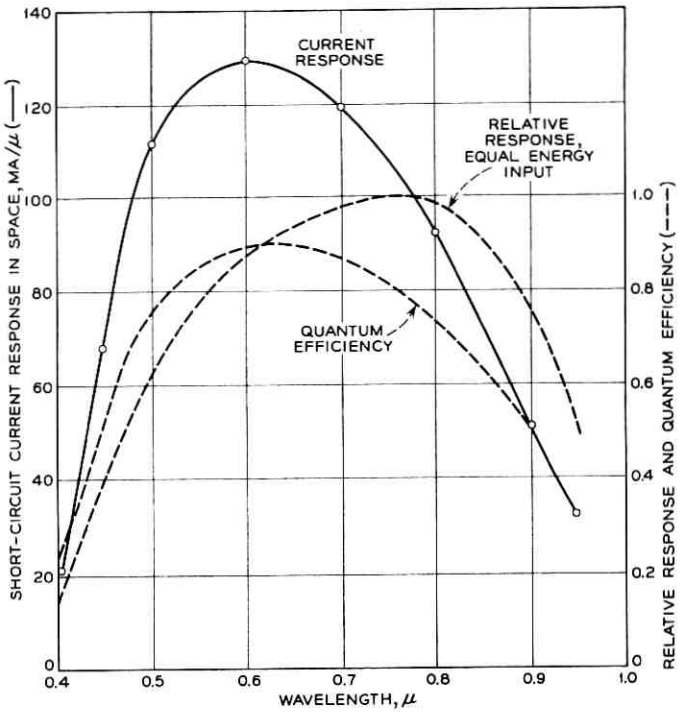

Fig. 12 — Spectral response, n-on-p solar cell.

3.3 *Fabrication Technology for N-on-P Cells*

3.3.1 *General*

This section describes some development experiments and the fabrication methods for making radiation resistant solar cells. During the period October 1960–June 1961, a moderate scale model fabrication operation was conducted in the laboratory. This model line was used for design experiments and to provide cells of specified characteristics for radiation damage study. The "going rate" was a fabrication of about 100 cells per week, and a total of some 2000 experimental cells was made in this period in the laboratory.

The first cells were delivered to the Laboratories by Western Electric Co. on January 28, 1961, and the desired program was completed about March 30, 1962. A total of approximately 100,000 n-on-p cells was made by Western Electric Co. for the program; however, not all of these re-

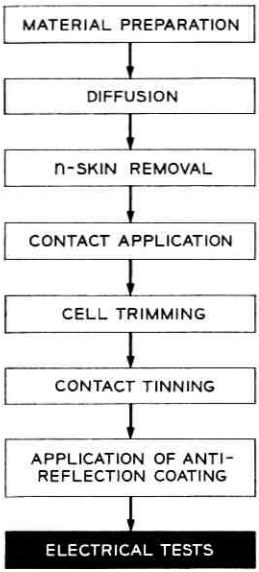

Fig. 13 — Fabrication sequence for n-on-p solar cells.

ceived antireflection coatings, and not all of those coated were considered acceptable for satellite use.

Fig. 13 indicates the principal steps in our fabrication of n-on-p solar cells. These steps are considered in sequence, and some of the development experiments and analyses leading to the final cell are mentioned. Since no n-on-p cells were in quantity manufacture (in the U. S. A.), considerable development engineering was required. Also, the time schedule for manufacture required that equipment and facility orders be placed on the basis of advance engineering judgment, without the benefit of a "proved in" process. Fortunately, it was not necessary to scrap any major equipment as the fabrication methods became shaken down.

3.3.2 *Silicon Material and Preparation*

3.3.2.1 *Material.* The material specified for the Telstar cells was p-type single-crystal silicon, sliced parallel to the [111] crystal plane with resistivity 1.0 ± 0.50 ohm-cm and minority-carrier lifetime greater than 5 μsec. No requirement was placed on etch pit density. The silicon slices were cut from the parent crystal with a multiple gang saw to a thickness of 20 mils, minimum. The slice was made 1.0 inch square (nominal),

in order that two cells could be prepared on one slice of the starting material. The crystals were pulled approximately one and one-half inches in diameter and from four to five inches long.

In laboratory experiments, material of resistivity in the range 0.05–20 ohm-cm was used. Several experimental fabrications were made, with material of different resistivity processed through the same operations at the same time to reduce the number of independent variables and establish the effects of material resistivity on cell performance. As previously indicated, optimum initial performance was obtained with silicon near 1 ohm-cm, and this was specified.

Silicon material was usually pulled into single-crystal form by Western Electric Co.; however, some single-crystal stock was obtained from other material suppliers and used for comparative fabrication. Little difference in cell performance was found attributable to the source of the single-crystal starting material, and for most of the operation no restrictions were placed on the source of the material used.

Experiments were also made in which solar cells were fabricated from twinned material, both with a single grain boundary and with many grain boundaries indicated on a cell. No significant deterioration in electrical performance was found until the number of grain boundaries became very large (of the order of 100), so that the material would more properly be called "multicrystalline, with large grain size" than "single-crystal, twinned." However, silicon slices showing grain boundaries were rejected for satellite use because of their inferior mechanical strength.

3.3.2.2 *Slice Preparation.* After the crystal was sawed into slices, the slices were lapped on both sides, and then one side was etch-polished; about three mils of material were removed by the etch. The slices were demounted from the etching racks, cleaned, and inspected for stains, scratches, and mechanical dimensions. The purpose of the etch-polishing step was to provide the best possible surface for the diffusion operation, to avoid crystal imperfections in the finished cell which would cause high surface recombination, and to facilitate application of an effective antireflection coating. A "modified CP4" type etch was usually used. To obtain consistent results, both the bath temperature and the agitation were carefully controlled.

3.3.3 *Diffusion, N-Skin Removal*

The diffusion process used for preparation of the thin n-layer is shown schematically in Fig. 14. This was chosen only after extensive development experiments using different methods of application, time-tem-

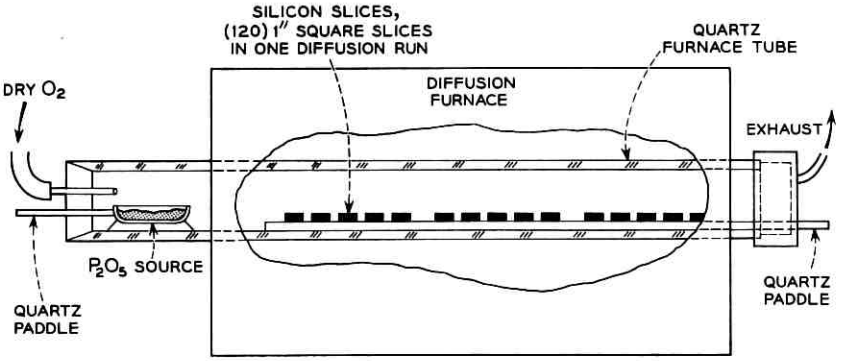

Fig. 14 — Schematic of phosphorus diffusion system.

perature programs, and sequences of operations. Significant factors in control of the diffusion process were found to be: cleanliness of silicon samples, temperature and quantity of the P_2O_5 source, method of introducing source and carrier gas, velocity of carrier gas flow, cleanliness of quartz trays and, of course, the time and temperature of the diffusion.

Fig. 15 shows the response of experimental (pre-antireflection-coated)

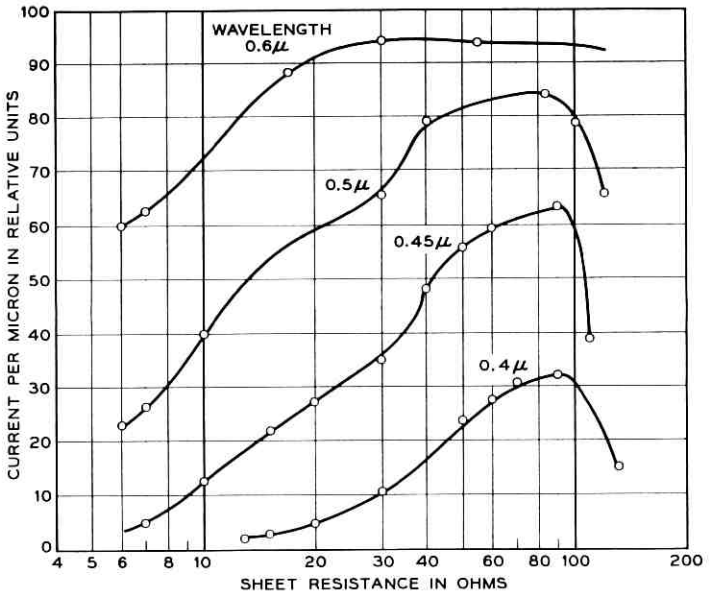

Fig. 15 — Spectral response vs sheet resistance.

cells vs the measured sheet resistance of the diffused layer at four wavelengths in the visible range. For these cells, it would at first appear that the optimum diffused layer sheet resistance would be about 90 ohms/square; however, attempts to fabricate cells in quantity with such thin diffused layers showed that further development would be required to obtain reasonable yields. A principal difficulty was local shorting of the cell in later process steps, particularly in contact application. As a compromise, the sheet resistance of production cells was specified to be greater than 30 and less than 60 ohms/square. The diffusion time and temperature were programmed to produce a diffusion depth in the order of 0.4–0.5 micron, with sheet resistance of perhaps 37 ± 5 ohms/square. As the diffusion depth was not subject to accurate measurement in the slightly irregular surface provided by the etch-polishing operation, this was not held as a requirement.

After diffusion and postdiffusion inspection, the n-skin was removed from the lapped side of the slice by a light abrasive blast, or by etching. Considerable care is required at this step, as the thin n-p junction on the polished face is quite sensitive to local damage if roughly handled in the presence of abrasive particles. It was found expedient to mask the face of the slice during the blasting or etching operation, as by cementing or waxing to a glass cover slide.

3.3.4 *Contact Application*

Adherent, low-resistance contacts to the n and p regions of the n-on-p solar cell presented a major problem. Electroless nickel plating followed by sintering would make a satisfactory mechanical connection, but was unacceptable for the n-layer, as the very thin diffused region would be penetrated during the sintering, and the n-p junction would be seriously degraded, if not shorted entirely. A new approach was needed. After some study, effort was concentrated on development of a new semiconductor contact, in which a reactive metal, titanium, is applied to the silicon surface in vacuum, and the titanium is covered with silver before removal from the vacuum chamber. The silver serves to protect the titanium from oxidation and permits ready tinning at a later point in the fabrication.

Silicon is normally covered with a thin SiO_2 layer, which is one cause of difficulty in forming good electrical contacts to it. In the titanium-silver contact process, the titanium is applied to this thin oxide layer. After removal from the vacuum station, the silicon slices are baked for a few minutes in an inert atmosphere at a temperature near 600°C.

During this heat treatment, the titanium reacts sufficiently with the SiO_2 surface layer to penetrate it and make electrical contact to the underlying silicon. This forms an adherent, low-resistance contact, without forming any liquid alloy and without damage to the n-p junction. If the surface is clean and if the vacuum deposition is properly carried out, the metal-silicon bond is very good. For example, if a heavy wire lead is soldered along the back of the cell and the combination is immersed in liquid nitrogen, thermal contraction differentials will rip the wire from the silicon body. However, the parting line is usually not at the metal-silicon interface, but rather inside the silicon. Because of the good electrical and mechanical properties of the Ti-Ag contact, it was used for both front and back contacts on all Telstar spacecraft cells.

Accessory contact "grid lines" or "fingers" are necessary on high-efficiency solar cells to reduce ohmic losses in the thin surface layer. This becomes more important as the diffused layer is made even thinner to optimize short-wave spectral response, as required for use in a radiation environment. However, the number of fingers should not be made too large, as the light which they intercept does not contribute to useful output. A compromise must be made. The "best" choice of finger array will depend on the width of the fingers, the cell geometry, and particularly on the diffused layer sheet resistance. For the Telstar spacecraft cell, five fingers were used. Experimental cells, fabricated alike up to the point of contact application, but made with both five fingers and seven fingers (each 0.006 inch wide) showed little difference in performance. If the sheet resistance of the diffused layer were increased, say to 60–80 ohms/square, then seven-finger cells would be preferred.

3.3.4.1 *Relief of Back Contact Margin.* The cells made early in the program had the rear contact applied over the entire rear surface of the slice. After assembly of several modules and thermal shock tests, it was found that small cracks would sometimes become evident at or near the edge of the cell beneath the top contact. This was attributed to strains set up by the solder and the metal mounting strip, these being attached directly to the bottom of the cell at the edge. Several means for avoiding this strain concentration were examined. The method adopted was to mask a narrow region along the edge of the cell, so that during evaporation of the rear contact this region would not be metallized and therefore, would not "take" solder. This operation required registration of front and back contact evaporation masks, however.

3.3.4.2 *Contact Adherence Tests.* After contact evaporation and heat treatment, the contacted slices were subjected to a "Scotch Tape" adherence test in which a strip of pressure-sensitive tape was applied to

each slice and stripped away. Defective contact adherence was shown by portions of the silver or silver and titanium adhering to the tape. Such slices were rejected at this point without further process effort.

3.3.5 *Cell Trimming and Tinning*

To this point in the process, two 1-cm × 2-cm cells have been prepared on a single silicon slice. These cells are now cut apart with a ganged diamond saw, which also trims the other edges of the cell to final dimension. Fig. 16 shows top and bottom views of the contacted slice with the trimming cuts. It will be evident that the width of the saw kerf in the cut which separates the cells must be allowed for in dimensioning the contact evaporation masks.

By trimming the cells on their entire perimeter after the contact application, any metallization across the exposed n-p junction is avoided. Also, some simplification of operations results from handling the cells as multiples of two through part of the fabrication. The cells, after trimming, are demounted from the cutting block, cleaned, and solder-tinned. This operation is done by dipping each cell in a bath of molten solder in an inert atmosphere. The solder contains about 3 per cent silver to prevent dissolving the silver already present on the cell. Some control of the amount and location of the solder on the rear face of the cell is available by adjustment of solder temperature, time of immersion, and method of removal of the cell from the solder bath. After tinning, the

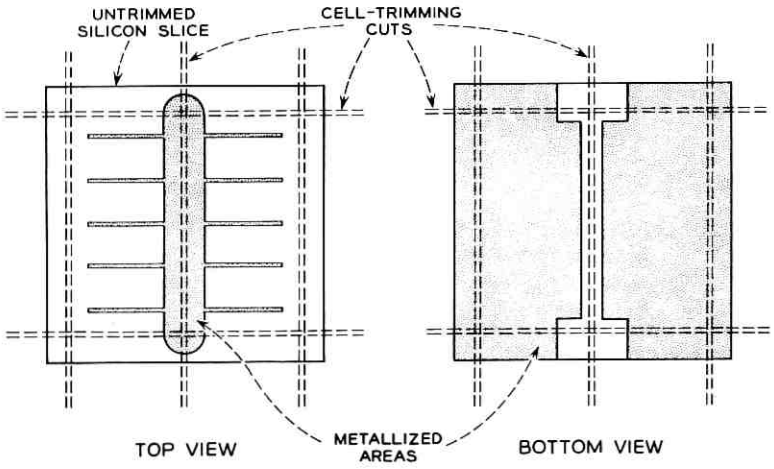

Fig. 16. — Contact configuration and cell trimming.

cells are cleaned with acetone and are delivered for preliminary electrical tests.

In our program, the edges of the cell were not given any etching or smoothing treatment after the diamond saw trimming operation. It was originally planned to provide some form of etch treatment to remove material damage introduced in sawing; however, experiments indicated that little improvement was obtained. The thin n-p junction is highly susceptible to mechanical damage on the face of the n-layer but is rather tolerant of damage at the exposed perimeter (6 cm) of the cell. The relative importance of etching the junction perimeter appears to diminish as the diffused layer is made very thin.

3.3.6 *Preliminary Electrical Tests*

Before application of the antireflection coating, the cells were subjected to electrical tests. All cells were tested for open-circuit voltage, short-circuit current, current into 0.45-volt load, reverse leakage current, and ac resistance at 50 ma dc. These tests were intended to serve as process checks and to weed out defective units before the coating process.

In addition to the above, 100 cells from each week's production were obtained, given identification numbers, and subjected to detailed spectral response tests; these cells were then antireflection coated and retested in detail. This permitted continued evaluation of the spectral behavior of the uncoated production cells, and of the improvement obtained by the coating process.

The test equipment for production line electrical tests used a slightly modified 35-mm slide projector as a light source. The heat absorbing glass filter in this projector cut off rather sharply in the near infrared; the resultant light was therefore "bluer" than sunlight at ground level. This test set was maintained by secondary standard cells which were calibrated in the laboratory spectral response set. As routine in-plant color tests were not made, the control of spectral response of the production cells was maintained indirectly — that is, by control of the diffused layer of the etched surface and of the antireflection layer later applied.

3.3.7 *Cell Antireflection Coating*

A single-layer interference antireflection film of SiO is vacuum evaporated onto the surface of the solar cell as the final step in its fabrication. SiO is generated by heating a mixture of pure Si and quartz (1:2 weight ratio, between 100 and 200 mesh) in a vertical tantalum tube

(0.157 inch ID, 2 inches long) pinched shut at the bottom and resistance heated. The solar cells are held by spring-loaded clips in a stainless steel dome of 13-inch radius, mounted 20 inches above the SiO source.

The film deposition is monitored by measuring the reduction in light reflection from a square of polished Si held in the center of the dome. A light source and blue-sensitive phototube pickup are mounted inside the vacuum chamber. A film about 800 Å thick is deposited in seven to ten minutes with a source heated to 1300°C and the vacuum at 5×10^{-6} torr or better. Deposition is stopped when the reflectance is a minimum for light between 0.50-μ and 0.55-μ wavelength.

The quality of the film is checked by suspending the coated cells for 30 minutes in steam over boiling water, and then visually inspecting them under diffuse light. Adherence of the film is tested by the simple Scotch Tape test. An acceptable coating shows no discoloration after steaming and none of it is stripped off by the Scotch Tape. Final electrical tests are relied upon to confirm the optical quality of the film.

3.4 *Initial Performance of Completed Cells*

Typical performance of production cells after antireflection coating is shown in Figs. 17 through 21, which summarize measurements on statistical samples from a group of more than 10,000 cells made in Sept., 1961. Fig. 17 shows the open-circuit voltage at 28°C. Although this is slightly lower than can be obtained with conventional p-on-n cells having a thicker diffused layer, the distribution of voltage values is consistent with a controlled process.

Fig. 18 shows the distribution of short-circuit currents and of cur-

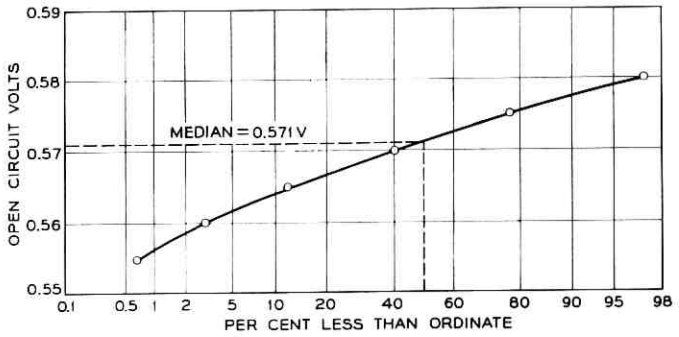

Fig. 17 — Open-circuit voltage distribution.

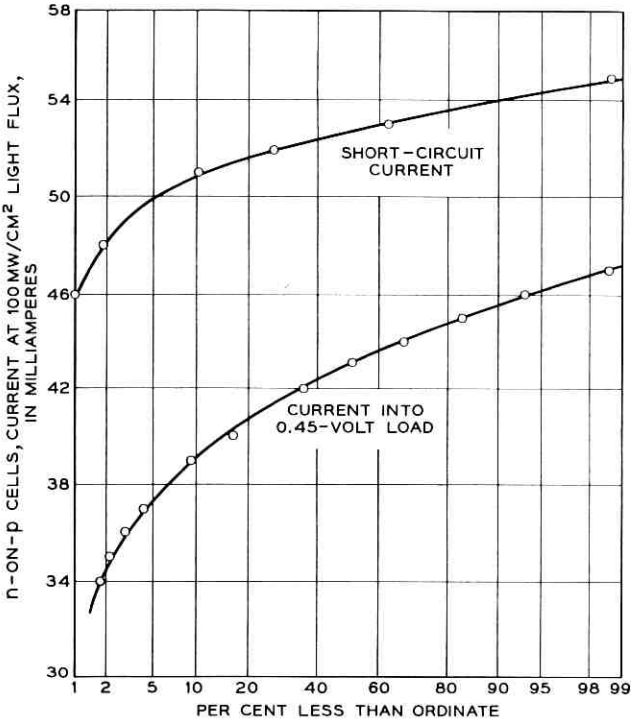

Fig. 18 — Short-circuit current and current into 0.45-v load.

rents into an output load of 0.45 volt, made at an equivalent light flux of 100 mw/cm² sunlight. Fig. 19 shows the electrical conversion efficiency at a load voltage of 0.45 volts for 100 mw/cm² illumination with the light source described in Section 3.3.6. Fig. 20 shows a typical *V-I* curve and conversion efficiency versus load voltage. Fig. 21 shows typical improvement in current output, resulting from the SiO coating operation, versus incident wavelength.

3.5 *Selection of Cells for Module Assembly*

The range in cell current output into a 0.45-volt load (see Fig. 18) was from less than 36 ma to 47 ma. Advantages in performance would result if all cells of like current were grouped together or, more generally, if knowledge of the voltage, current, and temperature characteristics of the cells were used to optimize the performance of the solar cell modules and strings. As a practical operation, such optimization could

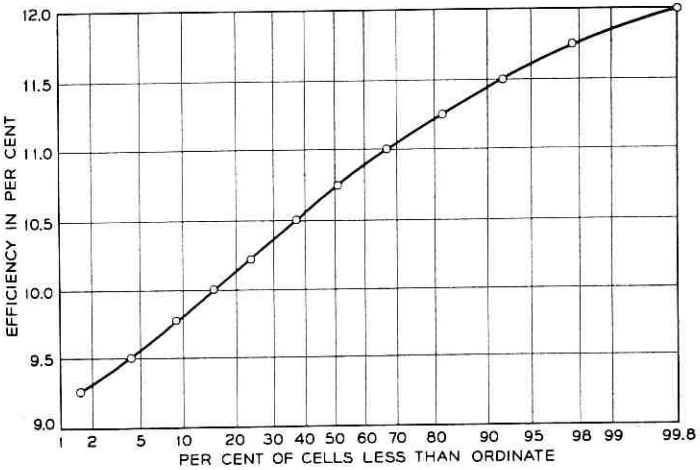

Fig. 19 — Conversion efficiency at 0.45 v.

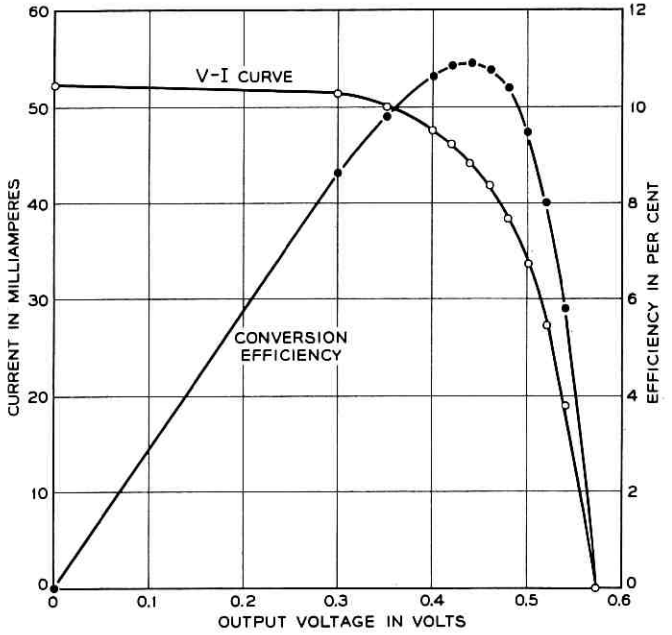

Fig. 20 — Solar cell V-I and conversion efficiency vs load voltage.

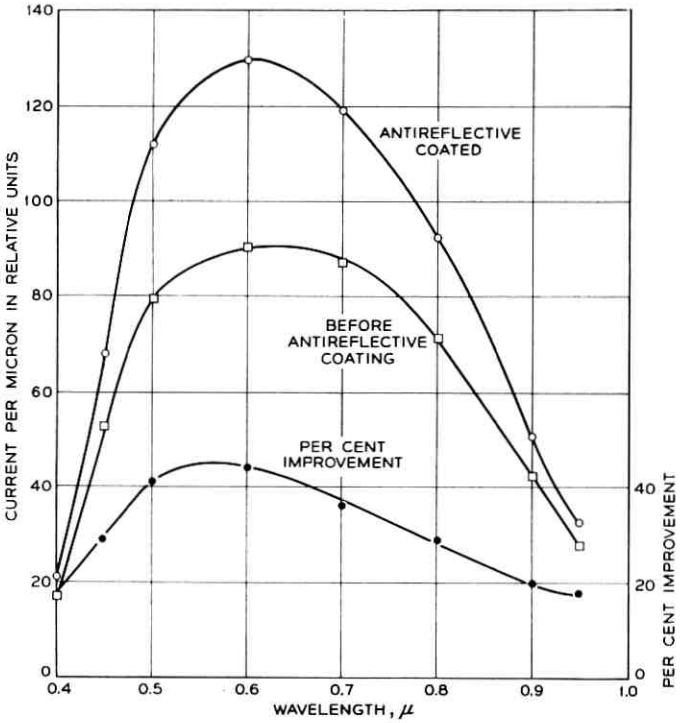

Fig. 21 — Improvement in current response after application of antireflection coating.

only be approximated. To this end, the cells were sorted into groups; the current range for all cells in one group was held to 1 ma. For a particular 12-cell module, only cells from a particular group were used. Records were kept in such form that the performance of the completed module could be compared to that expected from the cells with which it was made. This information could be used to find modules in which serious changes or deterioration of cell performance resulted from the assembly operation. In most cases, however, there appeared to be little change in the cell performance when assembled into modules.

IV. MODULE DESIGN AND CONSTRUCTION

4.1 *Solar Cell Module Requirements*

The module must withstand two widely different environments: the launching environment, where it is subjected to extreme mechanical

vibration stresses; and the orbital environment, where it is subjected to radiation and cyclic thermal stresses. The following list of items is given as the primary design requirements for the module:

(1) provide radiation protection
(2) withstand thermal cycling stresses
(3) withstand vibration during launch and
(4) minimize temperature of cells.

The need for radiation protection has been discussed earlier in this paper. The protection should be provided on all sides of the cells. The protective material over the active surface of the cell must be transparent and not be affected by the radiation bombardment.

As the satellite assumes various attitudes with respect to the sun, surface temperatures vary from $+69°C$ to $-100°C$. These extremes might occur once or twice during the life of the satellite should the spin axis point toward the sun. The normal temperature range is $+10°C$ to $-50°C$ for full sunlight and maximum eclipse with the spin axis nearly perpendicular to the sun. The differential expansion of the materials induces stresses in the component parts of the module, when cycled over the stated temperature range. Continuous thermal cycling will eventually result in fatigue failures if the stress is not limited.

The modules are mounted on the external surfaces of the satellite and measurements show that, at resonances in the structure, accelerations in excess of 200 g's are present.

As the temperature increases, the conversion efficiency of the cells decreases, making it desirable to minimize the temperature of the cell. Considerations of temperature effects in the design of the solar plant are given in Section V.

4.2 *Design Objectives*

The design of the module can be divided into four main sections: the electrical design, the mechanical design, the thermal design and the radiation protection. These, of course, are all closely interwoven: for example, the mechanical design might dictate the expansivity of a material being chosen for a particular application, the thermal requirements limit the choice to a single material, and the radiation protection dictates the thickness of the material for minimum weight.

Electrically, the design must provide a series connection between the cells, insulate them from the satellite structure and provide terminals for interconnecting the modules.

The major mechanical objective is that the module withstand the vibration during launch. Fortunately, the mass of the module is small

so that even with accelerations of 200 g's the forces are small. Damping has been provided in the spring tabs that are used to fasten the modules to the panels.

It is important to minimize the temperature of the solar cells. The incident power not converted into electrical power must be removed from the cells and eventually reradiated into space. Direct reradiation through the sapphire covers is not possible, because a "greenhouse" situation exists: i.e., at the wavelength of the black-body radiation of the cell, the cover is opaque. Thus a thermally conducting path to the cover is required, and this should be of low thermal impedance. As the modules must withstand a wide range of temperature, coexpansive materials must be used.

Radiation protection is provided by enclosing the cells in a box structure consisting of the ceramic mounting plate, the transparent covers and a metal frame to join these two. The thickness of the material is obtained by dividing the required protection of 0.3 gm/cm^2 by the density of the material. Using this relationship, the thickness of the cover plates and ceramic is 30 mils and the thickness of the platinum frame is 8 mils.

4.3 *Module Design*

The solar cell module, shown in Fig. 22, is $4\frac{5}{8}$ inches long, $\frac{7}{8}$ inch wide, and $\frac{1}{8}$ inch thick, and weighs 0.8 ounce. It is made of two assemblies: the cover assembly, which consists of sapphire cover plates brazed into the platinum frame; and the solar cell assembly, which consists of the solar cells, shingled to provide a series connection, mounted on the ceramic plate. The two assemblies are joined by soldering the cover assembly to the cell assembly along the edges of the ceramic plate.

Several materials were considered for the transparent cover over the solar cells. Measurements of the transmission before and after exposure to radiation showed the suitability of certain glasses, quartz and sapphire. In weighing the other characteristics of the materials, sapphire was chosen for its higher thermal conductivity and the availability of processes for joining it to metals.

Table I shows some of the properties of the materials used in the module. As can be seen, the thermal conductivity of sapphire is 20 to 30 times greater than that of glass or quartz. Alumina ceramic, which is a polycrystalline form of sapphire, has approximately the same expansivity as sapphire. Platinum was chosen to join these together because it provides the closest expansion match and is nonmagnetic.

The selection of coexpansive materials limits the stress where these

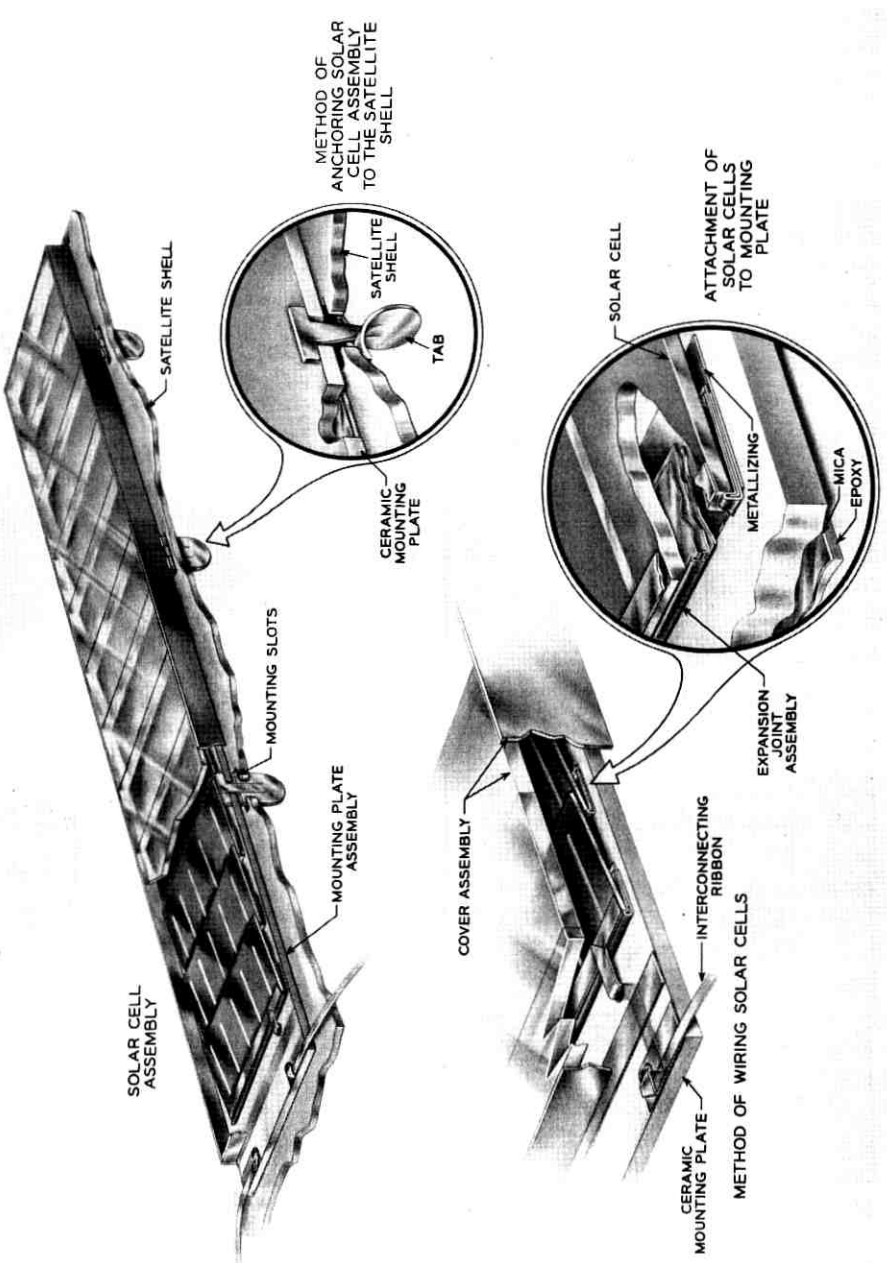
SOLAR CELL ASSEMBLY
SATELLITE SHELL
MOUNTING SLOTS
MOUNTING PLATE ASSEMBLY
METHOD OF ANCHORING SOLAR CELL ASSEMBLY TO THE SATELLITE SHELL
SATELLITE SHELL
TAB
CERAMIC-MOUNTING PLATE
SOLAR CELL
ATTACHMENT OF SOLAR CELLS TO MOUNTING PLATE
METALLIZING
MICA
EPOXY
COVER ASSEMBLY
EXPANSION JOINT ASSEMBLY
INTERCONNECTING RIBBON
CERAMIC MOUNTING PLATE
METHOD OF WIRING SOLAR CELLS

TABLE I — MATERIALS CONSIDERED FOR MODULE

Material	Expansivity, 10^{-6} in/in/°C	Thermal Conductivity, cgs Units
Silicon	2.4(20° C) −0.3(−173° C)	0.20
Sapphire	7.0	0.06
Fused quartz	0.5	0.003
Glass	10.0	0.002
Alumina ceramic	6.8	0.06
Platinum	8.0	0.16
Silver	19.0	1.06
Invar	0.5	0.03

materials are joined. The joints must have a low thermal impedance, since they are in the heat conduction path. A zirconium-silver active metal seal was developed for the joint between the sapphire and platinum.

Also shown in Table I is the expansivity of silicon. It should be noted that the expansivity decreases with temperature, reversing at a temperature of −180°C. Since no insulating material could be found which was coexpansive with the silicon, flexibility was provided by incorporating hinges or expansive joints between the cells and the ceramic. Silver is used for the expansion joints because of its ductility and good thermal conductivity. The conductance of the 1.5-mil silver expansion joint is the same as that of the 30-mil ceramic, since the coefficient of thermal conduction of silver is 20 times greater than that of the ceramic.

To compensate for the mismatch between the silver and the silicon, inserts of 0.001-inch thick Nilvar are used. When soldered between the silver and the silicon, the Nilvar retards the expansion of the silver and produces a joint capable of withstanding the thermal cycling.

4.4 *Module Fabrication*

4.4.1 *Cover Assembly*

The cover assembly is made by brazing 13 sapphire plates into a platinum frame with zirconium-silver. To minimize the gap between the covers, it is important that the long edges be parallel to and the short edges be perpendicular to them. Intimate contact for brazing was obtained by procuring the covers in sets matched within one mil in length.

The sapphire covers are brazed to the platinum frame in a fixture which maintains a planar surface for all covers and provides sufficient clamping pressure to insure intimate contact between the covers. The fixtures are placed in a retort which contains a purified nitrogen atmosphere and brazed at 975°C ± 10°C for 3 minutes. The temperature cycle during brazing is carefully controlled to minimize thermal shock.

4.4.2. *Antireflection Coating of Sapphire*

The polished sapphire covers placed over the solar cells to protect them from radiation damage transmit only 85 per cent to 87 per cent of the incident light. This loss, caused by surface reflection, reduces the solar cell output more than can be tolerated. An antireflection coating, therefore, is deposited on both sides of the sapphire cover assembly. The coating consists of a single-layer interference film of MgF_2 about 1000 Å thick. It increases the transmission to 90 per cent or more in the wavelength range from 0.4 μ to 1.0 μ, with a maximum transmission greater than 98 per cent between 0.5 μ and 0.6 μ. With this higher transmission, the covers reduce the solar cell module output by less than 5 per cent.

Micrometeorites will reduce the sapphire cover transmission by abrading the exposed surface. If this abrasion removes a 200 Å layer per year, as postulated by Jaffe and Rittenhouse,[14] the outer antireflection coating will be removed in three to four years, leading to a loss in initial cell output of about 6 per cent. Laboratory tests showed a 3 per cent loss in output for a mild abrasion of the antireflection-coated sapphire cover, and an 18 per cent loss for frosting of the sapphire. However, since the number and distribution of micrometeorites in space is not accurately known, a quantitative calculation of their effect on solar cell output cannot be made.

The antireflection coating is applied by evaporating MgF_2 from a hot, open tantalum boat in a vacuum of 9×10^{-5} torr or better. The boat is heated until the MgF_2 just melts, and the film is deposited in less than 3 minutes. The sapphire covers are held 20 inches above the boat on a stainless steel dome of 13-inch radius. Specially designed heaters are mounted on the dome so the sapphire covers can be kept at 300°C during the evaporation to assure a hard, adherent film. The film deposition is monitored by measuring the light reflected from one of the covers, using a blue-sensitive phototube as the pickup.

The quality of the antireflection film is checked by subjecting sample covers to 30 minutes in steam above boiling water in a covered vessel, then visually inspecting them. Transmission of the steamed covers is also measured at 0.4, 0.6, 0.8, and 1.0 μ.

4.4.3 *Mounting Plate Assembly*

The solar cell mounting plate consists of the solar cells, the expansion joints, the ceramic mounting plate and the electrical leads from the cells to the terminals.

The solar cells are delivered in matched sets as previously described. The expansion joint, which consists of a folded silver sheet with two narrow strips of Nilvar soldered to one edge and a mica sheet inserted in the fold, is soldered to the back edge of each cell. The mica insert prevents the solder from joining the flaps of the fold, which would spoil the flexibility of the expansion joint.

The cells are assembled in a fixture with the ceramic mounting plate for the soldering operation. The ceramic plates have metallized areas which are located to join the free end of the cell expansion joint. Prior to assembly in the fixture, the metallized areas are silver plated and coated with solder. Other metallized areas are provided on the ceramic that serve as the terminals and joining surfaces for the cover assembly. Individual weights on the cells force the expansion joints into contact with the ceramic. The fixtures are placed in a retort with a nitrogen atmosphere and heated to flow the solder. The nitrogen atmosphere is used in all soldering operations in lieu of organic fluxes. After removal from the fixture, the leads are connected to the terminals and the assembly is tested for continuity.

4.4.4 *Module Assembly and Test*

The two assemblies are soldered together at the joint between the platinum frame and the edge of the ceramic. This is done in a fixture in which pneumatic cylinders press electrically heated pads against the platinum frame and force it into contact with the ceramic plate. The temperature of the pads is controlled by thermocouples, and the soldering cycle is controlled by a timer.

The completed modules are evaluated mechanically, electrically and thermally. The mechanical test consists of a microscopic inspection which eliminates any obvious mechanical flaws such as cracked cells, incomplete solder joints or poor alignment of cells on their mounting plates. Because of the fragility of the cells and the inaccessibility of some solder joints for microscopic inspection, two stressing tests are used. The first of these tests is a vibration test during which the module is vibrated for 30 seconds at 20 g's at 600 cps. The second test is a thermal cycling test, in which the modules are cycled from $+65°C$ to $-100°C$ for a total of 6 cycles. The stresses induced by these tests eliminate the manufacturing freaks. The electrical tests are measurements of the electrical output of the module under a controlled illumination. The results of these tests are used for grouping the modules into different classes, and will be discussed in detail later.

4.5 *Module Mounting*

Each module is equipped with six beryllium-copper twist tabs for mounting. These tabs are inserted in slots in the reinforced aluminum panels. A molybdenum strip, with matching slots, is placed in back of the panel with the tabs projecting through the slots. The tabs are twisted a quarter turn, which causes slit ends to emerge from the slots and to form spring fingers which hold the module in contact with the panel.

Six modules are connected in series to form a string which provides the required 28 volts. Omega loops made of braided copper wire are soldered to adjacent terminals to connect the modules in series. The end terminals in the string are connected to glass seal terminals mounted in the panel. Two additional terminals are provided for each string of cells and are positioned approximately $\frac{3}{4}$ inch above the string terminals. A blocking diode is connected between the string terminal and the adjacent added terminal. A connection is provided between the upper terminals, so that the output of a string appears at one side of the panel. This arrangement has the advantage that all current paths are brought back upon themselves, so that no retarding torques due to current loops in the solar cell wiring are applied to the satellite. The same precautions are taken in the internal wiring harness that connects the solar cell plant to the electronics chassis.

4.6 *Solar Cell Module Testing*

Fig. 23 shows the expected temperature ranges on the surface of the satellite with the sun perpendicular (pos. 1) and parallel (pos. 2) to the spin axis. Thermal test ranges and test results are also given.

The slow cycling tests were conducted in an oven-refrigerator combination in which the maximum rate of change of temperature was 3°C/min. The temperature was varied from +65°C to −100°C. This rate of change was faster than the expected 2°C/minute in space, and the temperature excursion was greater than the 40° range expected for any module under orbital conditions. The results are indicated on the graph. After 800 cycles, 3 modules had failed, with the failures occurring at 300, 675 and 800 cycles. The failures were at solder joints.

For the thermal-vacuum tests, modules were sealed in evacuated glass vials. These were mounted on a sun-seeking servo system which maintained the surface of the module perpendicular to the sun. Maximum and minimum temperatures of +60°C and −10°C were observed. Twelve modules have been on test over a year with electrical checks at

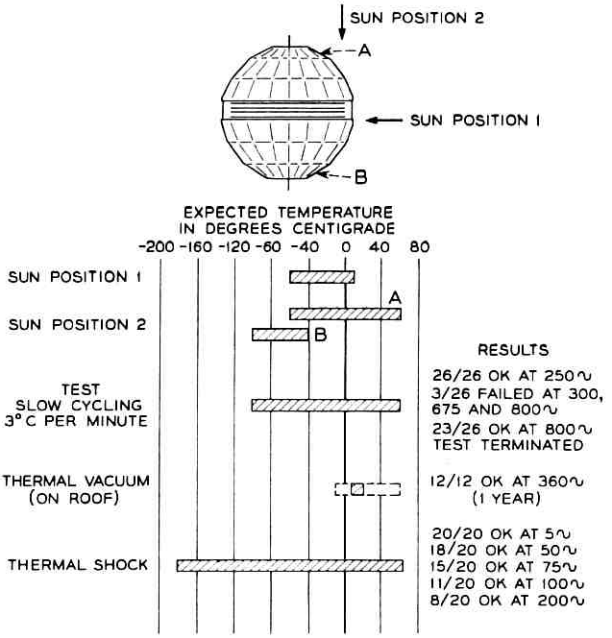

Fig. 23 — Expected satellite skin temperature for two conditions of illumination.

3-month intervals. There have been no significant changes in the modules on test.

For thermal shock tests, modules were sealed in polyethylene containers to prevent condensation. They were then heated and stabilized at 65°C in an oven. They were removed and immediately plunged into liquid nitrogen and held there until the temperature stabilized. The procedure was then repeated. After 200 cycles, 8 of the 20 modules were still operable. In all cases the failures occurred at the soft solder joints to the solar cells.

During early development, vibration tests were made on individual modules, using levels of 100 g's. These tests were all successful. However, it was not until a frame and panels were available that the transmissibility of the structure was known. A complete complement of 300 modules was mounted on the mechanical model satellite. Table II shows the tests to which the cells mounted on the satellite were subjected. Peak accelerations of 200 g's were measured. The failures that occurred at the fifth-resonance dwell test were all at solder joints. These

TABLE II — VIBRATION TESTS ON 300 MODULES MOUNTED ON MECHANICAL MODEL SATELLITE

Test	Number of Tests	Module Condition
Qualification level in thrust direction	5	ok
Resonance dwell	4	ok
Resonance dwell	fifth test	6/300 modules failed at soft solder joints

failures were due to fatigue of the solder, which had been subjected to 750,000 cycles at the time of failure.

The foregoing tests were in essence qualification tests of the module. During production of the module it was necessary to detect any modules that would not withstand the thermal or vibration environment. All modules were therefore subjected to two environmental tests: a thermal cycling test and a moderate-level vibration test. The purpose of these tests was to subject the module to cyclic stresses that would cause weak joints to fail.

The thermal test consisted of cycling the modules from +65°C to −100°C at a maximum rate of change of 3°C/min for a total of 6 cycles. The modules were evaluated by a microscopic inspection and electrical tests. Ninety-five per cent of the modules subjected to this test were later found acceptable.

All modules were vibrated at 600 cps for 30 seconds at an acceleration of 20 g's. Again, 95 per cent of the modules were acceptable, based on microscopic inspection and electrical tests.

V. SOLAR PLANT DESIGN AND PERFORMANCE

5.1 *General Design Considerations*

The integration of individual solar cells or of modules into a solar plant depends on several variables with strong interactions and possible trade-offs between them. The key variables are satellite shape and available surface area, operating temperature, satellite orientation in space, and required average output if chemical batteries are used, or required minimum output otherwise.

The Telstar spacecraft is a spherical, spin-stabilized satellite with solar cells attached to its surface. For such a solar plant the most favorable orientation is one where the spin axis and the sun-satellite line form an angle of 90°, i.e., equatorial illumination of the satellite. Such an

orientation of a spinning satellite will result in the lowest solar plant operating temperature. In the absence of perturbations, the satellite orientation will remain constant. However, interactions of the earth's magnetic field with any residual magnetic moment of the satellite cause precessions of the spin axis. Although ground commandable torquing coils are provided on the spacecraft for controlling such spin-axis precession, it was required for reasons of over-all reliability that the solar plant give usable power for any orientation. The design problem was thus to find the best distribution of the cells on the surface that would do this. Since the output current of series-connected cells is governed by the cell having the lowest output, all cells in a series string should have matched characteristics and should be mounted in one plane so as to receive the sunlight under the same angle of incidence. Thus, while electrically such a group of cells represents a string, in their geometrical layout they form a block or a patch.

If the temperature of the skin were uniform under all conditions, then the design objective would be achieved by distributing solar patches uniformly over the surface. However, since thermal conduction along the skin of the satellite is negligible, temperatures are established predominantly by radiative energy exchanges; therefore, the region facing the sun gets hottest. Under equatorial illumination, a given region near the satellite's equator receives sunlight at near normal incidence only a fraction of the time. Half of the time it is in the shade facing away from the sun. Thus, the average temperature on the equatorial band is low (1°C) and that of the poles is even lower (−3°C). Since the satellite's period of revolution is small compared to the thermal time constants, the instantaneous temperatures deviate little from the average temperature. Under polar illumination, however, one polar region faces the sun all the time and gets hot (+69°C) while the other gets very cold (−100°C). As the solar cell output in the voltage range of interest decreases with increasing temperature, the output under polar illumination would be lowest and that under equatorial illumination highest if solar patches of equal output characteristics were distributed evenly over the sphere. Some equalization is needed; it can be achieved by selective placement of high-output patches, and by increasing the patch density in the polar regions.

The output of the solar plant is connected directly across the batteries and the input regulator. The battery voltage, and thus the voltage into which the solar plant delivers its current, varies under normal operation between 25 and 28 volts, depending on the power demand schedule. One is thus interested, not in the solar plant current at a fixed voltage

only, but rather in the current-voltage output characteristic of the solar plant. Knowing the current-voltage characteristic of the individual cells as functions of temperature and angle of sunlight incidence, and knowing the temperatures of the solar patches for a given geometrical patch distribution and a given solar aspect (i.e., angle between sun-satellite direction and spin axis), the solar plant output characteristic can be calculated. While simple in principle, such calculations are quite lengthy and are most conveniently done on an electronic computer. The details of these calculations are presented in Section 5.5, and computed output curves representing the final design are shown in Figs. 28 and 29 of that section.

Finally, since the Telstar satellite operates with chemical storage batteries, it is the average output power which must satisfy the minimum output requirement, and not the instantaneous output power. Thus, the distribution of the solar cells need not be uniform over the entire surface — only the distribution averaged over one satellite rotation need be considered.

5.2 *Solar Plant Size and Configuration*

Since it is known that the output of the solar plant will decrease with time because of radiation damage, the most efficient use of this reduced output will be obtained if the solar plant delivers its maximum end-of-life power at the terminal voltage of the power plant when the batteries are being charged. Radiation damage studies have shown that a solar cell of the type used delivers its maximum power at approximately 0.4 volt after damage corresponding to about two years in orbit.[15] Since the terminal voltage of the power plant is roughly 28 volts when the batteries are being charged, strings of 72 series-connected solar cells were chosen to be the basic building blocks for the solar plant.

Considerations for the distribution of the patches were given above. One variable, however, has not been discussed yet, and that is the ratio of solar cell area to total satellite surface area. At places where there are no solar cells, the skin is covered with a material (aluminum oxide) which is highly reflective to or has a low absorptivity for sunlight in the 0.4-μ to 1.5-μ wavelength range containing most of the sunlight's power, but which is highly emissive at long wavelengths corresponding to the black body radiation at the temperature of the satellite. The ratio α/ϵ of the absorptivity at short wavelengths to the emissivity at long wavelengths is $\approx$0.22 for aluminum oxide and 1.7 for the solar cell

patches. Thus the larger the coverage with solar cells is, the higher will temperatures be. Since the canister is in radiative temperature equilibrium with the skin, its temperature is governed by the average skin temperature. For reliability reasons, a canister temperature near room temperature is highly desirable. Thus the canister temperature provided a strong constraint in decisions concerning the solar cell coverage. Another constraint was the weight per unit power. With higher coverage, a larger power output can be obtained on a sphere of given diameter. However, since the cells are then hotter, they work with lower efficiency, and the solar cell weight per watt goes up.

In the final design 50 parallel strings are used, incorporating a total of 3600 cells. This provides an initial power of about 14 watts and allows for an average of about 3.5 hours of transmission time per day — a reasonable figure, since the time of mutual visibility between Andover and Europe is about four hours when apogee is in its most favorable position. The distribution of cells on the surface is shown in Fig. 24.

5.3 *Selection and Placement of Modules*

The assembled modules were tested under a light source which provided uniform illumination over the 12-cell area of an intensity equivalent to 100 mw/cm^2 of solar illumination. The short-circuit current and the current at 5.4 volts (an average voltage of 450 mv per cell) were measured and recorded, and those modules having lower output than 38 ma at 5.4 volts were rejected for satellite use. The accepted modules were grouped into six-module strings by selection of modules which had matched short-circuit currents and currents at 5.4 volts under the test conditions. If there were insufficient modules having matched output currents to form a string, modules having higher current output under either or both test conditions were used to complete the string.

The six-module strings having the highest output currents were located on the bands nearest the poles of the satellite. This was done to provide the maximum output possible under the most unfavorable condition of illumination, namely, that of the spin axis of the satellite pointing toward the sun. The strings having the least output (of those selected for solar plant use) were located on the bands nearest the equator of the satellite, since cells on these bands operate at the lowest temperature.

Fig. 25 shows the distribution of currents at 5.4 volts obtained for 345 assembled modules at an equivalent light intensity of 100 mw/cm^2.

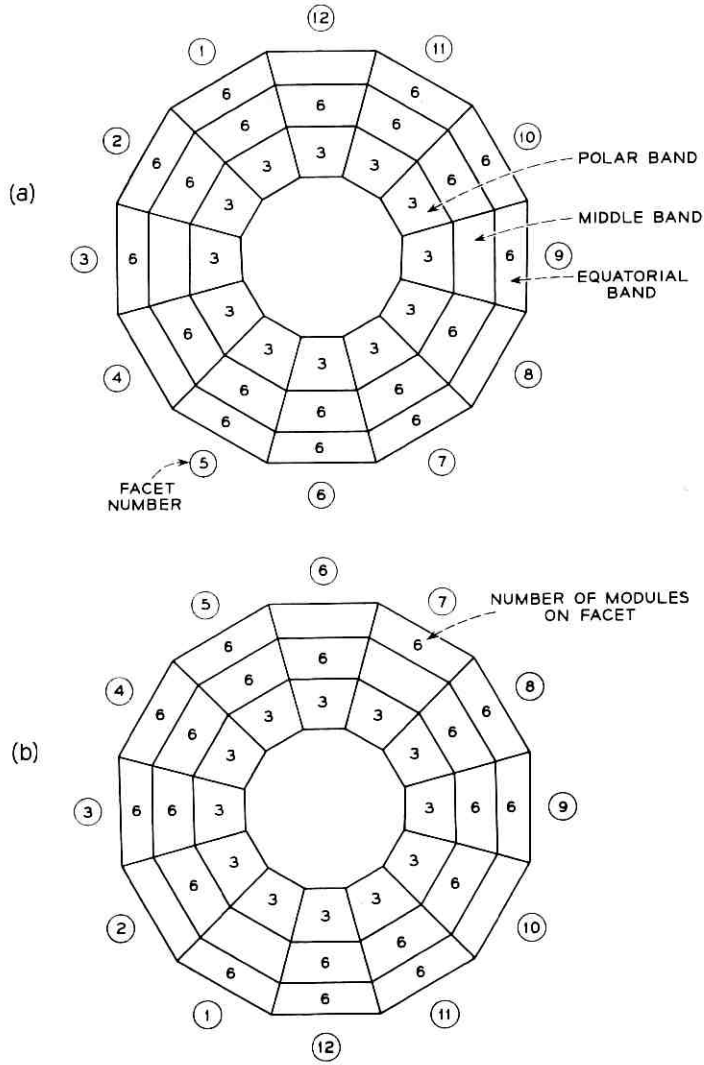

Fig. 24 — Distribution of solar cell modules on surface of Telstar spacecraft.

5.4 *Blocking Diodes*

The solar cell strings cannot be connected in parallel directly, since the dark cells would constitute a current drain. Instead, the positive terminals of all the strings are connected to the output bus by rectifier diodes. These diodes present a low impedance to the output current of

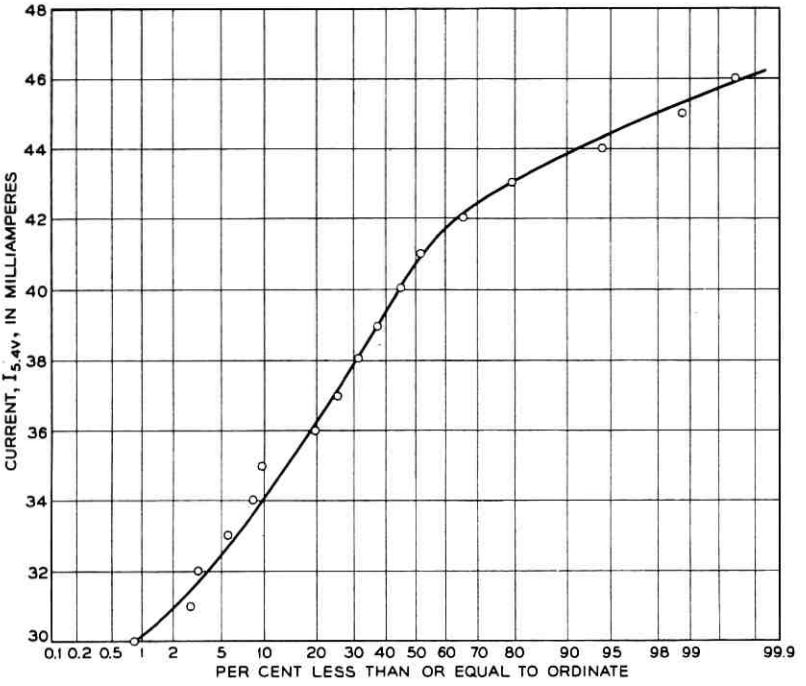

Fig. 25 — Module output current at 5.4 v.

illuminated strings, while their high reverse impedance prevents current leakage through dark cells. The rectifier diodes also prevent discharge of the batteries if a short from any portion of a string to the frame should develop, as might be the case under micrometeorite impact.

5.5 *Solar Plant Output Characteristic*

In the Telstar program, inspections and performance checks after each assembly step were undertaken whenever possible. The testing of the individual solar cells and of the modules was described above. However, adequate tests under simulated space environment of the completed solar plant on the satellite shell were not feasible. While thermal tests were made when the satellite was in a space-simulation chamber, the uniformity and collimation of the light source (3 carbon arc lamps) were insufficient to allow precision measurements of the expected outer space performance, and calculations had to be relied on. Such calculations were also important during the design phase, when the various trade-offs

were explored. These calculations were initially done by hand, but were later programmed for an IBM 7090 computer. We shall sketch below how the input information was obtained and present the important results of the calculations.

For convenience, all strings on a given band were considered to consist of 72 identical series-connected cells having characteristics representative of the cells used on the band. The output characteristic of a cell on the satellite shell depends on the angle of incidence and on temperature. In measuring cell characteristics, it was convenient to introduce the short-circuit current as an intermediate variable. One thus needed the output characteristic as a function of short-circuit current and temperature, and the short-circuit current as a function of angle. Simple geometrical reasoning would lead one to expect a cosine-law dependence for the latter; actually, however, between the incident light and the solar cell there is the antireflection coating of the solar cell and the sapphire cover with antireflection coatings on either side. Thus, a more complicated angular dependence results.

To determine the combined effect of these factors, as well as the effect of any shading or reflections caused by the module structure at near glancing angles of incidence, measurements were made of the short-circuit current output of sapphire-covered solar cells as a function of the angle of illumination using terrestrial sunlight. For these measurements, a baffle tube having a 0.1-radian acceptance angle was used to eliminate sky radiation, and the cells were mounted on a temperature-controlled base which could be rotated. Measurements were made at temperatures ranging from $-70°C$ to $+65°C$ on unbombarded cells and on cells bombarded with 2×10^{16} 1-Mev electrons/cm^2. The relative variation of short-circuit output current with the angle of illumination was found to be independent of both temperature and bombardment level. A normalized plot of this variation is shown in Fig. 26.

A typical output characteristic for short-circuit currents of 25 and 50 ma and temperatures of $-20°$ and $+40°C$ is shown in Fig. 27. To the first order, a change in short-circuit current corresponds to a shift of the characteristic parallel to the current axis. Second-order changes result from the front layer sheet resistance and contact resistance. To obtain the characteristic as a function of short-circuit current and temperature, precision measurements were made of the characteristic of a median cell at a set of 13 short-circuit currents and 6 temperatures. These are stored in the computer program, so that by interpolating between them reliable characteristics can be obtained for any short-circuit current and temperature required in the calculations.

Using the input data just described, the initial current and power out-

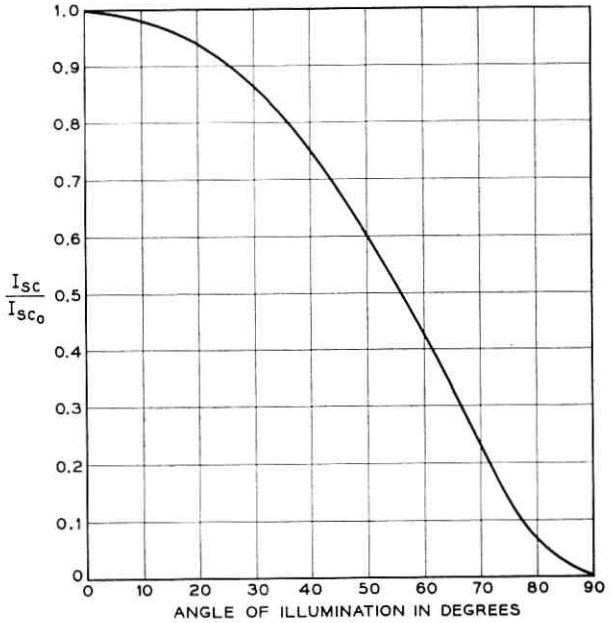

Fig. 26 — Normalized short-circuit current vs angle of illumination.

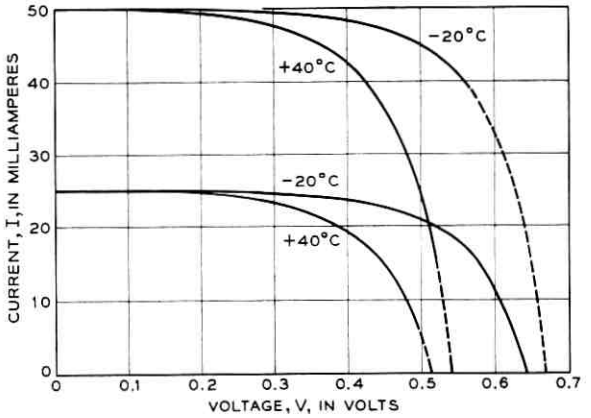

Fig. 27 — Typical solar cell output characteristic.

put characteristics of the spacecraft solar plant for four conditions of illumination were calculated and are shown in Figs. 28 and 29. The angles which identify each curve in these figures define the aspect angle between the spin axis of the satellite and the satellite-sun line. The time-

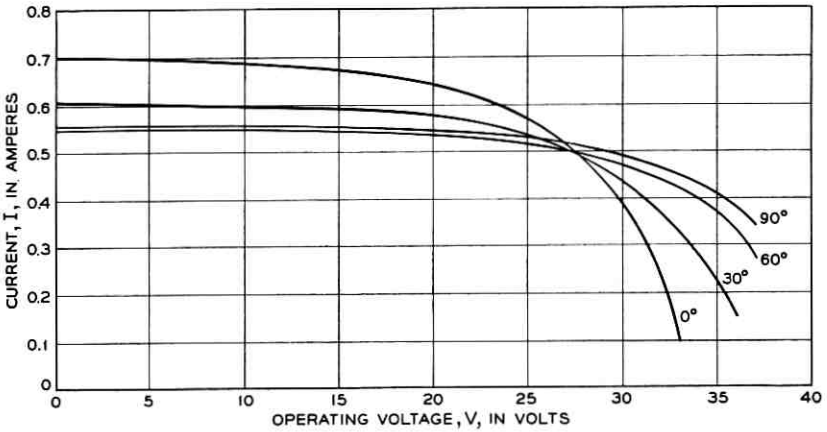

Fig. 28 — Calculated initial current output characteristic of the spacecraft solar plant.

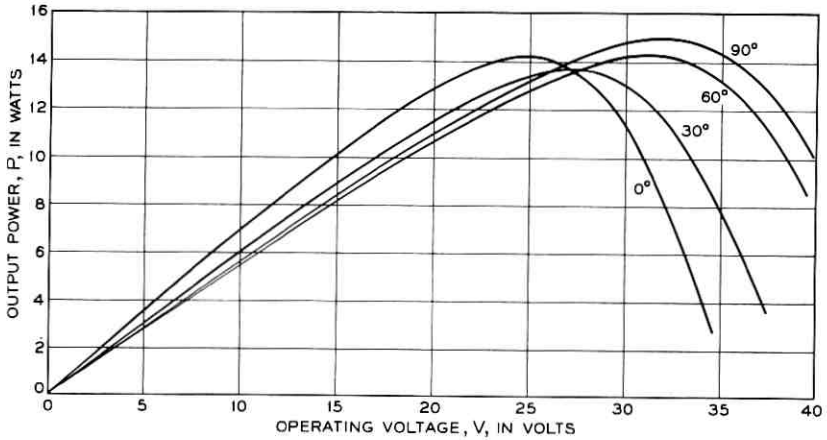

Fig. 29 — Calculated initial power output characteristic of the solar plant.

averaged output current contributed by each band was computed as a function of the operating voltage, taking into account the aspect angle, the calculated operating temperature of the cells on the band, the angle between the normal to the band and the spin axis, the efficiency of the strings and the number of strings on the band. The average solar plant output current is then the sum of the individual band outputs. The variation in the output characteristic with aspect angle is due primarily to the increased operating temperature of the solar cells as the aspect

TABLE III—CALCULATED BAND TEMPERATURES AS A FUNCTION OF ASPECT ANGLE

Band	Aspect Angle			
	0°	30°	60°	90°
1	69°C	49°C	15°C	−3°C
2	63°C	44°C	25°C	8°C
3	13°C	8°C	8°C	1°C
4		−70°C	−34°C	1°C
5			−41°C	8°C
6			−69°C	−3°C

angle changes from 90° to 0° as shown in Table III.[16] The increased short-circuit current at an aspect angle of 0° is the result of locating modules of a greater short-circuit current output near the poles of the satellite, as described earlier. The more rapid decrease of output current with increasing voltage at this aspect angle is entirely due to the high operating temperature of the modules. The solar plant was designed so that these two effects tend to compensate, and thus the initial output current at the battery charging voltage of about 28 volts is nearly constant, regardless of the orientation of the satellite in space.

5.6 *Flight Performance of the Solar Plant*

The first average current output from the Telstar solar plant after launch was obtained from telemetry data taken during pass 6. The average current during this pass was 492 ma at an average solar plant operating voltage of 24.8 volts. At the time of launch, the solar intensity was approximately 3.3 per cent less than mean solar intensity. Therefore, at mean solar intensity the output current would have been 509 ma for the same operating voltage. This is to be compared with the computed initial output current of 530 ma at 24.8 volts as shown in Fig. 28.

Immediately prior to launch it was discovered that one solar cell module in each of two strings had developed an open circuit due to thermally induced stresses during preflight testing. Since time did not permit replacement of these defective modules, they were electrically bypassed. Thus, two of the 50 strings of solar cells on the Telstar satellite are operating with only 60 series cells. Since near the operating point the output current varies only slowly with voltage, this defect has resulted in a loss of only about 0.2 per cent in average output current.

The average solar plant current for the first 160 days of operation is plotted as circles in Fig. 30. A number of corrections were applied in

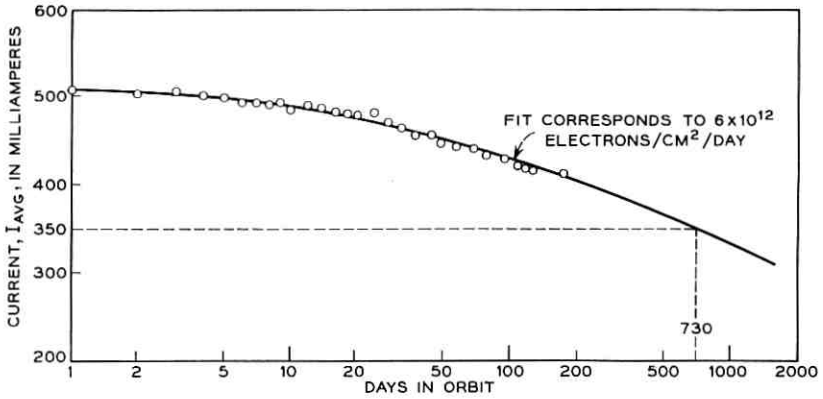

Fig. 30 — Average solar plant output current vs time in orbit.

Fig. 30 in order to suppress variations in output current that are not caused by radiation damage. The output current shows a peak-to-peak ripple of approximately 15 per cent. This ripple profile is scanned at a varying strobe rate as the spin rate changes. Care was taken to obtain a representative sample of the profile when extracting an average current. The variation due to solar distance changes was eliminated by normalizing to mean solar distance. The effect of changing load voltage was minimized by using only the measurements taken when the battery was near 25 volts. Corrections for temperature variations and variations in solar aspect were not applied. Thus the data in Fig. 30 must be considered preliminary; it is expected that the influence of the neglected corrections is small, but that their application may reduce the scatter in the points.

If the Telstar satellite had been exposed to a time-invariant radiation environment, then it should be possible to fit the observed output current points of Fig. 30 to a degradation curve under 1-Mev electrons similar to Fig. 4 by using a proper scale factor to convert time into 1-Mev electron flux. Fig. 4 shows the degradation of the short-circuit current of an average single cell; what is needed here is a corresponding curve for the output current of the solar plant at standard conditions (voltage, temperatures, solar aspect). Such a curve was computed, using the 1-Mev electron bombardment results of Section II, and is shown as the solid curve in Fig. 30. The ordinate scale was adjusted so that the initial value coincides with the measured one. The conversion factor for the abscissa which gives the best fit is 6×10^{12} electrons/cm^2 per day. Thus, the average radiation environment at the surface of the solar cell (i.e.,

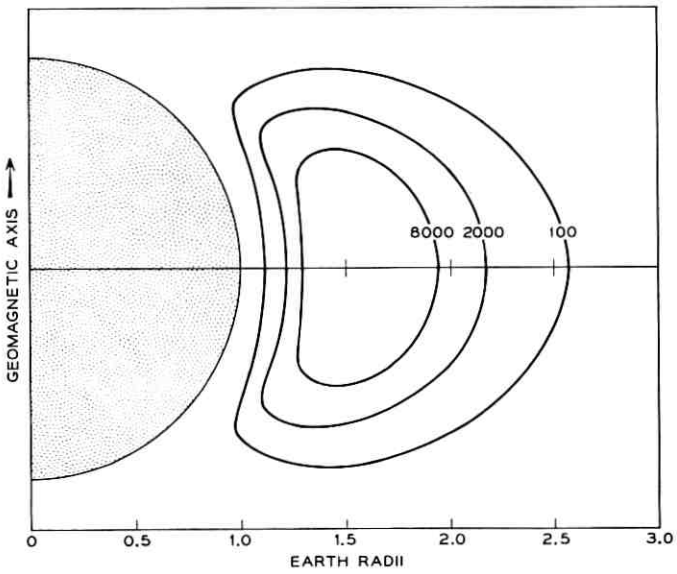

Fig. 31 — Isointensity contours of omnidirectional 24–36 Mev flux in protons/cm² per second.

behind the sapphire) can be characterized as being equivalent to a normal-incidence 1-Mev flux of 6×10^{12} electrons/cm² per day. We shall now compare this number with recently measured particle fluxes.

The satellite carries three proton counters, which cover the energy range of 3.5 to 80 Mev in three noncontiguous channels. Analysis of the counter data is only preliminary, and absolute flux values are of limited accuracy because of uncertainties in counter calibrations. The data of the counter whose sensitivity is in the 24 to 36 Mev range yield isointensity contours of omnidirectional flux as shown in Fig. 31 in equivalent dipole coordinates. Satellite perigee and apogee are at 1.15 and 1.9 earth radii, respectively, in geocentric coordinates, and are variable by about ±0.1 earth radius in dipole coordinates because of the magnetic irregularity of the earth. Measurements within the highest contour are not sufficiently extensive to allow the plotting of another contour, but they do indicate the existence of flux values three times as high as shown. Fluxes of this magnitude are not sufficient to account for the radiation damage observed in Telstar. More recent proton measurements on Explorer XV indicate fluxes of three orders of magnitude greater than the above for the energy range 4 to 12 Mev.[17] It thus appears reasonable that protons of energies greater than 14 Mev, which includes those protons able to penetrate the 30 mils of sapphire shielding, occur in

sufficiently high fluxes to produce an appreciable portion of the observed damage to the solar plant.

The electron counter on the satellite was designed to measure efficiently electrons of energy below 1 Mev.[18] The pulses are sorted into four channels, covering an energy-event range of 180 Kev to 990 Kev. The depletion layer width of the counter is such that electrons of energies between 200 Kev and 600 Kev are counted with relatively good efficiency as compared to those of higher energies. Thus, if the counter is operated in a radiation environment containing relatively high intensities of multi-Mev electrons, it is possible to get flux values only by making assumptions concerning their energy distribution. In arriving at the average electron flux to which the Telstar solar plant has been exposed, it has been assumed that in the high-intensity regions of the radiation belt the energy distribution is that of a uranium fission electron spectrum.[19] Under this assumption, the average intensity for the four-month interval from July to October, 1962, of the omnidirectional flux is found to be about 10^8 cm^{-2} sec^{-1}, for electrons of all energies.*

Time variation of the electron intensity arises from two causes: (1) a decay in intensity at a fixed position in space, the decay rate factor varying with position, and (2) a variation due to the precession of perigee. Both of these factors were estimated from the variation of counting rate in the third highest energy channel and were used in evaluating the July through October time average flux.

Preliminary experiments on the damage rates for multi-Mev electrons as a function of energy and absorber thickness indicate that a fission spectrum flux of omnidirectional intensity of 10^8 cm^{-2} sec^{-1} corresponds to an equivalent 1-Mev electron flux (normal incidence on an unshielded cell) of about 3×10^{12} cm^{-2} day^{-1}.

On the basis of the calculated equivalent electron flux of 3×10^{12} cm^{-2} day^{-1} for the radiation belt electron contribution to the solar plant degradation as compared to the observed 6×10^{12} cm^{-2} day^{-1} equivalent flux, it now appears that multi-Mev electrons are responsible for about half the observed damage, and protons are responsible for the remainder. A detailed comparison of the equivalent 1-Mev flux damage with the measured proton and electron fluxes is given in Ref. 20.

VI. SUMMARY AND CONCLUSIONS

Analysis of environmental effects on the performance of medium-altitude communication satellites showed that a severe radiation dam-

* Recent electron counter measurements on Explorer XV indicate that the average multi-Mev electron intensity may have been overestimated by about a factor of two.[17]

age problem exists. However, a useful power plant life on the order of years can be obtained by use of solar cells designed for high radiation resistance and by shielding of the solar cells.

Radiation resistance of silicon solar cells in space is achieved by designing them to be highly responsive to short-wave photons near the solar peak, by using the n-on-p structure, and by minimizing all losses which are not radiation-damage dependent. These include reflection losses, series and shunt resistive losses, and surface recombination losses. Special attention was given to development of a low-resistance electrical contact with good adherence to polished silicon surfaces.

The cells are mounted in 12-cell modules designed to be resistant to thermal shock and cycling, to provide a minimum of 0.3 gm/cm^2 protective shielding, and to withstand acceleration and vibration stresses encountered in launching. Inorganic materials are used in the module assembly to avoid deterioration in the space environment. Fifty strings of six modules each are connected in parallel to provide a nominal 28-volt output of 14 watts. The strings are mounted on the satellite skin in a configuration which provides substantially constant output for any orientation of the spin axis relative to the sun-satellite line.

The Telstar spacecraft solar plant output, as obtained from telemetry data, decreases with time as a result of particle irradiation. The time dependence agrees with that of an unbombarded solar cell that is exposed in the laboratory to a 1-Mev electron flux of 6×10^{12} electrons/(cm^2 day). From this comparison it is estimated that the plant will degrade to 68 per cent of its initial value after two years in orbit. Without other failures, occasional operation of the video channel should be possible even after 20 years in orbit, when the charging current will be in the order of one-half the initial value.

In future communication satellites, where switching is not used, the extension of solar power plant life to many years will be feasible by increasing the number of cells over that required initially. The penalty is not particularly severe, however, because of the logarithmic dependence of output on integrated radiation flux. For example, to extend the life of a particular power plant from two years to 20 years would require only about 20 per cent more cells on the satellite.

VII. ACKNOWLEDGMENT

The authors wish to express their appreciation for important contributions from many associates in Bell Telephone Laboratories and the Western Electric Co.; without their aid this work would not have been possible.

REFERENCES

1. Chapin, D. M., Fuller, C. S., and Pearson, G. L., A New Silicon p-n Junction Photocell for Converting Solar Radiation into Electrical Power, J. Appl. Phys., **25,** Jan., 1954, p. 676.
2. Smith, D. H., A 1-Watt Solar Power Plant, Communications and Electronics, No. 54, November, 1959.
3. Van Allen, J. A., Geomagnetically-Trapped Corpuscular Radiation, J. Geophys. Res., **64,** Nov., 1959, pp. 1683–1689.
4. Loferski, J. J., Rappaport, P., and Scott-Monck, J., Radiation Damage to Silicon Solar Energy Converters, R.C.A. Labs Quarterly Report No. 1, NASA Contract NAS5-47, October 15, 1960.
   Mandelkorn, J., Kesperis, J., McAfee, R., and Pharo, W., A New Radiation Resistant High Efficiency Solar Cell, NASA meeting on Radiation Damage to Semiconductors by High Energy Protons, Washington, D. C., October 20, 1960.
5. Naugle, J. E., and Kniffen, D. A., Flux and Energy Spectra of Protons in the Inner Van Allen Belt, Phys. Rev. L., **7,** July, 1961, pp. 3–6.
6. Freden, S. C., and White, R. S., Particle Fluxes in the Inner Radiation Belt, J. Geophys. Res., **65,** May, 1960, pp. 1377–1383.
7. Conference on Radiation Effects in Semiconductors, J. Appl. Phys., **30,** May, 1959.
8. Gummel, H. K., Smits. F. M., and Froiland, A. R., Method for Terrestrial Determination of Solar Cell Short Circuit Current under Outer Space Solar Illumination, I. R. E. WESCON Proc., July, 1961.
9. Gummel, H. K., and Smits, F. M., to be published.
10. Rosenzweig, W., Diffusion Length Measurement by Means of Ionizing Radiation, B.S.T.J., **41,** Sept., 1962, pp. 1573–1588.
11. Rosenzweig, W., Gummel, H. K., and Smits, F. M., Solar Cell Degradation under 1-Mev Electron Bombardment, B.S.T.J., **42,** Mar., 1963, pp. 399–414.
12. Rosenzweig, W., Smits, F. M., and Brown, W. L., Nuclear Electronic Effects Program, Tenth Triannual Note, July 15, 1962.
13. Naugle, J. E., and Fichtel, C. E., Flux and Energy Spectra of Protons in the Inner Van Allen Belt, Am. Phys. Soc. Bulletin II, **6,** Feb., 1961, p. 53.
14. Jaffe, L. D., and Rittenhouse, J. B., Behavior of Materials in Space Environment, Am. Roc. Soc., Meeting, Oct. 9–15, 1961.
15. Smits, F. M., Smith, K. D., and Brown, W. L., Solar Cells for Communication Satellites in the Van Allen Belt, J. Brit. Inst. Radio Eng., **22,** Aug., 1961, pp. 161–169.
16. Hrycak, P., Koontz, D. E., Maggs, C., Stafford, J. W., Unger, B. A., and Wittenberg, A. M., The Spacecraft Structure and Thermal Design Considerations, B.S.T.J., this issue, p. 973.
17. Brown, W. L., private communication.
18. Brown, W. L., and Gabbe, J. D., Electron Distribution in the Earth's Radiation Belts during July, 1962, as Measured by Telstar, J. Geophys. Res., **68,** Feb. 1, 1963, p. 607.
19. Carter, R. E., Reines, F., Wagner, J. J., and Wyman, M. E., Expected Cross Section from Measurements of Fusion Fragment Electron Spectrum, Phys. Rev., **113,** Jan., 1959, pp. 280–286.
20. Brown, W. L., Gabbe, J., and Rosenzweig, W., Results of the *Telstar* Radiation Experiments, B.S.T.J., this issue, p. 1505.

The Satellite Ferrimagnetic Power Limiter

By L. J. VARNERIN, R. L. COMSTOCK,
W. A. DEAN and R. W. KORDOS

(Manuscript received February 11, 1963)

To limit the 4080-mc local oscillator signal power input to the beat oscillator modulator of the Telstar satellite communications repeater, a subsidiary absorption limiter was used which consisted of an optically polished sphere of single-crystal yttrium iron garnet (YIG), placed in a resonant transmission cavity between the amplified 4080-mc output of the traveling-wave tube and the BO modulator input. The limiter holds the output power nearly constant above a given input threshold; below this threshold the YIG is linear and introduces only a small loss. The threshold is determined, for a given sample at a given frequency, by the external magnetic bias field. Temperature compensation over the desired range was obtained by orienting the crystal with the dc magnetic field along a [100] or "hard" axis. The total weight of the limiter package, including the bias magnet and cavity, is 13 ounces.

I. INTRODUCTION

The traveling-wave tube[1] in the Telstar communications repeater[2] serves to amplify both the 4170-mc output signal and the low-level (−12 dbm) 4080-mc local oscillator-beacon signal. The TWT gain for the 4080-mc signal is strongly dependent upon the 4170-mc signal level. If the signal to the satellite is lost, no 4170-mc signal is generated and the gain for the 4080-mc signal increases significantly. Additionally, temperature variations can cause undesired level changes. As can be seen from Fig. 1 of Ref. 2, the 4080-mc signal is the local oscillator for the beat oscillator modulator, which generates the 6300-mc local oscillator signal for the input down converter. This increased 4080-mc level can cause the modulator to oscillate.

To eliminate these effects a microwave ferrimagnetic power limiter was designed and incorporated to limit the 4080-mc level. Because this type of limiter incorporates a resonant cavity, it serves a required filter func-

tion of rejecting undesired signals which might cause instability. The limiter cavity loaded Q was designed to fulfill this need.

1.1 *Properties of Limiters*

Microwave power limiters are passive two-port devices which limit output power to a nearly constant value beyond some input threshold power level. Below this threshold limiters are linear and ideally introduce negligible loss. At a single frequency the power output (P_o) vs available power input (P_a) response of a limiter is shown in Fig. 1. The two thresholds, $P_{o\ crit}$ and $P_{a\ crit}$, are indicated as well as the shape of the limiting characteristic below and above the threshold. In the Telstar satellite application the limiter electrical and mechanical requirements are given in Table I and the mechanical requirements will be discussed in Section III. The temperature behavior of the device will be considered in detail in Section II.

Degenerate parametric oscillators make possible excellent power limiting devices, in which case the signal to be limited is used as the "pump" signal. Above the oscillation threshold the losses in the pump circuit increase since energy is required to sustain the oscillation, resulting in power limiting. For microwave ferrimagnets the pump circuit is the uniform precession motion of the magnetization coupled to a microwave circuit, and the parametrically excited systems are the "spin waves" which are bounded by the sample and not coupled to the external circuitry. A ferrimagnetic limiter employing single-crystal yttrium iron garnet (YIG) was chosen for the satellite requirements.

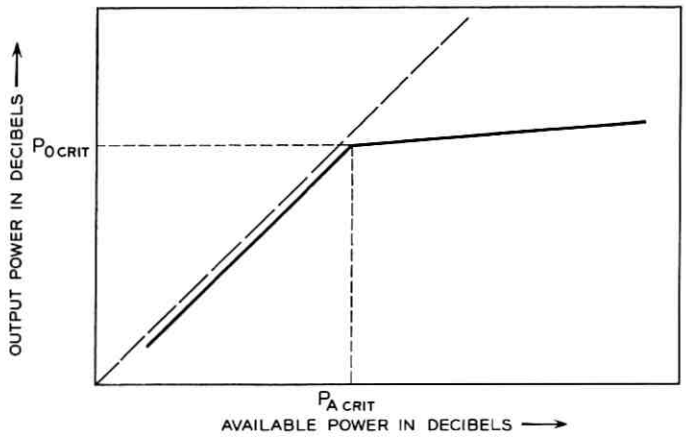

Fig. 1 — Output power (P_o) vs available power (P_a) for a power limiter.

TABLE I — POWER LIMITER REQUIREMENTS

Frequency of operation: 4080 mc
Bandwidth: to have a loaded Q of about 200
Quiescent point of operation: +14.5 dbm output power at +18.0 dbm input power
Output power at +26.0 dbm input power: < +17 dbm
Insertion loss below limiting level: <1.0 db
Temperature range of operation: +35°F to +120°F
Waveguide: silver-plated magnesium.

1.2 *The Subsidiary Absorption*

The degenerate parametric coupling of half-frequency spin waves in a ferrimagnet by the uniform precession has been discussed by Suhl.[3] Suhl's theory gives the threshold RF magnetic field at the sample (h_{crit}) as a function of the dc bias magnetic field, as shown in Fig. 2 for spherical samples. The ordinate is the ratio of h_{crit} to ΔH_k, the "spin wave" linewidth, while the abcissa is the ratio of the precession frequency, $\omega_o = \gamma H_e$ to the operating frequency ω, where γ is the gyromagnetic ratio. H_e is an effective bias field, the sum of the bias magnetic field H_{dc} and H_a the anisotropy field appropriate to the crystallographic axis with which H_{dc} coincides (see Section II). ω_m is $\gamma 4\pi M_s$, where $4\pi M_s$ (1750 oersteds for

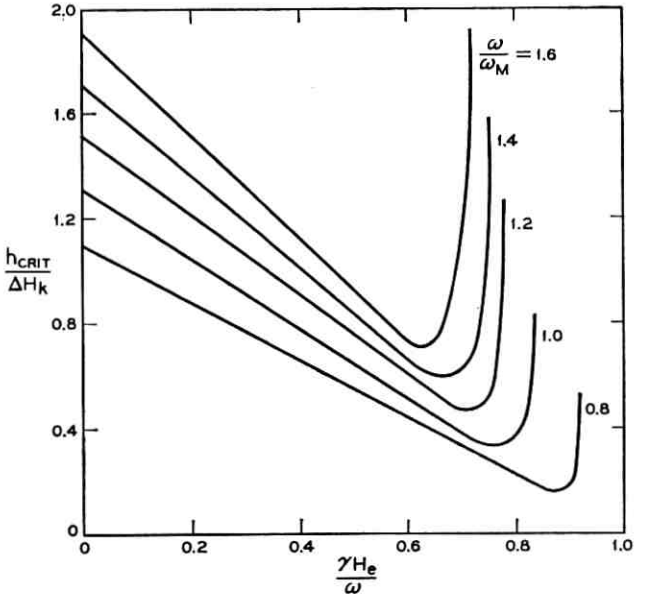

Fig. 2 — The subsidiary absorption threshold (h_{crit}) vs $\gamma H_e/\omega$ with ω/ω_M as a parameter (from Ref. 3).

YIG) is the ferrimagnetic saturation magnetization. The subsidiary absorption described by this curve always occurs at field values less than the resonance value, $(\omega_o/\omega) = 1$. For 4-kmc operation with YIG, ω/ω_M is 0.816. It is apparent from these curves that the threshold for the subsidiary absorption can be varied at a given frequency by varying the magnetic bias field. Above the threshold for the subsidiary absorption the losses in the ferrite sample increase, resulting in power limiting.

1.3 *The Ferrimagnetic Limiter*

A photograph of the completed limiter with the biasing magnet in position is shown as Fig. 3. A single-crystal spherical sample of YIG was mounted in the transmission resonant cavity and biased to the subsidiary absorption, with the external dc magnetic field perpendicular to the RF magnetic fields of the cavity mode. Single-crystal YIG was used since in this material the spin wave linewidth ΔH_k is extremely low

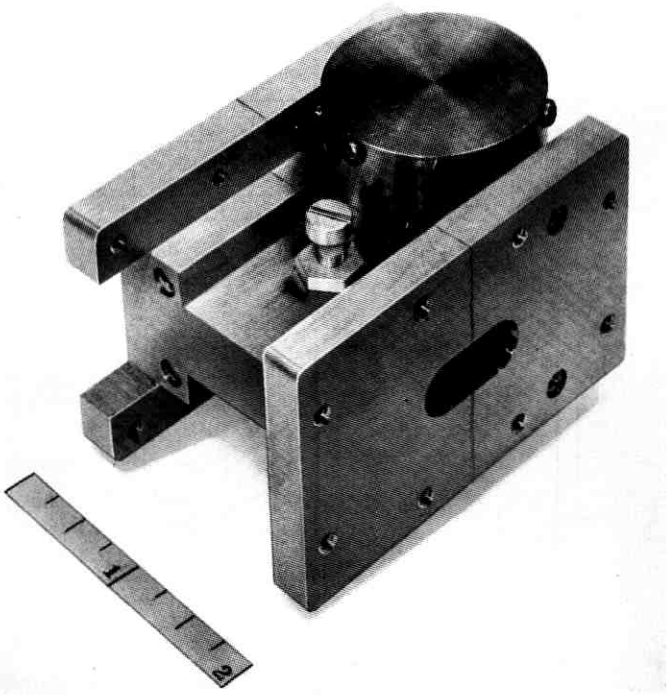

Fig. 3 — Ferrimagnetic limiter, showing the microwave cavity and external biasing magnet.

($\approx$0.3 oersteds) resulting in low thresholds (Fig. 2). Spherical geometry was chosen to minimize temperature effects since the ferromagnetic resonant frequency does not depend on the saturation magnetization, which varies with temperature.

II. ELECTRICAL DESIGN CONSIDERATIONS

2.1 *Insertion Loss and Limiting Threshold*

The transmission microwave cavity was made of reduced-height waveguide coupled to the external transmission lines with inductive irises. The cavity was excited in the TE_{101} mode as shown in Fig. 4. The YIG sphere was placed near the sidewall of the cavity and biased as shown. It is necessary to have a large ratio of sample to cavity volume so that the losses in the sample will represent a large change in the total cavity losses above the threshold (see Section 2.2). In this model it was found necessary to use spheres nominally 0.250 inch in diameter with cavities only slightly greater in height. Because of this large volume the sample contributes significant loss and reactance to the cavity mode below the threshold. The reactance contributed by a ferrimagnetic sample biased below the uniform precession resonance raises the cavity resonant frequency and thus can be compensated in part by a tuning screw placed in the maximum of the electric field, which will lower the cavity resonance by adding shunt capacitance. The transmission coefficient of the cavity at resonance is given by

$$T = \frac{1}{\left[1 + \frac{Q_e}{2Q_o}\right]^2} \tag{1}$$

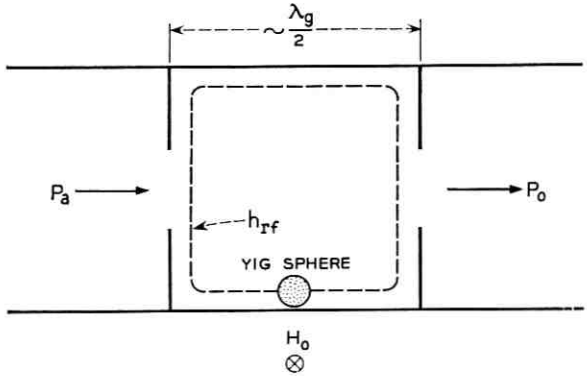

Fig. 4 — Schematic of the Telstar limiter.

where the loaded cavity $Q(Q_L)$ is given in terms of the external and unloaded Q's (Q_e and Q_o) by

$$\frac{1}{Q_L} = \frac{1}{Q_o} + \frac{2}{Q_e}.$$

In order to keep the low-level loss as low as possible, all precautions were taken to insure the largest value possible for Q_o. This included silver plating the cavity walls. (See Section III.) Thus the only electrical parameter available to maintain a low insertion loss is Q_e. However, the limiting threshold power also depends on Q_e as given by

$$P_{o\,\mathrm{crit}} = \frac{\omega}{Q_e} \frac{\mu_o h_{\mathrm{crit}}}{2} \int_{V_c} h^2 dV$$

where V_c is the cavity volume, with the sample placed where the RF magnetic field is maximum. Since the range of values of h_{crit}, at a given frequency, is bounded (Fig. 2) the specification of insertion loss and $P_{o\,\mathrm{crit}}$ are not independent. However, it was found possible to achieve a satisfactory insertion loss and still meet the threshold requirement given in Table I as well as the required Q (200) to serve the required filter function. The dc magnetic field required for this threshold was 1200 oersteds, resulting in $(\omega_o/\omega) = 0.840$ (neglecting the effect of crystalline anisotropy, as will be discussed presently). This operating point was chosen to lie somewhat on the low-field side of the minimum of the h_{crit} curve. The similar high-field point was found to have unsatisfactory temperature characteristics as well as a poorly defined break at threshold.

2.2 *Limiting Slope*

The behavior of the limiter in the nonlinear region of its operation depends critically on the ratio of sample to cavity volume. With the same cavity, reducing the sample size from 0.250 inch to 0.180 inch resulted in severe degradation of the limiting action. It was found that the limiting curve above the threshold was nearly a straight line over at least a 28-db dynamic range with a slope which decreased rapidly with sample volume. The sharpness of the discontinuity in the limiting curve from the linear to the nonlinear region was found to depend critically on the degree of sample polish. This result is unexplained on the basis of Suhl's theory. Experimental limiting curves are discussed in Section IV.

2.3 *Temperature Compensation*

Two limiter properties were found to vary to a significant degree over the temperature range given in Table I. These are the limiting threshold

and a thermal detuning resulting in increased low-level insertion loss. The variation in limiting threshold is due primarily to changes in h_{crit} caused by the temperature variation of the saturation magnetization ($4\pi M_s$), spin wave linewidth (ΔH_k), and anisotropy field (H_a). In the present case the crystal has cubic symmetry with the "easy" and "hard" magnetic axes long [111] and [100] directions, respectively. The temperature variations of $4\pi M_s$ and ΔH_k are such as to partially compensate the change in h_{crit} with respect to temperature, with the largest contribution being that due to variations in $4\pi M_s$; the net result is that h_{crit} increases with temperature. The anisotropy field can be used to compensate the residual temperature sensitivity, as can be shown using the curve in Fig. 5. This curve shows the variation in the effective bias magnetic field, including anisotropy, with respect to an angle θ measured from [100] as the sample is rotated about a [110] axis. In the two extreme cases $\theta = 0°, 54° 44'$, i.e., when the sample is oriented so that a "hard" and an "easy" axis are lined up along H_o , the effective field is given by

$$H_e\Big|_{[100]} = H_o - 2\frac{|K_1|}{M_s}$$
$$H_e\Big|_{[111]} = H_o + \frac{4}{3}\frac{|K_1|}{M_s} \qquad (2)$$

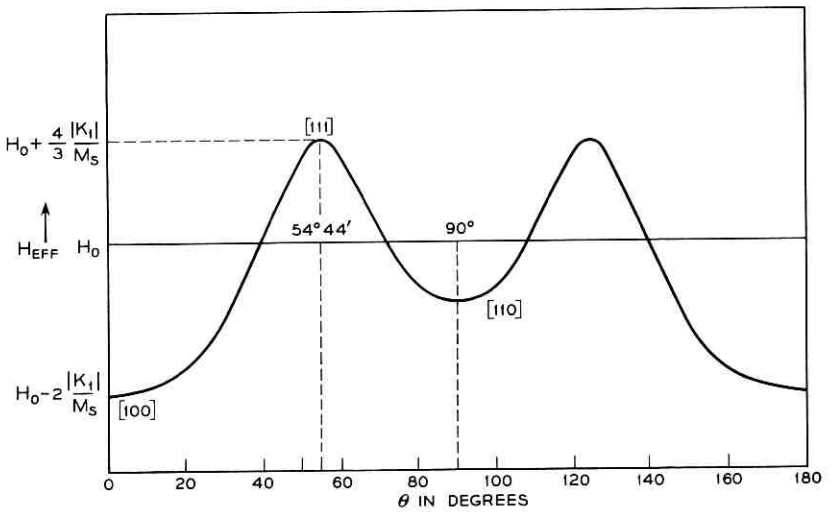

Fig. 5 — Effective static magnetic field, including anisotropy, for a cubic ferrimagnet for rotation about the [110] axis with $\theta = 0°$, corresponding to [100].

where K_1, the first-order anisotropy constant, is negative for YIG and decreases with temperature. The temperature variation of h_{crit} due to the temperature variation of H_e is given by

$$\frac{1}{h_{\text{crit}}}\frac{dh_{\text{crit}}}{dT} = \frac{1}{h_{\text{crit}}}\frac{\partial h_{\text{crit}}}{\partial H_e}\frac{dH_e}{dT}$$

where we see from Fig. 2 that $(\partial h_{\text{crit}}/\partial H_e) < 0$. Since it is necessary to compensate a positive value of $(1/h_c)(\partial h_c/\partial T)$ arising from changes in ΔH_k and $4\pi M_s$, it is seen that a positive value for dH_e/dT is needed, which can be obtained by orienting the sample with the dc magnetic field along [100]. Experimental results were obtained with orientation along both [100] and [111] which gave striking confirmation of the temperature compensation obtainable with this technique. The experimental results of Section IV show the effect of proper temperature compensation.

II. MECHANICAL DESIGN CONSIDERATIONS

13.1 *Cavity*

The limiter is constructed in a reduced-height, silver-plated magnesium cavity. The cavity is composed of two waveguide half-sections joined along the broad dimension, as shown in Fig. 3. Each half-section is of unit construction; the iris half-plates and the waveguide flanges at each end are an integral part of the machined piece to eliminate lowered Q's resulting from soldered iris plates. The over-all length of the cavity is 1.976 inches. The iris plates are 0.062 inch thick with centrally placed coupling irises (0.375 × 0.800 inch). Internal cross-section dimensions of the cavity are 0.400 inch high by 1.872 inches wide. The YIG sphere is placed 0.062 inch from the side wall of the cavity in a region of maximum RF magnetic field. The reduced-height cavity serves not only to give a large filling factor but to reduce appreciably the size and weight of the magnet required to bias the YIG sphere across the narrow waveguide dimension.

A silver-plated brass tuning screw is inserted in the broad dimension of the cavity and centrally placed along the length.

3.2 *Permanent Magnet*

An efficient permanent magnet capable of producing a field of approximately 1200 gauss across a 0.400-inch air gap was required in order to realize a practical limiter design. The magnet, designed for this application by M. S. Glass, contains two truncated cones of Alnico VI material of the proper length-to-diameter ratio to eliminate irreversible losses over the temperature range of interest. In addition it provides a very nearly

temperature-independent bias field. Two soft iron pole-pieces are used to concentrate the magnetic flux, and an outer case of heat treated tubing is used both as a return path and as an effective magnetic shield. The weight of the magnet assembly is approximately 9 ounces; the total weight of the limiter is 13 ounces.

3.3 *The YIG Sphere*

The diameters of the single-crystal YIG spheres used in the flight and test models of the satellite limiter ranged from 0.2470 inch to 0.2988 inch. Each sphere exhibited a highly polished surface which reduced the low-level insertion loss, made the slope transition more abrupt at the threshold and decreased the limiting slope.

The single-crystal YIG sphere was positioned in the cavity so that one of its three hard axes of magnetization was aligned along the direction of the static magnetic field. The hard magnetic axes of the YIG sphere were determined by first finding the four easy axes by allowing the sample to rotate freely in a uniform dc magnetic field so as to align itself along each of the [111] axes. Then a [100] or hard axis is uniquely defined and can be located and marked. This procedure eliminates the need for X-ray orientation and is sufficiently accurate for the required temperature compensation as shown in Section IV. The YIG sphere was supported 0.062 inch away from the cavity sidewall by encasing it in a Tellon package which was held firmly to the waveguide wall by a screw.

IV. PERFORMANCE

4.1 *Temperature Testing*

Fig. 6 shows the electrical characteristics of the 4080-mc limiter as a function of temperature. As noted, the compensated temperature performance of the device over the range from 35°F to 120°F was due to the alignment of a hard axis of magnetization of the YIG sphere with the direction of the applied dc magnetic field. All of the properties of the limiter fell within the specifications given in Table I over this temperature range.

4.2 *Mechanical Tests*

The limiter was subjected to the standard shock and vibration test with the following maximum test parameters:

Force	33 g
Frequency	40–2000 cps
Period	4.75 minutes

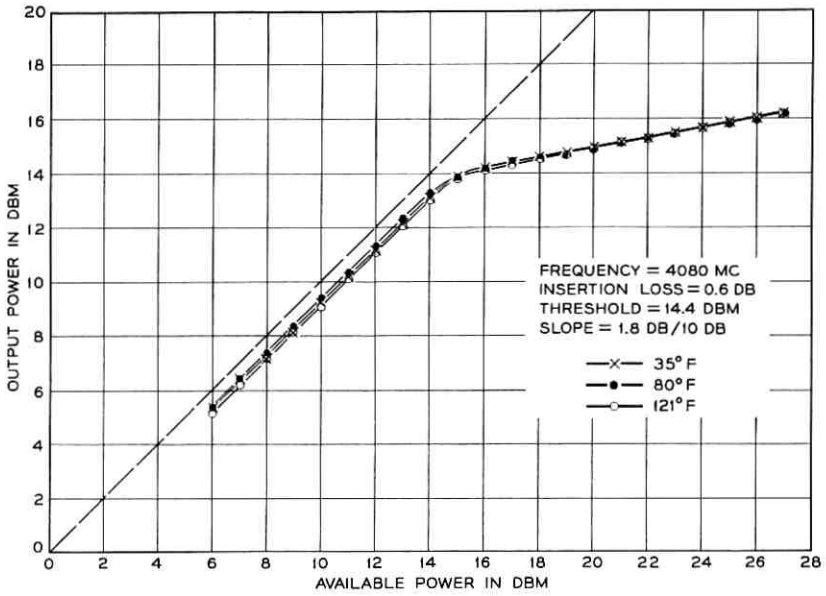

Fig. 6 — Experimental limiting curves for three operating temperatures. The YIG sample is oriented with a hard magnetic axis along the bias direction.

No degradation in the electrical performance of the limiter was observed following these tests. A centrifuge test was also performed with a maximum force of 30 g for three minutes and again no change in limiter performance was observed.

4.3 *Radiation Testing*

The ionizing radiation in the lower Van Allen belt consists of protons, electrons and gamma rays. The electrons have a moderate energy level (1 Kev to 100 Kev) and nearly all of them are stopped in the outer shell of the Telstar satellite. Nevertheless, electron radiation testing was conducted on the limiter, which is part of the electronic package within the satellite. Proton radiation testing was also performed on the limiter, since the protons of the lower Van Allen belt have relatively high energy (0.1 Mev to 1 Mev) and penetrate the entire satellite.

The irradiation test program on the limiter consisted of subjecting the single-crystal sphere of YIG and the Tellon package to the various types of radiation. Electrical tests were performed on a test limiter before and after radiation exposure, and it was found that the electron bombardment experiments had the largest effect. However, the electron energy

(1 Mev) corresponded to *unshielded* exposure in the lower Van Allen belt, and thus the effects under shielded conditions are expected to be much less than observed in this experiment. This effect probably is completely ascribable to electron radiation-induced dissipation in the Tellon holder. In the case of proton radiation with 10-Mev energy, slight degradation in the limiting slope characteristic was noted. It is conceivable that this also is attributable to the Tellon package; however, the highly polished YIG surface was observed to be slightly clouded. It is known that surface polish may have similar effects, and thus it is possible that there was an effect on the YIG sample primarily through surface damage. The gamma radiation test consisted of exposing the operating limiter to a low-intensity cobalt 60 source (1.3 curie) simulating conditions in the lower Van Allen belt. No effects on limiter characteristics were observed during the test.

V. CONCLUSIONS

As with many contributions to the Telstar project, the limiter development required considerable extension of existing device capabilities. Although the principle of ferrimagnetic limiting had been known for some time, there existed no well developed device technology or detailed design theory. The temperature stability requirements presented a particularly challenging problem. The basic understanding of ferromagnetic resonance and spin wave instability, particularly in single crystals, provided the basis for the rapid development of a design theory and limiter realization. The temperature dependence of the magnetocrystalline anisotropy (anisotropy field) provided the key which made possible the limiter design described in this paper.

VI. ACKNOWLEDGMENTS

The authors wish to acknowledge the many stimulating discussions with and contributions of R. C. LeCraw, E. G. Spencer, F. C. Rossol, V. Czarniewski, T. W. Mohr and J. Degan.

REFERENCES

1. Bodmer, M. G., Laico, J. P., Olsen, E. G., and Ross, A. T., The Satellite Traveling-Wave Tube, B.S.T.J., this issue, p. 1703.
2. Davis, C. G., Hutchinson, P. T., Witt, F. J., and Maunsell, H. I., The Spacecraft Communications Repeater, B.S.T.J., this issue, p. 831.
3. Suhl, H., Theory of Ferromagnetic Resonance at High Signal Powers J. Phys., and Chem. of Solids, **1**, April, 1957, pp. 209–227.

The Ground Station High-Power Traveling-Wave Tube

By R. J. COLLIER, G. D. HELM, J. P. LAICO and K. M. STRINY

(Manuscript received February 27, 1963)

The M4040 is a 2-kw CW traveling-wave tube developed specifically for communications applications. It was used as the power amplifier in the Project Telstar ground transmitter. Analytic methods employed in the design of the electron gun, the beam collector, the RF circuit and the output match are presented. Typical performance characteristics and drawings of the tube subassemblies serve to describe the electrical and physical features of the M4040 traveling-wave tube. Methods used to inhibit oscillation and the effects of ion drainage and collector depression on tube performance are also discussed.

I. INTRODUCTION

This paper describes the design of the M4040 2-kw CW traveling-wave tube amplifier which was developed specifically for communications applications. It was used as the final power amplifier in the Telstar transmitters at Andover, Maine, and Pleumeur-Bodou, France. It was necessary for the Telstar amplifier to meet the requirements shown in Table I.

The M4040 was designed to have sufficient instantaneous bandwidth to operate anywhere in the communications band from 5.925 to 6.425 gc. The design approach was a conservative one aimed primarily at delivering an operable tube in time for the Telstar experiment. The development time was approximately 18 months. In describing the M4040, we shall discuss only briefly its mechanical aspects. The prime intent is to present electrical design and operating information which may be applicable to future high-power traveling-wave tube development. Topics concerned with the electrical design of the electron gun, the beam collector, and the slow-wave structure will be discussed. Finally, some performance characteristics will be presented, accompanied by comments on the tube operation.

TABLE I — REQUIREMENTS

Output power (maximum)	2 kw CW
Small-signal gain	30 db
Large-signal gain	27 db
Bandwidth	25 mc
Center operating frequency	6.39 gc
Output amplitude ripple (small signal)	±0.5 db
Input signal amplitude range	30 db

II. GENERAL DESCRIPTION OF THE M4040

The M4040 is an all metal and ceramic electron tube 4 feet in length, 17 inches in diameter, and 230 pounds in weight. These dimensions include an aluminum foil solenoid which produces an axial beam-focusing field of 730 gauss along the 13 inches of slow-wave circuit. The electron gun is magnetically shielded, as is the solenoid and collector. The gun is a Pierce convergent type. The slow-wave circuit is a coupled-cavity structure with coupling slots rotated by 180° in each successive cavity. A single sever is employed. The sever attenuators are located in short waveguides matched to the circuit but are still in the vacuum. Microwave power is fed into and coupled out of the tube through ceramic windows, step transformers, narrow-height guide and matching cavities which form part of the slow-wave structure. The beam diverges into the beam collector under the action of space-charge forces alone. The slow-wave structure, solenoid and beam collector are separately water-cooled. Fig. 1 is a photograph of the M4040 located in the solenoid. The appendage ion pumps shown in the figure continuously pump the tube at the gun, as well as at the collector end. In the picture, the collector is at the top and the gun is at the bottom.

Fig. 2 is a cutaway section. Axial alignment of the tube in the magnetic field is preplumbed, and no adjustments are necessary to optimize their relationship. Figs. 3 to 7 are sketches showing more detail of the tube construction: respectively, the gun, RF circuit, collector, sever, and coupling assemblies. The construction materials are typical of those used in electron devices in that they have low vapor pressures and can withstand vigorous cleaning and the heating associated with outgassing. The residual gas pressure in a sealed-off M4040 is less than 1×10^{-8} torr. The tube is outgassed by heating, not only when the tube is finally processed, but also in the subassembly stages indicated in substance by Figs. 3 to 7, inclusive.

The gun shown in Fig. 3 is made of molybdenum, tungsten, and ceramic parts welded, brazed or glazed together. The spacing of the beam-forming electrode to the cathode is held to ±0.0003 inch, and the

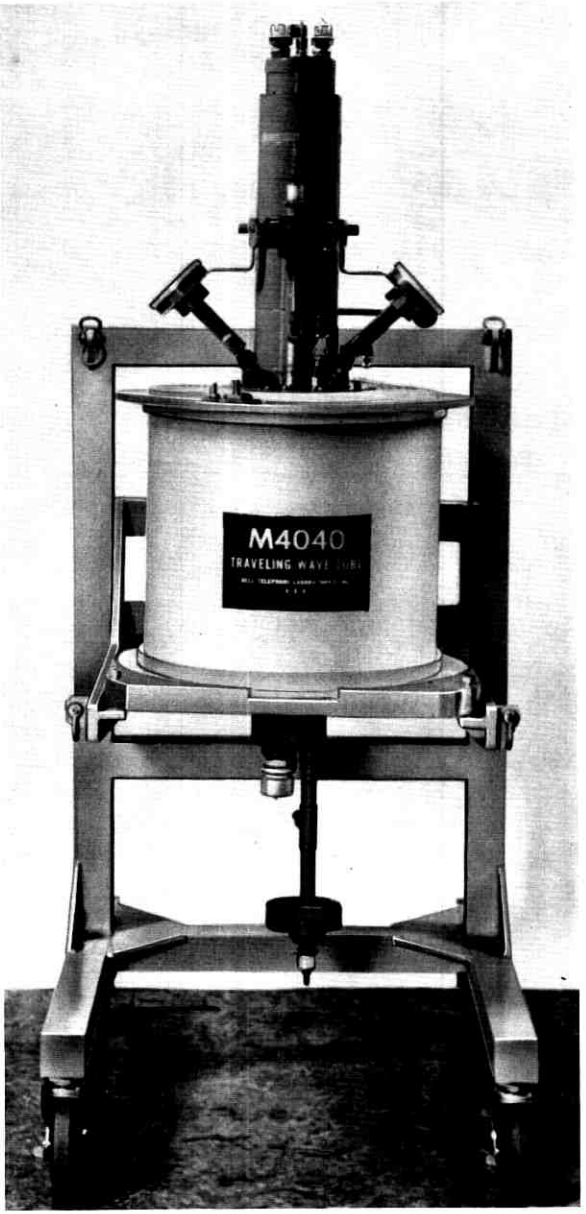

Fig. 1 — The M4040 traveling-wave tube.

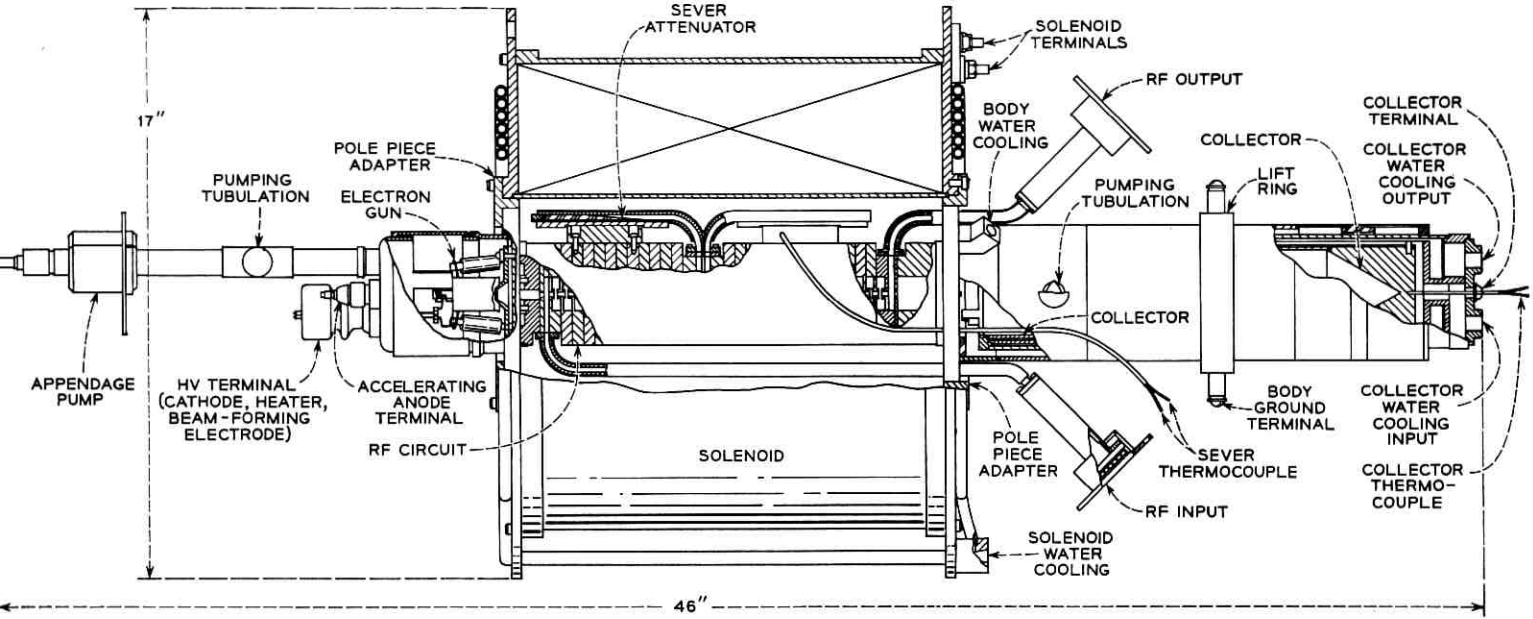

Fig. 2 — Internal structure of the M4040 tube.

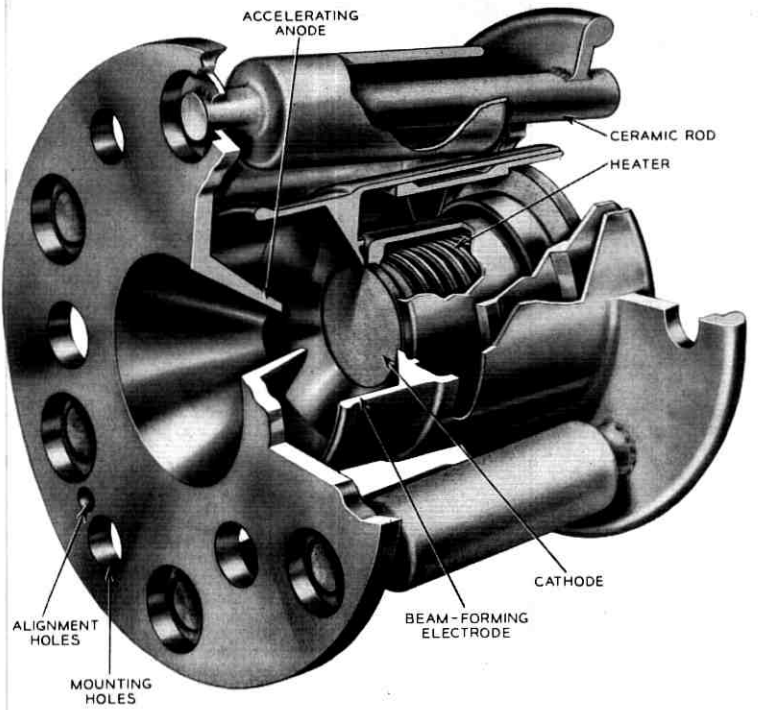

Fig. 3 — M4040 electron gun.

concentricity of these with respect to each other and to the accelerating anode is held to ±0.001 inch. Six Alsimag 475 insulators support and electrically isolate the accelerating anode from the cathode and the beam-forming electrode so as to safely withstand 18,000 volts. Re-entrant skirts are an integral part of these insulators and insure against electrical leakage arising from the deposition of metallic vapors emanating principally from the cathode; the latter is a Phillips Metallonics type B tungsten matrix cathode.

The RF structure identified in Fig. 4 consists of a stack of 29 copper cavities capped at each end by a steel pole-piece and machined at its center to provide for the addition of the sever sections. Adjacent to each steel pole-piece is the input or output waveguide, respectively. In each cavity and pole-piece, holes or channels are machined so that when the parts are finally brazed together, they not only form the RF circuit but also provide the path for circulating cooling water. The brazed assembly

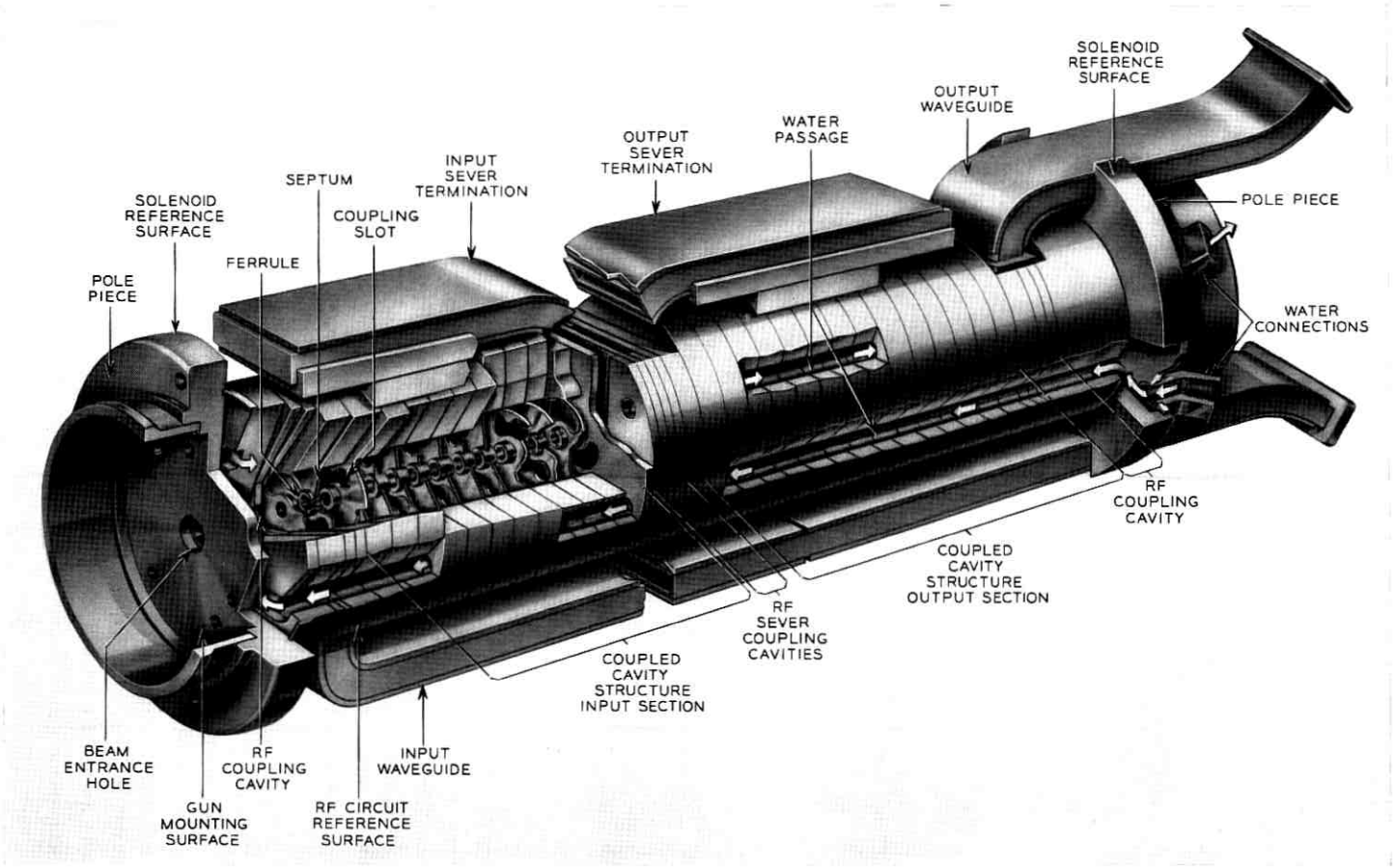

Fig. 4 — M4040 RF circuit.

meets the concentricity requirement of 0.004 inch on all central holes with respect to each other and to the outside diameter of the pole-pieces. After auxiliary subassemblies such as the sever sections and waveguides are assembled, the unit is outgassed by heating to about 500°C until a pressure of 5×10^{-6} torr is achieved.

In Fig. 5 the collector subassembly is shown. This is a set of concentric tubes of copper and steel to provide, in addition to the beam collector cavity, an annular channel for the passage of cooling water at the rate of 18 gpm. The collector is electrically isolated from the body of the tube by a ceramic insulator, allowing any beam current intercepted by the slow-wave structure to be monitored.

A sever section subassembly is shown in Fig. 6. A significant feature of this unit is the carbonized ceramic attenuator, which is a wedge of porous alumina 0.156×1.372 inches at one end and tapering to a point at the other end. To aid in dissipating some 300 watts of unwanted power, it is brazed to a molybdenum base plate. One surface of the ceramic is metallized with standard molybdenum manganese powder mixture in the empirically determined pattern shown in Fig. 6. Carbonizing is accomplished by soaking the unit in sugar solution and then converting the sugar to carbon by heating to 900°C in a purified dry hydrogen atmosphere.

The RF coupling assembly shown in Fig. 7 is the same for the input and output. It contains a step transformer section and an RF window which also forms part of the vacuum wall. The metal member of this vacuum seal is especially designed to provide sufficient elasticity to compensate for the mismatch in expansion between it and the ceramic and to better withstand thermal shocks.

An electrical description of the M4040 is furnished by Tables II, III and IV.

III. VOLTAGE SCALING OF AN ELECTRON GUN

To minimize development time, it was decided to scale in voltage a gun whose properties were previously measured at 1000 volts. We were able to predict the beam minimum radius and perveance quite successfully, enabling work on the slow-wave circuit to progress in parallel with the gun measurements program. The measurements of the beam cylindrical symmetry and the beam profile as a function of voltage and of distance from a reference surface on the beam-forming electrode were performed using the "pin-hole collector" technique.

Figs. 8(a) and 8(b) present measurements of the beam minimum radius and its location as a function of voltage. The radius is taken as

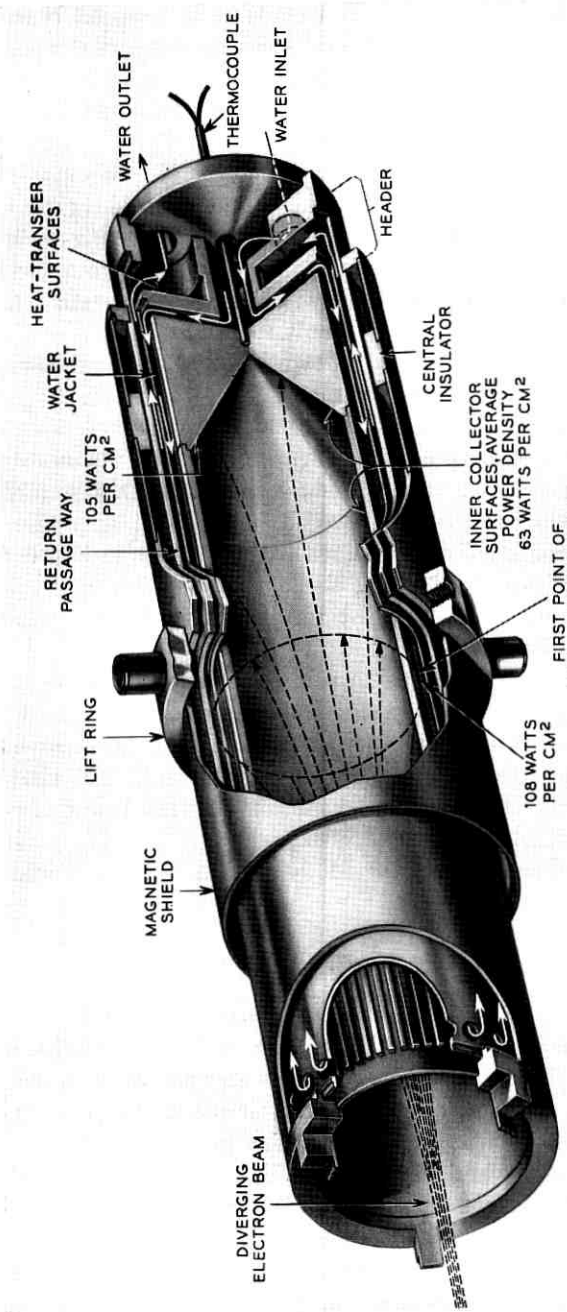

Fig. 5 — M4040 collector.

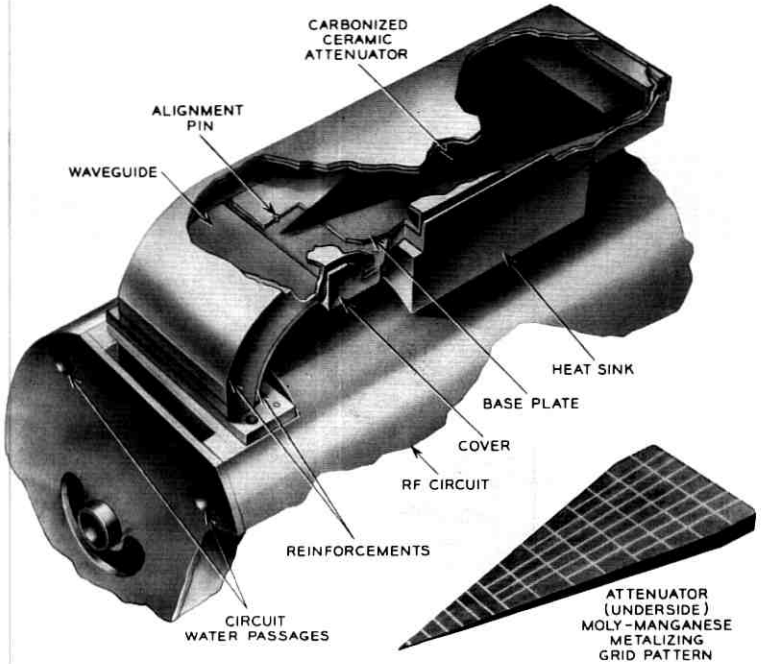

Fig. 6 — M4040 sever termination.

that which encloses 95 per cent of the total current. If the thermal motion of the electrons is neglected, these quantities are theoretically constant and are given by the curves labeled "universal beam spread." The latter were calculated by the methods described in Pierce[1] but with an additional correction for the focal length of the anode-aperture lens given by $\Gamma = 1.1$, where Γ is defined as in Danielson, Rosenfeld and Saloom.[2] On the other hand, transverse thermal velocities of the electrons cause the beam minimum radius to be smaller and closer to the cathode than predicted by the universal beam spread curve.

Danielson, Rosenfeld and Saloom have devised a theory which predicts the size and location of the beam minimum radius as a function of voltage and cathode temperature for several values of perveance. Their results were generalized by Herrmann[3] who presented curves having a wider applicability. The results predicted by Herrmann are shown in Figs. 8(a) and 8(b) for comparison with the experimental data and the universal beam spread values.

Fig. 8(a) suggests that a useful rule to apply when predicting the

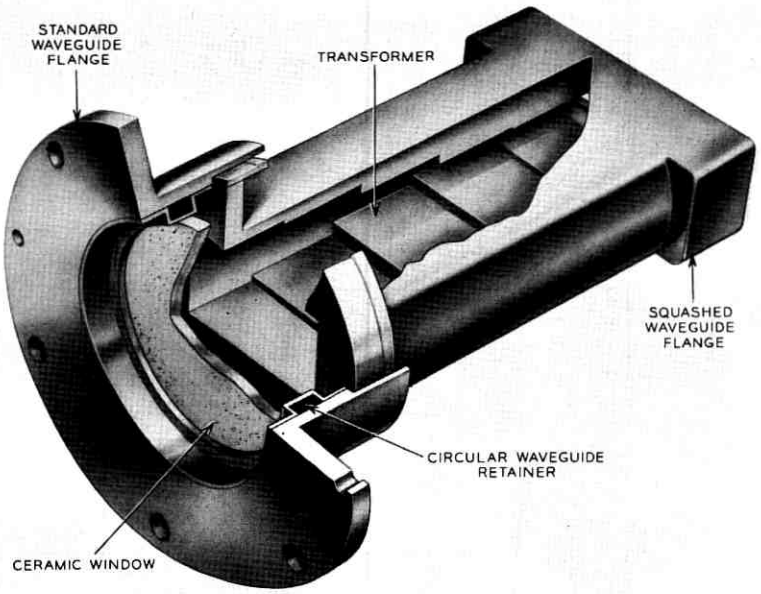

Fig. 7 — M4040 RF window assembly.

beam properties of an electron gun at a scaled voltage is that the theoretical behavior is given by the Herrmann curves up to the voltage at which they intersect the universal beam spread values and by the latter quantities at higher voltages. In comparing theory and experiment, we note that the experimental beam minimum radius is larger by 10 to 20 per cent, and its location falls within 10 per cent of the expected distance from the cathode.

TABLE II — ELECTRICAL DESIGN PARAMETERS AT MIDBAND

Midband frequency	6.15 gc
Gun perveance	0.47×10^{-6} amp/(volts)$^{\frac{3}{2}}$
Gain parameter, C	0.062
Space charge parameter, QC	0.3
(Radial phase constant) × (beam radius), γr_b	0.65
Growing wave parameter, X	0.65
Velocity parameter, b	1.0
No. of beam wavelengths, N	20
No. of active cavities	29
Beam radius (r_{95}), r_b	0.049 inch
Tunnel radius, a	0.082 inch
Cathode radius, r_c	0.205 inch

TABLE III — TYPICAL CHARACTERISTICS FOR M4040 OPERATED IN THE *Telstar* GROUND STATION

(a) Input	
Cathode potential	−17,000 v
Accelerator potential	+600 v
Circuit potential	0 v
Collector potential	0 v
Heater current	6.2 amps
Heater voltage	7.25 v
Solenoid current	23 amps
Solenoid voltage	15.3 v
Total cathode emission current	1030 ma
Collector water flow rate	18 gal/min
Circuit water flow rate	3.5 gal/min
Solenoid water flow rate	0.5 gal/min
Maximum signal power	3 watts
(b) Output	
Rated frequency range	6.35-6.45 gc
Rated maximum output power	2000 watts
Small-signal gain	31.8-30.8 db
Output amplitude ripple	±0.2 db
Gain at 2000-watt level	28 db
Magnetic field	730 oersted
Circuit interception current (no drive)	4 ma
Circuit interception current (with drive)	35 ma
Accelerator interception current	0.1 ma

TABLE IV — TYPICAL M4040 CHARACTERISTICS FOR BROADBAND HIGH-POWER OPERATION

(a) Input	
Cathode potential	−17,400 v
Total cathode emission current	1040 ma
Signal power	≈4 watts
(Other values are the same as in Table IIIa)	
(b) Output	
Center frequency, f_0	≈6.15 gc
Output power at center frequency	2500 watts
Gain at f_0 and at 2500-watt level	28 db
1-db instantaneous bandwidth (i.e., band edge power = 2 kw)	12.7% = 780 mc
Efficiency at f_0	13.8%

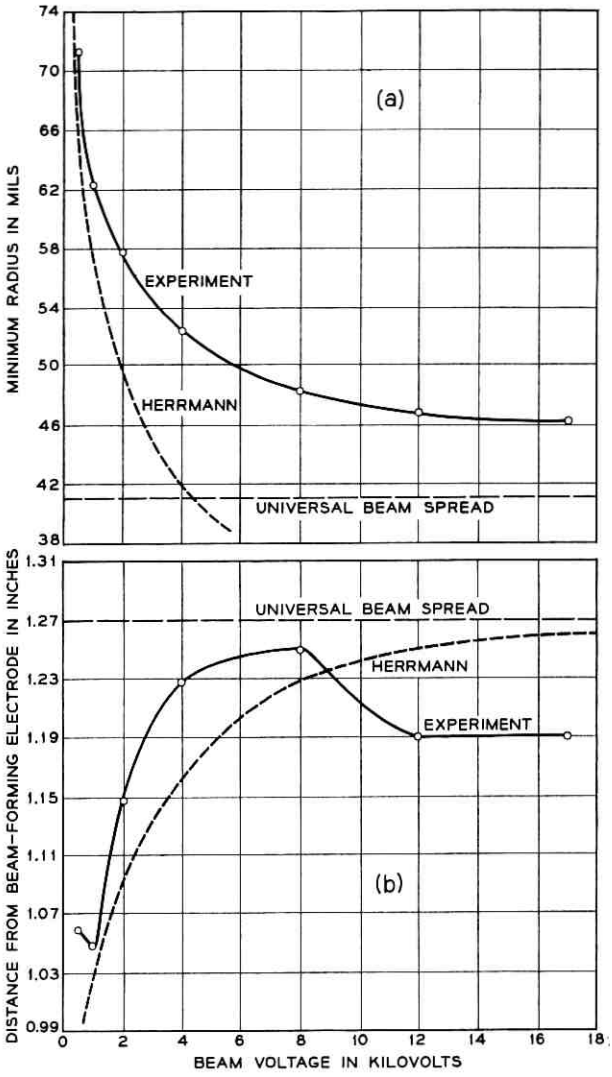

Fig. 8 — (a) Minimum beam radius (95 per cent of total current) vs beam voltage; (b) position of beam minimum vs voltage.

IV. DISTRIBUTION OF BEAM POWER IN THE COLLECTOR

If size and weight are of little consequence, the beam collector of a traveling-wave tube should be designed to minimize temperature inside the vacuum. Let us consider the spread of a monovelocity, homogeneous beam into an ideal hard-vacuum, field-free region. The universal beam

spread curve referred to in the previous section has been derived by several authors.[1,4] The relation between the axial distance the beam has drifted and the beam radius can be written as

$$z = \frac{r_0 Z}{\sqrt{K}} \tag{1}$$

where r_0 is the beam radius on entering the field-free region and

$$K = \frac{I}{V^{3/2}} \cdot \left(\frac{m}{e}\right)^{1/2} \cdot \frac{1}{2\sqrt{2}\pi\epsilon_0}. \tag{2}$$

The beam radius r_b appears in the expression for Z, viz.

$$Z = \int^{t} 2e^{t^2}\, dt \tag{3}$$

where $t = \sqrt{\ln R}$, in the form of a normalized radius $R = r_b/r_0$. The half-value of the integral in (3) is tabulated by Jahnke and Emde[5] for various values of t. One can plot the normalized radius R against the normalized axial distance Z to obtain the "universal beam spread curve." Applying the specific values of the normalizing constants associated with the M4040, we plot in Fig. 9 r_b versus z. Also plotted in

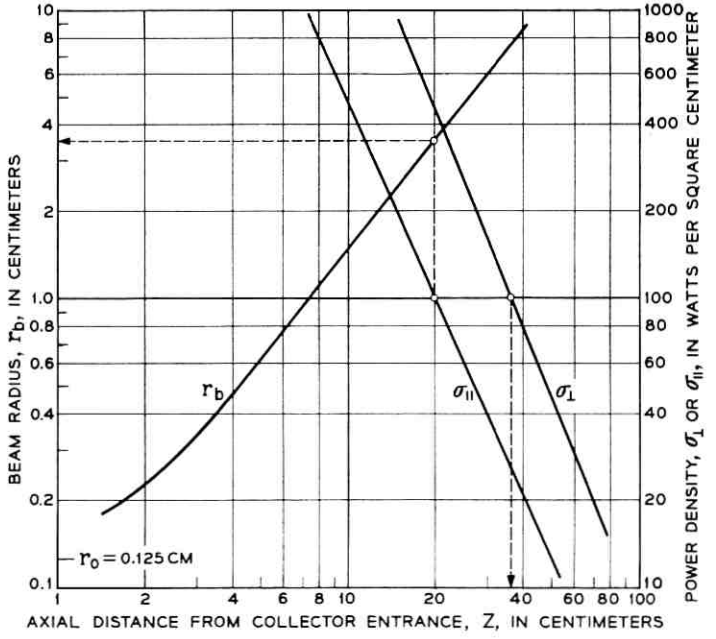

Fig. 9 — M4040 collector design chart.

Fig. 9 is the power density incident on a surface normal to the beam axis, $\sigma_\perp$, whose value is obtained for any value of z by dividing the total beam power by the area of a circle whose radius is read from the r_b versus z plot. The M4040 has been designed with a total beam power of about 17.7 kw so that the power density at the minimum radius of the beam ($r_0 \approx 0.125$ cm) is $\sigma_\perp \approx 360$ kw/cm^2.

If it is assumed that the collector is cylindrical in shape, the power density incident on a surface parallel to the beam axis, $\sigma_\parallel$, will be of interest. Consider the beam to be spreading such that the edge electrons make an angle φ with the initial beam axis. Then the power illuminating a small area, $A_\perp$, which is located at the beam edge and is perpendicular to the initial beam axis, is given by $\sigma_\perp A_\perp$. When $A_\perp$ is projected by the beam illumination onto the surface parallel to the initial beam axis, it takes the value $A_\parallel$ such that

$$\frac{A_\perp}{A_\parallel} = \tan \varphi = \frac{dr_b}{dz} = r_b'. \tag{4}$$

Equating the power incident on $A_\perp$ to that on $A_\parallel$

$$\sigma_\perp A_\perp = \sigma_\parallel A_\parallel \tag{5}$$

where $\sigma_\parallel$ is the power in the beam edge incident on a square unit area parallel to the initial beam axis. Upon the substitution of (4) into (5), we find that

$$\sigma_\parallel = \sigma_\perp r_b' = \sigma_\perp \sqrt{K}\, \sqrt{\ln r_b/r_0}\,. \tag{6}$$

The expression for r_b' is obtained in deriving (1). $\sigma_\parallel$ is plotted as a function of z in Fig. 9. Note that the interception of the beam edge on the cylindrical walls of the collector corresponds to the highest power density incident on those walls, since tan φ becomes smaller for all other conditions. Therefore, the collector may be designed such that the cylinder length determines when $\sigma_\perp$ equals the maximum desired and the cylinder radius determines the same value for $\sigma_\parallel$. The length and radius corresponding to a power density of 100 watts/cm^2 are indicated on Fig. 9 for the M4040. This chart indicates the hottest spots. The power density on the side wall will average to the order of half $\sigma_\parallel$.

V. ANALYTICAL METHODS FOR DESIGNING AND MATCHING THE SLOW-WAVE CIRCUIT

Fig. 4, the sketch of the RF circuit, indicates that a relatively rugged, easily fabricated slow-wave structure can be formed from an induc-

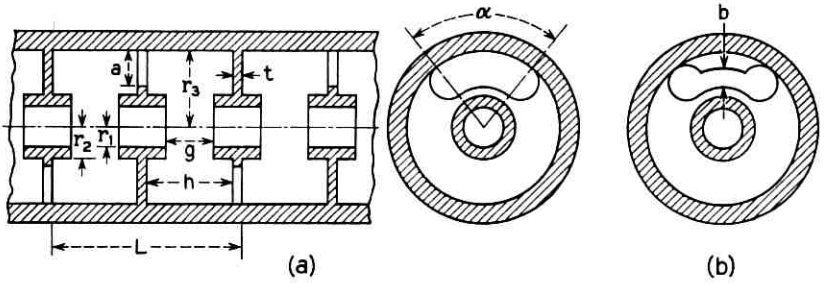

SUMMARY OF M4040 CIRCUIT DIMENSIONS			
a	0.325"	r_1	0.082"
b	0.1625"	r_2	0.122"
g	0.116"	r_3	0.5235"
h	0.294"	L	0.668"
t	0.040"	α	75°

Fig. 10 — (a) Slow-wave circuit dimensions showing unloaded coupling iris; (b) septum with a loaded coupling iris.

tively coupled chain of cylindrical cavities. Excellent heat dissipation properties are combined with a good impedance-bandwidth product. The important dimensional parameters are designated in Fig. 10; the parameter labels are those used in the analysis below.

ω-β diagrams for the four lowest modes are shown in Fig. 11. The M4040 is designed to operate on the first forward wave space harmonic of the TM_{01} cavity mode. Where the resonant frequency, ω_s, of the coupling slot is appreciably higher than the upper cutoff frequency, ω_2, of the cavity, the dispersion curve of the TM_{01} cavity mode may be approximated by the equation

$$\cos\left(\frac{\beta L}{2}\right) = 1 - 2\frac{\left[\frac{1}{\omega^2} - \frac{1}{\omega_2^2}\right]}{\left[\frac{1}{\omega_1^2} - \frac{1}{\omega_2^2}\right]}. \tag{7}$$

Here ω_1 is the lower cutoff frequency of the mode and L is the periodic length of the circuit.

The choice of the electron gun design establishes the electron beam radius, r_b, and the beam velocity, u_0. These in turn determine the cavity beam hole radius $r_1 \approx 1.67\ r_b$ and the periodic length $L \approx 3\pi u_0/\omega_0$,

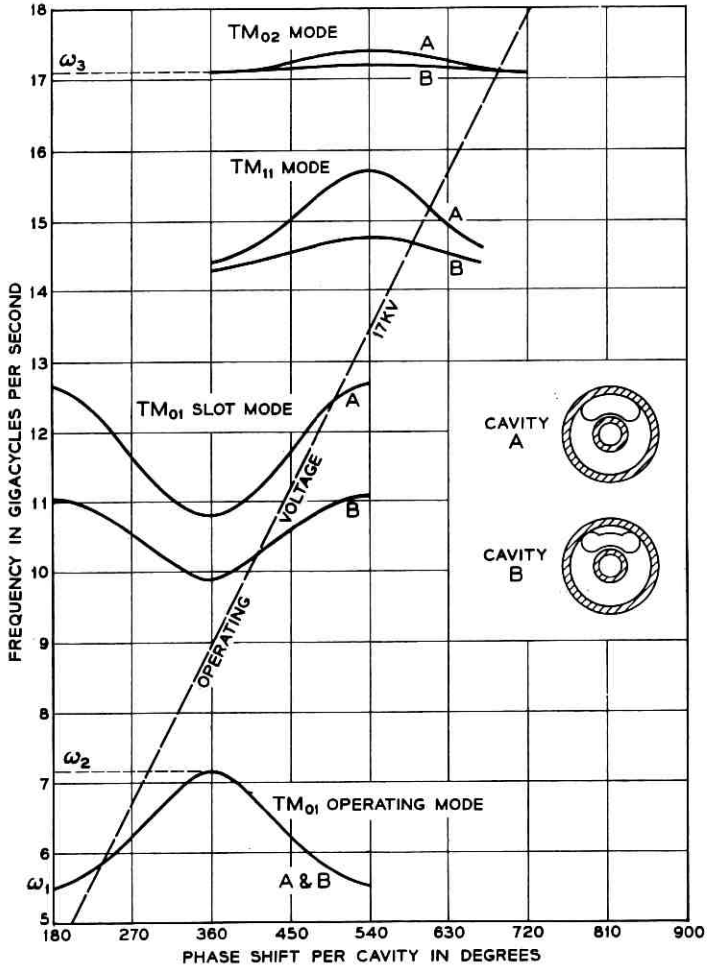

Fig. 11 — ω-β diagrams.

where ω_0 is the synchronous frequency. The gap, g, between the ferrules capacitively loading the cylindrical cavities, is used to optimize the interaction impedance of the forward wave space harmonic. To this effect the gap-to-period ratio g/L is selected to lie between 0.1 and 0.2. The outer radius of the ferrule, r_2, and the septum thickness, t, are designed to be as small as possible consistent with the heat energy to be dissipated.

Following Ramo and Whinnery,[6] the cavity may be analyzed as a

foreshortened radial line resonator. The major cavity radius, r_3, which sets the upper cutoff frequency, ω_2, may be calculated from the expression

$$\theta_3 = \tan^{-1}\left[\frac{\sin\theta_2 + (2\pi r_2/\omega_2 C_0 Z_{02} h)\cos\psi_2}{\cos\theta_2 - (2\pi r_2/\omega_2 C_0 Z_{02} h)\sin\psi_1}\right] \tag{8}$$

where

$$\theta_i = \tan^{-1}\left[\frac{N_0(kr_i)}{J_0(kr_i)}\right]$$

$$\psi_i = \tan^{-1}\left[-\frac{J_1(kr_i)}{N_1(kr_i)}\right]$$

$$Z_{0i} = 377\left[\frac{J_0^2(kr_i) + N_0^2(kr_i)}{J_1^2(kr_i) + N_1^2(kr_i)}\right]^{1/2}$$

and $k = \omega/c$, the wave number. J_0, J_1, N_0, N_1 are Bessel functions of the first and second kinds and C_0 is the loading capacitance. The latter is estimated as the sum of four parallel connected capacitances

$$C_0 = C_g + C_h + C_{d1} + C_{d2}. \tag{9}$$

The gap capacitance, C_g, is the equivalent parallel plate capacitance for an area equal to that on a ferrule edge, $\pi(r_2^2 - r_1^2)$, and a separation, g. Thus

$$C_g = \epsilon_0\pi(r_2^2 - r_1^2)/g. \tag{10}$$

The "hole" capacitance, C_h, is an artifice made by assuming a parallel plate capacitor with area equal to the beam hole area and a separation $L/2$. Then

$$C_h = 2\epsilon_0\pi r_1^2/L. \tag{11}$$

The capacitances C_{d1} and C_{d2} are the discontinuity capacitances located at r_1 and r_2, i.e., where the cavity height changes. For a symmetric step

$$C_{di} = \pi r_i C_d' \tag{12}$$

where the value of C_d' as a function of gap ratio is obtained from a curve in Ramo and Whinnery.[7] The gap ratio at r_1 is considered to be $2g/L$. (Note that once r_3 is calculated, it may be inserted back into (8) to obtain the higher order cavity mode resonant frequency, ω_3, corresponding to the TM_{02} mode.) The ratio of upper to lower cutoff

frequency of the operating mode is related to the coupling iris angle α in the following manner.

$$\frac{\omega_2}{\omega_1} = \sqrt{\frac{180}{180 - \alpha}} \tag{13}$$

for α in degrees. The final dimensions of the M4040 cavities are summarized in Fig. 10.

Some insight into the manner in which the slow-wave structure may be matched to rectangular waveguide can be obtained by considering a lumped-element equivalent circuit. One such circuit, suggested by Pierce,[8] appears in Fig. 12(a). Using the Tee equivalence in Fig. 12(b),

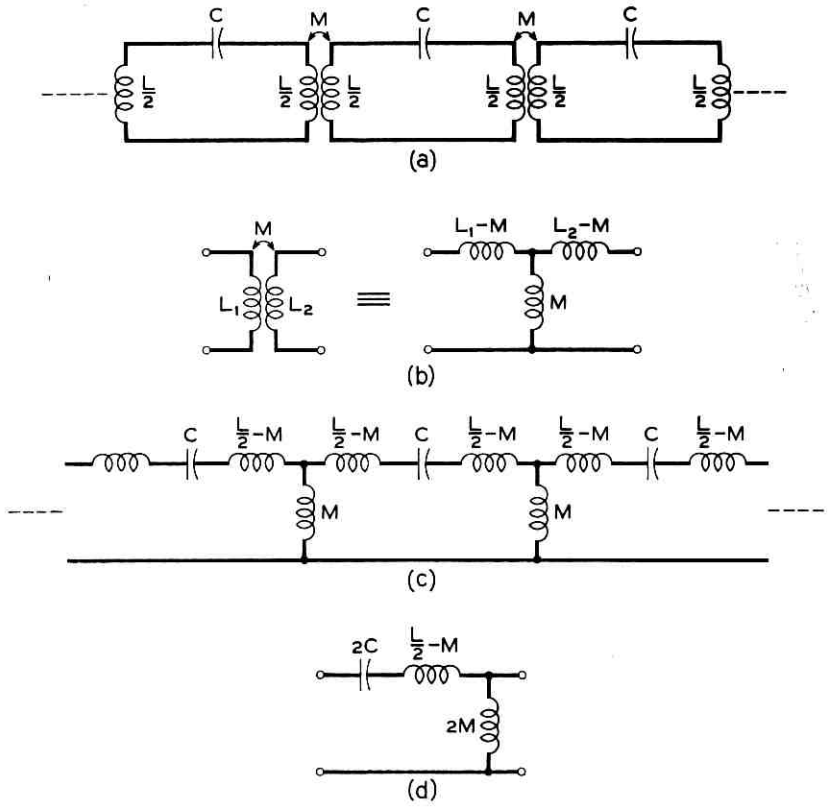

Fig. 12 — (a) Equivalent circuit for a chain of coupled cavities; (b) equivalent Tee circuit for a transformer; (c) transposition of circuit 12(a); (d) half section of circuit 12(c).

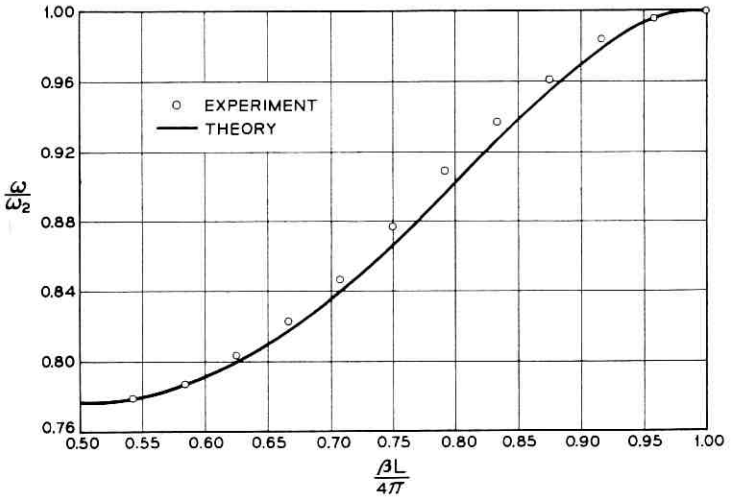

Fig. 13 — Comparison of an experimental ω-β curve with the theoretical dispersion curve of the assumed equivalent circuit.

the circuit of Fig. 12(a) may be transposed to that of 12(c), which in turn has the characteristic half-section of Fig. 12(d). The dispersion curve of this circuit (when the alternation of fields by π radians for adjacent cavities is properly accounted for) is precisely that of (7). Fig. 13 offers a comparison between a typical measured ω-β curve and the theoretical curve from the lumped-circuit approximation. The upper and lower cutoff frequencies are related to the circuit values as shown below.

$$\omega_2 = [C(L - 2M)]^{-\frac{1}{2}} \quad \text{upper cutoff} \tag{14}$$

$$\omega_1 = [C(L + 2M)]^{-\frac{1}{2}} \quad \text{lower cutoff} \tag{15}$$

whence

$$\frac{\omega_2}{\omega_1} = \left[\frac{(L - 2M) + 4M}{(L - 2M)}\right]^{1/2} \tag{16}$$

and

$$\frac{L}{M} = \frac{2(\omega_2^2 + \omega_1^2)}{\omega_2^2 - \omega_1^2} . \tag{17}$$

The equivalent circuit for the last two cavities and the terminating waveguide is represented in Fig. 14(a). The values L, C, and M define

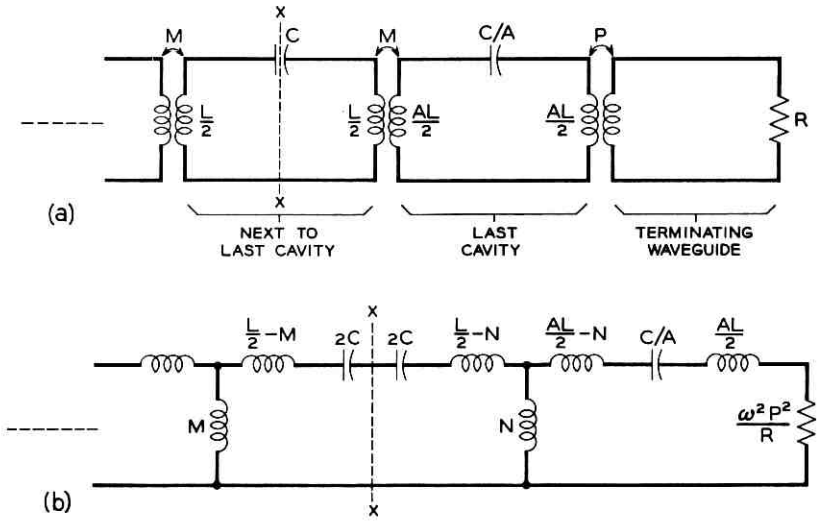

Fig. 14 — (a) Equivalent circuit of terminating cavities and waveguide; (b) transposition of circuit 14(a).

the general cavity circuit and the mutual coupling as before; the coupling between the last two cavities and between the last cavity and the waveguide, however, has been allowed to change to N and P, respectively. The inductance and capacitance of the last cavity have been modified by the factors A and $1/A$, which is roughly equivalent to changing the axial dimensions of the cavity by the factor A. We will assume the inductance of the waveguide termination is negligible. Again applying the circuit equivalence of Fig. 12(b), we arrive at the circuit of Fig. 14(b). Referring to the reference plane x-x, the impedance looking back to the left into the semi-infinite cavity chain is just the Tee impedance of the half-section circuit of Fig. 12(d)

$$Z_T = \sqrt{\omega^2 M^2 - \frac{K^2}{4}} \tag{18}$$

where

$$K = \omega L - \frac{1}{\omega C} = \frac{\omega^2 LC - 1}{\omega C}.$$

The impedance looking to the right of the reference plane can be written

$$Z_R = \frac{R(\omega^2 NP)^2}{(\omega P)^4 + (RAK)^2} + j2K\left[\frac{(\omega P)^4 + (RAK)^2 - 2A(\omega NR)^2}{(\omega P)^4 + (RAK)^2}\right]. \tag{19}$$

Z_R will be real if

$$(\omega P)^4 + (RAK)^2 = 2A(\omega NR)^2 \tag{20}$$

so that

$$R = \frac{(\omega P)^2}{2A\sqrt{\frac{(\omega N)^2}{2A} - \frac{K^2}{4}}}. \tag{21}$$

Substituting (20) and (21) back into (19) and equating Z_R to Z_T, we get

$$\sqrt{\omega^2 M^2 - \frac{K^2}{4}} = \sqrt{\frac{\omega^2 N^2}{2A} - \frac{K^2}{4}} \tag{22}$$

or

$$N = \sqrt{2A}\, M\,. \tag{23}$$

Let us assume that we may choose

$$P = \sqrt{B}\, M \tag{24}$$

where $\sqrt{B}$ is a constant. Then we have

$$R = \frac{B}{A}\left[\frac{(\omega M)^2}{2\sqrt{\omega^2 M^2 - \frac{K^2}{4}}}\right] \equiv \frac{B}{A} R_0. \tag{25}$$

For convenience the height of the last cavities in the M4040 was left unchanged. This implies that $A = 1$ and that $(L - 2M)$ in (16) is a constant quantity. Combining (13) and (16) with the above constraints yields a prediction for the coupling iris angle for N of

$$\alpha_N = 180^\circ\left[\frac{5.656}{L/M + 3.656}\right]. \tag{26}$$

Using $L/M = 8.09$ for the M4040, a figure evaluated from (17), we predicted a value of $\alpha_N = 86.7^\circ$, whereas the empirically determined angle turned out to be 92°.

An inherent difficulty arises when attempting to calculate R_0, since

(14) and (15) define three circuit values, L, C, and M, in terms of only two known parameters, ω_1 and ω_2. It remains then to select a suitable reference surface in the cavity in order to estimate one of the lumped-circuit values at that surface. The appropriate surface would seem to be a cylinder, concentric with the cavity, whose radius bisects the coupling iris since the waveguide impedance is presented to the final cavity in this region. The capacitance at this surface may be estimated by making an impedance transformation of the capacitance C_0, calculated in (9) through (12), over the radial waveguide from radius r_2 to $(r_3 - a/2)$. The calculation of R_0 may be simplified if the midband frequency is chosen as the mean of the cutoff frequencies ($\omega_M = \sqrt{\omega_1\omega_2}$). Combining (14), (15) and (25), one obtains

$$R_0 = \frac{(\omega_2 - \omega_1)(\omega_2 + \omega_1)^2}{16C(\omega_1\omega_2)^2}. \tag{27}$$

The resultant value for R_0 is 3.01 ohms. Since the midband impedance (on a voltage-current basis) of the reduced-height waveguide is 93.5 ohms, P is required to be

$$P = \sqrt{B}\,M = \sqrt{\frac{93.5}{3.01}}\,M.$$

Using the same procedure as when calculating α_N, we arrive at a predicted value of $\alpha_P = 141.7°$. The experimentally determined value is 132°.

Experimentally it was also found necessary to increase the ferrule separation in the last two cavities in direct proportion to the sum of the coupling iris angles on the two end walls of the cavity. Identical transition sections are used for input, output and sever waveguides. A typical curve of reflection coefficient versus frequency is shown in Fig. 15.

Considering the devious nature of the above calculations, plus all the usual inadequacies of a lumped-circuit approximation, the predicted and experimental values of iris angles show reasonable agreement. The equivalent circuit approach is valuable, however, even when it discloses only the qualitative aspects of the matching technique.

VI. METHODS USED TO INHIBIT OSCILLATION

The ω-β diagram, Fig. 11, shows the higher-order modes associated with the coupled cavity slow-wave structure. At the cutoff frequencies for these, as well as the fundamental mode, there is a substantial prob-

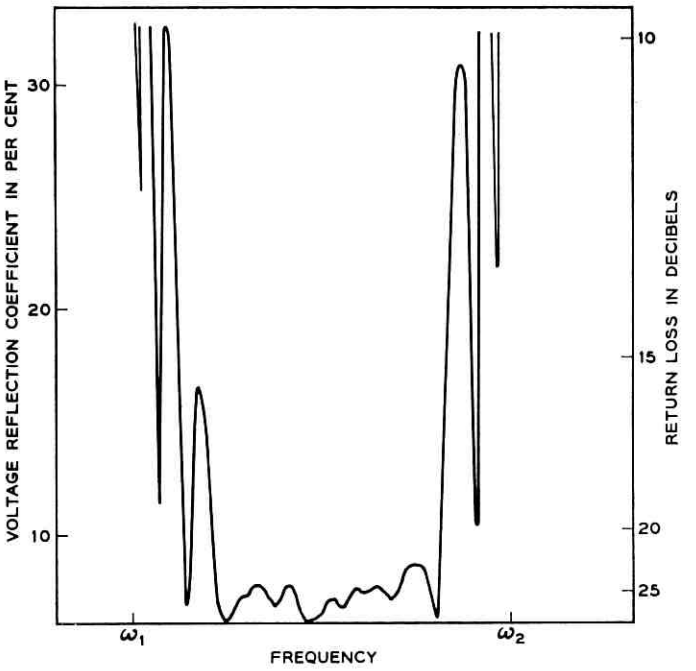

Fig. 15 — Reflection coefficient vs frequency looking into a single section of the slow-wave circuit.

ability that the tube will oscillate if the corresponding wave phase velocities lie close to the electron beam velocity. The intersection of the line, in Fig. 11, labeled "operating voltage" with any of the ω-β plots indicates a synchronism of the wave velocity, for the corresponding mode, with the beam velocity. The slope of the "operating voltage" line is proportional to the electron velocity. Thus, it may be seen that as the beam voltage is raised from 0 to the operating value, synchronism at a cutoff frequency can occur for many modes. The magnitude of the interaction impedance for these modes will determine whether oscillation can occur, and at the cutoff frequency this magnitude may be very large. Oscillations have definitely been identified at 7.1 gc, 12.7 gc and 17.1 gc and at voltages as low as 4 kv and as high as 18 kv. Several techniques have been used to inhibit and avoid the oscillations.

For normal operation, the beam is intended to interact with the first forward wave harmonic of the lowest-order mode. As the beam voltage is raised toward the operating value, the tube will break into a very

strong oscillation at the upper cutoff frequency of 7.1 gc. If one attempts to raise the voltage through the oscillation range with full beam power available, the tube will gas up; arcing will occur; and the beam supply will shut off. Since the Philips cathode can be run at full voltage under temperature-limited conditions, the following turn-up method was used. The cathode temperature is lowered until it is capable of emitting only 15 per cent of full current. The strength of the oscillation under these conditions will be greatly reduced. The beam voltage may now be turned up through the oscillating range to the operating point. Finally, the cathode temperature is returned to its normal value, resulting in full beam power at the operating point. After the tube is sufficiently aged in, the full beam power of 17.7 kilowatts can be applied abruptly by means of a vacuum relay connecting the tube to the power supply.

The original version of the slow-wave circuit had a kidney-shaped cavity coupling slot (cavity A in Fig. 11). The operating voltage line cut the phase-frequency curve for the first higher-order mode (slot-mode) at a high impedance point near the upper cutoff. Oscillation occurred at 12.7 gc. Fig. 11 shows that by capacity-loading the slot to produce the dumbbell shape (cavity B), the mode is lowered in frequency without affecting the operating mode. The impedance of the slot-mode decreases toward the low-frequency end of its passband. Therefore, the elimination of the slot-mode oscillation was accomplished by lowering its frequency until the operating voltage line intersected the phase-frequency curve for the slot-mode at a low impedance point.

A better understanding of the nature of the slot-mode can be obtained from the following analysis. It is assumed that the effects of the ferrule are merely to lower the various passband frequencies since it is placed in a region of large electric fields. This should not affect the slot-mode too greatly. A further assumption is that there is no reaction between slots, which will be nearly true if there is a 180-degree rotation from slot to slot. One may consider the coupled-cavity circuit as a TM_{01} circular waveguide of characteristic impedance Z_{01} and propagation constant β_{01} shunted by a normalized reactance jx corresponding to the circular end walls which form the cavities. If we treat a section, l, of this guide as a TEM transmission line, the eigenvalue equation is given by[9]

$$\cos \theta = \cos \beta_{01} l + \frac{1}{2x} \sin \beta_{01} l \tag{28}$$

where θ is the phase shift per section. The band edge frequencies may be solved for by setting $\theta = 0$ and $\theta = \pi$. For $\theta = 0$

$$\cot \frac{\beta_{01} l}{2} = 2x \quad \text{or} \quad \sin \frac{\beta_{01} l}{2} = 0, \qquad \text{i.e.,} \quad \beta_{01} l = 0, 2\pi, 4\pi, \cdots.$$

For $\theta = \pi$

$$\tan \frac{\beta_{01} l}{2} = -2x \quad \text{or} \quad \cos \frac{\beta_{01} l}{2} = 0, \qquad \text{i.e.,} \quad \beta_{01} l = \pi, 3\pi, \cdots.$$

If the periodic spacing, l, is small compared to a wavelength at the TM_{01} frequency, $\beta_{01} l = \pi, 2\pi \cdots n\pi$ will occur only at much higher frequencies. Thus, at $\theta = 0$

$$\cot \frac{\beta_{01} l}{2} = 2x \quad \text{or} \quad \beta_{01} l = 0; \tag{29}$$

at $\theta = \pi$

$$-\tan \frac{\beta_{01} l}{2} = 2x \tag{30}$$

where

$$(\beta_{01})^2 = \left(\frac{\omega}{c}\right)^2 - \left(\frac{\omega_2}{c}\right)^2 \tag{31}$$

and ω_2 is the cutoff frequency for the TM_{01} mode.

If the form of the reactance x can be determined, we can solve (29) to (31) for the band edge frequencies. For the TM_{01} mode in circular guide, an inductor would appear as a circular disc with a sector removed, while a capacitor would appear as a circular disc with an annular slot. The large slots generally used might be represented by a parallel LC circuit such that

$$x = \frac{\omega L}{1 - \left(\frac{\omega}{\omega_s}\right)^2} \tag{32}$$

where $\omega_s^2 = 1/LC$ the slot resonant frequency.

It is necessary to make an estimate of L and C and then solve (29) to (31) graphically. In the case of the M4040, the change to the dumbbell-shaped slot increased the slot capacity without changing the inductance. Thus, the main mode would not be much affected because its bandwidth is mainly determined by the slot inductance. However, ω_s/ω_2 is diminished, lowering the slot-mode passband center frequency and decreasing the ratio of upper to lower cutoff frequency in the slot-mode.

From the above discussion, one concludes that (*i*) the slot-mode is a perturbed TM_{01} mode; (*ii*) because of this, rotation of the slots (avoiding slot-to-slot coupling) would not be expected to change the slot-mode passband; and (*iii*) neither the upper nor the lower cutoff frequency corresponds to the slot resonant frequency.

The operating mode, high-frequency cutoff oscillation at 7.1 gc may also be "drive-induced." That is, when the input signal power (the drive level) is sufficiently high, the electron velocity can be reduced, by conversion of kinetic to microwave energy, to the point where it is again synchronous with the phase velocity corresponding to the 7.1-gc cutoff. Since this occurs at full beam power and the oscillation is very strong, it is necessary to limit the signal input level to prevent possible tube damage.

VII. ASPECTS OF TUBE PERFORMANCE

Figs. 16 to 22 are plots of power, gain and interception currents as functions of frequency, magnetic field, etc., for various parameter values. They were taken from the performance data of a tube presently located at the Andover station and are believed to be typical of the M4040. Although the graphs are self-explanatory, there are several points worth noting:

(*i*) The variation of small-signal gain with frequency is similar to that calculated, using the theory of Birdsall and Brewer,[10] except that

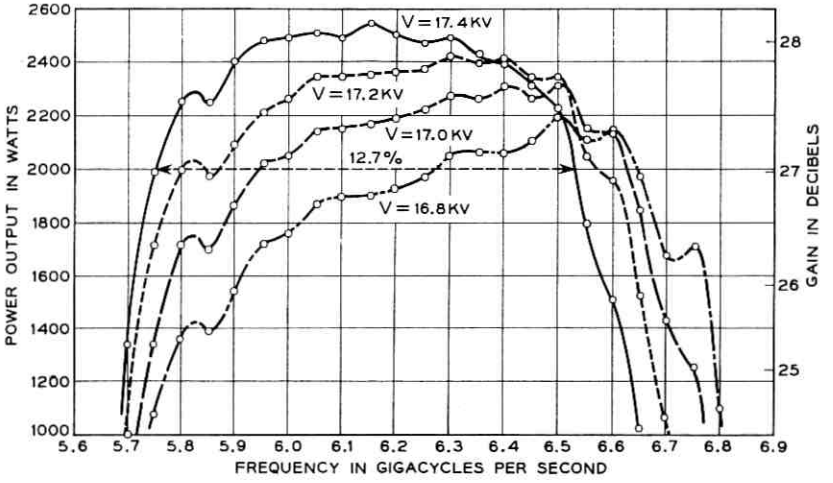

Fig. 16 — High-level output vs frequency [H = 1.2 H (Brillouin); power in = 4.2 watts; parameter is beam voltage].

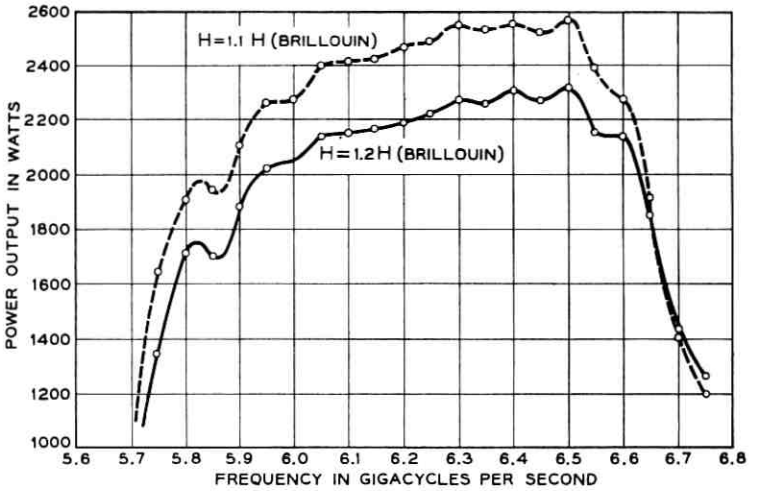

Fig. 17 — High-level output vs frequency [V = 17.0 kv; power in = 4.2 watts; parameter is magnetic field].

the tube requires slightly higher voltages than those calculated. The tube must operate at a voltage of 17.4 kv to achieve a gain-frequency curve similar to that calculated for 16.8 kv. (This latter voltage includes the relativistic correction.) The high-level output observed matches that calculated near the center frequency but is in disagreement at the low-

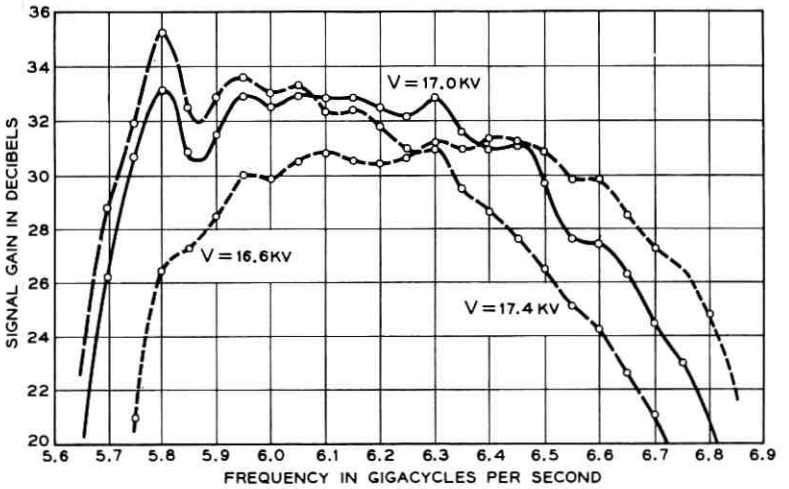

Fig. 18 — Small-signal gain vs frequency [H = 1.2 H (Brillouin); parameter is beam voltage].

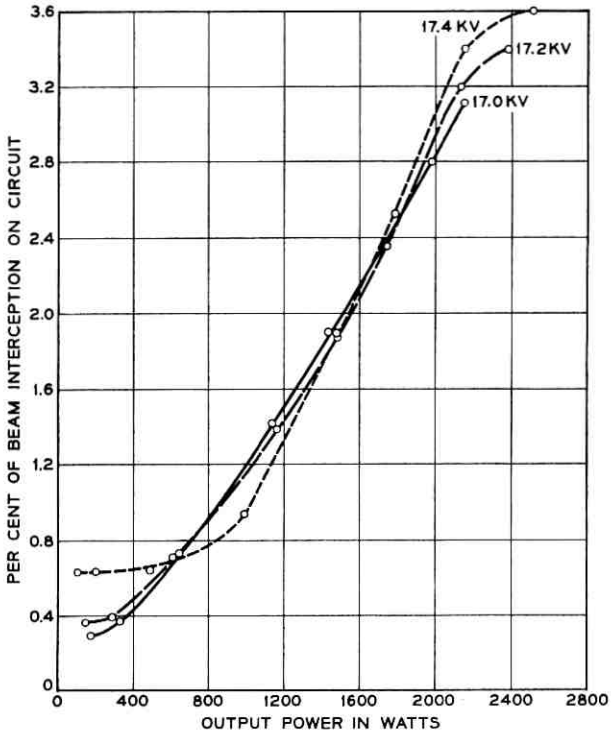

Fig. 19 — Beam interception vs output power [H = 1.2 H (Brillouin); parameter is beam voltage].

frequency end of the band. It is likely that a combination of higher applied voltage and higher input signal power might reproduce the curve shape of sharply rising power with decreasing frequency calculated for 16.8 kv. Here, the experimental data of C. C. Cutler[11] were combined with the small-signal calculations of Birdsall and Brewer to predict output power as a function of frequency.

(*ii*) The M4040 is operated with a focus field value fairly close to the Brillouin magnetic field value. To correlate the several parameters used as a measure of magnetic field, we note that

$$H \text{ (Brillouin)} \approx 600 \text{ oersted}$$

$$H = 1.1\ H \text{ (Brillouin)} \approx 660 \text{ oersted} \approx I_{\text{mag}} = 21 \text{ amps}$$

$$H = 1.2\ H \text{ (Brillouin)} \approx 720 \text{ oersted} \approx I_{\text{mag}} = 23 \text{ amps.}$$

(*iii*) The gross "wiggles" in the small-signal gain and high-level out-

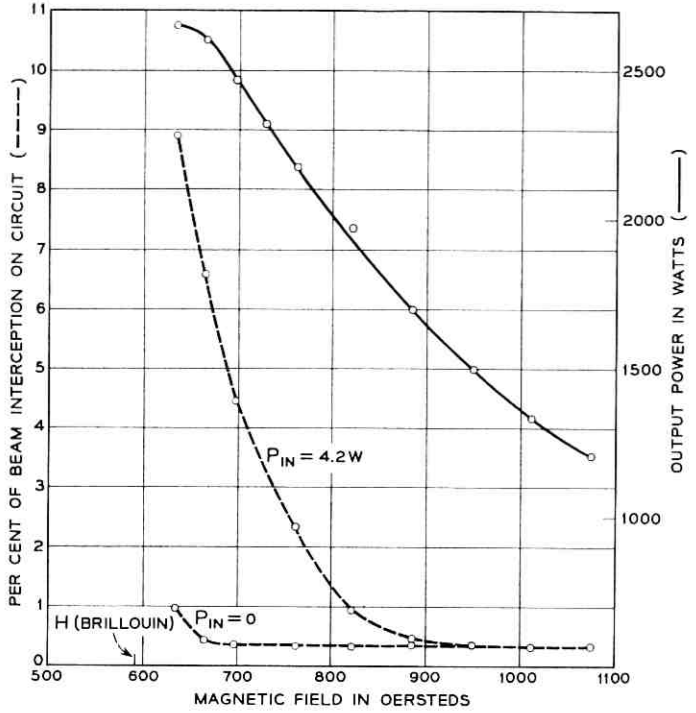

Fig. 20 — Output power and beam interception as a function of magnetic field [V = 17.0 kv; f = 6.4 gc].

put power versus frequency plots can be correlated with variations in the cold input and output matches.

(*iv*) The best explanation, at present, for the increase in gain with collector depression is that the resulting ion drainage from the beam allows the latter to expand. The increase in gain is about 1 db for a 300-volt depression. Not much is gained by going to higher potentials. Three hundred volts is about the magnitude of the potential of the beam center relative to the enclosing walls.

Particularly in the tubes produced early in the development period, positive ion effects were noticed. They can neutralize the beam and therefore change its diameter and, with it, the gain. Relaxation effects, much as described by Sutherland,[12] with frequencies dependent on nearly every adjustable parameter were observed. Improved vacuum processing has brought the magnitude of the effects to the point where they are of no concern. Ion effects were observed at an early stage in the electron gun region. It was necessary to maintain the accelerating

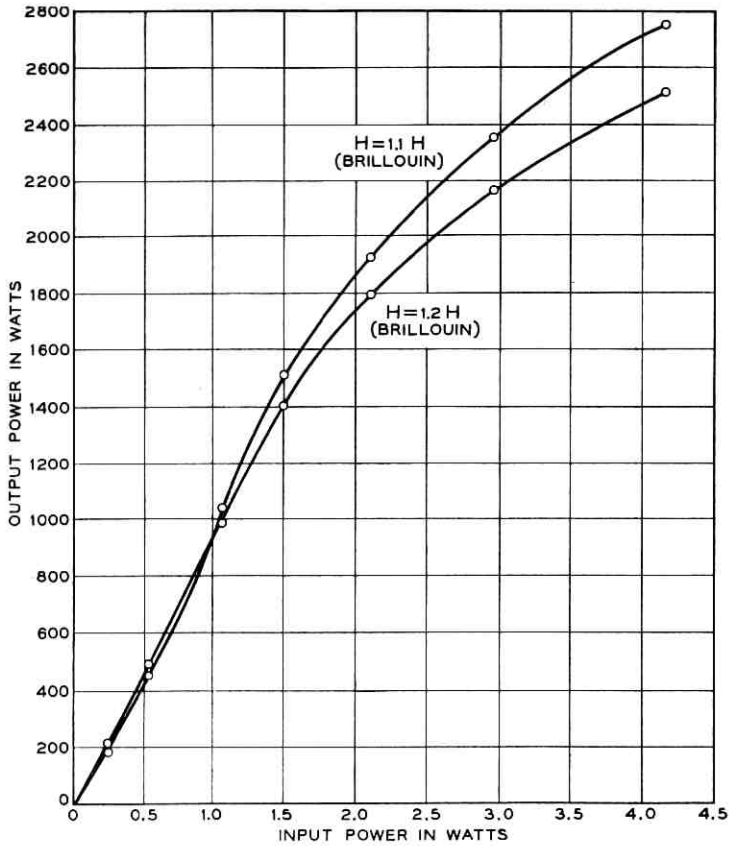

Fig. 21 — Output power vs input power for two values of magnetic field [V_k = 17.4 kv; f = 6.4 gc; parameter is magnetic field].

electrode positive relative to the slow-wave circuit by about 600 volts. If this voltage is allowed to drop below +450 volts, a poisoning of the cathode takes place, presumably due to ion bombardment.

To convince ourselves that the M4040 would indeed serve as a communications device and do its job in the Telstar system, we set up closed-circuit television apparatus to observe and compare a TV picture first transmitted through a straight waveguide and then transmitted through the M4040 substituted for the waveguide. No observable deterioration of the transmitted picture occurred with the M4040 included. The M4040 was operated over a 30-db range of signal power in these experiments. We also measured the second harmonic output power as

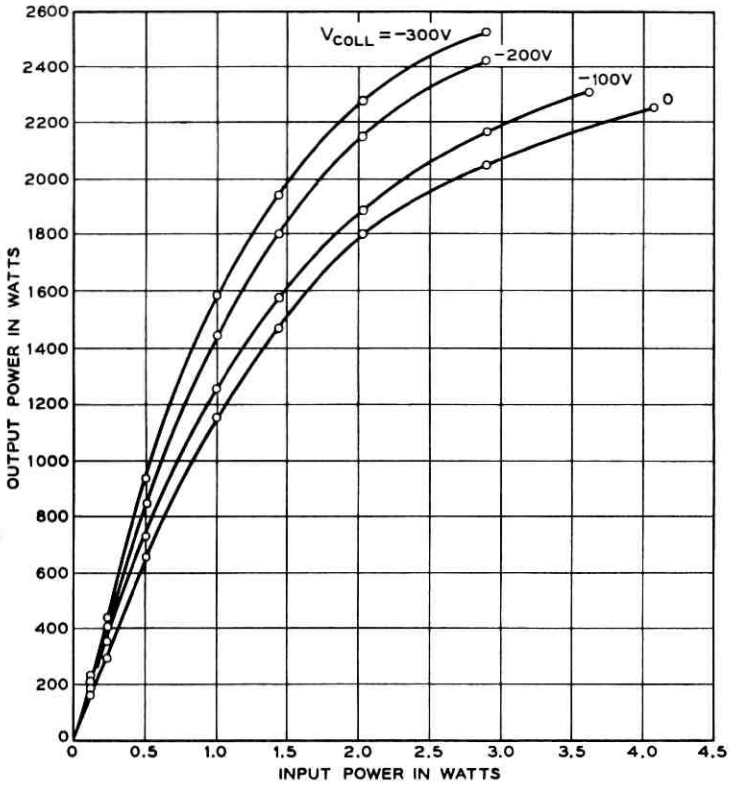

Fig. 22 — Output power vs input power [V_k = 17.0 kv; H = 1.2 H (Brillouin); f = 6.4 gc; parameter is collector depression].

30 db below the output signal level at full output level. With zero applied signal, the noise output is 2 milliwatts as detected through a low-pass filter cutting off at 7.2 gc. Over the narrow, 30-mc bandwidth of the Telstar system, this noise output is 0.4 milliwatt.

VIII. CONCLUDING REMARKS

The M4040 CW traveling-wave tube is capable of operation over a 12.7 per cent bandwidth centered at 6.15 gc with output power exceeding 2000 watts and a gain exceeding 27 db. In the Telstar experiment, the tube has performed satisfactorily as a television transmitter over a 30-db range of input signal power. At the time of writing, both the ground station at Andover, Maine, and the one at Pleumeur Bodou, France, are still using as the power amplifier the original M4040 tubes employed

during the first Telstar broadcasts. The tube at Andover has been operated for approximately 1500 high-power hours.

Recently, several experiments have indicated that much improved performance can be expected from the M4040. Two more cavities have been added to the output section of the tube, increasing the gain. At the midband frequency of 6.15 gc, the small-signal gain becomes 35 db and the gain, at the maximum output power of 2700 watts, is 30 db. Further experiments demonstrated that the water cooling rate could be drastically reduced and that ion drainage could be achieved by applying a negative voltage to a pair of electrodes concentric with the beam. The M4040 has been operated without the aid of appendage pumps after an age-in period of some 50 hours. Finally, and perhaps most significantly, the collector potential has been depressed 9 kv below the potential of the slow-wave circuit.[13] The resulting over-all tube efficiency becomes greater than 30 per cent, and a relatively unregulated power supply can be used to provide the beam power. The latter benefit is obtained because of the insensitivity of tube performance to collector voltages depressed beyond 400 volts. If one depresses the collector potential below 9 kv, undesirable effects of electrons returning to the gun region from the collector can be observed.

IX. ACKNOWLEDGMENTS

The development of the M4040 is the result of the cooperative efforts of a great many people in the engineering, assembly, and fabrication areas. The authors thank Messrs. J. W. Gewartowski, H. N. Carlson, and F. R. Ashley for allowing the inclusion of information developed during the course of their work on the M4040 traveling-wave tube.

REFERENCES

1. Pierce, J. R., *Theory and Design of Electron Beams*, Van Nostrand, New York, 1954, Chap. 10.
2. Danielson, W. E., Rosenfeld, J. L., and Saloom, J. A., Analysis of Beam Formation with Electron Guns of the Pierce Type, B.S.T.J., **35**, March, 1956, pp. 375–420.
3. Herrmann, G., Transverse Scaling of Electron Beams, J. Appl. Phys., **28**, April, 1957, pp. 474–478.
4. Spangenberg, K. R., Field, L. M., and Helm, R., *Production and Control of Electron Beams*, Federal Telephone and Radio Corp., New York, 1942.
5. Jahnke, E., and Emde, F., *Tables of Functions*, Dover Publications, New York, 1945, p. 32.
6. Ramo, S., and Whinnery, J. R., *Fields and Waves in Modern Radio*, John Wiley and Sons, First Edition, New York, 1944, pp. 406–408.
7. Ibid., p. 376.
8. Pierce, J. R., *Traveling-Wave Tubes*, D. Van Nostrand, New York, 1950, p. 68.

9. Collin, R. E., *Field Theory of Guided Waves*, McGraw-Hill Book Co., New York, 1960, p. 385.
10. Birdsall, C. K., and Brewer, G. R., Hughes Technical Memo, No. 396, June, 1955.
11. Cutler, C. C., The nature of Power Saturation in Traveling-Wave Tubes, B.S.T.J., **35,** July, 1956, pp. 841–876.
12. Sutherland, A. D., Relaxation Instabilities in High Perveance Electron Beams, I.R.E. Trans. on Electron Devices, ED-7, October, 1960, p. 268–273.
13. Melroy, D. O., private communication.

Masers for the *Telstar* Satellite Communications Experiment

By W. J. TABOR and J. T. SIBILIA

(Manuscript received January 28, 1963)

This paper discusses the design and characteristics of ruby traveling-wave masers operating at 4 gc. These masers, characterized by an average gain of ≈35 db over a bandwidth of 25 mc, are equipped with waveguide input transmission lines, rather than the previously employed coaxial cables. This change results in an over-all noise temperature of 3.5°K for these devices, rather than the 10°K exhibited by earlier masers. The maser noise temperature now closely approximates sky temperatures, which set the ultimate limit on earthbound receiver sensitivity. The improvements to be had by further reduction in amplifier noise are therefore almost negligible. A less well known maser property, i.e., its freedom from distortion, even when driven well into gain saturation, is discussed.

I. INTRODUCTION

In an active satellite communication system, the ultimate in ground station receiver performance is highly desirable, if not absolutely necessary. This follows directly from the limitations imposed by present rocketry on the payload, and thereby on the transmitter power, which can be placed in orbit. A major improvement in over-all system signal-to-noise ratio can be achieved much more easily and economically on the ground than in the satellite. Recognition of this fact led to the adoption of a giant horn-reflector antenna, and the selection of a ruby traveling-wave maser as a preamplifier in order to fully exploit this antenna's remarkable low-noise performance. The design considerations and performance of this maser are the subjects of this paper.

II. DESIGN OBJECTIVES AND THEIR SIGNIFICANCE

At the outset of the maser development program the following objectives and constraints were established:

(a) a minimum stable gain of 25 db

(b) an instantaneous bandwidth of 25 mc centered at 4170 mc

(c) lowest possible noise temperature

(d) an input impedance match better than or equal to 1.5:1 VSWR, and

(e) bath temperature of 4.2°K.

A minimum gain of 25 db is needed to render negligible the noise contribution of subsequent receiver stages. In the early receiver concept, the maser was to be followed by a low-noise traveling-wave tube. A typical value for the noise temperature of such a tube is 600°K. A maser with 25 db of gain would reduce the TWT noise contribution to the over-all system noise temperature to 1.9°K, a value which is small when compared to the initially projected total receiver noise temperature of approximately 50°K. Additional gain would reduce this even further, a point which will be pursued in a later paragraph.

The 25-mc instantaneous bandwidth requirement follows directly from consideration of the information transmission rate and wide index FM mode of transmission.

The demand for the lowest possible maser noise temperature is self-evident.

A good input impedance match is necessary in order to minimize delay distortion: i.e., the generation of weak reflected signals delayed in time with respect to the original. This could cause "ghosts" in TV transmission. In the Telstar system such distortion could arise through the following mechanism. A mismatch in the antenna-maser complex would reflect part of the incident signal, which would then be re-radiated. The radome, not being perfectly transparent, would in turn reflect a portion of this energy back to the receiver. Consideration of the path lengths and reflection coefficients in the entire system, together with the tolerable limits on delay distortion, led to the stipulation of maser input matching to a VSWR better than 1.5:1.

Operation at 4.2°K, rather than at some lower temperature where the gain and bandwidth requirements could be more easily satisfied, was dictated by the fact that this maser was intended to operate continuously over periods of several months. At 4.2°K, liquid helium is in equilibrium with its vapor at atmospheric pressure. If lower temperatures were required, the dewar would have to be maintained under a partial vacuum. This would mean periodic interruptions of service, since the dewar is opened to the atmosphere during each liquid helium transfer. Approximately two hours are needed to re-evacuate the dewar, thus lowering the temperature and restoring gain. For this reason, operation at 4.2°K was selected, and the attainment of the required gain-bandwidth product sought by means other than reduced temperature.

III. MASER DESIGN

3.1 *General Considerations*

The points of departure in maser design are the gain equation[1]

$$G = 27.3\ (-\chi'')(FfL/v_g) \tag{1}$$

where

G = electronic gain in db
χ'' = imaginary part of the ruby paramagnetic susceptibility
F = filling factor
f = frequency
L = maser physical length
v_g = group velocity of signal

and the gain-bandwidth relationship for the traveling-wave maser

$$B = \sqrt{\frac{3}{G-3}}\, B_m \tag{2}$$

where B is the 3-db bandwidth of the amplifier and B_m is the material linewidth (assuming a Lorentzian shape[1]).

If slowing, S, is defined as $S = (c/v_g)$, where c is the free-space velocity of light, (1) can be rewritten in a form more easily interpreted for practical design

$$G = 27.3(-\chi''F)\frac{1}{\lambda_0} SL, \tag{3}$$

where λ_0 = free-space signal wavelength. In this form, it is evident that increased gain can be achieved equally well by increasing either the slowing or the physical length of the maser. Since the maser requires a highly homogeneous transverse magnetic field, a very large magnet cross section is required. Therefore, a heavy penalty in weight is paid for gain achieved through increased maser length. This consideration led to the choice of a 5-inch maser length. The gain requirement has to be satisfied by maximizing the parameters χ'', F, and S. χ'' is a property of the active material and S is controlled by slow-wave structure design. F is partially determined by both.

The gain-bandwidth expression (2) in the case of a ruby (linewidth 60 mc) maser immediately leads to the conclusion that even for the minimum gain of 25 db, the obtainable bandwidth will be inadequate [taking an electronic gain of 30 db in order to allow for losses, the bandwidth would from (2) be 20 mc]. For this reason, the need for broad-

banding techniques, to be discussed in later paragraphs, was evident in the earliest stages of design.

3.2 *Ruby*

Amplification in a maser is the result of the interaction of a microwave signal with a paramagnetic crystal in which a negative susceptibility, χ'', has been established through the inversion of the spin populations of two energy levels. In ruby at 4 gc, χ'' is maximized when the C axis of the crystal is aligned perpendicular to the applied dc magnetic field ($\theta = 90°$). The signal transition occurs between the lowest two energy levels ($-\frac{3}{2}$, $-\frac{1}{2}$), and pump power is applied between the outermost levels ($-\frac{3}{2}$, $+\frac{3}{2}$).[2]

The susceptibility of a ruby crystal in thermal equilibrium can be calculated as outlined in the Appendix. However, what is needed in order to evaluate the gain obtainable with a particular maser design is the "inverted" susceptibility: i.e., the susceptibility when the population distribution of spins between two energy levels has been inverted through the application of microwave pump power. No reliable method exists for calculating this susceptibility. An experiment, together with the calculated equilibrium susceptibility, will provide the required information. One can measure the ratio of the microwave gain obtained from a ruby crystal when pump power is applied to the microwave absorption when the crystal is in thermal equilibrium. This ratio is just that of the magnitudes of the inverted to equilibrium susceptibilities. Therefore, one obtains the inverted susceptibility by simply multiplying the calculated equilibrium value by this empirically determined number.

The magnitude of the inverted χ'' is strongly dependent upon the concentration of chromium in the ruby. At low concentrations, where there is essentially no interaction between neighboring Cr^{+++} ions, the inverted susceptibility is directly proportional to the concentration. As the concentration is increased, the Cr^{+++} ions interact more strongly with one another because of their greater proximity, and this interaction (cross-relaxation) renders pumping less efficient, reducing the inversion ratio and, thereby, the available gain. Typical behavior of the inverted susceptibility as a function of chromium concentration (measured at 5.6 gc and 4.2°K) is presented in Fig. 1. The concentration at which χ'' is a maximum occurs in the range 0.03–0.04 atomic per cent. Operating at a temperature of 4.2°K, the optimum inversion ratio obtainable at 4 gc has been found to be approximately 5.0. The corresponding calculated values for the inverted susceptibilities are

$$\chi_{xx}'' = -0.028,$$

$$\chi_{yy}'' = -0.0054,$$

and

$$\chi_{xy}'' = i\,0.012,$$

where the Z direction is taken parallel to the dc magnetic field and the X axis parallel to the C axis of the ruby.

Since the paramagnetic susceptibility is a tensor, the interaction of a microwave signal with the ruby is highly dependent upon the spatial coincidence of the crystal and RF fields of the proper polarization. This leads to the inclusion of the filling factor F in the gain equation. The term $\chi''F$ when expanded is

$$\chi''F = \frac{\int_m [\chi_{xx}''\,|H_x|^2 + \chi_{yy}''\,|H_y|^2 - \chi_{xy}''(H_xH_y^* - H_x^*H_y)]\,dv}{\int_s [|H_x|^2 + |H_y|^2]\,dv} \tag{4}$$

where

$$H_x = h_x' + ih_x''$$

$$H_y = h_y' + ih_y''$$

and where $h_{x,y}'$ is the amplitude of the RF magnetic field along the x,y axis of the ruby (see Fig. 2) and $ih_{x,y}''$ is the amplitude of the RF magnetic field that is 90° out of phase with $h_{x,y}'$. The subscript m on the in-

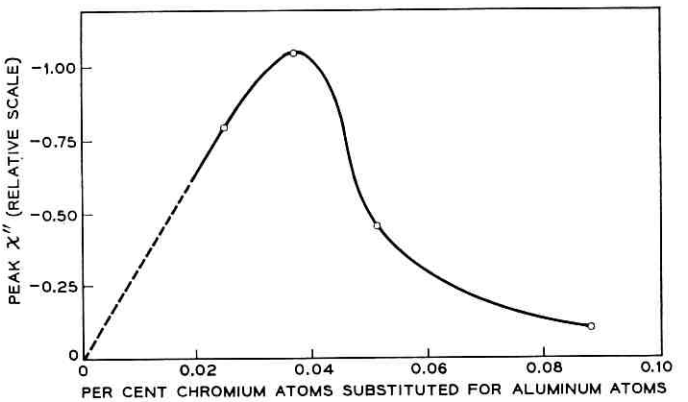

Fig. 1 — Inverted susceptibility vs concentration for ruby at 5.6 gc and 4.2°K.

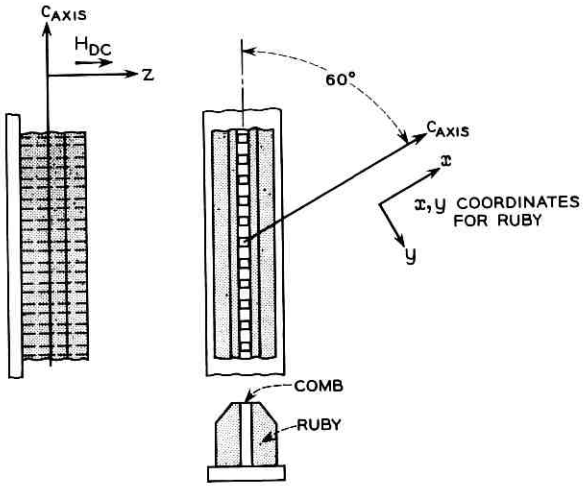

Fig. 2 — Orientation and coordinates for the ruby and comb structure.

tegral in the numerator means that the integral should be taken only over the volume occupied by the maser material, and the subscript s implies that the integral in the denominator should be taken over the entire volume of the structure. The term $|H_z|^2$ does not appear, since the fingers of the comb are resonating in a TEM mode and the Z direction is taken parallel to the fingers.

It is not possible to calculate the term $\chi''F$ with accuracy, since the configuration of the fields in the comb structure is only approximately known. An estimate can be made at the low-frequency edge of the traveling-wave structure passband where the RF magnetic field is approximately linearly polarized and parallel to the comb axis. At this frequency, $H_x = H \cos 60°$ and $H_y = H \sin 60°$ and, therefore, $\chi''F = -0.011$. This value for $\chi''F$, together with the 5-inch maser length, allows the evaluation of slowing required to achieve a given gain at 4 gc. Equation (1), with the insertion of the parameters

$$L = 5 \text{ inches}, \qquad f = 4 \text{ gc}, \qquad \chi''F = -0.011,$$

reduces to

$$G_{db} \approx 0.50\ S \text{ (from theory)}. \tag{5}$$

This calculated result led to the conclusion that it would not be difficult to design a maser with 40 db of net gain, since previous experience indicated that structures with slowings of 100 and losses of the order 10 db could be constructed.

It is possible to evaluate $\chi''F$ experimentally by building a trial structure of known slowing and measuring its electronic gain. This was done and a value of $\chi''F$, obtained from the gain equation (1), found to be -0.0076, i.e., 70 per cent of the theoretically derived value. This agreement, in view of the approximate knowledge of the RF fields in the comb structure, is surprisingly good. Equation (5) for a practical design should therefore read

$$G_{db} \approx 0.35\ S \text{ (experimental)}. \tag{6}$$

The ruby used in these masers was purchased from the Linde Company in the form of standard 60° boules; i.e., the angle between the C axis and the rod axis was approximately 60°. The boules were selected for a chromium concentration of $\approx$0.035 atomic per cent by comparing the paramagnetic absorption of small samples cut from each boule with standard samples.

3.3 *Structure*

It is evident from (6) that a high slowing is required in order to provide adequate gain. A comb type structure, consisting of sixty-two 0.040-inch square fingers spaced 0.080 inch on centers, loaded on both sides with ruby, was employed (see Fig. 3). The transmission characteristics of such a comb not only are determined by the geometry of the metallic structure, but are strongly dependent upon the dielectric loading pro-

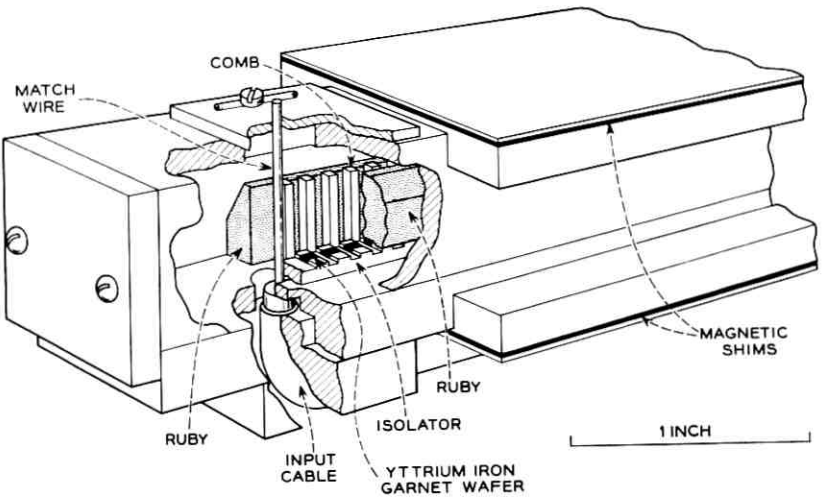

Fig. 3 — Cutaway view of structure.

vided by the ruby. Such a structure can be characterized by an ω-β response: i.e., the phase shift introduced per unit length (β) as a function of frequency (ω). The slowing is given by $c(d\beta/d\omega)$.

It is of advantage to use as much ruby as possible in such a structure, since by heavily loading with dielectric the structure size required for operation at a given frequency is reduced, thereby minimizing magnet weight. Further, the filling factor F is maximized.

When the cross section of the ruby loading is rectangular, the upper and lower cutoff frequencies of the loaded comb can be calculated. A variety of rectangular loadings was studied (see structures 1 and 2 of Fig. 4 and their ω-β diagrams), but it was found impossible to obtain sufficient slowing without the onset of "fold-over." "Fold-over" is the term applied to the occurrence of a double-valued ω-β diagram (curve 2 of Fig. 4). This phenomenon arises when the effective dielectric loading of the fingers of the comb is not a monotonic function of frequency. Knowledge of the field configuration within the structure is required

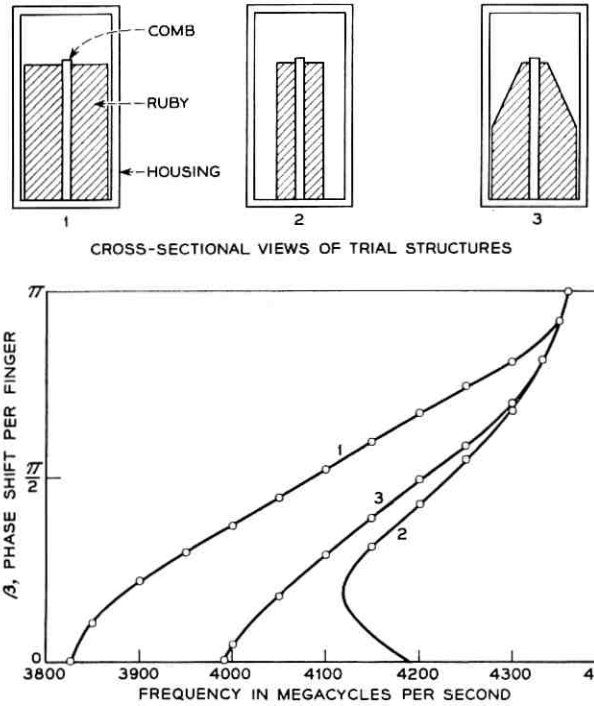

Fig. 4 — Bandpass characteristics for different types of dielectric loading.

for an understanding of this effect. At the lower cutoff frequency, the phase shift per unit length is zero, which implies that the electric field lines extend largely from the fingers to the side walls, as illustrated in Fig. 5. The effective loading is then a highly sensitive function of the gap between the ruby and wall. At the upper cutoff, there is a π phase shift per finger and the fields are concentrated in a region very near the fingers. The loading is then nearly independent of the ruby-to-wall gap. This can be summarized by the statement that the ruby-to-wall gap has a decreasing effect on the effective dielectric loading, and therefore the

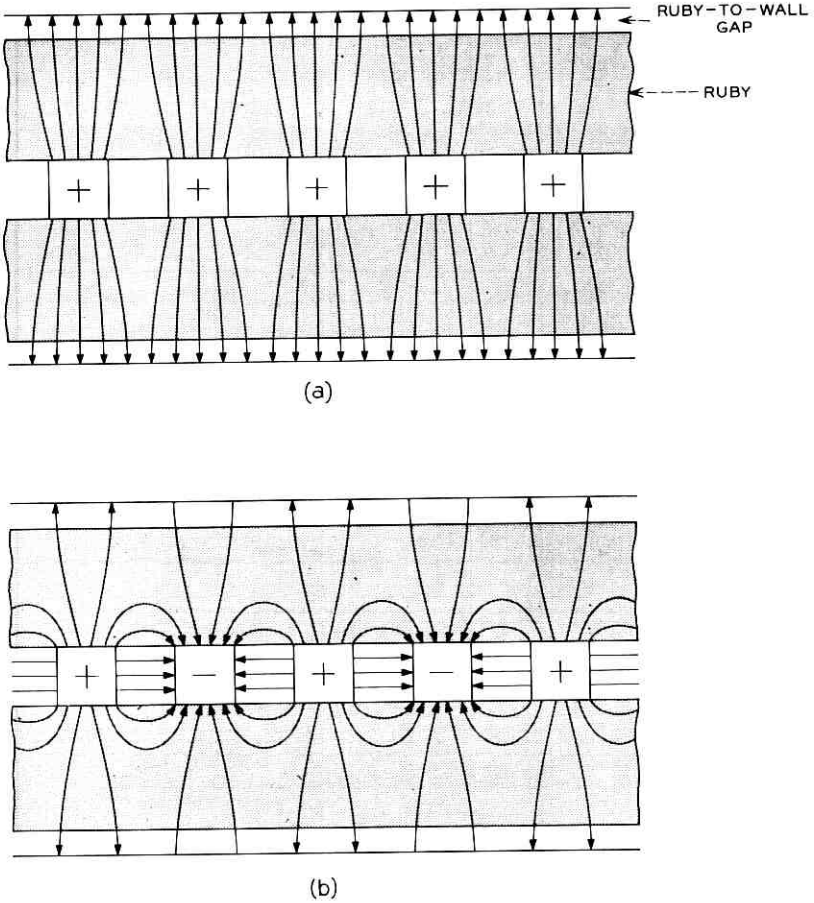

Fig. 5 — Field configuration in the comb structure: (a) zero phase shift condition at lower cutoff frequency; (b) π phase shift condition at upper cutoff frequency.

phase shift, as one traverses the passband from lower to upper cutoff. Increased slowing is achieved in a given structure by increasing the ruby-to-wall gap, thereby raising the lower cutoff frequency. If this process is carried too far, it is possible to reduce the effective loading at the lower cutoff to a value less than that present at a higher frequency. This results in the double-valued ω-β response. Maser operation under this condition is highly undesirable.[3] A "backward," as well as "forward" wave is supported. The sense of polarization associated with the "backward" wave is the reverse of that of the "forward" wave, and therefore the isolator (to be discussed) is rendered inoperative, leading to regeneration or oscillation. Therefore, other ruby geometries were tried in an attempt to account for the changing field configuration as a function of frequency and thereby obtain an effective loading which is monotonic. The cross section illustrated as structure 3 in Fig. 4 was selected as best. This gave the largest slowing ($S = 130$), with a single-valued ω-β characteristic. The slowing as a function of frequency is presented in Fig. 6.

With ruby symmetrically loaded on both sides of the comb as shown in Fig. 4, the maser will exhibit gain in either direction. Therefore, in order to prevent regeneration or oscillation, which would result from reflections due either to structure defects or imperfect input or output matches, an isolator must be incorporated within the structure. The amount of isolation provided should be sufficient for unconditional stability, so that the gain of the maser is not a function of the externally presented terminal impedances. The criterion for unconditional stability of a maser is that the round trip (input to output, back to input) loss must exceed the corresponding gain; i.e.

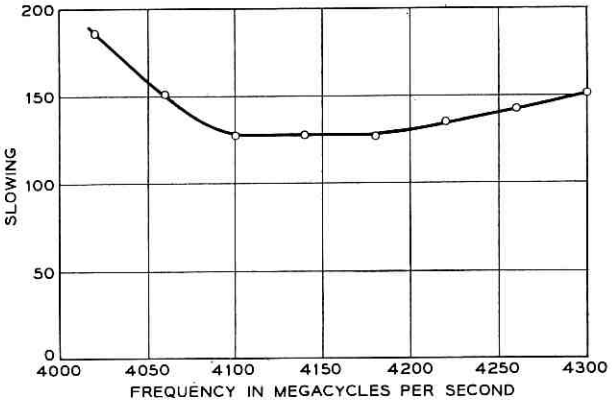

Fig. 6 — Slowing vs frequency for the masers at 4.2°K.

$$2(G_F - A_c) - A_{IF} - A_{IR} < 0 \qquad (7)$$

where all quantities are expressed in db and

G_F = forward electronic gain (equal to reverse gain)
A_c = forward copper attenuation
A_{IF} = forward isolator attenuation
A_{IR} = reverse isolator attenuation.

The isolator employed is a linear array of 0.040-inch square polycrystalline yttrium iron garnet (YIG) wafers 0.004 inch thick, bonded, 0.080 inch on centers (see Fig. 3), to an alumina substrate. The aspect ratio of these wafers is so chosen that they are resonant at the signal frequency in the dc magnetic field required by the ruby. This array is placed on one side at the base of the comb and positioned to occupy that region of RF field most nearly circularly polarized (this optimizes the ratio of reverse to forward insertion loss). Typical performance of this iterated isolator is: reverse attenuation > 120 db; forward insertion loss approximately 4 db, at center band. The isolator forward loss rapidly rises on either side, since the slowing increases, thereby strengthening the interaction; and further, the circularity of the RF field polarization deteriorates. This behavior, as well as that of the copper losses, is illustrated in Fig. 7. With a slowing factor of 130, these masers should exhibit electronic gains of the order of 50 db and copper losses of approximately 2–4 db. Substitution of these numbers into (7) shows that the maser short-cir-

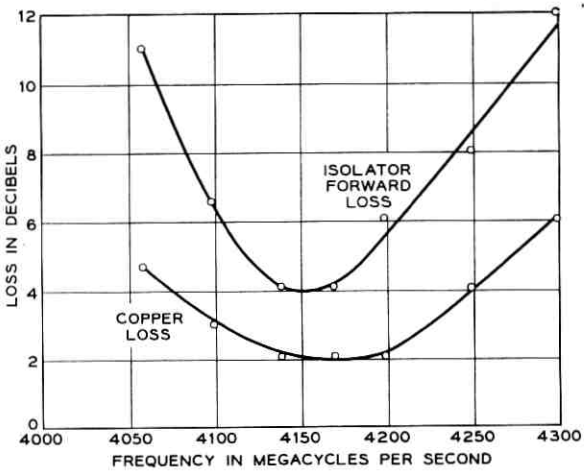

Fig. 7 — Typical losses for the structure at 4.2°K.

cuit stability margin should be greater than 30 db. In practice this is very desirable since it insures a smooth variation of the gain-frequency characteristic even in the presence of structural imperfections.

IV. MASER CHARACTERISTICS

4.1 *General*

In a uniform magnetic field the masers had net gains equal to or in excess of 42 db (corresponding to electronic gains $\geqq$ 47 db) and instantaneous 3-db bandwidths of approximately 16 mc centered at 4170 mc. These measured gains and bandwidths are in close agreement with those predicted by (5) and the bandwidth relationship. Since this was more gain and less bandwidth than required, it was necessary to correct this situation. Two distinct approaches were taken. The first of these was to exchange, within the maser, the excess center frequency gain for increased bandwidth by shaping the magnetic field along the length of the ruby, thereby broadening its effective linewidth. The second approach toward increasing the bandwidth was to consider the entire receiver as a whole, and to introduce equalization in the postamplifier. This latter course, which at first glance appears inefficient, actually leads to a larger effective gain-bandwidth product than broadening the ruby linewidth. This is illustrated in Fig. 8, which shows the ideal trade of center-frequency gain for effective bandwidth obtainable through the application of each technique. Both approaches were carried through experimentally, and will now be presented separately in the two following sections.

4.2 *Broad-Banding by Magnetic Field Shaping*

Since the resonant frequency of ruby is dependent upon the intensity of the dc magnetic field in which the crystal is immersed, its effective linewidth can be increased by making the field inhomogeneous over its volume. This was considered by Ostermayer[4] for several different variations of field along the maser length, and his results show that for a 25-mc bandwidth, the optimum exchange of gain for bandwidth is achieved if the magnetic field is made uniform for one-half the ruby length, and also uniform but of a different intensity over the remainder. A maser immersed in such a field is equivalent to two half-length masers in series tuned to different frequencies. It follows that for most effective inversion, two pump frequencies are required.

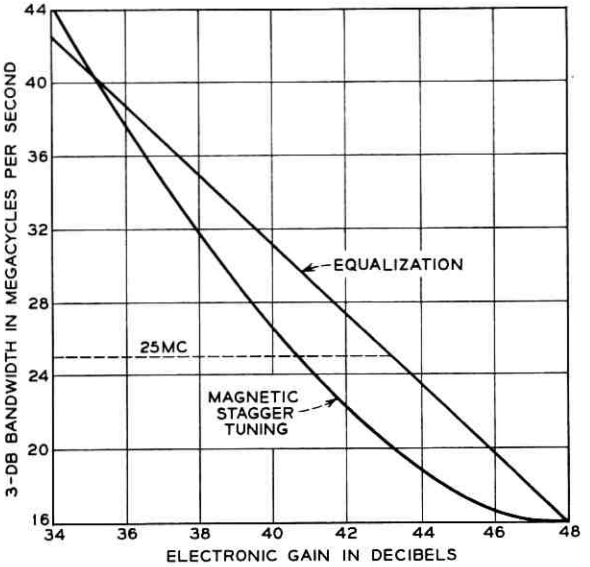

Fig. 8 — Trade of gain for bandwidth for a single-step stagger-tuned maser and for an equalized maser.

In practice it is not possible to achieve an abrupt step in magnetic field; there will be a finite transition region. In order to minimize this, the step in field was produced by inserting magnetic shims as close to the maser as possible, rather than by shaping the magnet pole pieces outside the dewar. The configuration of the shims used is illustrated in Fig. 3.

Using magnetic shims, the bandwidth was increased to 26 mc and the electronic gain reduced to 34 db, corresponding to a net gain of 28 db. Reference to Fig. 8 reveals that this loss in gain is 6 db greater than predicted by theory. There are two possible causes for this: first, a single-frequency pump was used; and second, the lateral homogeneity of the field may have been degraded by the shims, the width of which was severely limited by the dewar dimensions.

Fig. 9 is a plot of the electronic and net gain versus frequency over the tunable range of this maser. The electronic gain is nearly proportional to the slowing of the structure (Fig. 5); the small deviation (within 10 per cent) probably reflects slight changes with frequency of the filling factor. Fig. 10 is an oscillogram of instantaneous gain versus frequency. This maser was successfully employed at Holmdel, New Jersey, during the Telstar experiments.

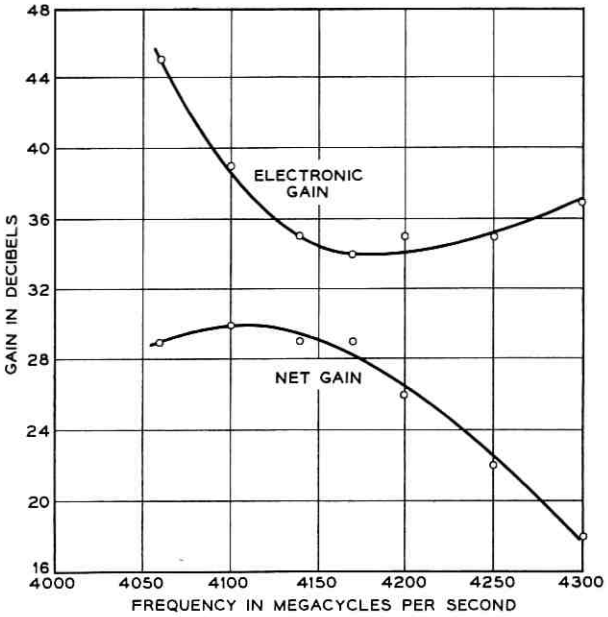

Fig. 9 — Gain of the stagger-tuned maser at 4.2°K.

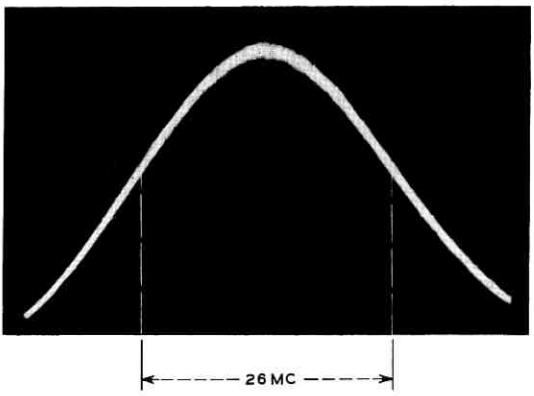

Fig. 10 — Oscillogram of instantaneous gain vs frequency for the stagger-tuned maser; the horizontal center line represents the 3-db point.

4.3 *Broad-Banding by Equalization of Amplifier following Maser*

In this approach, the maser is not modified, but rather the response of subsequent receiver stages is so equalized that the resultant over-all response has the required 25-mc bandwidth.

The gain-bandwidth relationship for equalization is simply generated by taking the electronic (not net) gain versus frequency characteristic of the maser, and finding the gain available at the appropriate deviation from center frequency as shown in Fig. 11. The shaded area then represents the excess gain to be absorbed by an equalizer. From Fig. 8, it is clear that the use of this technique would provide 2.5 db additional gain for a bandwidth of 25 mc beyond that ideally available by magnetic field shaping. Indeed, equalization is the more efficient method of increasing bandwidth up to approximately 40 mc. Magnetic field shaping should be employed for larger bandwidths. (The exact crossover is dependent upon both the detailed ruby line shape and the initial electronic gain.)

The theoretically ideal point for the insertion of an equalizer would be between the antenna and the maser input, for then the maser output would be flat over the band. Such an equalizer would have to be purely

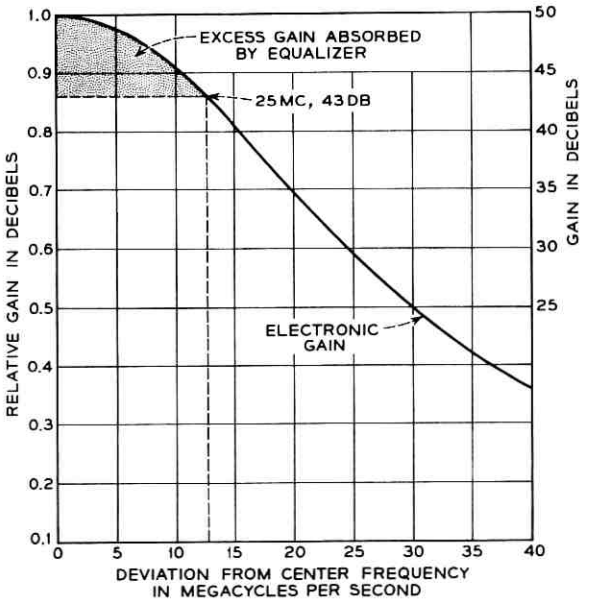

Fig. 11 — Determination of effective gain available with equalization.

reactive in nature in order not to seriously degrade the system noise temperature. The center band signal would have to be attenuated by approximately 7.5 db and this, if done resistively, would result in a noise temperature approaching 1500°K, which is clearly intolerable. A reactance in the input is, however, not acceptable in that it is incompatible with the requirement of a good input VSWR. For this reason, the equalizer was located after the maser in the receiver chain and took the form of a simple lumped RLC circuit at IF.

In going to IF equalization, one possible problem arises: maser gain saturation. The maser shows gain saturation; i.e., a monotonic decrease in gain when the signal level at its output exceeds −40 dbm. Since the center band gain of the unstaggered maser is 43 db, gain saturation will set in well below the level of the strongest signals to be encountered. This was investigated over the range of signal levels expected in the Telstar experiments (−90 to −70 dbm input). The results are presented in Fig. 12. When the input was increased from −90 to −70 dbm the gain of the maser decreased by 5 db, resulting in a signal level increase at the mixer of 15 db. This gain reduction will raise the system noise temperature somewhat, but since the gain reduction is present only when the signal level is high, the slight increase in system noise temperature is of no consequence. In this sense, the maser gain saturation does nothing more than to provide weak limiting action.

A second-order effect noted was a change in the shape of the gain-frequency characteristic arising from the fact that signals at the center frequency drive the amplifier further into saturation than do signals at the band edges. The maximum change was a 3-db reduction in center frequency gain compared to the band edge gain, as illustrated in Fig. 12. These measurements were made on a CW single-frequency basis, and could easily overemphasize, by an order of magnitude, the effect which would be found in an FM system. This effect would cause difficulty in designing a proper equalizer since exact compensation could be accomplished at only one signal level. However, it was decided that if the equalizer were so adjusted as to provide a low signal gain characteristic with a 1.5-db peak at center frequency relative to the band edge, then at high level, the response would at worst show a 1.5-db dip. This behavior would meet the normal 3-db bandwidth specification, and therefore this change in response with signal level was considered acceptable.

An additional factor to be considered when a maser is operated in the gain saturation regime is distortion. In conventional amplifiers, such as the electron tube, gain saturation and distortion are closely related, and formulae exist for the calculation of the distortion products from gain

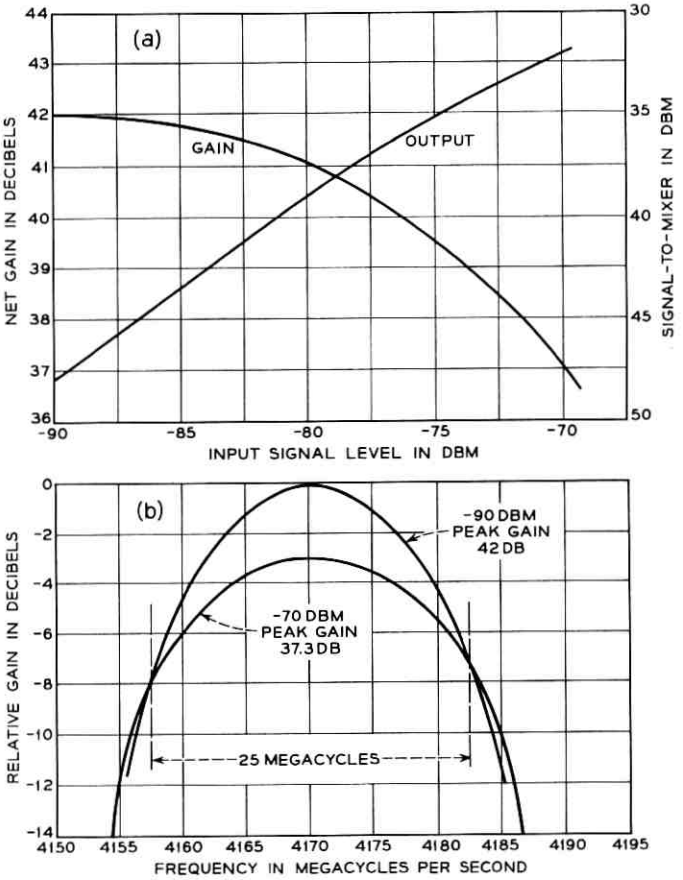

Fig. 12 — Maser signal saturation characteristics: (a) maser gain saturation; (b) maser response as a function of input level.

saturation curves. The behavior of a maser is, however, very different. This can be seen by considering the basic amplification process, stimulated emission.

The probability that photons will be added to the exciting RF field in a maser is given by the expression

$$W_{12} = K \mid \mu \mid^2 (N_2 - N_1) H_{rf}^2 \tag{8}$$

where

K is a collection of physical constants,

$\mid \mu \mid^2$ is the matrix element of the transition, a measure of the

intrinsic probability of the transition occurring, which to first-order approximation, (i.e., low RF fields), is a constant.

$(N_2 - N_1)$ is the difference in the spin population of the two levels under consideration,

and

H_{rf}^2 is a measure of the power level of the stimulating radiation.

The population difference $(N_2 - N_1)$ is a function of the signal power level at which a maser is operated, decreasing monotonically as the level is raised. At any fixed average power level it is a constant, since a time constant which is very long compared to the period of the carrier frequency is associated with it. The value of this time constant is different for each of two cases: a sudden increase in signal level or a sudden decrease in level. A calculation based on the reduction of the energy stored in the inverted spin system shows that for a typical ruby maser the time required for the gain to reach a new equilibrium after the input signal has been raised from zero to -70 dbm is approximately 1 second. The time characteristic of gain recovery, when the signal level is reduced, is approximately 0.1 second, as governed by the spin lattice relaxation times. Gain changes are therefore very slow at signal levels consistent with the use of a maser as a low-noise preamplifier. The distortion arising from these gain changes is therefore no more serious than that introduced by an AGC system.

Higher-order solutions for the matrix element $|\mu|^2$ do exhibit a dependence upon H_{rf}^2, and therefore a source of distortion exists. A theoretical analysis and experiments[5] both show that, at signal levels normally found in a low-noise maser preamplifier, the power in distortion products lying within the significant frequency range is well below the noise generated by the maser itself. For example, if two signals at frequencies f_1 and f_2 simultaneously emerge from a maser at a level of -30 dbm, the third-order intermodulation products, $2f_1 - f_2$ and $2f_2 - f_1$, will be found at a level of -185 dbm,[5] which is approximately 95 db below the output noise of a 4°K, 25-mc maser.

For the reasons presented, the maser is, from the system engineering point of view, a completely distortion-free amplifier.

The use of this combination of an unstaggered maser and IF equalizer provided an effective net gain of 34.5 db at the band edges. This gain was sufficient to allow feeding a mixer directly from the maser output without degradation of the receiver noise temperature. The mixer had a noise temperature of approximately 4300°K which, reflected back to the maser input through 34.5 db of gain, appears as 1.5°K.

Equalized receivers were employed at Andover, Maine, and Pleumeur-

Bodou, France, and will be provided for the German installation. The performance obtained was satisfactory in every respect.

V. MASER TERMINALS AND AUXILIARY STRUCTURE

In all previous masers, the largest contributor to the noise temperature has been the loss in the input transmission line. These, in the past, have been constructed of thin wall, stainless-steel coaxial cables in order to minimize heat conduction from their room temperature access to 4.2°K. A thin copper plating was employed to minimize electrical losses. (A delicate balance between electrical and thermal conductivity is required.) Masers using coaxial cables have had typical over-all noise temperatures of 10°K, of which only 2°K was inherent in the masers themselves. Waveguide, which intrinsically has lower loss than coaxial cable, was used for the input lead of the Telstar masers in an effort to obtain the lowest possible noise temperature. This waveguide was constructed of 0.020-inch thick seamless stainless steel and internally plated with 0.0002 inch of copper. The room temperature loss of such guide is approximately 0.1 db in the lengths required. The waveguides used in the final assemblies were selected for low-noise performance from many which had been initially prepared. This was accomplished by connecting the various waveguides, shorted at the far end, to an operating maser and noting the maser noise output.[6]

The waveguide extends from room temperature to well below the normal liquid helium level in the dewar. A transition to 0.140-inch diameter solid coaxial cable is employed (Fig. 13) and the center conductor of this cable is extended into the maser proper where it forms the final match to the comb structure (Fig. 3). Coaxial cable is permissible below the helium level, since the noise contributed by a given loss at 4.2°K is a factor of 70 less than would arise if the same loss were present at room temperature. The success of the arrangement can be judged by the measured noise temperature of these masers, approximately 3.5°K.

A new technique was employed to measure the noise temperature of these masers. The ratio of the noise power output of the maser with a matched load connected to its input to the noise power output with a short circuit at the input was determined. Since noise power is directly proportional to noise temperature, these quantities can be interchanged, provided one is consistent.

When a matched load is connected to the input of a maser whose input loss is small, the noise temperature observed at the output will be:

$$(T_{\text{out}})_1 = G(T_L + T_I + T_{\text{MF}}) \tag{9}$$

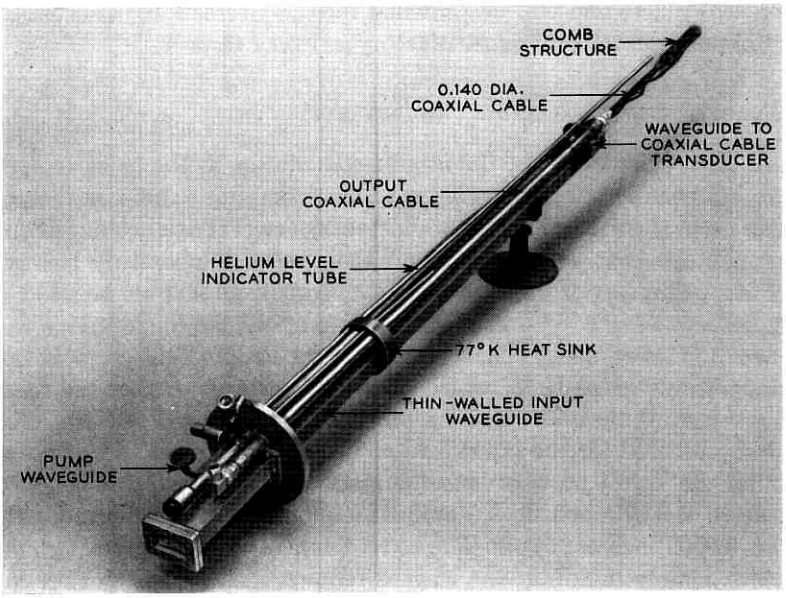

Fig. 13 — Maser head.

and when a short circuit is connected to the input, the output noise temperature is:

$$(T_{out})_2 = G(2T_I + T_S + T_{MF} + T_{MR}) \tag{10}$$

where

G = power gain of the maser
T_I = noise temperature due to losses in the input
T_{MF} = noise temperature of the maser in the forward direction
T_{MR} = temperature of the noise power emitted by the maser in the reverse direction
T_L = temperature of the matched load, and
T_S = noise temperature due to losses in the movable short.

The origin of (9) is clear, the noise contributed by the load and input losses being directly additive with forward-traveling maser noise. When the short is in position, the noise power generated by the input lead traveling away from the maser, as well as the noise power emitted in the reverse direction by the maser itself, are reflected, rather than absorbed, and therefore also contribute to the noise observed in the maser output. For this reason, the input noise appears doubly weighted, and the maser

reverse noise enters in (10). An observable quantity is the ratio of (9) to (10), i.e.

$$\frac{(T_{\text{out}})_1}{(T_{\text{out}})_2} = \frac{T_L + T_I + T_{\text{MF}}}{2T_I + T_S + T_{\text{MF}} + T_{\text{MR}}}. \tag{11}$$

The noise temperature of the maser, referred to the input terminals, is equal to $T_I + T_{\text{MF}}$. T_L is just equal to room temperature, approximately 300°K. T_{MF} and T_{MR} can be calculated from the theory of the traveling-wave maser and are typically 1.5°K and 6.5°K, respectively.

The one remaining parameter to be evaluated in (11) is T_S. This can be determined by any one of a number of standard techniques, and is typically found to be of the order of 1°K. Therefore, T_I can be calculated from the ratio and the maser noise temperature determined.

If the situation were as ideal as has been presented, the measurement of maser noise temperature would be well in hand. However, in practice the ratio of the maser noise outputs is found to vary as the position of the short circuit is changed. This is due to noise coherence effects which occur because of a limited bandwidth detection system and to small mismatches in the system. A detailed analysis of these effects by W. J. Tabor, which will be published separately, shows that the correct value for the noise temperature can be calculated, if one substitutes the average value of the ratio of observed noise powers into (11). This technique, which employs standard microwave components, i.e., a matched termination and a movable short in contrast to refrigerated loads, is capable of good accuracy. The range of uncertainty in the measurement of these masers was ±0.5°K.

The maser output is coaxial, since the noise contribution due to loss following the maser gain is negligible. The pump line is thin-walled WR28 waveguide. Fig. 13 is a photograph of the maser "head" which illustrates the various connections.

Fig. 14 shows the entire assembly except for the microwave pump source. The dc magnetic field is supplied by a 450-pound Alnico magnet, which allows the tuning of the maser over the entire structure passband by means of movable iron shunts. The dewar is of the standard type for liquid helium except for one innovation. A 77° heat station, in the form of a copper ring thermally tied to the liquid nitrogen jacket, was incorporated 10 inches below the room temperature flange (top). Its purpose is twofold: to reduce the thermal gradient to the liquid helium along the maser head, and to reduce the waveguide temperature in as short a length as possible in order to minimize thermal noise generation. With one filling of liquid helium (10 liters) the maser could be kept in opera-

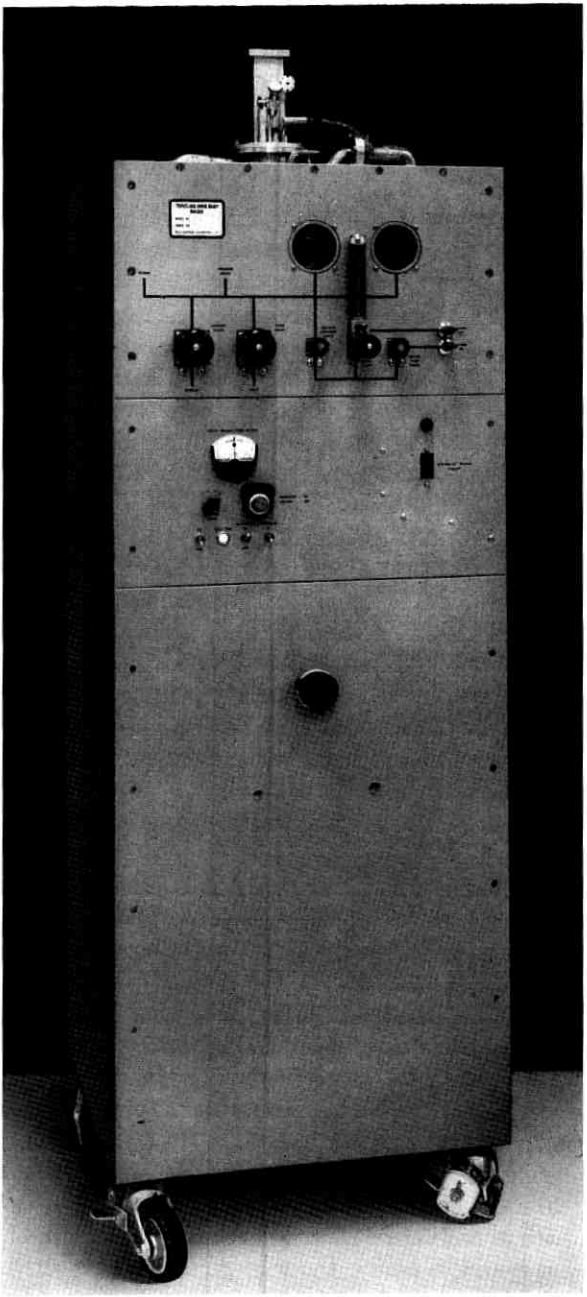

Fig. 14 — Complete maser package.

tion for approximately 20 hours. Refilling could be accomplished without disturbing maser performance.

VI. SUMMARY

The performance of the masers is given by the following data:

Center frequency:	4170 mc
Effective instantaneous bandwidth:	25 mc
Effective gain:	Approx. 34.5 db (equalized receiver) 28 db (magnetically staggered)
Pump frequency:	30,175 mc
Pump power:	70 mw
Magnetic field:	Approx. 3300 gauss
Over-all noise temperature:	3.5°K
Bath temperature:	4.2°K
Liquid helium consumption:	Approx. $\frac{1}{2}$ liter/hr
Helium capacity:	10 liters
Power output at 1-db gain compression:	−38 dbm.

The effective noise temperature, 3.5°K, of these amplifiers is almost a factor of 3 less than previously attained. Indeed, it is so low as to closely approximate the minimum noise temperature of the atmosphere itself. It therefore appears that the ultimate useful amplifier sensitivity has been achieved for application in terrestrial receivers.

VII. ACKNOWLEDGMENTS

The authors wish to acknowledge the role played by H. E. D. Scovil in the development of these masers. The importance of his insight and continued guidance cannot be overemphasized.

We are indebted to E. O. Schulz-DuBois and E. D. Reed for reading this manuscript and making valuable suggestions. We would like to thank P. J. Pantano for his valuable assistance in the mechanical design and microwave measurements; his enthusiastic efforts in the early stages of this program were invaluable.

The authors also wish to show appreciation to certain members of the group for access to unpublished data: namely, S. Harris and R. W. DeGrasse, for calculations involving the comb bandpass cutoff, and to F. W. Ostermayer for design equations used in broadbanding.

APPENDIX

Formulas for the Calculation of χ''

The tensor components of the susceptibility can be calculated from the following formulas

$$\chi_{xx}'' = \frac{\pi g^2 \beta^2}{\mu_0 h} g(f - f_0)(\rho_{-\frac{3}{2}} - \rho_{-\frac{1}{2}}) \mid \langle -\tfrac{1}{2} \mid S_x \mid -\tfrac{3}{2} \rangle \mid^2 \tag{12}$$

$$\chi_{xy}'' = \frac{\pi g^2 \beta^2}{\mu_0 h} g(f - f_0)(\rho_{-\frac{3}{2}} - \rho_{-\frac{1}{2}}) \langle -\tfrac{1}{2} \mid S_x \mid -\tfrac{3}{2} \rangle \langle -\tfrac{1}{2} \mid S_y \mid -\tfrac{3}{2} \rangle \tag{13}$$

etc., where μ_0 is the permeability of free space, h is Planck's constant, g is the spectroscopic splitting factor, β is the Bohr electronic magneton, ρ_i is the density of spins in the energy level i, and $g(f - f_0)$ is a normalized line shape function; i.e.,

$$\int g(f - f_0)\, df = 1.$$

All the units are expressed in mks units. If emu units are used, μ_0 must be replaced by $1/4\pi$.

In the case of ruby for operation at $\theta = 90°$, the transition probability between levels $-\frac{1}{2}$, $-\frac{3}{2}$ contain only S_x and S_y terms with $S_z = 0$, where the Z direction is parallel to the dc magnetic field and the X axis is parallel to the C axis of the ruby. Therefore, the susceptibility tensor for this case consists only of terms χ_{xx}'', χ_{xy}'' and χ_{yy}''. The values of the matrix elements can be computed from the data given by Schulz-DuBois.[7]

REFERENCES

1. DeGrasse, R. W., Schulz-DuBois, E. O., and Scovil, H. E. D., B.S.T.J., **38,** March, 1959, p. 305.
2. Geusic, J. E., private communication.
3. DeGrasse, R. W., Kostelnick, J. J., and Scovil, H. E. D., B.S.T.J., **40,** July, 1961, p. 1117.
4. Ostermayer, F. W., unpublished work.
5. Chen, F. S., Schulz-DuBois, E. O., and Tabor, W. J., to be published.
6. DeGrasse, R. W., Hogg, D. C., and Scovil, H. E. D., private communication.
7. Schulz-DuBois, E. O., B.S.T.J., **38,** January, 1959. p. 217.

4-gc Parametric Amplifier for Satellite Communication Ground Station Receiver

By M. UENOHARA, M. CHRUNEY, K. M. EISELE, D. C. HANSON and A. L. STILLWELL

(Manuscript received March 19, 1963)

This paper describes the design and performance of a 4-gc parametric amplifier which meets the stringent requirements of a satellite ground station receiver. It consists of two cascaded stages of similar design: the first of these is operated at liquid nitrogen temperature and the second at room temperature. One 23-gc pump source is used for both amplifier stages. The combination of the two amplifier stages provides 38-db over-all gain, 45°K over-all system input noise temperature, 60-mc bandwidth, 0.1-db short-term gain stability and 0.3-db long-term gain stability. A carefully designed cryogenic system maintains the amplifier refrigerated with only infrequent refilling of the dewar, i.e., once every 10 days.

I. INTRODUCTION

High sensitivity, stability and reliability are important requirements for a satellite communication ground station receiver. The maser has come to be considered the ideal preamplifier for satellite communication due to its superlative low-noise performance, and it is indeed ideal for cases where its cost and maintenance requirements are not of major concern. However, for lighter traffic routes where cheaper terminals are required, it is desirable to have a less expensive, more compact, and more easily maintained microwave preamplifier. This has motivated the development of the variable capacitance parametric amplifier described in this paper.

A block diagram of the parametric receiver is shown in Fig. 1. The receiver consists of four major sections: a circulator type parametric amplifier, an extremely stable 23-gc pump source, an efficient cryogenic system, and a control system. The first-stage amplifier is operated at liquid nitrogen temperature. The varactor diode mount, circulator,

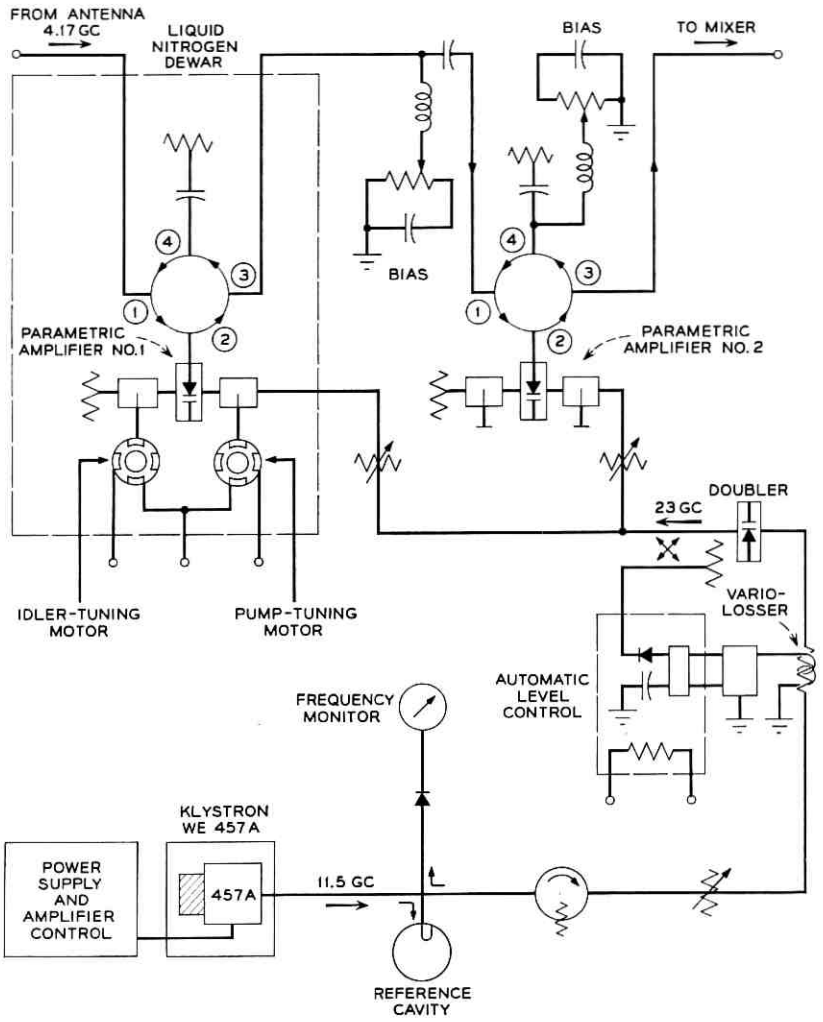

Fig. 1 — Block diagram of parametric receiver.

K-band termination for the external idler load, and two stepping motors for tuning the idler and pump circuits are all completely enclosed in a sealed copper can immersed in a liquid nitrogen dewar. This refrigerated amplifier is followed by a room temperature amplifier of the same design. Since the regenerative reflection mode of operation is used, there is no frequency conversion from input to output. The same 23-gc pump source supplies power to both amplifiers.

The gain stability of the parametric amplifier is largely dependent upon the stability of pump power level and frequency. Therefore, considerable effort has been spent to develop a pump source that would satisfy the most exacting requirements. The 23-gc source is derived from an X-band frequency-stabilized klystron of proven reliability (Western Electric 457A)[1] and a varactor frequency doubler.[2] An automatic level control is used to maintain a constant output power.

An efficient cryogenic system is required for operational simplicity and satisfactory amplifier performance. Such a system has been designed to maintain the amplifier at liquid nitrogen temperature. The dewar contains about 10 liters of liquid nitrogen and lasts more than ten days. This corresponds to an evaporation rate of 40 cc per hour or a heat inflow of 1.8 watts.

The two-stage amplifier provides a gain of 38 db at 4.17 gc with a minimum bandwidth of 60 mc. Over the entire band the effective system input noise temperature is less than 45°K. An input signal of −43 dbm produces 1-db gain compression when the small-signal gain is 38 db. Short-term gain fluctuations are less than 0.1 db and long-term gain variations are less than 0.3 db over periods of months. The amplifiers were installed in the ground station receivers at Andover and Holmdel and have been checked out to be satisfactory.

II. DESIGN CONSIDERATIONS

2.1 *Parametric Amplifier*

2.1.1 *Varactor Diode Considerations*

There are several factors which governed the choice of the varactor diode for the 4.17-gc refrigerated parametric amplifier. These include:

(a) A capacitive impedance of the same order as the circulator.[3]

(b) High dynamic quality factor[4] ($\tilde{Q}$) given by

$$\tilde{Q} = \frac{S_1}{2\omega R_s} = \frac{\text{Total reactance variation}}{4R_s}$$

where S_1 is the Fourier coefficient of the first-order term in the pumped variable elastance and R_s is the spreading resistance of the diode.

(c) Crystal suitability for operation at liquid nitrogen temperature.[5] The spreading resistance should decrease or at least remain constant down to liquid nitrogen temperature. To simplify amplifier design and adjustment, a small decrease in junction capacitance from room temperature to liquid nitrogen temperature is desirable.

(d) A self-resonant frequency of the diode higher than an idler frequency is preferred.

At the time this amplifier was designed no diode was available which would meet all these requirements. Since a gallium arsenide diode satisfied all conditions but the last, which was not essential, it was chosen for this application. It was originally developed by W. M. Sharpless[6] and was further developed by N. C. Vanderwal. The recent encapsulation of the sealed diode is shown in Fig. 2.

Typical data for the diode are tabulated in Table I.

The spreading resistance decreases about 10 per cent from room temperature to liquid nitrogen temperature, and the junction capacitance changes only 5 per cent. Representative impedance loci of the diode at 300°K and 77°K (measured at 5.85 gc) are plotted in Fig. 3. The normal bias voltage for operation at liquid nitrogen temperature is −1.1 volts.

2.1.2 *Amplifier Design Considerations*

The main objective of the amplifier design was to achieve the best possible noise performance with moderate bandwidth (i.e., 25-mc minimum, 50-mc desired) and thus satisfy the system requirement with the available diode described in the previous section. The amplifier was required to have stable and reliable performance.

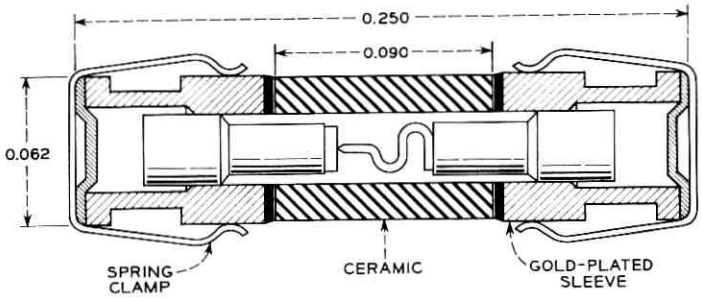

Fig. 2 — Encapsulation of sealed diode.

TABLE I

Static capacitance (C_0) at zero bias	0.37–0.46 pf (includes about 0.07 pf package capacitance)
Series inductance (L_s)	≈1.2 nh
Self-resonant frequency (f_{res})	7.3–8.4 gc
Dynamic quality factor (Q)	9.0–14 at 4.17 gc
Reverse breakdown voltage (V_b)	5.0–6.0 volts (at 1 μa current)

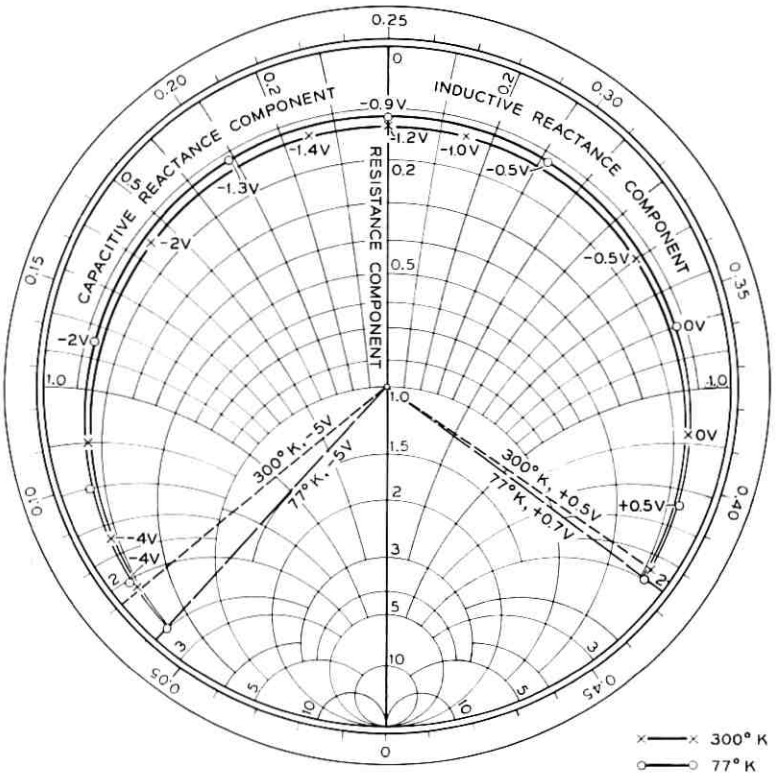

Fig. 3 — Impedance loci of input circuit at 300°K and 77°K (measured at 5.85 gc). Dynamic quality factor is 7.8 at 300°K and 9.3 at 77°K.

To achieve optimum performance, many factors, including the pump source, circuit elements and the cryogenic system, were carefully investigated. The detailed design considerations of the pump source and the cryogenic system are described in the following sections; however, selection of the pump frequency is discussed here since it primarily determines the circuit design of the amplifier.

The optimum ratio of idler frequency (f_2) to signal frequency (f_1) for best noise performance[3] is

$$\frac{f_2}{f_1} = \sqrt{1 + \frac{\tilde{Q}_1^2}{1 + \frac{R_L}{R_S}}} - 1 \qquad (1)$$

where $\tilde{Q}_1$ is the dynamic quality factor of the input circuit and R_L/R_S is the external idler loading factor. Assuming the external idler loading

factor $R_L/R_S = 0.8$, which is discussed later, and using a diode whose dynamic quality factor at the signal frequency is 10, the optimum pump frequency is 31.6 gc. Unfortunately, a reflex klystron with the desired reliability was not available near this frequency. In addition, most klystrons which provide more than 100 mw of power at K-band need very high voltage supplies. Another factor was that none of these tubes provide satisfactory frequency stability without an elaborate scheme to compensate for any large environmental temperature variation and for mechanical vibration. However, a Western Electric 457A klystron (available from 10.7 to 11.7 gc) has high frequency stability with a simple closed vapor-phase cooling system.[1] Typically, the frequency variation is less than 2 mc from $-20°$F to $+120°$F ambient temperature. This klystron provides more than 500 mw power at 11.5 gc with about 500 volts cavity voltage. With a varactor frequency doubler,[2] this klystron can generate about 100 mw of power at 23 gc even after taking an additional 2-db loss for an automatic level control. The increase in noise temperature due to the utilization of a 23-gc pump source instead of a 31-gc pump source is calculated from the following equation;[3] the effective input noise temperature for a reflection type amplifier

$$T_e = \left(1 - \frac{1}{G_{11}}\right) \frac{1 + \left(\frac{f_1}{f_2}\right)^2 \frac{\tilde{Q}_1^2}{1 + \frac{R_L}{R_S}}}{\left(\frac{f_1}{f_2}\right) \frac{\tilde{Q}_1^2}{1 + \frac{R_L}{R_S}} - 1} \cdot T \tag{2}$$

where G_{11} is a reflection power gain and T is the amplifier temperature. From (2), we obtain that the noise temperature degradation is only 1.5°K. Because of the reasons just described, a 23-gc pump was selected for this amplifier. This produces a center-band idler frequency of 18.83 gc. Fig. 4 shows curves of the effective input noise temperature of the amplifier at liquid nitrogen temperature for $f_2/f_1 = 4.52$. Curves are plotted as a function of external idler loading factor (R_L/R_S) for given values of input dynamic quality factor $\tilde{Q}_1$.

To achieve the noise performance shown in Fig. 4, the input circuit must be designed properly. The maximum normalized generator impedance (R_g/R_S) which provides 20 db of reflection gain for a given $\tilde{Q}_1$ and R_L/R_S is calculated[3] and plotted as a function of R_L/R_S in Fig. 5.

The first and second-stage amplifiers utilize the same design, a design

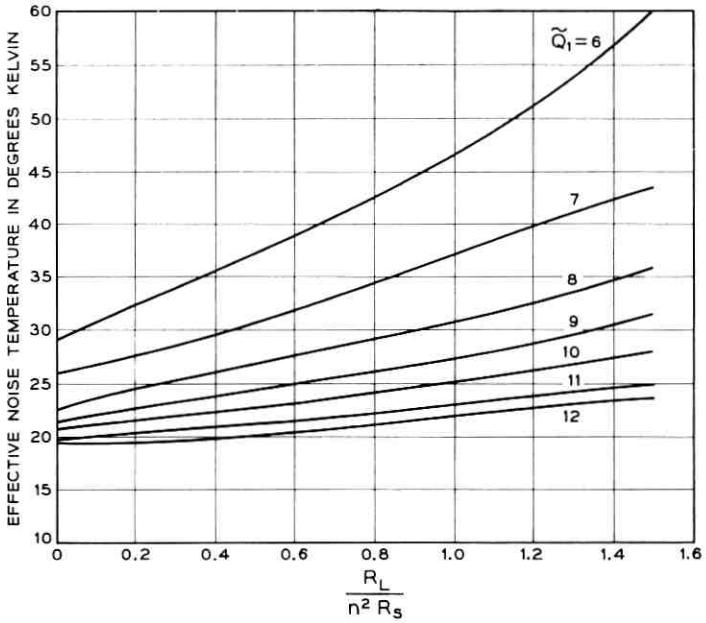

Fig. 4 — Effective input noise temperature of amplifier at liquid nitrogen temperature and room temperature as a function of external idler loading factor (R_L/R_S) for various $\tilde{Q}$.

which is similar to a 6-gc amplifier previously reported.[7] Fig. 6 shows a photograph of the amplifier mount with a four-port circulator. The input circuit is a 50-ohm coaxial line and the pump and idler circuits are in RG 66/U waveguide which houses a gallium arsenide point-contact diode at the end of the input center conductor. Since the diode sustains at least three frequencies (i.e., signal, idler and pump), filters must be arranged properly to eliminate unwanted interference among the three circuits. These filters are located as close as possible to the diode to minimize energy storage at the idler frequency. The input circuit contains two coaxial chokes for the pump and idler frequencies and a coaxial capacitor which is used to adjust the input coupling to the predetermined value of R_g/R_S and to tune the circuit at a desired bias voltage. These chokes and the rest of the mount are brazed into one piece for mechanical rigidity and electrical stability. The coaxial capacitor is movable along the center conductor to tune the circuit at a desired bias voltage. The input coupling is adjusted by using a different diameter coaxial capacitor.

One of the major design objectives was to increase the bandwidth

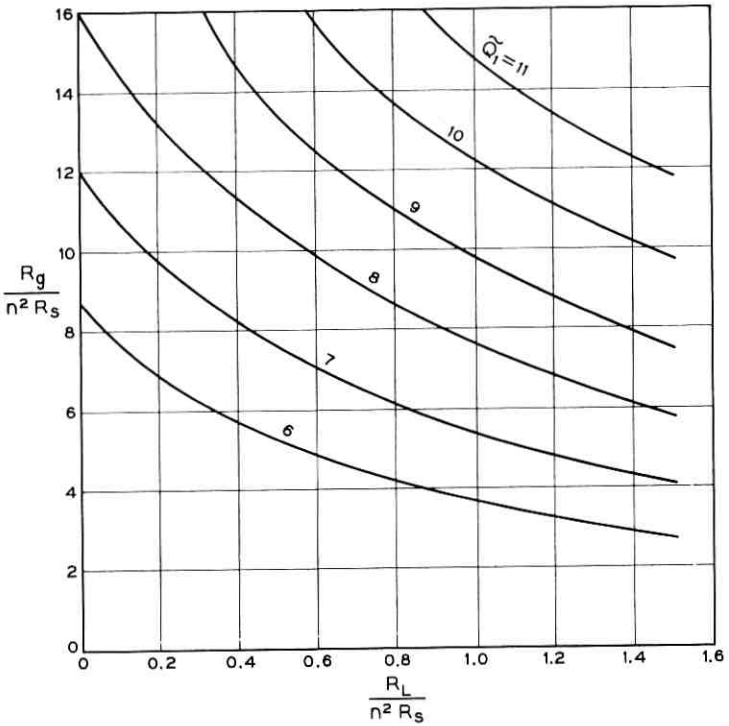

Fig. 5 — Normalized generator impedance R_g/R_S required for 20-db regenerative gain as a function of external idler loading factor R_L/R_S for given values of input circuit dynamic quality-factor $\tilde{Q}$.

without sacrificing noise performance. Since the self-resonant frequency of the diode is approximately 8 gc, it is unavoidable that an idler frequency much higher than the self-resonant frequency must be used. This resulted in an idler circuit of very high Q and complicated impedance. It was found that the 3-db bandwidth with 20-db center-band gain was less than 20 mc when there was no external idler loading or compensation circuit. Since the input circuit was broad enough, a compensation circuit was inserted in the idler circuit to improve the bandwidth. When the idler circuit Q is sufficiently high, the bandwidth can be improved by external idler loading. The optimum idler loading factor $(R_L/R_S)_{opt}$ for the case where the idler frequency is above the self-resonant frequency f_{res} of the diode is given in terms of $\tilde{Q}_1$, f_1/f_2 and f_{res}/f_1 as follows[8]

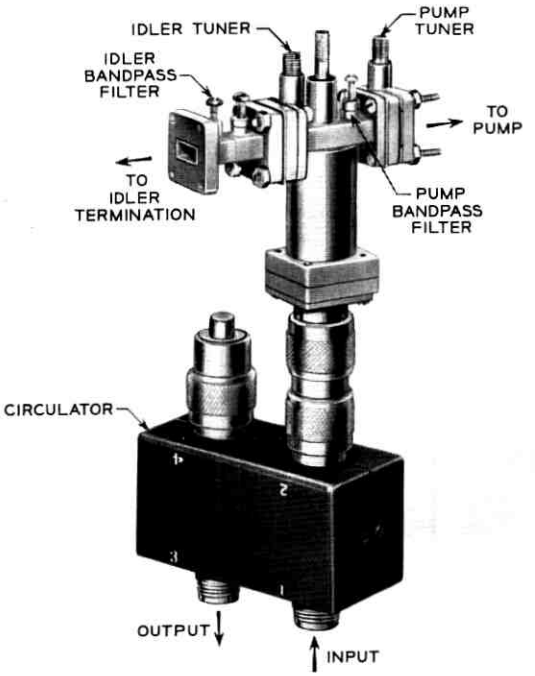

Fig. 6 — Photograph of 4.17-gc parametric amplifier and refrigerated circulator.

$$\left(\frac{R_L}{R_S}\right)_{\text{opt}} \approx \tilde{Q}_1^2 \left(\frac{f_1}{f_2}\right)\left[\frac{1}{1+\sqrt{1+\tilde{Q}_1^2\left(\frac{f_{\text{res}}}{f_1}\right)^2\left(\frac{f_1}{f_2}\right)}}\right] - 1 . \qquad (3)$$

For the case where $\tilde{Q}_1 = 10, f_1/f_2 = 0.22$ and $f_{\text{res}}/f_1 = 1.9$, this equation shows that $(R_L/R_S)_{\text{opt}} = 1.15$. According to the curves in Fig. 4, the noise degradation caused by this external load is about 5°K; a suitable compromise between optimum gain-bandwidth and optimum noise performance is $R_L/R_S = 0.8$. This reduces the noise degradation to about 3°K. As a compensation circuit, a two-cavity bandpass filter was added adjacent to the inductive iris which tunes the idler circuit at the prescribed diode bias voltage. This iris also determines the coupling between the diode and the external idler load. The electrical separation between the iris and the filter and the filter impedance characteristic were properly adjusted for the maximum bandwidth. A Teflon tuner

was located in the idler resonant cavity to compensate for the approximate 20 per cent change in circuit impedance from room temperature to liquid nitrogen temperature due to the reduction in junction capacitance and cavity volume.

The pump filter was built in the mount as close as possible to the diode to minimize idler frequency energy storage in the idler cavity. A Teflon tuner, an inductive iris adjacent to the amplifier, and a screw in the pump filter are used for critical matched tuning and compensation from room temperature to liquid nitrogen temperature operation.

The bias voltage of the diode was applied through the third or fourth port of the four-port circulator. Any loss and instability usually caused by the bias supply circuit in the diode mount were completely eliminated.

A circulator operated at liquid nitrogen temperature (Raytheon CCL-12) was specially designed for the refrigerated first-stage amplifier. It was designed to have a maximum insertion loss from port 1 to port 2 of 0.2 db and isolation of at least 30 db. The room temperature circulator for the second-stage amplifier is the broadband Melabs X-626. Its characteristics at room temperature are similar to those of the CCL-12 at liquid nitrogen temperature.

The main design features of the amplifier are given in Table II.

2.2 *Pump Source*

The design of parametric amplifiers usually calls for high stability in both the frequency and amplitude of the pump source. The troubles often ascribed to parametric amplifiers, such as frequent failure and high cost, can largely be attributed to unsatisfactory pump sources. Therefore, considerable effort was devoted to obtain the simplest pump source that would satisfy the exacting requirements.

For frequency stabilization and compactness an all solid-state source is most attractive. This would consist of a transistorized crystal oscillator at a relatively low frequency with power amplification and subse-

TABLE II

Input and output frequency	4.17 gc ± 30 mc
Pump frequency	≈23 gc
Dynamic quality factor $\tilde{Q}$ (including the circuit loss)	10 at 4.17 gc, 2.3 at 18.83 gc
Normalized generator impedance (R_g/R_S)	13.0
Normalized idler impedance (R_L/R_S)	0.8
Gain	20 db
Estimated noise temperature from (2) (amplifier alone)	94°K at 300°K 25°K at 77°K

quent multiplication by varactor diodes. While technically possible, such a device was not available in time for this project. Therefore, the WE 457A klystron was used as an 11.5-gc source to drive the varactor frequency doubler,[2] which produced the required 23-gc pump power.

For the automatic level control (ALC) the classical feedback approach has been used. A block diagram of the ALC arrangement is shown in Fig. 7. The output of the klystron is fed into the doubler through a Faraday rotational variolosser.[9] A small fraction of the 23-gc output is detected by a 1N26 crystal in the sampling port of a cross guide coupler. This output is compared with a reference voltage, amplified by a transistorized differential amplifier, and is fed to the variolosser. In this way the difference between the sampling voltage and the reference voltage is kept close to a preset constant value, and hence the 23-gc power output level is stabilized to better than 0.5 per cent over long time periods. Since the sensing diode characteristic is influenced by a large temperature change, this diode and the first stage of the differential amplifier are mounted in a small oven.

The second design, shown in Fig. 8, omitted the variolosser and operated directly on the doubler bias to control the output power. Although the performance was generally satisfactory, it demonstrated the need for an additional control factor. For feedback stability reasons, it is necessary to place a limit on the bias. However, this limit varies with input power to the doubler diode; hence, some additional circuitry is added to automatically set the maximum bias consistent with the input power.

The varactor frequency doubler from 11.5 gc to 23 gc used for this pump source can generate more than 200 mw of power at 23 gc with as low as 3.7-db conversion loss. The instantaneous 3-db bandwidth is about 300 mc, and no spurious oscillation is observable except at a bias

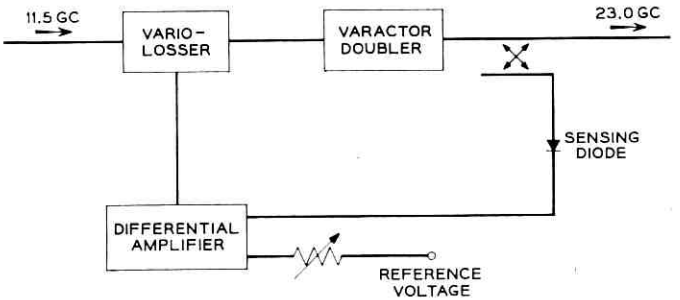

Fig. 7 — Block diagram of ALC arrangement. Power level is controlled by variolosser.

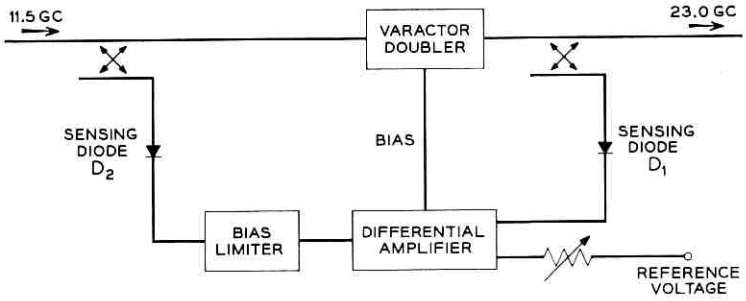

Fig. 8 — Block diagram of varactor diode bias-controlled ALC arrangement.

voltage which is much higher than the optimum. The varactor diode used is the epitaxial silicon mesa diode developed at Bell Telephone Laboratories. The diode has a cutoff frequency as high as 300 gc at −2.5 volts bias and a 25 volts average reverse breakdown voltage.

2.3 *Cryogenic System*

It was necessary for simple maintenance and satisfactory amplifier performance to design an efficient cryogenic system. Noise considerations dictate that not only the diode but also the total structure of the first-stage amplifier, including the circulator and the idler load, should be refrigerated. Immersing the whole amplifier in liquid nitrogen is a convenient way of refrigerating. However, it is very difficult to seal all parts of such a complex geometry in order to avoid liquid nitrogen leakage, which produces erratic electrical performance. Therefore, the whole unit is enclosed in a tight cylindrical copper vessel which is then immersed in liquid nitrogen. The walls of this vessel will assume a temperature of 77°K and cool the whole interior by conduction and radiation.

In order to achieve a long operating time with each filling of the dewar, the heat input must be minimized through the proper use of materials of low thermal conductivity. The design must make full use of the cryogenic value of the refrigerant. One liter of liquid nitrogen can absorb 38,600 cal. as heat of vaporization, and in addition the nitrogen gas which is produced can absorb 39,000 cal. when brought from 77°K to 273°K. If an arrangement can be made so that the nitrogen gas leaves the dewar with a temperature equal to that of ice, for instance, then the cryogenic value of one liter of liquid nitrogen is 77,600 cal. Furthermore, if the nitrogen gas escapes at room temperature there will be no condensation or freeze-out of moisture at the lid of the dewar, where many

electrical connections are located. A long operating time between refills can be obtained by immersing the amplifier deeply into the coolant; on the other hand, the input transmission line to the amplifier must be short to keep its loss and the corresponding noise contribution down. This imposes some restrictions on the cryogenic design. Fig. 9 shows a drawing of the cryostat. A commercial Linde Dewar featuring "Super Insulation" was chosen. It has a necktube of 5.5 inches diameter and holds 13.5 liters of liquid nitrogen. Part of this volume is taken up by the amplifier chamber, so that about 10 liters of liquid nitrogen are available for refrigeration. After immersion of the copper vessel the necktube is closed off by a lid consisting of a grooved Teflon plug, to the bottom of

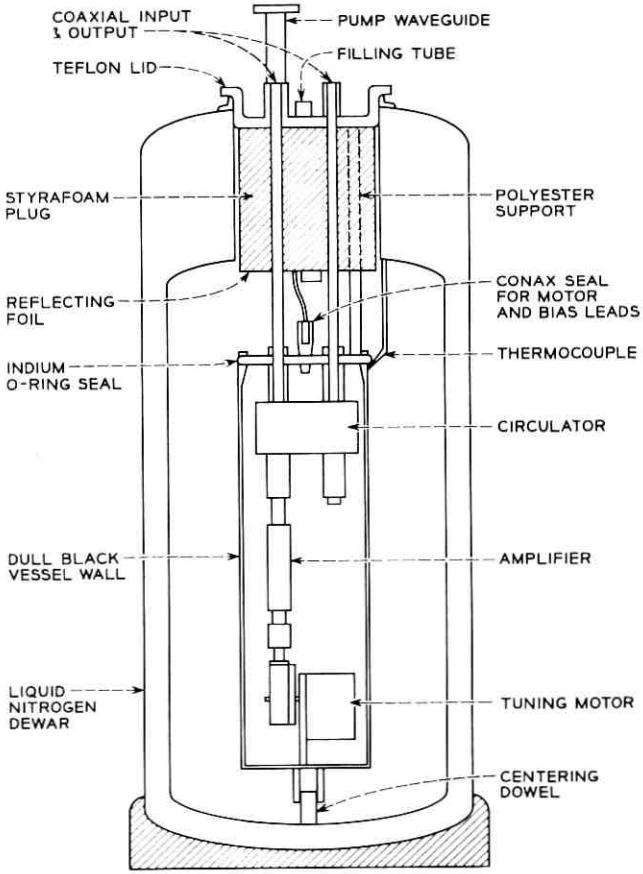

Fig. 9 — Cryostat for parametric amplifier.

which is glued a styrofoam cylinder 4 inches deep and $\frac{1}{8}$ inch smaller in diameter than the necktube. This arrangement forces the nitrogen gas to rise along the wall of the necktube and thereby cools it. The pump waveguide, two coaxial lines, a Teflon filling tube, and two polyester support rods (which add mechanical strength to the structure) pass through this lid down to the top of the amplifier chamber. The 11-inch input and output coaxial lines are made of 5-mil wall stainless steel tubes with 0.5-mil copper clad interior. Thin-wall stainless steel waveguide with silver plated interior is used for the pump waveguide. These transmission lines are vacuum sealed at the neck of the dewar (where the temperature is higher than the dew point) to prevent moisture condensation. The top of the copper chamber is sealed vacuum tight by an indium O-ring and the lower end extends almost to the bottom of the dewar, where it is held centered by a dowel pin. After all the parts are assembled, the copper chamber is tested on a helium leak tester for perfect sealing. The inside pressure of the chamber is left at atmospheric pressure to improve the speed of cooling.

With one filling of the dewar the amplifier was held for 10.5 days at liquid nitrogen temperature. This corresponds to an evaporation rate of 40 cc per hour or a heat inflow of 1.8 watts. Vertical temperature profiles which have been measured in the dewar reveal that the temperature of the gas above the liquid level stays within 2° of 77°K. This explains the constancy of the amplifier temperature over such a long time. The dewar can be refilled with liquid nitrogen without interrupting the performance of the parametric receiver.

For remote tuning of the idler and pump circuits, two tuning motors are mounted on the bottom of the copper vessel. Motors which are designed to be run at liquid nitrogen temperature must have a high starting torque, slow speed, and bearings which will not seize when the materials contract upon cooling. A stepping motor with 100 steps per revolution has been found to be the most reliable device to satisfy these requirements. The motors are operated by a transistorized multivibrator.

2.4 *Package*

One of the advantages of a parametric amplifier over a maser can be its compactness; however, its size is largely dependent upon the package design. Since the amplifier is highly susceptible to impedance variations and pump fluctuations, the package has to be designed not only for compactness but also to minimize any electrical malfunctions due to mechanical vibrations. Easier maintenance is also an important consideration for the package design.

Three different types of the package were constructed. Each of the first two amplifiers was packaged in a large 28 inch × 26 inch × 72 inch cabinet which can directly replace the maser cabinet and match mechanically to the horn antenna. This package was designed for operational convenience, reliability, simple maintenance and appearance. The front and back views of the amplifier are shown in Figs. 10 and 11. The dewar containing the refrigerated amplifier is in a frame at the top of the rack, with the input waveguide above the cabinet at a total height of 78 inches. The cabinet has four leveling jacks to enable an exact match to the antenna. The room temperature amplifier is mounted on

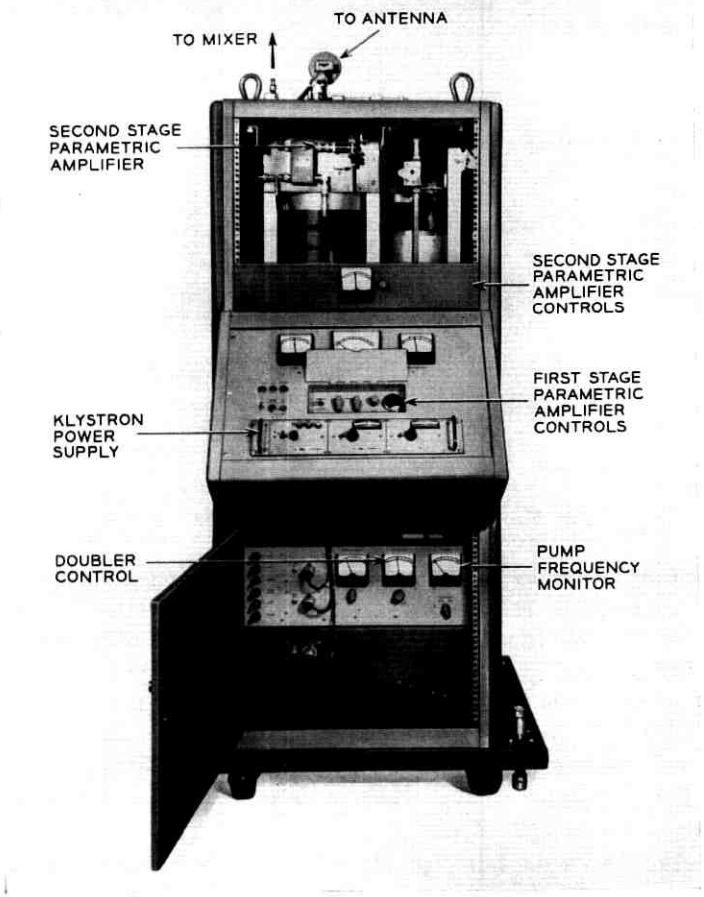

Fig. 10 — Front view of large amplifier package.

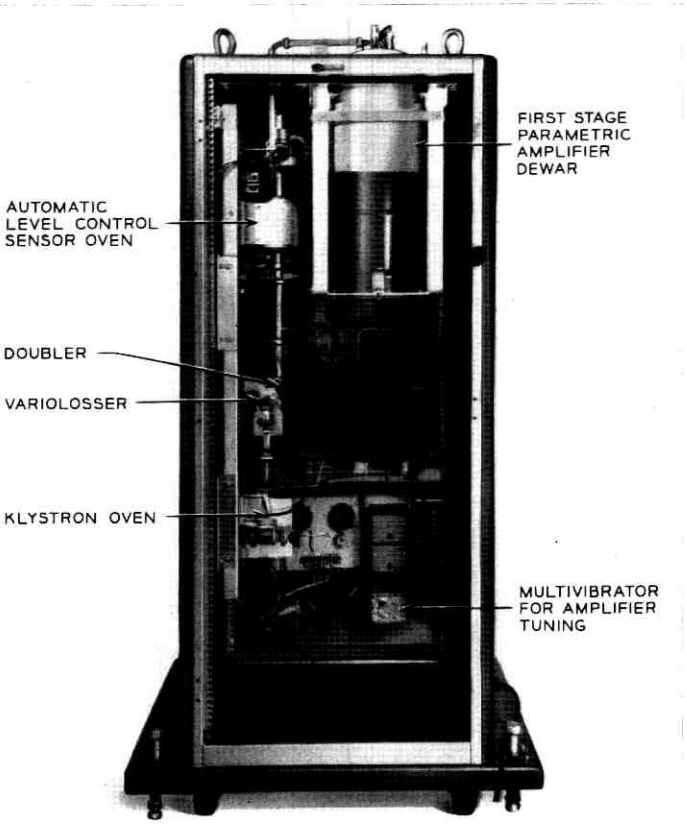

Fig. 11 — Back view of large amplifier package.

the dewar frame to minimize the interconnecting transmission line length and can be seen from the front of the rack with the top panel removed. The bias and pump power controls for the room temperature amplifier are located on the top control panel, and the controls for the liquid nitrogen temperature amplifier and the ALC are located in the recessed middle control panel. This section is usually covered and protected from accidental handling. The entire pump supply is mounted on a flat aluminum chassis which is fastened on the left side frame structure. The length of pump waveguides and the number of flange connections from the pump power sampling point to the amplifiers are minimized to maintain constant pump power levels against mechanical vibrations. The pump power level can be controlled by the motor-

driven waveguide attenuators from the front panel. One can see that the cabinet is only partially occupied.

To utilize full advantage of the parametric amplifier, a compact package was designed. This package consists of two cabinets: a control cabinet (17 inches × 18 inches × 10 inches) and an amplifier cabinet (14 inches × 14 inches × 32 inches), both shown in Fig. 12. The separation thus allowed the amplifier to be installed directly at the antenna output and the controls to be located at a convenient operating location. In this compact model, the doubler bias-controlled ALC is installed to ease the package design. Fig. 13 shows the amplifier and pump arrangement.

III. PERFORMANCE

Five parametric receivers were built: two were housed in large cabinets, two in compact cabinets, and one in a special cabinet for a sky

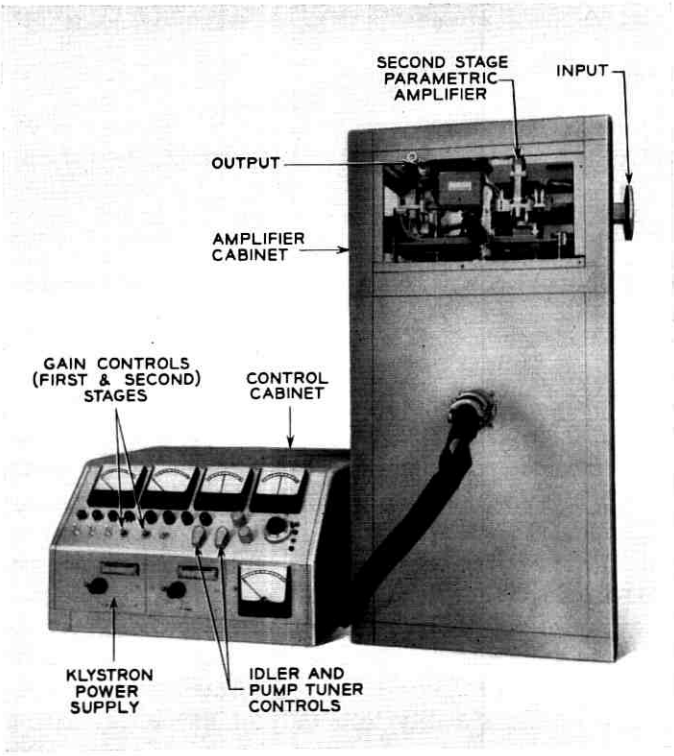

Fig. 12 — Photograph of compact package.

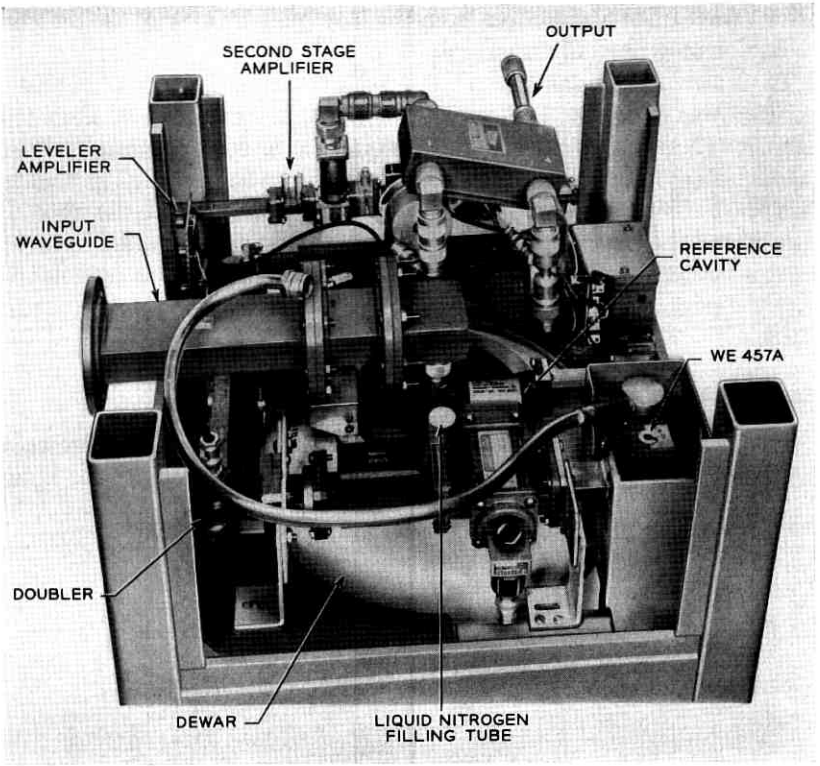

Fig. 13 — Photograph of amplifier and pump arrangement of compact package.

temperature measurement. The average values for the performance of these amplifiers are listed in Table III.

By December 1, 1962, amplifier no. 1 had been operated continuously for 6000 hours (since March 20, 1962) without any failure or degradation.

A representative gain-frequency band characteristic is shown in Fig. 14. Fig. 15 shows the recorded data on amplifier stability over a two-day period. The bottom f_p curve shows the pump frequency deviation from 23 gc. One inch on the original recording paper corresponds to about 200 kc deviation. The second curve from the bottom (gain) shows the gain of the refrigerated amplifier. One inch corresponds to 1-db change in gain. The P_{pump} curve indicates the pump power level. The scale is 0.25 db per 0.5 inch. Since the signal generator and the test receiver used for the stability tests did not themselves have absolute gain stability, both input and output signal level were detected by crystal detectors and were recorded simultaneously. The second (P_{in})

TABLE III

Gain	38 db (first stage 20 db, second stage 18 db)
Bandwidth	60 mc to 3-db points
Noise temperature	
First stage	<45°K
Contribution from second stage + mixer	<43°K
	<2°K
Gain stability	
Short-term	<0.1 db
Long-term	<0.3 db
Gain compression	1 db down at −5 dbm output
23-gc pump power required	≈20 mw for each stage
Pump stability	
Frequency	Short-term <100 kc
	Long-term <2 mc
Power	<0.02 db
Dewar — nitrogen service	Once a week (nitrogen lasts about 10 days)

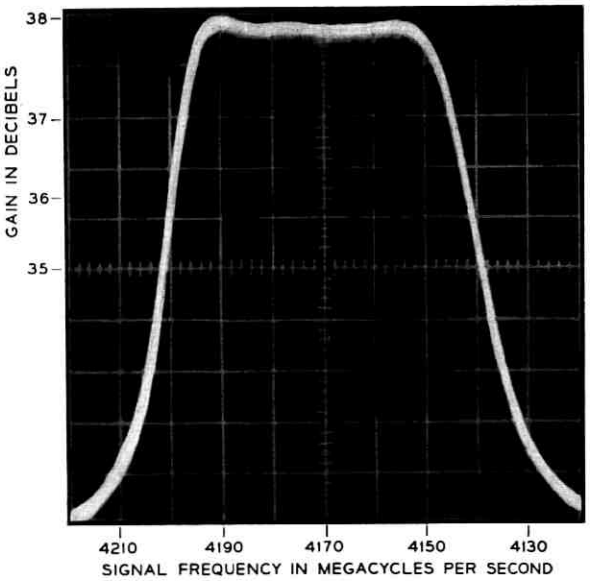

Fig. 14 — Gain-frequency band characteristic of parametric amplifier no. 2.

and third (P_{out} − 21 db) curves show these outputs. The controls were adjusted so that the separation between the two curves was 1 db when the gain of the amplifier was 20 db; the gain fluctuations were then deduced from the separation of these curves. The speed of the recorder was two inches per hour.

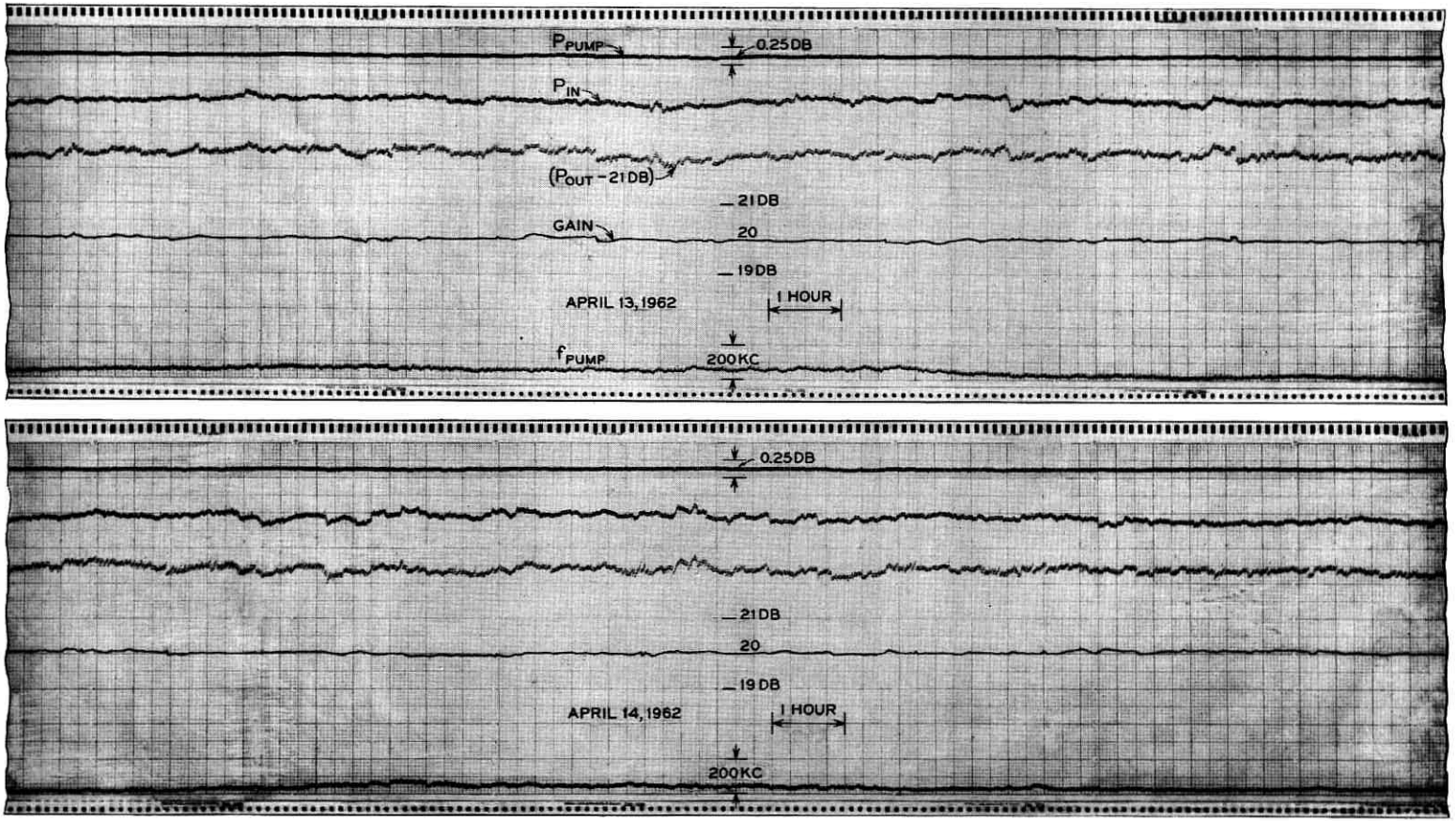

Fig. 15 — Recorded graph of amplifier stability. Pump line shows the pump power level; P_{in}, signal input; P_{out} − 21 db, 21 db below amplifier output; f_{pump} the pump frequency deviation from 23 gc.

The amplifiers were installed in the satellite ground stations both at Andover, Maine, and Holmdel, New Jersey, and were checked out as functioning satisfactorily. The complete system noise temperature of the receiver at the Andover station with the parametric amplifier was about 80°K when the antenna was directed at the zenith. This noise temperature includes about 28°K of noise from the sky, the radome, the antenna and the diplexer, and some noise from the 2.5-foot long waveguide which connects the amplifier to the diplexer.

IV. CONCLUSION

The noise temperature of the receiver with the parametric preamplifier is 2.5 times that with the maser. However, the parametric amplifier is much cheaper to operate. The results of laboratory and field tests demonstrate that the parametric receiver meets the stringent requirements of a satellite ground station receiver. The stability performance of the amplifier also proves that a carefully engineered parametric amplifier is as stable as conventional microwave amplifiers.

The amplifier and its associated devices have been designed for high sensitivity, stability, and reliability. To assure this performance, the bandwidth was sacrificed and in many places a conservative design has been adopted. With an improved diode—in particular, one in a more suitable package—and a completely transistorized pump source, the amplifier can be considerably simplified and made very compact without any degradation in its performance and with an improved bandwidth.

V. ACKNOWLEDGMENTS

During the course of this study many members of Bell Laboratories contributed valuable knowledge and skills. Unfortunately it is impractical to name them all here, but the authors are deeply grateful to them all. N. C. Vanderwal supplied the gallium arsenide diodes; R. L. Rulison developed the silicon epitaxial diodes; C. E. Barnes supplied the ferrite variolossers; and E. E. Prince did the initial package design. The authors wish to acknowledge their major contributions.

Acknowledgment is also made to K. D. Bowers for stimulating discussions and helpful criticism in the study of this project.

REFERENCES

1. Gucker, G. C., Long-Term Frequency Stability of a Reflex Klystron Without Use of External Cavities, B.S.T.J., **41**, May 1962, pp. 945–958.
2. Uenohara, M., Rulison, R. L., Bricker, C. H., Varactor Frequency Doubler from 11.5 to 23 gc, Proc. I.R.E, **50**, December, 1962, p. 2486.

3. Uenohara, M., Seidel, H., 961-mc Lower Sideband Up-Converter for Satellite-Tracking Radar, B.S.T.J., **40**, July, 1961, pp. 1183–1205.
4. Kurokawa, K., Uenohara, M., Minimum Noise Figure of the Variable-Capacitance Amplifier, B.S.T.J., **40**, May, 1961, pp. 694–722.
5. Uenohara, M., Extremely Low-Noise Variable-Capacitance Parametric Amplifier, Proc. of International Congress on Microwave Tubes in Munich, Germany, 22, 1961 Monograph 4031, pp. 334–337.
6. Sharpless, W. M., Gallium-Arsenide Point-Contact Diodes, I.R.E. Transactions on Microwave Theory and Techniques, **MTT-9**, January, 1961, pp. 6–10.
7. Uenohara, M., An Extremely Low-Noise 6-gc Nondegenerate Parametric Amplifier, Proc. I.R.E., **50**, February, 1962, p. 208.
8. DeJager, J. T., private communication.
9. Barnes, C. F., Broadband Isolators and Variable Attenuators for Millimeter Wavelengths, I.R.E. Trans. on Microwave Theory and Techniques, **MTT-9**, November, 1961, pp. 519–523.

Contributors to this Issue

J. V. Anders, B.E.E., 1953, University of Florida; Western Electric Co., 1953–1961; Bell Telephone Laboratories, 1961—. He has been engaged in guided missile systems test and evaluations programs and radar circuit design. He worked on the development of tracking receivers for the Telstar project and is presently engaged in the design of solid-state radar circuits. Member, IEEE, American Rocket Society, and American Ordnance Association.

John T. Bangert, B.S.E.E., 1942, University of Michigan; M.S.E.E., 1947, Stevens Institute; Bell Telephone Laboratories, 1942—. Mr. Bangert was first engaged in design of special circuits for military radar, investigation of fundamental problems in transmission theory, and exploration of new techniques for network analysis and synthesis in the time and frequency domain. Later he headed groups responsible for waveguide systems analysis, microwave network design and the application of analog and digital computers to the design of transmission systems. Since March, 1962, Mr. Bangert has been Director of the Transmission Technology Laboratory. Member, IEEE, Sigma Xi, Tau Beta Pi, Eta Kappa Nu, and Phi Kappa Phi.

Simon B. Bennett, B.E.E., 1959, City College of New York; M.E.E., 1961, New York University; Bell Telephone Laboratories, 1959—. He has been engaged in the study of noise in FM transmission systems and has participated in planning and performing the communications system tests for the Telstar and Relay projects. Member, IEEE, Tau Beta Pi and Eta Kappa Nu.

R. B. Blackman, A.B., 1926, California Institute of Technology; Bell Telephone Laboratories, 1926—. Mr. Blackman was first engaged in physical research in hearing, acoustics, and electromechanical filters. He later worked in applied mathematical research, specializing in linear networks and feedback amplifiers. Since 1940, he had been engaged in the development of data-smoothing and prediction techniques for anti-aircraft fire-control computers, air-to-ground bombing computers,

guided-missile computers and satellite launching computers. Member, IEEE and Tau Beta Pi.

R. W. Blackmore, B.S.M.E., 1940, Case Institute of Technology; Bell Telephone Laboratories, 1941—. He has engaged in mechanical design work on missile guidance systems, optical equipment for evaluating tracking performance of radar antennas, and flight control instruments. On the Telstar project he performed engineering liaison work with subcontractors and various Laboratories groups involved in the mechanical design, fabrication, erection, and alignment of the horn-reflector antenna. He is presently engaged in design and cost studies for future antennas. Member, Tau Beta Pi.

J. D. Bode, Ph.D., 1952, University of Pittsburgh; Bell Telephone Laboratories, 1960–63. Mr. Bode was first engaged in electroplating magnetic materials for the ESS semipermanent Twistor Memory Store. This was followed by work on the Telstar satellite project, which included the antireflection coating of the solar cells and their sapphire covers and work on the thermal control bellows. He was later involved in development work on long-wavelength sensitive photocathodes for laser applications. Member, American Chemical Society, Electrochemical Society, A.A.A.S., Electron Microscope Society of America, Faraday Society, Optical Society of America and Sigma Xi.

Max G. Bodmer, Dipl. El. Ing., 1946, Federal Institute of Technology, Zurich, Switzerland; Eng. D., 1950, Johns Hopkins University; Bell Telephone Laboratories, 1951—. Mr. Bodmer has specialized in the design and development of traveling-wave tubes, including exploratory development of TWT's, life studies for systems TWT's, the design of a high-power CW TWT for X-band, and the design and development of high-reliability long-life TWT's for satellite use. Member, IEEE and AIAA.

David C. Bomberger, B.S.E.E., 1934, and M.S.E.E., 1936, Lehigh University; Bell Telephone Laboratories, 1936—. He has worked on transmission measurements of coaxial cables, the design of broadband feedback amplifiers, the development of electromechanical gun director systems, and the analysis and simulation of complex dynamic systems. As Head, Power Systems Engineering Department, he was responsible for engineering the spacecraft power supply. Member, IEEE, Tau Beta Pi, Phi Beta Kappa; associate member, Sigma Xi.

STEPHEN J. BROLIN, B.S.E.E., 1957, M.S.E.E., 1959, New York University; Bell Telephone Laboratories, 1957—. He first worked on regulated power supplies for an experimental electronic telephone central office, and has since designed power supplies for a military project, a carrier system, and the Telstar project. He is currently working on power supplies for microwave radio relay systems. Member, IEEE, Tau Beta Pi, and Eta Kappa Nu.

W. L. BROWN, B.S., 1945, Duke University; A.M., 1947, Ph.D., 1951, Harvard University; Bell Telephone Laboratories 1950—. Mr. Brown has been engaged in research on the physical properties of semiconductor surfaces and the nature of defects produced in semiconductors by high energy radiation. He has recently been responsible for radiation experiments aboard the Telstar satellite. Fellow of American Physical Society, Sigma Xi and Phi Beta Kappa.

T. M. BUCK, B.S., 1942, Muskingum College; M.S., 1948, and Ph.D., 1950, University of Pittsburgh; Bell Telephone Laboratories, 1952—. He has been engaged in studies of the chemical and surface properties of semiconductor materials and devices. More recently, he has been responsible for development of the silicon p-n junction particle detectors for the Telstar satellite. Member, Electrochemical Society, Sigma Xi, Phi Lambda Upsilon, and Sigma Pi Sigma.

C. PAUL CARLSON, B.S. in E.E., 1926, University of Michigan; Bell Telephone Laboratories, 1926—. Until World War II he was engaged in equipment development of long-distance signaling, telephone repeaters, line balancing apparatus and transmission testing equipment. During the war he worked on radar test set development and has since been concerned with test sets, microwave radio, TASI, and undersea repeaters for transatlantic telephone cables. He presently supervises a group engaged in equipment design for the Andover, Maine, earth station. Registered Professional Engineer, State of New York.

J. G. CHAFFEE, S.B., 1923, Massachusetts Institute of Technology; Western Electric Co., 1923–25; Bell Telephone Laboratories, 1925—. He first engaged in short-wave transmission studies; this was followed by participation in the first ship-to-shore radiotelephone commercial installation. He then made extensive studies of frequency modulation and invented the FM-with-feedback receiver. During World War II he engaged in radar and guided-missile projects. Following this he spent the

next 15 years in studies for microwave radio relay systems. Since the inception of the Telstar project he has worked on circuit design, principally the design of the FMFB receiver for the ground station. Fellow of IEEE.

ROGER C. CHAPMAN, JR., B.S.E.E., 1954, University of Vermont; Bell Telephone Laboratories, 1954—. Mr. Chapman was first engaged in the study of pulse code modulation systems and pulse transmission. He developed circuits for regenerative repeaters, particularly the retiming and reshaping circuits. In 1961, he started work on command circuit design for the Telstar project, and later became supervisor of a group responsible for the command and telemetry portion of the ground station. Currently, Mr. Chapman is supervisor of a systems analysis group responsible for the Telstar systems tests and for analysis and system studies of possible future satellite communications systems. Member, IEEE; associate member, Sigma Xi.

MICHAEL CHRUNEY, B.S.E.E., 1948, and M.S.E.E., 1949, Pennsylvania State College; Bell Telephone Laboratories, 1949—. He has engaged in the design and development of beam devices such as the barrier-grid storage tube and the flying-spot scanner for the memory of an experimental electronic central office. He contributed to the microwave printed hybrids used in the Telstar satellite and the parametric amplifier used as a standby receiver at the Andover earth station. Member, IEEE.

A. J. CLAUS, B.S. in E.E. and M.E., 1956, University of Ghent, Belgium; Ph.D., 1961, University of Michigan; Bell Telephone Laboratories, 1961—. He has worked on orbit determination for the Telstar satellite and tracking studies for the Apollo project.

ROBERT J. COLLIER, B.S., 1950, M.S., 1951, and Ph.D., 1954, Yale University; Bell Telephone Laboratories, 1954—. He has been engaged in the development of microwave electron tubes, including the coaxial magnetron, the forward-wave crossed-field amplifier, and the traveling-wave tube for the Telstar transmitter. He presently heads a group which is designing high-power traveling-wave tubes for pulsed radar. Member, American Physical Society, Sigma Xi and Phi Beta Kappa.

R. L. COMSTOCK, B.S., 1956, and M.S., 1957, University of California; Ph.D., 1962, Stanford University; Bell Telephone Laboratories, 1957–58,

1961—. He has been concerned with the development of microwave solid-state devices, including isolators, power limiters and magnetoelastic devices. Member, IEEE, Eta Kappa Nu, Sigma Xi, and Tau Beta Pi.

J. S. Cook, B.E.E. and M.S., 1952, Ohio State University; Bell Telephone Laboratories, 1952—. He has engaged in microwave electron device research, including low-noise studies, coupled microwave circuits, electrostatic electron beam (slalom) focusing, and parametric amplification. He took part in the development of the autotrack system for the horn-reflector antennas used at Andover and Pleumeur-Bodou, France. He is presently engaged in studying special radar and communications antennas. Senior member, IEEE.

Arthur B. Crawford, B.S. in E.E., 1928, Ohio State University; Bell Telephone Laboratories, 1928—. Mr. Crawford has specialized in radio research, including work with measuring techniques, propagation, and antenna studies in the ultra-short-wave and microwave areas. He designed the horn-reflector antenna used in the Project Echo passive satellite communications experiments. As Head, Radio Research Department, he is in charge of a group which was responsible for transmission studies for the Telstar project. Fellow, IEEE; member, Eta Kappa Nu, Pi Mu Epsilon, Sigma Xi and Tau Beta Pi.

George F. Critchlow, B.E.E., 1942, and B.M.E., 1943, Cornell University; Bell Telephone Laboratories, 1943 —. He has been engaged in the development of precision impedance and transmission equipment and in the supervision of groups responsible for this work. He is presently head of a group which designs solid-state circuits for communications satellites. Member, IEEE, Eta Kappa Nu, Phi Kappa Phi and Tau Beta Pi.

C. Chapin Cutler, B.S., 1937, Worcester Polytechnic Institute; Bell Telephone Laboratories, 1937—. He has made significant contributions in the areas of microwave antennas, microwave tubes, and new radar and communication systems. As Director, Electronic Systems Research, he heads a group which has worked on communications engineering for both the Project Echo and Project Telstar satellite communications experiments. Fellow, IEEE.

Donald B. Cuttriss, B.S. in E.E., 1959, Newark College of Engineering; M.S. in E.E., 1961, New York University; Bell Telephone Labora-

tories, 1951—. Until 1959 Mr. Cuttriss worked on design and development of laminated-core inductors and semiconductor field-effect devices. In 1959 he transferred to semiconductor device development and was concerned with the development of diffused-base germanium transistors. Since 1960 he has been engaged in the evaluation of solar cell performance, particularly in the design and evaluation of solar power plants for communication satellites. Member, Tau Beta Pi.

J. B. D'Albora, Jr., B.S. in E.E., 1934, Massachusetts Institute of Technology; Research Assistant, M.I.T., 1935–40; Senior Radio Inspector for Inspector of Naval Material, N.Y.C., 1940–41; Western Electric Company, 1941–45; Bell Telephone Laboratories, 1945—. His early assignments at the Laboratories included development of shipborne fire control equipment and search radar for the DEW Line. In 1956 he was assigned responsibility for the ground guidance equipment for the Titan ICBM at Cape Canaveral, and since 1961 he has been in charge of the Cape Canaveral Laboratory as Resident Technical Director. Senior member, IEEE; member, American Rocket Society.

Claude G. Davis, B.S. in E.E., 1950, Case Institute of Technology; M.S. in Mathematics, 1960, Stevens Institute of Technology; Bell Telephone Laboratories, 1950—. He has specialized in transmission systems development, including the development of armorless submarine cable for a transoceanic telephone system, a PCM system for exchange trunks, PCM repeaters for an experimental waveguide transmission system, the Time Assignment Speech Interpolation (TASI) system, and satellite repeater design and data analysis. He is currently responsible for development of customer radio systems. Member, Eta Kappa Nu and IEEE.

W. A. Dean, Bell Telephone Laboratories, 1955—. He has worked on solid-state microwave device development, including devices for tropospheric scatter systems, Project Echo, and the Telstar project. He is presently engaged in circulator development for a carrier transmission system.

T. B. Delchamps, B.S.M.E., 1945, University of New Hampshire; B.S.M.E., 1947, Lehigh University; Bell Telephone Laboratories, 1959—. Mr. Delchamps is presently Head, Environmental Engineering Department of the Reliability Engineering Center.

Alton C. Dickieson studied electrical engineering at Brooklyn Poly-

technic Institute and joined the Western Electric Company Engineering Department in 1923. At Bell Laboratories, Mr. Dickieson's responsibilities have included long-distance communications systems; military telephone, sonar and torpedo-guidance systems during World War II; and transmission and radio systems engineering. In 1951 he became Director of Transmission Systems Development and subsequently directed the planning for the communication and detection systems used in the first Distant Early Warning stations. He became Executive Director of the transmission division in 1961, in which position he has general responsibility for the Telstar experiment. Naval Ordnance Development Award, 1945; Gen. H. H. Arnold Trophy of the Air Force Association (with Dr. J. R. Pierce), 1962; General Hoyt S. Vandenberg Award of the Arnold Air Society, 1963 (with Dr. J. R. Pierce); Fellow, IEEE.

J. C. Dolling, B.S. Eng., 1949, and M.S.M.E., 1952, Technical University of Hanover, Germany; Ph.D., Eng., 1955, Technical University of Brunswick, Germany; Weserhuette AG, Oeynhausen, Germany, Chief Development Engineer, 1954–56; Wuelfel AG, Hanover, Germany, Assistant to Vice-President, 1956–58; Bell Telephone Laboratories, 1958—. He has been engaged in electromechanical development of military radar and space communication antennas, including structural, mechanical, and system analyses for military projects. He was responsible for preliminary design of and engineering guidance on the Telstar horn-reflector antenna, and presently is developing this antenna for commercial use. Member of A.S.M.E. and German Engineers Association (VDI).

K. M. Eisele, Dipl. Phys., 1954, Institute of Technology, Stuttgart, Germany; M.A., 1955, and Ph.D., 1958, University of Toronto; Bell Telephone Laboratories, 1960—. He has been engaged in studies of low-noise performance in parametric amplifiers through cryogenic techniques and thermoelectric cooling. He is presently working on the noise performance figures of varactor diodes, determined independently of the system in which the diode is used.

Roy E. Elicker, B.S., 1950, and M.S., 1951, Michigan State University; Bell Telephone Laboratories, 1951—. He was first engaged in studies of low-temperature extrusion of aluminum as a sheath for cable. He then worked on development of a cooling system for an airborne bombing and radar system, after which he was concerned with the design and development of forward-scatter tropospheric antennas for early-

warning systems. He is currently engaged in development of communications structures and equipment resistant to nuclear blast effects. Member, Pi Mu Epsilon, Pi Tau Sigma, and Phi Lambda Tau.

RUDOLF S. ENGELBRECHT, B.S.E.E., 1951, and M.E.E., 1953, Georgia Institute of Technology; Bell Telephone Laboratories, 1953—. He was first engaged in the design of exploratory low-noise microwave receivers and parametric amplifiers for military projects. He presently supervises a group concerned with parametric device studies. Member, IEEE, Tau Beta Pi, and Eta Kappa Nu.

DAVID FELDMAN, B.S.E.E., 1947, M.S.E.E., 1949, Newark College of Engineering; Assistant Professor of Electrical Engineering, 1949–1954, Cooper Union School of Engineering; Bell Telephone Laboratories, 1956—. He was first engaged in the design of magnetic amplifiers and transistorized regulator circuits for military systems and later supervised activities in the field of energy conversion. He was responsible for the initial design of the Telstar spacecraft power supply and for development of the nickel-cadmium storage battery. Currently he is Head, Transmission Component Department, responsible for the design and development of reliable passive components for satellite and submarine cable systems. Member, A.A.S.E. and IEEE.

J. D. GABBE, B.A., 1950, New York University; M.S., 1951, University of Illinois; Ph.D, 1957, New York University; Bell Telephone Laboratories, 1956—. Mr. Gabbe was first associated with video telephone studies. At present, he is engaged in research on the earth's radiation belts.

ADOLF J. GIGER, Diploma in Electrical Engineering, 1950, and Doctor of Electrical Engineering, 1956, Swiss Federal Institute of Technology; Bell Telephone Laboratories, 1956—. Mr. Giger heads a group working on development of ground receivers for satellite communications systems. His earlier work was in development of circuits for the TH microwave transmission system. Senior member, IEEE.

JOHN A. GITHENS, B.S.E.E., 1951, Drexel Institute of Technology; Bell Telephone Laboratories, 1951—. He has been engaged primarily in computer research, including design of solid-state circuits, computer systems, and logical design. He took part in the design and develop-

ment of Tradic and Leprechaun, early transistorized computers. He later supervised logical design of the data conversion unit used for antenna steering on Project Echo. On the Telstar project, he was responsible for the digital control portion of the antenna pointing system. Member IEEE, Eta Kappa Nu, Tau Beta Pi, and Phi Kappa Phi.

HERMANN K. GUMMEL, Dip. Phys., 1952, Philipps University (Germany); M.S., 1952, and Ph.D., 1957, Syracuse University; Bell Telephone Laboratories, 1956—. His work has been in research and development of semiconductor devices. Member, American Physical Society and Sigma Xi.

EDWIN G. HALLINE, B.S.E.E., 1953, Bucknell University; Bell Telephone Laboratories, 1953—. He has primarily been concerned with computer programming for military research and development projects, including work with the Leprechaun computer for TRADIC and work on Project Mercury. He supervised the computer programming group on the Telstar project and is presently working on the Apollo project for Bellcomm, Inc. Member, IEEE and Tau Beta Pi.

D. C. HANSON, B.S. in E.E., 1959, University of Wisconsin; M.S. in E.E., 1961, New York University; Bell Telephone Laboratories, 1959—. He has been engaged in military system analysis, transistor circuit design for a Vocoder, the design and analysis of varactor diode amplifiers for the Telstar ground station receiver, the TD-3 radio relay system, and a parametric amplifier operating at liquid helium temperature. Member, Pi Kappa Delta, Tau Beta Pi, Eta Kappa Nu, and IEEE.

EARL T. HARKLESS, M.S., 1949, Case Institute of Technology; Bell Telephone Laboratories, 1949—. He has been engaged in the development of transmission systems, including the TH and TJ microwave radio relay systems, and the L3 coaxial cable system. He has worked on the exploratory development of millimeter-wave networks. On Project Telstar, he contributed to the antenna system design. Member, IEEE, Sigma Xi, and Tau Beta Pi.

RICHARD W. HATCH, B.S. in E.E., 1952, Northeastern University; M.S., 1958, Stevens Institute of Technology; Bell Telephone Laboratories, 1952—. For several years he worked on design of FM terminals for the TH microwave system. In 1961–62 he supervised a group working on systems analysis for a satellite communications system. Presently he is

Head, Transmission Studies Department, concerned with studies of objectives and maintenance of facilities for long-distance telephone transmission. Member, IEEE, Eta Kappa Nu, and Tau Beta Pi.

PAUL T. HAURY, B.E., 1941, Vanderbilt University; Bell Telephone Laboratories, 1942—. His first assignment was with the trial installation group preparing models of radar test equipment. Later he designed airborne and portable radar equipment, and after the war turned to equipment engineering related to carrier telephone systems. He worked on submarine cable systems for military communications from 1951 to 1956, and in 1957 he became supervisor of a group engaged in design of TH microwave equipment. Since early 1961 he has supervised mechanical design and construction work on electronic assemblies for satellite repeaters.

GEORGE D. HELM, B.S.E.E., 1947, Rensselaer Polytechnic Institute; M.S., 1955, Northeastern University; Bell Telephone Laboratories, 1956—. He first worked on long-range search radar, automatic data processing, and missile integration in connection with the SAGE system. More recently, he has worked on high-power microwave amplifiers for Telstar and other projects. Member, IEEE and Sigma Xi.

EDWARD F. HIGGINS, JR., B.S.E.E., 1961, Newark College of Engineering; Bell Telephone Laboratories, 1953—. He was first engaged in test and evaluation of missile ground guidance equipment and later worked on the development and evaluation of guided-missile systems. On the Telstar project, he was involved with system performance of the precision tracker receiver. At present he is concerned with the development of radio guidance systems.

J. NED HINES, B.S.E.E., 1943, University of Connecticut; M.Sc., 1949, Ohio State University; Bell Telephone Laboratories, 1958—. His first assignment was work on the design, construction and testing of an electronically scanned array. On the Telstar project he worked on the autotrack system and on measurements of the horn-reflector antennas at Andover and Pleumeur-Bodou. He is presently concerned with the design of a low-noise antenna for satellite communications systems. Member, IEEE and Sigma Xi.

WILLIAM C. HITTINGER, B.S. in Metallurgical Engineering, 1944, Lehigh University; Western Electric Co., 1946–52; National Union

Radio Corp., 1952–54; Bell Telephone Laboratories, 1954—. While with the Western Electric Co., Mr. Hittinger was concerned with the specification, testing and application of electron tube and semiconductor materials. After two years as Production Manager with the National Union Radio Corp., he joined Bell Laboratories, where he was initially engaged in exploratory and final development of semiconductor devices. He was appointed Director of Development at the Allentown, Pa., Laboratory in 1960, and Executive Director, Semiconductor Device and Electron Tube Division in 1962. Member, IEEE, Amer. Inst. of Mining, Metallurgical and Petroleum Engineers, Omicron Delta Kappa.

DANIEL F. HOTH, B.S. in M.E., 1935, Stevens Institute of Technology; Bell Telephone Laboratories, 1936—. Mr. Hoth was first concerned with studies of local plant transmission; he later engaged in the study and planning of development projects for wire and radio systems, engineering of initial Distant Early Warning (DEW) Line installations, and long-range planning studies for transmission systems. As Director, Transmission Studies Center, his responsibilities include engineering studies of satellite communication systems. Senior member, IEEE; member, Sigma Phi Epsilon.

PETER HRYCAK, B.S., 1954, M.S., 1955, and Ph.D., 1960, University of Minnesota; Instructor, Mechanical Engineering Dept. of University of Minnesota, 1955–60; Bell Telephone Laboratories, 1960—. He has worked on low-temperature refrigeration problems, thermal design and thermal testing of the Telstar satellite. Member, American Institute of Aeronautics and Astronautics.

P. T. HUTCHISON, B.S., 1944, Mississippi State University; M.S., 1947, California Institute of Technology; Ph.D., 1960, Georgia Institute of Technology; Bell Telephone Laboratories, 1960—. Mr. Hutchison was first engaged in development work on microwave reflectometers used in TH radio test equipment. He has done development work on the microwave portion of the 4-gc ground receiver used in the Telstar experiment. Later he was responsible for electrical aspects of the microwave repeater in the Telstar satellite. Currently, he is responsible for development work on microwave antennas and microwave circuitry to be used in future communications satellites. Member, IEEE and Sigma Xi.

MORIMI IWAMA, B.S., 1954, M.S., 1955, and Ph.D., 1960, University

of California; Bell Telephone Laboratories, 1961—. He has been engaged in the design of automatic control systems for satellite communication systems and was responsible for the design of the antenna servo for the Telstar project. Member IEEE, Tau Beta Pi and Sigma Xi.

WILLIAM C. JAKES, JR., B.S. in E.E., 1944; M.S. in E.E., 1947; Ph.D., 1949, Northwestern University; Bell Telephone Laboratories, 1949—. Mr. Jakes has been engaged in research in microwave radio antennas and microwave propagation. He was project engineer in charge of the Bell Laboratories team participating in the Project Echo passive satellite communication tests. During the Telstar system tests he has been test conductor at the Holmdel, N.J., satellite communication station. He is presently head of the Mobile Radio Research Department. Member, Eta Kappa Nu, Pi Mu Epsilon, and Sigma Xi; Fellow, IEEE.

GENE C. JONASSON, B.S.E.E., 1961, University of Washington; Western Electric Co., 1961—. He has been engaged in the development of environmental test specifications and in the environmental testing and evaluation of the Telstar satellite. He has also analyzed data received from the Telstar satellite and evaluated its performance in space. Member, IEEE.

H. P. KELLY, B.S.E.E., 1937, M.S.E.E., 1938, Virginia Polytechnic Institute; Bell Telephone Laboratories, 1943—. Mr. Kelly was first engaged in the design and development of military radio equipment. Later he was responsible for the design of transmission test equipment for telephone carrier systems and the development of video and microwave radio systems. At present he is Head of the Ground Station Design Department, responsible for planning, design, and coordination of construction of the satellite ground station near Andover, Maine. Member, IEEE, Tau Beta Pi and Phi Kappa Phi.

W. J. KINDERMANN, A.B., 1933, Columbia College; B.S., 1934, and M.E., 1935, Columbia University School of Engineering; New York Telephone Co., 1935–1941; Bell Telephone Laboratories, 1941—. He was first responsible for the design and construction of precision potentiometers employed in analog computers for missile guidance systems and flight instrumentation equipment. He later supervised work on data take-off devices for the Command Guidance system and Project Echo antennas. On the Telstar project, he performed liaison work with contractors on horn-reflector antenna mechanical design and supervised

work on data take-off devices, drives and electromechanical equipment for both the Andover and Pleumeur-Bodou antennas.

JOHN P. KINZER, M.E., 1925, Stevens Institute of Technology; B.C.E., 1933, Polytechnic Institute of Brooklyn; Bell Telephone Laboratories, 1925—. Except for an initial two years spent on loudspeakers for the first sound movies, and the four war years on radar test sets, he has been concerned with long-haul transmission systems. His work has included the development of two-wire and four-wire voice and program repeaters and the negative-feedback repeater used in cable carrier systems. Following the war, he was engaged in systems studies, first on the L1 and L3 coaxial systems and, more recently, on the TH microwave radio relay system. Since early 1961, he has been participating in the planning and analysis of the communications tests for the Telstar system. Senior member, IEEE.

A. ROBERT KOLDING, B.S.E.E., 1941, Polytechnic Institute of Brooklyn; Bell Telephone Laboratories, 1930—. Mr. Kolding first worked on the exploratory development of cable transmission of television, which later evolved into television transmission over the L1 system. During World War II he worked on the development and field evaluation of airborne radar bombing systems. He returned to television systems after the war, taking part in the development of the L3 coaxial system, the A2A local television system, and terminals for the TH microwave system. He supervised a development group on the TASI system. At present, he is supervisor of the Telstar Launch Operations Group. Member, IEEE, Eta Kappa Nu.

RUDOLF KOMPFNER, Diplom. Ingenieur, Technische Hochschule, Vienna, 1933; Ph.D., Oxford, 1951; Bell Telephone Laboratories, 1951—. Dr. Kompfner invented the traveling-wave tube while at Birmingham University during World War II. At Bell Laboratories, he has specialized in microwave electronics, work which has more recently been enlarged to include research on quantum electronics and satellite communications. Director of Electronics Research, 1955; Director of Electronics and Radio Research, 1957; Associate Executive Director, Research, Communications Systems Research Division, 1962. Fellow I.R.E., 1950; Duddell Medal, Physical Society, 1955; A.I.E.E. David Sarnoff Award, 1960; Franklin Institute Stuart Ballentine medal, 1960.

D. E. KOONTZ, B.S. in Chemistry, 1945, Youngstown University;

M.S. in Chemistry, 1948, Ph.D. in Chemistry, 1951, University of Pittsburgh; Bell Telephone Laboratories, 1952—. Mr. Koontz was first engaged in studies of electron tube materials and processing. For the Telstar project, he was responsible for the selection and application of materials for the space vehicle and their evaluation in simulated space environments. He is presently Head of the Electron Device Technology Department, responsible for chemicals and materials associated with the development of electron devices. Member, American Chemical Society, Sigma Xi and Phi Lambda Upsilon; Chairman of Committee F1-X of the American Society for Testing Materials.

Ronald W. Kordos, B.E.E., 1957, University of Detroit; M.S.E.E., 1959, Northeastern University; Bell Telephone Laboratories, 1957—. He has engaged in the design of microwave ferrite devices, including field-displacement and resonance isolators for several microwave radio relay systems. At present he is working on circulator development for a military radar system. Member, IEEE, Tau Beta Pi, and Eta Kappa Nu.

Joseph P. Laico, M.E., 1933, Brooklyn Polytechnic Institute; Bell Telephone Laboratories, 1929—. He has been engaged in the mechanical design and development of electron tubes from early amplifiers through magnetrons, klystrons, and traveling-wave tubes used in radar, coaxial cable, radio relay, missile guidance, and the Telstar satellite. He is presently engaged in the design and development of high-power traveling-wave tubes for use in a radar system.

Tingye Li, B.Sc., 1953, University of Witwatersrand (South Africa); M.S., 1955, and Ph.D., 1958, Northwestern University: Bell Telephone Laboratories, 1957—. He has been engaged in studies of microwave antennas and microwave propagation. Recently he has been primarily concerned with work on optical masers. Member, IEEE, Eta Kappa Nu, and Sigma Xi.

Robert Lowell, B.S.E.E., 1948, New York University; M.S.E.E., 1951, University of Maryland; M.S. (Applied Math), 1959, Stevens Institute of Technology; Bell Telephone Laboratories, 1953—. Mr. Lowell was first engaged in military systems studies. At present, he supervises a group in the military antenna and microwave research department. Member, IEEE.

John C. Lozier, A.B., 1934, Columbia University; Bell Telephone

Laboratories, 1936—. He was first concerned with the theoretical aspects of toll transmission systems, feedback amplifiers and control systems. On the Telstar project he headed a group which designed and developed the control system for the antennas. He presently supervises research and exploratory development work on military guidance and control systems. Senior member, IEEE.

A. A. LUNDSTROM, B.S.E.E., 1928, Oregon State University; Pacific Telephone and Telegraph Co., 1928–29; Oregon State University faculty, 1929–30; Bell Telephone Laboratories, 1930—. He first engaged in research on telephone transmission and signaling systems, including the first nationwide dialing system. He has since done research and development on radar, computer, and control systems. On the Telstar project he headed a group responsible for research and development work on the antenna direction systems. He is presently Head, Digital Technique Research, and is concerned with guidance and control system analyses and cryogenic digital techniques. Member, IEEE, Eta Kappa Nu, Tau Beta Pi, and Phi Kappa Phi.

CHARLES MAGGS, B.S. in M.E., 1941, New York University; Bell Telephone Laboratories, 1928—. He has chiefly been engaged in the design of electron tubes, including early magnetrons and klystrons and the close-spaced triode. More recently he has worked on magnetrons and supervised a group working on beam-deflection tubes. He headed a group which worked on the frame and solar power plant for the Telstar satellite and presently supervises a mechanical engineering group developing millimeter-wave power amplifiers and microwave printed circuits.

HENRY MANN, B.A., 1950, Brooklyn College; M.S. in E.E., 1955, Columbia University; Bell Telephone Laboratories, 1954—. His work has included the design of the synchronizing circuits, the demultiplex gate, and portions of the encoder for the experimental pulse code modulation system. He also engaged in the development of a system for the transmission of two PCM groups over short-haul microwave carrier circuits. He was responsible for the design and production of a command decoder for an experimental active satellite communications system. At the present time he supervises a group responsible for the design of an improved single-frequency signaling unit. Member, IEEE and Pi Mu Epsilon.

H. I. MAUNSELL, B.S., 1950, University of the Witwatersrand; Bell

Telephone Laboratories, 1957—. For several years he worked on the terminal equipment, test sets and protection switching circuits for the TH microwave radio relay system. In late 1960, he became concerned with communication circuits for the Telstar satellite, and he is presently responsible for transmitter design for the satellite system ground station. Member, IEEE.

JOHN S. MAYO, B.S. in E.E., 1952, M.S. in E.E., 1953, Ph.D. in E.E., 1955, North Carolina State College; Bell Telephone Laboratories, 1955—. He was first engaged in computer research, including studies relating to the use of digital computers for measurement and automatic tracking of pulsed radar range information, and in military weapons control systems. His recent work has involved the development of line repeaters for an exchange carrier PCM system, and high-speed PCM terminals for an experimental transmission system. He has been in charge of the PCM terminal department since December, 1960. Member, IEEE and Sigma XI.

ROBERT J. MCCUNE, B.S.E., 1948, U.S. Coast Guard Academy; Bell Telephone Laboratories, 1954—. He was first engaged in military systems engineering, concerned with operational studies and planning for SAGE and related air defense systems. In 1961–62 he worked on operational planning for the acquisition, tracking, and command complex of the Telstar ground station, and supervised a group responsible for design and operation of the control console, including provision of operations procedures and training of the operations team. He has since been engaged in special operations studies for Bellcomm, Inc., of communication and tracking system requirements for the Apollo project. Member, IEEE.

B. A. MCLEOD, B.S.E.E., 1954, Northeastern University; Bell Telephone Laboratories, 1954—. He first worked on the development of transmission systems, including test set development for the TH microwave radio relay system. He engaged in early studies for the TASI system and worked on TASI development until 1961, when he became associated with the launch operations group for the Telstar project. Member Tau Beta Pi, Eta Kappa Nu.

L. V. MEDFORD, Bell Telephone Laboratories, 1955—. At Bell Laboratories Mr. Medford has participated in the study of adsorption of gases on metal and semiconductor surfaces by use of the photoelectric effect.

Early in 1961 he began development of space radiation instrumentation for the Telstar project, followed by a similar and concurrent undertaking for the NASA Project Relay. Later he participated in the development of radiation instrumentation for the Explorer XV satellite and was active in the launch operations for Project Relay. At present, Mr. Medford is studying development problems related to future space radiation experiments.

G. L. MILLER, B.Sc. (Physics), 1949, M.Sc. (Mathematics) 1952 and Ph.D. (Physics), 1957, University of London; Brookhaven National Laboratories, 1957—. Since his association with Brookhaven Laboratories, he has been engaged in the study and development of nuclear instrumentation.

LOUIS F. MOOSE, B.S.E.E., 1940, University of California; Bell Telephone Laboratories, 1945—. After graduate study at the University of California and Massachusetts Institute of Technology, Mr. Moose joined the Laboratories and worked on microwave tubes for radio relay and radar applications, and semiconductor diodes for microwave usages. Currently, he is engaged in the final design of alloy transistors and applied mechanics at the Allentown Laboratory. Member, IEEE, Tau Beta Pi, Sigma Xi and Eta Kappa Nu.

J. L. MURRAY, B.E.E., 1955, Rensselaer Polytechnic Institute; Bell Telephone Laboratories, 1955—. He has specialized in missile electronics, including design of pulse logic circuitry, and has designed experiments to characterize the system aspects of several radars for a guided missile system. On the Telstar project, he supervised a group responsible for electronic design of the precision tracker. Since then, he has supervised a group responsible for the electronic design of a solid-state missile guidance radar transmitter and receiver. He presently supervises a group responsible for electronic design of the Nike Sprint missile-borne guidance transmitter and receiver. Member, IEEE.

R. J. NIELSEN, Bell Telephone Laboratories, 1941—. At Bell Telephone Laboratories, he was first engaged in design drafting of automatic central office equipment. He has also been concerned with the study of metal-ceramic sealing and other special problems in connection with the mechanical design of electron tubes. During this time he also studied at the University of Idaho and Fairleigh-Dickinson University. From 1960 to the present, Mr. Nielsen has worked on the Telstar project and

is now engaged in the mechanical design of special microwave oscillator tubes.

J. A. NORTON, B.A.Sc., 1957, University of Toronto; A.M., 1959, Princeton University; Bell Telephone Laboratories, 1960—. He has been engaged in the design of antenna control systems on the Echo and Telstar projects. He is also engaged in research in the stochastic aspects of nonlinear computer-controlled systems. Member, IEEE and Sigma Xi.

EDWARD G. OLSEN, Bell Telephone Laboratories, 1927—. He has specialized in the mechanical design and development of electron devices, including devices used in early radio transmission, special research structures, and traveling-wave tube amplifiers for microwave radio relay and guided-missile systems. On the Telstar project he was concerned with the mechanical design and development of the traveling-wave tube amplifier for the spacecraft repeater.

E. F. O'NEILL, B.S. and M.S. in Electrical Engineering, 1940 and 1941, Columbia University; Bell Telephone Laboratories, 1941—. Mr. O'Neill's early work was in the development of radar transmitters and of amplifiers and regulators for cable and radio-relay systems. Beginning in 1956 he headed a group responsible for the development of the Time Assignment Speech Interpolation (TASI) system terminals. Mr. O'Neill is Director, Satellite Communications Laboratory at Bell Laboratories, and is Project Manager for the Telstar experimental system. Member, Tau Beta Pi and Sigma Xi.

S. PARDEE, JR., A.B., 1939, Harvard University; M.S. in E.E., 1960, Stevens Institute of Technology; Bell Telephone Laboratories, 1946—. He has been engaged in the design and development of military electronic equipment, fire control radar, and missile guidance systems. At present, he is working on a military communications system. Member, IEEE.

D. STEWART PECK, M.S. in E.E., 1940, University of Michigan; Bell Telephone Laboratories 1947—. Mr. Peck has been concerned in the design for production of gas-filled electron tubes such as rectifiers, thyratrons and cold-cathode tubes. More recently, he has been in charge of work on reliability studies, applications engineering, and specifications for electron devices. On the Telstar project Mr. Peck's department has been generally responsible for the specification, aging and selection

programs for semiconductor components used in the satellite. Member, IEEE, American Standards Association, Tau Beta Pi, Eta Kappa Nu, Sigma Xi and Phi Kappa Phi.

T. R. PETERS, B.S.E.E., 1955, Virginia Military Institute; Bell Telephone Laboratories, 1955—. He has participated in the systems and logic design of a military special-purpose digital computer, studies of logic connectives for integrated circuits, and cryogenic logic studies. On the Telstar project he was involved in the system and logic design for the antenna pointing system and later was concerned with development, installation and maintenance of the digital equipment at Andover, Maine. He is currently working on studies for a military digital computer.

E. JARED REID, B.S., 1956, Trinity College; B.S.E.E., 1957, Rensselaer Polytechnic Institute; M.E.E., 1959, New York University; Bell Telephone Laboratories, 1957—. He was first engaged in development work on the TASI system, and took part in final field tests of TASI installations in the U.S. and overseas. He subsequently worked on the development of the Telstar satellite electronics system.

WILLIAM C. RIDGWAY, III, B.S.E., 1957, Princeton University; M.E.E., 1959, New York University; Ph.D., 1962, Stanford University; Bell Telephone Laboratories, 1957—. He has worked chiefly in the field of data processing, first for the Nike Zeus anti-missile system and more recently for the Telstar project. Member, A.C.M., IEEE, Phi Beta Kappa, Sigma Xi.

W. ROSENZWEIG, B.S., 1950, Rutgers University; M.S., 1952, University of Rochester; Ph.D., 1960, Columbia University. Brookhaven National Laboratory, 1951–1953; Radiological Research Laboratory, Columbia University, 1953–1960; Bell Telephone Laboratories, 1960—. At Bell Laboratories, Mr. Rosenzweig has been mainly engaged in studies of radiation damage to semiconductors. Member, American Physical Society, Radiation Research Society, Sigma Xi and Phi Beta Kappa.

A. THOMAS ROSS, B.S.E.E., 1939, Lafayette College; Bell Telephone Laboratories, 1946—. Mr. Ross was first engaged in the field of high-altitude bombing systems. Subsequently he worked on the development and testing of a high-powered, tunable magnetron. Prior to his work on

the Telstar project, he was concerned with the development of tubes for broadband submarine telephone cable systems. He is currently engaged in the development of parametric amplifiers. Senior member, IEEE.

R. E. SAGEMAN, B.E.E., 1944, and M.E.E., 1948, Renssalaer Polytechnic Institute; Long Lines Department of the American Telephone and Telegraph Co., 1948—. He has engaged in plant engineering for the overseas radiotelephone division and statistical analyses for the accounting and traffic operations departments. He has been Director of Electronic Data Processing Activities for the Long Lines Department and Satellite Projects Engineer, responsible for coordinating the activities of the Long Lines Department in the Telstar and Relay projects. He is presently Service Engineer, Southeastern Area, Long Lines. Member, Eta Kappa Nu, Tau Beta Pi, and Sigma Xi.

FRED J. SCHAEFER, B.E.E., 1950, Syracuse University; Bell Telephone Laboratories, 1951—. His early assignments included circuit design and field evaluation of a target designation system; operations and system planning for the DEW Line project, including evaluation of the VHF scatter system. He later supervised groups working on circuit design and performance analysis of missile systems, and is presently supervisor of a group developing missile guidance radar. He supervised a group responsible for the design of the Telstar precision tracker. Member, IEEE, Tau Beta Pi, and Eta Kappa Nu.

R. H. SHENNUM, B.S. in E.E., 1944, and M.S. in E.E., 1948, Montana State College; Ph.D., 1954, California Institute of Technology; Bell Telephone Laboratories, 1954—. He first worked on the design of microwave parts for the TJ microwave system. Later, he was responsible for companding, signaling, and voice-frequency development and field experiments for the T1 carrier system (PCM). As Head, Satellite Design Department, he was responsible for the development of the electronic circuits for the Telstar satellite. Mr. Shennum was also responsible for the assembly of the spacecraft and final testing at the Hillside, N. J., laboratory. Member, IEEE, Sigma Xi, Tau Beta Pi, and Phi Kappa Phi.

JOHN T. SIBILIA, B.S. in Physics, 1955, Rutgers University; M.A., 1957, and Ph.D., 1962, Princeton University; Bell Telephone Laboratories, 1960—. He has been engaged in maser development, including studies of the use of rutile for a 10-kmc maser. He presently supervises

a group responsible for the development of masers for the Telstar project and military projects.

D. H. SMITH, B.S.E.E., 1944, University of Minnesota; M.S. in Industrial Management, 1961, Stevens Institute of Technology; Bell Telephone Laboratories, 1947—. He has been engaged in development work on voltage regulating apparatus, including rectifiers and regulated exciters, and advance engineering and development of power systems, including long-range planning. From 1952 to 1961 he supervised a group concerned with power systems engineering. In 1961, as Head, Reserve Power Systems Department, he became responsible for development work on power systems, which included the power generating and reserve power systems at the Andover earth station, and for development of the timing mechanism to shut off the beacon transmitter in the Telstar satellite. Member, IEEE and its Subcommittee on Definitions, Magnetic Amplifier Committee; Chairman of American Standards Association Sectional Committee C85 on terminology for automatic control.

KENNETH D. SMITH, M.A. in Physics, 1930, Dartmouth College; Bell Telephone Laboratories, 1930—. He has worked on high-frequency test equipment, coaxial cable system development, proximity fuses, radar bombing equipment, and microwave radio relay systems. Since 1951, he has been engaged in semiconductor device development, including high-frequency transistors, power rectifiers, voltage limiters, and the Bell Solar Battery. He currently supervises a group concerned with high-frequency transistor development. Senior member, IEEE.

FRIEDOLF M. SMITS, Dipl. Phys., 1950, Dr. rer. nat., 1950, University of Freiburg, Germany; research associate, Physikalisches Institut, University of Freiburg, 1950–54; Bell Telephone Laboratories, 1954–62. Mr. Smits went to the Sandia Corporation in May 1962. His work at Bell Telephone Laboratories included studies of solid-state diffusion in germanium and silicon, device feasibility, and process studies, as well as the development of UHF semiconductor devices. He supervised a group that conducted radiation damage studies on components, particularly solar cells, used in the Telstar satellite. Member of the American Physical Society and the German Physical Society.

R. V. SPERRY, B.S.E.E., 1949, M.S.E.E., 1951, West Virginia University; Bell Telephone Laboratories, 1952—. Mr. Sperry was first engaged in the development of transmission networks for coaxial, radio

and military systems. He has worked on repeater development for an exploratory waveguide transmission system and on the antennas and several circuits used on the Telstar satellite. At present, Mr. Sperry supervises a group working on the development of repeaters for a high-speed PCM coaxial cable system. Member, Eta Kappa Nu, Pi Tau Sigma, and Tau Beta Pi.

JOHN W. STAFFORD, B.S.A.E., 1954, Massachusetts Institute of Technology; M.S.A.M.; 1959, Brooklyn Polytechnic Institute; Bell Telephone Laboratories, 1961—. Mr. Stafford participated in the mechanical design and testing of the Telstar satellite. He is now engaged in development studies of an orientation system for communications satellites. Member of American Institute of Aeronautics and Astronautics.

ALBERT L. STILLWELL, B.A., 1925, M.A., 1928, Gonville and Caius College, Cambridge, England; Bell Telephone Laboratories, 1927—. His early assignments included the design of filters, special networks, and the first three-stage cathode feedback amplifier for coaxial transmission. After wartime activity in the development of proximity fuses and radar, he worked on television transmission apparatus. Later he developed special circuits for the research department and is presently in a group concerned with the design of solid-state microwave circuits. Senior member, IEEE.

KURT M. STRINY, B.S.M.E., 1953, and M.S., 1961, Newark College of Engineering; Bell Telephone Laboratories, 1956—. He has been engaged in the mechanical design and development of electron tubes such as the coaxial magnetron and low-noise traveling-wave tubes. He is currently working on high-power traveling-wave tubes used for the Telstar ground transmitter and other applications. Member A.S.M.E.

R. A. SWIFT, B.S. in E.E., 1943, Union College; Bell Telephone Laboratories, 1946—. He has been engaged in mechanical and equipment design aspects of system design, and was responsible for mechanical design and evaluation of missile-borne guidance equipment for the Titan and Thor-Delta Missiles. On the Telstar project he was responsible for the formation and conduct of the design, qualification, and acceptance test program for the satellite. Member, IEEE.

WILLIAM J. TABOR, B.S. in Chemistry, 1953, Renssalaer Polytechnic Institute; A.M. (Physics) and Ph.D. (Chemical Physics), 1954 and 1957, Harvard University; Bell Telephone Laboratories, 1959—. Since

coming to the Laboratories, he has engaged in research and development work on microwave masers, including the maser for the Telstar ground station receiver.

E. W. THOMAS, Bell Telephone Laboratories, 1961—. He has contributed to the design and development of radiation experiments for the Telstar experimental communications satellite and other satellite programs. Following the Telstar satellite launch, he assisted in interpretation of the radiation data. He is currently conducting experiments to aid in more precise understanding of the Telstar results as well as results of other satellite radiation experiments.

LEROY C. TILLOTSON, B.S.E.E., 1938, University of Idaho; M.S.E.E., 1940, University of Missouri; Bell Telephone Laboratories, 1941—. Mr. Tillotson's early work included design of filters and networks; he has since been concerned with microwave radio relay systems. From June, 1958, to July, 1959, he served as a member of technical staff of the Advanced Research Projects Agency division of the Institute for Defense Analyses. As Assistant Director, Radio and Electronics Research, and Head, Radio Systems Research Department, he has been active in planning the communications aspects of Project Telstar. Senior member, IEEE; member, Sigma Xi.

DAVID E. TRUCKSESS, B.S.E.E., 1926, Pennsylvania State University; Bell Telephone Laboratories, 1926—. He has worked in the field of regulation for motor generators and rectifiers. During World War II, he supervised a group which designed power supplies for military systems. He is presently Head, Power Conversion Department, and is concerned with the development of power facilities for submarine cable systems, microwave communications systems, PBX equipment, and military sonar systems. Fellow and Deputy Director of Technical Operations, IEEE; member, N.S.P.E.

RICHARD H. TURRIN, B.S.E.E., 1956, Newark College of Engineering; M.S.E.E., 1960, New York University; Bell Telephone Laboratories, 1956—. He has been chiefly concerned with propagation and antenna work at micro and millimeter wavelengths. He participated in the design of the Telstar ground-station antennas. Member, IEEE, Eta Kappa Nu and Tau Beta Pi.

MICHIYUKI UENOHARA, B.E., 1949, Nihon University (Japan); M.S., 1953, and Ph.D., 1956, Ohio State University; D.E., Tohoku University

(Japan), 1958; Bell Telephone Laboratories, 1957—. He has been engaged in exploratory studies of microwave variable reactance amplifiers, Esaki diode amplifiers, and related devices. He was also engaged in microwave tube research at Nihon University from 1949 to 1952, and taught there in 1957. Member, American Physical Society, IEEE, Institute of Electrical Communication Engineers (Japan), Eta Kappa Nu, Pi Mu Epsilon, Sigma Xi, and R.E.S.A.

BURTON A. UNGER, B.S.M.E., 1954, Purdue University; M.S.M.E., 1960, Newark College of Engineering; Bell Telephone Laboratories, 1960—. Mr. Unger participated in the thermal test program of the Telstar satellite. He is now engaged in development studies of orientation systems for communication satellites.

H. NELSON UPTHEGROVE, B.S., 1945, U.S. Naval Academy; S.B., 1948, Massachusetts Institute of Technology; Ph.D., 1954, California Institute of Technology; Bell Telephone Laboratories, 1953—. Mr. Upthegrove served in the U.S. Navy, 1945–49, and was a Teaching Fellow in engineering at Cal. Tech., 1949–53. At the Laboratories, he was first engaged in submarine cable development and later in the planning and acquisition of new cable ships and equipment. On the Telstar project, he was Head of the Satellite Launch Operations Department, responsible for integration of the satellite and the Delta launch vehicle. He is presently Head of the Missile and Tracking Department. Member, IEEE, Sigma Xi, and Tau Beta Pi.

PAUL W. USSERY, B.S. in Physics, 1951, Upsala College; M.S.E.E., 1956, Newark College of Engineering; Bell Telephone Laboratories, 1957—. He has engaged in the development of regulated power supplies for an experimental electronic switching system, solid-state inverters and regulators, microwave radio relay systems and missile guidance equipment. He worked on the design of the Telstar spacecraft power supply system and is presently engaged in development work on thermoelectric regulators and power supplies for radio relay systems. Member, IEEE and Sigma Pi Sigma.

L. J. VARNERIN, S.B., 1947, Ph.D., 1949, Massachusetts Institute of Technology; Bell Telephone Laboratories, 1957—. He has been engaged in the development of components and solid-state devices, and was first concerned with the development of very high frequency germanium transistors, field-effect devices, thin film components and circuits. He is

presently Head, Solid-State Microwave Device Department, concerned with the development of microwave ferrite, magnetoelastic and optical devices. Fellow, American Physical Society; senior member, IEEE.

EDWARD J. WALSH, Bell Telephone Laboratories, 1928—. He has chiefly been engaged in the mechanical design of electron tube structures and enclosures, including the design during World War II of proximity fuse tubes and the thermally tuned klystron, and later of the frame-grid tube used in microwave radio relay systems. More recently he has supervised a group responsible for mechanical design of electron tubes for a submarine cable system; he is presently in charge of a group working on structures for the gaseous optical maser, photomultipliers, and other electron devices.

IRWIN WELBER, B.S.E.E., 1948, Union College; M.E.E., 1950, Rensselaer Polytechnic Institute; Bell Telephone Laboratories, 1950—. Mr. Welber has worked on the design and analysis of long-haul microwave radio relay circuits and the Time Assignment Speech Interpolation (TASI) switching system. As Head, Ground Station Design Department, he has been responsible for over-all systems analysis, ground communications equipment and technical planning with foreign participants for the Telstar project. Member, IEEE, and Sigma Xi.

PAUL R. WICKLIFFE, JR., B.S.E.E., 1949, Purdue University; S.M., 1951, Massachusetts Institute of Technology; Bell Telephone Laboratories, 1951—. He was first concerned with development of antennas and traveling-wave tube amplifiers for the TH microwave system. He later worked on a narrow-band radio system for order wire and alarms. In 1961 he became supervisor of a group engaged in the design of the ground transmitter for the Telstar project. Member, IEEE, Eta Kappa Nu, and Tau Beta Pi.

FRANCIS J. WITT, B.S.E.E., 1953, M.S.E.E., 1955, Johns Hopkins University; Bell Telephone Laboratories, 1954–55, 1957—. At Bell Laboratories, he has engaged in active and sampled-data network exploratory research and in solid-state circuit development for short-haul carrier systems. Later he was in charge of a group responsible for the development of some of the solid-state circuits in the Telstar experimental communications satellite. At present he is concerned with the development of digital processing circuitry for a high-speed PCM transmission system. Member, IEEE, Tau Beta Pi and Sigma Xi.

ALBERT M. WITTENBERG, B.S. in Physics, 1949, Union College; Ph.D., 1955, Johns Hopkins University; Bell Telephone Laboratories, 1955—. His early work at the Laboratories concerned the development of gas tube devices for switching applications. He later engaged in studies on photoconductive and electroluminescent materials. At present he is involved in developing techniques for space simulations, and is also concerned with the effects of space environment on the thermal and mechanical properties of satellites and satellite materials. Member, American Physical Society, Sigma Xi and Institute of Environmental Sciences.

K. B. WOODARD, B.S. in M.E., 1943, Georgia Institute of Technology; Bell Telephone Laboratories, 1946—. He has been engaged in the mechanical design and testing of components and structures for guided missile systems, including the antennas for the Nike Zeus system. For the Telstar project, he was responsible for mechanical design of the precision tracker antenna and the large air-supported structures and slip rings for the horn-reflector antenna. Member, A.S.M.E., Pi Tau Sigma, and American Rocket Society.

M. C. WOOLEY, B.S. in E.E., 1929, Ohio Northern University; Bell Telephone Laboratories, 1929—. He has been engaged in the design and development of inductors and capacitors, including capacitors for the Havana-Key West submarine cable. He has worked on fundamental development of capacitor materials and processes and presently supervises a group responsible for development capacitors and resistors for ultra-high reliability applications such as the Telstar experiment. Member, Nu Theta Kappa.